Vol. 69, No. 1 / 2023

e: ISSN 2068 – 2239
p: ISSN 2068 – 4215

INMATEH – AGRICULTURAL ENGINEERING

JANUARY - APRIL

No liability is assumed by the editorial staff for the content of scientific papers and opinions published in this volume. They represent the author's point of view

Managing Editorial Board - INMA Bucharest

Editor in Chief

Lucian-Ionel CIOCA, Professor, PhD.Eng., "Lucian Blaga" University of Sibiu

Executive Editor
Lucreţia POPA
PhD.Eng, SR I

Assistant Editor
Nicolae-Valentin VLADUŢ
PhD.Eng, SR I
Mihai-Gabriel MATACHE
PhD.Eng, SR I

Logistic support, database
Virgil MURARU
PhD.Eng, SR I

Scientific Secretary
Cârdei Petre, math.

Official translator
RADU Daniela-Cristina, English

Editorial Board

- *QUENDLER Elisabeth – Austria, Vienna, Univ. of Natural Resources & Applied Life Sciences;*
- *Ir. HUYGHEBAERT Bruno – Belgia, Walloon Agricultural Research Center CRA-W;*
- *Van IMPE F.M. Jan – Belgia, KU Leuven University*
- *FABBRO Dal Inacio Maria - Brazil, Campinas State University;*
- *ATANASOV Atanas – Bulgaria, "Angel Kanchev" University of Rousse*
- *MOLINOS-SENANTE María – Chile, Pontificia Universidad Católica - Vicedecana, Escuela de Ingeniería UC*
- *BILANDZIJA Nikola – Croatia, Zagreb University, Faculty of Agriculture;*
- *KOSUTIC Silvio – Croatia, Zagreb University, Faculty of Agriculture;*
- *KOVACEV Igor - Croatia, Zagreb University, Faculty of Agriculture;*
- *GONZÁLEZ Omar – Republic of Cuba, Central University "Marta Abreu" de las Villas;*
- *KATHIJOTES Nicholas – Cyprus, University of Nicosia;*
- *HERAK David - Czech Republic, Czech University of Agriculture Prague;*
- *BORCHARD Nils – Finland, Natural Resources Institute Finland (Luke);*
- *SAUER Johannes – Germany, Technical University Munich;*
- *FENYVESI László – Hungary, Hungarian Institute of Agricultural Engineering Godolo;*
- *PEEYUSH Soni - India, Indian Institute of Technology, Kharagpur;*
- *MOHAMMADREZA Alizadeh – Iran, Department of Agricultural Engineering, Rice Research Institute of Iran (RRII);*
- *De WRACHIEN Daniele - Italy, State University of Milan;*
- *BIOCCA Marcello - Italy, Agricultural Research Council, Agricultural Engineering Research Unit;*
- *COLANTONI Andrea – Italy, University Viterbo;*
- *SARAUSSKIS Egidijus – Lithuania, Vytautas Magnus University, Faculty of Agricultural Engineering;*
- *KRIAUCIUNIENE Zita - Lithuania, Vytautas Magnus University;*
- *DUKE Mike – New Zealand, University of Waikato, Faculty of Science and Engineering;*
- *EWEMOJE Temitayo Abayomy – Nigeria, University of Ibadan, Faculty of Technology, Department of Agricultural and Environmental Engineering;*
- *SKIERUCHA Wojciech – Poland, Institute of Agro-physics Polish Academy of Sciences, Lublin;*
- *EKIELSKI Adam - Poland, Warsaw University of Life Sciences;*
- *KOT Sebastian - Poland, Czestochowa University of Technology*
- *SAVIN Lazar– Serbia, University of Novi Sad, Faculty of Agriculture, Department of Agricultural Engineering;*
- *SIMIKIC Mirko– Serbia, University of Novi Sad, Faculty of Agriculture, Department of Agricultural Engineering;*
- *MARTINOV Milan - Serbia, Faculty of Agriculture, Department of Agricultural Engineering,*
- *TURAN Jan – Slovakia, Technical University Kosice, Dept Elect & Multimedia Commun, Kosice;*
- *MADYIRA M. Daniel - South Africa, University of Johannesburg, Mechanical Engineering Science Department*
- *COZ FERNANDEZ Alberto – Spain, University of Cantabria, School of Nautical Studies, Department of Chemistry and Process & Resource Engineering;*
- *ERTEKIN Can - Turkey, Akdeniz University Antalia;*
- *KABAŞ Önder –Turkey, Antalia, Agricultural Scientific Research Institute of Batı Akdeniz;*
- *SELVİ Kemal Çağatay - Turkey, Samsun, University of Ondokuz Mayıs, Faculty of Agriculture, Department of Machines for Agriculture;*
- *ÖTLEŞ Semih - Turkey, Ege University, Engineering Faculty, Food Engineering Department;*
- *MARUSCHAK Pavlo - Ukraine, Ternopil Ivan Pul'uj National Technical University, Department of Technical Mechanics and Agricultural Engineering;*
- *BULGAKOV Volodymyr – Ukraine, National University of Life and Environmental Sciences of Ukraine;*
- *PARASCHIV Gigel - Romania, Politehnica University of Bucharest;*
- *VOICU Gheorghe - Romania, Politehnica University of Bucharest;*
- *BIRIŞ Sorin - Romania, Politehnica University of Bucharest;*
- *MAICAN Edmond - Romania, Politehnica University of Bucharest;*
- *FILIP Nicolae - Romania, Technical University Cluj Napoca;*
- *COZAR Onuc-Romania, „Babes-Bolyai" University of Cluj-Napoca Romania, Faculty of Physics;*
- *VLASE Sorin - Romania, "Transilvania" University of Braşov;*
- *ŢENU Ioan - Romania, USAMV Iaşi;*
- *HERIŞANU Nicolae - Romania, Politehnica University of Timisoara;*
- *MARSAVINA Liviu - Romania, Politehnica University of Timisoara*
- *MARINCA Vasile - Romania, Politehnica University of Timisoara*
- *GERGEN Iosif - Romania, USAMVB Timişoara;*
- *BORDEAN Despina-Maria - Romania, USAMVB Timişoara;*
- *BUNGESCU Sorin - Romania, USAMVB Timişoara;*
- *VOICEA Iulian - Romania, INMA Bucharest*
- *DEAK Gyorgy - Romania, INCDPM;*
- *BELC Nastasia - Romania, IBA Bucharest;*
- *BUŢU Alina - Romania, INCDSB Bucharest;*
- *PAUN Mihaela - Romania, National Institute of Research and Development for Biological Sciences, INCDSB*

INMATEH - Agricultural Engineering **journal is indexed in the next international databases:**
ELSEVIER /SciVerse SCOPUS, CLARIVATE - WEB of SCIENCE- Emerging Sources Citation Index (ESCI), ULRICHS Web: Global Serials Directory, CABI, SCIPIO, Index COPERNICUS International, EBSCO Publishing, Elektronische Zeitschriftenbibliothek

INMATEH - Agricultural Engineering
vol. 69, no.1 / 2023
e-ISSN: 2068 – 2239; p: ISSN: 2068 – 4215

https://inmateh.eu/ *E-mail: inmatehjournal@gmail.com*

Edited by: INMA Bucharest
Copyright: INMA Bucharest / Romania
National Institute for Research-Development of Machines and Installations
Designed for Agriculture and Food Industry - INMA Bucharest
6, Ion Ionescu de la Brad Bvd., sector 1, Bucharest, ROMANIA

CONTENT

		Page(s)
1.	**REASEARCH ON PEAR INFLORESCENCE RECOGNITION BASED ON FUSION ATTENTION MECHANISM WITH YOLOV5 / *基于融合注意力机制的 YOLOv5 算法对梨花序的识别研究*** **Ye XIA [1, 2], Xiaohui LEI [*2], Andreas HERBST [3], Xiaolan LYU [*2]** [1] School of Agricultural Engineering, Jiangsu University, Zhenjiang/China; [2] Institute of Agricultural Facilities and Equipment, Jiangsu Academy of Agricultural Sciences / Key Laboratory of Modern Horticultural Equipment, Ministry of Agriculture and Rural Affairs, Nanjing/China; [3] Institute for Chemical Application Technology of JKI, Braunschweig Messeweg/Germany	11
2.	**RESEARCH ON OPTIMAL CONTROL ALGORITHM FOR POWER CHARACTERISTICS SEGMENTATION OF FORAGE HARVESTER / *饲草收获机动力特性分割优化控制算法研究*** **Zheng WANG [1,2], Qingfu GONG [1], Fade LI [1], Ang GAO [1], Longlong REN [1], Yuepeng SONG [1,2,*]** [1] Shandong Agricultural University, College of Mechanical and Electrical Engineering/ China; [2] Shandong Provincial Engineering Laboratory of Agricultural Equipment Intelligence/ China	21
3.	**APPLICATION OF INDUSTRIAL ROBOT AND MACHINE VISION IN INTELLIGENT CALDRON FEEDING PROCESS OF CHINESE BAIJIU / *工业机器人和机器视觉在中国白酒智能上甑工艺中的应用*** **ZhongLing XIA[1,2], WeiHan CHEN[1], Hang ZHAO[3], WeiDong SONG[*4], Ling YANG[1], MingJin YANG[*1]** [1]Southwest University, College of Engineering and Technology, Chongqing, China [2]Chongqing Yottametre Industry Automation Co., Ltd., Chongqing, China [3]Southwest University, College of Artificial Intelligence, Chongqing, China [4]Ministry of Agriculture and Rural Affairs, Nanjing Institute of Agricultural Mechanization, Nanjing, China	35
4.	**APPLICATION OF HYDROPONIC TECHNOLOGY TO THE YIELD AND QUALITY OF PURWOCENG "VIAGRA FROM ASIA" / *APLIKASI TEKNOLOGI HIDROPONIK PADA YIELD DAN KUALITAS PURWOCENG "VIAGRA DARI ASIA"*** **Eni SUMARNI[1]; Irmanida BATUBARA[2,3*]; Herry SUHARDIYANTO[4]; Slamet WIDODO[4]; Mohamad SOLAHUDIN[4]; Eti ROHAYATI[2,3]; Folkes LAUMAL[5]** [1] Department of Agricultural Technology. Faculty of Agriculture. General Sudirman University / Indonesia; [2] Department of Chemistry. Faculty of Mathematics and Natural Sciences, IPB University. Indonesia; [3] Tropical Biopharmaca Research Center, IPB University, Indonesia; [4] Department of Mechanical Engineering and Biosystems. IPB University / Indonesia; [5] Department of Mechanical and Biosystems Engineering. IPB University / Indonesia	46
5.	**DESIGN AND EXPERIMENTAL STUDY OF A VEHICLE-MOUNTED FERTILIZING AND SPRAYING MACHINE / *车载式施肥喷药机的设计与试验研究*** **Yujiang GOU, Huibo HE*, Huaying LI*, Daming WANG, Mian ZHANG** College of Engineering and Technology, Southwest University, Chongqing / P.R. China	55
6.	**RESEARCH ON PREDICTION OF SOIL ORGANIC MATTER CONTENT BASED ON HYPERSPECTRAL IMAGING / *土壤有机质含量的高光谱成像预测研究*** **Guoliang WANG[1,2]; Huiling DU[3]; Wenjun WANG[1]; Jiangui ZHAO[1]; Hong LI[2]; Erhu GUO[2]; Zhiwei LI[*1]** [1]College of Engineering, Shanxi Agriculture University, Taigu / China [2]Millet Research Institute, Shanxi Agricultural University, Changzhi / China [3]Department of Basic Education, Shanxi Agricultural University, Taigu / China	65
7.	**RESEARCH ON COMB BRUSH HARVESTER AND DAMAGE MECHANISM TO MATERIAL. A REVIEW / *梳刷式收获装置的研究现状及对物料的损伤机理综述*** **Junming HOU, Zhaotan REN, Liang ZHANG, Qijie SUN, Wei WANG** Shenyang Agricultural University, College of Engineering / China	74
8.	**ANOMALY DETECTION FOR HERD PIGS BASED ON YOLOX / *基于 YOLOX 的群养猪只异常检测*** **LI Yanwen[1], LI Juxia[*1], Liu Zhenyu[2], Bi Zhifang[3], Zhang Hui[1], Duan Lei[1]** [1] College of Information Science and Engineering, Shanxi Agricultural University, Taigu/China [2] Graduate School of Shanxi Agricultural University, Shanxi / China 3) Basic Department, Shanxi Agricultural University, Shanxi / China	88
9.	**STUDY ON THE INFLUENCE OF PCA PRE-TREATMENT ON PIG FACE IDENTIFICATION WITH SVM / *PCA 前处理对 SVM 识别猪脸的影响研究*** **Hongwen YAN*, Zhiwei HU, Qingliang CUI** College of Information Science and Engineering, Shanxi Agricultural University, Taigu / China	99
10.	**OPTIMAL DESIGN OF EJECTOR BELT SEEDLING COLLECTING MECHANISM BASED ON EDEM / *基于 EDEM 的顶杆输送带式取苗机构优化设计*** **Jin CHEN[1,2], Hua ZHOU[*1], Hailong CHE[1], Yuanyi LIU[1], Pei LI[1]** [1] College of Agricultural Engineering and Food Science, Shandong University of Technology, Zibo, China [2] Chinese Academy of Agricultural Mechanization Sciences Group Co., Ltd, Beijing, China	109
11.	**INVESTIGATION OF AN IMPROVED SIDE VENTILATION SYSTEM IN A POULTRY HOUSE USING CFD / *ДОСЛІДЖЕННЯ ВДОСКОНАЛЕНОЇ БОКОВОЇ СИСТЕМИ ВЕНТИЛЯЦІЇ В ПТАШНИКУ ЗА ДОПОМОГОЮ CFD*** **Viktor TROKHANIAK[1], Nadia SPODYNIUK[1], Taras LENDIEL[1], Petro LUZAN[2], Anatolii MISHCHENKO[1], Svitlana TARASENKO[1], Lucretia POPA[*3], Claudia IONITA [4]** [1] National University of Life and Environmental Sciences of Ukraine / Ukraine; [2] Central Ukrainian National Technical University / Ukraine; [3] National Institute of Research – Development for Machines and Installations Designed for Agriculture and Food Industry – INMA Bucharest / Romania; [4] Faculty of Mechanical Engineering and Mechatronics, University POLITEHNICA of Bucharest / Romania	121

		Page(s)
12.	**EXPERIMENTAL ANALYSIS OF THRESHING MAIZE SEEDS WITH HIGH MOISTURE CONTENT** ***高含水率玉米籽粒脱粒试验分析*** **Yujie DENG, Guohai ZHANG*, Aoqi ZHANG, Jitan LIAN, Jia YAO, Xin WANG, Xiaohui YANG** School of Agricultural Engineering and Food Science, Shandong University of Technology, Zibo, / China	131
13.	**DESIGN AND SIMULATION TEST OF DIGGING DEVICE FOR SMALL POTATO HARVESTER /** ***小型马铃薯收获机挖掘装置的设计与仿真试验*** **Yuan FU [1)], Shiyi REN [2)], Peng TANG [1)], Yuancai LENG [1)], Xiaohu CHEN [1)], Xinye TU [1)], Xiaorong LV [*1)]** [1)]College of Machinery & Electronics, Sichuan Agricultural University, Ya'an / China [2)]Faculty of Engineering, The University of Auckland, Auckland / New Zealand	145
14.	**DESIGN AND EXPERIMENT OF PRESSURE-HOLDING PRECISION SEED-METERING DEVICE FOR MAIZE /** ***压持式玉米精量排种器的设计与试验*** **YunHe ZHANG[1)], JinPeng CHENG[*2)], XueJun Zhang[2)], ZengLu SHI[2)], MeiJing WANG[2)], HaiFeng WU[2)], Hao FU[2)]** [1)] College of Electronic and Electrical Engineering, Lingnan Normal University, Zhanjiang/ China; [2)] College of Mechanical and Electrical Engineering, Xinjiang Agricultural University, Urumqi / China	159
15.	**DEVELOPMENT OF TUNA FISH SHREDDER FOR SMALL AND MEDIUM ENTERPRISES /** ***PENGEMBANGAN MESIN PENCABIK IKAN TUNA UNTUK PEMBUATAN ABON IKAN SKALA INDUSTRI RUMAH TANGGA*** **Mustaqimah MUSTAQIMAH *[1)], Syafriandi SYAFRIANDI [1)], Andriani LUBIS [1)], Nawawi JUHAN [2)], Diswandi NURBA [1)]** [1)] Department of Agricultural Engineering, Faculty of Agriculture, Syiah Kuala University, Indonesia [2)] Department of Mechanical Engineering, Lhokseumawe State Polytechnic / Indonesia	170
16.	**EXPERIMENT AND ANALYSIS OF MECHANIZED PICKING OF *CAMELLIA OLEIFERA* FRUIT BASED ON ENERGY UTILIZATION RATE /** ***基于能量利用率的油茶果机械化采摘试验与分析*** **Delin WU*[1)], Enlong ZHAO[1)], Dong FANG[1)], Ylin LIU[1)], Shunli WANG[1)], Cheng WU[1)], Feng GUO[1)]** [1)] School of Engineering, Anhui Agricultural University, Hefei, China	177
17.	**AN IMPROVED YOLOV4 METHOD FOR RAPID DETECTION OF WHEAT EARS IN THE FIELD /** ***一种改进型 YOLOv4 的田间麦穗快速检测方法*** **Zongwei JIA*[1)], Yi SHAO[2)], Yijie HOU[1)], ChenYu ZHAO[1)], ZhiChuan WANG[1)], Yiming HOU[3)] ,Jinpeng QIN[1)]** [1)] College of Information Science and Engineering, Shanxi Agricultural University, Taigu / China [2)] School of Software, Shanxi Agricultural University, Taigu / China [3)] School of hydraulic and Ecological Engineering, Nanchang Institute of Technology, Nanchang / China	185
18.	**REAPER BLADE SYSTEM FOR HARVESTING SUNFLOWERS /** ***НОЖОВА СИСТЕМА ЖАТКИ ДЛЯ ЗБИРАННЯ СОНЯШНИКУ*** **Olena NALOBINA [1)], Nazar VASYLCHUK [2)], Oleh BUNDZA [1)], Mykola HOLOTIUK [1)], PUTS Vitaliy [2)], Viktor MARTYNIUK [2)]** [1)]National University of Water and Environmental Engineering / Soborna str.11, Rivne, Ukraine; [2)]Lutsk National Technical University / Lvivska str., 75, Lutsk, Ukraine	195
19.	**MOVEMENT ANALYSIS AND EXPERIMENTAL STUDY ON PEANUT POD HARVEST SEPARATION CONVEYOR /** ***花生荚果收获分离输送装置运动分析与试验研究*** **Zengcun CHANG [1,2)] Dongjie LI [2)], Shuqi SHANG [2)], Xiaoning HE [2)], Baiqiang ZUO [2)] Cheng DONG [2)], Xu LI [2)], Dongwei WANG*[2)]** [1)] Shandong Agricultural University, College of Mechanical and Electrical Engineering/ China [2)] Qingdao Agricultural University, College of Mechanical and Electrical Engineering / China	205
20.	**STUDY ON THE MECHANISM OF INDOOR TEMPERATURE AND HUMIDITY CHANGE IN THE SUNKEN SOLAR GREENHOUSE DURING THE SMOTHERING PERIOD /** ***下沉式日光温室闷棚期间温湿度变化机制的研究*** **Weiwei CHENG [1)], Xin YOU [2)], Tao TIAN [2)], Jiaxuan LU [2)], Junlin HE [2)], Zhouhua LIU [*1)], Fei HAN [1)]** [1)] Shanxi Agricultural University, College of Urban and Rural Construction, Taigu / China [2)] Shanxi Agricultural University, College of Agricultural Engineering, Taigu / China	215
21.	**CERASUS HUMILIS CULTIVARS IDENTIFICATION WITH SMALL-SAMPLE AND UNBALANCED DATASET BASED ON EFFICIENT NET-B0+RANGER NETWORKS /** ***基于 EfficientNet-B0+Ranger 的小样本不平衡数据集欧李品种识别*** **Lili LI [1)]; Hua YANG [*1)]; Bin WANG [1)]** [1)] College of Information Science and Engineering, Shanxi Agricultural University, Taigu / China	225
22.	**DESIGN AND EXPERIMENT OF SUSPENDED ROTARY TILLAGE RIDGE AND FILM MULCHING MACHINE /** ***悬挂式旋耕起垄覆膜一体机的设计与试验*** **Dejiang LIU[1,2)], Jianling Hu[1)], Yan GONG [1*)], Xiao CHEN[1)], Guo WANG[1)], Xiao ZHANG [1)], Yingchun ZHU[2)]** [1)] Nanjing Institute of Agriculture Mechanization, Ministry of Agriculture and Rural Affairs, Nanjing, China [2)] Western agricultural research center, Chinese Academy of Agricultural Sciences, Changji, China	237
23.	**MULTI-OBJECTIVE OPTIMIZATION OF HOT BLAST STOVE HEAT EXCHANGER /** ***热风炉换热器多目标优化*** **Ye ZHANG[1)], Qing JIANG*[1,2)], Liangyuan XU[1,2)], Chao HUANG[1)], Huasheng GAN[1)]** [1)] College of Engineering, Anhui Agricultural University, Anhui/China [2)] Anhui Province Engineering Laboratory of Intelligent Agricultural Machinery and Equipment, Anhui/China	245

		Page(s)
24.	**FINITE ELEMENT SIMULATION OF INTER-PLANT WEED CONTROL DEVICE IN PADDY FIELD** ***稻田株间除草部件有限元模拟*** **Wenting JIN [1,2], Yuqi ZHUANSUN[1], Tengfei ZHUANG 1), Qi LU [1], Wenlong LI [2], Liuxuan MA *[2]** [1] Chinese Academy of Agricultural Mechanization Sciences Group Co.,Ltd, Beijing / China; [2] College of Mechanical Engineering, Jiamusi University, Jiamus / China	260
25.	**RECENT TECHNOLOGY IN CULTIVATING PIPER BETLE VAR NIGRA. A COMPREHENSIVE REVIEW / *TEKNOLOGI PEMBIAKAN TERKINI PIPER BETLE VAR NIGRA. SEBUAH REVIEW LENGKAP*** **Dewanto HARJUNOWIBOWO*[1], Anif JAMALUDDIN[1], Yudi RINANTO[2], Fajar PRASETYA[3]** [1]Physics Education, Universitas Sebelas Maret / Indonesia; [2]Biology Education, Universitas Sebelas Maret / Indonesia [3]Faculty of Pharmacy, Universitas Mulawarman / Indonesia	269
26.	**A WIRELESS REMOTE MONITORING SENSOR FOR AGRICULTURAL ENVIRONMENT BASED ON NB-IoT / *基于 NB-IoT 的农业环境无线远程监测传感器*** **Zhenfeng XU*[1], Jiajian YANG[1], Huan ZHOU[1], Yunfang HOU[2]** [1] School of advanced Manufacturing Engineering, Hefei University / China; [2] Fuyang Ziqing Agricultural Technology Co., Ltd / China	285
27.	**RESEARCH ON APPLE LEAF DISEASE SEGMENTATION AND CLASSIFICATION BASED ON SEMANTIC SEGMENTATION NETWORK / *基于语义分割网络的苹果叶片病害分割与分级研究*** **Bin WANG, Lili LI, Shilin LI, Hua YANG*** College of Information Science and Engineering, Shanxi Agricultural University, Taigu /China	295
28.	**RESEARCH OF THE AIR FLOW FORM IN THE INTAKE DEVICE FOR SAPROPEL EXTRACTION / *ДОСЛІДЖЕННЯ ФОРМИ ПОВІТРЯНОГО ПОТОКУ У ЗАБІРНОМУ ПРИСТРОЇ ДЛЯ ДОБУВАННЯ САПРОПЕЛЮ*** **Igor TSIZ, Serhii KHOMYCH, Vasyl SATSIUK, Victor TARASIUK** Lutsk National Technical University / Ukraine	305
29.	**MODELING OF SUBSTRATE AND AIR TEMPERATURE DYNAMICS IN THE MUSHROOM GREENHOUSE / *МОДЕЛЮВАННЯ ДИНАМІКИ ТЕМПЕРАТУРИ СУБСТРАТУ ТА ПОВІТРЯ У ГРИБНИЦІ*** **Gennadii GOLUB[1], Oleg KEPKO*[2], Olexander PUSHKA[2], Zoia KOVTUNIUK[2], Timofii KOTLIAR[3]** [1] National University of Life and Environmental Sciences of Ukraine, Kyiv, Ukraine; [2] Uman National University of Horticulture, Uman, Ukraine [3] Bila Tserkva National Agrarian University	315
30.	**DESIGN AND EXPERIMENT OF END EFFECT FOR KIWIFRUIT HARVESTING BASED ON OPTIMAL PICKING PARAMETERS / *基于最优采摘参数的猕猴桃采摘末端执行器设计与试验*** **Zhi HE [1,2], Zixu LI [1,2], Xingting DING [1,3], Kai LI [1], Yinggang SHI [1], Yongjie CUI *[1,3]** [1] College of Mechanical and Electronic Engineering, Northwest A&F University, Yangling / China; [2] Key Laboratory of Agricultural Internet of Things, Ministry of Agriculture and Rural Affairs, Yangling / China; [3] Shaanxi Key Laboratory of Agricultural Information Perception and Intelligent Service, Yangling / China	325
31.	**RICE MECHANIZATION IN ETHIOPIA: TRENDS, AND PROSPECTS / *የሩዝ ሜካናይዜሽን በኢትዮጵያ፡ አዝማሚያዎች እና ተስፋዎች*** **Tikuneh DESSYE *[1], Woldesenbet LAIKE[2]** [1]Ethiopian Institute of Agricultural Research, Fogera National Rice Research, and Training Center, Wereta, Ethiopia [2] Ethiopian Institute of Agricultural Research, Melkassa Agricultural Research Center, Adama, Ethiopia	335
32.	**EFFECT OF AGING TIME AND VACUUM DRYING ON PROXIMATE ANALYSIS AND AMINO ACID LEVELS OF GOAT MILK KEFIR / *EFEK WAKTU AGING DAN PENGERINGAN VAKUM PADA ANALISIS PROKSIMAT DAN TINGKAT ASAM AMINO DARI KEFIR SUSU KAMBING*** **Aman SANTOSO*[1], Lilik Eka RADIATI[2], Evi DAMAYANTI[3], Armaini ARMAINI[4], Amiroh NABILAH-MUJAHIDAH[1], Eli Hendrik SANJAYA[1], Muntholib MUNTHOLIB[1]; Muhammad Roy ASRORI[1]** [1] Dep.of Chemistry, Faculty of Mathematics and Natural Sciences, Universitas Negeri Malang / Indonesia; [2] Department of Animal Product Technology, Faculty of Animal Science, Universitas Brawijaya/ Indonesia; [3] Faculty of Human Ecology, IPB University; [4] Department of Chemistry, Faculty of Mathematics and Natural Sciences, Universitas Andalas/ Indonesia.	349
33.	**DEVELOPMENT AND PERFORMANCE EVALUATION OF A LIQUEFIED PETROLEUM GAS-POWERED FLUIDIZED COFFEE ROASTER / *PENGEMBANGAN DAN EVALUASI KINERJA PENYANGRAI KOPI FLUIDISASI BERTENAGA LIQUEFIED PETROLEUM GAS*** **Dadang Dayat HIDAYAT[1], Ari RAHAYUNINGTYAS[1], Diang SAGITA*[1], Maulana FURQON[1], Arie SUDARYANTO[1], Dadang GANDARA[1], Taufik YUDHI[1], Nandang JAENUDIN[1]** [1]Research Centre for Appropriate Technology, National Research and Innovation Agency	359
34.	**MODELING OF THE RUNNING SYSTEM PRESSURE ON THE SOIL DEPENDING ON THE STRUCTURAL PARAMETERS OF THE TRACTORS / *МОДЕЛЮВАННЯ ТИСКУ ХОДОВОЇ СИСТЕМИ НА ГРУНТ В ЗАЛЕЖНОСТІ ВІД КОНСТРУКТИВНИХ ПАРАМЕТРОВ ТРАКТОРІВ*** **Gennadii GOLUB*[1], Viacheslav CHUBA[2], Vasyl ACHKEVYCH[1], Victor KRUSHELNYTSKYI[1], Nataliya TSYVENKOVA[1]** [1] National University of Life and Environmental Sciences of Ukraine / Ukraine; [2] Bila Tserkva National Agrarian University / Ukraine	369

		Page(s)
35.	**MANUFACTURE OF A DEVICE FOR PRUNING FRUIT BRANCHES /** *تصنيع جهاز لتقليم الأفرع الثمرية* **Adel AL-GEZAWE, Mokhtar COTTB, Fatma ABD EL GAWAD, Mahmoud AWAD, Osama FOUDA, Mahmoud OKASHA*)** Agricultural Engineering Research Institute (AEnRI), Agricultural Research Center (ARC), Giza 12611/ Egypt	379
36.	**GRAIN MOISTURE MEASUREMENT SYSTEM WITH ROBUST TRANSFER FUNCTION, INVARIANT TO THE CHANGE OF A PHYSICO-CHEMICAL GRAIN COMPOSITION /** ***СИСТЕМА ВИМІРЮВАННЯ ВМІСТУ ВОЛОГИ ЗЕРНА З РОБАСТНОЮ ФУНКЦІЄЮ ПЕРЕТВОРЕННЯ, ІНВАРІАНТНОЮ ДО ЗМІНИ ФІЗИКО-ХІМІЧНОГО СКЛАДУ ЗЕРНА*** **Oleksandr ZABOLOTNYI [1)], Vitalii ZABOLOTNYI [1)], Nicolay KOSHEVOY [1)]** [1)] National Aerospace University «Kharkiv Aviation Institute» / Ukraine	389
37.	**PARAMETERS CALIBRATION OF DISCRETE ELEMENT MODEL FOR CRUSHED CORN STALKS /** ***碎玉米秸秆离散元模型参数标定*** **Min FU*, Xiaoqing CHEN, Zefei GAO, Chengmeng WANG, Bing XU, Yilin HAO** Northeast Forestry University, College of Mechanical and Electrical Engineering, Harbin / China	399
38.	**SIMULATION RESEARCH ON THE INFLUENCE OF INCLINATION ANGLE OF LINEAR VIBRATING SCREEN ON BUCKWHEAT SIZING EFFECT /** ***直线振动筛筛面倾角对荞麦分级效果影响的模拟研究*** **Bing XU[1,2)], Decong ZHENG *[1,2,3)], Qingliang CUI [1,2)], Hanqing YAO[1)]** [1)] College of Agricultural Engineering, Shanxi Agricultural University, Taigu / China; [2)] Dryland Farm Machinery Key Technology and Equipment Key Laboratory of Shanxi Province, Taigu / China [3)] Research centre of Shanxi modern agricultural facilities and equipment, Taiyuan / China	409
39.	**AN IoT-ENABLED DESIGN FOR REAL-TIME WATER QUALITY MONITORING AND CONTROL OF GREENHOUSE IRRIGATION SYSTEMS /** ***DESAIN PERANGKAT BERBASIS IoT UNTUK PEMANTAUAN DAN PENGENDALIAN KUALITAS AIR PADA SISTEM IRIGASI RUMAH KACA*** **Irfan ARDIANSAH[1*)], Ryan Ganesha CALIBRA[1)], Nurpilihan BAFDAL[2)], Awang BONO[3)], Edy SURYADI[2)], Siti NURHASANAH[4)]** [1)] Department of Agroindustrial Technology, Faculty of Agroindustrial Technology, Universitas Padjadjaran, Indonesia; [2)] Department of Agriculture Engineering and Biosystem, Faculty of Agroindustrial Technology, Universitas Padjadjaran, Indonesia; [3)] Department of Chemical Engineering, Faculty of Engineering, Universiti Malaysia Sabah, Malaysia; [4)] Department of Food Industrial Technology, Faculty of Agroindustrial Technology, Universitas Padjadjaran, Indonesia	417
40.	**AGRICULTURAL PLATFORM EQUIPPED WITH A HYDROSTATIC TRANSMISSION CAPABLE OF CONTINUOUSLY ADJUSTABLE TRAVEL VELOCITY AND NON-LINEAR DISTURBANCE COMPENSATION CAPABILITIES /** ***PLATFORMĂ AGRICOLĂ DOTATĂ CU O TRANSMISIE HIDROSTATICĂ CAPABILĂ SĂ REALIZEZE VITEZE DE DEPLASARE CONTINUU VARIABILE ȘI CAPABILITĂȚI DE COMPENSARE A PERTURBAȚIILOR NELINIARE*** **Alexandru-Polifron CHIRIȚĂ*[1),2)], Cristian PAVEL[2)]** [1)] INOE 2000 - Subsidiary Hydraulics and Pneumatics Research Institute / Romania; [2)] Faculty of Mechanical Engineering and Robotics in Construction, Technical University of Civil Engineering Bucharest / Romania	427
41.	**EFFECTS OF WATER-SAVING IRRIGATION COMBINED WITH CONDITIONER ON YIELD, NUTRIENT ABSORPTION AND QUALITY OF DRY DIRECT SEEDING RICE /** ***节水灌溉与调理剂结合对旱直播稻产量、养分吸收及品质影响*** **Shuchang LU [1)], Xiawen LI [1)]** [1)] College of Agronomy and Resources and Environment, Tianjin Agricultural University, Tianjin, China	437
42.	**RESEARCH ON SOIL MOISTURE DETECTION AND REMOTE PRECISION IRRIGATION OF SEEDLINGS BASED ON INTERNET OF THINGS /** ***基于物联网的苗木土壤墒情检测与远程精准灌溉研究*** **Yakun ZHANG[1,*)], Zihua FENG [1)], Yalin HUANG[1)], Tingting LI [1)], Xingyang YANG [1)], Hangxing ZHANG[1)], Libo WANG [1)]** [1)] College of Agricultural Equipment Engineering, Henan University of Science and Technology, Luoyang, China	449
43.	**DESIGN AND EXPERIMENT OF TRANSVERSE AXIAL FLOW CORN FLEXIBLE THRESHING DEVICE /** ***横轴流玉米柔性脱粒元件的设计与试验*** **Huabiao LI, Qihuan WANG, Jie MA, Yanan WANG, Dong YUE, Duanyang GENG*)** School of Agricultural and Food Engineering, Shandong University of Technology, Zibo, China	461
44.	**STUDY ON THE LOSS CONTROL SYSTEM OF WHEAT COMBINE HARVESTER /** ***小麦联合收获机损失控制系统研究*** **Jizhong WANG[1)], Xianfa FANG[1,*)], Fengzhu WANG[1)], Yangchun LIU[1)], Bo ZHAO[1)]** [1)] National Key Laboratory of Agricultural Equipment Technology, Chinese Academy of Agricultural Mechanization Sciences, Beijing, China	471
45.	**OPTIMIZATION AND APPLICATION OF IRRIGATION SCHEDULING BASED ON HYDRUS-2D AND STEWART MODEL IN A SEMI-ARID AREA OF CHINA /** ***基于 Hdyrus-2D 和 Stewart 模型的半干旱区灌溉制度优化及其应用*** **Haihua JING, Jing ZHANG, Kebao DONG*), Jiaqi MA, Zexu JIN** College of Water Conservancy, Shenyang Agricultural University, Shenyang, China	481
46.	**HYPERSPECTRAL IMAGE CLASSIFICATION IN DESERT GRASSLAND BASED ON THREE-DIMENSIONAL DEEP LEARNING MODEL /** ***基于 3D 深度学习模型的荒漠草原高光谱图像分类*** **Ronghua WANG [1)], Yanbin ZHANG [2*)], Jianmin DU [2)], Yuge BI[2)]** [1)] Inner Mongolia Technical College of Mechanics and Electrics, Hohhot, China [2)] Inner Mongolia Agricultural University, Hohhot, China	492

		Page(s)
47.	**RESEARCH ON KINEMATICS SIMULATION AND DYNAMIC ANALYSIS OF THE COLLECTION MECHANISM OF ORCHARD BRANCHES / *果园枝条收集机构的运动学仿真与动力学分析研究*** **Hui LI[1)], Xin YANG[2*)], Aiqian YANG[1)]** [1)]Hengshui University, Hengshui / China; [2)]College of Mechanical and Electrical Engineering, Hebei Agricultural University, Baoding / China	501
48.	**NUMERICAL SIMULATION AND EXPERIMENT ON AIRFLOW FIELD OF CORN SEED HARVESTER CLEANING DEVICE / *玉米籽粒收获机清选装置气流场数值模拟与试验*** **Zedong ZHAO[1)], Hongyong DU[2)], Xiaohui YANG[1)], Guohai ZHANG[1*)]** [1)] College of Agricultural Engineering and Food Science, Shandong University of Technology, Zibo, China [2)] Shandong Himile Mechanical Manufacturing Co., Ltd., Weifang, China	511
49.	**MANAGEMENT PRACTICES IN INDUSTRIAL HEMP HARVESTING AND STORAGE / *PRACTICI DE MANAGEMENT ÎN RECOLTAREA ŞI DEPOZITAREA CÂNEPEI INDUSTRIALE*** **Dragoș MANEA, Gheorghe STROESCU, Lucreţia POPA, Alexandru IONESCU, Alexandru ZAICA** National Institute of Research-Development for Machines and Installations designed for Agriculture and Food Industry – INMA / Bucharest, Romania	520
50.	**MECHANICAL MODEL OF *CERASUS HUMILIS* ESTABLISHED BY UNIAXIAL COMPRESSION PHYSICAL TEST AND VIRTUAL SIMULATION / *基于单轴压缩物理试验和虚拟仿真的钙果力学模型构建*** **Shilei KANG[1,2)], Jiaxuan LU[1)], Huhu YANG[1)], Yanxi GUO[1)], Junlin HE*[1,2)]** [1)]College of Agricultural Engineering, Shanxi Agricultural University, Taigu, China; [2)]Dryland Farm Machinery Key Technology and Equipment Key Laboratory of Shanxi Province, Taigu, China	527
51.	**CONFIGURATION OPTIMIZATION METHOD OF AGRICULTURAL MACHINERY CLUSTER OPERATION MAINTENANCE SERVICE VEHICLE / *农机集群作业维修服务车配置优化方法*** **Weipeng ZHANG, Bo ZHAO*, Guangrui LI, Liming ZHOU, Kang NIU, Shengbo GAO** State Key Laboratory of Soil Plant Machine System Technology, China Academy of Agricultural Mechanization Science Group Co., Ltd. Beijing, China	537
52.	**DETECTION OF FLAXSEED OIL ADULTERATION BASED ON TWO-DIMENSIONAL CORRELATION NEAR-INFRARED SPECTRA / *基于二维相关近红外光谱的亚麻籽油掺杂检测*** **Ning HAN, Tonghui WU, Qian WU, Hongzhi DU, Zhiyong ZHANG*, Yanqing ZHANG** College of Agricultural Engineering, Shanxi Agricultural University, Taigu/China	549
53.	**EXPERIMENT ON SPRAY FLOW FIELD CHARACTERISTICS AND DEPOSITION PERFORMANCE OF CONICAL WIND FIELD ANTI-DRIFT SPRAY / *锥形风场式防飘喷雾流场特性及沉积性能试验研究*** **Changxi LIU [1,2,3)], Jun HU *[1,2,3)], Yufei LI [1,2,3)], Wei ZHANG [1,2,)], Qingda LI [1,2,3)],** [1)]College of Engineering, Heilongjiang Bayi Agricultural University, Daqing / China; [2)]Heilongjiang Province Conservation Tillage Engineering Technology Research Center, Daqing / China; [3)]Key Laboratory of Soybean Mechanized Production, Ministry of Agriculture and Rural Affairs, Daqing / China	559
54.	**RESEARCH ON THE SPRAY CYLINDER INTERNAL FLOW FIELD AND ITS INFLUENCE ON SPRAYING QUALITY OF FORAGE SEED SPRAY SEEDING MACHINE / *牧草种子喷播机喷筒内流场及其对喷播质量影响研究*** **Yan CHEN, Hua GUO *), Shi FU, Rui ZHANG, Ming ZHANG** Department of Information Engineering, Ordos Institute of Technology, Compass, Ordos/ China	569
55.	**STUDY ON PHENOTYPIC CHARACTERISTICS OF MILLET BASED ON 3D MODEL / *基于三维模型的谷子表型特征分析研究*** **Lili SUN[1)], Yaoyu LI [2)], Yuzhi WANG [2)], Weijie SHI[2)], Wuping ZHANG [2)], Xiaoying ZHANG [3)], Huamin ZHAO [1)], Fuzhong LI [2,*)] [1)]** [1)] College of Agricultural Engineering, Shanxi Agricultural University, Taigu, Shanxi / China [2)] College of Software, Shanxi Agricultural University, Taigu, Shanxi / China [3)] Department of Basic, Shanxi Agricultural University, Taigu, Shanxi / China	579
56.	**STATISTICAL ANALYSIS OF FATIGUE DAMAGE LIFE OF CORN KERNELS / *玉米籽粒疲劳损伤寿命统计分析*** **Bolong WANG [1)], Zhiyong LIN [1)], Mingjie GAO [1)], Guohai ZHANG [1)], Duanyang GENG [1)], Zhou SHI [2*)]** [1)] School of Agricultural Engineering and Food Science, Shandong University of Technology, Zibo, China [2)]School of Mechanical Engineering, Shandong University of Technology, Zibo, China	589
57.	**HEAT TRANSFER CHARACTERISTICS OF AN EVAPORATOR EQUIPPING AN AIR HANDLING UNITS FOR CEREAL SEED STORAGE FACILITY/ *CARACTERISTICILE DE TRANSFER DE CĂLDURA ALE UNUI VAPORIZATOR CARE ECHIPEAZA O CENTRALA DE TRATARE A AERULUI DESTINATA UNUI DEPOZIT DE SEMINȚE DE CEREALE*** **Iulian UTA[1)], Valentin APOSTOL*[1)], Horatiu POP[1)], Viorel BADESCU[1)], Constantin PAVEL*[1)], Claudia IONITA[1)]** Faculty of Mechanical Engineering and Mechatronics, University Politehnica of Bucharest / Romania	597
58.	**ELECTRIC DRIVE SYSTEM POWERED BY Li-ION BATTERIES FOR AQUATIC BIOMASS HARVESTER / *SISTEM DE ACȚIONARE ELECTRICĂ PENTRU RECOLTATOR DE BIOMASĂ LACUSTRĂ ALIMENTAT DIN BATERII Li-ION*** **Emil TUDOR[1*)], Mihai-Gabriel MATACHE [2)], Ionuț VASILE[1)], Ion-Cătălin SBURLAN[1)], Vasilica ȘTEFAN[2)]** [1)] INCDIE ICPE-CA / Romania; [2)]INMA Bucharest / Romania	609

		Page(s)
59.	**CALIBRATION AND EXPERIMENTS OF THE SIMULATION BONDING PARAMETERS FOR PLUG SEEDLING SUBSTRATE BLOCK / *穴盘苗基质块仿真粘结参数标定与试验*** **Hongbin BAI[1)], Xuying LI*[1)], Fandi ZENG[1)], Qiang SU[1)], Ji CUI[1)], Junyue WANG[1,2)], Yongzhi ZHANG[1)]** [1)] Inner Mongolia Agricultural University, College of Mechanical and Electrical Engineering, Hohhot/China; [2)] China Academy of Agricultural Mechanization Science Hohhot Branch Co., Ltd. Hohhot/China	617
60.	**OPTIMIZATION OF SCREW CONVEYING OF KNEADED CORN STALKS BASED ON DISCRETE ELEMENT METHOD / *基于离散元法的揉碎玉米秸秆螺旋输送的优化*** **ZhiPeng FAN, Zhe MA, HongBo WANG*), ZhiHong YU** College of Mechanical and Electronic Engineering, Inner Mongolia Agricultural University, Hohhot / China	626
61.	**THREE-DIMENSIONAL RECONSTRUCTION AND CHARACTER EXTRACTION OF CORN PLANTS BASED ON KINECT SENSOR /** ***基于 Kinect 传感器的玉米植株三维重构与性状提取*** **Yuanyuan SUN[1)], Xuchang WANG*[2)], Kaixing ZHANG[3)]** College of Modern Equipment Academy, Changzhou Vocational Institute of Industry Technology / China; Yantai CIMC Raffies Offshore Ltd, Yantai / China College of Mechanical and Electronic Engineering, ShanDong Agricultural University, Tai'an / China	635
62.	**STUDY ON THE UNIFORMITY OF SPRAYING SEEDS WITH 4BQD-40C SPRAYING SEEDER MACHINE / *4BQD-40C 型喷播机喷播落种均匀性研究*** **Yan CHEN, Hua GUO *), Shi FU, Rui ZHANG, Ming ZHANG** Department of Information Engineering, Or595dos Institute of Technology, Compass, Ordos/ China	645
63.	**DESIGN AND EXPERIMENTAL STUDY OF A SMART TREE WHITEWASH DEVICE BASED ON HUMAN–COMPUTER INTERACTION /** ***基于人机交互智能树干涂白装置的设计与实验研究*** **Haichao WANG [1)], Zheying ZONG [2)], Yi QIN [2)], Yingjie DU2), Zhen WANG[2)], Chunhui ZHANG[2)]** [1)] Inner Mongolia Agricultural University, College of Energy and Transportation Engineering / China [2)] Inner Mongolia Agricultural University, College of Mechanical and Electrical Engineering / China	655
64.	**ON-STREAM SOIL DENSITY MEASURING /** **ПОТОКОВЕ ВИЗНАЧЕННЯ ЩІЛЬНОСТІ ҐРУНТУ** **Volodymyr KRAVCHUK [1)], Mikhailo IVANIUTA [1)], Viacheslav BRATISHKO [2)],** **Yuri HUMENIUK [2)], Vitaly KURKA [2)]** [1)]The Institute *of* Bioenergy Crops and Sugar Beet NAAS of Ukraine / Ukraine [2)] National University of Life and Environmental Sciences of Ukraine / Ukraine	665
65.	**EFFECT OF CONTROLLED-RELEASE FERTILIZER ON MAIZE YIELD AND NUTRIENT UPTAKE UNDER A FERTILIZER ONE-TIME POINT-APPLIED SYSTEM /** ***一次性机械化穴施缓释复合肥对玉米产量和养分吸收的影响*** **Xin DU[1, 2)], Cailing LIU*), Changqing LIU[1, 2)], Meng JIANG[1)], Hao YUAN[1)]** [1)] College of Engineering, China Agricultural University, Beijing 100083/ China; [2)] School of Mechanical Engineering, Jiangsu Ocean University, Lianyungang 222005/ China	673
66.	**DESIGN AND TEST OF POTATO CONVEYING AND GRADING DEVICE WITH VARIABLE SPACE /** ***变间距式马铃薯输送分级装置设计与试验*** **Xin HE[1)], Longfei LI [1)], Xing LIU [1)], Yumeng XIAO [1)], Taowei JIAO[1)], Wei LI*[1)]** [1)] Northwest A&F University College of Mechanical and Electronic Engineering, Shaanxi Yangling, China	681
67.	**ANALYSIS AND IMPROVEMENT OF SINGLE-PHASE FLOW FIELD INSIDE THE CRUSHING CHAMBER OF MACHINE FOR LENTINUS EDODES STIPE CRUSHING /** ***香菇柄成松机成松室内单相流场分析与改进*** **Yang LI [1,2)], Yanjun LI [3)], Pei LI [4)]** [1)] Chinese Academy of Agricultural Mechanization Sciences Group Company Limited, Beijing, China [2)] National Key Laboratory of Agricultural Equipment Technology, Beijing, China [3)] Weifang University, Weifang, Shandong, China [4)] Shandong University of Technology, Zibo, Shandong, China	693

REASEARCH ON PEAR INFLORESCENCE RECOGNITION BASED ON FUSION ATTENTION MECHANISM WITH YOLOV5
/
基于融合注意力机制的 YOLOv5 算法对梨花序的识别研究

Ye XIA [1, 2)], Xiaohui LEI *[2)], Andreas HERBST [3)], Xiaolan LYU *[2)] [1]

[1)] School of Agricultural Engineering, Jiangsu University, Zhenjiang/China;
[2)] Institute of Agricultural Facilities and Equipment, Jiangsu Academy of Agricultural Sciences / Key Laboratory of Modern Horticultural Equipment, Ministry of Agriculture and Rural Affairs, Nanjing/China;
[3)] Institute for Chemical Application Technology of JKI, Braunschweig Messeweg/Germany;
Tel: +86-025-84390082; E-mail: leixiaohui.2008@163.com

DOI: https://doi.org/10.35633/inmateh-69-01

Keywords: *agricultural machinery, pear inflorescence, object detection, YOLOv5, coordinate attention mechanism*

ABSTRACT
Thinning is an important agronomic process in pear production, thus the detection of pear inflorescence is an important technology for intelligentization of blossom thinning. In this paper, images of buds and flowers were collected under different natural conditions for model training, and the images were augmented by data augmentation methods. Model training was performed based on the YOLOv5s network with coordinate attention mechanism added to the backbone network and compared with the native YOLOv5s, YOLOv3, SSD 300, and Faster-RCNN algorithms. The mAP, F1 score and recall of the algorithm reached 93.32%, 91.10%, and 91.99%. The model size only took up 14.1 MB, and the average detection time was 27 ms, which are suitable for application in actual intelligent blossom thinning equipment.

摘要
疏花疏果是梨生产中一项重要的农艺环节，而梨树花序识别是疏花智能化过程中的一项重要技术。本文在不同的自然条件下采集了梨树花苞与花朵的图像，通过数据增强方法对图像进行了扩充。在 YOLOv5s 主干网络中增加 CA 注意力机制，将其与原生 YOLOv5s、YOLOv3、SSD 300、Faster-RCNN 算法进行对比。结果表明，改进的 YOLOv5s-CA 模型优于其他模型，其 mAP、F1 得分、Recall 分别达到了 93.32%、91.10%和 91.99%，模型大小仅为 14.1 MB，平均检测时间 27 ms，更适用于智能化疏花设备中。

INTRODUCTION
Under natural conditions, the number of blossoms in pear trees is far more than that of final fruit. Blossom thinning can save tree nutrients, avoid biennial bearing and improve fruit quality. At present, the method of pear tree thinning mainly adopts manual operation with mechanical tools, which is time-consuming with difficulty in controlling the thinning precision. Therefore, an intelligent blossom thinning method is necessary for the future development of blossom thinning equipment, especially the pear inflorescence detection algorithm based on deep learning.

With the rapid development of deep learning technology in agriculture, smart agriculture has ushered in a new era. The mainstream target detection algorithms can be divided into two-stage and one-stage algorithms according to the recognition process. Two-stage algorithms are represented by R-CNN series *(Girshick R. et al., 2013; Ren S. et al., 2016)* and SPP-Net *(He K. et al., 2014)*. This type of algorithm has a large number of parameters, and has the characteristics of high recognition accuracy but with slow recognition speed, and usually used for the tasks requiring high detection accuracy. One-stage algorithms filter the possible detection targets and return the category and classification of them. The mainstream one-stage algorithms include YOLO series *(Redmon J. et al., 2016; Bochkovskiy A. et al., 2020)* and SSD *(Wei L. et al., 2016)*, which have fast detection speed and are more suitable for deployment in embedded devices but with poor computing capacity.

[1] *Ye Xia, Master Candidate; Xiaohui Lei, Assistant Researcher; Andreas Herbst, Prof.; Xiaolan Lyu, Researcher.*

YOLO has been widely used in the field of target detection because it ensures the detection speed while taking into account the recognition accuracy. *Fan Z. et al., (2022),* compared several YOLO algorithms for the recognition of cucurbit fruits, and the results show that the YOLOv5 achieved the optimal effect, with mAP reaching 97.1% and fps reaching 90.9. *Yan L. et al., (2022),* used YOLOv4 to study the recognition of occluded orange fruits on trees, and the results showed that its detection accuracy reached 98.17%, showing a better effect on lightly occluded targets. *Jin Y., (2020),* used visual servo technology to identify the tomato in fruit picking task. The results show that the method can effectively identify and locate tomatoes during the picking process. *Wang D. et al., (2021),* used the YOLOv5 algorithm improved by the channel pruning method to detect multi-variety apple fruits. The average accuracy of the collected data set reached 95.8%, and the model size was reduced to 1.4 MB. *Farjon G. et al., (2020),* used Faster-RCNN for transfer learning and marked the flower information of apple by professional planters to realize the discrimination of different blooming intensities. The results showed that the model mAP reached 68%, and the flowering degree recognized by the model was similar to that of human discrimination in the range of 78% to 93%.

The researches above have detected the blossoms and fruits of different crops or trees with various target detection methods, but there is few related research on the detection of pear blossoms.

In this paper, pear inflorescence was taken as the research object for detection in different environments based on the improved YOLOv5s network, to provide a target positioning method for improving the operation accuracy of intelligent blossom thinning equipment in orchards.

MATERIALS AND METHODS

Image acquisition

The inflorescence data of pear trees were collected from March 10, 2022 to March 30, 2022 in Nan Jing, China. The pictures were collected in the environment of insufficient light, shadows, and overlapping occlusions. The data were captured by a smartphone, and the pictures were saved as *.jpg format with a resolution of 1920*1080. The pear trees in the data collection site were planted in horizontal trellis and the inflorescence on a single branch was used as the unit. The method of pear inflorescence data acquisition is shown in Fig. 1. A total of 1566 original pictures were collected from the sample data. The dataset was divided into 1200 training sets and 366 validation sets. Raw data was manually annotated by LabelIMG software.



Fig. 1 - Pear inflorescence data acquisition

Data augmentation

Due to the complex shape of pear inflorescence, a data augmentation strategy was adopted for the original data set to avoid overfitting. The processing program was compiled through the OpenCV library, and the original data was transformed by changing brightness, rotation angle, adding Gaussian noise, translation, mirroring, and clipping. The specific data augmentation logic is shown in Fig. 2.

Set the total transformation times and cycle after the pictures are input. In a cycle, each factor has a 50% probability of appearing until the set transformation times are met. The specific strategy was random rotation of 0 to 70°, random crop of 2*150*150 pt, random Gaussian noise of 0.1 to 0.2, brightness adjustment from -30% to +30%, random flip horizontally, vertically and on the original spot, 100 pt to 250 pt random shift in horizontal and vertical directions. In order to save the time for repeated manual labelling, the program adopts the same position transformation method for the objects that have been labelled in the original data, so as to directly generate the expanded data containing the annotation information. In the process of augmentation, the original data were expanded by 4 times, and each picture was subjected to 6 random transformation factors to generate its own quadruple-enhanced data. The dataset after data augmentation reached 7830 images.

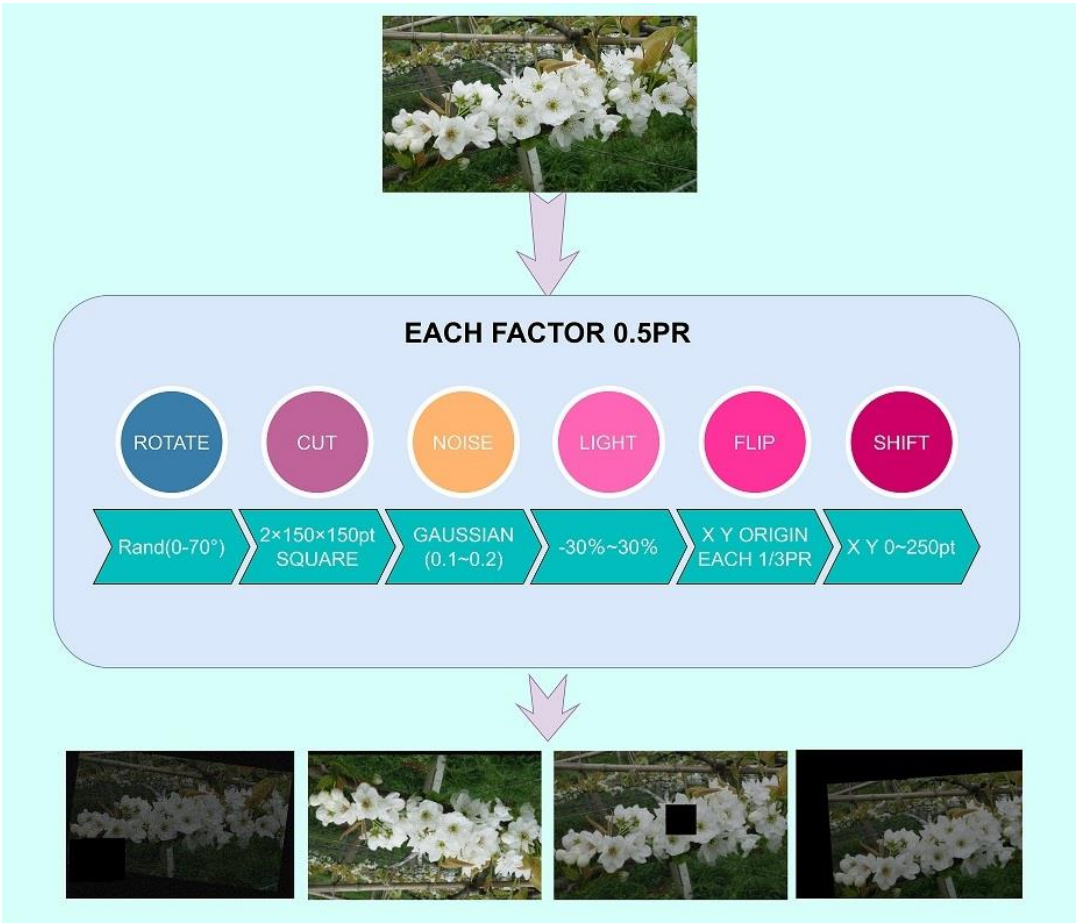


Fig. 2 - Data augmentation logic

The YOLOv5 algorithm

The YOLO algorithm transforms the object detection problem into a probabilistic regression problem by dividing the image into a finite number of anchor boxes and continuing to predict the edge box part of each anchor box. Through YOLO, the category and estimated probability of the target can be directly obtained, which greatly improves the detection speed compared with the two-stage detection network of RCNN. The standard version of YOLO can process 45 frames per second in real time, while the smaller, lighter version of YOLO can process 155 frames per second *(Shafiee M. et al., 2017)*. YOLOv5 uses the CSPDarkNet53 backbone network on the basis of the original framework. Compared with the DarkNet53 used in the previous version, CSPDarkNet53 can divide the feature map of the base layer into two parts, and merge them through the cross-stage hierarchy, which reduces the amount of calculation.

The Neck network of YOLOv5 adopts feature pyramid network (FPN) and pixel aggregation network (PAN) structure, with strong semantic and localization features. By fusing the two structures, the bidirectional aggregation of the features of different layers of the backbone network is achieved. The prediction head part makes predictions by performing probability regression judgment on the generated feature maps of different sizes using grid-based anchor boxes. The YOLOv5 algorithm organizes the network in a modular way, and the feature extraction module mainly includes convolution, batch normalization and SiLU (CBS), center and scale prediction (CSP), fast spatial pyramid pooling (SPPF). The CBS module mainly used in backbone network consists of the convolutional layer (Conv), the normalization layer (BN), and the SiLU activation function layer. The residual structure contained in it can increase the gradient value of back-propagation between layers to avoid gradient disappearing due to the deepening of the network. Finer features can be extracted without worrying about network degradation. The features of the input image are extracted by the convolution layer, normalized by the BN layer to speed up the network learning speed, and finally the features are retained and mapped by the activation function. The CSP_X consists of one CBS and X residuals, which are concatenated. SPPF first continues to pool one part of the features obtained after the maximum pooling of the small-sized feature map, and the other part is spliced with the results obtained by each pooling layer. Then the features are extracted by the CBS module and converted into fixed-size features. Let the network fuse local and global features of different sizes, and the structure diagram of each module and the entire network is shown in Fig. 3.

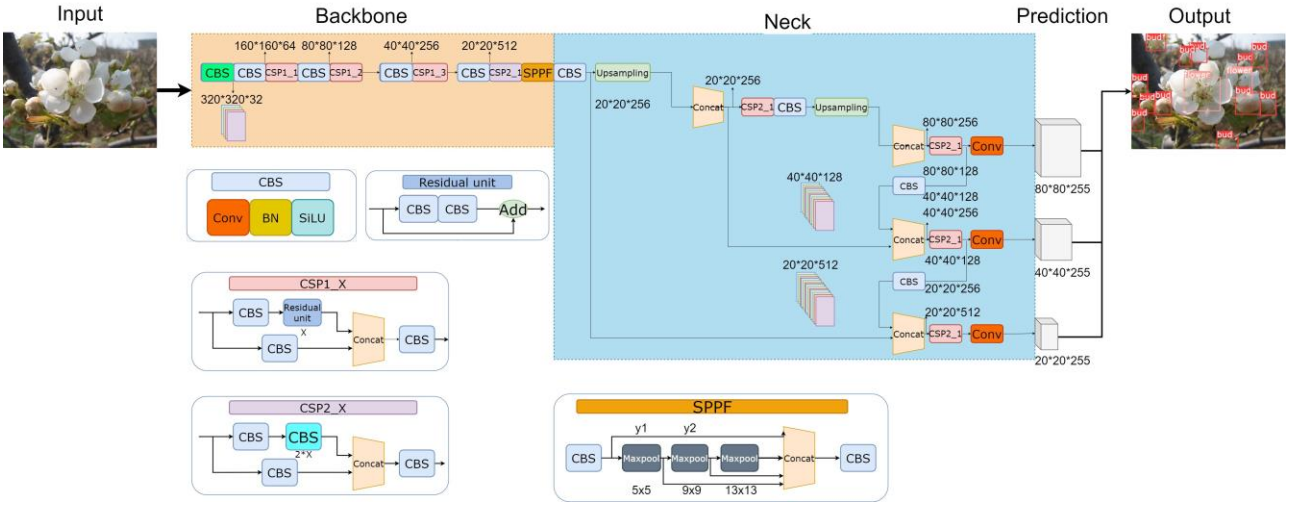


Fig. 3 – YOLOv5 network for pear inflorescence detection

The coordinate attention (CA) mechanism

The attention mechanism is a resource allocation scheme that allocates more resources to more important tasks when the computing power of the hardware platform is limited. The attention mechanism in CNN makes the network pay more attention to the information that is more critical to the current task by assigning weights to the feature maps of different parts, reducing the attention to irrelevant information or directly filtering irrelevant information, so as to improve the efficiency of the whole network processing task. Common attention mechanisms are mainly divided into two categories: spatial attention mechanism and channel attention mechanism. Typical attention mechanisms are SE-Net *(Jie H. et al., 2017)*, DRAW *(Gregor K. et al., 2015)*, which often pay attention to single-feature information, but in specific tasks, it is often necessary to take into account both attention mechanisms above in order to improve the attention to effective information.

CA mechanism *(Hou Q. et al., 2021)* is an attention mechanism embedded in mobile networks, which can transform any intermediate feature tensor in the network and output a tensor of the same size. The CA structure first divides the input feature maps into two directions by width and height, and performs global average pooling on them to obtain feature maps in both width and height directions. Then, the feature maps in the two directions of the global receptive field are spliced together for convolution, normalization, and activation operations.

Then a similar operation is performed, that is, convolve the feature map according to the original height and width to obtain a feature map with the same number of channels as the original, and then extract the attention weights in the width direction and height direction through the activation function. Finally, weighted fusion of feature maps in two directions is performed to obtain feature maps with attention weights in two directions. The CA structure is shown in Fig. 4.

For the pear inflorescence recognition task in this paper, both channel features and spatial features are meaningful, so this paper considers introducing a CA module into the network to improve the network's attention to target information. The specific way is to add the CA mechanism before the SPPF module after the last convolution operation of the backbone network part of YOLOv5s. Since the input and output feature maps of the CA module are of the same size, this addition does not change the network structure.

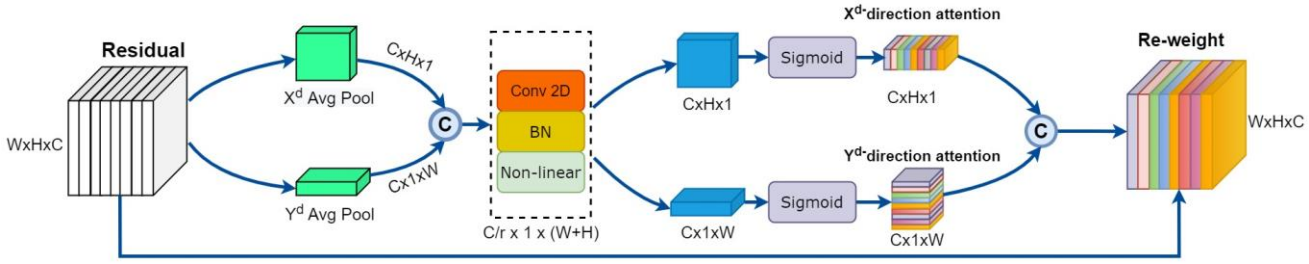


Fig. 4 – Structure of CA mechanism

Model training and evaluation indexes

The test hardware platform uses a desktop server equipped with Intel® Core E5 V3 CPU, 32 GB running memory, and 12 GB GeForce RTX 3090 GPU. The image input size is 640×640 pixels, the training epoch is set to 1000 rounds, the learning rate is initially 0.001, and hyperparameter evolution is used to dynamically adjust the learning rate through the loss rate of each round to speed up network training.

The accuracy evaluation mainly relies on the indicators of Precision, Recall, Mean Average Precision, and F1 score, which are calculated by formulas (1) to (5), respectively. In order to distinguish the recognition performance of the model, the parameter quantity, size and average run-time of the model are also important indexes for evaluation. The average run-time in this paper is obtained from running on the training platform.

$$P = \frac{TP}{TP + FP} \times 100\% \tag{1}$$

where:

P is precision, [%]; TP is true positive; FP is false Positive.

$$R = \frac{TP}{TP + FN} \times 100\% \tag{2}$$

where:

R is recall, [%]; FN is false negative.

$$AP = \int_0^1 P(R)dR \tag{3}$$

where:

AP is average precision of a class, [%].

$$mAP = \frac{\sum AP}{N(Class)} \tag{4}$$

where:

mAP is mean average precision, [%]; N is number of classes.

$$F1 = 2 \times \frac{P \times R}{P + R} \tag{5}$$

where: $F1$ is F1 Score, [%].

RESULTS AND DISCUSSION

In order to verify the superiority of the model that added CA mechanism, a comparative test between the original YOLOv5s network and the YOLOv5s network added with CA module (YOLOv5s-CA) was carried out. The performance indexes are shown in Tab. 1.

Table 1

Performance indexes of YOLOv5s and YOLOv5s-CA

Model	Class	Precision %	Recall %	F1 Score %	AP %	Parameter quantity	Average Run-Time / ms
YOLOv5s	Bud	87.33	84.16	85.72	88.54	7014617	21
	Flower	91.15	89.92	90.53	90.43		
YOLOv5s-CA	Bud	91.54	88.47	89.98	92.36	7041167	27
	Flower	94.27	93.73	94.00	94.27		

Tab. 1 shows that, the precision of YOLOv5s-CA network on the bud and flower object was increased by 4.21% and 3.12% respectively, and the recall was increased by 4.31% and 3.81% respectively, while the model parameter quantity was only increased by 0.3%. Compared with the quantity of model parameters, the precision and recall were greatly improved. In order to evaluate the contribution of CA mechanism to the network, the visual effect comparison of the two networks was carried out through gradient-weighted class activation mapping (Grad-CAM). Grad-CAM can convey network attention to the detection target through a heat map. The higher the heat value, the higher the attention of the network. Fig. 5 shows the heat map of target recognition using Grad-CAM for YOLOv5s and YOLOv5s-CA networks. The heat of the bud in Fig. 5c is higher than that in Fig. 5a, and obviously reduces in irrelevant background. For Fig. 5b and Fig. 5d, Fig. 5d removes the attention from the irrelevant background, while retaining the higher heat for the correct target and the area with high heat is better focused on the correct target area. Therefore, the network added CA module reduces attention to irrelevant information and increases the accuracy of the model. It can extract the overall feature information better than native YOLOv5.

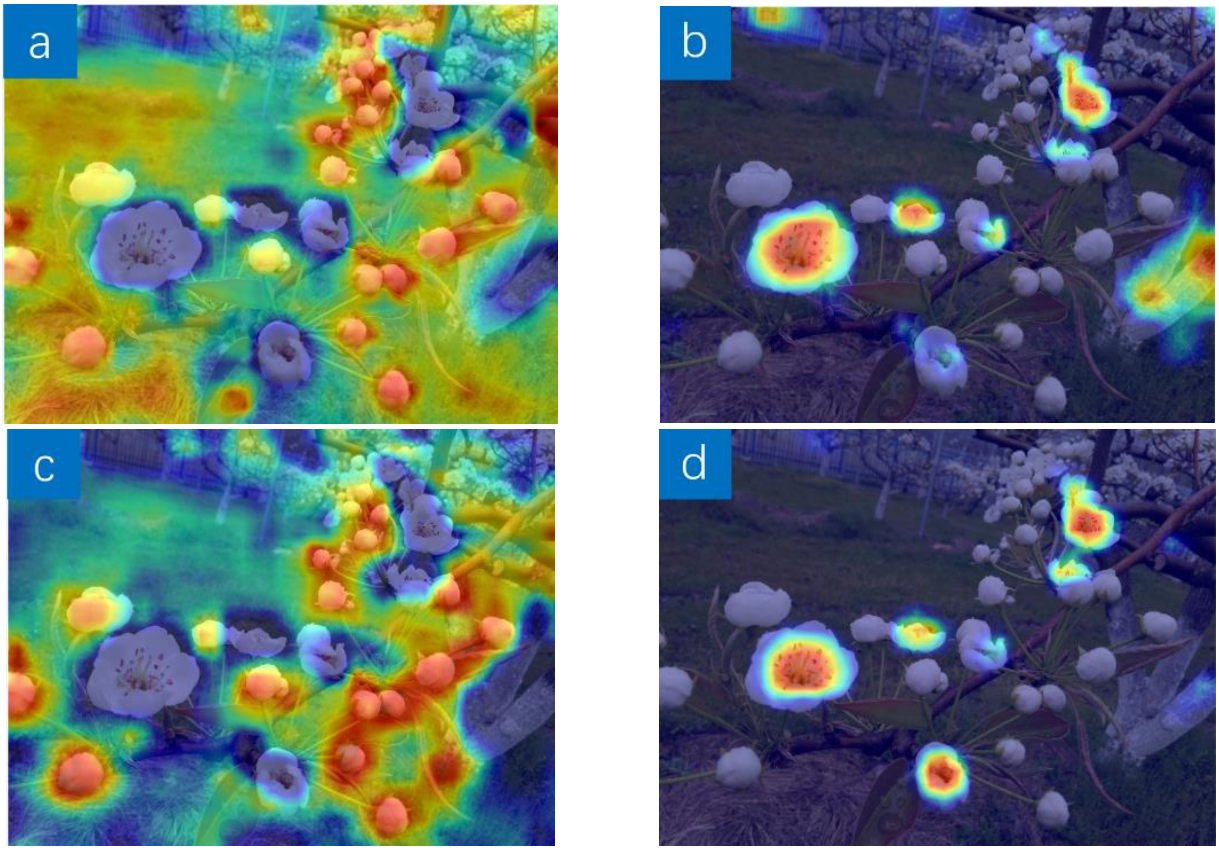


Fig. 5 – Network heat map

a, b represent the attention to buds and flowers without CA attention network;
c, d represent the attention to two types of targets after adding CA attention.

In order to compare the advantages of the model relative to other target recognition algorithms, general models SSD 300, Faster-RCNN and YOLOv3 were selected for performance comparison. In the test, the same data set and training platform were used for the 4 algorithms, and test results are shown in Tab. 2.

Table 2

Performance indexes of different detection algorithms

Algorithm	mAP %	Recall %	Model Size MB	Average Run-Time ms
SSD 300	81.53	82.76	36.71	25
Faster-RCNN	90.15	86.32	214.65	187
YOLOv3	89.71	87.46	206.36	23
YOLOV5s-CA	93.32	91.10	14.17	27

Tab. 2 shows that the mAP and recall rate of YOLOv5s-CA network is 93.32% and 91.10%, respectively, showing higher precision and recall rate than other algorithms. Compared with Faster-RCNN, the mAP and Recall of the YOLOv5-CA model were increased by 3.17% and 4.78%, respectively. At the same time, the model size was reduced by 200.48 MB and the detection speed was increased by 160 ms. Compared with SSD 300, which is also a one-stage algorithm, the mAP and recall of YOLOv5s-CA were increased by 11.79% and 8.34% respectively, the model size was reduced by 61%, and the detection time was increased by 2 ms. Compared with YOLOv3, the mAP and recall of YOLOv5s-CA was improved by 3.61% and 3.64%, the model size reduced by 192.19 MB, and the detection time increased by 4 ms. Although the detection accuracy of the two-stage algorithm was satisfactory, the detection speed was significantly lower than that of the one-stage algorithm. Therefore, two-stage algorithm is not suitable for intelligent blossom thinning equipment. In the one-stage algorithm, although YOLOv3 has better mAP and recall, its trained model is large and not suitable for actual deployment. The SSD 300 algorithm has a slight advantage in detection speed compared with YOLOv5s-CA, but it is almost negligible compared with the disadvantages of other indexes. In conclusion, YOLOv5s-CA algorithm has more advantages in actual deployment.

Pear trees are planted in relatively open orchards, and the actual detection environment is complex and has strong interference. Fig. 6 shows an example of the model recognition of some buds and flowers. From Fig. 6, it can be found that the model can effectively identify targets with different light intensities, shadows, occlusions, heterochromatic stamens, and slightly blurred targets.

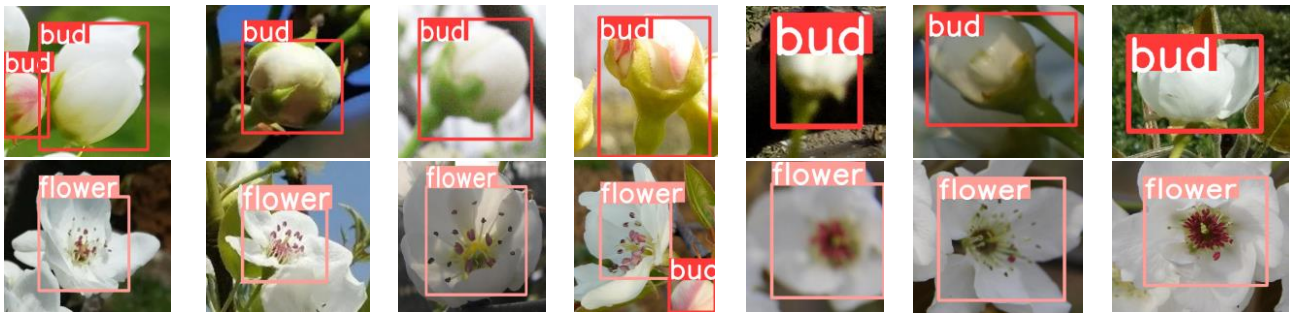


Fig. 6 – Bud and flower recognition

Although the model can work in most cases, there are many unrecognized cases in the actual application process. For example, the processing of small targets in target detection greatly affects the overall detection performance of the model. Fig. 7 shows the recognition effect of the model in this paper on small targets. When too many small objects appear, the model missed many objects. From the principle of the model, the reason is that the PAN feature fusion structure of the YOLOV5 network only fuses features of three different sizes. From the actual test effect, some targets can be detected using the feature fusion method of the original YOLOv5, but if these small targets need to be accurately detected, the current model is insufficient. In order to improve the problem of detection missing of small targets in the network, in future research, feature layers in the feature fusion network can be added according to the actual detection tasks and detection heads for small-scale targets in the detection heads of the network can also be added to improve the detection ability.



Fig. 7 – Small target detection

Similarly, the image blurring caused by camera performance also has a great impact on the target detection, as shown in Fig. 8. When the same branch is detected, the camera blurs the distant target and misses the detection. In the actual detection task, blurring will distort the characteristics of the target to a large extent, which will undermine the detection effect. In response to this problem, in this paper, Gaussian noise in the data enhancement part was added to improve the model processing capability. From the second picture of Fig. 8, it can be observed that some fuzzy targets were detected. However, due to the complexity of the specific recognition scene, there were still many virtual objects not detected. In order to improve the problem of detection missing caused by background blur, for future acquisition equipment, professional cameras without blur function can be adopted for data acquisition and detection to reduce detection missing caused by background blur.

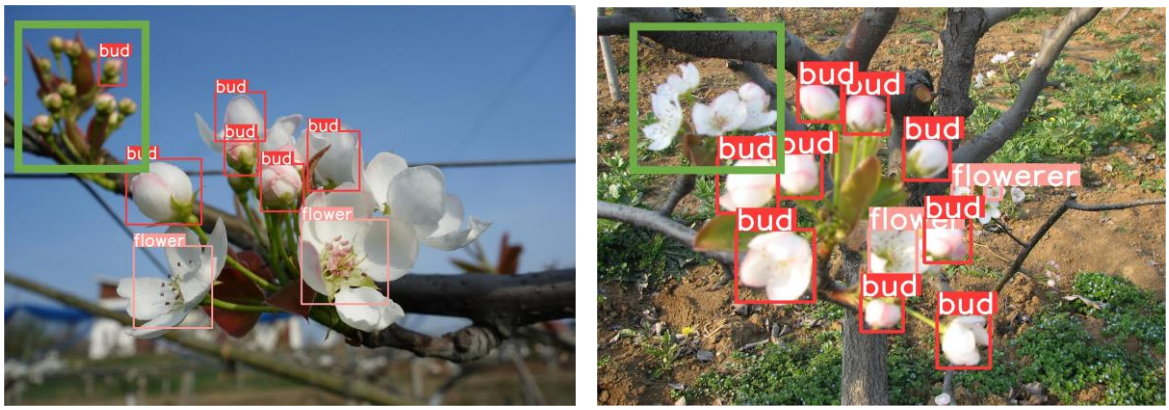


Fig. 8 – Image blurring

CONCLUSIONS

Thinning is a necessary agronomic section in pear orchard management. It can avoid biennial bearing and improve fruit quality. Intelligent blossom thinning method is necessary for the future development of blossom thinning equipment, especially the pear inflorescence detection algorithm based on deep learning. In this paper, an improved YOLOv5s model incorporating CA mechanism was proposed for identification of pear inflorescence. It can improve the network attention to the target information and improve the detection accuracy and efficiency.

(1) A total of 1566 original pictures were collected from the sample data. The pictures were captured in a real pear orchard environment with ideal conditions and possible lack of light, shadows, and overlapping occlusions. The augmentation program was compiled through the OpenCV library, and the original data were transformed by changing brightness, rotation angle, adding Gaussian noise, translation, mirroring, and clipping. The dataset after data augmentation reached 7830 images. Through data enhancement, more possible actual detection scenarios were expanded, and the generalization ability of the model was improved.

(2) The results of pear inflorescence test show that the improved YOLOv5s-CA model had a mAP of 93.32% and a recall of 91.10%. Compared with the native YOLOv5s network, the CA mechanism effectively increased the network's receptive field for the detection target, so that the network obtained higher mAP and Recall. Comparing YOLOv5s-CA with YOLOv3, SSD 300 and Faster-RCNN, the results show that the one-stage detection algorithm had better performance than the two-stage detection algorithm in the intelligent flower thinning recognition task. Among several one-stage algorithms, the YOLOV5s-CA model had better mAP and Recall. At the same time, the size of the model was only 14.1 MB, and the average detection speed was only 27 ms, which is more suitable for use in intelligent flower thinning embedded devices.

ACKNOWLEDGEMENT

The authors appreciate the financial support provided by National Natural Science Foundation of China (Grant No.32201680), China Agriculture Research System of MOF and MARA (Grant No. CARS-28-21), Jiangsu Modern Agricultural Machinery Equipment and Technology Demonstration Extension Fund (Grant No. NJ2022-14), National Science and Technology Development Program of China (Grant No. NK2022160104), Jiangsu Policy-guided Plans (Grant No. BX2019016) and Wuxi Science and technology development Fund (Grant No. N20221003).

REFERENCES

[1] Bochkovskiy, A., Wang, C. Y., & Liao, H. Y. M. (2020). Yolov4: Optimal speed and accuracy of object detection. *arXiv preprint arXiv:2004.10934*. https://doi.org/10.48550/arXiv.2004.10934

[2] Fan, Z. H. A. O., Zhang, J., Zhang, N., Zhiqiang, T. A. N., Yonghao, X. I. E., Zhang, S., ... & Mingbao, L. I. (2022). Detection of cucurbits fruits based on deep learning. *INMATEH-Agricultural Engineering*, *66*(1), pp.321-330. https://doi.org/10.35633/inmateh-66-32

[3] Farjon, G., Krikeb, O., Hillel, A. B., & Alchanatis, V. (2020). Detection and counting of flowers on apple trees for better chemical thinning decisions. *Precision Agriculture*, *21*(3), pp.503-521. https://doi.org/10.1007/s11119-019-09679-1

[4] Girshick, R., Donahue, J., Darrell, T., & Malik, J. (2014). Rich feature hierarchies for accurate object detection and semantic segmentation. *Proceedings of the IEEE conference on computer vision and pattern recognition.* pp. 580-587.

[5] Gregor, K., Danihelka, I., Graves, A., Rezende, D., & Wierstra, D. (2015). Draw: A recurrent neural network for image generation. In *International conference on machine learning,* pp.1462-1471. PMLR.

[6] He, K., Zhang, X., Ren, S., & Sun, J. (2015). Spatial pyramid pooling in deep convolutional networks for visual recognition. *IEEE transactions on pattern analysis and machine intelligence*, *37*(9), 1904-1916. https://doi.org/10.1109/TPAMI.2015.2389824

[7] Hou, Q., Zhou, D., & Feng, J. (2021). Coordinate attention for efficient mobile network design. *Proceedings of the IEEE/CVF conference on computer vision and pattern recognition,* pp. 13713-13722.

[8] Hu, J., Shen, L., & Sun, G. (2018). Squeeze-and-excitation networks. In *Proceedings of the IEEE conference on computer vision and pattern recognition,* pp. 7132-7141.

[9] Jin, Y. (2020). Recognition technology of agricultural picking robot based on image detection technology. *INMATEH-Agricultural Engineering*, *62*(3). https://doi.org/10.35633/inmateh-62-20

[10] Li, Y., Xiao, L., Li, W., Li, H., & Liu, J. (2022). Research on recognition of occluded orange fruit on trees based on YOLOv4. *INMATEH-Agricultural Engineering, 67(2)*. https://doi.org/10.35633/inmateh-67-13

[11] Redmon, J., Divvala, S., Girshick, R., & Farhadi, A. (2016). You only look once: Unified, real-time object detection. *Proceedings of the IEEE conference on computer vision and pattern recognition,* pp. 779-788.

[12] Redmon, J., & Farhadi, A. (2018). Yolov3: An incremental improvement. *arXiv preprint arXiv:1804.02767*. https://doi.org/10.48550/arXiv.1804.02767

[13] Ren, S., He, K., Girshick, R., & Sun, J. (2015). Faster R-CNN: Towards real-time object detection with region proposal networks. *Advances in neural information processing systems*, *28*.

[14] Shaifee, M. J., Chywl, B., Li, F., & Wong, A. (2017). Fast YOLO: A Fast You Only Look Once System for Real-time Embedded Object Detection in Video. *Journal of Computational Vision and Imaging Systems*, *3*(1). https://doi.org/10.15353/vsnl.v3i1.171

[15] Wang, D., & He, D. (2021). Channel pruned YOLO V5s-based deep learning approach for rapid and accurate apple fruitlet detection before fruit thinning. *Biosystems Engineering*, *210*, 271-281. https://doi.org/10.1016/j.biosystemseng.2021.08.015

[16] Liu, W., Anguelov, D., Erhan, D., Szegedy, C., Reed, S., Fu, C. Y., & Berg, A. C. (2016). SSD: Single shot MultiBox detector. *European conference on computer vision,* pp. 21-37. Springer, Cham.

RESEARCH ON OPTIMAL CONTROL ALGORITHM FOR POWER CHARACTERISTICS SEGMENTATION OF FORAGE HARVESTER
/
饲草收获机动力特性分割优化控制算法研究

Zheng WANG [1,2], Qingfu GONG [1], Fade LI [1], Ang GAO [1], Longlong REN [1], Yuepeng SONG[1,2,*]
[1] Shandong Agricultural University, College of Mechanical and Electrical Engineering/ China;
[2] Shandong Provincial Engineering Laboratory of Agricultural Equipment Intelligence/ China
E-mail: lntswangzheng@163.com
DOI: https://doi.org/10.35633/inmateh-69-02

Keywords: *Forage harvester; Dynamic allocation; Optimization control algorithm*

ABSTRACT
In order to improve the level of forage harvester automation and reduce damage, blockage and efficiency, based on the principle of minimum energy, fuzzy prediction theory and external characteristics of power, the mathematical model of the whole machine and each operating unit is established, and a set of forage harvester operating load adaptive feedback control system is designed; in order to make the power more scientifically and effectively distributed in real-time, the system adopts the simplified algorithm of operating unit efficacy threshold load splitting optimization control, with constant power and high efficiency. In order to make the power distribution more scientific and effective in real-time, the system adopts the simplified algorithm of operating unit efficacy threshold load splitting control to increase the load threshold of cutting and other operating units under constant power conditions, so that the operating efficiency of the whole machine can be improved. In the simulation test, the efficacy chopping load threshold ratio is about 1.08:1.01:1 for the three operation control methods of optimized control, fuzzy predictive control and PID control of the forage harvester, with 40% of the original feeding amount perturbation applied respectively, production efficiency was significantly improved.

摘要
为提高饲草收获机自动化作业水平和减损减堵提效，基于最小能量原理、模糊预测理论及动力外特性，建立整机及各作业单元的数学模型，并设计一套饲草收获机作业负荷自适应反馈控制系统：为使动力更加科学有效地实时分配，系统采用作业单元功效阈值负荷分割优化控制简化算法，恒动力条件下，提高切碎等作业单元的负荷阈值，从而使整机作业效能得到提升。仿真试验中，对饲草收获机的优化控制、模糊预测控制及 PID 控制三种作业控制方式，分别施加 40%的原喂入量扰动，功效切碎负荷阈值比约为 1.08:1.01:1。经现场试验，切碎负荷阈值比实际约为 1.078:1.004:1，该控制算法，使收获机的最大作业能力及其饲草生产效率都得到了明显提高。

INTRODUCTION

In recent years, many research attempts have been made at home and abroad to improve the automation and intelligence level of forage harvesters, select more appropriate feedback parameters, and innovate more advanced control algorithms to increase the efficiency and reduce the losses of forage harvesters, and great achievements have been made *(Chen et al., 2020; Chen et al., 2020; Li et al.2019)*.

Foreign scholar Jim Kruse used the engine load change to characterize the harvester load as a feedback parameter, and adjusted the walking speed of the whole machine in real time *(Jim,1983).* Kotyk et al. studied the load detection and feedback technology of the feeding amount of agricultural machinery, which reduced the operation power consumption and locked rotor failure rate, and improved the production efficiency *(Kotyk et al., 1991)*. Coen and others used fuzzy technology to build a control framework, and realized automatic operation of the combine based on model predictive control technology, reducing labour intensity *(Coen et al., 2006).* Baruah and others built the mathematical model of the whole machine based on the overall energy consumption *(Baruah et al., 2005)*; Reddy et al. fused explicit knowledge of design and implicit knowledge of design intent from the perspective of mechanical modeling technology of intelligent agricultural machinery to improve the flexibility, adaptability and reusability of the model *(Reddy et al., 2018)*.

Zheng Wang, Ph.D. Stud. Eng.; Qingfu Gong, M.Sc. Stud. Eng.; Fade Li, Prof. Ph.D. Eng.; Ang Gao, M.Sc. Stud. Eng.; Longlong Ren Lecturer Ph.D. Eng; Yuepeng Song, Prof. Ph.D. Eng.

Some students of China Agricultural University used digital modeling for high-end complex intelligent agricultural machinery and equipment to form a digital design technology system platform suitable for typical agricultural equipment products such as tractors and combine harvesters *(Du et al., 2019; Zhai et al., 2021).* Zhang Zhicheng et al. implemented intelligent control of work load based on fuzzy technology and variable quality working condition, proposed and implemented single-chip fuzzy control technology, which is not convenient for realizing strong nonlinear threshing drum of harvester when applied to traditional control theory automatic control of complex systems *(Zhang et al., 2001; Ji et al., 2008).* Li Guodong studies the constant speed of work based on pattern recognition technology, to further improve the robustness and discrimination of recognition. The low rank discriminant adaptive optimization algorithm is also proposed to solve the objective function and its effectiveness is verified *(Li et al., 2007)*. In addition, Ni Jun applied FPGA design speed fuzzy controller for specific real-time problems such as large inertia time delay *(Ni et al., 2009)*, and Qin Yun of Jiangsu University used neural network adaptive generalized predictive control technology to achieve control parameter output under different working conditions *(Zhao, 2009; Dong, 2010; Qi, 2012)*. However, they are often restricted by the level of software, hardware and other conditions. In terms of the specific application effect of the control algorithm for indicators such as steady-state accuracy, dynamic responsiveness and robustness, some studies can strengthen the characteristics of the controlled object, but are limited by the number of control parameters of the research object *(Yang, 2007)*; It ensures the dynamic stability output of the equipment, but the research on the time-delay control problem that may cause sudden changes in working conditions is relatively insufficient *(Rahman et al., 2020; Zakwan et al., 2021; Pan et al., 2010)*.

Therefore, the integration and optimization of control algorithms has gradually become a hot topic for many scholars at home and abroad. The literature *(EIOT Big Data Lab, 2018)* points out that optimization algorithms play an obvious role in the improvement of operation accuracy, energy saving etc., but the improvement of efficiency under the adaptivity and high computational difficulty needs to be researched and broken through.

On the basis of ensuring the effect of the above traditional control algorithm research and application, this paper establishes the mathematical model and control system design of the whole machine and each work unit, proposes and implements an optimal control algorithm for reasonably dividing the threshold load of work, that is, in the control process, the threshold load is divided into zero, the system output is efficiently transferred from any initial condition to another terminal condition in a limited time, and hierarchical closed-loop control is implemented (PID, Fuzzy and predictive, etc.). The system output controllability is enhanced, the operation threshold load is improved, and the operation is simplified and the output value is stable.

MATERIALS AND METHODS

Minimum power distribution model

Forage harvester

The structure of forage harvester test bench is shown in Figure 1.

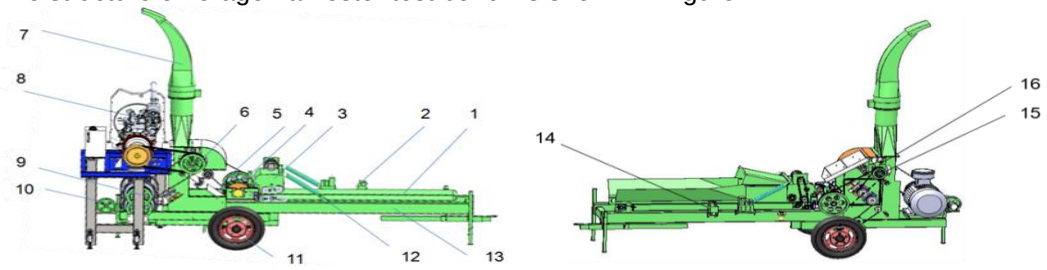


Fig. 1 - Forage harvester structure drawing
a) Right side of test bench; b) Left side of test bench

1. Feeding device; 2. Hydraulic signal proportional valve; 3. Cutting device; 4. Fixed knife and its regulating mechanism; 5. Grain crushing device; 6. Throwing mechanism; 7. Central tube bursting-type; 8. Diesel engine; 9. Motor; 10. Duplex hydraulic pump; 11. Traveling device; 12. Feed roll spring and tension sensor; 13. Frame; 14. Hydraulic flow signal proportional valve; 15. Speed Hall sensor; 16. Pressure sensor of drive belt

Table 1

Main operation technical parameters of forage harvester test bed

Project	Parameter
Length x Width x Height / mm	5454×2180×4319
Feeding system	belt
Feed inlet width / mm	535
Hobbing cutter rotation speed / $r \cdot min^{-1}$	1300
Feeding method	automatic straw feeder

Project	Parameter
Crop feeding per unit length kg / (m·s) Cutter roll type and specification Diameter x length / mm	5 Plate type drum cutter 476×560
Moving knife arrangement	"V" arrangement
Number of moving knives / piece Moving and fixed tool clearance / mm Slip cut angle / deg. Minimum working clearance of conditioner roll / mm	16 1 10° 1.5
Diesel engine power /kW	103.8
Rated speed / r·min^{-1}	2300
Maximum no-load speed / r·min^{-1}	2485±30
Idling / r·min-1	800±20
Maximum torque / N·m	562
Maximum torque speed / r·min^{-1}	1400～1800
Governor type	Whole process steel ball
Speed regulation range / r·min^{-1}	0～2300
Productivity /kg·h^{-1}	17×10^3（Fresh forage）

As shown in Figure 1, the forage harvester test-bed is mainly used for silage and yellow storage of forage. It can complete the feeding and conveying, chopping, crushing, throwing and loading of plants at one time. Its main operating loads and state quantities include feeding load, chopping roll speed, crushing roll speed, throwing fan speed, crop loss, crop height, etc. The operation characteristics of forage harvester (high-order nonlinearity, time variation, large inertia, pure time delay, parameter drift, asymmetry, etc.) are complex. In order to obtain better control effect, it is necessary to design and configure the automatic control system for the overall load of the harvester *(Ni et al., 2009)*, according to the actual working conditions reflected by the load data in the operation process, with the help of real-time optimal control of appropriate operation parameters. That is, the transmission belt pressure detection system detects the transmission belt load data in real time during the operation process, and timely feeds back the actual working conditions expressed by the data to the overall load of the harvester and the crop feeding control system. With the help of real-time control and adjustment of appropriate operating parameters, the control system realizes further automatic optimization and adjustment of the quality and efficiency of operations such as chopping, flattening and throwing, and reduces failures such as rotor blockage, wear and energy consumption, and ensure that the overall load of the harvester is in the best state for a long time *(Zhao, 2009)*. Table 1 shows the main operating parameters of the harvester. The rated productivity is 17×10^3 kg-h^{-1}, about 4.72 kg-s^{-1}. Since the cutting width of 535 mm is similar to the effective width of the chopping roller of 560 mm (feeding transverse length), the crop feeding volume per unit (cutting transverse) length was regularized to 5 kg/(m-s) in the field test.

The composition of main operation units of forage harvester is shown in Figure 2. The figure shows the specific installation and layout of the modules of each main operation unit of the forage harvester and the actual sample of the cutter roll of the shredding operation unit. The power transmission system structure of forage harvester is shown in Figure 3. The figure shows the power transmission system structure of the forage harvester, which is composed of belt transmission and hydraulic transmission.

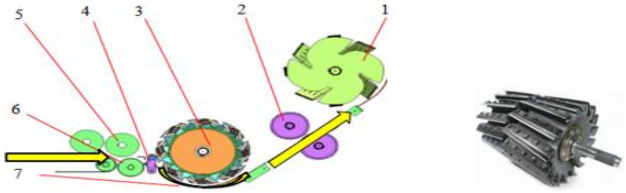


Fig. 2 - The main unit of work location and chopping unit diagram

1. Throwing device; 2. Grain crushing roller; 3. Chopping roller; 4. Fixed knife; 5. Upper feeding roller; 6. Lower feeding roller; 7. Chopping bottom arc plate

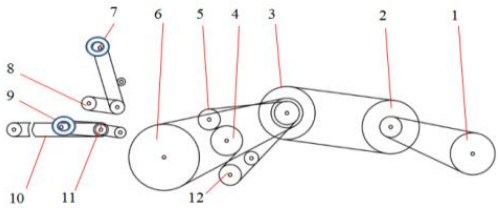


Fig. 3 - Schematic diagram on drive system for Forage Harvester

1. Hydraulic pump; 2. Engine pulley (largest); 3. Throwing device pulley (largest); 4. Lower grain crushing roller pulley; 5. Upper grain crushing roller pulley; 6. Chopper pulley; 7. Upper feed roller sprocket hydraulic motor; 8. Upper feed roller sprocket; 9. Lower feed roller sprocket hydraulic motor; 10. Conveyor belt; 11 Lower feed roller sprocket; 12. Tensioner wheel

The overall structure of the forage harvester operation load model is shown in Figure 4.

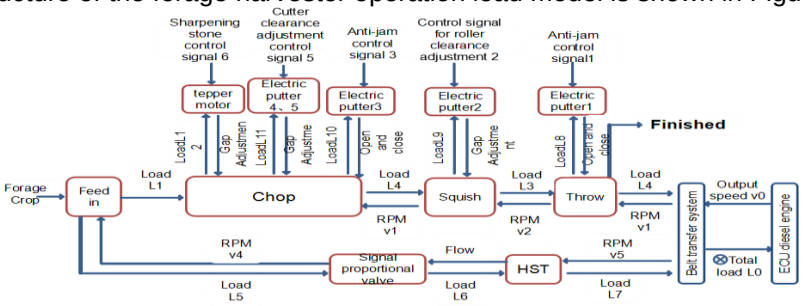


Fig. 4 - Load model structure of the forage crop harvester

Figure 4 shows that the main operating loads of the forage harvester test stand are, feeding load, chopping load, flattening load and throwing load, etc. The engine power is given to the main operating loads with reasonable algorithmic control distribution.

The functions of the control system are shown in Figure 5.

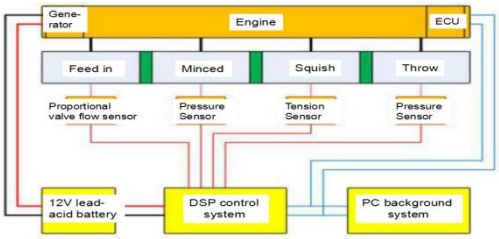


Fig. 5 - Functional Block Diagram on

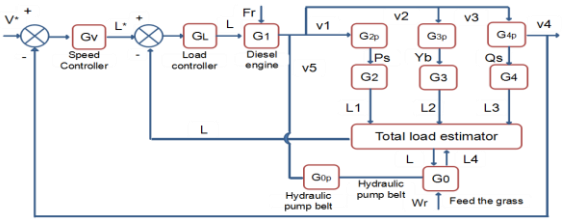


Fig. 6 - Forage harvester load control system structure drawing

The PID and other control systems of forage harvester operation are designed according to Fig. 5 and Fig. 6. The information of operating loads such as feeding, chopping, squashing and throwing are collected by the corresponding sensors and transmitted to the DSP information processing module of the main control board of the lower computer, and after the overall calculation, the control commands such as speed and torque are output to the engine through CAN bus to make the operating system run controllably in a stable and efficient way.

Minimum dynamic model and optimization objective

The power allocated to each operation unit in real time is the minimum, which can be equivalent to the minimum functional value of the objective function of the rotation angle and thrust of the main shaft of each operation unit of the harvester *(Gu et al., 2011)*. The objective function and constraint conditions of the rotation angle of the main shaft of the unit are:

$$J_{des} = \min\ J_i(\Delta\alpha, \Delta f, s) = \sum_{j=0}^{m}\left(\frac{dW_j}{df_j}(f_{0,j})\Delta f_j + \frac{d^2W_j}{df_j^2}(f_{0,j})\Delta f_j^2 + s^T Q s + \Delta\alpha^T \Omega \Delta\alpha\right) \quad (1)$$

The constraints are:

$$s.t. \quad s + B(\alpha_0)\Delta f + \frac{\partial}{\partial\alpha}(B(\alpha)f)\Big|_{\substack{\alpha=\alpha_0 \\ f=f_0}} \cdot \Delta\alpha = u - B(\alpha_0)f_0 \quad (2)$$

$$f_{min}/p - f_0 \le \Delta f \le f_{max}/p - f_0 \quad (3)$$

$$\alpha_{min} - \alpha_0 \le \Delta\alpha \le \alpha_{max} - \alpha_0$$

$$\Delta\alpha_{min} \le \Delta\alpha \le \Delta\alpha_{max}$$

where, J_i is the index value for the reduction of total power energy consumption of the unit; f_0 is the spindle thrust from the previous time's work unit; p is the force reduction factor *(Johansen et al., 2004)*; α is the spindle thrust angle; s is the spindle thrust error; The j operation period; m total of job periods; W is to minimize energy consumption; Q is the change rate of spindle thrust; Ω is the change rate of thrust azimuth angle of main shaft; u is the thrust command, and the first order inertia link of the low-pass filter is applied to it. Based on this objective function model, the dynamic and kinematic equations of each operation module and the whole machine of the equipment are established respectively.

The objective function and constraints of the spindle thrust of the work unit are:

$$\min\left\{J_i = f^T W f + s^T Q s\right\} \tag{4}$$

$$s.t. \quad B(\alpha) f = u + s \tag{5}$$

$$f_{\min} \le f \le f_{\max}$$

$$\Delta f_{\min} \le f - f_0 \le \Delta f_{\max}$$

Where, J_i is the optimal target value of the energy consumption reduction index of the work unit, f is the unit spindle thrust. Since the thrust azimuth of the main axis of the element $\alpha = \alpha_0 + \Delta\alpha$ can be calculated, the elements in the matrix $B(\alpha)$ are constant. In order to simplify the real-time calculation, u is a unit spindle thrust command with recursive relationship, so that the constraint conditions $B(\alpha) f = u + s$ are linear equations, which can avoid errors when the constraint conditions are linearized.

According to equations (2) and (5) below, the cutting operation unit of forage harvester is taken as the research object, and the control constraints of optimization algorithm are applied to the maximum value of real-time output of the cutting load division operation section, so as to reduce the load of the cutting operation system, reduce the energy consumption and locked rotor rate under the constant load, and finally improve the effective efficiency, where is the real-time load value of the operation; It is the load threshold of each divided operation segment. Therefore, it is proposed to optimize the control trajectory of the workload as shown in Figure 7.

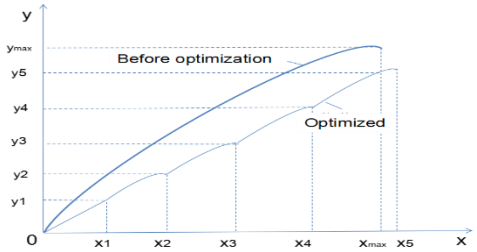


Fig. 7 - Schematic diagram of load control trajectory before and after optimization

In Figure 7, PID simplifies the design of the control system, and the traditional PID control algorithm expression is: $u(t) = K_p e(t) + K_i \int_0^t e(x)dx + K_d \frac{de(t)}{dt}$, where $u(t)$ is the output of the controller at t time, $e(t)$, $K_i \int_0^t e(x)dx$、$K_d \frac{de(t)}{dt}$ are the load control error, accumulation error and error change rate of the shredding and other operating units at time t respectively; K_p, K_i, K_d are the proportional, integral and differential parameters of PID control respectively. The fuzzy algorithm can enable the control system to define complex working conditions or have the strong robustness function of replanning definition and adaptation, and the predictive performance can eliminate the time delay in the operation process and save the system time to a certain extent. The above traditional algorithms adjust the control system according to deviation, deviation accumulation or deviation early warning value, and the internal constraints are small. Modern control is to adjust the performance of the system by entering and adjusting the characteristic values of the equation of state of the system, imposing constraints on both internal and external factors. The PID algorithm and fuzzy prediction algorithm with undivided task threshold load are pre-optimization algorithms. The fuzzy prediction algorithm of task threshold load segmentation is the optimization control algorithm of this study. The optimization control goal is that the load and energy consumption borne by the cutting knife with the same feeding amount at the same time are increased and reduced after optimization compared with before optimization.

Design of the chopping threshold load divider

Fitting and segmentation of engine external characteristic curve

The least square method is used to fit the fifth-degree polynomial of the dynamic characteristic curve, the equation derivation is used for quantitative prediction and segmentation, and the functional optimal trajectory algorithm is used.

The method steps are as follows:

Least square polynomial fitting equation of dynamic external characteristic curve. The least square fitting equation of engine speed torque external characteristic curve is obtained by Matlab:

$$\begin{cases} f(x) = 5.804\times10^{-13}x^5 - 4.378\times10^{-9}x^4 + 1.293\times10^{-5}x^3 - 0.019x^2 + 14.2x - 3874 \\ f'(x) = 2.902\times10^{-12}x^4 - 1.7512\times10^{-8}x^3 + 3.879\times10^{-5}x^2 - 0.038x + 14.2 \\ f''(x) = 1.1608\times10^{-11}x^3 - 5.2536\times10^{-8}x^2 + 7.758\times10^{-5}x - 0.038 \\ f'''(x) = 3.4824\times10^{-11}x^2 - 1.05072\times10^{-7}x + 7.758\times10^{-5} \end{cases} \quad (6)$$

Boundary value calculation and segmentation. Calculate the inflection point value of the above torque acceleration equation as the boundary value of the following functional prediction segmentation:

a. Boundary value calculation and segmentation

Calculate the inflection point value of the above torque acceleration equation as the boundary value of the following functional prediction segmentation:

The engine torque f value corresponding to the positive engine torque acceleration f ': (f 0 = 343.1, f '0=0); (f 1 =488.9, f '1=0); (f 2 = 497.3, f' 2=0.061); (f 3=507.8, f '3=0.122); (f 4 = 525.9, f '4 = 0.182); (f 5 = 562, f '5 = 0.182).

The engine torque f value corresponding to negative engine torque acceleration f' : (f 0 =562, f '0 = 0); (f 1 =561.6, f '1 = 0); (f 2 = 555.8, f' 2 = -0.102); (f 3 = 538.5, f '3= -0.203); (f 4 = 486.6, f '4 = -0.305); (f 5 =343.1, f '5 = -0.305).

Adopt the forecast segmentation method:

The engine torque f value corresponding to the positive engine torque acceleration f ': [343.1-525.9][0-0.182]; [488.9-525.9][0-0.182]; [497.3-525.9][0.061-0.182]; [507.8-525.9][0.122-0.182]; [525.9-525.9][0.182-0.182].

The engine torque f value corresponding to negative engine torque acceleration f ' : [525.9-437.5][-0.305-0]; [561.6-437.5][-0.305-0]; [555.8-437.5][-0.305--0.102]; [538.5-437.5][-0.305--0.203]; [486.6-437.5][-0.305--0.305].

Regularize the above segmentation into values in the interval [0,1] and [-1,0]:

Forward engine torque f and torque acceleration f ': (x1,x2)=[0,0]; [0.65, 0]; [0.93, 0]; [0.95, 0.33]; [0.97, 0.67]; [1, 1].

Negative engine torque f and torque acceleration f ': (x1,x2)=[0,0]; [0.20, 0]; [0.28, 0]; [0.27, -0.33]; [0.23, -0.67]; [0.11, -1]; [0, -1].

The power distributed to the shredder roll in real time is the minimum, which is converted into the minimum index function of the throttle thrust and angle of the diesel engine. The system state equation is set as: $\dot{x}_1(t)=x_2(t)$, $\dot{x}_2(t)=u(t)$; Boundary condition: the threshold load of shredding is measured through test, and it is also regular as 1 for convenience of programming and calculation; Initial state of engine torque *f* and torque acceleration *f'*: $[x_1(0), x_2(0)]$, final state $[x_1(t_r), x_2(t_r)]$.

b. Solution of optimal control trajectories of load functional

The fuzzy nonlinear predictive PID control with task threshold load segmentation is adopted. First, the shredding load algorithm is segmented and each boundary value is obtained. Then, the time-varying system is approximately simplified into a linear constant system through the generalized Lipschitz continuity condition (the minimum coefficient is taken in the test) and spline interpolation function applied in the prediction algorithm. Finally, the optimal control trajectory of each segment is solved using the minimum energy control principle. Construction of Hamiltonian function:

The control system is approximately a discrete steady system with fixed and free ends; According to equations (1), (2), (4) and (5), in order to avoid solving differential equations and singular structural terms, under the action of thrust reduction coefficient, p etc., to minimize the energy consumption, control constraints $|u(t)| \le 1$ are taken to determine the optimal control of all output solutions $u^*(t)$, and achieve the minimum energy performance index of equations (1) and (4). It can be equivalent to the shredding performance index:

$$J_{qdes} = \int_0^{tf} u^2(t)dt = \min$$

Sectional condition, boundary condition and law of variation H *(Hu,2007):*

$$x(t_0) = x_0,\ x(t_f) = x_f,\ \ H^*(t_f^*) = 0 \quad (7)$$

In order to turn the functional extremum with equality constraints into the functional extremum without constraints, according to formula (7), the Lagrangian multiplication operator is used to construct the Hamiltonian function $H(x, u, \lambda, t)=L(x, u, t)= \lambda^T(t)\, f(x, u, t)$, and the following results are obtained:

$$H = u^2 + \lambda_1 x_2 + \lambda_2 u = \left(u + \frac{1}{2}\lambda_2\right)^2 + \lambda_1 x_2 - \frac{1}{4}\lambda_2^2 \tag{8}$$

which:

$$\begin{bmatrix} x_1 \\ x_2 \\ u \\ \lambda \end{bmatrix}(t) = \begin{bmatrix} \frac{1}{12}C_1 t^3 - \frac{1}{4}C_2 t^2 + C_3 t + C_4 \\ \frac{1}{4}C_1 t^2 - \frac{1}{2}C_2 t + C_3 \\ \frac{1}{2}(C_1 t - C_2) \\ -\frac{\partial H}{\partial x_1}, -\frac{\partial H}{\partial x_2} \end{bmatrix} \tag{9}$$

where, $x_1(t)$ is speed, $x_2(t)$ is torque, $u(t)$ is control quantity, $\lambda_i \in R^n$ is Lagrange multiplier vector, H is Hamiltonian function, and C_i is undetermined coefficient.

From the minimum condition:

$$u^*(t) = \begin{cases} +1, & \lambda_2(t) < -2 \\ -\frac{1}{2}\lambda_2(t), & |\lambda_2(t)| \le 2 \\ -1, & \lambda_2(t) > 2 \end{cases} \tag{10}$$

The optimal control is determined by the combination of the optimal trajectory change law and the final state conditions, so that the forage crops are fed from the known initial state, the equal quality processing is transferred to the control target set, and the fuel consumption is:

Forward sectional load: $J = -W(t_f) \to \min$

Segment I boundary conditions: $x_1(0) = 0$, $x_2(0) = 0$; $x_1(t_f) = 1$, $x_2(t_f) = 1$;

⋮ ⋮

Segment VI boundary conditions: $x_1(0) = 0.97$, $x_2(0) = 0.67$; $x_1(t_f) = 1$, $x_2(t_f) = 1$.

Load of each section in negative direction:

Segment I boundary conditions: $x_1(0) = 0$, $x_2(0) = 0$; $x_1(t_f) = 0$, $x_2(t_f) = -1$;

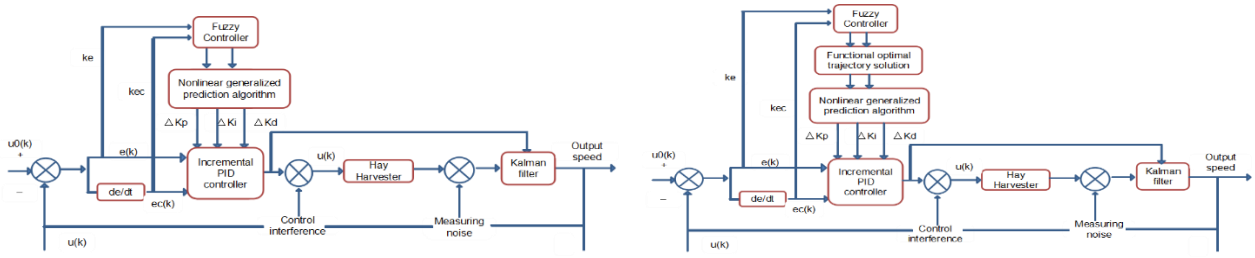
⋮ ⋮

Segment VI boundary conditions: $x_1(0) = 0.11$, $x_2(0) = -1$; $x_1(t_f) = 0$, $x_2(t_f) = -1$.

After checking the $u(t_f) = \frac{1}{2}(C_1 t_f - C_2)$ of each segment, the conditions of $[0, t_f]$ and $|u(t)| \le 1$ are met in the $|\lambda_2(t)| \le 2$ segment, and $x_2^*(t) = \int u^*(t)\, dt$ is obtained for each segment; $x_1^*(t) = \int x_2^*(t)\, dt$ optimal control trajectory equation.

Application of splitter

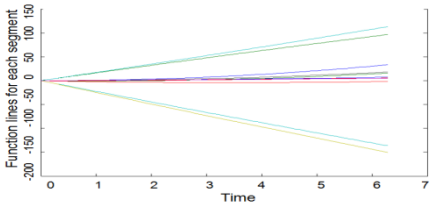
The structure of the shredding threshold load undivided Kalman fuzzy nonlinear generalized predictive controller *(Fan et al., 2017)* is shown in Figure 8a. The structure of the chopped threshold load split Kalman fuzzy nonlinear generalized predictive controller is shown in Figure 8b. This structure is based on the former with an optimization control algorithm module.



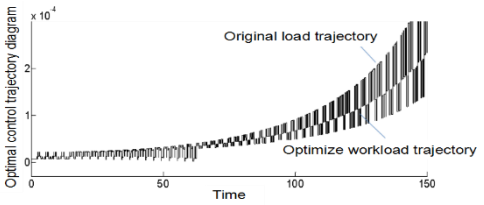
a Fuzzy Predictive PID Control Model b Fuzzy Predictive PID Optimal Control Model

Fig. 8 - Structure diagram of Emmerich Kálmán-fuzzy nonlinear generalized predictive controller

In the optimization control model, the shredding threshold load segmentation algorithm module is placed between the fuzzy algorithm module and the prediction algorithm module. After the fuzzy shredding load parameters are input. The output and prediction algorithm modules feedback control the shredding operation cycle. The function graph lines of each segment after segmentation are shown in Figure 9a, and the optimized trajectory graph lines in slope load control are shown in Figure 9b.



a Function lines of each segment after segmentation



b Optimal trajectory in slope load control

Fig. 9 - Split diagram and control application diagram

Figure 9a shows the optimal control trajectories of each load segment based on the segmentation and minimum energy principle algorithm, and the linear segments with different approximate slopes. Figure 9b controls and adjusts a slope load simulation optimization algorithm with random input, and compares the graph and line conditions before and after the optimization control, showing the control adjustment of the same load at the same time, which is finally reduced compared with that before the optimization.

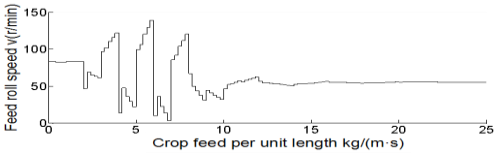
RESULTS

Simulation analysis

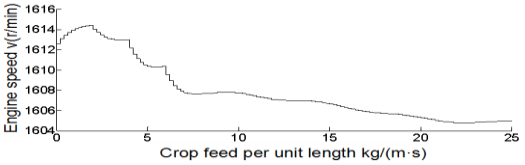
Under normal operation state, the simulation of steady state and disturbance transient response under PID control, fuzzy prediction (cutting threshold load is not divided) control, fuzzy prediction (cutting threshold load is divided) optimization control of forage harvester's cutting threshold load. After the normal operation is stable for a certain period of time, apply quantitative step and slope disturbance signals to the three working conditions respectively, detect the response of system parameters to the disturbance, and compare the operation effects before and after optimal control.

Steady state simulation of PID control, fuzzy predictive control and optimization control

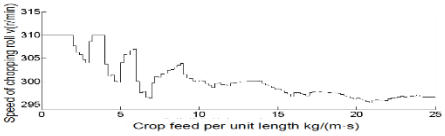
The PID load feedback control system is used to control the cutting threshold load of the forage harvester. Under the condition of a certain amount of crop feed input, after a long enough time, the steady-state values of the engine, the feed roll and the cutting roll are detected, and the steady-state control results are obtained, as shown in Figure 10.



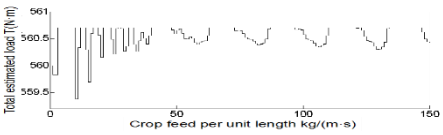
a) Rotation speed of closed-loop feeding roller and crop feeding amount



b) Closed loop engine speed and crop feed



c) Rotation speed of closed loop chopper roll and crop feeding rate



d) Closed loop population estimation load and crop feeding

Fig. 10 - Steady-state simulation diagram of closed-loop speed

The test results are shown in Figure 10. Engine: when the crop feeding amount is small, the controller automatically increases the speed of the chopping roll to obtain a larger feeding amount. When the crop feeding amount is less than 8 kg/(m▪s), the engine speed changes little. When the crop feeding amount exceeds 8 kg/(m▪s), the controller will gradually reduce the speed of the chopping roll, which will make the feeding amount tend to keep at the required level for operation. Feeding roller: the rotating speed is basically constant at about 55 r/min; The engine speed is still basically constant at about 1605 r/min; The speed of the chopping roll is basically constant at about 1295 r/min. Influenced by the real-time evaluation of the overall load estimator in the model, the feed roll speed, engine speed and chopping roll speed fluctuated during the stabilization process. See Table 2 for steady state deviation of feed roll, chopper roll and engine speed.

Table 2

Steady-state simulation deviation of operating unit speed for each model

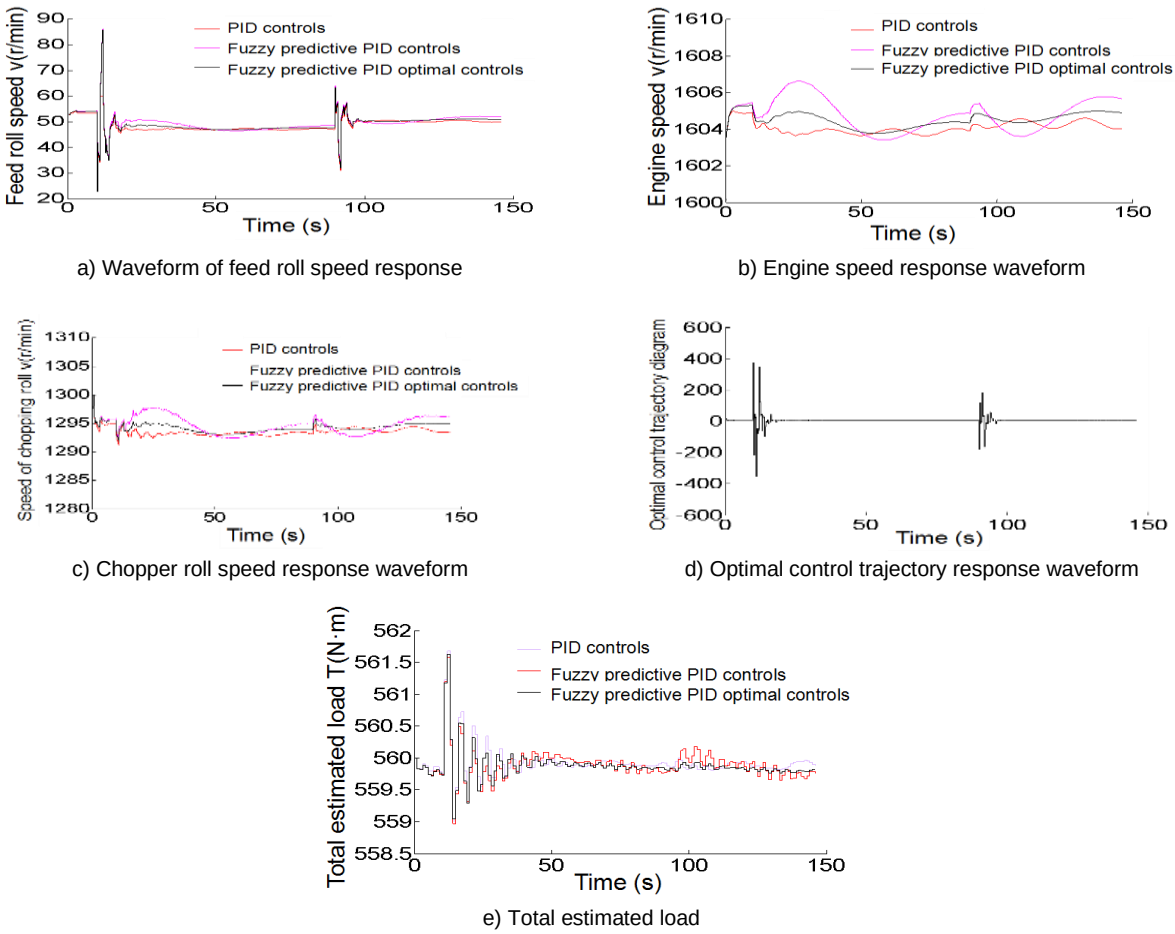
Model type	Steady state deviation of feed roll speed (r/min)	Steady state deviation of chopping roll speed (r/min)	Steady state deviation of engine speed (r/min)
PID control	0.393	5.16	0.23
Fuzzy predictive control	0.340	3.70	0.25
Fuzzy predictive optimal control	0.300	4.33	0.07

The steady state deviation of the feed roll speed, the optimal control<fuzzy predictive control<PID control; Steady state deviation of chopping roll speed, fuzzy predictive control<optimal control<PID control; Steady state deviation of engine speed, optimal control<PID control<fuzzy predictive control. The steady-state error of the overall optimal control is the smallest, and the steady-state error of the PID control is the largest.

PID control, fuzzy predictive control and their optimal control Simulation of transient response to step disturbance:

Positive disturbance feeding: First, the harvester shall be at 5 kg/(m▪s). And then apply 2 kg/(m▪s) at 15 s. Feed loaded, test the transient response of the harvester engine speed, chopping speed and feed roll speed. Negative disturbance feeding: The harvester shall be at 7 kg/(m▪s) for stable operation under feeding of, subtract 2kg/(m▪s) feed load, test the transient response of the harvester engine speed, chopping speed and feed roll speed.

The simulation results are shown in Figure 11.



a) Waveform of feed roll speed response

b) Engine speed response waveform

c) Chopper roll speed response waveform

d) Optimal control trajectory response waveform

e) Total estimated load

Fig. 11 - Closed-loop simulation of step-positive and negative-disturbance transient response of crop feed per unit length

The torque corresponding to each speed is calculated according to equation (6), and the product of the load disturbance response time is obtained. The energy consumption of each model for load control is shown in Table 3.

Table 3

Speed and disturbance response time of model engines

Model type	Chopper roll disturbance speed (r/min)	Chopper roll disturbance torque (N·m)	Chopper roll disturbance response time (s)	Chopping energy consumption (10^4J)
PID control	1308.2	535.57	12.2	3.296
Fuzzy predictive control	1292.2	532.85	15.2	3.913
Fuzzy predictive optimal control	1292.4	532.89	11.0	2.575
Energy consumption comparison of shredding	Fuzzy predictive optimal control<PID control<fuzzy predictive control			

According to the disturbance simulation analysis of steady state and positive and negative feeding loads, in terms of improving the maximum operating capacity, the optimal control>PID control>fuzzy predictive control; For the response time of disturbance load, the optimal control<PID control<fuzzy predictive control; In terms of control robustness, optimal control<fuzzy predictive control<PID control; In terms of disturbance energy consumption, PID control is superior to fuzzy predictive control, and optimal control is superior to PID control. It can be seen that the optimization algorithm based on fuzzy predictive control plays an obvious role.

Test and result analysis

The test crop is corn straw, and the forage harvester test bench is first set at 2.5 kg/(m▪s). After stable operation for a period of time, increase to 5 kg/(m▪s), implement the feedback control of the forage harvester's operating load, and test the relationship between the steady state and transient responses of the harvester's engine speed, feed roll speed and the pressure load change of the chopping drive belt, as shown in Figure 12.



a) Quantitative weighing of corn straw



b) Quantitative feeding of corn straw



c) Chopping transmission belt pressure detection mechanism and optimal control of processed straw

Fig. 12 - Corn stalk chopping and other work load feedback control experiment

The initial design speed of the engine is 1000 r/min, the initial design pressure of the liquid suspension jacking roller of the chopping drive belt is 2.04 MPa, the input value of the chopping drive Belt pressure is 3.28 MPa, and the different PI controller parameter input values (K_p, K_i) of the control model in different time periods are shown in Table 4. The operation control verification of the pure mechanical operation, PID control, fuzzy predictive control, and fuzzy predictive optimization models is carried out.

Table 4

K_p and K_i input values for different time periods

Time	[0,18465]	[18466,35757]	[35758,47102]	[47103, 50268]
Control	Pure	PID control	Fuzzy predictive	Fuzzy predictive optimal
K_p, K_i	(0, 0)	(0.72, 0.23)	(0.58, 0.14)	(0.80, 0.26)

The speed disturbance response of the work unit under the control of each model on site is shown in Table 5, the steady state deviation of the speed of the work unit is shown in Table 6, the speed change and response time of the work unit are shown in Table 7, and the maximum disturbance tracking deviation of the speed of the work unit is shown in Table 8.

Table 5

Speed and disturbance response time of model engines

Control model	Feed roll speed (r/min)	Chopper roll speed (r/min)	Engine speed (r/min)
Pure machinery	54.77	798.2	911
PID control	54.83	708.0	906.5
Fuzzy predictive control	54.86	676.4	919
Fuzzy predictive optimal control	54.86	679.1	906

Table 6

Steady-state simulation deviation of operating unit speed for each model

Control model	Steady state deviation of feed roll speed (r/min)	Steady state deviation of chopping roll speed (r/min)	Steady state deviation of engine speed (r/min)
Pure machinery	1.368	24.0	8.05
PID control	0.668	26.5	14.22
Fuzzy predictive control	0.892	21.2	16.40
Fuzzy predictive optimal control	1.793	18.6	6.12

Table 5 and Table 6 show that the engine speed under optimal control is the lowest, and the steady state deviation of the shredding unit and the engine is the lowest.

Table 7

Simulation of operating unit speed change and response time disturbance under each model

Control model	Speed variation of feeding roller (r/min)	Chopper roll speed variation (r/min)	Engine speed variation (r/min)	Response time (s)
Pure machinery	2.28	67.0	17.1	195.7
PID control	6.62	73.4	17.6	172.1
Fuzzy predictive control	9.55	58.6	13.3	196.5
Fuzzy predictive optimal control	14.40	87.6	9.4	129.6

Table 8

Maximum disturbance tracking error for model units

Control model	Maximum disturbance tracking deviation of feed roll speed (r/min)	Maximum disturbance tracking deviation of chopper roll speed (r/min)	Maximum disturbance tracking deviation of engine speed (r/min)	The disturbance deviation of engine speed is more than the steady-state deviation (times)
Pure machinery	0.684	7.97	68.3	8.48
PID control	0.205	5.55	37.3	2.62
Fuzzy predictive control	1.792	10.72	23.5	1.43
Fuzzy predictive optimal control	0.915	13.34	46.3	7.56

According to Equation (6), the torque corresponding to the chopped disturbance speed and the energy consumption of each model for load control are shown in Table 9.

Table 9

Speed and disturbance response time of model engines

Control model	Minimum speed of chopping roll disturbance (r/min)	Chopper roll disturbance torque (N·m)	Chopper roll disturbance response time (s)	Chopping energy consumption (10^7J)
Pure machinery	728.6	272.3	195.7	1.453
PID control	634.6	139.8	172.1	1.490
Fuzzy predictive control	617.9	110.3	196.5	1.388
Fuzzy predictive optimal	591.5	59.7	129.6	1.382
Energy consumption comparison of shredding	Fuzzy predictive optimal control<fuzzy predictive control<pure machinery<PID control			

Finally, the comparison and analysis of energy efficiency between field operation disturbance control and simulation of each model are shown in Table 10.

Table 10

Comparison of model control performance

Test method		Step simulation	Practical Operation
Feed roll speed (r/min)		v2≈v3≈v4	v1≈v2≈v3≈v4
engine speed (r/min)		v2<v4<v3	v4<v3<v2<v1
Chopper roll speed (r/min)		v2<v3<v4	v4<v3<v2<v1
Steady state accuracy of operation (r/min)		μ4>μ3>μ2	μ4>μ3>μ1>μ2
Operation disturbance accuracy (r/min)		μ3>μ2>μ4	μ2>μ1>μ3>μ4
Response time of operation disturbance (s)		t4<t2<t3	t4<t2<t1<t3
Feeding tension load (MPa)		F3<F2<F4	F1<F2<F3<F4
Energy consumption of feeding roller (J)		Q4>Q2>Q3	Q4>Q3>Q2>Q1
Maximum pressure value of chopping drive belt (MPa)		P3<P2<P4	P2<P1<P3<P4
Average pressure value of chopping drive belt (MPa)		p4<p2<p3	p4<p3<p1<P2
Energy consumption of shredding roll (J)	Short operation time	Q4<Q2<Q3	Q4<Q2<Q3<Q1
	Operation duration		Q4<Q3<Q2<Q1
Maximum operation capacity (N)		N3<N2<N4	N2<N1<N3<N4
Production efficiency (%)		M3<M2<M4	M2<M1<M3<M4
Overall energy consumption (J)		Q4<Q2<Q3	Q4<Q3<Q1<Q2

Note: 1 - pure machinery; 2-PID control; 3 - Fuzzy measurement control; 4-Fuzzy predictive optimal control

From the above analysis, it can be seen that the trend of field test and step disturbance simulation results is basically the same. Under the same conditions of other input parameters of each model, when optimizing control, the maximum value of the pressure of the chopping drive belt increases, which increases the chopping threshold load. The overall performance of the optimization control system is a good control performance with the highest efficiency, the lowest energy consumption and the shortest disturbance response time. The experimental results were in line with the characteristics of optimal control effect and the processing quality of corn straw was good. However, it was also found in the study that the simulation results in Table 3 showed that the optimized control obtained fuel savings of about 21.9% compared to the traditional PID control, which theoretically exceeded the 18% already achieved in the actual production of John Deere 8000 series silage harvesters (*Wu, 2021*) and 10.6% of CLAAS JAGUAR 800 series silage harvesters (*Li, 2021*).

However, the field test results in Table 9 showed that the actual fuel savings obtained from the optimized algorithm control alone are about 7.2% compared to the conventional PID control and only about 4.9% compared to the pure mechanical operation, both of which are still far less than 18%, indicating that other aspects of forage harvester research need to be continuously optimized in parallel with this.

Through the above research, it is concluded that: 1) optimal control is the largest and PID control is the smallest in terms of maximum operation capacity. 2) In terms of control robustness, the operation time is longer, the PID control is lower than the fuzzy predictive control, the operation time is shorter, and the fuzzy predictive control is lower than the PID control; The optimal control combines the advantages of PID control and fuzzy predictive control, and has strong adaptability to the changes of operating load parameters, the fastest disturbance response, and the best robustness. It tends to be suitable for the control characteristics of long-term and continuous uncertain load operations. 3) In terms of control accuracy, crops are subject to sudden change feeding operation for a long time, and the disturbance accuracy of fuzzy predictive control is better than that of PID control. For short-term slope feeding operation, the disturbance accuracy of PID control is better than that of fuzzy predictive control. The disturbance accuracy of optimal control still needs to be further studied and improved. 4) In terms of overall energy efficiency, the optimal control of the shredding unit operation has realized greater operational capacity (threshold load) of the forage harvester, higher production efficiency and less total energy consumption per unit operation.

CONCLUSIONS

An optimal control algorithm for reasonably dividing the task threshold load, that is, in the control process, the threshold load is divided into parts, the system output is efficiently transferred from any initial condition to another terminal condition in a limited time, and hierarchical closed-loop control is implemented so that the system output controllability is enhanced, the task threshold load is improved, and the operation is simplified and the output value is stable.

The simulation results of PID control, fuzzy predictive control, and fuzzy predictive optimal control system show that the system disturbance responsiveness and energy efficiency are better than those of PID control and fuzzy predictive control. The optimal control algorithm can improve the maximum operating capacity of the forage harvester again based on the original control effect.

Finally, the above algorithms were applied to the forage harvester workload optimization feedback control operating system, which to some extent made up for the shortage of simply relying on traditional algorithms to control the workload, and realized the timely and reasonable supply of power required by the operation units such as shredding. Through the on-site actual machine test, the maximum operating capacity of the equipment was significantly improved.

ACKNOWLEDGEMENT

This work was sponsored by National key research and development "13th Five Year Plan" project (2016YFD0701701); Shandong modern agricultural industrial technology system - special fund for fruit innovation team (SDAIT-06-12) - special fund for fruit facilities, machinery and equipment post.

REFERENCES

[1] Baruah, D. C., Panesar, B.S., (2005). Energy requirement model for a combine harvester, part I: development of component models. *Biosystems Engineering,* Vol. 90, pp. 9-25, India.

[2] Chen, G., Wen, J., Zhang, R., Pan, C., Zhao Y., (2020). Advances and progress of agricultural machinery and sensing technology fusion (农业机械与信息技术融合发展现状与方向). *Smart Agriculture*, Vol. 2, pp. 1-16, Xinjiang/China.

[3] Chen, L., (2020). Evaluation of the standard timeliness of agricultural machinery standard citation network (农业机械标准引用网络的标准时效性评价). *Zhongnan University of Economics and Law*, DOI:10.27660/d.cnki.gzczu.2020.000010, Hubei/China.

[4] Coen, T., Paduart, J., Anthonis, J., (2006). Nonlinear system identification on a combine Harvester. *Proceedings of the 2006 American Control Conference*, pp. 3074-3079, USA.

[5] Du, F., Fu, H., Mao, R., Zhu, X., Li, Z., (2019). Development situation and prospects of intelligent design for agricultural machinery (农业机械智能化设计技术发展现状与展望). *Transactions of the Chinese Society for Agricultural Machinery*, Vol. 50, pp.1-17, Beijing/China.

[6] Dong, Q., (2010). Development of load feedback equipment of combine harvester based on gray predictive fuzzy control (基于灰色预测模糊控制的联合收割机负荷反馈装置的研制). *Jiangsu University*, Jiangsu/China.

[7] Fan, J., Wang, Z., Zhang, H., Zhao, Y., Song, P., (2017). Design and experiment of automatic levelling control system for orchards lifting platform (果园升降平台自动调平控制系统设计与试验). *Transactions of the Chinese Society of Agricultural Engineering*, Vol. 33, pp. 38-46, Shandong/China.

[8] Gu N., Miu M., Kuang F., (2011). A new allocation method for dynamic positioning systems (一种新的动力定位系统推力分配算法). *China offshore platform*, Vol. 26, pp. 50-52, Jiangsu/China.

[9] Hu, T., (2007). Automatic control theory (自动控制原理). *Beijing:* Science *press*, pp.553-557, Jiangsu/China.

[10] Ji, T., Wang, X., Fu, J., (2008). Grey prediction fuzzy PID control of the feeding quantity in combine (联合收获机喂入量灰色预测模糊 PID 控制). *Transactions of the Chinese Society for Agricultural Machinery*, Vol. 39, pp. 63-66, Henan/China.

[11] Johansen, T. A., Fossen, T. I., Berge, S. P., (2004). Constraint nonlinear control allocation with singularity avoidance using sequential quadratic programming. *IEEE Transactions on Control Systems Technology*, Vol. 12, pp. 211-216, Norway.

[12] Kotyk, W.H., Kirk, T.G., Klassen, N.D., (1991). Control system for combine harvesters. *WESCAN,* pp.96-102, USA.

[13] Kruse, J., (1983). Computer controls for the combine. *Agricultural Engineering*, Vol. 64, pp. 7-9, USA.

[14] Li, H., (2019). Development and application prospect on self-propelled whole-plant feeding forage Harvester (自走式全株喂入青饲料收获机的研制及推广应用前景). *Hebei Agricultural Machinery*, pp. 27, Hebei/China.

[15] Li, D., Han, C, Sang, Z., (2007). Design of Intelligent Controller of Constant Pal stance of Cylinder of the Combine (联合收割机脱粒滚筒恒速智能控制器设计). *Control Engineering of China*, Vol. 14, pp. 154-156, Gansu/China.

[16] Liu, J.N., (2019). Innovative Technology of CLAAS harvester. *Journal of Agricultural Engineering*, Vol.9(08), pp. 18-21, Beijing/China.
[17] Muhammad, Z., Saeed A., (2021). Distributed output feedback control of decomposable LPV systems with delay and switching topology: application to consensus problem in multi-agent systems. *International Journal of Control*, Vol. 94, pp. 2428-2439, Turkey.
[18] Ni, J., Mao, P., Cheng, H., (2009). Fuzzy control system of combine cylinder based on FPGA (基于FPGA 的联合收获机脱粒滚筒模糊控制系统).*Transactions of the Chinese Society for Agricultural Machinery*, Vol. 40, pp. 83-87, Jiangsu/China.
[19] Pan, J., Shao, T., Wang, K., (2010). Detection method on feed density for rice combine (水稻联合收割机喂入密度检测方法). *Transactions of the Chinese Society of Agricultural Engineering*, Vol. 26, pp. 113-116, Anhui/China.
[20] Qin, Y., (2012). Study on load control system of combined harvester (联合收割机负荷控制系统研究). *Jiangsu University*, Jiangsu/China.
[21] Reddy, E.J., Rangadu, V.P., (2018). Development of knowledge based parametric CAD modeling system for spur gear: an approach. *Alexandria Engineering Journa*l, Vol. 57, pp. 3139-3149, India.
[22] Sayedur, Rahman, S.M., Diponkar, P., Masud, R.M., (2020). Performance evaluation & operation of DSP control UPS system. *Engineering*, Vol. 12, pp. 666-681, Bangladesh.
[23] Wu, G., (2017). Big Mac Silage Harvester, the Big Guy has the big brain (巨无霸青贮收获机,大块头有大智慧). Farm Machinery, pp. 39-41, DOI:10.16167/j.cnki.1000-9868, Beijing/China.
[24] Xiang, W.H, Ban, L.G, Zhou, P.P., (2021). Online prediction and optimal control method of wind power sub-synchronous oscillation based on machine learning interpretable agent model (基于机器学习可解释代理模型的风电次同步振荡在线预测及优化控制方法). *Power system protection and control*, Vol. 49 (16), pp. 67-75, Beijing/China.
[25] Yang, L., (2007). Research on underwater image segmentation and recognition algorithm based on fractal theory (基于分形理论的水下图像分割与识别算法研究). *Huazhong University of Science and Technology*, Hubei/China.
[26] Zhai, Q., Wang, Q., Wang, L., Zhu, X., Du, F., Mao, R., (2021). Collaborative path planning for autonomous agricultural machinery of master-slave cooperation (面向主从跟随协同作业的导航路径规划方法). *Transactions of the Chinese Society for Agricultural Machinery,* Vol. 52, pp. 542-547, Beijing/China.
[27] Zhang, C., Sang, Z., (2001). Simulation research on the fuzzy logic control of an axial threshing cylinder (轴流脱粒滚筒模糊控制仿真). *Transactions of the Chinese Society for Agricultural Machinery*, Vol. 32, pp. 45-48, Anhui/China.
[28] Zhao, B., (2009). Intelligent control system research of combine load feedback (联合收割机负荷反馈智能控制系统的研究). Jiangsu University, Jiangsu/China.

APPLICATION OF INDUSTRIAL ROBOT AND MACHINE VISION IN INTELLIGENT CALDRON FEEDING PROCESS OF CHINESE BAIJIU

/

工业机器人和机器视觉在中国白酒智能上甑工艺中的应用

ZhongLing XIA[1,2], WeiHan CHEN[1], Hang ZHAO[3], WeiDong SONG*[4], Ling YANG[1], MingJin YANG*[1]1)

[1]Southwest University, College of Engineering and Technology, Chongqing 400715, China
[2]Chongqing Yottametre Industry Automation Co., Ltd., Chongqing 401122, China
[3]Southwest University, College of Artificial Intelligence, Chongqing 400715, China
[4]Ministry of Agriculture and Rural Affairs, Nanjing Institute of Agricultural Mechanization, Nanjing 210014, China
Tel: +86 13883002509; E-mail: songwd@163.com; ymingjin@swu.edu.cn
DOI: https://doi.org/10.35633/inmateh-69-03

Keywords: *Chinese Baijiu, caldron feeding, industrial robot, machine vision, automatic distillation*

ABSTRACT

In traditional Chinese Baijiu (white wine) brewing factory, most processes were usually done manually. In order to promote industrial automation in liquor brewing industry and alleviate highly repetitive manual labor, an industrial robot operating system equipped with machine vision was designed to accomplish caldron feeding process during the distillation of Chinese Baijiu. Firstly, Modified D-H method was used to establish robot kinematics model. Shovel actuators and peripheral devices were designed to spread and transport grains during caldron feeding process. After that, an online detection system based on machine vision and master computer were designed to control key parameters of caldron feeding process, including grains height, caldron pressure, robot speed and waiting time, etc. Finally, multiple brewing experiments were carried out on crushed grains and spent grains. The experimental results showed that robot system maximum working space was 3.15 m, which could feed 3 caldrons at the same time. During Chinese Baijiu distillation, air pressure average error in caldron was 8.28 %. High proportion of first-class liquor and second-class liquor was obtained, which met engineering production requirements.

摘要

在中国传统的白酒酿造厂中，大部分工艺流程通常都是由人工完成。为了促进白酒酿造行业的工业自动化发展，减轻高重复性的人工劳作。本研究设计了一个配备机器视觉的工业机器人操作系统来完成中国白酒蒸馏过程中的上甑过程。首先采用改进的 D-H 方法对机器人进行数学建模，设计了铲式执行机构和外围设备用于上甑过程中大曲的铺料和运输。然后还开发了基于机器视觉的在线检测系统和上位机软件对上甑过程中的关键参数：料层高度，甑内压力，铺料速度和等待时间等进行控制。最后对大渣和丢糟两种原料进行多次酿造实验。实验结果表明：智能上甑机器人系统最大工作空间为 3.15m，可同时对 3 个甑桶进行上甑。白酒蒸馏过程中甑桶内气压平均误差为 8.28%。产出一级酒和二级酒的比例较高，符合工程生产要求。

INTRODUCTION

The six major distilled spirits in the world are brandy, whiskey, rum, vodka, gin and Chinese Baijiu (*Xie J. et al, 2022*). Chinese Baijiu uses solid-state fermentation and distillation process, which allows alcohol molecules in the fermented spirits to be distilled and purified. Through this process, flavor substances with special aromas are preserved intact (*Zhang G. Y. et al, 2017*). Caldron feeding process, as one of the core process steps in Chinese Baijiu brewing process, directly determines output rate and quality of liquor. In caldron feeding process, workers spread brewing ingredients in layers, evenly and loosely inside caldron to ensure that steam permeates upward from the bottom layer by layer to distill alcohol. Steam leakage or accumulation during spreading process will affect the quality of Chinese Baijiu (*Li Y., 2015*).

In traditional Chinese Baijiu brewing factory, caldron feeding process still required a lot of manual work (*Zhang J.S., 2017*). The process requires cooperation of two skilled operators, one of whom shovels ingredients from pile into dustpan, while the other spreads brewing ingredients from dustpan into 3m^2 caldron

1) ZhongLing Xia, M.S. Eng.; WeiHan Chen, M.S. Stud. Eng.; Hang Zhao, M.S. Eng.; WeiDong Son,; Prof. Eng.; Ling Yang, Prof. Eng.; MingJin Yang, Prof. Eng.

in layers. During the 35-40 min process, workers often have to repeat the shoveling and spreading action hundreds of times, and the total mass of brewing ingredients handled exceed 2000kg (*Yang Y. et al, 2021*). In addition, manual work was also accompanied by poor working conditions and inconsistent quality (*Qing Y. H., et al, 2020*). In recent years, industrial robots based on machine vision have been widely used to meet the automation and intelligence requirements of intelligent manufacturing. As the field of robotics continues to expand, it is possible for industrial robots to replace manual labor in caldron feeding process (*Jiang W.Y., 2022*). However, the caldron feeding machine on the market still suffers from poor accuracy in detecting the surface temperature of fermented grains, poor uniformity in spreading ingredients, and difficulty in controlling path planning and feeding time, etc. (*Li L.H. et al, 2018*).

In this paper, based on the traditional caldron feeding process and actual working requirements, an industrial robot operating system equipped with machine vision was designed, including robot arm, shovel actuator, machine vision system, master computer and control module, etc. According to layout of caldron and receiving port, the corresponding robot arm type and specification were selected. Modified D-H method was used to establish robot forward kinematics model. Then, applying Monte Carlo method to calculate robot working space to verify that the selected robot met caldron feeding requirements. An online detection system based on machine vision were designed to ensure quality of caldron feeding process. Finally, multiple brewing experiments were carried out on crushed grains and spent grains to verify feasibility of engineering application of intelligent robot caldron feeding system scheme.

MATERIALS AND METHODS

Mechanical system

Robotic arm and shovel actuators

The palletizing robot ABB IRB 660 was mainly composed of fixed base, rotary table, large arm, small arm, gripper mounting flange, joint drive motor, hydraulic cylinder and connecting rod. As shown in Fig. 1, IRB 660 with a 4-DOF parallelogram mechanism had 4 motors, driving rotary table rotation, large and small arms pitch, and gripper rotation, respectively. The working range of the four rotating parts was shown in Table 1. In addition, three links formed a double parallelogram mechanism, which was designed to always keep end-actuator parallel to the ground, so that palletizing robot gripped or placed objects smoothly. The stiffness to mass ratio of the robot was improved indirectly, then its weight and drive power were decreased.

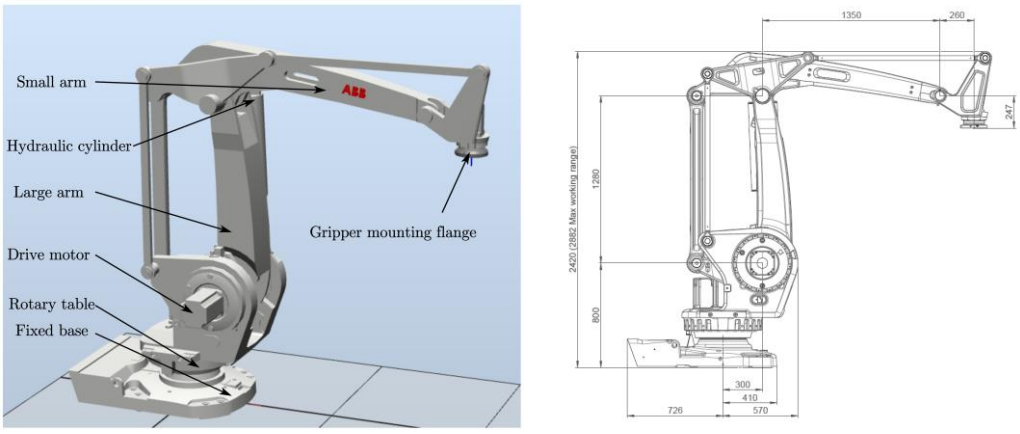


Fig. 1 – IRB 660 model drawing

Table 1

IRB 660 Performance Parameters

Type: 660-180		Max. load: 180 kg		Reach distance: 3.15 m		Number of axes: 4	
Sport performance							
Axis 1		**Axis 2**		**Axis 3**		**Axis 4**	
Rotation range of β_1 [°]	Max. velocity [°/s]	Rotation range of β_2 [°]	Max. velocity [°/s]	Rotation range of β_3 [°]	Max. velocity [°/s]	Rotation range of β_4 [°]	Max. velocity [°/s]
-180 ~ 180	130	-42 ~ 85	130	-20 ~ 120	130	-300 ~ 300	300

Shovel actuators were connected to robot arm by flanges. Fermented grains entered actuator at A, then they were transported by a conveyor belt at the bottom of actuator, and finally they spread by dispersing device at B. As shown in Fig. 2, the size of actuator was 475mm*600mm*400mm.

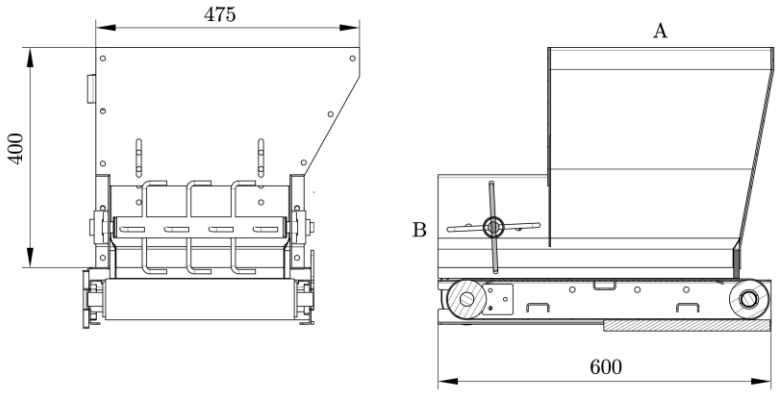
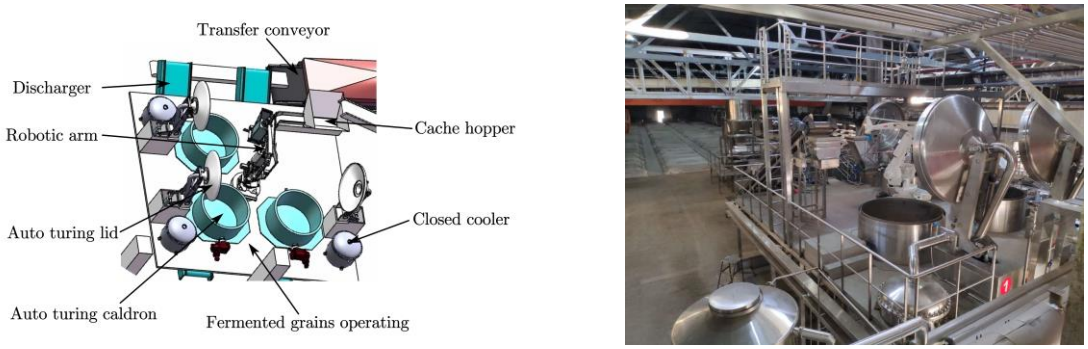


Fig. 2 – Shovel actuator model

Peripheral Institutions

Peripheral Institutions were equipped with cache hopper, fermented grains operating platform, closed cooler, auto-turning lid, auto-turning caldron, discharger and transfer conveyor. The 3-D diagram of system was shown in Fig. 3 (a), and physical diagram of system was shown in Fig. 3 (b).



(a) 3-D diagram (b) Physical diagram

Fig. 3 – Caldron feeding system

Control system

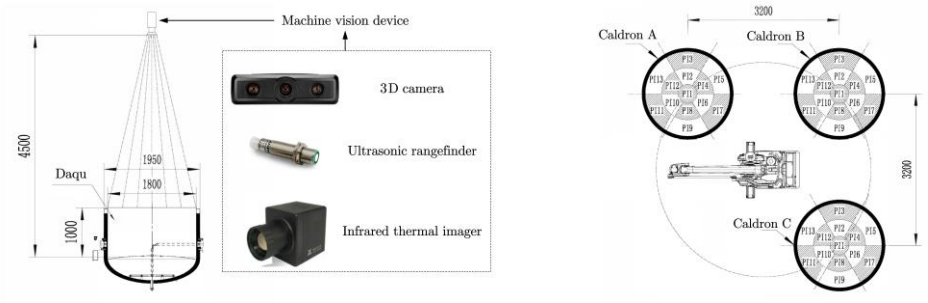
System device

The control system mainly included IPC, robot controller, PLC (Siemens, S7-1200), demonstrator (ABB). Machine vision system included ultrasonic rangefinder, 3D camera and infrared thermal imager, etc. IPC was responsible for receiving data from others to coordinate entire workstation. S7-1200, as the main motion control device, interacted with the robot via the profinet protocol. Ultrasonic rangefinder feeds detected distance data back to IPC or PLC to adjust the height of caldron feeding process. Three caldrons shared a common machine vision system, and inspection device was fixed on stand, which could rotate above caldron respectively. The machine vision device and spatial layout of caldrons were shown in Fig. 4(a). The installation height of device was 4.5m. As shown in Fig. 4 (b), the outermost feeding radius of caldron $R_{f\max}$ was calculated by:

$$R_{\mathrm{f\,max}} = \frac{\sqrt{2}L_{\mathrm{c}} + D_{\mathrm{c}}}{2} \tag{1}$$

Where:

$R_{\mathrm{f\,max}}$ is max feeding radius, [mm]; L_{c} is the distance between caldron, [mm]; D_{c} is the inner diameter of caldron, [mm]. $R_{\mathrm{f\,max}}$ is 3.06 m.



(a) Machine vision device and spatial layout of caldrons (b) Bird's view of caldrons

Fig. 4 – Machine vision device and layout of caldrons

Master host

During caldron feeding process, master host controlled robot operating parameters. Main parameters included total height, layer height, current layer number, chain plate velocity, robot velocity and waiting time, etc. Auxiliary parameters included time for stopping feeding in advance and adjustment times. Minimum, maximum and stable air pressure in caldron could be adjusted by master host. In addition, master host monitored running status of robotic arm parameters, such as feeding cycle status, robot power status, shovel actuator coordinate position and manual operation interface. The cooperation of manual operation interface and teach pendant could replenish fermented grains at air leakage area after feeding. The flow chart of control system was shown in Fig. 5.

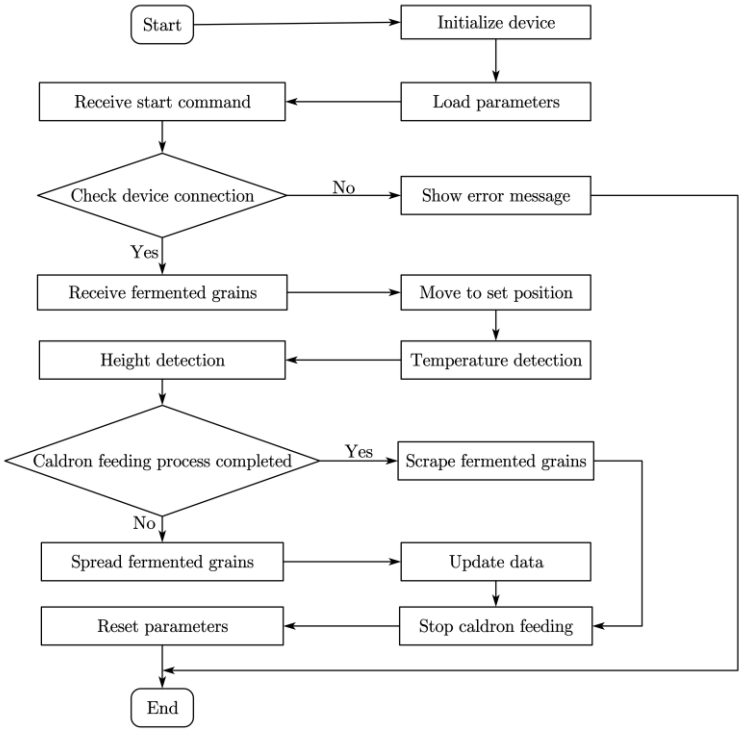
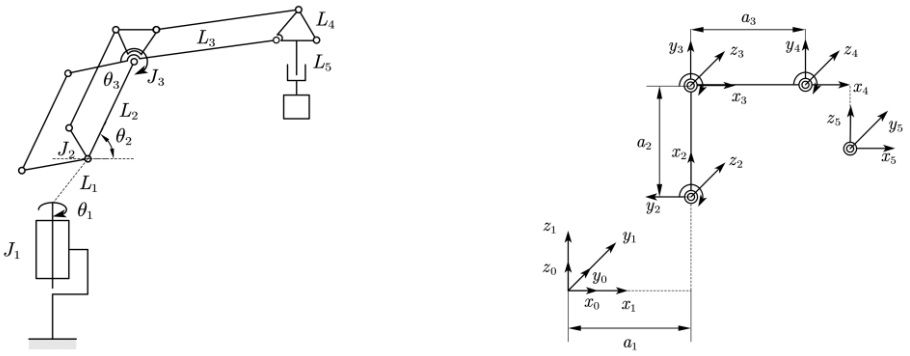


Fig. 5 - Control system flow chat

RESULTS

Motion model

According to above the analysis of palletizing robot IRB 660, a simplified structural diagram of robot was shown in Fig. 6 (a). θ_1, θ_2 and θ_3 are rotation angles of rotary table, large arm and small arm respectively; L_1, L_2, L_3, L_4 and L_5 are lengths of waist, large arm, small arm, wrist and actuator link, respectively. Using modified D-H method to establish 4-DOF robot coordinate system, as shown in Fig. 6 (b), where a_1=300mm, a_2=1280mm, a_3=1350mm.



(a) Robot structure diagram (b) D-H coordinate system

Fig. 6 - Robot structure diagram and D-H coordinate system

Forward kinematics was applied to solve posture of actuator in Cartesian space through the value of movement or rotation of each joint of robot arm. According to Modified D-H method, a homogeneous transformation matrix ${}_{i}^{i-1}T$ was used to represent transformation from coordinate system *i*-1 to *i*. The ${}_{i}^{i-1}T$ was determined by (*Rong S. L. et al, 2010; Craig J. J. 2006*):

$$ {}_{i}^{i-1}T = \begin{bmatrix} c\theta_i & -s\theta_i & 0 & a_{i-1} \\ s\theta_i c\alpha_{i-1} & c\theta_i c\alpha_{i-1} & -s\alpha_{i-1} & -s\alpha_{i-1}d_i \\ s\theta_i s\alpha_{i-1} & c\theta_i s\alpha_{i-1} & c\alpha_{i-1} & c\alpha_{i-1}d_i \\ 0 & 0 & 0 & 1 \end{bmatrix} \quad (2) $$

where $c\theta_i = \cos(\theta_i)$, $s\theta_i = \sin(\theta_i)$, $c\alpha_i = \cos(\alpha_i)$, $s\alpha_i = \sin(\alpha_i)$.

According to Fig. 6 and Table 1, robot modified D-H parameters were listed in Table 2.

Table 2

Modified D-H parameters

Joint i	α_{i-1}	a_{i-1}	d_i	θ_i	Range
1	0	0	*0*	θ_1	-180° ~ 180°
2	π/2	a_1	*0*	θ_2	-132 ~ -5
3	0	a_2	*0*	θ_3	20° ~ 160°
4	0	a_3	*0*	θ_4	$-\theta_2 \sim \theta_3$

When data in Table 2 were substituted into Eq. (2), the homogeneous transformation matrix between four coordinate systems were expressed as:

$$ {}^{0}T_1 = \begin{bmatrix} c\theta_1 & -s\theta_1 & 0 & 0 \\ s\theta_1 & c\theta_1 & 0 & 0 \\ 0 & 0 & 1 & 0 \\ 0 & 0 & 0 & 1 \end{bmatrix} \quad {}^{1}T_2 = \begin{bmatrix} c\theta_2 & -s\theta_2 & 0 & a_1 \\ 0 & 0 & -1 & 0 \\ s\theta_2 & c\theta_2 & 0 & 0 \\ 0 & 0 & 0 & 1 \end{bmatrix} $$

$$ {}^{2}T_3 = \begin{bmatrix} c\theta_3 & -s\theta_3 & 0 & a_2 \\ s\theta_3 & c\theta_3 & 0 & 0 \\ 0 & 0 & 1 & 0 \\ 0 & 0 & 0 & 1 \end{bmatrix} \quad {}^{2}T_3 = \begin{bmatrix} c\theta_4 & -s\theta_4 & 0 & a_3 \\ s\theta_4 & c\theta_4 & 0 & 0 \\ 0 & 0 & 1 & 0 \\ 0 & 0 & 0 & 1 \end{bmatrix} \quad (3) $$

The homogeneous transformation matrix of the end link relative to base coordinate system was defined as:

$$ {}^{0}T_4 = {}^{0}T_1 \, {}^{1}T_2 \, {}^{2}T_3 \, {}^{3}T_4 \quad (4) $$

$$ {}^{0}T_4 = \begin{bmatrix} c_1c_{234} & -c_1s_{234} & s_1 & c_1(a_1 + a_3c_{23} + a_2c_2) \\ s_1c_{234} & -s_1s_{234} & -c_1 & s_1(a_1 + a_3c_{23} + a_2c_2) \\ s_{234} & c_{234} & 0 & a_3s_{23} + a_2s_2 \\ 0 & 0 & 0 & 1 \end{bmatrix} \quad (5) $$

where $s_{234}=sin(\theta_1+\theta_2+\theta_3)$, $c_{234}=cos(\theta_1+\theta_2+\theta_3)$, $s_{23}=sin(\theta_2+\theta_3)$, $c_{23}=cos(\theta_2+\theta_3)$.

In addition, the positional relationship between shovel actuators and end link of robot was plotted in Fig.1. The posture matrix of shovel actuators was expressed as:

$$ {}^{0}T_5 = \begin{bmatrix} c_1c_{234} & -c_1s_{234} & s_1 & c_1(a_1 + a_3c_{23} + a_2c_2) + 260 \\ s_1c_{234} & -s_1s_{234} & -c_1 & s_1(a_1 + a_3c_{23} + a_2c_2) \\ s_{234} & c_{234} & 0 & a_3s_{23} + a_2s_2 - 247 \\ 0 & 0 & 0 & 1 \end{bmatrix} \quad (6) $$

Meanwhile, the general representation of end link posture matrix was defined as (*Li J. L. et al, 2021*):

$$ T_5^0 = \begin{bmatrix} n_x & o_x & a_x & p_x \\ n_y & o_y & a_y & p_y \\ n_z & o_z & a_z & p_z \\ 0 & 0 & 0 & 1 \end{bmatrix} \quad (7) $$

Simultaneously solve Eq. (5) and Eq. (6), the forward kinematic equation was calculated by:

$$ \begin{cases} n_x = c_1c_{234} \\ n_y = s_1c_{234} \\ n_z = s_{234} \end{cases} \begin{cases} o_x = -c_1s_{234} \\ o_y = -s_1s_{234} \\ o_z = c_{234} \end{cases} \begin{cases} a_x = s_1 \\ a_y = -c_1 \\ a_z = 0 \end{cases} \begin{cases} p_x = c_1(a_1 + a_3c_{23} + a_2c_2) + 260 \\ p_y = s_1(a_1 + a_3c_{23} + a_2c_2) \\ p_z = a_3s_{23} + a_2s_2 - 247 \end{cases} \quad (8) $$

When the motion conditions of each joint are known, posture of robot IRB 660 in base coordinate system can be calculated by Eq. (7).

Workspace and static moment

In order to express the working space of the robot visually, the Monte Carlo method in numerical method was used to calculated, and then MATLAB 2020b was used to draw a spatial point map to realize the visualization of working space of robotic arm. The detailed steps are as follows:

1. Forward kinematics equation was used to obatin transformation matrix of actuator in base coordinate system, where P_x, P_y, and P_z represent position in space.

2. The random function Rand (j) in MATLAB was used to generate *N* numbers between 0 and 1 over each point motion range. The random values of each joint variable are represented as:

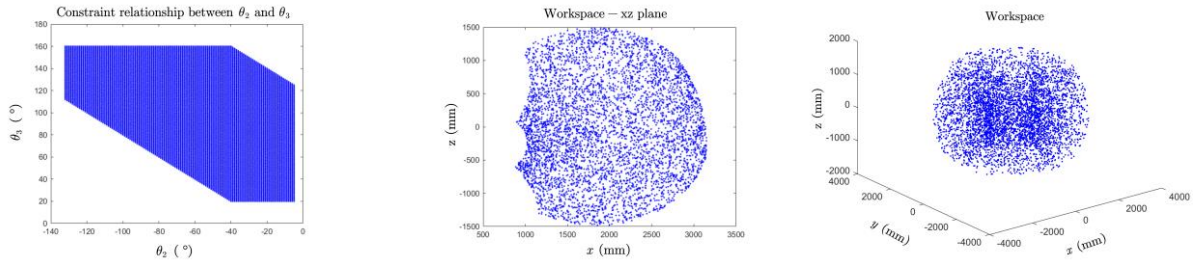
$$ \theta_i = \theta_{i\min} + (\theta_{i\max} - \theta_{i\min}) \times \mathrm{Rand}(j) \quad (9) $$

where $\theta_{i\min}$ and $\theta_{i\max}$ correspond to the minimum and maximum value of *i*-th joint variable, respectively.

3. Considering the influence of stop block and avoid mutual interference between members, there is a mutual constraint relationship between joint angles θ_2 and θ_3, as shown in Fig. 7 (a).

4. Marking the position of actuator in coordinate system to form three-dimensional point cloud image of the working space. The more random points there are, the closer to the actual working space of caldron feeding robot.

In this paper, the value of random point was set to 7000. The x-z plane and spatial result were displayed in Fig. 7 (b) and (c) respectively. There was no obvious hole in simulation, indicating that robot arm could move to various positions within working range. In the horizontal direction, the farthest distance that robot arm could reach was 3.15 m, which met the outermost caldron feeding radius 3.06 m. At the same time, in order to maximize production efficiency, three caldrons were arranged in working space to operate simultaneously.



(a) Mutual constraint relationship between joint angles

(b) Result of x-z plane

(c) Spatial result

Fig. 7 – Workspace of robot

When the shovel actuator was fully loaded, maximum weight was 150 kg. Static moment analysis of the robot was obtained according to Fig. 6 (a):

$$\begin{aligned} F_2 &= F_3 = F = 1500\text{N} \\ M_2 &= F \times (L_2 \sin(-\beta_1) + L_3 \cos\beta_2 + 0.26) = 1500(1.35\cos\beta_2 - 1.28\sin\beta_1 + 0.26) \\ M_3 &= F \times (L_3 \cos\beta_2 + 0.26) = 1500(1.35\cos\beta_2 + 0.26) \end{aligned} \quad (10)$$

where F, F_2, F_3 are the forces on wrist, large arm and small arm respectively, [N]; M_2, M_3 are the hinge point moments of large arm and small arm respectively, [kNm].

As shown in Fig. 8, MATLAB was used to draw the state moment of hinge point. The maximum torque of large and small arm was 4.33 kNm and 2.42 kNm, respectively. The robot could operate safely within the preset range.

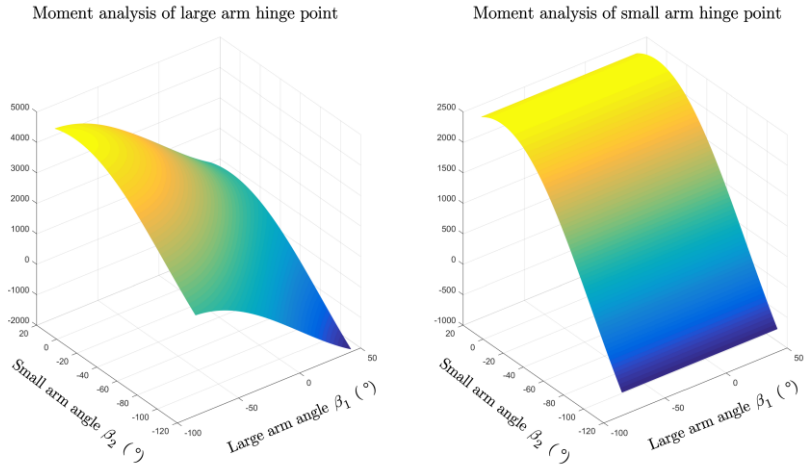
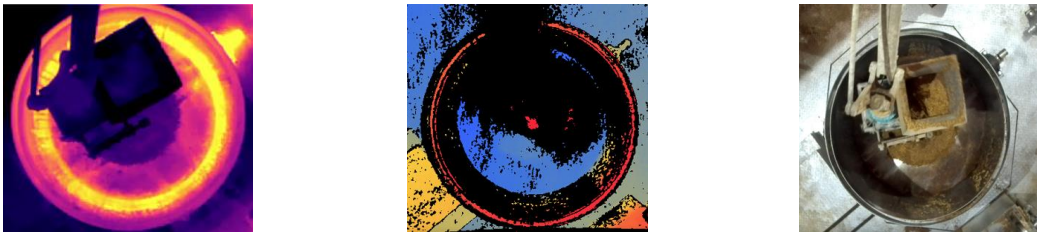


Fig. 8 – Hinge Moment Analysis

Online detection system

The online detection system of the intelligent caldron feeding system was divided into machine vision and air pressure monitoring system. The infrared thermal imager was used to monitor temperature of fermented grains surface inside the caldron in real time. When the surface occurred leaking gas, master host located position timely and accurately. Then the robot was controlled to feed fermented grains at leaking gas position. Simultaneously ultrasonic range finder and 3D camera worked together.



(a) Infrared image at start feeding

(b) 3D image at start feeding

(c) RGB image at start feeding



(d) Infrared image at midway feeding (e) 3D image at midway feeding (f) RGB image at midway feeding

Fig. 9 – Online machine vision system

As the height of the fermented grains increased, the area of lower temperature region photographed by infrared camera also increased. The fermented grains were spread evenly without air leakage on the surface, as shown in Figs. 9 (a) and (b). The increased blue area in Figs. 9 (b) and (e) taken by 3D camera also represented height increased. In addition, high resolution RGB photos of Figs. 9 (c) and (f) made it easy for operators to know feeding process of the caldrons.

Pressure monitoring system was shown in Table 2. Air pressure values in three caldrons were set in intelligent caldron feeding system and monitored every 10 minutes. According to Table 2, the average error of air pressure in caldron was 8.28 %, which met requirements of Chinese Baijiu production.

Table 2

Air pressure monitoring value

Caldron number	Current pressure [bar]	State pressure [bar]	Max. pressure [bar]	Min. pressure [bar]	Set pressure [bar]	Error [%]
1	2.2	2	2.2	1.7	2	10.00
1	2.05	2	2.2	1.7	2.2	6.82
1	1.98	1.8	2	1.7	1.8	10.00
2	1.97	1.7	2	1.6	2	1.50
2	1.84	1.7	1.8	1.5	1.8	2.22
2	1.8	1.7	1.8	1.5	1.7	5.88
3	1.17	1	1.2	0.9	1.2	2.50
3	1.07	0.8	1.1	0.7	0.8	33.75
3	1.12	0.8	1.1	0.7	1.1	1.82

Production test

The actual production application of the intelligent caldron feeding system was shown in Fig. 9. The states that fermented grains started to feed, feed in the midway and feed completed were shown in Fig. (a), (b) and (c) respectively.



(a) Feed starts (b) Midway of feeding (c) Feed complete

Fig. 9 – Caldron feeding process

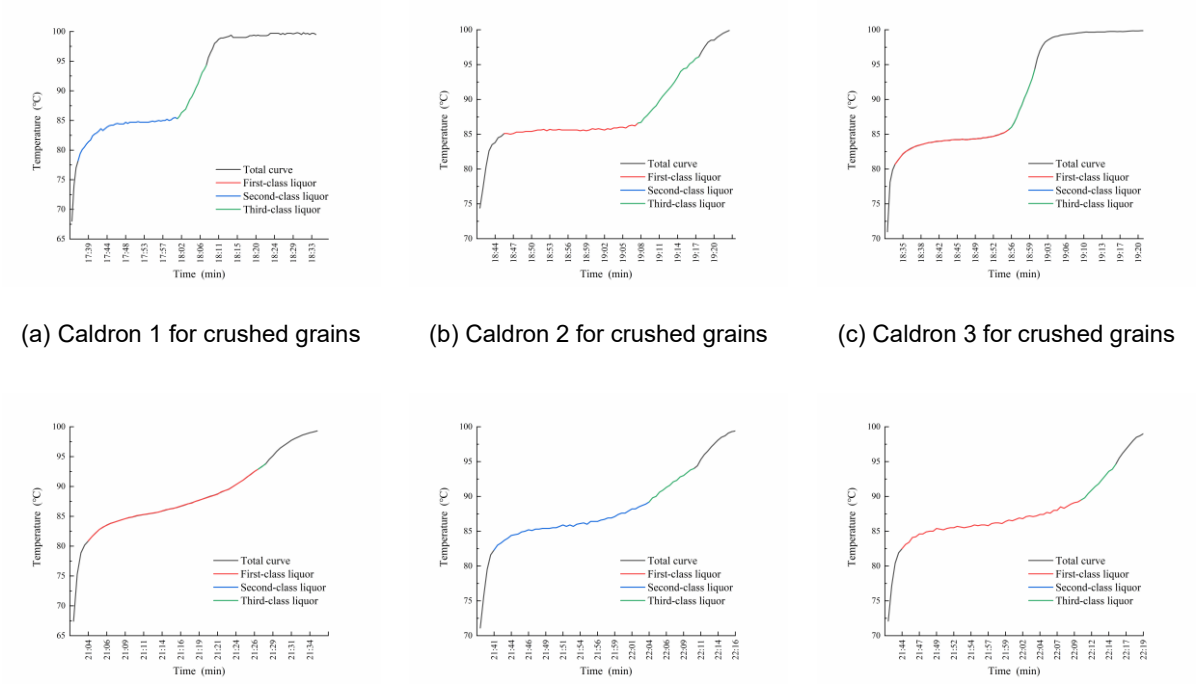
Finally, the surface of fermented grains was paved, and caldron lid cover preparation was done for the distilling, and the distilling process lasted 1h approximately. Taking feeding process of caldron 1 as an example, the sets of some operating parameters in master host were shown in Table 3.

Table 3

Sets of parameters of master host

Feed number	Inner-ring frequency [Hz]	Mid-ring frequency [Hz]	Outer-ring frequency [Hz]	Actual weight [kg]	Preset weight [kg]	Current height [mm]
1	38	42	67	60.0	45	42
2	35	40	70	68.5	45	84
3	38	42	70	70.1	45	129
4	30	40	70	71.3	45	174
5	30	44	72	67.1	45	219
6	30	44	72	65.2	40	264
7	33	45	72	64.8	40	309
8	33	45	72	65.6	40	354
9	33	45	72	64.2	40	399
10	33	45	72	64.7	40	444
11	33	45	72	66.6	40	489
12	33	45	72	64.2	40	534
13	33	45	72	64.2	40	579
14	33	45	72	63.6	40	624
15	33	45	72	66.5	40	664
16	33	45	72	61.7	40	704
17	33	45	72	66.4	40	741
18	33	45	72	65.8	40	778
19	33	45	72	66.6	40	815
20	33	45	72	65.8	40	820
21	33	45	72	65.8	40	825
22	33	45	72	64.5	42	850
23	33	45	72	68.7	42	885
24	33	45	72	70.6	42	920

There were two raw materials in the actual distillation, namely crushed grains and spent grains, and they were distilled several times separately. The grade of Chinese Baijiu was analyzed. Figs. 10 (a), (b) and (c) represented liquor production curves of crushed grains. Figs. (d), (e) and (f) represented liquor production curves of spent grains. As distillation proceed, the temperature in caldron increased and reached 100°C eventually. The quality of Chinese Baijiu was mainly manifested in different compound aromas, and ethyl caproate was the main component. According to the *Chinese national standard GB/T10781.1-2021 (China National standardizing committee, 2021*), Chinese Baijiu was divided into first-class, second-class, and third-class liquor, respectively (*Wu W. Y. et al, 2022*). As shown in Fig. 10, 3 minutes after the distillation, temperature stabilized at around 85°C and caldron began to produce first-class or second-class Chinese Baijiu. When the temperature increased above 85°C, caldron started to produce third-class liquor. The total curve showed that output time ratio for first-class and second-class was much higher than for third-class, so the intelligent feeding system met the actual Chinese Baijiu production requirements.



(a) Caldron 1 for crushed grains (b) Caldron 2 for crushed grains (c) Caldron 3 for crushed grains

(d) Caldron 1 for spent grains (e) Caldron 2 for spent grains (f) Caldron 3 for spent grains

Fig. 10 – Chinese Baijiu brewing analysis

CONCLUSIONS

In this paper, an intelligent Chinese Baijiu caldron feeding system was designed, including industrial robot selection, machine vision system construction, shovel actuator and peripheral device design, etc. The actual brewing experiments of crushed grains and spent grains were carried out and analyzed. Main conclusions were drawn as follows:

(1) Modified D-H method was used to establish robot kinematics model. Monte Carlo method was used to analyze working space of robotic arm. The robot IRB 660 reached 3.15 m in horizontal direction, which was larger than the outermost caldron feeding radius 3.06 m. The maximum torque of large and small arm was 4.33 kNm and 2.42 kNm respectively. The robot IRB 660 met space and moment requirements of caldron feeding.

(2) An online detecting system with machine vision and air pressure monitoring was built. The caldron feeding process was displayed clearly in master host. There was no air leak on the surface of fermented grains in the feeding process. The air pressure monitoring result showed that air pressure inside caldron was stable, and average error between actual and set value was 8.28%.

(3) The crushed grains and spent grains were brewing in intelligent caldron feeding system. The first-class liquor and second-class liquor were produced around 85 °C, accounting for a high proportion of total curve, which met the actual requirements of Chinese Baijiu production and saved a lot of manual work cost.

ACKNOWLEDGEMENTS

The study was funded by R & D Project of Chongqing Yottametre Industry Automation Co., Ltd. (No. ymdf20220909016).

REFERENCES

[1] Craig J. J., (2006). *Introduction to Robotics*, Ed. Pearson Education, New York/USA;

[2] Jiang W. Y., (2022). *Design and Research of Upper-Retort-Robot Based on Machine Vision* (*基于机器视觉的探气上甑机器人设计与研究*). Master dissertation, Qilu University of Technology, Ji' nan/P. R. C.

[3] Li J. L., Zhang B., Shu H. R., Yang X. S., Liu A. J., (2021). Joint Velocity Planning of Loading and Unloading Robot (上下料机器人关节速度规划), *Science Technology and Engineering*, vol. 21, issue 14, pp. 5784-5788, Ed. China Association for Science and Technology, Beijing/P. R. C.;

[4] Li L. H., Wang R. W., Wen X. B., (2018). Design of Efficient Detection Algorithm for Spreading Area of Intelligent Steamer Feeding System Based on Infrared Vision (基于红外视觉的智能装甑系统的撒料区域的高效检测算法设计), *Journal of Tianjin University of Technology*, vol. 34, issue 6, pp. 49-53, Ed. Tianjin University of Technology, Tianjin/P. R. C.

[5] Li Y., Hua Y., (2015). Design of Mechanical Steaming Bucket Feeding Control System Based on PLC (机械装甄布料控制系统 PLC 设计), *Food & Machinery*, vol. 31, issue 4, pp. 70-73, Ed. Changsha University of Science & Technology, Changsha/P. R. C.

[6] Qing Y. H., Wang S. Q., Zhang Z. P., Zhou X. Y., (2020). Kinematics Analysis and Trajectory Research for Upper-Retort-Robot (上甑机器人运动学分析及轨迹研究), *Food & Machinery*, vol. 36, issue 12, pp. 70-73, Ed. Changsha University of Science & Technology, Changsha/P. R. C.

[7] Rong S.L., Yan H. L., (2010). Development of Universal Environment for Constructing 5-Axis Virtual Machine Tool Based on Modified D–H Notation and OpenGL. *Robotics and Computer Integrated Manufacturing*, vol. 26, issue 3, pp. 253-262. Ed. Elsevier Sci Ltd.

[8] Wu W. Y, Yuan L., Song W. J., Yang X. J., Su Z. Y., Zheng, R. X., Li, F. F., (2022). Changes of Physicochemical Requirements in the 2021 Edition of the National Standard for Nongxiang Baijiu (浓香型白酒国家标准 2021 版理化要求的变化分析), *Liquor-Making Science & Technology*, issue 6, pp. 17-25, Ed. Guizhou Provincial Light Industry Scientific Research Institute, Guizhou/ P. R. C.

[9] Xie J., Luo H. B., Zeng Y., Huang D., Huang Z. G., Wei C. H., Zhu L. L., (2022). Evolution and Research Status of Distillation Device in Chinese Baijiu Industry (中国白酒产业蒸馏装置的演变历程及研究现状), *China Brewing*, vol. 41, issue 2, pp. 9-14, Ed. Beijing Academy of Food Sciences, Beijing/P. R. C.

[10] Yang Y., Wang H. B., Zhang L. Y., Liu C., Sheng X. J., (2021). Robot Operation System for Caldron Feeding in Traditional Distillation of Chinese Liquor (面向上甑工艺的机器人作业系统研究), *Science Technology and Engineering*, vol. 21, issue 36, pp. 15516-15528, Ed. China Association for Science and Technology, Beijing/P. R. C.;

[11] Zhang G. Y., Tou X. G., Li S., Chen L., Tang K. Y., Peng Y. J., (2017). Application Status and Study on Steamer－Filling Robot in Traditional Distillation of Chinese Liquor (上甑机器人在白酒固态蒸馏中的应用现状与探讨), *Science and Technology of food Industry*, vol. 38, issue 13, pp. 216-219+224, Ed. Beijing Industrial Technology Research Institute, Beijing/P. R. C.

[12] Zhang J. S., (2017). *Design and Analysis of a New Feeding Robot* (*一种新型上甄机器人的设计和分析*). Master dissertation, Tianjin University of Technology, Tianjin/P. R. C.;

[13] *** China National standardizing committee, (2021), *Quality Requirements for Baijiu-Part 1: Nongxiangxing Baijiu, GB/T10781.1-2021* (*白酒质量要求第 1 部分：浓香型白酒, GB/T10781.1-2021*), Ed. Chinese Standard Press, Beijing/P. R. C.

APPLICATION OF HYDROPONIC TECHNOLOGY TO THE YIELD AND QUALITY OF PURWOCENG "VIAGRA FROM ASIA"

/

APLIKASI TEKNOLOGI HIDROPONIK PADA YIELD DAN KUALITAS PURWOCENG "VIAGRA DARI ASIA"

Eni SUMARNI[1)], Irmanida BATUBARA[2,3*)], Herry SUHARDIYANTO[4)], Slamet WIDODO[4)], Mohamad SOLAHUDIN[4)], Eti ROHAETI[2,3)], Folkes LAUMAL[5)]

[1)] Department of Agricultural Technology. Faculty of Agriculture. General Sudirman University. Purwokerto, / Indonesia;
[2)] Department of Chemistry. Faculty of Mathematics and Natural Sciences, IPB University. Bogor / Indonesia;
[3)] Tropical Biopharmaca Research Center, IPB University, Bogor / Indonesia;
[4)] Department of Mechanical Engineering and Biosystems. IPB University. Bogor / Indonesia;
[5)] Doctoral program. Department of Mechanical and Biosystems Engineering. IPB University. Bogor / Indonesia
Tel: +622518347525.; E-mail: ime@apps.ipb.ac.id
DOI: https://doi.org/10.35633/inmateh-69-04

Keywords: *aerial part, cultivation, greenhouse, nutrient dose, recirculating drip, root*

ABSTRACT *Purwoceng (Pimpinella pruatjan Molkenb) is a medicinal plant native to Indonesia known as Indonesian Viagra from Java. The decline and scarcity of Purwoceng is an important obstacle in meeting the demands of harvesting from the original habitat without conservation and the extreme climatic conditions in the Dieng plateau. Therefore, it is necessary to apply controlled cultivation technology, namely hydroponic technology with drip irrigation in the greenhouse, to increase the yield and quality of Purwoceng. This study aimed to obtain the effect of hydroponic methods and hydroponic nutrition (EC) on the yield and quality of Purwoceng. The study was conducted from December 2020 to March 2021 at a greenhouse of ± 1500 m above sea level. The experiment used a randomized block design with three replications. Each replication consisted of 15 plants. Hydroponic type, which was recirculating drip, non-circulating drip, and nutrient concentration which were 1000 ppm, 1500 ppm, and 2000 ppm. The harvest weight (aerial part and root), moisture, ash, crude fat, crude fiber, water extractive, and ethanol extractive content, and the contaminant (microbial and heavy metal) content, were analyzed. In conclusion, to produce high-quality Purwoceng, a hydroponic system could be used using recirculating drip and 1000 ppm nutrient dose.*

ABSTRAK
Purwoceng (Pimpinella pruatjan Molkenb) adalah tanaman obat asli Indonesia yang dikenal dengan nama Viagra Indonesia dari Jawa. Penurunan dan kelangkaan Purwoceng merupakan kendala penting dalam memenuhi tuntutan panen dari habitat aslinya tanpa konservasi dan kondisi iklim ekstrim di dataran tinggi Dieng. Oleh karena itu, perlu diterapkan teknologi budidaya terkontrol yaitu teknologi hidroponik dengan irigasi tetes di rumah kaca, untuk meningkatkan hasil dan kualitas Purwoceng. Penelitian ini bertujuan untuk mengetahui pengaruh metode hidroponik dan nutrisi hidroponik (EC) terhadap hasil dan kualitas Purwoceng. Penelitian dilakukan pada bulan Desember 2020 hingga Maret 2021 di rumah kaca ± 800 m di atas permukaan laut. Percobaan menggunakan rancangan acak kelompok dengan tiga ulangan. Setiap ulangan terdiri dari 15 tanaman. Jenis hidroponik yaitu recirculating drip, dan non-circulating drip, serta konsentrasi nutrisi 1000 ppm, 1500 ppm, dan 2000 ppm. Berat panen (bagian udara dan akar), kadar air, abu, lemak kasar, serat kasar, ekstraktif air, dan ekstraktif etanol serta kandungan kontaminan (mikroba dan logam berat) dianalisis. Kesimpulannya untuk menghasilkan purwoceng yang berkualitas, sistem hidroponik dapat digunakan dengan menggunakan recirculating drip dan dosis nutrisi 1000 ppm.

INTRODUCTION

Purwoceng (*Pimpinella pruatjan Molkenb*) is a medicinal plant native to Indonesia from the highlands of Central Java, Indonesia (*Syahid et al., 2005; Nuryadin and Nabiila, 2018*). Traditionally, Purwoceng is used as an aphrodisiac and increases stamina. This traditional knowledge was supported by the report that Purwoceng extract tends to increase testosterone levels in male rats, indicating its functions as an aphrodisiac (*Arjadi et al., 2019; Bhagawan and Kusumawati, 2020*). In addition, Purwoceng has diuretic, anti-bacterial, and anti-fungal properties and can increase stamina, similar to ginseng plants (*Anwar, 2001*).

However, Purwoceng plants are currently experiencing scarcity due to using Purwoceng without any efforts to conserve/rejuvenate Purwoceng (*Balittro, 2000; Nuryadin and Nabiila, 2018*). This triggers fluctuations in Purwoceng production, which becomes a problem in meeting demand.

Purwoceng planted in open land in its natural habitat also has problems with the frost season, which can kill plants, and now Purwoceng is categorized as a rare and protected species *(Bhagawan and Kusumawati, 2020*). Therefore, the application of cultivation technology to increase the production and continuity of Purwoceng needs to be done as a development effort. In vitro cultivation started in 1990 to produce callus for both cultivation and in-vitro conservation, especially using root induction techniques (*Malda, Suzán and Backhaus, 1999; Srivastava et al., 2022*). However, the seed supply and suitable land to apply the ex-vitro root induction techniques in in-vitro culture are still constrained.

Our team used hydroponic technology and planted the Purwoceng in greenhouses. The greenhouse is provided a controlled environment for increasing yield and quality and reducing the scarcity of Purwoceng. Hydroponic technology is a cultivation technology that gets the best results, is controlled, and can be harvested according to plan *(Giurgiu et al., 2014*). Hydroponic technology has also been used for medicinal plants *(Ahmadi et al., 2021; Zarinkamar et al., 2021*), including Purwoceng (*Sumarni et al., 2017*).

Hydroponic technology with drip irrigation watering techniques can be an option for planting Purwoceng on medium plains. Drip irrigation is a technique of watering and providing nutrients for plants that are economical in a hydroponic system. Drip irrigation was proven to give the highest yield for zucchini plants (*Sałata et al., 2012*) and also Purwoceng, which reached 511 grams at the age of 70 days after planting (DAT) (*Sumarni et al., 2017*), and it is necessary to develop hydroponic techniques to obtain hydroponic techniques suitable for Purwoceng plants. Hydroponic applications with drip irrigation provide water and nutrient savings and high yields (*Morgan and Kadyampakemi, 2012*). From the things mentioned above, it is necessary to study the application of hydroponic techniques with drip irrigation for Purwoceng production in medium plains in the context of continuity, conservation, and increase in yield and quality.

The principle of drip irrigation is to provide water and nutrients in the form of drops that drip periodically according to the plant's needs through a PE pipe with the help of a pressure pump. According to *Wang et al., (2020)*, a drip irrigation system can save water use due to soil evapotranspiration reduction. Droplets on the system are directed right at the root area of the plant so that the plant can directly absorb the water and nutrients provided. Drip irrigation systems can be divided into recirculating drip irrigation and nonrecirculating drip irrigation. Recirculating drip irrigation is a system that utilizes runoff nutrient solutions to be reused as nutrients for plants. Meanwhile, nonrecirculating drip irrigation is a drip irrigation system that does not reuse runoff solutions as nutrients for plants. This study aimed to obtain the best hydroponic methods and hydroponic nutrition (EC) to produce a high-yield and quality Purwoceng.

MATERIALS AND METHODS

The study was conducted from December 2020 to March 2021. The research location was in a greenhouse on the Lembang medium plain ± 1500 m above sea level. The experiment used a randomized block design with three replications. Each replication consisted of 15 plants. The factors were hydroponic type and nutrition concentration as seen in Table 1.

Table 1

The experiment design

Hydrophobic type (N)	Nutrition concentration (ppm) (D)		
	1000 (D1)	1500 (D2)	2000 (D3)
Recirculating drip (N1)	D1N1 (4C)	D2N1 (4B)	D3N1 (4A)
Non-circulating drip (N2)	D1N2 (3C)	D2N2 (2B)	D3N2 (1A)

`

The Purwoceng seedlings were obtained from Dieng Plateau farmers in Central Java which was 1.5 months old. Seedlings were given acclimatization treatment for four days before being transplanted into the installation to be used for research. The type of hydroponics used is presented in Figure 1. The controlled conditions during planting in the greenhouse are the growing media, nutrient volume, temperature, and light intensity. After 240 days after planting (DAP), the aerial part and roots of Purwoceng were harvested. The growth and yield of Purwoceng plants which included plant height, number of leaves, harvest data (fresh weight of plants, fresh weight of aerial part, fresh weight of roots, dry weight of aerial part, dry weight of roots, and dry weight of plants) were analyzed by F test. and Duncan's Multiple Distance Test (DMDT) level 5%.



Fig. 1 - The hydroponic type in this research. Left: nonrecirculating drip, right: circulating drip

The harvest materials are divided into two parts, the aerial part, and the root part, which are traditionally used. The dried harvest materials were then used to determine their quality, such as the moisture content, ash content, fat content, fiber content, water extractive content, and ethanol extractive content.

For *Moisture Content Determination*, the sample was kept in a hot air oven at 105 ºC until dried. After cooling, the sample was placed in a desiccator and weighed to determine the moisture content.

For total *Ash Content Determination*, the sample is burned and put in a furnace at 45ºC for about three hours till no more organic components. Then, the ash's weight and content are determined *(WHO, 1998*). Crude Fat Determination, samples are refluxed with petroleum ether for 6 hours at 40–60°C in a Soxhlet extractor. Then, the extract was dried and weighed. The extracted content is the fat content.

Crude Fibre Content Determination, samples extracted with petroleum ether. The remaining residue was then boiled with 2% H_2SO_4 and NaOH solution for 30 minutes. The mixture was then filtered, and the residue was washed with boiling water and dried at 130 ºC for two hours. Finally, the residue was ignited at 550 °C and weighed. The water extractive and ethanol extractive content were measured using the cold maceration method *(WHO, 1998*). About 4.0g sample was macerated with 100ml of the solvent (water for water extractive content and ethanol for ethanol extractive content) for 24 hours. The filtrate then separated and evaporated to dryness on a water bath; continue with the drying process at 105°C for 6 hours. After cooling, the rest extract was weighed.

The safety of the harvest plant materials is also determined. It includes microbial safety, arsenic, and heavy metal safety. The microbial safety was determined based on WHO method no 18 (Determination of microorganism, WHO 1998), including total viable aerobic count (total plate count, TPC), yeast, and coliform. The arsenic and heavy metal content were determined using the WHO method no 17 (Determination of arsenic and heavy metal, WHO 1998).

RESULTS

1. Growth of Purwoceng plants cultivated in highland greenhouses

Purwoceng could grow well in hydroponic (drip recirculating and drip nonrecirculating) systems in altitudes only 1500m above sea level (asl). The growth performance is comparable with Purwoceng planted in the highlands as their natural habitat (higher than 2000 m) (Figure 2). The number of leaves and the number of branches is comparable. The leaves number, branches number, and leaves area of all groups are almost identical.

However, only Purwoceng cultivated at hydroponic drip nonrecirculating, and 2000ppm of concentration gave the significantly lowest leaves number, branches number, and area of leaves (Table 2).



(a) (b) (c)

Fig. 2 - Purwoceng cultivated in (a) recirculating drip at 1500 m s), (b) nonrecirculating drip at 1500 m asl, and (c) in its natural habitat higher than 2000 m asl

Table 2

The effect of drip irrigation hydroponic treatment and nutrient concentration on the growth of Purwoceng

Treatment combination	Growth per week		
	$\bar{x}$ Number of leaves	$\bar{x}$ Number of branches	$\bar{x}$ Leaf area
	[n]	[n]	[cm^2]
D1N1	5.66	1.69	6.679
D2N1	8.56	2.44	9.587
D3N1	7.80	2.09	7.098
D1N2	8.49	2.02	9.084
D2N2	7.49	1.36	6.142
D3N2	8.31	1.51	4.903

The hydroponic treatment did not affect the fresh-weight harvest product, but the different nutrient treatments significantly affected fresh and dry weight (Table 3). This is because the hydroponic type and the nutrients' EC interact with fresh and dry weight. The best treatment that produces the highest total plant fresh weight is obtained from the plant cultivated in 1500 ppm nutrient dose and non-circulating drip irrigation hydroponic type 211.81 gram. This total plant fresh weight was not significantly different with 2000 ppm nutrient dose and non-circulating drip irrigation hydroponic type, 1000 and 1500 ppm nutrient dose and recirculating drip irrigation hydroponic type. The highest aerial part fresh weight was obtained from nutrition with a dose of 1500 ppm and non-circulating irrigation of 85.88 grams, and the highest root fresh weight was obtained from the non-circulating hydroponic type with a dose of 1500 ppm.

Table 3

Interaction between hydroponic type treatment and nutrient dose (EC) on fresh weight characters of leaves, roots, and plants

Treatment combination	Aerial part weight		Root weight		All plant weight	
	[g]		[g]		[g]	
D1N1	72.54	ab	126.21	a	198.75	a
D2N1	61.79	ab	103.13	a	164.92	ab
D3N1	59.21	b	60.67	b	119.88	b
D1N2	25.92	c	14.25	c	40.17	c
D2N2	77.43	ab	134.38	a	211.81	a
D3N2	85.88	a	124.42	a	210.29	a

Note: Numbers followed by the same letter in one column are not different in DMDT level 5%

The interaction between hydroponic-type treatment and nutrient dose (EC) on aerial part, roots, and plant dry weight is shown in Table 4. The results showed that the highest plant dry weight was obtained from a nutrient dose of 1500 ppm and non-circulating drip irrigation, which was 16.93 grams. This result is consistent with the fresh weight of all plants (Table 3). Furthermore, the highest aerial part dry weight was obtained from the non-circulating drip irrigation hydroponic type and a dose of 1500 ppm (10.64 grams), while the highest root dry weight was obtained from the non-circulating drip irrigation hydroponic type with a nutrient dose of 1000 ppm (7.31 grams).

Drip irrigation is an efficient source of energy and water in the irrigation system. This technique delivers the required and appropriate amount to the plant roots and is applied periodically to reduce excessive evaporation from the area around the roots (*Bansal et al., 2021*) and can increase production (*Parthasarathi et al., 2018; El-Mageed et al., 2022*). In addition, non-circulating drip irrigation can reduce the impact of plant contamination from fungi/pathogens that attack and maintain the growing media's humidity, thereby optimizing plants' metabolic processes and the effectiveness of mineral nutrients absorbed by plants (*Moghadam et al., 2020; Esteves et al., 2022*).

Table 4

Interaction between hydroponic type treatment and nutrient dose (EC) on the dry weight of aerial part, roots, and plants

Treatment combination	Aerial part weight(g)		Root weight (g)		All plant weight (g)	
	[g]		[g]		[g]	
D1N1	6.65	abc	5.65	ab	12.30	a
D2N1	5.33	bc	6.93	a	12.26	a
D3N1	6.29	abc	4.19	b	10.48	ab
D1N2	8.50	ab	7.31	a	15.81	a
D2N2	10.64	a	6.29	ab	16.93	a
D3N2	3.24	c	1.51	c	4.75	b

Note: Numbers followed by the same letter in one column are not different in DMDT level 5%

2. Quality of harvest materials

The harvest materials determined their quality using specific proximate analysis such as moisture, ash, fat, and fiber content. In addition, the water and ethanol extractive content are also determined to find how many components could be extracted from the harvest materials.

The moisture content of the aerial part and root are not significantly different. It means that the treatment is not affected the moisture content. Moisture content mostly depends on the drying process. The moisture content in this research is about 10 – 11% (Table 5 and 6), which is higher than the previous report (about 9 – 10%) (*Rusmin, 2017*).

The ash content is also not affected by the treatment, which is from 8.46 to 12.22%. This content is the same as the previous report, from 10.25 – 12.60% (*Rusmin, 2017*). Fat content is also not significantly different among the treatment, aerial part, and root. However, the fat content in the aerial part is higher than in the root part. Different from the crude fat content, the crude fiber content varied among the treatment. The concentration of nutrition is affected by fiber content. The higher the nutrition concentration, the higher the fiber content found in the aerial part (Table 5). The lower the nutrition concentration, the higher the fiber content found in the root (Table 6). The highest fiber content is found in roots with a hydroponic recirculating drip system and 1000 ppm nutrition concentration.

Table 5

Quality of aerial harvest materials in each treatment combination

Treatment combination	Moisture content	Ash content	Fat content	Fiber content	Water extractive content	Ethanol extractive content
	[%]	[%]	[%]	[%]	[%]	[%]
D1N1	11.16	9.18	1.29	1.46a	21.55b	7.88
D2N1	11.82	10.65	1.05	5.34b	19.54b	7.14
D3N1	11.43	12.22	1.08	7.55b	17.75ab	6.38
D1N2	11.52	11.54	1.04	1.37a	13.25a	5.22

Treatment combination	Moisture content	Ash content	Fat content	Fiber content	Water extractive content	Ethanol extractive content
	[%]	[%]	[%]	[%]	[%]	[%]
D2N2	10.64	10.98	1.40	4.65b	14.50a	6.84
D3N2	10.51	11.96	1.07	6.87b	15.22a	7.13

Table 6

Quality of root harvest materials in each treatment combination

Treatment combination	Moisture content	Ash content	Fat content	Fiber content	Water extractive content	Ethanol extractive content
	[%]	[%]	[%]	[%]	[%]	[%]
D1N1	11.16	9.18	1.29	1.46a	21.55b	7.88
D2N1	11.82	10.65	1.05	5.34b	19.54b	7.14
D3N1	11.43	12.22	1.08	7.55b	17.75ab	6.38
D1N2	11.52	11.54	1.04	1.37a	13.25a	5.22
D2N2	10.64	10.98	1.40	4.65b	14.50a	6.84
D3N2	10.51	11.96	1.07	6.87b	15.22a	7.13

From an industrial point of view, water and ethanol extractive content is the most important quality. The industry produces the extract and then prepares the final product using the extract. The higher the extractive content, the quality of the material become better. The aerial part's water extractive content is higher than the root. The hydroponic type is affected by the water extractive content. The recirculating drip gave higher water extractive content compared with a non-circulating drip. The water extractive content in the aerial part of this research (13.25 – 21.55%) is lower than the previous report (26.55 – 46.25%, *Rusmin, 2017*).

Different from water extractive content in the aerial part, the ethanol extractive content in this research is higher (5.22 – 7.88%) than in the previous report (4.02 – 4.42%, *Rusmin, 2017*). However, the ethanol extractive content in the root part is lower than in the aerial part (Table 5 and 6). This is because the root part had lower extractive component content but higher fiber content, so this part is a fiber source. The results showed a tendency to increase the water and ethanol extractive content while the nutrient dose was low. It means that the extractive content produces more in lower nutrients. The low nutrient is a stress for Purwoceng, so this plant produces more secondary metabolites than high doses of nutrients.

Combining the dry weight of harvested materials in Table 4 and the extractive content in Table 5 and Table 6, the productivity of extractive content in each plant of cultivation treatment could be summarized in Table 7. For example, the high extractive content in root was found in the root that treated with 1000 ppm nutrient dose with recirculating drip could be applied to produce 1.22 g water extractive content/plant and 0.45 g ethanol extractive content/plant. On the other hand, to produce high extractive content in the aerial part, a 1500 ppm nutrient dose with a non-circulating drip could be applied to produce 1.54 g water extractive content/plant and 0.73 g ethanol extractive content/plant.

Table 7

The productivity of extractive content of all treatment combination

Treatment combination	Water extractive content		Ethanol extractive content	
	Aerial part	Root	Aerial part	Root
	[g/plant]	[g/plant]	[g/plant]	[g/plant]
D1N1	1.43	1.22	0.52	0.45
D2N1	1.04	1.35	0.38	0.49
D3N1	1.22	0.74	0.40	0.27
D1N2	1.13	0.97	0.44	0.38
D2N2	1.54	0.91	0.73	0.43
D3N2	0.49	0.23	0.23	0.11

3. Safety of Harvest Product

Microbiological safety was determined in each experimental group, aerial part, and roots. The determined microbiological safety includes total plate count (TPC), coliform, and mold/yeast. The results are shown in Table 8.

Based on the data in Table 8, it can be concluded that there is a diversity of measurement results for total plate number, coliform content, and yeast/mold content. Most of the samples showed the presence of microbes, and two herbal samples showed a negative test. From the positive, it appears that all samples of Purwoceng are still safe for consumption. This is based on the results of all samples showing the total plate number (TPC), the value of the coliform content, and the number of molds/yeasts below the standard, referred to as BPOM Regulation No. 13 of 2019 *(BPOM, 2019*).

Based on these regulations, the TPC for chopped products brewed with hot water or boiled before use is the maximum value of 5 x 10^7 colonies/gram. The Purwoceng sample showed a range of TPC values of 1.2 x 10^2 to 3.7 x 10^2 colonies/gram, namely the root sample of D2N2 treatment.

According to BPOM Regulation No. 13 of 2019, the molds/yeast number for chopped products that are brewed with hot water and boiled before use is the maximum value of 5 x 10^5 colonies per gram. The highest value of the Purwoceng sample for the molds/yeast number was 4.9 x 10^2, namely the D1N2 treatment root sample. For the coliform number, the limit of its presence for chopped products, according to the regulation, is 10^3 colonies/g. The D1N1 treatment root sample shows the highest coliform number in the Purwoceng sample of 2.9 x 10^2. Coliforms are only found in roots and not in the aerial part. In conclusion, all harvest materials are safe from microbial contaminants.

Table 8

The microbiology content of the harvested product

Treatment combination	Aerial part			Root		
	Total Plate Count (colony/g)	Coliform (colony/g)	Total Plate Count (colony/g)	Coliform (colony/g)	Total Plate Count (colony/g)	Coliform (colony/g)
	[colony/g]	[colony/g]	[colony/g]	[colony/g]	[colony/g]	[colony/g]
D1N1	1.6 x 10^2	negative	negative	2.3 x 10^3	2.9 x 10^2	Negative
D2N1	1.7 x 10^3	negative	negative	3.0 x 10^3	<10	2.5 x 10^2
D3N1	Negative	negative	negative	1.4 x 10^3	Negative	<10
D1N2	2.4 x 10^2	Negative	2.3 x 10^2	2.4 x 10^2	1.6 x 10^2	4.9 x 10^2
D2N2	1.2 x 10^2	negative	negative	3.7 x 10^2	negative	1.6 x 10^2
D3N2	negative	negative	negative	3.0 x 10^2	<10	2.5 x 10^2

The harvest materials' metal content analysis (Pb, Cd, and As) showed diversity (Table 9). Lead levels in the samples were in the range of 0.24 and 1.93 mg/kg. Cd was undetectable to 0.12 mg/kg, while As was undetectable to 0.72 mg/kg. Based on the reference to the BPOM regulation No. 13 of 2019 for chopped or simplified products, the safety requirements for heavy metals Pb, Cd, and As are 10, 0.3, and 5 mg/Kg, respectively. Based on this, it can be concluded that all samples are safe from contamination by the three metals. Lead metal was more dominant in the roots, arsenic metal in the aerials part, while cadmium did not show dominance in both parts of the sample.

Table 9

The heavy metal content of the harvested product

Treatment combination	Aerial part			Root		
	Pb	Cd	As	Pb	Cd	As
	[mg/Kg]	[mg/Kg]	[mg/Kg]	[mg/Kg]	[mg/Kg]	[mg/Kg]
D1N1	0.17	0.01	0.65	1.37	undetectable	undetectable
D2N1	0.56	0.02	0.48	1.93	0.12	undetectable
D3N1	0.71	0.01	0.72	0.25	undetectable	undetectable
D1N2	0.24	0.02	0.65	0.96	0.02	0.48
D2N2	0.24	undetectable	0.30	1.25	undetectable	undetectable
D3N2	0.36	0.01	0.28	0.85	0.01	0.11

Note: LOD As: 0.008 mg/kg; LOD Cd: 0.00011mg/kg

The presence of heavy metals in plants can come from the growing media. *Zarinkamar et al. (2021)* reported the presence of Cd content in flower parts of *Matricaria chamomilla* L. flowers grown in hydroponics media contaminated with Cd. The Cd content in flowers increases with Cd contaminants in the hydroponic media solution.

CONCLUSIONS

Drip hydroponic irrigation system is able to provide control of the growth environment for purwoceng plants well at lower altitudes (1500 m above sea level) than their natural habitat. The resulting growth performance is comparable to that of Purwoceng planted in the highlands as its natural habitat (higher than 2000 m). Recirculating and nonrecirculating drip hydroponic irrigation with a concentration of nutrients from 1000 – 2000 ppm could grow Purwoceng outside their natural habitat. Non-circulating drip irrigation with 1500 ppm of a nutrient is the best treatment to produce high water and ethanol extractive content in the aerial part, and circulating drip irrigation with 1000 ppm of the nutrient is the best treatment to produce high water and ethanol extractive content in the root of Purwoceng. All treatments produce safe harvest products based on microbial and metal contaminants (Pb, Cd, and As).

ACKNOWLEDGEMENT

This research was funded by RISPRO LPDP Republic of Indonesia (No: PRJ-46 / LPDP / 2020). The authors are grateful and honored to receive all the support.

REFERENCES

[1] Ahmadi, F., Samadi, A., Sepehr, E., Rahimi, A. and Shabala, S. (2021) Increasing medicinal and phytochemical compounds of coneflower (Echinacea purpurea L.) as affected by NO3−/NH4+ ratio and perlite particle size in hydroponics. *Scientific Reports*, 11, 15202.

[2] Anwar, N.S. (2001) Manfaat obat tradisional sebagai afrodisiak serta dampak positifnya untuk menjaga stamina. *Makalah pada Seminar Setengah Hari" Menguak Manfaat Herbal bagi Vitalitas Seksual". Jakarta*

[3] Arjadi, F., Kurniawan, D.W., Wibowo, Y., Siswandari, W. and Rujito, L. (2019) No acute toxicity tests of Purwoceng (Pimpinella pruatjan Molk.) ethanolic extract on male albino rat by determined hepatorenal function test and histopathology. *Molekul*, 14, 117–125.

[4] Balittro. (2000) Penggalian pemanfaatan dan karakterisasi mutu tumbuhan obat potensial dan langka. *Laporan Penelitian Balittro*, 47p.

[5] Bansal, G., Mahajan, A., Verma, A. and Singh, D.B. (2021) A review on materialistic approach to drip irrigation system. *Materials Today: Proceedings*, 46, 10712–10717.

[6] Bhagawan, W.S. and Kusumawati, D. (2020) Ethnobotanical medicinal plant study of Tengger tribe in Ranu Pani Village, Indonesia. *Proceedings of the the 3rd International Conference on Education \& Social Science Research (ICESRE)*

[7] BPOM. (2019) Peraturan BPOM 32 2019 tentang Persyaratan keamanan dan mutu obat tradisional.

[8] El-Mageed, A., Taia, A., El-Mageed, A., Shimaa, A., El-Saadony, M.T., Abdelaziz, S., et al. (2022) Plant growth-promoting rhizobacteria improve growth, morph-physiological responses, water productivity, and yield of rice plants under full and deficit drip irrigation. *Rice*, 15, 1–15.

[9] Giurgiu, R.M., Morar, G.A., Dumitraș, A., Boanciu, A.P., Duda, B.M. and Moldovan, C. (2014) Study regarding the suitability of cultivating medicinal plants in hydroponic systems in controlled environment. *Research Journal of Agricultural Science*, 46.

[10] Malda, G., Suzán, H. and Backhaus, R. (1999) In vitro culture as a potential method for the conservation of endangered plants possessing crassulacean acid metabolism. *Scientia Horticulturae*, 81, 71–87.

[11] Mohammadi Moghadam, M., Tavakkoli, A.R., Mohammadi, A.H., Moradi, M. and Hokmabadi, H. (2020) Effect of Irrigation Systems on the Contamination of Aspergillus flavus and Aflatoxin Production in Shahpasand Pistachio Cultivar. *Journal of Nuts*, 11, 237–244.

[12] Morgan, K.T. and Kadyampakemi, D. (2012) Open field hydroponics: Concept and application. *Advances in citrus nutrition* pp. 271–280. Springer.

[13] Nuryadin, E. and Nabiila, A. (2018) Potential Development of Purwoceng (Pimpinella pruatjan Molk or Pimpinella alpine Kds) Plant Scale Industry Using In-Vitro Culture Technique By Means of Rooting Induction. *Journal of Tropical Biodiversity and Biotechnology*, 3, 92–96.

[14] Parthasarathi, T., Vanitha, K., Mohandass, S. and Vered, E. (2018) Evaluation of drip irrigation system for water productivity and yield of rice. *Agronomy Journal*, 110, 2378–2389.
[15] Reyes Esteves, R.G., Gerba, C.P. and Slack, D.C. (2022) Control of Viral and Bacterial Contamination of Lettuce by Subsurface Drip Irrigation. *Journal of Irrigation and Drainage Engineering*, 148, 4022035.
[16] Rusmin, D. (2017) Pengembangan budidaya purwoceng (pimpinella pruatjan molk.) sebagai tanaman obat / The Development of Pruatjan (Pimpinella pruatjan Molk.) Cultivation as A Medicinal Crops. *Perspektif*, 16, 79–92.
[17] Sałata, A., Stepaniuk, R. and others. (2012) The effect of drip irrigation on zucchini cultivar'Soraya'yielding. *Annales Universitatis Mariae Curie-Skłodowska. Sectio EEE, Horticultura*, 22, 21–28.
[18] Srivastava, S., Nalla, V.K., Singh, V.P. and Prasad, R. (2022) Optimization of in vitro micropropagation and root establishment through combinatorial approaches for enhanced production of secondary metabolites in the endangered species Decalepis arayalpathra KMA 05 clones. *Brazilian Journal of Botany*, 45, 869–881.
[19] Sumarni, E., Farid, N. and Soesanto, L. (2017) A study of suitability of purwoceng medicinal plant on the hydroponic system with drip irrigation for preventing extinction. *Prosiding seminar nasional Perhimpunan Teknik Pertanian Indonesia. Unsyiah-Banda Aceh* pp. 2–3.
[20] Syahid, S., Rostiana, O., Miftakhurohmah, M. and others. (2005) Pengaruh naa dan iba terhadap perakaran purwoceng (Pimpinella pruatjan Molk.) 77V VITRO. *Jurnal Penelitian Tanaman Industri (Littri)*, 11.
[21] Wang, Y., Li, S., Qin, S., Guo, H., Yang, D. and Lam, H.-M. (2020) How can drip irrigation save water and reduce evapotranspiration compared to border irrigation in arid regions in northwest China. *Agricultural Water Management*, 239, 106256.
[22] World Health Organization (1998) *Quality Control Methods for Medicinal Plant Materials*. World Health Organization
[23] Zarinkamar, F., Moradi, A. and Davoodpour, M. (2021) Ecophysiological, anatomical, and apigenin changes due to uptake and accumulation of cadmium in Matricaria chamomilla L. flowers in hydroponics. *Environmental Science and Pollution Research*, 28, 55154–55165.

DESIGN AND EXPERIMENTAL STUDY OF A VEHICLE-MOUNTED FERTILIZING AND SPRAYING MACHINE
/
车载式施肥喷药机的设计与试验研究

Yujiang GOU, Huibo HE*, Huaying LI*, Daming WANG, Mian ZHANG [1]
College of Engineering and Technology, Southwest University, Chongqing/ P.R. China;
Tel: +86-23-68251265; E-mail: 1217968301@qq.com
DOI: https://doi.org/10.35633/inmateh-69-05

Keywords: *Agricultural machinery, Fertilizer application, Variable-rate spraying, Control system, Coefficient of variation*

ABSTRACT
In order to solve the problems of low efficiency of fertilization and spraying in the hilly mountains of China, a vehicle-mounted fertilization and spraying machine was designed. The whole structure and working principle of the machine were described, and the key components of fertilization and spraying are designed. The kinetics and kinematics of fertilizer particles and droplets were modeled by theoretical analysis of their motion characteristics in the air. The fertilization and variable spraying control system based on the core controller MCU (Microcontroller Unit) was set up. And the system can adjust the rotational speed of the disc and can automatically change the spraying volume by real-time detection of forward speed to achieve a constant spraying volume per unit area. The test results showed that: when the disc speed was greater than 90 r/min, the uniformity coefficient of variation was less than 15%, which satisfied the operational requirements; the uniformity coefficient of variation reached the minimum value of 10.03% when the disc rotation speed was 180 r/min, and the best fertilization performance was achieved at this time. In the spraying system, the actual spraying volume increased with the increased forward speed, and the relative error between the theoretical flow rate and the actual flow rate was 6.25% at most, and the average error was 5.94%, which could achieve the purpose of variable spraying. The research results can provide technical reference for the design and development of fertilization and spraying machinery in hilly areas.

摘要
针对中国丘陵山区施肥、喷药效率低的问题，设计了一种车载式施肥喷药机。介绍了该机的整机结构和工作原理，对施肥、喷药的关键部件进行了设计。通过对肥料颗粒和液滴在空气中的运动特性进行了理论分析，建立了其动力学和运动学模型。搭建了以单片机为核心控制器的施肥与变量喷药控制系统，该系统可调节圆盘转速，并能通过实时检测前进速度自动改变喷药量，实现单位面积喷药量恒定作业。试验结果表明: 当圆盘转速大于 90r/min 时，均匀性变异系数均小于 15%，满足作业要求；当圆盘转速为 180r/min 时,均匀性变异系数达到最小值 10.03%，此时施肥性能最好。喷药系统中，实际喷药量随前进速度的增大而增大，理论流量与实际流量的相对误差最大为 6.25%，平均误差为 5.94%，能够达到变量喷药的目的。研究结果可为丘陵山区施肥与喷药机械的设计与研制提供技术参考。

INTRODUCTION
Fertilization and spraying are important and effective ways to meet planting requirements and improve crop yield and quality in agricultural production (*Mueller et al., 2012; Owen-Smith et al., 2019*). According to reports, the consumption of fertilizers and pesticides in agricultural production in China is increasing year by year, and its average consumption is much higher than the global level (*Chen et al., 2015; Gargari et al., 2019; Chen et al., 2018*). However, the current utilization rate of fertilizers and pesticides in China is not high. Among them, the utilization rate of chemical fertilizers is only 30%-40%, and the utilization rate of pesticides is only 30%-50% (*Yang et al., 2020; Mei et al., 2016*). Therefore, it is necessary to achieve efficient fertilization and spraying by using machines to improve agricultural productivity and protect the environment.

In the research of fertilizer applicators, some scholars designed a layered and quantitative fertilization device and optimized its parameters, and field experiments showed that the device meets the requirements of fertilization (*Liu et al., 2021*).

[1] [1] *Yujiang Gou.,M.S.; Huibo He.;A. Prof.; Huaying Li,A. Prof.*

Some scholars developed a double-disc centrifugal variable rate fertilizer spreader by combining discrete element simulation and control algorithm (*Abbou-ou-Cherif et al., 2019*). Other scholars have designed a multi-reflux variable spraying control system. The control system can adjust the proportional control valve according to the driving speed of the spraying machine, and then change the spraying flow to realize the variable spraying (*Wang et al., 2019*).

The above research is mainly focused on the research of large and single operation machinery. However, it is difficult for large-scale fertilizer spreaders and sprayers to carry out field operations due to the complicated terrain in hilly areas of China (*Reyes et al., 2015; He, 2020*). Consequently, this paper proposes a vehicle-mounted fertilizing and spraying machine to meet the needs of agricultural production, which is small in size and light in weight. And it can improve people's work efficiency.

MATERIALS AND METHODS

General structure and operational principle

The vehicle-mounted fertilizing and spraying integrated machine was composed of four parts: control system; fertilization device; spraying device and walking device. Its general structure is shown in Fig.1.

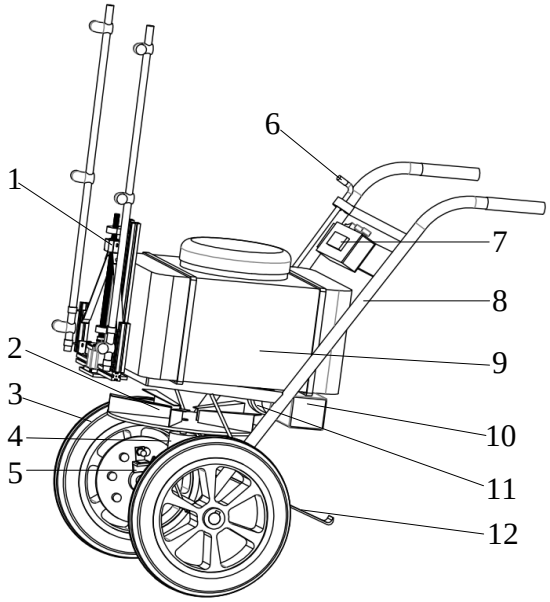


Fig. 1 - Structural diagram of vehicle-mounted fertilizer spreading and spraying machine

1. Multi-directional adjustable spray rod device; 2. Fertilizing disc; 3. Wheel; 4. DC motor of row of fertilizer; 5. Hall speed measuring device; 6. Fertilizer adjustment lever; 7. Control system; 8. Rack; 9. Water/Fertilizer box; 10. Battery; 11. Pump; 12. Brace

When the machine is running, fertilization or spray operations should be independently chosen by the staff according to their actual needs. If people choose fertilization operations, they can manually control the fertilizer adjustment rod to adjust the size of the opening of the fertilizer mouth, and the rotation speed of the fertilizer disc is set by manually adjusting the knob. The fertilizer falls onto the disc by gravity and is spread by the centrifugal force of the disc. If people want to carry out spraying operations, the angle of spread between the spray bars can be adjusted electrically through the knob, and users can independently select three different spraying modes: horizontal, vertical and tilt, in order to improve the coverage of fog drops. The amount of spray per unit area is set by the potentiometer, and the wheel speed is collected by the control system to change the amount of spray in real time, so as to achieve the purpose of variable spray.

Fertilizer application mechanism design

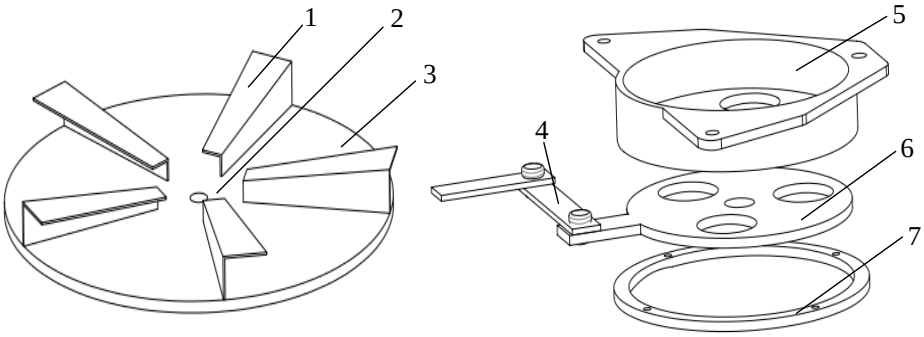
Fertilizer application mechanism mainly includes the fertilizer spreading disc and fertilizer volume adjustment device. Its structure is shown in Fig. 2. The fertilizer spreading disc is mainly composed of the disc, fertilizer bearing area and the blades. The fertilizer adjustment device mainly includes a fixed plate, moving plate, fixed ring and adjusting lever, which are used to adjust the fertilizer application amount by controlling the mutual position of the moving plate and the fixed plate.

Kinematics Analysis of fertilizer granules in air

According to theoretical mechanics, the centrifugal force on the fertilizer particle must be greater than or equal to its friction force in order for it to be thrown from the disk, which satisfies the formula:

$$\begin{cases} mr\omega^2 \geq \mu mg \\ \omega = 2\pi n \end{cases} \quad (1)$$

where: m is the mass of fertilizer particles, g; r is the distance between fertilizer particles and the center of the disc, mm; μ is the friction coefficient between the particles and the disc; ω is the rotational angular speed of the disc, rad/s; n is the rotational frequency of the disc, s^{-1}.



(a) Fertilizer spreading disc *(b)Fertilizer adjustment device*

Fig. 2 - The structure of fertilizer application mechanism

1. Disc; 2. Fertilizer bearing area; 3. Blade; 4. Adjusting lever; 5. Fixed plate; 6. Moving plate; 7. Fixed ring

Then, according to Equation (1), the rotation frequency n of the disk needs to meet:

$$n \geq \frac{1}{2\pi}\sqrt{\frac{\mu g}{r}} \quad (2)$$

Assuming that the rotation of the particles themselves and the influence of wind speed in the environment on fertilizer spreading are ignored, the fertilizer particles thrown into the air are mainly subjected to the action of air resistance F and gravity G and fall to the ground along a parabola (*Shi et al., 2018; Shi et al., 2021*). As shown in Fig. 3, the motion state can be divided into two stages: upthrow and descent. Then, the gravity and air resistance of the fertilizer particles, respectively, are:

$$\begin{cases} F = \frac{1}{2}\rho SCV^2, \quad S = \frac{\pi d^2}{4} \\ G = mg, \quad m = \frac{\pi}{6}\rho d^3 \end{cases} \quad (3)$$

where: C is the air resistance coefficient, sphere $C = 0.44$; ρ is the air density, kg/m^3; S is the windward area of fertilizer particles, m^2; V is the relative velocity of fertilizer particles with air, m/s.

In the upthrowing stage, the air resistance and gravity decomposition of fertilizer particles can be divided into horizontal and vertical directions. According to Newton's second law, it can be obtained:

$$\begin{cases} F_{X1} = \frac{\rho SC}{2}\sqrt{V_{X1}^2 + V_{Z1}^2}V_{X1} \\ \frac{\mathrm{d}^2 X_1}{\mathrm{d}t_1^2} = -\frac{F_{X1}}{m} \\ F_{Z1} = \frac{\rho SC}{2}\sqrt{V_{X1}^2 + V_{Z1}^2}V_{Z1} \\ \frac{\mathrm{d}^2 Z_1}{\mathrm{d}t_1^2} = -\frac{F_{Z1}}{m} - g \end{cases} \quad (4)$$

It can be obtained from Equation (4) that:

$$\begin{cases} t_1 = \sqrt{\frac{2mZ_1}{F_{Z1} + mg}} = \sqrt{\frac{4mZ_1}{\rho SC\sqrt{V_{X1}^2 + V_{Z1}^2}V_{Z1} + 2mg}} \\ X_1 = \frac{F_{X1}t^2}{2m} = \frac{\rho SC\sqrt{V_{X1}^2 + V_{Z1}^2}V_{X1}Z_1}{\rho SC\sqrt{V_{X1}^2 + V_{Z1}^2}V_{Z1} + 2mg} \end{cases} \quad (5)$$

where: V_{X1} is the horizontal component of the velocity of fertilizer particles in the upthrowing stage, m/s;

V_{Z1} is the vertical component of the velocity of fertilizer particles at the upthrowing stage, m/s;

t_1 is the movement time of the upthrowing stage, s;

Z_1 is the vertical displacement of fertilizer particles in the upthrowing stage.

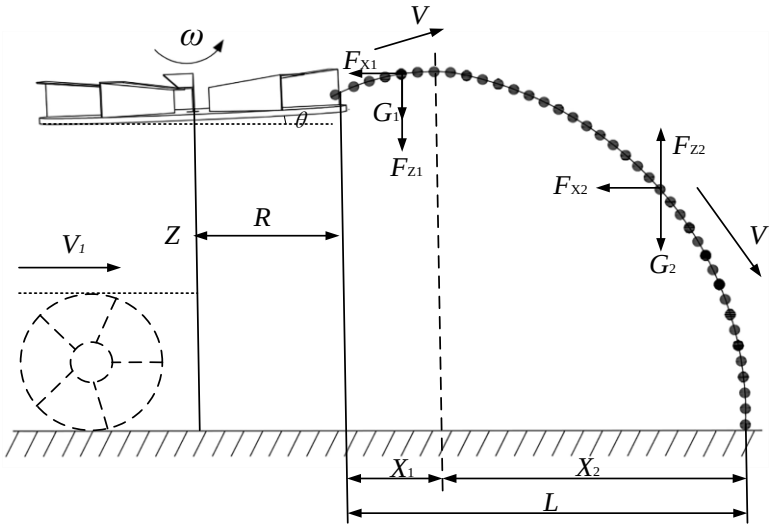


Fig. 3 - Analysis of movement and force of fertilizer particles in air

In the descending stage, the air resistance and gravity of fertilizer particles can also be decomposed in the horizontal and vertical directions. According to Newton's second law, it can be obtained:

$$\begin{cases} F_{X2} = \dfrac{\rho SC}{2}\sqrt{V_{X2}^2 + V_{Z2}^2}V_{X2} \\ \dfrac{\mathrm{d}^2 X_2}{\mathrm{d}t_2^{\,2}} = -\dfrac{F_{X2}}{m} \\ F_{Z2} = \dfrac{\rho SC}{2}\sqrt{V_{X2}^2 + V_{Z2}^2}V_{Z2} \\ \dfrac{\mathrm{d}^2 Z_2}{\mathrm{d}_2^{\,2}} = \dfrac{F_{Z2}}{m} - g \end{cases} \tag{6}$$

According to Equation (6), the time and horizontal displacement of the descending stage can be calculated as:

$$\begin{cases} t_2 = \sqrt{\dfrac{2mZ_2}{F_{Z2} + mg}} = \sqrt{\dfrac{4mZ_2}{\rho SC\sqrt{V_{X2}^2 + V_{Z2}^2}V_{Z2} + 2mg}} \\ X_2 = \dfrac{\rho SC\sqrt{V_{X2}^2 + V_{Z2}^2}V_{X2}Z_2}{2mg - \rho SC\sqrt{V_{X2}^2 + V_{Z2}^2}V_{Z2}} \end{cases} \tag{7}$$

Where, V_{X2} is the horizontal component of fertilizer particle velocity in descending stage, m/s; V_{Z2} is the vertical component of fertilizer particle velocity in descending stage, m/s; t_2 is the movement time of descending stage, s; Z_2 is the vertical displacement of fertilizer particles in descending stage.

From the above equations (5) and (7), the total time t and total displacement L of fertilizer particles moving in the air can be obtained as:

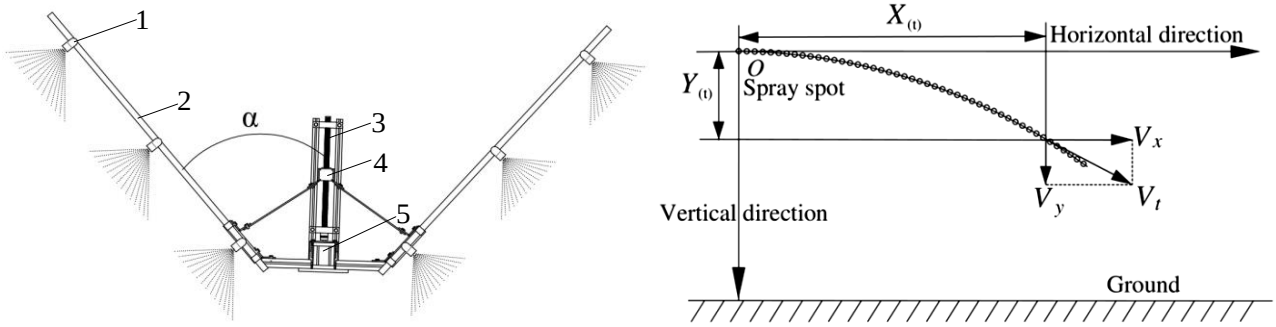
$$\begin{cases} t = t_1 + t_2 \\ L = X_1 + X_2 \end{cases} \tag{8}$$

According to the above equations (5), (7) and (8), it can be seen that the main factors affecting the distance and time of fertilizer particles are the motion speed and the height of the fertilizer disc in the process of scattering. Based on agronomic requirements and design experience, the diameter and height of the fertilizing disc were set to 250 mm and 500 mm respectively.

Adjustable spray rod mechanism design

The adjustable spray rod mechanism is mainly used to adjust the angle of spray rod expansion by a stepper motor and ball screw mechanism. Its structure is shown in Fig. 4(a). The nozzle is installed on the spray rod and it can be rotated, and the distance between the nozzles is 40 cm. The spray rod is installed on the spray rod, and its horizontal expansion length is 200 cm. The slider and the spray rod are connected by a connecting rod, and the spray rod is installed on the crank. And the control system can move the slider up and

down by controlling the forward and reverse rotation of the stepper motor to realize the adjustment of different spray modes.



(a) Structure drawing of adjustable spray rod *(b) Droplet trajectory*

Fig. 4 - Structure drawing of adjustable spray rod

1. Nozzle; 2. Spray rod; 3. Screw rod; 4. Slider; 5. Stepping motor

Kinematics Analysis of droplets in air

When the liquid droplet is ejected from the nozzle, it will make a variable speed movement in the air. Its movement trajectory is shown in Fig. 4(b). The volume and mass of the droplet during its motion are assumed to be constant. Considering that the droplets are fluid, it is known from fluid mechanics that if a single droplet is taken as the research object, the droplet is mainly affected by viscous resistance and gravity in the air. Decomposing the viscous drag f into two directions such as horizontal and vertical, the following formula can be obtained according to Newton's second law.

$$\begin{cases} f_x = -CV_x = m\dfrac{\mathrm{d}V_x}{\mathrm{d}t} \\ f_y = mg - CV_y = m\dfrac{\mathrm{d}V_y}{\mathrm{d}t} \end{cases} \tag{9}$$

where: C is the coefficient of viscous resistance; V_x is the partial velocity in the horizontal direction; V_y is the partial velocity in the vertical direction.

Given that the initial condition is $V_x=V, V_y=0$, the velocity of the droplet motion at moment t can be obtained by integrating equation (9) in the 0-t moment.

$$\begin{cases} V_x = Ve^{-\frac{C}{m}t} \\ V_y = \dfrac{mg}{C}\left(1-e^{-\frac{C}{m}t}\right) \end{cases} \tag{10}$$

The displacement of the droplet in the horizontal and vertical directions can be calculated.

$$\begin{cases} X_{(t)} = V_t\dfrac{m}{C}\left(1-e^{-\frac{C}{m}t}\right) \\ Y_{(t)} = \dfrac{m^2g}{C}\left(\dfrac{t}{m}+e^{-\frac{C}{m}t}-\dfrac{1}{C}\right) \end{cases} \tag{11}$$

The solve function in MATLAB is used to solve (11), and the trajectory equation of the droplet movement in the air can be obtained as:

$$Y_{(t)} = -\frac{mg}{CV}X_{(t)} - \frac{m^2g}{C^2}\ln\left(1-\frac{C}{mV}X_{(t)}\right) \tag{12}$$

As can be seen from the droplet motion track equation (12) above, when the droplet ejection height is certain, the droplet spray width in the horizontal direction mainly depends on the initial velocity V of the droplet when it leaves the nozzle. So, the droplet spray speed can be adjusted by changing the PWM duty cycle through the control system to improve the droplet coverage.

Hardware design of control system

According to the general principle of modular division, the control system of the vehicle-mounted fertilization and spraying machine is mainly composed of six parts: main control chip (STC89C52 microcontroller), user setting module, velocity detection module, prompt and alarm module, LCD display in module and motor drive module.

The design block diagram is shown in Fig. 5. These modules are described in detail below in turn.

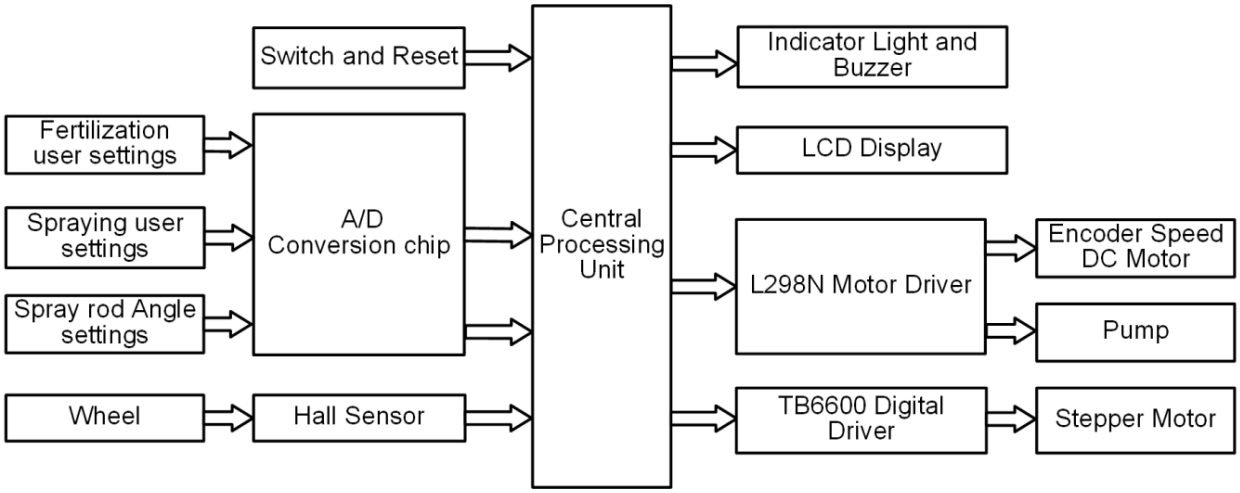


Fig. 5 - Schematics of control system of variable-rate spray

User setting module

User setting module includes three parts: setting unit of rotation speed of fertilization disk, setting unit of spraying volume per unit area and setting unit of spreading angle of spray rod. The operator adjusts the output voltage of the potentiometer by rotating the knob, and the signal is transmitted to the microcontroller through the A/D converter chip. As shown in Fig. 6 (a). The microcontroller receives the signal and outputs PWM pulse signals to control the operation of the coded DC gear motor, water pump and stepper motor after internal timer and counter calculation.

Velocity detection module

In order to achieve variable spraying, the forward speed of the vehicle needs to be collected. The speed detection module consists of a wheel and a Hall sensor mounted on the wheel hub, and a number of magnets are mounted on the disk directly opposite to the Hall sensor, as shown in Figure 1. When the disc rotates with the wheel, the magnetic induction signal received by the Hall sensor (A3144E) is input to the MCU. And the internal timer of the MCU can calculate, by processing the pulse frequency of the Hall sensor and combining with the wheel radius, the vehicle forward speed.

Prompt and alarm module

The prompt and alarm module is mainly composed of a buzzer and LEDs, and its circuit schematic is shown in Fig. 6(c) and (d). Since the operating voltage of the buzzer is so large that the output voltage of the microcontroller I/O cannot be driven directly, a triode amplifier circuit is used to drive it. In addition, the circuit module is designed with current-limiting resistors to prevent excessive current to ensure system safety. By setting the normal human walking speed of 0.4~1.2 m/s in the system, when the system detects that the forward speed is not within the normal operating range, the microcontroller controls the buzzer to make a sound and the LED light flashes continuously to prompt the operator to adjust the operating speed.

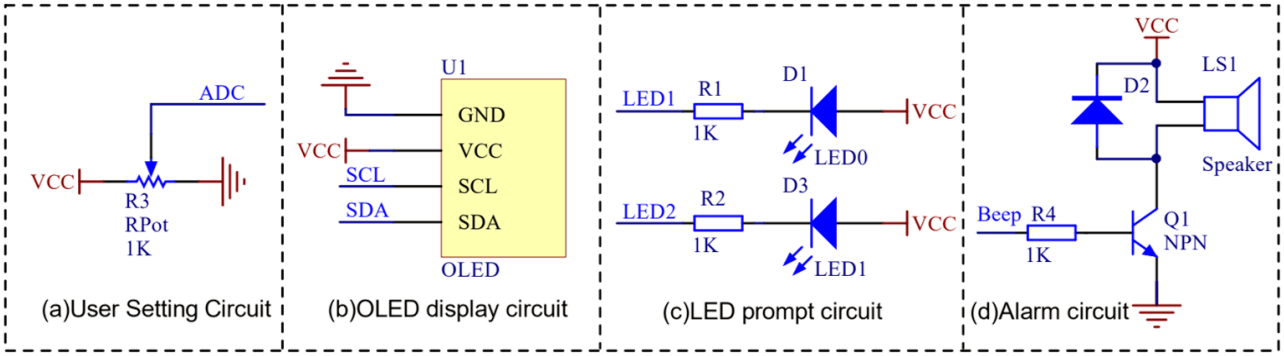


Fig. 6 - Control system submodule circuit schematic

OLCD display module

In order to monitor the operation status of fertilization and spraying operation in real time and facilitate human-computer interaction, liquid crystal display is used to display information such as forward speed, disc speed and spraying volume per unit area, as shown in Fig. 6(b). Since OLED has the advantages of self-illumination and high contrast, 0.96-inch OLED display is used as the display of the human-machine interaction interface. The SCL and SDA interfaces of the OLED display are connected to the I/O ports of the microcontroller, and the data display function can be realized through one-way data transmission.

Motor drive module

The motor drive module includes a DC geared motor drive circuit, a water pump drive circuit and a stepper motor drive circuit. The DC geared motor and the water pump are driven by the L298N motor drive module, and the speed of the motor can be adjusted by adjusting the PWM duty cycle of the MCU output. The DC geared motor has its own Hall encoder, which can measure the speed in real time and is mainly used to drive the rotation of the fertilizer spreading disc. The water pump changes the spraying flow rate in real time according to the forward speed detected by the system and the spraying volume per unit area set by the user to realize variable spraying. The stepper motor is driven by TB6600 digital driver. And the operator mainly uses the knob to control the output of the high and low level signals of the microcontroller to control the operation of the stepper motor.

Software system design

The software system is written in C language, and the modular design is based on the hardware circuit. The flow chart of the system control program is shown in Fig. 7.

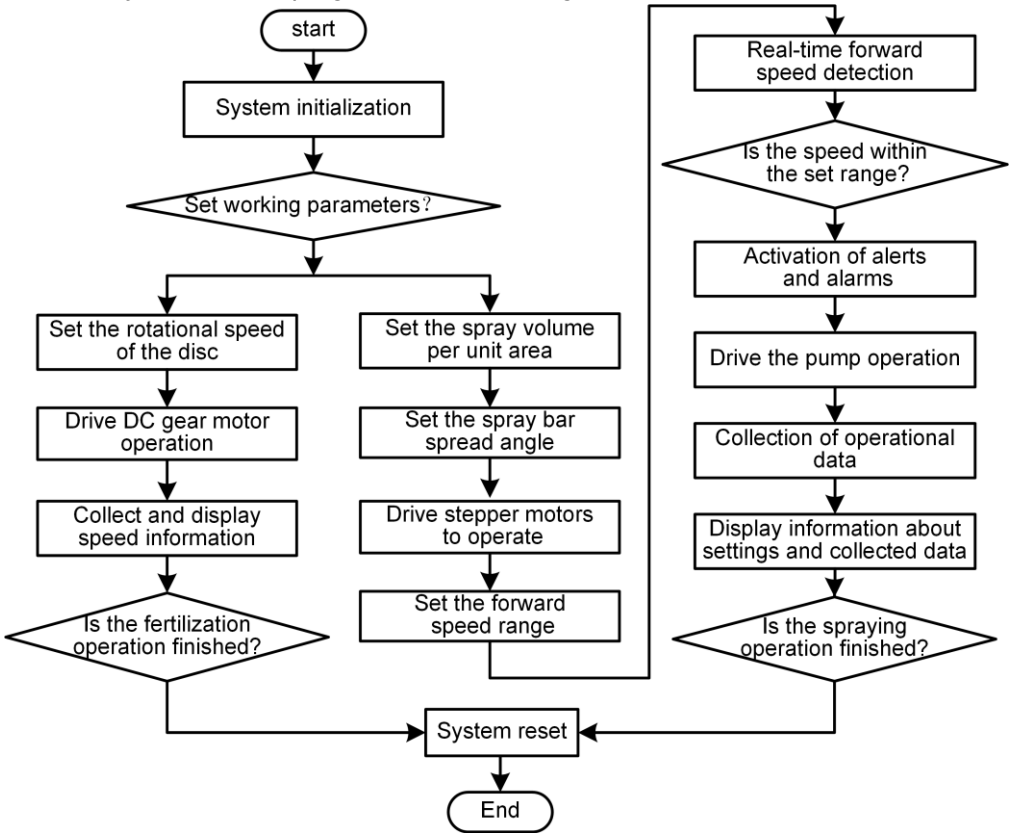


Fig. 7 - Software system flow chart

Firstly, the system is initialized after being powered on, the user selects either fertilizer application or spraying operation. For fertilizer application, the speed of the DC motor is set and the fertilizer spreading disc is driven to rotate for fertilizer application. If the spraying operation is selected, the spraying volume per unit area and the spraying angle of the spray rod are set first. After the system enters the operation state, the forward speed is detected automatically and the pump is controlled to carry out variable spraying. If the detected speed is not within the setting range, the system automatically enters the prompt and alarm program. In addition, the data information during fertilization and spraying is transmitted to the display screen in real time for display.

RESULTS AND ANALYSIS

Performance test of fertilization

The uniformity of fertilizer distribution is an important index to evaluate the effect of fertilization. Generally, the coefficient of variation of uniformity is used to evaluate the uniformity of fertilization (*Yu et al., 2019*). The calculation formula is:

$$\begin{cases} C_V = \frac{S_D}{\bar{m}} \times 100\% \\ S_D = \sqrt{\frac{1}{n-1}\sum_{i=1}^{n}(m_i - \bar{m})^2} \\ \bar{m} = \frac{1}{n}\sum_{i=1}^{n} m_i \end{cases} \quad (13)$$

where: C_V is the coefficient of variation of particle distribution, %; S_D is the standard deviation of fertilizer particle quality, g; m is the average mass of fertilizer particles, g; m_i is the quantity of fertilizer particles in the collection box, g; n is the number of collection boxes.

The test material is urea fertilizer pellets with particle size of 0.9~2.8 mm, and the test site is on cement ground. The test method is based on the test method of centrifugal fertilizer spreader as specified in ISO 5690 and ASAE 341.2, and the two-dimensional matrix collection method is adopted. A total of 48 collection boxes (25cm×19cm×6.5cm) were evenly arranged in the test area, with column spacing of 1.2 and row spacing of 1 m. According to the results of the previous study, the opening degree of the fertilizer outlet was set to 60%, because the best fertilization performance was achieved at the same rotation speed of the disk at this time. At the same time, the rotation speed range of the disc was set to 90~210 r/min, and the trolley was run at a certain speed through the collection area after stabilization. After the test, the mass of fertilizer particles in the collection box was weighed using an electronic scale, and the coefficient of variation of uniformity was calculated. The test was repeated three times to take the average value, and the results are shown in Table 1. The test scene is shown in Fig. 8.

Table 1

Test result of fertilizer uniformity

Number of test	Rotation speed of the fertilizer spreading disc /(r/min)				
	90	120	150	180	210
1	17.18	15.16	11.52	10.28	13.56
2	17.86	14.58	10.88	9.45	12.36
3	16.57	14.97	11.05	10.37	13.88
Average value/%	17.20	14.90	11.15	10.03	13.27

As shown in Table 1, the coefficient of variation of uniformity tended to decrease and then increase when the rotation speed of the disc was set to 90~210 r/min, indicating that too low or too high rotating speed of the disc would affect the uniformity of fertilizer spreading. When the rotation speed of the disc was greater than 90 r/min, the uniformity coefficient of variation was less than 15%, which satisfied the relevant regulations for fertilizer application machinery operation (*NYT1003-2006*). Therefore, the rotation speed of the disc should be set above 90 r/min as far as possible in the actual operation. The coefficient of variation of uniformity reached a minimum value of 10.03% when the disc speed was 180 r/min, indicating that the best performance of spreading fertilizer was achieved at this time.



Fig. 8 - Performance test of fertilization



Fig. 9 - Variable spraying performance test

Performance test variable spray

The variable spraying performance test was conducted with reference to the relevant national standard JB/T 9782-2014 "Equipment for crop Protection-General test methods". And the spraying performance was evaluated by using the spraying volume error per unit area *(Luck et al., 2015; Hussain et al.,2020)*. Assuming that the theoretical spraying amount per hectare (1000m^2) is K_0, it can be obtained:

$$Q_1 = \frac{K_0 vL}{600} \tag{14}$$

where:

Q_1 is the system's theoretical spray volume per minute, L/min;

K_0 is the unit area spray volume, L/hm^2;

v is the forward speed, km/h; L is the spray width, m.

In order to conduct the test more conveniently and accurately, the water liquid was used instead of the medicine solution, and the test was carried out in manual mode. When the test was turned on, the unit area spraying volume was set as 600 L/hm^2, the forward speed was set as 0.4, 0.8 and 1.2 m/s respectively, and the test time was set as 2 min. A bucket was used to take up the water solution flowing from the pump, and the electronic scale was used to weigh the mass of the water solution collected in the bucket. Finally, the test data is brought into equation (15) to calculate the actual flow rate value, and the test results are shown in Table 2, and the test scenario is shown in Fig. 9.

$$Q_2 = \frac{V}{t} = \frac{6m}{1000\rho} \tag{15}$$

where:

Q_2 is the actual flow, L/min; m is the mass of the water liquid, g;

ρ is the volume mass of water, kg/L; t is the time of the spray work, s.

Table 2

Test result of variable spray control precision

Forward speed (m/s)	Theoretical flow (L/min)	Actual flow (L/min)	Relative error (%)	Average error (%)
0.4	3.60	3.78	5.83	5.94
0.8	7.20	7.65	6.25	
1.2	10.80	11.42	5.74	

The test results show that: the actual spraying volume increases with the increase in forward speed when the variable spraying system is operating under the condition of setting the amount of spray per unit area. And the relative error between the theoretical flow and the actual flow is 6.25% at most, with an average error of 5.94%, which indicates that the system is reasonably designed and can achieve the purpose of variable spraying.

CONCLUSIONS

In this paper, a vehicle-mounted fertilization and spraying machine suitable for operation in hill and mountain operations, with contributions mainly reflected in three aspects.

(1) The structure and operating principle of the whole machine were determined, and the design and description of the fertilization device and the adjustable spray rod device were carried out. The kinetic analysis of the movement of fertilizer particles and droplets in the air was also carried out to determine the key design parameters.

(2) The hardware circuit was designed using a modular design method, and a control system with a microcontroller as the core controller was built. The system can adjust the disc speed in real time for fertilizer application operation; and can change the spraying volume according to the forward speed by setting the unit area spraying volume system to realize variable spraying operation.

(3) Fertilizer application and spraying performance tests were conducted on the developed prototype. The test results showed that the coefficient of variation of uniformity was less than 15% when the rotation speed of the disk is greater than 90 r/min, and the coefficient of variation of uniformity reached the minimum value of 10.03% when the rotation speed of the disk was 180 r/min, and the fertilizer application performance is the best at this time. In the spraying system, the actual spraying volume increased with the increased forward speed, and the relative error between the theoretical flow rate and the actual flow rate was 6.25% at most, and the average error was 5.94%, which could achieve the purpose of variable spraying.

ACKNOWLEDGEMENT

The authors acknowledge the financial support provided by the project of National College Students Innovation and Entrepreneurship Training Program [202110635066] and the project of Chongqing Science and Technology Commission [cstc2020jscx-msxmX0192].

REFERENCES

[1] Abbou-Ou-Cherif E., Piron E., Chateauneuf A. et al, (2019), On-the-field simulation of fertilizer spreading: Part 3-Control of disk inclination for uniform application on undulating fields, *Computers and Electronics in Agriculture*, Vol.158, pp.150-158;

[2] ASAE S341.2. *Procedure for measuring distribution uniform and calibrating granular broadcast spreaders*;

[3] Chen C., He P., Zhang J., (2018) A fixed-amount and variable-rate fertilizer applicator based on pulse width modulation, *Computers and Electronics in Agriculture*, Vol.148, pp.330-336;

[4] Chen Y., Long H., Liu Z., (2015), Actuality and measures of fertilization technology and machinery in China, *Journal of Agricultural Mechanization Research*, Vol.37, No.4, pp.255-260;

[5] Gargari H.P., Teimourlou R.F., Valizadeh M., (2019), Spray droplet characterization using a piezoelectric sensor through classification based on machine learning, *INMATEH-Agricultural Engineering*, Vol.59, No.3, pp.151-160;

[6] ISO 5690-2-1984 Equipment for distributing fertilizers-Test methods-Part 2: Fertilizer distributors in lines;

[7] Liu X., Wang X., Chen L., et al, (2021), Design and experiments of layered and quantitative fertilization device for rapeseed seeder (油菜直播机分层定量施肥装置设计与试验), *Transactions of the Chinese Society of Agricultural Engineering*, Vol.37, No.5, pp.1-10;

[8] Luck J.D., Shearer S.A., Sama M.P. et al. (2015). Control system development and response analysis of an electronically actuated variable-orifice nozzle for agricultural pesticide applications. *Transactions of the ASABE*, Vol.58, No.4, pp.997-1008;

[9] Mei Y., Qi L., Ji R. et al, (2016), Design and experiment of remote control system of greenhouse self-propelled mist sprayer (温室自走式弥雾机远程控制系统的设计与试验), *Journal of China Agricultural University*, Vol.20, No.1, pp.170-175;

[10] Mueller N.D., Gerber J.S., Johnston M. et al, (2012), Closing yield gaps through nutrient and water management, *Nature*, Vol.490, pp.254-257;

[11] NYT 1003-2006. *Technical specification of quality evaluation for fertilizing machinery*;

[12] Owen-Smith P., Perry R., Wise J. et al, (2019), Spray coverage and pest management efficacy of a solid set canopy delivery system in high density apples, *Pest management science*, Vol.75, No.11, pp.3050-3059;

[13] Reyes J.F., Esquivel W., Cifuentes D. et al, (2015), Field testing of an automatic control system for variable rate fertilizer application, *Computers and Electronics in Agriculture*, Vol.113, pp.260-265;

[14] Shi Y., Chen M., Wang X., et al, (2018), Numerical simulation of spreading performance and distribution pattern of centrifugal variable-rate fertilizer applicator based on DEM software, *Computers and Electronics in Agriculture*, Vol.114, pp.249-259;

[15] Shi Y., Xi X., Gan H. et al, (2021), Design and Experiment of Row-Controlled Fertilizing–Weeding Machine for Rice Cultivation, *Agriculture*, Vol.11, No.6, pp.527;

[16] Wang X., Hu Z., Li X., et al, (2019), Design and Experiment of Multi-reflux Variable Spraying Control System(多回流式变量喷药控制系统设计与试验), *Transactions of the Chinese Society for Agricultural Machinery*, Vol.50, No.2, pp.123-131;

[17] He X., (2020), Research progress and developmental recommendations on precision spraying technology and equipment in China (中国精准施药技术和装备研究现状及发展建议). *Smart Agriculture*, Vol.2, No.1, pp.133-146;

[18] Hussain, N., Farooque, A.A., Schumann, A.W. et al, (2020), Design and Development of a Smart Variable Rate Sprayer Using Deep Learning. *Remote Sensing*, Vol.12, No.21, pp.4091;

[19] Yu H., Ding Y., Fu X., et al, (2019), A solid fertilizer and seed application rate measuring system for a seed-fertilizer drill machine. *Computers and Electronics in Agriculture*, Vol.62, pp.836-844;

[20] Yang Q., Wang Q., Li H., et al, (2020), Development of layered fertilizer amount adjustment device of pneumatic centralized variable fertilizer system (气力集排式变量排肥系统分层施肥量调节装置研制), *Transactions of the Chinese Society of Agricultural Engineering*, Vol.36, No.1, pp.1-10.

RESEARCH ON PREDICTION OF SOIL ORGANIC MATTER CONTENT BASED ON HYPERSPECTRAL IMAGING
/
土壤有机质含量的高光谱成像预测研究

Guoliang WANG[1,2]; Huiling DU[3]; Wenjun WANG[1]; Jiangui ZHAO[1]; Hong LI[2]; Erhu GUO[2]; Zhiwei LI*[1]
[1]College of Engineering, Shanxi Agriculture University, Taigu/China
[2]Millet Research Institute, Shanxi Agricultural University, Changzhi/China
[3]Department of Basic Education, Shanxi Agricultural University, Taigu/China
Tel: +86-0354-6289384; E-mail: lizhiweitong@163.com
DOI: https://doi.org/10.35633/inmateh-69-06

Keywords: *hyperspectral imaging, content of soil organic matter, numerical transformation, key bands extraction*

ABSTRACT
*Soil nutrient content is an important index to evaluate the growing environment of crops. Rapid access to soil nutrient information is an important requirement for the development of modern precision agriculture, while the detection of soil organic matter content is a necessary condition for understanding basic soil fertility and implementing crop precision cultivation. In this paper, the soil of rural fields in the southeast of Shanxi Province before sowing was taken as the research object. 111 soil samples to be tested were collected. After the process of drying, impurity removal, and grinding, the hyperspectral data of the Region of interest (ROI) of the samples were collected, and then the chemical determination of soil organic matter content was conducted. The original spectral data matrix was pretreated by numerical transformation operations, such as arithmetic mean, average deviation, 1st derivation, natural logarithm, and mixed multiplication, and a Partial least square regression (PLSR) quantitative analysis model was established. In these models, the obtained prediction set RP value under the pretreatment of F(A)*ln(AD) was the highest, reaching 0.8859. For spectral data preprocessed by F(A)*Ln(AD), the Competitive adaptive reweighted sampling (CARS) algorithm and Random frog (RF) algorithm were used to select key variables. The PLSR model was established by using F(A)*Ln(AD)&CARS data processing method and the RP value was increased to 0.9545. The prediction results can accurately reflect the real content of soil organic matter. The results of this study can provide theoretical support for the application of hyperspectral imaging technology in the determination of soil organic matter content, and provide a reference for the rapid detection of other soil components.*

摘要
土壤养分含量是评价作物生长环境的重要指标，能够快速获取土壤养分信息是发展现代精准农业重要要求，而对土壤有机质含量检测，是了解土壤基础地力，实施农作物精细化耕作必要条件。本文以晋东南地区农家田播种前土壤为研究对象，采集待测土壤样本 111 份，经晾晒、去杂及研磨等工序后采集样本兴趣区域(Region of interest，ROI)高光谱数据，随后进行土壤有机质含量化学测定。对采集到原始光谱数据矩阵进行均值、均差、求导、取自然对数及混合相乘等数值变换运算预处理，并建立土壤有机质偏最小二乘回归(Partial least square regression，PLSR)定量分析模型，其中运用均值一阶导数乘以均差值取自然对数(F(A)∗ln(AD))建立 PLSR 模型这种预处理方式，所得预测集 Rp 值最高，达到 0.8859。对 F(A)∗ln(AD)预处理下光谱数据分别采用竞争性自适应重加权采样法(Competitive adaptive reweighted sampling，CARS)及随机蛙跳(Random frog，RF)法选择特征波段处理，并建立偏 PLSR 模型，采用 F(A)∗ln(AD)&CARS 数据处理方式建立的 PLSR 模型，Rp 值提高为 0.9545，预测结果能够较为准确反映土壤有机质真实含量水平。本研究结果可以为高光谱成像技术应用于土壤有机质含量检测提供理论支撑，并为土壤其他成分快速检测提供参考。

[1] *Guoliang Wang, Ph.D. Stud.; Wenjun Wang, Assoc. Prof. Ph.D., Jiangui Zhao Ph.D. Stud.; Zhiwei Li Prof. Ph.D.;*
[2] *Guoliang Wang, Assis. Prof.; Erhu Guo, Prof.; Hong Li, Prof.;*
[3] *Huiling Du, Prof. Ph.D.*

INTRODUCTION

Soil is a complex system, consisting of gas, liquid, and solid phases, organic matter, and microorganisms. As an important carrier for crop growth, the content of soil organic matter has also become an important index to evaluate the growing environment of crops. The traditional determination of soil organic matter content is completed by chemical determination in the laboratory, which has high accuracy, but it is time-consuming, laborious, and involves high-cost *(Soil agricultural chemical analysis methods, 2000)*. With the diversified development of detection technology, to meet the basic requirements of precision agriculture for the efficient and accurate detection of soil nutrients and realize the digital research of soil nutrients information, researchers have introduced hyperspectral imaging technology into soil nutrient detection *(Shi Zhou et al., 2014)*. The spectral reflectance of the region of interest (ROI) of soil samples is accurately collected by the hyperspectral instrument, the spectral data matrix is established in the spectral dimension, and multi-channel image information is obtained in the image dimension. This information is a comprehensive reflection of the soil internal material composition and molecular structure acting on the spectrum *(Wang Wenjun et al., 2018)*. At present, hyperspectral imaging technology has become a research hotspot in agricultural research institutions at home and abroad, and it has been widely used in quality classification, component detection, and other related studies of agricultural products. *Said Nawar et al., (2016),* used different pretreatment methods combined with multiple regression models to predict soil moisture and organic matter. The results showed that the Multivariate Adaptive Regression Splines model had the best effect in predicting soil moisture and organic matter, and the coefficient of determination (R^2) could reach 0.90 and 0.85, respectively. *Xu D.Y. et al., (2018),* found that the PLSR model can be used for classification and prediction of soil composition. By comparing the prediction accuracy of principal component analysis, partial least square method, least square support vector machine and Cubist algorithm in soil total nitrogen content, *Morellos A. et al., (2016),* found that the Cubist algorithm had a better prediction result for soil total nitrogen content. *Wang Wenjun et al., (2018),* proposed that statistical parameters such as the average spectral curve, standard deviation curve, and variance curve calculated combined with multiplication and division in the preprocessing of spectral data, and a PLSR model was established for the preprocessed data. The results showed that the spectral data could effectively predict the soil total nitrogen content through numerical transformation, which provides theoretical support for the application of hyperspectral to the prediction of soil total nitrogen content. At present, the spectral data processing using hyperspectral technology to predict the content of soil organic matter is almost based on average spectral data (*Nie Zhe et al., 2019; Zhu Yuanli et al., 2021; Tang Haitao et al., 2021*). However, combined with the characteristics of hyperspectral imaging technology, there are few pretreatment methods of data conversion through spectral data.

In this study, the pre-sowing soil of "Yangfei Millet" planting experimental area in Wuxiang County, southeastern Shanxi Province was taken as the research object, and hyperspectral data from 111 soil samples were obtained. Combined with the advantages of hyperspectral imaging technology, the collected original spectral data matrix was preprocessed by numerical transformation operations, such as arithmetic mean, average deviation, 1st derivative, natural logarithm, and mixed multiplication. The characteristic variables of spectral data were selected by chemometric methods, and the PLSR quantitative analysis model of soil organic matter was established. By comparing the quantitative analysis models of soil organic matter content with different pretreatment methods, a prediction model of soil organic matter content was established, which provided theoretical support for the rapid detection of soil organic matter content.

MATERIALS AND METHODS

Collection and preparation of samples

The soil samples were collected from the "Yangfei millet" planting trial plot in Wuxiang County, southeast Shanxi Province. The field covers an area of 100 mu, which is collected before the millet is sown. About 1000 g of fresh samples are collected from the plowing layer in a random checkerboard pattern and then put into aluminum boxes. 111 samples are collected, numbered, and recorded sequentially. Samples after drying, impurity removal, grinding and sieving, and quartering sampling, are under test for hyperspectral data acquisition. On the condition of the heating, add excessive potassium dichromate into the samples to oxidize the soil organic matter, and use standard ferrous sulfate to titrate the remaining potassium dichromate. The soil organic matter could be measured with the deviation of the soil quality and the potassium dichromate consumption.

The introduction of hyperspectral instrument

In this experiment, a hyperspectral imager produced by Headwall Photonics was used to collect spectral data main working parts of the instrument include imaging equipment, a light source, a moving object platform, a computer, etc. In this test, the acquisition parameters of the near-infrared band are as follows: the wavelength range of the near-infrared hyperspectral image is 900 nm-1700 nm, the channel interval is 4.715 nm, and the step number i =172. In the near-infrared band, the relationship between step number I and wavelength λ_i is:

$$\lambda_i = 895.285 + 4.715i \quad (1)$$

where:

λ_i is the bands of the spectrum, i is number of spectral bands.

In the process of data collection, the translation speed of the object platform was adjusted to 16 mm/s, the exposure time of the camera was 0.9 ms, and the distance of the sample surface from the lens was 25 mm, so as to collect clear images. Before data collection, black and white correction is carried out on the instrument, and dark background image B and white background image W are scanned, respectively. After the operation of the instrument, the experimental image I of the tested sample is collected. After calculation according to Equation (2), the relative image X is obtained.

The above correction process was repeated for every 3 hyperspectral images.

$$X = \frac{I - B}{W - B} \quad (2)$$

In the experiment, the tested samples were put into the experimental vessels with a diameter of 3 cm and a depth of 1 cm to ensure that the tested samples were smooth and compact. Spectral data were collected for three times for each sample under test, and the data were sequentially numbered and stored.

Processing methods of the soil organic matter hyperspectral data

Within the setting coordinate range, the pixel points are selected and judged one by one, and the spectral data conforming to the setting ROI conditions are screened out to form a matrix and calculate the mean results. The spectral data were divided into training set and prediction set according to 2:1 by the Kennard-Stone algorithm (K-S). The original spectral data were pretreated by the arithmetic mean, average deviation, 1st derivation, natural logarithm, and mixed multiplication, and then established a PLSR prediction model. The Correlation coefficient (R) was used for the model evaluation. To improve the efficiency of operation and the model precision, using CARS and RF algorithms to select the key variables (*Tang Haitao et al., 2021; Chen Junyu et al., 2020*), and establish the PLSR model. Spectral data processing software mainly includes image fetching point and spectral data pretreatments developed based on Visual Basic and MATLAB 2020b (*The MathWorks, USA*).

RESULTS AND DISCUSSION

The measure of the soil organic matter

The content of soil organic matter was determined by the oxidation capacity method of potassium dichromate heated in oil bath. Each sample was divided into two times to take the average value. The statistical results of soil organic matter content were shown in Table 1.

Table 1

Statistic results of the soil organic matter

Sample Number	Min (mg/kg)	Max (mg/kg)	Mean (mg/kg)	Standard deviation (mg/kg)
111	21510	77650	31625.68	10050.5

The processing of the soil organic matter hyperspectral data

The extraction of the hyperspectral data

Since the spectral reflectance of a single point on the soil surface varies greatly, the modeling error will be great if a small number of pixel points are selected to draw spectral characteristic curves. Therefore, in order to improve the accuracy of the inversion model by combining the advantages of hyperspectral imaging technology, the sampling method shown in Fig. 1 was adopted in this study.

The selection rules for the process of extracting a large number of pixels in the ROI area were shown as (3), (4), and (5).

$$x_i = x_c - a + \Delta x, \quad i = 0,1,2... \left[\frac{2a}{\Delta x} \right] \tag{3}$$

$$y_i = y_c - b + \Delta y, \quad i = 0,1,2... \left[\frac{2b}{\Delta y} \right] \tag{4}$$

$$\frac{x_i^2}{a^2} + \frac{y_i^2}{b^2} \leq 1 \tag{5}$$

Where:

The (x_c, y_c) in (3) and (4) is the coordinate position of the ROI center, a and b are the semi-axis length of the ROI in the two-dimensional coordinate axis, Δx and Δy are the interval parameters of pixel points in the image along the coordinate axis direction respectively. The interval points collect was set to 1, [X] were round-off numbers of x and y to ensure the selected pixels were within the ROI.

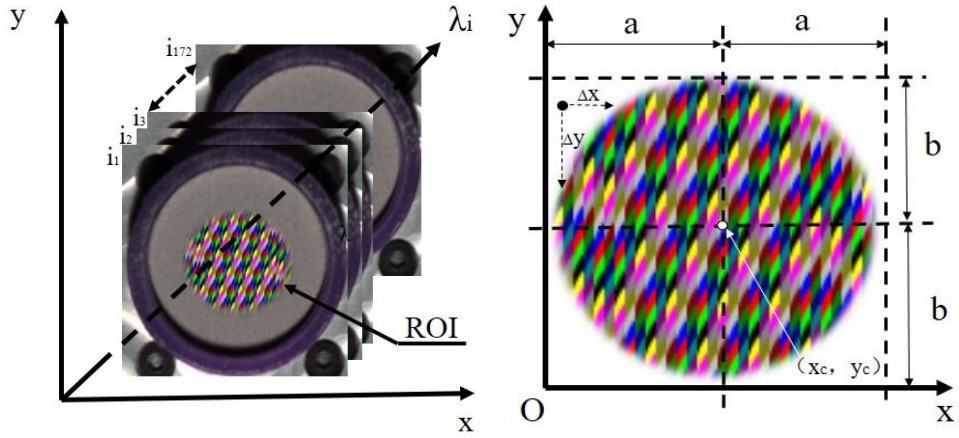


Fig. 1 - Extraction of the soil organic matter hyperspectral data

The tracking rule of pixel points was from top to bottom along the Y axis and from left to right along the X axis. The selected points were limited according to Equation (5), and 2000 fit pixel points were selected as the original spectral data.

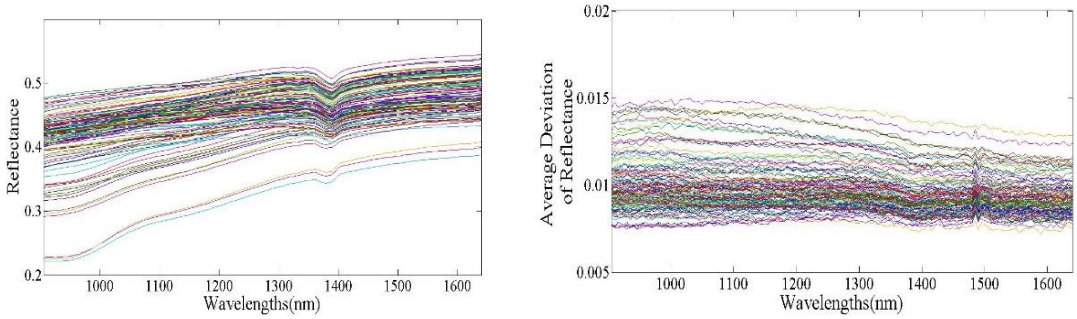
The calculation of hyperspectral data

The arithmetic mean (A) is the quotient of the sum of data divisive by the total number of data. It is widely used in the process of data statistics and analysis and has the characteristics of being sensitive, easy to be determined, and less affected by sample change (*Wang Wenjun et al., 2018*). The average deviation (AD) is the mean of the distance sum between each test value and its mean. It is sensitive and can better reflect the dispersion degree of the data to be analyzed. The calculations are shown in equations (6) and (7).

$$A_i = \frac{1}{n}(A_1 + A_2 + A_3 + \ldots + A_n) = \frac{1}{n}\sum_{i=1}^{n} A_{i,k} \tag{6}$$

$$AD_i = \frac{1}{n}\sum \left| AD_{i,k} - A_i \right| \tag{7}$$

In the equations, n is the sampling number in ROI. The number of sampling points of the near-infrared hyperspectral image is set to 2000, $A_{i,k}$ and $AD_{i,k}$ are the average spectral reflectance and the average deviation of reflectance respectively about the no. k sampling point and the no. i step length. Each step length was arranged in order to obtain the average spectral curve and average deviation spectral curve of the sample in the whole wave bands, as shown in Fig. 2.



a) b)

Fig. 2 - Spectral curves of the soil organic matter

a: Average spectral curves of the soil organic matter;
b: Average deviation spectral curves of the soil organic matter

At both ends of the near spectral range (<900 nm and >1700 nm), the spectral curve has a large disturbance, so the intercepted spectral range is 950-1650 nm, and the number of bands is reduced to 148. Soil organic matter has a variety of functional groups of organic compounds. Its spectral characteristics mainly describe the vibration in the molecules and lattice and the electron energy level transition in the atom of the high-molecular compound, spectral curve appears obvious wave was mainly caused by double frequency and co-frequency of the group like O-H and C-H in the organic matter. Figure 2 (a) shows that 1400 nm was the water absorption zone, taken as the boundary. From 950 nm-1400 nm, the spectral reflectance curve of the sample showed a monotonous upward trend and the curve shape was close to a straight line. From 1400 nm-1650 nm, the curve changed gently with a smaller slope than before (*Said Nawar et al., 2016*).

PLSR model for soil organic matter based on different pretreatments

The 1st derivative operation of the average spectral data can remove the linear part of the data and highlight the extreme value of the spectral data, which is conductive to observing the peak and valley characteristics of the data. The LN function has a good gain within the defined interval (0, 1]. The LN function operation of average spectral data can highlight the variation characteristics of spectral curves, enhance the difference of extreme values among data, and improve the accuracy of spectral feature recognition (*Wang Hongbo et al., 2017*). Table 2 lists 15 preprocessing methods results of spectral data A and AD that are calculated in 1st Derivative and LN functions, establishes PLSR model, obtains RP value of PLSR model under different pretreatments, and determines the best regression model. Among these methods, the highest RP value was based on the pretreatment F(A)*ln(AD), reaching 0.8859. The fit of the training set and prediction set was shown in Fig.3.

Table 2

PLSR modeling results of methods based on different pretreatments

Pretreatment	LVs	Calibration		Prediction	
		RMSEC (mg/kg)	R_C	RMSEP (mg/kg)	R_P
A	3	3388.29	0.9159	2793.53	0.6495
A*AD	3	6006.64	0.8271	4316.53	0.8691
A*F(A)	4	4172.7	0.9315	3897.68	0.7668
A*ln(A)	3	3518.65	0.9514	3455.46	0.7870
A*F(AD)	5	777.738	0.9898	14699.8	0.3300
A*ln(AD)	3	3518.65	0.9514	3455.46	0.7869
F(A)*AD	4	3278.6	0.9589	2864.37	0.8355
F(A)*F(AD)	1	16475.1	0.2085	6675.72	0.2396
F(A)*ln(AD)	**3**	**3417.68**	**0.9548**	**3037.72**	**0.8859**
ln(A)*AD	4	4344.2	0.9284	3553.94	0.1880
ln(A)*F(AD)	2	5147.83	0.8020	4478.75	0.4411
ln(A)*ln(AD)	3	3162.88	0.9612	3272.82	0.6675

Table 2
(continuation)

Pretreatment	LVs	Calibration		Prediction	
		RMSEC (mg/kg)	R_C	RMSEP (mg/kg)	R_P
AD	7	1669.34	0.9892	6992.65	0.4736
AD*F(AD)	1	9399.79	0.5894	2823.27	0.2283
AD*ln(AD)	3	6662.1	0.8073	4094.64	0.8136

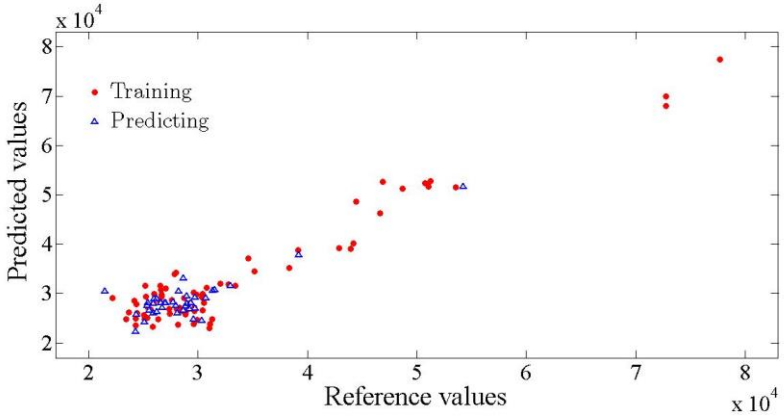


Fig. 3 - The fit of training set and prediction set by F(A)*ln(AD) pretreatment

Selection of key variables

Hyperspectral data has a large number of bands and high information redundancy, so it is easy to produce dimensionality disaster phenomena in the data processing, which leads to the decline of prediction accuracy. In this study, two key bands extraction methods, CARS and RF, were used to extract the feature band from the hyperspectral data of soil organic matter. The dimension of the hyperspectral data was reduced while the relatively complete spectral information was retained.

Selection of key variables based on CARS algorithm

Using Darwin's evolution theory as a reference, CARS algorithm selects the wavelength points with large absolute value of regression coefficient in PLSR model through adaptive reweighted sampling (ARS) technology, removes the wavelength points with small weight, selects the subset with the lowest root mean square error by cross-validation, and finds out the optimal variable combination. The algorithm was used to process spectral data and quickly select key spectral variables of samples. Fig. 4 shows the process of selecting key variables by CARS algorithm and the change curve of relevant parameters (*Tang Haitao et al., 2021*).

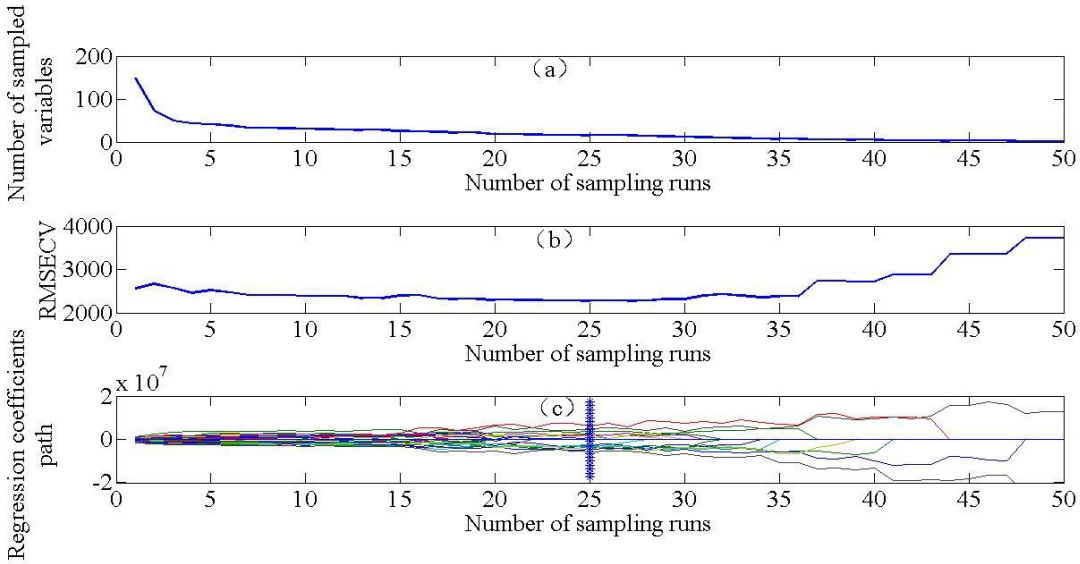


Fig. 4 - Selection of key variables using CARS algorithm
a: Changing trend of the number of sampled variables;
b: The variation of root-mean-square error of cross-validation values;
c: Regression coefficients of each variable with the increasing of sampling runs

Fig. 4(a) shows the trend of the number of samples tested with the increase of sampling times. Fig. 4(b) shows the change of Root mean square error (RMSECV) with the increase of sampling times through Cross validation (CV), with a trend of smooth decline from 1-25, 26-50 gradually rises and the minimum appears at 25, at which point RMSECV appears at its minimum. As can be seen from Fig. 4(c), the optimal selection of regression coefficients (RC) appears at the position marked with blue asterisk vertical line in the figure, where variable information can be retained as much as possible and the key variables can be selected. After the selection of key variables using CARS algorithm, as shown in Table 3, a total of 15 key variables were selected. The triple frequency of O-H appeared near 980 nm, the double frequency and co-frequency of C-H appeared near 1220 nm, and water molecular absorption peak appeared near 1400 nm.

Selection of key variables based on RF algorithm

With statistical ideas as the theoretical background, RF algorithm calculates the selection probability of each variable through multiple iterative operations. This algorithm has the advantage of not being easy to overfitting. Parameters were set before the RF algorithm. According to relevant references (*Chen Jianyu et al., 2020*), 0.4 was selected as the threshold value of the key variable. The execution was conducted for 50 times, and the running results were averaged. As shown in Fig. 5, some values in selection probability (SP) of some bands were high, and these wave peaks were highly correlated with the spectral characteristics of soil organic matter. Finally, 10 key variables were selected.

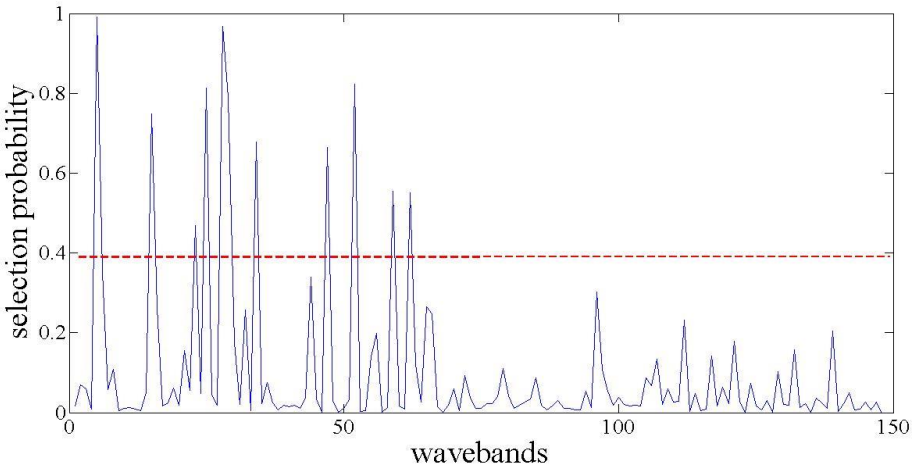


Fig. 5 - Selection probabilities of each wavelength using RF algorithm

As shown in Table 3, the key variables selected by RF and CARS algorithm almost overlap. In order to reduce the influence of random factors on the selection of key variables and ensure the effectiveness of the calculation process, the execution times of both algorithms were set at 50 times.

Table 3

Results of CARS&RF based on key wavelengths extraction

Pretreatment	Number of variables	Variables
CARS	15	959, 974, 1021, 1025, 1058, 1068, 1082, 1086, 1110, 1172, 1195, 1228, 1242, 1403, 1412
RF	10	974, 1021, 1068, 1082, 1086, 1110, 1172, 1195, 1228, 1242

Table 4 lists PLSR models of soil organic matter established by two data pretreatments, F(A)*Ln(AD)&CARS and F(A)*Ln(AD)&RF. As can be seen from the results, the RP value of PLSR established by using F(A)*Ln(AD)&CARS data pretreatments was 0.9545, while the RP value of PLSR established by using F(A)*Ln(AD)&RF decreased to 0.8834. This result may be due to the loss of relevant data in the process of using RF algorithm to extract key variables. It can be concluded from the above results that the PLSR model established by F(A)*Ln(AD)&CARS can be used to predict the hyperspectral reflectance of soil organic matter.

Table 4

PLSR modeling results of different methods based on key wavebands extraction

Pretreatment	LVs	Calibration		Prediction	
		RMSEC (mg/kg)	R_C	RMSEP (mg/kg)	R_P
F(A)*ln(AD)&CARS	3	4084.77	0.9208	3368.47	0.9545
F(A)*ln(AD)&RF	3	5128.9	0.9063	3880.41	0.8834

CONCLUSIONS

The hyperspectral data of 111 soil samples were obtained by taking the pre-sowing soil in "Yangfei millet" planting experimental area in Wuxiang County, southeast Shanxi Province as the research object.

Combined with the advantages of hyperspectral imaging technology, the collected original spectral data matrix was pretreated by numerical transformation operations, such as arithmetic mean, average deviation, 1st derivation, natural logarithm, and mixed multiplication, and the characteristic variables of spectral data were selected by the chemometric method, and then PLSR models were established respectively to realize the detection of soil organic matter. The main conclusions were as follows:

(1) Soil samples showed peaks and valleys in a specific spectral absorption zone, in which the water absorption zone was around 1400 nm and was taken as the boundary. Between 950 nm-1400nm, the spectral reflectance curve of the samples showed a monotonous upward trend and the curve shape was close to a straight line. From 1400nm-1650nm, the curve changes gently and the slope was smaller than before.

(2) The original spectral data were calculated by arithmetic mean, average deviation, 1st derivation, and natural logarithm, and then established the PLSR model of soil organic matter. In these PLSR models, the obtained prediction set R_P value under the pretreatment of F(A)*ln(AD) was the highest, reaching 0.8859.

(3) To further improve the precision of soil spectral inversion and reduce the amount of data computation, CARS and RF algorithms were used to extract the key variables from the spectral data preprocessed by F(A)*Ln(AD) and establish the PLSR model. The results showed that the PLSR model established by F(A)*Ln(AD)&CARS data pretreatment had a higher R_P value of 0.9545.

This study shows that the method of using the original spectral data arithmetic mean, average deviation, 1st derivation, and natural logarithm combined with the chemometric methods is feasible for the application of hyperspectral imaging technology in the detection of soil organic matter content and can provide a theoretical reference for the rapid detection of other soil components.

ACKNOWLEDGEMENT

This work was supported by Key Research and Development Program of Shanxi Province (No. 201903D211005), China Agriculture Research System of MOF and MARA, Technology Innovation Project of Shanxi Agricultural University (No. 2017YJ12), Shanxi Province Excellent Doctoral Work Award Fund (No. SXYBKY2019018).

REFERENCES

[1] Blasch Gerald, Spengler Daniel, Hohmann Christian, et al., (2015), Multitemporal soil pattern analysis with multispectral remote sensing data at the field-scale. *Computers and Electronics in Agriculture*, Vol. 2015, Issue 113, pp. 1-13, Oxford/England.

[2] Chen Jianyu, Li Guanghui, (2020), Prediction of moisture content of wood using Modified Random Frog and Vis-NIR hyperspectral imaging. *Infrared Physics & Technology*, Vol. 2020, Issue 105, Amsterdam/Netherlands, https://doi.org/10.1016/j.infrared.2020.103225.

[3] Gu Xiaohe, Wang Yancang, Sun Qian, et al., (2019), Hyperspectral inversion of soil organic matter content in cultivated land based on wavelet transform. *Computers and Electronics in Agriculture*, Vol. 2019, Issue 167, Oxford/England, https://doi.org/10.1016/j.compag.2019.105053.

[4] He Shaofang, Shen Luming, Xie Hongxia, (2021), Hyperspectral Estimation Model of Soil Organic Matter Content Using Generative Adversarial Networks. *Spectroscopy and Spectral Analysis*, Vol. 41, Issue 6, pp. 1905-1911, Beijing/China.

[5] Jin Xiuliang, Song Kaishan, Du Jia, et al., (2017), Comparison of different satellite bands and vegetation indices for estimation of soil organic matter based on simulated spectral configuration. *Agricultural and Forest Meteorology*, Vol. 2017, Issue 244, pp. 57-71, Amsterdam/Netherlands.

[6] Morellos A., Pantazi X.E., Moshou D., et al., (2016), Machine learning based prediction of soil total nitrogen, organic carbon and moisture content by using VIS-NIR spectroscopy. *Biosystems Engineering*, Vol. 2016, Issue 137, pp. 340–349, San Diego/U.S.A.

[7] Nie Zhe, Li Xiufeng, Lv Jiaxin, et al., (2019), Hyperspectral retrieval of surface soil organic matter content in a typical black soil region of northeast China. *Chinese Journal of Soil Science*, Vol. 50, Issue 6, pp. 1285-1293, Shenyang/China.

[8] Nowkandeh S.N., Noroozi A.A., Homaee., (2018), Estimating soil organic matter content from Hyperion reflectance images using PLSR, PCR, MinR and SWR models in semi-arid regions of Iran. *Environmental Development*, Vol. 2018, Issue 25, pp. 23-32, Amsterdam/Netherlands.

[9] Said Nawar, Henning Buddenbaum, Joachim Hill, et al., (2016), Estimating the soil clay content and organic matter by means of different calibration methods of vis-NIR diffuse reflectance spectroscopy. *Soil & Tillage Research*, Vol. 2016, Issue 155, pp. 510–522, Amsterdam/Netherlands.

[10] Samuel O Ihuoma, Chandra A Madramootoo, (2020), Narrow-band reflectance indices for mapping the combined effects of water and nitrogen stress in field grown tomato crops. *Biosystems Engineering*, Vol. 2020, Issue 192, pp. 133-143, Sandiego/U.S.A.

[11] Shi Zhou, Wang Qianlong, Peng Jie, et al., (2014), Development of a national VNIR soil-spectral library for soil classification and prediction of organic matter concentrations. *Science China: Earth Sciences*, Vol. 44, Issue 5, pp. 978-988, Beijing/China.

[12] Tang Haitao, Meng Xiangtian, Suo Xunxin, et al., (2021), Hyperspectral prediction on soil organic matter of different types using CARS algorithm. *Transactions of the Chinese Society of Agricultural Engineering*, Vol. 37, Issue 2, pp. 105-113, Beijing/China.

[13] Wang Wenjun, Wang Can, Li Zhiwei, et al., (2018), Prediction of total nitrogen content in brown soil based on hyperspectral technology. *Journal of Shanxi Agricultural University (Nature Science Edition)*, Vol. 38, Issue 9, pp. 71–76, Shanxi/China.

[14] Wang Hongbo, Zhao Ziqi, Lin Yi, et al., (2017), Leaf Area Index Estimation of Spring Maize with Canopy Hyperspectral Data Based on Linear Regression Algorithm. *Spectroscopy and Spectral Analysis*, Vol. 37, Issue 5, pp. 1489-1496, Beijing/China.

[15] Xu D.Y., Ma W.Z., Chen S.C., et al., (2018), Assessment of important soil properties related to Chinese Soil Taxonomy based on vis-NIR reflectance spectroscopy. *Computers and Electronics in Agriculture,* Vol. 2018, Issue 144, pp. 118–129, Oxford/England.

[16] Zhu Yuanli, Wang Dongyan, Zhang He, et al., (2021), Soil organic carbon content retrieved by UAV-borne high resolution spectrometer. *Transactions of the Chinese Society of Agricultural Engineering*, Vol. 37, Issue 6, pp. 66-72, Beijing/China.

[17] ***Soil science society of China, (2000), *Soil science society of China*. China Agricultural Science and Technology Press, Beijing/China.

RESEARCH ON COMB BRUSH HARVESTER AND DAMAGE MECHANISM TO MATERIAL. A REVIEW
/
梳刷式收获装置的研究现状及对物料的损伤机理综述

Junming HOU, Zhaotan REN, Liang ZHANG, Qijie SUN, Wei WANG
Shenyang Agricultural University, College of Engineering / China
Tel: +8602488487119; E-mail: junming_hou@163.com
DOI: https://doi.org/10.35633/inmateh-69-07

Keywords: *comb brush type, harvesting device, harvesting device, simulation, material fruit modeling*

ABSTRACT

Mechanized harvesting of crops is very important in the field of agricultural engineering, then the brush harvesting is a common way. The comb brush device is divided into four types: comb tooth type, roller spring finger type, belt comb finger type, and rod comb finger type. The picking rate and breakage rate are the indexes to evaluate the effect of comb brush harvesting devices. How to improve the picking rate and reduce damage rate is of great significance to the popularization of the devices. To improve the picking rate, the design of comb teeth should conform to the growth characteristics of crops. In this study, the application of four comb brush devices in harvesting crops was introduced, then the working principles and results were summarized. Meanwhile, the research status of a variable finger spacing device was summarized. In addition, to study fruit damage caused by brush devices during harvesting, three common analysis methods were summarized. The application situations and key steps were listed, and the modeling methods of material fruit in simulation analysis were analyzed. The study is intended to provide a reference for improving the harvesting effect of comb brush device. In the future, with the deepening combination of agronomy and agricultural machinery technology, comb brush harvesters will be more widely applied.

摘要

农作物的机械化收获是农业工程领域的一个重要环节，梳刷收获是一种常见的收获方式。目前梳刷装置分为梳齿型、滚筒弹齿型、带状梳指型以及杆条梳指型四种。采摘率和破损率作为评价梳刷装置优劣的指标，如何提高采摘率并降低破损率对梳刷装置的推广具有重要意义。提高采摘率，梳齿的设计要符合作物的生长特点，本文介绍了四种梳刷收获装置在收获不同作物时的应用情况，并归纳出其工作原理和优缺点，同时对变间距梳齿装置的研究现状进行了总结。此外，为了研究梳刷装置收获时对果实的损伤情况，总结了三种常用的分析方法，对其应用场景和关键步骤进行了总结，同时对仿真分析时物料果实建模的方法进行了归纳。本文旨在为提高梳刷装置的收获效果提供参考，未来随着农艺和农机技术不断深入结合，梳刷式收获装置将会得到更广泛的应用。

INTRODUCTION

With the improvement of living standards, people pay more and more attention to the quality of agricultural products, which has high requirements for the cultivation, management, harvest, transportation, and other links of crops, especially the harvest. It is easy to miss the best harvest period of crops, which affects the quality of agricultural products and causes economic losses. Therefore, the way to solve this problem is to apply machine harvesting.

Comb harvesting is a common harvest way at present, which is widely used in agricultural production. As one of the major food crops in the world, rice feeds more than half of the global population (*Li et al., 2020*). China is the world's largest producer of rice, with a planting area of 3×10^7 hm^2, accounting for about 23% of the world's total planting area (*Shen et al., 2016*). The common rice harvesting method is brush threshing (*Teng and Liu, 2020*). By the end of 2019, the comprehensive mechanization of rice production in China was 81% (*Feng and Liu, 2020*). Even so, problems such as unclean threshing and incomplete separation still exist in the process of rice harvest (*Hou, 2020*). Chili is a spicy crop with the widest planting area in the world. Since 1994, the planting area and total output of pepper in the world have been steadily increasing (*Hespeler et al., 2021; Jiang et al., 2018*). As a popular cash crop, chili harvester has been developed since the 1960s, and comb brush type device is a common type of harvest (*Funk and Walker, 2010*).

Up to now, chili harvester has developed relatively mature, to solve the problem of large breakage rate is still difficult. Lycium chinensis is mainly distributed in East Asia (*Potterat, 2010*). In China, the planting area of Lycium chinensis is about 1.333×10^5 hm^2, and the planting area is increasing year by year (*Hai et al., 2019*). Currently, the common mechanical picking is achieved by combing brush (*Wang et al., 2018*). However, due to the late start of the development of the harvesting device for Lycium chinensis, the mechanization degree of harvesting is still very low, which seriously restricts the development of the Lycium chinensis industry (*Teng, 2021*). Castor is one of the top ten oil crops, mainly grown in India, China, Brazil and other places. Its processed products are widely used in national defense, aviation, chemical industry and other fields *(Costa et al., 2018; Severino et al., 2013; Sun et al., 2012)*. At present, a common way to harvest castor beans is to brush it *(Kong et al., 2019)*. Cerasus Humilis *(Liu et al., 2021)*, Camellia Oleifera fruit *(Wu et al., 2022)* and other crops are also commonly harvested in this way, as shown in Fig.1. For the same crop, different types of comb and brush devices have different picking rates and damage rates. Therefore, it is of great significance to study the devices to improve harvesting efficiency and reduce damage rate.

The damage rate is one of the important indexes for harvest device. Research on the damage mechanism of materials during harvesting is the premise to obtain a low breakage rate. The damage in the process of comb brush harvesting is caused by the collision between the material fruit and the harvesting device. Its essence is that the material produced plastic deformation after beyond the yield point (*Celik, 2017*). With the development of computer technology, the simulation method has been widely applied to agricultural engineering (*Du et al., 2019*). It can analyze the process of material damage, which has become the main way to study material damage.

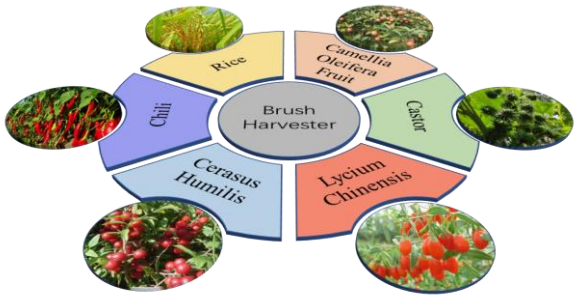


Fig. 1 - Application of brush harvesting

This study first summarizes the working principle and development status of brush harvesting and introduces four types of comb brush harvester. Then, the damage mechanism of the material fruit during the brush harvest was analyzed, the common methods and material modeling methods were summarized. Finally, the development of brush harvesting has been prospected.

COMB BRUSH TYPE OF HARVEST

The principle of comb brush harvesting is that the finger of comb moves periodically with the picking device. When the branch with fruit enters the finger of the comb, the fruit is forced to be separated from the stem by the impact force between the finger and the fruit. There are four types of brush which are comb tooth type, roller spring finger type, belt comb finger type, and rod comb finger type (*Hu et al., 2011*).

Comb tooth type brush harvesting device

The main working parts of the comb tooth type harvesting device are comb teeth, frame, and transmission device. The comb teeth moves according to a certain trajectory, and the plants are forced to be picked after entering the comb finger. These harvesting devices generally do not have collecting devices, so it is still necessary to collect the fallen fruit manually or by machine.

The structure design of the brush harvesting device needs to adapt to the growth characteristics of target crops. *Zhang et al.* (*2018*) designed a kind of Cerasus humilis brushing picking device, as shown in Fig. 2. When it works, the two brush parts open, then the finger of the comb enters the plant and gathers. The whole frame moves upward to complete the picking. It can harvest the fallen plants, and the harvesting efficiency is more than 80%. *Luo et al.* (*2017*) designed a tooth comb dial knife type picking device for Camellia oleifera fruit, as shown in Fig. 3. The device is carried out by hand, and its main parts are picking head, dial knife, pull wire, and long rod. It can effectively reduce the damage to Camellia oleifera fruit when picking. However, due to its lack of collection devices, the picked fruits directly fall to the ground and still

need to be picked up manually. The fruit is finally picked by manual pulling the ring, which has a large workload and intensity. To further reduce the working intensity, *Du et al.* (*2021*) designed a hand-held Camellia oleifera fruit brush picking machine with variable spacing. It is powered by a generator and enables variable-spacing combs. Field tests show that when the recovery rate is 480 r/min, the damage to the buds is reduced. Table 1 shows the comparison of the characteristics of the two crop picking devices.



Fig. 2 - Cerasus humilis brush picking device



Fig. 3 - Tooth comb dial knife type Camellia oleifera fruit picking device

Table 1

Comparison of different crop picking devices

Crops	Advantages	Disadvantages
Cerasus Humilis	High mechanization and high efficiency	Large damage, there is a phenomenon of omission of picking, the crop damage
Camellia Oleifera fruit	Small damage, high net recovery rate	Labor intensity, need to pick up manually

Roller spring finger type brush harvest device

Roller spring finger type brush harvest device mainly include picking roller, spring finger, conveyor belt, frame, transmission system, and other components. Its working principle is that the picking roller is powered by the machine itself while working, the spring fingers on the roller rotate with the roller and advance with the machine. Since the size of the fruit is larger than the distance of two springing teethes, the fruit after being picked continues to rotate with the springing teeth until it is thrown onto a conveyor belt behind.

Wang et al. (*2017*) optimized the threshing device because of the problem of poor threshing and separation capacity of the current longitudinal axial flow rice combine harvester. The threshing device is changed into the same diameter differential cylinder threshing device of the longitudinal axis. Through the test, it was found that the loss rate is reduced by 0.09%, and the breakage rate is reduced by 0.017%. *Dow* (*2003*) invented a tractor-type pepper picking device powered by a tractor. *Liu et al.* (*2020*) designed a comb-type cerasus humilis harvesting device, as shown in Fig. 4. To prevent the branches from being twined during work, the length of the comb was designed to be greater than 1/2 of the length of the cerasus humilis branches. The front section of the comb was set at 120°, which can not only prevent the fruits under the comb brush from falling to the ground but also facilitate the feeding of the branches. The test showed that the picking rate of the device can reach more than 95% when the roller speed is 25 r/min. *Ehlert et al.* (*2014*) designed a picking roller chamomile harvester, which adopted a double-blade picking comb. Field tests shows that the double-blade picking comb could play a certain role in preventing winding. *Li et al.* (*2016*) designed a comb-type castor harvest machine based on the bionics principle. The comb finger was designed into a finger-like structure, which could simulate manual picking to ensure the integrity of castor fruit. The results show that when the roller speed was 45 r/min and the unit forward speed was 2.5 m/s, most fruits can be harvested. *Hu et al.* (*2020*) designed a flexible comb brush device for apples planted with vertical fruiting wall architecture. The roller of the device is designed in the vertical direction, the comb finger and the harvesting platform can move up and down at the same time, which can reduce the falling height of apples and reduce the harvest damage of apples. Field experiments shows that the picking effect is better when the advance speed of the unit is 0.084 m/s and the rotation speed of the roller is 36 r/min.

Zhang et al. (*2018*) designed a hand-held variable spacing comb brush device of Lycium chinensis based on the principle of roller spring finger type device, as shown in Fig. 5. As the grooved cam rotates, the pressing plate rotates with it. When the pressing plate is at the end of the great arc of the cam, the comb finger is in a normal working state. When the platen is at the end of the small arc, the platen forces the comb to open laterally.

The picking device can effectively solve the problem of Lycium chinensis fruit stuck between two adjacent comb teeth when the comb brush is harvested. Field experiments show that when the tooth spacing is 8 mm and the finger length is 45 mm, the net recovery rate can reach 90% and the damage can be kept within 9%. This variable spacing comb brush device retains the characteristics of the roller spring-tooth type harvesting device but also can achieve a high net rate and low damage rate. Its processing accuracy requirements are high, which is not conducive to the research and development of large-scale harvesting devices.



Fig. 4 - Comb type Cerasus humilis harvesting device



Fig. 5 - Variable spacing Lycium chinensis brushing device

Belt comb finger type brush harvesting device

The main working parts of the picking device include grain distributor, picking belt, fan, drive system, frame, etc. The picking section consists of two picking strips, which are covered with snap fingers. The picking belt moves from bottom to top while moving along with the machine, as shown in Fig. 6. When the plant enters between the picking belt, the fruit is forced down by the comb fingers and continues to move with the picking belt.

This type of harvester was originally used to harvest tomatoes, then it was adapted in the late 20th century to harvest chilies. *Hu et al.* (*2012*) designed a belt comb finger type chili harvesting device and conducted prototype tests, as shown in Fig. 7. The picking device designs the comb finger on the picking belt with different lengths, the length of the front comb teeth is shorter than that of the back so that the front is easy to enter the chili plants, which is easy to pick the fruit of chili. Through the orthogonal test, it is found that the picking speed has the greatest influence on the picking performance, and the picking speed is the best as 2.17 m/s. This type of harvesting device has higher requirements on the material of the belt, and the processing is complex, which is not conducive to promotion.

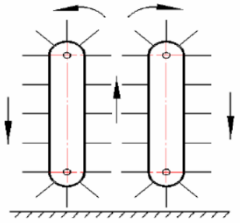


Fig. 6 - The movement direction of picking belt



Fig. 7 - Belt comb finger type chili harvesting device

Rod comb finger type brush harvesting device

Rod comb finger type picking device mainly includes grain distributor, picking roller, conveyor belt, rack, and so on. The working principle is that a pair of picking rollers rotate in reverse, and the comb finger moves with the picking rollers. When the plant enters the two picking rollers, the finger of the comb forces the fruit to be pulled down. The plucked fruit continues to rotate with the picking rollers until it is thrown to the two conveyor belts arranged parallel to the two picking rollers.



Fig. 8 - Roller brush type castor harvester

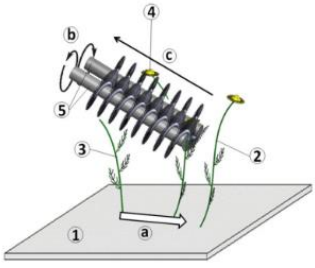


Fig. 9 - Rotary comb brush chamomile harvesting device

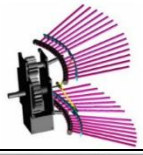
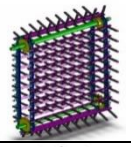
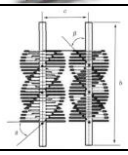
Zhang et al. (*2019*) developed a rolling brush-type castor picking device. This device changed the comb fingers used in the past and replaces them with power scrapers and auxiliary brushes. The power scraper used a longer power board to comb the castor fruit, and the auxiliary brush solved the loss caused by the fruit belt after picking and reduced the operating loss rate. *Liu et al.* (*2021*) improved the device in combination with the planting pattern and growth characteristics of castor beans, as shown in Fig. 8. The main working part of the device consists of a brush roller shaft and its surrounding flexible brush wire. The castor beans are picked by the impact generated by the rotation of the flexible brush wire. Results show that the picking rate of the device is more than 90%, and the breakage rate of the grain is only about 0.1%. *Liu et al.* (*2020*) designed an inclined double-helix finger comb chili harvesting device. The picking roller of the harvesting device is tilted and the comb fingers on it are arranged in a way of four spiral lines. *Brabandt et al.* (*2011*) designed a spiral chamomile harvesting device, as shown in Fig. 9, which chamomile is forced down by a pair of counter-rotating combs. *Di et al.* (*2020*) designed a brush-type Camptotheca Acuminata leaf-picking machine. The picking device arranged two picking axes horizontally, and the comb finger on the device was installed on the spring. When the comb finger touched the branch, the comb finger could automatically give way to avoid causing damage to the branch. To change the size of the picking roller can achieve the harvest of different height plants.

Table 2 is the comparison of the four brush harvesting methods. The comb tooth type brush device cannot achieve continuous operation, which is now mostly designed as a small machine to cooperate with manual use. The roller spring finger type device is used to harvest the fruits of dwarf plants and crops. It can also harvest crops with moderate plant height, but the roller size is larger.

Belt comb finger type or rod comb finger type device is generally used for crops with relatively tall plants. Due to the complex structure of the belt comb finger type device, low intensity of picking belt, it is mostly replaced by a rod comb finger type device. At present, the most commonly used picking methods are roller spring finger type and rod comb finger type.

Table 2

Comparison of four brush methods

Comb brush type	Structural diagram	Advantages	Disadvantages
Comb tooth type		Good picking effect, low damage, simple structure, convenient manufacture	Cannot operate continuously, operation efficiency is low
Roller spring finger type		Large operation width, simple structure, a wide range of application	It is easy to pull the stem into the roller when working
Belt comb finger type		Large area for simultaneous operation, high operating efficiency	Complex structure, difficult to manufacture, at the same time assembly fan, power consumption is large
Rod comb finger type		Can be picked on both sides of the plant at the same time, good picking effect	The distance between the two rollers is not easy to determine

SIMULATION OF MECHANICAL DAMAGE MECHANISM

In the process of brush picking, when the fruit collides with the machine, it is easy to produce damage. At the moment of contact between the material and the comb tooth, the contact position will be subjected to a large impact force which experiences elastic and plastic deformation processes. The elastic deformation will not cause material damage, while the plastic deformation will rupture, deformation, dislocation, or soft flesh inside the material cells, leading to collision damage (*Sang et al., 2008*). Therefore, it is extremely important to analyze the crop damage mechanism for picking. At present, there are three methods to analyze the mechanism of crop damage, which are finite element method, discrete element method, and test analysis method.

Finite Element Method

The finite element method (FEM), as a commonly used numerical method, is widely used to solve complex agricultural problems (*Du et al., 2019*). Through the simulation analysis and calculation of the material structure and characteristics, the influence of parameter changes on the material damage can be obtained.

Kang et al. (2017) used the finite element method to analyze the damage of calcium fruit when the comb teeth of different section shapes were harvested, and judged the damage degree by comparing the stress on the fruit. The results show that when the width between alveoli is 12 mm, the triangular comb tooth section shape has the least damage to fruit, which provides reference for the design of calcium fruit harvesting device. *Ji et al.* (*2017*) applied ANSYS software to study the damage of robot picking apple. They simulated the contact process between apple and plane and curved finger, which concludes that curved finger has less damage to apple. *Ahmadi et al.* (*2016*) studied the collision damage of apples in the transportation process, then analyzed the collision damage between apples and rigid bodies as well as between apples. It is concluded that the collision between apples and rigid bodies is the main cause of the damage, so it is very important to choose the appropriate material during transportation. *Li et al.* (*2021*) established an extended finite element model (XFEM) for tomato fruit to study the fracture mechanical response under mechanical compression. The model was applied to analyze the pre-crack propagation of tomato fruit under compression. The results shows that the pre-crack propagation would be rapid when the deformation percentage is more than 20%. *Celik et al.* (*2019*) used the FEM to simulate the collision between a single potato and a potato pile. The simulation results show that the stress values of impact and impact potatoes were 3.13 MPa and 1.40 MPa respectively, which provides a deeper understanding of dynamic bruise caused by potato transportation. *Zhao et al.* (*2019*) used finite element explicit dynamic simulation to evaluate impact scratch of fresh Lycium barbarum fruit. The results show that the fruit would not be damaged when the drop height is 0.2-0.5 m, the impact angle is 10-30°, and the impact materials are wood, foam, and nylon panels. *Zhu et al.* (*2016*) used FEM to study the fruit picking process of peanut harvesters. The impact response characteristics of the joint between peanut pod and roller blade after frontal impact were obtained. *Celik* (*2017*) used the FEM to study the impact deformation characteristics of pears. The bruise susceptibility of pear was analyzed by studying the impact height, impact surface, and impact direction, then the damage prediction model was established by using the response surface analysis method. After testing the prediction model, the maximum error between the simulation results and the empirical model results was about 7%. *Du et al.* (*2019*) analyzed the damage of kiwifruit at different ripening stages falling from different heights in horizontal and vertical directions by FEM. The severity of damage was determined by comparing the area of units exceeding the kiwi yield stress in the model. The maximum error between the simulation result and the experimental data is 17%.

FEM can be used to analyze the damage of materials to obtain the force size, stress-strain, and absorbed energy of the material at each time. By analyzing these parameters, the time, position, and final volume of material damage can be accurately obtained. However, there is a certain error between the data obtained by the finite element method and the experiment. Controlling mesh type and mesh size is a common method to improve simulation accuracy. Table 3 shows mesh types and mesh sizes used for some material fruits.

Table 3

Mesh division and simulation results of different fruit

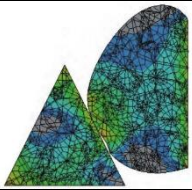
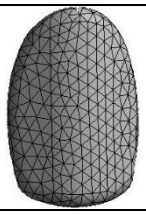
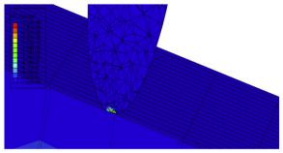
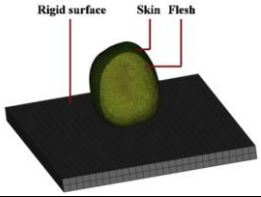
Material fruit	Divide area	Mesh type	Meshing result	Conclusion
Cerasus Humilis	Whole	Tetrahedron		When the load is 5N, the compressive contact stress of the comb teeth with triangular section is the least *(Kang et al.,2017).*
Castor	Castor shell	Tetrahedron		Dynamic analysis of different impact velocity, castor by the stress nomogram, when the impact velocity reaches 6 m/s, castor shell reached the yield limit of the material, the three chambers gradually separated *(Yang, 2019)*.

Table 3
(continuation)

Material fruit	Divide area	Mesh type	Meshing result	Conclusion
Castor	Castor bean seed	Tetrahedron		
Lycium chinensis	Whole	Tetrahedron		When the fall height is 0.2-0.5 m, the impact Angle is 10-30°, and the impact material is wood, foam board and nylon board, the fruit will not be damaged, and the impact damage is predicted successfully *(Celik, 2017)*.
Kiwifruit	Flesh	Tetrahedron		The higher the maturity is, the more likely it is to cause damage. Horizontal falls are more likely to cause damage than vertical falls. *(Du et al., 2019)*.
	Skin	Triangle		

Discrete Element Method

The discrete element method (DEM) can be used to analyze the force relationship between agricultural material particles (*Zeng et al., 2021*). It achieves the stimulation effect with the actual material damage by selecting the appropriate collision model and calibrating parameters. At the same time, the mechanical state and material to minimize the impact of the material are obtained by changing the mechanical parameters, so as to guide the practice according to the simulation results.

Hou et al. (2022) established a discrete element model of rice in order to analyze the grain breakage in the mechanical process of rice harvesting, and used discrete element method to simulate the process of harvesting and threshing. The simulation results showed that the normal force and tangential force were 28.4 N and 22.3 N, respectively, and 14.43 N and 8.74 N, respectively. The results indicate that the threshing roller with rigid and flexible coupling rod teeth could reduce the damage rate of rice.

Bao et al. (*2020*) used the DEM to analyze the collision damage of blueberries during mechanical picking and judged the damage degree of blueberries by analyzing the change of deformation energy value of blueberries. The results show that mechanical harvesting would only cause mechanical damage to a small part of fruits, and the probability of damage is about 20%. Blueberry fruits will be damaged not only in the picking stage but also in the conveying stage. Similarly, *Dariusz et al.* (*2020*) studied the damage of blueberry fruits when they are transported by reciprocating conveyor and vibrating conveyor. The simulation results show that the normal force and tangential force of conveying blueberries with a reciprocating conveyor belt are less than those with a vibrating conveyor.

Van Zeebroeck et al. (*2006*) studied the impact of vibration frequency, stacking height, and apple size on collision damage during apple transportation by applying DEM. The results show that vibration frequency is the main influencing factor of damage. *Scheffler et al.* (*2018*) used the DEM to predict the damage of fresh apples during handling and controlled the prediction accuracy of impact force of apples in drop test within 11%.

Pinto et al. (*2018*) used the DEM to study the deformation of peaches under cyclic load. At the same time, they used the same excitation conditions in the laboratory. Finally, it is concluded that the DEM could fully estimate the final deformation of peaches.

Wang et al. (*2019*) analyzed the impact force condition of a single corn kernel during threshing by using EDEM software and obtained that the maximum force received by the kernel in X, Y, and Z directions are 18.7 N, 92.5 N, and 22.0 N, respectively.

In order to study the damage of corn grains in the process of harvesting and transportation, *Li et al. (2022)* conducted simulation experiments in EDEM to verify the constitutive model and discrete element

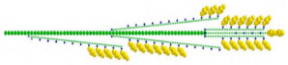
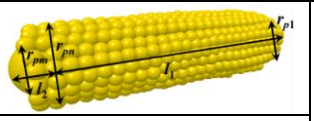
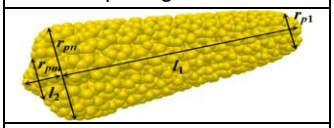
model of corn ear. The results show that the grain filling model could explain the mechanism of grain threshing and the stress of each grain in the process of grain threshing.

Liu et al. (*2018*) selected the Hertz-Mindlin contact mechanics model to calibrate parameters of virus-free micro potato, established the micro potato model as sphere and ellipsoid in EDEM. The impact recovery coefficients between the micro tubers, the steel plate and the micro tubers were measured. Compared with the real test, the simulation errors are 0.57% and 4.17% respectively.

Wei et al. (*2020*) used the DEM to analyze potato damage during operation on the undulating screen surface. Through simulation, they found that for the undulating screen surface with two peaks and two valleys, a small running speed is suitable when the inclination of the undulating screen surface is large. A large running speed is suitable when the inclination of the screen surface is small, and the rate of potato damage and the rate of broken skin are both less than 2%.

Table 4

Some collision models used in material simulation

Material	Discrete element model	Contact model	Conclusion
Rice		Hertz–Mindlin with Bonding V2, Hertz-Mindlin(no slip)	The mean normal force and tangential force of the rigid-flexible coupling rod teeth were smaller than those of the rigid rod teeth when they contacted the branches and ears, and the reduction rates were 21.48% and 39.43%, respectively *(Hou et al. 2020)*.
Corn	 Splicing model  Filling model	Hertz Mindlin with bonding, Hertz-Mindlin(no slip)	The average normal force on the filling model is 201.7 N, the maximum value is 342.0 N, and the minimum value is 104.3 N. The average normal force on the splicing model is 492.6 N, the maximum value is 823.7 N, and the minimum value is 362.6 N *(Li et al. 2022)*.
Potato	 	Hertz Mindlin with bonding, Hertz-Mindlin(no slip)	When the Angle of the undulating screen surface was 35° and the running speed of the separating screen was 1.0 m/s, the rate of potato damage and the rate of broken skin were 1.31% and 1.44%, respectively. When the Angle of the wavy screen surface was 15° and the running speed of the separating screen was 2.0 m/s, the potato injury rate and the skin breaking rate were 1.46% and 1.67%, respectively *(Wei et al. 2020)*.

In discrete element simulation, the similarity between the shape of the discrete element model and the actual shape and the selection of the collision model are particularly important. Table 4 shows the collision models and conclusions used in the simulation of some materials. Secondly, the parameters of the simulation model need to be calibrated. The physical parameters of the material are consistent with the real value, but because of the difference between the simulation model and the real particle in geometry, they are different from the real value. Therefore, the application of retrograde engineering to particle modeling is becoming more and more popular.

Test Analysis Method

The test analysis method is to carry out the mechanical test on the material through the test equipment, to obtain the physical parameters of the material itself. At the same time, a standard is used to judge the degree of damage. This method provides important data parameters for analyzing the mechanism of material damage and can analyze the cause and process of damage from inside the material, which is widely used at present.

Duan (*2014*) analyzed the collision damage mechanism by using Hertz rigid-flexible collision theory and von Mises criterion of plastic materials under the condition of plastic deformation of pepper fruit.

By observing the movement law of pepper fruit during picking with high-speed photography technology, it is concluded that the damage was mainly caused by the impact of the top and side of elastic teeth on pepper fruit. In order to study the impact damage of castor beans, *Hou et al. (2020)* conducted impact tests on two different varieties of castor beans respectively by means of high-speed photography equipment, and judged the degree of damage by comparing the maximum impact force and normal deformation. The results show that impact height has a significant effect on the maximum impact force, and impact height and impact angle have a significant effect on the normal deformation.

Sheng et al. (2022) studied the mechanical properties between tea shell and tea seed of camellia fruit through compression puncture test. The results showed that the higher the water content of camellia fruit, the lower the puncture power of tea shell and tea seed. When the water content was constant, the puncture force of tea shell and tea seed on the outside was greater than that on the inside. The relationship between water content and puncture force was found to provide theoretical basis for mechanized cleaning of camellia fruit. *Du et al.* (*2019*) studied the damage of kiwifruit through physical compression test and drop test. The results show that the bruise susceptibility of kiwifruit is correlated with the maturity of the fruit. The higher the maturity, the easier it is to scratch, while the fall height had little effect on the bruise susceptibility of the fruit. *An et al.* (*2020*) carried out a compression test on strawberries to study the damage mechanism of strawberry fruits and their internal tissues. By observing the area of fruit browning to judge the degree of damage, it was concluded that the percentage of fruit damage mass is only related to the direction of loading. *Yu* (*2020*) took three kinds of red jujube at a brittle maturity stage as research objects and carried out drop impact tests to explore the effects of varieties, impact materials and drop height on the damage. The regression model of collision damage was obtained by response surface analysis, which provides a reference for a mechanical damage theory of jujube. In the process of material harvesting, the collision between materials is inevitable. For this reason, *Wang et al.* (*2018*) used a pendulum impact device to study the collision damage between fruits in litchi harvest. The results show that fruit would be damaged significantly when impact speed was 2.8 m/s and impact times were 15. Therefore, mechanical damage during mechanical harvesting can be reduced by changing the parameters. Based on the Hertz contact theory, *Horabik et al.* (*2017*) used a high-speed camera to measure the rebound height of pea, soybean, and rapeseed seeds dropped and conducted an impact test. It is concluded that the recovery coefficient of seeds decreased with the increase of impact velocity, and the moisture content of different varieties seeds also had an impact on the recovery coefficient. *Hussein et al.* (*2019*) conducted a drop impact damage test on three kinds of pomegranates. It is found that the degree of damage of fruit is linearly related to impact energy. The damage volume and area of fruit increase with increasing temperature. *Fu et al.* (*2017*) used a pendulum impact device to study the impact of different buffer materials on apple damage and judged the damage condition by comparing the damaged area. The results show that the top area of the apple is most sensitive to bruising.

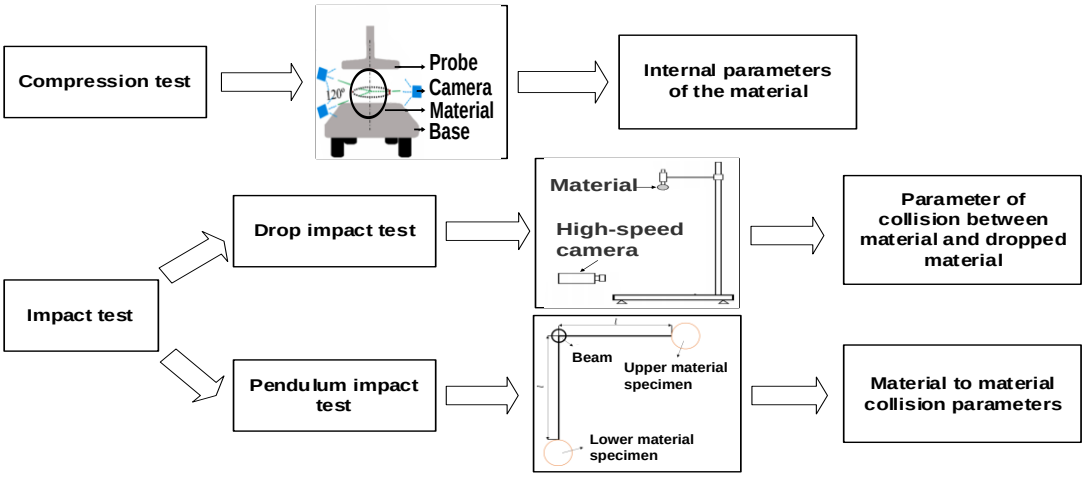


Fig. 10 - Two commonly used tests

The physical parameters of the material fruit can be obtained by using the method of experimental analysis. Common tests include compression test and impact test, as shown in Fig. 10. In addition, high-speed photography is used to observe the state of the harvest. The difficulty is how to determine the degree of damage, and cannot provide complete information to guide the design of machine.

Table 5

Comparison of different analysis methods

Analytical method	Advantage	Disadvantage
Finite element method	The stress and deformation of a single material are obtained	Material properties are difficult to set
Discrete element method	The collision parameters of mass materials are obtained	The setting of boundary conditions is complicated
Test analysis	The test data is true and reliable	Failure to provide complete information to adequately guide process and equipment design

It can be drawn that the impact damage mechanism of materials is mostly analyzed and processed by means of FEM, DEM, and experimental analysis. The comparison of the three methods is shown in Table 4. For simulation analysis, different methods are selected according to a different emphasis. For the impact damage of a single material fruit, the FEM is generally used to analyze, while for the impact damage of a material group, the DEM should be used. In addition, although the FEM and DEM can simulate the impact damage of materials, they are still different from the actual situation. Therefore, to judge the authenticity of the simulation, many researchers apply the experimental analysis. The relationship between the three methods of studying the mechanism of material damage is shown in Fig. 11.

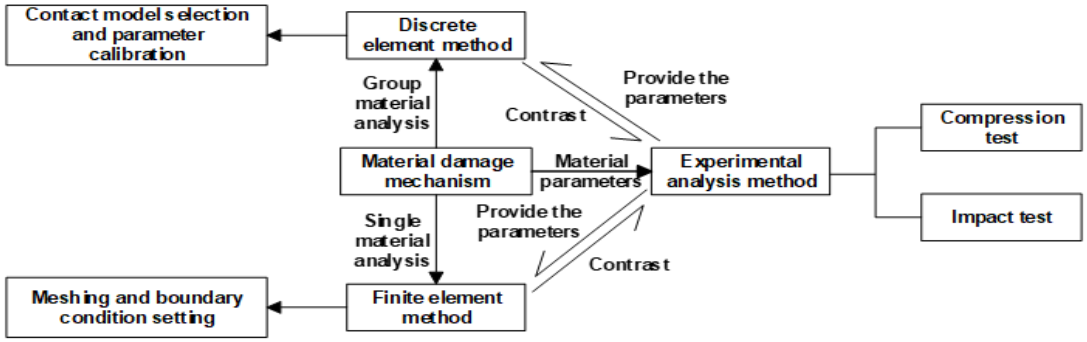


Fig. 11 – Relationships between the three methods

When using the method of simulation for damage analysis, it is necessary to model the fruit of the material. Since the shape of material fruit is not regular, the two commonly used modeling methods at present are to approximate the shape of the fruit to regular shape and modeling the fruit through reverse engineering. *Nikara et al.* (*2020*) approximated the potato to ellipsoid shape and carried out an impact test by using FEM. *Gharaghani et al.* (*2018*) established a citrus model as a sphere and conducted a drop finite element test. *Wang et al.* (*2018*) established a discrete element model of a single soybean by approximating the soybean seed as an ellipsoid and filling it with spheres. *Salarikia et al.* (*2017*) used a non-contact 3D scanner to generate the surface model of pear and used CATIA V5 software to process it into a 3D solid model. *Ji et al.* (*2019*) took the section of an apple with a camera and imported the image into AutoCAD to extract the contour curve of the apple with a spline curve. The real shape of the material can be restored by using the reverse engineering method, and the authenticity of the simulation can be improved.

CONCLUSIONS

Brush harvesting has been studied for more than 60 years since the 1960s. It has been widely used in harvesting different crops. At present, due to the continuous adaptation of agronomy to the development of agricultural mechanization, brush harvesting devices can harvest fruit crops, but has higher requirements for the damage rate. The focus of research on brush harvesters is to realize loss reduction while keeping the high harvest rate. We should further study the shape, structure, and material of the comb finger so that the comb brush harvester can get further development. The main conclusions of this paper are as follows:

(1) The comb brush device is divided into four types: comb tooth type, roller spring finger type, belt comb finger type, and rod comb finger type. Among them, roller spring finger type and rod comb finger type have become the two main types of research at present because of their strong applicability and wide range of crops. In addition, the technology of variable comb finger spacing can effectively improve the picking rate

of the brush device, while the existing variable finger spacing device can only realize the simultaneous change of finger spacing. In the future, it is possible to change the spacing of any part of the finger by developing the structure of the finger and adding sensors.

(2) Damage caused by harvesting with a brush device is collision damage. Three common analysis methods are FEM, DEM, and experiment analysis method. The FEM analysis the main collision between single part damage, while research on group collision damage produced is by DEM. Then the test analysis can obtain the physical parameters by material mechanics experiments. At the same time, it can also provide material parameters for the finite element method and discrete element.

(3) The application scope of comb brush harvesting has been expanded. Comb brush devices are often applied to harvest crops with small fruit mass but large stalk connections. For crops with large fruit mass, vibration is usually used. Compared with vibration harvester, brush harvester has the advantage of less damage to crop root. At present, some crops collected by vibration devices have been harvested by brush. The integration between agronomy and agricultural machinery technology, comb brush harvesting devices will be more widely used in the future.

REFERENCES

[1] Ahmadi, E., Barikloo, H., Kashfi, M., (2016), Viscoelastic finite element analysis of the dynamic behavior of apple under impact loading with regard to its different layers. *Computers and Electronics in Agriculture*, Vol.121, pp.1-11.

[2] An, X., Li, Z., Zude-Sasse, M., Tchuenbou-Magaia, F., Yang, Y., (2020), Characterization of textural failure mechanics of strawberry fruit. *Journal of Food Engineering*, Vol.282, pp.110016.1-110016.10.

[3] Brabandt, H., Ehlert, D., (2011). Chamomile harvesters: A review. *Industrial Crops and Products,* Vol.34, Issue 01, pp.818-824.

[4] Bao Y.D., Yang J., Zhao Y.L., Liu X.L., Liang Z., Guo Y.L., (2020), Numerical Simulation of Mechanically Harvested Blueberry Based on EDEM. *Journal of Harbin University of Science and Technology*, Vol.25, Issue 03, pp.88-93.

[5] Celik, H.K., (2017), Determination of bruise susceptibility of pears (Ankara variety) to impact load by means of FEM-based explicit dynamics simulation. *Postharvest Biology and Technology*, Vol.128, pp. 83-97.

[6] Celik, H.K., Cinar, R., Yilmaz, D., Ulmeanu, M.E., Rennie, A.E.W., Akinci, I., (2019), Mechanical collision simulation of potato tubers. *Journal of Food Process Engineering*, Vol.42, Issue 05, pp.e13078.1-e13078.7.

[7] Costa, A.G.F., Severino, L.S., Sofiatti, V., Freitas, J.G., Gondim, T.M.S., Cardoso, G.D., (2018). Pre-harvest desiccation of castor crop using 2,4-D and glyphosate. *Industrial Crops and Products*, Vol122, pp.261-265.

[8] Dow, P.W., NY B., (2003), Guard for crop pick up apparatus: United States, US2003/0110752A1.

[9] Du, D., Wang, B., Wang, J., Yao, F., Hong, X., (2019), Prediction of bruise susceptibility of harvested kiwifruit (Actinidia chinensis) using finite element method. *Postharvest Biology and Technology*, Vol.152, pp.36-44.

[10] Di L., Yang Z.D., (2020), Design of Brush-Type Camptotheca Acuminata Leaf Picking and Collecting Machine. *Agricultural Equipment & Vehicle Engineering*, Vol.58, Issue 08, pp.28-31.

[11] Du, X., Shen, T., Zhao, L., Zhang, G., Hu, A., Fang, S., Cao, Y., Yao, X., (2021), Design and experiment of the comb-brush harvesting machine with variable spacing for oil-tea camellia fruit. *International Journal of Agricultural and Biological Engineering*, Vol.14, Issue 01, pp.172-177.

[12] Duan Y.L. (2014), Damage Mechanism and Experimental Study of mechanical harvesting pepper. Shihezi University/China.

[13] Ehlert, D., Beier, K., (2014), Development of picking devices for chamomile harvesters. *Journal of Applied Research on Medicinal and Aromatic Plants*, Vol.1, Issue 03, pp.73-80.

[14] Fu, H., He, L., Ma, S., Karkee, M., Chen, D., Zhang, Q., Wang, S., (2017), 'Jazz' Apple Impact Bruise Responses to Different Cushioning Materials. *Transactions of the ASABE*, Vol.60, Issue 02, pp.327-336.

[15] Funk, P.A., Walker, S.J., (2010), Evaluation of Five Green Chile Cultivars Utilizing Five Different Harvest Mechanisms. *Applied engineering in agriculture*, Vol.26, Issue 06, pp.955-964.

[16] Feng Z.S., Liu J.H., (2020), Current Situation Analysis and Prospect of Agricultural Machinery Industry in China. *Agricultural Technology & Equipment*, Issue 07, pp.37-38.
[17] Hou M.K., (2020), Innovative structural design of rice threshing machine. *South Agricultural Machinery*, Vol.51, Issue 16, pp.32-34.
[18] Hu S.J., Chen Y.C., Yuan Y.X., Han L.L., (2011), The Present Research and Prospect of Pepper Harvester. *Journal of Agricultural Mechanization Research*, Vol.33, Issue 08, pp.237-240.
[19] Hu S.J., (2012), Design and Research of the comb-type picking device for Chili pepper. Shihezi University/China.
[20] Hespeler, S.C., Nemati, H., Dehghan-Niri, E., (2021), Non-destructive thermal imaging for object detection via advanced deep learning for robotic inspection and harvesting of chili peppers. *Artificial Intelligence in Agriculture*, Vol.5, pp.102-117.
[21] Hai S., Xiao H.R., Shi Z.G., Jiang Q.H., Zhao Y., Ding W.Q., (2019), Design and test of low-loss Lycium barbarum harvesting technology and equipment based on reciprocating vibration method. *Journal of Chinese Agricultural Mechanization*, Vol.40, Issue 11, pp.100-105,208.
[22] Horabik, J., Beczek, M., Mazur, R., Parafiniuk, P., Ryżak, M., Molenda, M., (2017), Determination of the restitution coefficient of seeds and coefficients of visco-elastic Hertz contact models for DEM simulations. *Biosystems Engineering*, Vol.161, pp.106-119.
[23] Hou, J., Yang, Y., Zhu, H., Hu, W., (2020). Experiment on Impact Damage of Castor Capsule and Its Influencing Factors Optimization. *INMATEH Agricultural Engineering,* Vol.61,Issue 2, pp.87-96.
[24] Hou, J., Wang, X.S., Xie, F.P., Liu, D.W., Chen, Z.G., (2022), Experiment of rigid flexible coupling threshing drum based on EDEM. *Journal of Hunan Agricultural University (Natural Sciences),* pp.1-9.
[25] Hu, G., Bu, L., Chen, J., (2020), Simulation to determination of significant parameters on apple stress for combing harvesting in trellis trained trees. *Scientia Horticulturae*, Vol.274, pp.109654.
[26] Hussein, Z., Fawole, O.A., Opara, U.L., (2019), Bruise damage susceptibility of pomegranates (Punica granatum, L.) and impact on fruit physiological response during short term storage. *Scientia Horticulturae*, Vol.246, pp.664-674.
[27] Ji, W., Qian, Z., Xu, B., Chen, G., Zhao, D., (2019), Apple viscoelastic complex model for bruise damage analysis in constant velocity grasping by gripper. *Computers and Electronics in Agriculture*, Vol.162, pp. 907-920.
[28] Ji, W., Qian, Z., Xu, B., Tang, W., Li, J., Zhao, D., (2017), Grasping damage analysis of apple by end-effector in harvesting robot. *Journal of Food Process Engineering*, Vol.40, Issue 06, pp.e12589.
[29] Jiang, J., Cen, H., Zhang, C., Lyu, X., Weng, H., Xu, H., He, Y., (2018), Nondestructive quality assessment of chili peppers using near-infrared hyperspectral imaging combined with multivariate analysis. *Postharvest Biology and Technology*, Vol.146, pp.147-154.
[30] Kang, S.L., He, J.L., (2017), Design and finite element analysis of harvesting device for the cerasus humilis. *Journal of Shanxi Agricultural University(Natural Science Edition),* Vol.37, Issue 6, pp.439-443.
[31] Kryszak, D., Bartoszewicz, A., Szufa, S., Piersa, P., Obraniak, A., Olejnik, T.P., (2020), Modeling of Transport of Loose Products with the Use of the Non-Grid Method of Discrete Elements (DEM). *Processes*, Vol.8, Issue 11, pp.1489.
[32] Kong F.T., Wu T., Shi L., (2019), Research status and development prospect of Ricinus communis harvester. *Journal of Chinese Agricultural Mechanization,* Vol.40, Issue1, pp.32-36.
[33] Li C.H., Liu C.C., Zhuang W.H., Zhu Z.W., (2016), The Structural Design and Motion Simulation of the Comb-type Castor Picking System. *Machinery Design & Manufacture*. Issue 05, pp.95-98,102.
[34] Li, D., Li, Z., Tchuenbou-Magaia, F., (2021), An extended finite element model for fracture mechanical response of tomato fruit. *Postharvest Biology and Technology*, Vol.174, pp.111468.
[35] Liu G., Lin S.Y., Liang Y., Tang Y., Xu W.P., (2020), Design of Inclined Double Spiral Comb Finger Type Pepper Harvesting Test Bed. *Journal of Agricultural Mechanization Research*, Vol.42, Issue 08, pp.133-137.
[36] Liu L., Wu T., Kong F.T., Sun Y.F., Chen C.L., Xie Q., Shi L., (2021), Optimized design and experiment of the picking mechanism for brush-roller castor harvesters. *Transactions of the Chinese Society of Agricultural Engineering*, Vol.37, Issue 08, pp.19-29.
[37] Li, M., Fu, Q., Singh, V.P., Liu, D., Li, T., Li, J., (2020), Sustainable management of land, water, and fertilizer for rice production considering footprint family assessment in a random environment. *Journal of Cleaner Production*, Vol.258, pp.120785.1-120785.14.

[38] Li, X., Du, Y., Liu, L., Mao, E., Yang, F., Wu, J., Wang, L., (2022). Research on the constitutive model of low-damage corn threshing based on DEM. *Computers and Electronics in Agriculture,* Vol.194.
[39] Liu S.H., He J.L., Wu N., He Y.Q., Yi M., Du J.J., (2020), Design and Optimization of Comb-type Cerasus humilis Harvesting Test Bench. *Agricultural Engineering*, Vol.10, Issue 03, pp.81-85.
[40] Liu, S., He, J., Wu, N., (2021), Design and Experimental Study of the Comb-Type Harvesting Test Bench for Cerasus Humilis. *INMATEH Agricultural Engineering*, Vol.63, Issue 1, pp.261-270.
[41] Liu W.Z., He J., Li H.W., Li X.Q., Zheng K., Wei Z.X., (2018), Calibration of Simulation Parameters for Potato Minituber Based on EDEM. *Transactions of the Chinese Society for Agricultural Machinery*, Vol.49, Issue 05, pp.125-135,142.
[42] Luo S.T., Rao H.X., Zhang L.Y., Yu J.J., Xu X.Q., Li T., Liu M.H., (2017), Design and Experiment of Tooth Comb Type Device for Camellia Fruits Picking. *Journal of Agricultural Mechanization Research,* Vol.39, Issue 02, pp.84-88,157.
[43] Namdari Gharaghani, B., Maghsoudi, H., (2018), Free fall analysis of orange fruit using numerical and experimental methods. *International Journal of Food Properties*, Vol.21, Issue 01, pp.484-495.
[44] Nikara, S., Ahmadi, E., Alavi Nia, A., (2020), Finite element simulation of the micromechanical changes of the tissue and cells of potato response to impact test during storage by scanning electron microscopy. *Postharvest Biology and Technology*, Vol.164, pp.111153.
[45] Pinto, E.M., Ferraz, A.C.d.O., (2018). Deformation of Peaches Submitted to Cyclic Loading Using the Discrete Element Method. *Engenharia Agrícola*, Vol.38, Issue 03, pp.434-442.
[46] Potterat, O., (2010), Goji (*Lycium barbarum* and *L. chinense*): Phytochemistry, pharmacology and safety in the perspective of traditional uses and recent popularity. *Planta Med*, Vol.76, Issue 01, 7-19.
[47] Qiang S., Wang G., Deng Y.J., Lai Q.F., Liu M.H., Hu S.F., Xiao B.G, Cao X.Y., Liao Y.S., Zeng Y.F., (2022), Experimental study on puncture force of camellia oleifera seed shell under different moisture content. *Acta Agriculturae Universitatis Jiangxiensis,* Vol.44, Issue 6, pp.1478-1487.
[48] Salarikia, A., Miraei Ashtiani, S.-H., Golzarian, M.R., Mohammadinezhad, H., (2017), Finite element analysis of the dynamic behavior of pear under impact loading. *Information Processing in Agriculture*, Vol.4, Issue 01, pp.64-77.
[49] Sang Y.Y., Zhang D.X., Zhang M.M., (2008), Study on bruising damage experiment of potato and finite element analysis. *Journal of China Agricultural University*, Issue 01, pp.81-84.
[50] Scheffler, O.C., Coetzee, C.J., Opara, U.L., (2018), A discrete element model (DEM) for predicting apple damage during handling. *Biosystems Engineering*, Vol.172, pp.29-48.
[51] Severino, L.S., Auld, D.L., (2013). A framework for the study of the growth and development of castor plant. *Industrial Crops and Products,* Vol.46, pp.25-38.
[52] Sheng Y.H., Sun S.L., Qiu J., (2016), Research status and development trend of longitudinal axial flow threshing and separation system for small rice harvester. *Contemporary Farm Machinery*, Issue 06, pp.70-73.
[53] Sun Z.J., Lü L.Y., Wu Y.P., (2012), Castor industry development: from cultivation to product exploitation. *Journal of China Agricultural University*, Vol.17, Issue 6, pp.204-214.
[54] Teng Y.J., Jin C.Q., Chen Y.P., Liu P., Yin X., Wang Y.E., Yu K., (2020), Design and optimization of segmented threshing device of combine harvester for rice and wheat. *Transactions of the Chinese Society of Agricultural Engineering*, Vol.36, Issue 12, pp.1-12.
[55] Teng W.H., (2021), Baiyin city wolfberry production weak link agricultural machinery technology test. *Farm Machinery*, Issue 04, pp.65-66.
[56] Van Zeebroeck, M., Tijskens, E., Dintwa, E., Kafashan, J., Loodts, J., De Baerdemaeker, J., Ramon, H., (2006), The discrete element method (DEM) to simulate fruit impact damage during transport and handling: Case study of vibration damage during apple bulk transport. *Postharvest Biology and Technology*, Vol.41, Issue 01, pp.92-100.
[57] Wang, J., Mei, S., Xiao, H., Zhao, Y., Zhou, H., (2018), Research on Mechanized Harvesting Methods of Lycium barbarum Fruit. *IFAC-PapersOnLine*, Vol.51, Issue 17, pp. 223-226.
[58] Wang, J.S., Xiong Y.S., Xu Z.W., Ma G., Wang Z.M., Chen D.J., (2017), Improved design and test of key components for longitudinal axial flow combine harvester. *Transactions of the Chinese Society of Agricultural Engineering*, Vol.33, Issue 10, pp.25-31.

[59] Wang, M.M., Wang W.Z., Yang L.Q., Zhang H.M., Zhong D.F., (2019), Bench experiment and discrete element simulation analysis of corn threshing process. *Journal of Henan Agricultural University*, Vol.53, Issue 03, pp.365-373.
[60] Wang, W., Yang, Z., Lu, H., Fu, H., (2018), Mechanical damage caused by fruit-to-fruit impact of litchis. *IFAC-PapersOnLine*, Vol.51, Issue 17, pp.532-535.
[61] Wei, Z.C., Su G.L., Li X.Q., Wang F.M., Sun C.Z., Meng P.X., (2020), Parameter Optimization and Test of Potato Harvester Wavy Sieve Based on EDEM. *Transactions of the Chinese Society for Agricultural Machinery*, Vol.51, Issue 10, pp.109-122.
[62] Wu D.L., Yang J.H., Liu Y., Zhao E.L., Liu L., Cao C.M., (2022), Research progress and trend of camellia fruit picking equipment in China. *Journal of Chinese Agricultural Mechanization,* Vol.43, Issue 1, pp.186-194.
[63] Xu, T., Yu, J., Yu, Y., Wang, Y., (2018), A modelling and verification approach for soybean seed particles using the discrete element method. *Advanced Powder Technology*, Vol.29, Issue 12, pp.3274-3290.
[64] Yang, Y., (2019), Damage law and experimental on shelling collision of castor capsule based on finite element method. Shenyang Agricultural University/China.
[65] Yu, F.F., (2020), Experimental study on physical characteristics and mechanical damage of jujube during crisp ripening period. Tarim University/China.
[66] Zhao, J., Sugirbay, A., Chen, Y., Zhang, S., Liu, F., Bu, L., Chen, Y., Wang, Z., Chen, J., (2019), FEM explicit dynamics simulation and NIR hyperspectral reflectance imaging for determination of impact bruises of Lycium barbarum L. *Postharvest Biology and Technology*, Vol.155, pp.102-110.
[67] Zhang, W., Du X.B., He J.L., Du J.J., (2018), Simulation Analysis and Experiment of Combing Pluck of Cerasus humilis. *AGRICULTURAL ENGINEERING*, Vol.8, Issue 05, pp.89-94.
[68] Zhang, W.Q., Li Z.Z., Tan Y.Z., Li W., (2018), Optimal Design and Experiment on Variable Pacing Combing Brush Picking Device for Lycium barbarum. *Transactions of the Chinese Society for Agricultural Machinery*, Vol.49, Issue 08, pp.83-90.
[69] Zhu, W.W., Yang Y., Li A., Nie M.L., Chen C.J., (2016), Finite element simulation of physical process of nut picking by peanut combine harvester. *Journal of Chinese Agricultural Mechanization*, Vol.37, Issue 01, pp.13-17.
[70] Zhang, Y.T., Shi L., Kong F.T., Sun Y.F., Chen C.L., Xie Q., (2019), The utility model relates to a rolling brush picker suitable for harvesting castor beans: CN208908604U[P]
[71] Zeng Z.W., Ma X., Cao X.L., Li Z.H., Wang X.C., (2021), Critical Review of Applications of Discrete Element Method in Agricultural Engineering. *Transactions of the Chinese Society for Agricultural Machinery*, Vol.52, Issue 04, pp.1-20.

ANOMALY DETECTION FOR HERD PIGS BASED ON YOLOX
/
基于 YOLOX 的群养猪只异常检测

Yanwen LI [1], Juxia LI [*1], Zhenyu LIU [2], Zhifang BI [3], Hui ZHANG [1], Lei DUAN [1]
[1] College of Information Science and Engineering, Shanxi Agricultural University, Taigu/China
[2] Graduate School of Shanxi Agricultural University, Shanxi / China
[3] Basic Department, Shanxi Agricultural University, Shanxi / China
Tel: +86-15803446486; E-mail: lijxsn@126.com
DOI: https://doi.org/10.35633/inmateh-69-08

Keywords: *Abnormal behavior, Target detection, Deep Learning, YOLOX*

ABSTRACT
In order to solve the problem that the complex pig house environment leads to the difficulty and low accuracy of abnormal detection of group pigs, the video of 9 adult fattening pigs were collected, and the video key frames were obtained by the frame differential method as the training set, and the YOLOX model for abnormal detection of group pigs was constructed. The results show that the average accuracy of YOLOX model on the test set is 98.0%. The research results can provide a reference for the detection of pig anomalies in the breeding environment of pig farms.

摘要
为了解决复杂的猪舍环境导致对群养猪只异常检测困难和准确率较低的问题，本研究采集 9 头成年育肥猪视频图像，采用帧间差分法获取视频关键帧作为训练集，构建群养猪只异常检测 YOLOX 模型。结果表明，YOLOX 网络模型在测试集上平均准确率达 98.0%。研究结果可为猪场养殖环境中针对猪只异常检测提供参考。

INTRODUCTION
The monitoring of abnormal behaviors such as attack, ear-biting and other conditions of pigs is mainly conducted in a manual way, which not only increases the cost of pig breeding management, but also leads to stress response of pigs or even results in cross-infection between human and animals *(He et al., 2019)*. With the development of computer vision technology, it becomes possible that this technology can be used for the health monitoring of pigs in a non-contact and low-stress way. Target detection and behavior recognition of pigs are the premises for achieving automatic monitoring and intelligent analysis of pigs *(Hua et al., 2019)*. Rapid and accurate detection of abnormal behavior of pigs is of great significance for achieving accurate, personalized and intelligent health monitoring of pigs.

At present, some progress has been made in the research of abnormal behavior of pigs. In 2014, Viazzi extracted motion features from the historical data of motion images of pigs to classify their abnormal behavior by Linear discriminant analysis (LDA) *(Viazzi et al., 2014)*. Ocazk used BP neural network to classify the degree of aggressive behavior of pigs via having a statistical calculation of their activity indexes *(Oczak et al., 2014)*. In 2016, Lee classified the two abnormal behaviors of chase and attack of pigs by support Vector Machine (SVM) after having the activity features of pigs extracted by Kinect depth sensor *(Lee et al., 2016)*. In 2017, Chen extracted the acceleration features of pigs by analyzing the displacement changes of pig targets between adjacent key frame images, and had the degree of aggressive behavior of pigs classified with the hierarchical clustering method adopted *(Chen et al., 2017)*. All the studies about detection of abnormal behavior of pigs as listed above are based on extracting a feature in pig images Based on image processing technology before machine learning and other means are combined to process the feature. However, in practical application, extra feature extraction is needed in traditional image processing technology, which leads to the problems of low efficiency and large workload. What's more, due to adhesion, occlusion, poor lighting conditions as well as complex abnormal behaviors of pigs in the piggery environment, it is difficult to detect abnormal behavior of pigs in intensive breeding piggeries efficiently and in real time by traditional methods.

In recent years, deep learning has shown its superiority over traditional methods in the fields of image and vision. From the extraction and learning of low-dimensional features to high-dimensional features, deep learning can detect and recognize various tasks in most cases *(Ren et al., 2017, Zeiler et al., 2014, Zhang et al., 2015)*.

Demonstrating strong learning and generalization ability in various fields, deep learning has also been widely used in behavior detection of pigs. In 2018, Yang proposed to use Faster R-CNN to locate and identify individual pigs from a group-housed pen *(Yang et al., 2018)*. Zheng also used Faster R-CNN to identify five postures (standing, sitting, sternal recumbency, ventral recumbency and lateral recumbency) and obtain sows accurate location in loose pens *(Zheng et al., 2018)*.

Xue introduced the Center Loss monitoring signal into the Faster R-CNN training to enhance the cohesion of intra-class features, so as to improve the accuracy of identification of postures of lactating sows *(Xue et al., 2018)*. In 2019, Li used Resnet-FPN network to improve the Mask R-CNN deep learning model to identify the mounting behavior of pigs *(Li, et al., 2019)*. Yan proposed a detection model of DAT-YOLO, which is a combination of both attention mechanism and Tiny-YOLO, to detect the facial postures of herd pigs *(Yan et al., 2019)*.

Gao constructed a 3D convolutional neural network model that is used to identify the aggressive behavior of herd pigs *(Gao et al., 2019)*. In 2020, Yan proposed a model of FPA-Tiny-YOLO, which is a combination of feature pyramid attention FPA and Tiny-YOLO, for the shape detection of pigs, so as to achieve multi-target detection of herd pigs *(Yan et al., 2020)*. In 2021, Li used YOLOv4 model to detect the dietary behavior of pigs *(Li et al., 2021)*. Xue proposed a convolutional network model that integrates 2D-3D convolution features together to identify postures of sows *(Xue et al., 2021)*. By introducing lightweight MobileNet and feature pyramid structure FPN in, Fang improved the CenterNet model and conducted a target detection of herd pigs *(Fang et al., 2021)*. Deep learning has shown excellent performance in both target and simple behavior detection of pigs, but few studies on advanced abnormal behavior of herd pigs in interactive states are available at the moment. In this study, inter-frame difference method was adopted to obtain key frames to form a data set for the detection of abnormal behavior of herd pigs, so as to construct a deep learning target detection model YOLOX, which shall be used for the detection of abnormal behavior of herd pigs, so that the problems of both difficulty and low accuracy in detection of abnormal behaviors of pigs that are there because of the complicated postures of pigs and the complex piggery environment may get solved. By training the model, an effective model for detection of abnormal behavior of pigs was constructed, and the generalization and feasibility of the algorithm were verified by having model prediction tests carried out on the test set in different time buckets.

MATERIALS AND METHODS

Data acquisition and pre-processing

The experimental data in this study were collected in July 2020 at Fenxi Pig Breeding Base in Linfen City, Shanxi Province within 24 hours without interruption. The piggery was of closed-type brick-concrete structure. A total of 9 five-month-old finishing pigs were selected and placed in an enclosed piggery of size of 4.5m×4m×2.8m. As for the selection of camera position, the conventional aerial view and flat view acquisition method have the following disadvantages: the images collected from aerial view Angle are mainly the back area of pigs, which cannot be obtained for the face or other key parts, and the specific behavioral characteristics of pigs cannot be obtained. The horizontal Angle of view will show a lot of occlusion in the barn environment. Therefore, this paper innovatively adopted a tilt down 60 degrees Angle of view for data collection, so as to obtain different behavior characteristics of pigs while avoiding large area occlusion of herd pigs.

In this study, a large amount of manual screening was performed on the daily video of pigs, and 185 video segments of pigs with abnormal behaviors were observed and intercepted. Finally, the abnormal behaviors of pigs included four kinds of attack, wall climbing, ear biting and stride climbing. Then, the inter-frame difference method is used to extract key frames, so as to avoid the following problems: Pig daily movement is relatively slow and the pigs rest and are dormant for a long time, if consecutive frames are used as training samples, there may be a large number of repeated samples during training, which can result in an ill-fitted model and decrease the robustness of the test due to a large number of similar samples being present. In order to improve the goodness of fit and robustness of the model, this paper uses the inter-frame difference method to extract key frames as valid images. When the difference between the sum of gray values of pixels between two frames is greater than the set threshold, it is defined as a key frame, and the key frame acquisition formula is shown in Equation (1):

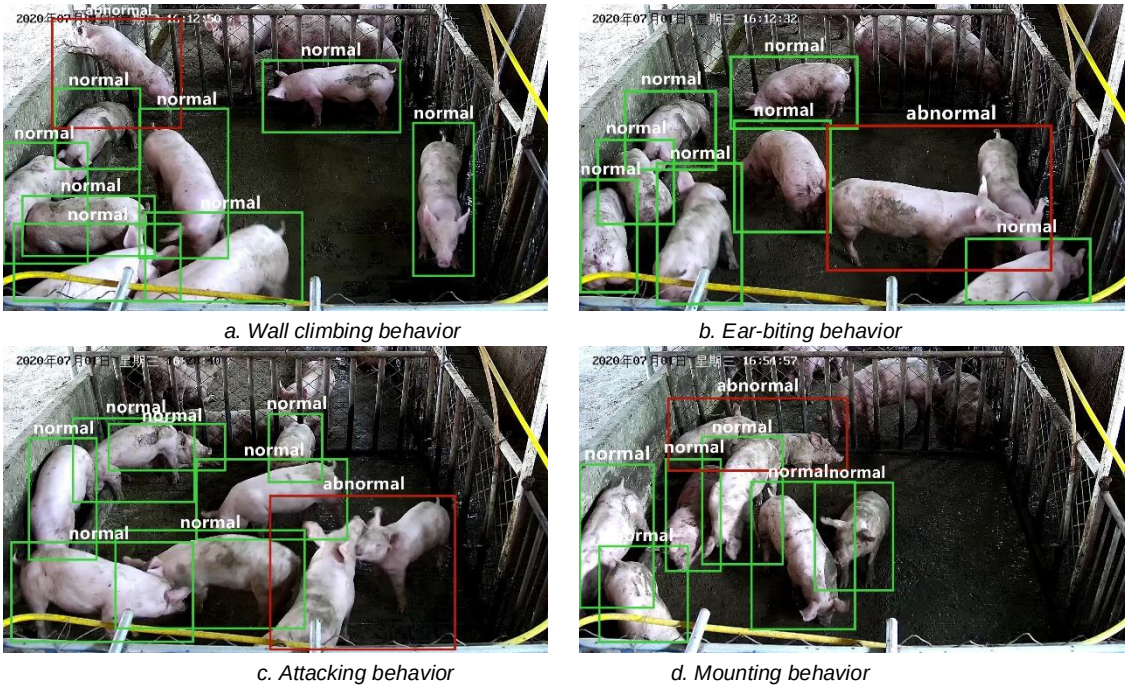
$$D(i,j)=\begin{cases}1, & \sum\left|f_i(x,y)-f_j(x,y)\right|>T_i \quad (j>i)\\ 0, & others\end{cases} \tag{1}$$

wherein: $f_i(x,y)$ represents the gray value at the pixel point (x,y) of frame i, $f_j(x,y)$ represents the gray value at the pixel point (x,y) of frame j, and T_i represents the threshold value. In this study, it is set as 20% of the sum of the gray values of each pixel point of frame i, $D(i,j)=0$ represents that frame j is a key frame relative to frame i, $D(i,j)=0$ indicating that frame j is not a key frame relative to frame i, and frame i is a key frame relative to the previous key frame, where $j>i$.

In this study, the following two steps are used to process the obtained images and obtain the final experimental data set.

(1) In order to improve the computing speed and reduce the amount of calculation, this paper adjusts the image with a resolution of 1920×1080 pixels, and finally gets a resolution of 640×640 pixels.

(2) In order to make the data set required by the experiment conform to PASCALVOC format requirements, the data set needs to be labeled. In this study, LabelImg was used to label the pig image data set, and the behavior label of the pig was set as Normal (normal behavior). Green label boxes were used. Abnormal is highlighted in red, as can be seen in Fig. 1.



a. Wall climbing behavior *b. Ear-biting behavior*

c. Attacking behavior *d. Mounting behavior*

Fig. 1 - Data annotation

(Note: Abnormal behavior of pigs is shown in Fig. 1a to Fig. 1d, where a shows wall-climbing behavior, b shows ear-biting behavior, c shows attacking behavior, and d shows mounting behavior.)

After the above steps, a total of 1105 valid labels were obtained, including 323 for wall climbing, 356 for aggression, 302 for ear biting and 124 for climbing and crossing.

Deep Learning YOLOX Algorithm

Although currently, YOLOv5 is already performing well, some recent work on object detection has triggered the development of this new YOLOX algorithm *(Ge et al., 2021)*. The most important focus points in object detection are anchor-free detectors, advanced label assignment strategies, and end-to-end detectors. These new focal points are still not integrated into the YOLO algorithm, and YOLOv4 *(Bochkovskiy et al., 2020)* and YOLOv5 are still anchor-based detectors and use hand-crafted assigning rules for training. The backbone network of the YOLOX network structure, or Darknet53, had the Input layer, Neck layer as well as the Prediction layer improved. To address the problem that coupling of detection heads may affect the model's performance, in YOLOX, the decoupled head got improved. By replacing YOLO's detection head with a coupled head, the convergence rate of the model was significantly improved. To better the performance of YOLOX, Mosaic and MixUp strategies were added in data enhancement. As Anchor mechanism solves the problems of both complex detection heads and poor generalization performance in some way, in YOLOX, it was improved to be of Anchor-free mechanism, in which 3 groups of Anchor predictions were reduced to only 1 group of prediction for a feature map, thus reducing the number of parameters and GFLOPs and making the detection much faster.

To reduce training time and avoid extra super-parametric problems, in YOLOX, the OTA tag allocation was improved to get an approximate solution (SimOTA) with a dynamic top-k strategy employed. After undergoing a series of improvements and compared with other advanced target detection models, YOLOX showed significant improvements in both speed and accuracy to some extent. Network structure of YOLOX can be seen in Fig. 2.

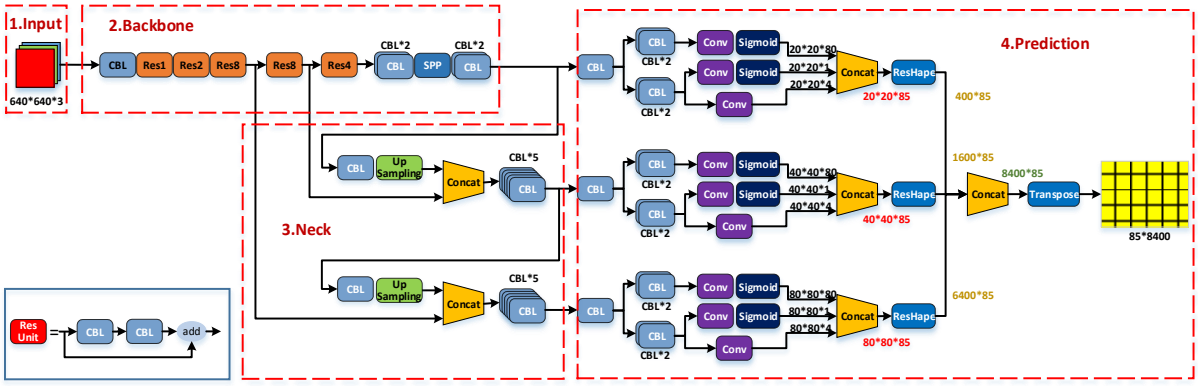


Fig. 2 - Network structure of YOLOX

As shown in Figure 2, CBL is widely used as a component of YOLOX network structure. CBL consists of three network layers (convolution layer, Batch Normalization layer, and Leaky ReLU function). In the convolution layer, multiple different convolution kernels are used to process the input image and different response characteristic graphs are obtained. The BN layer optimizes the network structure by normalizing the scattered data. To address the issue of neuron exhaustion in the ReLU function, the Leaky ReLU function introduces a non-zero slope in the negative half of the function, resulting in improved performance.

$$LeakyReLU(x) = \begin{cases} x, & x > 0 \\ ax, & x \le 0 \end{cases} \tag{2}$$

The output of this function has a small slope for negative input. Since the derivative is not zero, this can reduce the presence of silent neurons, allowing gradient-based learning, although sometimes slower, but solves the problem that neurons remain silent after negative ReLU function input. Network structure of CBL can be seen in Fig. 3.



Fig. 3 - CBL structure

In YOLOX, ResNet *(He et al., 2016)* is a residual block, which contains two convolution blocks and an Add layer. The Add layer is the addition of tensors of the same dimension. The residual structure can ensure that the network structure can still converge at a very deep level, so that the model can continue to train.

ResX in YOLOX is composed of a CBL and X residual components. The CBL in front of each Res module plays a role of down-sampling, and each ResX contains 1+2*X convolution layers. Figure 4 shows the ResX structure.



Fig. 4 – ResX structure

The SPP component consists of four parallel branches, which are the maximum pooling of kernel size 5×5, 9×9, 13×13 and a jump connection respectively. The main function of the SPP component is to effectively avoid image region clipping and zoom operations caused by image distortion. Additionally, it solves the problem of repeated feature extraction from images by the convolutional neural network, greatly improving the speed of candidate frame generation and saving computational cost.

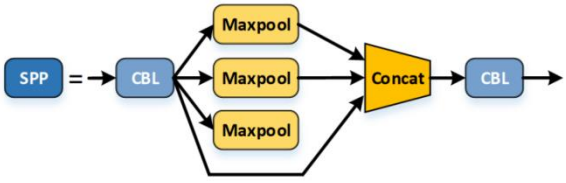


Fig. 5 - SPP structure

Model Evaluation Metrics

In this study, the commonly used evaluation indexes in target detection field, including IoU, Precision, Recall, P-R curve, AP value and mAP value, were used. IoU refers to the ratio of intersection and union of two detection frames, as shown in Equation (3):

$$IoU = \frac{S_A \cap S_B}{S_A \cup S_B} \tag{3}$$

where:

S_A represents the collection of pixels in the Prediction frame area, S_B represents the collection of pixels in the True frame area.

Precision represents detection precision, and Recall represents detection recall rate, for which the *equation* is as follows:

$$Precision = \frac{TP}{TP + FP} \tag{4}$$

$$Recall = \frac{TP}{TP + FN} \tag{5}$$

where:

TP (True Positive) refers to number of samples predicted by the model as individual frames of pigs (whose IOU is greater than the threshold) with a category tag that is consistent with the actual tag. FP (False Positive) refers to number of samples predicted by the model as individual frames of pigs with a category tag that is inconsistent with the actual tag. FN (False Negative) refers to the number of samples in which no individual pig is detected.

In the graph of P-R curve, Recall was taken as the abscissa and Precision was taken as the ordinate. Precision was negatively correlated with Recall. The larger the area (AP value) surrounded by P-R curve was, the better the model effect was. The mAP value represents the average accuracy of the model, as defined in equation (6) and (7):

$$AP = \int_0^1 p(r)dr \tag{6}$$

$$mAP = \frac{\sum_{i=1}^{N} AP_i}{N} \tag{7}$$

Considering that different IoU thresholds may have a direct impact on TP and FP values and thus cause fluctuations in mAP values, in this study, ten IoU thresholds of 0.5:0.05:0.95 (where 0.05 represents the grown step length) were used to calculate the mAP value. Finally, $mAP_{0.5}$, $mAP_{0.75}$, $mAP_{0.5:0.95}$, $mAP_{0.5:0.95\text{-}medium}$ and $MAP_{0.5:0.95\text{-}large}$ were used to measure the detection performance of the model, where $mAP_{0.5}$ represents the mAP value when the IoU threshold is 0.5, $mAP_{0.75}$ represents the mAP value when the IoU threshold is 0.75, $mAP_{0.5:0.95}$ represents the average value of mAP under the 10 thresholds of IoU at 0.5:0.05:0.95 respectively, while $mAP_{0.5:0.95\text{-}medium}$ indicates the median mAP value under the 10 thresholds of IoU at 0.5:0.05:0.95 respectively, and $mAP_{0.5:0.95\text{-}large}$ indicates the maximum mAP value under the 10 thresholds of IoU at 0.5:0.05:0.95 respectively.

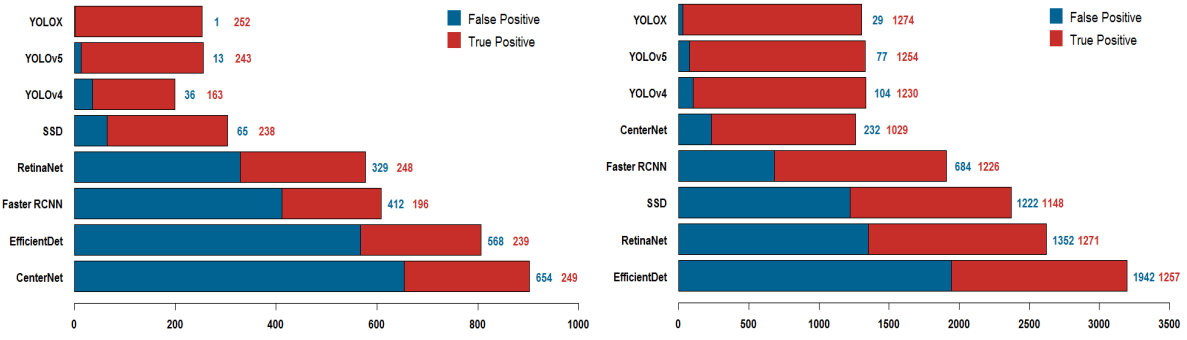
RESULTS

In this experiment, with PyTorch deep learning framework adopted, the operating system was Windows10, and GPU was RTX2080Ti. There were 1105 labels of abnormal behaviors in pigs, including 323 wall-climbing behaviors, 356 aggression behaviors, 302 ear-biting behaviors and 124 crawling behaviors. The 1105 collected image data sets were divided into training sets and test sets according to the ratio of 8:2, including 884 training sets and 221 test sets.

In the experiment, eight target detection models were used for comparison, respectively YOLOX *(Ge et al., 2021),* YOLOv5, YOLOv4 *(Bochkovskiy et al., 2020)*, RetinaNet *(Lin et al., 2017)*, EfficientDet *(Tan et al., 2019)*, Faster R-CNN *(Ren et al., 2017)*, CenterNet *(Duan et al., 2019)* and SSD *(Liu et al., 2016)*. In this study, the size of input image was set as 640*640 pixels, and epoch was set as 200, momentum 0.9, regular coefficient for weight decay 0.005. With learning rate decay mechanism adopted, the initial learning rate was set as 0.0001. Once the learning got stagnating, the learning rate of the model would attenuate at 2~10 times the rate, and the attenuation frequency was set as 80% and 90% of the maximum number of iterations.

TP/FP and P-R curve

In this study, the training set with the same experimental data was used to train eight models before tests were conducted on the same test set. With results compared and analyzed, the respective performance of the eight models was evaluated. In order to refine the results in the detection of abnormal behavior of pigs by models of YOLOX, YOLOv5, YOLOv4, RetinaNet, EfficientDet, Faster R-CNN, CenterNet and SSD, the TP and FP values predicted by the eight models were respectively calculated, as shown in Fig. 6. In the 221 images in the test data set of this paper, 260 frames of actual abnormal behavior and 1,326 frames of actual normal behavior were there.



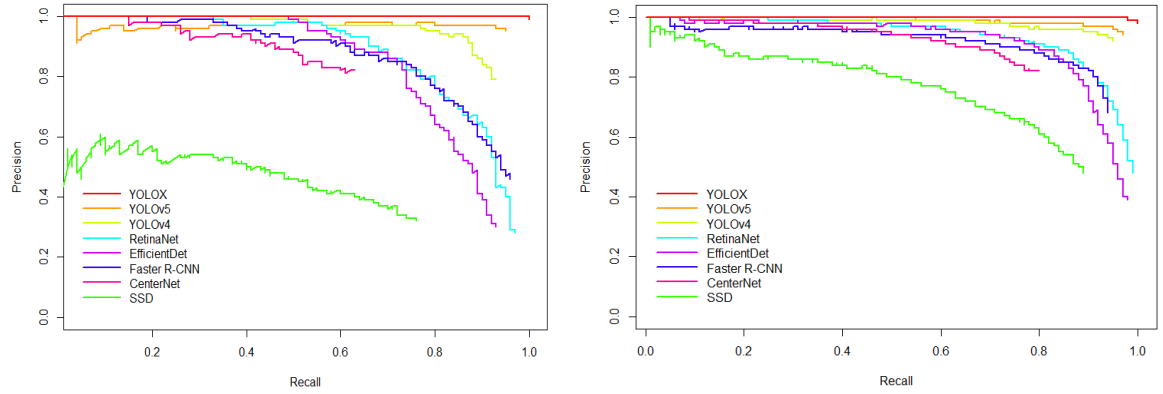
(a) Abnormal behavior *(b) Normal behavior*

Fig. 6 - TP and FP values predicted in detection by eight models

(Note: In case of the number of TP, the higher the value is, the better the model is; in case of the number of FP, the lower the value is, the better the model is.)

For the detection of abnormal and normal pigs, the TP value represents the number of pigs that correctly detected normal or abnormal behavior, and the FP value represents the number of pigs that incorrectly detected normal or abnormal behavior. As shown in Fig. 6, the TP numbers of the YOLOX model were 252 and 1274, respectively, which were 3-245 more than the other seven models. In addition, the FP numbers of the YOLOX model are 1 and 29, which are 12~1913 less than other models. The FP value of the YOLOX model is much lower than the other seven models. Although the difference in TP values of the eight models is not obvious, the huge difference in FP values finally makes the advantage of the YOLOX model more obvious.

In object detection, the P-R curve reflects the trade-off between the recognition accuracy and coverage ability of the model's correct object detection. The P-R curve for abnormal and normal behaviors of pigs detected by eight models, respectively YOLOX, YOLOv5, YOLOv4, RetinaNet, EfficientDet, Faster R-CNN, CenterNet and SSD, were as shown in Fig. 7.



(a) Abnormal behavior *(b) Normal behavior*

Fig. 7 - P-R curve

(1) As can be seen in Fig. 7, in the P-R curve for abnormal and normal behaviors of pigs, the curves for models YOLOX, YOLOv5 and YOLOv4 in YOLO series were all located at the upper right of the figure in comparison with that for other mainstream models, indicating that the models in YOLO series were better than other mainstream models in the detection of abnormal and normal behaviors of pigs. The curve for YOLOX model was above that for models YOLOv5 and YOLOv4, indicating that YOLOX model was superior to other models in the same series.

(2) As shown in Fig. 7(a), for abnormal behaviors of pigs, when the Recall value was less than 0.15, the Precision value for models YOLOX, YOLOv4, RetinaNet, EfficientDet, Faster R-CNN and CenterNet maintained around 1.0, and the difference was not significant, while the Precision value of SSD model remained around 0.6. As the Recall value increased, when the Recall value was greater than 0.6, the Precision value for models of YOLO series changed slightly, while the Precision value for other models decreased significantly, indicating that the models of YOLO series kept stable in the detection of abnormal behavior of pigs, and the YOLOX model owned the optimum detection performance.

(3) As can be seen in Fig. 7(b), for the normal behavior of pigs, as the Recall value increased, the Precision value for the models in YOLO series decreased slightly, while the Precision value for the YOLOX model kept staying at the top of the same series all the time, indicating that the YOLOX model had the optimum performance in the detection of normal behavior of pigs.

Detection accuracy of the model

In order to better evaluate the performance of the model, eight target detection models, respectively YOLOX, YOLOv5, YOLOv4, RetinaNet, EfficientDet, Faster R-CNN, CenterNet and SSD were used to predict the abnormal behavior of pigs on the same test set. The detection effects of the eight models were compared through different values of the mAP index, as can be seen in Table 1.

Table 1

Different values of mAP index for eight models

Model name	$mAP_{0.5}$	$mAP_{0.75}$	$mAP_{0.5:0.95}$	$mAP_{0.5:0.95\text{-}medium}$	$mAP_{0.5:0.95\text{-}large}$
YOLOX	98.0%	92.6%	81.2%	96.7%	98.0%
YOLOv5	94.5%	90.9%	86.3%	91.8%	94.5%
YOLOv4	92.3%	47.5%	58.6%	76.3%	92.3%
RetinaNet	90.1%	34.3%	51.7%	62.9%	90.1%
EfficientDet	86.7%	24.2%	46.3%	53.0%	86.7%
Faster R-CNN	86.6%	22.5%	45.6%	51.9%	86.6%
CenterNet	67.6%	15.2%	35.4%	39.6%	67.6%
SSD	54.3%	4.20%	21.6%	54.3%	54.3%

The experiment result showed that:

(1) In the detection of abnormal behavior of pigs, models of YOLO series behaved obviously much better than other mainstream target detection models. In $mAP_{0.5}$ index, the index value for YOLO series was 43.7 percentage points higher than that for other models; in $mAP_{0.75}$ index, the index for YOLO series was 88.4 percentage points higher than that for other models; in $mAP_{0.5:0.95\text{-}medium}$ index, the index for YOLO series was 59.6 percentage points higher than that for other models; in $mAP_{0.5:0.95\text{-}large}$ index, the index for YOLO series was 43.7 percentage points higher than that for other models. It can be seen that models of YOLO series performed significantly better than other target detection models. The pig detection process in the YOLO series models was completed in a neural network which can optimize the pig detection performance in an end-to-end way, while in other detection models, with sliding window or region proposal adopted, the detector could only get partial information of the image, though YOLO series models could obtain the target feature information of a whole image during training, that is why models in YOLO series could make good use of context information to not to make wrong predictions in the background, thus the detection accuracy was assured.

(2) Compared with the same series of YOLOv5 and YOLOv4 models, YOLOX model had the highest index value of 98.0 percentage points in $mAP_{0.5}$ index, 3.5 percentage points higher than that of YOLOv5 and 5.7 percentage points higher than that of YOLOv4 model, respectively; in $mAP_{0.75}$ index, YOLOX model owned the highest index value of 92.6 percentage points, 1.7 percentage points higher than that of YOLOv5 and 45.1 percentage points higher than that of YOLOv4. The $mAP_{0.5:0.95\text{-}large}$ index value was completely consistent with the $mAP_{0.5}$ index value, though the maximum value was in the YOLOX model. It can be seen that after the improved decoupled head and label allocation strategy were used in YOLOX model, the performance of YOLOX model got improved.

In $mAP_{0.5:0.95\text{-}medium}$ index, the index value for YOLOX model was 5.1 percentage points lower than that for YOLOv5, which may be influenced by the fact that a full consideration of reducing the complexity of the model is given in YOLOX and thus the detection accuracy was affected in some way.

Analysis of detection results of models

To further show the effects of eight kinds of models on prediction of abnormal behavior of pigs, different abnormal behaviors of pigs were predicted on the test set, among which four visualized results are as shown in Fig. 8. In the first row was the TP labeling frame, while all the other rows showed the prediction map for different models. In each prediction map, the displayed value at the top left corner of the prediction frame showed the confidence coefficient. The red frame in the map indicates abnormal behavior, while the green frame indicates normal behavior.

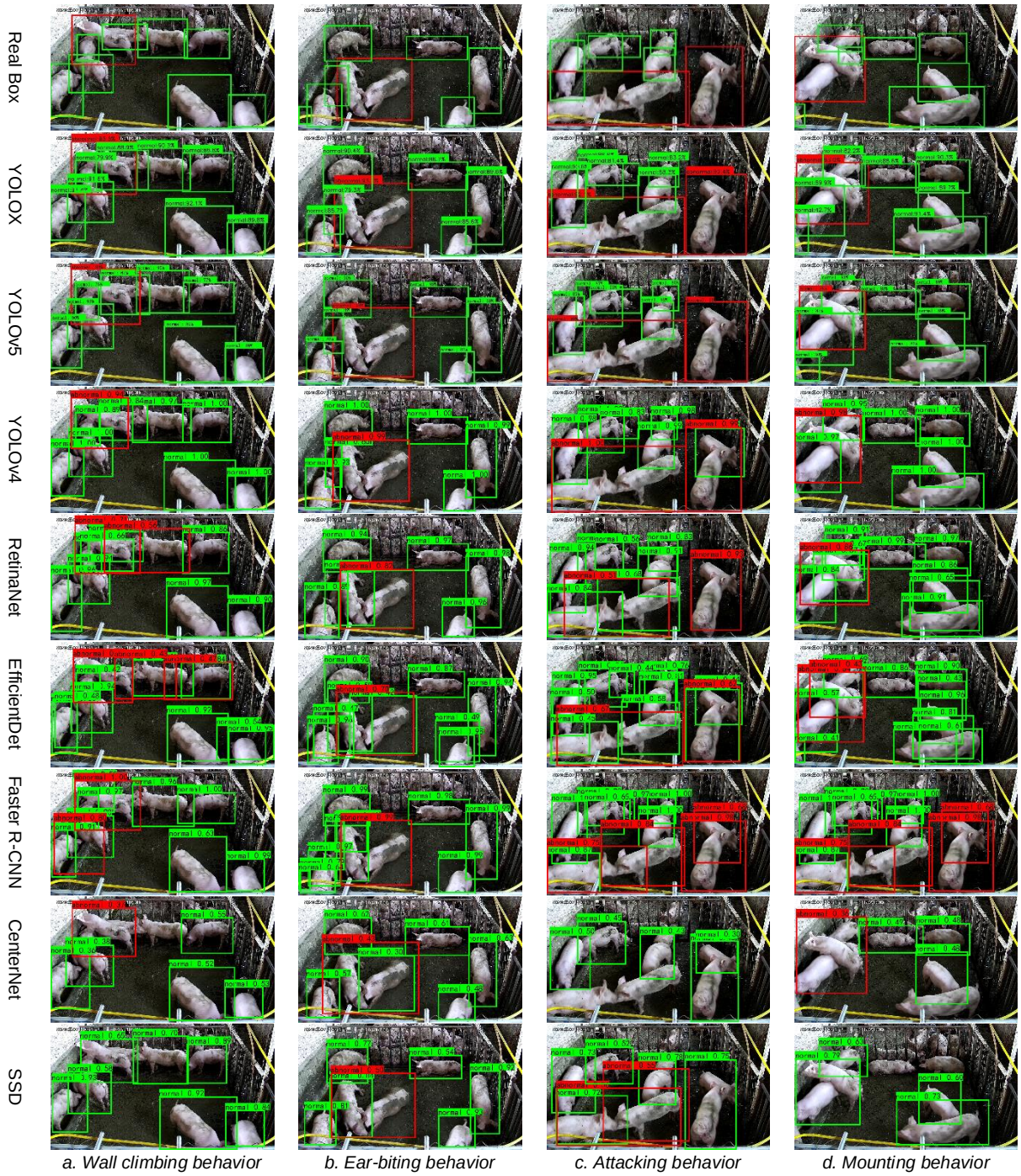


Fig. 8 - Prediction results of eight models

1) In case of wall climbing, models YOLOX, YOLOv5, YOLOv4, RetinaNet, EfficientDet, Faster R-CNN and CenterNet could all detect the wall climbing behavior of pigs, while SSD model could not. Among all the models, false detection occurred in RetinaNet model for it detected the normal behavior of pigs as abnormal, also false detection and over-detection occurred in the EfficientDet model. In addition, false detection and missed detection of the normal behavior of occluded pigs occurred in the Faster R-CNN and CenterNet models.

2) In case of ear biting, all the eight models could detect abnormal behavior of pigs, among which missed detection occurred in SSD, RetinaNet and CenterNet models for normal behavior of occluded pigs could not be predicted, also false detection occurred in the Faster R-CNN and EfficientDet models.

3) In the case of attacking, as shown in Fig. 8(c), two groups of pigs displayed attacking behavior at the same time. YOLOX, YOLOv5, YOLOv4, RetinaNet, and EfficientDet models were all able to detect the attacking behavior of the two groups of pigs. False detections occurred in the EfficientDet and RetinaNet models as they detected abnormal behavior of pigs as normal behavior. Additionally, false detection occurred in the Faster R-CNN model because the pigs displaying attacking behavior were not in the same frame at all. Furthermore, missed detection occurred in CenterNet and SSD models as they failed to detect the normal behavior of occluded pigs.

4) In case of mounting, all the models could detect abnormal behavior of pigs, while SSD could not. Among the models that could detect normal behavior of pigs, false detection occurred in the EfficientDet model, and missed detection occurred in YOLOv4, RetinaNet, Faster R-CNN as well as CenterNet models for they could not detect the normal behavior of occluded pigs.

In conclusion, different degrees of missed detection and false detection occurred in the prediction of different abnormal behaviors of pigs in models YOLOv4, RetinaNet, EfficientDet, Faster R-CNN, CenterNet and SSD. Both YOLOX and YOLOv5 models could detect behaviors of pigs in a correct way, though between the two, the YOLOX model had the maximum confidence in the prediction results, so the YOLOX model owned a better detection effect, being able to have the abnormal behavior of pigs detected effectively under different background conditions, thus the occurrence of missed detection and false detection was lowered, also the detection confidence coefficient for it was higher than that for the other seven models.

CONCLUSIONS

1) The image obtained by the frame differential method is used as the research material for pig anomaly detection, which overcomes the problems of adhesion and occlusion that are easy to occur in the pig house environment, and makes the 24-hour anomaly detection application possible.

2) Compared with other target detection models, the YOLO series models have stronger detection performance, and the detection accuracy of the YOLOX model in the YOLO series models reaches 98.0%.

3) The P-R curves of the YOLOX model are all located at the upper right of the figure, and the precision value changes very little, while other models have a significant decrease, indicating that the YOLOX model has better stability for the detection of abnormal behavior of pigs.

4) A comparative analysis is undertaken of different model prediction results in the detection of abnormal pig behaviour under conditions of adhesion and obstruction. The YOLOX model has the lowest false detection and missed detection rates, and can correctly detect abnormal pig behavior, indicating that the YOLOX model has better detection effect and can provide technical reference for real-time monitoring of scientific pig breeding.

ACKNOWLEDGEMENT

This research, titled ‘Anomaly Detection for Herd Pigs Based on YOLOX’, was funded by the Basic Research Program of Shanxi Province (202103021223241), the National Natural Science Foundation of China (31772651).

REFERENCES

[1] Bochkovskiy, A., Wang, C. Y., & Liao, H. Y. M. (2020). Yolov4: Optimal speed and accuracy of object detection. *arXiv preprint arXiv*:2004.10934. https://doi.org/10.48550/arXiv.2004.10934

[2] Cao, Y., Chen, K., Loy, C. C., & Lin, D. (2020). Prime sample attention in object detection. *In Proceedings of the IEEE/CVF Conference on Computer Vision and Pattern Recognition*. pp.11583-11591. https://doi.org/10.48550/arXiv.1904.04821

[3] Chen, C., Zhu, W., Ma, C., Guo, Y., Huang, W., & Ruan, C. (2017). Image motion feature extraction for recognition of aggressive behaviors among group-housed pigs. *Computers and Electronics in Agriculture*, 142, 380-387. https://doi.org/10.1016/j.compag.2017.09.013

[4] Duan, K., Bai, S., Xie, L., Qi, H., Huang, Q., & Tian, Q. (2019). Centernet: Keypoint triplets for object detection. *In Proceedings of the IEEE/CVF international conference on computer vision*. pp. 6569-6578. https://doi.org/10.48550/arXiv.1904.08189

[5] Fang, J., Hu, Y., Dai, B., & Wu, Z. (2021). Detection of group-housed pigs based on improved CenterNet model. *Transactions of the Chinese Society of Agricultural Engineering*, 37(16), 136-144. https://doi.org/10.11975/j.issn.1002-6819.2021.16.017

[6] Gao Y, Chen B, Liao H M, et al. (2019). Recognition method for aggressive behavior of group pigs based on deep learning. *Transactions of the Chinese Society of Agricultural Engineering*, 35(23), 192-200. https://doi.org/10.11975/j.issn.1002-6819.2019.23.024

[7] Ge, Z., Liu, S., Wang, F., Li, Z., & Sun, J. (2021). Yolox: Exceeding yolo series in 2021. *arXiv preprint arXiv*:2107.08430. https://doi.org/10.48550/arXiv.2107.08430

[8] He, K., Zhang, X., Ren, S., & Sun, J. (2016). Deep residual learning for image recognition. *In Proceedings of the IEEE conference on computer vision and pattern recognition*. pp. 770-778.

[9] https://doi.org/10.1109/CVPR.2016.90

[10] He, Z., Yu, S., Li, H., Li, S. & Li, M. (2019). Biological characteristics of African swine fever virus and its prevention and control measures in pork food production. *Transactions of the Chinese Society of Agricultural Engineering*, (10), 299-304. https://doi.org/10.11975/j.issn.1002-6819.2019.10.038

[11] Lee, J., Jin, L., Park, D., & Chung, Y. (2016). Automatic recognition of aggressive behavior in pigs using a Kinect depth sensor. *Sensors*, 16(5), 631 − 641. https://doi.org/10.3390/s16050631

[12] Li, D., Zhang, K., Li, X., Chen, Y., Li, Z., & Pu, D. (2019). Mounting Behavior Recognition for Pigs Based on Mask R-CNN. *Transactions of the Chinese Society for Agricultural Machinery*, 50(S1), 261-266+275. https://doi.org/10.6041/j.issn.1000-1298.2019.S0.041

[13] Li, J., Li, Y., Niu, F., Li, R., Zhang, T., & Jing, B. (2021). Pig Diet Behavior Detection Method Based on YOLOv4. *Transactions of the Chinese Society for Agricultural Machinery*, 52(03), 251-256.

[14] https://doi.org/10.6041 / j.issn.1000-1298.2021.03.028

[15] Lin, T. Y., Goyal, P., Girshick, R., He, K., & Dollár, P. (2017). Focal loss for dense object detection. *In Proceedings of the IEEE international conference on computer vision.* pp. 2980-2988.

[16] https://doi.org/10.1109/TPAMI.2018.2858826

[17] Liu, W., Anguelov, D., Erhan, D., Szegedy, C., Reed, S., Fu, C. Y., & Berg, A. C. (2016, October). Ssd: Single shot MultiBox detector. *In European conference on computer vision*. pp. 21-37. Springer, Cham. https://doi.org/10.1007/978-3-319-46448-0_2

[18] Oczak, M., Viazzi, S., Ismayilova, G., Sonoda, L. T., Roulston, N., Fels, M., & Vranken, E. (2014). Classification of aggressive behaviour in pigs by activity index and multilayer feed forward neural network. *Biosystems Engineering*, 119, 89-97. https://doi.org/10.1016/j.biosystemseng.2014.01.005

[19] Ren, S., He, K., Girshick, R., & Sun, J. (2017). Faster R-CNN: towards real-time object detection with region proposal networks. *IEEE Transactions on Pattern Analysis & Machine Intelligence*, 39(6), 1137-1149. https://doi.org/10.1109/TPAMI.2016.2577031

[20] Tan, M., Pang, R., & Le, Q. V. (2020). EfficientDet: Scalable and efficient object detection. *In Proceedings of the IEEE/CVF conference on computer vision and pattern recognition*. pp.10781-10790. https://doi.org/10.48550/arXiv.1911.09070

[21] Viazzi, S., Ismayilova, G., Oczak, M., Sonoda, L. T., Fels, M., Guarino, M., Berckmans, D. (2014). Image feature extraction for classification of aggressive interactions among pigs. *Computers and Electronics in Agriculture*, 104, 57-62. https://doi.org/10.1016/j.compag.2014.03.010

[22] Xue, Y., Li, S., Zheng, C., Gan, H., Li, C., & Jiu, H. (2021). Posture change recognition of lactating sow by using 2D-3D convolution feature fusion [J]. *Transactions of the Chinese Society of Agricultural Engineering*, 37(09), 230-237. https://doi.org/10.11975/j.issn.1002-6819.2021.09.026

[23] Xue, Y., Zhu, X., Zheng, C., Mao, L., Yang, A. et al. (2018). Lactating sow postures recognition from depth image of videos based on improved Faster R-CNN. *Transactions of the Chinese Society of Agricultural Engineering*, 34(9), 189-196. https://doi.org/10.11975/j.issn.1002-6819.2018.09.023

[24] Yang, Q., Xiao, D., & Lin, S. (2018). Feeding behavior recognition for group-housed pigs with the Faster R-CNN. *Computers and electronics in agriculture*, 155, 453-460. https://doi.org/10.1016/j.compag.2018.11.002

[25] Yan, H., Lu, Z., Cui, Q., Hu, Z., & Li, Y. (2019). Detection of facial gestures of group pigs based on improved Tiny-YOLO. *Transactions of the Chinese Society of Agricultural Engineering*, 35(18), 169-179. https://doi.org/10.11975/j.issn.1002-6819.2019.18.021

[26] Yan, H., Lu, Z., Cui, Q., & Hu, Z. (2020). Multi-target detection based on feature pyramid attention and deep convolution network for pigs. *Transactions of the Chinese Society of Agricultural Engineering*, 36(11), 193-202. https://doi.org/10.11975/j.issn.1002-6819.2020.11.022

[27] Zeiler, M. D., & Fergus, R. (2014). Visualizing and understanding convolutional networks. *In European conference on computer vision*. Springer, Cham. https://doi.org/10.1007/978-3-319-10590-1_53

[28] Zhang, Z., Fidler, S., & Urtasun, R. (2016). Instance-level segmentation for autonomous driving with deep densely connected MRFs. *In Proceedings of the IEEE Conference on Computer Vision and Pattern Recognition.* pp. 669-677. https://doi.org/10.1007/978-3-319-46466-4_19

[29] Zheng, C., Zhu, X., Yang, X., Wang, L., Tu, S., & Xue, Y. (2018). Automatic recognition of lactating sow postures from depth images by deep learning detector. *Computers and electronics in agriculture*, 147, 51-63. https://doi.org/10.1016/j.compag.2018.01.023

STUDY ON THE INFLUENCE OF PCA PRE-TREATMENT ON PIG FACE IDENTIFICATION WITH SUPPORT VECTOR MACHINE (SVM)

/

PCA 前处理对 SVM 识别猪脸的影响研究

Hongwen YAN*, Zhiwei HU, Qingliang CUI [1]

College of Information Science and Engineering, Shanxi Agricultural University, Taigu / China

Tel: +86-0354-6288165; E-mail: yhwhxh@126.com

DOI: https://doi.org/10.35633/inmateh-69-09

Keywords: *pre-treatment, pig face, individual identification, intelligent management of pig breeding*

ABSTRACT

To explore the application of traditional machine learning model in the intelligent management of pigs, in this paper, the influence of Principal Components Analysis (this method is simply referred to as PCA) pre-treatment on pig face identification with Support Vector Machine (this method is simply referred to as SVM) is studied. By testing method, the kernel functions of two testing schemes, one adopting SVM alone and the other adopting PCA+SVM, were determined to be poly and Radial Basis Function, whose coefficients were 0.03 and 0.01, respectively. With individual identification tests carried out on 10 pigs respectively, the identification accuracy was increased to 88.85% from 83.66% by the improved scheme, also the training time as well as testing time were reduced to 30.1% and 20.97% of the original value in the earlier scheme, respectively. It indicates that PCA pre-treatment had a positive effect on improving the efficiency of individual pig identification with SVM. It provides experimental support for the mobile terminals and embedded application of SVM classifiers.

摘要

为探索传统机器学习模型在生猪智能管理中的应用，本文研究了 PCA 前处理对 SVM 识别猪脸的影响，采用试验方式分别确定仅采用 SVM 以及 PCA+SVM 两种试验方案的核函数为 poly、RBF，其系数为 0.03、0.01，分别对 10 头生猪进行个体识别试验，优化方案将识别准确率从 83.66%提高到 88.85%，训练时间和测试时间缩减为原来的 30.1%、20.97%，结果表明，使用 PCA 前处理对采用 SVM 进行生猪个体识别的效率具有增益作用，可为 SVM 分类器的移动端和嵌入式应用提供试验支持。

INTRODUCTION

The management of individual identification and behaviour analysis of pigs, an important part in the intelligent management of pigs, can be divided into three categories: the first category is based mainly on RFID (Radio Frequency Identification) technology *(Maselyne et al., 2014; Hahnel et al., 2016)*, while the second category is based mainly on traditional machine learning model: LASSO (Least absolute shrinkage and selection operator). Regression and random forest model were used to predict the weight of pigs at 159 days to 166 days under four scenarios *(He et al., 2021)*; random forest and generalized linear regression were used to predict physiological temperature of piglets, though the prediction error was relatively high *(Gorczyca et al., 2018)*; auto-regression model (AR) and improved local linear embedding (LLE) were used to estimate pig weight in actual farm environment *(Wongsriworaphon et al., 2015)*. The third category is based mainly on the application of deep learning model and improved computer vision technology. Tu Shuqing et al. explored a PigMS R-CNN (Region Convolutional Neural Networks) framework based on mask scoring R-CNN (MS R-CNN) to segment the adhesion regions in images for herd pigs as well as identify and locate them *(Tu et al., 2021)*. Zhang Jianlong et al. modified DenseNet201, ResNet152 V2, Xception and MobileNet V2 to be a multi-output regression CNN (Region Convolutional Neural Networks) before getting them trained on modelling data, and modified Xception was selected as the optimal estimation model. In order to improve the real-time performance of the model, Residual learning structure was introduced in, with its MSE (Mean Squared Error) reaching 0.092 *(Zhang et al., 2021)*.

[1] *Hongwen Yan*, As. Ph.D. Prof. Eng.; Zhiwei Hu, Lect. Ph.D. Eng.; Qingliang Cui, Prof. Ph.D. Eng.*

Cheng et al. used the deep learning algorithm of recurrent neural network with few layers to identify pigs' preferences for objects. With the full connection layer and Softmax classifier, pigs' preferences were recognized, and the identification accuracy was high; convolutional neural network as well as Long and short term memory Network (LSTM) were combined to identify pigs' aggressive behaviours, with the accuracy reaching 97.2%, though the operation efficiency was only 15 fps *(Cheng et al., 2020)*. To better the interpretability and controllability of the model, Mathieu Marsot et al. used the cascade classifier with Haar features to intuitively see how neural network learns to distinguish parameters by using the category activation diagram generated by Grad-CAM (Gradient-weighted Class Activation Mapping), with an accuracy for 320 test images reaching 83% *(Marsot et al., 2020)*. With GPU being applied, the high precision advantage of computer vision technology has gradually been revealed. In the management of small and medium-sized farms, the needs for mobile terminals and embedded apps has gradually been increasing. For the deep learning model has a high requirement to hardware, it is difficult to adapt to wide application, while the RFID technology is easy to be simulated in the management *(Shi et al., 2012; Zhou et al., 2018)*, also it violates the animal welfare breeding thinking, so it has been gradually eliminated. Only the requirements to hardware by traditional machine learning model conform to the standards for mobile terminals and embedded apps, though there is still room for improvement in its identification accuracy and running time. With principal component analysis, the main features of the images to be tested can be extracted, thus reducing the computation burden, improving operation efficiency, eliminating noise interference and improving identification accuracy.

To promote the application of traditional machine learning model in mobile terminals and embedded apps, in this paper, SVM is adopted for improving the pig face identification efficiency in this study, and its influence on the efficiency of pig face identification is further studied by adding PCA pre-treatment in, which provides experimental support for its application in both mobile terminals and embedded application.

MATERIALS AND METHODS

Sample collection

As shown in Fig.1, the experimental materials of this study were collected on a small farm in Dongsongjiazhuang Village, Jicun Town, Fenyang City, Shanxi Province, China (111º95′ E, 37º26′ N), and the sampling date was in June 2019. Pictures of a total of 10 pigs were collected, including 768 training samples, 85 validation samples and 258 test samples.



Fig.1 - Pig Samples

The computer used in the experiment is configured with 64-bit windows system, Intel Core i7-6700, 8GB memory, 6GB video memory capacity, and Program development uses python v3.5 version language.

Principle of pig face identification with SVM

Support vector machine (SVM) is a machine learning method based on structural risk minimization that is based on statistical learning theory. According to the finite sample information, it seeks the best compromise between the model complexity and the ability to learn to obtain the best generalization ability. In addition, in the process of learning, no shortcomings such as over-fitting and local minimization are there. Thus, it has been widely used in practical identification and control *(Alex et al., 2004; Suykens et al., 1999; Suykens et al., 1999; Suykens et al., 2001)*.

SVM, whose model is related to neural network, classifies by constructing N-dimensional hyperplane. In fact, SVM model adopting S-shape kernel function is equivalent to a two-layer perceptron neural network. In SVM, kernel alternative training methods, in which include polynomial functions, radial basis functions and multi-layer perceptual classifiers, are used. Solution of their network weight is then transformed into the optimization of quadratic programming with linear constraints. With this transformation, it can be ensured that the parameters are the same when two functions get their optimal solutions. The main reason for making this transformation is that mature calculation methods and theoretical support, namely Lagrange optimization theory, are there for quadratic convex functions and constraints. In essence, SVM aims to find a predictive variable called attribute and a transform attribute of hyperplane called feature *(Du et al., 2006)*, also known as feature selection. SVM model has achieved to find the optimal hyperplane, which separates vector clusters in a certain way, and the vectors on different sides of the hyperplane are classified into different categories, while the vectors near the hyperplane are support vectors. SVM was invented by Vapnik *(Vladimir et al., 1979)* in 1979. In its linear form, SVM is a hyperplane that separates a set of positive instances and negative instances. With a maximum margin, it does not minimize training errors. Instead, it minimizes the upper limit of the generalization error and maximizes the margin between the separating hyperplane and the training data.

The key to the classification problem is that to separate the positive and negative instances, it is necessary to set up a traditional classifier. If the data point in the training set is a vector for m numbers, then the task of this kind of classifier is to find a hyperplane that may separate its members, though always linear inseparable data are there, which means that there may be no hyperplane, which can then be solved by SVM classifier nonlinear kernel function. In it, the space of its input instance x⊂R^n is mapped to the high-dimensional feature space, so that the optimal separating hyperplane built on this space has good generalization ability. SVM can select the plane with the maximum margin in the training set, so that it has the maximum generalization ability when unknown data are classified.

For the linear case, the margin is defined by the distance from the hyperplane to the nearest positive and negative instances, and the output formula for linear SVM is

$$u = w \times x - b \tag{1}$$

where: w represents Normal vector to the hyperplane, [dimensionless];
p represents the Input vector, [dimensionless];
b represents threshold for classification, [dimensionless].

For separating hyperplane, the plane u = 0 and the nearest point is on the plane where u = +1 and u = -1. The margin is

$$m = \frac{1}{\|w\|^2} \tag{2}$$

where: w represents normal vector to the hyperplane, [dimensionless];
m represents the margin of the hyperplane, [dimensionless].

SVM can be further extended to nonlinear classifiers. Lagrange multiplier is adopted to calculate the output of nonlinear SVM

$$u = \sum_{j=1}^{N} y_j a_j K(x_j, x) - b \tag{3}$$

where: K represents function used to measure the similarity or distance between input vector x and all training vectors x_j,[a];
y_j represents the classification tag of the training vector x_j, [dimensionless];
a_j represents the Lagrange multiplier for the jth sample, [dimensionless];
b represents the threshold for classification, [dimensionless];
j represents the sample size, [a];
u represents discriminant function, [dimensionless].

In this study, SVM was adopted to realize pig face classification, which is a multi-classification problem. According to its guiding principles, two SVM multi-classification methods are there:

(1) Multi-class identification tasks can be realized by multiple binary classification SVM, and the output result is determined jointly by the results of multiple SVM solutions.

(2) The initial optimization of SVM is changed in some way so that SVM can calculate the multi-classification decision functions to complete the multi-classification task.

This assorting thought was adopted in this study to realize the classification of pig face data. Thus, the original problem as listed above can be rewritten as:

$$min: 1/2 \sum_{m=1}^{k} ||w_m||^2 + C \sum_{i=1}^{n} \sum_{m \neq y_i} \xi_i^m \quad (4)$$

where: i represents the sample size, [a];

w represents normal vector to the hyperplane, [dimensionless];

m represents the number of categories, [a];

y_i represents the classification tag of the training vector x_i, [dimensionless];

ξ_i represents the Lagrange multiplier for the i[th] sample, [dimensionless].

$$S.T. (w_i \cdot x_i) + b_i \geq (w_m \cdot x_i) + b_m + 2 - \xi_i^m, \quad (5)$$
$$\xi_i^m \geq 0$$

where: i represents the sample size, [a];

w represents normal vector to the hyperplane, [dimensionless];

m represents the number of categories, [a];

x_i represents the i[th] sample, [dimensionless];

b represents the threshold for multiple-classification, [dimensionless];

ξ_i represents the Lagrange multiplier for the i[th] sample, [dimensionless].

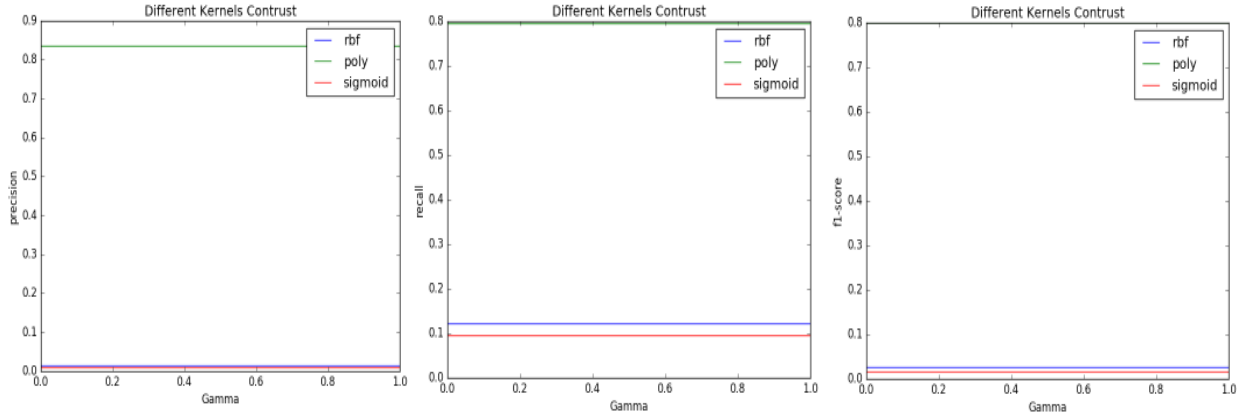
Thus, the decision function $f(x) = max\,[(w_i \cdot x_i) + b_i]$ can be obtained, and the discriminant result is for the i[th] category.

COMPARISON PROCESS IN THE EXPERIMENT

Pig face identification test carried out with SVM alone

SVM model parameter determination

When SVM is used to have pig face data classified, the determination of its kernel function and coefficient is the key to the establishment of an SVM classifier model. In this study, to select the optimal kernel function and its coefficient, the performance of different kernel functions under different coefficients was tested. The RBF radial kernel function, the polynomial kernel function called poly as well as sigmoid kernel function of SVM were selected respectively to ensure that its kernel function coefficient Gamma changes within the range of 0.0~1.0. The curves for classification accuracy, recall rate and *f1* value changing were drawn respectively, as can be seen in Fig. 2.



a. accuracy *b. recall rate* *c. f1 value*

Fig. 2 - The relationship between the evaluation index of SVM model and its kernel function and coefficient

Fig. 2a shows the relationship between the kernel function coefficient Gamma and the classification accuracy. The blue line represents the RBF radial kernel function, while the green line represents the polynomial kernel function called poly, and the red line represents the sigmoid kernel function.

As can be seen from the figure, the three curves were basically smooth and steady, which means that the value of the kernel function coefficient Gamma had little correlation with the classification accuracy. The accuracy of the polynomial kernel function called poly reached 82%, while the accuracy of RBF radial kernel function and sigmoid kernel function was about 1%. Fig. 2b shows the relationship between the kernel function coefficient Gamma and classification recall rate. As can be seen from the figure, compared with the RBF radial kernel function and sigmoid kernel function, the polynomial kernel function called poly had a higher recall rate for pig face data and the identification effect was better. Fig. 2c shows the relationship between the kernel function coefficient Gamma and *f1* value. It can be seen from the figure that the polynomial kernel function called poly had the best classification effect on the pig face data. With all these factors taken into consideration, in this experiment, the polynomial kernel function called poly was adopted as the kernel function for SVM.

Evaluation index of SVM model

By using the parameter determined by the above test, or the polynomial kernel function called poly selected as the kernel function for SVM, the kernel function coefficient was determined to be 0.03 before it was tested on the test set. A confusion matrix was obtained according to the test results, as shown in Fig. 3.

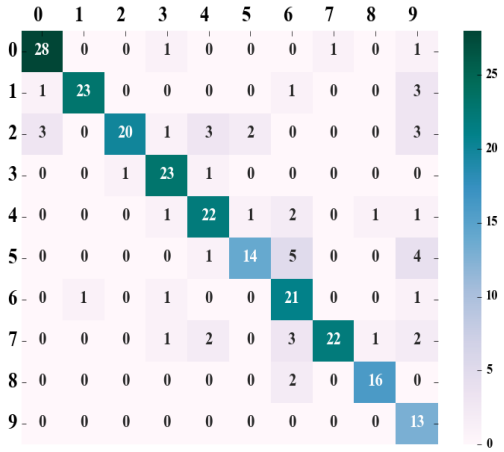


Fig. 3 - SVM prediction result confusion matrix

The leftmost column of the confusion matrix represents the real category, the top row represents the predicted category, and the diagonal line represents the number of correct predictions. The precision, recall and *f1*-core values of ten different pigs were obtained respectively in accordance with the confusion matrix and formulas (6) ~ (8), as shown in Table 1, the precision ratio was defined as:

$$precision = \frac{TP}{TP + FP} \tag{6}$$

Recall ratio was defined as:

$$recall = \frac{TP}{TP + FN} \tag{7}$$

Recall ratio was also called recall rate. Recall ratio and precision ratio changed in opposite trend. The *f1*-score can measure the different preferences of these two indexes, and the formula was as follows:

$$f1 - score = 2 \times \frac{precision \times recall}{precision + recall} \tag{8}$$

where: TP represents the number of positive samples that are actually positive samples, [a];

FP represents the number of positive samples that are actually negative samples, [a];

FN represents the number of negative samples that are actually positive samples, [a].

Table 1

SVM model prediction performance table

Category	Precision [%]	Recall [%]	*f1*-score [%]	Count [a]
1	88	90	89	31

Table 1
(continuation)

Category	Precision [%]	Recall [%]	*f1*-score [%]	Count [a]
2	96	82	88	28
3	95	62	75	32
4	82	92	87	25
5	76	79	77	28
6	82	58	68	24
7	62	88	72	24
8	96	71	81	31
9	89	89	89	18
10	46	100	63	13
average	83.66	79.53	79.95	25

As can be seen from Table 1, the average accuracy of classification and identification of pig face data with SVM adopted reached 83.66%, with the recall rate and the *f1* value reaching 79.53% and 79.95%, respectively.

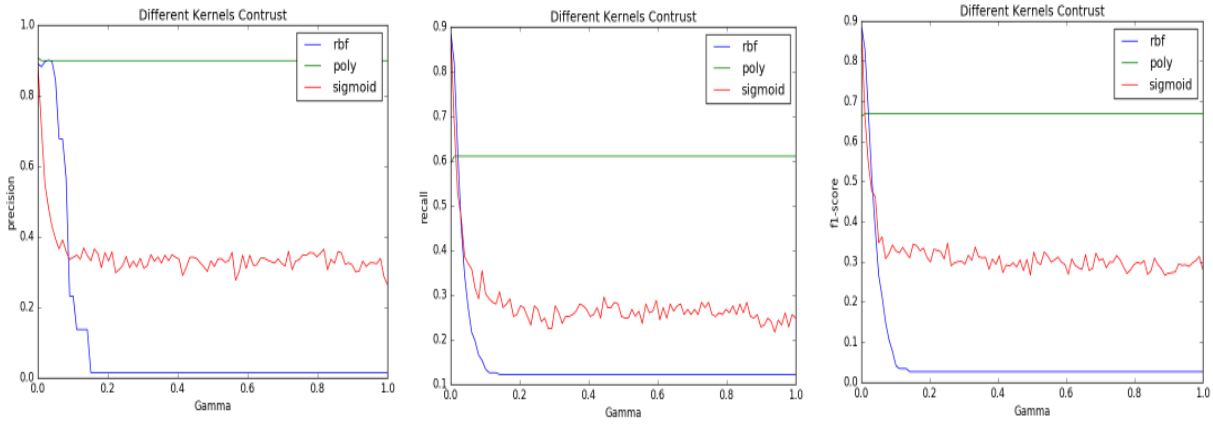
Experiment of pig face identification with SVM + PCA pre-treatment

Determine the *k* value in principal component analysis

At the first stage of the experiment, the number of principal components needs to be determined for principal component analysis. Here the *k* value was taken as 300, with the variance explanation rate reaching over 95%.

Determination of SVM parameters in the optimization plan

Determining the kernel function and the coefficient for support vector machine (SVM) is the key to the establishment of a SVM classifier model. After going through PCA treatment, the data distribution of the pig face images may change in the same way. That is to say, to continue the test with the parameters determined in the above test, it is possible that the optimal result cannot be obtained. That is to say, the kernel function and the coefficient for SVM model needs to be re-determined. With the testing method in "**SVM model parameter determination**" adopted, the kernel function and coefficient for SVM, whose input is the pig face image going through PCA treatment, is determined. The performances under different kernel functions and coefficients were compared, and their relationship is as shown in Fig. 4.



a. accuracy *b. recall rate* *c. f1 value*

Fig. 4 - The relationship between SVM model performance and parameters after pre-PCA processing

In Fig. 4a, the abscissa shows the coefficients for polynomial kernel function, radial basis kernel function and Sigmoid kernel function, the value for which is within the range of 0.0~1.0, while the ordinate shows the precision whose value is also within the range of 0.0~1.0.

As can be seen from the figure, the polynomial function reached a smooth and steady state quickly, and its precision remained to be at 0.91 as the coefficient increased. The precision of the radial basis kernel function decreased slightly when the coefficient was very small, for which the reason is that when the RBF coefficient was so small, the kernel function could fit all data points, thus over-fitting occurred; though after a slight decrease, it started to rise again, and when the coefficient was 0.01, it reached the maximum, and when the coefficient was over 0.01, it decreased rapidly. The accuracy rate decreased to the lowest---close to 0 when the coefficient was about 0.18. The precision of sigmoid kernel function decreased rapidly as the coefficient increased. When the coefficient was close to 0.05, the precision dropped to about 0.39 and was in an oscillating state. It can be concluded from the above analysis that polynomial kernel function and radial basis kernel function should be selected, and the coefficient shall be 0.01. As the precision for RBF function exceeds that for polynomial kernel function, priority was given to RBF function.

It can be seen from Fig. 4b and Fig. 4c that recall and $f1$-score showed basically the same trend. When the coefficient was very small, their values were relatively high, close to 0.9, though the recall value of polynomial kernel function remained unchanged at 0.61, while the *f1*-score value was a little larger, it remained unchanged at 0.68. The recall and $f1$-score of RBF and polynomial kernel decreased rapidly as the coefficient increased. Recall and $f1$-score reached the lowest values when the RBF coefficient was about 0.1, and they remained unchanged as the coefficient increased. At this time, the precision value was below 0.2, which means that the prediction was meaningless for practice. The performance curve of sigmoid kernel function was in an oscillating state when the coefficient was about 0.05, with recall value remaining around 0.3 and $f1$-score value around 0.35.

With the accuracy, recall rate and $f1$ value all considered, when the RBF kernel function coefficient was close to 0.01, the classification performance reached optimum. Therefore, in this paper, the kernel function was taken as RBF and the coefficient 0.01 was selected as a parameter for the SVM validation set to be tested.

Model evaluation index of optimization plan

With the parameters determined in the training set, or RBF selected as a kernel function for SVM, used, the coefficient was taken as 0.01 for the test to be carried out on the verification set. With the prediction accuracy, recall rate and *f1* value of each category calculated, the confusion matrix was drawn, as is shown in Fig. 5.

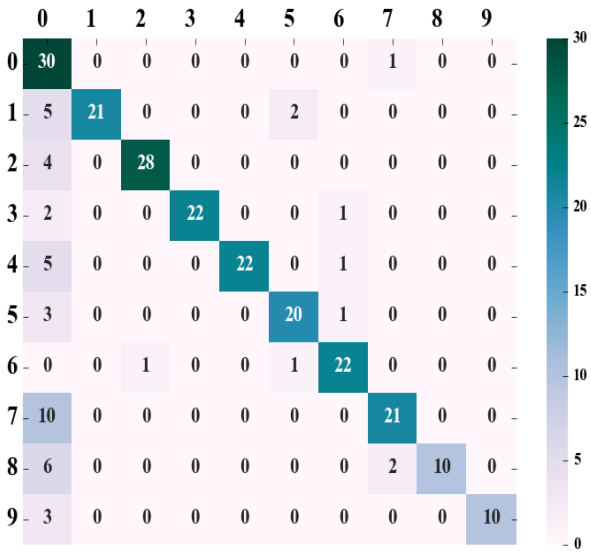


Fig. 5 - PCA+SVM prediction result confusion matrix

The precision, recall and $f1$-core values of 10 different pigs were obtained in accordance with the confusion matrix and formulas (6) ~ (8), as shown in Table 2.

Table 2

PCA+SVM model prediction performance table

Category	Precision [%]	Recall [%]	$f1$-score [%]	Count [a]
1	44	97	61	31
2	100	75	86	28
3	97	88	92	32
4	100	88	94	25
5	100	79	88	28
6	87	83	85	24
7	88	92	90	24
8	88	68	76	31
9	100	56	71	18
10	100	77	87	13
average	88.85	81.10	82.69	25

SVM classifier with PCA pre-treatment adopted was used for individual pig identification, which not only improved the identification accuracy but also reduced the training time as well as testing time of the model. The specific test indexes for the two schemes are as shown in Table 3.

Table3

The optimization result of SVM model by PCA pre-processing

model	precision [%]	precision change	test_time [ms]	test_new/ old[%]	train_time [ms]	traintest_ new/old[%]
SVM	83.66		329		12,823	
PCA+SVM	88.85	+5.19	69	20.97	3,861	30.10

RESULTS AND DISCUSSION

As can be seen in Table 2, the classification effect of PCA+SVM classifier is significantly better than that of SVM classifier alone, with the accuracy of the 2nd, 4th, 5th, 9th and 10th categories reached 100% in accuracy while the average accuracy was 88.85%. As can be seen in Table 3, for PCA+SVM scheme, the training time was 3,861 ms, the identification time was 69 ms, while the corresponding indexes for the SVM classifier alone scheme were 83.66%, 12,823 ms and 329 ms respectively. With PCA+SVM scheme employed, the accuracy of the classification test got improved by 5.19 percentage points, while its training time and the identification time were only 30.1% and 20.97% of the SVM classifier alone scheme, respectively. Although the identification accuracy was increased by only 5.19 percentage points, it was difficult to improve from 83.66% to 88.85%. The operation efficiency of the algorithm was obviously improved, and the identification time was only 20.97% of that of SVM classifier alone scheme. This provides theoretical support for the embedded application of the algorithm.

The operating efficiency of the algorithm got improved mainly for three reasons: first, after features of pig face samples were selected via principal component analysis, features participating in calculation were reduced, thus reducing the amount of calculation, which means that the running time of the algorithm was bound to get reduced; second, while the main features were selected via PCA, the secondary features were filtered, also the noise interference was eliminated, thus there would be no over-fitting in the model training, which was beneficial to not only the reduction of running time but also the improvement of identification accuracy, as has been verified by the experimental results; third, for PCA treatment, indeed additional time cost was needed, though the additional time cost can almost be ignored considering the overall operating efficiency of the algorithm. This method can be used to identify pigs through their face pictures, improve the efficiency of identification by adding PCA pre-processing, and realize the personalized feeding of pig breeding more effectively, so as to provide a reference for intelligent pig breeding.

CONCLUSIONS

In this paper, the influence of PCA pre-treatment mode on the efficiency of identification of 10 different pigs with SVM classifier was studied. The kernel function and the coefficient of the classifier were determined via tests. With the influence of two test schemes on identification efficiency compared, in which one adopting the SVM classifier alone and the other adopting PCA+SVM, we got the following conclusions:

(1) When SVM classifier was used for individual pig identification, the selection of kernel function was related to the pre-treatment method. When the SVM alone scheme was adopted, the poly function was appropriate and the coefficient shall be 0.03; while the PCA+SVM scheme was adopted, RBF function was appropriate, and the coefficient shall be 0.01.

(2) PCA pre-treatment can benefit the efficiency of individual pig identification with SVM adopted, with the accuracy increasing to 88.85% from 83.66%, and the training time as well as testing time reduced to 30.1% and 20.97% of the original values respectively.

(3) This method can improve the recognition accuracy and reduce the recognition time, SVM classifier going through PCA pre-treatment is more suitable for mobile terminals and embedded application, and it can improve the efficiency of intelligent pig breeding.

ACKNOWLEDGEMENTS

This research, titled ‘Study on the Influence of PCA Pre-treatment on Pig Face Identification with SVM’, was funded by the National Key Research and Development Plan of China (2016YFD0701801), the Shanxi Province Basic Research Program Project (Free Exploration) (Grant No. 20210302124523, 202103021224149, 202103021223141), the Doctor Scientific Research Foundation of Shanxi Agricultural University (2020BQ14). The authors are grateful and honoured to have obtained support from the Key Laboratory of Biomechanics.

REFERENCES

[1] Alex J. S., Bernhard S., (2004), A tutorial on support vector regression. *Statistics and Computing,* Vol.14, Issue 3, pp.199–222, Kluwer Academic Publishers / Netherlands;

[2] Cheng C., Zhu W.X., Juan S., et al., (2020), Recognition of aggressive episodes of pigs based on convolutional neural network and long short-term memory. *Computers and Electronics in Agriculture*, Vol.169, pp.105166, Oxford / England;

[3] Cheng C., Zhu W.X., Oczak M. et al., (2020), A computer vision approach for recognition of the engagement of pigs with different enrichment objects. *Computers and Electronics in Agriculture*, Vol.175, pp.105580, Oxford/England;

[4] Du K.L., Swammy M.N.S., (2006), *Neural Networks in a Softcomputing Framework*, pp.458-463, Springer, London / England;

[5] Gorczyca M.T., Milan H.F.M., Maia A. S. C. et al., (2018), Machine learning algorithms to predict core, skin, and hair-coat temperatures of piglets. *Computers and Electronics in Agriculture,* Vol.151, pp.286–294, Oxford / England;

[6] Hahnel D, Burgard W, Fox D, et al., (2016), Mapping and localization with RFID technology. *IEEE International Conference on Robotics and Automation*, pp.1015-1020, Los Angeles/USA;

[7] He Y.Q., Tiezzi F., Jeremy H., et al., (2021), Predicting body weight in growing pigs from feeding behaviour data using machine learning algorithms. *Computers and Electronics in Agriculture*, Vol.184, pp.106085, Oxford / England;

[8] Marsot M., Mei J.Q., Shan X.C. et al., (2020), An adaptive pig face recognition approach using Convolutional Neural Networks. *Computers and Electronics in Agriculture*, Vol.173, pp.105386, UK;

[9] Maselyne J., Saeys W., Ketelaere B. et al., (2014), Validation of a High Frequency Radio Frequency Identification (HF RFID) system for registering feeding patterns of growing-finishing pigs. *Computers and Electronics in Agriculture*, Vol.102, pp.10-18, Elsevier, Oxford / England;

[10] Shi Y.W., Zhang Y.Q., Liu K.S., (2012), Research on Security Issues Based on RFID System, Computer Science, Vol.39, Issue 6A, pp.214-216, Chongqing / China;

[11] Suykens J.A.K., Vandewalle J., (1999), Least Squares Support Vector Machine Classifiers. *Neural Processing Letters,* Vol.9, pp.293–300, Dordrecht / Netherlands;

[12] Suykens J.A.K.; Vandewalle, J. (1999), Training multilayer perceptron classifiers based on a modified support vector method, *IEEE Transactions on Neural Networks,* Vol.10, Issue 4, pp.907–911, New Jersey / United States;

[13] Suykens J.A.K., (2001), Support Vector Machines: A Nonlinear Modelling and Control Perspective, *European Journal of Control,* Vol.7, pp.311–327*,* Cachan / France;
[14] Tu S., Yuan W., Liang Y., Wang F., Wan H., (2021), Automatic Detection and Segmentation for Group-Housed Pigs Based on PigMS R-CNN. *Sensors,* Vol.21, Issue 9, pp.3251, Basel / Switzerland;
[15] Vladimir N. V., (1979), *Estimation of dependencies based on empirical Data*, pp. 430-436, Springer, New York/USA;
[16] Wongsriworaphon A., Arnonkijpanich B., Pathumnakul S., (2015), An approach based on digital image analysis to estimate the live weights of pigs in farm environments*. Computers and Electronics in Agriculture*, Vol.115, pp.26–33, Oxford / England;
[17] Zhang J.L., Zhuang Y.R., Ji H.Y., Teng G.H., (2021), Pig Weight and Body Size Estimation Using a Multiple Output Regression Convolutional Neural Network: A Fast and Fully Automatic Method. *Sensors*, Vol.21, Issue 9, pp.3218, Basel / Switzerland;
[18] Zhou J., Lu J.Z., Tu Y.Z., (2018), Discussion on the use of intelligent recognition terminal to promote the management of animal ear tags, *The Chinese Livestock and Poultry Breeding*, Vol.14, Issue 5, pp.33-34, Beijing / China.

OPTIMAL DESIGN OF EJECTOR BELT SEEDLING COLLECTING MECHANISM BASED ON EDEM
/
基于EDEM的顶杆输送带式取苗机构优化设计

Jin CHEN[1,2], Hua ZHOU*[1], Hailong CHE[1], Yuanyi LIU[1], Pei LI[1]

[1] College of Agricultural Engineering and Food Science, Shandong University of Technology, Zibo 255000, China
[2] Chinese Academy of Agricultural Mechanization Sciences Group Co., Ltd, Beijing 100083, China
Tel: +86-13336722406; E-mail: CJ82912@163.com
DOI: https://doi.org/10.35633/inmateh-69-10

Keywords: *transplanting; seedling structure; fragmentation rate; EDEM simulation; experimental research*

ABSTRACT
In the seedling extraction mechanism of the ejection type, because the ejector rod is in direct contact with the seedling substrate, the fragmentation rate of the seedling is high, the success rate is low, and the seedling effect is poor. In order to solve this problem, combined with the interaction between the ejector rod and the bowl seedling, this paper analyzes the working principle of the ejector rod conveyor belt seedling harvesting mechanism, and optimizes the design of the ejector rod conveyor belt seedling harvesting mechanism. By using the method of EDEM simulation analysis and orthogonal experiment, taking the breaking rate and success rate of bowl seedling as the test response index, the effects of ejector rod end form, ejector rod diameter and seedling extraction speed were studied, and the results were analyzed by range analysis and variance analysis to analyze the influence law of the interaction of various factors on bowl seedling extraction. The simulation results show that the crushing rate of bowl seedlings increases with the increase of seedling speed and the decrease of ejector diameter. Among the three different types of ejectors, the effect of round head ejector is the best. The best parameter combination of the seedling mechanism is the diameter of the ejector rod 10mm, the seedling speed 2m/s, and the ejector rod in the form of round head ejector rod. The verification experiment shows that the seedling extraction effect of the optimized seedling extraction mechanism is better than that of the original seedling extraction mechanism. The results show that when the best combination of working parameters is used to collect seedlings, the qualified rate of seedlings is not less than 90%, the fragmentation rate is not higher than 20%, and the seedling performance is relatively stable. The optimized seedling extraction mechanism can be used in the automatic dryland bowl seedling transplanter to meet the operational requirements of the automatic transplanter.

摘 要
在顶出式取苗机构中，由于顶杆与钵苗基质直接接触，钵苗破碎率高，成功率低，育苗效果差。为解决这一问题，结合顶杆与钵苗的相互作用，分析了顶杆输送带取苗机构的工作原理，并对顶杆输送带取苗机构进行了优化设计。采用 EDEM 模拟分析和正交试验的方法，以钵苗基质破碎率和取苗成功率为试验响应指标，研究了顶杆端部形状、顶杆直径和取苗速度对取苗效果的影响，并对结果进行极差分析和方差分析，分析各因素交互作用对取苗效果的影响规律。模拟结果表明，钵苗破碎率随取苗速度的提高和顶杆直径的减小而增大。在三种不同类型的顶杆中，球头顶杆的效果最好。取苗机构的最佳参数组合为顶杆直径 10 mm，取苗速度 2m/s，顶杆形式为球头顶杆。验证实验表明，优化后的取苗机构取苗效果好于原取苗机构。结果表明，采用最佳工作参数组合取苗，取苗合格率不低于 90%，破碎率不高于 20%，取苗表现相对稳定。优化后的取苗机构可用于旱地钵苗自动移栽机，满足自动移栽机的作业要求。

INTRODUCTION
Vegetables are an indispensable food for people's daily life. According to the statistics of the National Bureau of Statistics, the national vegetable output was 770 million tons in 2021. At present, the process of urbanization in China is accelerating, and there is a shortage of labor force in agricultural production *(Liu et al., 2022)*, which has a certain impact on agricultural production and life. In order to adapt to the development of modern agricultural production, there is an urgent need to upgrade and transform the existing transplanting technology.

The technology of automatic seedling collection in hole plate is the core part of the automatic transplanting technology of vegetable seedling in hole tray. The quality of seedling collection has a direct impact on the success rate of transplanting pot seedlings *(Wang et al., 2016; Wen et al., 2021; Hu, 2021)*. At present, the main model in the market is the semi-automatic bowl seedling transplanter, which still uses manual seedling collection, which has the advantages of low working efficiency and high labor cost. The semi-automatic transplanter uses manual seedling collection, and then sends the seedling into the planting mechanism for planting, which is the most widely used and the largest existing transplanter type *(Lv, et al. 2017)*. At present, the automatic seedling extraction technology is mainly divided into two types: the clamping type and the ejection type. The pinch type seedling extraction mechanism works stably, but the mechanism is more complex, and the structure of the ejection type seedling extraction mechanism is simple, but if the working parameters are not selected properly, it is easy to penetrate the bowl seedling and the deviation rate of falling seedling position is large. Therefore, for the top-out seedling extraction device, it is necessary to optimize the working parameters of the seedling extraction device to improve the success rate and reduce the loss of bowl seedlings in the process of seedling extraction.

At present, there are many types of dryland transplanters in China, but most of them use foreign machines for reference, and the situation at home and abroad is quite different. Foreign transplanting machines are not matched with the situation of our country, and the cost is high *(Wen et al., 2020; Yu et al., 2014; Choi et al., 2016; Karayel, D., 2023; Porteus, Sc.,1988; Kornecki, TS., 2022)*. Many scholars at home and abroad have applied discrete element simulation technology to the field of agricultural machinery *(Wang et al., 2022; Zhang et al., 2022; Yan et al., 2022; Yu et al., 2020; Liu et al., 2022; Zhou et al., 2022; Feng et al., 2016)*, which has greatly reduced the cost of research and development. Wen Yongshuang *(Ren et al., 2011)* designed a kind of plug-in type seedling extraction device, analyzed the force of the ejection process of the bowl seedling from the seedling plate, and the kinematics analysis of the motion process after the bowl seedling was thrown out. The influence factors of the bowl seedling rolling were obtained, and the force analysis and parameter optimization were carried out on the plate feeding mechanism and seedling picking mechanism of the structure.

Feng Tianxiang *(Yao et al., 2019)* and others designed the existing transplanting claws, measured the physical and mechanical property parameters of Anthurium andraeanum seedling substrate through matrix mechanical test and physical test, used different oblique insertion methods to clamp seedlings, and compared the seedling clamping effect. Combined with discrete element method, the model was established by EDEM software, and the damage of steel needle to substrate was simulated. The damage of matrix with different insertion angle, depth and position of insertion point is analyzed, and the experimental verification is carried out. At present, China's transplanting machinery has developed some transplanting equipment, mainly semi-automatic vegetable seedling transplanter, but its seedling extraction link is still completed manually, which cannot really solve the problems of high labor cost and high labor intensity. The automatic seedling collecting device of transplanter is the key to solve the above problems.

In order to further improve the working performance of the automatic seedling harvesting mechanism, this paper first measured the basic physical parameters of the seedling and analyzed the movement of the seedling in the process of seedling extraction. Secondly, the EDEM simulation analysis is used to analyze the seedling extraction mechanism with different structure, different seedling speed and different ejector diameter, and the optimal working parameters are determined. Finally, the optimal working parameters of the seedling harvesting mechanism are verified by bench test. In this study, aiming at the top-out seedling harvesting mechanism, the working performance of the seedling harvesting mechanism can be improved through the optimization analysis of modern simulation technology.

MATERIALS AND METHODS

Determination of basic parameters

- **Determination of moisture content of potted seedlings**

The bowl seedling matrix is similar to the soil, the moisture content is different, and the physical properties are quite different. Soil shows bonding characteristics due to the interaction of ion molecules and water film, which is an important factor of soil strength *(Zhang et al., 2008)*.

Because it is necessary to overcome the friction and adhesion between the acupoint plate and the seedling, the friction force is related to the material of the burrow plate and the physical characteristics of the seedling matrix, and the adhesion force is mainly related to the type of substrate, texture, water content and soil surface state, and varies greatly with the moisture content.

According to the relevant literature, in a certain range, the higher the moisture content of the matrix is, the greater the bonding force between the disk and the matrix is, and the subsequent simulation parameters need to select the bonding radius of the particles according to the moisture content of the seedling matrix. Therefore, the moisture content of the bowl seedling matrix was measured before the forward compression test to ensure the consistency of the moisture content.

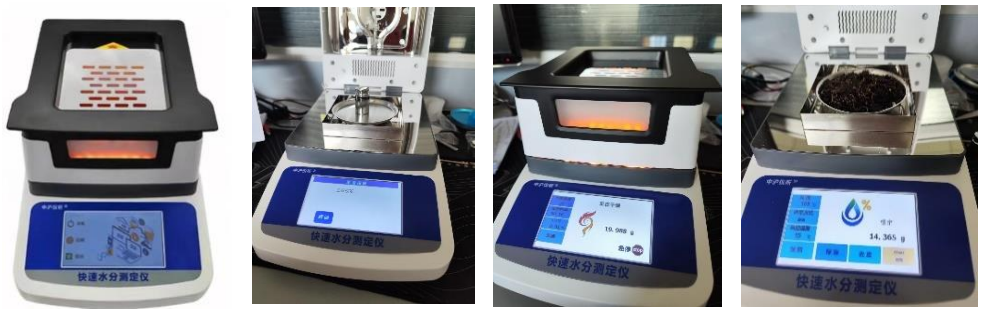


Fig. 1 - Rapid moisture meter

First of all, the weight calibration and preheating of the rapid moisture measuring instrument are carried out. Put the weight, tray and triangle bracket on the measuring instrument to calibrate the standard weight. Select the automatic mode, set the heating time to 30 minutes, and preheat the rapid moisture meter. In order to improve the testing accuracy of moisture content and shorten the drying time, the seedling matrix was mashed and laid flat on the tray as far as possible. Set the drying temperature and choose the end mode automatically. The measurement results are shown in Table 1.



a) ***b)***

Fig. 2 - Seedling matrix granule

a) Before drying b) After drying

Table 1

Measurement results of moisture meter

Parameter	drying temperature (℃)	standby temperature (℃)	initial weight (g)	Drying weight (g)	drying time	water loss (%)	drying rate (%)	wet weight (%)	moisture regain (%)
Numerical value	105	56	14.355	4.036	48min32s	71.88	28.12	355.67	255.67

Analysis of ejection time and conveyor belt speed of seedling

The seedling collecting mechanism is composed of synchronous belt pulley, bottom plate, customized synchronous belt, guide rod, seedling guide plate side plate, seedling top rod, horizontal conveyor belt, seedling guide bucket, etc., which is installed at the back of the transplanter through the frame, as shown in Fig 3. The custom conveyor belt is fixed on the frame through the synchronous belt pulley, and the guide rod is fixed on the base plate, which is used to fix the synchronous belt pulley. The seedling ejector rod is located on the back of the base plate, and the seedlings in the hole plate are taken out. The point plate is placed through the limit block on the custom synchronous belt, the side plate is fixed on both sides of the frame by screws, and the horizontal conveyor belt is fixed under the base plate. It is used to send the removed seedlings to the seedling guide bucket.

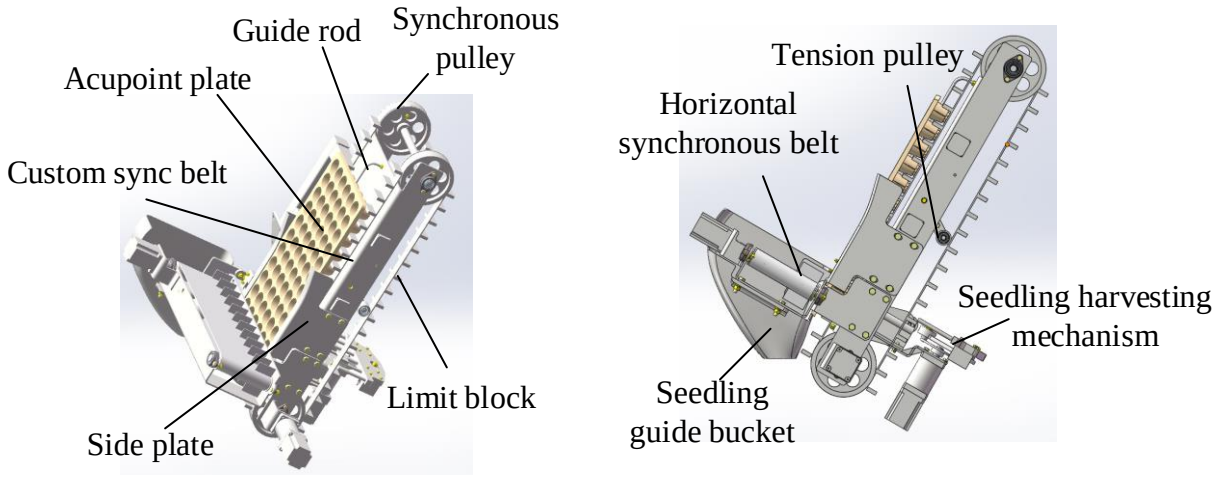


Fig. 3 - Overall structure of transplanter

a) Transplanting machine axonometric map b) transplanting machine side view

- **Establishment of Model of Seedling Mechanism**

In the process of ejecting the seedling from the seedling plate by the ejector rod, the matrix of the seedling will be broken to a certain extent under the action of ejection force. Because there are many kinds of particles in the matrix and the structure is complex, it is difficult to obtain various crushing parameters of the bowl seedling, so the discrete element analysis software is used to simulate and analyze the ejection process of the bowl seedling, which provides the basis for the parameter optimization of the ejection process.

When the seedling is ejected by the ejector rod, the force and breaking rate of the seedling will be affected due to the difference of the structure, ejection speed and diameter of the ejector rod. In this study, three kinds of ejector rod structures are designed, namely, flat head ejector rod, round head ejector rod and cone head ejector rod. The specific structure is shown in Fig 4.

The process of ejecting the bowl seedling from the seedling plate by the ejector rod was simulated, and through the comparison of the number of connecting bonds between the bowl seedling particles before and after the ejector rod ejection, the fragmentation rate and stress condition of the bowl seedling were obtained. Thus, the end structure, ejection speed and diameter of the ejector rod are selected and determined.

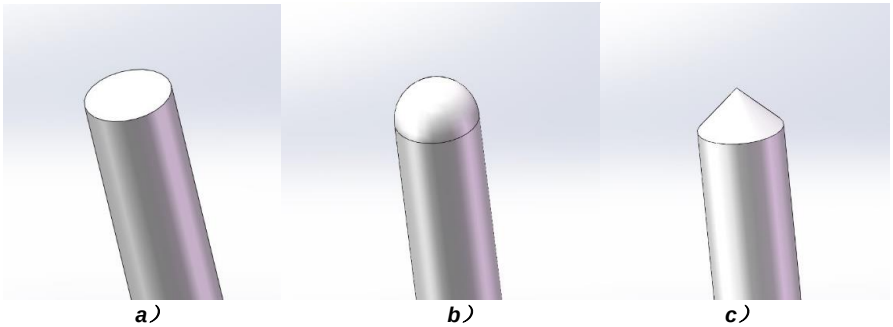


Fig. 4 - Ejector rods with different end types

a) Flat head ejector rod; b) Round head ejector rod; c) Conical ejector rod

- **Test factors and indicators**

Ejector rod diameter: the diameter of the ejector rod is too small, which will lead to penetration in the ejection process, damage the seedling matrix, cause the seedling adhesion to fall off smoothly at the end of the ejector rod, and the ejector rod diameter is too large, so that the ejector rod cannot smoothly pass through the drainage hole at the bottom of the hole plate. Easy to rub with the drainage hole. Therefore, the diameter of the ejector rod plays a key role in the success rate of seedling extraction.

The shape of the jacking rod: the overall shape of the bowl seedling is round table, and the flat head jacking rod form can basically meet the requirements of taking seed-lings, but the simulation shows that the force of the bowl seedling is mainly concentrated in the edge part of the ejector rod, relative to the bottom center position. The root effect of the edge position is poor, the breaking rate is high, and the stress state is un-reasonable, so the end form of the ejector rod is optimized, and different end structures are selected for ejection test.

Ejection speed: the seedling extraction mechanism is the ejector rod conveying belt type, and the ejection process of the bowl seedling from the point plate is a collision process, the ejection speed is too large, and the collision between the ejector rod and the bowl seedling is intensified, which can easily lead to a high fragmentation rate of the bowl seedling and serious damage to the bowl seedling; the ejection speed is too small, so that the initial speed of the bowl seedling is not enough, which cannot be thrown to the ideal position, resulting in the waste of the bowl seedling.

Based on the above analysis, the diameter, end form and ejection speed of the ejector rod in the seedling harvesting mechanism were tested. According to the leaf growth and root condition of pepper, the seedling age was selected as 33 days. The level of moisture content will affect the adhesion between the pot and the bowl seedling and the position of the center of gravity, too low moisture content will lead to the survival rate of the bowl seedling substrate is low, too high will lead to the reduction of the compressive capacity of the bowl seedling, and it is difficult to maintain the original shape, so the bowl seedling with 40% moisture content is selected.

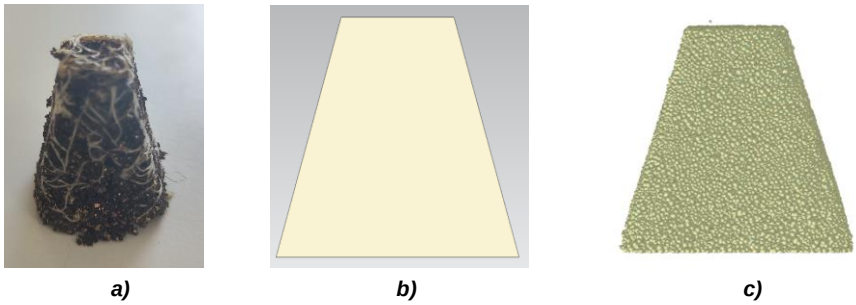
According to the overall performance of the seedling extraction device, the pepper seedling was taken as the seedling object, the ejection speed, diameter and structure of the ejector rod as the influencing factors, and the qualified rate of the seedling was taken. The orthogonal experiment of three factors, three levels and two indexes were carried out to explore the effects of different parameters and structural combinations of the ejector rod on the seedling harvesting effect. The factor level table is shown in Table 2.

Table 2

Level table of test factors

level	Factors		
	Ejector rod diameter /mm	Ejector rod speed /m/s	Ejector rod end form
1	6	1.5	Plane type
2	8	2	Cone type
3	10	2.5	Arc type

- **Establishment of discrete element simulation model of bowl seedling**



a) ***b)*** ***c)***

Fig. 5 - Rapid moisture meter

a) The physical picture b) Three-dimensional map c) Potted seedling granule bond diagram.

First of all, we need to establish the geometric model of the seedling plate and the geometric model of the ejector rod. Model the seedling plate and ejector rod by SolidWorks, then save the model in x_t format and import it into EDEM. The Poisson's ratio, shear modulus and density of ejector rod and seedling plate are set, and with reference to the previous literature, the static friction coefficient, rolling friction coefficient and collision recovery coefficient between geometry and particles are set.

In order to carry out the discrete element simulation of the bowl seedling ejection process, it is necessary to model the particles that make up the bowl seedling matrix, as shown in Fig 5, which is followed by the physical map of the bowl seedling matrix, the 3D diagram and the particle bonding diagram from left to right. The main materials of the existing matrix are peat, perlite and vermiculite at the proportion of 3:1:1. According to the relevant literature *(Pan, 2019)* and particle test, the basic structure of peat particles is mainly massive particles, nuclear particles and columnar particles, the main structure of perlite is spherical particles, and the main structure of vermiculite is flake particles.

Table 3

Simulation parameter

Parameters	Numerical value
Matrix density (kg·m^{-3})	790
Matrix shear modulus (Pa)	1.59×10^{6}
Matrix Poisson's ratio	0.25
Density of ejector rod and hole plate (kg·m^{-3})	1380
Shear modulus of ejector rod and hole plate (Pa)	1.28×10^{8}
Poisson's ratio of ejector rod to hole plate	0.35
Static friction coefficient	0.40
Rolling friction coefficient	0.44
Collision recovery coefficient	0.27

To carry out the generation of matrix particles, we should set up a particle factory, adjust the size and position of the generated particles, and set it to virtual, the generation speed is set to 10000 per second, the generation position is randomly generated, and the initial velocity is generated in the direction of -z. The purpose of setting the initial velocity is to make the soil particles move downward and prevent the formation of accumulation too fast. In the solver, the time integral is set to Euler, and the total simulation time is 3s. When the bowl seedling is ejected from the seedling plate by the ejector, the bowl seedling is subjected to gravity, the ejection force of the ejector rod to the bowl seedling, the adhesion between the seedling plate and the bowl body, and the supporting force of the seedling plate to the bowl seedling.

Because of the adhesion between soil particles, the contact model between soil particles is Hertz-Mindlin with bonding model, and the bonding parameters are shown in Table 4.

The best parameters obtained in the previous calibration are used to bond the particles. The bonding start time is set to 0.5s, and the total bonding time lasts about 0.2s. In the setting of the simulation environment, all models are subject to gravity, and the displayed area is set to the area where the model exists, and a large space should be left above the model to show the damage and bonding after the seedling is ejected.

Table 4

Bonding bond parameters

Parameters	Numerical value
Normal stiffness per unit area (N/m^{3})	2.6×10^{6}
Shear stiffness per unit area (N/m^{3})	2.6×10^{6}
Critical normal stress (Pa)	710000
Critical shear stress (Pa)	710000
Bonded disk radius (m)	0.001

Bench test method

In order to test the seedling harvesting mechanism and verify the simulation experiment, and to test the influence of three types of ejector on the seedling harvesting mechanism, the seedling extraction experiment was carried out in the State key Laboratory of soil Plant Machinery system of Chinese Academy of Agricultural Mechanization on December 10, 2022. The experimental seedlings were pepper seedlings, and the pepper burrow plates with seedling age of 35 days were used for the experiment. The experimental seedlings were cultivated in Beijing Zhongnong Futong Horticultural Co., Ltd., the seedling substrate was imported substrate, the proportion of peat, perlite and vermiculite was 3:1:1, and the experimental seedlings grew evenly.

In the control system of the seedling collecting mechanism, the experiment is carried out with the optimal working parameters. The stm32f407 chip is used as the main controller and the stepper motor is used as the driving part. After the seedlings were evenly watered, they were placed in a cool and ventilated place, and the moisture content of the bowl was measured with a moisture meter. When the moisture content of the bowl was reduced to 40%, the seedling extraction test was carried out. When picking up the seedlings, the links such as sending the plate, collecting the seedlings and sending the seedlings were completed successively. After the completion of each group of experiments, they were repeated five times and the experimental data were counted.

RESULTS

Determination of substrate ratio of bowl and seedling



a) *b)*

Fig. 6 - Screening of substrate by soil sieve

a) Soil sieves with different grids; b) 10g Matrix sample

By consulting the data, it was found that the main components of the seedling matrix were peat, perlite and vermiculite at the ratio of 3:1:1 *(Gao et al., 2017)*. In order to simulate the real composition of pot seedlings and provide data support for follow-up simulation, the particle size composition of bowl seedlings was screened by new standard soil sieve. Because the substrate of the bowl seedling is soft and contains a certain amount of water, in order to facilitate the screening of the substrate by the soil sieve, the substrate of the bowl seedling is crushed and dried in the sun, and then the substrate of the pot seedling is screened by using soil sieves with different meshes (as shown in Fig 7), and the distribution of the substrate in each screen is obtained. 10.02g matrix is selected to weigh on the electronic scale, and the particle size distribution is shown in Table 5.

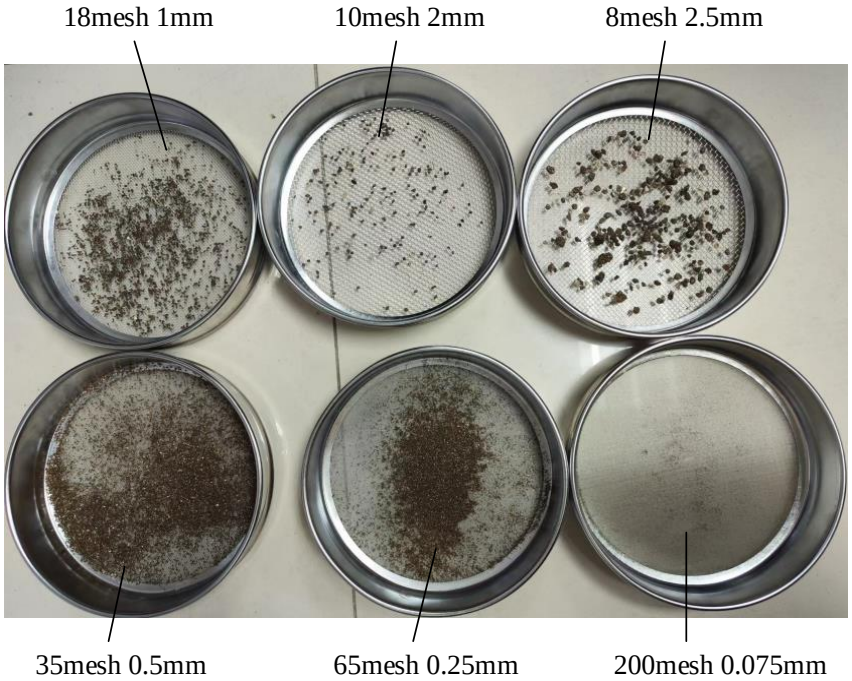


Fig. 7 - Screening results

From Table 5, it can be seen that the matrix particle size is mainly distributed between 0.25mm - 1.0mm.

Particle size distribution of matrix **Table 5**

Aperture size [mm]	Particle mass [g]	Mass proportion [%]
2.5	2.62	0.262
2	0.50	0.050
1	2.16	0.216
0.5	3.41	0.341
0.25	1.29	0.129
0.075	0.02	0.002

Simulation result

When the particle bonding is completed, the number of connection bonds between the particles can be obtained through the bonds module in the data browser of the software itself. After the bowl seedling is ejected from the bowl seedling plate, the number of connection bonds between the particles is recorded again. The ratio of the number of connection bonds reduced after ejection to the number of connection bonds between the particles before ejection is the breaking rate of the bowl seedling. According to the flight track after taking out the seedling and the distance between the center of gravity of the seedling and the hole plate, the qualified rate of the seedling is determined. The simulation is shown in Fig 8. Each group of simulation is repeated five times, taking the average value, and the experimental results are shown in Table 6.

In the simulation, the method for calculating the qualified rate of seedlings n_1 is as follows：

$$n_1 = \frac{a}{A} \times 100\% \quad (1)$$

a is total number of connection keys after ejection, A is total number of connection keys before ejection.

The crushing rate n_2 is calculated as follows：

$$n_2 = \frac{b}{B} \times 100\% \quad (2)$$

b is the number of seedlings ejected in a specified range, B is the total number of seedlings ejected from the bowl.

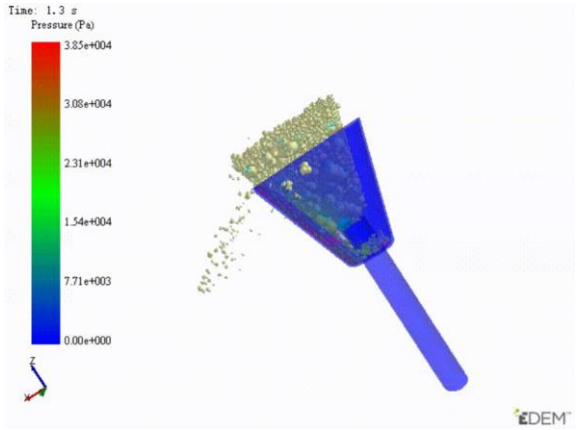


Fig. 8 - Seedling ejection process

Table 6

Simulation Scheme and results of orthogonal experiment of Seedling Mechanism

Serial number	Ejector rod diameter (mm)	Ejector rod form	Ejector rod speed (m/s)	Breakage rate n1 (%)	Qualified rate of seedling n2 (%)
1	6	Plane type	1.5	16.5	88.3
2	6	Cone type	2	20.2	94.5
3	6	Arc type	2.5	22.1	89.6

Table 6
(continuation)

Serial number	Ejector rod diameter (mm)	Ejector rod form	Ejector rod speed (m/s)	Breakage rate n1 (%)	Qualified rate of seedling n2 (%)
4	8	Plane type	2	14.8	95.3
5	8	Cone type	2.5	18.6	91.2
6	8	Arc type	1.5	16.3	89.3
7	10	Plane type	2.5	12.3	93.2
8	10	Cone type	1.5	13.6	87.5
9	10	Arc type	2	10.3	96.4

Range analysis and variance analysis were used to analyze the experimental results. The results were shown in Table 7 and Table 8. The range of fragmentation rate and qualified rate of seedling collection were R_1 and R_2, respectively. As can be seen from Table 7, for crushing rate $R_{1A} > R_{1C} > R_{1B}$, the primary and secondary factors of crushing rate are A, C, B, the optimal scheme of crushing rate is $A_1B_2C_3$, the qualified rate of seedling is $R_{2A} > R_{2C} > R_{2B}$, the factor of qualified rate of seedling is A, C, B, and the optimal scheme of qualified rate of seedling is $A_3B_3C_2$.

Table 7

Range analysis

Index	Factors	K1	K2	K3	Extreme difference R	Optimal scheme
n1	A	19.60	14.50	15.40	7.50	A1
	B	16.56	17.46	15.10	2.90	B2
	C	12.06	16.23	17.66	2.50	C3
	Primary and secondary				A>B>C	
n2	A	90.80	92.26	88.36	1.60	A2
	B	91.93	91.07	95.40	1.20	B3
	C	92.36	91.76	91.33	7.00	C1
	Primary and secondary				C>A>B	

The three optimization schemes are not exactly the same. The better parameters are selected by using the basic principle of comprehensive balance method, and each factor is analyzed.

The diameter of ejector rod A: for the crushing rate, the range of A is the largest, so A is the biggest factor affecting the crushing rate, A1 is the best for the crushing rate, A3 is the best for the seedling qualified rate, and A3 is the best for the comprehensive effect of seedling qualified rate and crushing rate on transplanting effect. The form of ejector rod B: for the breaking rate and the qualified rate of seedlings, the range of B is the smallest, which is the least influencing factor. Select B3. Ejector speed C: for the crushing rate, the range of C is smaller, which is a smaller influencing factor. For the qualified rate of seedlings, the range of C is larger, which is the larger influence factor of the crushing rate.

Table 8

Analysis of variance

Index	Variance source	Sum of squares of deviation	Degree of freedom	Mean square	F value	P value
n1	A	86.20	2.00	43.10	19.17	0.05
	B	13.02	2.00	6.51	2.90	0.26
	C	11.56	2.00	5.78	2.57	0.28
	D（Error）	4.50	2.00	2.25	1.00	0.50
	Summation	115.28	8.00			
n2	A	3.93	2.00	1.96	1.02	0.49
	B	2.18	2.00	1.09	0.57	0.64
	C	74.81	2.00	37.40	19.45	0.05
	D（Error）	3.85	2.00	1.92	1.00	0.50
	Summation	84.76	8.00			

Note: $P \leq 0.01$ means extremely significant, $P \leq 0.05$ means significant, $P \leq 0.1$ means significant, $P > 0.1$ means not significant.

From Table 7 and Table 8, it can be seen that the significant order of the factors of range analysis and variance analysis on each index is basically the same. The comprehensive balance valve is used to analyze each factor, and it is concluded that the better seedling selection scheme is A3B3C2, that is, the diameter of the ejector rod is 10mm, the end form is round head, and the seedling speed is 2 m/s. In order to verify the rationality of the optimization scheme, the optimization scheme is selected for verification experiment.

Bench test result

In order to further verify the results of the above simulation test, the bench test of the seedling harvesting mechanism was carried out, and the ejection mechanism with the optimal working parameters was used to carry out the top seedling experiment, and the qualified rate and breaking rate of the seedling extraction mechanism were calculated and analyzed.

The method for calculating the qualified rate of seedlings N_1 is as follows:

$$N_1 = \frac{W - W_1 - V_1 - V_2}{W} \times 100\% \quad (1)$$

where:

W is the total number of plants, W_1 is the number of seedlings without ejection, V_1 is the number of damaged or broken stems and leaves, and V_2 is the number of loose dunes.

The crushing rate N_2 is calculated as follows:

$$N_2 = \frac{P - M - N}{P} \times 100\% \quad (2)$$

where:

P is the total quality of seedling plate before seedling collection, N is the sum of seedling quality after seedling collection, kg; M is the mass of pot seedling after seedling collection, kg.



a) ***b)*** ***c)***

Fig. 9 - Seedling extraction process test

a) Before taking seedlings *b) When collecting seedlings* *c) After the seedling is taken*

The experiment shows that under the optimal working parameters, the qualified rate of seedling collection mechanism is 91.2%, and the breaking rate is 18.3%, which meets the working standard of seedling collection mechanism. Through the experiment, it can be found that the loss of the seedling matrix is mainly caused by the collision between the seedling collecting mechanism and the substrate, and between the horizontal conveyor belt and the substrate, and the loss part is mainly peat and perlite outside the matrix.

Basically, damage was not caused to the main part of the internal matrix-root complex. In order to reduce the damage rate, the diameter of the ejector rod can be increased as much as possible, the speed of seedling extraction can be reduced, and the impact and pressure of the ejector rod on the bottom of the seedling can be reduced.

However, the bottom space of the hole plate is relatively small, in order to ensure that the ejector rod can smoothly pass through the bottom hole plate for normal work, the diameter of the ejector rod cannot be set too large, and the decrease of seedling speed plays a significant role in reducing the breaking rate of the matrix. However, too small seedling speed will affect the qualified rate of seedling extraction. The end form has a certain effect on the matrix fragmentation rate, but has little effect on the qualified rate of seedlings.

CONCLUSIONS

In view of the problems of high breaking rate and low qualified rate of the existing top-out seedling extraction mechanism, this paper optimizes the design of the top-out automatic seedling extraction device, measures the moisture content and particle size distribution of bowl seedlings, calculates and analyzes the speed of bowl seedling movement and conveyor belt, and simulates the effects of seedling extraction speed, ejector rod diameter and end type on seedling collection qualified rate and fragmentation rate by using EDEM discrete element simulation method. The following conclusions are drawn:

(1) the speed of seedling collection, the diameter of ejector rod and the type of end of ejector rod have important influence on the crushing rate and qualified rate of seedling. Too high or too small seedling speed will lead to the seedling not being able to fall to a reasonable position, and the qualified rate of seedling will be reduced. Increasing the diameter of ejector rod in a certain range and selecting the end form with better effect can effectively reduce the breaking rate of bowl seedling matrix and the effect is better.

(2) through the design of orthogonal experiment, the ejection process of the seedling was simulated and analyzed, and the crushing rate of the seedling was evaluated by using the number of connecting bonds between particles, and the best working parameters of the seedling mechanism were obtained, so as to improve the seedling quality.

(3) the verification test of the seedling harvesting mechanism was carried out, and the verification test of seedling ejection was carried out by using the optimal parameter combination in the simulation. The test results show that when the round head ejector rod is used, the ejection speed is 2m/s, and the diameter of the ejector rod is 10mm, the fragmentation rate of the seedling is 80%, and the qualified rate of the seedling is 90%, which meets the requirements of the dryland transplanter.

ACKNOWLEDGEMENT

This work was supported by Natural Science Foundation of Shandong Province (Grant No. ZR2022QE150) and Shandong Agricultural Machinery Equipment R&D Innovation Plan Project (Grant No. 2018YF005).

REFERENCES

[1] Choi, Young, Lee, Chai-Sig, Lee, Jae-Sun. (2012). Comparison of Labor-Saving and Economical Efficiency on Mechanical Transplants of Ginseng Seeding (묘삼 이식기종에 따른 생력화와 경제성 비교). *The Journal of the Korean Society of International Agriculture*, Vol. 24, pp. 203-206, South Korea.

[2] Feng, T.X. et al. (2016) Optimization design and test research of plug seedings end-effector in greenhouse (温室穴盘苗移栽手爪改进设计及试验研究). *Beijing University of technology*, Beijing/China.

[3] Gao, G.H. et al. (2017) Verification for EDEM simulation of process of jacking tray-seedling by steel needle in grafting machine and parameter optimization (嫁接机钢针顶起穴盘苗过程 EDEM 模拟验证及参数优化). *Transactions of the Chinese Society of Agricultural Engineering,* Issue 7, pp. 29-35, Beijing / China.

[4] Hu, M.Y. (2021) Structure design and research of semi-automatic transplanting machine for vegetable plug seedlings (蔬菜穴盘苗半自动移栽机结构设计与研究). *Hubei University of Technology*, Wuhan/China.

[5] Karayel, D., Canakci. M, Topakci. M, Aktas. A. (2023). Technical evaluation of transplanters' performance for potted seedlings. *Turkish Journal of Agriculture and Forestry*, Vol. 47, pp. 116-123, Turkey.

[6] Kornecki, TS., Kichler, C. (2022). Development of a No-Till Transplanter for Walk-Behind Tractors. *Applied Engineering in Agriculture*. Vol. 38, pp. 865-872, United States of America.

[7] Liu R., et al. (2022), Optimization and Experiment of a Disturbance Assisted Seed Filling High-Speed Vacuum Seed-Metering Device Based on DEM-CFD. *Agriculture,* Vol.12, Issue 1304, Switzerland.

[8] Lv, Z.J. et al. (2017). Research progress of vegetable transplanting machine and prospects of seedling-picking machinery of transplanter (蔬菜移栽装备研究现状和钵苗移栽装备展望). *Journal of Chinese Agricultural Mechanization*, Issue 5, pp. 30-34, Heilongjiang/China.

[9] Liu, R. et al. (2022). Numerical Simulation of Seed-Movement Characteristics in New Maize Delivery Device. *Agriculture,* Vol.12, Issue 1944, Switzerland.

[10] Pan, J. (2019). *Design and Key Technology Research of Hand-held Vegetable Tray Seedling Automatic Transplanting Machine (手扶式蔬菜穴盘苗自动移栽机设计及关键技术研究).* Jiangsu University, Nanjing/China.
[11] Ren, L.Q. et al. (2011). Soil adhesion mechanics (土壤粘附力学). *China machine press*, Beijing/China.
[12] Porteus, Sc., Parish, Rl., Wright, Me. (1988). A Mechanical Transplanter for Coastal Marsh Stabilization. *Louisiana Agriculture*, Vol. 31, pp. 12, United States of America.
[13] Wang, D.Y. et al. (2016). Design and Experiment of Fully Automatic Ejection and Picking-up Seedlings Mechanism of Transplanter. *Journal of Agricultural Mechanization Research*, Issue 5, pp. 64-68, Heilongjiang/China.
[14] Wen, Y.S. et al. (2021). Current situation and analysis of automatic pick-up technology for vegetable plug seedlings (蔬菜穴盘苗移栽自动取苗技术现状与分析). *Journal of China Agricultural University*, Issue 15, pp. 128-142, Beijing /China.
[15] Wen, Y.S. et al. (2020). Development of insertion and ejection type seedling taking device for vegetable plug seedlings (蔬菜穴盘苗插入顶出式取苗装置研制). *Transactions of the Chinese Society of Agricultural Engineering,* Issue 9, pp. 96-104, Beijing/China.
[16] Wang, Y. et al. (2022). Design of and Experiment on Reciprocating Inter-Row Weeding Machine for Strip-Seeded Rice. *Agriculture,* Vol.12, Issue 1956, Switzerland.
[17] Yan, D. et al. (2022). Soil Particle Modeling and Parameter Calibration Based on Discrete Element Method. *Agriculture,* Vol.12, Issue 1421, Switzerland.
[18] Yao, Y.J. et al. (2019). Research on the Movement of Paddy Pot Seedlings in the Process of Pneumatic Ordered Throwing Transplantation (水稻气力有序抛栽钵苗运动过程研究). *Journal of Agricultural Mechanization Research,* Issue 7, pp. 158-165, Beijing / China.
[19] Yu, W.J. et al. (2020). Parameter Calibration of Pig Manure with Discrete Element Method Based on JKR Contact Model. *AgriEngineering,* Issue 2, pp. 367-377, Switzerland.
[20] Yu, X.X. et al. (2014) Current Situation and Prospect of Transplanter (移栽机械发展现状与展望). *Transactions of the Chinese Society for Agricultural Machinery*, Issue 45, pp. 45-53, Beijing/China.
[21] Zhang, X., et al. (2022). The Design and Experiment of Vertical Variable Cavity Base Fertilizer Fertilizing Apparatus. *Agriculture,* Vol.12, Issue 1793, Switzerland.
[22] Zhou, L. et al. (2022). Analysis and Design of Operating Parameters of Floor-Standing Jujube Pickup Device Based on Discrete Element Method. *Agriculture,* Vol.12, Issue 1904, Switzerland.

INVESTIGATION OF AN IMPROVED SIDE VENTILATION SYSTEM IN A POULTRY HOUSE USING CFD

/

ДОСЛІДЖЕННЯ ВДОСКОНАЛЕНОЇ БОКОВОЇ СИСТЕМИ ВЕНТИЛЯЦІЇ В ПТАШНИКУ ЗА ДОПОМОГОЮ CFD

Viktor TROKHANIAK[1)], Nadia SPODYNIUK[1)], Taras LENDIEL[1)], Petro LUZAN[2)], Anatolii MISHCHENKO[1)], Svitlana TARASENKO[1)], Lucretia POPA[*3)], Claudia IONITA [4)]

[1)] National University of Life and Environmental Sciences of Ukraine / Ukraine;

[2)] Central Ukrainian National Technical University / Ukraine;

[3)] National Institute of Research – Development for Machines and Installations Designed for Agriculture and Food Industry – INMA Bucharest / Romania;

[4)] Faculty of Mechanical Engineering and Mechatronics, University POLITEHNICA of Bucharest / Romania

Tel: +380673513082; E-mail: Trohaniak.v@gmail.com

DOI: https://doi.org/10.35633/inmateh-69-11

Keywords: *CFD, side ventilation system, aerodynamics, poultry house, inlet valves*

ABSTRACT

One of the main factors in the poultry house is maintaining a standardized microclimate. The quality of the product output in the final result depends precisely on the quality indicators of the air parameters. Poultry during its maintenance requires significant efforts and technological solutions. In this regard, authors improved microclimate system in air environment of the poultry house by installing exhaust fans on the side wall in a total number of 8 units. CFD modeling using ANSYS Fluent is a powerful tool for predicting the air flow scheme in a poultry house and is considered an alternative to experimental studies. Based on the obtained results of CFD modeling, it was established that the valves located at a height of 210 mm from the ceiling work most efficiently. Pressure drop for the inlet valves is 45.85 Pa. Air velocity at the inlet of the supply valves is equal to 9.17 m/s. Air velocity at a height of 0.7 m from the floor level varies within 0.57 m/s, the temperature is 9.91°C.

РЕЗЮМЕ

Одним із основних факторів у птахівничому приміщенні є підтримання нормованого мікроклімату. Якість виходу продукції в кінцевому результаті залежить саме від якісних показників параметрів повітря. Птиця під час її утримання вимагає значних зусиль та технологічних рішень. В зв'язку із цим авторами виконувалось вдосконалення системи мікроклімату у повітряному середовищі пташника за допомогою монтажу витяжних вентиляторів на боковій стінці в загальній кількості 8 шт. Моделювання CFD за допомогою ANSYS Fluent є потужним інструментом прогнозування схеми повітряного потоку в пташнику і вважається альтернативою експериментальним дослідженням. На основі отриманих результатів CFD моделювання встановлено, що клапани най ефективніше працюють ті, які розташовані на висоті 210 мм від перекриття. Перепад тиску для припливних клапанів становить 45,85 Па. Швидкість повітря на вході припливних клапанів рівна 9,17 м/с. Швидкість повітря на висоті 0,7 м. від рівня підлоги коливається в межах 0,57 м/с, температура – 9,91 °С.

INTRODUCTION

Evaluating the performance of new ventilation systems can be a difficult task because it is time-consuming and quite expensive. As an alternative to field measurements, Computational Fluid Dynamics (CFD) modeling is a powerful tool for predicting air flow patterns, particle and gas concentrations, and the thermal environment in livestock premises. It has also been used to evaluate the effectiveness of existing ventilation systems and new designs (*Manbeck H.B. et al., 2016; Ionita C. et al., 2022*).

[1] *Trokhaniak V.I., Assoc. Prof. Ph.D. Eng.; Spodyniuk N.A., Assoc. Prof. Ph.D. Eng.; Lendiel T.I., Assoc. Prof. Ph.D. Eng.; Luzan P.H., Assoc. Prof. Ph.D. Eng.; Mishchenko A.V., Assoc. Prof. Ph.D. Eng.; Tarasenko S.V., Assoc. Prof. Ph.D. Eng., Popa L., Ph.D. Eng.; Ionita C., Lecturer Ph D. Eng.*

According to authors *Ma, Y.X. and Zou H.F.,* (*2020*), the design of air intake devices was optimized for this typical broiler house in a cold region with cross ventilation based on two influencing factors: the length of the device and the direction of the air flow.

The optimized air supply devices helped to improve the air flow in the broiler house, thereby changing environmental factors such as internal temperature distribution, wind speed distribution and carbon dioxide distribution. The length of an ideal flow direction device should be approximately 1 m and no more than 2 m.

In the cold regions of northern China, the summer temperature is high, the winter is long and cold, and the spring and autumn are short, which makes it necessary to use a closed structure of broiler poultry houses (*Jinguo N. et al., 2016*). In this study, a typical broiler plant in the cold regions of northern China was chosen as the research object. Air supply devices commonly used in broiler houses in northern China were studied and optimized using simulation software.

The purpose of this work is to create a 3D CFD model using *ANSYS,* (*2020*), capable of reproducing real operating conditions inside the poultry house. The improvement consists in the integration of the main apparent and latent heat sources according to the procedure described in *Rojano F. et al.,* (*2015*), which was previously applied to a 2D CFD model. Model results were first validated against experimental data to assess the model's performance in predicting temperature and humidity gradients. Then the simulated field velocity was used to calculate the ventilation intensity.

In order to make the most of the advantages of weather conditions, the authors *Rojano F. et al., (2016*) analyze the effect of natural ventilation on the dynamics of the internal climate of the poultry house with an emphasis on the role of external climatic parameters, except for the direction of the wind. According to the experimental data, seven periods with a stable wind direction of at least 4 hours were selected with the prevailing north-easterly wind direction. Three of these periods were chosen as typical examples and used to validate a three-dimensional CFD model for the integration of the main elements, indoor climate: release of heat by animals and water vapor, radiative heat transfer and ventilation. The predictions of the 3D CFD model were then analyzed using the air residence time concept to estimate the ventilation rate and to investigate the apparent and latent heat transfer.

Authors *Tong, X. et al.,* (*2019a*), developed a 3D CFD model to simulate air velocity, air temperature, humidity, and heat stress in a commercial poultry house for laying hens. The model was successfully confirmed by field measurements in warm, transitional and cold periods of the year. Heat stress was detected in 69.1%, 78.0% and 18.4% of nurseries in summer, autumn and winter according to the temperature-humidity index at the incoming air temperature of 26.0°C, 15.0°C and 2.5°C with the intensity of ventilation 85.8, 15.5 and 11.7 air changes per hour, respectively. As a continuation of the research, the authors *Tong, X. et al.,* (*2019b*), developed a new ventilation system, a ventilation system with upward displacement of air flow (UDAF), which allows fresh air to enter the poultry house through air ducts located in the lower part of the cages, move upward due to the thermal buoyancy caused by the poultry and the static pressure difference caused by the exhaust fans and eventually exit the house through the fans installed on the roof. The results showed that the UDAF system resulted in a 46-129% increase in cage air exchange efficiency and provided a more uniform thermal environment with 9.4% less heat stress in summer and 68% less cold stress in winter compared to the TV system.

The article authors *Dudnyk, A. et al.,* (*2019*), gives the results of the study of intelligent management systems of biotechnological facilities using the example of a greenhouse. A measuring system has been developed for effective solar radiation research and forecasting of possible information violations. Neural networks have been used as a mathematical tool for forecasting temperature time series. Later, in *Lysenko V. et al., (2020), Lendiel T. Et al., (2021*), a software-hardware subsystem of phytomonitoring was created in a modern greenhouse building, provided with the help of LabVIEW software and Arduino equipment, which is tested directly in production. To conduct experiments, *Lysenko, V.P. et al.,* (*2021*), developed a mobile robot for monitoring the state of the atmosphere and phytostatus in protected ground facilities for the formation of control strategies that maximize production profit. As a final stage, the authors *Lysenko, V.P. et al.,* (*2019*), developed an energy-efficient control system for the electrotechnological complex of an industrial greenhouse - evaluation of the quality of plant products based on the use of Harrington's desirability functions. This allows to determine the microclimate parameters (plant temperature, air temperature and humidity), maximizing the profit of products. All these methods that were used to create, analyze and forecast the microclimate in greenhouses can be used to a large extent for poultry farms.

The authors *Spodyniuk N. and Lis A.* (*2020*), *Trokhaniak V.I. et al.,* (*2021*), conducted a study of modular poultry housing. The design of the module for growing poultry with an infrared heater has been developed.

The proposed design is energy efficient and recommended for installation in poultry houses. Microclimate in the module was analyzed. The air temperature near the poultry in the module reaches 18.6 ºC, and the average velocity does not exceed 0.75 m/s.

This publication is a continuation of scientific and practical research on improving the aerodynamic characteristics of the air environment in the poultry house (*Trokhaniak V.I. et al., 2021*). Thus, the purpose of the article is to improve the microclimate system in the air environment of the poultry house due to the installation of exhaust fans on the side wall in the total number of 8 pcs.

MATERIALS AND METHODS

According to the purpose of the work, the location of the exhaust fans was changed. The essence is summed up in the following. In the traditional design of the poultry house, the exhaust fans are not mounted on the back end wall of the poultry house, but on the side (Fig. 1), four pieces for each wall, a total of 8 pieces. Current indicators in the poultry house can be seen in Table 1.

Table 1

Current indicators in the poultry house

Current indicators	Livestock	Cross	Age/ Weight, g	Density of poultry heads/m²	Density kg/m²	Outside temperature, °C	Internal humidity, %	External humidity, %
	57971	ross	18/707	24.15	15.46	2	72	92

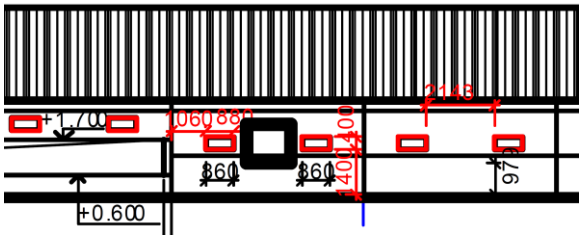
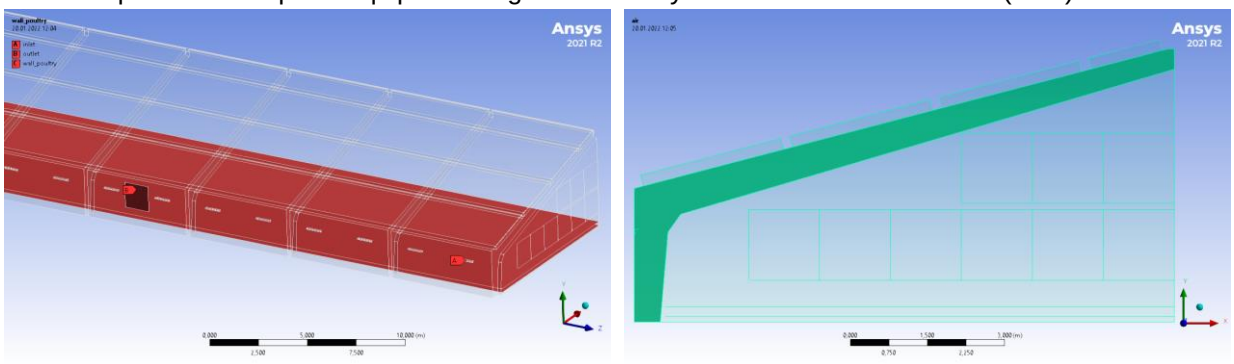


Fig. 1 – Location of the first exhaust fan on the side wall

In Fig. 2 is shown the 3D geometry of the poultry house for CFD simulation, made in 100% scale, but only half of the poultry house. The limit condition "symmetry" is set at the center of the poultry house. The rest of the boundary conditions are shown in Fig. 2a. These measures were taken in connection with the insufficient power of computer equipment. Figure 2b clearly shows the concrete frame (stick).



a) b)

Fig. 2 - 3D geometry of the poultry house

a - with the indication of boundary conditions, b – with the selection of a concrete frame.

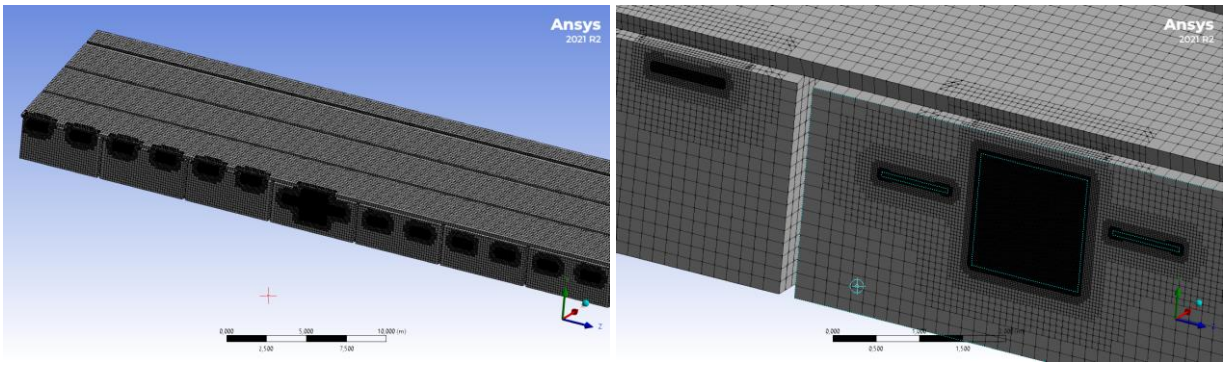
Table 2 shows the design parameters of the mesh in air environment of poultry house. Using the ANSYS Meshing software in particular volumetric element method, a 3D calculation grid was constructed. CutCell mesh construction method was applied. The number of elements reached 4.3 million. The mesh orthogonal quality index was equal to 0.22. The minimum size of the element of exhaust fans on the side wall of the poultry house was 0.01 m. It was smaller than the element size of the inlet valves by 0.03. This decision was made due to the fact that this study is more interested in the nature of air movement in exhaust fans. How the air behaves in the inlet valves was already studied in the publication (*Trokhaniak V.I. et al. 2021*).

In Fig. 3 is shown the constructed mesh in the air environment of the poultry house from the side. The openings of exhaust fans and supply valves are presented in a close-up view (see Fig. 3b). In the openings of exhaust fans and supply valves, the mesh is reduced relative to the rest of the wall area, also near the floor, where the poultry is located. Mesh refinement was carried out for more accurate calculation of hydrodynamics and heat and mass transfer by numerical method.

Table 2

Mesh construction parameters for a poultry house

Settings options	Indicator	Dim.
Mesh quality index (orthogonal quality)	0.22	–
Number of elements	4291613	piece
Number of nodes	4849379	piece
Method	CutCell	–
Maximum face size	0.16	m
Minimum face size	0.04	m
Minimum size of the supply valve element	0.04	m
Minimum size of the element of exhaust fans	0.01	m



a) b)

Fig. 3 – Mesh in the air environment of the poultry house
a – distant, b – close.

Calculations were carried out at an air consumption of 21.5 kg/s. Temperature of the outside air was assumed equal to +2°C and the parameters of thermal radiation were entered. The walls were made of concrete and insulated with foam plastic with a density of 35 kg/m^3 and a thickness of 60/100/60 mm, respectively. The roof was insulated with "Izovat" with a density of 30 kg/m^3, and a thickness of 100 mm. The floor was insulated with polystyrene foam with a density of 45 kg/m^3 and a thickness of 100 mm on a width of 2 m from the wall along the perimeter, the entire remaining area was 50 mm. In poultry houses, poultry grown on the floor is a source of heat and has a temperature of +41 °C. The heating system was not provided. Exhaust fans of the type Munters EM50 1.5Hp in the amount of 4 pcs. were used for air removal. Inflow valves Wlotpowietrza 3000-VFG were installed in a total number of 79 pcs. Spoilers were mounted above the valves at an angle of inclination of 75º from the vertical.

The CFD model was performed on the Navier-Stokes equations for convective flows (*Khmelnik S.I., 2018; Trokhaniak V. and Klendii O., 2018; Marzouk S.A. et al., 2022*). The Spalart-Allmaras turbulence model (*Allmaras S.R. et al., 2012*) and the Discrete Ordinates radiation model were used in calculations (*ANSYS, 2017; Moreno J. et al., 2019*).

RESULTS

This section presents the results of numerical simulation of poultry house in 3D using ANSYS Fluent. This makes it possible to evaluate hydrodynamic air flows in the poultry house. For numerical modeling, a 3D grid is first constructed using the method of volumetric elements in ANSYS Meshing.

In Fig. 4–9 the results of numerical modeling of the poultry house on three sections along the length of the room - 16.23 m, 50.78 m and 85.25 m are shown. The first section is the middle of the 6th inlet valve, the second is the 2nd exhaust fan (between the 17th and 18th supply valve) and the third section is in the middle of the 29th inflow valve. There are 40 inlet valves along the length of the poultry house.

In Fig. 4 is shown the temperature field in different areas of the poultry house at a constant air flow rate of 77402 m^3/h and an inlet air temperature of +2 °C. The upper air layers near the ceiling and near the side wall have a slightly higher temperature. This is accompanied by radiation from the sun and ranges from +22 to +24°C. Since the poultry is a source of heat, as well as in combination with radiation, the air in the room is partially heated. In the center of the room along the entire height, the temperature reaches +16 °C. Cool air with a temperature of +2°C is directed to the center of the room and bypasses the poultry. In the area where the incoming air actively mixes with the air in the poultry house, the air temperature does not exceed +9.85 °C (Fig. 4 a, c). In Fig. 4 b, can be observed how the exhaust fan extracts part of the heat from the poultry, which is unacceptable. The average air temperature at the exhaust fans is +8.535 °C.

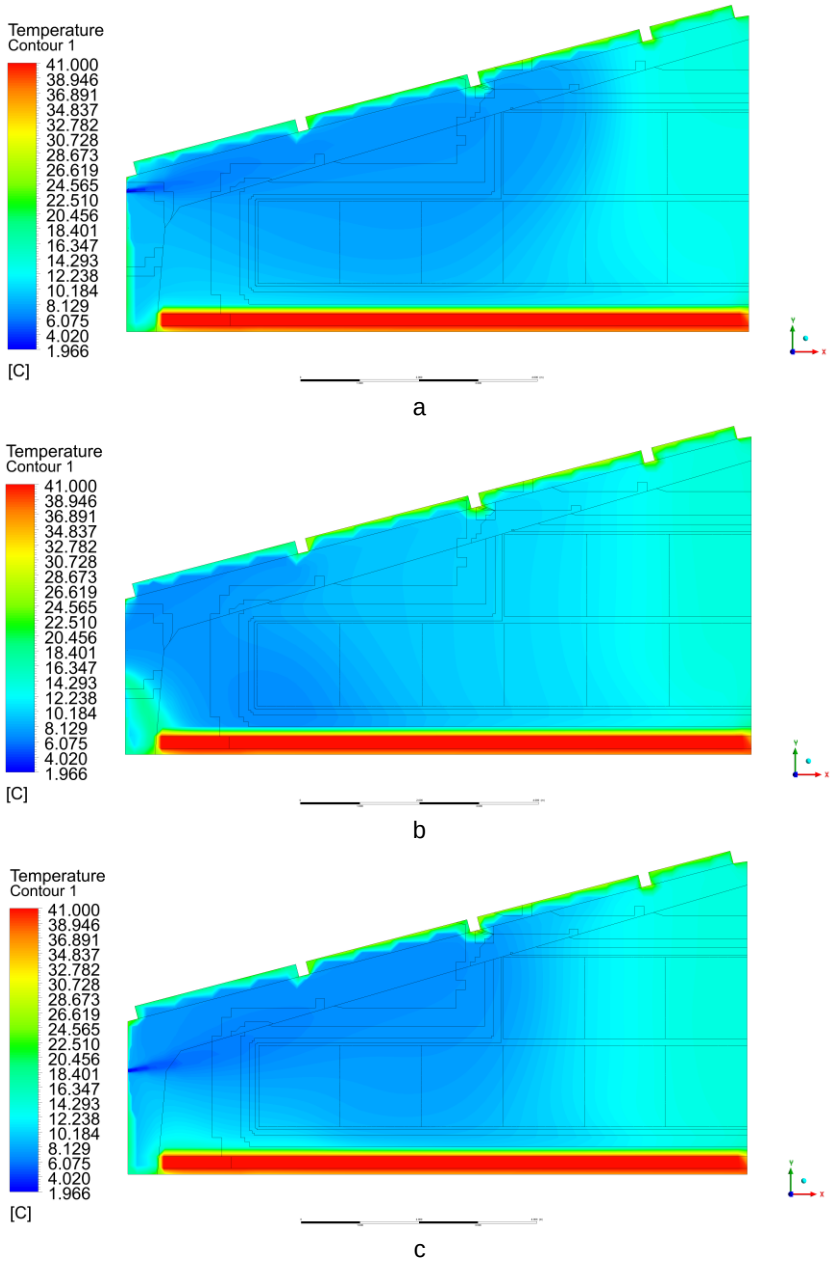


Fig. 4 – Temperature field (°C) in the poultry house at a distance from the front end wall at:
a – 16.23 m.; b – 50.78 m.; c - 85.25

In Fig. 5 is shown the pressure field in the poultry house. At the inlet of the inlet valves, the pressure is 45.846271 Pa (Fig. 5 a, c). A certain vacuum can be observed on the exhaust fans -8.4171922 Pa (Fig. 5 b). At certain points, the maximum pressure reaches 54.505 Pa.

Fig. 6 shows the hydrodynamics of air flow in the poultry house. As already mentioned above, the air flow is directed upwards by the inlet valves. However, due to low pressures and velocities at the entrance, the air falls down after passing a third of the room. Only in the case of valves that are at a height of 210 mm. from the ceiling (Fig. 6a, c; Fig. 6a, c), the air flow smoothly passes near the surface of the ceiling. The air is partially trapped due to the concrete protrusions of the floor (see Fig. 2.a).

After that, it goes to the center of the room, but reaches a third of the room. The average air velocity at the inlet of the inlet valves is 9.166368 m/s. At certain points of the poultry house, the maximum velocity can reach up to 9.871124 m/s. Two vortices are formed in the center along the length of the poultry house at 16.23 m (Fig. 6a).

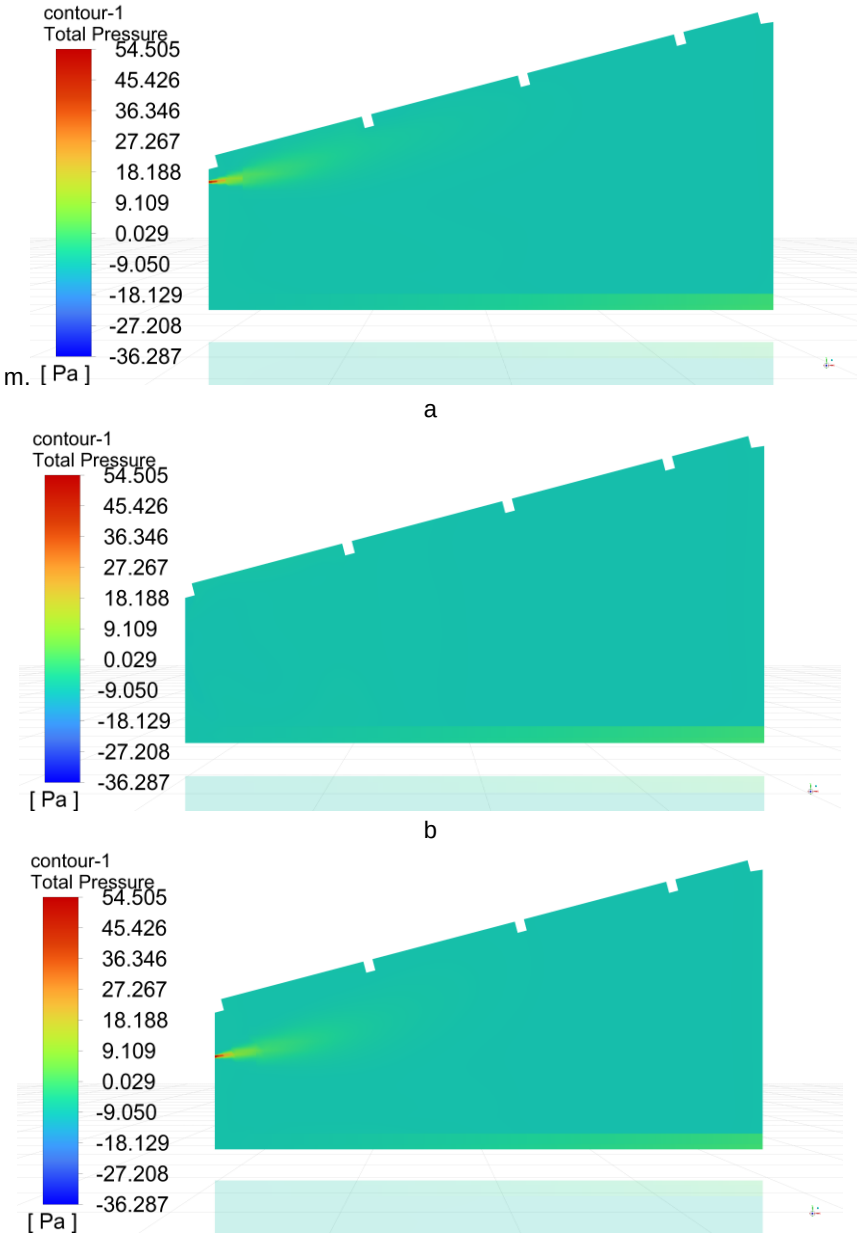
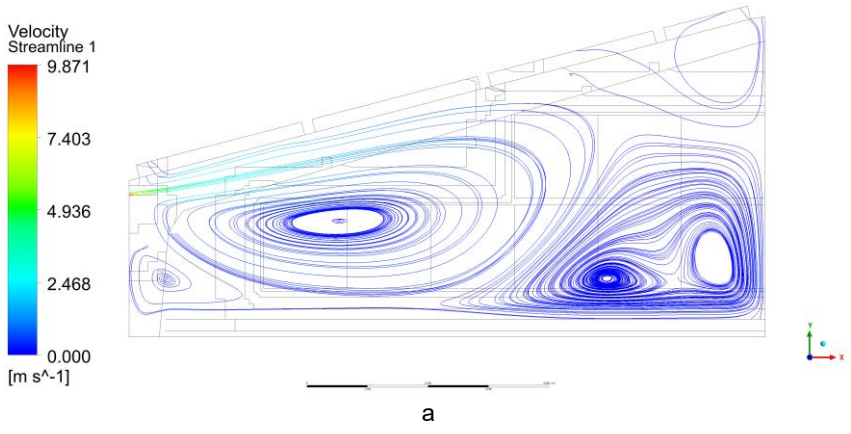
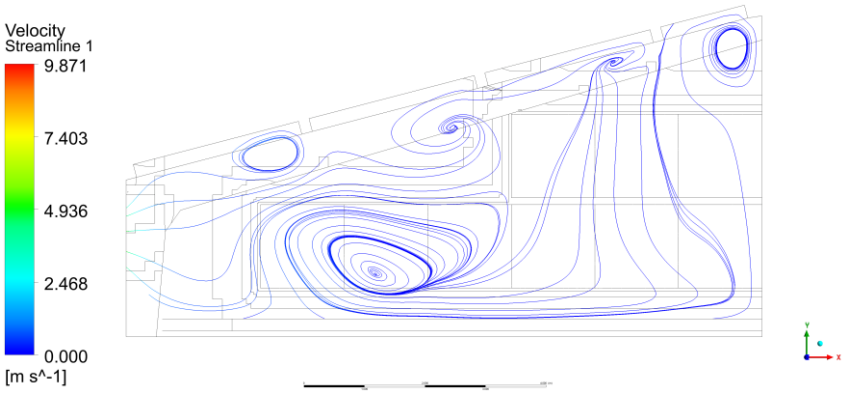
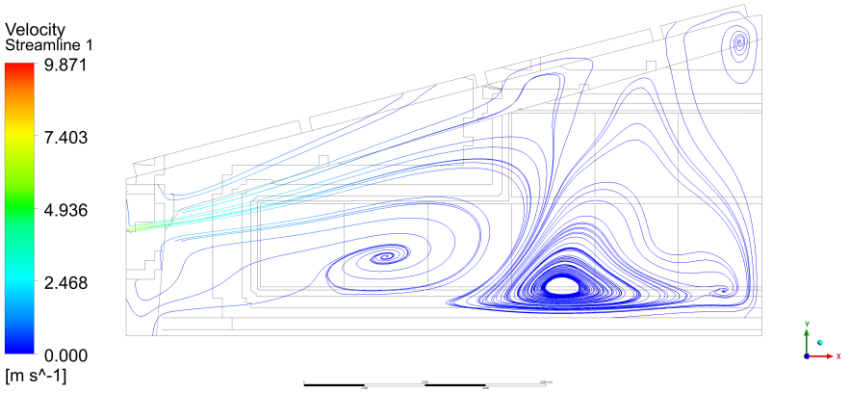


Fig. 5 – Pressure losses (Pa) in the poultry house at a distance from the front end wall at:
a – 16.23 m.; b – 50.78 m.; c - 85.25 m.





b

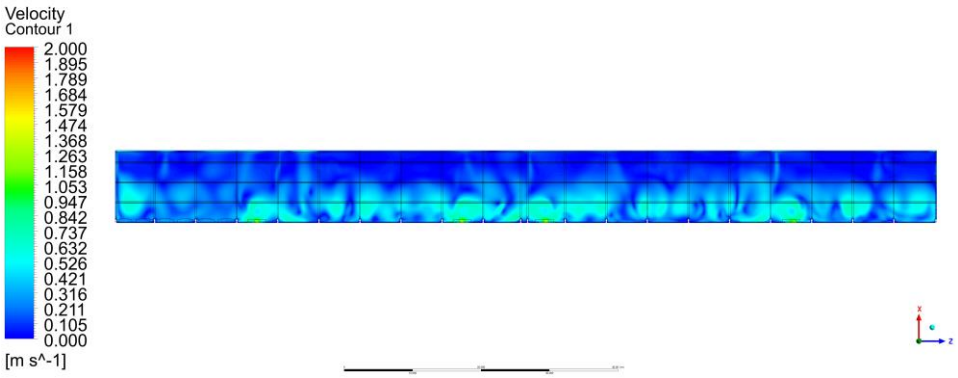


c

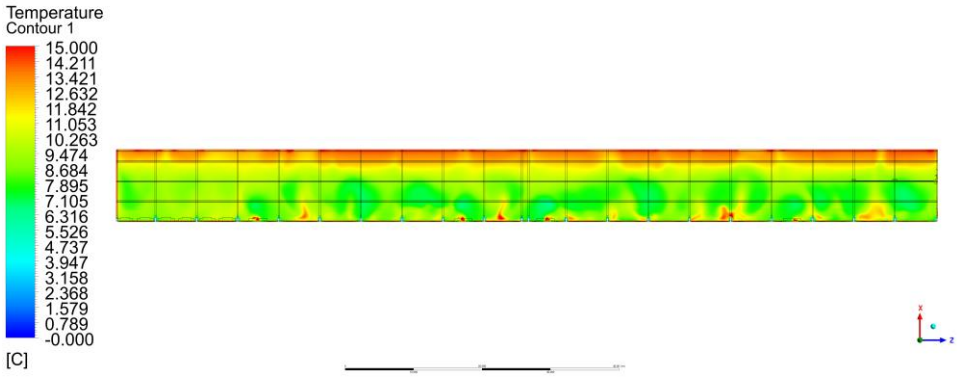
Fig. 6 – Flow lines (m/s) in the poultry house at a distance from the front end wall at:
a – 16.23 m.; b – 50.78 m.; c - 85.25 m.

Due to disturbance near the exhaust fans, along the length of the poultry house for 50.78 m (Fig. 6b), stagnant zones occur near the overlap. A vortex forms at a distance of 4.15 m from the side wall. This is due to low velocities at the outlet of the fan. In the section of exhaust fans, the average velocity is 3.4614946 m/s (Fig. 6b). Several vortices are formed at a distance of 85.25 m from the front end wall of the poultry house (Fig. 6c). The air that is pumped through the supply valves at a height of 810 mm does not reach the center of the room. This can be caused by the disturbance that occurs due to the large volumes of the room. And it is also due to low air velocity, low pressures on these inlet valves and protrusions in the concrete floor.

Figure 7 shows the field of velocities and temperatures along the plane of the room at a height of 0.7 m from the floor level. These results are the most interesting, which will help to evaluate the hydrodynamics and heat exchange of air above the poultry. The average air velocity is 0.57 m/s, the temperature is 9.91 °C. Only at some points the velocity is slightly higher than 2 m/s. The main array of poultry will not feel discomfort.



a



b

Fig. 7 – Velocity field, m/s (a), and temperature field, °C (b) in the poultry house at a height of 0.7 m from the floor level

Due to disturbance and stagnant zones in the center of the poultry house, the air velocity is about 0.32156 m/s. It was indicated above that the temperature reaches +16°C throughout the height. In the scientific work of *Trokhaniak V.I. et al., (2022*), the exhaust fans are located on the upper line of the rear end wall. This arrangement accompanies the creation of a tunnel effect in the center of the poultry house. In this regard, in the future, the authors propose to install two additional exhaust fans on the rear end wall to the already existing ones. This will increase the air velocity in the center of the poultry house.

Fig. 8-9 present 3D streamlines and visualization of volumetric air flow in the range from 0 to 2 m/s for a poultry house. The results show that the valves located 810 mm from the ceiling do not work efficiently. Valves located at 210 mm work a little better. The first valves located to the right and left of the exhaust fans practically do not work. All air enters through them, immediately entering the exhaust fan. The authors suggest that these 8 valves be closed and not used. In this way, there will not be such a large disturbance in certain areas of the poultry house. And also the velocity of the remaining valves will rise to 0.1-0.2 m/s.

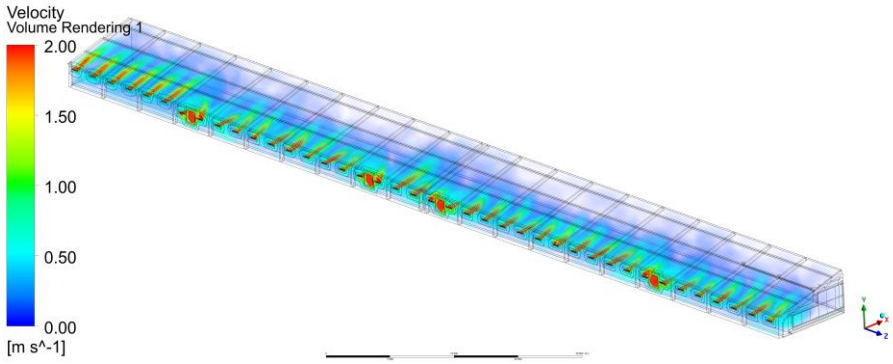


Fig. 8 – Visualization of the volume flow rate of the poultry house in the range from 0 to 2 m/s

Detailed information on the average parameters of the air environment in the poultry house as a result of the numerical simulation is presented in Table 3.

Table 3

Average indicators of the air environment in the poultry house

Parameter	Dim.	Inlet valves (inlet)	Exhaust fans (outlet)
Air consumption at the entrance for half of the poultry house	kg/s	21.5	21.50209
Air consumption at the entrance for half of the poultry house	m^3/h	77402	77402
Air consumption at the entrance for a full poultry house	m^3/h	154804	154804
Air pressure	Pa	45.846271	-8.4171922
Air temperature	°C	2.0757952	8.5349084
Air velocity	m/s	9.166368	3.4614946
Air density	kg/m^3	1.2816432	1.2532063
Thermal conductivity coefficient of air	w/m·K	0.024559	0.025
Kinematic air viscosity	kg/m·s	$1.68137 \cdot 10^{-5}$	$1.71239 \cdot 10^{-5}$

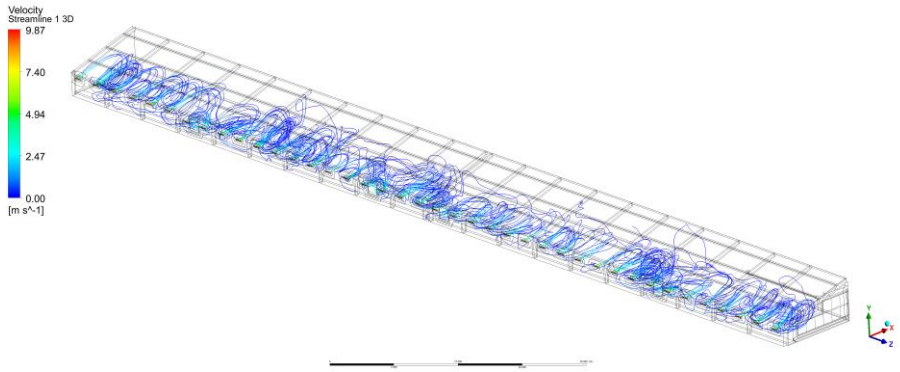


Fig. 9 – 3D streamlines (m/s) in the poultry house

With the practical experience of raising poultry, traditional poultry farms are divided into 16 uniform zones according to the output and quality of meat. Along the perimeter of the zone near the side walls of the poultry house, the quality of the meat is much worse. In the center of the poultry house, the output quality of the products is much better. From the obtained results of CFD modeling, it can be seen that due to lower speeds over the poultry and more uniform temperatures, the quality of products will be higher, compared to the traditional arrangement of exhaust fans. However, the presented results have both positive and negative effects on poultry as a whole. The authors evaluated all the pros and cons of the proposed ventilation system and will work on eliminating the shortcomings in the future.

CONCLUSIONS

1. CFD modeling of heat and mass transfer in the poultry house was carried out. To carry out CFD modeling, a mesh was built using the method of volumetric elements of the air environment of the poultry house in 3D. The CutCell method was used to build the mesh in the ANSYS Meshing preprocessor. The maximum size of the grid face is 0.16 m. The number of elements is about 4.3 million. Mesh quality indicator Orthogonal Quality is 0.22.

2. The results of the numerical modeling showed that the valves located at a height of 210 mm from the ceiling work most efficiently. The pressure drop at the inlet valves is 45.85 Pa. The air velocity at the inlet of the supply valves is 9.17 m/s. The air velocity at a height of 0.7 m from the floor level varies within 0.57 m/s, the temperature is 9.91 °C. The angle of inclination of the valve relative to the wall is 75°. The opening of the valve is 49 mm. However, with the proposed arrangement of exhaust fans on the side wall of the poultry house, the ventilation system does not work efficiently enough.

3. Authors recommend not to use two supply valves (total of 8 pcs) located on the right and left of the exhaust fans in the future. This will make it possible to increase the velocity of the remaining valves to 0.1-0.2 m/s, also include two additional fans on the rear end wall of the poultry house along the top line. This will make it possible to create a tunnel effect in the center of the poultry house. And this accompanies an increase in air velocity and at the same time reduces disturbances in the air environment of the poultry house.

ACKNOWLEDGEMENT

Supported by Affiliate «Poultry Complex» LLC Vinnytsia Poultry Farm (Ladyzhyn), Project No. 4/81 and Education and Science of Ukraine projects of scientific works of young scientists (Kyiv), Project No. 110/1m-pr-2022.

REFERENCES

[1] Allmaras S.R., Johnson F.T., Spalart P.R., (2012), Modifications and Clarifications for the Implementation of the Spalart-Allmaras Turbulence Model, *7th International Conference on Computational Fluid Dynamics*, pp. 9-13, Big Island / Hawaii;

[2] Dudnyk A., Lysenko V., Zaets N., Komarchuk D., Lendiel T., Yakymenko I. (2019), Intelligent control system of biotechnological objects with fuzzy controller and noise filtration unit, Paper presented at the *2018 International Scientific-Practical Conference on Problems of Infocommunications Science and Technology*, p. 8632007. doi:10.1109/INFOCOMMST.2018.8632007 Kharkiv / Ukraine;

[3] Ionita C., Vasilescu E.E., Popa L., Pop H., (2022), Energy and exergetic analysis of an air-conditioning system for a fruit warehouse, *INMATEH-Agricultural Engineering*, vol. 66, no. 1, pp. 403-412. https://doi.org/10.35633/inmateh-66-41. Bucharest / Romania;

[4] Jinguo N., Lizhen S., Binlin R., Binbin W. (2016), Poultry, *J. China National Poultry*, vol.2, pp.43-46;
[5] Khmelnik S.I., (2018), Navier-Stokes equations. On the existence and the search method for global solutions, *Mathematics in Computers – MiC*, 134 p., Bene-Ayish / Israel;
[6] Lendiel T., Lysenko V., Nakonechna K. (2021), Computer-integrated technologies for fitomonitoring in the greenhouse, *Lecture Notes on Data Engineering and Communications Technologies*, vol. 48, pp. 711–729, https://doi.org/10.1007/978-3-030-43070-2_30, Switzerland;
[7] Lysenko V., Bolbot I., Lendel T. (2019), Energy efficient system of electrotechnological complex control in industrial greenhouse, *Technical Electrodynamics*, vol.2, pp.78-81. Kyiv / Ukraine;
[8] Lysenko V., Zhyltsov A., Bolbot I., Lendiel T., Nalyvaiko V. (2020), Phytomonitoring in the phytometrics of the plants, Paper presented at the *E3S Web of Conferences*, vol. 154, p. 07012.
[9] Lysenko V.P., Bolbot I.M., Lendiel T.I., Nakonechna K.V., Kovalskiy V.P., Rysynets N.O., Gromaszek K., Amirgaliyev Y., Nurseitova K. (2021), Mobile robot with optical sensors for remote assessment of plant conditions and atmospheric parameters in an industrial greenhouse, Paper presented at the *International Society for Optical Engineering*, p. 12040. Warsaw / Poland;
[10] Ma Y.X., Zou H.F. (2020), Optimized design of air inlet devices based on environmental analysis of a broiler house model. Paper presented at the *2020 IOP Conf. Ser.: Mater. Sci. Eng*., vol. 789, p. 012036 doi:10.1088/1757-899X/789/1/012036. Brașov / Romania;
[11] Manbeck H.B., Hofstetter D.W., Murphy D.J., Puri V.M. (2016), Online design aid for evaluating manure pit ventilation systems to reduce entry risk, *Frontiers in Public Health*, vol. 4, no. 2, pp. 1-16, https://doi.org/10.3389/fpubh.2016.00108. Lausanne / Switzerland;
[12] Marzouk S.A., Abou A.M.M., El-Fakharany M.K., El-Said E.M.S. (2022), A comparative numerical study of shell and multi-tube heat exchanger performance with different baffles configurations, *International Journal of Thermal Sciences*, vol.179, p.107655. France;
[13] Moreno J., Casado C., Marugán J. (2019), Improved discrete ordinate method for accurate simulation radiation transport using solar and LED light sources, *Chemical Engineering Science*, vol. 205, pp. 151-164. https://doi.org/10.1016/j.ces.2019.04.034. United Kingdom;
[14] Rojano F., Bournet P.-E., Hassouna M., Robin P., Kacira M., Choi C. Y. (2015), Modelling heat and mass transfer of a broiler house using computational fluid dynamics, *Biosystems Engineering*, vol. 136, pp. 25-38. San Diego / USA;
[15] Rojano F., Bournet P-E., Hassouna M., Robin P., Kacira M., Choi C.Y. (2016), Computational modelling of thermal and humidity gradients for a naturally ventilated poultry house, *Biosystems Engineering*, vol. 151, pp. 273-285, San Diego / USA;
[16] Spodyniuk N., Lis A. (2020), Research of temperature regime in the module for poultry growing, *Lecture Notes in Civil Engineering*, vol. 100, pp. 451-458. Lviv / Ukraine;
[17] Tong X., Hong Se-W., Zhao L. (2019a), CFD modelling of airflow pattern and thermal environment in a commercial manure-belt layer house with tunnel ventilation, *Biosystems Engineering*, vol. 178, pp. 275-293, https://doi.org/10.1016/j.biosystemseng.2018.08.008. San Diego / USA;
[18] Tong X., Hong Se-W., Zhao L. (2019b), Using CFD simulations to develop an upward airflow displacement ventilation system for manure-belt layer houses to improve the indoor environment, *Biosystems Engineering*, vol. 178, pp. 294-308, San Diego / USA;
[19] Trokhaniak V., Klendii O., (2018), Numerical simulation of hydrodynamic and heat-mass exchange processes of a microclimate control system in an industrial greenhouse, *Bulletin of the Transilvania University of Brasov, Series II: Forestry, Wood Industry, Agricultural Food Engineering*, vol. 11 (60), no. 2, 171-184, Brasov / Romania;
[20] Trokhaniak V.I., Rogovskii I.L., Titova L.L., Dziubata Z.I., Luzan P.H., Popyk P.S. (2020), Using CFD simulation to investigate the impact of fresh air valves on poultry house aerodynamics in case of a side ventilation system, *INMATEH-Agricultural Engineering*, vol. 62, no. 3, pp. 155-164. https://doi.org/10.35633/inmateh-62-16. Bucharest / Romania;
[21] Trokhaniak V.I., Spodyniuk N.A., Antypov I.O., Shelimanova O.V., Tarasenko S.V., Mishchenko A.V. (2021), Experimental research and CFD modeling of modular poultry breeding, *INMATEH - Agricultural Engineering*, vol. 65, no. 3, pp. 303-311. Bucharest / Romania;
[22] Trokhaniak V.I., Spodyniuk N.A., Trokhaniak O.M., Shelimanova O.V., Luzan P.H., Luzan O.R. (2022). Investigation of the influence of exhaust fans location on the upper line on poultry house aerodynamics with the use of CFD. *INMATEH-Agricultural Engineering*, vol. 67, no. 2, pp. 425-432. https://doi.org/10.35633/inmateh-67-43. Bucharest / Romania;
[23] *** ANSYS, (2020), ANSYS Fluent theory guide. Release 2020 R1, Published in the USA, 982 p.

EXPERIMENTAL ANALYSIS OF THRESHING MAIZE SEEDS WITH HIGH MOISTURE CONTENT
/
高含水率玉米籽粒脱粒试验分析

Yujie DENG, Guohai ZHANG*, Aoqi ZHANG, Jitan LIAN, Jia YAO, Xin WANG, Xiaohui YANG [1]
School of Agricultural Engineering and Food Science, Shandong University of Technology, Zibo, 255000, China
Tel: +86-15965534882; E-mail: guohaizhang@163.com
DOI: https://doi.org/10.35633/inmateh-69-12

Keywords: *maize harvesting; maize threshing; orthogonal test*

ABSTRACT
To address the problems of high breakage rates, high entrainment losses and many unthreshed kernels when harvesting high moisture content maize seeds, a high moisture content maize seed threshing test was designed based on a multifunctional seed harvester stand designed by this group. In order to determine the optimum operating parameters of the threshing unit, single-factor experiments and orthogonal tests were carried out using the threshing drum speed, concave plate clearance and feed rate as test factors and the crushing rate, un-threshing rate, entrained loss rate and trash content rate as test evaluation indicators. The optimum combination of test factors obtained for the harvesting of maize at 32% to 34% moisture content was a drum speed of 346.55 r/min, a concave plate clearance of 44.39 mm and a feed rate of 9.739 kg/s. After repeated experiments on the bench, the test results with optimum parameters were 6.311% crushing rate, 0.187% un-threshing rate, 0.912% entrained loss rate and 4.251% impurity rate, at which point the crushing rate was the lowest and the other three met national standards.

摘要
针对高含水率玉米籽粒收获时破碎率高、夹带损失大、未脱净籽粒多的问题，基于本课题组设计的多功能籽粒收获机台架设计了高含水率玉米籽粒脱粒试验。为确定脱粒装置的最佳工作参数，以脱粒滚筒转速、凹板间隙和喂入量为试验因素，以破碎率、未脱净率、夹带损失率和含杂率为试验评价指标，进行了单因素实验与正交试验。在进行 32%~34%含水率的玉米收获试验时获取的试验因素最优参数组合为滚筒转速为 346.55r/min，凹板间隙为 44.39mm，喂入量为 9.739Kg/s，经过台架的重复实验，最优参数下的试验结果为破碎率为 6.311%，未脱净率为 0.187%，夹带损失率为 0.912%，含杂率为 4.251%，此时破碎率最低，其他三项符合国家标准。

INTRODUCTION
In recent years, with the development of China's agricultural mechanization, the level of maize mechanization harvesting has been increasing, and the national average maize harvesting rate reached 80% by 2021, but maize harvesting is mostly based on cob harvesting, and seed harvesting accounts for less than 10%, compared with the United States in the 1980s, which has achieved all maize harvesting for maize seed harvesting (*Pan, 2017; Zhang, 2017; Xie, 2021)*. Maize seed harvesting has the advantages of a short operating process, few intermediate links, low costs and high efficiency compared to cob harvesting, and has become an important means of addressing the high quality development of maize harvesting in China. For the harvesting of maize kernels, the axial threshing device has the advantages of low drum speed, gentle threshing process, long threshing time, thorough threshing, low breakage rate and high removal rate (*Zhao et al., 2010*). Longitudinal axial flow threshing drums are widely used in medium and large combine harvesters because they offer more advantages in terms of spatial layout of the combine harvester.

To solve the problem of low loss and efficient threshing of high moisture content maize, the process of threshing maize cobs in the threshing system was studied and a maize seed threshing test was designed. A review of data and field research revealed that in field trials of whole maize seed threshing and harvesting machines, maize seed threshing and stripping entered the scavenging system and re-screening device,

[1] *Yujie Deng, M.S. Stud. Eng.; Guohai Zhang, As. Ph.D. Eng. Aoqi Zhang M.S. Stud. Eng.; Jitan Lian, M.S. Stud. Eng.; Jia Yao, M.S. Stud. Eng.; Xin Wang, M.S. Stud. Eng.; Xiaohui Yang, M.S. Stud. Eng.*

increasing the crushing rate and reducing the un-threshing rate, making it impossible to collect data on the trash content rate. During threshing the maize kernels are not evenly distributed over the entire length of the drum, in a single longitudinal axial flow threshing drum the maize kernels are 90% threshed in the input and threshing section. It is therefore necessary to carry out segmental tests on the threshing process of maize kernels and to analyze the threshing material in segments, to study the rate of contamination, fragmentation, loss and uncleaning of the material, in order to carry out an in-depth study of the threshing mechanism of maize.

Many studies have been carried out by domestic and foreign scholars on maize grain harvesting: Some scholars have developed a mathematical model of material movement in a longitudinal axial flow threshing device, which can be used to guide the design and optimization of the longitudinal axial flow threshing device, and can also analyze the movement of grain in the threshing device (*Miu et al., 2007*). Some scholars concluded that for different varieties of maize cobs, increasing the speed of the threshing drum helps to increase the threshing capacity of the drum (*Tiwari et al., 2010*). Some scholars presented a mathematical model that characterizes the process of threshing and separation from the threshing machine with an axial flow of a thresher, taking into account the following input parameters: material flow, rotor speed, distance between rotor and counter rotor, mean density of processed material, feed speed, length of thresher and separating surface. The mathematical model has been experimentally validated to be a good fit (*Vlădut N.V. et al., 2022*). Some scholars have designed a fuzzy logic controller (FLC) incorporating human expert knowledge to automatically adjustment and control of the harvester to achieve minimal grain losses especially at the position of straw walker and upper sieve (*Omid et al., 2010*). Some scholars have designed a fuzzy control system which combines the knowledge of experienced operators with these data-based models (*Craessaerts et al., 2010*). Some scholars have designed a combine chassis leveling control system. Starting from the identification of a gray box model, a two-layer cascade regulator is designed to control the body roll and pitch angles. In addition, an automatic, data driven tuning protocol that cuts down the time needed for the traditional manual tuning procedure is proposed (*Federico et al., 2023*). Some scholars have recorded the actual field speed of the rice combine used by the operator on a daily basis through field observation measurements. In addition, its impact on grain losses in the rice field was assessed (*Shamilah et al., 2020*). Some scholars have developed mathematical models for the operation of combine harvester cleaning system screens based on the nodal coordinates, velocities and motion acceleration of the combine harvester cleaning system screens (*Ildar et al., 2020*).

A researcher has designed a low-damage combination round-headed spiked tines and segmented circular tube threshing screen plate that can be used for efficient, high-performance maize harvesting (*Qu, 2018*). Some scholars designed a longitudinal axial flow type variable diameter and variable pitch conical threshing drum, which was tested and proven to be suitable for harvesting maize with high moisture content (*Song et al., 2022*). Some scholars have designed an adjustable threshing and separating device. It solves the problem of unstable feeding volume of combine harvesters in the field leading to poor harvesting performance (*Wang et al., 2019*). Some scholars have designed a threshing and separating device for regenerated rice combine harvesters. The device achieves the purpose of making full use of space and improving threshing efficiency (*Li et al., 2022*).

Given the difficulty of collecting experimental data on the threshing and removal of trash residues in maize seed harvesting experiments in the field, this affects the effectiveness of the experiment and increases experimental error. The multifunctional seed harvesting test stand designed by the group is therefore used. The test stand is not equipped with a travelling device and is fed to the cutting table by a conveyor belt. The other working parts are designed and assembled according to the mainstream domestic models. The test stand is powered by 7 motors and the speed of each motor is controlled by a PLC control cabinet. After testing and verification, the stand can simulate the complete threshing process of a combine harvester and meets the requirements of this experiment.

MATERIALS AND METHODS

General design of the multifunctional seed harvesting test stand

The designed test stand consists of a feeding, threshing, scavenging and chopping system. The PLC control cabinet included in it enables the independent speed regulation of each of the seven motors by controlling seven frequency converters. The parameters of each device can be adjusted infinitely. The structure of the test stand is shown in Figure 1.

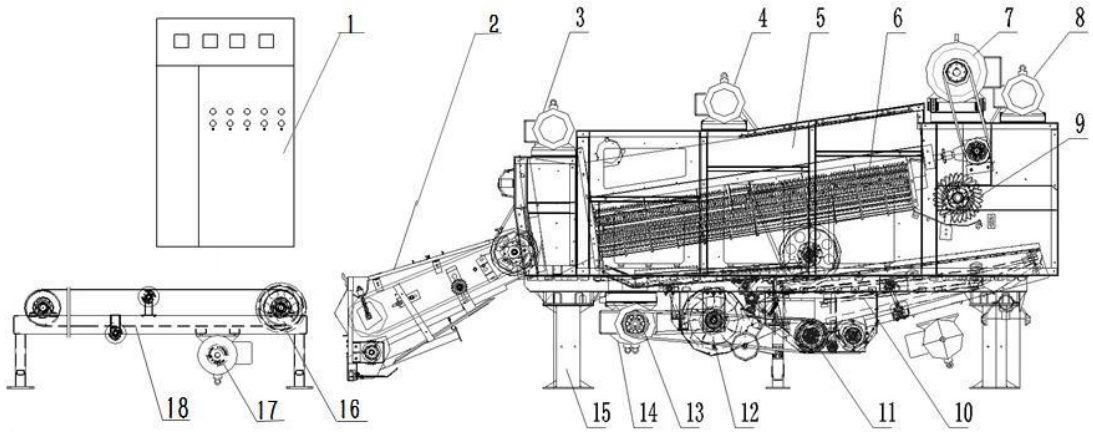


Fig. 1 - Structure of the test bench

1. PLC control cabinet; 2. Over bridge assembly; 3. Over bridge motor; 4. Scavenging motor; 5. Machine wall; 6. Axial flow assembly; 7. Axial flow reluctance motor; 8. Chopper motor; 9. Chopper assembly; 10. Scavenging sieve assembly; 11. Scavenging chamber bottom shell; 12. Scavenging fan; 13. Belt drive; 14. Fan motor; 15. Frame; 16. Conveyor belt drive roller; 17. Conveyor belt motor; 18. Conveyor belt assembly

Operating principle of the multifunctional seed harvesting test stand

When the table is in operation, the crop first enters the spiral conveyor through the conveyor belt and enters the conveyor overpass under the action of the spiral conveyor; the crop enters between the threshing drum and the gap between the concave plates under the action of the rotating screw feed head for threshing and separation; the threshed material enters the sorting system after threshing is completed, and the other miscellaneous residues are conveyed through the drum to the rear shredding system for shredding and discharge (*Shen et al., 2013*). The threshed material entering the sorting system is sorted under the action of the fish scale screen and the fan. The seeds are discharged through the discharge opening by means of a conveyor churn and finally collected by hand, most of the trash is discharged from the tail screen and a part of the mixture of seeds and trash is conveyed by the trash churn to the front of the threshing drum for secondary re-threshing.

EXPERIMENTAL RESEARCH ON MAIZE THRESHING

Test methods

The influence of moisture content on the threshing of maize kernels is mainly generated during the threshing process, so the feeding rate, drum speed and threshing gap, which have a greater influence on the threshing effect, were selected as the test factors, and a single-factor test was conducted at 5 levels within the parameter adjustment range. To study the effect of different levels of each parameter on the threshing effect at different water contents, three excellent levels were selected and then orthogonal tests were carried out to obtain the optimal ratio of threshing parameters at different water contents using response surface analysis.

The test indicators are calculated as follows:

$$Y = \frac{W_3}{W_1} \times 100\% \quad (1)$$

$$S = \frac{W_2}{W_4} \times 100\% \quad (2)$$

$$Z = \frac{W_5}{W_4} \times 100\% \quad (3)$$

$$Q = \frac{W_7}{W_6} \times 100\% \quad (4)$$

where: S is the crushing rate, %;

Y - the impurity rate, %;

Z - the undefined rate, %

Q - the loss rate, %;

W_1 - the total mass of seeds and trash in the material box, kg;

W_2 - is the mass of crushed maize kernels in the material box, kg;

W_3 - is the mass of trash in the material box, kg;

W_4 - is the mass of maize seeds in the material box, kg;

W_5 - is the mass of un-threshing maize seeds in the material box, kg;
W_6 - is the mass of all maize seeds, kg;
W_7 - is the quality of maize seeds on receiving tarp, kg.

Based on the actual operational characteristics of the single longitudinal axial flow maize seed harvester, the adjustment range of the threshing test parameters was determined, as shown in Table 1 below.

Table 1

Adjustment range of bench parameters

Parameters	Adjustment range	Measurement unit
Feeding volume	6~14	kg/s
Roller speed	250~600	r/min
Threshing clearance	25~55	mm
Deflector angle	50~70	°

Test materials

The maize variety tested was Zhengdan 958, taken from a field grown by a local farmer in Zibo, with the parameters shown in Table 2 below. The test material was unthreshed maize cobs taken by hand and harvested in September 2022.

Table 2

Corn size parameters

Parameters	Numerical values
Maize varieties	Zhengdan 958
Maize cob length, mm	175-202
Diameter of the top of the corn, mm	30-36
Maize cob tail diameter, mm	49-51
Maize seed weight per 100 kernels, g	40
Initial moisture content of the seeds, %	32-34

The maize was selected for harvesting from the same lot, with essentially the same growth. At harvesting, the maize was required to be fully mature and free from collapse, and to prevent the loss of moisture from the kernels, a bench test of the highest moisture content was carried out immediately after harvesting, with a theoretical dosage of 2.35 t and an actual estimate of 2.5 t.

Test site: Shandong Yafeng Agricultural Machinery & Equipment Co.

Test apparatus: single longitudinal axial flow maize combine harvesting stand, moisture tester, weighing apparatus.

Test procedure

Before the test starts, carry out the inspection of the threshing and cleaning test bench, check whether the machine chain, pulley, etc. are connected normally; switch on the power, check whether the frequency converter, instrument panel, indicator lights and other parts are displayed normally; press the click start button and check whether there are any strange noises in the motors (*Du et al., 2020*). After the threshing and cleaning test bench has been inspected, the material boxes are placed on the first cleaning sieve surface to catch and release the maize kernels and debris after threshing. 50 material boxes of 300 mm x 250 mm x 150 mm in length, width and height are densely placed on the sieve surface according to the length and diameter of the threshing drum; the discharge tarp is laid flat at the rear of the test bench to catch and release the maize kernels and debris lost during threshing.

To start the test, first fill a woven bag with maize cobs, 10 kg per bag, and after determining the amount to be fed for this test take a sufficient amount of maize cobs and pour them onto the conveyor belt 1.5 m from the end and lay them backwards for 4 m. Before starting the machine, adjust the threshing gap to meet the test requirements. When starting the machine, start it from the rear of the stand in order to the front, start the stand in the order of the crushing roller, threshing drum and cutting table, and start the conveyor belt when it is running smoothly. After the corn cob has been threshed, the machine is switched off from the front to the rear of the frame, in the order of the conveyor belt, the cutting table, the threshing roller and the crushing roller.

At the end of each trial, the mixture on the discharge tarp was collected, the trash and maize kernels were separated manually and their kernel mass was weighed on an electronic scale to calculate the entrainment loss rate. Samples are removed from the receiver box using the quadratic method, the total mass is weighed using an electronic scale, then the trash, broken kernels and un-threshing kernels are separated manually and the mass of each is weighed using an electronic scale to calculate the percentage of broken, trash and un-threshing kernels. In order to reduce measurement errors, the test data from the three material boxes were combined and the average value was taken as the final maize kernel breakage rate, un-threshing rate and trash content rate.

Single-factor tests

In order to investigate the effect of drum speed, concave plate clearance and cob feed on the rate of broken and unthreshed kernels in a single longitudinal axial threshing device, the range of values for each factor level in the orthogonal test was determined and a single factor threshing test was conducted on maize cobs in the 32-34% moisture content range. All three factors examined were tested in a 5-level single-factor test on the basis of prior art, with three replications of each level and the mean value taken as the final result.

Speed single factor test: The basic parameters in the speed single factor test are determined with reference to existing threshing techniques and requirements. At this stage of the multi-row high efficiency maize seed combine harvester, its threshing device cob feeding capacity needs to reach about 10 kg/s, so the cob feeding capacity in the speed single factor test is 10 kg/s. The gap between the concave plates is set at 40 mm in reference to the well-established spike-tooth threshing devices in the market. The speed of the roller has been explored in preliminary tests to find a better value at around 400 r/min. The speed test was conducted at 75 r/min as a unit and five levels were selected for threshing at 250/325/400/475/550 r/min respectively.

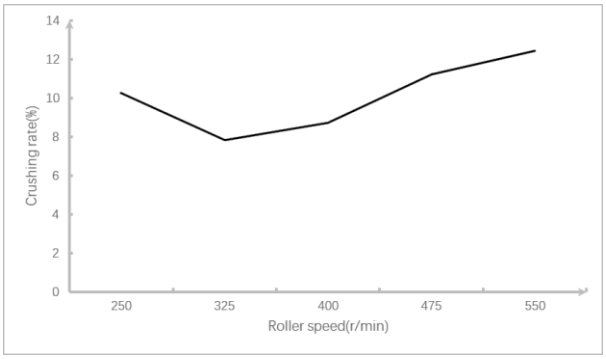
RESULTS

The results of the single-factor test on roller speed are shown in Table 3 below. A line graph of drum speed versus test indexes based on the test results is shown in Figure 2.

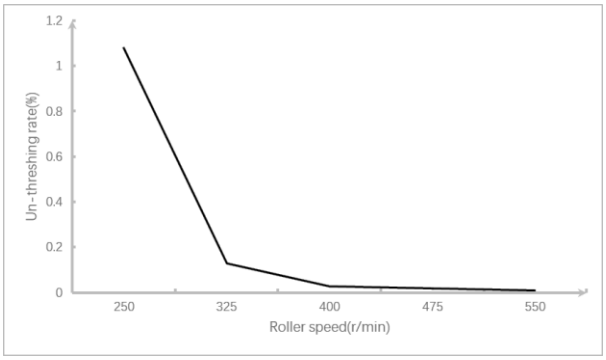
Table 3

Results of single factor tests on drum speed

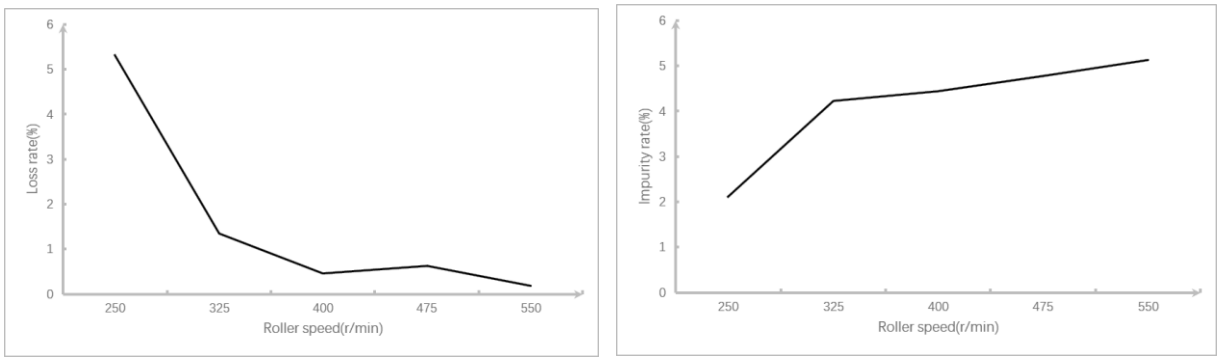
Test serial number	Test factors			Test indicators			
	Roller speed (r/min)	Concave plate clearance (mm)	Feeding volume (kg/s)	Crushing rate (%)	Un-threshing rate (%)	Loss rate (%)	Impurity rate (%)
1	250	40	10	10.264	1.080	5.310	2.120
2	325	40	10	7.845	0.130	1.345	4.230
3	400	40	10	8.716	0.028	0.456	4.450
4	475	40	10	11.233	0.018	0.631	4.780
5	550	40	10	12.452	0.009	0.185	5.130



(a)



(b)



(c) (d)

Fig. 2 - Effect of drum speed on test index

Incomplete threshing at low roller speed, high un-threshing rate and low crushing rate. When the drum speed is low, the threshing is incomplete, the un-threshing rate is high and the crushing rate is low; when the speed is increased to a suitable level, the un-threshing rate is effectively reduced and the crushing rate is at a low level; when the drum speed is continued to be increased, the impact of the rod teeth on the seeds is increased and the crushing rate rises faster, but the reduction is not significant because the un-threshing rate is at a low level. The loss rate is higher at lower speeds because the threshing element fails to separate out the seeds caught in the bracts and leaves. Significant improvement in loss ratio after increasing speed. The trash content increases at higher speeds as a result of stronger drum strikes on the mandrel.

Single factor test for concave plate clearance: The basic parameters in the single-factor test for concave plate clearance were determined with reference to the results of the single-factor test for speed and the requirements of high-feed maize seed harvesting machinery. Based on the results of the single-factor test on speed, the drum speed was set at 325 r/min for the 32-34% moisture content corn cob threshing test; the cob feeding rate was set at 10 kg/s for the corn cob threshing test in both moisture content zones based on the efficiency requirements of the multi-row high efficiency corn seed harvester.

The concave plate gap test was still selected at 5 levels, with a single factor threshing test for the gap at 30/35/40/45/50 mm respectively.

The results of the single factor test for the concave plate clearance are shown in Table 4 below. A line graph of concave plate clearance versus test index based on the test results is shown in Figure 3.

Table 4

Single-factor test results for concave plate clearance

Test serial number	Test factors			Test indicators			
	Roller speed (r/min)	Concave plate clearance (mm)	Feeding volume (kg/s)	Crushing rate (%)	Un-threshing rate (%)	Loss rate (%)	Impurity rate (%)
1	325	30	10	8.245	0.052	0.683	4.210
2	325	35	10	7.537	0.049	0.532	4.780
3	325	40	10	7.215	0.076	0.465	4.650
4	325	45	10	7.657	0.113	0.895	3.650
5	325	50	10	7.983	0.253	1.214	7.240

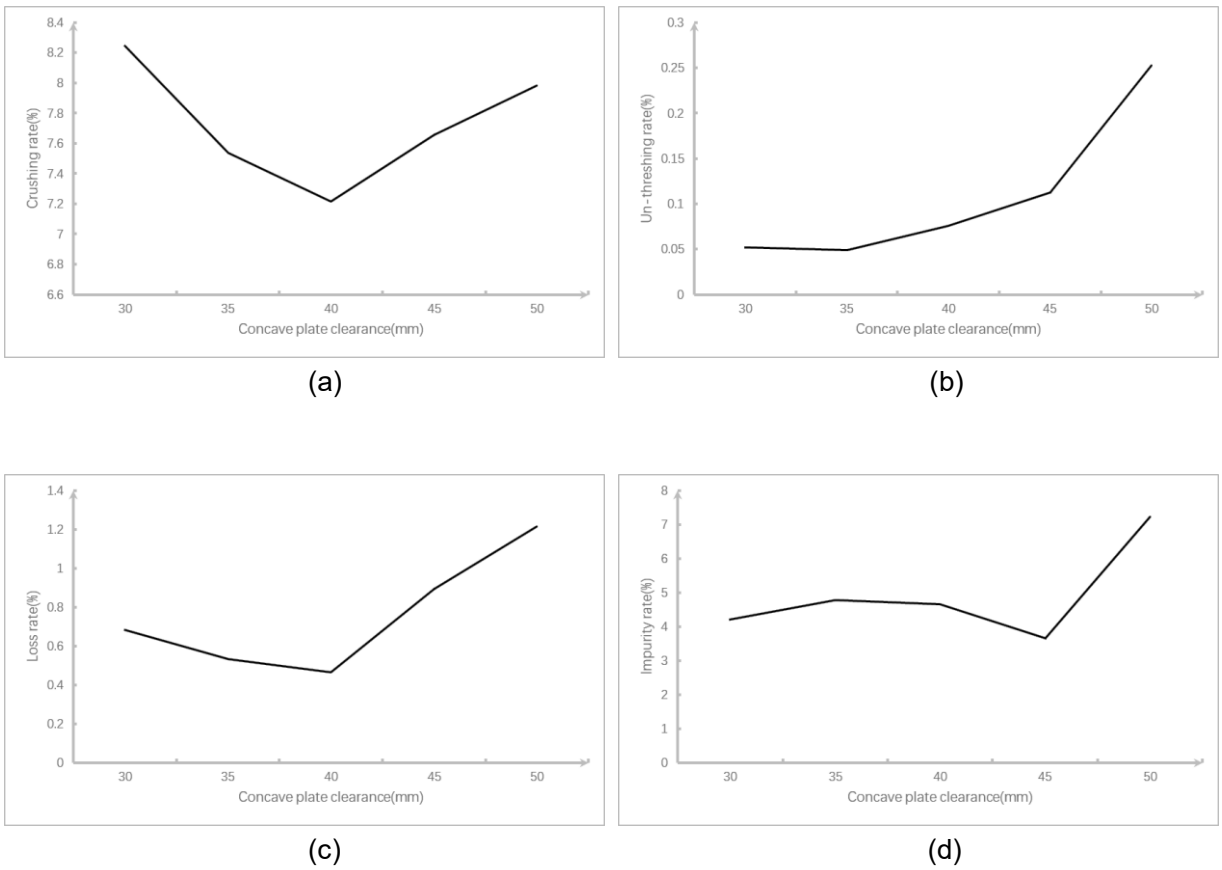


Fig. 3 - Effect of concave plate gap on test index

The gap between the threshing drum and the threshing concave plate is called the threshing gap or concave plate gap. When the gap between the concave plates is small the crop layer thickness is thin, allowing full contact with the threshing drum, resulting in a high rate of threshing but also a high rate of crushing. The increase in the gap between the concave plates to the right size and the increase in the crop layer thickness reduces the frequency of the rod tooth strikes on the seeds, the crushing rate decreases and the increase in the unstripped rate is not significant. The concave plate gap continues to increase, the un-threshing rate increases significantly, the flow rate of the crop layer thickness gradually decreases, the corn threshing time increases and the crushing rate increases.

Loss rate increases and then decreases with increasing clearance. The loss rate increases and then decreases as the gap increases, because the initial gap is small, the threshing time is short and some of the kernels are carried out by the maize bracts, after increasing the gap the threshing time is extended and the bracts and kernels are completely separated.

The gap continues to increase, the effect of the threshing element on the layer thickness diminishes and entrapment losses increase. The increased threshing gap extends the threshing time and leads to increased fragmentation of the mandrel and consequently increased trash content.

One-way test of feeding rate:

The basic parameters in the single-factor test for feed rate are determined by the results of the single-factor test for speed and the single-factor test for the gap between the concave plates. Based on the results of the single-factor test on speed, the drum speed was set at 325 r/min for the 32-34% moisture content maize threshing test. Based on the results of the single-factor test on the gap between the concave plates, the gap between the concave plates for the 32-34% moisture content maize threshing test was 40 mm. Five levels of maize cob feeding were still selected, with 2 kg/s as a unit, and feeding rates were tested at 6/8/10/12/14 kg/s for one-way feeding rates.

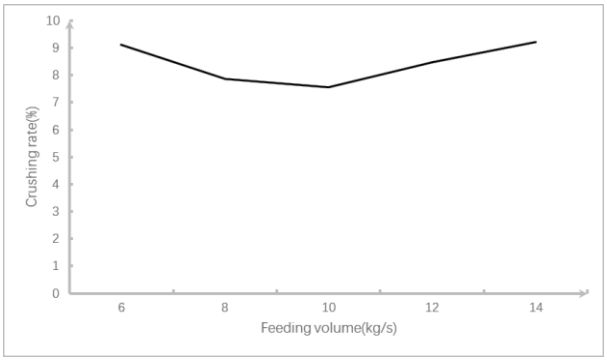
The results of the single-factor test for the feed rate are shown in Table 5 below.

A line graph of feeding rate versus test index based on the test results is shown in Figure 4.

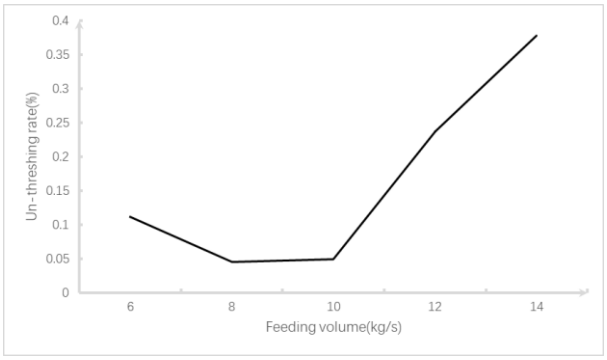
Table 5

Results of the one-way feeding rate test

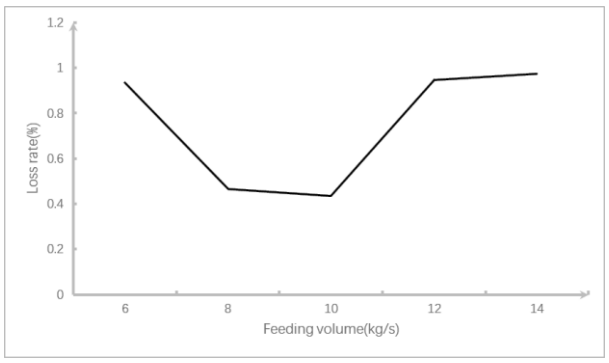
Test serial number	Test factors			Test indicators			
	Roller speed (r/min)	Concave plate clearance (mm)	Feeding volume (kg/s)	Crushing rate (%)	Un-threshing rate (%)	Loss rate (%)	Impurity rate (%)
1	325	40	6	9.107	0.111	0.935	2.750
2	325	40	8	7.853	0.045	0.465	3.570
3	325	40	10	7.557	0.049	0.435	4.210
4	325	40	12	8.475	0.237	0.946	2.000
5	325	40	14	9.229	0.378	0.975	2.660



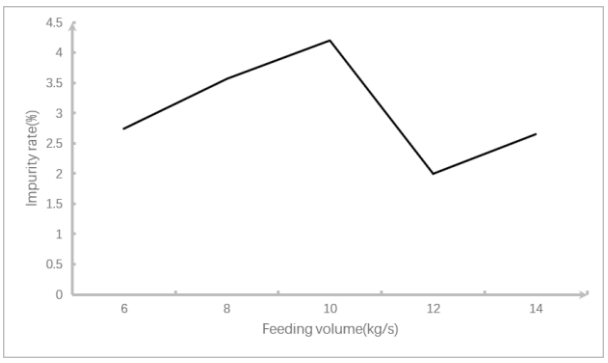
(a)



(b)



(c)



(d)

Fig. 4 - Effect of feeding rate on test indicators

The crop does not flow steadily in the gap when the feed rate is small, which increases the threshing time, the crushing rate is high, the un-threshing rate is low and the loss rate and the trash rate of the threshing product are high; as the feed rate increases, the layer thickness increases, the trash rate of the threshing product increases, the loss rate decreases, the crop flows steadily in the gap, the crushing rate decreases and the un-threshing rate decreases; as the feed rate continues to increase, the layer thickness of the crop increases, the bottom crop does not have sufficient contact with the drum, the top crop is hit too often and the flow rate decreases.

The bottom layer of crop does not have sufficient contact with the drum, the top layer of crop is hit too often and the flow rate decreases, at this time the crushing rate continues to increase, the unthawed rate increases significantly, the loss rate increases, the trash rate increases and the risk of clogging of the threshing device increases.

Orthogonal tests

In order to obtain the optimum ratio of parameters for the single longitudinal axial threshing device for threshing maize cobs in different moisture content zones, orthogonal tests were conducted based on the results of single-factor tests.

Based on the results of the single-factor test, three optimal levels were selected for each of drum speed, notch gap and cob feed, and a four-factor, three-level orthogonal test was arranged according to the L9(34) orthogonal table, with an empty column for the fourth factor. Analysis of variance (ANOVA) and response surface analysis (RSA) were conducted to obtain the significance of the three investigated factors on the investigated indexes and the optimum parameter ratios for the threshing device.

Based on the results of the 32-34% maize single-factor threshing test, three better levels were selected from each of the single-factor tests of drum speed, notch gap and feed rate to form the test factor arrangement table, as shown in Table 6.

Table 6

Test factors and levels

Factors / Levels	Roller speed A (r/min)	Concave plate clearance B (mm)	Feeding volume C (kg/s)
-1	325	35	9
0	350	40	10
1	375	45	11

The orthogonal tests were conducted according to the standard four-factor, three-level test factor arrangement table, with each group of tests repeated three times and the mean value taken as the final result. The arrangement of the test factors and the results are shown in Table 7.

Table 7

Results of orthogonal tests

Test serial number	Test factors			Test indicators			
	Roller speed A	Concave plate clearance B	Feeding volume C	Crushing rate (%)	Un-threshing rate (%)	Loss rate (%)	Impurity rate (%)
1	0	-1	1	7.244	0.199	1.001	6.738
2	-1	0	-1	7.102	0.256	1.201	4.378
3	0	0	0	6.376	0.159	0.890	4.722
4	0	1	1	7.024	0.189	0.952	6.210
5	1	0	-1	9.112	0.251	1.125	4.504
6	-1	1	0	7.410	0.304	1.524	4.772
7	0	0	0	6.396	0.155	0.890	4.754
8	0	0	0	6.588	0.151	0.881	4.708
9	1	-1	0	10.002	0.238	1.257	4.448
10	0	0	0	6.540	0.161	0.904	4.810
11	-1	0	1	7.562	0.272	1.121	7.114
12	1	1	0	7.476	0.281	1.085	4.024
13	0	1	-1	6.828	0.197	0.926	4.874
14	-1	-1	0	7.404	0.268	1.101	4.302
15	0	0	0	6.560	0.158	0.895	4.750
16	1	0	1	9.548	0.221	0.997	6.442
17	0	-1	-1	7.244	0.199	1.001	6.738

Crushing rate analysis

Analysis of variance (ANOVA) was carried out using Design-Expert 10 software on the crushing rate and test factors as shown in Table 8 below; A, B, AB and A^2 were highly significant for crushing rate, C^2 was significant for crushing rate and all other factors were not significant for crushing rate, the fitted curve for crushing rate was obtained by removing the insignificant items.

Table 8

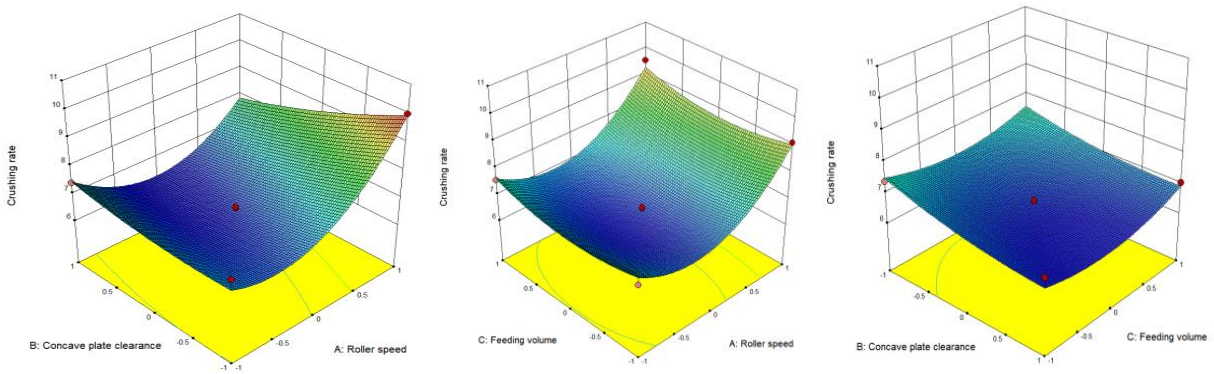
Correlation analysis between crushing rate and test factors

Test factors	P
A	0.0002
B	0.0088
C	0.3268
AB	0.0058
AC	0.9714
BC	0.6317
A^2	< 0.0001
B^2	0.2823
C^2	0.0264

Note: $P < 0.01$ (extremely significant); $0.01 < P < 0.05$ (significant); $P > 0.05$ (not significant).

Fitted curve after removal of insignificant terms:

$$S = 6.57 + 0.83 \times A - 0.41 \times B - 0.63 \times AB + 1.14 \times A^2 + 0.45 \times C^2 \quad (5)$$



(a) (b) (c)

Fig. 5 - Response surface analysis of crushing rate

The response surface analysis shown in Figure 5 gives a minimum crushing rate of 6.241% at a drum speed level of -0.138, a concave plate gap level of 0.878 and a feed rate level of -0.261. At this point the drum speed level is 346.55 r/min, the concave plate gap level is 44.39 mm and the feed rate level is 9.739 kg/s.

Analysis of the non-decontamination rate

The analysis of variance (ANOVA) was carried out using Design-Expert 10 software on the undelivered rate and the test factors, as shown in Table 9 below; A, B, A^2 and B^2 were highly significant for the undelivered rate, while the other factors were not significant for the undelivered rate.

Table 9

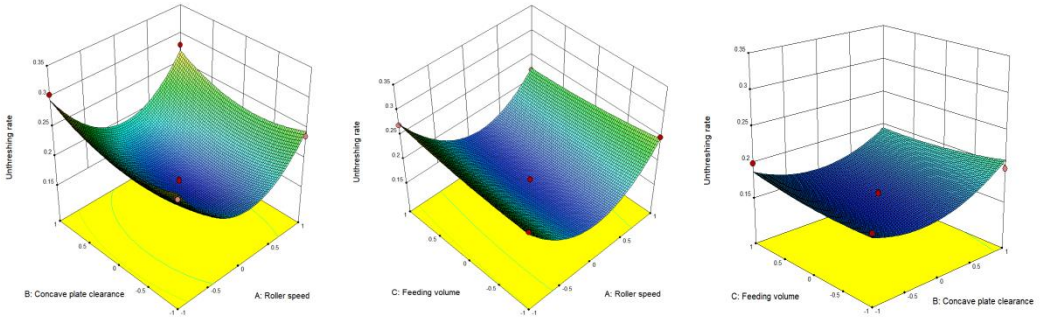
Correlation analysis of the non-decontamination rate with the test factors

Test factors	P
A	0.0081
B	0.0223
C	0.9484
AB	0.7494
AC	0.0653
BC	0.2255
A^2	< 0.0001
B^2	0.0009
C^2	0.3015

Note: P < 0.01 (extremely significant); 0.01 < P < 0.05 (significant); P > 0.05 (not significant).

Fitted curve after removal of insignificant terms:

$$Z = 0.15921 - 0.013625 \times A + 0.010875 \times B + 0.087776 \times A^2 + 0.028776 \times B^2 \quad (6)$$



(a) (b) (c)

Fig. 6 - Response surface analysis of the unpurged rate

The response surface analysis shown in Figure 6 gives a minimum uncut rate of 0.155% at a drum speed level of 0.079, a concave plate gap level of -0.196 and a feed rate level of -0.026. At this point the drum speed level is 351.975 r/min, the concave gap level is 39.02 mm and the feed rate level is 9.74 kg/s.

Loss ratio analysis

Analysis of variance (ANOVA) was carried out on the loss rates and test factors using Design-Expert 10 software, as shown in Table 10 below; AB and A^2 were highly significant for loss rates, A and B^2 were significant for crushing rates and all other factors were insignificant for loss rates.

Table 10

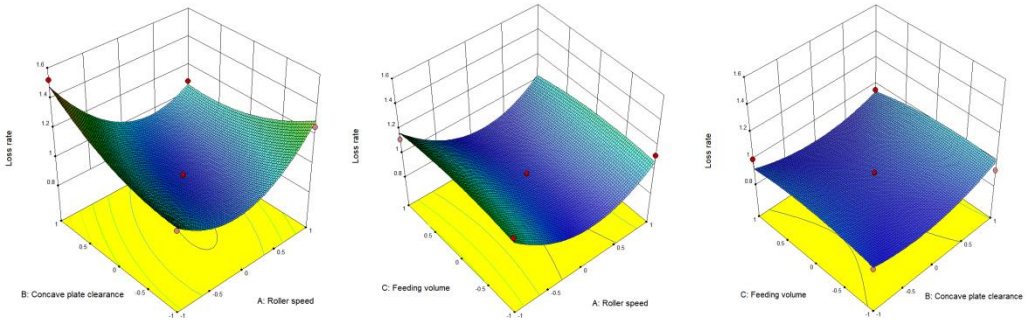
Correlation analysis of loss rates with test factors

Test factors	P
A	0.0245
B	0.1828
C	0.7374
AB	0.0016
AC	0.7000
BC	0.4439
A^2	< 0.0001
B^2	0.0184
C^2	0.1949

Note: P < 0.01 (extremely significant); 0.01 < P < 0.05 (significant); P > 0.05 (not significant).

Fitted curve after removal of insignificant terms:

$$Q = 0.87 - 0.06 \times A - 0.15 \times AB + 0.26 \times A^2 + 0.087 \times B^2 \quad (7)$$



(a) (b) (c)

Fig. 7 - Loss rate response surface analysis

The response surface analysis shown in Figure 7 gives a minimum loss rate of 0.841% at a drum speed level of 0.137, a concave plate gap level of 0.161 and a feed rate level of 0.964. At this point the drum speed level is 353.425 r/min, the concave gap level is 40.805 mm and the feed rate level is 10.964 kg/s.

Analysis of trash content

Analysis of variance (ANOVA) was carried out using Design-Expert 10 software on the impurity rates and the test factors as shown in Table 11 below; A, C, AB, AC, BC, B^2 and C^2 were highly significant for the impurity rates, while the other factors were not significant for the impurity rates.

Table 11

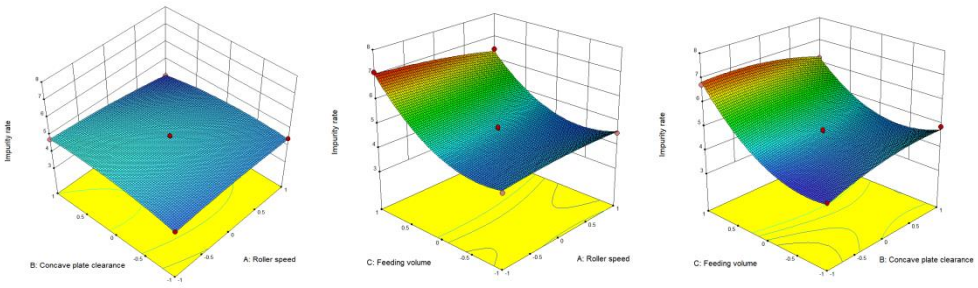
Correlation analysis of trash content with test factors

Test factors	P
A	0.0042
B	0.2445
C	< 0.0001
AB	0.0025
AC	0.0046
BC	0.0002
A^2	0.0546
B^2	0.0011
C^2	< 0.0001

Note: $P < 0.01$ (extremely significant); $0.01 < P < 0.05$ (significant); $P > 0.05$ (not significant).

Fitted curve after removal of insignificant terms:

$$Y = 4.7 - 0.14 \times A + 1.09 \times C - 0.22 \times AB - 0.2 \times AC - 0.34 \times BC - 0.26 \times B^2 + 0.96 \times C^2 \quad (8)$$



(a) (b) (c)

Fig. 8 - Response surface analysis of the impurity rate

The response surface analysis shown in Figure 8 gives a minimum contamination rate of 3.676% at a drum speed level of -0.845, a concave gap level of -0.976 and a feed level of -0.769. At this point the drum speed level is 328.875 r/min, the gap between the concave plates is 35.12 mm and the feed rate is 9.231 kg/s.

Analysis of test results

In order to compare the crushing rate with the entrainment loss rate, the lowest crushing rate is more representative of the total harvest loss, so the response surface analysis in Design-Export 12.0 is used to find the best parameters for the lowest crushing rate. The lowest crushing rate of 6.241% was taken, when the drum speed level was 346.55 r/min, the concave plate gap level was 44.39 mm and the feed rate level was 9.739 kg/s.

All other parameters were held constant and the test was repeated three times using a harvester test rig. To facilitate the adjustment of equipment parameters, the drum speed level was taken to be 346.5 r/min, the concave plate gap level was 45 mm and the feed rate level was 9.7 kg/s. The average crushing rate for the three times was taken to be 6.311%, which was similar to the 6.241% obtained from the response surface analysis, at which time the un-delivered rate was 0.187%, the entrained. The loss rate was 0.912% and the impurity rate was 4.251%. The test proved that the results from the experimental analysis were consistent with the actual working results.

CONCLUSIONS

This study addresses the problem of high moisture content maize harvesting losses by designing a maize harvesting trial based on a harvester test bed designed by our group, effectively simulating a maize harvesting field trial and collecting accurate data parameters.

In order to determine the optimum operating parameters of the harvester for maize harvesting, single-factor tests and orthogonal tests were conducted using threshing drum speed, threshing clearance and feed rate as test factors, and crushing rate, un-threshing rate, entrainment loss rate and trash content rate as evaluation indicators. The response surface analysis of the test factors was used to derive the influence of the factors on the response indicators.

The optimum operating parameters were obtained when harvesting maize at 32% to 34% moisture content with the lowest crushing rate. The optimum operating parameters were: drum speed of 346.55 r/min, concave plate clearance of 44.39 mm and feed rate of 9.739 kg/s, at which time the crushing rate was 6.311%, the un-threshing rate was 0.187%, the entrained loss rate was 0.912% and the trash content was 4.251%. The results of the verification experiments show that the test results are consistent with the actual work.

ACKNOWLEDGEMENT

The work was supported by the High Efficiency and Low Loss Single Longitudinal Axial Flow Threshing and Separation Technology and Development of Intelligent Flexible Threshing Device, (Grant No.2021YFD200050204), and the Development of Intelligent Multifunctional Wheat Corn Grain Combine Harvester, (Grant No.2016YF026).

REFERENCES

[1] Craessaerts G., Baerdemaeker J.D., Missotten B. et al. (2010). Fuzzy control of the cleaning process on a combine harvester. *Biosystems Engineering*, Vol. 106, No. 2, 103-111.

[2] Du Hongyong, Zhang Heng, Li Haoze et al. (2020). Research on Optimization of Cleaning Parameters of Corn Threshing and Cleaning Test Bench. (玉米脱粒清选试验台清选参数优化研究). *Journal of Agricultural Mechanization Research*, Vol. 42, No. 9, 166-172+180.

[3] Federico Dettù, Matteo Corno, Daniele D'Ambrosio, et al. (2023). Modeling, control design and experimental automatic calibration of a leveling system for combine harvesters. *Control Engineering Practice*, Vol.132, No. 105411.

[4] Ildar Badretdinov, Salavat Mudarisov, Ramil Lukmanov et al. (2019). Mathematical modeling and research of the work of the grain combine harvester cleaning system. *Computers and Electronics in Agriculture,* Vol.165, No. 104966.

[5] Li Jiasehng, Li Yaoming, Xu Lizhang et al. (2022). Design and performance test of ratoon rice threshing separation device. (再生稻联合收获机脱粒分离装置的设计与试验). *Journal of Agricultural Mechanization Research*, Vol. 44, No. 2, 85-89.

[6] Miu P.I.，Kutzbach H.D. (2007). Mathematical model of material kinematics in an axial threshing unit. *Computers & Electronics in Agriculture*, Vol. 58, No. 2, 93-99.
[7] Omid M., Lashgari M., Mobli H. et al. (2010). Design of fuzzy logic control system incorporating human expert knowledge for combine harvester. *Expert Systems with Applications*, Vol. 37, No. 10, 7080-7085
[8] Pan Xiaofeng. (2017). *Research on the Development of Agricultural Mechanization in Shandong Province* (*山东省农业机械化发展研究*) [Master's dissertation, Shandong Agricultural University].
[9] Qu Zhe. (2018). *Research on Combined Maize Threshing and Separating Device with Low Damage.* (*低损伤组合式玉米脱粒分离装置的研究*). [Doctoral dissertation, China Agricultural University].
[10] Shamilah Ahmad Mokhtor, Darius El Pebrian, Nor Azi Asminda Johari. (2020). Actual field speed of rice combine harvester and its influence on grain loss in Malaysian paddy field. *Journal of the Saudi Society of Agricultural Sciences,* Vol.19, No. 6, 422-425.
[11] Shen Yufeng, Wu Mingliang, Wu Zigao et al. (2013). Structural design of a longitudinal axial flow rice combine harvester cleaning system. (纵轴流式水稻联合收割机清选系统结构设计). *Journal of Hunan Agricultural University (Natural Sciences),* Vol. 39, No. S1, 94-96.
[12] Song Zhicai, Diao Peisong, Chen Meizhou et al. (2022). Analysis Design and Test of Longitudinal Flow Corn Threshing and Separating Plant. (纵轴流玉米脱粒分离装置设计与试验). *Journal of Agricultural Mechanization Research*, Vol. 44, No. 2, 58-66.
[13] Tiwari P.S., Pandey M.M., Gite L P, et al. (2010). Effect of operating speed and cob size on performance of a rotary maize sheller. *Journal of Agricultural Engineering*, Vol.47, No.2, 1-8.
[14] Vlădut N.V., Biris S.St., Cârdei P. et al. (2022). Contributions to the mathematical modeling of the threshing and separation process in an axial flow combine. *Agricultural,* Vol. 12, No. 10, 1520.
[15] Wang Xunwei, Xie Fangping, Li Xu et al. (2019). Design and experiment on threshing and separation device with adjustable concave clearance. (可调间隙脱粒分离装置的设计与试验). *Journal of Hunan Agricultural University (Natural Sciences)*, Vol. 45, No. 2, 205-211.
[16] Xie Dongmei. (2021). *Study on the Influence of Agricultural Mechanization Development on China's Grain Production.* (*农业机械化发展对中国粮食生产的影响研究*) [Doctoral dissertation, Southwest University of Finance and Economics].
[17] Zhang Lina. (2017). *Study on the Influence of Mechanized Production on Competitiveness of Maize Industry in China.* (*机械化生产对我国玉米产业竞争力影响的研究*) [Doctoral dissertation, China Agricultural University].
[18] Zhao Dechun, Yu Tao, Cai Xiaohua. (2010). Design on Ordinate Axial Threshing and Separating Test-bed. (纵轴流脱粒分离试验台的设计). *Journal of Agricultural Mechanization Research*, Vol. 22, No.7, 121-123.

DESIGN AND SIMULATION TEST OF DIGGING DEVICE FOR SMALL POTATO HARVESTER

/

小型马铃薯收获机挖掘装置的设计与仿真试验

Yuan FU [1)], Shiyi REN [2)], Peng TANG [1)], Yuancai LENG [1)], Xiaohu CHEN [1)], Xinye TU [1)], Xiaorong LV [*1)]

[1)]College of Machinery & Electronics, Sichuan Agricultural University, Ya'an / China

[2)]Faculty of Engineering, The University of Auckland, Auckland / New Zealand

Tel: 08352882182; E-mail: lxrxj2008@163.com

DOI: https://doi.org/10.35633/inmateh-69-13

Keywords: *Potato harvest, digging device, discrete element method, simulation test*

ABSTRACT

Aiming at the potato cropping pattern in the hilly area of southwest China, a small digging device for potato harvester was designed. First, the overall structure of the harvester was determined according to the soil physical characteristic and cropping pattern of the test site. Then, the digging shovel, the key components of harvester were designed and was analyzed the relationship between the inclination of the digging shovel and the power loss under the conditions of different digging speed, digging depth and soil bulk density by MATLAB software, and the mathematical models were established. Finally, the three-dimensional model of the whole machine was established by SolidWorks, and the simulation experiment was carried out with the model of soil particles, potato particles and potato ridges created by the discrete element (DEM) software. The simulation results show that when the working speed of the harvester is 1 m/s, the digging depth is 170 mm, and the potato expose rate is 87.3%. Under normal working conditions of the digging device, appropriately reducing the digging depth can reduce the resistance and wear of the digging shovels.

摘要

针对西南丘陵地区马铃薯种植模式，设计了一款小型马铃薯收获机挖掘装置。首先根据试验场地的土壤物理特性和种植模式，确定了收割机的整体结构；然后设计了关键部件挖掘铲，并利用 MATLAB 软件分析了在不同挖掘速度、挖掘深度和土壤容重条件下挖掘铲的倾角与消耗功率之间的关系，建立了数学模型；最后使用 SolidWorks 建立整机三维模型，结合 DEM 软件建立的土壤颗粒、马铃薯颗粒和马铃薯种植垄的模型，进行了仿真试验。仿真结果表明：当收割机的工作速度为1m/s 时，开挖深度为170mm，马铃薯的明薯率为87.3%，在挖掘装置正常工作条件下，适当减小其挖掘深度，可以减小挖掘铲的阻力和磨损情况。

INTRODUCTION

Potatoes, typical root crops, are widely planted and used for food and vegetables, but also has a certain energy value (Nobuhisa K et al.,2013; Kang Wenqin et al., 2014; Yang Bingnan et al.,2015). As the world's largest potato producer, China produces about a quarter of the world's potato production where Sichuan Province is one of the main potato planting areas. However, because of the complexity of terrain, potato scale, standardization and mechanization production are still relatively weak. Mechanized potato harvesting is the key link to realize the whole process of potato mechanized production, which can improve its working efficiency and ensure the increase of production and income (*Lv Jinqing et al., 2015; Lv Jinqing and Tian Zhongen et al., 2015; Liu Chonglin et al., 2019; Wang Gongpu et al., 2014*). Potato harvesters in many developed countries have been at the world's leading level, can complete one-time digging, potato and soil separation, automatic sorting of potato size, automatic loading, small damage to potato (*Chuai Deming, 2017*). These potato harvesters have the characteristics of high efficiency, high technical level, high stability. However, potato harvesters in developed countries are mostly used on large areas of cultivated land, which are not suitable for small and medium-sized plots in the main potato producing areas in southwest China, and this type of machine is more expensive. (*Wei Hongan et al., 2013; Kempenaar C. and Struik P.C., 2008; Li Zihui et al., 2019*).

---

[1] *Lv Xiaorong, Prof. Ph. D. Eng.; Fu Yuan, Chen Xiaohu, MA. Stud. Eng.; Ren Shiyi, Ph. D. Eng.; Tang Peng, Leng Yuancai, Tu Xinye, MA. Stud. Agr.;*

The research of potato harvester in China started late, the technical reserve is insufficient and the development speed is slow (*Ke Jianhong et al., 2017*). At present, the potato harvester produced by our country is mainly a small and medium potato harvester, which mainly takes the method of multi-stage harvest. To deal with the phenomenon that the soil block area is small and the surface is uneven in the hilly area of the south, the small and medium potato harvester can realize the digging and the separation of potato and soil in the early stage, and the later stage needs for potatoes to be picked up manually.

In view of the above problems, this paper designs a small potato harvester, using SolidWorks to create a three-dimensional model of the harvester, using EDEM to carry out discrete element simulation experiments, creating soil particles and potato particles, establishing a potato ridge simulation model, simulating the harvester to dig potatoes, analyzing the position and velocity changes of potato particles, soil particle position and potential energy changes and the wear of the harvester.

MATERIALS AND METHODS

Overall Scheme Design and Working Principle

The design of the potato harvester is based on the project of the research group to carry out research, and the design and experiment are carried out in accordance with the agronomic requirements of the experimental demonstration base in Pengzhou City, Sichuan Province. The overall structure of the potato harvester is shown in Fig.1. The main work components include the digging shovel mechanism, the vibration shovel mechanism, the lifting chain mechanism, the buffer regulating mechanism and the frame. The whole machine is towed by a tractor. After the digging shovels dig up the potato-soil mixture, the vibrating shovel shakes and separates the potato soil mixture. Then the potato soil mixture is lifted and sieved by the elevator chain, and finally the potatoes are fall on the soil ridge. The digging shovel mechanism is composed of multiple digging shovels. Vibration shovel mechanism is forced vibration, which is the vibration transfer of eccentric wheel under the rotation of drive shaft. The lifting chain mechanism rotates under the action of both sides of the chain drive to separate the potato soil mixture from the potato soil. The convey chain conveys potatoes to reduce the collision damage caused by parabolic motion. The adjusting mechanism is composed of screw and nut, and the back end of the digging device is raised and lowered by spiral drive, which realizes the adjustment of the digging inclination angle of the digging device.

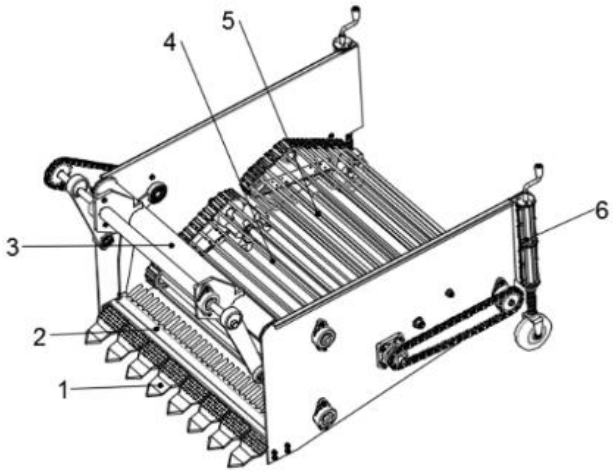


Fig. 1 - Overall structure of potato harvester

1-digging shovel mechanism; 2-Vibration shovel structure; 3-Frame;
4-Lifting chain mechanism; 5-Conveying chain mechanism; 6-Adjusting mechanism

Key component design

According to the agronomic requirements of potato planting and the experimental data obtained from the test, the digging shovel shape is designed as a triangular curved surface structure, as shown in Fig.2.

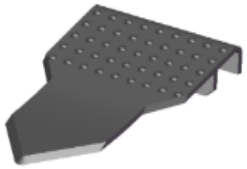


Fig. 2 - Triangular Surface Digging

Statics Analysis of digging Potato-soil Mixture

To smoothly shovel the potato-soil mixture during the working process of the digging device, it is necessary to overcome the reaction force of the traction resistance of the digging device; Analyze the force of the digging shovel, and establish the traction resistance model of the shovel using the concept of the virtual dip angle of the plane shovel (*Li Jinchuan et al., 2017; Li Baoling et al., 2016*).

$$W = G\tan(\alpha+\varphi) = SL\rho g(\alpha+\varphi) \quad (1)$$

$$Q = W + K_s + K_W G \quad (2)$$

where: L is the length of digging shovel, m; S is the cross-sectional area for cropping ridges, m^2; K is the soil specific resistance in furrow, N/m^2, (Medium solid soil, K=24000~30000 N/m^2); ρ is the soil density, kg/m^3; φ is the inner friction angle of soil, º; α is the angle of the digging shovel, º; K_W is the resistance coefficient of the machine driving along the ridge, (Medium solid soil, K_W =0.14~0.17); G is the machines and soil gravity on shovels, N; Q is the tractor traction force, N; K_S is the force needed to dig up the soil, N; $K_W G_1$ is the resistance the machine needs to overcome as it moves along the ridge, N.

To facilitate the creation of the model, the influence of impurities is ignored in the Digging process. The mixture of rising potato and soil, ignoring the phenomenon that the distribution of potato in soil is not continuous and uniform. The resistance that the shovel needs to overcome when shoveling up the potato soil mixture was analyzed, as shown in Fig. 3. In the process of rising, the potato soil mixture mainly undergoes three processes of cutting, squeezing and raising. Squeezed section of the potato-soil mixture is shown in Fig.4.

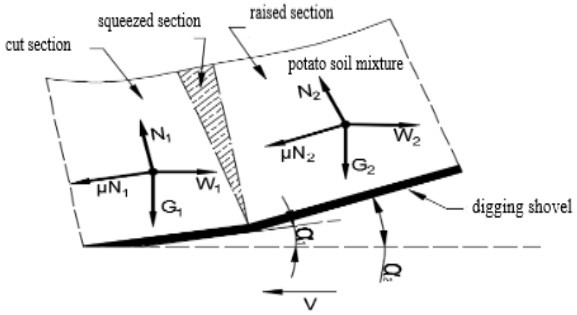


Fig. 3 - Force analyze of the mixture of potato and soil on the digging shovel

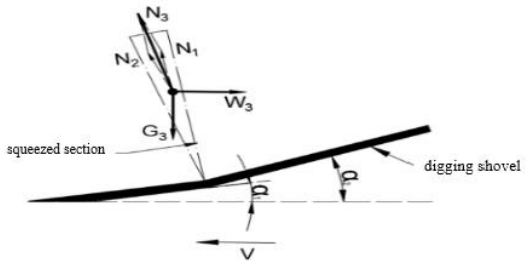


Fig. 4 - Squeezed potato-soil mixture

The potato-soil mixture in the squeeze section is subjected to the positive pressure of the cut section and the rising section. Because of the small inclination angle of the shovel surface on the cut section and the large inclination angle of the raised section, the soil will squeeze each other at the intersection.

The digging shovel surface force diagram is shown in Fig. 5. In the process of rising up, the digging device keeps the speed as far as possible, and the potato soil mixture is conveyed backward in an orderly manner. In order to simplify the force model and ignore the cohesion between soil particles and between soil and potato, the movement of the soil mixture is set to be in equilibrium.

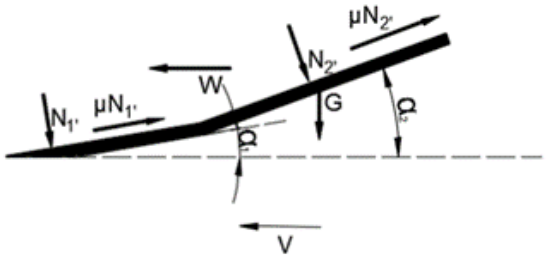


Fig. 5 - Force analysis of the digging shovel

$$W_1\cos\alpha_1 + W_2\cos\alpha_2 - G_1\sin\alpha_1 - G_2\sin\alpha_2 - \mu N_1 - \mu N_2 = 0 \quad (3)$$

$$N_1 + N_2 - G_1\cos\alpha_1 - G_2\cos\alpha_2 - W_1\sin\alpha_1 - W_2\sin\alpha_2 = 0 \quad (4)$$

$$W = W_1 + W_2 + W_3 \quad (5)$$

$$N_3 = N_1\cos\beta_2 + N_2\cos\beta_1 \quad (6)$$

$$\beta_1 + \beta_2 = \alpha_2 - \alpha_1 \quad (7)$$

where: β_1 is the angle between the positive pressure of the rising section and the upward force of the squeeze section along the shovel surface, N; β_2 is the angle between the positive pressure of cut section and the upward squeeze pressure along the shovel surface, N;

The digging resistance coefficient Z_1 and Z^2:

$$Z_1 = \cos\alpha_1 - \mu\sin\alpha_1 \tag{8}$$

$$Z_2 = cos\alpha_2 - \mu sin_{\alpha_2} \tag{9}$$

Bring in the above equations:

$$Z_1 W_1 + Z_2 W_2 = G_1 \sin\alpha_1 + G_2 \sin\alpha_2 + \mu G_1 \cos\alpha_1 + \mu G_2 \cos\alpha_2 \tag{10}$$

Analysis of angle range of digging shovel

According to the force analysis of the digging shovel during the digging process, the inclination angle of the digging shovel is related to the working speed, the digging depth and the soil type. Ignoring the local force of the shovel, the equation can be obtained:

$$\alpha = \text{arctg}e\frac{W - \mu G}{G = \mu W} \tag{11}$$

$$W = \frac{P}{V} \tag{12}$$

Where: P is the digging consumption power; V is the digging shovel forward speed;

Bring in the equation:

$$\alpha = arctg\frac{P - \mu GV}{GV + \mu P} \tag{13}$$

$$P = \frac{\tan\alpha GV + \mu GV}{1 - \tan\mu} \tag{14}$$

According to the physical characteristics of the soil, the soil can be divided into sandy soil, clay soil and loam soil, and the bulk density between the soils is different, which determines the different digging inclination angle needed for digging shovels between different types of soils. Ignoring the partially raised soil, the cross section of the ridge mixture can be simplified to elliptical (*Cheng Huidong et al., 2007*). Establish soil bulk density model. The cross section of potato planting ridges is shown in Fig. 6:

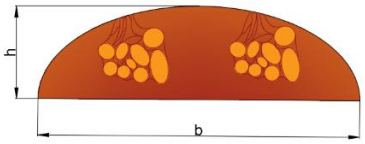


Fig. 6 - Cross section of potato planting ridge

The coordinate system is established along the center of potato ridge bottom. The ridge height direction is X axis, the ridge bottom width direction is Y axis, and the ridge bottom length direction is Z axis. The mathematical model of potato ridge section is established. The surface equation of potato ridge is as follows:

$$\frac{y^2}{h^2} + \frac{z^2}{(b/2)^2} = 1 \tag{15}$$

$$y = h\sqrt{1 - \frac{z^2}{(b/2)^2}y} \tag{16}$$

$$S = \iint_{\Sigma} dS = \iint_{D}\sqrt{1 + \frac{4h^2z^2}{b^2\left((b/2)^2 - z^2\right)}}dzdx \tag{17}$$

Volume equation of potato ridge:

$$V = Sl \tag{18}$$

$$S = \frac{\pi hb}{4} \tag{19}$$

$$M = \rho v \tag{20}$$

$$G = Mg \tag{21}$$

where: ρ is the soil bulk density, kg/m^3; l is the digging shovel length, mm; h is the maximum digging depth, mm; b is the maximum depth ridge width, mm;

The above joint equations can be obtained:

$$G = \frac{\pi\rho glhb}{4} \tag{22}$$

The relationship between the loss power needed to dig the potato soil mixture and the working speed, digging depth, and soil type is shown in equation (23).

$$P = \frac{\pi\rho glhb}{4} \cdot \frac{V(\tan\alpha + \mu)}{1 - \tan\alpha\mu} \tag{23}$$

Relationship between digging loss power and digging dip angle per unit time at different operating speeds, digging depth and soil bulk density

In the actual digging process, different digging speed corresponds to different digging dip angle, and the setting of digging dip angle is the key factor to reduce the digging power loss.

Operating speeds, digging depth and soil bulk density are the main parameters in this experiment. When one parameter is a variable, the other two parameters are set as constants. For example, when the operating speed is determined as a variable, the digging depth and soil bulk density are determined as constants. The experimental parameters are determined as shown in Table 1.

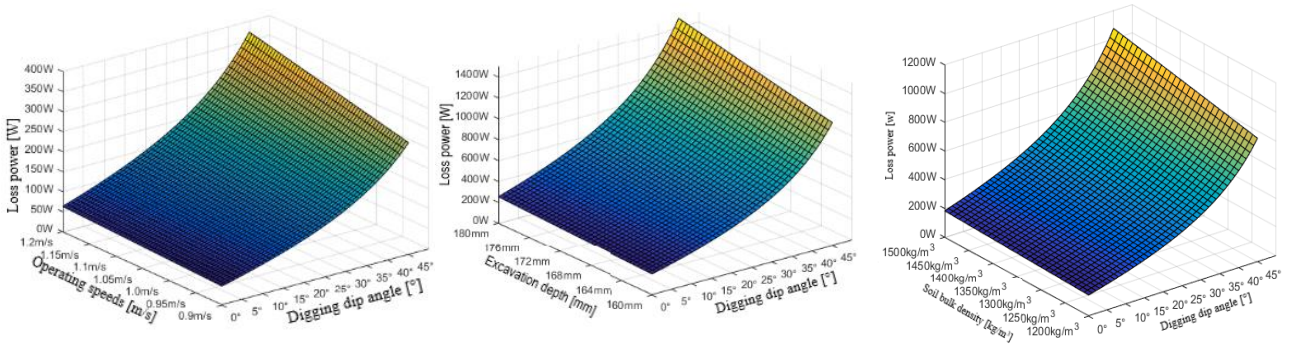
Table 1

Parameters		Operating speeds	Digging depth h	Length of shovel surface l	Soil bulk density ρ		Friction angle of soil	Rest angle of soil
					sandy soil	clay soil		
		[m/s]	[mm]	[mm]	[g/cm3]		[°]	[°]
Ranges		0.9~1.2	160~180	350-400	1.2~1.8	1.0~1.5	18~20	30~40
Value	(a)	0.9~1.2	170	350	1.3		20	35
	(b)	1	160~180		1.3			
	(c)	1	170		1.2~1.5			

The width of ridge section is related to the rest angle of soil, and the maximum ridge width is obtained:

$$b = \frac{h}{\tan\alpha} \tag{16}$$

Based on the balance equation and experimental parameters of potato soil mixture, the relationship between digging loss power and digging dip angle per unit time is determined at different operating speeds, digging depth and soil bulk density are shown in Fig. 7.



(a) (b) (c)

Fig. 7 - Relationship between digging loss power and digging dip angle per unit time at different operating speeds, digging depth and soil bulk density

From Fig. 7, the following analysis can be made: (a) The loss power per unit time increases with the increase of soil bulk density and digging dip angle when the digging dip angle is constant. The ratio of the loss power per unit time to the change of working speed tends to be stable during the period of 15º~30º, which is beneficial to the digging shovel under the specified working speed. (b) The loss power increases with the increase rate of digging speed change in unit time when the digging dip angle is constant.

When the dip angle is less than 10º, the loss power per unit time tends to be stable under the change of digging depth, which is beneficial to the shear effect of the shovel blade on the soil and ridge bottom. The dip angle of digging shovel increases gradually, the digging shovel is between 10º~30º, and the ratio of loss power to digging depth is stable in unit time, which is beneficial to the rise of potato soil mixture at the end of digging shovel. If the digging dip angle is more than 30º, the loss power per unit time has a sharp upward trend from both the digging dip angle and the digging depth, which is not conducive to the digging shovel under the condition of the change of the digging dip angle and the digging depth. (c) The loss power per unit time increases with the increase of soil bulk density and digging dip angle. When the digging dip angle is less than 8º, the loss power per unit time increases with the increase of soil bulk density, but the increment is small, which is suitable for the design of the digging shovel front dip angle. The digging dip angle is in the range of 8º~30º. With the increase of soil bulk density and digging dip angle, the loss power per unit time increases slowly and the increment is stable. If the digging dip angle is more than 30º, the loss power per unit time increases sharply with the increase of digging dip angle and soil bulk density, and the increment is large, and the loss power per unit time changes greatly and is unstable.

According to the relationship between soil loss power and digging dip angle under different digging conditions, the digging shovel force model is established. The relationship between working speed, digging depth and soil bulk density are analyzed as shown in Fig. 8.

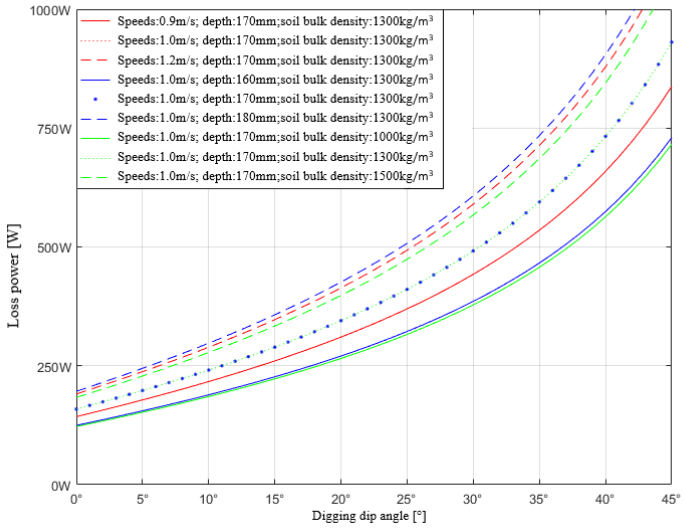


Fig. 8 - Relationship between digging loss power and digging dip angle per unit time under different digging conditions

The analysis shows that the loss power per unit time increases with the increase of digging dip angle under the condition of certain operating speed, digging depth and soil bulk density. From the analysis of the change of digging dip angle, the change of digging depth unit increment has the greatest influence on the loss power, followed by soil bulk density, and the change of operating speed unit increment has little effect on the change of loss power. When the dip angle is less than 25º, the loss power per unit time is less than 500 W, which is an ideal traction state for walking tractor. If the digging dip angle is less than 15º, the increment of the loss power is smaller and the loss power is lower, so it is suitable for the design of the front end of digging shovel dip angle.

Parameter Design of Digging Shovel

According to the potato planting scale and the power required by the digging device, the traction power of the digging device is to choose a small tractor. In potato digging process, the forward speed of the digging shovel generally needs to be maintained between 0.9 ~ 1.2 m/s. Therefore, the forward speed of the digging shovel is taken as 1 m/s; theoretically, the digging depth of the digging shovel needs to be greater than the maximum potato Bury depth to avoid damage to potatoes during the digging process. After field measurement, the general burial depth of potatoes is about 150 mm. Therefore, in order to ensure the quality of potato harvest, the digging depth of the shovel is 170 mm.

Width Design of Digging Shovel

The width of the digging shovel mainly depends on the distribution width of the potato underground and the uniformity between its row spacing. The gap between the shovels should be less than the average triaxial size of the potato. During the digging process, the connection between the digging shovel and the frame is subject to greater stress and the stress is concentrated, which is likely to cause damage to the digging shovel. In order to ensure that the digging shovel has good soil penetration and rigidity, the selection of the width of the shovel surface is very important. The shape of the shovel adopts a canard-type design, which can ensure that the front section of the digging shovel has a good soil penetration capacity. The larger width of the digging shovel is to improve the stability of the digging shovel; the blades on both sides of the digging shovel play the role of cutting grass roots and potato roots, avoiding the clogging of the potato soil mixture due to the accumulation of grass roots and roots.

On the basis of the measured data, the average row spacing of potato planting ridges is 170 mm, the average width of potato block distribution of double row potato is 501.6 mm, and the working width of potato harvesting device is 500 mm, and the working width is small. The running deviation of the machine can be controlled. In this paper it is set as 40 mm.

The comprehensive standard deviation can be calculated from the following formula:

$$\sigma = \sqrt{\sigma_M^2 + \sigma_b^2} \tag{24}$$

where: σ_m is the standard deviation of line spacing, mm; σ_b is the standard deviation of distribution width of potato, mm;

The comprehensive standard deviation is 8.83 mm, the integral is 10 mm, and the working width of the digging device is B=780 mm.

The digging shovel assembly diagram is shown in Fig. 9:

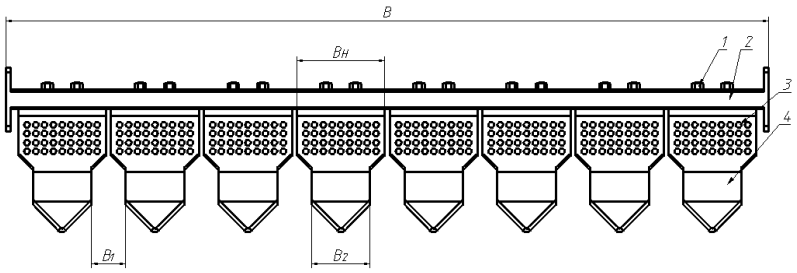


Fig. 9 - Digging shovel assembly

1–bolts; 2 - installing-frame; 3-bulge; 4-digging shovel

Digging shovel width and clearance satisfied:

$$\lambda B_2 + (\lambda - 1)B_1 < B, C > \mathrm{D} \tag{25}$$

where: λ is the number of digging shovels (pieces); B_2 is the width of digging shovels, mm; B_1 is the slide gap of digging shovels, mm; B is the width of digging device, mm;

This design adopts the multi-face digging shovel combination, the digging shovel piece quantity λ takes 8 pieces.

Calculated: B_2<66.875 mm

A certain gap is reserved between the shovels, the digging shovel is assembled reasonably, and the width of the shovel surface at the front end is 60 mm. The distance between the two sides of the shovel is determined according to the slip clearance. For the convenience of assembly, there is a certain gap between the shovels. The blade clearance on both sides is 15 mm.

Calculated: B_H=90 mm

Design of dip angle of shovel blade

The force on the shovel blade is shown in Fig. 10.

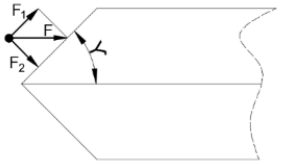


Fig. 10 - The force diagram of digging shovel blade

$$F\sin(90^\circ-\gamma)=F_1 \tag{26}$$

$$F\cos(90^\circ-\gamma)=F_2 \tag{27}$$

$$F_1=F_2\tan\varphi \tag{28}$$

where: F is the total resistance to shovels; F_1 is the friction on the blade of a shovel; F_2 is the vertical splitting force on the blade surface of the digging shovel; γ is the digging shovel blade dip angle; φ is the inner friction angle of soil.

In the process of digging, the soil at the bottom of the planting ridge is cut smoothly, and the cross section of the digging blade is in direct contact with the soil. According to the corresponding friction law, the friction force overcome by the digging shovel needs to be greater than the total resistance of the digging shovel.

$$F_2\tan\varphi<F\sin(90^\circ-\gamma) \tag{29}$$

$$\cos(90^\circ-\gamma)\tan\varphi<\sin(90^\circ-\gamma) \tag{30}$$

Calculated: $$\varphi<90^\circ-\gamma$$

The larger the dip angle of the shovel blade, the more soil the ridge has, the flatter the ridge bottom and the greater the resistance of the digging; the smaller the dip angle of the shovel blade, the more serious the wear of the shovel tip. When the internal friction angle of the soil is 20º, digging shovel blade dip angle γ<70º.In this paper γ is set to 45º.

Design of dip angle of shovel surface

According to the conclusion of the force analysis of the shovel above, the digging resistance of the shovel is mainly related to the mixture of potato and soil and the dip angle of the shovel. The relationship between shovel dip angle and digging resistance is shown in Fig. 11.

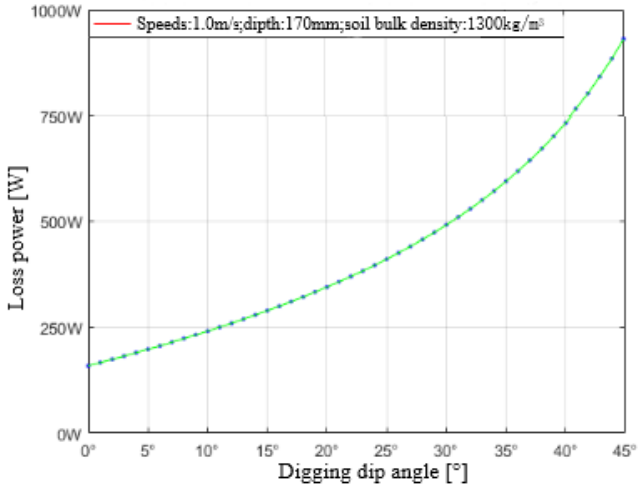


Fig. 11 - Relationship between inclination angle of shovel surface and digging resistance

It can be seen from the diagram that the surface digging shovel is used to minimize the digging resistance under the condition of a certain dip angle of the digging shovel surface. In order to meet the requirements of small digging resistance and backward transportation height, the digging shovel is designed with two sections, the front section dip angle is small and the back section of dip angle is large. The detailed size of the shovel is shown in Fig.12.

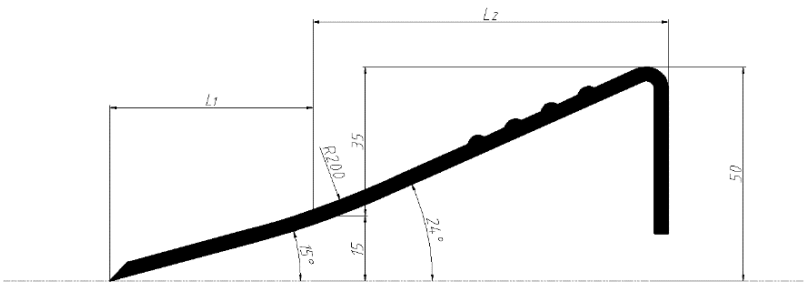


Fig. 12 - Inclination of digging shovel

In the first part of digging shovel, the angle is 15º, the shovel height is 15 mm. In the second part, the angle is 24º, the shovel height is 35 mm, the total shovel height is 50 mm. The front and rear sections of the shovel have rounded corners, R=200 mm.

Design of Length of Digging Shovel

In the Fig. 12.

L_1 is the length of first part digging shovel; L_2 is the length of second part digging shovel;

According to the angle of the digging shovel surface and the height of the cross section of the two sections of the shovel surface can be calculated:

$$L_1 = \frac{15}{\tan 15^\circ} \tag{31}$$

$$L_2 = \frac{35}{\tan 24^\circ} \tag{32}$$

Calculated: L_1=55.98mm; L_2=78.61mm

The total shovel length: $L=L_1+L_2$=134.59mm

Simulation model

The soil model and potato model were established by EDEM, in order to increase the accuracy of the simulation experiment, the soil particles use the soil model library in the material library, and the potato particles were conducted by SolidWorks, and then the particle unit is filled, and the degree of filling meets the triaxial size of the particles. Four kinds of soil particles were set up in the simulation experiment to represent surface soil, middle soil, deep soil and ground soil respectively. the model shape of each layer of soil particles was the same, but the physical parameters were different.

According to the measured triaxial size of potato particles, the average triaxial size of potato particles was 80×50×40 mm. Create a 3D model of potato by SolidWorks. Soil particle model and potato particle model are shown in Fig. 14 and Fig.15. According to the actual situation, the potato-soil mixture is modeled by simulation. The potato-soil mixture consists of compacted soil particles, ridge bottom sparse soil large particles, middle layer tight soil particles, surface layer small particles and potato particles. The ground size was set to 3000×1500×100 mm. The ridge width is 620 mm, the ridge height is 210 mm, the ridge length is 2800 mm.

The potato ridge model is shown in Fig. 16:

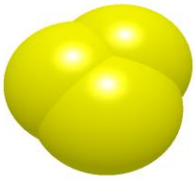


Fig. 14 - Soil particle model



Fig. 15 - Potato particle model

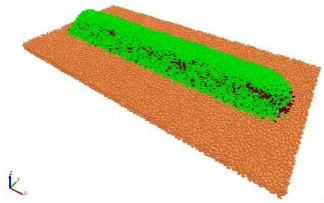


Fig. 16 - Ridge Model of potato

The simulation parameters and characteristics were set as shown in Table 2 and Table 3.

Table 2

Simulation parameters

Items	Poisson's ratio	shear modulus [Pa]	Density [kg·m^{-3}]
Surface soil	0.32	3×10^6	800
Middle soil	0.4	5×10^6	900
Deep soil	0.5	10×10^6	1000
potato	0.4	1.99×10^6	1200
Shovel	0.3	7.8×10^{10}	7850

Table 3

Simulation characteristics of soil, potato and shovel

Items	Coefficient of restitution	Coefficient of static friction	Coefficient of dynamic friction
Surface Soil - Middle Soil	0.145	0.52	0.245
Surface Soil -Deep Soil	0.150	0.53	0.250
Middle Soil -Deep Soil	0.155	0.54	0.255
Potato - potato	0.13	0.2	0.01
Potato -shovel	0.523	0.644	0.0221
Potato -surface soil	0.06	0.48	0.01
Potato -middle soil	0.06	0.50	0.01
Potato -deep soil	0.055	0.51	0.01
Shovel-surface soil	0.17	0.49	0.39
Shovel-middle soil	0.18	0.50	0.40
Shovel-deep soil	0.19	0.51	0.41

Simulation process

(1) Experimental particle contact model using Hertz-Mindlin with JKR model, The Surface Energy between particles is set to 3.75 J/m^3;

(2) Importing the 3D model of potato digging device and setting up the material parameters and contact model of digging device. Set the speed of digging device to 0.8 m/s, lifting-chain line speed of 2 m/s (*Li Xiaopeng et al., 2019*). A Hertz-Mindlin with JKR model is used to simulate the contact model between potato digging device and particle, Surface Energy is set to 3.5 J/m^3.

The simulation process of the potato digger is shown in Fig.17.

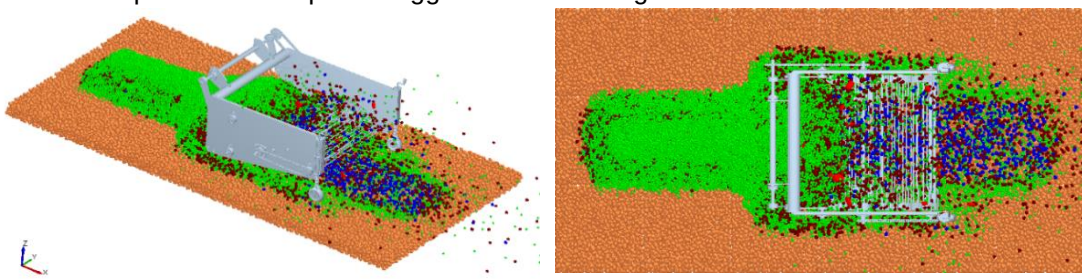


Fig. 17 - The simulation process of the potato digger

According to the figures above, after the digging device slowly shovel into the ridge, the potato ridge section began to deform slowly; The potato particles and soil particles are mainly concentrated between the vibrating shovel and the lifting chain, and start conveying backward under the rotation of the lifting chain. During the transportation process, part of the surface soil particles falls to the ground along the lifting chain, and the middle soil particles and the deep soil particles fall less due to the large particle size. Potato particles and soil particles will beat during the rise of the lifting chain, and the contact between the particles and the lifting chain causes a certain impact. Therefore, a reasonable control of the line speed of the lifting chain is an important measure to reduce the potato damage.

RESULTS

Simulation Results

The experimental results of potato mining simulation are shown in Fig.18.

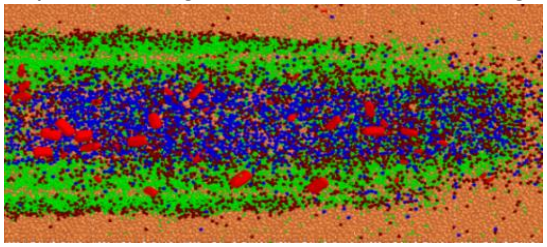


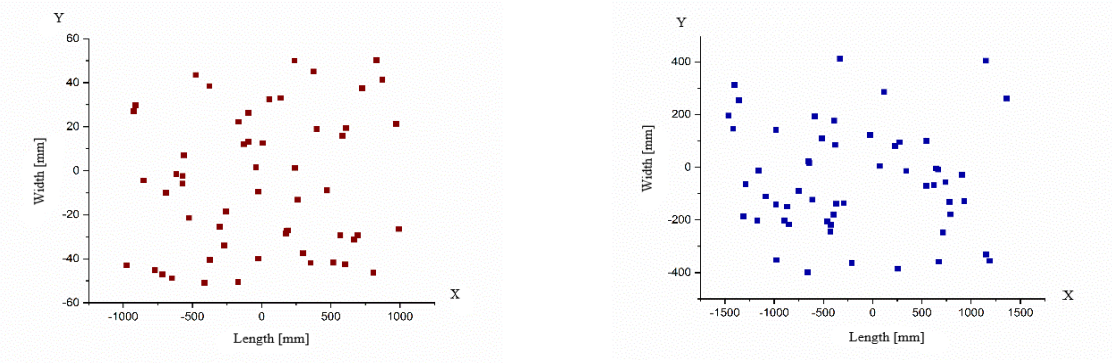
Fig. 18 - Experimental results of potato digging simulation

Simulation results show that the total number of potatoes is 55, 48 were exposed after shovel digging, and 7 potatoes were not exposed. The exposed potato rate was 87.3% and the buried potato rate was 12.7%. The potato digging effect was good.

Analysis of Simulation Results

1. Analysis on the Distribution of Potato Particles before and after Digging

Refer to Fig.18 to establish a coordinate system, which is X along the direction of the harvester, the Y direction along the ridge section direction. The position distribution before and after potato digging is shown in Fig.19.



before **after**

Fig. 19 - Top view of potato digging before and after

According to the change of the position of the potato before and after digging, it can be seen that the potato particles are concentrated in the X direction in the range of -1000~1000 mm, and in the Y direction in the range of -60~60 mm, which conforms to the position distribution of the potato in the potato cropping ridge; After the potatoes are dug, the X direction is concentrated in the range of -1500~1200 mm, and the Y direction is concentrated in the range of -400~400 mm. It can be seen that the distribution of the positions of the potatoes before and after the digging in both the X and Y directions has increased. The analysis shows that since the forward speed of the digging device is 1 m/s and the linear speed of the lifting chain is 1.5 m/s, the speed direction is opposite to the forward direction of the digging device, and the linear speed of the lifting chain is greater than the forward speed of the digging device; After digging, the Y-direction width is close to the working width of the digging device 780 mm. The analysis shows that the potato moves to both sides of the digging device while moving backwards on the lifting chain. The width of the digging device determines the width of the potato in the Y direction after digging. The increase of the width in the Y direction can increase the landing area of potato, and reduce the collision between the potato and the potato, thereby reducing the damage of the potato.

2. Analysis of Speed Change in Potato particle Digging

The speed changes during potato particle digging are shown in Fig. 20:

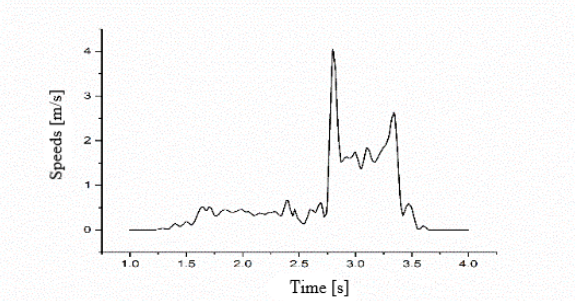


Fig. 20 - Changes of potato particle velocity

According to the diagram, the time experienced by potato particles on the digging device is about 2.5 s, and the speed and state of potato in each time period are shown in Table 4.

Table 4

Changes of velocity and state of potato granules in different time periods

Time period [s]	Changes in potato speed	State
1.25~1.75	A slow increase from 0 to 0.5 m/s	Potatoes in the potato-soil mixture start to contact the shovel
1.75~2.30	At about 0.5 m/s speed	Potato soil mixture moves backward on a shovel
2.30~2.75	Velocity fluctuates greatly, keeping up and down 0.5 m/s	Potato soil mixture moves backward on a vibrating shovel
2.75~2.80	Velocity increases dramatically, reaching maximum speed of 4 m/s	Potatoes are exposed to ascending chains
2.80~2.85	A sharp drop in speed 1.5 m/s	Potatoes are transported backward on the lift chain
2.85~3.30	Velocity fluctuates greatly, keeping up and down 1.5 m/s	The gap between the potato transport chain and the transport chain

Time period [s]	Changes in potato speed	State
3.30~3.40	A sharp increase in speed, maximum 2.7 m/s	Potato contact transport chain
3.40~3.75	The velocity drops sharply and the final velocity is 0	Potatoes are transported backward on the conveyor chain and fall to the ground

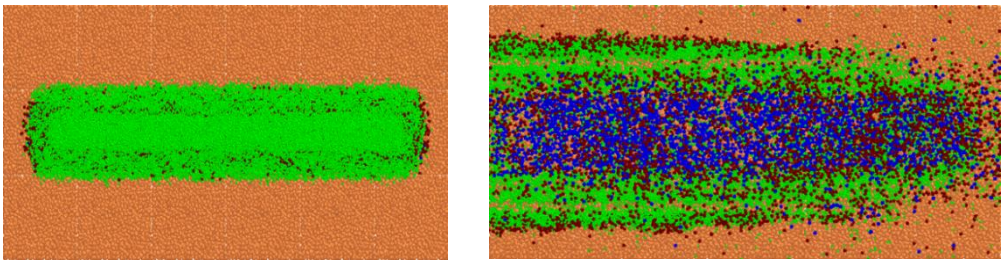
It can be seen from the data in Table 4 that the speed of potato movement has two sharp increases, which are the moment when the potato touches the lifting chain and the moment when it touches the conveyor chain. This is caused by the impact generated by the potato contacting them. When the potato touches the elevator chain, the speed of the potato will increase sharply to about 4 m/s, and then it will drop to the line speed of the lifting chain about 1.5 m/s, and the potato will continue to be lifted. When the potato is in contact with the conveyor chain, the speed of the potato gradually increases from 1.5 m/s to 2.7 m/s, and then decreases to the linear speed of the conveyor chain. Then, under the conveying chain, the potato particles slide down from the end of the conveyor chain until on the ground, the speed drops to 0 m/s.

Analysis of potato particle velocity changes can be concluded:

(1) The conveyor chain added at the back end of the lifting chain can reduce the landing speed of potato particles and reduce the damage to the potato skin; (2) In the process of potato soil separation and transportation, potato particles are impacted and rubbed many times, which is directly related to the linear velocity of the lifting chain, which ensures the good separation of potato soil, and reduces the linear velocity of the lifting chain is helpful to reduce the impact effect of potato; (3) The speed of potato on the conveying chain fluctuates, but the fluctuation times and frequency are small. The combination of straight rod and curved rod can effectively reduce the impact and rolling friction of potato on the conveying chain.

3. Analysis on the Change of Position Distribution before and after Soil Particle Digging

The location distribution of soil particles before and after digging is shown in Fig. 21.



before **after**

Fig. 21 - Location distribution of soil particles digging

According to Fig.21, after digging the soil ridge, most of the soil particles are distributed in a certain regularity. Due to the propulsion of the digging device, the loose soil particles on the surface layer slowly move to both sides; Most of the soil particles are located in the middle of the digging track of the digging device. Since the bulk density of the middle soil and the bottom soil is larger than that of the surface soil, the lifting chain bears a larger load during the transportation process. Therefore, it can be appropriately used to ensure normal digging. In this case, reduce the digging depth, thereby reducing the working load of the lifting chain.

4. Analysis of Potential Energy Change in Soil Particle Digging

The analysis of potential energy changes during soil particle digging is shown in Fig.22.

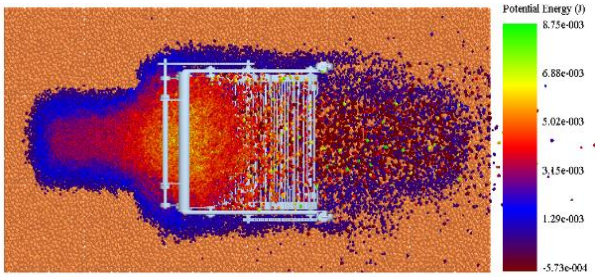


Fig. 22 - Location distribution of soil particles digging

During the process of digging potatoes by the digging device, the overall potential energy of the soil particles changes in a 'T' shape. The maximum potential energy of the soil particles is 8.75×10^{3} J, and the minimum potential energy is -5.73×10^{4} J. The potential energy of the soil particles in contact with the working parts of the digging device and the soil particles in the middle of the planting ridge along the forward direction

of the digging device vary greatly. The potential energy of the soil particles above the working parts of the digging device presents a "circular" shape. The soil particles located in the center above the digging shovel and the vibrating shovel have the largest potential energy, and the potential energy changes in the range of 5.02×10^3~6.88×10^3 J. The surrounding soil includes: the potential energy of the soil at the front end of the lift chain, the soil between the two side plates and the surface soil particles varies in the range of 3.15×10^3 to 5.02×10^3 J. The potential energy of soil particles in the middle of the planting ridge along the forward direction is greater than that on both sides of the ridge. The potential energy of soil particles on both sides of the ridge is maintained at about 1.29×10^3 J, and the potential energy of soil particles in the middle of the ridge is maintained at about 3.15×10^3 J. The analysis shows that the soil particles in the forward direction are propelled by the digging device, and the potential energy of the soil particles in the middle increases.

The following conclusions can be drawn from the digging of potato soil potential energy:

(1) The potential energy of the soil particles on the potato planting ridge gradually increases from the periphery to the middle of the ridge, and the soil particles gradually move to the surrounding to prevent clogging.

(2) Under the traction of the tractor, the soil particles in the front middle of the digging device are pushed by the digging device. The greater the digging depth, the greater the shovel force required by the soil particles, and the greater the power loss of the digging device. Properly controlling the digging depth of the digging device is the key factor to reduce resistance.

5. Wear analysis of excavating equipment

The digging device is in close contact with soil particles during the digging process, and the digging parts will cause surface wear when working for a long time. It can be analyzed by investigating the pressure of the digging parts during the digging process. The force distribution of the digging parts during the digging process is shown in Fig.23.

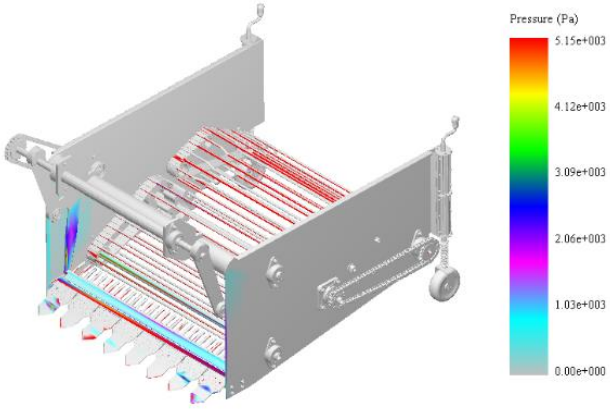


Fig. 23 - Force Wear Distribution of Excavator

During the digging process, each digging component will produce some wear, but the degree of wear is not uniform. The main worn parts of the shovel are at the junction of the shovel tip, the blade and the curve of the shovel surface. The most worn part is subjected to a pressure of 5150.24 Pa. Among them, the tip of the shovel is severely worn. The wear of the digging shovel in the middle is more serious than that of the shovel on both sides. The abrasion effect of the curve connection of the shovel surface is greater.

The analysis shows that due to the change of the curve curvature, the friction of the soil particles on the joints is increased, and the abrasion of the excavating shovel is increased. The wear of the digging shovel shaft is mainly concentrated in the middle, and the pressure range is between 2000-5000 Pa. Long-term wear is easy to cause deformation of the shaft and affect the assembly accuracy between the digging shovel. The chain rods of the rear lift chain are subject to wear, and the pressure range is between 5000-5100 Pa. The wear makes the lift chain thinner and reduces the stability of the lift chain. The pressure range of the two side plates of the digging device is between 500-800 Pa.

CONCLUSIONS

(1) A digging device of potato harvester is designed. The force analysis is carried out on the digging shovel. The relationship between the inclination angle of the digging shovel and the power consumption under different digging speed, digging depth and soil bulk density was analyzed by MATLAB software, and the mathematical models of the three were established.

(2) According to the structure size of potato digging device, the 3D model of key parts and frame of digging device is created by SolidWorks, and the complete potato digging device model is assembled. Using the discrete element analysis method, DEM software was used to create soil particles and potato particles, build a simulation model of potato planting ridges, and conduct simulation experiments for potato digging. the position change, velocity change, soil particle position change, potential energy change and the wear of the digging device before and after the potato particle digging were analyzed. The simulation results show that when the working speed of the digging device is 1 m/s, the digging depth is about 170 mm and the linear speed of the lifting chain is 1.5 m/s, the potato's exposed potato rate is 87.3%, which meets the requirements of potato harvesting operations.

ACKNOWLEDGEMENT

The study was supported by the National Key Research and Development Program, Intelligent Agricultural Machinery Equipment, (2018YFD0701100-03).

REFERENCES

[1] Cheng Huidong, Meng Xinzhu. (2007). Mathematical model of crop ridge, *Mathematics in Practice and Theory*, Vol.18, pp.107-110. Qingdao/China

[2] Chuai Deming. (2017). Current Situation and Development Trend of Potato machinery harvesting, *Agriculture and technology*, Vol.37, Issue 06, pp.85, Huludao/China

[3] Kang Wenqin, Fan Mingshou, Ma Zhong et al. (2014). Luxury absorption of potassium by potato plants, *American Journal of Potato Research*, Vol.91, Issue 5, pp.573 – 578. Hohhot/China. https://doi.org/10.1007/s12230-014-9386-8

[4] Ke Jianhong, Yang Bohua, Jiao Dachun et al. (2017). Present Situation and Countermeasures of Potato Mechanization Production in China, *Southern agriculture*, Vol.11, Issue 19, pp.72–75. Chongqing/China

[5] Kempenaar C., Struik P. C. (2007). The canon of potato science: 33. haulm killing, *Potato Research*, Vol.50, Issue 3, pp. 341 – 345, Wageningen/The Netherlands.

[6] Li Baoling, He Bing, Liu Xuhong et al. (2016). Force Analysis and Optimization of Digging Shovel of Cassava Harvester, Journal of Agricultural Mechanization Research, Vol. 38, Issue 08, pp.64-67, Liuzhou/China

[7] Li Jinchuan, Zheng Yimin, Shang Xin et al. (2017). Optimization of the angle of artichoke harvester's second-order flat shovel based on Mathematica, *Agricultural Research in the Arid Areas,* Vol. 35, Issue 02, pp.282-288. Yinchuan/China

[8] Li Xiaopeng, Liao Min, Hu Ben et al. (2019), Study on the Bionic Digging Shovel of Potato and Its Reduced Resistance Characteristics, *Journal of Agricultural Mechanization Research*, Vol.41, Issue 06, pp.19-25+31. Chengdu/China

[9] Li Zihui, Wen Xinyu, Lv Jinqing et al. (2019). Analysis and prospect of research progress on key technologies and equipments of mechanization of potato planting, *Transactions of the CSAM*, Vol.50, Issue 3, pp. 1–16, Harbin/China

[10] Liu Chonglin, Hu Jun, Zhao Shengxue, et al. (2019). Research progress on potato harvesting equipment, J*ournal of Chinese Agricultural Mechanization*, Vol.40, Issue 4, pp.31-35, Daqing/China

[11] Lv Jinqing, Tian Zhongen, Yang Ying et al. (2015). Design and experimental analysis of 4U2A type double-row potato digger, *Transactions of the CSAE*, Vol. 31, Issue 6, pp.17－24. Harbin/China

[12] Lv Jinqing, Tian Zhongen, Wu Jin'e, et al. (2015). Design and experiment on 4U1Z vibrating potato digger, *Transactions of the CSAE*, Vol.31, Issue 12, pp. 39－47. Harbin/China

[13] Nobuhisa K., Tsutomu K., Keiichi S. et al. (2013). Energy efficiency of potato production practices for bioethanol feedstock in northern Japan, *European Journal of Agronomy*, Vol.44, pp.1-8. Hokkaido/Japan. https://doi.org/10.1016/j.eja.2012.07.001.

[14] Wang Gongpu, Jiang Jinlin, Tian Yanqing et al. (2014). Present status and prospects of mechanical potato harvest technology, *Journal of Chinese Agricultural Mechanization*, Vol.35, Issue 1, pp.11-15

[15] Wei Hongan, Wang Di, Lian Wenxiang et al. (2013). Development of 4UFD-1400 type potato combine harvester, *Transactions of the CSAE*, Vol.29, Issue 1, pp.11－17, Lanzhou/China

[16] Yang Bingnan, Zhang Xiaoyan, Zhao Fengmin et al. (2015). Suitability evaluation of different potato cultivars for processing products, *Transactions of the CSAE*, Vol.31, Issue 20, pp.301-308. Beijing/China.

DESIGN AND EXPERIMENT OF PRESSURE-HOLDING PRECISION SEED-METERING DEVICE FOR MAIZE
/
压持式玉米精量排种器的设计与试验

YunHe ZHANG[1)], JinPeng CHENG*[2)], XueJun ZHANG[2)], ZengLu SHI[2)], MeiJing WANG[2)], HaiFeng WU[2)], Hao FU[2)]
[1)] College of Electronic and Electrical Engineering, Lingnan Normal University, Zhanjiang/ China;
[2)] College of Mechanical and Electrical Engineering, Xinjiang Agricultural University, Urumqi / China
Tel: +86 18653786713; E-mail: chengludan369@Gmail.com
DOI: https://doi.org/10.35633/inmateh-69-14

Keywords: *agricultural machinery, seed-metering device, maize, precision-seeding, experiment*

ABSTRACT
In order to further improve the seeding performance of the maize seed-metering device, a pressure-holding precision seed-metering device for maize was designed. The seed-metering device is made up of several seed rowing modules, which effectively solves the problems of inconvenient disassembly and complex maintenance of the current maize seed-metering device. The working principle of the device was introduced, and the mechanical and kinematic analysis of the maize seeds during the seeding operation was carried out. The orthogonal test was carried out with the installation diameter of seed-metering device's guide plate, torsion spring's wire diameter and seed-metering device's rotational speed as the test factors, the single-seeding rate, missed-seeding rate and multiple-seeding rate as the indexes, and the relationship between different test factors on the performance of seed-metering device was obtained. By optimizing the model, the best performance of the seed-metering device was obtained when the installation diameter of the guide plate was 92.32 mm, the wire diameter of the torsion spring was 1.59 mm, and the rotational speed of the seed-metering device was 0.41 rot/s. At this time, the single-seed rate was 93.08%, the missed-seeding rate was 3%, and the multiple-seeding rate was 3.9%, which met the requirements of the industry standard.

摘要
为了进一步提高玉米排种器的排种性能，设计了一种压持式玉米精量排种器。该排种器由多个排种模块组合而成，有效解决了目前玉米排种器存在的拆装不方便、维修复杂等问题。介绍了排种器的工作原理，对作业过程中的玉米种子进行了力学和运动学分析。以排种器导引板安装直径、扭簧丝径及排种器转速为试验因素，以单粒率、漏播率及多粒率为指标进行正交试验，得到了不同试验因素对排种器性能的影响关系。通过对模型进行优化，得到了当导引板安装直径为 92.32mm、扭簧丝径为 1.59mm、排种器转速为 0.41r/s 时，排种器工作性能最佳，此时的排种单粒率为 93.08%、漏播率为 3%、多粒率 3.9%，满足行业标准要求。

INTRODUCTION

Maize is an important food cash crop and its yield has a profound impact on the development of a country's agricultural economy *(Feng et al., 2022)*. Precision seeding technology is the key technology to realize maize yield increase and reasonable use of soil resources, and it is also an important part of maize mechanized planting *(Ding et al., 2021; Wu, 2020)*. The core component of this technology is the seed-metering device, and its reasonable design directly affects the performance of the whole precision seeder *(Wang et al., 2021; Fang et al., 2022)*. At present, there are two main types of maize seed-metering device, pneumatic and mechanical *(Bai et al., 2021; Li et al., 2021)*, and mechanical maize precision seed-metering device have been widely used in maize agricultural production because of their reliable operation, simple structure, and stable operation *(Wang et al., 2019; Liu et al., 2018)*.

In recent years, scholars in the industry have conducted a lot of research on mechanical maize precision seed-metering device *(Wan, 2021; Ren, 2021)*. *Wang et al*., *(2022)*, designed a maize seed-metering device for sloping land, which improved the degree of adaptation of the device to different operating environments. *Du et al*., *(2019)*, designed a self-disturbing in-fill type maize precision seed-metering device to improve seed filling performance by increasing the activity of the population.

[1] *Yunhe Zhang, M.S.Eng*; *Jinpeng Cheng, M.S.Eng*; *Xuejun Zhang, Prof. Ph.D.Eng*; *Zenglu Shi, Ph.D.Eng, Meijing Wang, M.S.Stud. Eng*; *Hao Fu, M.S.Stud. Eng*; *Haifeng Wu, M.S.Stud. Eng* .

Wang et al., *(2019)*, designed a clamping type maize precision seed-metering device to complete the process of seed picking and seed dropping by controlling the clamping block to pick and release the seeds at different positions. *Inderpal et al., (2020)*, designed a tilting disc type of maize seed-metering device and determined the optimum operating parameters of the seed-metering device through experiments. *Cortez et al*., *(2020)*, studied the effect of the forward speed of the seed rower and the tractor on the agronomic traits of maize and obtained the optimum operating speed suitable for the seed-metering device. However, the current mechanical corn precision seed-metering device has the disadvantage of having too much structural integrity and not being easy to repair in case of failure.

In order to solve this problem, this paper designs a pressure-holding maize precision seed-metering device with a modular design to facilitate maintenance and replacement in case of failure. The design and analysis of the structural parameters and working process of the seed-metering device were carried out, and the rationality of the mechanism design was verified by the test bench test.

MATERIALS AND METHODS

STRUCTURE OF SEED-METERING DEVICE

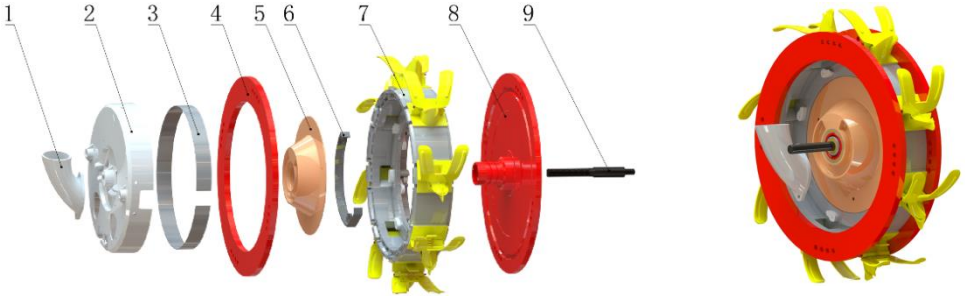


Fig. 1 - Structure diagram of pressure-holding maize precision seed-metering device

1. Seed feeding cylinder; 2. End-cap fixing disc; 3. Steel Belt 4. Fixed Plate; 5. Spaced core tray; 6. Guide plate; 7. Seed displacement module assembly; 8. Motion disc; 9. Shaft

As shown in Figure 1, the pressure-holding maize precision seed-metering device consists of a seed feeding cylinder, end-cap fixing disc, fixed plate, seed core tray, guide plate, seed displacement module assembly (including duckbill, seed picking block, seed storage box, driving arm and torsion spring), motion disc, shaft, etc. In order to facilitate the rapid replacement of damaged parts in case of device failure, the seed releasing module assembly is designed so that each individual seed releasing module is interconnected by means of a slot. Finally, the seeding module is fixed axially by the fixing and motion discs mounted on both ends of the seeding module assembly. The components of the pressure-holding maize precision seed-metering device is fixed by bolts that work together to form the seeder as a whole. Its working parameters are shown in Table 1.

Table 1

Operating parameters of the seed-metering device

Parameters	Value
Diameter [mm]	385
Working width [mm]	90
Quality of the whole machine [kg]	23.5
Working rotational speed [rot/s]	0.3-0.5
Number of seeds per lap	8-10

The seed picking mechanism is the main working part of the seed-metering device, through which the process of seed picking, seed holding and seed dropping can be completed. The structure of seed picking mechanism is shown in Figure 2, which mainly consists of seed picking block, torsion spring, rotary shaft and driving arm.

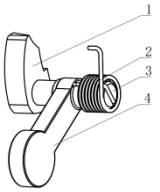
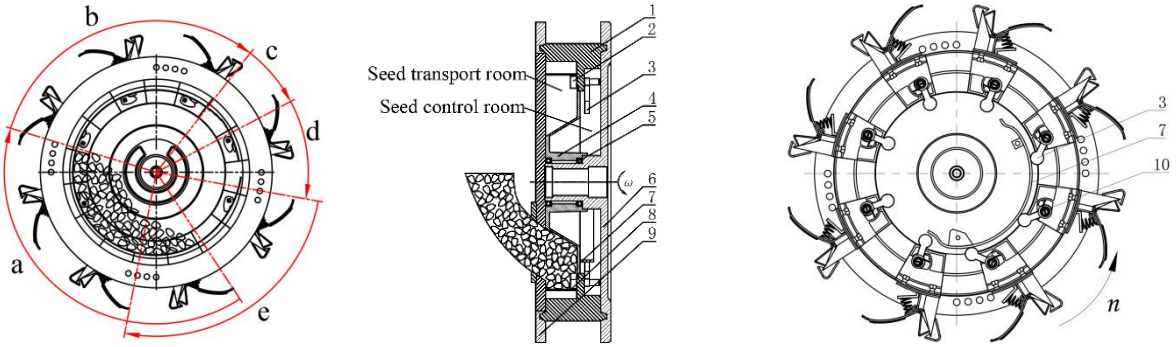


Fig. 2 - Structure diagram of seed picking mechanism

1. Seed picking block; 2. Torsion spring; 3. Rotary shaft; 4. Driving arm

WORKING PRINCIPLE

As shown in Figure 3a, the pressure-holding maize precision seed-metering device can be divided into five working areas. When working, the seeds enter from the seed feeding cylinder, and with the rotation of the seed-metering device, they finish the process of taking, holding, cleaning and dropping seeds in different working areas in turn. A cross-sectional view of the seed-metering device is shown in Fig. 3b, in which it can be seen that the spaced core tray divides the device into a seed transport room and seed control room, with the seed picking block in the transport room and the driving arm in the control room. As shown in Figure 3c, with the rotation of the device, the driving arm in the control room is in constant contact with the guide plate, thus driving the seed picking block to open and close the movement, and then driving the seed to complete a series of processes from seed taking to seed dropping in the seed transport room.



a. Working area division *b. Cutaway view of seed-metering device* *c. Working principle diagram*

Fig. 3 - Working principle of pressure-holding maize precision seed-metering device

a. Seed-taking area; b. Seed-holding area; c. Seed-cleaning area; d. First seed-dropping area; e. Second seed-dropping area

1. Seed storage box; 2. Seed picking block; 3. Driving arm; 4. Spaced core tray; 5. Bearing; 6. Motion disc; 7. Guide plate; 8. Steel Belt; 9. Fixed Plate; 10. Torsion spring;

ANALYSIS OF SEED-TAKING PROCESS

Seed-taking is a relatively complex process in which maize seeds are subject to the combined effects of gravity, friction, centrifugal forces and other seeds' forces, forming a dynamic mechanical system that changes in real time. Since the seed taking process is the first step in the whole seeding cycle, it is particularly important to analyse the movement of the maize during the seed taking process.

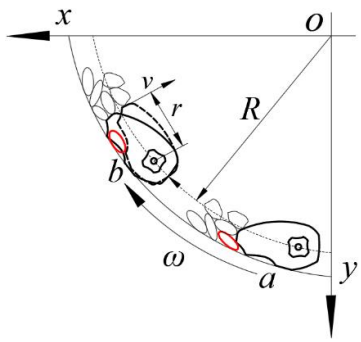


Fig. 4 - Diagram of seed-taking process

As shown in Figure 4, the maize seeds enter the seed-metering device and forms a self-flowing seed cluster under the action of the rotation of the device. For the kinematic analysis of the seed-picking block at this time, a is the start of the seed-taking block opening movement and b is the end in the figure.

In order to reduce the rigid impact of the seed picking block on the maize during the opening and closing process, the motion of the seed picking block is set as a flexible transition, i.e., the seed picking is considered as a simple harmonic motion during the opening and closing process, and the equation of its motion trajectory is:

$$S = A\sin(\frac{2\pi}{T}t + \psi_0) \tag{1}$$

$$T = \frac{2\pi}{\omega} \tag{2}$$

where:

S - The displacement of the simple harmonic motion of the seed picking block, mm;
A - Movement amplitude of seed picking block, mm;
T - Twice the value of the time taken for the seed picking block from a to b, min;
Ω - Rotation Speed of seed metering device, r/min;
ψ_0 - Initial phase angle of seed picking block, °;
t - Movement time of the seed picking block, min.

Taking the first order derivative of both ends of equation (1) with respect to t yields the equation for the velocity of motion of the seed picking block as:

$$v = A\omega\cos(\omega t) \tag{3}$$

The actual velocity v_1 of the seed picking block is the vector sum of its simple harmonic velocity and the velocity v_0 of the circular motion with the seed picking block, i.e.;

$$v_0 = \omega R = 2\pi n R \tag{4}$$

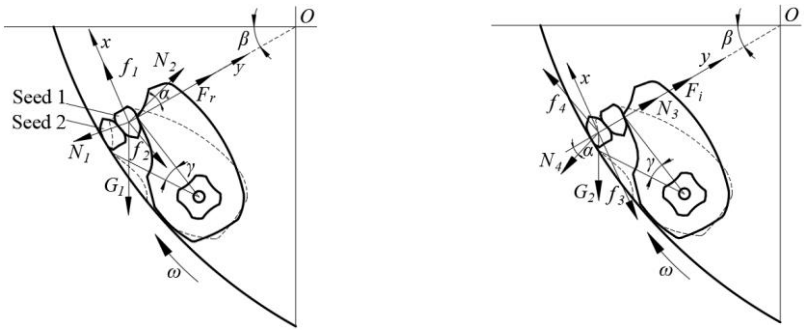
$$v_1 = \sqrt{v^2 + v_0^2} = \sqrt{A^2\omega^2\cos(\omega t)^2 + 4\pi^2 n^2 R^2} \tag{5}$$

where:
R - Turning radius of seed picking block, mm;
n - Rotational speed of seed metering device, r/min.

It is clear from the analysis that the opening and closing of the seed picking block and its rotation during the seed taking process will have a disturbing effect on the flow movement of the seed cluster itself, which in turn will affect the seed-taking effect of maize seeds. When the seed picking block has a certain radius of rotation, the rotational speed of the seed-metering device is the main factor affecting the movement of the seed picking block, so setting a better value will increase the probability of taking the maize kernels and prevent the phenomenon of missed seeding.

FORCE ANALYSIS OF SEED GRABBING

Because of the large differences in maize seed size parameters, there is a possibility of seeds grabbing each other's position during seed-picking process, resulting in maize seeds not entering the seed filling space effectively and causing missed seeding. The maize seeds that grabbed each other's position during seed taking are now studied and mechanically analysed separately, as shown in Figure 5.



a. Force analysis of seed 1 *b. Force analysis of seed 2*

Fig. 5 – Force analysis of seed grabbing

In Figure 5a, with the centre of mass of seed 1 as the coordinate origin, the direction of the tangent to the velocity of the seed-metering device as the x-axis and the normal direction as the y-axis to establish a right-angle coordinate system, the force on seed 1 can be decomposed as:

$$\begin{cases} f_1 + N_2\sin\alpha + N_1\sin\gamma = G_1\sin\beta + f_2\cos\alpha \\ F_r + N_2\cos\alpha + f_2\sin\alpha = N_1\cos\gamma + G_1\cos\beta \end{cases} \tag{6}$$

The force on seed 2 can be decomposed as:

$$\begin{cases} f_4\cos\alpha = N_3\sin\alpha + G_2\sin\beta + f_3 \\ F_i + N_4 = f_4\sin\alpha + N_3\cos\alpha + G_2\cos\beta \end{cases} \tag{7}$$

Of which:

$$\begin{cases} F_r = \omega^2 R_1 \\ F_i = \omega^2 R_2 \\ f_1 = N_1 \mu_1 \\ f_2 = N_2 \mu \\ f_3 = N_3 \mu_3 \\ f_4 = N_4 \mu \end{cases} \quad (8)$$

where:

μ - Friction coefficient between seed 1 and seed 2;
μ_1 - Friction coefficient between the seed picking block and the seed 1;
μ_3 - Friction coefficient between steel belt and seed 2.

From the above equation, it can be seen that when the opening angle γ of the seed picking block changes, the force equilibrium between the maize seeds that grab each other's position will be disrupted, i.e., the support force on seed 1 and seed 2 will change. Since the sliding friction f_3 of the steel belt on seed 2 points in the direction of seed filling, an acceleration along the negative direction of the x-axis can be obtained. At this point, seed 2 is successfully grabbed and seed 1 falls back to the seed filling area. Therefore, by setting the seed picking block to open its own motion while passing the seed group in the seed-filling area, it can make it easier for the picked up seeds to obtain acceleration towards the seed filling space, effectively improving the seed filling rate and avoiding missed seeding.

DESIGN OF GUIDE PLATE'S PROFILE

To enable the seed picking block to open and close precisely and smoothly in the seed-filling area, the profile contour of the guide plate is designed in the shape of a swing follower cam. The swing angle of the driving arm is controlled through calculation of the cam profile parameters to control the opening and closing of the seed-picking block. To prevent damage to the seeds caused by the impact of the seed-picking block's movement, the opening and closing process of the seed-picking block is set as a flexible transition, and the follower motion method uses simple harmonic motion. Focus on the design of the push section entering the seed-filling area and the return section entering the seed-holding area.

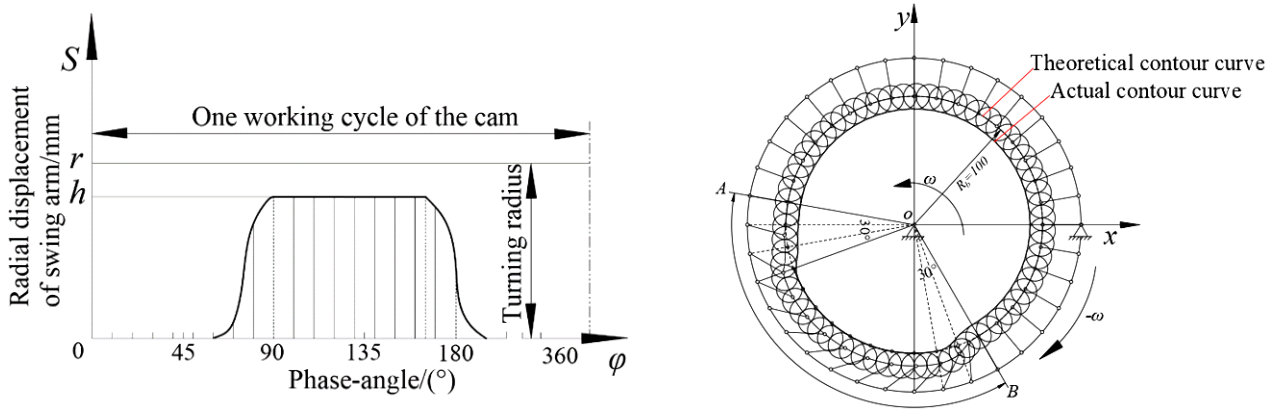
The phase curve equation is:

$$\begin{cases} S_1 = \dfrac{h}{2}\left(1 - \cos\dfrac{\pi\varphi}{\varphi_1}\right) & \left(\dfrac{\pi}{3} \le \varphi \le \dfrac{\pi}{2}\right) \\ S_2 = h\left(1 - \dfrac{\varphi}{\varphi_2} + \dfrac{1}{2\pi}\sin\dfrac{2\pi\varphi}{\varphi_2}\right) & \left(\dfrac{8}{9}\pi \le \varphi \le \dfrac{19}{18}\pi\right) \end{cases} \quad (9)$$

where:

S_1 - length of the pushing displacement into the seed-filling area, mm;
S_2 - length of the return displacement into the seed-holding area, mm;
h - length of the far resting stroke of the driving arm in the seed-clearing area, mm;
φ – phase angle, (°);
φ_1 - angle of the pushing motion, (°);
φ_2 - angle of the return motion, (°).

The resulting phase angle curve is shown in Figure 6a. The driving arm in the seed extraction mechanism is used in conjunction with the torsion spring to form a force locking cam mechanism. Furthermore, the theoretical and actual contours of the cam are plotted according to the phase curve diagram using the inverse rotation method, as shown in Figure 6b.



a. Phase relationship diagram *b. Cam profile curves*

Fig. 6 – Design drawing of guide plate profile

The *AB* section of the actual contour curve is the outer profile curve of the guide plate. The value of the base circle's radius (noted as R_b) is 100 mm. To make the arms open and close smoothly, the angle of thrust movement (noted as φ_1) into the seed-filling area is set to 30°. The angle of return movement of the seed-filling area into the seed-holding area (noted as φ_2) has a value of 30°. The seed-filling process is the initial step in the seeding process. The seed-filling area's operating range and the seed-picking block's opening angle are the keys to the seed-filling effect. Too large an opening angle of the seed-picking block can easily trap too many seeds, resulting in difficulties in clearing the seeds and causing multiple seeding. Too small an opening angle makes it difficult to fill the seed-filling area, resulting in missed seeds. The length of pushing displacement of the seed-filling area determines the size of the opening and closing angle of the seed-picking block. The value of the length of the pushing displacement is set to 10-15 mm, taking into account the parameters of the mechanism and the size of the opening and closing angles of the seed-picking blocks required for the different sizes of maize kernels. The guide plate's installation radius has a value of 90 to 96 mm, where the exact value is to be obtained through subsequent bench tests. The cam profile curve can be found by bringing the above values into Equation (9).

BENCH TESTING

A pressure-holding maize precision seed-metering device was built for bench testing. The test seeds were selected from Denghai 8883 maize seeds, which are widely grown in China. The device was mounted on the test bench, and the single-seeding rate, multiple-seeding rate and missed-seeding rate of the seeding process were counted by recording the number of seeds discharged from each seed row port, as shown in Figure 7, and was calculated according to the following equation:

$$\theta = \frac{g}{G} \times 100\% \tag{10}$$

where:

θ - the single grain rate, multiple grain rate and missed seeding rate, %;
g - the number of single grains, the number of multiple seeds and the number of missed seeds;
G - the total number of holes measured.



Fig. 7 - Bench test of seed-metering device

1. Seed box; 2. Feeding tube; 3. Seed-metering device; 4. Bracket; 5. Conveyor belt; 6. Control box; 7. Voltage stabilizer

RESULTS

According to the theoretical analysis and pre-experiments, the main factors are the rotational speed of the seed-metering device, the installation diameter of the guide plate and the spring force of the torsion spring. The torsion spring force can be adjusted by changing the wire diameter of the torsion spring. Therefore, a three-factor, five-level orthogonal test was conducted with the rotational speed of seed-metering device, installation diameter of guide plate and wire diameter of torsion spring as the test factors, and the single seeding rate, multiple seeding rate and missed seeding rate as the evaluation index. The values of each factor are shown in Table 2, and the test results are shown in Table 3.

Factor and levels of experiment **Table 2**

Level	Installation diameter of guide plate / X_1	Wire diameter of torsion spring / X_2	Rotational speed of seed-metering device / X_3
	[mm]	[mm]	[rot/s]
-1.682	88	1.43	0.23
-1	90	1.5	0.3
0	93	1.6	0.4
1	96	1.7	0.5
1.682	98	1.77	0.56

Experiment results **Table 3**

No.	Experimental factors			Experimental index		
	Installation diameter of guide plate / X_1	Wire diameter of torsion spring / X_2	Rotational speed of seed-metering device / X_3	Single seeding rate Y_1 / %	Missed seeding rate Y_2 / %	Multiple seeding rate Y_3 / %
1	-1	-1	-1	92.62	3.18	4.2
2	1	-1	-1	92.2	3.37	4.43
3	-1	1	-1	92.46	3.22	4.32
4	1	1	-1	92.12	3.41	4.47
5	-1	-1	1	92.52	3.11	4.37
6	1	-1	1	92.54	3.26	4.2
7	-1	1	1	92.38	3.36	4.26
8	1	1	1	92.46	3.24	4.3
9	-1.682	0	0	92.63	3.22	4.15
10	1.682	0	0	92	3.55	4.45
11	0	-1.682	0	92.71	3.11	4.18
12	0	1.682	0	92.38	3.26	4.36
13	0	0	-1.682	92.38	3.34	4.28
14	0	0	1.682	92.62	3.22	4.16
15	0	0	0	92.97	3.07	3.96
16	0	0	0	93.04	3.03	3.93
17	0	0	0	93.17	2.95	3.88
18	0	0	0	93.05	3.05	3.9
19	0	0	0	93.07	2.98	3.95
20	0	0	0	93.07	3.05	3.88
21	0	0	0	93.13	3.03	3.84
22	0	0	0	92.99	3.07	3.94
23	0	0	0	93.04	2.99	3.97

As can be seen from Table 3, the single seed filling rate of the pressure-holding maize precision seed-metering device is greater than 92%, and the missed and multiple seeding rates are less than 5%, meeting the industry requirements. The regression models of single seeding rate, missed seeding rate, multiple seeding rate and guide plate's installation diameter, torsion spring wire's diameter and seed metering-device's rotational speed were obtained by analysing the test results.

Analysis of variance was performed on the model and the results are shown in Table 4.

Table 4

Factor and levels of experiment

Source	Single seeding rate /Y_1				Missed seeding rate /Y_2				Multiple seeding rate /Y_3			
	Sum of squares	Degree of freedom	*F*	*P*	Sum of squares	Degree of freedom	*F*	*P*	Sum of squares	Degree of freedom	*F*	*P*
Model	2.68	9	52.77	< 0.0001	0.5127	9	21.81	< 0.0001	0.9101	9	29.33	< 0.0001
X_1	0.2165	1	38.39	< 0.0001	0.0682	1	26.11	0.0002	0.0417	1	12.09	0.0041
X_2	0.0754	1	13.38	0.0029	0.0231	1	8.86	0.0107	0.0150	1	4.35	0.0572
X_3	0.0598	1	10.60	0.0063	0.0124	1	4.76	0.0482	0.0177	1	5.14	0.0411
X_1X_2	0.0025	1	0.4344	0.5213	0.0091	1	3.49	0.0845	0.0021	1	0.6127	0.4478
X_1X_3	0.0925	1	16.39	0.0014	0.0153	1	5.86	0.0308	0.0325	1	9.43	0.0089
X_2X_3	0.0001	1	0.0089	0.9264	0.0028	1	1.08	0.3183	0.0036	1	1.05	0.3247
X_1^2	1.11	1	196.16	< 0.0001	0.2334	1	89.37	< 0.0001	0.3234	1	93.79	< 0.0001
X_2^2	0.5294	1	93.88	< 0.0001	0.0405	1	15.51	0.0017	0.2771	1	80.36	< 0.0001
X_3^2	0.6257	1	110.96	< 0.0001	0.1123	1	43.00	< 0.0001	0.2079	1	60.29	< 0.0001
Residual	0.0733	13			0.0340	13			0.0448	13		
Lack of fit	0.0422	5	2.17	0.1574	0.0197	5	2.22	0.1512	0.0294	5	3.06	0.0778
Error	0.0311	8			0.0142	8			0.0154	8		
Total	2.75	22			0.5467	22			0.9549	22		

Note: $P<0.01$ is highly significant; $P<0.05$ is significant

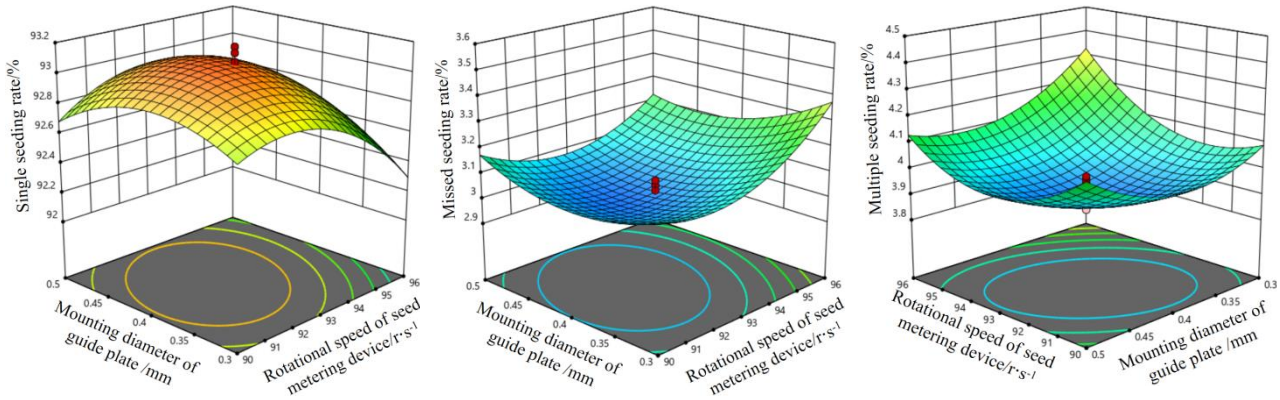
As can be seen from Table 5, the regression model for the single seeding rate Y_1 was significant, where X_1, X_2, X_3, X_1X_3, X_1^2, X_2^2, X_3^2 had a highly significant effect on Y_1. The regression model for the missed seeding rate Y_2 was significant, with X_1, X_1^2, X_2^2, X_3^2 having a highly significant effect on Y_2 and X_2, X_3, X_1X_3 having a significant effect on Y_2. The regression model of multiple seeding rate Y_3 was significant, where the effects of X_1, X_1X_3, X_1^2, X_2^2, X_3^2 on Y_3 were highly significant and X_2, X_3 on Y_3 were significant. After removing the insignificant term, the regression equations of the installation diameter of the guide plate, the wire diameter of the torsion spring and the rotational speed of the seed-metering device on the single seeding rate Y_1, the missed seeding rate Y_2 and the multiple seeding rate Y_3 were obtained as:

$$Y_1 = 93.06 - 0.12X_1 - 0.07X_2 + 0.06X_3 + 0.1X_1X_3 - 0.26X_1^2 - 0.18X_2^2 - 0.19X_3^2 \quad (11)$$

$$Y_2 = 3.03 + 0.07X_1 + 0.04X_2 - 0.03X_3 - 0.4X_1X_3 + 0.12X_1^2 + 0.05X_2^2 + 0.08X_3^2 \quad (12)$$

$$Y_3 = 3.92 + 0.05X_1 - 0.04X_3 - 0.06X_1X_3 + 0.142X_1^2 + 0.132X_2^2 + 0.114X_3^2 \quad (13)$$

In order to visually analyse the influence of the interaction of the influencing factors on each evaluation index, the response surface is plotted by Design-Expert 12.0 software, as shown in Figure 8.



a. $Y_1=f(X_1,1.6,X_3)$ b. $Y_2=f(X_1,1.6,X_3)$ c. $Y_3=f(X_1,1.6,X_3)$

Fig. 8 - Response surface curves

From Fig. 8, it can be seen that when the seed-metering device rotates at a certain speed, the single seeding rate increases and then decreases as the diameter of the guide plate installation increases. This is due to the fact that when the diameter of the guide plate is too small, the opening and closing angle of the seed picking block is too small, which is not conducive to the entry of seeds with larger characteristic sizes into the seed filling space, resulting in missed seeding. When the diameter of the guide plate is too large, the opening and closing angle of the seed picking block is too large, and the seeds with small characteristic size cannot be effectively pressed and held, so that the seeds fall off in the process of seed filling, resulting in increased missed seeding rate.

When the installation diameter of the guide plate is fixed, the single seeding rate increases and then decreases with the increase of the seed-metering device's rotational speed. The reason is that when the rotational speed of the seed-metering device is too low, the self-rotating flow rate of the seed population is slow, so that the seeds do not have enough speed to enter the seed filling space, resulting in missed seeding. When the speed is too high, the time for the seed picking block to pass through the seed population is reduced, and the contact time between the picking block and the seeds is lowered, so that the seeds cannot enter the seed filling space in a limited time, resulting in missed seeding.

In order to obtain the best combination of parameters affecting the performance of the pressure-holding maize precision seed-metering device, the multi-objective optimization analysis of the guide plate's installation diameter, torsion spring's wire diameter and device's rotational speed was carried out with the objectives of improving the single seeding rate and reducing the missed seeding rate and multiple seeding rate, and the optimization model was obtained as:

$$\begin{cases} \max Y_1(x_1, x_2, x_3) \\ \min Y_2(x_1, x_2, x_3) \\ \min Y_3(x_1, x_2, x_3) \\ 88\ mm \le x_1 \le 98\ mm \\ 1.43\ mm \le x_2 \le 1.77\ mm \\ 0.23\ rot/s \le x_3 \le 0.56\ rot/s \end{cases} \quad (14)$$

Through analysis and calculation, the optimal combination of parameters was obtained as follows: 92.32 mm diameter of guide plate installation, 1.59 mm diameter of torsion spring wire, and 0.41 rot/s rotational speed of seed-metering device, and the single seeding rate in this case was 93.08%, 3% missed seeding rate, and 3.9% multiple seeding rate, which meets the operational requirements.

CONCLUSIONS

(1) This paper designed a pressure-holding type maize precision seed-metering device, and introduced its structure and working principle. The shape of the guide plate profile was designed, a mechanical model of the seeds in the seeding operation was developed, and mechanical and kinematic analyses were conducted to derive the influence of the device's rotational speed on the operational performance. The mechanical analysis of the robbed seeds obtained that when the opening and closing angle of the seed picking block changed, it was beneficial for the seeds to enter the seed filling space and improve the seed filling rate.

(2) A three-factor, five-level orthogonal test was carried out with the single seeding rate, missed seeding rate and multiple seeding rate as the test indexes, and the installation diameter of guide plate, wire diameter of torsion spring wire diameter and rotational speed of seed-metering device as the test factors to obtain the influence parameters of each influencing factor on the operational performance of the seed-metering device.

(3) By analysing the test results and optimizing the regression model, the optimum working parameters of the pressure-holding maize precision seed-metering device were 92.32 mm installation diameter of the guide plate, 1.59 mm diameter of the torsion spring, and 0.41 rot/s rotational speed of the device, at which the single seeding rate was 93.08%, 3% missed seeding rate, and 3.9% multiple seeding rate, meeting the industry regulations and usage requirements.

ACKNOWLEDGEMENT

This work was supported by the regional Collaborative Innovation Special Project (Science and Technology Assistance Program) in the Autonomous Region, China (No.2021E02055).

REFERENCES

[1] Bai, H. C., Yi S. J., Feng, Z. H. (2021). Maize precision seeding technology development status and outlook（玉米精密播种技术发展现状与展望), *China Southern Agricultural Machinery,* vol. 52, issue 15, pp. 74-75.

[2] Cortez, J. W., Anghinoni, M., Arcoverde, S. N. S. (2020). Seed metering mechanisms and tractor-seeder forward speed on corn agronomic components, *Engenharia Agrícola,* vol. 40, issue 1.

[3] Ding, L., Yang L., Zhang, D. X., Cui, T., Zhang, K. L., Zhong, X. J. (2021). Effect of seed adsorption posture of corn air-suction metering device on seed feeding performance, *Transactions of the Chinese Society of Agricultural Machinery,* vol. 52, issue 07, pp. 40-50.

[4] Du, X., Liu C. L., Jiang, M., Zhang, F. Y., Yuan, H., Yang, H. L. (2019). Design and experiment of self-disturbance inner-filling cell wheel maize precision seed-metering device, *Transactions of the Chinese Society of Agricultural Engineering,* vol. 35, issue 13, pp. 23-24.

[5] Fang, L. F., Cao C. M., Qin, K., Ge, J. (2022). Design and experiment of wheel seed metering device with guide ring groove combining U-hole for radix peucedani（导种环槽 U 型孔组合型轮式前胡排种器设计与试验), *Transactions of the Chinese Society of Agricultural Machinery,* vol. 53, issue 4, pp. 21-32+51.

[6] Feng, S. H., Yi S. J., Li, Y. F., Chen, T., Zhang, D. M. (2022). Experimental study on performance of air suction electric drive high speed precision metering device for corn（气吸式电驱动玉米高速精量排种器性能试验研究), *Journal of Agricultural Mechanization Research,* vol. 44, issue 12, pp. 192-198.

[7] Inderpal, S., Anand, G., Anoop, K. D., Gursahib, S. M., Arshdeep, S. (2020). Development and evaluation of inclined plate metering mechanism for the sowing of maize (Zea mays L) seed, *Current Journal of Applied Science and Technology*.

[8] Li, Y. H., Yang L., Zhang, D. X., Cui, T., He, X. T., Hu, H. (2021). Design and test of double-side cleaning mechanism for air-suction maize seed-metering device（气吸式玉米精量排种器双侧清种装置设计与试验), *Transactions of the Chinese Society of Agricultural Machinery,* vol. 52, issue 07, pp. 29-39.

[9] Liu, C. L., Wang C., Song, J. N., Du, X., Zhang, F. Y. (2018). Design and seed-filling test of cell-type precision seed-metering device with vibration technology（振动供种型孔轮式非圆种子精密排种器设计与试验), *Transactions of the Chinese Society of Agricultural Machinery,* vol. 49, issue 05, pp. 108-115.

[10] Ren, J. D. (2021). Design and test of swinging finger clip corn seed-metering device（摆动指夹式玉米排种器设计与试验), *Heilongjiang: Northeast Agricultural University.*

[11] Wan, C. H. (2021). Design and experiment of chain clip corn seed metering device（链夹式玉米排种器设计与试验), *Heilongjiang: Northeast Agricultural University.*

[12] Wang, J. W., Wang, Z. M., Xu, C. W., Zhou, W. Q., Du, M. J., Tang, H. (2022). Design and experiment of intermittent synchronous seeding and reseeding device of duck-billed corn seed metering machine in sloping farmland (坡耕地鸭嘴式玉米排种器间歇同步充补装置设计与试验), *Transactions of the Chinese Society of Agricultural Machinery,* vol. 53, issue 05, pp. 57-66.

[13] Wang, Q., Zhu L. T., Li, M. W., Huang, D. Y., Jia, H. Z., Zhuang, J. (2019). Vibration characteristics of corn no-tillage finger-type precision planter and its effect on seeding performance, *Transactions of the Chinese Society of Agricultural Engineering,* vol. 35, issue 09, pp. 9-18.

[14] Wang, Y. C., Gao Y. P., Tai, W. S., Li, B. Q., Zhang, W., Han, X. (2019). Design and experiment of clamping maize precision seed-metering device（夹持式玉米精密排种器设计与试验), *Transactions of the Chinese Society of Agricultural Machinery,* vol. 50, issue 09, pp. 40-46.

[15] Wang, Y. C., Gao Y. P., Tai, W. S., Wang, Y., Lv, J. Q., Yang, D. Q. (2021). Design and test of pickup finger potato precision seed metering device（指夹式马铃薯精密排种器设计与试验), *Transactions of the Chinese Society of Agricultural Machinery,* vol. 52, issue 11, pp. 49-58.

[16] Wu, N. (2021). Comparative Research on miss-seeding reseed method in no-tillage corn planter（玉米免耕播种机漏播补偿方法对比研究), *Transactions of the Chinese Society of Agricultural Machinery,* vol. 51, issue S2, pp. 41-46+78.

DEVELOPMENT OF TUNA FISH SHREDDER FOR SMALL AND MEDIUM ENTERPRISES
/
PENGEMBANGAN MESIN PENCABIK IKAN TUNA UNTUK PEMBUATAN ABON IKAN SKALA INDUSTRI RUMAH TANGGA

Mustaqimah MUSTAQIMAH *[1)], Syafriandi SYAFRIANDI [1)], Andriani LUBIS [1)], Nawawi JUHAN [2)], Diswandi NURBA [1)]

[1)] Department of Agricultural Engineering, Faculty of Agriculture, Syiah Kuala University, Indonesia
[2)] Department of Mechanical Engineering, Lhokseumawe State Polytechnic / Indonesia
Tel: +62 921-6484-6042; E-mail: mustaqimah@ussyiah.ac.id
https://doi.org/10.35633/inmateh-69-15

Keywords: *shredder machine, shredded fish, performance optimization, statistical analysis*

ABSTRACT

This study aims to develop a fish grater machine to produce shredded fish on a household scale. The development of this fish shredder machine considers getting the maximum capacity, a minimum percentage of losses, a maximum percentage of the samples with short grade and middle grade size, and a maximum percentage of the samples with rough grade size with limited sources specified power. The method used in this research is the machine manufacturing and testing approach. Three types of shredder machine teeth (K-type, P-type, and B-type) are the main focus of this research to optimize the quality of the shredded material and the machine's performance. The machine capacity, the percentage of losses, and the optimal quality of the counting size of the developed machine can be achieved using K-type shredder machine teeth. Analysis of variance and the t-test are used simultaneously to determine the optimal performance of this machine. The results of this study suggest that using a K-type shredder machine teeth is the most appropriate shredder machine for shredded fish.

ABSTRAK

Penelitian ini bertujuan untuk mengembangkan mesin pencabik ikan untuk menghasilkan abon ikan skala rumah tangga. Pengembangan mesin pencabik ikan ini mempertimbangkan untuk mendapatkan kapasitas maksimum, persentase susut minimum, persentase maksimum sampel yang dicabik dengan ukuran pendek dan sedang, serta persentase maksimum sampel yang dicabik dengan ukuran kadar kasar dengan daya yang ditentukan sumber terbatas. Metode yang digunakan dalam penelitian ini adalah pendekatan manufaktur dan pengujian. Tiga jenis gigi pencabik (tipe-K, tipe-P, dan tipe-B) menjadi fokus utama penelitian ini untuk mengoptimalkan kualitas cabikan dan kinerja mesin. Kapasitas mesin, persentase losses dan kualitas optimal dari ukuran ikan yang dicabik dari mesin yang dikembangkan dapat dicapai dengan menggunakan mata pencabik tipe-K. Analisis varians dan uji-t digunakan secara bersamaan untuk mengetahui kinerja optimal dari mesin ini. Hasil penelitian ini menunjukkan bahwa menggunakan mata pencabik tipe-K adalah yang paling cocok untuk pembuatan abon ikan tuna.

INTRODUCTION

Tuna has a high protein content, vitamins A and B, omega 3, minerals, and amino acids that are good for growth and intelligence *(Usydus and Szlinder-Richert, 2012; Saleh et al., 2021; Parletta et al., 2013*). The body quickly digests them, which is perfect if humans consume them. In some ports, fishermen throw some fish out in the sea because they have rotted due to the limited facilities and infrastructure owned by fishermen. Another problem is the lack of knowledge of fishermen on post-catch fish handling. They do not understand that handling fresh fish is one of the most critical links in creating diversified fish products. An alternative that can be made to prevent a decrease in fishing income is to innovate the manufacture of processed products such as salted fish, ikan kayu, shredded fish, etc.

Shredded fish is one of the processed foods made from raw fish, which is obtained by boiling, cutting, and frying, then adding spices and herbs so that the shredded meat has a distinctive taste (*Latif et al.*, *2017*; *Rosalina et al.*, *2021*; *Fahmi and Purnamayati*, *2020*).

Shredded fish is classified as processed dry food, so it can be stored for a long time without changing its shape, aroma and taste. Drying and storage is a process that involves a lot of energy (*Sitorus et al.*, *2021*).

In the process of making shredded fish in most of Indonesia, it is still straightforward to use hands, knives, mortar, and hammers to grate the fish that will be transformed into shredded fish (*Putri and Rukmana*, 2021; *Rihayat et al.*, *2019*; *Dewi et al.*, *2020*). Using a manual system to produce shredded materials requires more time and human labour, which will result in high production costs. To solve this problem, a fish shredder machine facilitates shredding to increase production yields and shorten working time. Therefore, this study aims to develop a fish shredder machine for small and medium enterprises considering the aspect of the shredder teeth.

MATERIALS AND METHODS

Design of fish shredder machine

The driving motor used in this fish shredder machine is an electric motor with engine specifications of 220 V, 0.18 KW, 2.49 A, and 50 Hz. The type of electric motor used is an alternating current electric motor with a rotational speed of 1450 rpm. In the K-type shredder machine teeth (Figure 1a), the material used is a stainless-steel pipe with a thickness of 2 mm, the width of the cylinder is 93.80 mm, and the diameter of the cylinder is 88.10 mm. The weight of the K-type teeth is 498 g. The number of teeth for this type is 654 pieces. In the P-type shredder machine teeth (Figure 1b), the material used is a stainless-steel pipe with a thickness of 3 mm, the width of the cylinder is 93.80 mm, and the diameter of the cylinder is 88.10 mm. The weight of the P-type teeth is 437 g. The number of teeth for this type is 70 pieces. In B-type shredder machine teeth (Figure 1c), the material used is a stainless-steel pipe with a thickness of 3 mm, the width of the cylinder is 93.80 mm, and the diameter of the cylinder is 88.10 mm. The weight of the B-type teeth is 422 g. The number of teeth for this type is 70 pieces.

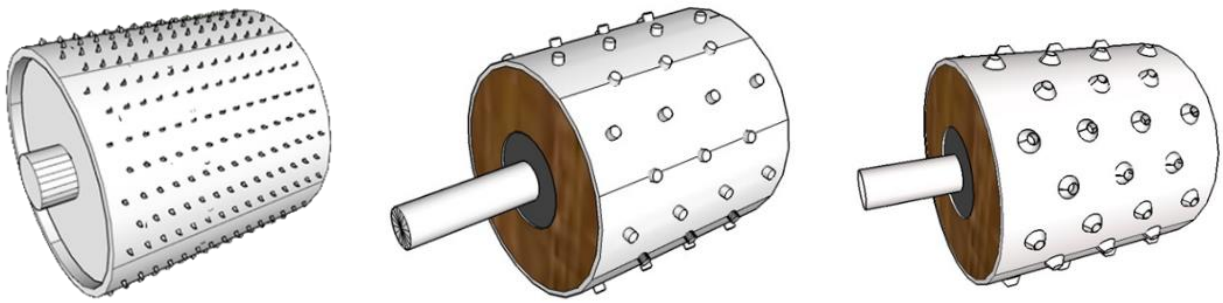


Fig. 1 – Teeth shape for shredder machine (a) K-type, (b) P-type, (c) B-type

Sample preparation

The raw material is the tuna cleaned of dirt, scales, and entrails. Furthermore, the fish is boiled to facilitate the separation of bones from meat. Three replications use 500 g of tuna fish that are fed into the shredder to test its performance. The total tuna fish used was 1500 g for each testing of the tooth shape.

Observation parameters

The performance test of the fish shredding machine is carried out to determine the machine's performance and the quality of the shredding results. In this test, measurements and calculations will be carried out, including the capacity of the machine (*Bulan et al.*, 2019), the percentage of losses, and the uniformity of the shredding results (percentage of the sample that is grated with short, middle, and rough grade). The uniformity of the shredding is then carried out by sieving with a 25 size mesh. The weight of the sample that passes will be compared with the initial weight of the fish before being shredded. Furthermore, statistical analysis, including ANOVA and *t-test*, is carried out on the experimental parameters (*Perdana et al.*, 2021; *Abbey et al.*, *2018*; *Ardiansyah and Sahubawa*, *2020*). All analyses are performed using the MS Excel application.

RESULTS AND DISCUSSIONS

Machine capacity

Table 1 shows the results of the analysis of variance of the capacity parameters using the shredder machine developed in this study and compared to the manual shredding. The results indicate at least one different treatment of the three types of shredding compared to manual shredding.

This can be seen in the *F-value*, which is much higher than the *F-crit*, 98.329 > 4.066. Therefore, more analysis is needed to determine the difference between each treatment in this machine capacity parameter.

Table 1

Analysis of variance of machine capacity parameters

Source of variation	Sum of square	Degrees of freedom	Mean squares	F	P-value	F-critical
Between groups	458.123	3	152.708	98.329	1.183×10^{-6}	4.066
Within groups	12.424	8	1.553			
Total	470.55	11				

The results of the *t-test* on the capacity parameters for using this machine compared with manual shredding are presented in Figure 2. In general, the shredding capacity using the machine developed in this study was significantly greater, eight times higher than that of manual shredding. Additionally, the use of the K-type teeth resulted in a significant difference (p<0.05) in engine capacity performance compared to the use of the P- type and B-type teeth. However, using P-type and B-type teeth did not differ significantly (p<0.05) on the machine capacity achievement. This *t-test* indicates that the use of P-type and B-type can be used equally well to achieve the maximum capacity for making fish floss. In addition, the use of K-type teeth should be avoided so that the machine can work optimally.

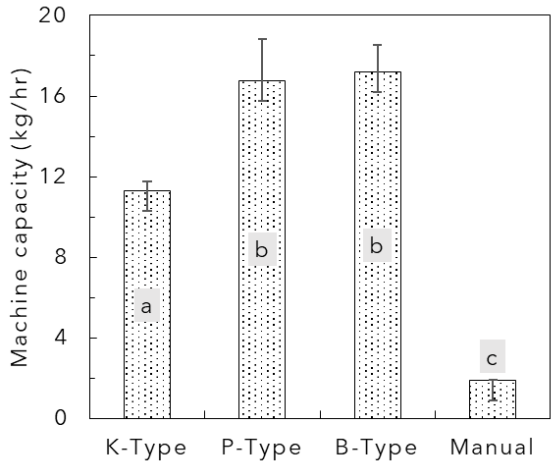


Fig. 2 – The results of the *t-test* on the machine capacity parameter compared with manual shredding

Percentage of losses

Table 2 shows the results of the analysis of the percentage of variance of losses using the shredder machine developed in this study and compared to the manual shredding. The results indicated at least one different treatment among the three types of shredding compared to manual shredding. This can be seen from the *F-value*, which is much higher than the *F-crit*, namely 12.804 > 4.066. Therefore, further analysis is needed to determine the difference in each treatment in the parameter percentage of losses from this machine.

Table 2

Analysis of variance to a percentage of losses

Source of variation	Sum of square	Degrees of freedom	Mean squares	F	P-value	F-critical
Between groups	15.237	3	5.079	12.804	0.002	4.066
Within groups	3.173	8	0.397			
Total	18.41	11				

The results of the *t-test* on the percentage of losses parameter using either the machine or manual shredding are presented in Figure 3. This shows statistically that any type of shredder teeth can be used for this developed fish shredding machine without affecting the percentage of losses. In general, the percentage of losses using the machine designed in this study is significantly greater than manual shredding, 5.5 times. Furthermore, the use of shredder teeth of all types in this study did not produce a significant difference (p<0.05) in the percentage of losses. However, to subjectively minimize the percentage of losses by observing the average percentage of losses from using the three types of shredder teeth, it can be recommended to use a shredder teeth of type K-type > P-type > B-type.

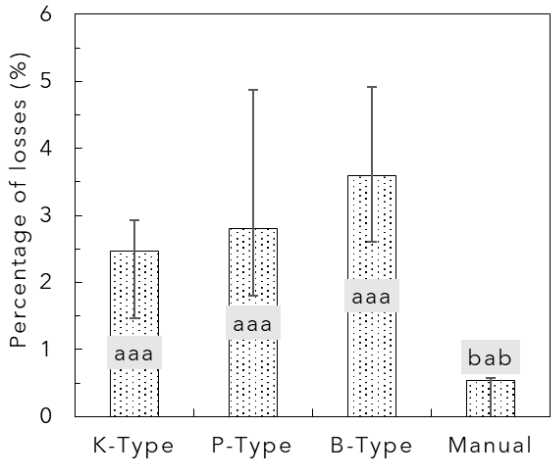


Fig. 3 – The results of the *t-test* on the percentage of losses from machine shredder parameter compared with manual shredding

Percentage of the sample that shredded with size short grade

Table 3 shows the results of the analysis of the variance percentage of the sample shredded with short grade size using the shredder machine developed in this study. The results indicate that at least one treatment differs from the three types of shredder teeth treatments in the percentage of the sample that is shredded with short grade size. This can be seen in the *F-value*, which is much higher than the *F-crit*, 11.523 > 5.143. Therefore, more analysis is needed to determine the difference between each treatment in the sample percentage more significant with the short-grade parameter size.

Table 3

Analysis of variance of the sample shredded with short grade size

Source of variation	Sum of square	Degrees of freedom	Mean squares	F	P-value	F-critical
Between groups	185.761	2	92.880	11.523	0.009	5.143
Within groups	48.362	6	8.060			
Total	234.123	8				

The results of the *t-test* on the percentage of parameters in the sample that is shredded with a short grade size is presented in Figure 4. In general, there is a difference between the use of brittle tooth type on the achievement of the percentage of the sample that is higher with short grade size. The K-type shredded teeth were significantly different (p<0.05) in achieving the percentage of the sample that is grater with a short grade size against the P-type teeth. However, the K-type and B-type teeth did not significantly affect the achievement of the percentage of the sample that was shredded with short grade size. In addition, using P-type teeth also did not have a significant effect achieving the percentage of the sample that was shredded with short grade size. Therefore, from the point of view of the percentage of the sample that is shredded with a short grade size, the use of K- type and B-type is the best option. But when the two are compared, the K-type teeth option is the best.

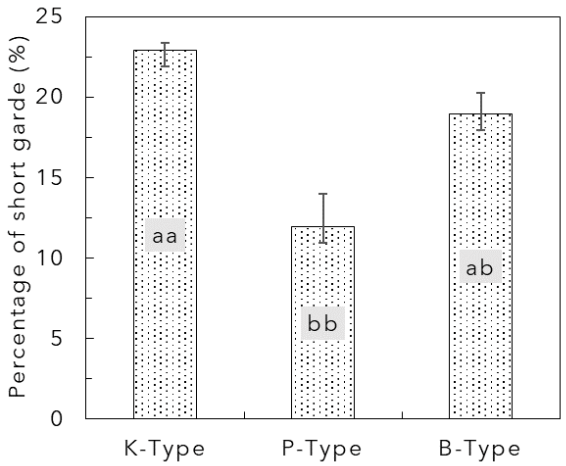


Fig. 4 – The results of the *t-test* on the percentage of the sample that is shredded with short grade size

Percentage of the sample that shredded with size middle grade

Table 4 shows the results of the analysis of the variance percentage of the sample that is shredded with middle grade size using the shredder machine developed in this study. The results indicate that at least one treatment differs from the three types of shredder teeth treatment in the percentage of the sample that is shredded with middle grade size. This can be seen in the *F-value*, which is much higher than the *F-crit*, which is 78.613 > 5.143. Therefore, further analysis is needed to determine the difference between each treatment in the percentage of parameter of the sample shredded with a middle grade size.

The results of the *t-test* on the percentage of parameters in the sample that is shredded with a middle grade size is presented in Figure 5. In general, there is a difference between the use of the type of shredder tooth and the achievement of the percentage of the sample that is shredded with middle grade size. The K-type teeth were significantly different (p<0.05) in achieving the percentage of the sample that was shredded with a short grade size against the P-type and B-type teeth.

However, the P-type and B-type teeth did not significantly affect the achievement of the percentage of the sample that was shredded with a middle grade size. Therefore, from the point of view of the percentage of the sample that was shredded with a middle grade size, the use of K-type teeth is optimal.

Table 4

Analysis of variance percentage of the sample shredded with middle grade size

Source of variation	Sum of square	Degrees of freedom	Mean squares	F	P-value	F-critical
Between groups	2985.093	2	1492.546	78.613	0.000050	5.143
Within groups	113.916	6	18.986			
Total	3099.009	8				

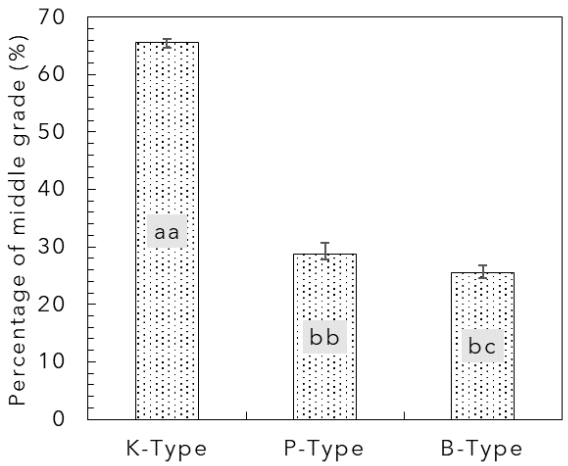


Fig. 5 – The results of the *t-test* on the percentage of the sample that is shredded with middle grade size

Percentage of the sample that was shredded with rough grade size

Table 5 shows the results of the analysis of the variance percentage of the sample shredded with rough grade size using the shredder machine developed in this study. The results indicate that at least one treatment differs from the three types of teeth treatments in the percentage of the sample that is shredded with rough grade size. This can be seen in the *F-value*, which is much higher than the *F-crit*, which is 158.927 > 5.143. Therefore, further analysis is needed to determine the difference between each treatment in the percentage of parameter of the sample shredded with rough grade size.

The results of the *t-test* on the percentage of parameters in the sample that is shredded with rough grade size are presented in Figure 6. In general, there is a difference between the use of the teeth type on the achievement of the percentage of the sample shredded with middle grade size. The K-type teeth were significantly different (p<0.05) in achieving the percentage of the sample shredded with a short grade size against the P-type and B-type teeth. In addition, the P-type teeth also significantly influence the achievement of the percentage of the sample shredded with rough grade size against the B-type teeth. Therefore, from the point of view of the percentage of the sample shredded with rough grade size, using K-type teeth is optimal.

Table 5

Analysis of variance percentage of the sample shredded with rough grade size

Source of Variation	Sum of square	Degrees of freedom	Mean squares	F	P-value	F-critical
Between groups	4148.570	2	2074.285	158.927	6.359×10^{-6}	5.143
Within groups	78.311	6	13.052			
Total	4226.881	8				

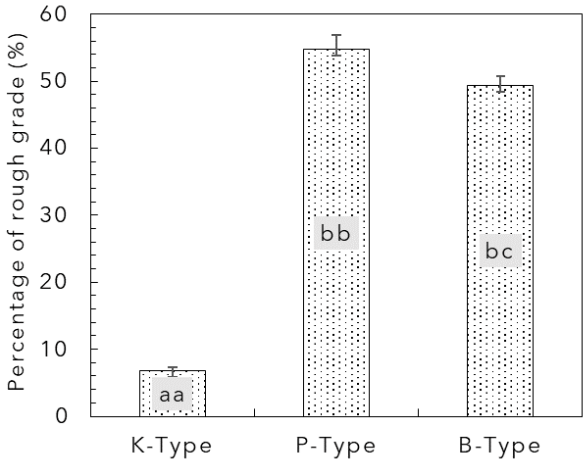


Fig. 6 – The results of the *t-test* on the percentage of the sample that shredded with size rough grade

CONCLUSIONS

A fish shredding machine for small and medium enterprises has been successfully designed and its performance tested. The developed machine has a capacity in the range of 11.29±0.46 kg/hr to 17.21±1.31 kg/hr with optimization on the K-type shredder teeth. The parameter percentage of machine loss is at a maximum of 3.60±0.60%. The best percentage of the sample shredded with a short grade size was achieved using K-type teeth, which was 22.92±1.97%. The best percentage of the sample shredded with middle grade size was performed with K-type teeth, namely 65.67±2.02%. The best percentage of the sample shredded with rough grade size was achieved using K-type teeth, namely 6.80±1.99%. On the basis of these parameters, the results of this study conclude that using a K-type shredder tooth is the most appropriate for developing a fish shredder machine for tuna fish.

REFERENCES

[1] Abbey, L., Annan N., Asiedu S. K., Esan E. O., Iheshiulo E. M.-A. (2018). Amino acids, mineral nutrients, and efficacy of vermicompost and seafood and municipal solid wastes composts. *International journal of agronomy*. Volume 2018, Issue 6. ISSN : 1687-8167. https://doi.org/10.1155/2018/6419467

[2] Ardiansyah, A., Sahubawa L. (2020). "Restructuring steak from flakes of yellowfin tuna meat using low salt microbial transglutaminase (MTGase)." In *IOP Conference Series: Earth and Environmental Science*, 012073. IOP Publishing
[3] Bulan, R., Yasar M., Nata Y., Sitorus A. (2019). Design and construction of chopper machine AE02-type for oil palm frond. *INMATEH - Agricultural Engineering*, 57(1). 165-172.
[4] Dewi, E. N., Nurbaiti A. A., Purnamayati L. (2020). Chemical Changes of Shredded Catfish (Clarias gariepinus) Added with Different Concentration of Sucrose During Storage at Room Temperature. *E3S Web of Conferences*, 03001. EDP Sciences
[5] Fahmi, A. S., Purnamayati L. (2020). Cholesterol content, fatty acid composition and sensory analysis of deep fried and roasted Abon Ikan (fish floss/shredded fish flesh). *E3S Web of Conferences*, 03009. EDP Sciences
[6] Latif, R., Dirpan A., Indriani S. (2017). The status of implementation of Good Manufacturing Practices (GMP) shredded fish production in UMKM Az-Zahrah, Makassar. *IOP Conference Series: Earth and Environmental Science*, 012040. IOP Publishing
[7] Parletta, N., Milte C.M., Meyer B.J. (2013). Nutritional modulation of cognitive function and mental health. *The Journal of nutritional biochemistry*, 24(5). 725-743.
[8] Perdana, W., Widowaty W., Sofia D., Setiawan Y., Hadayanti D., Zakaria A. (2021). Chemical analysis and organoleptic properties of banana blossoms (Musa paradisiaca) as filler for catfish (Clarias sp.) fish floss. *Journal of Physics: Conference Series*, 012008. IOP Publishing
[9] Putri, A., Rukmana I. (2021). Additional Value of Bandeng Fish Fishing Business in The District Pinrang. *IOP Conference Series: Earth and Environmental Science*, 012088. IOP Publishing
[10] Rihayat, T., Putra A., Fona Z., Riskina S., Syahputra W. (2019). Effect of Determination Temperature on Nutrition and Organoleptic Tuna Fish Floss. *IOP Conference Series: Materials Science and Engineering*, 012055. IOP Publishing
[11] Rosalina, L., Manvi K. I., Pramudia H. (2021). A Great Food for Children Base on Rinuak Shredded Fish (Psilopsis Sp). *IOP Conference Series: Earth and Environmental Science*, 012059. IOP Publishing
[12] Saleh, A. A., Amber K. A., Soliman M. M., Soliman M. Y., Morsy W. A., Shukry M., Alzawqari M. H. (2021). Effect of low protein diets with amino acids supplementation on growth performance, carcass traits, blood parameters and muscle amino acids profile in broiler chickens under high ambient temperature. *Agriculture*, 11(2), 185.
[13] Sitorus, A., Putra S. A., Cebro I. S., Bulan R. (2021). Modelling drying kinetics of paddy in swirling fluidized bed dryer. *Case Studies in Thermal Engineering*, 28.
[14] Usydus, Z., Szlinder-Richert J. (2012). Functional properties of fish and fish products: A review. *International journal of food properties*, 15(4). 823-846.

EXPERIMENT AND ANALYSIS OF MECHANIZED PICKING OF *CAMELLIA OLEIFERA* FRUIT BASED ON ENERGY UTILIZATION RATE
/
基于能量利用率的油茶果机械化采摘试验与分析

Delin WU*[1)], Enlong ZHAO[1)], Dong FANG[1)], Yilin LIU[1)], Shunli WANG[1)], Cheng WU[1)], Feng GUO[1)]
[1)] School of Engineering, Anhui Agricultural University, Hefei, China
Tel: +86 15805602399; E-mail: wudelin@126.com
https://doi.org/10.35633/inmateh-69-16

Keywords: *Camellia oleifera, vibration harvest, energy utilization rate, parameter optimization*

ABSTRACT
In order to use the resonance principle for vibratory picking of Camellia oleifera fruit, the frequency sweep tests were carried out on the fruiting branches of Camellia oleifera trees. The results showed that the acceleration response of fruit-bearing branches had good consistency. The use of fruit removal rate alone to evaluate the picking effect is not reliable, and the introduction of energy utilization to evaluate the vibration picking effect is significant. The best results were a vibration frequency of 8 Hz and an excitation time of 10 s. The fruit removal rate was 88.12% and the energy utilization rate was 36.72%. Compared with the traditional fruit shedding rate, the application of energy utilization rate to evaluate the picking effect can improve the reliability of the results and reduce the energy loss.

摘要
为了利用共振原理对油茶果进行振动采摘，对油茶树挂果枝条进行扫频试验。结果表明：挂果枝条的加速度响应具有较好的一致性。仅使用果实去除率不能准确评价采摘效果，引入能量利用率评价振动采摘效果是显著的。采用 8Hz 振动频率和 10s 激振时间的振动采摘效果最佳，此时油茶果实去除率为 88.12%，能量利用率为 36.72%。与传统果实脱落率相比，应用能量利用率评价采摘效果可以提高结果的可靠性，同时降低能量的损失。

INTRODUCTION
Camellia oleifera is unique oilseed species to China and is one of the world's four major woody oil crops, along with olive, coconut and palm *(Peng Shaofeng et al.,2021; Zhang Liwei et al.,2021)*. For those who grow Camellia oleifera, labour costs and economic efficiency are the two main issues. As *Camellia oleifera* is characterized by random spatial location and orientation of the fruit within the growing canopy and varying spatial location and orientation, manual harvesting is work intensive and inefficient. Although labour-saving *Camellia oleifera* fruit harvesting techniques plays a vital role in the development of the *Camellia oleifera* industry, no commercial *Camellia oleifera* fruit harvesting machines have been available to growers up to date. In the long run, advances in mechanized *Camellia oleifera* fruit harvesting technology will help the *Camellia oleifera* industry become more competitive and sustainable.

Research has shown that mechanical harvesting based on vibration technology is an effective technique for improving harvesting efficiency and reducing costs *(Brondino et al.,2021)*. The fruit is picked by vibration. When picking fruit by vibration, the fruit is shed by means of excitation device that provides vibration energy with the right combination of vibration parameters (frequency, amplitude and duration of vibration) *(Sargent, S.A. et al., 2020)*. The main study is the effect of vibration mode and vibration parameters on fruit drop rate and fruit damage rate *(Zhang Z. et al., 2020; Wang, W.Z. et al., 2019; Castro-Garcia, S. et al., 2018; Castro-Garcia, S. et al., 2019)*. *Wu Delin et al. (2022)* theoretically analysed the whole acceleration process of mechanical vibration picking according to different vibration positions (heights), and carried out vibration picking experiments. *He et al., (2013)* found a relationship between frequency and harvest efficiency, with higher frequencies associated with easier fruit shedding. *Guangrui Hu et al., (2020)* inserted the comb finger into the apple tree model by simulation to comb and pick apples, and determined the important parameters of

[1] *Delin WU, A.Prof.; Enlong ZHAO, M.S. Stud.; Dong FANG, M.S. Stud.; Yilin LIU, M.S. Stud.; Shunli WANG, M.S. Stud.; Cheng WU, M.S. Stud.; Feng GUO, M.S. Stud.*

apple in the combing and harvesting of vertical structure. *Kang et al., (2021)* optimal Camellia fruit picking parameters were obtained by designing the canopy Camellia fruit picking gear and calculating the key position acceleration. The device designed by *Gao Zicheng et al., (2019),* fruit collecting by vibrating the main branches of the *Camellia oleifera* tree through a suspended vibrating mechanical arm. The test results show that the removal rate of the device can reach 95% and the damage rate of the flower bud can be as low as 5%. *Rao Honghui et al., (2018, 2019)* used an electric rubber roller rotating *Camellia oleifera* picking actuator to achieve fruit removal rate of 86.4% by creating extrusion on *Camellia oleifera* fruit impact through upper and lower rubber roller rotation. *Wu Delin et al., (2020),* analysed the main factors affecting the shedding of *Camellia oleifera* fruits as the amplitude, vibration frequency, vibration time and clamping position of the excitation device, and designed a shaking branch type *Camellia oleifera* fruit picking device, and the removal rate of *Camellia oleifera* fruits was 89.13% under the optimal combination of vibration parameters.

In summary, the best way to mechanize the harvesting of forest fruits is vibration, and the effect of vibration on the mechanized harvesting of *Camellia oleifera* is more significant. The current research on vibration harvesting of *Camellia oleifera* is limited to the development of excitation devices, the correspondence between excitation parameters and fruit removal rate, and the evaluation of excitation effect only relying on fruit removal rate. In this paper, it is studied the acceleration response of fruiting branches in the *Camellia oleifera* canopy, using the resonance principle to conduct excitation picking tests and introducing energy utilization rate to evaluate vibration picking. The results of this study can provide a basis for understanding the vibration response characteristics of the fruiting branches of *Camellia oleifera* trees, reducing energy consumption and improving harvesting efficiency during *Camellia oleifera* fruit harvesting.

MATERIALS AND METHODS

Healthy and well-managed *Camellia oleifera* trees of the XIANGLIN 210 variety were tested in November 2020 at the 'Uncle Lei' *Camellia oleifera* site in Yongzhou, Hunan Province, China. Some of the orchard, tree and fruit characteristics are given in Table 1 and these data are taken from the mean of 100 samples. The field trials were conducted in two sessions. The first field trial is the frequency scan test of the acceleration response amplitude of hanging fruit branches in the canopy of oilseed tea trees, during which the corresponding optimum vibration frequency to the extreme value of the acceleration response was detected. The fruiting branches are relatively thin and can easily break when the vibration frequency is too high, the vibration frequency was set in the range of 0 - 20 Hz with an interval of 1 Hz, a vibration time of 8 s and an amplitude of 50 mm. 20 vibration tests were conducted with similar *Camellia oleifera* trees at each vibration frequency. The second field trial utilized the excitation frequency with the larger acceleration response in the frequency scan results for the canopy vibration picking test on Camellia oleifera.

Table 1

Basic parameters of XIANGLIN 210 Camellia oleifera

Row spacing [m]	Plant spacing [m]	Tree height [m]	Canopy height [m]	Canopy diameter [m]	Branches length [m]
3.9±0.35	2.4±0.26	2.0±0.45	1.5±0.34	2.28±0.21	0.63±0.15

Canopy vibrating camellia fruit harvester

As shown in Figure 1. A prototype "Canopy Vibrating *Camellia Oleifera* Fruit Harvester" developed and built by the research group was used in the trials.



Fig. 1 - Vibrating camellia fruit harvester used in the canopy experiment

The prototype consists of a vehicle body and a vibrating device. The vehicle body is made from a small tracked excavator with a telescopic arm, and bucket of the excavator removed and replaced by a lifting platform, telescopic rod and rack and pinion mechanism which changes in the spatial position of the vibrating device. The mini excavator is powered by a hydraulic motor, the movement of the lifting platform, telescopic rod and rack and pinion mechanism is achieved by the hydraulic motor driving the hydraulic cylinder.

Table 2

Basic parameters of the vibrating camellia fruit harvesting prototype

Number	Project		Parameters
1	Boundary dimension	Long [mm]	2300
2		Wide [mm]	1480
3		High [mm]	2180
4	Displacement distance [mm]		2400~2680
5	Rotation angle [°]		180
6	Rising height [mm]		990~1860
7	Motor rated power [KW]		1.5
8	Rotary table eccentricity [mm]		40, 50, 60, 70, 80
9	Excitation frequency [Hz]		0-50
10	Running speed [m/s]		0.3

Acceleration measurement

For the acceleration response of hanging fruit branches, the acceleration response of each test point was measured by inserting the vibration actuator of the canopy vibration *Camellia oleifera* fruit harvester into the *Camellia oleifera* tree canopy and excitation of the *Camellia oleifera* tree canopy by varying the vibration frequency. The test equipment consisted of an excitation device, an accelerometer (CA-YD-141, Jiangsu Zhongke Ceramic Piezoelectric Company, Yangzhou, China), a charge amplifier (YE5853A, Jiangsu Zhongke Ceramic Company, Yangzhou, China), and a data acquisition unit (NI cDAQ-9174, China). Data analysis software (CRAS V7.1, First Test Software Engineering Co., Ltd., Nanjing, China). The accelerometer was fixed to a small wooden block (15 mm x 15 mm x 15 mm) and the block was attached to the test points of the branch using hot melt glue.

As shown in Figure 2, the accelerometer is placed on the hanging branch (point C) at a distance of 500 mm from the excitation positions B and C. The analysis is carried out using the synthetic acceleration values. Equation as:

$$a = \sqrt{a_x^{\,2} + a_y^{\,2} + a_z^{\,2}} \tag{1}$$

where:

a_x, a_y and a_z are the instantaneous acceleration values for each axis at the same moment, [m/s^2].

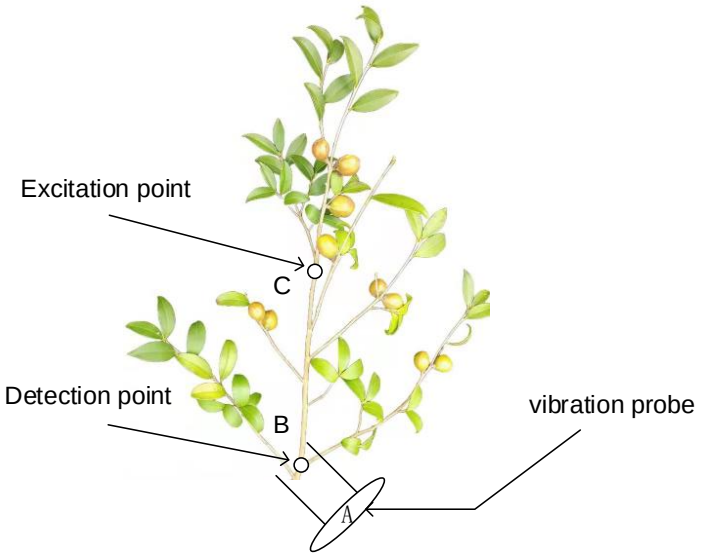


Fig. 2 - Accelerometer installation position

Determine the energy utilization rate

For the canopy vibration *Camellia oleifera* fruit process, by inserting the vibration actuator of the canopy vibration *Camellia oleifera* fruit harvester into the canopy of the *Camellia oleifera* tree, the canopy of the *Camellia oleifera* tree is stimulated by varying the vibration frequency and the vibration time, the vibration harvested *Camellia oleifera* fruit is collected after the vibration is over and the unshed *Camellia oleifera* fruit is manually removed and weighed and recorded separately. Energy utilization was introduced to collaboratively evaluate the effect of canopy vibration on *Camellia oleifera* fruit harvesting. Defined as the efficiency of fruit removal per unit amount of energy consumption during harvesting, expressed as:

$$\mu = \frac{C}{E} \tag{2}$$

where:

μ is the energy efficacy of a harvesting operation, [%/kJ];

C is the fruit removal efficiency, [%];

E is the energy consumption of the harvester, [kJ].

Fruit removal efficiency is defined as the weight of mechanically harvested fruit as a percentage of the weight of all fruit on the tree. The fruit removal efficiency can be mathematically expressed by the following equation:

$$C = \frac{M_1}{M} \times 100\% \tag{3}$$

where:

M_1 is the weight of the mechanically harvested fruit, [kg];

M is the weight of all fruit grown on the tested tree, [kg].

The energy consumption of the shaker during the harvesting operation is determined by the input power used during the total harvesting time with the following equation:

$$E = P \times t \tag{4}$$

where:

E is the shaker energy consumption in certain shaking durations, [kJ];

P is the input power to the shaker in operation, [KW];

t is the duration of harvesting, [s].

The input power of the shaker is expressed as:

$$P = \frac{P_0 \times f}{f_0} \tag{5}$$

where:

P_0 is motor rated power, [W];

f_0 is the power frequency, take 50 Hz;

f is the power frequency adjusted by the frequency converter is the motor rotation frequency, [Hz].

RESULTS

The acceleration response of the test point

The vibration response of the hanging fruit branches of the *Camellia oleifera* tree is caused by the excitation of the branches driven by the excitation device. In order to use the resonance characteristics for vibration picking of *Camellia oleifera* fruit, the acceleration response of *Camellia oleifera* tree fruit branches to the harmonic excitation of *Camellia oleifera* tree fruit branches need to be studied to obtain the acceleration-spectrum curve.

The excitation device was inserted into the canopy of the *Camellia oleifera* tree and the vibration signal was directed to the hanging branches of the tree. The accelerometer was fixed at test point C on the hanging branches. The acceleration signals a_x, a_y and a_z were recorded in three directions during the experiment, and the acceleration curve with time was intercepted after the motor had stabilized in operation. The acceleration response values in the X, Y and Z directions were different at each frequency.

Figure 3 shows that acceleration values of the three directions of the branches of *Camellia oleifera* varied greatly. Compared to the other two axes, the acceleration response value in the X direction is the largest, the acceleration response value in the Z direction is the smallest, and the acceleration response value in the Y direction is slightly larger than that in the Z direction. When the excitation frequency is 8 Hz, the acceleration value in the Z direction is only 13 m/s^2, while the acceleration values in the X and Y directions are 6.15 and 1.92 times higher respectively.

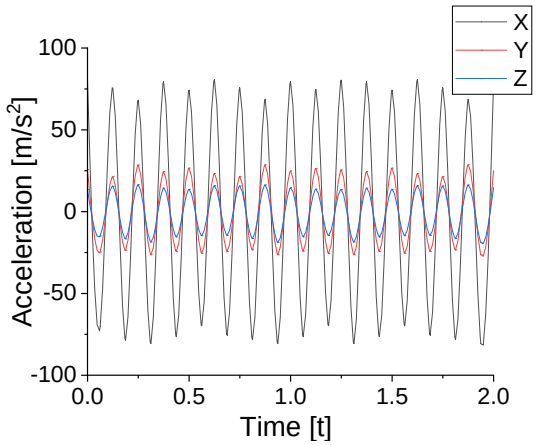


Fig. 3 - Acceleration time domain response

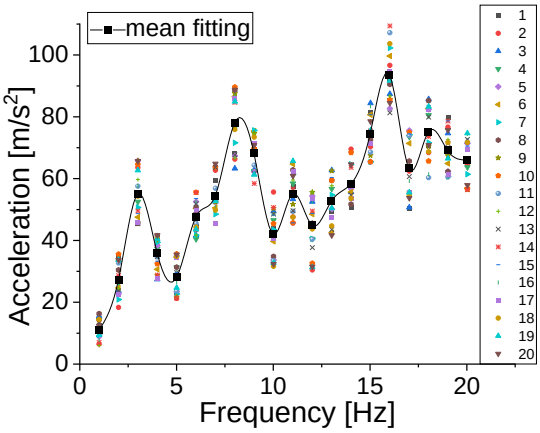


Fig. 4 - Acceleration frequency domain response

The curve of acceleration versus frequency obtained from experimental measurements is shown in Figure 4. Generally, the excitation frequency range of the crank linkage based on excitation method used in *Camellia oleifera* harvesting does not exceed 20 Hz. Moreover, the diameter of the hanging branches of the *Camellia oleifera* tree is small and the relative stiffness is low, when the excitation frequency exceeds 20 Hz, the hanging branches are extremely vulnerable to injury and even break, which causes great damage to Camellia oleifera tree. Therefore, this paper focuses on the acceleration-spectrum curve below 20 Hz.

The range of spectral curves used in this paper is from 1 to 20 Hz. This may be the different number of fruits and leaves on the different branches, as denser leaves can produce higher aerodynamic damping; This may also be the different thickness of the branches, the thinner the branch, the higher the structural damping of the branch. Fortunately, the overall trend of the measured acceleration response of the hanging branches of the *Camellia oleifera* tree with respect to frequency were similar, and the acceleration-frequency response curve of the hanging branches of the *Camellia oleifera* tree was obtained by fitting the average value of the acceleration response at the same frequency. The peak frequencies in the test frequency range are the resonant frequency that are likely to cause resonance in the fruiting tree, namely 3 Hz, 8 Hz, 11 Hz, 16 Hz and 18 Hz, and the corresponding accelerations are 55.1 m/s^2, 80 m/s^2, 55 m/s^2, 93.6 m/s^2 and 75.03 m/s^2.

Energy delivery efficiency

In the vibration harvesting tests, field trials were carried out for the test points for 3 Hz, 8 Hz and 16 Hz, where the sweep test results had a significant and abrupt change in acceleration, as the excitation frequencies. Vibration times of 5 s, 10 s and 15 s were applied respectively.

Table 3

Results of vibration picking test with 5 s vibration time

Frequency [Hz]	3			8			16		
Energy consumption[KJ]	0.45			1.2			2.4		
Fruit removal rate [%/KJ]	15.38	16.48	15.07	42.08	35.07	43.22	65.78	58.73	69.78
Energy utilization [%/KJ]	34.19	36.61	33.49	35.07	29.23	36.02	27.41	24.47	29.07

Table 4

Results of vibration picking test with 10 s vibration time

Frequency [Hz]	3			8			16		
Energy consumption[KJ]	0.9			2.4			4.8		
Fruit removal rate [%/KJ]	29.35	35.29	30.63	88.58	83.24	92.55	89.33	85.6	94.9
Energy utilization [%/KJ]	32.61	39.22	34.03	36.91	34.68	38.56	18.61	17.83	19.78

Table 5

Results of vibration picking test with 15 s vibration time

Frequency [Hz]	3			8			16		
Energy consumption[KJ]	1.35			3.6			7.2		
Fruit removal rate [%/KJ]	28.26	29.55	26.98	88.96	84.27	91.59	89.71	86.04	90.83
Energy utilization [%/KJ]	20.93	21.89	19.98	24.71	23.41	25.44	12.46	11.95	12.61

For 5 s continuous vibration, with the increase of excitation frequency, the removal rate of *Camellia oleifera* fruits showed an upward trend. However, the energy utilization rate increased first and then decreased. When the vibration frequency was 3 Hz, the average value of fruit removal rate was 15.64% and the average value of energy utilization rate was 34.76%/KJ; when the vibration frequency was 8 Hz, the fruit removal rate was 40.12% and the energy utilization rate was 33.44%/KJ; when the vibration frequency was 16 Hz, the fruit removal rate was 64.76% and the energy utilization rate was 26.98%/KJ.

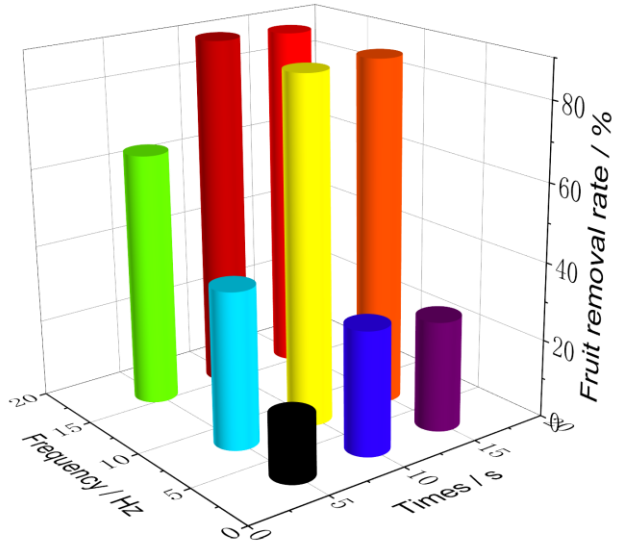


Fig. 5 - Camellia fruit removal rate

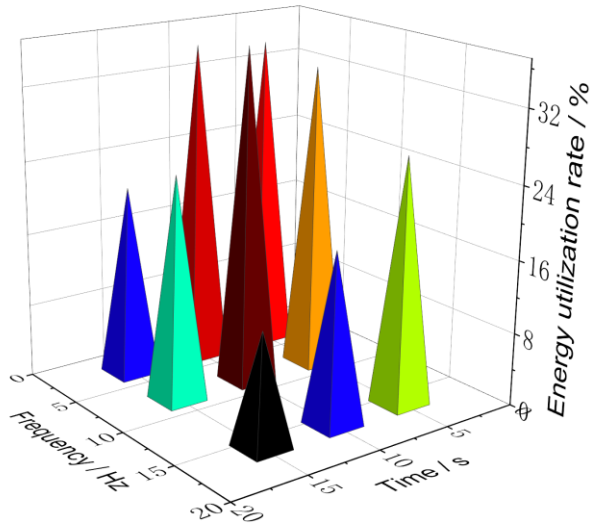


Fig. 6 - Energy utilization rate

At 10 s of continuous vibration, the fruit removal rate at an excitation frequency of 8 Hz was significantly higher than that at a vibration frequency of 3 Hz. However, the fruit removal rates at excitation frequencies of 8 Hz and 16 Hz were essentially the same; the energy utilization rate at an excitation frequency of 3 Hz was slightly lower than that at an excitation frequency of 8 Hz and much higher than that at an excitation frequency of 16 Hz. When the vibration frequency was 8 Hz, the fruit removal rate was 88.12% and the energy utilization rate was 36.72%/KJ. Compared to the vibration effect at 8 Hz, the fruit removal rate at 3 Hz decreased by 56.36% and the energy utilization increased by 1.43%/KJ, and the fruit removal rate at 16 Hz increased by 1.84% and energy utilization decreased by 17.98%/KJ.

The variation trend of fruit removal rate (Figure 5) and energy utilization rate (Figure 6) of *Camellia oleifera* at 15 s of continuous vibration were basically the same as the excitation effect at 10 s of vibration duration. When the vibration frequency was 3 Hz, the fruit removal rate was 28.26% and the energy utilization rate was 20.93%/KJ, while the fruit removal rate at a vibration frequency of 8 Hz was 3.12 times higher than that at a vibration frequency of 3 Hz, and the fruit removal rate at a vibration frequency of 16 Hz was 3.14 times higher than that at a vibration frequency of 3 Hz, and the energy utilization rate at a vibration frequency of 8 Hz was 1.17 times higher than at 3 Hz and 0.59 times higher at 16 Hz than at 3 Hz.

Vibration parameters have a great influence on the harvesting fruits. In this study, different vibration parameters were used for harvesting *Camellia oleifera* fruit to investigate the effects of two excitation parameters, vibration frequency and vibration time, on the harvesting effect of *Camellia oleifera* fruit. As the excitation frequency increased, the removal rate of *Camellia oleifera* fruits shows an increasing trend. However, when the vibration frequency reached a certain value, the removal rate of *Camellia oleifera* fruits does not keep increasing.

Only when the free vibration frequency of the *Camellia oleifera* branch reaches the resonance, the vibration amplitude is maximum and the acceleration of the *Camellia oleifera* fruit reaches the abscission condition, the *Camellia oleifera* fruit may be absconded. At 3 Hz, 8 Hz and 16 Hz excitation frequencies, the maximum values of *Camellia oleifera* fruit removal rate were 35.29%, 92.55% and 94.96% at different excitation times respectively. This indicates that 3 Hz is not the optimum excitation frequency, although in the sweep test, the *Camellia oleifera* canopy branches showed a higher acceleration response at 3 Hz. The removal rates of *Camellia oleifera* fruit at 8 Hz and 16 Hz were generally consistent and could be used as the excitation frequency for vibratory harvesting of *Camellia oleifera* fruit canopies.

Discussions

The same relationship exists between *Camellia oleifera* fruit removal rate and vibration duration, that is, with the rate increasing, the vibration duration increases. The results of the picking trials showed a common trend for the three tested excitation frequencies, with a surge in *Camellia oleifera* fruit removal rate at 10 s excitation duration relative to 5 s excitation duration, but when the excitation duration was increased to 15 s, the *Camellia oleifera* fruit removal rate was essentially the same as that at 10 s excitation duration, with a maximum *Camellia oleifera* fruit removal rate of 92.55%.

The energy utilization was similar at 5 s and 10 s, reaching 39.22%/KJ, however, when the excitation duration was extended to 15 s, the energy utilization decreased rapidly by almost 50%. The energy utilization was higher when the excitation duration was 5 s or 10 s and the removal rate of *Camellia oleifera* fruit was higher when the excitation duration was 10 s or 15 s. This indicates that an excitation duration of 10 s is the optimum vibration time for vibratory harvesting of *Camellia oleifera* canopy. From the perspective of energy utilization, the energy utilization at a vibration frequency of 8 Hz was significantly higher than at a vibration frequency of 16 Hz for different vibration durations. With the same *Camellia oleifera* fruit removal rate, choosing 8 Hz as the vibration frequency for *Camellia oleifera* fruit canopy can effectively reduce energy consumption.

The experimental results of *Camellia oleifera* canopy vibration picking showed that the best effect of *Camellia oleifera* fruit removal rate does not reach 100%, which may be caused by the following reasons:

1. When vibration picking, the maturity of camellia fruit is different. The binding force between stalk and branch of the fruit with higher maturity is smaller than that of the fruit with lower maturity. The smaller the binding force, the easier it is to fall off.

2. The distance between the camellia fruit and the excitation point is different. The inertial force generated by the fruit with a shorter distance is larger than that of the fruit with a longer distance, and the closer the distance, the easier it is to fall off. Therefore, the use of a single vibration frequency vibration picking can't make all camellia fruits obtain enough inertia force, that is, a single vibration frequency can't make all camellia fruits removed. In the next study, multiple vibration frequencies will be used simultaneously to achieve higher fruit removal rate and energy utilization rate of camellia oleifera. Future work will focus on expanding the study to include other controllable factors, including differences in camellia canopy structure and species.

CONCLUSIONS

The results of the study on the acceleration response characteristics of *Camellia oleifera* showed that the acceleration response of fruit was consistent with different test results. The acceleration responses at 3 Hz, 8 Hz, 11 Hz, 16 Hz and 18 Hz were higher, which was most likely the natural frequency of *Camellia oleifera* branches.

When the vibration result was evaluated by fruit removal rate, the vibration effect was basically the same when the excitation frequency was 8 Hz and 16 Hz, and the excitation duration was 10 s and 15 s. When the vibration frequency was 8 Hz and the vibration duration was 10 s, the optimal vibration parameters of *Camellia oleifera* canopy were 88.12% of fruit removal rate and 36.72%/KJ of energy utilization rate.

ACKNOWLEDGEMENT

The project was supported by Natural Science Foundation of Anhui Province (NO. 2208085ME132) and the National Key Research and Development Program of China (NO. 2016YFD0702105).

REFERENCES

[1] Brondino, L., Borra, D., Giuggioli, N.R., Massaglia, S. (2021). Mechanized Blueberry Harvesting: Preliminary Results in the Italian Context. *Agriculture*, 11, 1197. https://doi.org/10.3390/agriculture11121197

[2] Castro-Garcia, S., Aragon-Rodriguez, F., Sola-Guirado, R.R., Serrano, A.J., Soria-Olivas, E., Gil-Ribes, J.A. (2019). Vibration Monitoring of the Mechanical Harvesting of Citrus to Improve Fruit Detachment Efficiency. *Sensors*, 19, 1760. https://doi.org/10.3390/s19081760

[3] Castro-Garcia, S., Sola-Guirado, R.R., Gil-Ribes, J.A. (2018). Vibration analysis of the fruit detachment process in late-season 'Valencia' orange with canopy shaker technology. *Biosystems Engineering*,170,130–137. https://doi.org/10.1016/j.biosystemseng.2018.04.007

[4] D. Kang, Z.J. Chen, Y.H. Fan, C. Li, C. Mi, Y.H. Tang. (2021). Optimization on kinematic characteristics and lightweight of a camellia fruit picking machine based on the Kriging surrogate model, *Mechanics & Industry* 22, 16. https://doi.org/10.1051/meca/2021017

[5] Delin Wu, Enlong Zhao, Shan Jiang, Ding Da, Yangyang Liu. (2022). Influence of Excitation Position on Mechanized Picking Effect of Camellia Oleifera. *Engenharia Agrícola*, v. 42, n. 4. https://doi.org/10.1590/1809-4430-Eng.Agric.v42n4e20220040/2022

[6] Wu, D.; Zhao, E.; Fang, D.; Jiang, S.; Wu, C.; Wang, W.; Wang, R. (2022). Determination of Vibration Picking Parameters of *Camellia oleifera* Fruit Based on Acceleration and Strain Response of Branches. *Agriculture*, *12*, 1222. https://doi.org/10.3390/agriculture12081222

[7] Gao Zicheng, Zhao Kaijie, Li Lijun, Pang Guoyou, Wang Xiaochen. (2019). Design and experiment of suspended vibratory actuator for picking Camellia Oleifera fruits. *(悬挂振动式油茶果采摘执行机构设计与试验)*. *Transactions of the Chinese Society of Agricultural Engineering*, 35(21):9-17.

[8] Guangrui Hu, Lingxin Bu, Jun Chen. (2020). Simulation to determination of significant parameters on apple stress for combing harvesting in trellis trained trees. *Scientia Horticulturae*, Volume 274,2020 https://doi.org/10.1016/j.scienta.2020.109654

[9] Long He, Jianfeng Zhou, Xiaoqiang Du, Du Chen, Qin Zhang, Manoj Karkee. (2013). Energy efficacy analysis of a mechanical shaker in sweet cherry harvesting. *Biosystems Engineering*, 116(4):309-315. https://doi.org/10.1016/j.biosystemseng.2013.08.013

[10] Peng Shaofeng, Wu Hong, Lu Jia, MA Li, Chen Yongzhong, WU Rongling, WANG Ganchun. (2021). Simultaneous extraction and determination of oil and tea saponin contents in semi-trace kernel of Camellia oleifolia. *(油茶半微量种仁中油脂和茶皂素含量的同步提取测定)*. *Journal of Central South University of Forestry and Technology*, 41(05):133-141.

[11] Rao Honghui, Huang Dengsheng, Wang Yulong, Chen Bin, Liu Muhua. (2019). Design and Experiment of Hydraulic-driven Camellia Fruit Picking Machine. *(液压驱动式油茶果采摘机设计与试验)*. *Transactions of the Chinese Society for Agricultural Machinery*, 50(5):133-139+147.

[12] Rao Honghui, Zhang Liyong, Huang Dengsheng, Chen Bin, Liu Muhua. (2018). Design and Test of Motor-driven Picking Actuator of Camellia Fruit with Rotate Rubber Roller. *(电动胶辊旋转式油茶果采摘执行器设计与试验)*. *Transactions of the Chinese Society for Agricultural Machinery*, 49(9):115-121.

[13] Sargent, S.A., Takeda, F., Williamson, J.G., Berry, A.D. (2020). Harvest of Southern Highbush Blueberry with a Modified, Over-The-Row Mechanical Harvester: Use of Handheld Shakers and Soft Catch Surfaces. *Agriculture*, 10, 4. https://doi.org/10.3390/agriculture10010004

[14] Wang, W.Z., Lu, H.Z., Zhang, S.M., Yang, Z. (2019). Damage caused by multiple impacts of litchi fruits during vibration harvesting. *Computers and Electronics in Agriculture*, 162,732–738. https://doi.org/10.1016/j.compag.2019.04.037

[15] Wu Delin, Li Chao, Cao Chengmao, Fan Erbo, Wang Qi. (2020). Analysis and experiment of the operation process of branch-shaking type camellia oleifera fruit picking device. *(摇枝式油茶果采摘装置作业过程分析与试验)*. *Transactions of the Chinese Society of Agricultural Engineering*, 36(10):56-62.

[16] Wu Delin, Fu Liqiang, Cao Chengmao, Li Chao, Xu Yanping, Ding Da. (2020). Design and Experiment of Shaking-branch Fruit Picking Machine for Camellia Fruit. *(摇枝式油茶果采摘机设计与试验)*. *Transactions of the Chinese Society for Agricultural Machinery*, 2020,51(11):176-182,195.

[17] Zhang, Z., Igathinathane, C., Li, J., Cen, H., Lu, Y., Flores, P. (2020). Technology progress in mechanical harvest of fresh market apples. *Computers and Electronics in Agriculture*, 175, 105606. https://doi.org/10.1016/j.compag.2020.105606

[18] Zhang Liwei, Wang Liaowei. (2021). Development status and prospect of China oil tea industry. *(我国油茶产业的发展现状与展望)*. *China Oils and Fats*, 46(6):6-9+27.

AN IMPROVED YOLOV4 METHOD FOR RAPID DETECTION OF WHEAT EARS IN THE FIELD
/
一种改进型YOLOv4的田间麦穗快速检测方法

Zongwei JIA *[1)], Yi SHAO [2)], Yijie HOU [1)], ChenYu ZHAO [1)], ZhiChuan WANG [1)], Yiming HOU [3)], Jinpeng QIN [1)][1]
[1)] College of Information Science and Engineering, Shanxi Agricultural University, Taigu / China
[2)] School of Software, Shanxi Agricultural University, Taigu / China
[3)] School of hydraulic and Ecological Engineering, Nanchang Institute of Technology, Nanchang / China
Tel:13835441286; E-mail: jiazw@sxau.edu.cn
DOI: https://doi.org/10.35633/inmateh-69-17

Keywords: *Field wheat ears, MobileNet, Deep separable convolution, Alpha*

ABSTRACT
The automatic detection of wheat ears in the field has important scientific research value in yield estimation, gene character expression and seed screening. The manual counting method of wheat ears commonly used by breeding experts has some problems, such as low efficiency and high influence of subjective factors. In order to accurately detect the number of wheat ears in the field, based on MobileNet series network model, deep separable convolution module and alpha channel technology, the YOLOv4 model is reconstructed and successfully applied to the task of wheat ear yield estimation in the field. The model can adapt to the accurate recognition and counting of wheat ear images in different light, viewing angle and growth period. At the same time, the model volume with different alpha parameters is more suitable for mobile terminal deployment. The results show that the parameters of the improved YOLOv4 model are five times smaller than the original model, the average detection accuracy is 76.45%, and the detection speed FPS is two times higher than the original model, which provides accurate technical support for rapid yield estimation of wheat in the field.

摘要
田间麦穗的自动检测在产量估计、基因性状表达及种子筛选等方面都具有较为重要的科学研究价值，育种专家常用的麦穗人工计数方法存在效率低，主观因素影响较高等问题。为了精确检测田间麦穗数量，本文基于MobileNet系列网络模型，深度可分离卷积模块及Alpha通道等技术，重构了YOLOv4模型并成功应用到田间麦穗估产任务上，模型能够适应不同光照，视角，不同生长时期麦穗图像的准确识别和计数，同时采用不同Alpha参数的模型体积更加适应移动终端部署。结果表明，改进型YOLOv4模型参数量较原始模型体积缩小了5倍，平均检测精度达76.45%，检测速度FPS比原模型提升了2倍，为田间小麦快速估产提供准确的技术支撑。

INTRODUCTION
As one of the important food crops in the world, wheat has an annual output of 700 million tons *(http://faostat3.fao.org/faostat-gateway/go/to/browse/Q/QC/E)*. With the global climate change, natural disasters, regional economic fluctuations and other factors, the global food demand and price are increasing year by year, and the food crisis facing mankind is becoming more and more serious. This poses a higher challenge to agricultural breeding experts. Human beings need more cold resistant and high yield crop varieties to increase crop yield and improve crop tolerance to biological and environmental stresses. In order to find new varieties with high yield and stress tolerance, many breeding experts increasingly rely on high-throughput phenotypic technology to measure different crop traits, so as to understand the response and adaptability of crops to the surrounding environment, hoping to improve crop yield and quality. The phenotypic development technology of high-throughput images has been experienced for nearly a decade. In the early stage, it was mostly through special laboratories or greenhouses. *Li et al., (2017),* proposed a method to detect, count and measure the panicles of plants under the automatic control environment. *Bi et al. (2010)* and *Bi et al. (2011)* measured the different morphological characteristics of potted plants through the plant imaging device in the special laboratory, but the effect of such potted plants on water and nutrient absorption is greatly affected by the laboratory environment.

[1] *Zongwei Jia*, A.P. M.; Yi Shao, M. Stud.; Yijie Hou, M. Stud.; Chenyu Zhao, M. Stud.; Zhichuan Wang, M. Stud.; Yiming Hou, M. Stud; Jinpeng Qin, M. Stud.*

The results are quite different from the field natural environment data. In recent years, a series of large-scale plant phenotype image capture systems *(Perez-Sanz et al., 2017; Araus et al., 2014; Montes et al., 2007)*, UAVs *(Holman et al., 2016; Khan et al., 2018; Shi et al., 2016; Madec et al., 2017)* and satellite remote sensing images *(Azzari et al., 2015; Lobell et al., 2015)* have emerged. These methods can capture a wide range of crop phenotype information, but most of them can only carry out rough statistical information, such as average canopy coverage and average canopy color characteristics. It is worth noting that the field situation is often affected by the environment such as weather, light and wind speed, which brings great difficulties to image acquisition and image analysis algorithms. In order to adapt to the changing experimental conditions and improve the robustness of the algorithm, researchers usually need to manually analyze a large amount of data.

In this paper, tripod and single RGB camera are used to obtain real field crop images, which can capture high-resolution crop phenotype images. At the same time, the imaging device is simple, easy to operate and cost-effective, which is also convenient for the rapid implementation of breeding experiments of various scientific research groups. The challenge of this paper is how to extract quantitative information from these high-resolution images, mainly the number and density of wheat ears. The field data acquisition perspective of this paper selects oblique top photography instead of the common head up angle photography. Under the oblique angle, more phenotypic information can be obtained, involving the texture, color, shape and other information of wheat ears. These traits can provide data support for the application of wheat phenotype, such as ear count, ear area, ear texture, disease monitoring, yield estimation and so on. Using a single RGB image to obtain data and study the phenotype of machine vision technology has been favored by most breeders.

Fernandez-Gallego et al. (2018) used RGB camera to obtain the image from the head up angle of the top of the plant canopy, and then processed it with Laplace operator and median filter algorithm to identify the local maximum as wheat ears, with an accuracy of 92%, but for wheat ears in different growth stages, the algorithm recognition rate is quite different. *Alharbi et al. (2018)* used Gabor filter, principal component analysis and K-means clustering technology, and the average recognition rate of wheat ear is 90.7%. However, this method is seriously limited by ear density, ear and straw color, texture and ear angle. *Zhou et al. (2018)* et al. used multispectral cameras to collect data and used the improved maximum entropy segmentation algorithm to identify wheat ears in the field, which achieved good results when the wheat ear density and wheat ear occlusion were small.

In recent years, deep learning is gradually surpassing the previous image analysis and machine learning methods, and has brought significant changes in the field of plant phenotype analysis, especially the rapid application of convolutional neural network in image analysis tasks, such as in agricultural crop organ detection tasks based on target detection models such as YOLO-v3 *(Gao et al., 2019)*, mask RCNN, Alex net *(Khan et al., 2018)*, YOLO-v4 *(Gong et al., 2020)*. Extensive research has been carried out to solve agricultural science problems such as plant leaf classification *(Wilf et al., 2016)*, root structure analysis *(Kumar et al., 2014; Kumar et al., 2015)*, plant stress degree measurement *(Singh et al., 2016)*, determination of crop growth period *(Sadeghi-Tehran et al., 2017)*. This paper presents a depth learning model designed to quickly detect and count the number of wheat ears in the field wheat ear dense image. This method relies on the wheat ear image training data set manually marked with rectangular box, and outputs a complete boundary box position and size information to detect the number of wheat ears in the unit area, so as to realize wheat yield estimation. Field wheat yield estimation is an important data in wheat breeding. The combination of deep learning theory and field wheat ear counting task has strong application value and practical significance.

MATERIAL AND METHODS

DATA ACQUISITION AND PREPROCESSING

Data sources

The experimental wheat ear data in this paper are from the global wheat target detection competition (gwhd)*(https://www.kaggle.com/c/global-wheat-detection.)* and the wheat experimental base of Shanxi Agricultural University (sxau_wheat). The images of the sxau_wheat dataset are all wheat from April to June. At this time, the wheat ears are relatively full, most of them are still in an upright state, and the color is more prominent. Finally, 11 wheat ear image subsets were obtained, a total of 3487, with a resolution of 1024 × 1024 field wheat ear image.

Data enhancement

In order to better improve the generalization ability and robustness of the model, data enhancement on the original data set is performed, which is divided into offline enhancement and online enhancement.

1) For offline enhancement, set the random chromaticity interval of wheat ear image as (0.4-2.6), contrast interval as (0.6-1.6) and sharpness change interval as (0.4-4.0) for enhancement, and randomly apply enhancement operations such as salt and pepper noise, Gaussian blur, rotation, horizontal flip, vertical flip and zoom. Fig. 1 shows the comparison of enhancement effect of wheat ear data.

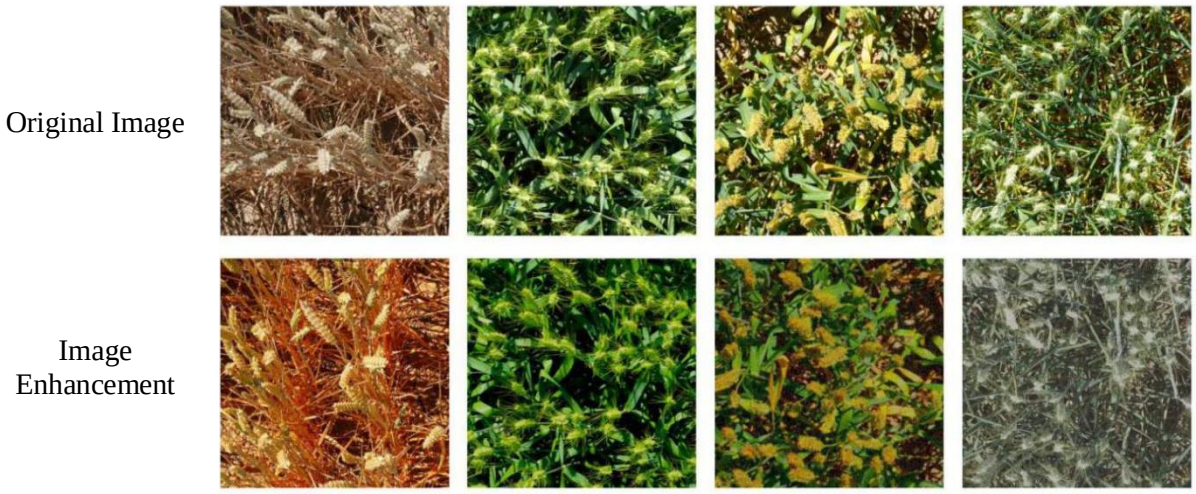


Fig. 1 - Contrast Map of Wheat Spike Image Enhancement Effect

2) Online image enhancement is carried out by turning, brightness adjustment, contrast, random clipping and scale transformation. In order to take into account the corresponding changes of image scale transformation and image file and annotation file after random clipping, a random online preprocessing function get for real-time data enhancement is designed in this get_random_data, through the online enhancement before each epoch to further improve the robustness of the model. Fig. 2 shows an example of online enhancement of wheat ear image.

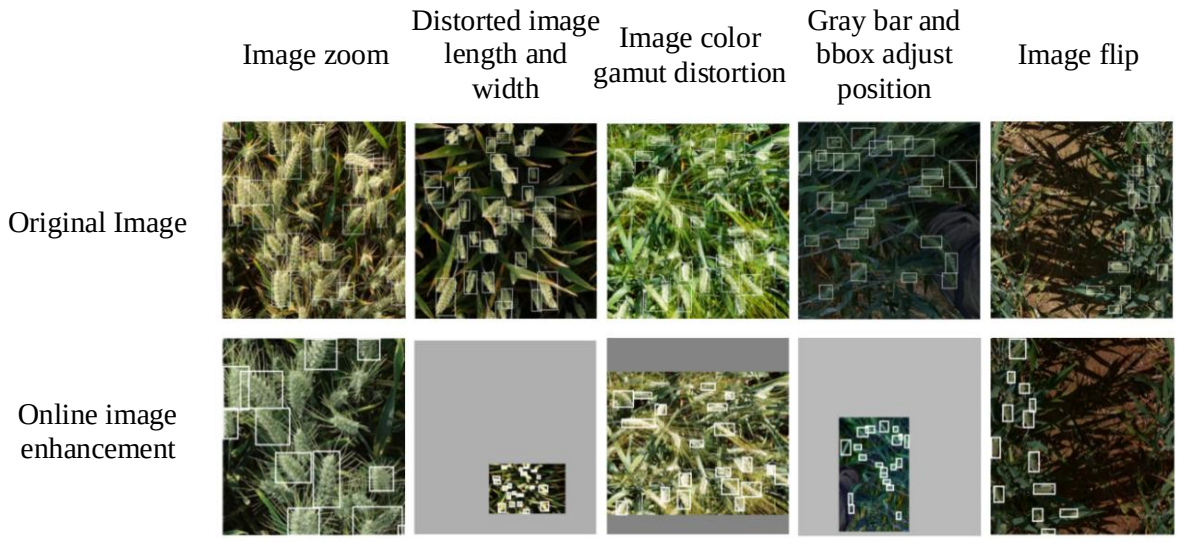


Fig. 2 - Example of Online Enhancement of Wheat Spike Image

OPTIMIZATION MODEL CONSTRUCTION

Backbone feature extraction and network replacement

YOLOv4 is one of the current YOLO series models with high accuracy, but its backbone feature extraction network CSPdarknet53 has the characteristics of large amount of parameters and slow model convergence. In this paper, the MobileNet series network is selected to replace the original CSPdarknet53 network *(Howard et al., 2017)*, and the specific selection of Mobilenetv1, Mobilenetv2 Mobilenetv3 is one of the three models to obtain effective features. The shape sizes of the three effective feature layers feat1, feat2 and feat3 corresponding to the three models are shown in Table 1.

Table 1

Effective Feature Sizes Corresponding to Different Replacement Models

Model	Feat1 shape	Feat2 shape	Feat3 shape
MobileNetV1	(52, 52, 256)	(26, 26, 512)	(13, 13, 1024)
MobileNetV2	(52, 52, 32)	(26, 26, 92)	(13, 13, 320)
MobileNetV3	(52, 52, 40)	(26, 26, 112)	(13, 13, 160)

MobileNet series models are selected as the backbone feature extraction network to replace CSP-Darknet53 network. The reconstructed models are named mnv1-YOLOv4, mnv2-YOLOv4 and mnv3-YOLOv4 respectively.

At this time, the replacement of the YOLOv4 backbone feature extraction network is completed, as shown in Table 2. After analyzing the size of the replaced model parameters, it can be found that the number of model parameters is reduced by nearly 30% compared with the original YOLOv4 model, effectively improving the detection speed of the model.

Table 2

Number of Model Parameters after Backbone Network Replacement

Model name	Parameter quantity
YOLOv4	64,429,405
MNV1-YOLOv4	41,005,757
MNV2-YOLOv4	39,124,541
MNV3-YOLOv4	40,043,389

PANet enhances feature extraction and network optimization

For the PANet enhanced feature extraction network, its parameters are mainly concentrated on many ordinary 3 × 3 convolution. If these ordinary 3 × 3 convolution can be modified, the parameter quantity and volume of the whole model can be greatly reduced.

In this paper, the deep separable convolution block *(Sandler et al., 2018)* in the MobileNet network is used to replace the ordinary 3 used in the enhanced feature extraction network PANet in the original YOLOv4 × 3, the overall parameters of the model are further reduced, and the enhanced extraction of image edge features by the model is also improved. At this time, the YOLOv4 network structure after two-step optimization is shown in Figure 3.

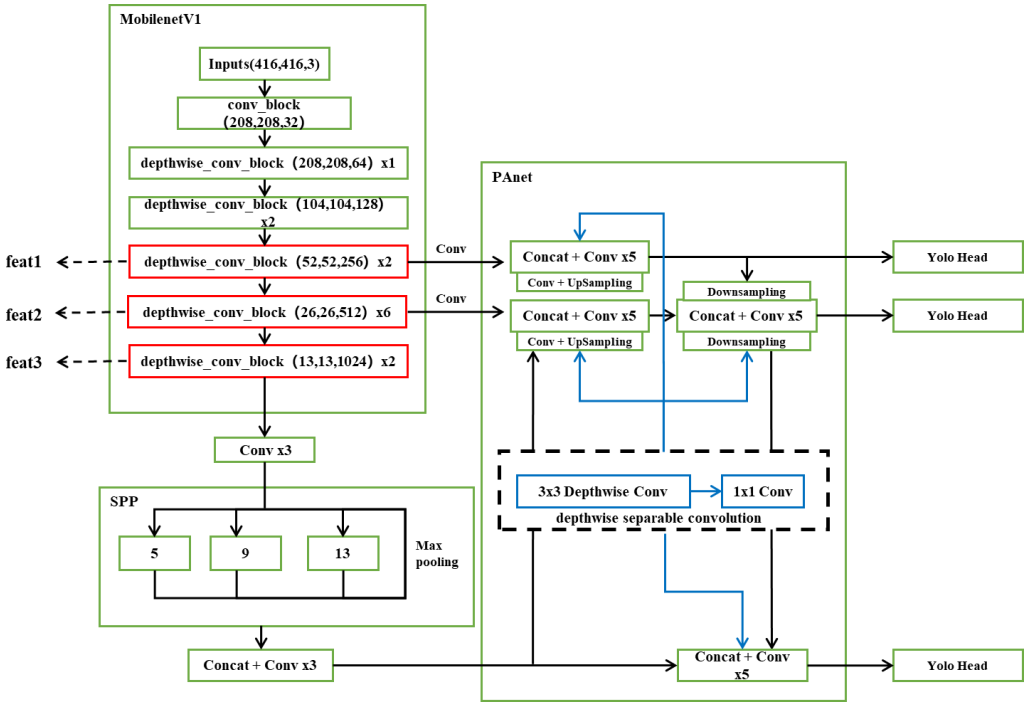


Fig.3 - Optimized YOLOV4 Network Structure

As shown in Table 3, by comparing and analyzing the parameters of the optimized PANet model, it can be seen intuitively that the parameters of the optimized PANet model are nearly 70% less than the total parameters of the model after the backbone feature extraction network is replaced, which basically meets the deployment requirements of mobile devices.

Table 3

Parameter Quantities after PANet Model Optimization

Model name	Model parameters after backbone network replacement	Model parameters after optimizing PANet
MNV1-YOLOv4	41,005,757	12,754,109
MNV2-YOLOv4	39,124,541	10,872,893
MNV3-YOLOv4	40,043,389	11,791,741

Alpha parameter channel adjustment

In order to further reduce the volume of the model, this paper modifies the number of channels by adjusting the alpha parameter value, and sets the alpha parameters for the number of channels such as 128, 256, 512 and 1024 in the model, replacing (128 * alpha) with 128 channels, replacing (256 * alpha) with 256 channels, replacing (512 * alpha) with 512 channels and replacing (1024 * alpha) with 1024 channels to complete the replacement operation. Next, you can directly set and change the alpha parameter according to your needs. The smaller the alpha parameter setting, the fewer channels of the whole model will be.

Through the replacement of backbone feature extraction network and PANet, strengthen the modification of feature extraction network and the application and setting of alpha parameters. Select the backbone feature extraction network to be used in mobilenetv1, mobilenetv2 and mobilenetv3, which is represented by backbone parameters. The alpha parameter is 1 by default (setting the alpha parameter to 1 means that the number of channels of the whole model has not been adjusted). The optional range is set to 0.25, 0.5, 0.75 and 1.0. Continuous comparison is made within this range. The comparative analysis of the parameters of the optimized and improved model is shown in Table 3. The total parameters of the original YOLOv4 model are 64429405. Through the reconstruction and optimization of the YOLOv4 model, the changes of the parameters of the whole model are shown in Table 4.

Table 4

Comparative Analysis of the Number of Model Parameters after Improvement and Optimization

Model name	Model parameters after backbone network replacement	Model parameter quantity after optimizing PANet (Alpha parameter is 1.0 by default)	Model parameter quantity with Alpha parameter = 0.75	Model parameter quantity with Alpha parameter = 0.5	Model parameter quantity with Alpha parameter = 0.25
MNV1-YOLOv4	41005757	12754109	7299789	3356125	680381
MNV2-YOLOv4	39124541	10872893	6257773	2370541	476568
MNV3-YOLOv4	40043389	11791741	6315309	2823754	568156

Evaluating indicator

For the wheat ear detection model, the most important is the AP value, FPS and the size of model parameters. The AP value mainly reflects the relationship between the accuracy and recall of the model. The higher the AP value, the better the overall detection effect of the model. FPS represents the image detection speed, and the model parameter refers to the size of the parameters in the internal network of the model.

(1) AP (average precision) and PR curve

Because the object category detected in the whole experiment is only wheat, mAP is not used as an index in the model test effect, but AP value is used to measure the performance of target detection algorithm. AP value refers to the average accuracy rate of a certain category. AP value is the combination of different precision and recall points. The larger the area under the PR curve, the larger the AP value, and the higher the average accuracy rate of the model, the better the performance of the model and the better the effect of the model in detecting wheat ears.

AP value is defined as equation (1).

$$AP = \int_0^1 P(R)dR = \sum_{k=0}^{n} P(k)\Delta R(k) \quad (1)$$

(2) TP and FP

TP is used to represent the number of positive samples predicted by the model and actually positive samples, and FP is used to represent the number of positive samples predicted by the model and actually negative samples.

(3) FPS (frames per second) image detection speed

FPS simply means that it can detect the number of pictures in one second. FPS can well evaluate the real-time performance of model detection, in seconds. Generally, the speed is measured by the number of frames of input video processed in one second. The higher the FPS, the better the real-time performance of the trained model.

(4) Model size and parameter quantity

The unit of model size is usually expressed in megabytes (MB), which is also one of the important factors of wheat ear target detection and evaluation indicators. The target detection model includes backbone network architecture information, optimization information and parameter information. If the model is too large to affect the portability of transplantation, the unit of parameter is usually expressed in "pieces".

TRAINING AND EVALUATION

The field wheat ear enhancement data set selected in this paper has a total of 5632 wheat ear images, all of which are labeled with labelimg to generate a VOC format data set *(Everingham et al., 2010)* , in which the number of bounding box wheat ears is 242309.

The data set is divided into training set, test set and verification set according to 8:1:1, which are 4505, 563 and 564 respectively. The wheat ear detection model was trained and tested on NVIDIA geforce RTX 2080 Ti GPU.

Model training

Set the number of iterative training to 100 rounds, of which the first 50 rounds are frozen training. Freeze some features to extract the weight of the network, so that the network weight of the frozen part is not updated, and other parts of the network are trained first. After 50 rounds of thawing, the network layer to be trained shall be trained. Freeze the number of pictures entered in each training batch_size is set to 8 and the learning rate is 1e-3. Unfreeze training number of pictures input each time batch_size is set to 6 and the learning rate is 5e-5. The training learning rate adopts the adjustment strategy of linear attenuation, that is, if the loss value does not decrease after 5 epochs, the learning rate becomes one-half of the original.

During the training process, the model is constantly updated and adjusted, and the parameters are set to save the best model every 5 epochs. Finally, after continuous iterative training, the model structure and parameters are saved to obtain the wheat ear real-time detection model. If the loss value of the model does not decrease under 10 consecutive epochs, it indicates that the model has fitted the data, and the model will automatically stop training.

RESULTS AND ANALYSIS

It can be seen from Figure 4 that the five models can detect wheat ears in different growth periods, varieties, light and dark, and the confidence values are not different. When the alpha coefficient is adjusted to 0.25, the effect of the prediction model is the worst, and there are many missed errors, which is directly due to the lack of model parameters.

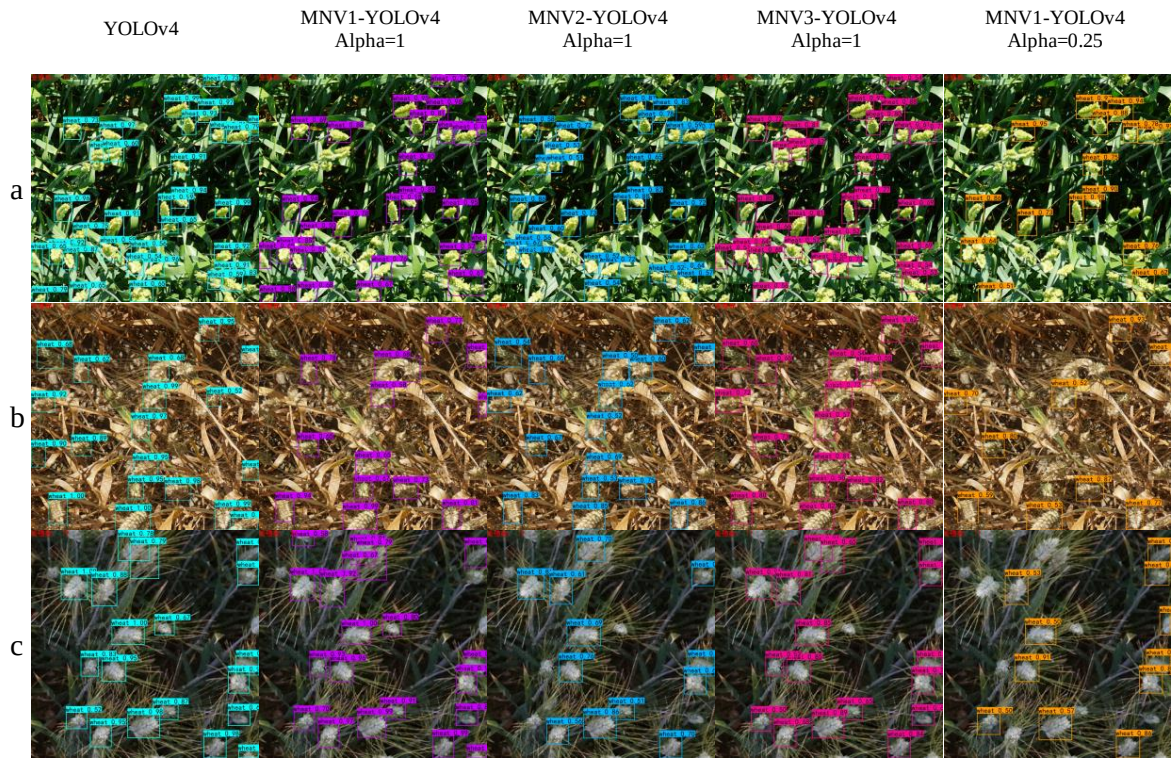


Fig.4 - Some Forecast Results

Figure a shows the test results of wheat ears under insufficient light; Figure b shows the test results of wheat ears under sufficient light; Figure c shows the detection results of dark light and only part of wheat ears in the image

Table 5

Comparative Analysis of Wheat Spike Detection Models

Target detection Model	Average accuracy AP（%）	Image detection speed FPS （Frame/s）	Model size （MB）	Model parameter quantity（PCs.）
YOLOv4	76.74	13.03	751.2	64,429,405
MNV1-YOLOv4-Alpha=1	74.83	22.52	145.1	12,754,109
MNV2-YOLOv4-Alpha=1	73.65	23.64	110.9	10,872,893
MNV3-YOLOv4-Alpha=1	76.45	24.82	124.2	11,791,741
MNV1-YOLOv4-Alpha=0.25	62.8	44.69	10.4	680,381

It can be seen from table 5 that the AP value of YOLOv4 detection model is higher than that of the improved model, which is 1.91, 3.09 and 0.29 percentage points higher than mnv1-YOLOv4-alpha = 1, mnv2-YOLOv4-alpha = 1, mnv3-YOLOv4-alpha = 1 and mnv1-YOLOv4-alpha = 0.25 respectively.

On the premise of sacrificing part of the accuracy, the detection speed and model parameters of the model have been highly optimized and improved. Mnv1-YOLOv4-alpha = 0.25 model pursues the ultimate detection speed and minimal volume, resulting in low AP of the model, but it provides a reference for the transplantation of the model to embedded device terminals in the future.

The optimized model has been greatly optimized in terms of detection speed and model volume, and the accuracy sacrifice is small.

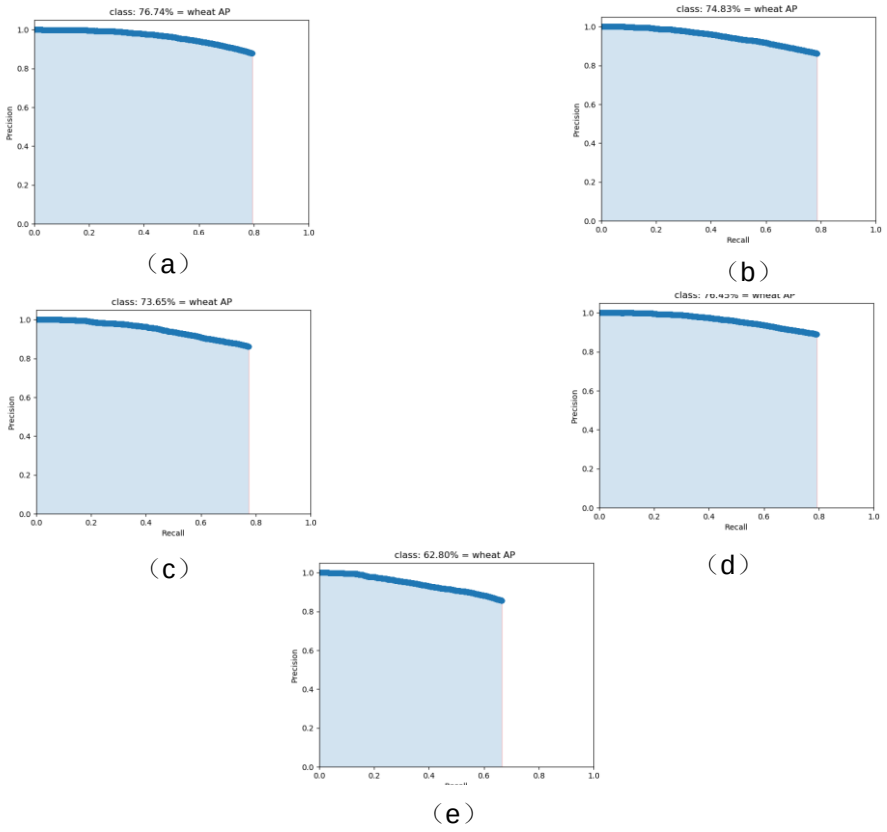


Fig. 5 - P-R Curve

Fig. 5 (a-e) shows the P-R curves of YOLOv4, MNV1-YOLOv4-Alpha = 1, MNV2-YOLOv4-Alpha = 1, MNV3-YOLOv4-Alpha = 1 and MNV1-YOLOv4-Alpha = 0.25. The confidence of the model is set to 0.5 and the IOU is set to 0.3 to obtain the AP values of five wheat ear detection models.

Figure 6 shows the TP and FP results of five wheat ear detection models, which are obtained from 563 pictures in the test set. The number of frames manually labeled in 563 pictures is 13399, (a-e) respectively represents the TP / FP results of five models: YOLOv4, MNV1-YOLOv4-Alpha = 1, MNV2-YOLO4-Alpha = 1, MNV3-YOLOv4-Alpha = 1 and MNV1-YOLOv4-Alpha = 0.25.

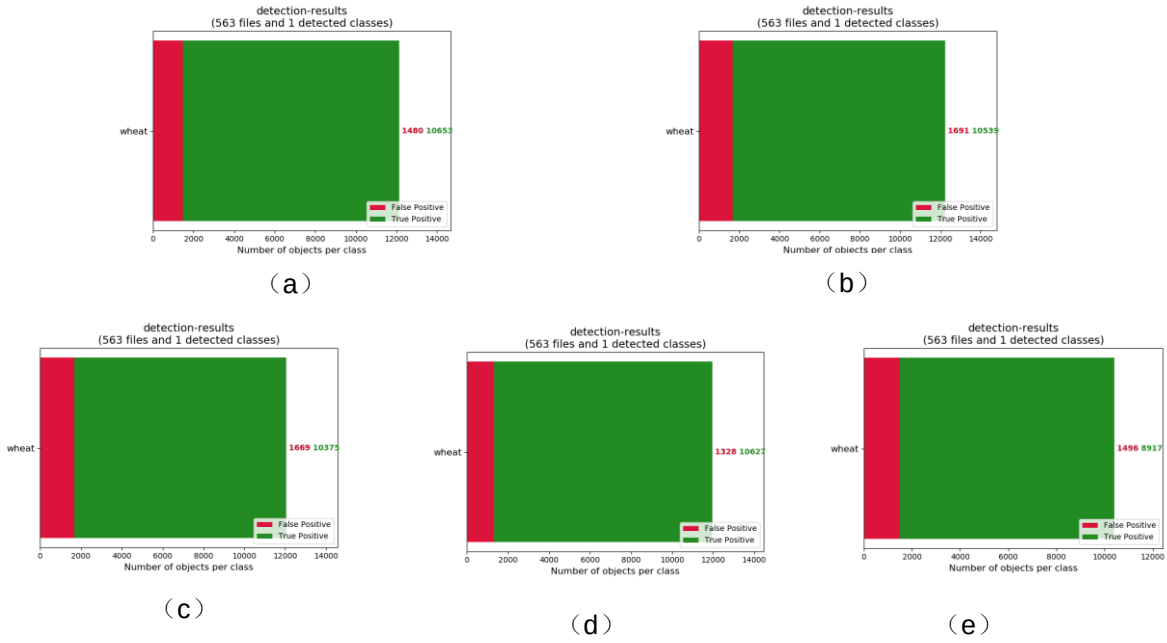


Fig. 6 - TP/FP of Wheat Spike Detection Model

It can be concluded from Fig.6 that except for figure (e), the TP values of other optimized models are similar, but the number of false detections of the model changes greatly. Among them, the number of false detections of mnv3-YOLOv4-alpha = 1 model is 152 less than that of the original YOLOv4 model, indicating that the performance of the optimized model has been effectively improved compared with the original YOLOv4 model.

CONCLUSIONS

In this paper, MobileNet series backbone network, deep separable convolution module and alpha channel number dynamic adjustment technology are used to improve and optimize the YOLOv4 model, and it is applied to the field wheat ear detection and counting task. When the detection accuracy is very close, the detection speed of the optimized detection model is increased by two times, and the volume of the model is reduced to one fifth. At the expense of small accuracy, the model can adapt to the rapid detection and counting tasks of wheat ears in the field under different illumination, angles and growth periods, provide support for agricultural breeding experts to estimate yield quickly and accurately, and provide possibility for the transplantation and deployment of mobile terminals.

ACKNOWLEDGEMENT

This research, titled ‘AN IMPROVED YOLOV4 METHOD FOR RAPID DETECTION OF WHEAT EARS IN THE FIELD’, was funded by Shanxi Province Basic Research Program (Free Exploration) Project(NO:202103021224149), Shanxi Province Postgraduate Education Teaching Reform Project (NO:2021YJJG087), Shanxi Province Educational Science "14th Five-Year Plan" Education Evaluation Special Project (NO:PJ-21001). The authors are grateful and honored to receive this support.

REFERENCES

[1] Alharbi N., Zhou J., Wang W., (2018), Automatic counting of wheat spikes from wheat growth images. In: *7th International Conference on Pattern Recognition Applications and Methods*, p. 346–355.

[2] Araus J.L., Cairns JE., (2014), Field high-throughput phenotyping: the new crop breeding frontier. *Trends Plant Sci*, 19(1):52–61.

[3] Azzari G., Lobell DB., (2015), Satellite estimates of crop area and maize yield in Zambia’s agricultural districts. In: *Proceedings of the AGU fall meeting*.

[4] Bi K., Jiang P., Li L., Shi B., Wang C., (2010), Non-destructive measurement of wheat spike characteristics based on morphological image processing. *Trans Chin Soc Agric Eng*, 26(12):212–6.

[5] Bi K, Jiang P., Wei T., Huang F., Wang C., (2011), The design of wheat variety BP classifier based on wheat ear feature. *Chin Agric Sci Bull*, 28(6):464–8.

[6] Everingham M., Van Gool L., Williams C K I., et al. (2010), The Pascal Visual Object Classes (VOC) challenge[J]. *International journal of computer vision*, 88(2): 303-338.

[7] Fernandez-Gallego JA., Kefauver SC., Gutiérrez NA., Nieto-Taladriz MT., Araus JL., (2018), Wheat ear counting in-field conditions: high throughput and low-cost approach using RGB images. *Plant Methods*, 14(1):22.

[8] Gong B., Ergu D., Cai Y., et al. (2020), Real-Time Detection for Wheat Head Applying Deep Neural Network[J]. *Sensors*, 21(1):191.

[9] Gao Y.P., (2019), Study on field wheat ear detection method based on depth neural network[D]. Beijing: *Master Thesis of Beijing Forestry University*.

[10] Holman FH., Riche AB., Michalski A., Castle M., Wooster MJ., Hawkesford MJ., (2016), High throughput field phenotyping of wheat plant height and growth rate in field plot trials using UAV based remote sensing. *Remote Sens*, 8(12):1031.

[11] Howard A.G., Zhu M., Chen B, et al. (2017), Mobilenets: Efficient convolutional neural networks for mobile vision applications[J]. arXiv preprint arXiv:1704.04861.

[12] Khan Z., Rahimi-Eichi V., Haefele S., et al. (2018), Estimation of vegetation indices for high-throughput phenotyping of wheat using aerial imaging[J]. *Plant Methods*, 14(1): 20.

[13] Kumar P., Cai J., Miklavcic SJ., (2015), A complete system for 3D reconstruction of roots for phenotypic analysis. *Adv Exp Med Biol*, 823:249–70.

[14] Kumar P., Huang C., Cai J., Miklavcic SJ., (2014), Root phenotyping by root tip detection and classification through statistical learning. *Plant Soil*, 380(1):193–209.

[15] Li Q, Cai J., Berger B., Okamoto M., Miklavcic SJ., (2017), Detecting spikes of wheat plants using neural networks with Laws texture energy. *Plant Methods*, 13(29046709):1–13.
[16] Lobell DB., Thau D., Seifert C., Engle E., Little B., (2015), A scalable satellite-based crop yield mapper. *Remote Sens Environ*, 164:324–33.
[17] Madec S., Baret F., deSolan B., Thomas S., Dutartre D., Jezequel S., Hemmerle M., Colombeau G., Comar A., (2017), High-throughput Phenotyping of Plant Height: Comparing Unmanned Aerial Vehicles and Ground LiDAR Estimates. *Front Plant Sci*, 8:2002.
[18] Montes JM., Melchinger AE., Reif JC., (2007), Novel throughput phenotyping platforms in plant genetic studies. *Trends Plant Sci*, 12(10):433–6.
[19] Perez-Sanz F., Navarro PJ., Egea-Cortines M., (2017), Plant phenomics: an overview of image acquisition technologies and image data analysis algorithms. *GigaScience*, 6(11):1–18.
[20] Sadeghi-Tehran P., Sabermanesh K., Virlet N., Hawkesford MJ., (2017), Automated method to determine two critical growth stages of wheat: heading and flowering. *Front Plant Sci*, 8(252):1–14.
[21] Sandler M., Howard A., Zhu M., et al. (2018), MobileNetV2: Inverted Residuals and Linear Bottlenecks[J]. *The IEEE Conference on Computer Vision and Pattern Recognition(CVPR)*, 4510-4520.
[22] Shi Y., Thomasson JA., Murray SC., Pugh NA, Rooney WL., Shafian S., Rajan N., Rouze G., Morgan CLS., Neely HL., (2016), Others: unmanned aerial vehicles for high-throughput phenotyping and agronomic research. *PLoS ONE*, 11(7):1–26.
[23] Singh A., Ganapathysubramanian B., Singh AK., Sarkar S., (2016), Machine learning for high-throughput stress phenotyping in plants. *Trends Plant Sci*, 21(2):110–24.
[24] Wilf P., Zhang S., Chikkerur S., Little SA., Wing SL., Terre T., (2016), Computer vision cracks the leaf code. *Proc Natl Acad Sci*, 113:3305–10.
[25] Zhou C., Liang D., Yang X., Xu B., Yang G., (2018), Recognition of wheat spike from field based phenotype platform using multi-sensor fusion and improved maximum entropy segmentation algorithms. *Remote Sens*, 10(2):246.
[26] *http://faostat3.fao.org/faostat-gateway/go/to/browse/Q/QC/E*
[27] *http://www.kaggle.com/c/global-wheat-detection*.

REAPER BLADE SYSTEM FOR HARVESTING SUNFLOWERS
/
НОЖОВА СИСТЕМА ЖАТКИ ДЛЯ ЗБИРАННЯ СОНЯШНИКУ

Olena NALOBINA [1)], Nazar VASYLCHUK [2)], Oleh BUNDZA [1)], Mykola HOLOTIUK [1)], PUTS Vitaliy [2)], Viktor MARTYNIUK [2)]

[1)]National University of Water and Environmental Engineering / Soborna str.11, Rivne, Ukraine;
[2)]Lutsk National Technical University / Lvivska str., 75, Lutsk, Ukraine
Tel: +380960825360; E-mail: o.z.bundza@nuwm.edu.ua

DOI: https://doi.org/10.35633/inmateh-69-18

Keywords: *header, sunflower, cutting, knife system, losses, cutting force*

ABSTRACT

The relevance of the study is due to the need to reduce the energy intensity of the process of cutting sunflower stalks by choosing a rational profile of knives. The research is based on a comparative analysis of experimental values of cutting forces for the proposed and manufactured design of the knife system and known knife systems. The studies have shown that the implementation of the retaining and main knives of the header in the form of a curved spiral of Archimedes allowed to reduce the cutting force. It was also found that the cutting force for the proposed design of the knife system, unlike other studied, practically does not change with the removal of the stem from the axis of rotation of the knives, which does not require an increase in energy costs for the cutting process.

РЕЗЮМЕ

Актуальність дослідження зумовлена необхідністю зменшення енергоємності процесу зрізання стебел соняшнику за рахунок вибору раціонального профілю ножів. Дослідження базуються на порівняльному аналізі експериментальних значень сил різання для запропонованої та виготовленої конструкції ножової системи та відомих ножових систем. Проведені дослідження довели, що виконання підпорного і основного ножів жатки у вигляді кривої спіралі Архімеда дозволило зменшити зусилля різання. Також встановлено, що сила різання для запропонованої конструкції ножової системи, на відміну від інших досліджуваних, практично не змінюється за умови віддалення стебла від осі обертання ножів що не потребує збільшення енергетичних витрат на здійснення процесу різання.

INTRODUCTION

World production of sunflower seeds is constantly growing. Ukraine, Russia, the European Union, and Argentina are the main seed-producing countries; Ukraine and Russia account for more than half of the world's sunflower seeds and almost 60% of oil production.

The high interest of agricultural companies in growing this crop can be explained by waste-free and, relatively, high profitability. Sunflower allows you to get not only oil but many related products - a protein-rich livestock feed, alcohol; potassium, and nitrate are extracted from sunflower ash; the flowers are used to make an extract that replaces quinine. Sunflower can also be used as a source of biodiesel, biogas, raw materials for the paper industry (*Kovacic D., Kralik D. et al., 2017; Perea-Moreno Manzano-Agugliaro, & Perea-Moreno, 2018; Pari Luigi, Latterini Francesco, Walter Stefanoni, 2020*).

In addition to being used as a source of oil, the plant remains of sunflower stalks, pre-shredded, are used to increase the content of organic matter in the soil (*Martens DA, Frankenberger WT, 1992*), as well as reducing the tightness of the soil surface (*Le Bissonnais and Arrouays, 1997*). In addition, the distribution of crushed remains of sunflower stalks in the field provides increased macroporosity and water infiltration (*Glab T., Kulig B., 2008*).

Scientists have also proven that grinding and mixing into the soil-plant waste (stubble) that remains after harvest in the field prevents erosion (*Gonulol E., Dalmis I.S. et al, 2009*).

Currently, after the passage of the combine with the reaper, quite strong sunflower stalks remain in the field, which complicates the preparation of the field for the next growing season (fig.1).



Fig. 1 - Sunflower stubble

Sunflower crop residues need to be shredded and incorporation into the soil after harvesting in order to decompose them quickly and prevent disease. At the same time, additional damage to the top layer of soil contributes to the development of water and wind erosion. Post-harvest treatment requires additional energy and human resources. In addition, it was found that additional mechanized tillage leads to deterioration of its nutrient content. Thus, in particular, Chinese scientists have found that the traditional mechanized system of agriculture will reduce the content of soil organic matter per year, on average, by 0.01–0.02% (*Honglei J, Chenglin L. et al., 2007*).

Post-harvest treatment involves the use of additional equipment. Most often used are disc harrows, toothed rotors, and cutters. The equipment is used after the harvest and this leads to additional costs of energy, material, and labour resources. All this prompted researchers to improve the design of sunflower headers in the direction of installing additional cutting-type working bodies for shredding sunflower stalks during the technological process of harvesting.

Dalmis, Kayisoglu et al., (2013), in their study proposed the installation under the reaper of a combine harvester shredder unit with knives. The introduction of this device allowed to grind the remnants of sunflower stalks.

The authors performed a number of experiments in the field using specially manufactured cutting modules equipped with flat and curved blades. The relationship between the number of cutting modules, the configuration of blades and the height of cutting stems, fuel consumption was investigated. A significant influence of blade configuration on fuel consumption was found.

Due to the high energy intensity of the cutting process, the study of the process of cutting crop stems and devices for its implementation is of great scientific interest. The theory of cutting with a knife blade was initiated by academician *V.P. Goryachkin, 1968*.

The author divides the process of cutting fibrous materials into two types: the first - the knife blade moves in the direction of the cut only in the direction normal to its edge; the second - at the same time it moves parallel to the edge. The first type of cutting is chopping, the second is sliding cutting. It is proved that sliding cutting occurs with a decrease in friction force, part of the force is transferred in the direction perpendicular to the direction of the cut. As a result, the knife blade enters the material more easily.

This theory is confirmed in the works of many authors: *Johnson P.C., Clementson C.L., 2012; Zhang C.L., Chen L.Q. et al, 2019; Song S., Zhou, H.; Xu L., et al, 2022; Daipeng Lu, Wei Wang et al, 2022*.

In particular *Zhang C.L., Chen L.Q. et al, 2019,* during experiments with rice stalks studied the effect of the sliding effect during cutting and the value of the cutting angle on the cutting energy. It is proved that the energy per unit area of the stem was the lowest when sliding cutting without a support blade, with a cutting angle of 45°.

Daipeng Lu, Wei Wang, et al, 2022, in the course of multifactorial orthogonal experiment and mathematical modeling established the factors that affect the cutting stress: sliding angle, cutting edge angle, cutting speed. It was found that the factor of greatest importance is the sliding angle.

The influence of sliding and cutting angles, as well as the parameters of plant material on the energy consumption of the cutting process and the cutting force was proved by *Wang, Y., Yang, Y. et al, 2020; Song S., Zhou H., Jia Z. et al, 2022*.

Analysis of studies of the process of harvesting sunflower and machines and mechanisms for its implementation, found that improvements in the design of reapers for harvesting sunflower are also carried out in the direction of reducing losses and damage to seeds (*Shaforostov V. D., Makarov S.S., Yelizarov P.A., 2018; Startswv A.S., 2017; Nalobina O.O., Vasylchuk N.V. and others., 2019; Liu Y., Luo C., Zong W., et al, 2021; Ali K.A.M., Zong W. et al.,2021; Ali K.A.M., Zong W. et al., 2022; Stepanenko S., Aneliak M. et al., 2022.*

In particular, this problem is solved by reducing the length of the segment of the stem, which together with the head falls on the auger for threshing (*Shaforostov V.D., Makarov S.S., Yelizarov P.A., 2018*). The authors propose the design of a four-row reaper in which sunflower plants are captured at a height equal to the minimum height of the location of the heads above ground level during the movement of the combine. This is done by installing the inlet of the dividers with hydraulic cylinders to the desired height. Due to such a high grip, the heads fall into the area of action of the threshing auger with a minimum length of the stem, which allows to increase the efficiency of threshing and reduces seed injuries.

The model of the sunflower harvester was developed by the authors to solve two problems: 1) reducing the height of the stubble; 2) reducing the length of the segment of the stem that comes with the head for threshing (*Nalobina O.O., Vasylchuk N.V., and others, 2019*).

According to the analysis of known studies in sunflower harvesters, the stems are cut to separate the sunflower heads from the stem for further transport to the main part of the combine and some models of modern reapers use additional knives for completion of the collection process.

Cutting plant materials during production processes is one of the most energy-intensive and complex technological operations. Most often, modern reapers use flat-rotating cutters with the traditional rectilinear shape of the knife blade profile. Such knives are characterized by ease of manufacture and subsequent maintenance. The disadvantage is the high energy consumption of the cutting process.

Given the above, the task of reducing the energy consumption of the cutting process by choosing a rational profile of knives for cutting sunflower stalks is relevant.

MATERIALS AND METHODS

At the beginning of the study, the possibility of reducing the energy consumption of the cutting process by developing a knife support cutting system was hypothesized. It is necessary to use a shape of the knife at which the sliding angle (the ratio of radial and tangential cutting force) will be the same along the entire length of the cut for any point of the knife with a curved edge profile.

As a result of analysing the known research directed on the substantiation of choosing an optimum profile of cutting knives (*Goriachkin V.P., 1958, Lvov D.V., 2009, Braginets M.V., 2013; Zhang C.L., Chen L.Q. et al, 2019; Daipeng Lu, Wei Wang et al, 2022*) it is proposed to execute a knife system consisting of a supporting knife and cutting knives made in the form of an Archimedes spiral. This design, according to the conceptual hypothesis of the research, will ensure the maximum quality of cutting and will minimize energy consumption throughout the cutting area of the stem for both the main and the support knife.

In order to test the accepted hypothesis, studies were conducted to determine the cutting forces for different configurations of knives: John Deer S690I and Massey Ferguson 1006 reapers; knife system made according to the recommendations of the founder of agricultural mechanics, Goryachkina V.P. (*Goryachkin V.P., 1968*) and the knife system proposed by the authors.

In the knife system, made according to the recommendations of *Goryachkin V.P. (1968),* (Fig. 2), the profile of the cutting knife is made in the form of an Archimedes spiral, which allows cutting by sliding along the entire length of the cut. Support knife 1 (Fig. 2) is made in the form of a concentric curve. This allows you to ensure complete cutting of the stem and also prevents the stem from slipping out from under the knives. To construct a curve of a cutting knife Goryachkin's technique will be used (*Goryachkin V.P., 1968*).

The optimal curve according to the author's research is the Archimedean spiral. The equation of such a spiral: $r = r_0 + A\Theta$, where r_0 initial knife radius, A- helix pitch, Θ - the polar flow (Fig. 2,a).

Cutting with such a knife occurs with sliding, and it is the Archimedean spiral that gives the same coefficient of sliding τ when turning the knife to any angle. Therefore, the energy intensity of cutting will be uniform along the entire length of the cut without maximum and minimum points, which allows the use of a lower power drive.

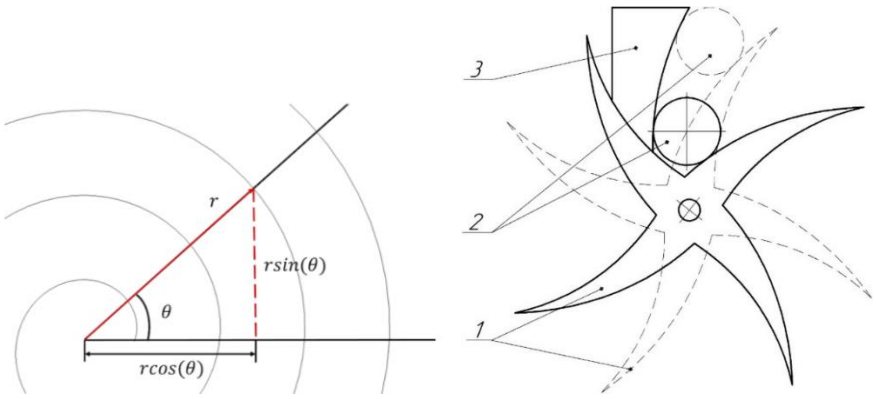


Fig. 2 - Scheme of the knife system according to Goryachkin's recommendations
1 - support knife, 2 - sunflower stalk, 3 - cutting knife

This design of the knife system has a drawback. As the distance from the cut to the axis of rotation of the knife increases, the total cutting angle decreases.

It is proposed to make a knife system in which the support knife serves not only to support the sunflower stalk but is fully used in the cutting process and also has the shape of an Archimedes spiral. The total cutting angle is 50° (Fig. 3).

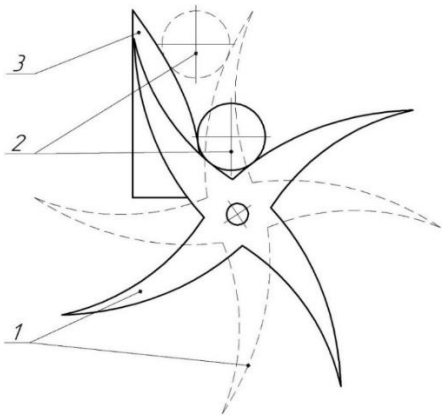


Fig. 3 – The proposed scheme of the knife system
1 - support knife, 2 - sunflower stalk, 3 - cutting knife

To compare the cutting efficiency of the selected knife system designs (John Deer S690I, Massey Ferguson 1006, Goryachkin knife system, and our proposed design), the total cutting force in each case was determined. Cutting forces (Fig. 4) were determined from experimental studies by measuring cutting angles α (fig.4), for stem diameters of 10, 20, 30, 40, and 50 mm and at a distance of 60, 80, 100, 115, and 125 mm from the axis of rotation of the knives. To make experimental studies, a laboratory setup was made (Fig. 4, a), which was equipped with knives corresponding to the knives of the above designs (Fig. 4, b shows a knife whose edge is made in the form of an Archimedean spiral)

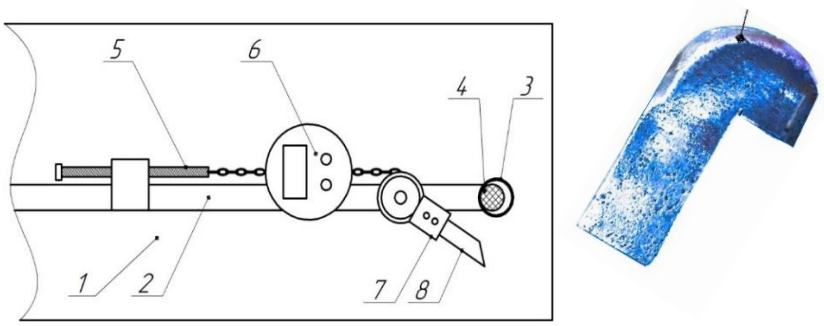


Fig. 4 - Study of the cutting force of the stem
a - scheme of the laboratory installation; b - knife, the edge of which is made in the form of an Archimedean spiral
1 - platform; 2 - frame; 3 - glass for installing the stem; 4 - stem; 5 - screw-nut transmission; 6 - dynamometer

Below is a diagram of the forces acting on the sunflower stalk during retaining cutting (Fig. 5) and diagrams for determining the cutting angles for the knives that were subject to the study (Figs. 6-8).

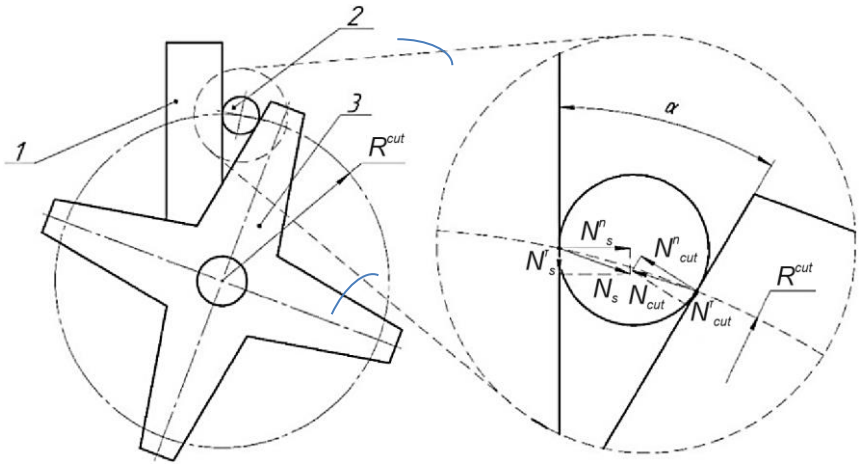


Fig. 5 - Scheme of forces acting on the sunflower stalk during support cutting:
1 - support knife, 2 - the stem, 3 - cutting knife, R^{cut} - distance from the axis of the knife to the axis of the stem, N^n_{cut}, N^τ_{cut}, N_{cut}, N^n_s, N^τ_s, N_s - respectively normal, tangential, equivalent cutting forces of the cutting and support knife

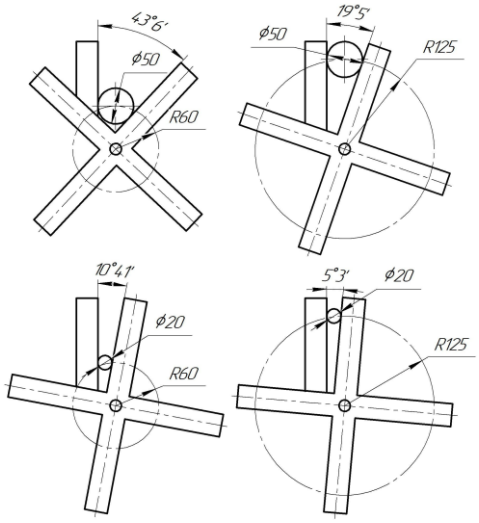


Fig. 6 - Diagram for determining the cutting angles for John Deer S690I reaper blades

We see that with increasing distance from the axis of rotation of the knives to the cutting point and increasing the diameter of the stem, the angle between the knives decreases, which will increase the total cutting force.

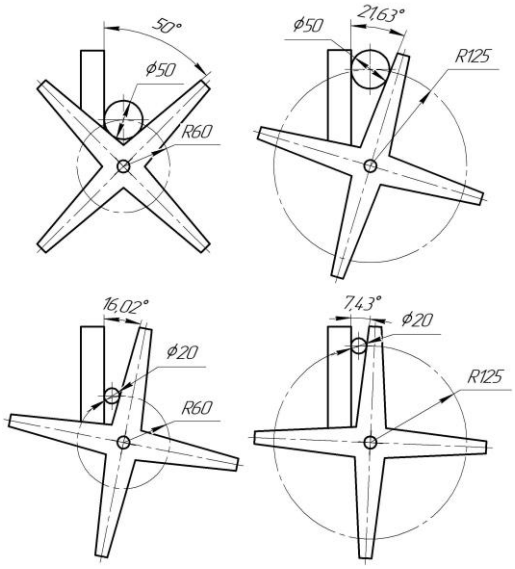


Fig. 7 - Diagram for determining the cutting angles for Massey Ferguson 1006 reaper blades

The pattern of reducing the angle between the blades from the stem diameter and the distance from the centre of the blades to the cutting point is maintained for Massey Ferguson 1006 reaper blades. However, the value and the law itself is slightly different from similar values for John Deer S690I cutterbars.

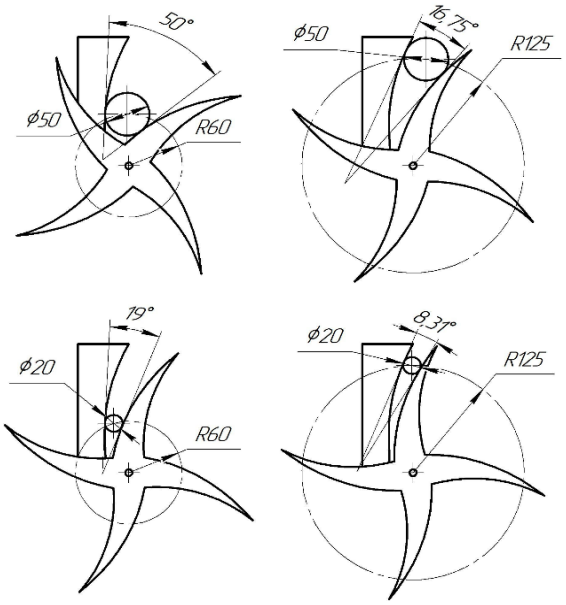


Fig. 8 – Scheme for determining the cutting angles for knives according to Goryachkin's scheme

The angles between the cutting and support knives, than in the similar positions for the knives Massey Ferguson 1006 and John Deer S690I, but they are smaller than for the knife system of our proposed design (Fig. 8).

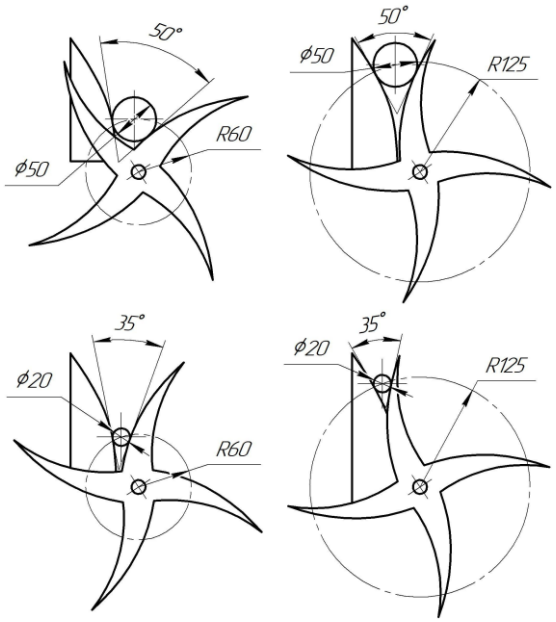


Fig. 9 - Scheme for determining the cutting angles for knives

For the experiments, stems were selected in the field during the period when 14% of plants with yellow heads remained in the field (which corresponds to the agrotechnical requirements for harvesting).

RESULTS

As a result of the research, the values of the cutting force were obtained under the condition of changing the diameters of the stem and the distance from the axis of rotation of the knives. Depending on the cutting angles, the values of the tangent and normal components and the resulting one for all cases were obtained. The average values of cutting forces are given in Table 1.

Table 1

Cutting force values (N)

Distance from the axis of rotation to the centre of the stalk (mm)	Stalk diameter (mm)				
	50	40	30	20	10
The Massey Ferguson 1006 system					
60	7282	4987	2918	1303	332
80	8057	5285	2995	1315	332
100	8367	5403	3028	1320	336
115	8494	5452	3042	1322	338
125	8553	5475	3048	1323	338
The John Deer S690I knife system					
60	7674	5170	2980	1317	333
80	8232	5373	3023	1322	333
100	8482	5458	3049	1335	338
115	8571	5487	3155	1339	340
125	8624	5512	3169	1342	340
For Goryachkin knife system					
60	7282	5369	2952	1313	331
80	8126	5373	2991	1329	332
100	8325	5422	3022	1332	332
115	8583	5468	3049	1422	338
125	8677	5496	3052	1422	338
For the proposed blade system					
60	7182	4666	2687	1209	312
80	7182	4666	2687	1209	312
100	7182	4666	2687	1209	312
115	7184	4667	2687	1209	312
125	7184	4667	2687	1209	312

From the data presented in tab. 1 we can see that the smallest cutting force was obtained by using the proposed knife system; in addition, its value remains virtually unchanged with the removal of the stem from the axis of rotation of the knife, which does not require an increase in energy for the cutting process.

Below, figs. 10-12 show the graphical dependences of the cutting force on the diameter of the sunflower stem and the distance from the knife rotation to the stem axis: for the proposed knife system of normal and tangential components of the main knife cutting force and the distance from the axis of rotation of the knife system for a stem diameter of 40 mm and the cutting force depending on the diameter of the sunflower stem and the distance from the knife rotation to the stem axis.

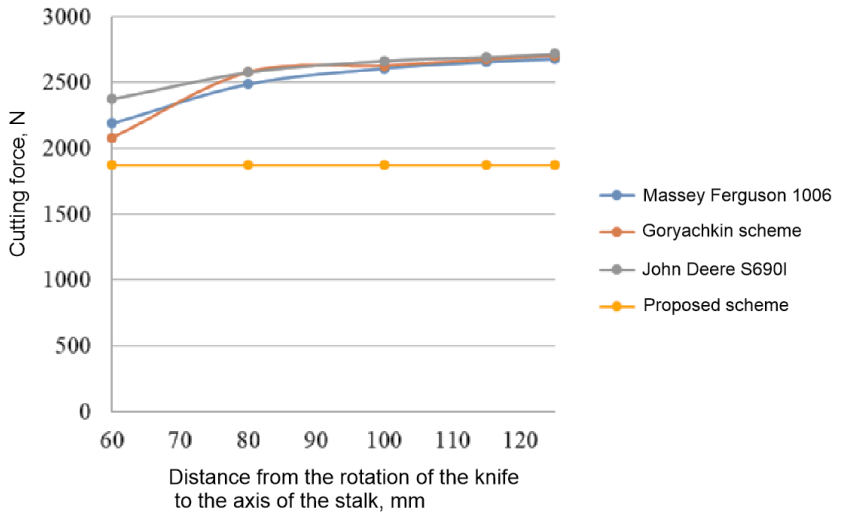


Fig. 10 - Dependence of the normal component of the main knife cutting force and the distance from the axis of rotation of the knife system for a stem diameter of 40 mm

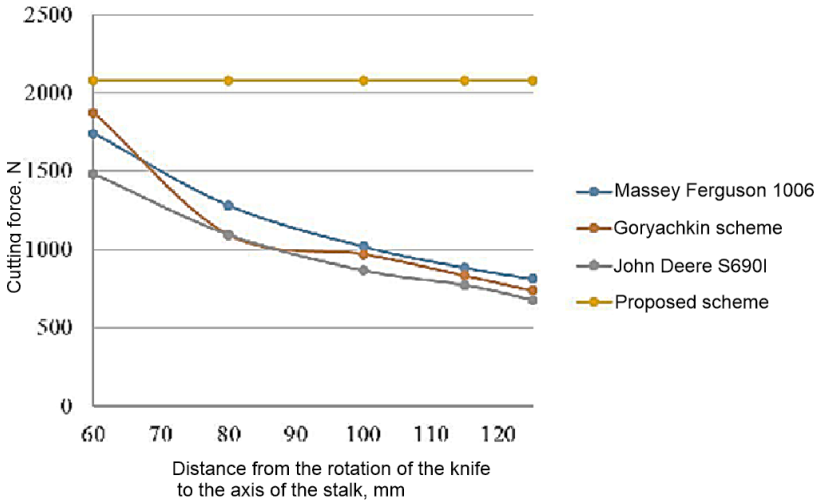


Fig. 11 - Dependence of the tangential component of the main knife cutting force and the distance from the axis of rotation of the knife system for a stem diameter of 40 mm

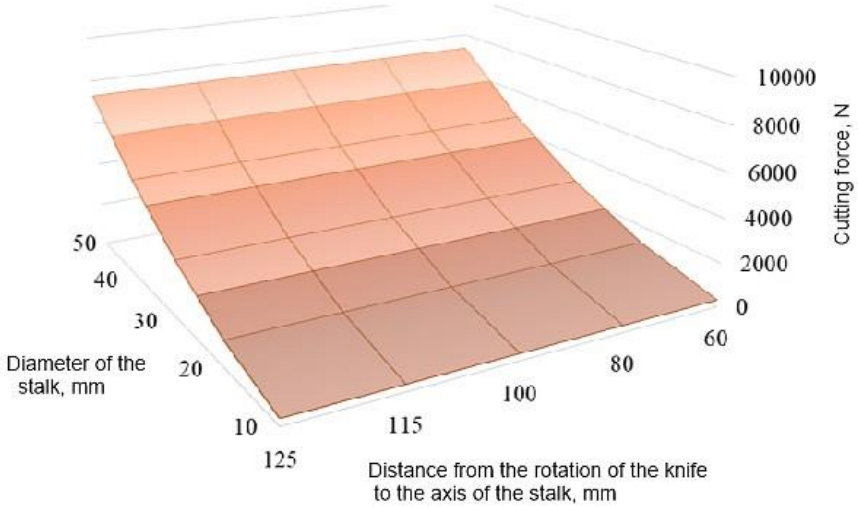


Fig. 12 - The value of cutting force depending on the diameter of the sunflower stem and the distance from the knife rotation to the stem axis: for the proposed knife system

CONCLUSIONS

The analysis of the results allows us to draw the following conclusions:

1. The use of a knife system where the retaining and main knives are made according to the Archimedes spiral allows cutting with less effort.

2. Compared to the knife system of the Massey Ferguson 1006 cutterbar, the reduction in cutting force is: 1.3 - 16% (for stems with a diameter of 50 mm), 6.4-14.8% (40 mm), 7.9-11.8% (30 mm), 6.02 -7.7% (10 mm).

3. Compared to the knife system of the John Deer S690I cutterbar, the reduction in cutting force is: 6.4-16.7% (50 mm), 9.7-15.3% (40 mm), 9.8-15.2 (30 mm), 8.2-9.9 (20 mm), 6.3-8.2% (10).

4. In comparison with the Goryachkin knife system: the reduction in cutting force is: 1.4-17.2% (50 mm), 13.1-15.1% (40 mm), 8.97-11.9 (30 mm), 7.9-14.97% (20 mm), 5.7-7.7% (10 mm).

5. The cutting force for the proposed design of the knife system, unlike the other studied, practically does not change with the removal of the stem from the axis of rotation of the knives, which does not require an increase in energy consumption for the cutting process.

6. The installation of the proposed design of the knife system where the profiles of the support and cutting knives are made according to the Archimedes spiral will allow to ensure complete cutting of the stem, and also makes it impossible for the stem to slip out from under the knives; to perform sliding cutting along the entire length of the cut with the least effort.

REFERENCES

[1] Ali K. A. M., Zong W., Md-Tahir H., Ma L., Yang L. (2021). Design, simulation and experimentation of an axial flow sunflower-threshing machine with an attached screw conveyor. *Applied Sciences*, *11*(14), 6312. https://doi.org/10.3390/app11146312

[2] Ali K.A.M., Zong W.Y., Ma L.N., El-Wahhab A., Galal G., Li M. (2022). Testing, Evaluating and Simulate the Performance of the Newly Designed Drum for a Sunflower Threshing Machine. In *International Journal of Engineering Research in Africa.* Vol. 60, pp. 29-41. doi: https://doi.org/10.4028/p-8s4erw

[3] Braginets M. V., Kovalov S.V., Volvak S.F., Bahariev D.M., (2013). *Rounding the curvature of the knife cut podribnyuvacha roots (Обгрунтування кривизни леза ножів подрвбнювача корнеплодів), Bulletin of Uman National University of Gardening (Вісник Уманського національного університету садівництва)*, Vol. 1-2, pp. 70-75, Uman / Ukraine;

[4] Daipeng Lu, Wei Wang, Encai Bao, Shilin Wang, Xue Wu, Zongchun Bai, Yuxin Tang, (2022). Cutting Mechanical Properties of Pumpkin Grafted Seedling Investigated by Finite Element Simulation and Experiment, *Agriculture, MDPI*, Vol. 12(9), pages 1-18. http://dx.doi.org/10.3390/agriculture12091354

[5] Dalmis I.S., Kayisoglu B., Bayhan Y. et al. (2013). Development of a chopper unit for chopping of sunflower stalk during harvesting by combine harvester, *Bulgarian Journal of Agricultural Science*, 19 (No 5), ISSN: 1310-0351, pp. 1148-1154, Sophia / Bulgaria;

[6] Glab T, Kulig B., (2008). Effect of mulch and tillage system on soil porosity under wheat (*Triticum aestivum*). *Soil & Tillage Res.*, 99: 169– 178. DOI:10.1016/j.still.2008.02.004, Kraków / Poland;

[7] Gonulol E., Dalmis I.S. et al. (2009). The evaluation of alternative stalk chopping methods in sunflower farming. *African Journal of Agricultural Research*, Vol. 4 (12), ISSN 1991-637X, pp. 1398-1403, Shagamu / Nigeria;

[8] Goryachkin V.P. (1965). *Collected works in three volumes (Собрание сочинений в трех томах).* Vol. *2,* Kolos publishing house (Издательство Колос), 720 p., Moscow / Russia;

[9] Honglei J., Chenglin M., Guangyu L., Dongyan H. and Zhaochen L., (2007). Combined rototilling-stubble-breaking-planting machine. *Soil and Tillage Research*, 96: 73–82. DOI: doi.org/10.1016/j.still.2007.03.002, Changchun / China;

[10] Kovacic D., Kralik D., Rupcic S., Jovicic D., Spajic R. & Tisma M., (2017). Soybean straw, corn stover and sunflower stalk as possible substrates for biogas production in Croatia: A review. *Chemical and biochemical engineering quarterly*, 31(3), 187–198. DOI: doi.org/10.15255/CABEQ.2016.985, Zagreb / Croatia;

[11] Johnson P.C., Clementson C.L., Mathanker S.K., Grift T.E., & Hansen A. C. (2012). Cutting energy characteristics of Miscanthus x giganteus stems with varying oblique angle and cutting speed. *Biosystems engineering*, 112(1), 42-48. https://doi.org/10.1016/j.biosystemseng.2012.02.003

[12] Le Bissonnais Y., Arrouays D. (1997). Aggregate stability and assessment of soil crustability and erodibility: II. Application to humic loamy soils with various organic carbon contents. *European Journal of Soil Science*, Vol. 48, pp. 39–48. DOI: doi.org/10.1111/j.1365-2389.1997.tb00183.x, Exeter / UK;

[13] Liu Y., Luo C., Zong W., Huang X., Ma L., & Lian G. (2021). Optimization of clamping and conveying device for sunflower oil combine harvester header. *Agriculture*, 11(9), article number 859. doi: http://dx.doi.org/10.3390/agriculture11090859

[14] Lvov D.L. (2009), *Improving the process of sliding cutting of food semi-finished products with lamellar knives (Совершенствование процесса скользящего резания пищевых полуфабрикатов пластинчатыми ножами): Author. dis. for the sake of science*. PhD: 05.18.12. 136 p., Kemerovo / Russia;

[15] Martens D.A., Frankenberger W.T. (1992). Modification of infiltration rates in an organic-amended irrigated soil. Agron. J. 84, 707–717. DOI: doi.org/10.2134/agronj1992.00021962008400040032x, California / USA;

[16] Nalobina O.O., Vasylchuk N.V. et al. (2019). A new technical solution of a header for sunflower harvesting. *INMATEH Agricultural Engineering*, Vol. 58, No.2, pp. 129-136., DOI: https://doi.org/10.35633/inmateh-58-14, Bucharest / Romania;

[17] Pari Luigi, Latterini Francesco, Walter Stefanoni. (2020). Herbaceous Oil Crops, a Review on Mechanical Harvesting State of the Art. *Agriculture,* 10(8), 1-25. doi: http://dx.doi.org/10.3390/agriculture10080309

[18] Perea-Moreno M. A., Manzano-Agugliaro, F., Perea-Moreno, A. J. (2018). *Sustainable energy based on sunflower seed husk boiler for residential buildings. Sustainability*, 10(10), 3407. DOI: doi.org/10.3390/su10103407, Kraków / Poland;

[19] Shaforostov V., Makarov S., Elizarov P. (2018), *A harvester to a breeding and seeds growing combine for sunflower harvesting (Жатка к селекционно-семеноводческому комбайну для уборки подсолнечника)*, *All-Russian Research Institute of Oil crops by V.S. Pustovoit (VNIIMK) (Всероссийский научно-исследовательский институт масляничных культур)*, Vol. 3 (175), pp. 76–80, Krasnodar / Russia;

[20] Song S., Zhou H., Xu L., Jia Z., Hu G. (2022). Cutting mechanical properties of sisal leaves under rotary impact cutting. *Industrial Crops and Products*, Vol.182, 114856. https://doi.org/10.1016/j.indcrop.2022.114856

[21] Song S., Zhou H., Jia Z., Xu L., Zhang C., Shi M., Hu G. (2022). Effects of cutting parameters on the ultimate shear stress and specific cutting energy of sisal leaves. *Biosystems Engineering*, 218, 189-199. https://doi.org/10.1016/j.biosystemseng.2022.03.011

[22] Stepanenko S., Aneliak M., Kuzmych A., Kustov S., Lysaniuk V. (2022). Improving the efficiency of harvesting sunflower seed crops. *INMATEH Agricultural Engineering*, 67(2), 331-340. doi: https://doi.org/10.35633/inmateh-67-34

[23] Wang Y., Yang Y., Zhao H., Liu B., Ma J., He Y., ... & Xu H. (2020). Effects of cutting parameters on cutting of citrus fruit stems. *Biosystems Engineering*, Vol.193. pp. 1-11. https://doi.org/10.1016/j.biosystemseng.2020.02.009

[24] Zhang C.L., Chen L.Q., Xia J.F., Zhang J.M. (2019). Effects of blade sliding cutting angle and stem level on cutting energy of rice stems. *International Journal of Agricultural and Biological Engineering*. 12(6): 75–81 DOI: 10.25165/j.ijabe.20191206.4604

MOVEMENT ANALYSIS AND EXPERIMENTAL STUDY ON PEANUT POD HARVEST SEPARATION CONVEYOR
/
花生荚果收获分离输送装置运动分析与试验研究

Zengcun CHANG [1,2] Dongjie LI [2], Shuqi SHANG [2], Xiaoning HE [2], Baiqiang ZUO [2]
Cheng DONG [2], Xu LI [2], Dongwei WANG*[2]
[1] Shandong Agricultural University, College of Mechanical and Electrical Engineering/ China
[2] Qingdao Agricultural University, College of Mechanical and Electrical Engineering / China;
Tel: +86-0532-58957391; E-mail: 200701031@qau.edu.cn
DOI: https://doi.org/10.35633/inmateh-69-19

Keywords: *Peanut reacquiring; Removing-soil; Equipment; ADAMS*

ABSTRACT
A peanut harvest separation and conveying device was designed considering the shortage of peanut harvest machinery and poor harvesting effect in China. The interaction between mechanism and pod-soil mixture was analysed to obtain the motion state of peanut relative separation conveyor. ADAMS simulation was applied to obtain the spatial curve of peanut trajectory in the separation process. The study determined that the optimum operating parameters of the separation conveyor were a drum speed of 280 r/min and an inclination angle of 19^o. This study provides a theoretical basis for the further design of efficient peanut harvesting device.

摘要
针对我国花生复收机械短缺、复收效果差的现状，设计一种花生荚果收获分离输送装置。对机构-果土混合物进行互作分析，得到花生荚果相对分离输送装置运动状态。运用 ADAMS 对果土分离输送过程进行仿真，得到花生荚果在分离输送装置上的运动轨迹空间曲线。研究确定分离输送装置最佳工作参数为滚筒转速 280 r/min、倾角 19^0。为进一步设计高效的花生果土分离机械提供理论基础。

INTRODUCTION
Peanut is an important oil crop and cash crop in China. It is the main crop for China's export earnings. The planting area and output are among the highest in the world. At present, the problems of disordered peanut harvesting methods and poor harvesting effect are still prominent in China. Thus, peanut mechanized harvesting has become one of the important factors affecting peanut production. And picking matters most in peanut harvesting process, directly related to the efficiency and quality of the peanut harvest *(Pari et al, 2020*) The loss rate of mechanized harvesting peanut in sandy land is generally about 2%. With the increase of soil viscosity, the loss rate increases to 3%~5%. The loss of artificial harvesting (*Wang et al., 2013*) is especially high. The reference article introduces the methods and technical means to improve the efficiency of grain washing machine (*Babic et al, 2013*). At present, the total loss rate of missing and falling pods of domestic peanut harvesters is 1.8%~4.2%. The loss is about 235.5 kg/hm2 measured in the field.

The pods soil separation and conveying device is the core working mechanism of the peanut harvester. Its quality directly affects the working performance of the peanut harvester. A peanut falling pick-up machine was designed by Li X. et al. The pods soil separation device uses centrifugal force to separate. This machine is controlled by multiple motors. Its pods soil separation effect is good, but the cost is high and the failure rate is high (*Li et al., 2020*). A peanut groundnut picking machine designed by Chen H. and others consists of a lifting mechanism, a soil crushing mechanism, a cleaning mechanism, a vibrating screen and a pods collecting box. The machine has the characteristics of large size and high production cost (*Chen et al., 2019*).

In view of the above problems, this paper deeply studies the theory of pods soil separation of the separation conveyor and obtains the optimal parameter combination of the separation conveyor. The research results can improve the technical level of peanut harvester, enrich the relevant theories of pods soil separation, and reduce the cost of peanut harvester. It is of great significance to promote the development of peanut harvesting machinery in China (*Gao et al., 2017*).

MATERIALS AND METHODS

Determination and analysis of mechanical properties of peanut pods

Recovery of peanut pods is an important part of peanut harvesting. Peanut pods are susceptible to impact, extrusion, vibration and other conditions in the process of mechanized harvesting. These effects can lead to different degrees of damage to peanut pods (*Liu et al., 2022*). These processes are closely related to their basic physical properties (*Li et al., 2017, Hou, 2017*). According to the physical characteristics of peanut fruit, the separation and conveying roller device is designed. The purpose is to accurately design the gap between each separation conveying roller. The triaxial dimension index of peanut pod was selected as the evaluation index of geometric characteristics in this study. The size mark of peanut triaxial is shown in Fig.1.

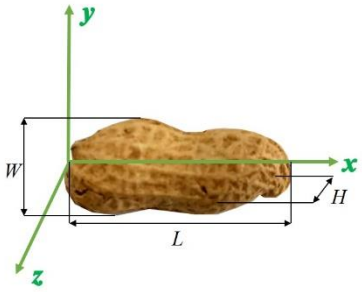


Fig. 1 - Peanut triaxial dimension marking

Dabaisha, Silihong and high oleic acid peanut Jihua 16 were used as experimental materials in this study. The moisture content of peanut pods for this trial is 11.2%~14.7%. The trial adopts the method of taking the average value by repeated measurement. The measurement result record is shown in Table 1.

Table 1

Pod parameters of three peanut varieties

Name	L/mm	W/mm	H/mm	Minimum Length/mm	Minimum Width /mm	Minimum Height /mm
Da Baisha	39.84	17.88	16.12	24.52	15.17	13.90
Si Lihong	47.83	14.69	14.57	22.62	11.77	11.69
Ji Hua 16	40.11	18.99	17.03	24.87	16.33	14.94

Structure and working mechanism

The working principle of the drum type separation conveyor is as follows. Use six groups of rollers to collide the pod-soil mixture during the rotating work. The crushed soil blocks leak through the gap between the grid bars and the rollers. The soil adhered to the peanut pod is separated by the continuous impact between the grid and the pod-soil mixture. Impurities such as broken soil are removed with the continuous rotation of the separation drum. Peanut pods are transported to the rear of the machine in a jumping shape (*Wei et al., 2019*). The rubber products wrapped on the fence strip can reduce the damage to the peanut pods (*Wang et al., 2020*).

The conditions that can ensure the smooth backward separation and transportation of peanut pods are as follows. The diameter of roller bar is 12 mm. Screen surface width is 1900 mm. The minimum diameter of peanut pod between rods and rollers is 11.69 mm. In addition, the length of conveyor is 1600 mm.

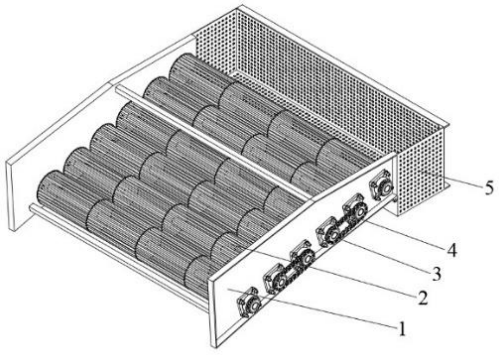


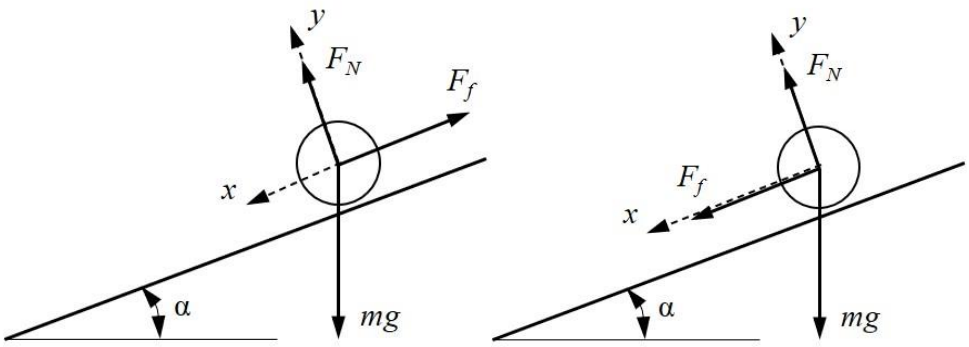
Fig. 2 - Structural diagram of separation conveyor

1. Connecting plate; 2. separating roller conveyor device; 3. Roller shaft; 4. Drive chain; 5. Pods collecting box

Movement analysis of peanut pod relative separation conveyor

It is easy to produce vibration when the separation conveying device is working, which leads to the phenomenon of "jumping" and "backflow" of pod-soil mixture. There are problems such as unclean separation of pods and soil, high damage rate of peanut, etc. In order to avoid the above problems, the movement analysis of peanut pod relative separation conveyor was carried out (*Zhang et al., 2012, Yang et al., 2016*). The optimal parameters are designed through theoretical calculation and analysis.

The separating and conveying device needs to transport the materials on the screen back while separating the pods and soil. The pod-soil mixture will appear relatively static, reciprocating sliding and throwing away from the screen surface when the mechanism of the separation conveyor is different from the selection of working parameters. Fig. 3 shows the forward and reverse slipping force of peanut relative separation sieve.



a) Forward slip **b) Reverse slip**

Fig. 3 - The forward and reverse slipping force of peanut relative separation sieve

The dynamic equation of forward and reverse sliding of peanut pod is as follows according to Fig.3.

$$\begin{cases} m\left(a_{x_{12}} + a_x\right) = mg\sin\alpha \mp F_f \\ ma_y = F_N - mg\cos\alpha \\ F_f = \mu F_N \end{cases} \quad (1)$$

where:

F_f- frictional force, N;

F_N- supporting force, N;

α- Angle between screen surface and horizontal plane, ^{0}.

The instantaneous acceleration of forward slipping can be solved as follows:

$$a_x = g\sin\alpha - \frac{F_f}{m} \quad (2)$$

The instantaneous acceleration of reverse slipping can be solved as follows:

$$a_x = g\sin\alpha + \frac{F_f}{m} \quad (3)$$

The critical conditions when peanut pods are thrown off the screen are as follows:

$$k_2 r\omega^2 \cos\omega t \bullet \sin(\beta + \alpha) = g\cos\alpha \quad (4)$$

The acceleration of peanut thrown away from the screen surface relative to the screen is obtained from formula 6 as follows:

$$\begin{cases} a_x^{'} = k_1 r\omega^2 \sin\omega t \bullet \cos(\beta + \alpha) + g\sin\alpha \\ a_y^{'} = k_2 r\omega^2 \sin\omega t \bullet \sin(\beta + \alpha) - g\cos\alpha \end{cases} \quad (5)$$

According to the above derivation formula, the motion state of the peanut pod relative separation conveyor can be obtained by substituting the known parameters into the solution. This provides an analytical basis for the problem of high damage rate of peanut.

Analysis of separation conditions between peanut and soil

The reason why the surface of peanut pod is easy to bond with soil is that the soil has high moisture content (*Kong, 2016*). The separation conditions of pods and soil were obtained through the mechanical analysis of the adhesion between peanut pods and soil (*Cao et al., 2019*). Thus, it provides a theoretical basis for achieving high-quality separation performance.

In order to facilitate analysis and calculation, peanut and soil are ideally equivalent into two parts for stress analysis. The stress analysis diagram is shown in Fig.4.

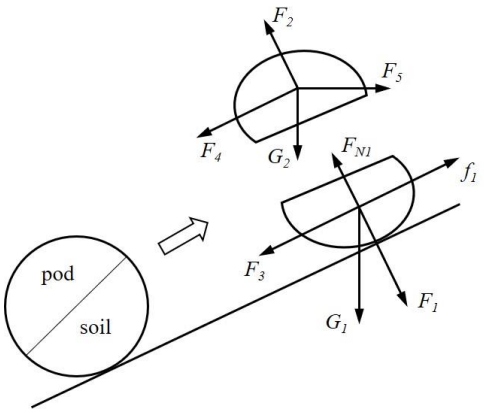


Fig. 4 - Stress analysis of pod soil separation

It can be seen from Fig. 4 that the force required to realize the separation of pod and soil is greater than the bonding force.

$$f_1 + G_1 \sin\theta > F_3 \tag{6}$$

According to the data, the calculation formula of soil adhesion is as follows:

$$F_3 = cS \tag{7}$$

where:

c - the soil bond strength, kPa.

S - the area of the soil fracture surface, cm^2.

It can be calculated according to the friction principle:

$$f_1 = \mu F_{N1} \tag{8}$$

where: μ- friction factor.

The simultaneous equation is solved to obtain F_{N1} as follows:

$$F_{N1} = \frac{mg}{(\mu+1)\sin(\beta-\theta)+(1-\mu)\cos(\beta-\theta)} \tag{9}$$

where:

$$\beta = \arccos\frac{l}{a+b+D} \tag{10}$$

The friction force of peanut is related to its own weight which can be seen from the above analysis. In addition, it is also related to the inclination of the device and the size of the drum gap.

Dynamics analysis of peanut and separating conveyor

The peanut soil mixture is excavated by the excavation device. The peanut soil mixture is lifted backward to the separation conveyor as the machine moves forward (*Fan et al., 2019*).

The stress analysis of peanut on the separation conveyor is shown in Fig. 5. For the convenience of calculation and analysis, the peanut is simplified as an ellipsoid. Define the length of the long axis and short axis of peanut as a and b respectively, the diameter of the separation and conveying drum as D, and the gap between the two drums as l.

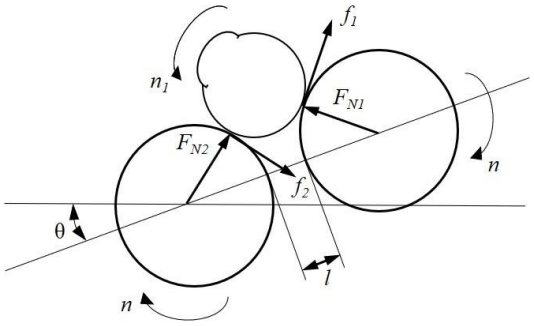


Fig. 5 - Stress Analysis of peanut

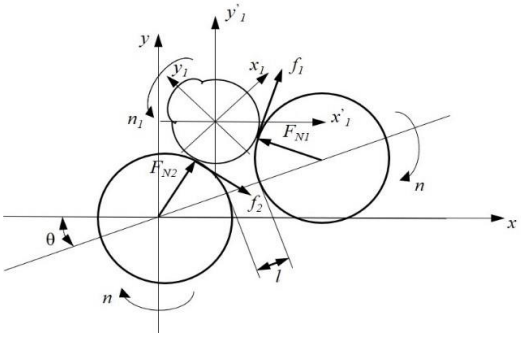


Fig. 6 - Schematic diagram of coordinate transformation

The stress of peanut on the separation conveyor is as follows: the supporting forces F_{N1} and F_{N2} of the two rollers, the gravity mg of the peanut pod, the friction f_1 and f_2. In order to ensure the smooth backward lifting and transportation of peanut pods, the resultant moment of each force on the contact point must be greater than zero.

In order to facilitate the stress analysis when the position of peanut changes at any time, the coordinate transformation method is used for analysis and calculation. The schematic diagram of coordinate transformation is shown in Fig. 6.

Therefore, the elliptic equation of peanut pod in x_1y_1 coordinate system is as follows:

$$\frac{x_1^2}{a^2}+\frac{y_1^2}{b^2}=1 \tag{11}$$

According to the rotation formula transformation of the coordinate system, the solution is obtained in the $x'_1y'_1$ coordinate system:

$$\frac{(x_1^{'}\cos\theta+y_1^{'}\sin\theta)^2}{a^2}+\frac{(y_1^{'}\cos\theta-x_1^{'}\sin\theta)^2}{b^2}=1 \tag{12}$$

where, θ - is the angle between screen surface and horizontal plane, °.

The formula of the coordinate system is as follows after transverse transformation.

$$\begin{cases} x=x_1^{'}+x_0 \\ y=y_1^{'}-y_0 \end{cases} \tag{13}$$

By combining the above equations, the relative coordinates of the peanut centre are as follows:

$$\begin{cases} x_0=-\dfrac{2l\cos\theta}{a+b+D}\cos(\alpha+\theta) \\ y_0=\dfrac{a+b+D}{2}\sin(\alpha-\theta) \end{cases} \tag{14}$$

The coordinates of the right roller in the xy coordinate system is as follows:

$$\begin{cases} x_{o2}=-\dfrac{4Dl\cos(\alpha+\theta)\bullet\cos\theta}{2\sqrt{\left[4l\cos(\alpha+\beta)\bullet\cos\theta\right]^2+(a+b+D)^4\sin(\alpha-\theta)}} \\ y_{o2}=\dfrac{a+b+D}{2}\sin(\alpha-\theta) \end{cases} \tag{15}$$

Calculate the distance from the right roller to F_{N2} as follows:

$$S=\frac{k_1x_{o2}-y_{o2}+k_1l\cos\theta+l\sin\theta}{\sqrt{k_1^2+1}} \tag{16}$$

The distance from the right roller to f_2 is as follows:

$$t = x_{o2} - x_o \, \mathrm{t} \tag{17}$$

The distance from the right roller to the peanut gravity mg is as follows:

$$s_2 = \frac{k_2 x_{o2} - y_{o2} - \frac{(a+b+D)^2 \sin(\alpha-\theta)}{4l\cos\theta\cos(\alpha+\theta)}}{\sqrt{k_2^2+1}} \tag{18}$$

where:

k_1-The slope of the straight line where the supporting force F_{N2} is located;

k_2 -The slope of the straight line where the supporting force F_{N1} is located.

Combining the above formula, the resultant torque is obtained as follows:

$$\sum M_{O2} = F_{N2} s - f_2 s_2 - mgt \tag{19}$$

Through the analysis of the above formula and calculation results, it can be seen that as follows: Peanut is mainly affected by the inclination of the device on the separation conveyor. In addition, it is also vulnerable to the impact of other peanut pods in the actual harvest process.

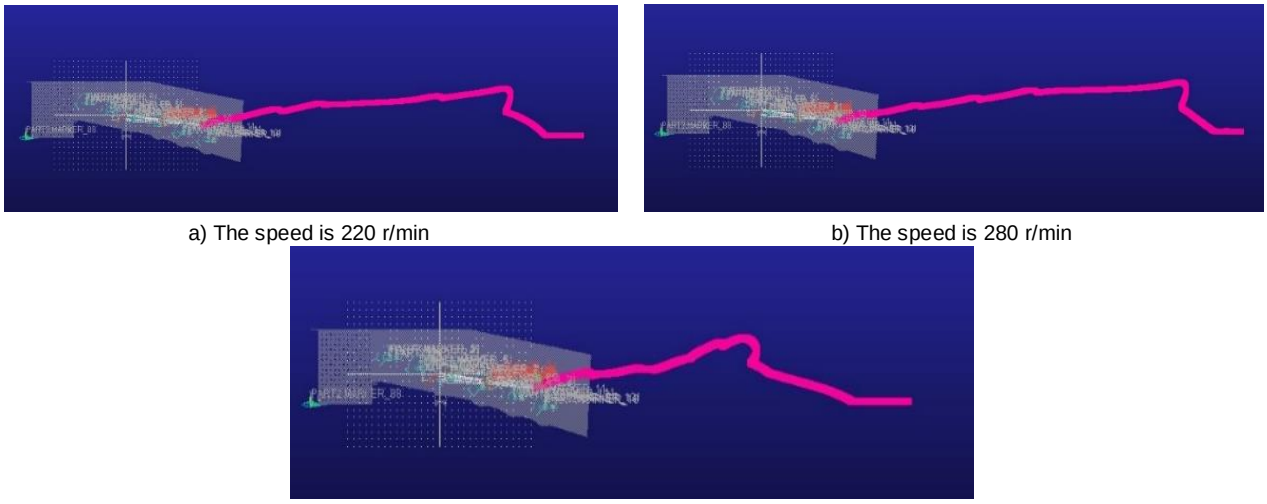
RESULTS

Simulation analysis of separation conveyor

The whole simulation process of peanut on the separation and conveying device is carried out in Adams view environment. Set the unit system as MMKS. The forward speed of the virtual prototype is set to 1.67 m/s. The rotating speed of the drum of the separation conveyor is 280 r/min. The total time of the whole virtual simulation process is set to 1.8 s, and the step size is set to 800 steps.

Selecting two marker points in the middle of peanut and recording the whole process of its movement can simulate the trajectory and movement law of peanut in the process of separation and transportation (*Wang et al., 2021*). At first, peanuts are excavated and picked up by the excavation device. The peanut enters the separation conveyor and moves forward with the machine. The separating conveying drum rotates, and the peanut jumps backward under the impact force. Finally, all the peanuts enter the rear pods collecting box.

The forward speed of the implement remains unchanged during the simulation. The rotating speed of the separation conveying drum is 220 r/min, 280 r/min and 310 r/min respectively. Record the movement track and law of peanut under different parameters. After the simulation, the simulation trajectory of peanuts at other three different speeds is shown in Fig. 7.



a) The speed is 220 r/min

b) The speed is 280 r/min

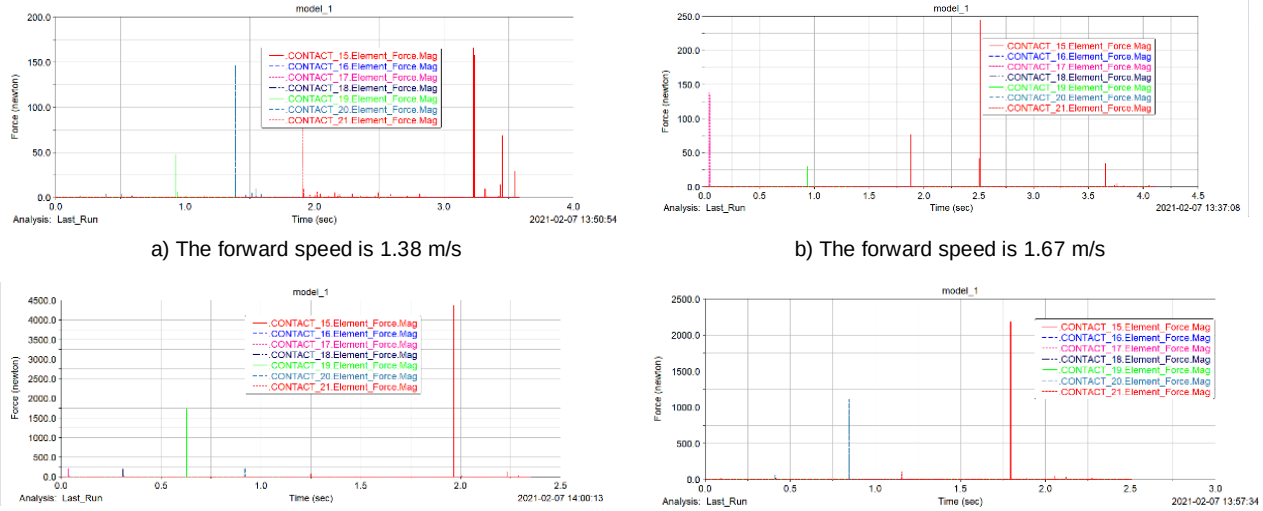
c) The speed is 310 r/min

Fig. 7 - Simulated trajectory of peanut pods at three different speeds

Compared the motion simulation tracks of different drum speeds. It can be seen that the trajectory and motion law of peanut simulation are roughly the same when the forward speed of the machine is the same and the rotating speed of the drum is different.

The jumping phenomenon of peanut is more serious with the continuous increase of drum speed. In particular, "backflow" occurs in some nodes of peanuts as shown in Fig. 7.

The rotating speed of the drum is set at 280 r/min, and the forward speed of the simulated machine is selected as 1.38 m/s, 1.67 m/s, 1.94 m/s and 2.22 m/s respectively. The impact force on peanuts is shown in Fig. 8.



a) The forward speed is 1.38 m/s

b) The forward speed is 1.67 m/s

c) The forward speed is 1.94 m/s

d) The forward speed is 2.22 m/s

Fig. 8 - The impact force on peanut at different forward speeds

The following results can be found by comparing the impact force on peanuts obtained from ADAMS simulation process in different states. When the forward speed of the machine is 1.67 m/s and the rotating speed of the drum is 280 r/min, the impact force of the two working parameters is smaller than that of the matched peanut.

Field test conditions and schemes

Si Lihong peanut varieties were selected for field experiment in Pingdu experimental field. The test adopts the method of taking the average value of multiple groups of repeated tests. Select 30 meters as the harvest operation test area each time, and randomly select 6 test areas.



Fig. 9 - The test process

Field test results and analysis

The Box Behnken test design scheme is adopted with the damage rate, soil content and pod leakage rate of peanut as the evaluation indexes. The inclination angle of the separation conveyor, the rotating speed of the drum and the forward speed of the machine are tested and studied. The level code of test factors is shown in Table 2.

Table 2

Test factor level code

	Declination angle of separator (°)	Drum speed (r/min)	Forward speed (m/s)
-1	19	220	1.38
0	21	250	1.67
1	23	280	1.94

This test plan is designed according to the Box-Behnken test principle. The test design scheme and results are shown in Table 3, where the inclination of the separating device is A, the rotation speed of the drum is B, and the forward speed of the machine is C.

Table 3

Test design scheme and test results

Serial number	Declination angle of Separator A / (°)	Drum speed B / (r/min)	Forward speed C / (m/s)	Soil content Y_1/ (%)	Breakage rate Y_2 / (%)	Pod leakage rate Y_3/ (%)
1	1	1	0	2.03	2.44	0.24
2	-1	1	0	2.31	1.13	0.18
3	1	-1	0	3.07	2.46	0.22
4	-1	-1	0	2.27	1.19	0.19
5	1	0	1	4.21	2.66	0.24
6	-1	0	1	2.48	2.07	0.23
7	1	0	-1	3.62	2.43	0.24
8	-1	0	-1	2.67	2.39	0.29
9	0	1	1	3.28	2.15	0.27
10	0	-1	1	3.41	2.22	0.31
11	0	1	-1	2.34	2.19	0.22
12	0	-1	-1	2.63	2.15	0.22
13	0	0	0	2.98	2.11	0.24
14	0	0	0	2.77	2.16	0.26
15	0	0	0	3.02	2.11	0.19
16	0	0	0	2.76	2.33	0.25
17	0	0	0	2.77	2.41	0.24

It can be directly seen from table 3 that the soil content of peanut is generally between 2.03% and 3.62% during the above test and research. After excavation, separation and transportation, the damage rate of peanuts is generally in the range of 1.13% - 2.66%. The average pod leakage rate is about 2%. It can be directly seen that the device can better ensure the net harvest quality of peanuts. The device is designed to work well.

Analysis of variance

The test results were imported into SPSS for variance analysis (Tanner-Smith, E.E., 2014, Guo M. et al., 2017). The results were shown in Table 4. The model P for soil content, breakage rate and pod leakage rate were 0.0008, <0.0001 and <0.0001 ($p < 0.01$), respectively, as analysed by the data in the table 4. The data from this regression model are highly significant. The model fit was good and it argues that the error during this experiment is small, and the experimental data has strong reliability. At this time, you can select the combination of A1, B3, and C2 to form the optimal combination of A1B3C2. The resulting optimal combination plan A1B3C2 exists in the orthogonal test table 3. Therefore, the combination of A1B3C2 was the best. The optimal combination plan was that the speed of the separation drum is 280 r/min, the inclination of the separation conveyor is 190, and the forward speed of the machine is 1.67 m/s.

Table 4

Variance analysis table

Source of variation	Sum of squares	Degree of freedom	F	p-Value
X_1	153.29	9	15.41	0.0008
X_2	7.81	9	31.41	<0.0001
X_3	95.532	9	14.10	<0.0001
Error	52.53	16	/	/

Field test verification

The average value is obtained through multiple groups of repeated field experiments, and the test results are shown in Table 5.

Table 5

Test results

Peanut varieties	Soil content / %	Breakage rate / %	Pod leakage rate / %
Sili-hong peanut varieties	3.99	1.16	0.18

It can be seen from the above table that the damage rate and pod leakage rate of peanuts are low, and the overall harvest effect is great. The damage rate is less than 2.5%, and the pod leakage rate is less than 0.25%.

The walking of machines and tools, soil hardening and other factors cause the soil blocks that are not easy to be broken after re-harvest during the harvest process. This puts forward higher requirements for the structural design of the separation and conveying device.

It can be seen from the test results that the test effect is good when the speed of the separation drum is 280 r/min, the inclination of the separation conveyor is 190, and the forward speed of the machine is 1.67 m/s. The recovery rate of peanut is guaranteed, and the damage and leakage of peanut pods are avoided. The performance of the machine is great.

CONCLUSIONS

This paper aims at the problems such as poor soil removal effect of peanut recovery. A new type of separating and conveying device is designed. The main conclusions are as follows:

(1) Through the dynamic analysis of the separation conveyor and the analysis of the peanut soil separation conditions, it is found that the peanut is mainly affected by the inclination of the device on the separation conveyor. The influencing factors of peanut and soil separation are mainly related to the inclination of the separation conveyor and the gap between the two rollers.

(2) Through field experiments, it is concluded that the working effect of the machine is the best when the inclination of the separation conveyor is 190, the rotation speed of the separation drum is 280 r/min, and the forward speed of the machine is 1.67 m/s.

ACKNOWLEDGEMENT

This research was funded by Modern Agricultural Industrial Technology System Project (CARS-13) and Shandong Provincial Key Science and Technology Innovation Engineering Project (2021CXGC010813).

REFERENCES

[1] Babic L., Radojcin M. and others, (2013), Physical properties and compression loading behaviour of corn seed, *International Agrophysics*, №27, pp. 119–126.

[2] Cao Q., Fan L., & Yuan P. (2019). Comparative test of two peanut harvesters(两种花生分段挖掘收获机对比试验). *Agricultural Development & Equipments*, vol.02, pp.109.

[3] Chen H., Xiao W., & Jiang J. (2019), A kind of peanut fallen fruit picking machine (一种花生地落果捡拾机). Patent. No.2018106105575. China.

[4] Fan L., Cao Q., &Yuan P.(2019). Design and test of roller peanut segmented digging harvester(辊式花生分段挖掘收获机的设计与试验). *Agricultural Development & Equipments*, vol.02, pp.95.

[5] Gao L., Chen Z., Charles C., & Butts C.L. (2017), Development course of peanut harvest mechanization technology of the United States and enlightenment to China (美国花生收获机械化技术衍变历程及对中国的启示). *Transactions of the Chinese Society of Agricultural Engineering*, vol.33.issue 12, pp.1-9.

[6] Guo, M., Feng, B., Guan, Y. (2017). Experimental Design and Software Application (实验设计与软件应用). *Beijing: Chemical Industry Press, 7*.

[7] Hou M. (2017). *Study on Mechanical Properties of Corn Kernel and Design of Threshing Test Bed* (玉米籽粒力学特性试验与脱粒试验台设计研究) [Master dissertation, Henan Agricultural University]. China National Knowledge Internet.

[8] Kong P. (2016). *Experiment on Small Scale Shove-roller type Peanut Harvester* (小型铲辊式花生起收装置的试验研究) [Master dissertation, Shenyang Agricultural University]. China National Knowledge Internet.

[9] Liu L., Liu D., Sun Q., Qian K., & Li X. (2022), Experiment and Analysis of the Harvest and Picking Ability of Peanut (花生收获摘果力试验及分析). *Journal of Agricultural Mechanization Research*, vol.44, issue 06, pp.139-144+151.

[10] Li X., Liu H., & Qi L. (2020), Peanut drop pod picking machine (花生落果拾捡机). Patent. No. 2020100406025. China.

[11] Li X., Liu X., & Pei X. (2017), Model Analysis of corn Harvester Threshing Device Based on Ansys Workbench (基于 ANSYS Workbench 的玉米籽粒收获机脱粒装置的模态分析). *Xinjiang Agricultural Mechanization,* vol.03, pp.16-19.

[12] Pari, L.; Latterini, F.; Stefanoni, W. Herbaceous oil crops, a review on mechanical harvesting state of the art. *Agriculture* 2020, 10, 309.

[13] Tanner-Smith, E.E., Tipton, E. (2014). Robust variance estimation with dependent effect sizes: practical considerations including a software tutorial in Stata and SPSS. *Research Synthesis Methods*, Vol.5, issue 1, pp.13-30, Nashville/USA.

[14] Wang B., Yu Z., Hu Z., Cao M., Zhang P., & Wang B. (2021). Numerical Simulation and Experiment of Flow Field in Air Separation System of Peanut Pickup Harvester (花生捡拾收获机风选系统流场数值模拟与试验). *Transactions of the Chinese Society for Agricultural Machinery*, vol.52, issue 11, pp.103-114.

[15] Wang B., Zhang X. (2020), Design and Experiment of Peanut Harvester in South China (南方花生收获机的设计与试验). *Modern Agricultural Equipment*, vol.41, issue 04, pp.33-38.

[16] Wang D., Shang S., Zhao D., & Zhu H. (2013), Type-4HBL-4 Two-ridges and Four-lines Semi-feeding Self-propelled Peanut Combine Harvester (4HBL-4 型二垄四行半喂入自走式花生联合收获机). *Transactions of the Chinese Society for Agricultural Machinery*, vol.44, issue 10, pp.86-92.

[17] Wei Z., Li H., Mao Y., Sun C., Li X., Liu W., & Su G. (2019), Experiment and analysis of potato-soil separation based on impact recording technology. *International Journal of Agricultural and Biological Engineering*, vol.12, issue 5, pp.71－80.

[18] Yang R., Yang H., Shang S., Xu P., Cui G., &Liu L. (2016). Design and Test of Poking Roller Shoving Type Potato Harvester (拨辊推送式马铃薯收获机设计与试验). *Transactions of the Chinese Society for Agricultural Machinery*, vol.47, issue 07, pp.119-126.

[19] Zhang H., Zhao F. (2012). Stress Analysis for Dig Shovel based on ANSYS (基于 ANSYS 的挖掘铲静力分析). *Agricultural Science & Technology and Equipment*, vol.05, pp.13-15.

STUDY ON THE MECHANISM OF INDOOR TEMPERATURE AND HUMIDITY CHANGE IN THE SUNKEN SOLAR GREENHOUSE DURING THE SMOTHERING PERIOD
/
下沉式日光温室闷棚期间温湿度变化机制的研究

Weiwei CHENG [1)], Xin YOU [2)], Tao TIAN [2)], Jiaxuan LU[2)], Junlin HE [2)], Zhouhua LIU [*1)], Fei HAN [1)]
[1)] Shanxi Agricultural University, College of Urban and Rural Construction, Taigu / China
[2)] Shanxi Agricultural University, College of Agricultural Engineering, Taigu / China
Tel: +86-0354-6287420; E-mail: lzh6175305@163.com
Corresponding author: Zhonghua LIU
DOI: https://doi.org/10.35633/inmateh-69-20

Keywords: *sunken solar greenhouse, solar radiation, temperature and humidity, sterilization*

ABSTRACT
A sunken solar greenhouse is the original type of greenhouse in China, its soil wall thermal storage performance is better and low cost. Higher benefits of stereoscopic planting in sunken solar greenhouses, while repeated use of the substrate can produce pathogens, so high-temperature smothering is used for sterilization in the summer months of June to August. To investigate the mechanism of indoor temperature and humidity variation and fungicidal effect in a sunken solar greenhouse, a single cross-sectional test of temperature and humidity in sunken solar greenhouse during the smothering period was conducted using wireless sensors. The results showed that: The maximum value of indoor temperature at noon was 69.5°C the temperature value of all measurement points was greater than 50°C for 3h, when removing the measurement points at the upper surface of the ground, the relative humidity value of other measurement points was less than 60% for 5h. During the daytime period, when the indoor temperature is greater than 28°C in the interval 7:00-12:00, the initial relative humidity value of each measurement point is located at 70%-85%; when the weighted temperature of each measurement point starts to rise at a rate of 1.1°C/10min, the weighted humidity of each measurement point declining is 1.3%/10min; the determination of the rate of change of indoor temperature and humidity during the daytime and the starting value can provide a basis for indoor plants to take measures to sterilize at high temperature.

摘要
下沉式日光温室是我国[1]原创型式的温室，其土质墙体储热性能好且造价低廉。在下沉式日光温室中采用立体栽培收益较高，而基质重复使用会产生病菌，因此在夏季 6-8 月份采用高温闷棚杀菌。为探究下沉式日光温室室内温湿度变化机制和杀菌效果，利用无线传感器对闷棚期下沉式日光温室的温湿度进行单横截面试验，结果显示：室内温度在中午时刻的最高值为 69.5℃，所有测点的温度值大于 50℃的时长为 3h，去除地面上表面处测点时，其他测点的相对湿度值小于 60%的时长为 5h；白天期间，在 7:00-12:00 时间段内，当室内温度都大于 28℃，各测点的初始相对湿度值位于 70%～85%，当各测点加权温度以 1.1℃/10min 速度开始上升，各测点加权湿度的下降速率为 1.3%/10min，白天期间室内温湿度变化速率和起始值的确定，可为室内有植物采取闷棚的措施提供依据。

INTRODUCTION
The solar greenhouse is an essential agricultural facility in China, which is often referred to as "conservation farming," "controlled environment farming," "greenhouse farming," and "facility farming". (*Steven et al, 2017; Jia et al, 2016*). There are three types of facility farming facilities in China, namely plastic greenhouses, solar greenhouses, and attached greenhouses, among which solar greenhouses are the original agricultural facilities in China (*Peng P et al., 2019*). Moreover, the COVID-19 pandemic is threatening the world's food security, depriving 265 million individuals of food by the end of 2020 (*Lal R., 2020*).

Greenhouses are used to mitigate the harsh weather conditions and allow for a full year-round production of crops (*Morshed W. et al., 2022*) by controlling the microclimate and ensuring that the crops acquire the required level of temperature, humidity, water, and light (*Ghani S. et al., 2019*).

[1] *Weiwei Cheng, As Lec.Ph.D. Eng; Xin You, M.S. Eng; Tao Tian, M.S. Eng; Jiaxuan Lu, M.S. Eng; Junlin He, Prof.Ph.D.Eng; Zhonghua Liu Asoc.Prof.Ph.D. Eng; Fei Han, M.S. Eng;*

A solar greenhouse is a facility that uses solar energy resources so that the indoor air absorbs solar heat during the daytime and the indoor walls and soil absorb heat during the day and exotherm at night, thus providing a suitable microclimate inside the greenhouse. The sunken solar greenhouse is an original structural type of greenhouse in China, and its outstanding advantages are low cost and good heat storage performance, which is very suitable for Chinese vast land and weak economy (*Zhang LH et al., 2010*). The temperature value inside the sunken solar greenhouse is 2°C higher than that of the greenhouse built on flat ground, and the sunken solar greenhouse can also reduce the influence of external low temperature on the soil, and the low-temperature value of its south margin area is greater than that of the south margin area of the non-digging solar greenhouse, so the application of the sunken solar greenhouse is widely promoted in production. The sunken solar greenhouse originated in northeastern China to improve the thermal insulation performance of the greenhouse, and the initial concave depth of the sunken solar greenhouse was 0.5-1 m. At the present stage, the concave depth is 1.2-2 m, equivalent to a 1-m-high wall around the southern ground margin, which is better than the general greenhouse thermal insulation effect.

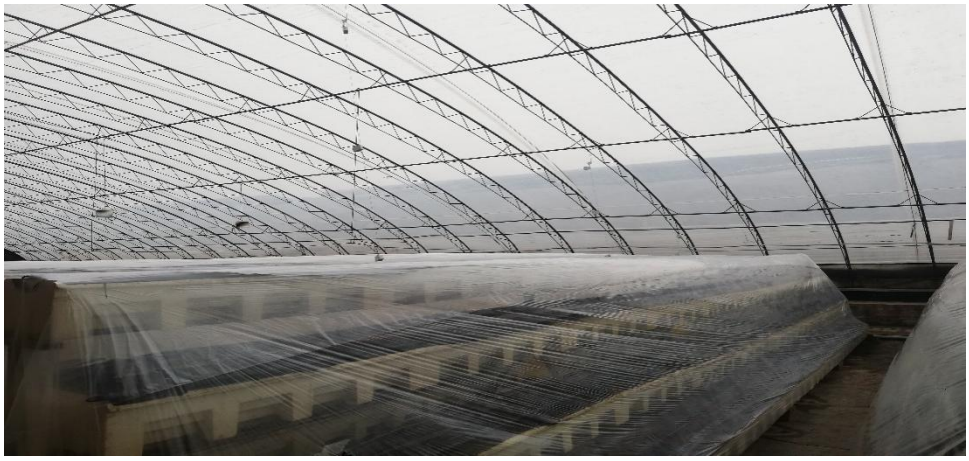
Substrate stereo culture and soil cultivation can be used in daylight greenhouses, which can cause the soil and substrate to carry pathogens during repeated planting. Continuous planting of strawberries in the soil or substrate provides conditions for the development of a large number of pathogens (*Chen P et al., 2020*), which can lead to a reduction in yield and, at a later stage, to the death of the strawberry plant. Smothering means that during the summer period, no plants are grown indoors and all air vents in the solarium are closed to take advantage of the high indoor temperatures generated by the solar radiation absorbed by the greenhouse to kill harmful bacteria. To alleviate the trend of soil deterioration and improve the growing environment of crops, high-temperature smothering is usually carried out during the high-temperature crop vacancy period from June to August in summer, i.e., the greenhouse is sterilized by using high temperature above 70°C (*Shi L.J. et al., 2021*). *Li J.C. et al*., *(2015),* studied the physicochemical characteristics of soil during the high-temperature smothering period and found that irrigation smothering can help promote soil restoration, which can increase yield and improve economic efficiency, and can be actively applied in continuous crop production. After smothering there is also a reduction in beneficial bacteria such as Phytophthora and Helicobacter nitrificans, which play an important role in the nitrogen cycle in the soil (*Sun B.et al., 2020*). Smothering can be effective in controlling root knot nematodes and affecting the microbial community structure in the soil (*He Wei et al., 2022*). The result (*Hu Q.Q. et al., 2015*) showed that the plants in the irrigation and high-temperature smothering treatment were better than the control in terms of plant height, stem thickness, leaf growth and fruit quality. It was confirmed that adding corn straw combined with high-temperature smothering, not only has a strong disinfection effect on the soil, but also accelerates the decomposition of straw, increases soil organic matter content, reduces soil salt content, and improves the soil microbiological environment (*He Z.G. et al., 2018*). *Fu G.H.* and *Liu W.K., (2016*), verified that the temperature of the substrate rooting area in the heliostat was significantly and positively correlated with the daily indoor and outdoor temperatures. Therefore, the studying of indoor temperature and humidity during the smothering period of sunken solar greenhouse can provide theoretical data and reference for farmers to smother their greenhouses for sterilization. The process of sunken solar greenhouse smothering in the three-dimensional planting method is as follows: the three-dimensional planting facilities are covered with plastic film, the substrate is filled with water, all indoor wind vents are closed, and the quilt is not pressed into the shed.

MATERIALS AND METHODS

Greenhouse tested

The sunken solar greenhouse was smothered from June 30, 2019 to August 7, 2019. The tested greenhouse was a sunken three-dimensional planting solar greenhouse, as shown in Figures 1 and 2. The greenhouse was north-facing, with a length of 108 m and a span of 12 m. The sunken solar greenhouse had a concave depth of 1.2 m on the south wall, a width of 1.1 m on the south aisle, and a width of 1.2 m on the north aisle. The external height of the rear wall of the sunken solar greenhouse is 4.3 m, and the ridge height is 5 m. The width of the north wall is 6 m at the bottom and 2 m at the top. The main bearing skeleton is made of elliptical steel pipe with a skeleton spacing of 1 m, and the covering material is plastic film.

All air vents of the greenhouse were closed during the smothering period, the base tank was filled with water, the water outlet at the bottom of the base tank was closed, the A-frame was covered with plastic film, and the greenhouse was shown in Figure 1.



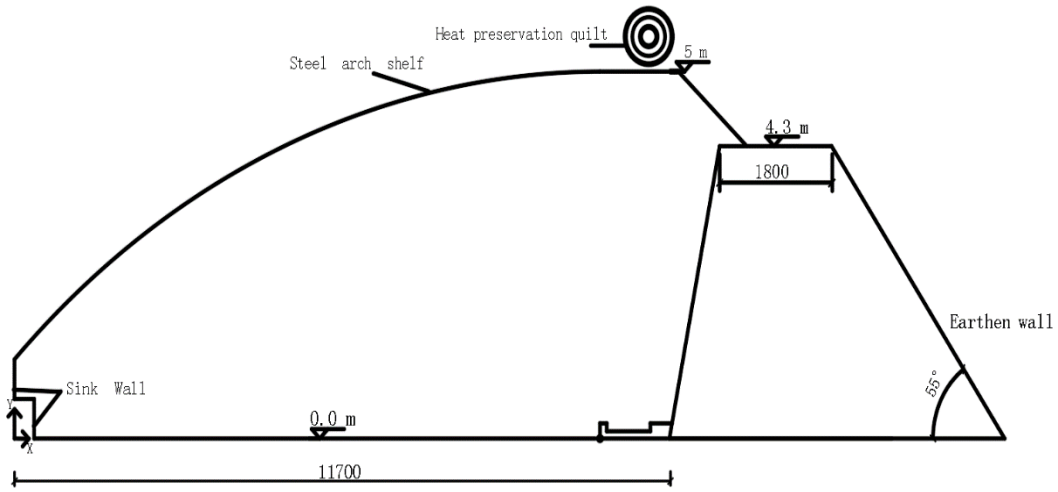


Fig. 1 - Sunken Solar Greenhouse and cross-sectional view

Theoretical basis

Area heat received by space points in indoor air (q_{total})(*Cheng W.W. et al., 2021*):

$$q_{total} = a \cdot S_{total} = S_1^{'} \cdot T_1 \cdot \alpha \cdot (1 - \eta \cdot H_{aze}) + S_2^{'} \cdot T_1 \cdot \alpha \cdot (1 - \eta) \quad (1)$$

where:

q_{total} is the total solar radiation at a point in the indoor space, W/m^2;

$S_1^{'}$ - the direct solar radiation illumination of the light passing through the atmosphere to the outer surface of the greenhouse membrane, W/m^2;

$S_2^{'}$ - the solar scattering radiation illumination of the light passing through the atmosphere to the outer surface of the greenhouse membrane, W/m^2;

T_1 - the direct light transmittance of the film at different roof angles, %;

T_2 - the transmittance of scattered light of the film at different roof angles, %;

S_{Qs} - the amount of scattered solar radiation received by space point Q in the greenhouse W/m^2.

S_{Qz} - the amount of direct solar radiation received by space point Q in the greenhouse, and the incidence angle of light is θ, W/m^2.

H_{aze} - the Haze of covering material, %; q is heat per unit area, W/m^2;

S_{total}- the total solar irradiance of the outdoor horizontal plane, W/m^2;

A_s - the greenhouse ground area, m^2;

α - the correction coefficient of the heated area;

ρ - the indoor sunshine reflectance;

η - the influence coefficient of point scattering quantity, which is related to the coordinate values of y and z of the section where it is located, and has nothing to do with the longitudinal coordinate *x*.

Testing instruments

Wireless sensors are used to collect data at different heights. The indoor temperature and humidity collection instrument in the solar greenhouse is an HT59-Li-A1 wireless temperature and humidity collector developed by Shenyang Weien Technology Co., LTD and calibrated by Liaoning Provincial Institute of Metrology Science, and coordinated with WG59 gateway. The wireless temperature and humidity collector transmits the temperature and humidity data collected by the wireless temperature and humidity collector to the WG59 gateway through GPRS. The WG59 gateway collects the private network data to the cloud server through the Internet and obtains the data information through mobile phones or computers. Temperature measurement range of wireless temperature and humidity collection instrument: 40 ~ 85°C, accuracy: ±0.2° (0 ~ 65°C), ±1° (other temperature range). The transmission period of the wireless temperature and humidity collector and the gateway is 6 minutes, and the data is measured and transmitted continuously 24 hours a day.

Testing methods

To explore the variation law of temperature and humidity in the greenhouse, the duration of indoor high temperature and the maximum indoor temperature value during the stuffy greenhouse period, the temperature and humidity of the sunken solar greenhouse during the stuffy conservatory were measured experimentally. Because the high temperature and high humidity will damage the sensor, the single cross section method is used to measure the temperature and humidity value of sunken solar greenhouse. The cross-section 30 m from the west wall was selected as the cross-section to be measured, and the coordinate system was established in the cross section. The intersection point between the indoor ground and the extension line of the sinking wall was 0, the vertical upward was the positive *y* axis, and the north direction of the line of intersection between the interior floor and the cross section is the *x* axis. The coordinate system was established, as shown in Figure 2. Four positions were selected along the section to be measured from south to north, and s-type hooks were hung on the lower chord of the steel truss at the corresponding positions. The height of the s-type arches was 300 mm, and wire ropes were suspended at the lower end of the arches. Wireless temperature and humidity acquisition instruments were arranged at different heights of the wire ropes. The measurement lines are numbered 1, 2, 3, and 4, and the number of sensors placed on the corresponding lines is 4, 5, 5, and 5. The vertical and horizontal spacing is shown in Table 1. A wireless temperature recorder is placed 1.5 m outside to measure outdoor temperature and humidity.

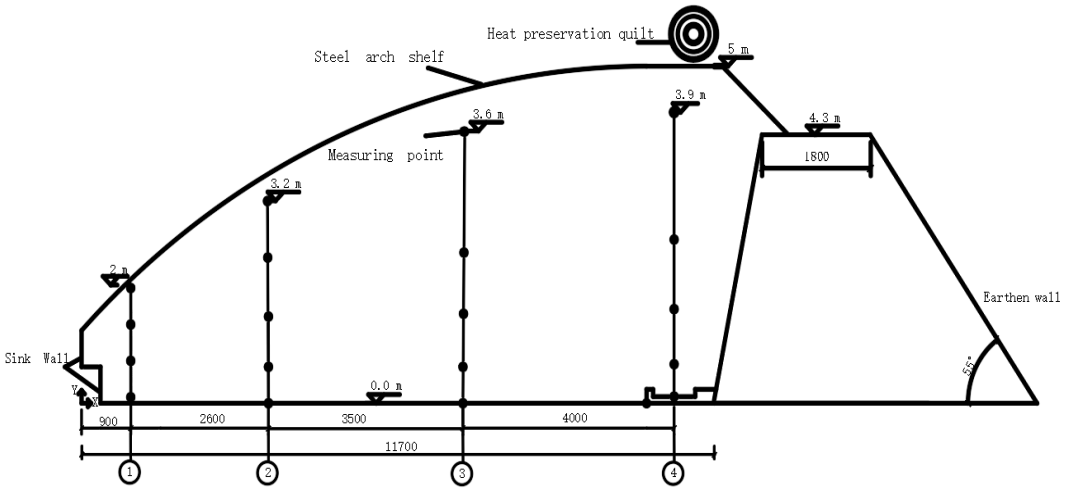


Fig. 2 - Schematic diagram of survey line layout indoor

Table 1

Height from the measuring point to the indoor ground during the closed canopy period (m)

Line number	1	2	3	4
The x coordinate [m] / Measurement point number	0.9	3. 5	7	11
1	2.0	3.2	3.6	3.9
2	1.6	2.4	2.4	2.4
3	0.8	1.6	1.6	1.6
4	0	0.8	0.8	0.8
5		0	0	0

Data processing methods

Origin 8.5 and Excel 2010 were used for data analysis and 2D chart making.

RESULTS AND DISCUSSION

According to the theoretical formula (1): the smaller the horizontal distance from the north wall, the higher the height from the indoor ground, the higher the temperature would be. The temperature value of the measuring point closest to the wall on the north side and the maximum indoor ground height were selected for analysis, that was, the temperature value of measuring point 4-1. In the middle of July 2019, the highest temperature value of the 4-1 measuring point was 69.5°C, 14:30 on July 13, 2019. At this time, it was sunny outdoor, and the outdoor temperature had the lowest value of 19°C and the highest value of 38°C.

The change law of indoor temperature

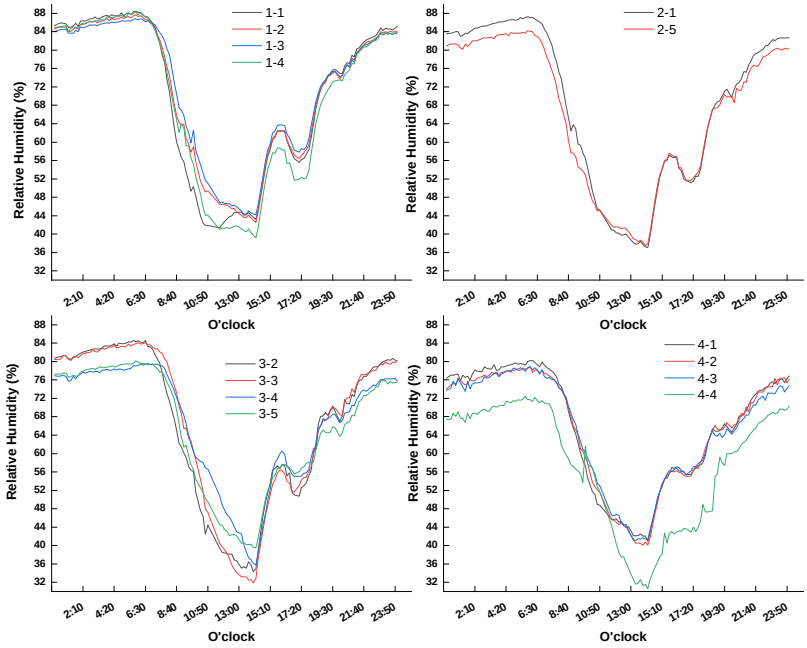


Fig. 3 - The curve of temperature outdoor and measuring points indoor with time

Figure 3 showed that the temperature difference between indoor and outdoor was significant. The maximum temperature difference between indoor and outdoor occurred at 14:10, and the maximum temperature difference between indoor and outdoor was 31.1 °C. At night (00:00-6:00), the temperature value of each measuring point decreased linearly with time. The smaller the indoor ground surface height was, the higher the temperature value was. During this period, indoor air exchanged heat with outdoor through plastic shed film, and indoor wall and indoor soil continued to release heat. Not considering the temperature of the indoor floor, the nighttime temperature difference between measuring points on Line 3 was between 0.1 °C and 0.5 °C. The nighttime temperature difference between measuring points on measuring line 4 was between 0.1 °C and 0.5 °C. At the same time and on the same measuring line, the temperature difference at night between the measuring point at 0 m on each measuring line and the adjacent measuring point was 0.8 ~ 1.2 °C on measuring line 1, No. 3 measuring line was 0.8 ~ 1.1 °C and measuring line 4 was 0.8 ~ 1.1 °C. Therefore, at the same time, the temperature difference at night between the measuring point 0 m away from the upper surface of the indoor ground and the measuring point 0.8 m away from the upper surface of the indoor ground on the same measuring line was more significant than that between the measuring points above 0.8 m.

Between 6:00 and 14:30, the temperature curve of indoor measuring points increased and reached the maximum at about 14:30. The indoor temperature increased because of solar radiation, and the wall and soil on the north side of the room were in an endothermic state. During this period, the temperature of each measuring point increased by 36-43 °C. The maximum temperature of each measuring point on the same measuring line was the point in the middle of the measuring line and the temperature value of the measuring point at 0m on the ground surface was the smallest. This is due to the large difference between indoor and outdoor temperature, resulting in more significant indoor heat loss.

The maximum temperature difference between other measuring points on the same measuring line was 1.2 °C on line 1, 2.9 °C on line 3 and 2.2 °C on line 4, except for the measuring point at 0 m above the ground surface (0 m away from the indoor ground). 14:10 The temperature difference between the temperature value of the measuring point at 0 m on the same measuring line and the adjacent measuring point (the height between each measuring line and the upper surface of the indoor ground is 0.8 m) was 5.6 °C on Line 1, 5.1 °C on Line 3 and 6.6 °C on Line 4. Therefore, it could be seen that the temperature difference between measuring points at 0 m above the indoor ground surface and adjacent measuring points (0.8 m above the indoor ground surface) was more significant than that between measuring points above 0.8 m above the same measuring line.

From 14:00 to 14:30, the temperature of most of the measuring points reached the maximum value, and the time difference of the temperature of each point reaching the maximum value was less than 20 min. The maximum temperature of the indoor measurement point was 69.5 °C, and the outdoor temperature value at the same time was 38.4 °C. At this time, it was the ultimate outdoor temperature, and the difference between indoor and outdoor temperature was 31.1 °C, indicating a significant indoor and outdoor temperature difference. From 14:00 to 14:30, the lowest temperature of each measuring point was 57.1 °C, which was a 4-5 measuring point, located on the upper surface of the indoor ground in the north corridor. The period when the temperature value of all measuring points was greater than 40 °C was 9:50-19:00, up to 9h; The period when the temperature value of all measuring points was greater than 50 °C was 11:40-15:00 for 3 hours. The duration of maintaining room temperature above 40 °C was similar to that of Li JC's research (*Li J.C., 2015*), and its research results showed that it could meet the sterilization requirements.

From 14:30 to 16:00, the temperature values of each measuring point gradually decreased, because the outdoor light intensity gradually reduced, and the heat loss of the greenhouse was more significant than the heat absorption, so the indoor air temperature decreased. From 16:00 to 18:00, the temperature value of each measuring point increased slightly, due to the increase of outdoor light intensity, and the indoor heat absorbed was more significant than the heat loss due to the temperature difference between indoor and outdoor. The temperature values of each measuring point decreased linearly with time from 19:00 to 24:00. To verify whether it was a linear model, a scatter plot was made for the temperature values of each measuring point from 19:00 to 24:00 , and a linear fitting was conducted. The fitting coefficient R^2 was ≥0.9, indicating an excellent proper relationship.

Table 2

The maximum temperature changes at different heights in the room (m)

Height of the point [m]	Line number	1	2	3	4
	The *x* coordinate [m]	0.9	3.5	7	11
0		56.6	-	64	57.1
0.8		62.2	-	69.5	63.4
1.6		63.4	-	67.9	64.1
2.0		62.8			
2.4		-	66.1	-	63.9

It can be seen from Table 2 that the temperature value of the measuring point 0 m away from the upper surface of the indoor ground was the lowest among all measuring lines, and the temperature difference with the adjacent measuring point was the largest. At the same time and line, the temperature of the most significant point was not the biggest point with indoor ground height on the line 3, it was because of the A-frame, which covered strawberries with plastic wrap during the smothering period. No. 3 line measuring point was located on the outer surface of the plastic films, plastic films having a reflection effect on indoor sunlight, in the middle point to receive plastic greenhouse films of reflected light. Therefore, the temperature value of the measuring point at the medium height of No. 3 measuring line was higher. At the same height, with the increase of Y-axis coordinates, the temperature first increased and then decreased. The temperature at line 3 was the highest. This was because line 3 was located in the middle of the greenhouse and received more reflected light from plastic shed film, resulting in a higher temperature at the measuring point of this line.

The change law of indoor relative humidity

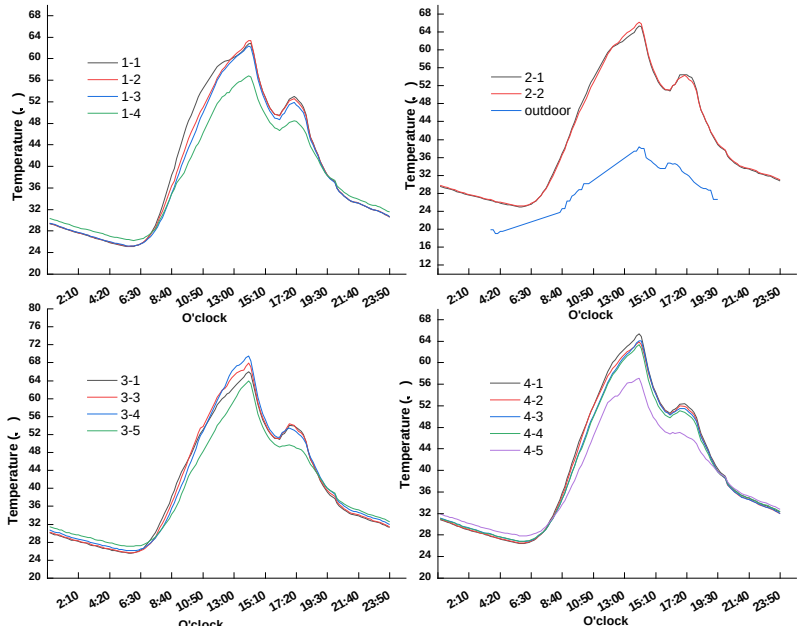


Fig. 4 - Curve of relative humidity measuring points with the time

Figure 2 and Figure 4 showed that: (1) the relative humidity of indoor air was relatively high from 00:00 to 6:00, and the relative humidity of each measuring point was above 67%, and the highest was 90%. During this period, with the decrease of indoor temperature, the relative humidity of each measuring point gradually increased, and the relative humidity of each measuring point decreased between 1.6% and 4.7%.

(2) Between 6:00 and 12:00, the indoor humidity curve decreased, and the lowest relative humidity value was between 30% and 45%; the inflection point of relative humidity at each measuring point was different. The inflection point of most measuring point curves was 6:20, and the latest measuring point of an inflection point in the measuring point curve was the measuring point at 0 m on the surface of the ground, and its time was 8:00. At the inflection point of the relative humidity value of each measuring point over time, the temperature value of each indoor measuring point was more significant than 25°C. During 6:20-7:20, the average temperature drop rate of each measuring point was 0.27°C/10min, and the average relative humidity drop rate of each measuring point was 0.43%/10min. The time when the relative humidity of each measuring point began to drop significantly was 7:30, and the temperature of each indoor measuring point was higher than 29°C. Between 6:00 and 12:00, the average decrease rate of relative humidity of all measuring points was 1.3%/10min, and the average rise rate of the temperature of each measuring point was 1.1 °C/10min.

(3) From 12:00 to 14:00, the relative humidity at each measuring point decreased at a slowly rate. During this stage, the average temperature rise rate at each measuring point was 0.5°C/10min, and the average decrease rate of relative humidity was 0.37%/10min. At this time, the temperature value of all measuring points is more significant than 57°C, and the relative humidity value of all measuring points (excluding 1-4 measuring points and measuring points near the ground) was between 40% and 46%. This was because measuring points 1-4 are located at the beginning of planting, below the upper water pipe and return water pipe of drip irrigation, and there was leakage at the interface. Therefore, the relative humidity value of the measuring points here was around 59%. When 1-4 measuring points were removed, the relative humidity of other measuring points was less than 60% for 5 h, and the relative humidity of other measuring points was less than 50% for 2.2 h.

(4) From 14:00 to 16:00, the relative humidity value of each measurement point increased, which was because outdoor light intensity decreased, indoor air heat absorption was less than the energy loss of indoor and outdoor temperature, resulting in indoor temperature decrease and relative humidity increase. From 16:00 to 17:30, the outdoor light intensity increased, leading to indoor temperature increase, and indoor relative humidity value decreased during this period.

(5) The relative humidity of each measuring point increased from 18:00 to 24:00, and the increased range of relative humidity during this period was more significant than that during 00:00 to 6:00. From 18:00

to 24:00, the average relative humidity drop value of all measuring points was 19.8%, and the average temperature drop value of all measuring points during this period was 12.9°C.

It can be seen that during the stuffy greenhouse period, the indoor relative humidity curve with time and the indoor temperature curve with time in the sunken solar greenhouse showed opposite laws in the same period, and the humidity was at the lowest value, when the temperature was the highest. The relationship between indoor temperature and humidity should be established during the stuffy shed period, to provide a theory for production practice.

The relation between indoor temperature and relative humidity

As can be seen from the change law of indoor relative humidity, when the indoor air temperature was higher than 29°C, the relative humidity of indoor air decreased significantly with the increase of indoor air temperature. Therefore, the relative humidity and temperature at different measuring points from 7:30 to 12:00 were established, providing a theoretical reference for the measures of greenhouse temperature rise and humidity reduction. Since water droplets on the inner surface of the greenhouse film would drop to the ground, resulting in high humidity on the surface of the greenhouse, the relationship between relative humidity and temperature at the measuring point 0 m on the surface of the indoor ground was not considered.

The relative humidity value of each measurement point during 7:20-12:00, on July 13, 2019 was taken as the *Y*-axis, and the temperature value of the corresponding measurement point was taken as the *X* value. The temperature and humidity scatter plot was drawn and linear fitting was carried out. The temperature and humidity curve equation of each measurement point during 7:20-12:00 is shown in Table 3.

Table 3

Temperature and humidity relation diagram of different measuring points from 7:30 to 12:00

Code number	Fitting equation	The correlation coefficient
1-1	y=-1.3405x+115.45	0.94
1-2	y=-1.2788x+115.4	0.96
1-3	y=-1.3502x+119.5	0.97
2-1	y=-1.3193x+116.51	0.97
2-2	y=-1.3285x+116.61	0.98
3-1	y=-1.1763x+107.81	0.97
3-3	y=-1.2778x+113.76	0.98
3-4	y=-1.4094x+122.96	1
4-1	y=-1.2027x+112.14	0.98
4-2	y=-1.1924x+111.58	0.98
4-3	y=-1.1789x+110.6	0.99
4-4	y=-1.1282x+109.29	1

N-M in Table 3 represents the *M* measuring point on measuring line *N*, for example, *4-3* represents the 3rd measuring point on measuring line 4.

It can be seen from Table 3 that: during the period from 7:30 to 12:00, the curve fitting of relative humidity and temperature at different measuring points was good, and the correlation coefficient R^2 was > 0.94. In this period, over time, the indoor light intensity increased, and the relative humidity of the indoor measurement point and the temperature of the corresponding measurement point were linearly negative correlation, that was, with the increase of temperature, the indoor relative humidity gradually decreased. At different measuring points, the change rate of the curve equation was between -1.1 and -1.4. The temperature of each measuring point reached 57°C at noon, and the humidity of each measuring point at this time was less than 50%.

In order to study the relationship between temperature and humidity in the sunken solar greenhouse during the period from 7:30 to 12:00, the weighted average value of the change rate of temperature and humidity curves at each measuring point was calculated, and the formula was as follows:

$$\bar{v} = \frac{\sum y_i z_i v_i}{y_i z_i} \quad (2)$$

In formula (2), y_i and z_i were the coordinate values of the measuring points, and were the change rates of the relative humidity and temperature curves of the measuring points. Thus, the weighted average speed can be obtained as -1.23. During the stuffy period, the indoor temperature increased by 1°C, and the indoor relative humidity decreased by 1.23%. At 7:00, the relative humidity of each measuring point was located near (78±2)%, so the humidity value of the corresponding measuring point can be obtained according to the temperature of different measuring points, thus providing a theoretical basis for the relationship between indoor temperature and humidity.

CONCLUSIONS

This paper analyzed the pattern of temperature and humidity changes in the sunken solar greenhouse. The following conclusions were drawn:

(1) Temperature and humidity relationships during the day in a sunken solar greenhouse were reversed during smothering. There were three phases of temperature change during the day: the rising curve, the fluctuating phase and the falling curve.

(2) The maximum value of indoor temperature at noon was 69.5°C. When the measurement points at the upper surface of the floor were removed, the relative humidity value of other measurement points was less than 60% for a period of 5 h, which can meet the requirements of greenhouse sterilization for high temperature and low humidity environments.

(3) During the 7:00-12:00 time period, when the room temperature was all greater than 28°C and the initial relative humidity values at each measurement point were located between 70% and 85%, the weighted temperature at each measurement point began to rise at a rate of 1.1°C/10min and the weighted humidity at each measurement point fell at a rate of 1.3%/10min. There was a relationship between the temperature and humidity changes in the greenhouse.

ACKOWLEDGEMENT

I am very grateful to Prof. Shuangxi Wang, Prof. Junlin He and Associate Prof. Zhonghua Liu. I am very grateful to the College of Urban and Rural Construction for their help during the experiment and to Shanxi Agricultural University for the PhD start-up costs.

REFERENCES

[1] Cheng Weiwei (2021). *Study on thermal environment and marginal effect of sunken solar greenhouse (下沉式日光温室三维热环境及边际效应的研究).* College of Agricultural Engineering, Shanxi Agricultural University.

[2] Chen P., Wang Y.Z, Liu Q.Z. et al (2020). Phase changes of continuous cropping obstacles in strawberry (Fragaria × ananassa Duch) production[J]. *Applied Soil Ecology*, 155:103626.

[3] Fu G.H., Liu W.K. (2016). Sunlight greenhouse pepper ridging embedded substrate cultivation root zone temperature variation characteristics (日光温室甜椒起垄内嵌式基质栽培根区温度日变化特). *Chinese journal of eco-agriculture,* 24(1):47-55.

[4] Hu Q.Q., LI Y., Lu G.Q. (2015). Effect of high temperature smoking-shed technology on continuous cropping obstacle control of pepper greenhouse (高温闷棚技术对设施辣椒 连作障碍防治效果的研究). *Journal of pepper science,* 13(1): 23-25.

[5] He Z.G., Lou C.R., Dong H. (2018). Effects of straw returning on soil microhabitat and growth and development of tomato under continuous cropping (秸秆还田与高温闷棚对设施连作土壤微生境及番茄生长发育的影响). *Journal of Henan agricultural sciences.* 47(10):87-91.

[6] He Wei, Luo Wenfang, Yu Zhenhua et al (2022). Higher temperature Influence on the control effect of the root-knot nematode and soil microbial community structure of vegetables in the facility (高温闷棚对设施蔬菜根结线虫的防治效果及土壤微生物群落结构的影响). *Xinjiang Agricultural Science*, 59(1):179-189.

[7] Jia W.S., Li M.N., LI Y. (2016). Application of Key Internet Thing Technologies in Facility Agriculture. *Journal of Food Safety and Quality,* 7(11):4401-4407.

[8] Lal R. (2020). Home gardening and urban agriculture for advancing food and nutritional security in response to the COVID-19 pandemic, *Food Secur*. 12 (4): 871–876.

[9] Li J.C. (2015). *Effect of irrigated high temperature smothered shed on soil remediation of continuous cropping in greenhouse (灌水高温闷棚对温室连作土壤修复效果的研究).* Xi'an: College of Horticulture, Northwest A&F University.

[10] Morshed W., Abbas L., Nazha H. (2022). Heating performance of the PVC earth-air tubular heat exchanger applied to a greenhouse in the coastal area of west Syria: An experimental study, *Therm. Sci. Eng. Prog*. 27:101000.

[11] Peng P., Liang L., Li H.L., Zhao G.S. (2019) Current situation, Problems and development suggestions of Facility agriculture in China (我国设施农业现状、问题与发展建议). *Northern Horticulture* (05):161-168.

[12] Shi L.J., Sun J.Q., Cai C. (2021) Methods of swarming greenhouse in Shandong province and matters needing attention (山东地区常用的闷棚方法及注意事项). *Modern Agricultural Science and Technology* (17):88-89.

[13] Sun B., Bai Z., Bao L. et al. (2020). Bacillus subtilis biofertilizer mitigating agricultural ammonia emission and shifting soil nitrogen cycling microbiomes[J]. *Environment International*, 144: 105989.

[14] Ghani S. et al. (2019). Design challenges of agricultural greenhouses in hot and arid environments – A review, *Eng. Agric. Environ*. *Food.* 12 (1):48–70.

[15] Steven W., Van G., Thomas I. (2017). Energy Water and Nutrient Impacts of California-grown Vegetables Compared to Controlled Environmental Agriculture Systems In Atlanta, GA. *Resource, Conservation and Recycling*. 122:319-325.

[16] Wang S.Q., Zhang Z.L., Hou W.N. (2012) Characteristics of soil temperature variation in southern marginal area of sunken solar greenhouse (下沉式日光温室南侧边际区域土壤温度变化特征). *Transactions of the Chinese society of agricultural engineering*. 28 (8): 235-240.

[17] Zhang L.H., Zhang F., Liu S., Xu L. (2010) Three-dimensional unsteady simulation of indoor temperature field of sunken earth wall greenhouse (下沉式土质墙体温室室内温度场的三维非稳态模拟). *Acta Solar Energy Sinica.* (31).

CERASUS HUMILIS CULTIVARS IDENTIFICATION WITH SMALL-SAMPLE AND UNBALANCED DATASET BASED ON EFFICIENT NET-B0+RANGER NETWORKS
/
基于 EfficientNet-B0+Ranger 的小样本不平衡数据集欧李品种识别

Lili LI [1]; Hua YANG [*1]; Bin WANG [1] [1]
[1] College of Information Science and Engineering, Shanxi Agricultural University, Taigu 030800/China
Tel: 13466883256; E-mail: yanghua@sxau.edu.cn
DOI: https://doi.org/10.35633/inmateh-69-21

Keywords: *cerasus humilis cultivars, efficientNet-B0+Ranger, small-sample, unbalanced dataset, complex environment*

ABSTRACT

Because of the high similarity of leaves of different Cerasus humilis varieties, it is difficult to identify them with the naked eye. In this study, the leaves of four different Cerasus humilis varieties collected in the field were used as the research objects, and a new leaf recognition model based on the improved lightweight convolution neural network model EfficientNet-B0 was proposed. Firstly, the performance of the network models Efficientnet-B0 and ResNet50, GoogleNet, ShuffleNet, and MobileNetV3 were compared based on two different learning methods. Then, the influence of different optimizers on model recognition accuracy was compared based on the optimal model. Finally, different learning rates were used to optimize the optimal model. The results show that the recognition rate of the proposed Efficientnet-B0 +Ranger+0.0005 model was up to 86.9%, which was 2.23% higher than that of the original Efficientnet-B0 model. The results show that this method can effectively improve the recognition accuracy of Cerasus humilis auriculate leaves, which can provide a reference for the deployment of the leaf identification model of Cerasus humilis variety on the mobile terminal.

摘要

针对不同欧李品种叶片相似度高，用肉眼难以鉴别的问题。本研究以田间收集的4种不同欧李品种叶片为研究对象，提出一种基于改进轻量级卷积神经网络模型EfficientNet-B0的欧李品种叶片识别模型。首先，基于2种不同学习方式对比EfficientNet-B0与ResNet50, GoogleNet, ShuffleNet, MobileNetV3等网络模型的性能；然后，基于最优模型对比不同优化器对模型识别准确率的影响；最后采用不同学习率（0.0001, 0.0005, 0.001, 0.005, 0.05)对优选出的模型进行优化。结果表明该研究提出的EfficientNet-B0+Ranger+0.0005模型识别率达到86.9%，相比于改进前的EfficientNet-B0模型，其识别率提高了2.23%。研究结果表明，该方法可有效提高欧李品种叶片的识别准确率，可为移动端部署欧李品种叶片识别模型提供参考。

INTRODUCTION

Cerasus humilis (Bge.) Sok. belongs to the Rosaceae cherry genus shrub fruit tree. It is a unique fruit tree resource in China. Cerasus humilis fruit is rich in active calcium and easy to be absorbed by the human body, it is also known as the “fruit rich in calcium”. It has the ability of early fruiting, high yield, cold resistance, drought resistance, stubble resistance, wind and sand fixation, and soil erosion control. It is a strategic tree species for sustainable development *(Bai et al., 2015)*.

In recent years, with the increasing variety of Cerasus humilis cultivars, the planting area has gradually expanded. However, the pest control and management of different cultivars of Cerasus humilis are different. The identification of Cerasus humilis cultivars is mostly carried out by plant protection experts, which often has a high recognition rate, but it is time-consuming, labor-consuming, subjective, and with the given scientific and genetic advances, many of the hybrid Cerasus humilis cultivars cannot be identified by ordinary individuals and even gardening experts *(Ferentinos et al., 2018)*. So, computer vision and machine learning techniques are used to solve these problems. The images of leaves had been used by many researchers of computer vision to identify species of plants *(Kalyoncu et al., 2015; John et al., 2021).*

[1] *Lili Li, Lec. Ph.D.; Hua Yang*, Prof. Ph.D.; Bin Wang, Ph.D.*

Leaf shape is the feature most commonly used to develop automated plant classification systems. Other than the shape *(Mouine et al., 2012)*, the leaf can provide some additional information such as textures *(Naresh et al., 2016)*, venation *(Charters et al., 2014)*, and colors *(Tan et al., 2018)*. Although there are many studies aimed to classify different plant species, they were based on the common fact that the leaves they used had different colors and shapes, which made the classification task easier. In contrast, the leaves of Cerasus humilis cultivars are generally of the same color and similar in shape, so using these methods to classify Cerasus humilis cultivars with leaf images used the method of computer vision is challenging and problematic.

Recently, deep learning methods especially the Convolutional Neural Network (CNN) had been employed for the automated extraction of features. It can extract more detailed information as compared to conventional machine learning techniques. And deep learning models have been well used in the field of agriculture, such as weed and seed detection, counting, plant disease identification, root segmentation, etc. The common deep learning classification methods based on the convolutional neural network (CNN) are AlexNet, VGGNet, GoogleInceptionNet, and ResNet.

Liu et al. (2018) proposed a ten-layer CNN for plant leaf classification on a leaf database of Flavia which contains 4,800 leaf images and 32 kinds of leaves, and the result showed that the proposed method achieved a high overall accuracy of 87.92%. *Beikmohammadi et al. (2020)* proposed a new method and compared it with three deep learning-based models (S-Leaf Net, W-Leaf Net, and P-Leaf Net). The tests were conducted on the two well-known datasets of leaf identification, i.e. MalayaKew (MK) and Flavia. The results showed that the proposed method obtained 99.81% and 99.67% of accuracy and outperformed all the other methods. Unfortunately, when transferring these methods from species identification to cultivar identification, most of them performed worse due to the high similarity of leaves among different cultivars.

Although the deep network model had achieved excellent performance in the plant leaf classification task. However, considering the real environment of crop growth, deploying trained deep network models on mobile phones or embedded devices still faces significant challenges. The main influencing factors include huge model parameters, long training time, and large storage space *(Li et al., 2019)*. Therefore, the current research tends to miniaturize and apply the model structure. Among them, *Sun et al. (2017)* proposed an improved convolutional neural network model that combines batch normalization (BN) and global pooling to train 21917 leaf images collected by PlantVillage. After only three training sessions, the recognition accuracy reached over 90%.

Guo et al. (2019) proposed a convolutional neural network image recognition method for plant leaves based on transfer learning, and the recognition accuracy achieved by AlexNet and InceptionV3 models reached 95.31% and 95.40%, respectively.

Liu et al. (2019) proposed two lightweight convolution neural network models for crop disease classification based on MobileNet and Inception V3, comprehensively considered the recognition accuracy, operation speed, model size, and other indicators to select the best, and realized the leaf detection of a mobile terminal. At present, most of the methods are based on public datasets, which contain simple backgrounds and many plant species, and there is little research on the identification of the plant cultivars, such as the author *Zhang et al. (2021)* proposed an automatic leaf image-based cultivar identification pipeline called MFCIS (Multi-feature Combined Cultivar Identification System), to identify 88 Sweet cherry cultivars and 100 Soybean cultivars and achieved an overall accuracy of 83.52% and 91.4%, respectively.

Liu et al. (2020) proposed an efficient and convenient method for the classification of 14 apple cultivars using a deep convolutional neural network and achieved an overall accuracy of 97.11%. Although these studies aimed to classify different plant cultivars the images they used were also simple backgrounds. However, there is little research on the identification of plant cultivars in the field environment.

Based on these problems, this paper used the classic lightweight CNN structure EfficientNet to identify 4 Cerasus humilis cultivars by using the leaf images collected in the natural environment. To deploy the trained model to the mobile terminal to establish an intelligent detection system, and realize the rapid identification of Cerasus humilis cultivars according to the leaves.

The remainder of this paper is organized as follows. In section 2 the datasets, data augmentations performed, and Cerasus humilis cultivars diagnosis model are presented, Section 3 presents the experimental setup as well as analyzes the experimental results provided by the identification approach to Cerasus humilis cultivars based on CNNs. In section 4 the significance of the identification of Cerasus humilis cultivars is discussed. Finally, this paper is concluded in Section 5.

MATERIALS AND METHODS

In this section, the procedure of identifying Cerasus humilis cultivars by using leaf is segregated into seven steps processes which showed in Fig. 1.

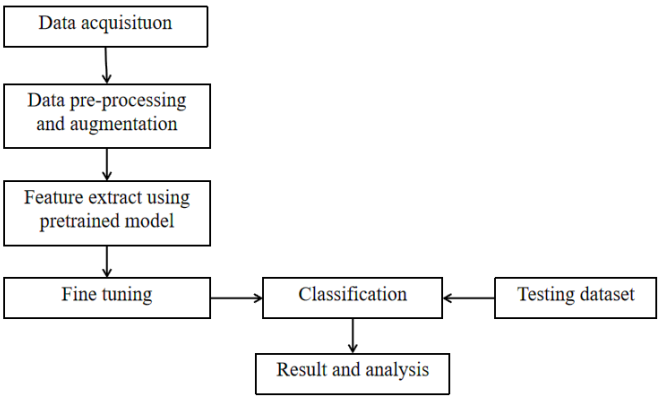


Fig. 1 - The procedure of the work

Dataset

The 4 Cerasus humilis cultivars leaf images used in this study were collected from the Cerasus humilis planting demonstration base in the national (Jinzhong) agricultural high-tech industry demonstration zone. The base covers an area of about 6000 square meters, with a total of 1000 Cerasus humilis trees, all of which are 4 years old. In the process of taking photos, it is also considered the influence of angle, illumination, occlusion, and other complex environments, to take into account the influence of as many environmental conditions as possible in the process of data acquisition. And the samples were labeled according to the cultivars of the Cerasus humilis plant, and the label name was the name of Cerasus humilis cultivars.

Under the natural environment conditions, multi-angle collections were carried out at different times. The mobile phone camera lens was used to take images 10~20 cm away from the Cerasus humilis leaf. The images dataset includes 4 Cerasus humilis cultivars, that is Nongda-4 Cerasus humilis leaves (403 images), Nongda-5 (476 images), Nongda-6 (581 images), and Nongda-7 (558 images). Examples of leaf images for all 4 Cerasus humilis cultivars are shown in Fig. 2.



a) Nongda-4 *b) Nongda-5* *c) Nongda-6* *d) Nongda-7*

Fig. 2 - Leaves of different varieties of Cerasus humilis

Fig. 2 reveals that the leaves of 4 Cerasus humilis cultivars are generally very simple and similar to each other, and they have an elliptical-to-ovate shape and small difference in length and width, with a sharp apex and round and blunt serrated edges. Due to these similarities, there are challenges in classifying Cerasus humilis cultivars.

Image Preprocessing and Augmentation

Image Preprocessing

Image preprocessing helps to improve data quality and enhance transform information features. The preprocessing of experimental data in this study includes redefinition of image size, pixel averaging, and normalization of each batch of samples. In this experiment, the image is redefined as 224×224×3. The purpose of image de-averaging is to standardize the image and remove the average brightness value of the image. The specific operation is as follows: for the given size redefined image, each pixel value of each sample subtracts the average pixel value of the whole training sample. In many cases, it is not sensitive to the brightness of the image but pays more attention to its content. For CNNs, data normalization is necessary for gradient descent, and it can also prevent gradient explosion, accelerate network convergence and further reduce the number of feature maps. The batch normalization method is used in this experiment,

and each sample image in the batch needs to be normalized. The processing of the image x is shown in Equations (1) and (2):

$$\mu = \frac{1}{n}\sum_{i=1}^{n} x_i \quad (1)$$

$$\sigma = \frac{1}{n}\sum_{i=1}^{n} (x_i - \mu)^2 \quad (2)$$

Where x_i represent the value of the i-th pixel of the sample, n is the total number of pixels of the sample, μ represents the mean value, and σ represents the variance.

The normalization is shown in Equation (3):

$$\hat{x}_i = \frac{x_i - \mu}{\sqrt{\sigma^2 + \varepsilon}} \quad (3)$$

Where $\hat{x}_i$ is the normalized pixel value of the i-th pixel of the image x, ε is a small value greater than 0 to ensure that the denominator is greater than 0.

Image Augmentation

Image augmentation can increase the diversity of images, reduce the dependence of the model on some attributes, and improve the performance and generalization ability of the model. The following image augmentation technique was mainly used: random rotation angle (the maximum rotation angle is 30º), random horizontal or vertical translation (the maximum translation distance is 0.1× image width or height), random horizontal flip and other operations, and slight disturbance were introduced to realize data expansion, the missing pixels were filled with the adjacent pixels after image enhancement. In deep learning, the uneven distribution of samples will affect the accuracy. Finally, in order to meet the data balance of each category, after image augmentation, the image became Nongda-4 (3180 images), Nongda-5 (2555 images), Nongda-6 (3140 images), Nongda-7 (3095 images). Whereafter, according to the ratio of 8:1:1, it was randomly divided into the training set, validation set, and test set.

Convolutional Neural Network Models

Actually, for obtaining an optimal model, we tried several deep learning models. In this section, there will be simply introduced state-of-the-art CNNs such as ResNet50, GoogleNet, MobileNetV3, ShuffleNet, EfficientNet-B0 *(Tan et al., 2018)*, and improved EfficientNet-B0.

EfficientNet Model

The birth of CNNs promotes the development of deep learning, from the original convolutional layer, pooling layer, and full connection layer, which consists of simple network LeNet, AlexNet, and VGG-16 *(Charters et al., 2014)*, to ResNet, Inception, and GoogleNet.

In order to improve the accuracy and efficiency of the model, the current general method is to amplify the depth, width, and resolution of CNN. Previously, it was used to amplify one of the three dimensions alone. For example, ResNet18 to ResNet152 increased the network depth to improve the accuracy. Although it is possible to enlarge two or three dimensions arbitrarily, it needs tedious manual parameter adjustment and may produce a suboptimal accuracy and efficiency. The experimental study in reference showed that the three dimensions of depth, width, and resolution affect each other. How to balance these three dimensions is crucial. It is verified that such a balance can scale each dimension by simply using a set of constant ratios. On this basis, the latest network EfficientNet was proposed. In the model, a simple and efficient multi-dimensional hybrid scaling method was proposed, that is to find a set of fixed scaling factors that can take into account both speed and accuracy to scale the depth, width, and resolution of the network.

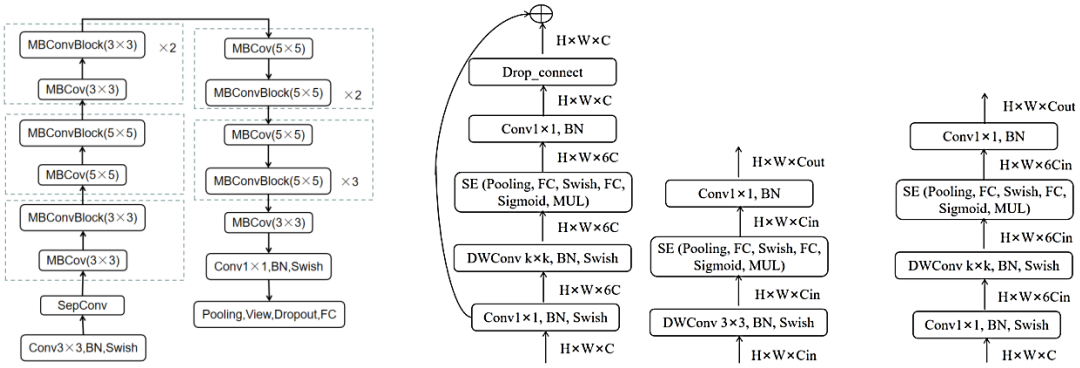
The EfficientNet group consists of 8 models between B0 and B7, and the EfficientNet-B0 network structure consists of 16 MBConv+2 Conv+1 Global average pooling + 1 FC classification layer. In addition, MBConv (mobile inverted bottleneck convolution) module is used in the network, and the attention idea of the SENet (Squeeze-and-Excitation Network) is introduced.

The overall structure of the EfficientNet-B0 was shown in Table 1, and the network structure can be seen in Figure 3. Where (a) is a representative model selected from Table 1; (b)-(d) are a few corresponding layer structures. MBCov denotes mobile inverted bottleneck Conv, DWCov denotes depthwise Conv, k3×3/k5×5 denotes kernel size, BN is batch normalization, and H×W×C denotes tensor shape (height, width, channel).

Table 1

The overall structure of the EfficientNet-B0

Stage	Operator	Resolution	#Channels	#Layers
i	$\hat{F}_i$	$\hat{H}_i \times \hat{W}_i$	$\hat{C}_i$	$\hat{L}_i$
1	Conv3×3	224×224	32	1
2	MBConv1,k3×3	112×112	16	1
3	MBConv6,k3×3	112×112	24	2
4	MBConv6,k5×5	56×56	40	2
5	MBConv6,k3×3	28×28	80	3
6	MBConv6,k5×5	14×14	112	3
7	MBConv6,k5×5	14×14	192	4
8	MBConv6,k3×3	7×7	320	1
9	Conv1×1&Pooling&FC	7×7	1280	1



a) The EfficientNet-B0 structure *b) MBConvBlock(k×k)* *c) SEPConv* *d) MBconv (k×k)*

Fig. 3 - The EfficientNet-B0 structure

Unlike other CNN models, EfficientNet uses a new activation function called Swish instead of the Rectifier Linear Unit (ReLU) activation function. And the EfficentNet-B0 contains 5.3M parameters, as it is suitable according to our resources and purpose.

Swish

The choice of activation functions in deep networks has a significant effect on the training dynamics and task performance. Currently, the most successful and widely-used activation function is the Rectified Linear Unit (ReLU). Although various alternatives to ReLU have been proposed, none have managed to replace it due to inconsistent gains. In 2017, *Ramachandran et al. (2017)* proposed to leverage automatic search techniques to discover new activation functions named Swish, that is, $f(x) = x \cdot sigmoid(\beta x)$. Where β is a hyperparameter.

The form of the Swish function is very simple, and almost a patchwork of Sigmoid and ReLU, with characteristics of smooth, non-monotonic, with no upper bound but a lower bound. The Swish tends to work better than ReLU on deeper models across several challenging datasets. And the simplicity of Swish and its similarity to ReLU make it easy for practitioners to replace ReLUs with Swish units in any neural network.

Improved EfficientNet-B0 Model

To further improve the accuracy of the EfficientNet model, we adopted the current state-of-the-art Ranger optimizer proposed by Dang. The Ranger optimizer combines the ideas of RAdam and LookAhead. Among them, RAdam (Rectified Adam) is a variant of Adam, which utilizes dynamic rectifiers to adjust Adam's adaptive momentum according to variance, and provides an automatic warm-up mechanism effectively customized based on the current dataset to ensure a solid first step in training. LookAhead was inspired by the latest developments in deep neural network loss surface understanding and provided a breakthrough in robust and stable exploration throughout the entire training period. The LookAhead optimizer

reduces the need for extensive hyperparameter adjustment, while achieving faster convergence of different depth learning tasks with minimal computational overhead. Therefore, the combination of RAdam and LookAhead optimizers had high synergy and can provide the best improvement in deep learning optimization.

Metrics

In order to evaluate the results of the proposed method for the identification of Cerasus humilis cultivars, the average identification accuracy, and the model parameters were considered respectively.

Average Accuracy (AA)

Average Accuracy (AA) represents the proportion of currently classified predictions, it refers to the ratio of the predicted correct samples to all the observed samples. It is the most important metric index to evaluate the performance of the model, and is calculated as equation (4):

$$\mathrm{AA} = \frac{1}{n_s}\sum_{i=1}^{n_s}\frac{n_{ii}}{n_i} \tag{4}$$

Where n_s is the total number of sample categories (in this paper, the focus is on the four sample categories of Cerasus humilis cultivars, so $n_s = 4$), i is the label of the sample category, n_i is the total number of class i samples, n_{ii} is the total number of class i samples (that is, the number of correctly predicted samples in each type).

Model Parameters

With the improvement of the accuracy of the network models, the hardware resources required for the deployment and operation of the models are considered while improving the identification accuracy. Too complex network models occupy a lot of storage and computing resources, which limits their deployment and operation in the scenario of limited hardware resources. Therefore, the size of the model is also one of the key factors to be considered.

Transfer Learning

Deep learning usually requires a large number of training samples, and the models with small images are prone to over-fitting, thus reducing the generalization ability of the models. Deep learning involves initializing weights on pre trained networks on large labeled datasets (such as ImageNet datasets), rather than randomly initializing from existing sample sets.

However, transfer learning is to adapt the convolutional neural network model trained on a task to a new task through simple adjustment. And it can reduce the number of images, save time, and improve the accuracy of training models.

The cerasus humilis leaf dataset in this study is a small sample dataset. The transfer learning method will be used to fully train the pre trained models (such as MabileNetV3, ResNet50, GoogLeNet, ShuffleNet, and EfficientNet-B0) and apply them to the recognition of different kinds of leaf images.

Experiment Setup

The training and testing of the model were completed under the Cuda deep learning framework. Hardware environment of the platform: NVIDIA GTX 1650 GPU, 16G graphics memory, Intel Xeon Gold 6271C @2.60GHz CPU, 32GB of memory. Software environment: Python 3.7, Cuda10.1.

To avoid memory overflow, batch training methods were used to compare the EfficientNet-B0 model with Google Net, MobileNetV3, ShuffleNet, and ResNet50 on the training and validation sets. During the training and validation process, 16 images were set for each batch. In this paper, the number of iterations was set to 50, and the Categorical-cross entropy in Keras was used as the cost function. In order to solve the problem of gradient disappearance and explosion in the process of backpropagation, using batch normalization (BN) to normalize the characteristic map of each sample formed after the convolution layer can well solve the problem that the distribution of data in the middle layer changes during the training process of the model, accelerate convergence, improve accuracy, and reduce overfitting.

To accurately obtain the parameters of the training model, the optimal model is determined by observing the change of the loss function of the validation set after each iteration, and the model is applied to the test set to realize the prediction of leaf varieties.

RESULTS AND ANALYSES

The Compared Results of Different Transfer Learning Strategies

The main purpose of this study is to examine the success of EfficientNet-B0 deep learning architecture in the identification of Cerasus humilis cultivars and compare it with the performances of state-of-the-art CNN models in the literature. Three sets of comparative experiments of different learning methods, different optimizers, and different learning rates are carried out.

Two transfer learning strategies had been considered as follows. One is that instead of random initialization, the network weights are initialized by the pre-trained network model in the ImageNet data set and global fine-tuning is performed. Another method was that freeze the weights of all networks, except for the final fully connected layer. And use the pre trained model as a feature extractor (ResNet50, MobileNetV3, and EfficientNet-B0) to learn the corresponding features of the target dataset by fine-tuning the fully connected layer. In this section, the optimizer selected is Adam, and the learning rate was set to 0.0001.

The First Transfer Learning Strategy

In this section will be given the testing results of 5 kinds of deep learning models, including MobileNetV3, GoogleNet, ResNet50, ShuffleNet, and EfficientNet-B0, by using the transfer learning method of strategy one. Among them, ResNet50 and GoogleNet belong to traditional CNNs, and the other three belong to lightweight CNNs.

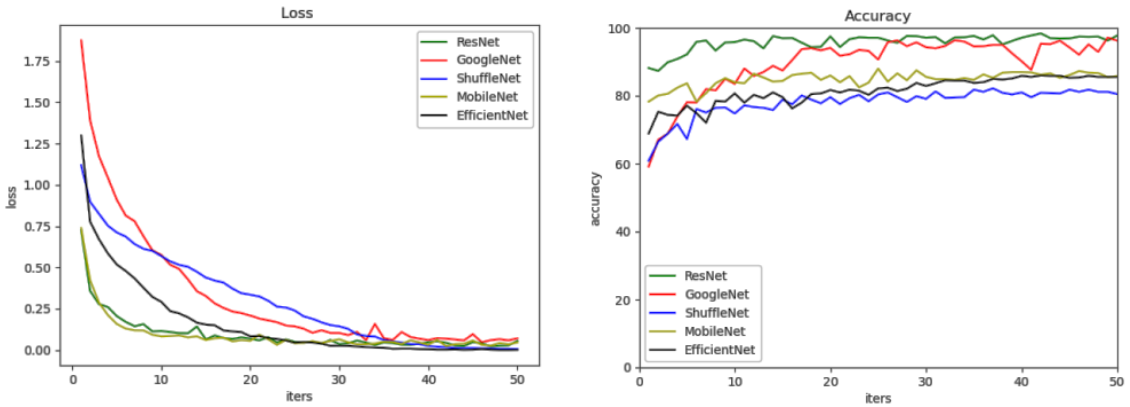
In this context, the average accuracy on the test set, and model parameters obtained by all models were given in Table 2 for the 4 Cerasus humilis cultivars leaf datasets.

Table 2

The comparison results of different models

Model	Model parameters	Average accuracy(%)
ResNet50	25,664,453	97.89
GoogleNet	10,318,655	95.72
MobileNetV3	4,232,837	84.29
ShuffleNet	1,274,909	75.12
EfficientNet-B0	4,055,976	84.67

The results showed that although the recognition accuracy of the traditional deep learning model ResNet50 and GoogleNet was higher than that of the lightweight model, their model size and average recognition time were also much larger than the other three lightweight models. The accuracy rates of the two lightweight models are all above 84.0%, except for ShuffleNet 75.12%, which proved the feasibility of applying transfer learning to identify the 4 Cerasus humilis cultivars in the real environment. In addition, considering that it will be deployed on the mobile terminal to identify the Cerasus humilis cultivars in the future, the lightweight model will be selected for research later.



a) Loss function value *b) Average accuracy*

Fig. 4 - The accuracy and loss function on the verification set

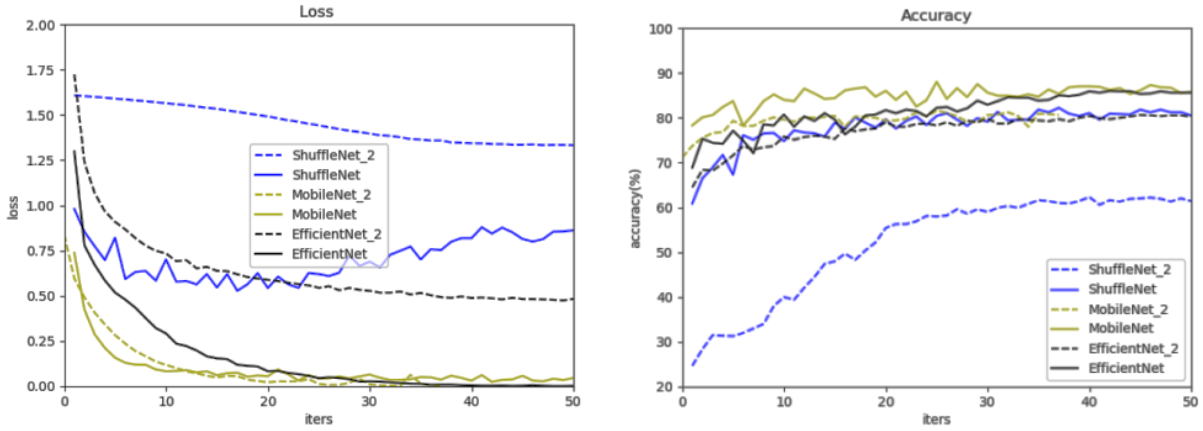
Fig. 4 shows the change of precision and loss function of each model in the validation set when the number of training iters was set to 50. From Fig. 4(a), it can be seen that the lightweight model EfficientNet-

B0 has a very smooth loss on the validation set, while the models MobileNetV3 and ShuffleNet have a relatively smooth loss on the validation set.

As shown in Fig. 4(b), the models showed that different characteristics in the validation accuracy change during the training. The overall recognition accuracy of EfficientNet-B0 and MobileNetV3 models was higher than ShuffleNet. MobileNetV3 had a higher verification accuracy in the initial iteration, and its accuracy shook during the iteration process. For EfficientNet-B0 with the number of iterations increases the accuracy had been showing an upward trend, and the shaking phenomenon was not obvious, indicating that the EfficientNet-B0 model, which had been co-expanded in depth, width and resolution, compared with the MobileNetV3 and ShuffleNet model has higher stability and can steadily improve the accuracy of the model.

The Second Transfer Learning Strategy

In this section will be given the testing results of 3 kinds of lightweight deep learning models by using the transfer learning strategy two, utilizing the pre-trained neural network architectures such as MobileNetV3, ShuffleNet, and EfficientNet-B0 as feature extractors, and the top layers are truncated by defining a new fully-connected layer with the practical number of classification and fine-tuned the higher dimensional layers.



a) Loss function value *b) Average accuracy*

Fig. 5 - The results of different transfer learning strategies

Fig. 5 showed the average precision and loss function values of different network models on the validation set when two transfer learning methods are applied. In Fig. 5, the first transfer learning method was represented by a solid line, and the second transfer learning method was represented by a dotted line. From the training results, it can be seen that the accuracy curves that for all models, fine-tuning the parameters of a pre-trained neural network architecture achieved higher classification accuracy as compared to using the neural network architecture with feature extraction only. Therefore, it is necessary to fine tune all layers of the network model using the transfer learning method.

Second, since the early stopping technique was used during the training, Fig. 5 showed that MobileNetV3 triggers early stopping in iteration 38 when using the neural network architecture as feature extractors only, while ShuffleNet and EfficientNet-B0 do not trigger early stopping during training. So the ShuffleNet and EfficientNet-B0 had better stability than MobileNetV3. From Fig. 5(a), it can be seen that the lightweight model EfficientNet-B0 has a very smooth loss on the validation set, while the model MobileNetV3 and ShuffleNet have a relatively smooth loss on the validation set, but the ShuffleNet has Serious oscillation.

The analysis results indicate that compared with other models, the EfficientNet-B0 model has the best classification accuracy in the four types of leaf datasets.

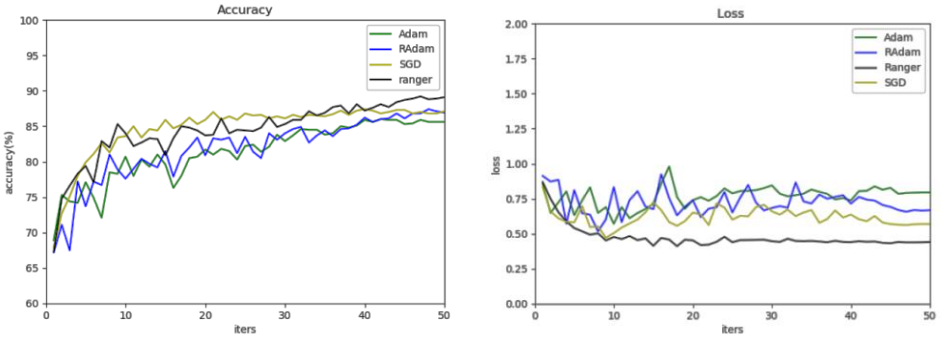
The Improved EfficientNet-B0

In this section, EfficientNet-B0 is used with Adam, RAdam, SGD, and Ranger optimizers respectively, and the accuracy of the models with different optimizers in the validation set and test set were shown in Table 3. In this section, the learning rate was set to 0.0001. The results in Table 3 showed that the accuracy of EfficientNet-B0 + Ranger was the highest in both the validation set and test set, and the other three had little difference.

Table 3

Comparison of EfficientNet-B0 with different optimizers

Model	Verification accuracy (%)	Test accuracy (%)
EfficientNet-B0+Adam	86.0	84.7
EfficientNet-B0+RAdam	87.4	85.3
EfficientNet-B0+SGD	87.4	85.1
EfficientNet-B0+Ranger	89.2	86.8



a) Accuracy rate curve *b) Loss curve*

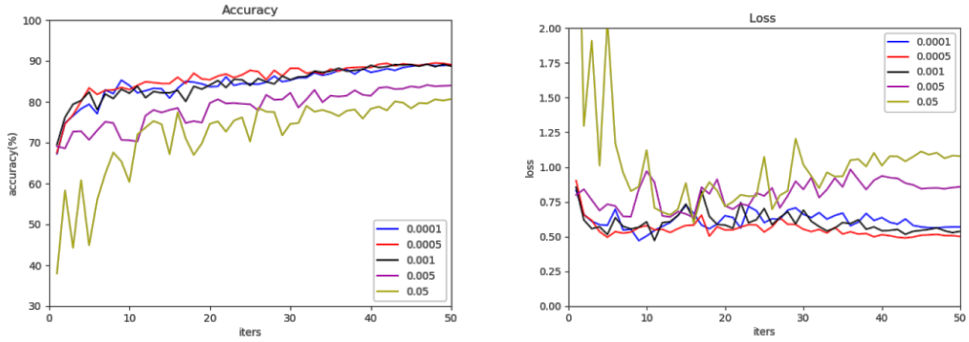
Fig. 6 - The accuracy and loss value of the model with different optimizers

Fig. 6 showed the changes in the accuracy of the EffiientNet-B0 with different optimizers in the verification set during 50 iterations. It can be concluded from Fig. 6 that the performance of the proposed EffiientNet-B0+Ranger outperformed all other pre-trained models achieving high overall accuracy of 86.8%. The reason was that EfficientNet-B0+Ranger with the optimizer of Ranger, which combines two very new optimizers (RAdam + Lookahead) into one optimizer, and had the advantages of RAdam and LookAhead at the same time. It can speed up the convergence speed and improve recognition accuracy. EfficientNet-B0+Ranger showed a steady increase in accuracy compared to other optimizers.

Effect of Learning Rate on The Model

Choosing the optimal learning rate is important as it determines whether the neural network can converge to the global minimum. It is used to control the update amplitude of weights and bias terms in order to achieve the optimal solution. The proper learning rate can accelerate the convergence of model training and achieve good classification results.

In order to find the most suitable learning rate for the Cerasus humilis cultivars leaf data set, five groups of learning rates (0.0001, 0.0005, 0.001, 0.005, and 0.05) were selected respectively for the EfficientNet-B0+Ranger model. Comparing the effects of different learning rates on the performance of the EfficientNet-B0+Ranger model, the comparison of model performance is shown in Fig. 7 (a) and (b).



a) Accuracy rate curve *b) Loss curve*

Fig. 7 - EfficientNet of learning rate on training accuracy and training loss

It can be seen from Fig. 7 that the convergence rate of the model does not accelerate with the increase of the learning rate. When the learning rate was 0.05 or 0.005, the curve oscillated seriously, the

convergence was slow, and when the maximum number of iterations was reached, the model had not yet reached a convergence state. This indicates that when the learning rate was too high, it will cause the parameters to be optimized to fluctuate around the minimum value and not converge. When using a learning rate of 0.001, the loss value curve and average accuracy change curve of the model were more stable than the model curve when using a learning rate of 0.001 and 0.0001, and the model had a lower loss value and higher accuracy.

When fine-tuning the model, the performance of the model was better when the initial learning rate was set to a small value. The reason was that: in the transfer learning mode, all the layers of the network had been well trained, and the weight parameters of the model were close to the optimal solution, if the higher learning rate was used in the fine-tuning training phase, the model will skip the optimal solution and produce more oscillation, which will made the loss larger and the accuracy lower.

The network model of EfficientNet-B0+Ranger converged fastest and had higher accuracy when the learning rate was 0.0005, so the following research will choose the learning rate of 0.0005.

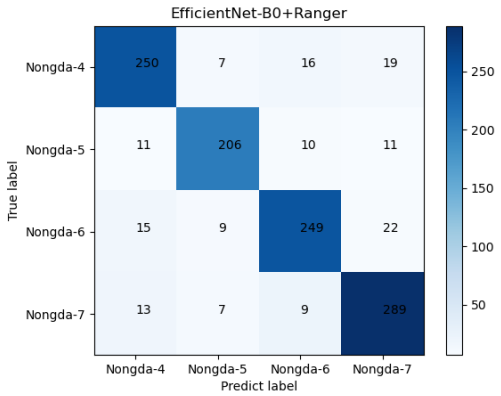


Fig. 8 - The confusion matrix of EfficientNet-B0+Ranger on the test set

To further evaluate the performance of the improved model, the confusion matrix of EfficientNet-B0+Ranger on the test set is shown in Fig. 8. The classification performance of the model was evaluated by precision, recall rate and average accuracy *(Powers et al., 2020)*, and the results were shown in Table 4. The Accuracy, Recall, and Precision, as defined in Equations (5-7).

$$Accuracy = \frac{TP + TN}{TP + TN + FP + FN} \tag{5}$$

$$\mathrm{Re}\,call = \frac{TP}{TP + FN} \tag{6}$$

$$\mathrm{Pr}\,ecision = \frac{TP}{FP + TP} \tag{7}$$

Where true positive (TP) denotes the number of instances that the classifier accurately identifies, false negative (FN) is the reverse, which is the number of instances that are incorrectly identified, and false positive (FP) represents the number of cases that are mistakenly marked as such, and true negative (TN) is the number of samples that they are not in such disease and accurately identified by the classifier.

Table 4

The results of different metrics

Category name	Identified samples	Correct samples	Accuracy (%)	Precision (%)	Recall (%)
Nongda-4	292	250	85.6	95.0	86.5
Nongda-5	238	206	86.6	96.5	90.0
Nongda-6	295	249	84.4	94.6	87.7
Nongda-7	318	289	90.9	93.7	93.8

According to the confusion matrix of Fig. 8, the 4 Cerasus humilis cultivars leaves have the possibility of error, mainly because the 4 Cerasus humilis cultivars leaves are very similar, so if the image with low resolution or there is other interference factors will lead to more difficult to distinguish correctly.

As seen in Table 4, most of the samples in each class are correctly identified by the EfficientNet-B0+Ranger approach, and the average accuracy of the experimental results achieved 86.9% on the test set, which presents that the proposed approach had an impressive capability to recognize the Cerasus humilis cultivars in the field condition.

In a word, the experimental studies showed that EfficientNet-B0+Ranger models with the learning rate of 0.0005, offered the best classification performance and could be successfully used in Cerasus humilis cultivars recognition.

Discussion

Cultivar identification has long been dependent on visual recognition by experts, which highly relies on personnel skills. Therefore, accuracy cannot be guaranteed. It is of great significance to speed up the recognition process and make it accessible for non-experts. Although leaf image-based methods have been widely adopted in plant species identification. *Zhang et al. (2021)* proposed an Xception network to identify 88 sweet cherry cultivars and 100 soybean cultivars under controlled conditions, with an accuracy of 83.52% and 91.4%, respectively. *Liu et al. (2020)* proposed an efficient and convenient method for the classification of 14 apple cultivars with a sample background using a deep convolutional neural network and achieved an overall accuracy of 97.11%. However, the images they used were simple backgrounds, when transferring those methods from plant cultivars identification with simple backgrounds to the field of complex background, most of them performed worse, due to the high similarity of leaves among cultivars and other interfering factors in the field of complex background. As the field image acquisition is simple and has more practical significance, this study proposes an effective lightweight CNN for Cerasus humilis cultivars with complex background identification and achieved a high overall accuracy of 86.9%.

CONCLUSIONS

In this work, the lightweight EfficientNet-B0 deep learning architecture was proposed and compared with the state-of-the-art deep learning architectures ResNet50, GoogleNet, ShuffleNet, and MobileNetV3. The performance of the models with different transfer learning methods, different learning rates, and optimizers had been validated on an 1143 Cerasus humilis leaf dataset.

The experimental results confirmed that considering both the average accuracy and the model size on datasets, the lightweight models MobileNetV3, ShuffleNet, and EfficientNet-B0 were found to be superior to other traditional CNNs architectures. Furthermore, it was confirmed that for all models, fine-tuning the parameters of a pre-trained neural network architecture achieved better classification accuracy as compared to using the neural network architecture with feature extraction only. Moreover, the comparative experiments were carried out on EfficientNet-B0 with Adam, RAdam, and Ranger optimizers, and the experimental results confirmed that the optimizer of Ranger performed better with a faster convergence rate and higher accuracy compared to SGD, Adam, and RAdam. At last, the EfficientNet-B0+Ranger with the learning rate of 0.0005 had the best performance and achieved a high overall accuracy of 86.9%.

In summary, the improved EfficientNetB0+Ranger had smaller parameters and higher average accuracy, making it an ideal model for use in embedded devices.

In future work, it is planned to collect the hundreds of Cerasus humilis cultivars' leaf images from different planting areas to increase the generalization performance and efficiency of the model on more Cerasus humilis cultivars. By deploying these improved models in mobile environments, this presented model will also be used to identify other Cerasus humilis cultivars and even other plants. Furthermore, it is aimed to identify Cerasus humilis cultivars in real-time by studying other targets detection models such as Faster RCNN (Regions with Convolutional Neural Network), YOLO (You Only Look Once), and SSD (Single Shot MultiBox Detector).

ACKNOWLEDGEMENT

This work was supported by the Teaching and Research Management Fund Project of Shanxi Agricultural University, China (XK19207), Basic Research Project of Shanxi Province (Free Exploration) (Project No. 202203021212426).

REFERENCES

[1] Bai Z. H. (2015). Study on biological characteristics and drought resistance of cerasus humilis in the different site conditions and leaf size types. Inner Mongolia Agricultural University: Huhehot, China.

[2] Beikmohammadi, A., Faez, K., Motallebi, A. (2020). SWP-Leaf NET: a novel multistage approach for plant leaf identification based on deep learning. arXiv:2009.05139.

[3] Charters, J., Wang, Z., Chi, Z., Tsoi, A. C., Feng, D. D. (2014). Eagle: a novel descriptor for identifying plant species using leaf lamina vascular features. In 2014 IEEE international conference on multimedia and expo workshops (ICMEW), Chengdu, China, 14-18 July, 1-6.

[4] Ferentinos, K. P. (2018). Deep learning models for plant disease detection and diagnosis. Comput. Electron. Agric. 145, 311-318.

[5] Guo, X. Q., Fan, T. J., Shu, X. (2019). Tomato leaf diseases recognition based on improved multi-scale AlexNet. Transactions of the Chinese Society of Agricultural Engineering, 35(13), 162-169.

[6] John, S., Rose, A. L. (2021). Machine learning techniques in plant disease detection and classification-a state of the art. INMATEH-Agricultural Engineering, 65(3), 362-372.

[7] Kalyoncu, C., Toygar, Ö. (2015). Geometric leaf classification. Comput. Vis. Image Und. 133, 102-109.

[8] Li, J. Y., Zhao, Y. K., Xue, Z. E. (2019). A survey of model compression for deep neural networks. Chinese Journal of Engineering, 41(10), 1229-1239.

[9] Liu, C., Han, J., Chen, B., Mao, J., Xue, Z., Li, S. (2020). A novel identification method for apple (Malus Domestica Borkh.) cultivars based on a deep convolutional neural network with leaf image input. Symmetry, 12(2), 217.

[10] Liu, J., Yang, S., Cheng, Y., Song, Z. (2018). Plant leaf classification based on deep learning. In 2018 Chinese Automation Congress (CAC), Xi'an, China. 30 November-2 December, 3165-3169.

[11] Liu, Y., Feng, Q., Wang, S. Z. (2019). Plant disease identification method based on lightweight CNN and its mobile application. Transactions of the Chinese Society of Agricultural Engineering, 35, 194-204.

[12] Mouine, S., Yahiaoui, I., Verroust-Blondet, A. (2012). Advanced shape context for plant species identification using leaf image retrieval. In Proceedings of the 2nd ACM international conference on multimedia retrieval, New York, United States, 5-8 June, 1-8.

[13] Naresh, Y. G., Nagendraswamy, H. S. (2016). Classification of medicinal plants: An approach using modified LBP with symbolic representation. Neurocomputing, 173, 1789-1797.

[14] Powers, D. M. (2020). Evaluation: from precision, recall and F-measure to ROC, informedness, markedness and correlation. arXiv:2010.16061.

[15] Ramachandran, P., Zoph, B., Le, Q. V. (2017). Searching for activation functions. arXiv:1710.05941.

[16] Sun, J., Tan, W., Mao, H., Wu, X.; Chen, Y. (2017). Recognition of multiple plant leaf diseases based on improved convolutional neural network. Trans. Chin. Soc. Agric. Eng. 33(19), 209-215.

[17] Tan, J. W., Chang, S. W. (2018). Deep learning for plant species classification using leaf vein morphometric. IEEE/ACM Transactions on Computational Biology and Bioinformatics, 17(1), 82-90.

[18] Zhang, P., Yang, L., Li, D. (2020). EfficientNet-B4-Ranger: A novel method for greenhouse cucumber disease recognition under natural complex environment. Comput. Electron. Agric., 176, 05652.

[19] Zhang, Y.; Peng, J.; Yuan, X.; Zhang, L. (2021). MFCIS: an automatic leaf-based identification pipeline for plant cultivars using deep learning and persistent homology. Hortic. Res., 8(1), 1-14.

DESIGN AND EXPERIMENT OF SUSPENDED ROTARY TILLAGE RIDGE AND FILM MULCHING MACHINE
/
悬挂式旋耕起垄覆膜一体机的设计与试验

Dejiang LIU[1,2)], Jianling HU[1)], Yan GONG [1*)], Xiao CHEN[1)], Guo WANG[1)], Xiao ZHANG [1)], Yingchun ZHU[2)]

[1)] Nanjing Institute of Agriculture Mechanization, Ministry of Agriculture and Rural Affairs, Nanjing 210014, China
[2)] Western agricultural research centre, Chinese Academy of Agricultural Sciences, Changji 831199, China
Tel: +86 025-84346227; E-mail: gongyan@caas.cn
DOI: https://doi.org/10.35633/inmateh-69-22

Keywords: *hanging vine melon; rotary tillage; ridging; field experiment*

ABSTRACT
Considering the planting mode and agronomics requirements of the existing facilities, the high-power rototilling ridge hoisting and lamination machine is difficult to operate in the greenhouse of the facility, and the small hanging rotary ridge raiser has technical problems such as insufficient horsepower. This paper designs the hanging rotary tillage ridging and film - covering machine. The machine realizes a single operation process to complete rotary tillage, ridging, drip irrigation, film laying and film edge covering soil suppression and other mechanized compound operations. The innovatively designed adjustable ridging device of this machine can steplessly adjust the size of the ridge. The ridge height after operation of the machine is 25-35 cm, the ridge width is 70-80 cm, the ridge shape is arc-shaped, the size is adjustable, and the operation efficiency is improved being 0.17-0.23 hectares/hour, the machine driving speed is set at low speed 1 gear. The machine has high operating efficiency, the arc-shaped ridge body is uniform and compact. the ridge body has a large lighting surface, the film is tightly laid, and it is close to the ridge surface without wrinkling. By test data analysis, the tillage depth stability is 93%, the ridge height qualified rate is 100%, the ridge width qualified rate is 85%, the ridge spacing qualified rate is 95%, the film edge covered soil thickness is 40 mm, the working efficiency is 0.802 hm²/h, the fuel consumption per hectare is 9.02 kg·h/m², and the three shifts work without fault. To sum up, it meets the agronomic requirements of ridging and film planting.

摘要
针对现有设施吊蔓西甜瓜种植模式与农艺要求，市场上已有大功率旋耕起垄覆膜机难以进入设施温室中作业，小型旋耕起垄机又会有马力不足等技术难题，本文设计了悬挂式旋耕起垄覆膜复式作业机，该机具实现了一个作业流程即可完成旋耕、起垄、铺滴灌带、铺膜及膜边覆土镇压等机械化复式作业。该机具创新设计的垄形可调式起垄器，可无级调整垄形大小，该机作业后的起垄高度 25-35cm，垄宽 70-80cm，垄形弧形、大小可调，作业效率 0.17-0.23 公顷/小时，拖拉机行驶速度挂在低速 1 挡，该机具作业效率高，圆弧形垄体均匀紧实，垄体采光面大，铺膜严实，紧贴垄面，不起皱，无破损，通过试验数据分析，耕深稳定性 93%，垄高合格率 100%，垄宽合格率 85%，垄间距合格率 95%，膜边覆土厚度 40mm,作业效率 0.802hm2/h,每公顷燃油消耗量 9.02kg·hm-2，并且三班次作业无故障。综上，可满足设施吊蔓西甜瓜耕整地机械化作业需求。

INTRODUCTION
With the adjustment of agricultural industry institutions, China's "rural revitalization" supporting policy implementation, agricultural efficiency, the effect of increasing farmers' income, the initiative of Chinese farmers to develop superior crops, especially cash crops such as watermelon and melon on raised beds in winter,which have been at an unprecedented high, farmers urgently need a complete function, price appropriate, suitable for greenhouse rotary tillage ridge mulching operation duplex machine, to reduce labour intensity, improve work efficiency, save operation cost, increase the production income. In northern China, such machines are relatively numerous, but most of them are high-power large machines, which are not suitable for greenhouse rotary farming ridge operation; in southern China, rotary tillage machinery supporting with walking tractors has been widely used, but the single function cannot achieve multifunctional duplex operation.

The planting mechanical ridging and film covering soil mainly have artificial and mechanical operation. The artificial ridge surface is uneven, the ridge is not straight and is time-consuming, and the production efficiency is low [1]. The machine is mainly ridging (*Zhang Jin, 2021; Wang Xiaomei, 2019*) the whole land should be ploughed and cleared before ridging, which consumes the most power in the process of western melon planting. Besides, the land preparation and ridge film mulching are conducted separately and the operation efficiency decreases, which seriously restricts the rapid development of the whole technology on double ridges.

In the 1970s, developed countries such as European countries began to develop and promote new agricultural machinery and tools adapted to the requirements of high-yield agriculture, and study the operation technology and supporting machinery and tools for rational utilization of water and soil resources (*Wang Xiaome, 2019*; *Liang Zheng, 2008*). For example, MAS5 made in Spain and 506 made in Germany are hand wheeled rotary cultivators (*wEISE G, 2008*; *Wang Wenzhi, 2013*). In the early stage of Chinese research on rotocultivator, the rotocultivator is mainly matched with walking tractor. In recent years, microcultivator and compound or combined operation machine have become a research hotspot. *Zong Minhua et al.* designed corn rotary tillage ridge-raising and film-laying machine, which is mainly used for furrow and furrow setting, spraying (herbicide), fertilizing (granular fertilizer), film-laying and film-edge soil pressing before seeding of corn with whole film on double ridges. Reducing the number of operations, greatly saves costs and increases agricultural production efficiency. It is suitable for the whole film mulching operation on double ridges and ridges in hilly and Sichuan areas with relatively flat surface, suitable humidity and less debris such as weeds and stones (*Shahgolig, 2010; Zong Minhua, 2022*). Some authors designed and developed a rotary ridge hoisting machine for Arbor planting that integrates deep rotary tillage and high ridging operation (*Prasanna, 2011; Fu Jie, 2020*). Chen Yanyu et al. designed an all-in-one scallion furrow and ridge fertilization machine and conducted field experiments (*Chen Yanyu, 2019*). Tang Fei et al designed a double spiral rotary tillage ridger for tobacco fields (*Hua Jianpin, 2014; Tang Wei, 2018*). All the above designed tools have large vibration, high oil consumption, uneven soil breakage rate and other phenomena in the process of rototillage ridging operation, which are mainly caused by the unreasonable installation angle and distribution of the tool holder, the unbalanced force of the tool shaft and other factors, and the optimization design is carried out by changing the form of blade arrangement and the installation Angle of the tool holder.

According to the preliminary calculation of the technical parameters of the machine, the machine can improve the operation effect by 40%~60% compared with the traditional artificial planting, each machine can replace 15~30 labour force, and the work efficiency can be improved by 5~20 times. Mechanized joint operation reduces the number of operation links and machines into the land, reduces the labour intensity, improves the efficiency of agricultural production, realizes soil moisture conservation, drought resistance, water saving and cost saving, and reduces the damage of the machines and tools, reduces the unit operation cost and fuel consumption, and can effectively save energy. The large-scale application of machines and tools will provide strong technical support for the water-saving technology of whole membrane ridge cultivation and the planting technology of western melon ridge membrane furrow, promote the development level of mechanized operation in other major producing areas in China, and will radiate and drive the rapid development of agriculture in the main production areas of western melon ridge planting. On the basis of sufficient market research, through the optimization and innovation of a number of parameters, the "greenhouse hanging vine and melon ridge mulching film seeder" was developed, which integrates ridging, drip irrigation belt, film covering, soil covering and other processes into one, and that can realize labour saving and high efficiency.

MATERIALS AND METHODS

Whole structure and working principle - Whole structure of the machine

1GQS-80 rotary tillage ridge and film mulching machine is mainly composed of rotary tillage device, ridging device, soil mulching device and frame and other components.

The specific structure is shown in Figure 1. The whole machine has the following overall dimensions (length x width x height) 1700 mm x 1300 mm x 1100 mm. The rotary tillage device and ridging device are fixed through the front frame beam of the machine, and the length of the front frame beam is 1350 mm. The gearbox of rotary tillage ridge machine is designed to have low speed, neutral and high speed gear, low speed gear for rotary tillage ridge operation, and high speed gear for film mulching operation. After the operation, the machine walks in neutral, and the knife shaft does not rotate at this time. The speed of knife shaft is 350 r/min in low speed gear and 860 r/min in high speed gear. The 3D final assembly drawing is shown in Figure 1, and its physical diagram is shown in Figure 2.



Fig. 1 – Overall rotary tillage ridging mulch applicator



Fig. 2 – Appearance

For operation, as shown in Figure 3, the power transmission of rotary farming ridge laying machine is transmitted from the universal coupling and transmission shaft to the transmission through the supporting tractor power output shaft. The knife shaft is arranged in the middle of rotary farming knife on both sides of the ridge cutter. The power of the transmission is driven by the gear box to rotate the rotary farming knife shaft to complete the ploughing. The film mulching device covers the agricultural film on the ridges in sequence under the traction of the tractor, at the same time the soil mulching device will cover the soil evenly to both sides of the film longitudinal, the suppression wheel compacts the overlying soil of the mulch film, thus completing the compound working procedures of rotating tillage, ridging and mulching.



Fig. 3 –Field operation

Planting agronomic qualification

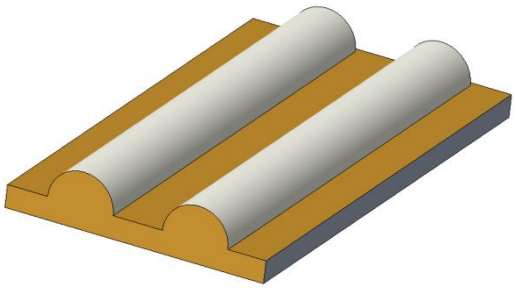


Fig. 4 - Ridging type cantaloupe cultivation and planting mode

Ridging type cantaloupe cultivation and planting technology has been studied for many years by agricultural technology department, promotion of a new type of drought resistance farming technology will be combined with ridge planting of new planting technology, the agronomy requirements being: ridge width 70-80

cm, ridge height 25~35 cm, ridge spacing 70 cm, mulching film covering ridge, plant spacing according to local agronomic requirements (*Chen Xinyu, 2021*). The main characteristics of this planting mode include tilting the soil, rotating tilling, fertilizing, mulching, and then sowing on the top of the ridge when the appropriate planting time, which can effectively increase the temperature, reduce evaporation, effectively improve the environment of the growth of the crops, improve the water utilization.

Combined with the agronomic characteristics of ridge planting, the main parameters of rotary-tillage ridging filming machine are shown in the table1.

Table 1

Rotary-tillage ridging filming machine technical parameters

No.	Project	Technical parameters
1	Version	1GQS-80
2	Type of power	traction type
3	Tractor power（kW）	25.7
4	Ridge width（tunable, cm）	70-80
5	Ridge height (cm)	25-35
6	The shape of the ridge	Round arch
7	Number of rotary cutting blades (put)	18
8	Number of ridge knives (put)	24
9	Outline dimensions length × width × height: (cm)	170 x 130 x 110
10	Rotary tillage depth (cm)	10-15
11	Operation speed（km·h）	4.5
12	Machine weight/kg	~ 500 kg
13	Number of operators (including tractor driver)	3

Design analysis of key rotary-tillage ridging filming machine

Design of rotary tillage and ridge lifting knife shaft

The main difference in the design of ridging and rotary knife shaft is the welding angle of the knife holder on the shaft. The lateral view direction of the rotary tillage cutter seat is 90° from the axis of the cutter shaft, while the ridge base and the tool axis have a certain angle (*Jiang Weiwen, 2022*). When the angle between the ridge holder and the knife shaft axis is out of scope, the soil resistance of the ridge cutter is too large, and the small angle will lead to the insufficient amount of soil and the height of the ridge lifting cannot meet the requirements of ridging (*Gu Yang, 2022; Luo Yanlei, 2021*). *Yong-Joo's* test results show that (*Yong-Joo Kim, 2013*), the most suitable angle between ridge cutter seat and ridge cutter axis is 20°. In the rotary farming industry, the working load is larger than the ridge operation, and the diameter of the rotary blade shaft is greater than the diameter of the ridge blade, the design is 55 mm, the casting blade base is welded on the knife shaft, the ridge blade shaft diameter is 45 mm, and the 8 mm thick steel plate is welded on the knife shaft.

The welding position of rotary plough holder and ridge holder on the knife shaft is arranged according to the agronomic requirements of planting hanging vines and melon ridges, which can meet the requirements of ridge size and reduce the area of rotary tillage. The rotary tiller and ridge cutter seats are shown in Figure 5，the physical picture is as shown in Figure 6.

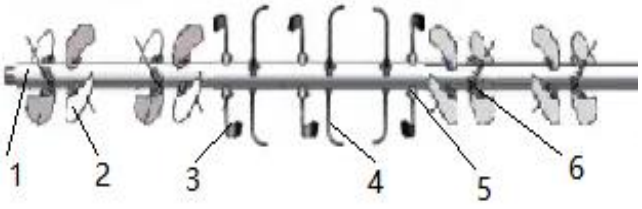


Fig. 5 -Rotary tillage ridge blade shaft assembly

1- Cutter shaft；2-Ridge knife；3-Right curved knife；4-Left curved knife；5-Rotary plough knife seat；6-Ridge knife seat.



Fig. 6 - Physical picture of the rotary tillage ridge blade shaft

Design of rotary-plough knife and ridge-raising knife

The function of rotary tillage device is mainly to break the soil ploughing, so the curved blade with strong soil turning function is selected, and the blade is narrow. The curved blade is divided into left and right cutlass, the left and right scimitars are interleaved on the tool shaft. Install the shaft staggered to ensure the radial force balance of the knife shaft. The shape of the rotary ploughing blade and the installation on the blade shaft are shown in Figure 7. The ridge blade mainly piles the soil from the middle to the sides, so the knife body is wide and the blade mouth is slightly curved, in the shape of a fan blade. The arrangement of the ridge blade on the shaft should also balance the radial force of the shaft. The shape of the ridge blade and the mounting on the blade shaft are shown in Figure 8.



Fig. 7 - Spinning knife



Fig. 8 - Ridging knife

Optimization of the blade and its arrangement

In order to reduce the power consumption of rotary tillage ridge machine, this paper is based on the traditional national standard rotary tillage knife, the rotary plane and the forward direction of the unit are appropriately tilted at a certain angle, and the Archimedes spiral line is still used in the rotary tillage blade mouth. The test shows that the power consumption of oblique rotary knife is 8. 75% lower than that of national standard rotary knife.

The arrangement of rotary ridge blade determines the performance of rotary ridge machine. This paper adopts the double-head screw blade arrangement, and the number of knives meets the array 4n ± 2 = the total number of blades (*Mo Cankun, 2006; Sui Xiuxu, 2016*). There are 18 rotary ploughing knives and 24 ridge knives, of which n is the natural number.

The blades were arranged as shown in Figure 9. There are two spiral blades on the entire segment; the adjacent blades are 40, or 20 per turn. There was a machete buried in the ground; the peripheral angle between two adjacent blades is 180; the axial distance between two adjacent blades is 45 mm.

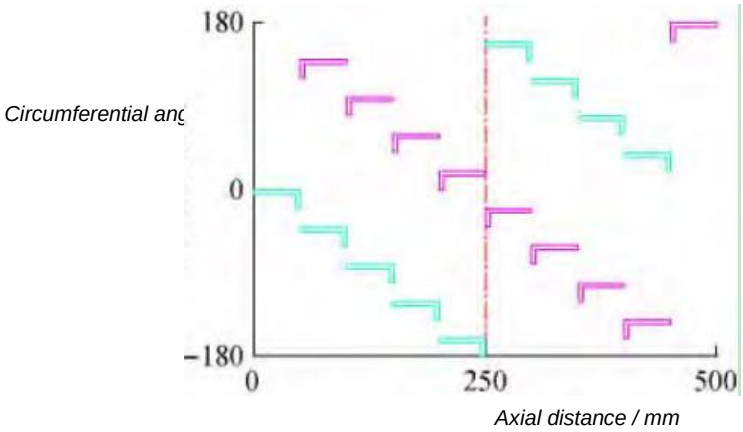


Fig. 9 - Blade layout

Transmission system design

The transmission mode is gear transmission. The transmission diagram of the rotary tillage machine is shown in Figure 10. The power is transmitted to the reducer gear of the rotary tillage machine through the PTO shaft, transmitted to the chain gear through the drive shaft, and then transmitted to the knife shaft by the chain shaft, which drives the rotary shaft to cut the soil and drives the ridge knife to ridge the soil block (*Xie Bin, 2016; Wang He, 2022*).

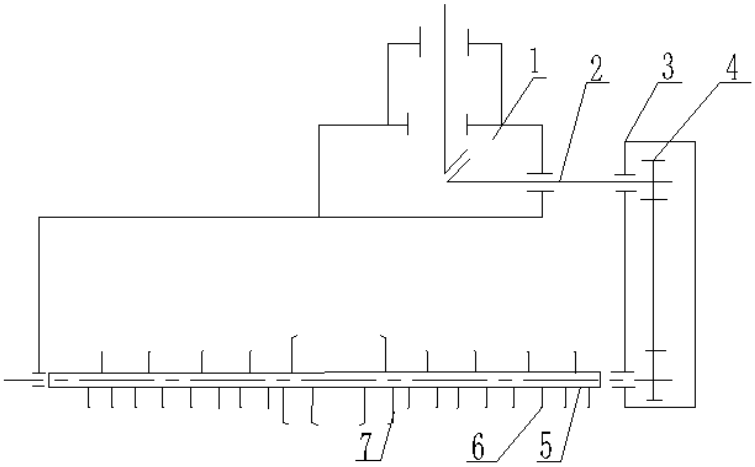


Fig. 10 - Transmission system diagram of rotary tillage ridge lifting machine

1- Decelerator; 2 - Transmission shaft; 3 - Chain box; 4 – Chain; 5 - Knife pivot; 6 -Spinning knife;7 - Ridge knife

According to the established optimization model of power consumption per unit volume, the range of n is 180 ~ 250 r/min, the standard speed of the transmission shaft is 540 r/min, and the transmission ratio from the drive shaft to the knife shaft is 2.25, where the gearbox transmission ratio i_1 = 1.5; the transmission ratio of the chain transmission i_2 = 1.5.

Field experiment and data analysis

Test site and equipment

The test field was dry land with deep soil layer, loose soil and medium fertility. The previous crop was corn planted on double ridges with whole film, and the experiment was conducted after the previous crop was cleared. The test area is 6 hectares (*Shu-yi wang, 2013; Wang Jianchao, 2011*). The Yellow Sea Jinma 354 tractor, which is matched with the prototype, was used for the test. The Yellow Sea Jinma 354 tractor has a power output of 25.7 kW.

Test instruments and equipment

Stopwatch, leather tape, steel tape, steel tape and post are used in the test, which can meet the test requirements.

Test time and place

The prototype was tested on January 20, 2022. The test site was conducted in the field of Baima Base, Nanjing City, Jiangsu Province, China. The test plot was flat with a length of 400 m and a width of 200 m. The soil quality was sandy loam, which could meet the test requirements.

RESULTS

Test items and test results

In order to understand and master whether the prototype can meet the design requirements and technical performance indexes, the stability of tillage depth, the qualified rate of ridge height and width, the qualified rate of ridge spacing, the shape of ridge, the thickness and width of soil cover and the working efficiency were tested. The results are shown in Table 2.

Table 2

Test result of miniature ridge mulcher

No.	Project	Agronomic and technical requirements	Determination results	Determinant
1	Deep tillage stability （%）	≥80	93	qualified
2	Ridge high pass rate （%）	≥75	100	qualified
3	Ridge width pass rate （%）	≥70	85	qualified
4	The qualified rate of ridge spacing （%）	≥75	95	qualified
5	The thickness of the membrane side cover （mm）	30-50	40	qualified
6	Working performance （hm^2/h）	0.802		
7	Fuel consumption per hectare （$kg \cdot hm^{-2}$）	9.02		
8	Fault situation	Three shift operation without fault	meet the requirement	qualified

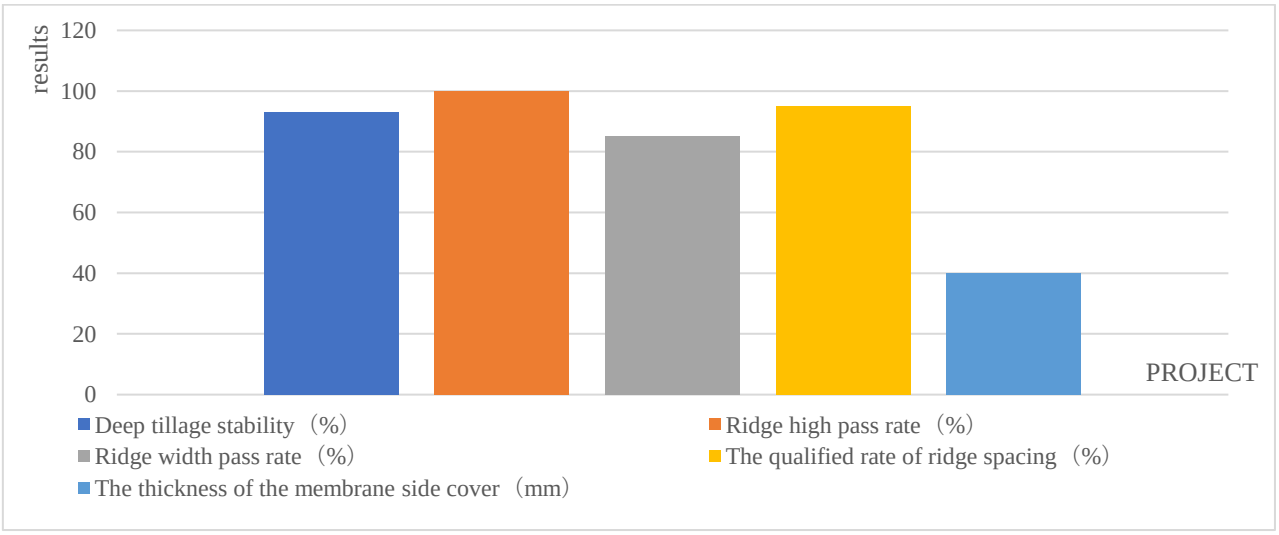


Fig. 11 – Graphical variation of the analysed parameters

Through the field test, the main performance index of this machine has reached the design requirements, and can meet the agronomic requirements of rotary tillage, ridging and film laying.

CONCLUSIONS

(1) The successful research of the hanging rotary tillage ridging and film laying machine provides an advanced, reliable and applicable model for the operation of rotary tillage ridging and film laying in the greenhouse environment. The model is reasonable in design, compact in structure, simple in operation and convenient in use, and can be matched with small and medium-sized four-wheel tractor. After rotating tillage and soil preparation, the machine carries out ridging and film laying in time according to soil moisture. It has the characteristics of high operation speed and good film laying quality. This machine can further improve the working efficiency, reduce the labour intensity and reduce the working cost, and has a good prospect of popularization and application.

(2) According to the above test results, the statistical calculation of the stability of rotating tillage depth, the width and height of ridges, the thickness and width of longitudinal soil cover, the qualified rate of ridge spacing, the thickness of film edge soil cover and the working efficiency can be obtained. The tillage depth stability is 93%, the ridge height qualified rate is 100%, the ridge width qualified rate is 85%, the ridge spacing qualified rate is 95%, the film edge covered soil thickness is 40 mm, the working efficiency is 0.802 hm^2/h, the fuel consumption per hectare is 9.02 $kg \cdot hm^{-2}$, and the three shifts work without fault. To sum up, it meets the agronomic requirements of ridging and film planting.

ACKNOWLEDGEMENT

This research was supported by the China Agriculture Research System (CARS-25), the National Key Research and Development Programme of China (2020YFD1000300).

REFERENCES

[1] Chen Xinyu, Shi Yuliang, Chen Mingdong. (2021). Simulation test of rotary performance of sweet potato ridging machine based on discrete element method (基于离散元法的甘薯起垄机旋耕刀抛土性能仿真试验). *Agricultural Engineering*, 11(02), pp.117-120.

[2] Chen Yanyu, Li Tianhua, Niu iru u, Li Yong, Hou Jialin. (2020). Design and test of fertilization machine for opening and ridging of green onion (大葱开沟起垄施肥一体机的设计与试验). *Agricultural Mechanization Research*, 42(07), pp.77-87.

[3] Fu Jie, Feng Yan, Xiao Jia, Wu Penghui. (2021). Development of rotary ridge machine for the root of kudzu vine planting (葛根种植旋耕起垄机的研制). *Agricultural mechanization research*, 43(08), pp.88-95.

[4] Gu Yang, Jiang Xinbo, Dunguoqiang. (2022). Research status and development trend of rotary tiller (旋耕机研究现状与发展趋势). *Southern agricultural machinery*, 53(23), pp.44-46.

[5] Hua Jianping, Yan Xiaoyue，MA Jun et al. (2014). Dimensional synthesis and kinematics simulation of a high-speed plug seedling transplanting robot [J]. *Computers and Electronics in Agriculture,* 107: 64-72 .

[6] Jiang Weiwen, Zhu Xiangdong. (2022). Design and mode analysis of horizontal rotary tiller knife roller (卧式旋耕机刀辊设计与模态分析). *Journal of Jiamusi University (Natural Science Edition)*, 40(01), pp.83-87.

[7] Luo Yanlei, Du Li, Li Yi. (2021). Analysis of the load-sensitive system of the hydraulic rotary tiller working device (液压旋耕机工作装置负载敏感系统分析). *Hydraulic and pneumatic*, 45(09), pp.52-57.

[8] Liang Zheng. (2008). Rototiller is modified for design and manufacture of rotary machine (旋耕机改进为旋耕起垄机的设计与制造). *Modern agricultural equipment*，08 (5), pp. 47-49 .

[9] Mo Cankun, Lin Qikuan, Xiong Yuanfang et al. (2006). Design and test analysis of GQS-1201(GQS-120 型旋耕起垄机的设计与试验分析). *Modern agricultural equipment*, (06). pp.50-54.

[10] Prasanna K.G.V., Rahemanb H. (2011). Development of a walk-behind type hand tractor powered vegetable transplanter for paper pot seedlings [J]. *Biosystems Engineering*, 110: 189－197.

[11] Sui Xiuxu. (2016). *Design and experimental study of ridge mulching machine in sweet potato (甘薯起垄覆膜机的设计与试验研究)*. Qingdao Agricultural University.

[12] Shu-yi Wang. (2013). High yield and high efficiency of purple sweet potato (机械起垄覆膜栽培 实现紫甘 薯高产高效). *Tianjin Agriculture and Forestry Technology*, (02):8, pp.10-15.

[13] Shahgoli G, Fielke J, Desbiolles J, et al. (2010). Optimising oscillation frequency in oscillatory tillage [J]. *Soil & Tillage Research*, 106(2): 202-210.

[14] Tang Wei, Luo Junyong, Hu Lei, Song Zhihua, Xiao Shumin. (2018). Design of double spiral rotary machine in tobacco field (烟田双螺旋旋耕起垄机的设计). *Southern Agricultural Machinery*, 49(15), pp.63-70.

[15] Wang Jianchao, Zhang Fan, Zhang Jianling, He Dunqing. (2011). Stress simulation of knife shaft of rotary ridge machine（旋耕起垄机刀轴的应力仿真研究). *Anhui Agricultural Science*, 39(19): pp.154-163.

[16] Wang Bo. (2018). Development and test of small ridge and film laying machine (小型起垄铺膜机研制与 试验). *Agricultural engineering*, 8(09), pp.9-12.

[17] Wang Wenzhi, Tan Jing. (2013). Development and test of 1 GZ-60V mountain rotary ridge machine (1GZ-60V 型山地旋耕起垄机研制与试验). *China Agricultural Machinery and Chemical News*, 34(02). pp.67-69.

[18] Wang He, Hu Haoran and Chen Zhenglong. (2022). Development of type 1MC-150 stubble extinguishing rotary tiller (1MC-150 型灭茬旋耕机研制). *Agricultural Engineering* ,12(09). pp:107-110.

[19] Wang Xiaomei, Liu Hongyan, Zhou Yarong. (2019). Current situation and development countermeasures of mechanization of facility agriculture (设施农业机械化现状与发展对策). *Agriculture and technology*，29(6), pp. 9-10.

[20] Weise G. (2008). Active and passive elements of a combined tillage machine: interaction, draught requirement and energy consumption [J]. *Journal of Agricultural Engineering Research,* 56(4): 287-299.

[21] Xie Bin, Sun Hongxia, Mao Enrong et al. (2016). Design and test of rotary tillage ridge lifting machine (旋 耕起垄机设计与试验). *Laboratory research and exploration*, 35(04), pp.55-62.

[22] Yong-Joo Kim，Sun-Ok Chung，Chang-Hyum Choi. (2013). Effects of gear selection of an agricultural tractor on transmission and PTO load during rotary tillage. *Soil & Tillage research*，134, pp. 90-96.

[23] Zhang Jin, Chen Wei, and Zhu Jiping et al. (2021). Research status and prospect of energy-saving technology of rotary tiller (旋耕机节能技术研究现状及展望). *China Agricultural Machinery and Chemical News*, 42(07), pp.182-189.

[24] Zong Minhua. (2022). Maize rotary tillage ridge and film laying machine (玉米旋耕起垄铺膜机). *Agricultural Machinery*, (08). pp.75-80.

MULTI-OBJECTIVE OPTIMIZATION OF HOT BLAST STOVE HEAT EXCHANGER
/
热风炉换热器多目标优化

Ye ZHANG[1)]; Qing JIANG*[1,2)]; Liangyuan XU[1,2)]; Chao HUANG[1)]; Huasheng GAN[1)]
[1)] College of Engineering, Anhui Agricultural University, Anhui/China
[2)] Anhui Province Engineering Laboratory of Intelligent Agricultural Machinery and Equipment, Anhui/China
Tel: +86_0551-65786450; E-mail: jtao@ahau.edu.cn
Corresponding authors: Qing Jang
DOI: https://doi.org/10.35633/inmateh-69-23

Keywords: *Heat exchanger, Hot-blast stove, Multi-objective genetic algorithm, Numerical simulation, Response surface method*

ABSTRACT
Shell-and-tube heat exchangers are widely used in many research fields and industrial production processes, but little research has been conducted on the use of heat exchangers for drying crops. This study conducted a numerical simulation of the temperature, velocity, and pressure fields based on the shell-and-tube fluids of a heat exchanger in a biomass particle hot-blast stove. The correctness of the simulation results was verified by test data before simulation, and the mesh was verified to be irrelevant. The application of a multi-objective genetic algorithm in heat exchanger design and optimization was explored, considering five design variables, such as hot tube diameter, transverse pitch, longitudinal pitch, cold flow velocity, and hot flow velocity for optimization. The Nusselt number, friction factor, and comprehensive performance coefficient were used as objective functions for 2D and 3D response surface analysis. The final design variables P1=74.91 mm, P2=104.23 mm, P3=121.37 mm, P4=4.83 m/s, and P5=8.48 m/s were obtained to improve the comprehensive performance coefficient by 16.11%. The heat transfer performance was improved by 9.55% and the resistance performance was reduced by 15%.

摘要
管壳式热交换器在许多研究领域和工业生产过程中被广泛使用，但对热交换器用于干燥农作物的研究却很少。本研究对生物质颗粒热风炉中基于壳管式流体的热交换器的温度、速度和压力场进行了数值模拟。仿真前通过测试数据验证了仿真结果的正确性，并验证了网格的无关性。探讨了多目标遗传算法在换热器设计和优化中的应用，考虑了热管直径、横向间距、纵向间距、冷流速、热流速等五个设计变量进行优化。以努塞尔数、摩擦系数和综合性能系数作为目标函数进行二维和三维响应面分析。最终得到的设计变量 P1=74.91㎜，P2=104.23㎜，P3=121.37㎜，P4=4.83m/s，P5=8.48m/s，综合性能系数提高了 16.11%。传热性能提高了 9.55%，阻力性能降低了 15%。

INTRODUCTION
Despite the global shortage of energy, most traditional drying devices are coal fired. As an alternative, biomass pellet hot-air stoves are energy-saving and environmentally friendly drying devices that provide a heat source for drying crops. These furnaces are fueled by renewable energy sources such as plants (including algae, wood chips, and crops) and organic substances such as livestock manure, with improved combustion conditions (*Wickramaarachchi and Narayana, 2020; McKendry, 2002*). The parts comprising these furnaces include a heat exchanger, combustion chamber, and blower. The role of the heat exchanger is to transfer heat from the hot fluid to the cold fluid device, and its performance directly affects the applicability and reliability of the biomass pellet hot-air furnace. Many experimental and numerical methods have been proposed to obtain the natural-convection heat transfer and fluid flow characteristics of shell-and-tube tube heat exchangers.

Numerical simulations and computer techniques are increasingly used by scholars to analyze and solve a multifaceted range of drying problems. Numerical simulation has developed relatively quickly in China and has evolved from being used to validating models to solving practical problems, which requires a rigorous combination of theory with practice (*Jiang et al., 2021*).

[1] *Ye Zhang, M.S. Stud. Eng.; Qing Jiang, Prof. M.S. Eng.; Liangyuan Xu, Prof. Ph.D. Eng.; Chao Huang, M.S. Stud. Eng.; Huasheng Gan M.S. Stud. Eng.*

As for the structure of a heat exchanger, to improve performance to reduce the drop in the pressure of the shell-side fluid, scholars have investigated the thermal performance of tie round tubes, embedded ties, spiral ties, spiral bellows, and spiral folded plates at different shell velocity (*Guo et al., 2011; Liu et al., 2015; Tan et al., 2012; Sharifi et al., 2018; Dong et al., 2015*). In addition, some scholars have studied the effect of different heat exchanger tube diameters and different baffle sizes on the thermal performance of heat exchangers at different shell velocity (*Chen et al., 2016; Xie et al., 2019; Naqvi et al., 2019; Shahril et al., 2017*), and other scholars have studied the effect of different fluid materials on heat exchanger performance. *Sheikholeslami et al., (2015),* studied the fluid flow and heat transfer in an air–water double tube heat exchanger, and *Heydari et al., (2018),* used numerical simulations to study how the addition of different nanoparticles to the fluid affects the performance of a folded plate shell and tube heat exchanger. *Kim and Cho (2018)* analyzed the airside heat transfer and pressure drop of louver-finned parallel flow heat exchanger. In summary, many scholars have formulated schemes to improve heat exchanger performance in terms of structure, dimensions, and fluid materials—achieving great breakthroughs in numerical simulations, whether in China or abroad. However, the final goal of these studies was to improve heat exchanger performance.

Thus, in this study, the boundary conditions were calculated for a heat exchanger according to the design requirements of a biomass pellet hot-blast furnace. Ansys Fluent software was used to perform numerical simulations of two-phase flow heat transfer, and the structural and flow parameters of the heat exchanger were optimized with multi-objective optimization methods (*Kamiyama et al., 2022; Tharakeshwar et al., 2017; Mirzaei et al., 2017; Raja et al., 2017a, 2017b; Gu et al., 2019*). The optimal parameters under different operating conditions were summarized by response surface analysis, and the adequacy was analyzed to prove the reliability of the results; the sensitivity was analyzed to determine the weights of the design variables on the output parameters. For single-objective optimization problems, it is difficult to weigh the contradictions of multiple objective functions, whereas multi-objective optimization methods can solve such problems. This method enables simultaneous optimization of multiple variables, with a high degree of continuity in optimization, and provides good predictability and intuition for heat exchanger design, which ultimately leads to optimal design parameters.

MATERIALS AND METHODS

Establishment of heat exchanger model

The focus of the research was on heat exchangers in biomass particle hot-blast furnaces. In this study, the heat exchanger was composed of four tube processes and one shell process. The gas in the tube side was a high-temperature flue gas produced through combustion in a biomass pellet furnace, and the air in the shell side was at room temperature. High-temperature air is obtained through heat exchange in a hot tube, and at a certain temperature, the air enters the dryer to dry the grain. The total length of the heat exchanger was 1,900 mm, the total width was 610 mm, the total height was 1,540 mm, and the tube diameter of the heat exchanger tube was 76 mm. The computational domain in this paper consists of a solid domain and two fluid domains (air domain and flue gas domain) as shown in Fig. 1. The simplified model of heat exchanger is mainly consisted of shell, heat transfer tube bundle and baffle plate.

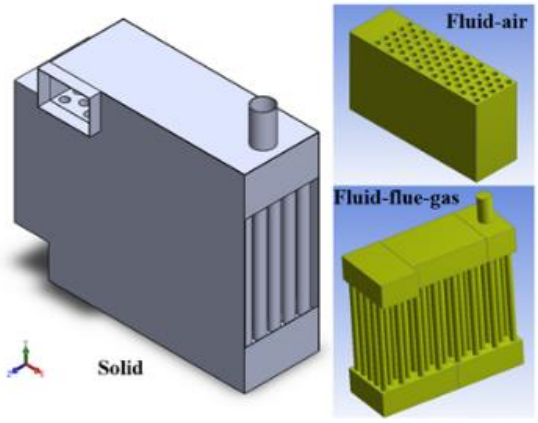


Fig. 1 - Simplified heat exchanger model

Setting materials and boundary conditions

The heat exchanger of the biomass pellet hot-blast stove was made of Q235 steel, when analyzing the flow field of the heat exchanger model, the material properties of the air and high-temperature flue gas should be fully considered. The materials were defined through the Fluent software, and the specific material parameters (*Zhang et al., 2009*) are presented in Table 1.

Table 1

Material characteristics set

Materials	Density (kg/m^3)	Specific Heat [J/(kg-K)]	Thermal conductivity [W/(m-K)]	Viscosity (m^2/s)
Steel	7850	502	48.6	
Air	1.205	1005	0.0259	1.81×10 $^{-5}$
Flue gas	0.363	1239	0.0827	4.07×10 $^{-5}$

According to the design requirements, 200,000 kcal of heat is generated per hour:

$$W = Q_{out} = 200000\ kcal/h = 232.60\ kW \tag{1}$$

Because of the design of the hot-air stove, the thermal efficiency cannot reach 100%. Due to the thermal resistance between the solid wall of the heat exchanger and the fluid, and the heat loss from the environment was considered. Thus, a 20% heat transfer loss was therefore considered:

$$Q_{in} = W \times (1-20\%) = 186.08\ kW \tag{2}$$

$$Q_{in} = C_{air} m_{air} \Delta t_1 \tag{3}$$

$$Q_{out} = C_{fume} m_{fume} \Delta t_2 \tag{4}$$

$$m_{air} = \rho_{air} v_{air} A_{in} \tag{5}$$

$$m_{fume} = \rho_{fume} v_{fume} A_{out} \tag{6}$$

$$D = \frac{4S}{L} \tag{7}$$

where:

Q_{in}, Q_{out} is the heat absorbed by air per hour and the heat emitted by the flue gas per hour, (kW). C_{air}, C_{fume} is the average specific heat capacity of air and the average specific heat capacity of flue gas, [kJ/(kg/K)]. m_{air}, m_{fume} is the mass flow of air and the mass velocity of flue gas, (kg/s). Δt_1, Δt_2 is the air temperature difference and the flue gas temperature difference, (°C). ρ_{air}, ρ_{fume} is the average density of air and the average density of flue gas, (kg/m^3). v_{air}, v_{fume} is the air velocity and the flue gas velocity, (m/s). Ain, $Aout$ is the air inlet area and the flue gas inlet area, (m^2). D is the hydraulic diameter, (m). S is the effective area of total flow, (m^2), and L is the wet circumference, (m).

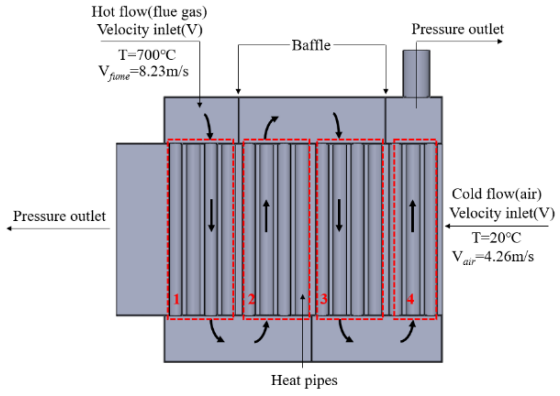


Fig. 2 - Heat exchanger boundary condition profile

The air inlet is calculated using a normal air temperature of 20°C. However, according to the design requirements of the hot-air outlet, the temperature must reach 80°C. The temperature difference is therefore 60°C. If the average specific heat of the air is 1.007 kJ/(kg/K), the density of the imported 20°C air is 1.205 kg/m^3, and the air inlet cross-sectional area is 0.6 m^2, using equations (1), (3), and (5), the air inlet velocity is approximately 4.26 m/s.

During the heat exchange between the flue gas and air, the temperature of the flue gas changes with time. According to the test experience, the temperature of the flue gas produced by the combustion of biomass particles can reach 700°C. According to the design requirements, to make full use of the heat generated by the high-temperature flue gas, the flue gas outlet temperature must be below 100°C. The temperature difference is therefore 600°C. If the average specific heat is 1.1535 kJ/(kg/K), the density of the 700°C flue gas is 0.363 kg/m^3, and the flue gas inlet cross-sectional area is 0.1125m^2, using equations (2), (4), and (6), the flue gas inlet velocity is approximately 8.23 m/s.

The hydraulic diameter is a common physical quantity used when dealing with flow in non-circular pipes and is defined as four times the ratio of the total flow effective area to the perimeter. It is necessary to calculate the hydraulic diameter because of the setting requirement during the simulation. According to equation (7), the hydraulic diameter of the air velocity inlet can be calculated as 0.75 m and the hydraulic diameter of the flue gas velocity inlet is 0.3263 m. The boundary condition profiles are indicated in Fig. 2.

Method for evaluating the heat transfer performance of the heat exchanger

Researchers continually strive to improve heat exchange with less power consumption, and numerous evaluation indexes to assess the performance of heat exchangers have been proposed. The main parameters evaluated are Nusselt number, pressure drop, heat transfer factor, friction factor, etc. The standard for measuring heat exchangers investigates heat transfer and resistance performance. The balance between the two has attracted much attention. The heat transfer factor and friction factor comparison method was proposed by Kays and London (1984).

In this paper, the optimized output parameters: the heat transfer performance is evaluated by the Nusselt number *Nu*, the resistance performance by the friction factor f, and the comprehensive performance by Pec, which are denoted by P6, P7, and P8, respectively.

$$Nu = \frac{hD}{k} \tag{8}$$

$$f = \frac{\triangle p(2D / L_0)}{\rho v^2} \tag{9}$$

$$Pec = \frac{Nu}{f^{1/3}} \tag{10}$$

where: h is the convective heat transfer coefficient, D is the hydraulic diameter, k is the thermal conductivity of fluids, ρ is the fluid density, v is the fluid inlet velocity, Δp is the differential pressure between the fluid inlet and outlet within the unit, and L_0 is the heat exchanger tube length (1m).

The convective heat transfer coefficient:

$$h = \frac{Q}{A_{\triangle} t_m} \tag{11}$$

where: Q is the heat flux of fluid, A is the heat transfer area, Δt_m is the logarithmic mean temperature difference.

RESULTS

Grid independence verification

Fluent meshing is a powerful and highly robust mesh generation software with high-quality tetrahedral mesh and hexahedral core mesh generation algorithms. To get the grid-independent results, different cell sizes were set and the mesh models with 390W, 261W, 197W and 128W grid cells were obtained.

Setting the same boundary parameters, the shell-side outlet temperature and the pressure drop are obtained as shown in Table 2.

Table 2

Result of grid-independence

Grid number/(W)	Pressure drop/(Pa)	Relative error/(%)	Outlet temperature(°C)	Relative error/(%)
390	372.12	—	88.71	—
261	377.55	1.46	88.33	0.43
197	386.73	3.93	87.53	1.33
128	419.62	12.76	90.04	1.50

It can be found from Table 2 that the relative error of the grid model with a grid number of 261w is the lowest at 1.46% and 0.43%. It indicated that the difference between the calculation results of the two grid models was small, which reduced the number of grids by about 130W and shortened the calculation time. Therefore, the final heat exchanger was calculated using the 261W cell grid model.

The accuracy of the simulation was verified, the air outlet temperature was monitored, and the outlet temperature reached stability at about 300 steps (Fig. 3) and 88°C. This temperature deviates slightly from the calculated value of 80°C obtained under ideal conditions but meets the design requirements; thus, the simulation results are credible.

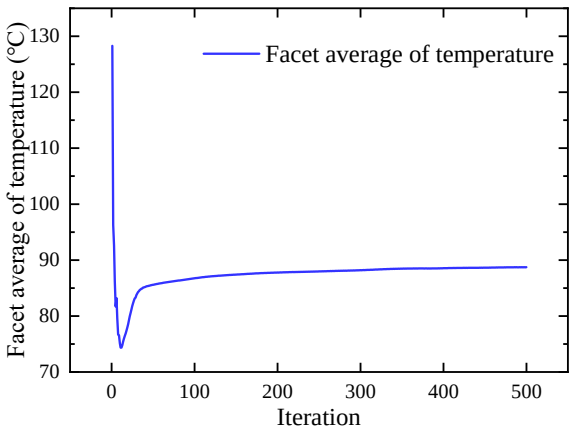


Fig. 3 - Variation of air outlet temperature with the iteration

Verification of numerical simulation correctness

In order to verify the correctness of the numerical simulation, the temperature variation of the hot air stove from ignition to hot air outlet temperature stabilization in 60 min was collected during the test of the hot air stove product as shown in Fig. 4.

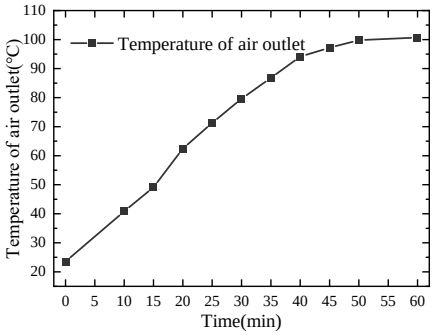


Fig. 4 - Variation of air outlet temperature with time

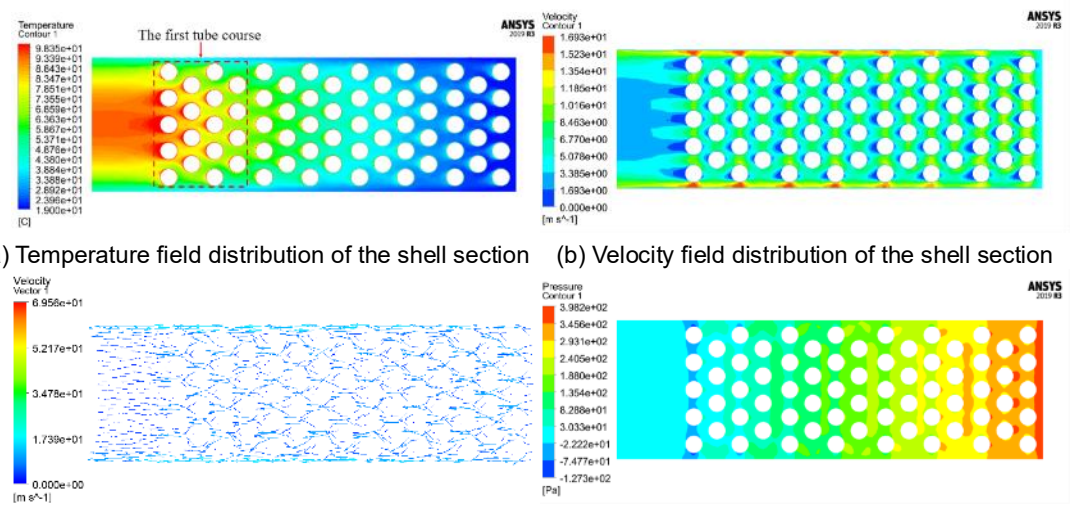


Fig. 5 - Biomass pellet hot air stove test device

The biomass pellet hot air stove test device is shown in Fig. 5. The temperature was measured every 5 min during the machine operation. The temperature was stabilized at about 100°C after 50 min of machine operation, and the temperature at 60 min was 100.7°C. The cold flow rate under this test condition is 4.5m/s, the ambient temperature is 23°C, and the hot flow rate is 7.8m/s. The simulation of this test condition results in an outlet temperature of 90.67°C. The difference between the simulation result and the test result under this condition is about 10.03°C, and the error is about 9.96%. The temperature difference of simulation result is 70.67°C in this condition, and the temperature difference of test is 77.7°C, and the error of both is 9.05%. Although there are some errors between the simulation results and the experimental results, these differences are attributed to the simplification of the model and the unavoidable measurement errors, which are also within the error tolerance. In the simplification of the heat exchanger model, the features irrelevant to the simulation will be reasonably deleted, simplified as follows: 1. Hot blast stove in the process of combustion, the ash cleaning port is closed, so the ash cleaning port at the bottom of the heat exchanger will be simplified. 2. The connection of the hot tubes will appear welded seams, the impact of the weld is ignored. 3. The bottom of the hot blast stove is connected by the channel steel, this paper analyzes the heat exchanger flow field, so the impact of the bottom channel steel is ignored. It is necessary to ensure the accuracy of the measurement, and high-precision sensors should be used to reduce the instrument error.

Numerical simulation results of the shell side

After modeling, meshing, determining the solution model, and defining the boundary conditions, the model was imported into a computational fluid dynamics program to obtain a numerical solution. The distribution of the temperature, air velocity, and pressure field inside the tube and shell side of the heat exchanger were obtained, and the accurate temperature distribution required for the finite element structural analysis was obtained for fluid mechanics and heat transfer. The temperature, velocity, and pressure field distribution in the middle section of the heat exchanger shell (Y = 0 mm) is presented in Fig. 6.



(a) Temperature field distribution of the shell section (b) Velocity field distribution of the shell section

(c) Velocity vector diagram of shell section (d) Pressure field distribution of the shell section

Fig. 6 - The result of shell side simulation

The clouds for the distribution of the cross-sectional temperature of the heat exchanger shell at Y = 0 mm are illustrated in Fig. 6(a). The change in the temperature of the shell side was large; the temperature of shell-side fluid increased after absorbing heat along the direction of fluid flow; and room-temperature air rushed toward the heat exchanger tube wall surface from the inlet to the outlet, which lowered the temperature inside the heat exchanger tube while initiating the process of heat exchange with the high-temperature flue gas. The lowest temperature at the inlet end of the heat exchanger was approximately 20°C, which was the boundary temperature set before the heat exchanger calculation, whereas the highest temperature at the outlet end reached approximately 98°C and the high-temperature region was concentrated on the first tube section. The average surface temperature at the outlet was calculated to be approximately 88°C in Fluent software. The end product was high-temperature air of 80°C, indicating that the product met the design requirements under the speed conditions.

The cross-sectional velocity of the heat exchanger shell at Y = 0 mm and the distribution clouds of the velocity vectors are presented in Fig. 6(b) and (c). Due to the obstruction of the heat exchanger tube when the air flowed through the heat exchanger tube bundle, the air on either side of the heat exchanger tube entered the narrow space between the two heat exchanger tubes separately. Because of the rapid decrease in flow space, the velocity of air in this narrow channel then suddenly increased. At the back of each heat exchanger tube, the speed value was low and the degree of thermal mixing was therefore small, resulting in poor local heat transfer and the formation of a flow “dead zone.” In this zone, the heat exchanger heat transfer area could not be fully utilized; thus, the heat transfer coefficient and heat transfer efficiency decreased and this area was easy to scale.

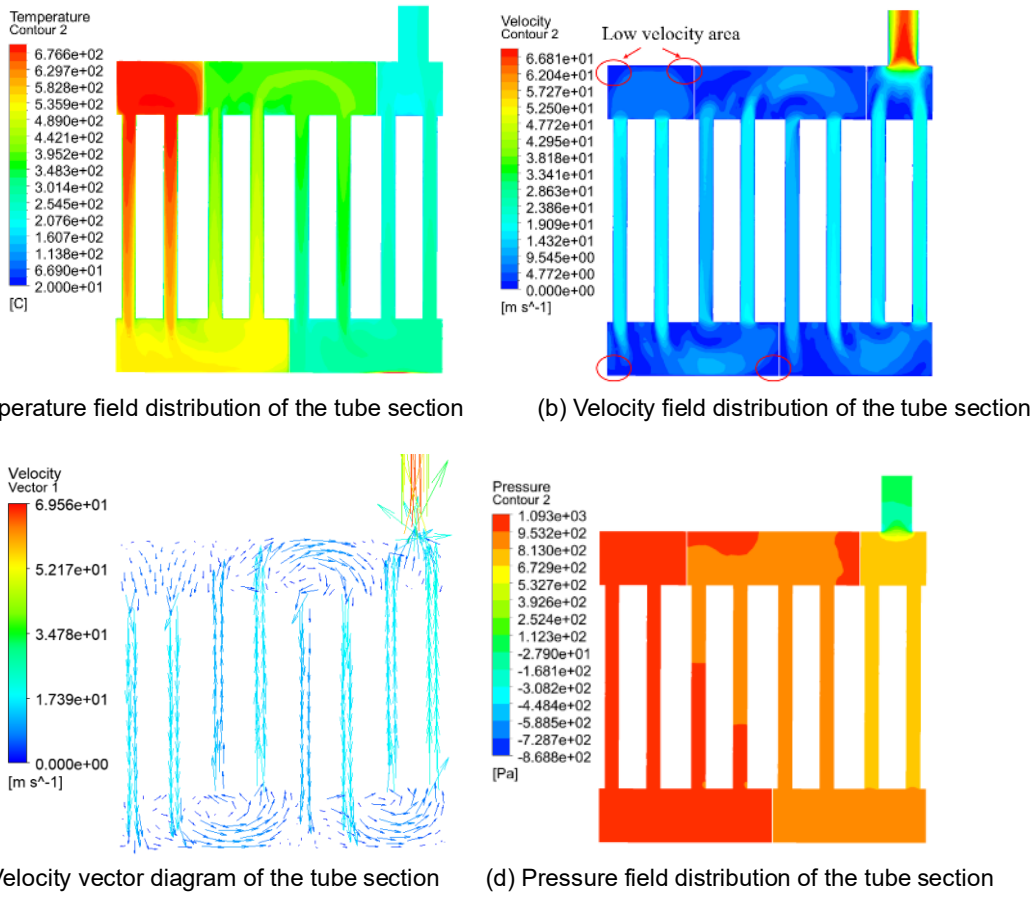
The distribution cloud of the cross-sectional pressure of the heat exchanger shell side at Y = 0 mm is presented in Fig. 6(d). Air flowed in the shell side of the heat exchanger, and the effect of the blockage on the heat exchanger tube bundle became increasingly obvious, gradually decreasing the shell side pressure. From the perspective of the Bernoulli equation (equation 12), the total energy of the inlet section is equal to the total energy of the outlet section, which includes pressure potential energy, position potential energy, and kinetic energy. In the same section, the position potential energy is equal, and the loss of pressure reflects the change of kinetic energy at the inlet and outlet.

$$P_1 + \frac{1}{2}\rho v_1^2 + \rho g h_1 = P_2 + \frac{1}{2}\rho v_2^2 + \rho g h_2 \quad (12)$$

where: P_1, P_2 is the inlet and outlet pressure, h_1, h_2 is the position height.

Numerical simulation results of the tube side

The temperature, velocity, and pressure field distribution in the middle section of the heat exchanger tube side (Z = 0 mm) is illustrated in Fig. 7.



(a) Temperature field distribution of the tube section (b) Velocity field distribution of the tube section

(c) Velocity vector diagram of the tube section (d) Pressure field distribution of the tube section

Fig. 7 - The result of tube side simulation

Fig. 7(a) presents the distribution of the temperature of the heat exchanger tube in the section at Z = 0 mm. The high-temperature flue gas moved in the flow direction, and the temperature differences in the different tube side were clearly observable. When the high-temperature flue gas was in the narrow flow channel, the heat transfer through the wall of the heat exchanger tube could increase the shell side air temperature. In the Z = 0 mm cross-section of the first, second, third, and fourth tubes, the temperatures were 676°C and approximately 400°C, 300°C, and 160°C, respectively.

The velocity and the distribution of the velocity vectors of the heat exchanger tube in the Z = 0 mm section are illustrated in Fig. 7(b) and (c). The distribution of the tube range velocity was relatively uniform, and the velocity above the heat exchanger tube was less than the velocity inside the tube. This was because the cross-sectional area decreased when the high-temperature flue gas entered the heat exchanger tube, thus increasing the velocity of the tube. There are low-velocity areas at the corners of the heat exchanger, which are dead angles of the flow, which leads to uneven velocity field distribution. This was because the flue gas rotated and could not flow out. These areas can accumulate dust. Therefore, a switch-type door plate should be added above this area in the structure design, which makes it easy to clean to prevent the heat exchanger tube from becoming blocked. An ash cleaning port should be installed below the heat exchanger tube to allow the furnace ash in the flue gas to be regularly removed to extend the service life of the equipment, reducing the impact of dirt on product performance and improving the product's efficiency. Fig. 7(c) depicts the heat exchanger tube side with high-temperature flue gas flowing from the fourth tube to the outlet, reaching its maximum flow at the outlet.

Fig. 7(d) presents the pressure distribution in the Z = 0 mm section of the heat exchanger tube, the pressure decreases gradually from the first to the fourth tube section. The overall pressure of the tube side is larger than that on the shell side. This was because the tube-side fluid velocity was greater than the shell-side fluid velocity, which resulted in the tube-side pressure being greater than the shell-side pressure.

Multi-objective optimization of shell and tube heat exchangers

The project input parameters include three structural dimensional design variables (hot tube diameter, transverse pitch, and longitudinal pitch) and two boundary parameter design variables (cold flow and hot flow velocity), denoted by P1, P2, P3, P4, and P5, respectively. In addition, the horizontal spacing between the circle centers of two hot tubes is defined as the transverse pitch; the vertical spacing between the circle centers of two hot tubes of the same centerline is defined as the longitudinal pitch. The diagram of the structure of the tube bundle arrangement is shown in Fig.8. In the optimization process, the number of hot tubes is 68 and the three parameters a, b, and c are constant values of 62 mm, 62 mm, and 342 mm, respectively. The variation of transverse pitch and longitudinal pitch will change the overall length and width of the heat exchanger but not the overall shape. The range of values of the design variables is shown in Table 3.

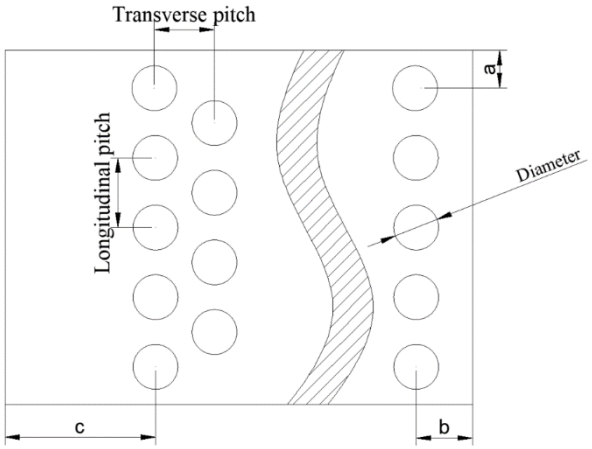


Fig. 8 - The diagram of tube bundle structure

Table 3

Range of variation of design parameters

Limit	Design Variables				
	P1/(mm)	P2/(mm)	P3/(mm)	P4/(m/s)	P5/(m/s)
Initial Value	76	102	118	4.26	8.23
Lower limit	70	90	100	2	3
Upper limit	80	112	130	6	9

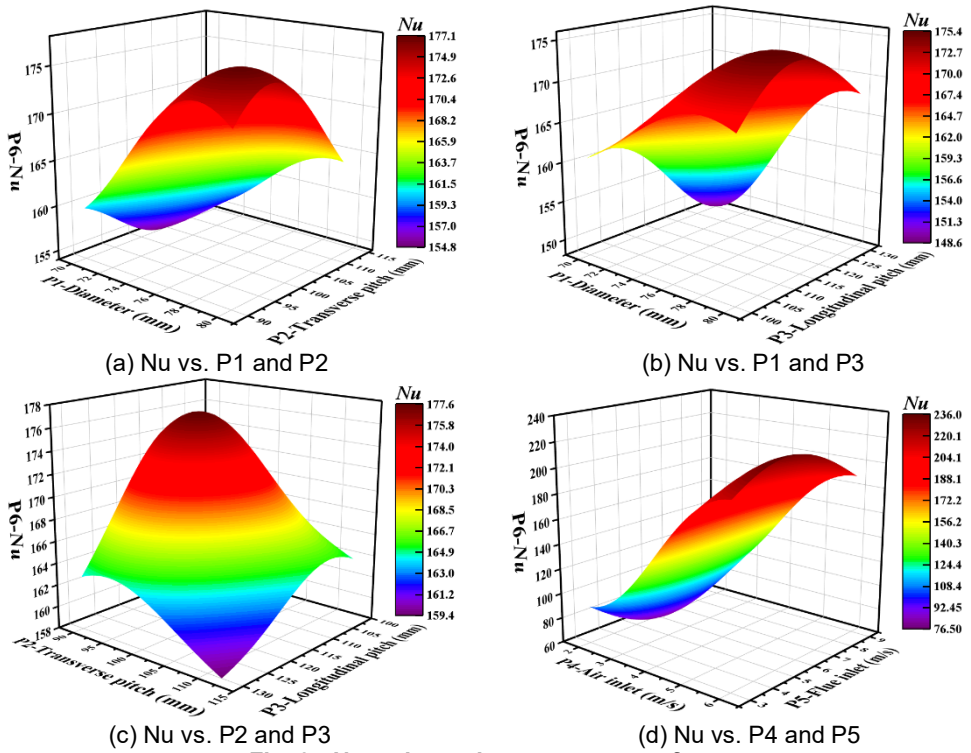
The project output parameters are *Nu*, friction factor *f*, and Pec, which are expressed by P6, P7, and P8, respectively. Because the final export temperature of the product needs to reach 80°C, the final decision target is shown in Equation 13.

$$\begin{cases} \max Nu \\ \min f \\ \max Pec \\ t \geq 80 \end{cases} \tag{13}$$

In the Design of Experiment (DOE) setup for multi-objective optimization, the optimization space-filling design method with high filling capacity and low response surface error was selected, the number of samples was 40 groups, and the response surface type was set as a non-parametric regression type. The multi-objective genetic algorithm (MOGA) was selected in the final optimization combination, with 5000 response surface sample points, 1000 iteration samples, 70% maximum allowable Pareto percentage, and 20 maximum iterations.

Influence of optimization parameters on Nusselt number

After the design variables of the optimization model were confirmed, the range of variables was determined and the multi-objective optimization experimental design was completed. The first obtained is the influence between the design variables P1-P5 on the Nusselt number. The three-dimensional response surface variation of Nusselt number with hot tube diameter, transverse pitch, longitudinal pitch, cold flow velocity, and hot flow velocity is shown in Fig. 9. The input parameters that do not participate in the response in each figure take default values: P1 = 76 mm, P2 = 102 mm, P3 = 118 mm, P4 = 4.26 m/s, P5 = 8.23 m/s.

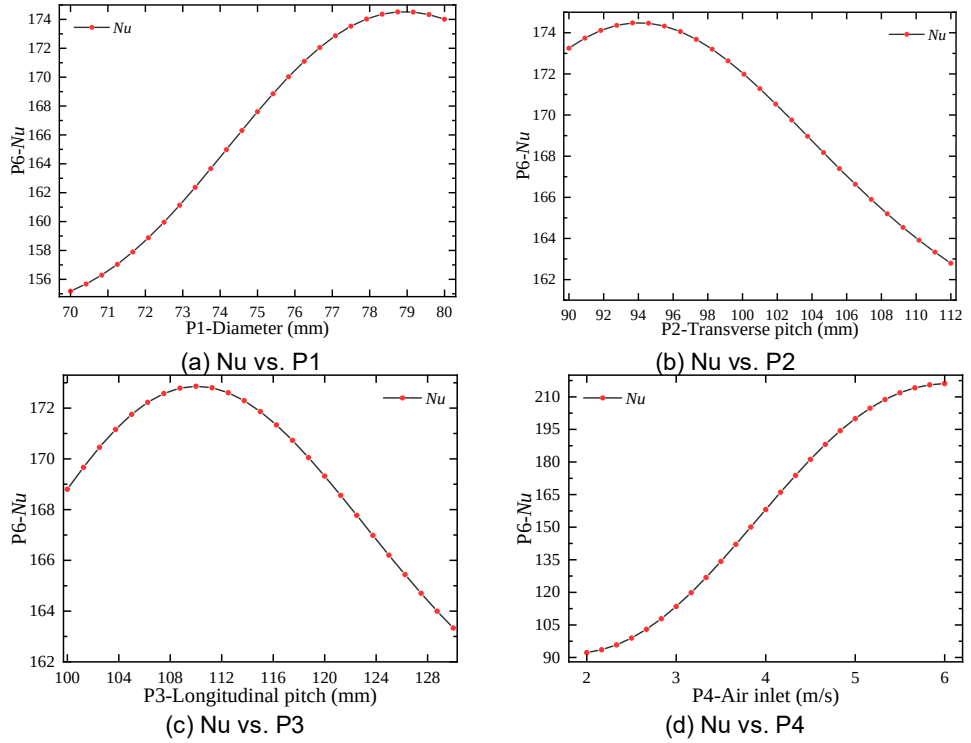


(a) Nu vs. P1 and P2 (b) Nu vs. P1 and P3

(c) Nu vs. P2 and P3 (d) Nu vs. P4 and P5

Fig. 9 - Nusselt number response surface

Figure 9(a) shows the response surface of the Nusselt number when the hot tube diameter and transverse pitch work together. When the hot tube diameter is between 70 and 80 mm, the Nusselt number increases and then decreases with increasing transverse pitch; when the transverse pitch is between 90 and 112 mm, the Nusselt number increases and then decreases with increasing hot tube diameter. When P1 = 78.33 mm and P2 = 95.50 mm, the maximum response value of Nusselt number is 177.07. It can be found in Fig. 9(b) that when the hot tube diameter is between 70 and 80 mm, the Nusselt number increases and then decreases with increasing longitudinal pitch. When P1 = 78.75 mm and P3 = 112.50 mm, the maximum response value of Nusselt number is 175.40. It can be found from Fig. 9(c) that the maximum response value of Nusselt number up to 177.55 when P2 = 93.67 mm and P3 = 110 mm. It can be found from Fig. 9(d) that when P4 = 6 m/s and P5 = 5.5 m/s, the maximum response value of Nusselt number is 235.71.



(a) Nu vs. P1 (b) Nu vs. P2

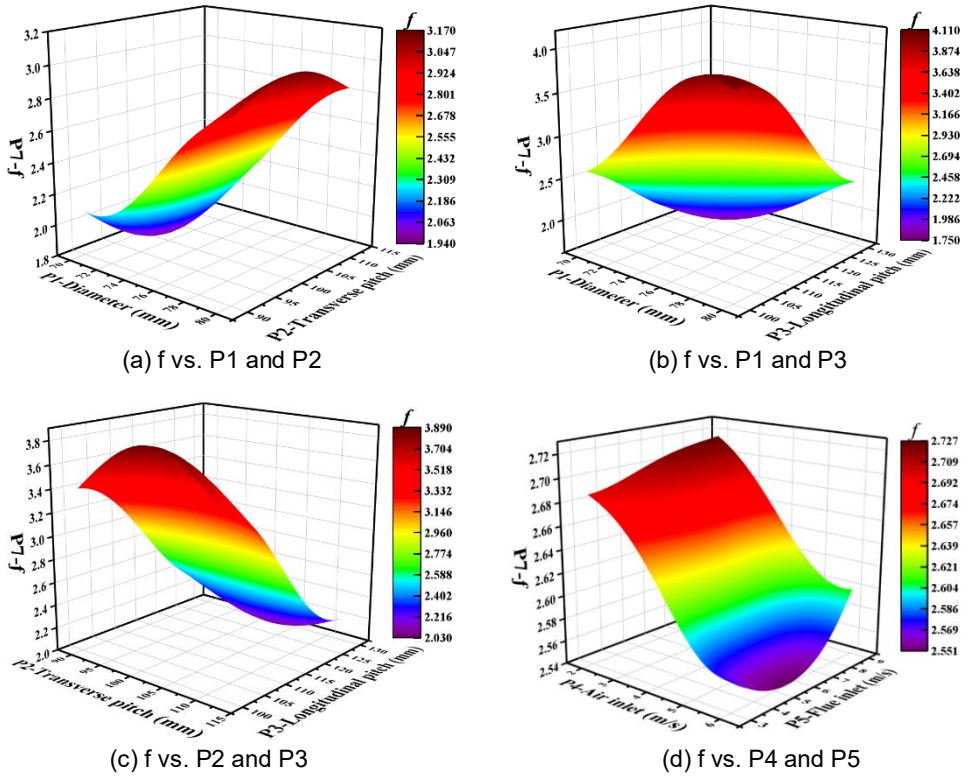
(c) Nu vs. P3 (d) Nu vs. P4

Fig. 10 - Nusselt number 2D response curves

The influence of the one-factor design variables on the two-dimensional response curves for the Nusselt number is shown in Fig. 10. As it can be found in Fig. 10. The Nusselt number tends to increase overall with the increase of heat pipe diameter and air velocity, and the peak Nusselt number is 174.36 when P1 = 78.33 mm. The heat exchange area is appropriately increased, so the heat dissipation per unit time will increase, thus increasing the convective heat transfer coefficient *h* and making the Nusselt number larger. When P2 = 94.58 mm and P3 = 111.25 mm the Nusselt number reached the maximum value of 174.48 and 172.86 respectively.

Influence of optimization parameters on friction factor

The next obtained is the influence of design variables P1-P5 on the friction factor of the heat exchanger, the influence of two factors of the design variables on the friction factor was analyzed separately. The three-dimensional response surface variation of friction factor with hot tube diameter, transverse pitch, longitudinal pitch, cold flow velocity, and hot flow velocity is shown in Fig. 11. The input parameters that do not participate in the response in each figure take default values.



(a) f vs. P1 and P2

(b) f vs. P1 and P3

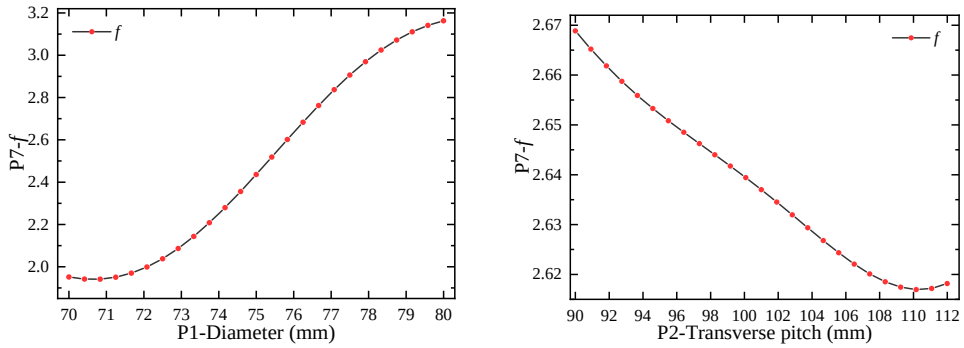
(c) f vs. P2 and P3

(d) f vs. P4 and P5

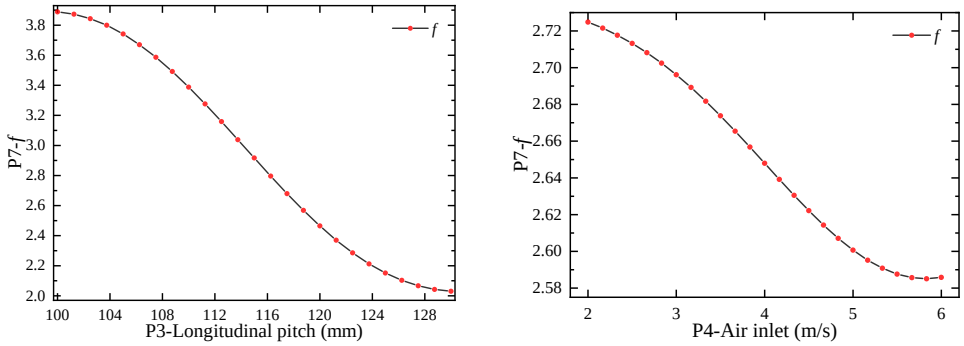
Fig. 11 - Friction factor response surface

Figure 11(a) shows the response surface of the friction factor when the hot tube diameter and transverse pitch work together. It can be found from Fig. 11(a) that the friction factor shows a trend of increasing and then decreasing with increasing hot tube diameter and transverse pitch. The minimum response value of the friction factor is 1.94 when P1 = 70.83 mm and P2 = 101.92 mm. It can be found from Fig. 11(b) that the minimum response value of the friction factor is 1.75 when P1 = 72.08 mm and P3 = 126.25 mm. It can be found from Fig. 11(c) that the minimum response value of the friction factor is 2.03 when P2 = 102.83 mm and P3 = 130 mm. It can be found from Fig. 11(d) that the minimum response value of the friction factor is 2.55 when P4 = 5.67 m/s and P5 = 5.25 m/s.

The influence of the one-factor design variables on the two-dimensional response curves for the friction factor is shown in Fig. 12. Based on the two-dimensional response curve in Fig. 12(a), it can be found that the friction factor is proportional to the hot tube diameter, which is because the increase of the diameter in a certain space increased the heat transfer area, decreased the airflow area and increased the resistance. On the contrary, it can be found from Fig. 12(b-d) that the friction factor decreases with increasing transverse pitch, longitudinal pitch, and air flow rate. This is because the increase of transverse pitch and longitudinal pitch increases the airflow area and the resistance gradually decreases.



(a) *f* vs. P1 (b) *f* vs. P2

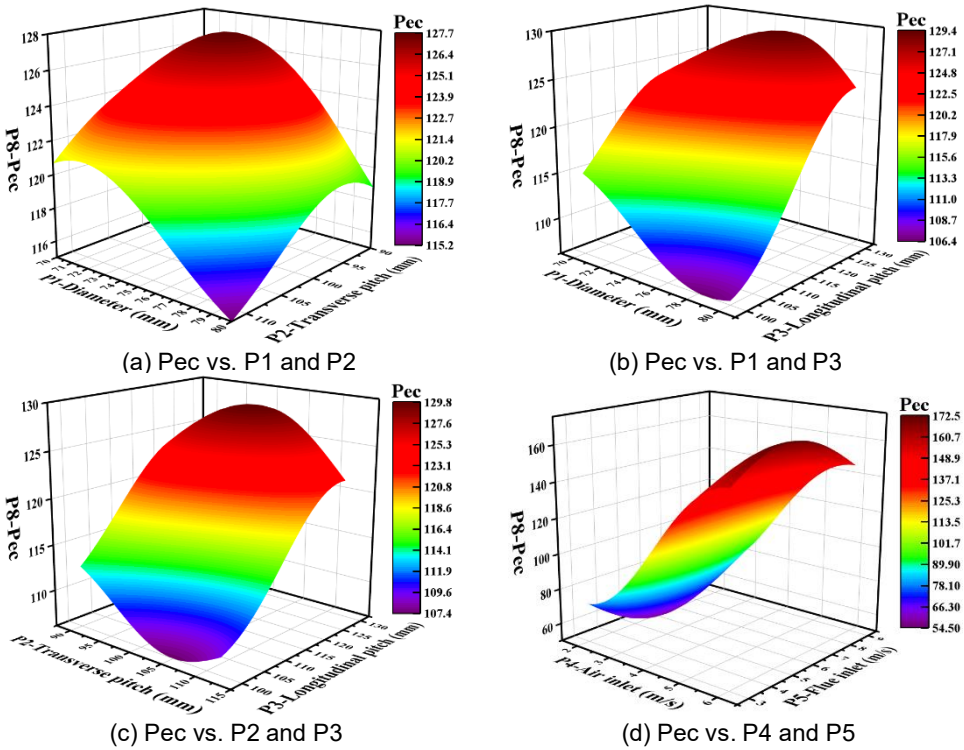


(c) f vs. P3 (d) f vs. P4

Fig. 12 - Friction factor 2D response curves

Influence of optimization parameters on comprehensive performance coefficient

The last obtained is the influence of the design variables P1-P5 on the comprehensive performance coefficient of the heat exchanger. The three-dimensional response surface variation of comprehensive performance coefficient with hot tube diameter, transverse pitch, longitudinal pitch, cold flow velocity, and hot flow velocity is shown in Fig. 13.



(a) Pec vs. P1 and P2 (b) Pec vs. P1 and P3

(c) Pec vs. P2 and P3 (d) Pec vs. P4 and P5

Fig. 13 - Comprehensive performance coefficient response surface

Figure 13(a) shows the response surface of the comprehensive performance coefficient when the hot tube diameter and transverse pitch work together.

It can be found from Fig. 13(a) that the maximum response value of the comprehensive performance coefficient is 127.60 when P1 = 73.75 mm and P2 = 96.42 mm. As shown in Fig. 13(b), the maximum response value of the comprehensive performance coefficient is 129.35 when P1 = 75.42 mm and P3 = 127.50 mm. It can be found in Fig. 13(c) that the maximum response value of the comprehensive performance coefficient is 129.74 when P2 = 99.17 mm and P3 = 127.50 mm. Figure 13(d) shows the response surface of the comprehensive performance coefficient when the boundary parameters air flow rate and flue gas flow rate work together. The maximum response value of the comprehensive performance coefficient is 172.35 when P4 = 5.83 m/s and P5 = 5.75 m/s.

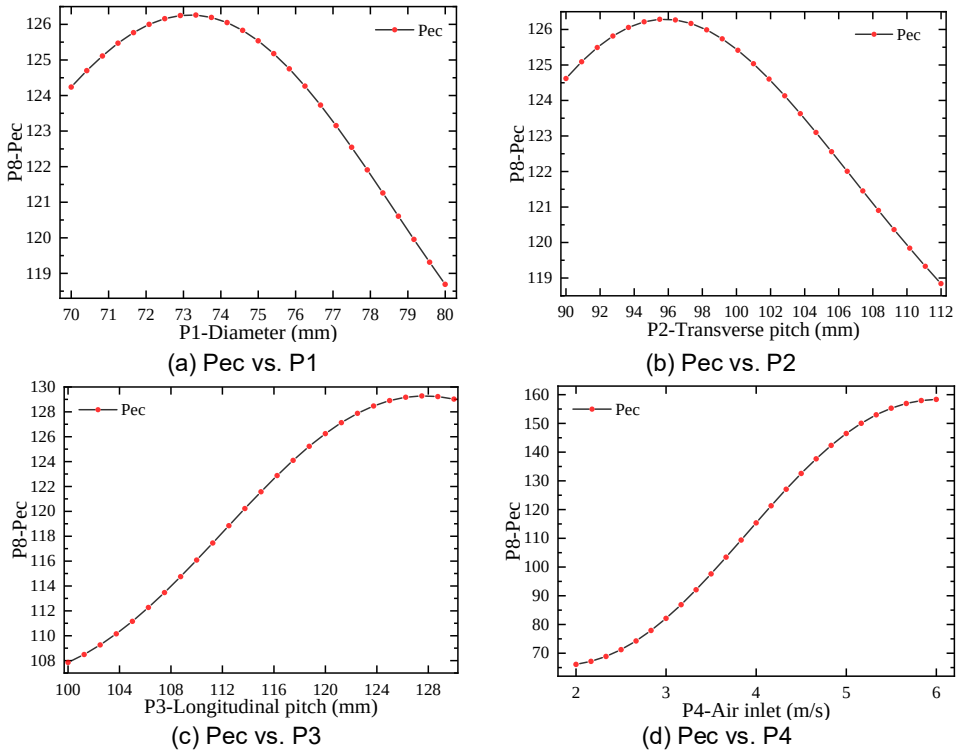


Fig. 14 - Comprehensive performance coefficient 2D response curves

The influence of the one-factor design variables on the two-dimensional response curves for the comprehensive performance coefficient is shown in Fig. 14. Based on the two-dimensional response curves in Fig. 14(a) and Fig. 14(b), it can be found that there is a peak in the effect of hot tube diameter and transverse pitch on the comprehensive performance coefficient. The comprehensive performance is best around this point, and above or below this value will have a bad effect on the performance of the heat exchanger. When P1 = 73.33 mm and P2 = 95.50 mm, the maximum response values of the comprehensive performance coefficient are 126.26 and 126.29, respectively. Figure 14(c) and Figure 14(d) show the two-dimensional response curves of the comprehensive performance coefficient with the longitudinal pitch and air flow rate, and the comprehensive performance coefficient increases with the increase of the longitudinal pitch and air flow rate.

Adequacy analysis

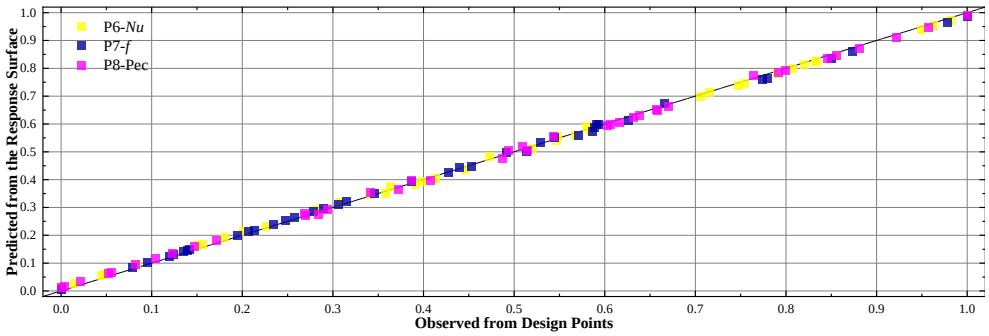


Fig. 15 - Adequacy of output parameters

After the optimization is completed, the fit can be used to determine whether the response surface predicted value fits the test value accurately. The figure of adequacy is shown in Fig. 15, the horizontal axis is

the standardized value of the observed value from the design point, and the vertical axis is the standardized value of the predicted value from the response surface. The discrete points in the figure represent the ratio between the response surface predicted value and the observed value at the design point, and the closer the discrete points are to the diagonal line, the better the response surface predicted point fits the test point. It can be seen from Fig. 15 that the fit points of the three output parameters obtained from the response surface prediction are close to the diagonal line, which further illustrates the accuracy of the simulation.

Optimization parameter sensitivity analysis

The local sensitivity reflects the closeness of the relationship between the output parameters and the input parameters. The larger the local sensitivity, the stronger the effect of the input parameters on the output parameters. Take the sensitivity of the Nusselt number as an example (equation 14):

$$Sensitivity = \frac{Nu_{max} - Nu_{min}}{Nu_{ave}} \tag{14}$$

If the input parameter is positively correlated with the output parameter, it means that the output parameter increases with the increase of the input parameter and the local sensitivity is positive. If the input parameter is negatively correlated with the output parameter, it means that the output parameter decreases with the increase of the input parameter and the local sensitivity is negative.

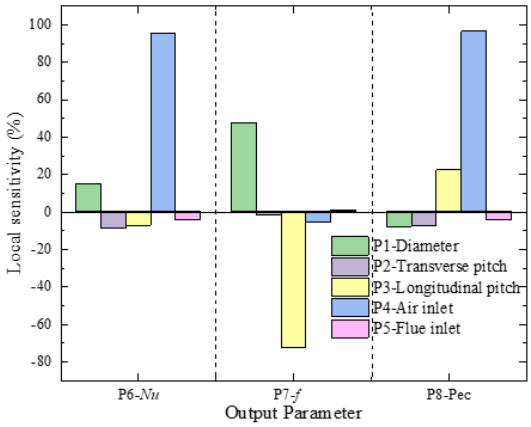


Fig. 16 - Local sensitivity of output parameters

The sensitivity of each input parameter to the output parameter is shown in Fig. 16. Air velocity and longitudinal pitch perform the most significant influence on the overall performance, followed by hot tube diameter, transverse pitch, and flue gas velocity. An increase in air velocity is beneficial for comprehensive performance. The influence of air velocity on heat transfer performance is the largest and is positively correlated; the influence of longitudinal pitch on resistance performance is the largest and is negatively correlated. A simulation result is needed to confirm an optimal value.

Optimization results

After the response surface of the heat exchanger was completed, and the accuracy of the response surface prediction was demonstrated by the fit. Based on the DOE simulation results, three sets of relatively optimal solutions were screened out as shown in Table 4.

Table 4

Results of multi-objective optimization

Plan	P1/(mm)	P2/(mm)	P3/(mm)	P4/(m/s)	P5/(m/s)	*Nu*	*f*	Pec
Initial	76	102	118	4.26	8.23	167.96	2.60	122.15
1	74.91	104.23	121.37	4.83	8.48	184.00	2.21	141.83
2	74.30	99.83	123.98	4.66	8.83	175.20	2.05	137.76
3	75.67	101.76	119.86	4.67	7.92	187.39	2.39	140.85

It can be found from Table 4 by comparing the performance parameters with the initial structure that the *Nu* of schemes 1-3 increased by 9.55%, 4.31%, and 11.57%, respectively, and *f* decreased by 15%, 21.15%, and 8.08%, and Pec increased by 16.11%, 12.78%, and 15.31%. According to the equation of Pec, the Nusselt number of all three structures is increased and the friction factor is decreased after optimization, thus the Pec is increased. In this study, the maximum value of Pec increase was adopted as the best design point: P1=74.91 mm, P2=104.23 mm, P3=121.37 mm, P4=4.83 m/s, and P5=8.48 m/s.

Table 5

Design point verification results and optimization results

Plan	*Nu* optimized results	*Nu* validated results	*Nu* error (%)	*f* optimized results	*f* validated results	*f* error (%)	Pec optimized results	Pec validated results	Pec error (%)
1	184.00	180.36	1.98	2.21	2.27	2.71	141.83	137.27	3.22
2	175.20	172.14	1.75	2.05	2.10	2.44	137.76	134.38	2.45
3	187.39	179.93	3.98	2.39	2.45	2.51	140.85	133.54	5.19

In order to analyze the reliability of the optimization results, the three optimization results were reinserted as design points in the DOE scheme for simulation validation again. The validation results are shown in Table 5. It can be found from Table 5 that the maximum error between the optimization results and the validation results is 5.19%. Therefore, the accuracy of the genetic algorithm calculation was proved, and the optimization of the heat exchanger structure can be completed by the ANSYS response surface module.

CONCLUSIONS

(1) According to the calculated boundary conditions, when the simulated air velocity is 4.26 m/s and flue gas velocity is 8.23 m/s, the outlet temperature obtained is 88°C, which is higher than the product design requirement of 80°C. The numerical simulation results agree well with the calculation results, with a maximum deviation of 10%, and the results can be considered reliable.

(2) The structural parameters and flow parameters are considered. The results of single-factor and multi-factor analyses of input parameters by 2D and 3D response surfaces show that the influence of multiple input parameters is more complex and correlated with each other. Response surface optimization provides a novel method for optimizing shell and tube heat exchangers.

(3) Within the range of input parameters selected in this study, air velocity and longitudinal pitch most affect the comprehensive performance, followed by hot tube diameter, transverse pitch, and flue gas velocity. The multi-objective optimization of the heat exchanger by genetic algorithm finally determined the best design points in this study as P1=74.91 mm, P2=104.23 mm, P3=121.37 mm, P4=4.83 m/s, and P5=8.48 m/s. The comprehensive performance is improved by 16.11%.

ACKNOWLEDGEMENTS

The authors thank Fund Project: Anhui Province Science and Technology Major Special Project and Anhui Province Engineering Laboratory of Intelligent Agricultural Machinery and Equipment and Anhui Agricultural University for their funding support.

REFERENCES

[1] Chen, H. T., Lin, Y. S., Chen, P. C., & Chang, J. R. (2016), Numerical and experimental study of natural convection heat transfer characteristics for vertical plate fin and tube heat exchangers with various tube diameters. *International Journal of Heat and Mass Transfer*, *100*, 320-331. England. https://doi.org/10.1016/j.ijheatmasstransfer.2016.04.039

[2] Dong, C., Chen, Y., & Wu, J. (2015). Comparison of heat transfer performances of helix baffled heat exchangers with different baffle configurations. *Chinese Journal of Chemical Engineering*, *23*(1), 255-261. China https://doi.org/10.1016/j.cjche.2014.10.014

[3] Gu, X., Wang, T., Chen, W., Luo, Y., & Tao, Z. (2019). Multi-objective optimization on structural parameters of torsional flow heat exchanger. *Applied Thermal Engineering*, *161*, 113831. England https://doi.org/10.1016/j.applthermaleng.2019.113831

[4] Guo, J., Fan, A., Zhang, X., & Liu, W. (2011). A numerical study on heat transfer and friction factor characteristics of laminar flow in a circular tube fitted with center-cleared twisted tape. *International Journal of Thermal Sciences*, *50*(7), 1263-1270. France. https://doi.org/10.1016/j.ijthermalsci.2011.02.010

[5] Heydari, A., Shateri, M., Sanjari, S. (2018). Numerical analysis of a small size baffled shell-and-tube heat exchanger using different nano-fluids. *Heat Transfer Engineering*, *39*(2), 141-153. USA. https://doi.org/10.1080/01457632.2017.1288052

[6] Jiang, Q., Zhang, Y., Yan, S., & Xu, L. (2021). Optimal Design of an Angular Box for a Mixed Flow Grain Dryer. *Applied Engineering in Agriculture*, *37*(4), 555-562. USA. https://doi.org/10.13031/aea.14643

[7] Kamiyama, A., Inokuma, K., Murata, A., Yamamoto, S., Iwamoto, K., & Konno, T. (2022). Multi-objective optimization of multi-stage heat sink of electric aircraft using three-dimensional thermal network analysis. *Journal of Thermal Science and Technology*, *17*(1), 21-00421. Japan. https://doi.org/10.1299/jtst.21-00421

[8] Kays, W. M., & London, A. L., (1984) *Compact heat exchangers*, New York: McGraw-Hill Book Company.

[9] Kim, N. H., & Cho, H. (2018). Airside heat transfer and pressure drop of louver-finned parallel flow heat exchanger having a drainage channel. *Journal of Thermal Science and Technology*, *13*(1), JTST0018-JTST0018. Japan. https://doi.org/10.1299/jtst.2018jtst0018

[10] Liu, J. J., Liu, Z. C., & Liu, W. (2015). 3D numerical study on shell side heat transfer and flow characteristics of rod-baffle heat exchangers with spirally corrugated tubes. *International journal of thermal sciences*, *89*, 34-42. France. https://doi.org/10.1016/j.ijthermalsci.2014.10.011

[11] McKendry, P. (2002). Energy production from biomass (part 1): overview of biomass. *Bioresource technology*, *83*(1), 37-46. Netherlands. https://doi.org/10.1016/S0960-8524(01)00118-3

[12] Mirzaei, M., Hajabdollahi, H., & Fadakar, H. (2017). Multi-objective optimization of shell-and-tube heat exchanger by constructal theory. *Applied Thermal Engineering*, *125*, 9-19. England. https://doi.org/10.1016/j.applthermaleng.2017.06.137

[13] Naqvi, S. M. A., & Wang, Q. (2019). Numerical comparison of thermohydraulic performance and fluid-induced vibrations for STHXs with segmental, helical, and novel clamping antivibration baffles. *Energies*, *12*(3), 540. Switzerland. https://doi.org/10.3390/en12030540

[14] Raja, B. D., Jhala, R. L., & Patel, V. (2017). Many-objective optimization of cross-flow plate-fin heat exchanger. *International Journal of Thermal Sciences*, *118*, 320-339. France. https://doi.org/10.1016/j.ijthermalsci.2017.05.005

[15] Raja, B. D., Jhala, R. L., & Patel, V. (2017). Many-objective optimization of shell and tube heat exchanger. *Thermal Science and Engineering Progress*, *2*, 87-101. England. https://doi.org/10.1016/j.tsep.2017.05.003

[16] Shahril, S. M., Quadir, G. A., Amin, N. A. M., & Badruddin, I. A. (2017). Thermo hydraulic performance analysis of a shell-and-double concentric tube heat exchanger using CFD. *International Journal of Heat and Mass Transfer*, *105*, 781-798. England. https://doi.org/10.1016/j.ijheatmasstransfer.2016.10.021

[17] Sharifi, K., Sabeti, M., Rafiei, M., Mohammadi, A. H., & Shirazi, L. (2018). Computational fluid dynamics (CFD) technique to study the effects of helical wire inserts on heat transfer and pressure drop in a double pipe heat exchanger. *Applied Thermal Engineering*, *128*, 898-910. England. https://doi.org/10.1016/j.applthermaleng.2017.08.146

[18] Sheikholeslami, M., Gorji-Bandpy, M., & Ganji, D. D. (2015). Fluid flow and heat transfer in an air-to-water double-pipe heat exchanger. *The European physical journal plus*, *130*, 1-12. Italy. https://doi.org/10.1140/epjp/i2015-15225-y

[19] Tan, X. H., Zhu, D. S., Zhou, G. Y., & Zeng, L. D. (2012). Experimental and numerical study of convective heat transfer and fluid flow in twisted oval tubes. *International Journal of Heat and Mass Transfer*, *55*(17-18), 4701-4710. England. https://doi.org/10.1016/j.ijheatmasstransfer.2012.04.030

[20] Tharakeshwar, T. K., Seetharamu, K. N., & Prasad, B. D. (2017). Multi-objective optimization using bat algorithm for shell and tube heat exchangers. *Applied Thermal Engineering*, *110*, 1029-1038. England. https://doi.org/10.1016/j.applthermaleng.2016.09.031

[21] Wickramaarachchi, W. A. M. K. P., & Narayana, M. (2020). Pyrolysis of single biomass particle using three-dimensional Computational Fluid Dynamics modelling. *Renewable Energy*, *146*, 1153-1165. England. https://doi.org/10.1016/j.renene.2019.07.001

[22] Xie, C. Y., Tao, H. Z., Li, W., & Cheng, J. J. (2019). Numerical simulation and experimental investigation of heat pipe heat exchanger applied in residual heat removal system. *Annals of Nuclear Energy*, *133*, 568-579. USA. https://doi.org/10.1016/j.anucene.2019.07.009

[23] Zhang, H., Yang, J., Zhuang, J., (2009), *Energy saving technology of heat pipe*, China, Beijing: Chemical Industry Press. (In Chinese)

FINITE ELEMENT SIMULATION OF INTER-PLANT WEED CONTROL DEVICE IN PADDY FIELD
/
稻田株间除草部件有限元模拟

Wenting JIN [1,2], Yuqi ZHUANSUN [2], Tengfei ZHUANG[1], Qi LU [1], Wenlong LI [2], Liuxuan MA *[2]
[1] Chinese Academy of Agricultural Mechanization Sciences Group Co.,Ltd, Beijing 100083, China;
[2] College of Mechanical Engineering, Jiamusi University, Jiamus 154007, China
Tel: +86-15145498846; E-mail: 198053043@stu.jmsu.edu.cn
DOI: https://doi.org/10.35633/inmateh-69-24

Keywords: *weeding machinery, inverted V-shaped component, finite element method, dynamic behavior*

ABSTRACT
Mechanical weeding in paddy fields is a green and environmentally friendly way to control weeds, which has the advantages of reducing the amount of pesticides and improving the physical structure of the soil. This paper briefly describes the composition and relevant parameters of the mechanical weeding environment in rice fields. Using Creo 5.0, HyperMesh 2017, and LS-PrePost and LS-DYNA software to jointly simulate the interaction process between inverted V-shaped inter-plant weeding component and the soil in the paddy field, the single-point ALE multi-material unit algorithm is used to couple the soil and water with multiple substances, and realize the material movement between the soil and the water layer. Using the penalty function method, a fluid-solid coupling finite element modelled on the interaction between inter-plant weeding components and soil-water was established. The dynamic behavior of the interactions shows that the coupling stress increases and then decreases periodically, and the teeth of the spring cross the soil with a "bending moon (fish scale)" scratch, which can effectively avoid rice seedlings and reduce the injury rate.

摘要
稻田机械除草是一种绿色环保的控草方式，具有降低农药用量、改善土壤物理结构等优点。本文简要介绍了稻田机械除草环境组成及相关参数。运用 Creo 5.0、HyperMesh 2017 和 LS-PrePost 及 LS-DYNA 软件联合模拟了倒 V 型株间除草部件与水田土壤间的互作过程，其中，采用单点 ALE 多物质体单元算法，对土壤与水进行多物质耦合，实现了在株间除草部件扰动下土壤与水层间的物质运动；运用罚函数法建立了株间除草部件与土壤-水互作的流固耦合有限元模型。由互作动态行为过程可知：耦合应力呈先增后减周期性变化；弹齿划过土壤呈现“弯月（鱼鳞）”状划痕，可有效避让水稻秧苗，降低伤苗率。

INTRODUCTION
Compared with the numerical simulation method, the traditional experimental research method has a long cycle and is time-consuming and labor-intensive *(Wu et al., 2019)*. Choosing the numerical simulation method for preliminary exploration and research and applying the research results to the test will greatly shorten the test period and reduce the research and development cost *(Qi et al., 2020)*. At present, domestic and foreign scholars widely use virtual simulation methods for agricultural machinery-soil interaction problems. Commonly used 3D modeling software are CREO, SOLIDWORKS and UG *(Abo-Elnor et al., 2004)*; ANSYS, ADAMS and ABAQUS are widely used for finite element analysis *(Shinde et al., 2011)*. *Bentaher et al.* used 3D reconstruction combined with the finite element method to simulate the process of ploughing body cutting soil. The simulation results show that the best working angle of the plough body is 22° *(Bentaher et al., 2013)*. *Qi Long et al.* used ANSYS software to simulate the interaction process between the paddy field raking-pressed inter-row weeding wheel and soil, and explored the effects of soil type, water depth and weeding wheel speed on the coupling stress and soil disturbance rate *(Qi et al., 2015)*. *Tian Liang et al.* used the discrete element method to simulate and analyze the interaction process between the weeding wheel and the soil in paddy fields, and obtained the influence of the depth of the weeding wheel, the speed of the weeding wheel and the forward speed of the machine on the torque and soil disturbance rate, and verified through soil trough and field experiments *(Tian et al., 2021)*.

[1] *Wenting JIN, Ph.D.Stud; Tengfei ZHUANG, Engineer; Qi LU, Ph.D.Stud;*
[2] *Liuxuan MA*, Professor (Corresponding author); Yuqi ZHUANSUN, Undergraduate; Wenlong LI, Master Degree*

To sum up, it is feasible to use virtual simulation method to study the interaction between agricultural machinery and soil. In this paper, the joint modeling finite element virtual simulation is used for the inverted V-shaped inter-plant weeding component, and the interaction process between the weeding component and the paddy soil coupling model is simulated, in order to improve the effect of mechanical weeding between rice fields and accelerate the process of weeding mechanization in paddy fields.

MATERIALS AND METHODS

WEEDING ENVIRONMENT AND WORKING PRINCIPLE

The inter-plant mechanical weeding environment in a rice field includes inter-plant weeding machinery, rice seedlings, weeds, soil and water, as shown in Fig 1. The row spacing is 0.2 ~ 0.3 m; the plant spacing is 0.1 ~ 0.12 m. Various weeds are randomly distributed throughout the paddy field *(Jin et al., 2021)*. When the rice had been transplanted for about 20 days, the root depths of rice and weed were 0.08 ~ 0.1 m and 0.03 ~ 0.07 m, respectively. Paddy soil can be divided into soil layer and mud layer after soaking and beating, and the depths are 0.16 ~ 0.18 m and 0.03 ~ 0.05 m respectively *(Tao et al., 2015)*. Different growth stages of rice seedlings have different water requirements, and the water layer is generally not more than the leaf core.

The inverted V-shaped between plant weeding device consists of a weeding claw, an inverted V mechanism and a transmission mechanism. The transmission mechanism mainly includes an inverted V-shaped transmission shaft, a transverse transmission shaft and a gear composed of a large bevel gear and two small bevel gears group. The weeding claw is the part of the device that directly contacts the soil and plants in the paddy field, and is welded by spring teeth and a claw plate. Two weeding claws are symmetrical and have a phase angle of 36° between the spring teeth of the same No.. The distance between the center of the claw plate is L, the rotation center line extends and the intersection angle α is 50°, and the shape is like an inverted V, so it is called "inverted V mechanism".

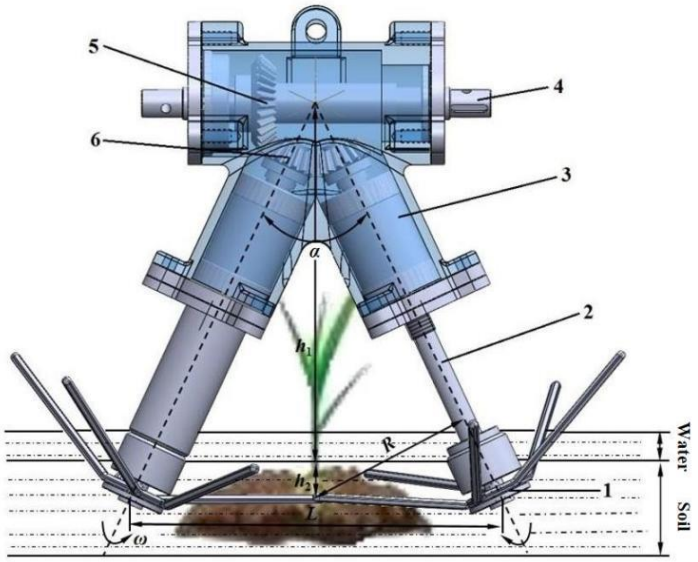


Fig. 1 - Schematic diagram of the environmental structure of mechanical weeding among rice fields
1. Weeding claw; 2. Inverted V-shaped drive shaft; 3. Inverted V-shaped cover; 4. Lateral drive shaft; 5. Large bevel gear; 6. Small bevel gear

For each row of between plant weeding operations, the weeding claws are powered by a diesel engine through a gearbox through a series of transmissions (chain transmission, gear transmission), and move in a counter-rotating trochoidal motion in the direction opposite to the machine operation. The depth of the spring teeth into the soil is h_2. The soil is cut in sequence to muddy the water. When the spring teeth touch the main root of the rice seedling without touching the secondary root, the secondary root produces a certain pulling force on the main root and resists the partial thrust of the spring teeth, so that the growth posture of the seedling is less affected; But when the spring teeth come into contact with the secondary roots of the rice seedling, the rice seedlings move away from the soil with the spring teeth, causing damage to the seedling. Since weed has only main roots, they can easily be separated from the original floating water surface or buried in the soil, inhibiting their growth.

FINITE ELEMENT SIMULATION

The "joint modeling" is used to carry out finite element simulation analysis on the interactive relationship between paddy field weeding components and soil. The simulation process flow chart is shown in Fig. 2.

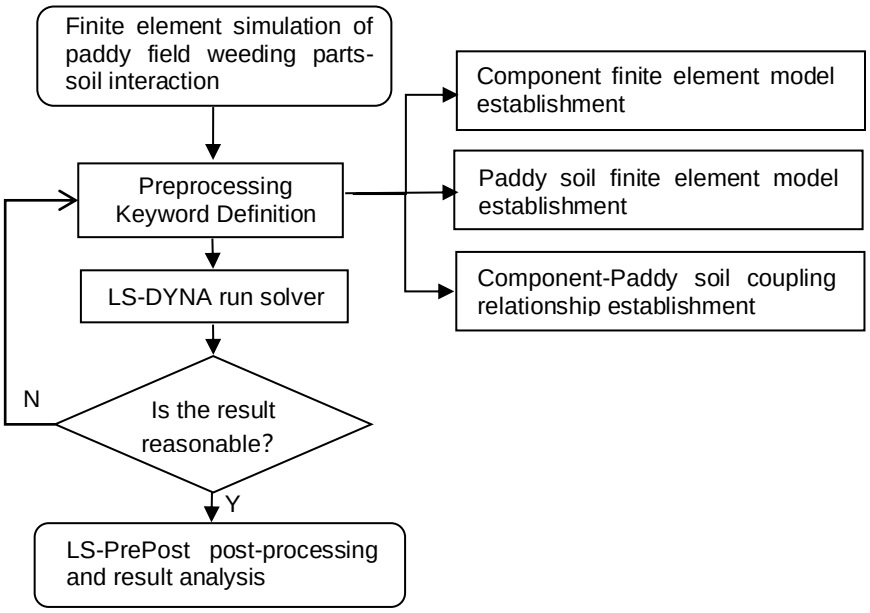


Fig. 2 - Simulation process flow chart

Establishing a finite element model of the component

Import the inter-plant weeding component model into HyperMesh software and find that the boss information of the cutter plate is missing. Select "Geom" in the page menu bar to modify and operate the inter-plant weeding component model. Click "surfaces", select the stretching command, click the missing surface *(Zhou et al., 2015)*, select the positive direction of the *Y*-axis of the coordinate system as the stretching direction, set the stretching length to 4, and complete the repair of the model, as shown in Fig 3.

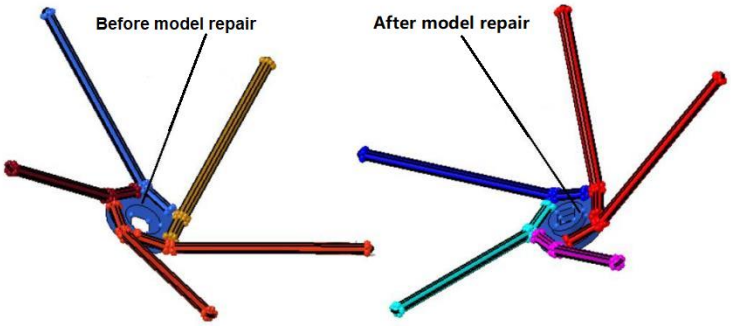


Fig. 3 - Comparison before and after model repair

Due to the different contact between the cutter plate and the spring teeth, the meshes of it are different. The cutter plate is divided into Solid meshes, and the spring teeth are divided into Shell meshes. The mesh size of the cutter plate and spring teeth is both set to 0.001 m, with a total of 31795 nodes and 31892 elements.

The inter-plant weeding component work in a high-moisture soil environment, and have strong impact under high-speed rotation and forward speed. Therefore, 65Mn spring steel with strong oxidation resistance, corrosion resistance and wear resistance is selected, and rigid material (*MAT_RAGID) is selected as the simulation material, and the parameters are set as: density 7.85×103 kg/m^3, Young's modulus 2.1×103 MPa, Poisson's ratio 0.3. In addition, the degrees of freedom in the *X* and *Z* axes of the movement direction and the *Y* axes degrees of freedom of rotation direction are constrained, and other parameters are selected by default.

Establishing a finite element model of paddy soil

In order to ensure that the water layer and the soil share the grids and nodes on the cutting plane, and the watershed boundary is not distorted during the process of cutting the paddy field soil by the inter-plant

weeding component *(Liu, 2020)*. Creo 5.0 software is used to establish a solid with length × width × height [soil height + water layer height (W_h:W_{h1}-W_{h2}-W_{h3})] with a size of 0.5m × 0.6m × [0.1+(0.01-0.04-0.07)] m to represent a rectangular. Then use the segmentation function to divide the model into two layers, the upper layer represents water, and the lower layer represents soil, as showed in Fig 4.

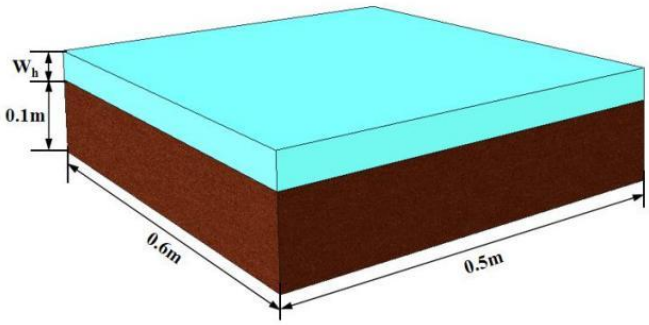


Fig. 4 - 3D model of water-soil

The soil layer material is selected from No. 147 material (*MAT_FHWA_SOIL) in the material library. The main parameters are set according to the paddy soil parameters in Table 1, and the default values are selected for other parameters. The soil failure criterion of paddy field generally adopts the Mohr-Coulomb yield criterion (M-C criterion) *(Yang., 2014)* with the addition of the similar factor modified Drucker-Prager criterion (D-P criterion), as showed in formula (1):

Table 1

Soil parameters of sampling paddy field

Soil density	Moisture content	Cohesive strength	Friction angle	Bulk modulus	Poisson's ratio	Shear modulus
[g/cm^3]	[%]	[MPa]	[°]	[MPa]		[MPa]
1.681	68.3	0.0037	19.022	21.8	0.51	7.22

$$F = -p\sin\phi + \sqrt{J_2 K(\theta)^2 + \alpha^2 \sin^2\phi} - c\cos\phi = 0 \quad (1)$$

$$K(\theta) = \cos\theta + \frac{1}{\sqrt{3}}\sin\theta\cos\phi \quad (2)$$

where:

F is the model surface yield force, N; P is the pressure, MPa; $\varnothing$ is the Friction angle, °; J_2 is the second invariant of deviatoric stress; α is the similarity factor between the corrected yield surface and the standard M-C yield surface; c is the cohesive strength, MPa.

The upper layer of the model is actually a mixture of water and various substances. In order to facilitate the definition of simulation parameters, the upper layer is water by default. No. 9 material (*MAT_NULL) in the material library is selected for the water layer. This material is an empty material model, which can provide movement space for the soil, which is suitable for the large deformation problem of cutting soil by weeding parts between plants *(Zhao., 2017)*. The pressure-volume relationship of the water layer adopts the Grüneisen equation of state, as shown in formula (3):

$$P = \frac{\rho C^2 \mu\left[1+\left(1-\frac{\gamma_0}{2}\right)\mu - \frac{\alpha_2\mu^2}{2}\right]}{\left[1-(S_1-1)\mu - \frac{S_2\mu^2}{\mu+1} - \frac{S_3\mu^3}{(\mu+1)^2}\right]} + (\gamma_0 + \alpha_2\mu)E \quad (3)$$

$$\mu = \frac{\rho}{\rho_0} - 1 \quad (4)$$

where:

ρ is the density of water, g/cm^3; C is the impact velocity-particle velocity curve intercept; S_1, S_2 and S_3 are the impact velocity-particle velocity curve coefficients; μ is volume strain; E is the initial energy, J/Kg; γ_0 is the Grüneisen constant; α_2 is the order volume correction factor.

Using the single-point ALE multi-material unit body algorithm in the ALE method, and using the keyword *ALE_MULTI_MATERIAL_GROUP to perform multi-material fluid-structure coupling on the soil layer and the water layer. The two are bound in a unit algorithm to realize the material exchange and transportation between water and soil *(Wang et al., 2021)*.

Establishment of fluid-solid coupling relationship between components and paddy soil

After completing the finite element model of the inter-plant weeding component and the paddy soil, it is necessary to establish the fluid-solid coupling relationship between the two to solve. Use the keyword *CONSTRAINED_LAGRANGE_IN_SOLID to define the contact form between the inter-plant weeding components and the paddy field-soil, set the Lagrange unit (a pair of inter-plant weeding components) as SLAVE, the ALE multi-substance unit (soil-water) as MASTER, and set the kinetic friction coefficient as 0.1, the static friction coefficient as 0.5, and other parameters are selected as default.

The penalty function method is used to perform fluid-solid coupling between the inter-plant weeding component and the paddy field soil. This method can track the relative displacement between the inter-plant weeding component and the paddy field soil, and detect whether penetration occurs on the paddy field soil surface, so that the system maintains kinetic energy conservation *(Wang et al., 2021)*.

In the fluid-structure interaction, the Lagrange dynamic equation is adopted, such as formula (5):

$$M\ddot{U} + D\ddot{U} + KU = F^{S} + F^{FSI} \tag{5}$$

where:

M is the mass matrix of the Lagrange unit cell, kg;
D is the damping matrix of the Lagrange unit cell, N/(m/s);
$\ddot{U}$ is the acceleration of the Lagrange unit cell, m/s^2;
K is the stiffness matrix of Lagrange unit cell, N/m;
U is the displacement of the Lagrange unit cell, m;
F^{S} is the external load vector without fluid force;
F^{FSI} is the coupled stress of the fluid acting on the Lagrange unit cell, which can be expressed by formula (6).

$$F^{FSI} = -\int_{\Gamma_{FSI}} N^{T} n_f \sigma_f d\Gamma \tag{6}$$

where:

Γ_{FSI} is the fluid-solid coupling contact surface, which can be deformed; N^{T} is the velocity interpolation matrix after transposition; n_f is the outer normal vector of the fluid domain Neumann boundary unit; σ_f is the Cauchy stress tensor within the fluid.

In order to simulate the infinite space of real paddy soil, all the degrees of freedom at the bottom of the paddy soil model are constrained, and non-reflection boundary conditions are added to the other five surfaces. In addition, to achieve the purpose of mutual transport between soil and water, the keyword *CONTROL_ALE is defined, as showed in Fig 5.

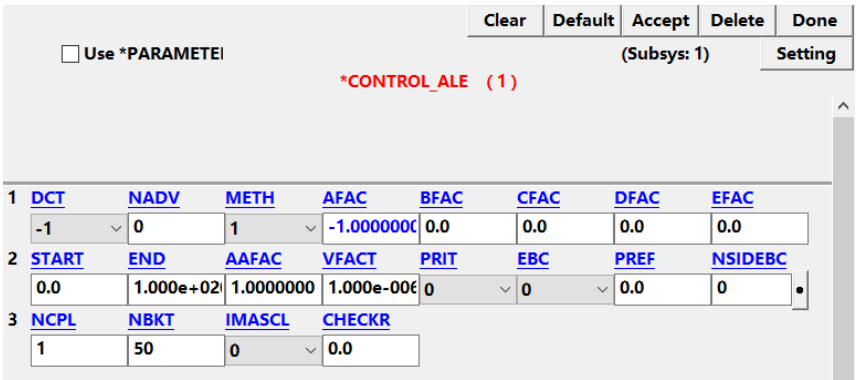


Fig. 5 - ALE control algorithm parameters

Combined with the coupled stress-time curve diagram (as shown in Fig 6) and the coupled stress nephogram (as shown in Fig 7), the stress field of the finite element simulation model of the interaction between the inter-plant weeding component in the paddy field and the soil is analyzed, and it is known that: The inter-

plant weeding component in the paddy field cuts the paddy field soil inward. Under the cutting disturbance of the inter-plant weeding component, the water-soil coupling interface is destroyed, resulting in coupling stress.

When t_1=0.028 s, the No. 0 spring tooth of the right inter-plant weeding component cuts the coupling interface, and the tooth tip completely enters the soil, and the coupling stress reaches the first peak point of 0.5134 MPa, as shown in Fig 7 - a); When t_2=0.073 s, the No. 0 spring tooth of the left inter-plant weeding component cuts the coupling interface, and the tooth tip completely enters the soil, and the coupling stress reaches the second peak point of 0.5555 MPa, as shown in Fig 7 - b); When t_3=0.110 s, the No. 1 spring tooth of the right inter-plant weeding component cuts the coupling interface, and the tooth tip completely enters the soil, and the coupling stress reaches the third peak point of 0.5490 MPa, as shown in Fig 7 - c); When t_4 = 0.142 s, the No. 1 spring tooth of the left inter-plant weeding component cuts the coupling interface, and the tooth tip completely enters the soil, and the coupling stress reaches the fourth peak point of 0.5543 MPa, as shown in Fig 7 - d).

RESULTS

The results after the operation was solved, were imported into LS-PrePost 4.3 for dynamic behavior analysis. In order to facilitate the observation of the dynamic behavior of the inter-plant weeding components in the soil, the water layer was hidden, and the stress and density of the water layer-soil coupling interface were selected to analyze the stress field and flow field of the interaction process of the inter-plant weeding component in the paddy field soil.

Stress Field Analysis

Combined with the coupled stress-time curve diagram (as shown in Fig. 6) and the coupled stress nephogram (as shown in Fig.7), the stress field of the finite element simulation model of the interaction between the inter-plant weeding component in the paddy field and the soil is analyzed, and it is known that: the inter-plant weeding component in the paddy field cuts the paddy field-soil inward. Under the cutting disturbance of the inter-plant weeding component, the water-soil coupling interface is destroyed, resulting in coupling stress.

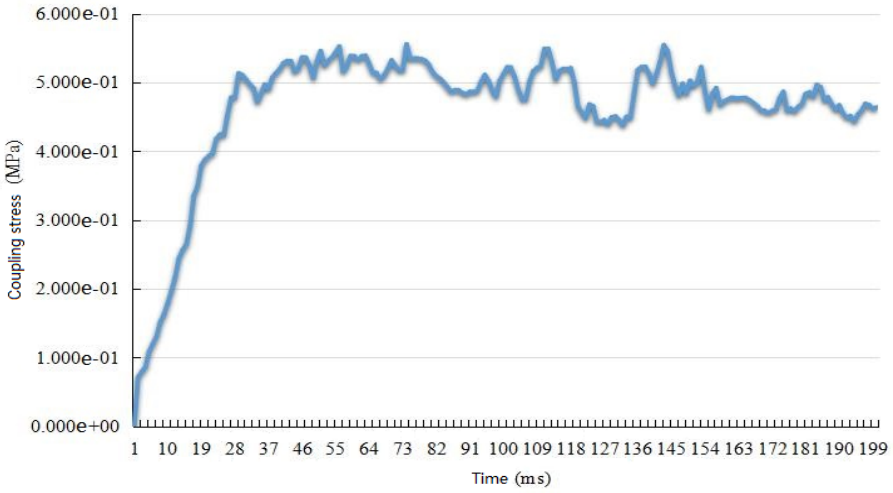
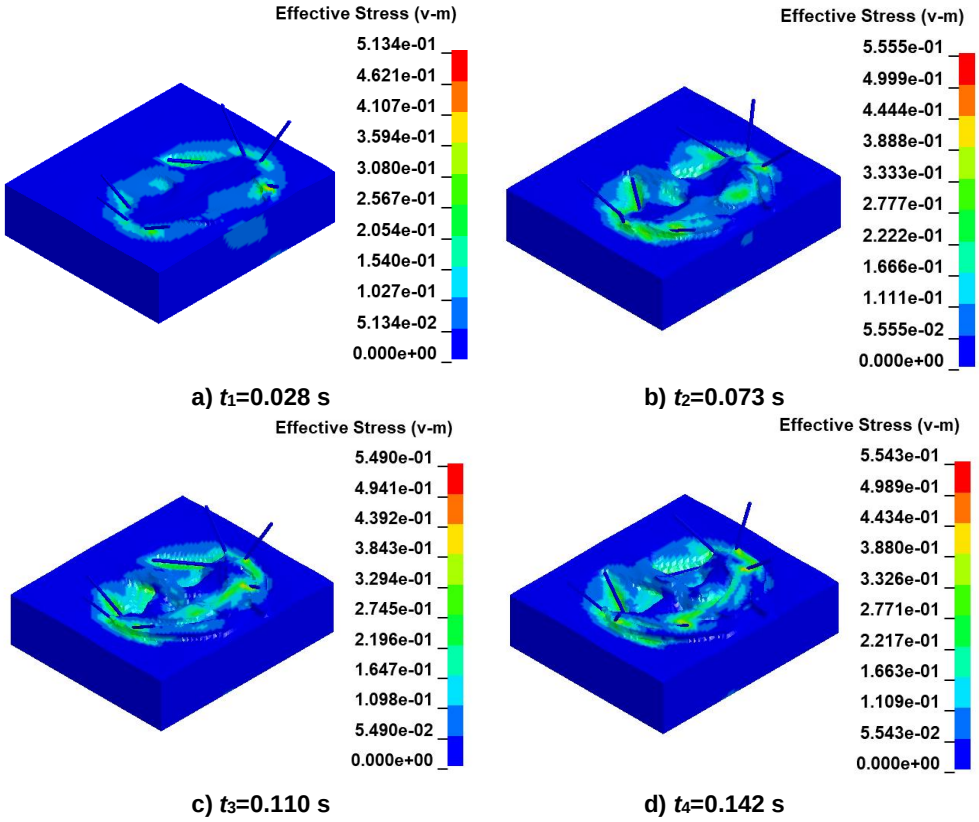


Fig. 6 - Coupling stress-time graph

When t_1=0.028 s, the No. 0 spring tooth of the right inter-plant weeding component cuts the coupling interface, and the tooth tip completely enters the soil, and the coupling stress reaches the first peak point of 0.5134 MPa, as shown in Fig 7 - a); When t_2=0.073 s, the No. 0 spring tooth of the left inter-plant weeding component cuts the coupling interface, and the tooth tip completely enters the soil, and the coupling stress reaches the second peak point of 0.5555 MPa, as shown in Fig 7 - b); When t_3=0.110 s, the No. 1 spring tooth of the right inter-plant weeding component cuts the coupling interface, and the tooth tip completely enters the soil, and the coupling stress reaches the third peak point of 0.5490 MPa, as shown in Fig 7 - c); When t_4 = 0.142 s, the No. 1 spring tooth of the left inter-plant weeding component cuts the coupling interface, and the tooth tip completely enters the soil, and the coupling stress reaches the fourth peak point of 0.5543 MPa, as shown in Fig 7 - d).



a) t_1=0.028 s b) t_2=0.073 s

c) t_3=0.110 s d) t_4=0.142 s

Fig. 7 - Coupling stress cloud diagram

Flow field analysis

The water-soil model adopts the single-point ALE multi-substance unit algorithm, and the simulation model is a fluid state. By observing the water-soil fluid flow change diagram (as shown in Fig 8) and the soil density-time curve (as shown in Fig 9), the flow field of the finite element simulation model of paddy field weeding component-soil interaction is analyzed, and it is known that: since the fluid-structure coupling keyword is defined between the water layer and the soil, the water and soil can flow freely and exchange substances. Therefore, under the disturbance of the rotating spring teeth of the inter-plant weeding component, the soil grid contacted by the spring teeth is destroyed, the soil is forced to flow backward and upward, and the water flows downward to the space where the soil is destroyed. Each spring tooth scratches the soil to present a "meniscus (fish scale)"-like scratch, and the water molecules and soil particles are mixed and stirred to make the water layer turbid.

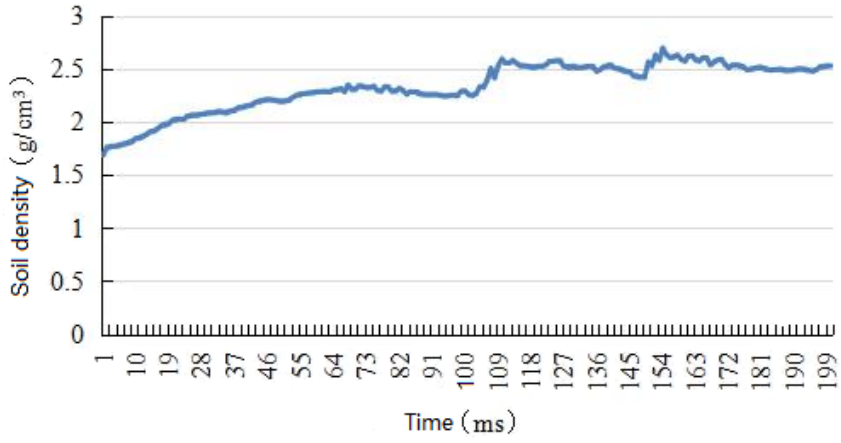
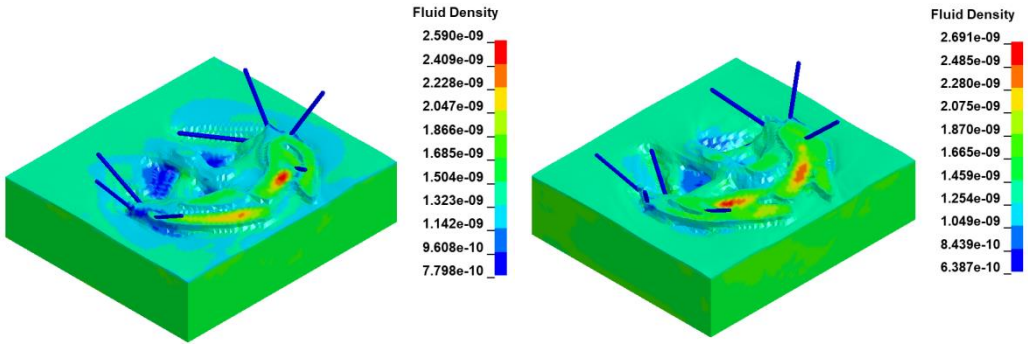


Fig. 8 - Soil density-time curve diagram

When T_1=0.109 s, the No. 0 spring tooth of the right inter-plant weeding component has just crossed the lowest point of rotation, and the No. 0 spring tooth of the left inter-plant weeding component is about to reach the lowest point of rotation.

The soil is flowing backwards and upwards accumulated in the water layer to form the first "meniscus (fish scale)"-shaped bulge. At this time, the No. 4 spring tooth of the right inter-plant weeding component just rotated and impacted this watershed. Make the density of fluid (soil) reach the first peak point of 2.590 g/cm^3, as shown in Fig 9 - a); When T_2=0.153 s, the No. 1 spring tooth of the right inter-plant weeding component is about to reach the lowest point of rotation, and the soil is transported backward and upward to accumulate in the water layer to form a second "meniscus (fish scale)"-shaped bulge. At this time, the No. 4 spring tooth of the left inter-plant weeding component just rotated and impacted the watershed, and fluid (soil) density reached the second peak point of 2.691 g/cm3, as shown in Fig 9 - b).



a) T_1=0.109 s **b) T_2=0.153 s**

Fig. 9 - Fluid Density Diagram

CONCLUSIONS

(1) Using the idea of "joint modeling", the material exchange between the soil and the water layer was realized under the disturbance of the inter-plant weeding component; the dynamic behavior process of the inter-plant weeding component and the soil was established and analyzed.

(2) Through the analysis of the stress field, it can be concluded that when the spring tooth cuts the coupling interface and the tooth tip completely enters the soil, the interface coupling stress is the largest. Because the paddy soil has a certain fluidity, compactness around the soil decreases under the disturbance of the previous spring teeth, and the coupled stress first increases and then decreases cyclically during the forward movement of the inter-plant weeding components. The lower the coupling stress, the lower the resistance of the inter-plant weeding components during weeding operation and the lower the power consumption of the machine.

(3) Through the analysis of the convective flow field, it can be concluded that during the rotation of the inter-plant weeding components, the lower end of the soil grid is not damaged because it is not in direct contact with the spring teeth, but is compressed by downward pressure. In addition, the soil is forced to flow backwards and upwards, and accumulates and squeezes in a certain watershed of the water layer, which makes the fluid density increase. The greater the variation in fluid density, the greater the rate of soil disturbance and the greater the rate of weed control during inter-plant weeding component operation.

ACKNOWLEDGEMENT

This work was supported by the Natural Science Foundation of Heilongjiang Provincial (No. LH2020E026). National Modern Agricultural Industrial Technology System Construction Special Fund (No. CARS-01) and the Basic Scientific Research Business Expenses of the Department of Education of Heilongjiang Province (No. 2019-KYYWF-1378).

REFERENCES

[1] Abo-Elnor M., Hamilton R., Boyle J.T. (2004) Simulation of soil–blade interaction for sandy soil using advanced 3D finite element analysis[J]. *Soil and Tillage Research*, 75(1): 61-73.

[2] Bentaher H., (2013). Finite element simulation of moldboard-soil interaction. *Soil & Tillage Research*, Vol. 134, pp. 11-16.

[3] Jin W.T., Ge Y.Y., Fan W W. et al., (2022). Virtual simulation and verification of inverted V-shaped inter-plant weeding device for paddy field（倒 V 型稻田株间除草装置虚拟仿真及验证). *Journal of Chinese Agricultural Mechanization*, Vol. 43, Issue 10, pp. 72-77.

[4] Liu X.D., (2020). *Development and experiment of combined operation machine for split deep rotary tillage and soil disinfection* (分体式深旋耕土壤消毒联合作业机研制与试验). [D], Jiangsu University.

[5] Qi L, Liang Z W, Ma X., (2015). Validation and analysis of fluid-structure interaction between rotary harrow weeding roll and paddy soil（耙压式除草轮与水田土壤作用的流固耦合仿真分析及验证). *Transactions of the Chinese Society of Agricultural Engineering*, Vol. 31, Issue 05, pp. 29-35+37+36.

[6] Qi L., Liu C., Jiang Y. et al., (2020). Present status and intelligent development prospects of mechanical weeding technology and equipment for rice (水稻机械除草技术装备研究现状及智能化发展趋势). *Journal of South China Agricultural University*, Vol.41, Issue 06, pp. 29-36.

[7] Shinde G.U., Kajale S.R. (2011) Computer aided engineering analysis and design optimization of rotary tillage tool components [J]. *International Journal of Agricultural and Biological Engineering*, 4(3): 1-6.

[8] Tian L., (2021). Design and test of post-seat weeding machine for paddy. *Int. J. Agric & Biol Eng*, Vol.14, Issue 03, pp. 112–122.

[9] Tao G.X., Wang J.W., Zhou W.Q. et al., (2015). Herbicidal mechanism and key components design for paddy weeding device (水田株间除草机械除草机理研究与关键部件设计). *Transactions of the Chinese Society for Agricultural Machinery*, Vol.46, Issue 11, pp. 57-613.

[10] Wang Q., Zhou W.Q., Tang H. et al., (2021). Design and Experiment of Arc-tooth Reciprocating Motion Type Seedling Avoided Weeding Control Device for Intertillage Paddy (弧齿往复式稻田株间自动避苗除草装置设计与试验). *Transactions of the Chinese Society for Agricultural Machinery*, Vol.52, Issue 06, pp. 53-61+72.

[11] Wang J.W., Ma X..C, Tang H. et al., (2021). Design and Experiment of Curved-tooth Oblique Type Inter-row Weeding Device for Paddy Field (曲面轮齿斜置式稻田行间除草装置设计与试验). *Transactions of the Chinese Society for Agricultural Machinery*, Vol.52, Issue 04, pp. 91-100.

[12] Wu T., Zeng S., Zhao R.M. et al., (2019). Analysis and study on intelligentialized technologies of intra-row weeding mechanical control（智能化作物株间机械除草技术分析与研究). *Journal of Agricultural Mechanization Research*, Vol.41, Issue 06, pp. 1-6+12.

[13] Yang J., (2014). *Validation and analysis of fluid-structure interaction between rotary harrow weeding roll and paddy soil* (基于扩展有限元法和离散元法的土壤-耕具接触研究). Master dissertation, Kunming University of Science and Technology.

[14] Zhou X.Q., Zhang J., Xiao J. et al., (2015). Simulation of cutting process with double disc colter based on LS-dyna (基于LS—dyna的双圆盘开沟器切削过程的仿真). *Journal of Chinese Agricultural Mechanization*, Vol.36, Issue 05, pp. 288-291+307.

[15] Zhao L.L., (2017). *Study on the key technology of riding paddy field cultivator* (乘坐式水田中耕除草机关键技术研究). Master dissertation, South China Agricultural University.

RECENT TECHNOLOGY IN CULTIVATING PIPER BETLE VAR NIGRA. A COMPREHENSIVE REVIEW
/
TEKNOLOGI PEMBIAKAN TERKINI PIPER BETLE VAR NIGRA. SEBUAH REVIEW LENGKAP

Dewanto HARJUNOWIBOWO*[1)], Anif JAMALUDDIN[1)], Yudi RINANTO[2)], Fajar PRASETYA[3)]
[1)]Physics Education, Universitas Sebelas Maret/ Indonesia;
[2)]Biology Education, Universitas Sebelas Maret/ Indonesia
[3)]Faculty of Pharmacy, Universitas Mulawarman/ Indonesia
Tel: (62) 82258919195; E-mail: dewanto_h@staff.uns.ac.id
Corresponding author: Dewanto Harjunowibowo
DOI: https://doi.org/10.35633/inmateh-69-25

Keywords: *Betel vine, Piper betle var. Nigra, cultivation, human health, herbs*

ABSTRACT
The betel vine, a species of Piper, has organic impacts on human health through its secondary metabolites. Historically, it has been used to treat various illnesses including liver and stomach problems, inflammation, and as an antioxidant, antipyretic, and antimicrobial. Despite its medicinal benefits, the black betel vine (Piper betle var. Nigra) is not widely cultivated. This review summarises traditional and advanced methods of betel cultivation, including the habitats and diseases affecting Piper Betle L. There are two cultivation systems: closed-type and open-type, each with its own advantages and disadvantages. The modern method of propagation through callus induction is gaining popularity, but requires specialised knowledge and is more costly. Traditional cultivation is less complicated, but exposes young plants to disease. Implementing smart farming practices, maintaining optimal growth conditions, and utilizing a screen house with artificial shading and lighting may lead to higher-quality crops with reduced losses. Before planting, the cuttings should be soaked in a fungicide mixture and grown as individual plants to avoid bacterial leaf blight from occurring.

ABSTRAK
Tanaman betel, spesies dari Piper, memiliki dampak alami pada kesehatan manusia melalui metabolit sekundernya. Sejarahnya, tanaman ini digunakan untuk mengatasi berbagai penyakit termasuk masalah hati dan lambung, inflamasi, dan sebagai antioksidan, antipiretik, dan antimikroba. Meskipun memiliki manfaat obat, tanaman sirih hitam (Piper betle var. Nigra) tidak banyak dibudidayakan. Tinjauan ini menguraikan metode budidaya betel tradisional dan modern, termasuk habitat dan penyakit yang mempengaruhi Piper Betle L. Ada dua sistem budidaya: tipe tertutup dan tipe terbuka, masing-masing memiliki kelebihan dan kekurangan. Metode modern reproduksi melalui induksi callus sedang populer, tetapi membutuhkan pengetahuan khusus dan lebih mahal. Budidaya tradisional lebih sederhana, tetapi membuat tanaman muda rentan terhadap risiko penyakit. Penerapan praktik pertanian cerdas, menjaga kondisi pertumbuhan yang optimal, dan memanfaatkan screen membran dengan pencahayaan buatan dapat menghasilkan tanaman berkualitas tinggi dengan kerugian yang lebih sedikit. Sebelum ditanam, potongan tanaman harus direndam dalam campuran fungisida dan harus ditanam sebagai satu tanaman untuk menghindari terjadinya penyakit bakteri layu.

INTRODUCTION

Recently, the concept of utilising natural medication (*Kano et al., 2017)* and preserving food has gained increased popularity (*Salehi et al. 2019; Sahlan, Mandala et al., 2020*), particularly in the era of the COVID-19 pandemic. Science has developed new methods for evaluating herbs utilised in different cultures *(Salehi et al., 2018; Madhumita, Guha and Nag 2020*). The pharmacological properties of plant life, such as food, medicine *(Daud et al., 2020)*, energy *(Ayadi et al., 2020; Sahlan, Muryanto et al. 2020; Kuncoro and Purwanto, 2020*), industrial *(Izzah et al., 2020*), and religious functions, have been demonstrated through improved analysis methods over the centuries (*Dwivedi and Tripathi, 2014; Shukla et al., 2015*).

[1] *Dewanto Harjunowibowo, Assistant Professor; Anif Jamaluddin, Assistant Professor; Yudi Rinanto, Associate Professor; Fajar Prasetyo, Associate Professor.*

The secondary metabolites of Piper betle L. plants *(Prasetya et al., 2022)* such as flavonoids, polyphenols, tannins, saponins, alkaloids, and steroids have significant impacts on human health, exhibiting antimicrobial (*Prasetya et al., 2021*), anti-rheumatic *(Murugesan et al., 2020)*, anti-diabetic, anti-thrombin and Cytotoxic bioactive *(Yogeswari et al., 2020*), anti-cancer (*Wang et al., 2014*), anti-tumour *(Kangralkar and Kulkarni, 2013*), anti-asthma *(Hajare et al., 2011)*, anti-oxidant and anti-fungal *(Li Y. et al. 2020)*, gastroprotective (*Arawwawala, Arambewela, and Ratnasooriya, 2014*), and anti-bacterial *Bintang et al.* (2014);*Taukoorah et al.* (2016) (in mouth) properties (*Teanpaisan et al, 2016)*.

The genus Piper is an abundant group of plants found in pantropical regions such as India (*Sengupta, 2019*), Indonesia (*Patra et al., 2016*), and Sri Lanka (*Arambewela et al., 2011*). These species are classified as aromatic plants due to the presence of essential oil-producing cells (*Dyer and Palmer, 2004*). Chemical analysis of a fresh leaf revealed that it consists of 85.4% moisture, 6.1% carbohydrates, 3.1% protein, 2.3% minerals, 2.3% fibre, and 0.8% fat. Additionally, the leaf contains various minerals and vitamins, including magnesium, iron, carotene, calcium, niacin, riboflavin, vitamin C, and thiamine *(Shah et al., 2016*). Betel leaves are consumed by 2 billion people in India annually and have a significant economic impact, contributing to the national income to the tune of Rs 7000 million annually (*Das et al., 2016*).

In fact, the information about the various biological activities of piper plants comes from in vitro *(Muttaleb et al., 2018; Ghazali et al., 2016; Prasetya et al., 2021; Murugesan et al., 2020; Kangralkar and Kulkarni, 2013*), while cultivation studies are still limited. However, these plants have potential for multiple applications, and the mechanisms of their fundamental cultivation are yet to be investigated. Among the species, cultivation of Piper betle is the most challenging (*Raja et al., 2018*). In particular, the cultivation of betel vine, especially black betel vine, is not yet done effectively and efficiently. Therefore, this current work reviews available literature on traditional and advanced methods of cultivation, specifically for *Piper betle var Nigra*.

MATERIALS AND METHODS

The manuscript has been compiled through a comprehensive literature review. To determine the current understanding of the potency and cultivation of black betel vines, over a hundred articles from various sources around the world were analysed. The literature review commenced with an examination of the potential and utilisation of black betel vines, followed by a general overview of the factors affecting plantation growth. This was followed by a discussion of traditional and contemporary techniques for farming Piper betle. For the reader's convenience, brief findings were provided in each sub-discussion, leading to a comprehensive conclusion based on the results obtained.

RESULTS AND DISCUSSION

1. General factors influencing the plant's growth

The quality of medicinal plants is verified by their prevalent hereditary properties and also large biomass, with reliable and high content of secondary metabolites (*Mosaleeyanon et al., 2005b*). The concentration and chemical profile of secondary metabolites in plants grown outdoors are affected by environmental conditions such as temperature, light quality and intensity *(Mosaleeyanon et al., 2005b; Kozai, Afreen, and Zobayed, 2005*).

The characteristics of in vitro plants in terms of physiology and anatomy are related and primarily governed by the microclimate of the culture container, which includes factors such as relative humidity, light, air movement within the container, carbon dioxide, and the nutrient composition of the medium. All of these factors interact and influence the growth and output of seedlings *(Salehi et al., 2019*).

1.1. Light

All organisms that possess chlorophyll require sunlight to synthesise organic compounds such as carbohydrates. These organic compounds serve as an energy source for cellular mechanisms in plants and for other forms of life. Photosynthesis, the process by which plants synthesise organic compounds from light, occurs in the visible light spectrum (*Singh et al., 2015*) between 400 nm-700 nm (*Bhatia, 2014*). Hence, light is a crucial factor in the production of fruits and vegetables in greenhouse farming (*Messinger and Lauerer, 2015; Choi, Moon, and Kang, 2015; Cossu et al., 2014; Mosaleeyanon et al., 2005a; Rahman, Prihantini, and Nasruddin, 2020)*. In greenhouse cultivation, the choice of cladding material for the facade is a critical factor in providing natural light. Some authors have recommended the use of glass, polyethylene, acrylic, and polycarbonate cladding materials, which have transmission percentages of Photosynthetically Active Radiation (PAR) of 90%, 88%, 86%, and 75%, respectively *(Both, 2013)*.

Under controlled environmental conditions, an increase in photosynthetic photon flux (PPF) and CO_2 concentration leads to an increase in the leaf net photosynthetic rate (*Mosaleeyanon et al., 2005b*). The addition of artificial light in controlled environments enables the maximisation of plant output while minimising the release of resources and pollutants into the environment, thus reducing environmental degradation (*Hoque, 2022*).

Additionally, it facilitates the planning of plant growth, scheduling, and production, and reduces the risk of contamination from diseases, metals, insects, and other harmful substances *(Toyoki Kozai, 2020*).

Studies have shown that environmental factors such as CO_2 concentration and light intensity can have a significant impact on metabolite concentrations. For example, elevated light intensity of 400 mmol $m^{-2}s^{-1}$ leads to a significant increase in hypericin concentration in St. John's *wort* plants *(Briskin and Gawienowski, 2001*). Kurata et al. found that high light irradiation enhances the production of purine alkaloids in *Coffea arabica* cell suspension cultures (*Kurata, Matsumura, and Furusaki, 1997*), and the production of anthocyanin in *Perilla frutescens* cell culture (*Zhong et al., 1991*).

LED lighting has been shown to enhance lettuce growth when using a Red-Blue-White (RBW) spectrum (*Lin et al., 2013*). The highest yield of volatile terpenoids in vegetable plants (*Gynura bicolour*) was obtained using RB20 LED lighting under ambient CO_2 (*Ren, Guo, Xin et al., 2014*). The quality of broccoli seedlings was found to be improved more by red LED light compared to white or blue light *(Wilson, Iwabuchi, & Rajapakse, 1998; Wilson, Iwabuchi, Rajapakse, et al., 1998)*. Despite this, LED lighting is regarded as the most suitable light source for crop cultivation *(Bula et al., 1991; Singh et al., 2015)*.

Ouzounis et al. conducted a study to examine the impact of light spectrum on plant growth and secondary metabolites in *Chrysanthemum morifolium*, *Campanula portenschlagiana*, and *Rosa* hybrida, with a focus on photosynthesis. The findings showed that the levels of flavonoids and phenolic acids increased when the plants were exposed to higher ratios of blue light from LED sources *(Ouzounis et al. 2015; Matysiak, 2021*). It is well established that these compounds play a crucial role in plant stress defence and pathogen resistance, as well as contributing to pigmentation (*Jensen et al., 2011*). Furthermore, the study also revealed that a 40% blue LED light ratio was less supportive of terpene accumulation in the roots of *Gynura bicolour* compared to a 20% ratio *(Ren, Guo, Cheng, et al., 2014)*.

1.2. Brief findings on light effect against plants

Blue light helps plants better handle stress due to the function of secondary metabolites. Additionally, blue LED lighting is more practical for low-temperature storage due to its smaller light fixture size and lower reduction in irradiance compared to fluorescent lamps. If cost-effective, using blue LED lights under dim conditions in low-temperature environments would be ideal for various agricultural operations, including tissue culture production.

1.3. Carbon dioxide (CO_2) concentration

Seedling growth in vitro is reliant on both the CO_2 levels in the growing microclimate (endogenous source) and the sugars in the growth medium (exogenous source), known as *photomyxotrophic* growth. Photoautotrophic growth occurs when CO_2 serves as the sole carbon source through photosynthesis in an air microclimate culture *(Afreen, Zobayed, and Kozai, 2001*). As plants grow, their CO_2 demand increases, leading to enhanced net photosynthetic rate, growth, rooting, and development through CO_2 enrichment. Stomata density also increases significantly in photoautotrophic conditions with CO_2 enrichment *(Kirdmanee, Kitaya, and Kozai, 1995*).

A recent study showed that growing St. John's *wort* in 1500 mmol/mol CO_2-enriched conditions boosted secondary metabolite production and net photosynthetic rate (*Zobayed and Saxena, 2004*). Kim et al. similarly increased the production of secondary metabolites (berberine) in Thalictrum rugosum non-photosynthetic cell culture grown in a CO_2-enriched air transport bioreactor (*Kim, Pedersen, and Chin, 1991*). Plant secondary metabolites are valuable natural compounds and play a critical role in stress defence and pathogen resistance (*Yang et al., 2018*).

The development and survival of in-vitro generated plants require a substantial root system. CO_2 increase (450 to 1200) enhances phenol production including anthocyanin, flavonoids, and phenolics. However, further increase in CO_2 (1200 to 2000) seems to negate this promotion *(Ren, Guo, Xin, et al., 2014*). Modifying storage atmosphere (low O_2 and CO_2) can effectively preserve vegetable soybeans' green colour and mass (*Makino et al., 2020*). The CO_2 storage fertiliser (CO_2SMs), derived from captured CO_2, applied as an energy source has been shown to significantly increase stem diameter, height, and root growth of vegetable crops (*Zhao et al., 2018*).

Increased CO_2 (827 mmol mol^{-1}) can result in 34% higher vegetable yields and reduce drought stress (*Dong et al., 2020*). However, elevated CO_2 enrichment has no effect on the constant ratio of night respiration to day photosynthesis (*Nomura et al., 2021*). Moreover, increased CO_2 can increase DDT absorption in the shoots of B. Lee and B. Bailey, posing a risk to human health upon consumption (*Wu et al., 2019*).

1.4. Brief findings on CO_2 effect against plants

Elevated CO_2 levels improve photosynthetic rate, resulting in increased biomass and nutrient content and improved tolerance to drought stress in plants. However, prolonged exposure to high levels of CO_2 may negatively impact human health and reduce plant secondary metabolite production. Therefore, using the climate change effect (*Lestari, 2019*) could be a good step for cleaner vegetable production.

1.5. Relative humidity (RH)

The relative humidity (RH) during the light period has been found to have a greater effect on the growth of rice seedlings than during the dark period (*Hirai et al., 2000*). When high RH is combined with an increase in CO_2, it can also promote photosynthesis and growth of tomato plants. However, it is important to exercise caution in controlling air moisture levels (*Sultan et al., 2014*) and monitoring transpiration rates, as crops grown in high relative humidity can be prone to instability (*Suzuki et al., 2015*). For tropical crops, such as watermelon, which are subject to cold stresses of 10°C (during the day) and 5°C (at night), increasing RH may be beneficial in reducing cold tolerance (*Lu et al., 2021*). The increase in RH reduces the potential for water loss in leaves, reduces electrolyte leakage, increases photosynthetic stability, and reduces chilling damage.

A study by *Mortensen (1986)* found that the dry weight of several flower plants including *Saintpaulia ionantha* (17-36 percent), *Lycopersicon esculentum* (20 percent), *Euphorbia pulcherrima* (31 percent), *Chrysanthemum* (31 percent), *Begonia* (47 percent), and *Nephrolepis exaltata* (17-36 percent) showed a significant increase in dry weight with increasing RH (from the lowest level to the highest level, by 68%). However, RH had no effect on the dry weight of *Rosa*, *Campanula isophylla*, *Cucumis sativa*, or *Lactuca sativa*, and negatively affected *Soleirolia soleirolii*.

In conventional micropropagation systems, high relative humidity levels, resulting from sealing culture vessels, can pose challenges for plant growth. When the relative humidity is too high or air circulation is inadequate, plants are unable to extract nutrients or allow water to evaporate from the soil. To mitigate this, lowering relative humidity through forced ventilation can significantly aid in the normal functioning of plant stomata (*Kozai, Afreen, and Zobayed, 2005*).

1.6. Brief findings on relative humidity effect against plants

The relative humidity within a plantation is crucial for maintaining optimal plant growth. It is imperative to note that both excessively low and excessively high levels of relative humidity can prove detrimental to the health of plants, regardless of the growing method being utilised, be it traditional or modern. It is therefore imperative to exercise caution when adjusting the relative humidity within a plantation, and to ensure that any changes made are based on the specific needs of the plants in question.

1.7. Temperature

Numerous studies have explored the impact of temperature on plant growth within a plantation setting *(Ito, 2014)*. The utilization of forced ventilation has been shown to aid in maintaining a suitable culture environment by reducing relative humidity. As temperatures rise, plants undergo morphological, anatomical, physiological, and biochemical changes that ultimately influence growth and agricultural yields *(Wahid et al., 2007)*. The role of temperature in root plasticity against pathogen and biocontrol agent inoculation has also been explored, with Seflo et al. finding that temperature plays a critical role in this process *(Sefloo et al., 2021)*. Results from the study by Seflo et al. indicated that at 24°C, there was no significant change in the morphological properties of *Fusarium oxysporum f.sp. lycopersici* roots, but at 28°C, inoculation with *Fusarium oxysporum f.sp. lycopersici* reduced root volume, surface, and length.

MacAlister et al., (2020), investigated the effects of temperature on the growth and stress tolerance properties of A. linearis, and found that, with the exception of phenolics content, increasing temperature and altering soil nutrients had a negative impact on plant biomass. Additionally, *Li et al., (2020),* examined the impact of temperature fluctuations, including day/night cycles and heat waves, on *Gossypium hirsutum L.*, and found that higher daytime temperatures reduced leaf carbon production and yield, while nighttime warming did not compensate for these negative effects.

Temperature has a direct impact on photosynthesis, a highly temperature-dependent biochemical process regulated by enzymes *(Afreen, 2005, p. 65)*. As depicted in Fig. 1, temperatures that are too low or

too high can inhibit photosynthesis by affecting enzyme activity. Furthermore, decreases in temperature can indirectly reduce the net photosynthetic rate by reducing the rate of CO_2 diffusion. Plant species that are more resistant to heat stress tend to have a higher content of secondary metabolites *(Wahid et al., 2007)*, increased carbohydrate availability (*Liu and Huang, 2000*), higher photosynthesis rates *(Scafaro, Haynes, and Atwell, 2010; Bita and Gerats, 2013*), and lower chlorophyll concentrations (*MacAlister et al., 2020*).

1.8. Brief findings on temperature effect against plants

In order to maximize the effect of temperature on plantation growth, it is crucial to maintain temperatures within the range of heat stress tolerance. This can be challenging in traditional growing methods, particularly in regions with extreme climates. In these instances, the utilization of a glasshouse equipped with a temperature control system can greatly aid the growth process.

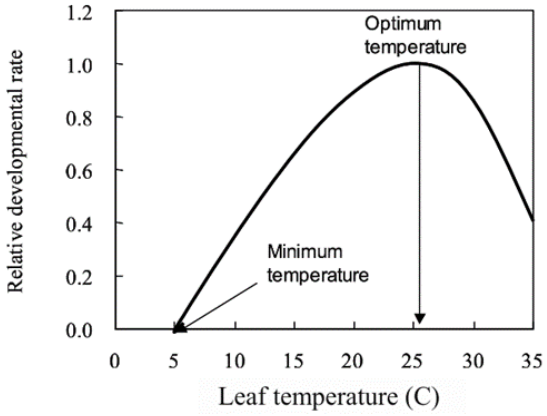


Fig. 1 – General plant developmental rate response to temperature (*Afreen, 2005*)



Fig. 2 – Piper betle var Nigra (*Harjunowibowo, 2021)*

1.9. Substrate or supporting medium

Water and fertiliser are essential factors that influence agricultural production (*Du et al., 2015*). Under photoautotrophic conditions, using fibrous planting media materials with high air porosity, such as florialite *(Nguyen & Kozai, 2001)*, vermiculite *(Feng & Zhang, 2021)*, humic acid *(Feng & Zhang, 2021),* and rockwool *(Acuña et al., 2013)*, promotes root development and enhances plant growth. The use of hydrogels as a planting medium can also improve soil biological properties and enhance the growth of water-stressed tomato plants *(Nassaj-Bokharaei et al., 2021)*. In a study by *Sefloo, et al. (2021)*, root growth was found to be high in perlite soil, with an increase of only 2% in root growth observed in the sucrose treatment.

Soilless culture involves growing seedlings without soil as the rooting medium. This technique is divided into substrate culture and water culture, with floating hydroponics being a widely used aquaculture technique for the cultivation of fresh vegetables and aromatic plants *(Tüzel et al., 2019)*. In soilless agriculture, all essential plant nutrients are supplied through a nutrient solution, with the exception of carbon which is taken up from the air as CO_2. The soil in greenhouses must be periodically changed to address soil structure, fertility, and pest issues. However, soilless agriculture is not yet a widely accepted alternative in organic farming. The recycling and biological treatment of municipal waste to produce fertilizer is preferable for supporting plant growth and reducing greenhouse gas emissions *(Berisha & Osmanaj, 2021)*.

1.10. Brief findings on Substrate or supporting medium effect against plants

The reduction of water consumption and the optimization of nutrient utilization are becoming increasingly recognised as critical components of sustainable agriculture globally. The implementation of these strategies in growing media can lead to improved soil moisture management, increased plant growth, and enhanced soil microbial activity and nutrient availability.

2. Ecology of *Piper Betle L.*

Betel (Piper betle) is a vine species belonging to the family Piperaceae that thrives in warm and humid environments with diffused sunlight *(Sengupta, 2019)*. It is often cultivated under an artificial structure known as Barouj, which provides high humidity and moisture levels *(Dasgupta and , 2017)*. Due to its widespread use, betel has earned the nickname "green gold" in Southeast Asia and India *(Vikas Bajpai, 2020)*.

For optimal cultivation, betel requires porous and fertile soil in upland sites, as it is sensitive to waterlogging. In India, there are three distinct cultivation systems, ranging from natural to fully controlled, with

varying degrees of anthropogenic interventions aimed at regulating light, temperature, and humidity. To ensure proper growth, saplings should be planted in parallel rows with a two-foot spacing, with reeds providing support as they mature and twined around upright sticks of split bamboo to avoid reciprocal shading *(Jane, Deshmukh and S., 2014)*.

The cultivation of Piper betle L. (betel), a vine of the Piperaceae family, is influenced by various factors, including temperature and light. Cold temperatures, particularly low frost, can result in crop damage, particularly in subtropical regions. The sensitivity to cold varies among landraces, with some, such as *Madras Paan Kapoori* and *Kapoori Vellaikodi*, being more sensitive than others, such as *Deshi Bangla*, *Kaker*, and *Bangla Mahoba (Tripathi, Khare, and Kumar, 2000; Gupta et al., 2012)*. This sensitivity is more pronounced in male landraces than in female landraces, as demonstrated by molecular studies using DNA markers *(Ranade et al., 2002; Samantaray and Phurailatpam, 2012)*.

The growth of Piper betle L is influenced by the presence of shade and the application of nitrogen. Phytochemical production in the plant is positively impacted by these factors *(Muttaleb et al., 2018)*. Betel is a commercially valuable plant that is propagated asexually and exhibits a range of cultivars *(Patra, Mukherjee and Acharya, 2011).* Cultivation of betel nut in partial shade, with a 30 percent to 50 percent canopy and 100 kg/ha nitrogen application, has been shown to result in increased chlorophyll content. Conversely, full sun exposure with 0 kg/ha nitrogen application is unfavourable for the growth of betel plants, resulting in leaf scorch, stunted growth, and the accumulation of secondary metabolites and antioxidants.

Secondary metabolites produced by the betel plant serve important ecological functions, such as providing resistance against diseases and herbivores. The biosynthesis of these metabolites is influenced by environmental factors, including temperature, light, soil fertility, groundwater, and soil salinity *(Yang et al., 2018).* These environmental factors can impact the concentration of specific compounds required for plant survival. However, changes in phytoconstituents cannot be distinguished through morphological features or traditional methods, highlighting the need for chemical-based discrimination methods for quality control purposes.

The Black betel (*Piper betle L. var. nigra*), an endemic species of Indonesia, has potential as a medicinal plant *(Junairiah et al., 2021)*. Unlike other closely related species, Black betel thrives in shady environments, climbing and clinging to nearby plants, and is able to grow on most trees. The plant is characterized by its dark green, stiff, and smooth heart-shaped leaves with a distinctive aroma, black stems, and a growing habit at altitudes of 500-700 m above sea level *(Suriani et al., 2020)*, as shown in Fig. 2. Black betel is a rapidly growing perennial herb that can reach heights of 5 to 15 meters, leaving a ring-shaped mark on the stem when its fallen leaves decompose.

The plant species, Black betel, is a source of secondary metabolites, including flavonoids, alkaloids, steroids, tannins, terpenoids, and saponins *(Junairiah, Ni'matuzahroh et al., 2019; Junairiah et al., 2021).* It has been investigated for its antimicrobial activity, with studies demonstrating its efficacy against tooth decay and gum inflammation *(Prasetya and Cipta Narsa, 2013).* Additionally, two amide derivatives, piperenamide A-B, have been shown to act against oral pathogens *(Prasetya, Salam, Rahmadani, Haikal, et al., 2021)*. Fatty acid derivatives, *2-octenoic acid* and *2-hexenoic acid*, have also been identified in this species and have potential health benefits *(Prasetya, Salam, Rahmadani, Kuncoro et al., 2021)*. The health-related benefits of betel leaves are largely attributed to its bioactive phenolic compounds, the content and composition of which vary according to genotype, agronomic practices, and climatic conditions *(Gagnon and Berrouard, 1994)*. Extracts from this perishable product have potential applications in the food, beverage, organic synthesis, and medicinal industries to address environmental problems *(Madhumita, Guha, and Nag, 2020).* Despite its potential, research on the cultivation of black betel vine is limited, and further studies are required to fully understand the method of cultivation for this species.

2.1. Traditional Cultivation

In a closed-type cultivation system, the common betel vine is grown in square or rectangular man-made structures constructed from locally available and economical materials such as bamboo, bamboo sticks, and jute sticks. These structures are designed to provide ideal growing conditions for the betel vine in terms of light, humidity, temperature, and soil moisture.

The betel vine is well-suited for cultivation in well-drained fertile soil in both wet and dry climates. A well-drained sandy loam soil or loam soil with a pH of 6.8-7.5, as well as a porous substrate, is ideal for betel culture *(Sengupta, 2019)*. The soil must be properly prepared and arranged in furrows 75 cm wide, 10-15 m long, and 75 cm deep. Soil that has been tilled with solarisation and dry soils are most suitable for planting.

However, freshly tilled or recently collected soil should not be used directly, and instead, should be opened and stacked for at least 6-10 months to sterilise the soil and eliminate soil-borne pathogens. Single node vine cuttings are planted with proper dressing between February and June, depending on the location and prior to the onset of the monsoon season and mild winter *(Das et al., 2016)*.

The cultivation of betel vine is negatively impacted by alkaline soil and waterlogging, thus saline or alkaline soil is unsuitable for its growth. Chemical fertilisers, particularly those containing nitrogen, have been shown to exacerbate leaf disease and reduce the shelf life and durability of leaves. Leptolyngbya HS-16 demonstrated better growth in NPK medium at a concentration of 80 ppm *(Prihantini et al., 2020)*. The combination of *Synechococcus sp*. HS-9 and NPK media with a tubular photobioreactor (tPBr) system has the potential to produce biomass feedstock for biofuels *(Ardiansyah et al., 2019)*, highlighting the cost-effectiveness of using NPK media as a growth medium. However, some studies have indicated that while nitrogen from organic sources may reduce disease incidence, it does not improve storage quality *(Sengupta, 2019).*

The combination of organic fertilisers derived from algae *(Kaur et al., 2013)* and nitrogenous fertilisers has been found to be effective in increasing betel leaf yields. Vermicompost and cow dung have also been shown to be suitable for betel cultivation. Scientific studies have indicated that phosphorous (100 kg P_2O_5/ha) and potassium (100-125 kg K_2O/ha) have a positive effect on crop yields, maintenance quality, and the spread of disease outbreaks. Additionally, the administration of zinc (0.25-0.5%), manganese (0.5%), and molybdenum (0.1%) has been shown to increase leaf yields through studies on micronutrients.

Betel is best cultivated under the ecologically shady conditions found in tropical forests, with a relative humidity ranging from 40% to 80%, rainfall between 2250 and 4750 millimetres, and a mild temperature range between 15°C and 40°C *(Vikas Bajpai, 2020)*. Irrigation throughout the year is necessary for the optimal growth of the plant *(Sengupta, 2019)*. The cultivation of betel vine in India demonstrates the plant's ability to thrive in both mild and highly variable climatic conditions. However, the quality of betel leaves is generally better in wet and medium environments compared to dry areas. Extremely hot and dry winds can have a negative impact on the growth of the vines, as hot air causes wilting and burning of the soft leaves, while cold waves lead to yellowing.

Black betel is propagated through cuttings. The cuttings should be taken from healthy, high-yielding mother vines, with large, dark green leaves. The cuttings should be 15-50 cm in length, with 2-8 internodes, and taken from the top of the betel tree *(Sengupta, 2019)*. They can be planted directly in the field or as rooted cuttings in a polybag mixture of mother soil, cow dung, coconut dust, and sand (Fig. 3).



Fig. 3 – Cultivating from stem cutting



Fig. 4– Betel vine planting field

Betel is typically planted in indented beds (Fig. 4). The soil must be level and free from any contamination by bacterial leaf blight for at least two years prior to planting. Beds measuring 1.2 meters by 7.5 meters are created to facilitate maintenance. Spacing between beds should be cleared to prevent the spread of illnesses and facilitate management. The beds should be sterilised by burning straw. A seepage canal, 30 cm in width and 60 cm in depth, should be constructed around the cluster of beds. A stake should be provided for the betel vine to climb, with two cuttings planted close to each stake at a 45 cm^2 spacing.

Before planting, the cuttings should be soaked in a fungicide mixture for two minutes. They are then planted in 30 cm^2 holes in the beds. The beds should be covered with shading material for 4-6 weeks to support the growth of seedlings from the cuttings, which take 20-45 days to establish. Intercropping is not recommended, as it may serve as a host plant for diseases *(Sengupta, 2019)*. Hence, betel should be grown as a single plant, in addition to the indented beds.

After planting the cuttings, the initial watering schedule should be twice daily for the first 3-4 days, once daily for the next 3 days, and once every 2 days for the following 6 days. Subsequently, irrigation water should be applied judiciously and slowly, for which the drip irrigation method is recommended as the ideal option *(Sengupta, 2019)* (Fig. 5). The flood method of irrigation should be avoided to prevent the spread of disease pathogens.



Fig. 5 – Drip Irrigation



Fig. 6 – Lowering the vines *(Dr Ysrhu Hortiportal, 2021)*

When the betel vines reach a height of approximately 2 meters, they come close to touching the roof of the barouj. The lowering of the vines should be performed regularly, approximately 5-6 times per year, with due care taken during the monsoon months as most pathogens are soil-borne. Once lowered, the vine can be covered with soil or kept coiled just above the ground (Fig. 6). When lowering the vine, it is necessary to spray a copper fungicide solution on the bottom and roll up parts of the vine, then tie it to the support sticks *(Sengupta, 2019).*

2.2. Finding for traditional cultivation on black betel

There are two methods of cultivating betel vine: the closed-type system and the open-type system. Each method has its own advantages and disadvantages. While the open-type system may be cost-effective, it is susceptible to disease and lacks the ability to make necessary adjustments. The closed-type system requires a higher initial investment in facilities and control systems, but helps to avoid harmful diseases and offers the potential to produce high quality and quantity of leaves at low operating costs.

3. Recent Cultivation Technology

Closed greenhouses provide an environment that facilitates the cultivation of insect and pesticide-free transplant seedlings, with a 40% reduction in production time as compared to conventional greenhouses that employ optimal environmental controls, including CO_2 enrichment *(Kozai, 2020).*

3.1. Callus induction

The *Piper betle L. var Nigra* plant is a valuable source of secondary metabolites, which can be obtained through the extraction of various plant parts. However, this approach requires a large supply of fresh herbs and incurs significant costs associated with isolation, purification, and extraction. As an alternative, callus culture technology has been proposed as a means of maintaining the availability of secondary metabolites while also increasing production in a more time-efficient manner.

Junairiah et al. has investigated the combination of growth regulators on callus induction of black betel leaf explants *(Junairiah et al., 2017)*. Based on their research, the concentration of *Indole-3-Acetic Acid* (IAA) 1.0 mg/L and 1.5 mg/L of kinetin is the best recipe for callus induction from black betel leaf. The resulting fresh weight was 0.2972 grams with a dry weight of 0.1660 grams. Furthermore, the growth regulator 2.4-D given at kinetin (2.5 mg/L) was able to induce callus with an average induction time of 14 days *(Junairiah, Mahmuda et al., 2019)*. Meanwhile, a combination for callus induction of P. betle L. var. Nigra leaf explants in the form of addition of 2.0 mg/l BAP and 0.5 mg/L 2.4 D combined with coconut water (5%) resulted in callus induction time of 13 days *(Junairiah et al., 2021)*. Furthermore, the growth regulators IBA (2 mg/L) and BAP (2 mg/L) is combined and resulted in a callus induction time of nine days *(Junairiah, Rahmawati et al., 2020).* While callus of black betel had a compact texture in all the treatments (brownish yellow colour), in the eighth week the callus mostly turned black (

Fig. **7**).

In a study by *Junairiah et al. (2018),* the objective was to identify the bioactive compounds present in black betel fruit through the use of ethyl acetate, n-hexane, and methanol extracts. The n-hexane extract was found to contain three main components: *3-butenoic acid*, *1-pentene*, and *furan*.

Further research conducted by *Junairiah et al. (2020)* explored the impact of varying concentrations of cobalt (II) chloride ($CoCl_2$) on black betel leaf callus biomass and terpenoid profiles. It was found that the addition of 1.0 mg/L $CoCl_2$ to the callus resulted in a 5.95% production of terpenoids, which was higher compared to the control. Additionally, the fresh and dry weights of the callus increased over three weeks of growth. However, it should be noted that this technique requires specialised skills and must be conducted under strict sterile conditions. It also takes up to 8 weeks for induction, and even longer to cultivate plantlets.

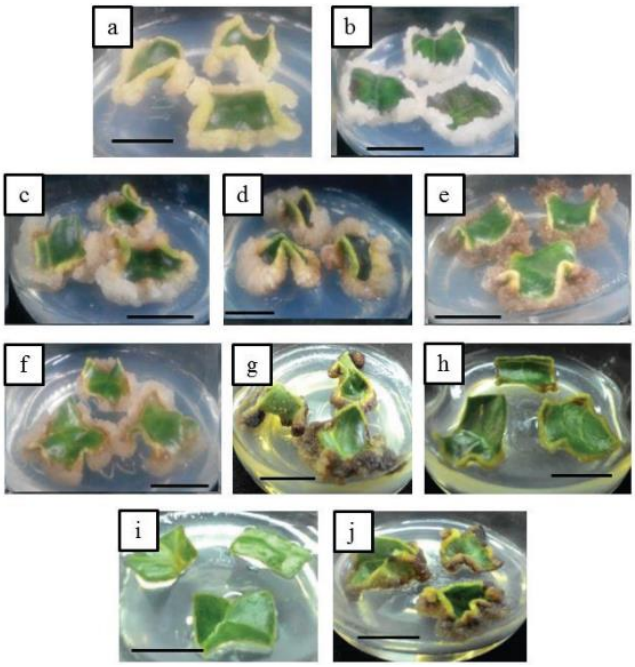


Fig. 7 – Callus morphology of Piper betle L. Var Nigra in some treatments *(Junairiah et al., 2017)*

3.2. Finding for callus method of black betel

The cultivation of betel vine and black betel vine shares similar physical requirements for optimal growth, including adequate light, temperature, relative humidity, irrigation, and substrate nutrition. Both traditional and modern cultivation methods can be utilised, although the traditional method of soil-based cultivation may require a longer period of time to produce high-quality crops in significant quantities. Callus induction technology may provide a solution to these challenges.

However, it should be noted that callus induction technology is delicate and sensitive to changes in growth parameters, and requires careful attention to ensure successful outcomes. Nevertheless, it is well suited for large-scale production or for cultivating species that are limited in availability, such as black betel vine. Typically, callus induction takes between 8 to 14 weeks before the plantlets are ready for transplantation into soil.

CONCLUSIONS

Betel vine holds significant potential both for its health-promoting secondary metabolites and as a source of income, making the cultivation of high-quality crops in economic quantities a crucial goal. The recent discovery of a new genus of *Piper betle L.*, known as "*Piper betle var Nigra*", adds further interest to this species. However, cultivating betel vine presents several challenges.

Traditional cultivation techniques, including open- and closed-type systems, have been used, while the modern method of callus induction is becoming increasingly popular, particularly for mass production. Each of these technologies has its own advantages and limitations, with the modern technique requiring specialized skills, being more time-consuming, and more expensive, while traditional techniques are simpler but face the

risk of disease.

By utilising a closed system, such as a greenhouse, it may be possible to produce higher-quality crops than with open systems. Through the implementation of smart farming practices and maintaining optimal conditions for betel vine growth, any losses can be reduced, particularly through the use of appropriate lighting. As betel vine requires low levels of sunlight, tropical temperatures, and protection from insects, a screen house with artificial shading and lighting may be an appropriate choice for subtropical regions.

ACKNOWLEDGEMENTS

The authors thank Ministry of Research and Technology/National Agency for the funding support through Research and Innovation (RISTEK-BRIN) Grant no 11/E1/KP.PTNBH/2021, Productive Innovative Research (RISPRO) PRJ-52/ LPDP/2019 and ESMART for the facilities given.

REFERENCES

[1] Acuña, R. A.Bonachela, S.Magán, J. J.Marfà, O.Hernández, J. H.& Cáceres, R. (2013). Reuse of rockwool slabs and perlite grow-bags in a low-cost greenhouse: Substrates' physical properties and crop production. *Scientia Horticulturae*, *160*, 139–147. https://doi.org/https://doi.org/10.1016/j.scienta.2013.05.031

[2] Afreen, F. (2005). Physiological and anatomical characteristics of in vitro photoautotrophic plants. In *Photoautotrophic (sugar-free medium) micropropagation as a new propagation and transplant production system* (pp. 61–90). Springer Netherlands.

[3] Afreen, F.Zobayed, S. M. A.& Kozai, T. (2001). Mass-Propagation of Coffee from Photoautotrophic Somatic Embryos. In N. Morohoshi & A. Komamine (Eds.), *Molecular Breeding of Woody Plants* (1st ed., Vol. 18, pp. 355–364). Elsevier Masson SAS. https://doi.org/10.1016/S0921-0423(01)80092-7

[4] Arambewela, L. S. R.Arawwawala, L. D. A. M.Kumaratunga, K. G.Dissanayake, D. S.Ratnasooriya, W. D.& Kumarasingha, S. P. (2011). Investigations on Piper betle grown in Sri Lanka. *Pharmacognosy Reviews*, *5*(10), 159–163. https://doi.org/10.4103/0973-7847.91111

[5] Arawwawala, L. D. A. M.Arambewela, L. S. R.& Ratnasooriya, W. D. (2014). Gastroprotective effect of Piper betle Linn . leaves grown in Sri Lanka. *Journal of Ayurveda & Integrative Medicine*, *5*(1), 38–42. https://doi.org/10.4103/0975-9476.128855

[6] Ardiansyah, S. R.Orlando, A. M.Rahman, A.Prihantini, N. B.& Nasruddin. (2019). Tubular photobioreactor: A preliminary experiment using synechococcus sp. (cyanobacteria) cultivated in NPK media for biomass production as biofuel feedstock. *Evergreen*, *6*(2), 157–161. https://doi.org/10.5109/2321011

[7] Ayadi, M.Ahou, S.Awad, S.Abderrabba, M.& Andres, Y. (2020). Production of biogas from olive pomace. *Evergreen*, *7*(2), 228–233. https://doi.org/10.5109/4055224

[8] Berisha, A.& Osmanaj, L. (2021). Kosovo scenario for mitigation of greenhouse gas emissions from municipal waste management. *Evergreen*, *8*(3), 509–516. https://doi.org/10.5109/4491636

[9] Bhatia, S. C. (2014). *Advanced renewable energy systems* (1st ed.). Woodhead Publishing India Pvt. Ltd.

[10] Bintang, M.Safira, U. M.Kusumawati, D. E.Pasaribu, F. H.Template, A. D. N. A.& Isolate, B. S. (2014). *Analysis of 16S rRNA Sequence of Endophytic Bacteria Isolate BS1 from Piper betle [L.] Stem*. 69–70.

[11] Bita, C. E.& Gerats, T. (2013). Plant tolerance to high temperature in a changing environment: Scientific fundamentals and production of heat stress-tolerant crops. *Frontiers in Plant Science*, *4*(JUL), 1–18. https://doi.org/10.3389/fpls.2013.00273

[12] Both, A. J. (2013). *Measuring LED Lighting Systems and Developing l Guidelines d l for f Evaluation , Comparison and Use*. 1–8.

[13] Briskin, D. P.& Gawienowski, M. C. (2001). Differential effects of light and nitrogen on production of hypericins and leaf glands in Hypericum perforatum. *Plant Physiology and Biochemistry*, *39*(12), 1075–1081.

[14] Bula, R. J.Morrow, R. C.Tibbitts, T. W.Barta, D. J.Ignatius, R. W.& Martin, T. S. (1991). Light-emitting Diodes as a Radiation Source for Plants. *HortScience*, *26*(2), 203–205. https://journals.ashs.org/hortsci/downloadpdf/journals/hortsci/26/2/article-p203.pdf

[15] Choi, H. G.Moon, B. Y.& Kang, N. J. (2015). Effects of LED light on the production of strawberry during cultivation in a plastic greenhouse and in a growth chamber. *Scientia Horticulturae*, *189*, 22–31. https://doi.org/10.1016/j.scienta.2015.03.022

[16] Cossu, M.Murgia, L.Ledda, L.Deligios, P. a.Sirigu, A.Chessa, F.& Pazzona, A. (2014). Solar radiation distribution inside a greenhouse with south-oriented photovoltaic roofs and effects on crop productivity.

Applied Energy, *133*, 89–100. https://doi.org/10.1016/j.apenergy.2014.07.070

[17] Das, S.Parida, R.Sriram Sandeep, I.Nayak, S.& Mohanty, S. (2016). Biotechnological intervention in betelvine (Piper betle L.): A review on recent advances and future prospects. *Asian Pacific Journal of Tropical Medicine*, *9*(10), 938–946. https://doi.org/10.1016/j.apjtm.2016.07.029

[18] Dasgupta, B.& Sarkar, S. (2017). Changes in crop canopy architecture on the incidence of major foliar diseases of betelvine (Piper betle L.). *Journal of Applied Horticulture*, *19*(2), 135–138. https://doi.org/10.37855/jah.2017.v19i02.24

[19] Daud, D.Yang, S. C.Balaja, C. C.Ja'afar, F.Yasin, H. M.Kusrini, E.Prihandini, W. W.& Usman, A. (2020). Radical scavenging activity assay and red fluorescence microscopy studies: Antioxidant properties of selected young and mature leaves for application in pharmaceutical industry. *Evergreen*, *7*(2), 216–220. https://doi.org/10.5109/4055222

[20] Dong, J.Gruda, N.Li, X.Tang, Y.Zhang, P.& Duan, Z. (2020). Sustainable vegetable production under changing climate: The impact of elevated CO2 on yield of vegetables and the interactions with environments-A review. *Journal of Cleaner Production*, *253*, 119920. https://doi.org/10.1016/j.jclepro.2019.119920

[21] Dr YSRHU Hortiportal. (2021). *betelvine.pdf*. Dr YSRHU Hortiportal. www.drysrhu.edu.in/crops/betelvine.html

[22] Du, T.Kang, S.Zhang, J.& Davies, W. J. (2015). Deficit irrigation and sustainable water-resource strategies in agriculture for China's food security. *Journal of Experimental Botany*, *66*(8), 2253–2269. https://doi.org/10.1093/jxb/erv034

[23] Dwivedi, V.& Tripathi, S. (2014). Review study on potential activity of Piper betle. *Journal of Pharmacognosy and Phytochemistry JPP*, *93*(34), 9398.

[24] Dyer, L. A.& Palmer, A. D. N. (2004). *Piper : A Model Genus for Studies of Phytochemistry , Ecology , and Evolution Piper* (Kluwer Academic (ed.)). Plenum Publishers. https://doi.org/10.1007/978-0-387-30599-8

[25] Feng, X.& Zhang, L. (2021). Vermiculite and humic acid improve the quality of green waste compost as a growth medium for Centaurea cyanus L. *Environmental Technology & Innovation*, *24*, 101945. https://doi.org/https://doi.org/10.1016/j.eti.2021.101945

[26] Gagnon, B.& Berrouard, S. (1994). Effects of several organic fertilizers on growth of greenhouse tomato transPlants. *Canadian Journal of Plant Science*, *74*(1), 167–168. https://doi.org/10.4141/cjps94-035

[27] Ghazali, N. A.Elmy, A.Yuen, L. C.Sani, N. Z.Das, S.Suhaimi, F.Yusof, R.Yusoff, N. H.& Thent, Z. C. (2016). Piper betel leaves induces wound healing activity via proliferation of fibroblasts and reducing 11β hydroxysteriod dehydrogenase-1 expression in diabetic rat. *Journal of Ayurveda and Integrative Medicine*, *7*(4), 198–208. https://doi.org/10.1016/j.jaim.2016.08.008

[28] Gupta, S.Gupta, S. M.Sane, A. P.& Kumar, N. (2012). Chlorophyllase in Piper betle L . has a role in chlorophyll homeostasis and senescence dependent chlorophyll breakdown. *Molecular Biology Reports*, *39*(6), 7133–7142. https://doi.org/10.1007/s11033-012-1545-8

[29] Hajare, R.Darvhekar, V. M.Shewale, A.& Patil, V. (2011). *Evaluation of antihistaminic activity of Piper betel leaf in guinea pig*. *5*(February), 113–117. https://doi.org/10.5897/AJPP09.376

[30] Harjunowibowo, D. (2021). *Pembuatan Protected Crop untuk Pemeliharaan Sirih Hitam*. Kompasiana. https://www.kompasiana.com/dewantoharjunowibowo9651/611e06ea06310e2d85167502/pembuatan-protected-crop-untuk-pemeliharaan-sirih-hitam?page=all#section1

[31] Hirai, G. I.Okmura, T.Takeuchi, S.Tanaka, O.& Chujo, H. (2000). Studies on the effect of the relative humidity of the atmosphere on the growth and physiology of rice plants: Effects of relative humidity during the light and dark periods on the growth. *Plant Production Science*, *3*(2), 129–133. https://doi.org/10.1626/pps.3.129

[32] Hoque, M. J. (2022). Causes, Mechanisms and Outcomes of Environmental Degradation in Bangladesh: a Study in Sylhet. *Evergreen*, *9*(2), 310–325. https://doi.org/10.5109/4793670

[33] Ito, K. (2014). Micro- and macro-scale measurement of fungal growth under various temperature and humidity conditions. *Evergreen*, *1*(1), 32–39. https://doi.org/10.5109/1440974

[34] Izzah, N.Zamri, I.Fields, M.Izzah, N.Zamri, I.Lailatul, S.Zulmajdi, N.& Kusrini, E. (2020). *Rhodamine B Photocatalytic Degradation using CuO Particles under UV Light Irradiation for Applications in Industrial and Medical Fields Rhodamine B Photocatalytic Degradation using CuO Particles under UV Light Irradiation for Applications in Industrial an*. *7*(2), 280–284.

[35] Jane, N. S.Deshmukh, A. P.& S, J. M. (2014). Review Of Study Of Different Diseases On Betelvine Plant and Control Measure. *International Journal of Application or Innovation in Engineering &*

Management (IJAIEM), *3*(3), 560–563. https://www.ijaiem.org/volume3issue3/IJAIEM-2014-03-31-157.pdf

[36] Jensen, B.Shetty, N. P.Jensen, J. D.Shetty, R.Frette, X.Jørgen, H.Jørgensen, L.Newman, M.& Christensen, L. P. (2011). Silicon-Induced Changes in Antifungal Phenolic Acids , Flavonoids , and Key Phenylpropanoid Pathway Genes during the Interaction between Miniature Roses and the Biotrophic Pathogen Podosphaera pannosa 1 [W]. *Plant Physiology*, *157*(4), 2194–2205. https://doi.org/10.1104/pp.111.185215

[37] JunairiahEly, T. W.Manuhara, Y. S. W.Ni'Matuzahroh& Sulistyorini, L. (2021). Optimation of callus induction from piper betle l . Var . nigra explants with various concentrations of coconut water and addition of 2 , 4-d and bap. *Annals of Biology*, *36*(2), 324–328. http://agribiop.com/optimation-of-callus-induction-from-piper-betle-l-var-nigra-explants-with-various-concentrations-of-coconut-water-and-addition-of-24-d-and-bap/

[38] Junairiah, J.Mahmuda, A.Manuhara, Y. S. W.Ni'Matuzahroh& Sulistyorini, L. (2019). Callus Induction and Bioactive Compounds from Piper betle L. var nigra. *IOP Conference Series: Earth and Environmental Science*, *217*(012026), 1–8. https://doi.org/10.1088/1755-1315/217/1/012026

[39] JunairiahNi'matuzahroh& Sulistyorini, L. (2018). GCMS analysis of bioactive compounds in n-hexane, ethyl acetate, and methanol extract of P iper betle L.var. nigra. *Bioscience Research*, *15*(3), 472–1479. https://www.isisn.org/BR15(3)2018/1472-1479-15(3)2018BR18-204.pdf

[40] JunairiahNi'matuzahrohZuraidassanaaz, N. I.& Sulistyorini, L. (2019). Isolation and identification of secondary metabolites of black betel (Piper betle L. var Nigra). *Jurnal Kimia Riset*, *3*(2), 131. https://doi.org/10.20473/jkr.v3i2.12064

[41] JunairiahRahmawati, R. K.Manuhara, Y. S. W.Ni'matuzahrohPramudya, M.& Sulistyorini, L. (2020). Induction and identification of bioactive compounds from callus extract of Piper betle L . var . Nigra. *Malaysian Journal of Analytical Sciences*, *24*(6), 1024–1034.

[42] JunairiahZuraidassanaaz, N. I.Izdihar, F. N.& Manuhara, Y. S. W. (2017). Callus induction of leaf explant Piper betle L . Var Nigra with combination of plant growth regulators indole-3-acetic acid (IAA), benzyl amino purin (BAP) and kinetin Callus Induction of Leaf Explant Piper betle L . Var Nigra with Combination of Plan. In H. Y. Abdullah (Ed.), *6th International Conference And Workshops On Basic And Applied Sciences* (Vol. 1888, pp. 020028.1-11). AIP Publishing. https://doi.org/10.1063/1.5004305

[43] JunairiahZuraidassanaaza, N. I.Manuhara, Y. S. W.Ni'matuzahroha& Sulistyorini, L. (2020). Biomass and terpenoids profile of callus extract of Piper betle L . var . Nigra with abiotic elicitor cobalt (II) chloride. *Moroccan Journal of Chemistry*, *1*(1), 88–98. https://revues.imist.ma/index.php/morjchem/article/download/19129/10475

[44] Kangralkar, V. A.& Kulkarni, A. R. (2013). In vitro antitumor activity of alcoholic extract of piper betel leaf. *Research Journal of Pharmaceutical, Biological and Chemical Sciences*, *4*(4), 1558–1561.

[45] Kano, A.Kamita, M. K.Iwasaki, T.& Shindo, M. (2017). Bongkrekic acid induces selective cytotoxicity in tumor cells, revealed by CCK-8. *Evergreen*, *4*(2–3), 23–27. https://doi.org/10.5109/1929661

[46] Kaur, G.Singh, S.Kuppan, P.Goto, M.Sugiura, N.Johari, M.Mohd, M.& Ujang, Z. (2013). Physical Water Quality and Algal Density for Remediation of\nAlgal Blooms in Tropical Shallow Eutrophic Reservoir. *Journal of Novel Carbon Resource Science*, *7*(feb 2013), 33–41. http://ncrs.cm.kyushu-u.ac.jp/assets/files/JNCRS/JNCRS_Vol.7_33-41.pdf

[47] Kim, D.-I.Pedersen, H.& Chin, C.-K. (1991). Cell Suspension in an Improved Airlift Bioreactor : Stimulatory Effect of Carbon Dioxide and Ethylene on Alkaloid Production. *Biotechnology and Bioengineering*, *38*(4), 331–339. https://doi.org/10.1002/bit.260380403

[48] Kirdmanee, C.Kitaya, Y.& Kozai, T. (1995). Effects of CO2 Enrichment and Supporting Material In vitro on Photoautotrophic Growth of Eucalyptus Plantlets In vitro and Ex vitro. *In Vitro Cellular & Developmental Biology. Plant*, *31*(3), 144–149. http://www.jstor.org/stable/4293078

[49] Kozai, T. (2020). Transplant production in closed systems. In M. T. Toyoki Kozai, Genhua Niu (Ed.), *An Indoor Vertical Farming System for Efficient Quality Food Production* (2nd ed., pp. 299–332). Academic Press. https://doi.org/10.1016/B978-0-12-816691-8.00022-4

[50] Kozai, T.Afreen, F.& Zobayed, S. M. A. (2005). *Photoautotrophic (sugar-free medium) Micropropagation as a New Micropropagation and Transplant Production System* (T. KOZAI, F. AFREEN, & S. M. A. ZOBAYED (eds.)). Springer Netherlands. https://link.springer.com/content/pdf/10.1007%2F1-4020-3126-2.pdf

[51] Kuncoro, A.& Purwanto, W. W. (2020). Analysis of energy-water nexus palm oil biodiesel production in riau using life cycle assessment and water footprint methods. *Evergreen*, *7*(1), 104–110.

https://doi.org/10.5109/2740965
[52] Kurata, H.Matsumura, S.& Furusaki, S. (1997). Light irradiation causes physiological and metabolic changes for purine alkaloid production by a Coffea arabica cell suspension culture. *Plant Science*, *123*(1), 197–203. https://doi.org/https://doi.org/10.1016/S0168-9452(96)04588-8
[53] Lestari, N. A. (2019). Reduction of CO2 emission by integrated biomass Gasific ation-solid oxide fuel cell combined with heat recovery and in-situ CO2 utilization. *Evergreen*, *6*(3), 254–261. https://doi.org/10.5109/2349302
[54] Li, X.Shi, W.Broughton, K.Smith, R.Sharwood, R.Payton, P.Bange, M.& Tissue, D. T. (2020). Impacts of growth temperature, water deficit and heatwaves on carbon assimilation and growth of cotton plants (Gossypium hirsutum L.). *Environmental and Experimental Botany*, *179*(June), 104204. https://doi.org/10.1016/j.envexpbot.2020.104204
[55] Li, Y.Zhang, C.Pan, S.Chen, L.Liu, M.Yang, K.Zeng, X.& Tian, J. (2020). LWT - Food Science and Technology Analysis of chemical components and biological activities of essential oils from black and white pepper (Piper nigrum L .) in five provinces of southern China. *LWT - Food Science and Technology*, *117*(September 2019), 108644. https://doi.org/10.1016/j.lwt.2019.108644
[56] Lin, K. H.Huang, M. Y.Huang, W. D.Hsu, M. H.Yang, Z. W.& Yang, C. M. (2013). The effects of red, blue, and white light-emitting diodes on the growth, development, and edible quality of hydroponically grown lettuce (Lactuca sativa L. var. capitata). *Scientia Horticulturae*, *150*, 86–91. https://doi.org/10.1016/j.scienta.2012.10.002
[57] Liu, X.& Huang, B. (2000). Carbohydrate accumulation in relation to heat stress tolerance in two creeping bentgrass cultivars. *Journal of the American Society for Horticultural Science*, *125*(4), 442–447. https://doi.org/10.21273/jashs.125.4.442
[58] Lu, J.Shireen, F.Cheng, F.& Bie, Z. (2021). High relative humidity improve chilling tolerance by maintaining leaf water potential in watermelon seedlings. *Plant Physiology and Biochemistry*, *166*(May), 818–826. https://doi.org/10.1016/j.plaphy.2021.06.037
[59] MacAlister, D.Muasya, A. M.Crespo, O.Ogola, J. B. O.Maseko, S. T.Valentine, A. J.Ottosen, C. O.Rosenqvist, E.& Chimphango, S. B. M. (2020). Effect of temperature on plant growth and stress tolerant traits in rooibos in the Western Cape, South Africa. *Scientia Horticulturae*, *263*(December 2019), 109137. https://doi.org/10.1016/j.scienta.2019.109137
[60] Madhumita, M.Guha, P.& Nag, A. (2020). Bio-actives of betel leaf (Piper betle L.): A comprehensive review on extraction, isolation, characterization, and biological activity. *Phytotherapy Research*, *34*(10), 2609–2627. https://doi.org/10.1002/ptr.6715
[61] Makino, Y.Nishizaka, A.Yoshimura, M.Sotome, I.Kawai, K.& Akihiro, T. (2020). Influence of low O2 and high CO2 environment on changes in metabolite concentrations in harvested vegetable soybeans. *Food Chemistry*, *317*(June 2019), 126380. https://doi.org/10.1016/j.foodchem.2020.126380
[62] Matysiak, B. (2021). The effect of supplementary led lighting on the morphological and physiological traits of miniature rosa × hybrida 'aga' and the development of powdery mildew (Podosphaera pannosa) under greenhouse conditions. *Plants*, *10*(2), 1–14. https://doi.org/10.3390/plants10020417
[63] Messinger, J.& Lauerer, M. (2015). Solanum quitoense, a new greenhouse crop for Central Europe: Flowering and fruiting respond to photoperiod. *Scientia Horticulturae*, *183*, 23–30. https://doi.org/10.1016/j.scienta.2014.11.015
[64] Mortensen, L. M. (1986). Effect of relative humidity on growth and flowering of some greenhouse plants. *Scientia Horticulturae*, *29*(4), 301–307. https://doi.org/10.1016/0304-4238(86)90013-0
[65] Mosaleeyanon, K.Zobayed, S. M. A.Afreen, F.& Kozai, T. (2005a). Relationships between net photosynthetic rate and secondary metabolite contents in St . John ' s wort. *Plant Science*, *169*, 523–531. https://doi.org/10.1016/j.plantsci.2005.05.002
[66] Mosaleeyanon, K.Zobayed, S. M. A.Afreen, F.& Kozai, T. (2005b). Relationships between net photosynthetic rate and secondary metabolite contents in St. John's wort. *Plant Science*, *169*(3), 523–531. https://doi.org/10.1016/J.PLANTSCI.2005.05.002
[67] Murugesan, S.Ravichandran, D.Lakshmanan, D. K.Ravichandran, G.Arumugam, V.Raju, K.Geetha, K.& Thilagar, S. (2020). Evaluation of anti rheumatic activity of Piper betle L. (Betelvine) extract using in silico, in vitro and in vivo approaches. *Bioorganic Chemistry*, *103*(May), 104227. https://doi.org/10.1016/j.bioorg.2020.104227
[68] Muttaleb, Q. A.TL, A.SA, H.AA, R.S, T.OA, A.& DA, A. (2018). The Role of Shade and Nitrogen on Physiological Traits and Secondary Metabolites of Piper betle L. *Journal of Horticulture*, *05*(02), 1–8.

https://doi.org/10.4172/2376-0354.1000230
[69] Nassaj-Bokharaei, S.Motesharezedeh, B.Etesami, H.& Motamedi, E. (2021). Effect of hydrogel composite reinforced with natural char nanoparticles on improvement of soil biological properties and the growth of water deficit-stressed tomato plant. *Ecotoxicology and Environmental Safety*, *223*, 112576. https://doi.org/10.1016/J.ECOENV.2021.112576
[70] Nguyen, Q. T.& Kozai, T. (2001). Photoautotrophic Micropropagation of Tropical and Subtropical Woody Plants. In N. Morohoshi & A. B. T.-P. in B. Komamine (Eds.), *Molecular Breeding of Woody Plants* (Vol. 18, pp. 335–344). Elsevier. https://doi.org/https://doi.org/10.1016/S0921-0423(01)80090-3
[71] Nomura, K.Yasutake, D.Kaneko, T.Takada, A.Okayasu, T.Ozaki, Y.Mori, M.& Kitano, M. (2021). Long-term compound interest effect of CO2 enrichment on the carbon balance and growth of a leafy vegetable canopy. *Scientia Horticulturae*, *283*, 110060. https://doi.org/10.1016/j.scienta.2021.110060
[72] Ouzounis, T.Fretté, X.Rosenqvist, E.& Ottosen, C. O. (2015). Corrigendum to 'Spectral effects of supplementary lighting on the secondary metabolites in roses, chrysanthemums, and campanulas' [J. Plant Physiol. 171 (16) (2014) 1491-1499] 10.1016/j.jplph.2014.12.006. *Journal of Plant Physiology*, *175*, 192. https://doi.org/10.1016/j.jplph.2014.12.006
[73] Patra, A. P.Mukherjee, A. K.& Acharya, L. (2011). Comparative Study of RAPD and ISSR Markers to Assess the Genetic Diversity.pdf. *American Journal of Biochemistry and Molecular Biology*, *1*(2), 200–211. https://doi.org/10.3923/ajbmb.2011.200.211
[74] Patra, B.Das, M. T.& Dey, S. K. (2016). A review on Piper betle L. *Journal of Medicinal Plants Studies*, *4*(6), 185–192.
[75] Prasetya, F.& Cipta Narsa, A. (2013). Aktivitas gel mulut berbahan aktif ekstrak daun sirih hitam kalimantan sebagai antimikroba penyebab radang gusi (Gingivitis) dan gigi berlubang (Caries). *Journal Of Tropical Pharmacy And Chemistry*, *2*(3), 146–151. https://doi.org/10.25026/jtpc.v2i3.60
[76] Prasetya, F.Salam, S.Rahmadani, A.Haikal, K.Febrina, L.Anshory, H.Arifuddin, M.Siregar, V. O.Narsa, A. C.Herman, H.Ahmad, I.Indriyanti, N.Ibrahim, A.Rusli, R.Rijai, L.& Kuncoro, H. (2021). Novel Amides Derivative with Antimicrobial Activity of Piper betle var . nigra Leaves from Indonesia. *Molecules*, *26*(335), 1–8. https://doi.org/10.3390/molecules26020335
[77] Prasetya, F.Salam, S.Rahmadani, A.Kuncoro, H.Rusli, R.Ruchaemi, A.& Sukartiningsih. (2021). Chemical constituents from Piper betle L. Var Nigra (Piperaceae). *Journal of Tropical Pharmacy and Chemistry*, *5*(3), 229–232. https://doi.org/10.25026/jtpc.v5i3.322
[78] Prasetya, F.Salam, S.Rijai, H. R.Kuncoro, H.& Rusli, R. (2022). Pharmacognostic Profile of Simplicia and Ethanolic Leaves Extract from Indonesian Piper betle var . nigra. *Pharmacogn J.*, *14*(5), 610–618. https://doi.org/10.5530/pj.2022.14.143
[79] Prihantini, N. B.Rakhmayanti, N.Handayani, S.Sjamsuridzal, W.Wardhana, W.& Nasruddin. (2020). Biomass production of indonesian indigenous leptolyngbya strain on npk fertilizer medium and its potential as a source of biofuel. *Evergreen*, *7*(4), 593–601. https://doi.org/10.5109/4150512
[80] Rahman, A.Prihantini, N. B.& Nasruddin. (2020). Biomass production and synthesis of biodiesel from microalgae synechococcus hs-9 (Cyanobacteria) cultivated using bubble column photobioreactors. *Evergreen*, *7*(4), 564–570. https://doi.org/10.5109/4150507
[81] Raja, M. B.Parthiban, S.Anandhan, M.Venkadeswaran, E.Pandi, K.Suganthi, S.& Prakash, M. S. (2018). Rooting and sprouting performance of nodal cutting of cultivated and wild inter specific Piper rootstocks. *International Journal of Chemical Studies*, *6*(2), 20–24.
[82] Ranade, S.Verma, A.Gupta, M.& Kumar, N. (2002). RAPD profile analysis of betel vine cultivars. *Biologia Plantarum*, *45*(4), 523–527. https://bp.ueb.cas.cz/pdfs/bpl/2002/04/09.pdf
[83] Ren, J.Guo, S.-S.Xin, X.-L.& Chen, L. (2014). Changes in volatile constituents and phenols from Gynura bicolor DC grown in elevated CO2 and LED lighting. *Scientia Horticulturae*, *175*, 243–250. https://doi.org/10.1016/j.scienta.2014.06.023
[84] Ren, J.Guo, S.Cheng, Q.Shen, Y.& Feng, H. (2014). Synergistic Effects of CO2 and LED Lighting on Accumulation of Terpenes in Roots of Gynura bicolor. *Chinese Herbal Medicines*, *6*(3), 228–236. https://doi.org/10.1016/S1674-6384(14)60033-2
[85] Sahlan, M.Mandala, D. K.Pratami, D. K.Adawiyah, R.Wijarnako, A.Lischer, K.& Fauzi, A. (2020). Exploration of the antifungal potential of indonesian propolis from Tetragonula biroi bee on Candida sp. and Cryptococcus neoformans. *Evergreen*, *7*(1), 118–125. https://doi.org/10.5109/2740968
[86] Sahlan, M.MuryantoHermansyah, H.Wijarnako, A.Gozan, M.Lischer, K.Ahmudi, A.& Pujianto, P. (2020). Ethanol production by encapsulated rhizopus oryzae from oil palm empty fruit bunch. *Evergreen*, *7*(1),

92–96. https://doi.org/10.5109/2740963

[87] Salehi, B.Javier Hernández-Álvarez, A.Del Mar Contreras, M.Martorell, M.Ramírez-Alarcón, K.Melgar-Lalanne, G.Matthews, K. R.Sharifi-Rad, M.Setzer, W. N.Nadeem, M.Yousaf, Z.& Sharifi-Rad, J. (2018). Potential Phytopharmacy and Food Applications of Capsicum spp.: A Comprehensive Review. *Natural Product Communications*, *13*(11), 1543–1556. https://ndb.nal.usda.gov/ndb/;

[88] Salehi, B.Zakaria, Z. A.Gyawali, R.Ibrahim, S. A.Rajkovic, J.Shinwari, Z. K.Khan, T.Sharifi-Rad, J.Ozleyen, A.Turkdonmez, E.Valussi, M.Tumer, T. B.Fidalgo, L. M.Martorel, M.& Setzer, W. N. (2019). Piper Species : A Comprehensive Review on Their and Applications. *Molecules*, *24*(1364), 1–118. https://doi.org/10.3390/molecules24071364

[89] Samantaray, S.& Phurailatpam, A. (2012). *Identification of sex-specific DNA markers in betel vine (Piper betle L .)*. 645–653. https://doi.org/10.1007/s10722-011-9707-4

[90] Scafaro, A. P.Haynes, P. A.& Atwell, B. J. (2010). Physiological and molecular changes in Oryza meridionalis Ng., a heat-tolerant species of wild rice. *Journal of Experimental Botany*, *61*(1), 191–202. https://doi.org/10.1093/jxb/erp294

[91] Sefloo, N. G.Steinkellner, S.& Hage-Ahmed, K. (2021). The bioprotective effect of root endophytic Serendipita herbamans against Fusarium wilt in tomato and its impact on root traits are determined by temperature. *Rhizosphere*, 100453. https://doi.org/10.1016/J.RHISPH.2021.100453

[92] Sengupta, K. (2019). Agronomy of Betelvine Crop. In M. Hasanuzzaman (Ed.), *Agronomic Crops: Volume 1: Production Technologies* (1st ed., Vol. 1, pp. 533–543). Springer Singapore. https://doi.org/10.1007/978-981-32-9151-5_2

[93] Shah, S. K.Garg, G.Jhade, D.Patel, N.& Sciences, M. (2016). *Review Article Piper Betle: Phytochemical, Pharmacological and Nutritional Value in Health Management*. *38*(34), 181–189.

[94] Shukla, R.Sachan, S.Mishra, A.& Kumar, S. (2015). A scientific review on common chewing plant of Asians : Piper Betle Linn. *Journal Of Harmonized Research in Pharmacy*, *4*(1), 01–10.

[95] Singh, D.Basu, C.Meinhardt-Wollweber, M.& Roth, B. (2015). LEDs for energy efficient greenhouse lighting. *Renewable and Sustainable Energy Reviews*, *49*, 139–147. https://doi.org/10.1016/j.rser.2015.04.117

[96] Sultan, M.El-Sharkawl, I. I.Miyazaki, T.Saha, B. B.& Koyama, S. (2014). Experimental study on carbon based adsorbents for greenhouse dehumidification. *Evergreen*, *1*(2), 5–11. https://doi.org/10.5109/1495157

[97] Suriani, N. L.Suprapta, D. N.Nazir, N.Made, N.& Parwanayoni, S. (2020). Potential of Bioactive Substances of Piper caninum and Piper betle Var . Nigra Leaves as Biopesticide in Organic Bali Rice. *Preprints*, *August*, 1–19.

[98] Suzuki, M.Umeda, H.Matsuo, S.Kawasaki, Y.Ahn, D.Hamamoto, H.& Iwasaki, Y. (2015). Effects of relative humidity and nutrient supply on growth and nutrient uptake in greenhouse tomato production. *Scientia Horticulturae*, *187*, 44–49. https://doi.org/10.1016/j.scienta.2015.02.035

[99] Taukoorah, U.Lall, N.& Mahomoodally, F. (2016). South African Journal of Botany Piper betle L . (betel quid) shows bacteriostatic , additive , and synergistic antimicrobial action when combined with conventional antibiotics. *South African Journal of Botany*, *105*, 133–140. https://doi.org/10.1016/j.sajb.2016.01.006

[100] Teanpaisan, R.Kawsud, P.& Pahumunto, N. (2016). Screening for antibacterial and antibio film activity in Thai medicinal plant extracts against oral microorganisms. *Journal of Traditional Chinese Medical Sciences*, 6–11. https://doi.org/10.1016/j.jtcme.2016.06.007

[101] Tripathi, R. Khare, G.& Kumar, N. (2000). Effect of low temperature stress on betel vine (Piper betle L.) types , Bangia and Desavari. *Journal of Spices and Aromatic Crops*, *9*(2), 141–143. https://updatepublishing.com/journal/index.php/josac/article/download/4564/4064

[102] Tüzel, Y.Gül, A.Tüzel, I. H.& Öztekin, G. B. (2019). Different Soilless Culture Systems and Their Management. *Journal of Agricultural, Food and Environmental Sciences*, *73*(3), 7–12.

[103] Vikas Bajpai, N. K. and B. K. (2020). *Phytochemistry of Piper betle Landraces* (B. Kumar (ed.); 1st ed). Taylor & Francis Group, LLC.

[104] Wahid, A.Gelani, S.Ashraf, M.& Foolad, M. R. (2007). Heat tolerance in plants: An overview. *Environmental and Experimental Botany*, *61*(3), 199–223. https://doi.org/10.1016/j.envexpbot.2007.05.011

[105] Wang, Y. H.Natschke, S. L. M.Yang, J.Niu, H. M.Long, C. L.& Lee, K. H. (2014). Anticancer Principles from Medicinal Piper (胡椒 Hú Jiāo) Plants. *Journal of Traditional and Complementary Medicine*, *4*(1),

8–16. https://doi.org/10.4103/2225-4110.124811

[106] Wilson, S. B.Iwabuchi, K.& Rajapakse, N. C. (1998). Responses of broccoli seedlings to light quality during low-temperature storage in vitro.pdf. *HortScience*, *33*(7), 1253–1257. https://irrecenvhort.ifas.ufl.edu/microprop/HortScience 1998-microprop-I.pdf

[107] Wilson, S. B.Iwabuchi, K.Rajapakse, N. C.& Young, R. E. (1998). Responses of Broccoli Seedlings to Light Quality during Low-temperature Storage in Vitro_ II. *HortScience*, *33*(7), 1258–1261. https://journals.ashs.org/hortsci/downloadpdf/journals/hortsci/33/7/article-p1258.xml

[108] Wu, X. R.Li, Y. P.Tu, S. X.Ding, Y. Z.Wang, R. G.Rensing, C.& Feng, R. W. (2019). Elevated atmospheric CO2 might increase the health risk of long-term ingestion of leafy vegetables cultivated in residual DDT polluted soil. *Chemosphere*, *227*, 289–298. https://doi.org/10.1016/j.chemosphere.2019.04.024

[109] Yang, L.Wen, K.-S.Ruan, X.Zhao, Y.-X.Wei, F.& Wang, Q. (2018). Response of Plant Secondary Metabolites to Environmental Factors. *Molecules*, *23*(762), 1–26. https://doi.org/10.3390/molecules23040762

[110] Yogeswari, S.Bindu, K. H.Kamalraj, S.Ashokkumar, V.& Jayabaskaran, C. (2020). Antidiabetic, Antithrombin and Cytotoxic bioactive compounds in five cultivars of Piper betle L. *Environmental Technology and Innovation*, *20*, 101140. https://doi.org/10.1016/j.eti.2020.101140

[111] Zhao, L.Liu, C.Yue, X.Ma, L.Wu, Y.Yang, T.& Zhang, J. (2018). Application of CO2-storage materials as a novel plant growth regulator to promote the growth of four vegetables. *Journal of CO2 Utilization*, *26*(January), 537–543. https://doi.org/10.1016/j.jcou.2018.06.011

[112] Zhong, J.Seki, T.Kinoshita, S.& Yoshida, T. (1991). *Effect of Light Irradiation on Anthocyanin Production by Suspended Culture of Perilla frutescens*. 0–5.

[113] Zobayed, S.& Saxena, P. K. (2004). Production of St . John ' s wort plants under controlled environment for maximizing biomass and secondary metabolites. *In Vitro Cell. Dev. Biol.*, *40*(February), 108–114. https://doi.org/10.1079/IVP2003498

A WIRELESS REMOTE MONITORING SENSOR FOR AGRICULTURAL ENVIRONMENT BASED ON NB-IoT
/
基于 NB-IoT 的农业环境无线远程监测传感器

Zhenfeng XU*[1)], Jiajian YANG[1)], Huan ZHOU[1)], Yunfang HOU[2)]
[1)] School of advanced Manufacturing Engineering, Hefei University / China;
[2)] Fuyang Ziqing Agricultural Technology Co., Ltd / China
Tel: 86+019810957375; E-mail: xuzhf@hfuu.edu.cn
DOI: https://doi.org/10.35633/inmateh-69-26

Keywords: *NB-IoT, agricultural environment, wireless monitoring, remote monitoring*

ABSTRACT

This paper describes the design and implementation of a wireless sensor based on NB-IoT (Narrow Band Internet of Things) for monitoring agricultural environmental information. The sensor is capable of real-time monitoring of four environmental parameters, including ambient temperature, relative humidity, illuminance, and CO_2 concentration. In the hardware design, sensor elements are selected based on the measurement ranges and accuracies specified in agricultural environmental monitoring industry standards. The hardware circuit is designed using the BC35-G type NB-IoT module and STM32 MCU (Microcontroller Unit). In the software design, data from the environmental parameters are collected and processed by the STM32 MCU and sent to the OneNET cloud platform through the NB-IoT module. The OneNET cloud platform enables users to view the relevant environmental data collected by the sensors using mobile phones and other mobile terminals. To test the effectiveness of the developed sensors, they were tested in a glass greenhouse at Fuyang Ziqing Agricultural Technology Co., Ltd. in Anhui Province. The results demonstrate that the sensors can accurately collect the data of relevant environmental parameters and can provide stable wireless transmission of data remotely, making them suitable for practical engineering applications. In summary, this wireless remote monitoring sensor based on NB-IoT represents a significant advancement in the field of agricultural automation. The sensor's ability to accurately monitor and wirelessly transmit data in real-time provides farmers with valuable information to optimize crop growth and maximize yields.

摘要

本文描述了一种基于窄带物联网（NB-IoT）的无线传感器的设计和实现，用于监测农业环境信息。该传感器能够实时监测四个环境参数，包括环境温度、相对湿度、照度和 CO_2 浓度。在硬件设计中，传感器元件的选择是基于农业环境监测行业标准中规定的测量范围和精度。硬件电路采用 BC35-G 型 NB-IoT 模块和 STM32 MCU 进行设计。在软件设计中，环境参数的数据由 STM32 MCU 收集和处理，并通过 NB-IoT 模块发送到 OneNET 云平台。OneNET 云平台允许用户使用手机和其他移动终端查看传感器收集的相关环境数据。为了测试所开发传感器的有效性，在阜阳紫青农业科技股份有限公司的玻璃温室中进行了测试。结果表明，该传感器能够准确地采集相关环境参数的数据，并能够提供稳定的远程无线数据传输，适用于实际工程应用。总之，这种基于 NB-IoT 的无线远程监测传感器代表了农业自动化领域的重大进步。该传感器能够准确监测并实时无线传输数据，为农民提供了有价值的信息，以优化作物生长并最大限度地提高产量。

INTRODUCTION

Real-time monitoring of agricultural environmental information provides valuable data for farmers to understand the growing environment of crops and enables precise and intelligent agriculture management. The methods used for agricultural environmental monitoring depend on the planting area and geographical location. Wired or wireless LAN technology is typically used for data transmission in facility agriculture (*Lihong et al., 2011; Feng et al., 2019*), while satellite remote sensing and other technologies are used for field agriculture due to the vast area (*Sishodia et al., 2020*). Some researchers have explored the use of UAV remote sensing technology in field agricultural environment monitoring (*Radoglou-Grammatikis et al., 2020*).

In recent years, short-range wireless communication technology has been applied to the field of agricultural environmental monitoring.

Zhenfeng Xu, Ph.D. Eng.; Jiajian Yang, M.S.Stud. Eng.; Huan Zhou, B. S.; Yunfang Hou, Eng.

For instance, Du et al. proposed a low-power Bluetooth gateway system to monitor breeding environments in a large pig farm equipped with LAN *(Du et al., 2021*). Wang et al. developed a monitoring system for agricultural greenhouses based on ZigBee technology and particle filter optimization to reduce measurement errors (*Wang et al., 2021*). Liang et al. proposed a dynamic monitoring method for greenhouse environments using WiFi to remotely monitor parameters such as temperature, relative humidity, and illumination (*Liang et al., 2018*). To meet the needs of agricultural production, Wang et al. designed a wireless sensor network system for meteorological monitoring using LoRa communication technology (*Wang et al., 2020*). Yang et al. designed a greenhouse remote monitoring system based on NB-IoT and uploaded data to the cloud platform, facilitating the viewing of environmental monitoring data on mobile terminals (*Yang et al., 2021*). Some researchers summarized the characteristics of these short range wireless communication technologies, including Bluetooth, ZigBee, WiFi, LoRa, and NB-IoT (*Farooq et al., 2019; Mekki et al., 2019; Tang et al., 2021; Elijah et al., 2018*). Here, the characteristics of these wireless communication technologies were also summarized, focusing on their application in agricultural environmental monitoring, as shown in Table 1.

Table 1

The characteristics of existing wireless communication technologies

Type	Transmission range	Maximum data rate	Communication quality
Bluetooth	<100m	3Mbps	High
ZigBee	<1km	250kbps	Low
WiFi	100m	10Mbps	High
LoRa	5km	50kbps	Low
NB-IoT	15km	200kbps	High

Both Bluetooth and WiFi have high communication rates, so they are very suitable for transmitting information such as agricultural images. However, their transmission ranges are very short, which severely limits their application in the field of agricultural environmental monitoring. In contrast, ZigBee wireless communication technology has a longer transmission range, making it suitable for small-scale facility agriculture. However, ZigBee is a low-rate wireless communication technology that is not suitable for transmitting image information, but can meet the wireless transmission of agricultural environmental parameter monitoring data. LoRa has a longer communication distance, but its data transmission speed is also lower. NB-IoT has the longest communication distance, and its data transmission rate is similar to ZigBee, and significantly superior to LoRa. Currently, both LoRa and NB-IoT are low-power WAN communication technologies with broad development prospects (*Sinha et al., 2017; Popli et al., 2018*).

Compared to LoRa, NB-IoT has the advantages of high communication quality and long communication distance. The sufficiently long communication distance not only makes NB-IoT suitable for facility agriculture, but also for field agriculture. Excellent wireless communication quality is desired in the field of agricultural environmental monitoring and control. Compared to the transmission of environmental monitoring data, the transmission of control command information has high requirements for the quality of wireless communication to ensure reliable control of environmental control devices, and NB-IoT can well meet this requirement. The disadvantage of NB-IoT is that it requires a small amount of annual fees to be paid annually, but generally no more than EUR 2, which many businesses and individuals can fully afford.

In this paper, the focus was on the design and implementation of a wireless sensor system for monitoring agricultural environmental parameters using NB-IoT technology. The novelty of our research lies in the integration of four environmental parameters, namely air temperature, relative humidity, CO_2 concentration, and illuminance, into one compact and easy-to-use system. Additionally, our system features excellent wireless communication quality, making it well-suited for use in both facility and field agriculture. Compared to existing research on IoT-based environmental monitoring systems, our system offers a unique combination of features and performance, providing accurate and real-time data for environmental control and decision-making in agriculture.

MATERIALS AND METHODS

Architecture of remote monitoring system based on NB-IoT

The Internet of Things (IoT) has been widely utilized in various fields, but there is still no unified standard architecture. Different IoT system architectures exist in different application fields (*Burhan et al., 2018; Raj et al., 2021; Silva et al., 2018*).

Even for the same engineering problem, the architecture of IoT systems can still differ from different perspectives. Various IoT architectures have been proposed so far (*Samizadeh Nikoui et al., 2021*). In the field of agricultural environmental monitoring, the architecture of IoT systems can be divided into five layers, as illustrated in Figure 1. The perception layer is located at the bottom, where various sensors detect real-time environmental information, such as temperature, humidity, illuminance, CO_2 concentration, etc. The edge computing layer is composed of microcontrollers or microprocessors in various sensor nodes. In the edge computing layer, the microcontroller obtains environmental information from the various sensor nodes in the perception layer. Data compression is one of the main tasks of the edge computing layer. Data compression can reduce both the wireless transmission of useless data and the communication energy consumption, thus avoiding bandwidth congestion and reducing the amount of data involved in cloud computing.

The transport layer is primarily composed of 4G/5G base stations and the internet, and its function is to receive the data sent by the edge computing layer and reliably transmit them to the cloud server. In the cloud computing layer, in addition to the functions of storing massive agricultural environmental information data, complex tasks such as crop yield prediction, disease and pest prediction can also be accomplished by deep learning and other methods. The top layer is the application layer. Users can access the cloud through mobile phones, iPads, computers, and other terminals to view relevant environmental information remotely.

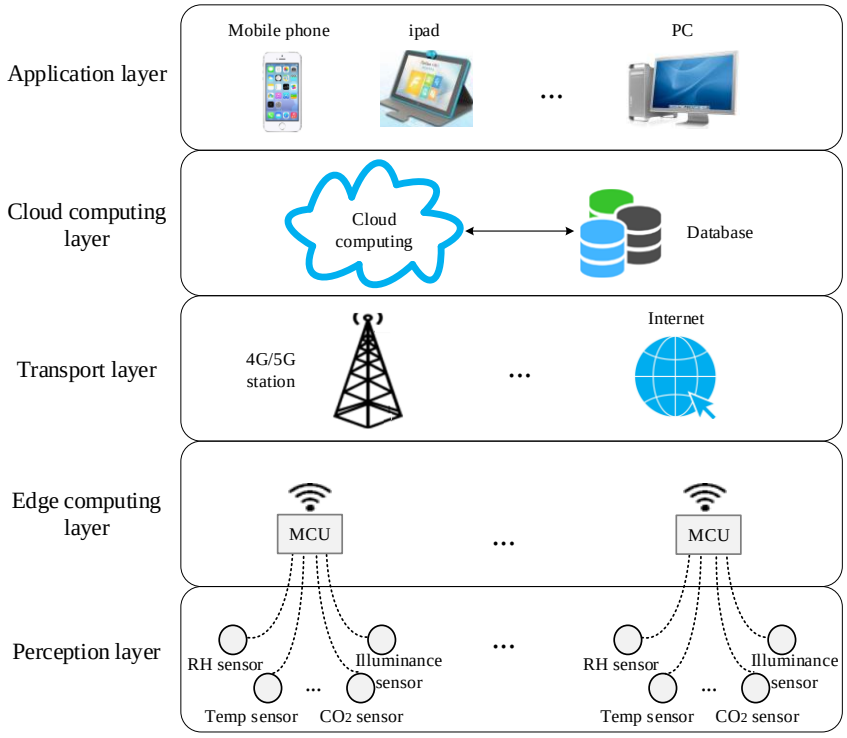


Fig. 1 - The monitoring system architecture of agricultural environment based on NB-IoT

Hardware design of wireless sensor

Environmental parameters vary in different agricultural fields, and growers' concerns depend on the type of crops or livestock. In crop farming, environmental parameters of interest include air temperature, relative humidity, illuminance, CO_2 concentration, and soil moisture. In livestock breeding, farmers may be more interested in parameters such as ammonia and hydrogen sulfide concentration, in addition to air temperature, humidity, illumination, and CO_2 concentration. For our design, the focus was on the four common parameters of air temperature, relative humidity, illuminance, and CO_2 concentration, while also reserving communication interfaces for other environmental sensors on the hardware circuit.

When selecting sensors for specific environmental parameters, various types of sensors are available, and the choice should depend on the specific application's environmental characteristics and technical specifications in relevant national, industry, and local standards. For example, Taizhou City's latest local standard, DB3212T 2024-2021 Technical Specifications for the Construction of Facility Plants Networking (*Taizhou Local Standards, 2021*), provides measurement requirements for environmental parameters such as air temperature, relative humidity, illuminance, and CO_2 concentration in the agricultural IoT monitoring field.

Table 2 shows the main measurement requirements, including the measurement ranges, accuracies, working temperature and humidity ranges, and other relevant factors.

Table 2

The main measurement requirements of agricultural environmental parameters

Environmental parameters	Measurement range	Measurement accuracy	Working temperature range	Working relative humidity range
Temperature	-10°C~65°C	±0.4°C	----	----
Relative humidity	0%~100%	±3%	----	----
Illuminance	0~200000 lux	±7%lux	-10~50°C	0~95%
CO_2 concentration	0~5000 ppm	±2% (20ppm reading)	-10~50°C	0~95%

The measurement requirements outlined in Table 2 serve as an important basis for selecting appropriate sensing devices. However, there are other factors that should also be considered when selecting the appropriate sensor devices, such as price and ease of use.

After comparing several typical sensor devices, the SHT30 digital sensor module was selected for temperature and humidity measurement. The temperature and humidity measurement ranges of the SHT30 sensor device are -40~125℃ and 0~100%, respectively, with measurement accuracies of ±0.3℃ and ±2.0%, respectively (Datasheet of SHT3x sensor, 2016), which meet the measurement requirements specified in Table 1. The physical photo of the SHT30 sensor module is shown in Fig.2. The sensor module is connected to the STM32 MCU through an I^2C interface, and the specific interface circuit is shown in Fig.3. The SCL pin serves as the serial clock signal input terminal, while the SDA is the serial data transmission pin.



Fig. 2 - The SHT30 sensor module

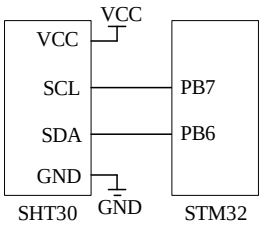


Fig. 3 - The interface circuit between SHT30 sensor and STM32 MCU

There are various types of illuminance sensors available on the market, including TSL2561 and BH1750, which have been used in previous research designs (*Bachuwar et al., 2018; Arvind et al., 2020*). However, the measurement ranges of these sensors, which are all 0-66535lx, do not meet the requirements outlined in Table 1, as the illuminance at noon on sunny days in most regions of China exceeds 10000lx in summer. Therefore, the B-LUX-V30B illuminance sensor module was chosen, having a measurement range of 0-200000 lx, a measurement accuracy of 4%, and a working temperature range of -40~85℃, with no specific requirements for humidity environment (Instructions of the B-LUX-V30B illuminance sensor). This sensor module meets the measurement requirements given in Table 1.

The physical photo of the B-LUX-V30B sensor module is shown in Fig.4, and it also uses the I^2C communication interface.



Fig. 4 - The B-LUX-V30B sensor module

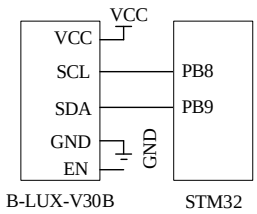


Fig. 5 - The interface circuit between B-LUX-V30B sensor and STM32 MCU

Although the STM32 MCU has two I2C interfaces, the common GPIO (General-purpose input/output) pins of the STM32 MCU were used to connect with the illuminance sensor module to make it easier to add other sensor devices in the future, such as soil sensors, etc. The sensor data acquisition can be simulated in software by implementing the I2C communication timing. The interface circuit between the B-LUX-V30B sensor module and the STM32 MCU is shown in Fig.5, and the sensor module has an enable pin (EN) that is valid for high level and can be connected to high level or suspended.

For the CO_2 concentration measurement, the JX_CO2_102 sensor module was selected after comparing various types of sensors. The measurement range is 0~5000 ppm, and the measurement accuracy is 2% of the measurement range. The working temperature range is -1060℃, and the working humidity range is 0~95% (Instructions of the JX_CO2_102 CO_2 concentration sensor). It meets the measurement requirements given in Table 1. The physical photo of the JX_CO2_102 type sensor module is shown in Fig.6. The sensor has the function of automatic zero calibration, which is convenient to use. The sensor module has three output signal modes, namely, analogue voltage signal, UART (Universal Asynchronous Receiver/Transmitter) signal, and PWM (Pulse Width Modulation) signal, and the UART mode is selected for our design. The interface circuit between the sensor module and the STM32 MCU is shown in Fig.7. The PA2 and PA3 pins are the TX pin and RX pin of the UART interface of the STM32 MCU, respectively.

As for the narrowband IoT module, the BC35-G NB-IoT module was selected, which is a multi-band wireless communication module with high performance and low power consumption. The NB-IoT module supports B1/B3/B8/B5/B20/B28 bands, and the size is only 23.6mm×19.9mm×2.2mm. To simplify the hardware circuit design, a development board with this model of NB-IoT module as the core board was selected, which is equipped with the STM32F103 single-chip microcomputer. In addition to the NB (Narrow Band) module and the STM32 MCU, there are some other interface circuits and GPIO pins led out on the development board, which is convenient for future functional enrichment.



Fig. 6 - The JX_CO2_102 sensor module

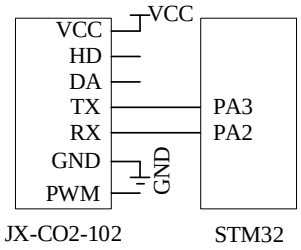


Fig. 7 - The interface circuit between JX_CO2_102 sensor and STM32 MCU

The hardware circuit of the sensor node has been designed based on the information provided above. To ensure practical application, the circuit system has been enclosed in a waterproof junction box with a round hole at the top centre, suitable for the diameter of the illumination sensor. Both the SHT30 type sensor module and the JX_CO2_102 sensor module have been positioned outside the box to enable real-time monitoring of temperature, humidity, and CO_2 concentration. Two holes have been made in the bottom centre of the box to allow the two sensor modules to extend out of the box, and PG series waterproof connectors have been used to secure the modules. To eliminate the impact of solar radiation on the measurement accuracy of temperature and humidity, a multi-layer radiation shield has been fixed at the bottom of the box, with the two sensors placed in the middle of the radiation shield.

Software design of wireless sensor for agricultural environment

The program for the node circuit was developed using Keil professional software. The primary function of the sensor node is to periodically collect information on four environmental parameters, process the data using the STM32 MCU, and wirelessly transmit the processed data to the cloud through the NB module.

The main program completed by the STM32 MCU includes system initialization, timer settings, and other related tasks. System initialization includes initializing the GPIOs connected to each sensor module, initializing the timers, initializing each sensor module, and initializing the NB module. In the timing interrupt subprogram, environmental data acquisition and wireless transmission are completed. The flow of the timing interrupt program is illustrated in Fig.8.

After collecting data from the three sensors, the STM32 MCU processes the data and combines them into a data packet, then attempts to connect to the cloud server. If a connection fails, the MCU re-establishes the connection until it succeeds, and then sends the data packet to the cloud.

The process of collecting temperature and humidity data is described as follows. The SHT30 sensor has two measurement modes: single shot mode and periodic data acquisition mode. In order to reduce the energy consumption of the sensor module, the single shot mode was adopted. Firstly, the STM32 MCU sends a data acquisition command to the SHT30 sensor. After the measurement is completed, the MCU obtains a sampling value through the read command. Then, the SHT30 sensor enters the idle state. To ensure high detection accuracy, the command 0x2C06 was used, which has the highest reproducibility and a relatively long delay time of about 20 ms. For more detailed data reading flow, please refer to SHT30 work sequence flow (Datasheet of SHT3x sensor, 2016). The temperature value and humidity value obtained are both two bytes. The temperature value is denoted as temp, and the relative humidity value is denoted as hum.

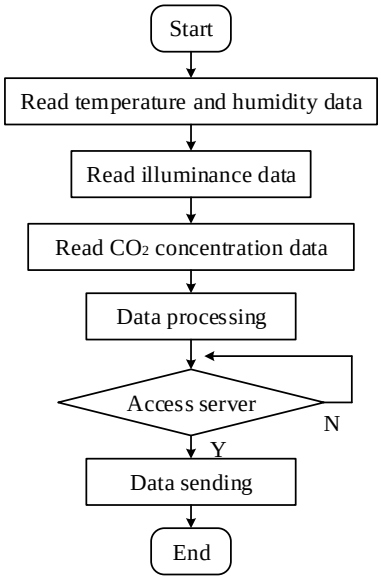


Fig. 8 - The main program flow completed by the STM32 MCU

The calculation formulas for converting the temperature value T[°C] and relative humidity RH[%] are shown in Equation (1) and Equation (2), respectively.

$$T[℃] = -45 + 175 \times temp/(2\text{^}16 - 1) \quad (1)$$

$$RH[\%] = 100 \times hum/(2\text{^}16 - 1) \quad (2)$$

The collecting process of illuminance data is described as follows. When data acquisition is not being performed, both SDA and SCL are high. When data acquisition starts, the STM32 MCU sends a start signal to the B-LUX-V30B illuminance sensor. Specifically, when SCL is at a high level, SDA changes from a high level to a low level. Then, the MCU sends the device address signal and data reading command to the illuminance sensor successively and obtains 6 bytes of data from it. Since the data directly obtained from the sensor contains 3 decimal places, the measured value needs to be divided by 1000 to obtain the correct illumination value. In the actual design, the illumination sensor module is sealed in a transparent housing to protect it. Since the enclosure attenuates the illumination to a certain extent, it is necessary to correct the measured data. The manufacturer has provided a correction factor of 1.4.

The measured value of illuminance is denoted as "light," and the calculation formula for obtaining the actual value L[lux] is shown in equation (3).

$$L[lux] = light/1000 \times 1.4 \quad (3)$$

The collection process for CO_2 concentration data is as follows: the JX_CO2_102 sensor has two operating modes - active reporting mode and passive response mode. In the active reporting mode, the sensor sends the current concentration value once every second. In contrast, in the passive response mode, the sensor measures the current CO_2 concentration only when the MCU sends the data

measurement command to the sensor. To reduce energy consumption, the sensor is set to work in the passive response mode. The sensor returns the CO_2 concentration value in parts per million (ppm), with numbers in different counting units presented in ASCII code. The concentration value of CO_2 can be obtained after simple conversion.

Experimental setup

The designed system was completed with the support of the Agricultural Science and Technology Innovation Project of Anhui Province and other projects. The system was installed in a large glass greenhouse at Fuyang Ziqing Agricultural Technology Co., Ltd. The greenhouse measures approximately 130 m in length and 50 m in width, and the plants being cultivated are longevity flowers.

The sensor nodes are powered by an AC 220V to DC 5V power circuit, which is easily accessible in the greenhouse. This ensures stable sensor operation and reduces the impact of factors such as power instability. Eight sensor nodes were developed, which are uniformly deployed in the 130 m x 50 m glass greenhouse of Fuyang Ziqing Agricultural Technology Co., Ltd. The greenhouse is used for cultivating longevity flowers. The sampling period is 5 minutes, and after the successful system debugging, an actual test experiment is conducted. The monitoring period is from 0:00 on April 23, 2022, to 0:00 on April 28, 2022, for a total of five days. Some field photos of the sensor nodes are shown in Fig.9.



Fig. 9 - Some wireless sensor nodes in the field experiment

The eight sensor nodes are registered on the open cloud platform OneNET, and the detected data of environmental parameters can be displayed in various forms such as instrument panel, table, etc. An example of data display is shown in Fig.10, taken from a screenshot of a mobile phone.

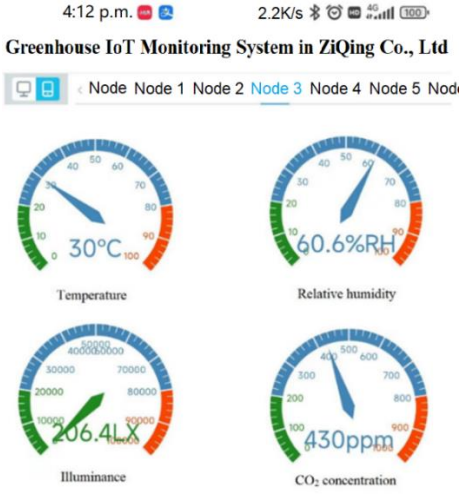


Fig. 10 - The real time environmental data displayed in the form of instrument panel

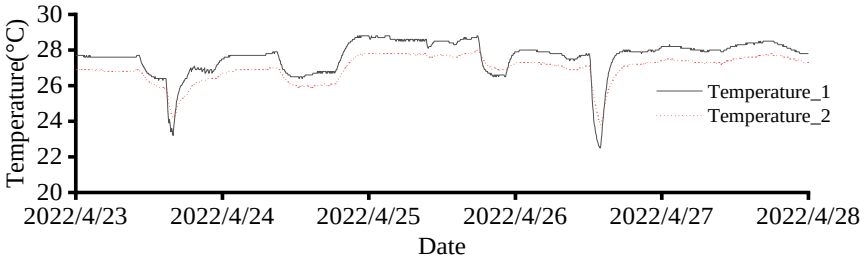
An automatic temperature and humidity recorder of type RC-4HA was used and placed alongside the 8 sensor nodes in the same greenhouse for simultaneous measurement. The purpose was to compare the temperature and humidity data measured by the designed sensor nodes with that of the recorder, which would help verify the accuracy of the sensor nodes' measurements to some extent.

RESULTS

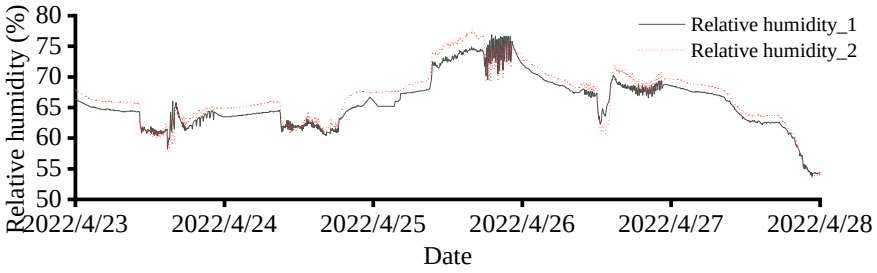
The measured data collected over the five-day monitoring period was exported from the OneNET cloud platform. With a sampling period of 5 minutes, there were 1441 sets of data. The curve displays of the four environmental parameters after mean filtering are shown in Fig.11, which includes the measured data of the RC-4HA type recorder. The black solid lines "temperature_1" and "relative Humidity_1" represent the data detected by the SHT30 type sensors, while the red dotted lines "temperature_2" and "relative humidity_2" represent the data detected by the RC-4HA recorder. The RC-4HA automatic recorder uses a temperature and humidity sensor of SHT11 type, with a temperature measurement accuracy of ±0.4°C and a relative humidity measurement accuracy of ±3.0%.

During the five-day monitoring period, each sensor node successfully uploaded 1441 sets of measured data without any loss of data packets. This shows that the designed sensor nodes can achieve real-time monitoring and reliable transmission of environmental parameters and demonstrates the high wireless communication quality of NB-IoT technology. Compared with other low-rate wireless local area communication technologies, NB-IoT technology has a significant advantage in wireless communication quality. This advantage is not only important for environmental monitoring but also for the regulation of environmental parameters in the future.

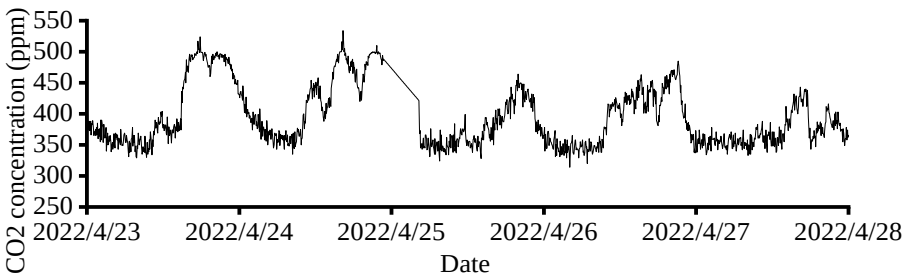
The deviation of the data average value collected by the designed sensor nodes compared to the measured data of the RC-4HA automatic temperature and humidity recorder can be calculated. The mean square error (MSE) and maximum absolute error (MAE) are shown in Table 3. The MSE and MAE of temperature measurement deviation were 0.55°C and 0.71°C, respectively, while the MSE and MAE of relative humidity were 2.01% and 1.25%, respectively. These measured deviations are normal when considering the measurement accuracy of the RC-4HA automatic recorder and the SHT30 type sensor used in the designed sensor nodes. Furthermore, all three sensor modules used in the sensor nodes have calibration functions internally, and their outputs are digital signals. Therefore, accurate measurement results can be obtained by using the calculation formula given in their instructions. The experimental results show that the designed sensor nodes can be used for real-time monitoring of agricultural environmental parameters.



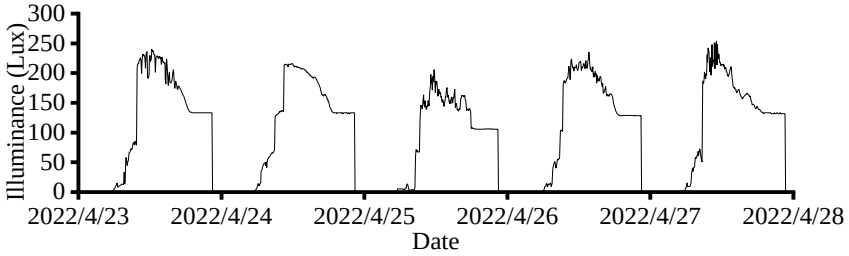
(a) The measured data of temperature



(b) The measured data of relative humidity



(c) The measured data of CO_2 concentration



(d) The measured data of illuminance
Fig.11 - The measured data of environmental parameters

Table 3

Measurement deviation of temperature and humidity

Environmental parameters	MSE	MAE
Temperature	0.55°C	0.71°C
Relative humidity	2.01%	1.25%

The AC 220V to DC 5V power supply was chosen in the experiment to prevent monitoring results from being affected by unstable power supply. In future practical applications, wired power supply can still be used, especially in facility agriculture where 220V AC power is commonly available. However, for field agriculture, a solar power supply circuit would be necessary. This can be easily achieved in practice.

CONCLUSIONS

The wireless sensor nodes designed in this study utilize NB-IoT technology to monitor and transmit real-time and accurate data on air temperature, relative humidity, CO_2 concentration, and illuminance. The system demonstrated excellent wireless communication quality, indicating the potential for widespread use in wireless remote monitoring of agricultural environments. Users can easily access the data through cloud platforms and other Internet-connected devices. The system's existing hardware provides a foundation for future data analysis and acquisition, with reserved GPIO pins available for the addition of soil sensors and control equipment. Future developments will include the design of a solar power supply circuit to expand the system's applicability beyond facility agriculture to field agriculture, providing valuable environmental data for agricultural decision-making.

ACKNOWLEDGEMENT

This work was funded by the Talent Research Fund of Hefei University (18-19RC35), Hefei University graduate innovation and entrepreneurship program (21YCXL08) and Agricultural Science and technology innovation project of Anhui Province “Development of Remote Wireless Monitoring System for Greenhouse Environment Based on NB-IoT”.

REFERENCES

[1] Arvind C S, Jyothi R, Kaushal K, et al. (2020). Edge computing based smart aquaponics monitoring system using deep learning in IoT environment. *IEEE Symposium Series on Computational Intelligence*, 1485-1491. https://doi.org/10.1109/ssci47803.2020.9308395

[2] Bachuwar V D, Ghodake U R, Lakhssassi A, et al. (2018). WSN/WiFi microchip-based agriculture parameter monitoring using IOT. *International Conference on Smart Systems and Inventive Technology*, 214-219. https://doi.org/10.1109/icssit.2018.8748638

[3] Burhan M, Rehman R A, Khan B, et al. (2018). IoT elements, layered architectures and security issues: A comprehensive survey. *Sensors*, 18(9), 2796. https://doi.org/10.3390/s18092796

[4] Datasheet of SHT3x sensor. (2016). Available online: https://pdf1.alldatasheetcn.com/datasheet-pdf/view/897974/ETC2/SHT30.html

[5] Du Y, Sun G, Zheng B, et al. (2021). Design and implementation of intelligent gateway system for monitoring livestock and poultry feeding environment based on Bluetooth low energy. *Information*, 12(6), 218. https://doi.org/10.3390/info12060218

[6] Elijah O, Rahman T A, Orikumhi I, et al. (2018). An overview of Internet of Things (IoT) and data analytics in agriculture: Benefits and challenges. *IEEE Internet of Things*, 5, 3758-3773. https://doi.org/10.1109/jiot.2018.2844296

[7] Farooq M S, Riaz S, Abid A, et al. (2019). A Survey on the Role of IoT in Agriculture for the Implementation of Smart Farming. *IEEE Access*, 7, 156237-156271. https://doi.org/10.1109/access.2019.2949703

[8] Feng X, Yan F, Liu X. (2019). Study of wireless communication technologies on Internet of Things for precision agriculture. *Wireless Personal Communications*, 108, 1785-1802. https://doi.org/10.1007/s11277-019-06496-7

[9] Liang M H, He Y F, Chen L J, et al. (2018). Greenhouse environment dynamic monitoring system based on WiFi. *IFAC-PapersOnLine*, 51(17), 736-740. https://doi.org/10.1016/j.ifacol.2018.08.108

[10] Lihong Z, Lei S, Shufen H, et al. (2011). Measurement and control system of soil moisture of large greenhouse group based on double CAN bus. *In proceedings of the 3rd International Conference on Measuring Technology and Mechatronics Automation*. Shanghai, China. https://doi.org/10.1109/icmtma.2011.416

[11] Mekki K, Bajic E, Chaxel F, et al. (2019). A comparative study of LPWAN technologies for large-scale IoT deployment. *ICT express*, 5(1), 1-7. https://doi.org/10.1016/j.icte.2017.12.005

[12] Popli S, Jha R K, Jain S. (2018). A survey on energy efficient narrowband internet of things (NBIoT): architecture, application and challenges. *IEEE Access*, 7, 16739-16776. https://doi.org/10.1109/access.2018.2881533

[13] Radoglou-Grammatikis P, Sarigiannidis P, Lagkas T, et al. (2020). A compilation of UAV applications for precision agriculture. *Computer Networks*, 172, 107148. https://doi.org/10.1016/j.comnet.2020.107148

[14] Raj A, Shetty S D. (2021). IoT eco-system, layered architectures, security and advancing technologies: A comprehensive survey. *Wireless Personal Communications*, 1-37. https://doi.org/10.1007/s11277-021-08958-3

[15] Samizadeh Nikoui T, Rahmani A M, Balador A, et al. (2021). Internet of Things architecture challenges: A systematic review. *International Journal of Communication Systems*, 34(4), e4678. https://doi.org/10.1002/dac.4678

[16] Silva B N, Khan M, Han K. (2018). Internet of things: A comprehensive review of enabling technologies, architecture, and challenges. *IETE Technical Review*, 35(2), 205-220. https://doi.org/10.1080/02564602.2016.1276416

[17] Sinha R S, Wei Y, Hwang S H. (2017). A survey on LPWA technology: LoRa and NB-IoT. *ICT Express*, 3(1), 14-21. https://doi.org/10.1016/j.icte.2017.03.004

[18] Sishodia R P, Ray R L, Singh S K. (2020). Applications of remote sensing in precision agriculture: A review. *Remote Sensing*, 12, 3136. https://doi.org/10.3390/rs12193136

[19] Tang Y, Dananjayan S, Hou C, et al. (2021). A survey on the 5G network and its impact on agriculture: Challenges and opportunities. *Computers and Electronics in Agriculture*, 180, 105895. https://doi.org/10.1016/j.compag.2020.105895

[20] Technical specification for construction of facility plant networking, DB3212T 2024-2021. (2021). *Taizhou Local Standards*. https://www.doc88.com/p-43547141687747.html

[21] Wang D, Hu H, Yang H, et al. (2020). A real-time LoRa-based IoT system for intelligent meteorological monitoring. *In proceedings of the 6th International Conference on Computer and Communications*. Tokyo, Japan. https://doi.org/10.1109/iccc51575.2020.9344917

[22] Wang Z. (2021). Greenhouse data acquisition system based on ZigBee wireless sensor network to promote the development of agricultural economy. *Environmental Technology & Innovation*, 24, 101689. https://doi.org/10.1016/j.eti.2021.101689

[23] Yang J, Xu Z, Sun Q. (2021). Research and design of greenhouse environment monitoring system based on NB-IoT. *In proceedings of the 33rd Chinese Control and Decision Conference*. Kunming, China. https://doi.org/10.1109/CCDC52312.2021.9601377

[24] B-LUX-V30B Illuminance Sensor Instructions. Taobao. Retrieved May 10, 2022, from https://item.taobao.com/item.htm?spm=a1z09.2.0.0.2d5f2e8dajZ9WV&id=616892137767&_u=33fmhdrd918

[25] Instructions of the JX_CO2_102 CO_2 concentration sensor. (n.d.). Retrieved May 10, 2022, from https://b2b.baidu.com/land?id=a1c3ffe524df7ecea31899bd88fe3ed610

RESEARCH ON APPLE LEAF DISEASE SEGMENTATION AND CLASSIFICATION BASED ON SEMANTIC SEGMENTATION NETWORK
/
基于语义分割网络的苹果叶片病害分割与分级研究

Bin WANG, Lili LI, Shilin LI, Hua YANG* [1]
College of Information Science and Engineering, Shanxi Agricultural University, Taigu 030800/China
Tel: 13466883256; E-mail: yanghuaxky@126.com
DOI: https://doi.org/10.35633/inmateh-69-27

Keywords: *apple leaf, disease degree, semantic segmentation, U2Net*

ABSTRACT

The key to diagnosing the types and degree of apple leaf diseases is to correctly segment apple leaf disease spots. Therefore, in order to effectively solve the problem of poor segmentation of leaves and diseased areas, the U2Net semantic segmentation network model was used in the research of apple leaf disease identification and disease diagnosis, and compared with the classic semantic segmentation network model DeepLabV3+ and UNet. In addition, the effects of different learning rates (0.01, 0.001, 0.0001) and optimizers (Adam, SGD) on the performance of U2Net network model were compared and analyzed. The experimental results showed that the learning rate is 0.001 and the optimizer is Adam, the average pixel accuracy (MPA) and mean intersection over union (MIoU) of the research model for lesion segmentation reach 98.87% and 84.43%, respectively. The results of this study were expected to provide the theoretical basis for the precise control of apple leaf disease.

摘要

诊断苹果叶病类型和程度的关键是正确分割苹果叶部病斑区域。因此，为有效解决叶片及病斑区域分割效果不佳的问题，提出将U2Net 语义分割网络模型用于苹果叶片病害识别及病害诊断的研究，并与经典语义分割网络模型DeepLabV3+和UNet进行对比分析。此外，比较和分析了不同学习率（0.01、0.001、0.0001）和优化器（Adam、SGD）对U2Net网络模型性能的影响。实验结果表明，学习率为0.001，优化器为Adam，U2Net网络模型的平均像素准确率（MPA）和平均交并比（MIoU）分别达到98.87%和84.43%。该研究结果以期为苹果叶片病害的精准化防治提供理论依据。

INTRODUCTION

In the process of apple growth, its leaves are extremely vulnerable to diseases (such as ring rot, rust, early leaf disease, scab, etc.). The occurrence of leaf diseases also easy to causes changes in leaf color, and in serious cases, leaves fall off, and even affect the resistance of fruit trees to diseases, resulting in reduced fruit yield or quality *(Wang et al., 2019)*. Therefore, the realization of intelligent, rapid, and accurate identification of apple leaf disease is of great significance for improving apple yield, quality, and safety, and promoting the sustainable development of the apple industry.

Deep learning has a higher recognition ability than traditional models in image classification, target detection, image segmentation, and other aspects. Therefore, more and more scholars have applied it to the disease identification of apple leaves *(Li et al., 2022)*. For example, *Ding et al. (2021)* improved the Internet model algorithm by introducing the CBAM attention mechanism and multi-scale feature fusion for apple leaf disease under complex background. *Li et al. (2022)* identified the types of corn diseases in the field environment by improving the RegNet model, with an average recognition accuracy of 95.33% for the three diseases. *Yu et al. (2022)* applied the MSO ResNet network model to the recognition of apple leaf disease images. Using the transfer learning method can improve the recognition rate of the model and provide a reference for the intelligent diagnosis of apple leaf disease. *Jiang et al. (2019)* used the target detection algorithm SSD to detect three common diseases of apple leaves. The results show that this model can automatically extract disease features and has high detection accuracy.

The deficiency of these studies is that the whole disease image is classified or the target is roughly framed by the bounding box, but the contour and shape information of the disease spot cannot be extracted.

[1] *Bin Wang, Lec. Ph.D. Eng.; Lili Li, Lec. Ph.D. Eng.;Shilin Li, Lec. Ph.D. Stud.; Hua Yang*, Prof. Ph.D.*

Therefore, it is of great significance to achieve accurate segmentation of leaf lesion area and leaf area to improve the diagnosis of disease degree. *(Li et al., 2021; Boulent et al., 2019; Sharma et al., 2020)*.

Some scholars also use deep learning models to complete semantic segmentation of plant leaf images and then use traditional image analysis methods to complete subsequent disease recognition, diagnosis, and other work *(Ganesh et al., 2019; Santos et al., 2020; Manso et al., 2019)*. It is proved that the deep learning semantic segmentation model based on plant disease spot image semantic segmentation performance is good. The image semantic segmentation model based on deep learning is used for semantic segmentation of the disease image, which realizes the classification of pixel level, and omits the tedious image preprocessing work, the design of the disease segmentation method, and the process of the disease feature extraction. It can directly calculate the proportion of the leaf spot area to the leaf area, and then evaluate the degree of disease according to the relevant standards.

However, to our knowledge, only the author Chao et al. (2021) proposed a semantic segmentation-based approach for segmenting apple leaf lesion areas, but the drawback is that the study did not include diagnostic work on disease severity.

In this study, it is proposed using semantic segmentation network models (U2Net, UNet, and DeepLabV3+) to segment apple leaf lesions and leaf areas, and based on this, calculate the area of the lesion and leaf areas, to estimate the degree of disease according to corresponding standards.

MATERIALS AND METHODS

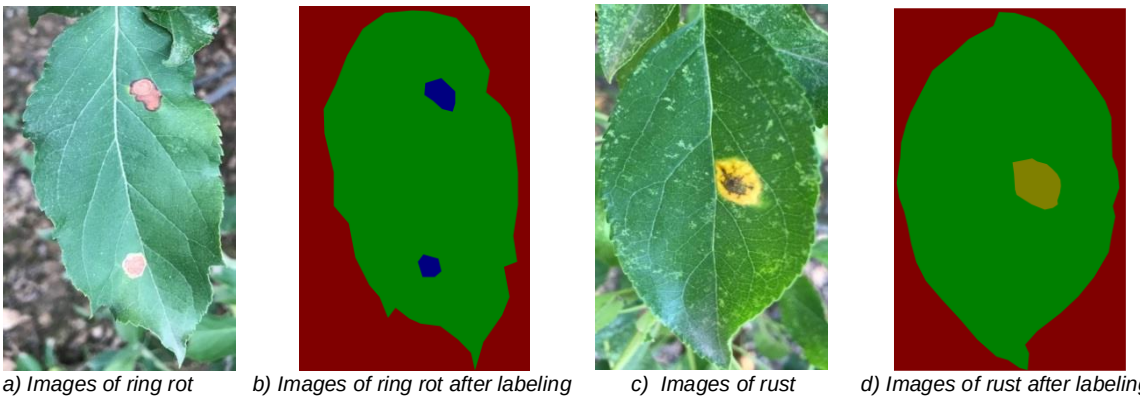
Sample Dataset

In order to identify apple leaf diseases, it is necessary to collect relevant images to establish an image dataset. The image data of apple leaf disease in this study was collected from the Fruit Tree Research Institute of Shanxi Agricultural University. A smartphone (iPhone 13) was used to capture 152 images of ring rot disease and 115 images of rust disease in a natural environment from multiple angles and periods, with an image resolution of 3024×4032, the image format is JPEG, and the color mode is RGB. An example image sample is shown in Fig. 1(a) and Fig.1(c).

Data Set Calibration

The convolutional neural network requires supervised training and learning, so the sprite marking assistant software was used to manually mark polygons in the area where the disease spots were located in the image, while also labeling the leaf area and background area. The method of horizontal, vertical, and rotation was used for data expansion. The original data set was expanded three times to improve the quantity and diversity of samples collected. The data set was divided into training sets (477), verification sets (162), and test sets (54) according to the ratio of 6:2:2. An example of marking the lesion area in the image was shown in Fig. 1.

When training a deep learning model, the more and more comprehensive the training data, the stronger its recognition ability. However, due to the difficulty in collecting disease samples, there is currently a lack of a large number of disease image datasets. Many researchers use a variety of data augmentation methods to expand the original image samples, reduce the over-fitting in the training stage and improve the generalization performance of the network model. The category and quantity of image data sets in this study were shown in Table 1.



a) Images of ring rot *b) Images of ring rot after labeling* *c) Images of rust* *d) Images of rust after labeling*

Fig. 1 - Examples of labeled disease images

Table 1

Distribution of experimental sample data

Classes	Original dataset	Training set	Validation set	Augmented training set	Augmented validation set	Test set
Ring rot	152	90	31	270	93	31
Rust	115	69	23	207	69	23
Total	267	159	54	477	162	54

Experimental Environment

The experiment was implemented based on Python 3.9.1, Pytorch 1.9.0, and Cuda 11.2 deep learning frameworks. Both training and testing are conducted on a PC with an R7-5800H CPU and a GeForce RTX 3070 8G GPU.

Semantic Segmentation Network Model

U2Net Network Model

The U2Net network model is a new network structure proposed by the author Qin et al *(2020)*. by adding a new module RSU (ReSidual U-blocks) based on the UNet network model. The network structure is shown in Fig. 2. It can be seen from the figure that each En_x in the U2Net network model uses an RSU module, and the structure of the RSU module is shown in Fig. 3(a). By using dilation convolution, U2Net can obtain a larger receptive field without increasing the amount of computation, and the whole network structure looks very deep, but the number of parameters does not increase significantly.

It can be easily seen from the RSU structure Fig. 3(a) that the so-called RSU is actually a simple UNet. The final mask is obtained by combining and merging the output results of multiple UNets. The function of the RSU module is to obtain multi-scale features of different stages (L refers to the number of layers in the encoder, C_{in} and C_{out} respectively refer to the number of input channels and output channels, and M represents the number of channels in the internal layer of RSU). The essence of the corresponding structure diagram of the module is shown in Fig. 3(b).

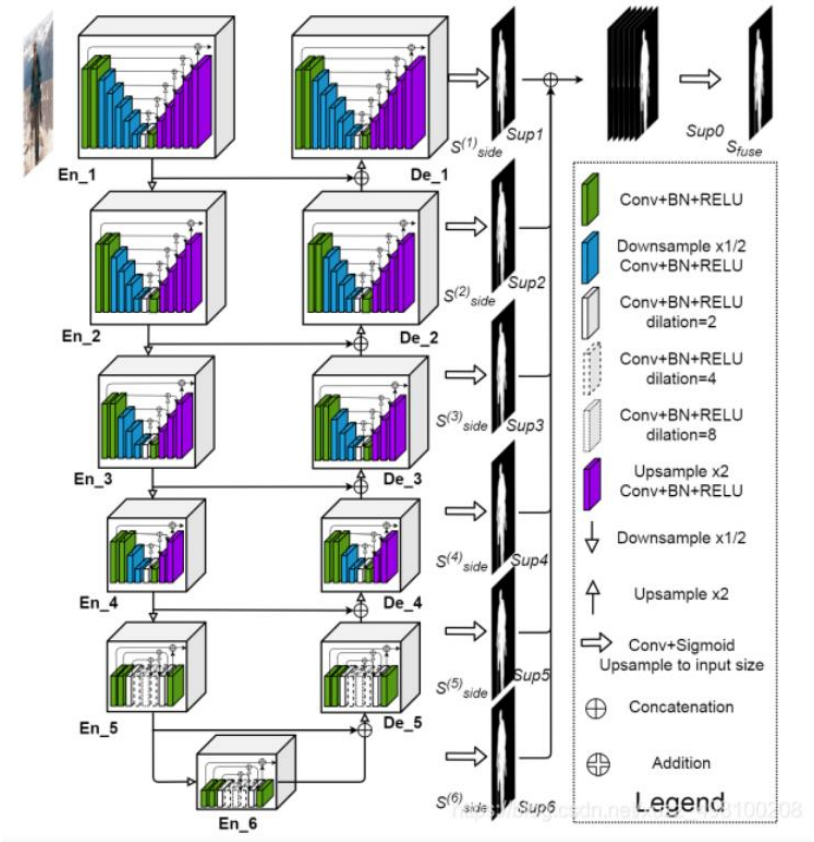
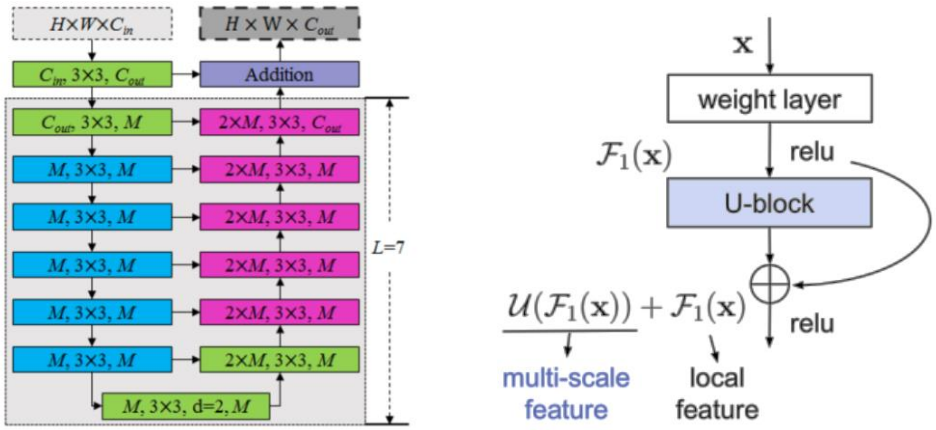


Fig. 2 - Schematic diagram of the overall structure of the U2Net model



a) RSU-L(Cin,M,Cout) *b) ReSidual U-block(RSU)*

Fig. 3 - Structure diagram of the RSU module

Since U2Net can be divided into multiple blocks, and each block outputs a loss, the loss of the whole model can be expressed as Equation (1).

$$L = \sum_{m=1}^{M} \omega_{side}^{(m)} I_{side}^{(m)} + \omega_{fuse} I_{fuse} \quad (1)$$

Where I_{side}^{m} (M=6, as the Sup1, Sup2, … Sup6 in Fig.2) in the loss of the side output saliency map $\omega_{side}^{(m)}$ and I_{fuse} (Sup 0 in Fig.2) is the loss of the final fusion output saliency map $\omega_{side}^{(m)} I_{fuse}$ and ω_{fuse} are the weights of each loss term. For each term L, the standard binary cross-entropy is used to calculate the loss:

$$L = -\sum_{(r,c)}^{(H,W)} \left[P_{G(r,c)} \log P_{S(r,c)} + (1 - P_{G(r,c)} \log(1 - P_{S(r,c)}) \right] \quad (2)$$

Where (r,c) are the pixel coordinates and (H,W) image size: height and width. $P_{G(r,c)}$ and $P_{S(r,c)}$ denote the pixel values of the ground truth and the predicted saliency probability map, respectively. The training process tries to minimize the overall loss L of Eq.(1). In the testing process, the fusion output I_{fuse} is chosen as the final saliency map.

Model Evaluation Indicators

In order to comprehensively evaluate the performance of the models, pixel accuracy (PA), Mean pixel accuracy (MPA), intersection over union (IoU), Mean intersection over union (MIoU), and model size were used to evaluate the model performance.

EXPERIMENTAL RESULTS AND ANALYSIS

Model performance comparison

In this study, the three models selected (U2Net, UNet, and DeepLabV3+) used the original network structure to complete the segmentation task of apple leaf disease data sets. The parameters of all models were set as follows: the optimizer selected Adam, the epoch was set to 50, the initial learning rate was 0.001, the batch size was 4, and the backbone network of UNet and DeepLabV3+ used ResNet50 *(He et al., 2016)*. The network training process includes two stages: freezing training and total training. In the first stage, freeze training is carried out to keep the parameters of the feature extraction stage unchanged and only train the decoder layer. In the training process, when the training loss remains low among the two epochs, the learning rate is adjusted to 1/2 of the original. The second stage is a comprehensive training, with all network parameters participating in the training. During the training process, when the training loss remains unchanged in one epoch, the learning rate is adjusted to half of the original rate, and the training is set to stop early. If the loss of the training set remains unchanged in 10 epochs, the training of the model will be ended.

By comparing the segmentation performance indicators MPA and MIoU of the three models in the test set, the segmentation performance of the model was analyzed. Table 2 list information on the hyperparameters, size of the model, MIoU, and MPA used by the models.

Table 2

Analysis of semantic segmentation performance of compared models

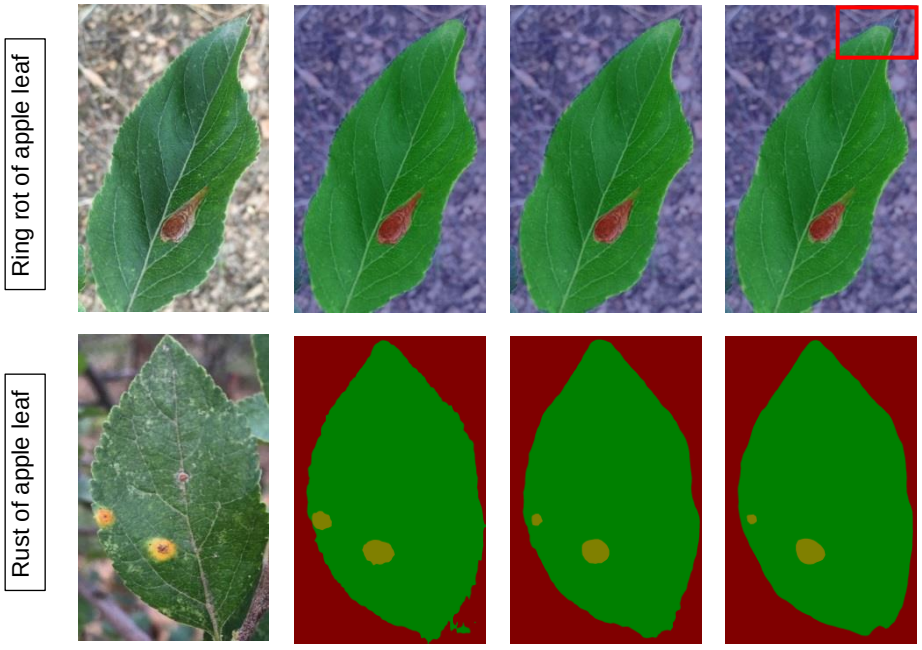
Model	Initial learning rate	Size (MB)	MPA (%)	MIoU (%)
DeepLabV3+	0.001	37.3	97.21	83.40
U2Net	0.001	176.3	98.87	84.43
UNet	0.001	7.76	93.31	81.51

As can be seen from Table 2 that the satisfactory segmentation of MPA and MIoU had been obtained in the apple leaf disease segmentation task for the three classical segmentation network models.

When the initial learning rate was set to 0.001, the MPA values of the three models were all above 93.00%, and the MIoU values were all above 80.00%. The U2Net network model had the best segmentation effect on apple leaf diseases (MPA=98.87%, MIoU=84.43%), followed by the DeepLabV3+ network model, and the UNet network model had the worst segmentation performance.

Considering the size of the models, U2Net had the biggest size (176.3MB), and the size is more than four times the size of the DeepLabV3+ network model (37.3MB). And the size of the UNet model was 7.76MB which was the least, this was one of the reasons leading to the worst model segmentation effect. While the MPA and MIoU indexes of the UNet network model are nearly 6 and 3 percentage points lower than the best network model respectively.

Based on the above analysis, the segmentation accuracy of the U2Net model was significantly improved compared to DeepLabV3+ and UNet models, indicating that the model had good segmentation performance for apple leaf diseases, and the model can be embedded in mobile devices in the future. Figure 4 shows the segmentation effects of two diseases on U2Net, DeepLabV3+, and UNet models.



a) Original image *b) U2Net* *c) DeepLabV3+* *d) UNet*

Fig. 4 - The segmentation effect of different models

As can be seen from Fig. 4, for apple rust, from the segmentation results of the three network models on the leaf area, it can be seen that U2Net had the best segmentation effect on the leaf area, and the segmentation results of the leaf area can be seen in Fig.4 showing that the segmentation of the leaf area was relatively complete and the blade edge burrs could be clearly seen. DeepLabV3+ occupied the second place in leaf area segmentation, and only slight burrs could be seen on the edge of the leaf. However, UNet had the worst segmentation effect, almost no burr could be seen and the segmented blade contour was poor. From the segmentation results of the three network models for the lesion area, it can be seen that the U2Net had the best segmentation effect also, and could segment the two lesions better.

However, DeepLabV3+ and UNet had a satisfactory segmentation effect for large lesions, but the segmentation effect for small lesions was not ideal.

For the ring rot disease, the U2Net network model was the best for the segmentation of leaves and diseased areas. DeepLabV3+network model had little difference in the segmentation of leaf area and U2Net, but the segmentation effect of the diseased area was worse than U2Net. The UNet had the worst segmentation effect on the leaf area and the diseased spot area (the part framed by the red line in the figure).

Comprehensive analysis showed that the segmentation effect of the U2Net network model was better than the other two models, DeepLabV3 and UNet.

Comparison of Segmentation on Different Disease Categories

To further compare and analyze the segmentation performance of three semantic segmentation network models, Table 3 lists the PA and IoU of the four categories in the dataset used for the three models (U2Net, UNet, and DeepLabV3+), where the ones highlighted in bold in the table are the best semantic segmentation network models among the current category and indicators.

Table 3

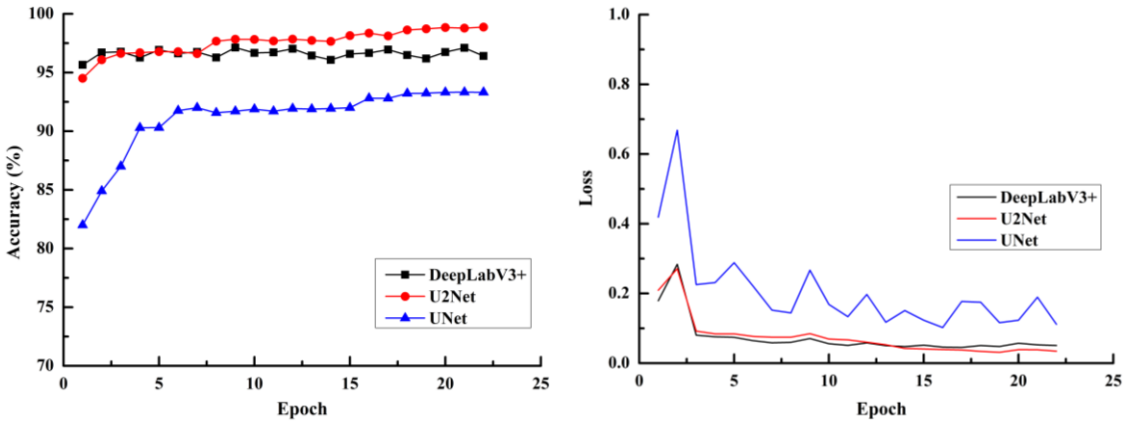
The PA and IOU of different models on different diseases

Evaluation indicators	Network model	Background (%)	Leaves (%)	Rust (%)	Ring rot (%)
IoU	DeepLabV3+	93.89	94.51	71.35	73.86
	U2Net	**95.21**	**94.62**	**74.92**	**73.90**
	UNet	83.24	80.13	78.43	70.96
PA	DeepLabV3+	**96.63**	97.28	89.2	84.67
	U2Net	96.59	**98.90**	**90.12**	**89.19**
	UNet	93.10	93.38	84.38	79.44

It can be seen from Table 3 that compared with the other two network models, the U2Net model had the highest IoU for the four categories, followed by the DeepLabV3+ network model, and the IoU index of the UNet network model was the lowest for the four categories. In addition to the background area, the PA index of the U2Net network model was the highest among the three semantic segmentation network models, and the PA for the background area was only 0.04 percentage points lower than the highest 96.63%. According to Tables 3 and 2, it can be seen that compared to other network models, the network model U2Net had the best comprehensive segmentation effect.

Comparison of Model Convergence Performance

By comparing the convergence performance of the three models (DeepLabV3+, U2Net, and UNet), Fig. 5 compared the convergence performance of three models in the validation set, showing the curves of PA accuracy and loss curves of the four models on the validation set as a function of the number of training rounds.



a) Variation of pixel accuracy with training rounds *b) Variation of validation set loss values with training rounds*

Fig. 5 - Convergence of different models

It can be seen from Fig. 5 that the models had high convergence starting points and fast convergence speed, for the reason that the weight parameters of the backbone network pre-trained on the ImageNet dataset were directly loaded into the model at the initial stage of training.

From the perspective of convergence point, the convergence point of DeepLabV3+ was the highest (95.65%), followed by the convergence point of the U2Net model (94.50%), and the convergence point of UNet model was the lowest (72.00%).

From the perspective of convergence speed and convergence stability, the U2Net network model had the best stability with the highest MPA of 98.87%, followed by the DeepLabV3+ network model with the highest accuracy of 96.4%, while the UNet network model had the worst convergence performance with the highest MPA of 93.30%. Comprehensive analysis showed that the U2Net model was the best model for the apple leaf disease segmentation task.

Hyperparameter Optimization of U2Net

The segmentation results of U2Net with different hyperparameter combinations (learning rates and optimizers) is shown in Table 4.

Table 4

Performance comparison of the U2Net

Model	Initial learning rate	Optimizer	MPA (%)	MIoU (%)
U2Net	0.01	Adam	97.30	83.81
	0.001		98.87	84.43
	0.0001		98.88	84.41
	0.01	SGD	96.16	83.19
	0.001		97.23	83.88
	0.0001		97.97	84.23

It can be seen from Table 4 that when the same Adam optimizer was used and the learning rate was 0.01, 0.001, and 0.0001, the MPA values obtained by the U2Net model on the test set were 97.30%, 98.87%, and 98.88%, and the MIoU values were 83.81%, 84.43%, and 84.41%, respectively.

On the whole, when the learning rate was 0.01, the segmentation performance of the U2Net model was the worst; When the learning rate was 0.001 and 0.0001, the difference in segmentation performance of the U2Net model was small and the same. When the learning rate was adjusted from 0.001 to 0.0001, the MPA value of the U2Net model was only increased by 0.01%, while the MIoU value was reduced by 0.02%, which leads to longer training time.

When the SGD optimizer was used and the learning rate was 0.01, the MPA and MioU of the U2Net model in the test set were the lowest, with values of 96.16% and 83.19% respectively. When the learning rate was adjusted from 0.01 to 0.001, the MPA value of the U2Net model increased by 1.07%, and the MIoU value only increased by 0.69%. When the initial learning rate was 0.0001, U2Net had the highest MPA and MIoU on the test set, which was 97.97% and 84.23%, respectively.

According to the above analysis, when the learning rate was 0.001 and the optimizer was Adam, the segmentation performance of the U2Net model was the best.

Diagnosis of Leaf Disease Degree

Generally speaking, the degree of apple leaf disease varies with the proportion of the diseased area to the entire leaf area. Therefore, according to the relevant standards of Air Assisted Orchard spray Operation Quality (NY/T 992-2006), which was issued by the Ministry of Agriculture and Rural Affairs of the People's Republic of China, list the classification standards for the disease degree of apple leaves, as shown in Table 5.

Table 5

Classification standard of apple leaf disease degree

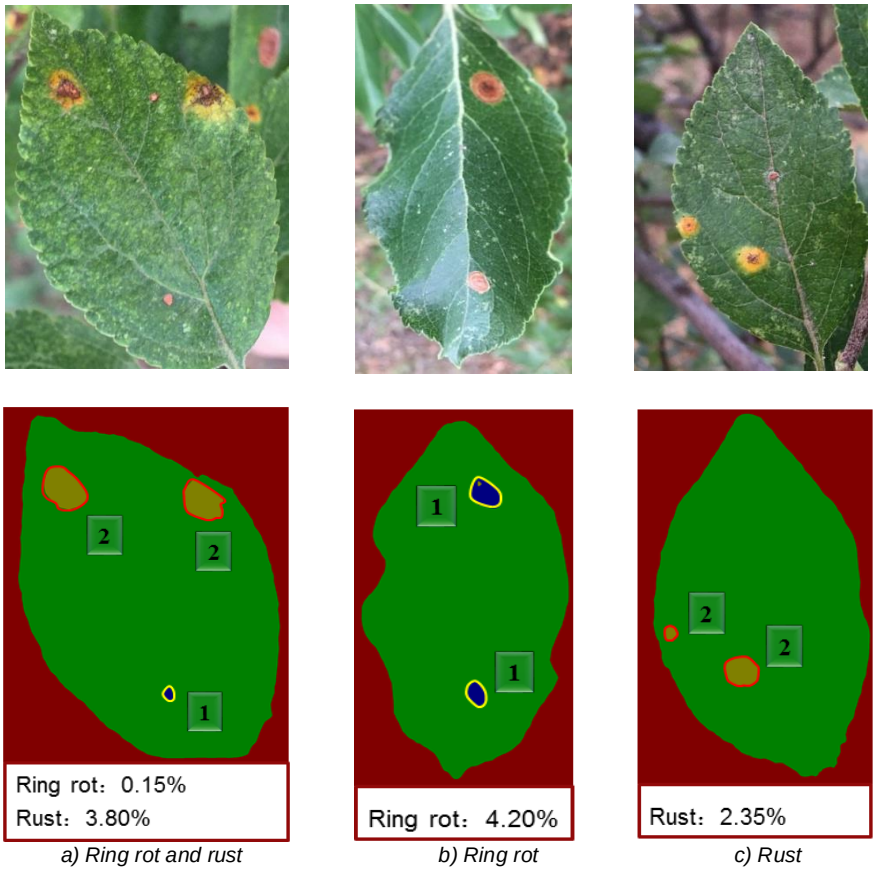
Grade	The proportion of lesion area to leaf area (%)
0	0
1	<=10
3	11~25
5	26~40
7	41~65
9	>=65

According to the segmentation results of the leaf area and lesion area of apple diseased leaves using semantic segmentation methods, the proportion of the total number of pixels in the lesion area to leaf area was calculated. Finally, the disease degree of apple leaves is inferred based on the disease degree classification criteria in Table 5. The calculation method is shown in Equation (3).

$$DD = \frac{S_d}{S_d + S_h} \tag{3}$$

where: DD is the disease degree of the apple diseased leaf, S_d is the number of pixels in the lesion area, S_h is the total number of pixels in the apple leaf area.

Fig. 6 shows the results of the semantic segmentation network model U2Net in symptom classification and severity estimation with ResNet50, Adam, and 0.001 as the backbone network, optimizer, and learning rate, respectively.



a) Ring rot and rust *b) Ring rot* *c) Rust*

Fig. 6 - Examples of the segmentation effect obtained by U2Net

Fig. 6 (a) showed the segmentation result of semantic segmentation network U2Net on apple leaf rust and ring rot, and it was calculated from the segmentation result that the lesion area ratio of rust and ring rot is 1.87% and 0.12%, respectively. Similarly, in Fig. 6 (b), the lesion area of ring rot was 1.98%, and in Fig. 6 (c), the lesion area of rust was 1.82%. Based on the above analysis, the proposed semantic segmentation network model has achieved satisfactory results. The disease grade of apple leaves was determined according to Table 5. The result showed that the method proposed in this study was effective for the segmentation of apple diseased leaves under complex field background.

CONCLUSIONS

In this paper, the classical semantic segmentation models (U2Net, UNet, and DeepLabV3+) were used for semantic segmentation of apple leaf area and diseased area, transfer learning was used for the reason of limited data set, and the U2Net network model was fine-tuned to select the most suitable combination of hyperparameter. Finally, the grading diagnosis of apple leaf disease was studied. The main research conclusions are as follows:

(1) By comparing MPA, MIoU, PA, IoU, average pixel accuracy curve, and loss function curve, the comprehensive performance of three semantic segmentation network models U2Net, UNet, and DeepLabV3+ (when using the learning rate of 0.001, the optimizer selected Adam) on apple leaves and diseased areas were analyzed. The research showed that the segmentation performance of the U2Net network model was superior to the other two segmentation network models (DeepLabV3+, UNet).

(2) The influence of three groups of different learning rates and two different optimizers on the performance of the U2Net network model was analyzed through experiments. The research showed that when the learning rate of the U2Net network model was set to 0.001 while the Adam optimizer was selected, the segmentation performance indicators MPA and MIoU of the model reached the highest, 98.87% and 84.43% respectively.

This study can achieve accurate segmentation of leaf area and lesion area, and provide a basis for the diagnosis of disease degree. At the same time, this study can provide more accurate information for subsequent disease prevention and early warning.

ACKNOWLEDGEMENT

This work was funded by Basic Research Project of Shanxi Province (Free Exploration) (Project No. 202203021212426), "Introduction of Talents and Scientific Research Initiation Project" of Shanxi Agricultural University (Project No. 2023YJ52).

REFERENCES

[1] Boulent, J., Foucher, S., Théau, J., & St-Charles, P. L. (2019). Convolutional neural networks for the automatic identification of plant diseases. *Frontiers in plant science*, *10*, 941. https://doi.org/10.3389/fpls.2019.00941

[2] Chao, X. F. (2021). *Research on the Methods of Identification and Lesion Segmentation of Common Apple Leaf Diseases*. Northwest A&F University: Xianyang, China.

[3] Ding, X., Song, Y., & Liu, M. (2021). Based On the Improved Neural Network Anchor Free Apple Leaf Disease Detection Algorithm. *International Journal of Computational and Engineering*, *6*(4), 133-146. https://doi.org/10.326/ijce.2021.034268

[4] Ganesh, P., Volle, K., Burks, T. F., & Mehta, S. S. (2019). Deep orange: Mask R-CNN based orange detection and segmentation. *IFAC-PapersOnLine*, *52*(30), 70-75. https://doi.org/10.1016/j.ifacol.2019.12.499

[5] He, K., Zhang, X., Ren, S., & Sun, J. (2016). Deep residual learning for image recognition. In Proceedings of the *IEEE Conference on Computer Vision and Pattern Recognition*, Las Vegas, USA. https://openaccess.thecvf.com/content_cvpr_2016/html

[6] Jiang, P., & Chen, Y. (2019). Detection method of apple leaf disease based on SSD. *Electronic Technology & Software Engineering*, *10*, 56. https://doi.org/10.3389/etse.2019.02349

[7] Li, L., Zhang, S., & Wang, B. (2022). Identification of apple leaf diseases based on improved convolutional neural network. *INMATEH - Agricultural Engineering*, *67*(2), 553-561. https://doi.org/10.35633/inmateh-67-54

[8] Li, L., Zhang, S., & Wang, B. (2022). Apple leaf disease identification with a small and imbalanced dataset based on lightweight convolutional networks. *Sensors*, *22*(1), 173. https://doi.org/10.3390/s22010173

[9] Li, X. R. (2021). Research on apple leaf disease detection method based on deep learning. Northwest A&F University: Xianyang, China.

[10] Manso, G. L., Knidel, H., Krohling, R. A., & Ventura, J. A. (2019). A smartphone application to detection and classification of coffee leaf miner and coffee leaf rust. *arXiv preprint arXiv:1904.00742*. https://doi.org/10.48550/arXiv.1904.00742

[11] Pan, S. J., & Yang, Q. (2010). A survey on transfer learning. *IEEE Transactions on knowledge and data engineering*, *22*(10), 1345-1359. https://doi.org/10.1109/TKDE.2009.191

[12] Qin, X., Zhang, Z., Huang, C., Dehghan, M., Zaiane, O. R., & Jagersand, M. (2020). U2-Net: Going deeper with nested U-structure for salient object detection. *Pattern recognition*, *106*, 107404. https://doi.org/10.1016/j.patcog.2020.107404

[13] Santos, T. T., de Souza, L. L., dos Santos, A. A., & Avila, S. (2020). Grape detection, segmentation, and tracking using deep neural networks and three-dimensional association. *Computers and Electronics in Agriculture*, *170*, 105247. https://doi.org/10.1016/j.compag.2020.105247

[14] Sharma, P., Berwal, Y. P. S., & Ghai, W. (2020). Performance analysis of deep learning CNN models for disease detection in plants using image segmentation. *Information Processing in Agriculture*, *7*(4), 566-574. https://doi.org/10.1016/j.inpa.2019.11.001

[15] Wang, C. L., Lu, C. Y., Chen, W. Z., Li, H. W., He, J., & Wang, Q. J. (2019). Image segmentation of maize stubble row based on genetic algorithm and threshold filtering noise. *Transactions of the Chinese Society of Agricultural Engineering*, *35*(16),198-205. https://doi.org/10.11975/j.issn.1002-6819.2019.16.022

[16] Yu, H., Cheng, X., Chen, C., Heidari, A. A., Liu, J., Cai, Z., & Chen, H. (2022). Apple leaf disease recognition method with improved residual network. *Multimedia Tools and Applications*, *81*(6), 7759-7782. https://doi.org/10.1007/s11042-022-11915-2

RESEARCH OF THE AIR FLOW FORM IN THE INTAKE DEVICE FOR SAPROPEL EXTRACTION

/

ДОСЛІДЖЕННЯ ФОРМИ ПОВІТРЯНОГО ПОТОКУ У ЗАБІРНОМУ ПРИСТРОЇ ДЛЯ ДОБУВАННЯ САПРОПЕЛЮ

Igor TSIZ, Serhii KHOMYCH, Vasyl SATSIUK, Victor TARASIUK
Lutsk National Technical University / Ukraine
Tel: +38 050 147 28 44; E-mail: igor-71@ukr.net
DOI: https://doi.org/10.35633/inmateh-69-28

Keywords: *sapropel, trajectory, motion, air, bubble, liquid, viscosity*

ABSTRACT

For many years, global researches that focus on improving soil fertility have been conducted. Nowadays, innovative inculcations of environmentally (ecologically) friendly organic agriculture are becoming quite popular. One of the most effective indicators is the use of alternative types of fertilizers. As part of large-scale experiments, researchers propose to use fertilizers made from organic sapropel concentrated in freshwater lakes. Analysis of such studies shows that the impact of sapropel on soil fertility is significant and complex. The main problem they faced is the extraction of these deposits from underwater deposits (fields). Ukrainian scientists have proven the effectiveness of sapropel extraction by means of a pneumatic intake device. To substantiate the rational parameters of this device and visualize the processes, experimental studies of the work of the pneumatic working body were carried out. Namely, experimental studies of the determination of the trajectories of air bubbles in liquids of different viscosity were carried out. According to received trajectories, the boundaries of airflow and its shape are determined. Limpid liquids of different viscosities were used specially in order to see and fix the flow parameters, because it is impossible to observe such a phenomenon in sapropels placed in underwater deposits, due to their opacity and change of viscosity with depth of the bedding. Therefore, the experiment was considered as close as possible to the real one, and the environment of realization of the experiment was simulated. Water, industrial oil and concentrated detergent were selected as investigated liquids. Research data indicate that one can use a whirling airflow for better loosening of deposits of reduced humidity. Whirling occurs when there is a horizontal position of the outlet axis with a diameter in the range of 1-1.5 mm and air pressure of 300-400 kPa.

РЕЗЮМЕ

Протягом багатьох років проводяться світові дослідження, які зосереджені на підвищенні родючості ґрунту. На сьогодні досить популярним стають інноваційні впровадження з ведення екологічно чистого органічного землеробства. Одним з найбільш результативних показників є застосування альтернативних видів добрив. В межах масштабних експериментів дослідники пропонують застосовувати добрива, які виготовлені з органічного сапропелю зосередженого в прісноводних озерах. Аналіз таких досліджень показує, що вплив сапропелю на родючість ґрунту є значним та комплексним. Основна проблема з якою вони зустрілись є видобування даних покладів з підводних родовищ. Українськими науковцями доведено ефективність добування сапропелів засобом із пневматичним забірним пристроєм. Для обґрунтування раціональних параметрів цього пристрою, та візуалізації процесів проведено експериментальні дослідження, роботи пневматичного робочого органу. А саме проведені штучні експериментальні дослідження визначення траєкторій руху повітряних бульбашок у прозорих рідинах різної в'язкості. За отриманими траєкторіями встановлено межі повітряного потоку та його форму. Прозорі рідини різної в'язкості застосовували спеціально, для того щоб бачити і фіксувати параметри потоку. Оскільки спостерігати таке явище в сапропелях розміщених у підводних родовищах неможливо, через їх непрозорість та зміну в'язкості з глибиною залягання. Тому експеримент вважали максимально наближеним до справжнього, а середовище проведення досліду моделююче. У якості рідин було вибрано воду, оливу індустріальну та концентрований миючий засіб. Результати дослідження вказують, що з метою кращого розпушення покладів пониженої вологості можна використовувати завихрений повітряний потік. Завихрення досягається під час горизонтального розташування осі вихідного отвору із діаметром у діапазоні 1-1.5 мм та тиску подачі повітря 300-400 кПа.

INTRODUCTION

It is known that the most accessible sources of fresh water for economic needs are lake reservoirs. At the same time, Ukraine occupies one of the last places in Europe in terms of fresh water reserves per capita. Due to the processes of eutrophy, existing lakes in our country are turning into swamps. Since nature cannot cope with such problems on its own, scientifically based human intervention is necessary. The most radical and effective method of lake restoration is the removal of accumulated sediments (sapropels) (*Gafsi et al., 2009; Lewtas et al., 2016*). But at the same time this method is the most costly. The efficiency of this method can be increased by using the extracted sediments in various industries, especially in agriculture. The extracted organic deposits are used as raw materials for the production of highly effective environmentally friendly fertilizers, which in turn form a favourable soil climate for the development of nutrients for plants and increase soil fertility. Analysis of research sources shows that the impact of sapropel on the increase of humus in the soil is quite significant and complex (*Stankevica, 2020; Tsiz et al., 2021*). Especially bright effect is observed from the use of organic sapropel on sandy and sandy loam soils (*Baksiene et al., 2015*). Therefore, the purification of lakes by extracting sapropel primarily gives the opportunity to get environmentally friendly organic and organomineral fertilizers that improve the structure of the soil and they are a quality source of humus replenishment, and makes it possible to use natural organic raw materials in other industries (chemical industry, medicine, stockbreeding, biotechnology).

Machines with mechanical and hydraulic working bodies are widely used for sapropel removal and dredging (*Bulik et al., 2014; Vanags, 2015*). However, their designs are complicated and carry out multi-operational working processes with high energy consumption (*Bodak et al., 2020; Khlopetskyi, 2016*). The design can be considerably simplified by means involving the use of compressed air energy (*Tsiz and Homich, 2013*).

For getting sapropel an important element in pneumatic means is the intake device, in which the formation of air-sapropel mixture forms. To ensure high-quality operation of the tool in general, and to justify the shape of the intake device body in particular, it is necessary to understand the laws governing the interaction between the flow of air bubbles and sapropel. Since the pneumatic sapropel extraction device is a new design, experimental and theoretical studies of the interaction between air bubble flow and sapropel have not been conducted before. However, sapropel in its natural state can be considered a viscous liquid, and the processes of interaction between the flow of air (or other gases) bubbles and viscous liquids are utilized in a wide range of technological processes. Therefore, studies of such processes have been analysed.

The processes of interaction of the flow of air (or other gases) bubbles with liquids are used in a large number of technological processes. In *Brevik and Kristiansen, (2002)*, a systematization of studies of air bubble flow in water by industries where it is used is carried out. Thus, the flow of air bubbles is used in the restoration (renewal) of eutrophic lakes by aeration. Studies in this direction made by *Gafsi et al., (2009),* refer to the methodology for studying of water aeration in lakes at different air supply parameters, bubble size distribution, and theoretical modelling of vertical air bubble flow. Experimental studies of air bubble flow during the dissolution of solids in liquids involved the use of a laboratory setup for the formation of quasi-static conditions (*Danylyuk et al., 2018*). As a result of the studies, the detachment size of air bubbles from the bubbler orifices was established and the energy distribution in the dissolution apparatus during pneumatic mixing of liquids within the quasi-static mode of motion at different air rates was determined. The study of turbulence of air bubbles flow created in the tank at the wastewater treatment plant is given in the work (*García and García, 2006*). Experiments were carried out to establish the velocity of water in a large volume outside the core of the bubble plume using Laser Doppler Anemometry. The flow of air bubbles in water was investigated to simulate the processes occurring in a foundry ladle by introducing gasified elements into the liquid metal (*Sheng and Irons, 1995*). The results of the physical model study were used to refine the mathematical model of the real process. The studies given by *Milelli, (2002)*, concern the flow of air bubbles, which takes place in nuclear reactors with boiling water of the passive type. The researchers' experiments concerned establishing the empirical coefficients needed to refine the mathematical model of large vortices.

A study of the hydrodynamics of a bubble plume in media characterized by different viscosities in the range of 1-100 mPa·s was conducted by Laupsien et al. They studied the effect of viscosity on the oscillations of the bubble plume, as well as on the velocity fields of liquid and gas. Membrane and tubular atomizers were used in the study. The results of the study were obtained in terms of porous fraction profiles, plume oscillation periods, and bubble size distribution.

A considerable amount of theoretical research of air-bubble flow modelling was carried out by *Brevik I.* (*Brevik, 1977; Brevik and Kristiansen, 2002*). His research is based on the energy approach and contains simple dependencies for engineering calculations of the geometric parameters of the flow of air bubbles in water. In order to theoretically study the mechanism of the transverse velocity effect on the plume of air bubbles in open channels, Xu et al., (2022) developed a numerical model of this process. This study provides an opportunity for engineering programs to model the movement of air bubble flows in water.

Original methods of experimental studies of air bubble flow are given in works made by *Kitagawa et al., (2004); Lima-Ochoterena and Zenit, (2003); Metz et al., (2010); Qin et al., (2016); Tian et al., (2020); Wang et al., (2019)*. According to these studies, pretreatment fluids, additional illumination sources, and high-speed digital video cameras were used to visualize the air bubble flow.

Thus, a large number of experimental studies have been carried out in the field of air bubble flow research, which allow us to understand many of its features and involve the use of a wide range of experimental equipment. However, the information from available sources on determining the boundaries of the flow, which is necessary to know in order to justify the shape of the body of the intake device of the sapropel production means, is insufficient. Therefore, it requires the study of the process of air bubble flow specifically in the sapropel environment. But, by analogy with the studies considered above in this case simulating transparent liquids was used since visual observation of the flow of air bubbles in sapropel is limited by its transparency.

MATERIALS AND METHODS

Since the state of natural sapropel deposits does not allow visual observation of the movement of air bubbles inside them, a modelling fluid that was sufficiently transparent was selected. In terms of viscosity, the closest liquids were concentrated detergents (TU U 24.5 23731918-010-2003). To verify the validity of the research and to determine the effect of fluid viscosity on the shape of the air bubble flow, water (coefficient of dynamic viscosity at 20°C η = 0.001004 Pa·s) and industrial oil (coefficient of dynamic viscosity at 20°C η = 0.0275 Pa·s) was also used as test fluids.

While studying the motion trajectory of air bubbles in liquids of different viscosity, the setup shown in Fig. 1 was used, photo and 3D model.

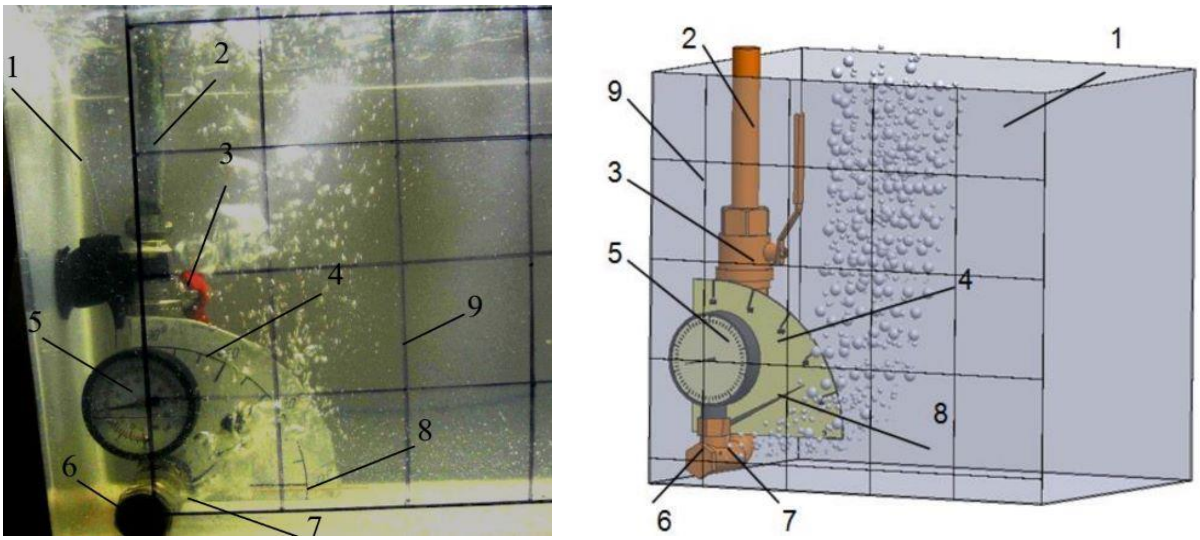


Fig. 1 - Photo of the setup for studying airflow motion in liquids of different viscosity (a), (b) - 3D model

This setup consists of a plastic reservoir *1*, which has marked coordinate grid *9* on the front wall. Within the reservoir *1*, a piece of pipeline *6* with a nozzle *7* of the determined diameter is fixed. A flexible armature hose *2* is used to supply air from the compressor to the pipeline. Preliminary pressure regulation of air supply was made with the setup valve *3*, and precise - with spool mechanism of the compressor. The current value of the air outlet pressure from the nozzle *7* was recorded with the manometer *5*. To determine the angle of inclination of the nozzle axis *7* to the horizon an arrow *8* is fixed on the pipeline *6* and on the tap body *3* - the scale graded in degrees. The change of the angle of inclination of the nozzle axis *7* to the

horizon was made by weakening of the connecting sliding coupling with its subsequent tightening. Pipeline segments with a cylindrical nozzle with diameters of 0.5, 1.0; 1.5 mm were used during the research.

The fixation of airflow motion trajectory in liquid medium was done using a tripod-mounted digital camera. A pipeline segment with a nozzle, the diameter of which was determined by the experiment plan with an angle of inclination at 0° to the horizon, had been fixed in the sliding coupling before the research. Then this element together with the pressure gauge and compressed air supply hose were installed in the reservoirs of the setup. Afterwards, the assembled setup was installed on the horizontal surface and a zero scale-reading division of the angle of inclination of the output nozzle was aligned with the horizontal scale axis, drawn on the front wall of the device.

To set a required air pressure range in the output nozzle, its preliminary regulation using the setup valve was done so that the compressor valve motion allowed to provide pressure regulation in the range from 100 to 500 kPa.

The filling of the setup capacity with the investigated liquid was done without violation of previous regulations. The filling was stopped after liquid reached the level lower by 20-30 mm of the upper end of the container.

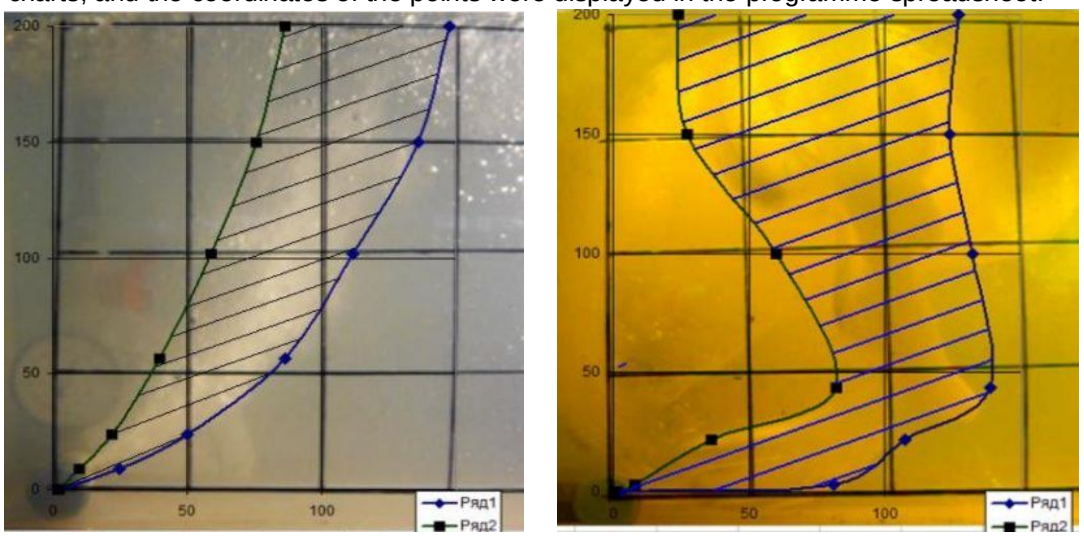
Next, a digital camera was mounted on the tripod so that the camera lens was on a level with the pipeline outlet and the plane of the camera front board was parallel to the plane of the front wall of the setup reservoir. The camera mode - video recording was set.

Then the supply of compressed air was turned on, the appropriate to the experiment plan pressure was set and the button “start” of the video camera was pressed. A 6-second video clip was recorded. Afterwards, the air supply pressure was changed and the video of the defined duration was recorded one more time. After that the liquid was drained off, the angle of inclination of the nozzle was set at 45° and the experiment was repeated in the sequence described above.

While carrying out the experiment, the recorded video was processed in order to obtain curves that limited the space where airflow was moving after its exit from the nozzle. For this purpose, using Media Window programme, the continuous video was converted into discrete images corresponding to video frames. As the quality of the video was characterized by 30 frames per second, 180 digital discrete images were obtained from a six-second video. Next, every thirtieth image that corresponded to the end of each second of the experiment was selected, and thus 6 selected images were obtained which provided a sixfold repetition of the experiment.

The images, selected in the way described above, were exported to the Microsoft Excel. Then each image overlapped a coordinate grid and two-point charts of this programme, which for first approximation corresponded to the curves, which limited the space where airflow was moving after the exit from the nozzle. By scaling the image data, the coincidence of the divisions of the chart axes and a coordinate grid of the setup front wall was provided (Fig. 2).

After that, their form was compared with the form of the real airflow by moving the points of the previous charts, and the coordinates of the points were displayed in the programme spreadsheet.



a) b)

Fig. 2 - A sample of the processed snapshot of the airflow motion in the liquid (a) water, (b) in detergent

RESULTS

According to the coordinates of the lines received in such a way, which limited the airflow, point charts were built. In Fig. 3-5, the results of the research on this phenomenon in water are demonstrated, in Fig. 5, b – 7, a – in industrial oil and in Fig. 7, b – 9 – in concentrated detergent. The indicated figures show pairs of points that limit the airflow from the right and left sides at designated air supply pressure in sixfold repetition (six points are given).

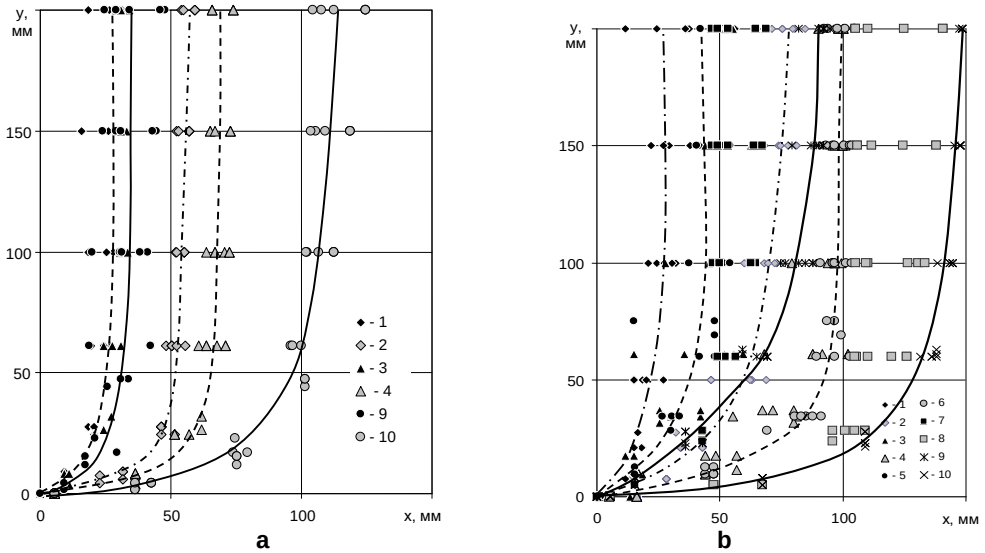


Fig. 3 – The boundaries of airflow during its motion in water after exiting the horizontal (a) and deviating from the horizon by 45° (b) nozzle with a diameter of 0.5 mm at supply pressure:
1-2 – 100 kPa; 3-4 – 200 kPa; 5-6 – 300kPa; 7-8 – 400 kPa; 9-10 – 500 kPa

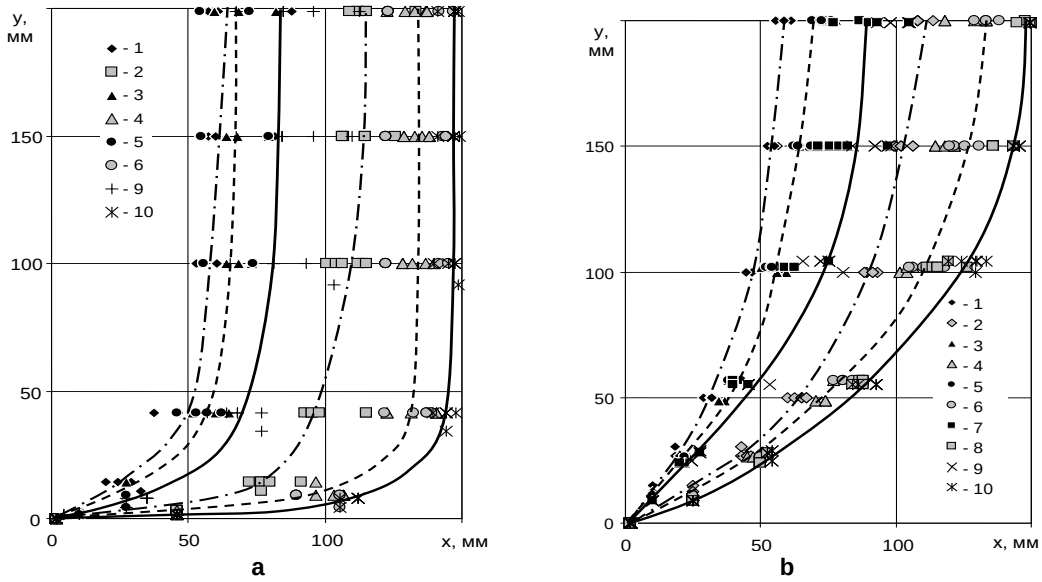


Fig. 4 – The boundaries of airflow during its motion in water after exiting the horizontal (a) and deviating from the horizon by 45° (b) nozzle with a diameter of 1.0 mm at supply pressure:
1-2 – 100 kPa; 3-4 – 200 kPa; 5-6 – 300 kPa; 7-8 – 400 kPa; 9-10 – 500 kPa

The analysis of the obtained point charts confirmed a significant influence of liquid viscosity on the shape of the airflow. Thus, in case of air supply at pressure 400 kPa from the outlet with diameter of 1.00 mm deviating from the horizon by 45° to water with viscosity η = 0.001004 Pa·s the most horizontal displacement of air bubbles at an altitude of y=200 mm reaches x=150 mm (Fig.4b), and under the same conditions in the case of supply to the industrial oil medium with viscosity η = 0.0275 Pa·s this indicator is equal to x=110-120 mm (Fig.6b). During air supply at pressure 500 kPa from the outlet with diameter of 1.0 mm deviating from the horizon by 45° to the concentrated detergent, the viscosity of which depends on the speed of layers displacement and for the conditions of the experiment is in range of η = 0.5 – 1.5 Pa·s, the most horizontal displacement of air bubbles at an altitude of y=200 mm does not exceed x=100 mm (Fig.8b).

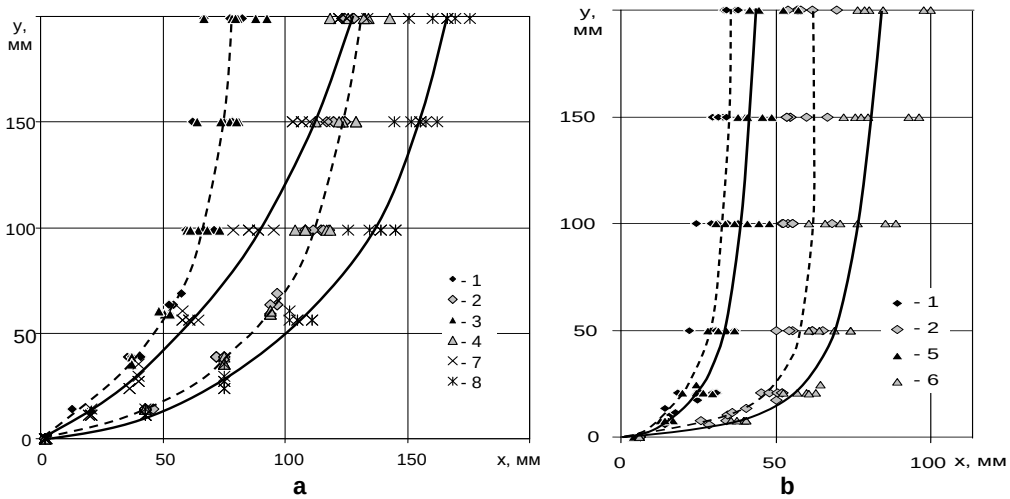


Fig. 5 – The boundaries of airflow during its motion in water after exiting the nozzle with a diameter of 1.5 mm (a) and in industrial oil after exiting the nozzle with a diameter of 0.5 deviating from the horizon by 45^0 (b) at supply pressure: *1-2 – 100 kPa; 3-4 – 200 kPa; 5-6 – 400 kPa; 7-8 – 500 kPa*

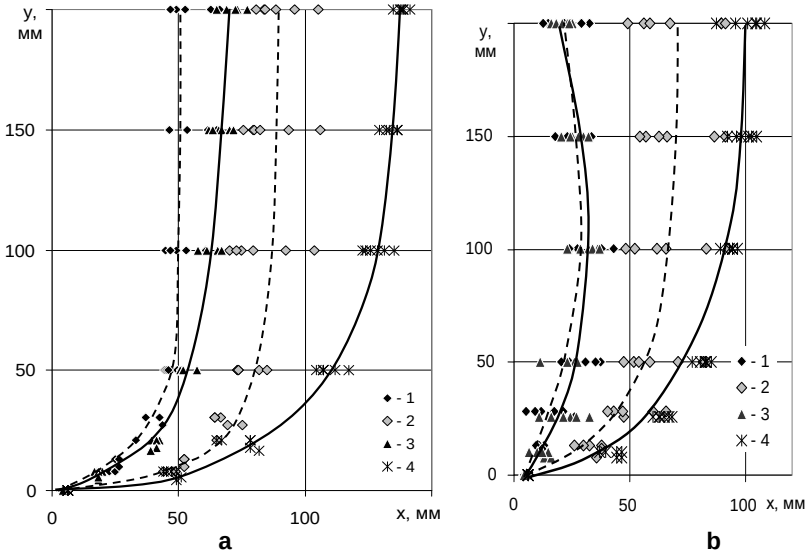


Fig. 6. – The boundaries of airflow during its motion in industrial oil after exiting the horizontal nozzle with a diameter of 0.5 mm (a) and diameter of 1.0 mm deviating from the horizon by 45^0 (b) at supply pressure: *1-2 – 200 kPa; 3-4 – 400 kPa*

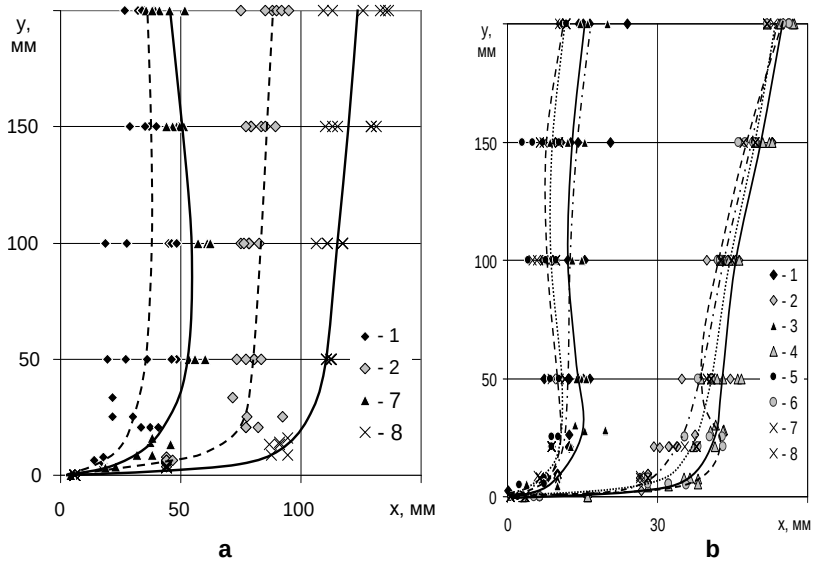
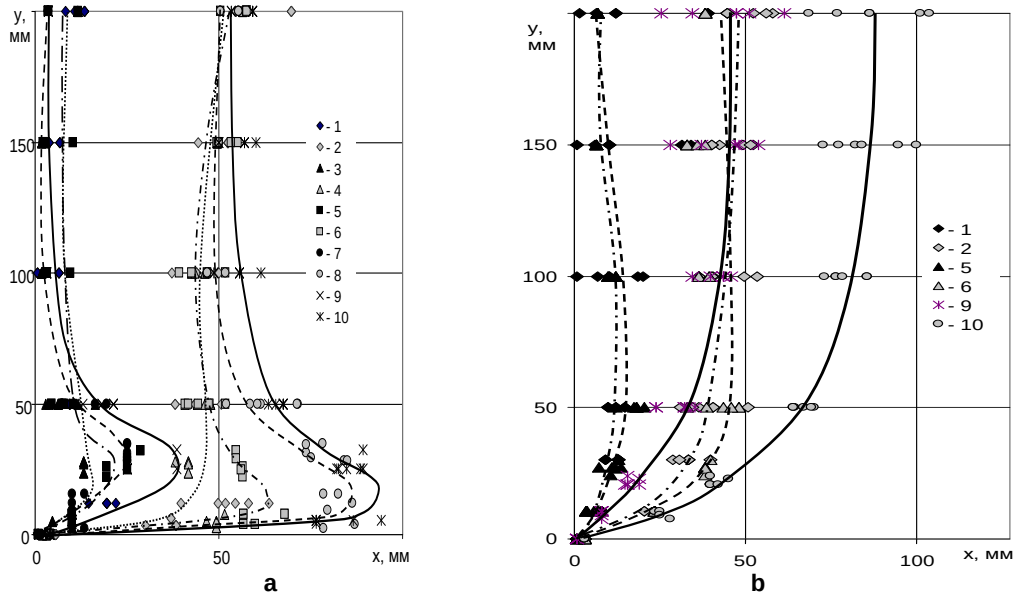


Fig. 7 – The boundaries of airflow during its motion in industrial oil after exiting the horizontal nozzle with a diameter of 1.5 mm (a) and in detergent after exiting the horizontal nozzle with a diameter of 0.5 mm (b) at supply pressure: *1-2 – 100 kPa; 3-4 – 200 kPa; 5-6 – 300 kPa; 7-8 – 400 kPa*

It is also found that for liquids with low viscosity (water and industrial oil) the change of angle of inclination of the outlet axis from 0° to 45° has an influence on the shape and coordinates of airflow limiting curves only within the height of rise $y = 150$ mm (Fig.4 a, b and Fig. 5a; 6a).

At the same time, during air supply through a horizontally placed nozzle with diameter of 1.0-1.5 mm to the concentrated detergent air whirling is observed (Fig.8a; 9a). Intensification of this phenomenon is observed for the outlet with diameter of 1.0 mm at air supply pressure in the range of 300-500 kPa (Fig. 8, and curves 6, 8, 10) and for the outlet with diameter of 1.5 mm – 200-300 kPa (Fig. 9, and curves 4 and 6). For the outlet with diameter of 1.5 mm at air supply pressure of 500 kPa (Fig.9 and curve 8), and also for the outlet with diameter of 0.5 mm at pressure in the range of 100-500 kPa (Fig.7b) this phenomenon disappears. For the experiment with concentrated detergent and angle of inclination of the outlet axis at 45° air whirling does not occur, therefore the maximum horizontal deviation of airflow at an altitude of y=200 mm is greater than in cases of air whirling (Fig. 8, b curve 6, Fig. 9, b curves 4 and 6).

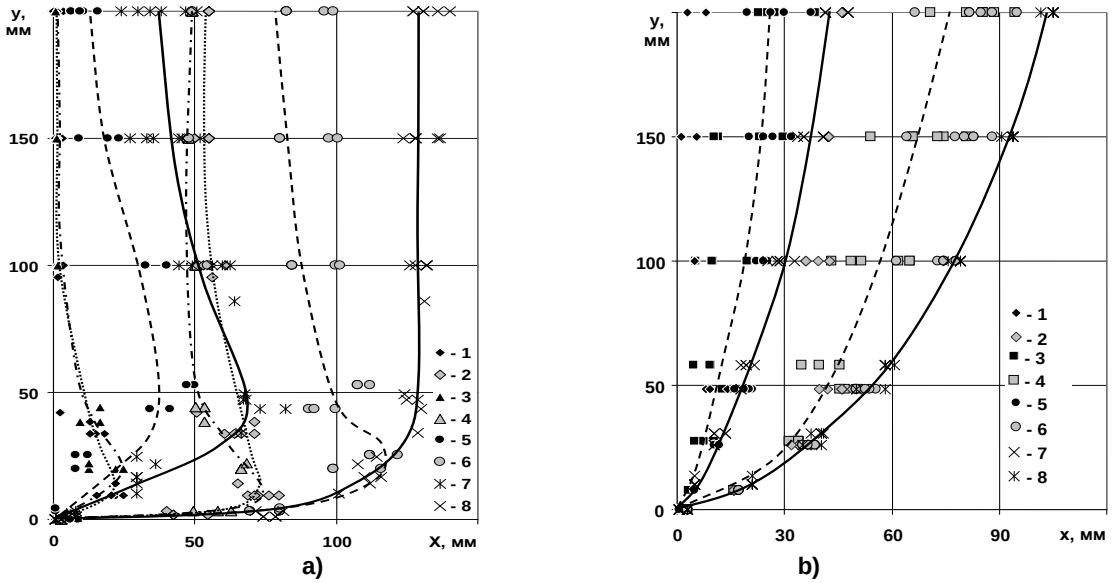
An increase in the outlet diameter and air supply pressure and hence the volume of air supply lead to an increase in the cross-section area of the flow (Fig.3b; 3a; 6a). Slowing down the airflow with the height of rise causes an extension of its cross-section area. The stabilization of this indicator is observed at heights of rise ranging from y=50…100 mm.



a b

Fig. 8 – The boundaries of airflow during its motion in detergent after exiting the horizontal (a) and deviating from the horizon by 45° nozzle (b) with a diameter of 1.5 mm at supply pressure:

1-2 – 100 kPa; 3-4 – 200 kPa; 5-6 – 300 kPa; 7-8 – 400 kPa; 9, 10 – 500 kPa



a) b)

Fig. 9 – The boundaries of airflow during its motion in detergent after exiting the horizontal (a) and deviating from the horizon by 45^0 (b) nozzle with a diameter of 1.5 mm at supply pressure:

1-2 – 100 kPa; 3-4 – 200 kPa; 5-6– 300 kPa; 7-8 – 500 kPa

To determine the design parameters of the intake device for the extraction of sapropel, namely: the diameter of the inlet and outlet opening of the intake cone (body), its height and the angle of inclination; the diameter of the lifting pipeline; the number of loosening-feeding nozzles and the step of their placement in the pressure pipeline; based on the average values of the point graphs, 3-D models of effective flows in more viscous liquids were depicted (Fig. 10).

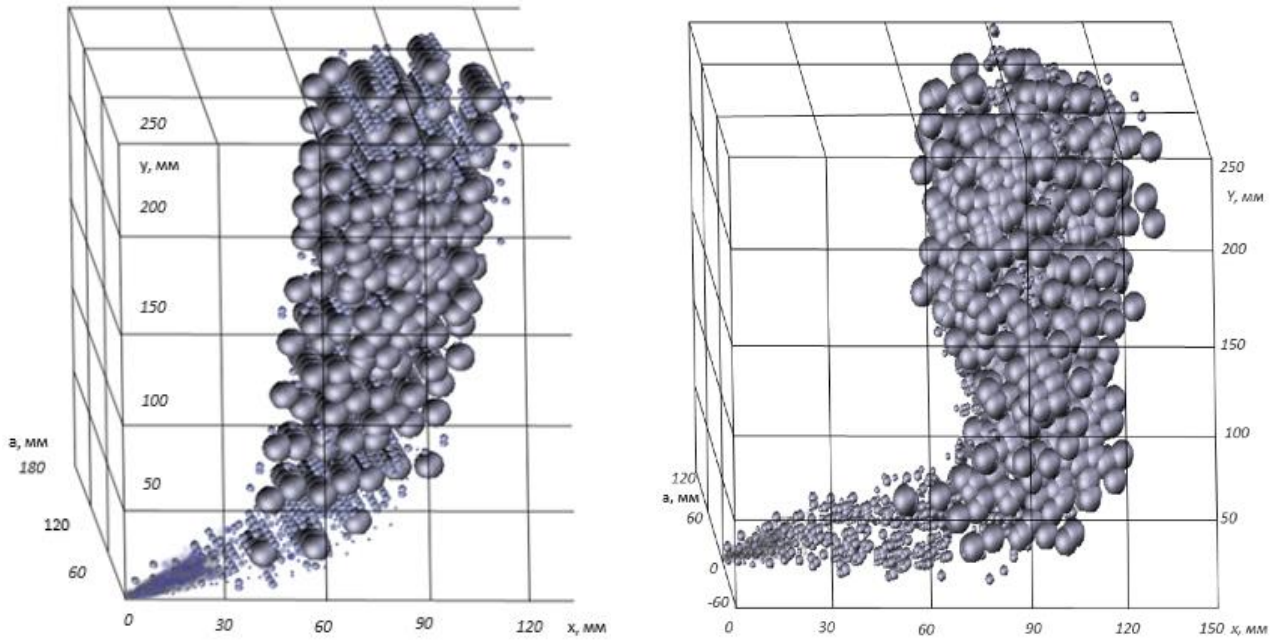


Fig. 10 – 3-D model of air sweat during its movement in the detergent after leaving the horizontal (a) and deviated from the horizon by 450 (b) nozzle with a diameter of 1.5 mm at an air supply pressure of 500 kPa

Accordingly, by selecting the viscosity of the fluid, the parameters of the air supply pressure and the angle of inclination of the nozzles, it can be argued that the height of the intake cone, which can be used for the extraction of sapropel, can be more than 200 mm, with a diameter of the outlet of the body and a diameter of the transport pipeline of 50 mm. Such a selection of parameters can be explained by the fact that the flow with the height of lifting expands and acquires a maximum diameter of 40...60 mm at a height of about 180...200 mm, and then stabilizes and does not change in cross section. The pitch of the nozzles in the pressure pipeline should be approximately 40...60 mm, this indicates that the flow has approximately the same diameter in the upstream position at the 200 mm mark. The diameter of the inlet cavity of the intake body should be more than 260 mm, since the maximum flow outlet from the nozzle is 90...130 mm. Taking into account that this distance falls only on the side of the casing according to its diameter, it is also worth considering a small gap in the central part of the casing where the sapropel for the intake could fit. The number of nozzles can be calculated on the basis of the length of the circle, which is calculated from the diameter of the inlet cavity of the body, and the angle of inclination of the generating cone in height and inlet and outlet diameters.

The height of the casing should be increased by a correction factor of 40...50 %, since at a height of 100...120 mm, adjacent streams begin to merge and form an air pressure medium in the upper part of the casing, which can increase and, under initial operating conditions, go beyond the casing. It is possible to prevent such a fact by increasing the central gap where the sapropel is concentrated, then in the additional space of the cone a quality sparging will be formed, which will pass into the lifting pipeline.

Based on the parameters substantiated experimentally and refined by the computer model, a pneumatic intake device was manufactured (Fig. 10). Tests of this device during the extraction of sapropel revealed its effectiveness and confirmed the adequacy of the research.

CONCLUSIONS

Thus, the studies show that in order to intensify the process of extracting low moisture (high viscosity) sapropel, a swirling flow of air bubbles can be created in the collecting device.

Whirling occurs in case of the horizontal position of the outlet nozzle axis with a diameter ranging from 1 to 1.5 mm and air supply pressure 300...400 kPa. And while extracting the deposits that do not require preliminary significant disintegration, it is advisable to use a nozzle with an angle of inclination of their axis to the horizon 45°. As in this case, the energy of airflow will be maximally used for lifting the deposits in the pipeline.

It was also established that the height of the intake device body should be more than 200 mm, with the diameter of the outlet of the body and the diameter of the transport pipeline being 50 mm. The pitch of the nozzles in the air supply pressure pipeline should be within 40...60 mm, and the inlet diameter of the intake device body should be more than 260 mm. Tests in production conditions of the pneumatic intake device manufactured according to the above parameters confirmed the adequacy of the studies.



Fig. 10 – Photo of the manufactured intake device

REFERENCES

[1] Bodak V.I., Hailis G.A., Dubytskyi O.S, Mazyliuk P.V., (2020), Investigation of the movement of a sapropel particle in a final intake part of a screw mechanism (Дослідження руху частинки сапропелю в конічній забірній частині шнекового механізму), *Agricultural machines (Сільськогосподарські машини),* vol. 44, pp. 7-17. LNTU, Lutsk. https://doi.org/10.36910/agromash.vi44.30.

[2] Baksiene E., Asakaviciute R., Romanovskaja D., Tripolskaja L., Razukas A., (2015), The influence of lake sediments on sandy loam soil properties and crop yield, *Romanian agricultural research*, No. 32., ISSN 1222-4227, pp. 183-190.

[3] Brevik I., Kristiansen O., (2002), The flow in and around air-bubble plumes, *International Journal of Multiphase Flow,* vol. 28, pp. 617–634.

[4] Brevik I., (1977), Two-dimensional air-bubble plume, *Journal of Waterway, Port, Coastal and Ocean Division*, ASCE 103, pp. 101–115.

[5] Bulik Y.V., Pavlova I.O., Ilyushyk I.M., (2014), The experimental studies of the dynamics of the process of excavation sapropel with the grapple (Експериментальні дослідження динаміки процесу екскавації сапропелів грейфером), *Agricultural machines (Сільськогосподарські машини),* vol. 29-30, LNTU, Lutsk, ISSN 2307-1699, pp. 3-8.

[6] Danylyuk O.M., Atamanuk V.M., Gumnitsky J.M., (2018), Simulation of the movement of compressed air bubbles in the apparatus with pneumatic mixing (Моделювання руху бульбашок стисненого повітря у апараті з пневматичним перемішуванням), *Scientific Works (Наукові праці)*, vol. 82, Issue 1, Odessa National Academy of Food technologies, Odessa, ISSN: 2073-8730, pp. 61-65.

[7] Gafsi M., Kettab A., Benmamar S., Benziada S., (2009), Comparative studies of the different mechanical oxygenation systems used in the restoration of lakes and reservoirs, *Journal of food, agriculture & environment*, vol.7 (2), pp. 815-822.

[8] García C. M., García M. H., (2006), Characterization of flow turbulence in large-scale bubble-plume experiments. *Experiments in Fluids*, 41(1), pp. 91-101. https://doi.org/10.1007/s00348-006-0161-6.

[9] Khlopetskyi R.A., (2016), *Improvement of technology and means for extraction of lake sapropels from under water layer (Удосконалення технології та засобу для добування озерних сапропелів з-під шару води)*. PhD dissertation, Lviv National Agrarian University, Lviv/Ukraine.

[10] Kitagawa A., Sugiyama K., Murai Y. (2004), Experimental detection of bubble–bubble interactions in a wall-sliding bubble swarm, *International journal of multiphase flow*, vol. 30, Issue 10, pp. 1213-1234. https://doi.org/10.1016/j.ijmultiphaseflow.2004.07.002.

[11] Laupsien D., Le Men C., Cockx A., Line A., (2022), Effects of liquid viscosity and bubble size distribution on bubble plume hydrodynamics, Chemical engineering research and design, vol. 180, pp. 451-469.

[12] Lewtas K., Roy D., Paterson, M. (2016). Manitoba prairie lakes: In-lake remediation treatment summary. International Institute for Sustainable Development (IISD), from https://www.iisd.org/publications/report/manitoba-prairie-lakes-lake-remediation-treatment-summary.

[13] Lima-Ochoterena R., Zenit R., (2003), Visualization of the flow around a bubble moving in a low viscosity liquid. *Revista mexicana de fisica,* vol.49, Issue 4, pp. 348–352.

[14] Metz T., Paust N., Zengerle R., Koltay P., (2010), Capillary driven movement of gas bubbles in tapered structures. *Microfluid Nanofluid 9*, Springer, pp. 341–355. https://doi.org/10.1007/s10404-009-0551-1

[15] Milelli, M. (2002), *A numerical analysis of confined turbulent bubble plumes*. A dissertation submitted to the Swiss federal institute of technology Zurich, Switzerland.

[16] Qin S., Liu J., Miao T., Wu D., (2016), Experimental study on gas-liquid flow characteristics of submerged air jets, *IOP Conference Series: Materials Science and Engineering*, vol. 129, Hangzhou, China.

[17] Sheng Y., Irons G., (1995), The impact of bubble dynamics on the flow in plumes of ladle water models, *Metallurgical and materials transactions*, vol. 26B, pp. 625-635.

[18] Stankevica K., (2020), *Character of sapropel properties based on its formation conditions and possibilities of its use*, PhD dissertation, University of Latvia, Riga/Latvia.

[19] Tian W., Xingxing Y., Wen C., Jiehui R., Min W., Ting M., Lei L., Ran F., Kun Y., (2020), Effect of aerated pore distribution on bubble plume movement in a cylindrical aerated tank, Revista de Chimie, vol.71(6), pp. 408-417. https://doi.org/10.37358/RC.20.6.8207.

[20] Tsiz I., Homich S., (2013), Experimental research of working process of pneumatic intake device for sapropel extraction, *INMATEH, Agricultural Engineering,* Vol. 40, No. 2., pp. 67-72.

[21] Tsiz I., Khomych S., Satsiuk V., (2021), Agro-ecological aspects of mining and use of sapropel (Агро-екологічні аспекти добування та використання сапропелю). *Сільськогосподарські машини),* vol. 47, LNTU, Lutsk, ISSN 2307-1699, pp. *37-45*. https://doi.org/10.36910/acm.vi47.625.

[22] Wang Y., Zegao Y., Wenming Z., Zhu D., (2019), Computational study of bubbly jets in stagnant water, *Journal of Hydrodynamics*, Vol.31. ISSN 1001-6058, pp. 1021-1033. https://doi.org/10.1007/s42241-018-0147-x.

[23] Vanags R., (2015), Investigation of sapropel extraction technical tools. *Engineering for Rural Development*, vol. 14, ISSN 1691-5976, Jelgava/LATVIA, pp.151-154.

[24] Xu J., Wang X., Zhu L., Zhou D., Zhao J., (2022), Study on air bubble plume in open channel with CFD-PBM coupling model. Proceedings of PIANC Smart Rivers 2022. PIANC 2022. Lecture Notes in Civil Engineering, vol. 264, Springer, Singapore, pp. 1261-1270. https://doi.org/10.1007/978-981-19-6138-0_110.

MODELING OF SUBSTRATE AND AIR TEMPERATURE DYNAMICS IN THE MUSHROOM GREENHOUSE
/
МОДЕЛЮВАННЯ ДИНАМІКИ ТЕМПЕРАТУРИ СУБСТРАТУ ТА ПОВІТРЯ У ГРИБНИЦІ

Gennadii GOLUB[1)], Oleg KEPKO*[2)], Olexander PUSHKA[2)], Zoia KOVTUNIUK[2)], Timofii KOTLIAR[3)]
[1)] National University of Life and Environmental Sciences of Ukraine, Kyiv, Ukraine;
[2)] Uman National University of Horticulture, Uman, Ukraine
[3)] Bila Tserkva National Agrarian University, Ukraine
Tel: +380630499929; E-mail kepko@meta.ua
DOI: https://doi.org/10.35633/inmateh-69-29

Keywords: *heat exchange, ventilation system, mathematical modeling, plant greenhouse, mushroom greenhouse*

ABSTRACT
Economic efficiency of greenhouse vegetable growing depends quite significantly on the cost of energy carriers, which is why the introduction of energy-saving technologies in greenhouse vegetable growing is an urgent issue. One of the ways to save energy resources can be the use of a closed ventilation system of the "plant greenhouse - mushroom greenhouse" type, which is based on the opposite type of respiration of plants and mushrooms. A closed ventilation system includes air exchange between the greenhouse with growing plants and the cultivation room for growing mushrooms. The closed ventilation system allows you to save energy by reducing the heating of the incoming air, as well as increasing the yield of vegetable products due to the increased concentrations of carbon dioxide in the air that flows from the cultivation room for mushrooms to the greenhouse and mushrooms due to the increased concentrations of oxygen in the air that flows into the cultivation room for mushrooms from the greenhouse. Mathematical modeling of the process of heat transfer between greenhouses makes it possible to simulate transitional processes between rooms in order to assess the quality and accuracy of regulation, as well as to evaluate the parameters of the object in transitional modes. Mathematical modeling of dynamic processes is the basis for the formulation of transfer functions for the automatic control system. As a result of the study, mathematical models of the temperature dynamics of the substrate of mushrooms and greenhouse vegetables were obtained due to the analytical solution of the system of differential equations. The adequacy of the solution was verified by the Runge-Kutta method and compared with experimental data. The difference between the theoretical and experimental values is not significant and amounted to -3 % for the substrate temperature and -3.2 % for the air temperature.

АНОТАЦІЯ
Економічна ефективність тепличного овочівництва досить суттєво залежить від вартості енергоносіїв, у зв'язку з чим впровадження енергозберігаючих технологій у тепличному овочівництві є питанням актуальним. Одним із способів економії енергоресурсів може бути використання замкнутої системи вентиляції типу «рослинна теплиця - грибниця» яка основана на протилежному типі диханні рослин та грибів. Замкнута система вентиляції включає в себе повітрообмін між теплицею з вирощуванням рослин та культиваційним приміщенням для вирощування грибів. Замкнута система вентиляції дозволяє економити енергоносії за рахунок зменшення нагріву припливного повітря, а також збільшити вихід овочевої продукції завдяки підвищеним концентраціям вуглекислоти у повітрі, яке поступає із культиваційного приміщення для грибів в теплицю та грибів завдяки підвищеним концентраціям кисню у повітрі, яке поступає в культиваційне приміщення для грибів із теплиці. Математичне моделювання процесу переносу тепла між теплицями дає можливість моделювати перехідні процеси між приміщеннями з метою оцінки якості та точності регулювання, а також для оцінки параметрів об'єкту у перехідних режимах. Математичне моделювання динамічних процесів є підставою для формулювання передаточних функцій для системи автоматичного управління. У результаті дослідження були отримані математичні моделі динаміки температури субстрату грибів та тепличних овочів за рахунок аналітичного вирішення системи диференційних рівнянь. Перевірка адекватності рішення була перевірена методом Рунге-Кутти та порівняна із експериментальними даними. Розходження між теоретичними та експериментальними значеннями не суттєва і склала по температурі субстрату – 3 % і по температурі повітря – 3,2 %.

INTRODUCTION

The energy efficiency of a closed ventilation system and the dynamics of temperature changes in the buildings of this system were studied, which made it possible to use the ventilation system to carry out gaseous inter-fertilization of plants and mushrooms, since it is well known that plants absorb CO_2 and release O_2 during photosynthesis, and mushrooms, on the contrary, during respiration absorb O_2 and emit CO_2. CO_2-enriched air from the mushroom greenhouse and O_2-enriched air from the greenhouse circulates in a closed circuit using the ventilation system, and supply air is supplied to the system only when the concentration of CO_2 in the mushroom greenhouse exceeds the set norm. At the same time, the air that moves between the greenhouses has some thermal potential. That is, there is not only gas exchange, but also heat transfer (*Girchenko, et al., 2003)*. These studies are a continuation of the studies presented in *(Golub & Kepko, 2017*).

In addition to technological advantages, such a ventilation system provides significant savings in thermal energy for heating supply air. To ensure automatic control of the temperature regime in the "plant greenhouse - mushroom greenhouse" system, it is necessary to know its dynamic characteristics as an object of automatic control of temperatures of the substrate and circulating air.

Interest in the automation of greenhouses has now reached a significant level. The introduction of digital technologies into agricultural production has made it possible to introduce new technologies, technical information and ease of management, making crop production manageable on the basis of such technologies *(Achour, et al., 2021), (Tokmakov & Hrudynyn, 2008), (Rodrıŕguez, et al., 2001)*.

Transient processes in closed heating and ventilation systems can be quite complex, therefore, to assess the quality and accuracy of regulation, as well as to evaluate the object at any part of the transient process, it is desirable to have simulated mathematical models of these processes *(Dudnyk, et al., 2020*), (*Johansson, 1993*), which will make it possible to reduce the use of fuzzy conclusions in the microclimate management system in greenhouses, which leads to the need to use fuzzy neural networks in management *(Lysenko, et al., 2022*).

In many cases, when studying complex dynamic processes in greenhouses, systems of differential equations are solved using numerical methods (*Lendyel, 2016*).

The nature and duration of transient processes in greenhouses with large volumes of production *(Sethi, et al., 2013), (Costantino, et al., 2021)* requires modeling of these processes to evaluate the object at any part of the transient process *(Gorobec & Yatsenko, 2014), (Dudnyk, 2014)*. This issue is especially relevant for closed ventilation systems, due to their complexity.

Formulation of mathematical models for temperature dynamics in cultivation rooms with their subsequent analytical solution for plant greenhouses *(Koshkin & Babenko, 2011), (Voynova, 2007), (Berzan, et al., 2012), (Semenov & Krushel', 2009), (Takakura & Son, 2004)* and mushroom greenhouses *(Koshkin, 2015), (Peshko, 2011)*, did not consider models of temperature dynamics for the "plant greenhouse - mushroom greenhouse" system.

The task of the study was to investigate the transition processes in the system "plant greenhouse - mushroom greenhouse" and to obtain an analytical solution of the mathematical model of the dynamics of the substrate temperature and air in the system and to compare them with the results of investigational studies.

MATERIALS AND METHODS

During the investigation, differential equations characterizing the dynamic properties of objects in the "plant greenhouse - mushroom greenhouse" system were formulated and analytically solved by creating a mathematical model of air and substrate temperature dynamics.

In order to check and confirm the analytical dependences, studies of changes in air and substrate temperature were carried out in experimental greenhouses, which were connected to the "plant greenhouse - mushroom greenhouse " system (Fig. 1), where green onion was grown in the plant greenhouse, and in the mushroom greenhouse – oyster fungus. The choice of research methodology and processing of experimental data was based on the recommendations outlined in *(Hashchuk, 2002), (Trehub, 2017), (Pushkar & Protsenko, 2013)*.

The research on temperature dynamics was carried out with the aim of obtaining dynamic (accelerating) characteristics and comparing them with dynamic characteristics obtained from experimental dependencies. The method of active experiment was used to study the dynamic characteristics *(Pushkar & Protsenko, 2013), (Ryss & Hurvych, 1986)*.

During the investigation, differential equations characterizing the dynamic properties of control objects, existing schemes of ventilation systems of greenhouses and cultivation rooms for growing mushrooms were used.

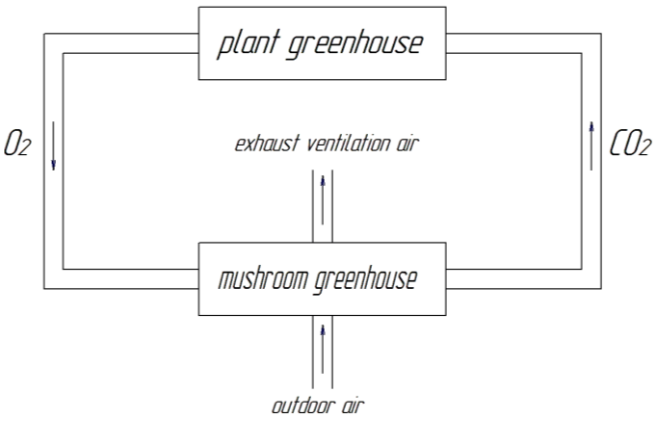


Fig. 1 - Schematic diagram of the closed system of heating and ventilation "plant greenhouse – mushroom greenhouse"

To determine the impact of the studied parameters on the processes that take place in the "plant greenhouse – mushroom greenhouse" system, a pairwise comparison of two factors was carried out, with other factors constant.

The assessment of the accuracy and reliability of the results of experiments, which contain systematic and random errors, is carried out using the methods of probability theory and mathematical statistics *(Vedenyapyn, 1973), (Drahanov, et al., 1993).*

To assess the state of the "plant greenhouse – mushroom greenhouse" system, the heat balance equation will be used (*Stroy, 1983*):

$$Q_{T.I} - Q_{H.ios} = Q_{exc} \tag{1}$$

where: $Q_{T.I}$ – total heat input to the room, [W]; $Q_{H.ios}$ – total heat loss from the room, [W]; Q_{exc} – excess ("–" deficit) of heat in the room, [W].

A positive value of Q_{exc} determines the power of the heating system, a negative value – the power of the air conditioning system.

Representing equation (1) through its components, the heat balance equation for rooms operating in the "plant greenhouse - mushroom greenhouse" system is obtained:
for the greenhouse:

$$-Q_{T.I.1} - Q_{H.1} + Q_{HL.1} - c_a \cdot \left[G_{M.1.1} \left(t_{in.2} - t_{in.1} \right) + G_{M.1.2} \left(t_{out} - t_{in.2} \right) \right] = 0 \tag{2}$$

for mushroom greenhouse:

$$-Q_{T.I.1} - Q_{H.1} + Q_{HL.1} - c_a G_{M.1.1} \left(t_{in.1} - t_{in.2} \right) = 0 \tag{3}$$

where: *1,2* – respectively, a mushroom greenhouse and a plant greenhouse; $Q_H = Q_{exc}$, [W]; Q_{HL} – heat losses due to enclosing structures, [W]; c_a – heat capacity of air, [J/(kg·K)]; $G_{M.1.1}$ – air exchange between rooms, [kg/s]; $G_{M.1.2}$ – air exchange with the outside environment [kg/s]; t_{out} – outside air temperature, [°C]; $t_{in.1}$ – air temperature in the mushroom greenhouse, [°C]; $t_{in.2}$ – air temperature in the vegetable greenhouse, [°C].

Air and substrate temperature are the main factors affecting the process of mushroom cultivation in a mushroom greenhouse, and air temperature is the main factor in growing vegetable crops in a vegetable greenhouse. To determine the dependence between the temperature of the substrate and the air in time, we will use the theoretical prerequisites outlined in (*Golub, 2003)*, where it is proposed to determine this dependence by a system of differential equations. Assuming that the air temperature in the plant greenhouse is maintained by a separate control system, then in this case the temperature of the air entering the greenhouse from the greenhouse is assumed to be constant, which makes it possible to compile the following system from two differential equations:

$$\begin{cases} \dfrac{dt_S}{d\tau} = \dfrac{q_S m_S - r m_{EV}}{m_S c_S} - \dfrac{a_S S_S}{m_S c_S} \left(t_S - t_{in.1} \right) \\ \dfrac{dt_{in.1}}{d\tau} = -\dfrac{k_{EN} S_{EN}}{m_a c_a} \left(t_{in.1} - t_{out} \right) + \dfrac{a_S S_S}{m_a c_a} \left(t_S - t_{in.1} \right) + \dfrac{k_{HD} S_{HD}}{m_a c_a} \left(t_{HD} - t_{in.1} \right) + \ldots \\ \quad \ldots + k_{E1} \left(t_{in.2} - t_{in.1} \right) + k_{E2} \left(t_{out} - t_{in.1} \right) + k_{A.INF} \left(t_{out} - t_{in.1} \right) \end{cases} \tag{4}$$

where: t_S – substrate temperature, [°C]; m_S – mass of the substrate in the mushroom greenhouse, [kg]; c_S – specific heat capacity of the substrate, [J/(kg°C)]; q_S – heat release of the substrate, [W/kg]; α_S – coefficient of heat transfer from the substrate, [W/(m^2·°C)]; S_S – the surface area of the substrate that is blown by air, [m^2]; r – specific heat of vaporization of water, [J/kg]; m_{EV} – intensity of water evaporation, [kg/s];

τ – time, [s]; m_a – air mass in the mushroom greenhouse, [kg]; k_{E1} – the multiplicity of air exchange in the "plant greenhouse – mushroom greenhouse" system, which is organized between the premises of the system, [s^{-1}]; k_{E2} – the multiplicity of air exchange in the "plant greenhouse – mushroom greenhouse" system, which is organized between the mushroom greenhouse and the external environment, [s^{-1}]; k_{EN} – coefficient of heat transfer through enclosing structures, [W/($m^2 \cdot$°C)]; S_{EN} – surface area of fences, [m^2]; S_{HD} – surface area of heating devices, [m^2]; k_{HD} – coefficient of heat transfer from heating devices, [W/m^2 °C]; t_{HD} – water temperature in heating devices, [°C]; $k_{A.INF}$ – air exchange rate of infiltration, [s^{-1}].

The general solution of the system of differential equations will be as follows:

$$t_S = C_1 \exp\left(k_1 \tau\right) + C_2 \exp\left(k_2 \tau\right) + t_S^c \quad (5)$$

$$t_{in.1} = \left(\frac{k_1}{c} + 1\right) C_1 \exp\left(k_1 \tau\right) + \left(\frac{k_2}{c} + 1\right) C_2 \exp\left(k_2 \tau\right) + t_{in.1}^c \quad (6)$$

where: k_1, k_2 – roots of the characteristic equation; C_1, C_2 – permanent solutions of the differential equation; t_S^c – constant value of the temperature of the substrate, [°C]; $t_{in.1}^c$ – constant value of the air temperature in the mushroom greenhouse, [°C]; $C = a_S S_S / m_S c_S$.

Permanent solutions of differential equations are determined from the condition that at the initial moment of time the temperature of the substrate and air are equal to their initial constant values. In the presence of incoming exciting influences (changes in the temperature of the outside air, the amount of heat released by the substrate, which depends on the intensity of the passage of biological processes in the substrate or the temperature of the supply air), new constant values of the temperature of the substrate and air are established. Therefore, this can be written as:

$$C_1 = -\frac{\left(k_2 + C\right)\left(t_S^{CB} - t_S^{CE}\right) - C\left(t_{in.1}^{CB} - t_{in.1}^{CE}\right)}{k_1 - k_2} \quad (7)$$

$$C_2 = -\frac{\left(k_1 + C\right)\left(t_S^{CB} - t_S^{CE}\right) - C\left(t_{in.1}^{CB} - t_{in.1}^{CE}\right)}{k_1 - k_2} \quad (8)$$

where: t_S^{CB}, t_S^{CE} – initial and final constant value of substrate temperature, [°C]; $t_{in.1}^{CB}$, $t_{in.1}^{CE}$ – initial and final constant value of the air temperature in the mushroom greenhouse, [°C].

The inhomogeneous differential equation of the second order that can be obtained by solving the system of equations (4), which describes the dynamic properties of the cultivation room – greenhouse system, can be represented through the Laplace transform in the form of a transfer function, which is important for the performance of functions of automatic control of the temperature of the substrate:

$$W\left(p\right) = \frac{k}{\left(T_1 + 1\right)\left(T_2 + 1\right)} \quad (9)$$

where: T_1 – response time for the substrate, [s]; T_2 – response time for the air, [s].

Checking the analytical solution of the system of differential equation (4) by solving the second-order differential equation by the Runge-Kutta method using MathCad software showed the coincidence of the results.

The experimental greenhouse of the Horticulture Department of Uman National University of Horticulture was used to check analytical dependences on temperature dynamics. The premises were equipped with a heating and ventilation system and a temperature control and regulation system.

A production inspection was carried out, the task of which was to determine the energy indicators of a closed heating and ventilation system and to compare them with the indicators obtained as a result of analytical and experimental studies.

RESULTS

Modeling of the power of the heating installation of the mushroom greenhouse and the plant greenhouse in the range of internal temperatures from 10 to 22°C according to (2) and (3) is shown in Figures 2 and 3, respectively.

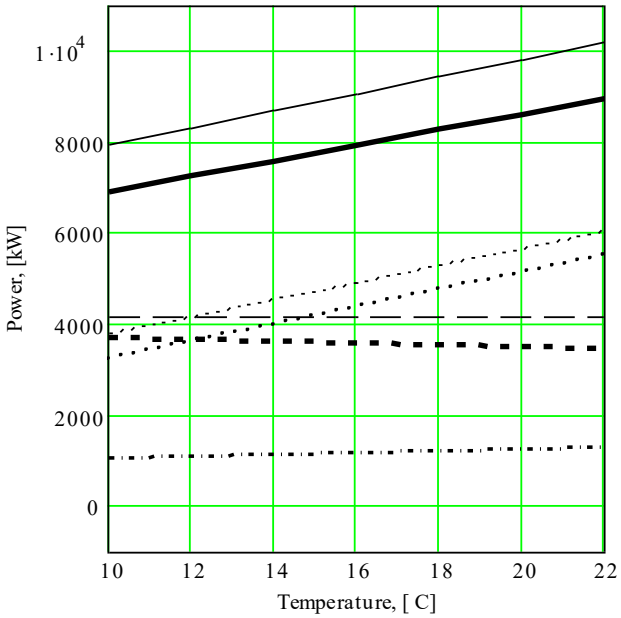


Fig. 2 - Dependence of the power of the heating system on the temperature of the internal air in the mushroom greenhouse (night)

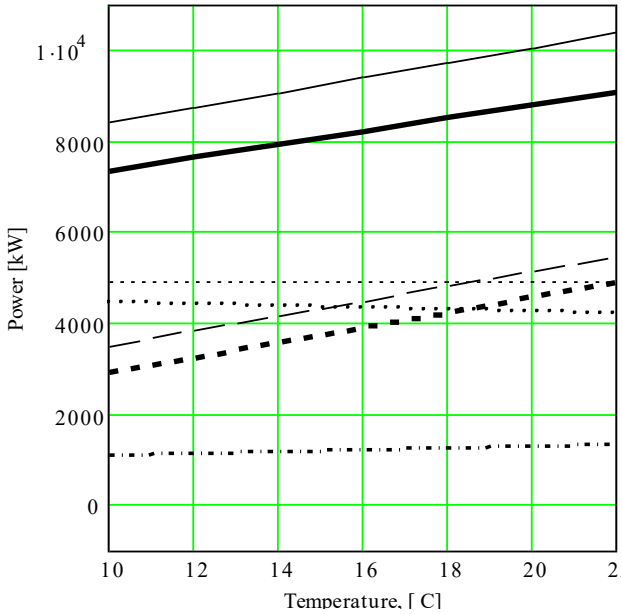


Fig. 3 - Dependence of the power of the heating system on the temperature of the internal air in the plant greenhouse (night)

Power of an open system
Power of the mushroom greenhouse in the open system
Power of the plant greenhouse in the open system
Power saving with a closed system
Power of the closed system
Power of the mushroom greenhouse in the closed system
Power of the plant greenhouse in the closed system

Heat and heat air balances for experimental mushroom greenhouse and plant greenhouse are given in Tables 1-4.

Table 1

Heat balance of the cultivation room for mushrooms

Indicator	Winter	Transition period	Summer
Outdoor air temperature, t_{out}, °C	–21	5	24
Air temperature in the room, t_{in}, °C	16	16	16
Heat input: from solar radiation, $Q_{s.r}$, kW	1.444	2.403	3.105
Other, Q_{OTH}, kW	0.599	0.599	0.5985
Total, $Q_{T.I}$, kW	2.042	3.002	3.703
Heat losses: due to enclosing structures, Q_{HL}, kW	3.857	1.131	–0.86
on infiltration, Q_{INF}, kW	0.249	0.055	–0.03
on evaporation, Q_{EVA}, kW	0.408	0.408	0.408
on heating the supply air, $Q_{I.AIR}$, kW	1.995	0.593	–0.431
Total, $Q_{H.ios}$, kW	6.508	2.188	–0.914
Excess ("-"deficit) of the heat flow, Q_{exc}, kW	–4.466	0.814	4.617

Table 2

Heat-air balance of the cultivation room for mushrooms

Indicator	Winter	Transition period	Summer
Excess ("-"deficit) of the heat flow, Q_{exc}, kW	–4.466	0.814	4.617
Inflow of air into the room, GM, kg/s	0.054	0.054	–0.523
Outdoor air temperature, t_{out}, °C	–21	5	24
Heat flow with supply air, Q_{IA}, kW	–1.132	0.27	–12.6
Heat flow for room heating, Q_H, kW	4.466	–0.814	–
Heat flow for heating supply air, $Q_{I.AIR}$, kW	1.995	0.593	–
Extraction (removal) of the air from the room, G_M, kg/s	0.054	0.054	–0.523
Air temperature in the room, t_{in}, °C	16	16	16
Heat flow with exhaust air, Q_{OA}, kW	0.863	0.863	–8.4
Balance: in the air, $G_м$, kg/s	0	0	0
in the heat flow, $Q_{баланс}$, kW	0	0	0

Table 3

Heat balance of a plant greenhouse

Indicator	Winter	Transition period	Summer
Outdoor air temperature, t_{out}, °C	– 21	5	24
Air temperature in the room, t_{in}, °C	14	14	14
Heat input: from solar radiation, $Q_{s.r}$, kW	1.197	2.462	3.387
other, Q_{OTH}, kW	0	0	0
Total, $Q_{T.I.}$, kW	1.197	2.462	3.387
Heat losses: due to enclosing structures, Q_{HL}, kW	3.983	0.992	–1.194
on infiltration, Q_{INF}, kW	0.231	0.044	–0.037
on evaporation, Q_{EVA}, kW	0.116	0.116	0.116
on heating the supply air, $Q_{I.AIR}$, kW	0.681	0.175	–0.194
Total, $Q_{H.ios}$, kW	5.011	1.327	–1.309
Excess ("-"deficit) of the heat flow, Q_{exc}, kW	– 3.814	1.135	4.696

Table 4

Air and heat balance of a plant greenhouse

Indicator	Winter	Transition period	Summer
Excess ("-"deficit) of the heat flow, Q_{exc}, kW	–3.81	1.135	4.696
Inflow of air into the room, G_M, kg/s	0.0194	0.0194	–0.448
Outdoor air temperature, t_{out}, °C	–21	5	24
Inflow of air into the room, G_M, kg/s	–0.408	0.097	–10.8
Heat flow for room heating, Q_H, kW	3.814	–1.135	–
Heat flow for heating supply air, $Q_{I.AIR}$, kW	0.681	0.175	–
Extraction (removal) of the air from the room, G_M, kg/s	0.0194	0.0194	–0.448
Air temperature in the room, t_{in}, °C	14	14	14
Heat flow with exhaust air, Q_{OA}, kW	0.272	0.272	–6.3
Balance: in the air, G_{bal}, kg/s	0	0	0
in the heat flow, Q_{bal}, kW	0	0	0

Production inspection was carried out at LLC "Slavuta" of Bila Tserkva district, Kyiv region, in order to check the efficiency of the "plant greenhouse – mushroom greenhouse" system, where oyster fungus culture (strain NK 35) was cultivated in the mushroom growing workshop (Fig. 4). The production inspection was carried out for 30 days.



Fig. 2 – Production premises (general view)

The energy efficiency of the close system of ventilation in the mushroom room was carried out as follows: one day the heating and ventilation system worked in a closed mode, and the next – in an open mode, on the third day again – in a closed mode, etc. During the inspection, the following parameters were recorded: the temperature of the external and internal air in the cultivation room and the temperature of the water in the

heating system at the entrance and exit from the room, the temperature of the water at the entrance and exit from the heater, the temperature of the air at the entrance and exit from the heater, and the temperature of the substrate. Two arrays of data, i.e. data on a closed and an open system, were statistically processed and grouped by outdoor air temperatures. Graphs constructed based on these data are shown in Figures 5, 6 and 7.

According to the obtained data, thermal energy savings during the inspection period (30 days) at "Slavuta" LLC amounted to 1,980 kW/h of heat energy, which made it possible to reduce heating and ventilation costs by 10.7%. When using "plant greenhouse – mushroom greenhouse" system during the entire cycle of mushroom fruiting, the saving of heat energy will be 4032 kW/h with a payback period of 0.64 per year.

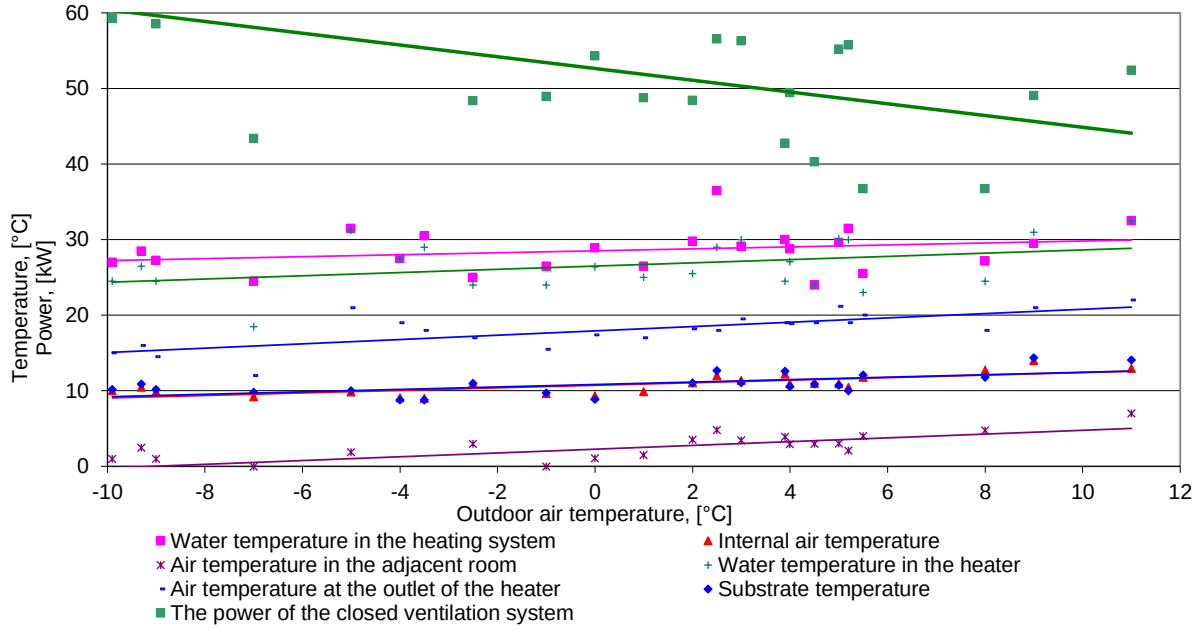


Fig. 5 – Mushroom greenhouse parameters in a closed ventilation system

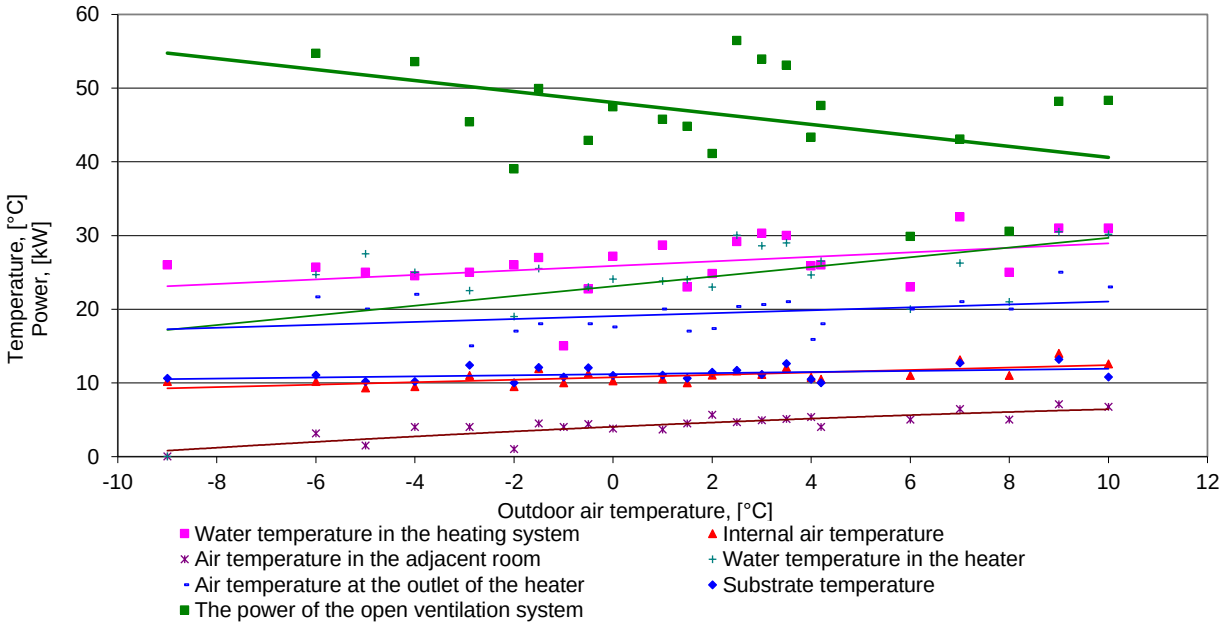


Fig. 6 – Mushroom greenhouse parameters in an open ventilation system

Experimental studies were carried out at a constant air temperature in the plant greenhouse of 14°C and at an initial temperature of the substrate of 15.2°C and air in the mushroom greenhouse of 12.9°C. An increase in the temperature of the water in the heating system of the mushroom greenhouse from 50°C to 60°C led to a transition process (Fig. 8), and new constant values of substrate and air temperatures were set at 18.8°C and 16.4°C.

Approximation of experimental data was carried out using exponential regression:

$$f\left(x\right)=a\cdot e^{bx}+c \tag{10}$$

where: a, b, c – are exponential regression coefficients.

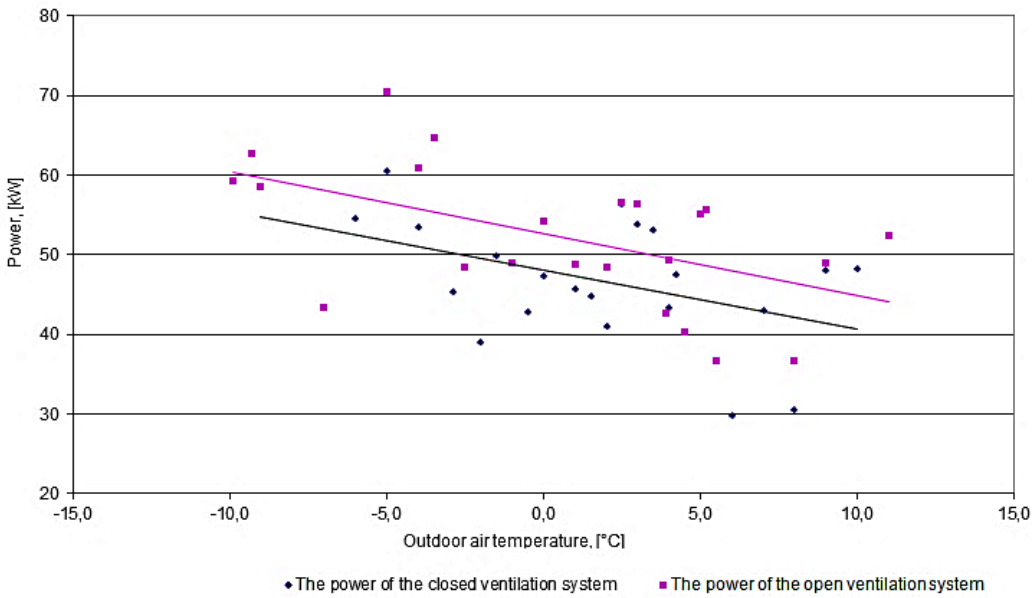


Fig. 7 – Power of mushroom greenhouse in closed and open ventilation systems

Exponential regression coefficients are given in Table 5.

Table 5

Exponential regression coefficients

Parameter	Regression coefficients		
	a	***b***	***c***
Internal air temperature	–2.55	–0.089	15.99
Substrate temperature	–3.87	–0.041	18.89

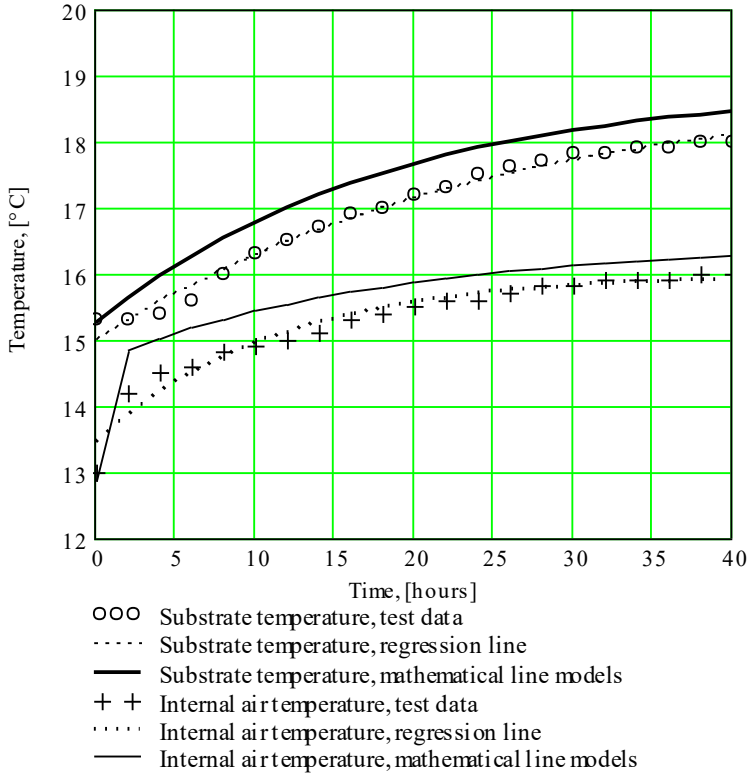


Fig. 8 - Dynamics of changes in the temperature of the substrate and air in the mushroom greenhouse when the temperature of the water in the heating system changes from 50 to 60 °C

CONCLUSIONS

1) The inspection showed that the difference between the theoretical and experimental values is not significant and amounted to 3% for the substrate temperature and 3.2% for the air temperature. Correlation coefficients, respectively, were: 0.99, 0.98.

2) The conducted comparative theoretical and experimental studies make it possible to assert the adequacy of the obtained solution of the differential equation of the temperature change of the substrate and air.

3) Depending on the conditions, the use of the "plant greenhouse – mushroom greenhouse" system makes it possible to reduce heat energy consumption by 12-20%.

REFERENCES

[1] Achour, Y., Ouammi, A., & Zejli, D., (2021), Technological progresses in modern sustainable greenhouses cultivation as the path towards precision agriculture. *Renewable and Sustainable Energy* Reviews, vol.147. https://doi.org/10.1016/j.rser.2021.111251;

[2] Berzan, V. P., Shyt, M. L., Tymchenko, D. V., Shvydchenko, S. D., Nykonorova, Y. V., Kotrutsa, A. B., (2012), Autonomous heat supply system for consumers with significantly different thermal inertia (Автономная система теплоснабжения потребителей со значительно различающейся тепловой инерцией). *Problems of regional energy*, no.1(18), pp. 64-77. https://cyberleninka.ru/article/n/avtonomnaya-sistema-teplosnabzheniya-potrebiteley-so-znachitelno-razlichayuscheysya-teplovoy-inertsiey;

[3] Costantino, A., Comba, L., Sicardi, G., Bariani, M., Fabrizio, E., (2021), Energy performance and climate control in mechanically ventilated greenhouses: A dynamic modelling-based assessment and investigation. *Applied Energy*, 288. https://doi.org/10.1016/j.apenergy.2021.116583. ISSN 0306-2619;

[4] Drahanov, B. K., Sazhyna, S. O., Serhiyenko, Y. M., Fedorov, V. H., (1993), *Thermometry in agriculture (Теплометрія у сільському господарстві).* Kyiv/Ukraine, Publishing House of the UAA, ISBN 5-7987-0144-1;

[5] Dudnyk, A. O., (2014), Synthesis and research of mathematical models of energy consumption for heating greenhouses in winter (Синтез та дослідження математичних моделей витрат енергоресурсів на опалення теплиць у зимовий період). *Scientific Bulletin of the National University of Bioresources and Nature Management of Ukraine. Series: Technology and energy of agricultural industry, no.194(3)*, pp. 218-222;

[6] Dudnyk, A., Zayets', N., Lendyel, T., Hachkovs'ka, M., & Yakymenko, I., (2020), *Development of resource-efficient modes of growing vegetable products in greenhouse complexes: monograph (Розроблення ресурсоефективних режимів вирощування овочевої продукції в тепличних комплексах : монографія).* Kyiv/Ukraine: Pritenko, ISBN 978-617-7876-19-8;

[7] Girchenko M., Golub H., Zhorov V., Vdovenko, S., Kepko O., Shapovalov L., (2003), The method of ventilation of closed soil structure (Спосіб вентиляції споруд закритого грунту)), *Patent No. 57956A*, Ukraine;

[8] Golub, G., & Kepko, O., (2017), Modelling the work of closed system of heating and ventilation of greenhouses. *INMATEH - Agricultural Engineering, Vol. 52, Issue 2*, pp. 85-90.

[9] Golub, H. A., (2003). Microclimate of mushroom growing facilities (Мікроклімат споруд для вирощування грибів). *Herald of Agrarian Science, no.*10, pp. 46-49.

[10] Gorobec, V., & Yatsenko, O., (2014), Development and heating systems mathematical model of heat and mass transfer in the greenhouse with alternative energy sources. *Energy and automation, no.1,* ISSN 2223-0858*;*

[11] Hashchuk, P. M., (2002), *Linear dynamic systems and ordinary differential equations (Лінійні динамічні системи і звичайні диференціальні рівняння)*. L'viv/Ukraine, Ukrainian technologies, ISBN 966-666-024-5;

[12] Johansson, R., (1993), *System Modeling and Identification.* NJ/USA, Prentice Hall, Englewood Cliffs, ISBN 0-13-482308-7

[13] Koshkin, D. L., (2015), Simulation model of the mushroom greenhouse microclimate control system (Імітаційна модель системи керування параметрами мікроклімату грибної теплиці). *Proceedings of the Tavri State Agro-Technological University. Technical sciences*, Melitopol/Ukraine, Vol. 2, Issue 15, pp. 230-236. ISSN 2078-0877;

[14] Koshkin, D. L., & Babenko, D. V., (2011), Dynamic model of greenhouse microclimate management (Динамічна модель керування мікрокліматом теплиці). *Herald of Agrarian Science of the Black Sea Region*(3 (60)), pp. 160-164. http://hdl.handle.net/123456789/623;

[15] Lendyel, T. I., (2016), *Energy-efficient control of the electrotechnical complex of the greenhouse taking into account the state of the biological object (Енергоефективне керування електротехнічним комплексом теплиці з урахуванням стану біологічного об'єкта : автореф. дис. ... канд. техн. наук). Abstract PhD dissertation,* National University of Bioresources and Nature Management of Ukraine, Kyiv/Ukraine, http://dglib.nubip.edu.ua/handle/123456789/3189;

[16] Lysenko, V.; Polishchuk, D.; Zaiets, N., (2022), Machine learning in scenarios of control of temperature-humidity regime for greenhouse complexes (Машинне навчання в сценаріях керування температурно-вологісним режимом для тепличних комплексів). Kyiv/Ukraine, *Scientific Works of NUFT,* Volume 28, No. 1, pp. 7-17, http://dspace.nuft.edu.ua/bitstream/123456789/37361/1/Tom_28_%23_1.pdf#page=7;

[17] Peshko, M. S., (2011), Disclosed mathematical model of the microclimate of a mushroom greenhouse (Раскрытая математическая модель микроклимата грибной теплицы). *Young scientist,* Chita. Russia, no.9(32), pp. 42-48. ISSN 2072-0297, https://moluch.ru/archive/32/3649/;

[18] Pushkar, M. S., & Protsenko, S. M., (2013), *Design of automation systems (Проектування систем автоматизації).* Dnipropetrovsk/Ukraine, National Grid University. ISBN 978-966-350-423-0;

[19] Rodrıґguez, F., Berenguel, M., Arahal, M. R., (2001). Feedforward controllers for greenhouse climatecontrol based on physical models, *European Control Conference (ECC), Porto/Portugal,* pp. 2158-2163, *DOI: 10.23919/ECC.2001.7076243, ISBN:978-3-9524173-6-2;*

[20] Ryss, A. A., Hurvych, L. Y., (1986), *Automatic temperature control in greenhouses (Автоматическое управление температурным режимом в теплицах).* Moscow/Russia Agropromizdat, P. 128;

[21] Semenov, V. H., Krushel', E. H., (2009), Mathematical model of the greenhouse microclimate (Математическая модель микроклимата теплицы). *Proceedings of the Volgograd State Technical University*, Volgograd/Russia, No.6, pp. 32-35, https://www.vstu.ru/uploadiblok/files/izvestiya/archive/2/2009-06.pdf#page=32;

[22] Sethi, V. P., Sumathy, K., Lee, C., Pal, D. S., (2013), Thermal modeling aspects of solar greenhouse microclimate control: A review on heating technologies. *Solar Energy, Vol.96*, pp. 56-82. https://doi.org/10.1016/j.solener.2013.06.034;

[23] Stroy, A. F., (1983), *Heat supply and ventilation of agricultural buildings and structures (Теплоснабжение и вентиляция сельскохозяйственных зданий и сооружений).* Kyyiv: Vishcha school.

[24] Takakura, T., Son, J. E., (2004), *Simulation of biological and Environmental Processes.* Kyushu University Press, P. 139, ISBN 487378848X, 9784873788487;

[25] Tokmakov, N. M., Hrudynyn, V. S., (2008). Mathematical model of the microclimate control system for hangar greenhouses (Математическая модель системы управления микроклиматом ангарных теплиц). *Havrysh*, no.3, pp. 28-32;

[26] Trehub, V. H., (2017), *Design of automation systems (Проектування систем автоматизації).* Kyiv: Publishing house Lira-K. ISBN 978-966-2609-58-5;

[27] Vedenyapyn, H. V., (1973), *General methodology for experimental research and processing of experimental data (Общая методика экспериментального исследования и обработки опытных данных).* Moscow/Russia: Kolos;

[28] Voynova, N. F., (2007), *Methods and systems of adaptive control of the temperature regime of greenhouses (Методы и системы адаптивного управления температурным режимом теплиц: автореф. дис. канд. техн. наук).* Abstract PhD dissertation, RSACU, Moscow/Russia.

DESIGN AND EXPERIMENT OF END EFFECT FOR KIWIFRUIT HARVESTING BASED ON OPTIMAL PICKING PARAMETERS
/
基于最优采摘参数的猕猴桃采摘末端执行器设计与试验

Zhi HE [1,2], Zixu LI [1,2], Xingting DING [1,3], Kai LI [1], Yinggang SHI [1], Yongjie CUI [*1,3]
[1] College of Mechanical and Electronic Engineering, Northwest A&F University, Yangling / China;
[2] Key Laboratory of Agricultural Internet of Things, Ministry of Agriculture and Rural Affairs, Yangling / China;
[3] Shaanxi Key Laboratory of Agricultural Information Perception and Intelligent Service, Yangling / China
E-mail: robotagricultural@163.com
Corresponding author: Yongjie Cui
DOI: https://doi.org/10.35633/inmateh-69-30

Keywords: *Kiwifruit, harvesting, robot, end effector, response surface*

ABSTRACT
A kiwifruit harvesting end effector was designed and developed to improve the efficiency of mechanized kiwifruit harvesting. Firstly, the automated kiwifruit picking process was determined according to the kiwifruit orchard working environment. Secondly, the end effector was designed and analyzed based on the principle of kiwifruit picking. Finally, an orchard experiment was conducted with the clamping force, rotation angle and rotation speed of the end effector as test factors, and the separation success rate, separation time and damage rate of kiwi fruit as test indicators. A regression model between the test factors and test indicators was established using a quadratic fitting equation to analyze the influence between the test factors and indicators. The experimental results showed that the optimal parameter was a clamping force of 3.05 N, a separation angle of 65.75°, and a separation speed of 60.03°/s. The results of the study provide theoretical basis and technical support for automated kiwifruit harvesting.

摘要
为提高猕猴桃机械化收获效率，设计并开发了一款用于猕猴桃采摘的末端执行器。首先，根据猕猴桃果园作业环境，确定出猕猴桃机械化采收作业原理。其次，根据猕猴桃采摘机理，对末端执行器的结构进行设计和分析。最后，进行果园试验，以末端执行器的夹持力，旋转角度和旋转速度为试验因素，以猕猴桃果实的分离成功率，分离时间和损伤率为试验指标，采用二次拟合方程建立试验因素和试验指标之间的回归模型，分析试验因素和指标间的影响。试验结果表明最优参数中夹持力为 3.05N，分离角度为 65.75°，分离速度为 60.03°/s。研究结果为实现猕猴桃自动化高效采摘提供理论依据和技术支持。

INTRODUCTION
China has the largest area and production of kiwifruit in the world, with a cultivation area of 193,000 hectares and an annual yield of 2.2 million tons (*Li et al., 2022; Suo et al., 2020*). Compared to other industries in the agricultural field, kiwifruit picking is still a labor-intensive industry, especially in the time-consuming and laborious harvesting process (*Mu et al., 2018; Fu et al., 2020*). Therefore, the development of kiwifruit harvesting robots is crucial to reduce the risk of artificial injury and promote the development of the kiwifruit industry (*Jin, 2020*).

In recent years, harvesting robots have achieved remarkable results in the design of end effectors (*Li et al., 2020*), picking mechanism research (*Liu et al., 2022; Bu et al., 2020*), fruit identification (*Mu et al., 2019*). However, the harvesting efficiency has always been affected by the long picking cycle of the single fruit. At present, fruit information perception is mainly studied in the mechanized picking operation of kiwifruit (*Zhou et al., 2020*), improving the mechanized picking efficiency with the improvement of fruit recognition accuracy. The existing research on kiwifruit harvesting robots reflects the problems of long picking time and low picking efficiency of kiwifruit (*Williams et al., 2020*). However, less research on improving operational efficiency is on motion control of kiwifruit harvesting robots.

In this paper, the kiwifruit picking end effector was designed and developed to solve the low efficiency of mechanized harvesting of kiwifruit. The field experiment was carried out.

He Zhi, Ph.D. Stud. Eng.; Zixu Li, M.S. Stud. Eng; Xingting Ding, Ph.D. Stud. ; Kai Li, Ph.D. Stud.; Yongjie Cui Prof. Ph.D. Eng.

The response surface method was used to determine the optimal range of picking parameters to improve the picking efficiency of the robotic arm in the fruit separation stage, taking the success rate, separation time and damage rate of kiwifruit fruit separation as the dependent variable, and the clamping force, rotation angle and rotation speed of the end effector as independent variables.

MATERIALS AND METHODS

The working principle of the kiwifruit harvesting robot

Kiwifruit adopts the planting management mode of scaffolding cultivation as shown in Figure 1(a). The trellis canopy is suitable for mechanized harvesting due to its large and flat bottom (4 m wide× 2 m spacing between fruit trees× 1.8 m high). In addition, kiwifruit show a natural drooping state due to their own gravity, as shown in Figure 1(b).



(a)Pergola planting mode *(b)Clusters of kiwifruit*

Fig.1 – Kiwifruit planting patterns

The harvesting robot was built according to the Kiwifruit harvesting operation environment as shown in figure 2. Harvesting robots mainly included the main components such as a six-degree-of-freedom robotic arm, a mobile platform, an end effector and a depth camera. The mobile platform moves the harvesting robot to the picking position. At the same time, the depth camera sends this coordinate information to the controller by obtaining the three-dimensional spatial coordinate information of the kiwifruit. Then, the robotic arm drives the end effector to pick according to the joint movement trajectory planned by the controller.

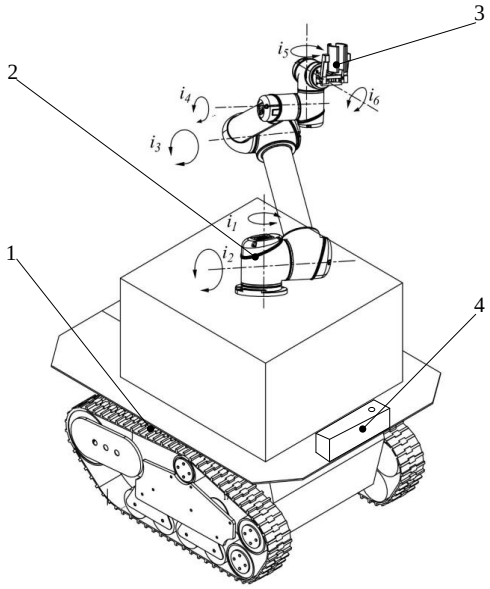


Fig. 2 – Overall structure diagram of kiwifruit harvesting robot

1 Mobile chassis; 2 Robotic arm with six degrees of freedom; 3 End effector; 4 Depth camera

The principle of kiwi fruit picking

During the manual picking operations, the separation of kiwifruit and fruit stem is often achieved by bending the fruit stalk. The resulting shear force separates the fruit from the peduncle by holding the fruit body and rotating it in an arc motion. So, inspired by the above manual picking methods, the separation law between the kiwifruit and the fruit stalk was studied in the early stage.

The results show that when the angle between kiwifruit and fruit stalk is 60°-90°, the separation force required for the fruit is the smallest (*Mu et al., 2020*). The separation process is shown in Figure 3, the separation of fruit and stem is realized, when the kiwifruit stalk moves from point B to point B1, the bending angle of the fruit stem α reaches the separation threshold.

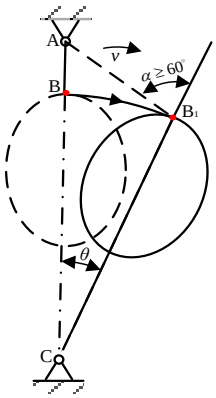


Fig. 3 – Geometric model of the kiwifruit picking method

Note: Line AB is the initial position of fruit stem of kiwifruit under natural growth; Point B is the connection point between the fruit stem and the fruit; Point C is the rotation center point of the end actuator finger; V - is the rotation speed of the end actuator around point C; θ - Rotation angle for end actuator.

During the manual picking operations, the separation of kiwifruit and fruit stem is often achieved by bending the fruit stalk. The resulting shear force separates the fruit from the peduncle by holding the fruit body and rotating it in an arc motion. So, inspired by the above manual picking methods, the separation law between the kiwifruit and the fruit stalk was studied in the early stage. The results show that when the angle between kiwifruit and fruit stalk is 60°-90°, the separation force required for the fruit is the smallest (*Mu et al., 2020*). The separation process is shown in Figure 3, the separation of fruit and stem is realized, when the kiwifruit stalk moves from point B to point B1, the bending angle of the fruit stem α reaches the separation threshold.

The overall structure design of the end effector

The end effector is mainly composed of three parts: mounting base, pneumatic hand claw and clamping device as shown in Figure 4. The mounting base forms a fixed connection between the end effector and the sixth joint of the robotic arm through screws; Under the control of the solenoid valve, the pneumatic hand claw realizes the effective grasp of kiwi fruits by driving the clamping device; The clamping device is made using 3D printing to minimize the mass of the picking end effector mechanism itself and achieve lightweight processing. The finger dimensions of the picker end effector gripper are designed to be 75 mm long× 65 mm wide × 5 mm thick.

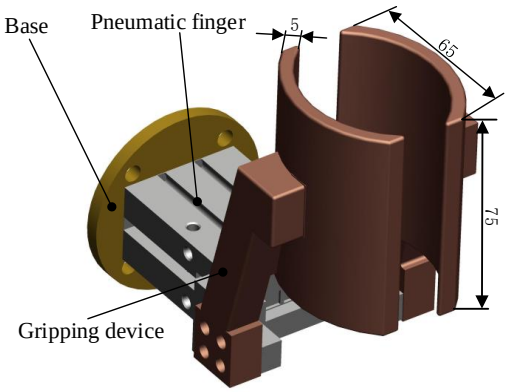


Fig. 4 – Overall Structure of End Actuator

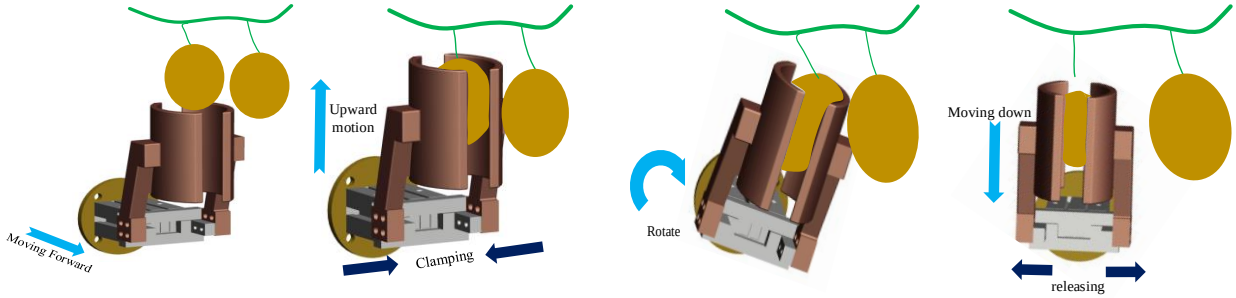
As shown in Figure 5, the kiwi fruit is spherical-like, and the kiwifruit is harvested by bottom-up picking. The process of harvesting kiwifruit with an end effector can be described as:

(1) Close to the fruit. The robotic arm moves the end effector to the base of the kiwifruit so that the center of the finger aligns with the center of the fruit.

(2) Grab the fruit. The end effector moves upwards and the fingers are closed under the drive of the cylinder to achieve the purpose of grabbing the fruit.

(3) Pick the fruit. The end effector rotates to achieve separation of fruit and stem, according to the kiwifruit picking mechanism. The kiwifruit stalk and fruit are successfully separated, when the bending angle of the kiwifruit stem reaches the separation threshold.

(4) Unload the fruit. Spread your fingers to finish picking the fruit. Then get the coordinates of the next target space to be picked.

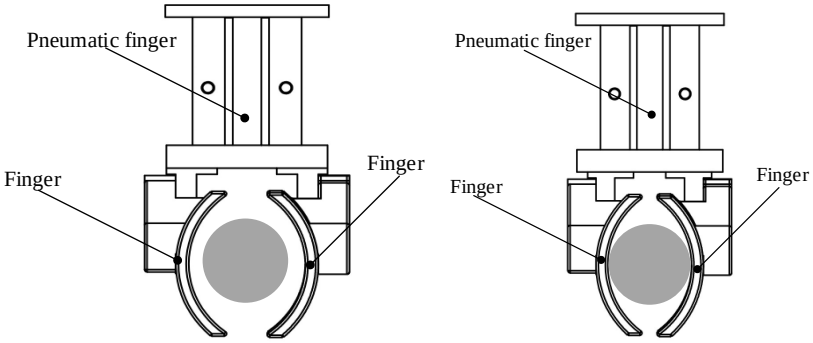


(a) Close to the fruit (b) Grab the fruit (c) Pick the fruit (d) Unload the fruit

Fig. 5– Picking Diagram of End Actuator

Dynamic analysis of the clamping mechanism

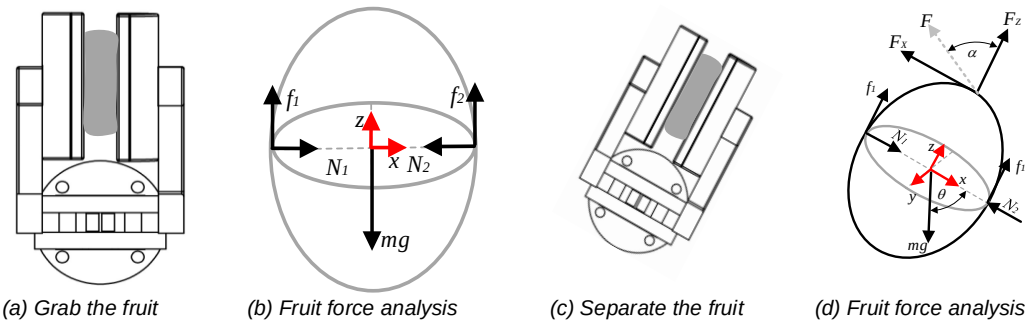
The clamping mechanism consists of two fingers, as a part in direct contact with the fruit. As shown in Figure 6, it has two open and gripping states under the drive of pneumatic hand jaws. The mechanical gripping device cannot apply dynamic pressure through the soft and hard state of the fruit, unlike manual gripping. Therefore, it is necessary to adjust the finger support force, by calculating the movement law of the grasping mechanism and by analyzing the dynamics of the grasping mechanism.



(a) Open state (b) Grasping state

Fig. 6 – Operating schematic diagram of the clamping device

The grasping device needs to complete the two actions of grasping the fruit and separating the fruit, according to the picking mechanism of kiwifruit. The force on the kiwifruit itself is analyzed, during of grasping and separating the kiwi fruit with the designed end effector. The fruit force of the two stages is shown in Figure 7. In the grasping of the fruit, there are two contact points between the fingers and the fruit, the positive pressure between the two contact points is N_1 and N_2 , and the friction in the vertical direction is f_1 and f_2. In the fruit separation stage, the rotation angle of the grasping mechanism is θ , and the separation force between the fruit and the peduncle is F.



(a) Grab the fruit (b) Fruit force analysis (c) Separate the fruit (d) Fruit force analysis

Fig. 7 – Kinetic analysis of end effector

In the fruit grasping stage, to ensure that there is no slippage between the fingers and the fruit, it is necessary to meet:

$$\begin{cases} N_1 = N_2 \\ f_1 + f_2 = mg \end{cases} \quad (1)$$

To ensure that there is no relative movement between the fruit and fingers, the friction force is expressed as:

$$\begin{cases} f_1 = \mu N_1 \\ f_2 = \mu N_2 \end{cases} \quad (2)$$

Where:

μ is coefficient of friction, m is fruit mass, N_1, N_2 is normal force, f_1, f_2 is frictional force.

It can be concluded from Formula (1) and Formula (2) that the normal force between fingers and fruit should meet:

$$N_1 \geq \frac{m \cdot g}{2\mu}$$

As shown in Figure 7(d), the fruit breaks apart from the peduncle under tangential shear force by rotating the end effector until the angle between the fruit and the peduncle reaches the separation threshold.

The separation process of the fruit is a uniform movement, so all directions need to meet:

$$\begin{cases} F\cos\alpha + f_1 + f_2 = mg\cos\theta \\ F\cos\alpha + N_1 = N_2 + mg\sin\theta \end{cases} \quad (3)$$

Where:

F is separation force, θ is rotation angle, α is separation threshold.

In addition, considering that kiwifruit is a non-rigid body, it is prone to deformation during the picking process. Therefore, in order to successfully separate the fruit and achieve the purpose of non-destructive harvesting, the gripping force of the fruit needs to meet:

$$N_1 \geq \frac{mg\sin(\alpha - \theta)}{2\mu\sin\alpha} \quad (4)$$

Experimental conditions

The test site was selected at the Kiwifruit Experimental Station of Meixian County of Northwest A&F University (geographical location is 34°07'39" north latitude, 107°59'50" east longitude, altitude 648 m). The test was carried out using a prototype of a kiwifruit harvesting robot as shown in Figure 8. The prototype mainly included end effectors (pneumatic claws: SMC, MHZL2-20D; Solenoid valve: OLK, 4V210-08), depth camera Kinect 2.0 (Microsoft, USA), mobile platform with tracked chassis (Guoxing Intelligence, China), robotic arm UR5 (Universal Robot, Denmark).

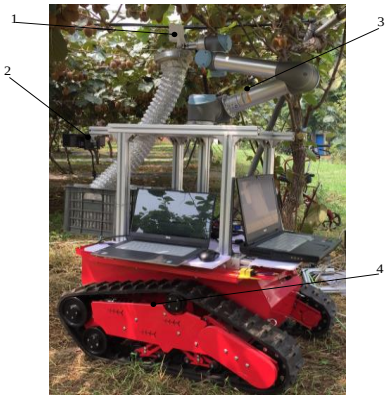


Fig. 8 – Kiwi fruit harvesting robot

1 - End effector; 2 - Kinect camera; 3 - UR5 Mechanical arm; 4 - Mobile chassis

Test parameters and methods

To optimize and determine the optimal conditions for fruit separation, picking tests of scaffolding cultivated kiwifruit were carried out. Firstly, the picking area is randomly selected, the picking area is 600mm*650mm. Secondly, the number of kiwifruits in the picking area was counted.

Each group of experiments operated on 5 picking areas, 20 kiwifruits were picked in each area. If there are less than 20 kiwifruits, the next picking area is selected. Then, the end effectors are set up and adjusted for picking. Finally, the number of successful separations, separation time and damage during the picking process is counted.

The harvesting robot adjusts and sets the end effector before the kiwifruit harvest. Firstly, the air pressure of the pneumatic grip is adjusted to control the clamping force of the fingers. Secondly, the rotation angle and speed of the end effector are adjusted by planning the joint angle movement of the sixth joint of the robotic arm. Finally, positioning accuracy in picking operations is improved by hand-eye calibration and calibration of the end effector dimensions.

The factors affecting the separation efficiency of the robot mainly include finger clamping force, end effector rotation angle and speed. Experimental studies are carried out on finger gripping force, end effector rotation angle and speed to obtain the best parameters. Taking the success rate of fruit separation, fruit separation time and damage rate as evaluation indexes, according to the agronomic requirements of kiwifruit harvesting process. The success rate of fruit separation is the ratio of the number of successfully picked fruits to the total number of fruits that can be picked. The separation time is the time spent in the four stages of fruit picking at the end effector; The damage rate is the ratio of the number of damaged fruits to the total number of fruits successfully picked. The previous studies have shown that when the pressure is less than 15N and the corresponding pressure is 18.8KPa, the fruit is not damaged at this time, so the pressure sensor is used to judge the measured pressure value to judge the fruit damage during the picking process.

Experiment design and analysis

The quadratic regression orthogonal rotation combination test scheme was adopted. The quadratic regression orthogonal rotation combination test scheme was adopted. Finger clamping force X1, end effector rotation angle X2 and rotation speed X3 were taken as test factors, success rate of fruit separation Y1, fruit separation time Y2 and harvesting damage rate Y3 were taken as the evaluation indicator of the test. Table 1 shows the controlling factors and their levels. Quadratic regression equations for the test factors and test indicators are established, using Design-Expert software and experimental design schemes and results. The experimental design scheme and results are shown in Table 2.

The regression equation is:

$$Y_1 = 84.40 + 2.13X_1 + 1.88X_2 - 0.25X_3 - 0.25X_1X_3 - 0.25X_2X_3 - 1.95X_1^2 - 1.45X_2^2 - 1.20X_3^2$$

$$Y_2 = 1.89 - 0.04X_1 + 0.4963X_2 - 0.5738X_3 + 0.08X_1X_2 - 0.015X_1X_3 - 0.2075X_2X_3 + 0.0323X_1^2 + 0.1398X_2^2 + 0.4447X_3^2$$

$$Y_3 = 7.2 + 4.13X_1 + 0.375X_2 + 3.0X_3 + 0.50X_1X_2 + 1.25X_1X_3 + 0.25X_2X_3 + 3.15X_1^2 - 0.85X_2^2 + 0.40X_3^2$$

Table 1

Experimental factor coding

Code	Finger clamping force (N)	End effector rotation angle (°)	Rotation speed (°/s)
-1	1N	50	30
0	3N	65	60
1	5N	80	90

Table 2

Experimental design and protocol

Serial No	factor			index		
	X1	X2	X3	Y1	Y2	Y3
1	-1	-1	0	77	1.74	5
2	1	-1	0	81	1.51	13
3	-1	1	0	81	2.45	5
4	1	1	0	85	2.54	15
5	-1	0	-1	79	2.94	5
6	1	0	-1	84	2.82	10
7	-1	0	1	79	1.88	9

Serial No	factor			index		
	X1	X2	X3	Y1	Y2	Y3
8	1	0	1	83	1.82	19
9	0	-1	-1	80	2.34	4
10	0	1	-1	84	3.87	4
11	0	-1	1	80	1.49	9
12	0	1	1	83	2.19	10
13	0	0	0	85	1.65	6
14	0	0	0	84	1.95	7
15	0	0	0	83	1.71	9
16	0	0	0	87	2.01	7
17	0	0	0	83	2.12	7

The analysis of variance of the experimental results is shown in Table 3. The significance level of the experimental index model is in a state of extremely significant difference, and the misfit term is greater than 0.05. Experimental results show that the three regression equations have high fitting degree and the model is statistically significant.

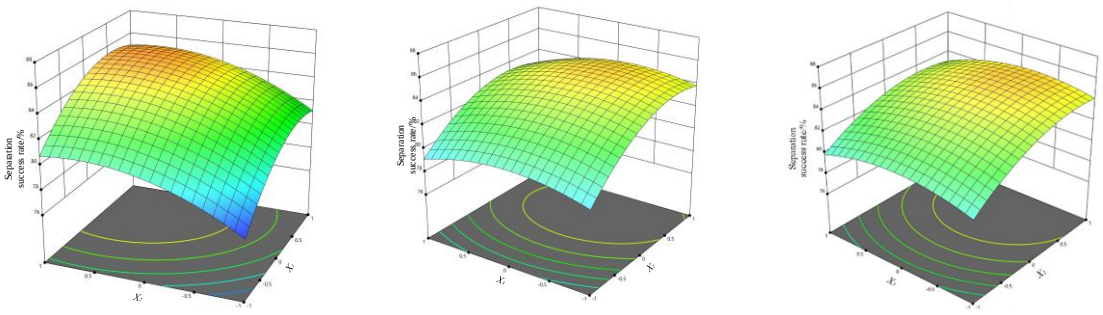
In the Y_1 model, X_1 and X_2 had a significant impact on the model, X_1^2 had a significant impact on the model, and other factors had no significant impact on the model. In the Y2 model of separation time, X_2, X_3 and X_3^2 had a significant effect on the model, while other factors had no significant influence on the model. In the Y_3 model of damage rate, X_1, X_2 and X_1^2 had a significant impact on the model, X_2X_3 factors had a significant impact on the model, and other factors had no significant influence on the model.

Table 3

Analysis of variance

variance source	Separation success rate Y_1				Separation time Y_2				Damage rate Y_3			
	Sum of squares	Free degree	F	p	Sum of squares	Free degree	F	p	Sum of squares	Free degree	F	p
model	99.61	9	6.77	0.0098**	5.78	9	20.52	0.003**	261.69	9	31.07	<0.0001**
X1	36.13	1	22.09	0.0022**	0.0128	1	0.4097	0.5425	136.13	1	145.48	<0.0001**
X2	28.13	1	17.19	0.0043**	1.97	1	63.06	<0.0001**	1.13	1	1.20	0.3091
X3	0.5000	1	0.3057	0.5976	2.63	1	84.29	<0.0001**	72.00	1	76.95	<0.0001**
X1 X2	0.0000	1	0.0001	1.0000	0.0256	1	0.8194	0.3955	1.0000	1	1.07	0.3356
X1 X3	0.2500	1	0.1528	0.7075	0.0009	1	0.0288	0.8700	6.25	1	6.68	0.0362*
X2 X3	0.2500	1	0.1528	0.7075	0.1722	1	5.51	0.0513	0.2500	1	0.2672	0.6212
X12	16.0105	1	9.79	0.0166*	0.0044	1	0.1402	0.7192	41.78	1	44.65	0.0003**
X22	8.8526	1	5.41	0.0529	0.0822	1	2.63	0.1488	3.04	1	3.25	0.1144
X32	6.0632	1	3.71	0.0956	0.8329	1	26.66	0.0013**	0.6737	1	0.7200	0.4242
residual	11.45	7			0.2187	7			6.55	7		
Misfit term	0.2500	3	0.0298	0.9920	0.0578	3	0.4792	0.7140	1.75	3	0.4861	0.7101
error	11.20	4			0.1609	4			4.8	4		
sum	111.06	16			6.00	16			268.24	16		

Note : indicates significant difference (P<0. 05); **Indicates a very significant difference (P<0. 01)*



(a) (b) (c)

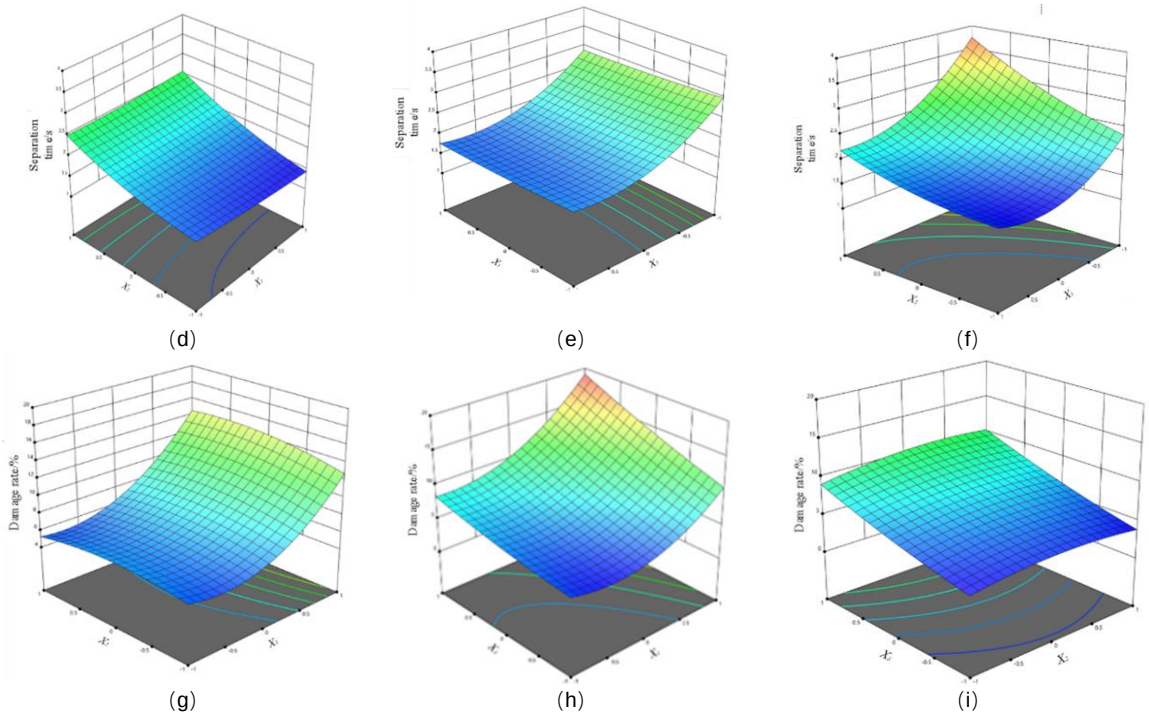


Fig. 9 – Response surface of interaction factors to performance indicators

Analysis of the effect of interaction factors on performance

Fig. 9(a)(b)(c) shows the influence of interaction factors on the success rate of fruit separation. Overall, the end effector rotation speed is moderate, and the higher the clamping force and rotation angle, the higher the success rate of fruit separation. The greater the clamping force, the fewer times the kiwifruit will slip during the separation process and the higher the success rate of separation. In addition, kiwifruit stalks and trunks are non-rigid materials. Deformation occurs during fruit separation: the rotation angle of the end effector is too small to make the separation angle not reach the separation threshold. As a result, the kiwifruit peduncle is not separated. The greater the rotation angle, the greater the success rate of separation between the stem and the kiwifruit. The rotation speed has no effect on the success rate of fruit separation.

Figure 9(d)(e)(f) shows the effect of interaction factors on fruit separation time. In general, the lower the angle of rotation of the end effector, the faster the rotation speed and the less time for kiwifruit separation. In addition, the size of the clamping force has no effect on the kiwifruit separation time.

Figure 9(h)(i)(j) shows the effect of interaction factors on fruit damage rate. In general, the greater the end effector clamping force, the faster the rotation speed, and the higher the kiwifruit damage rate. The greater the clamping force, the greater the pressure per unit area of the kiwifruit, resulting in damage during the harvesting process. In addition, if the rotation speed is too large, it will cause the surrounding branches and fruits to vibrate in the moment of separating the fruit. This vibration causes fruit to collide with fruit. During the next harvesting process, the vibrating fruit and the end effector are prone to collision. The effect of rotation angle on damage rate is not obvious.

Optimal parameter combination solution

The separation success rate, separation time and damage rate of each parameter are optimized to improve the fruit separation efficiency and determine the optimal picking parameters of the kiwifruit harvesting robot.

According to the module Numerical, the optimal combination of picking parameters is solved, where the optimization constraints are:

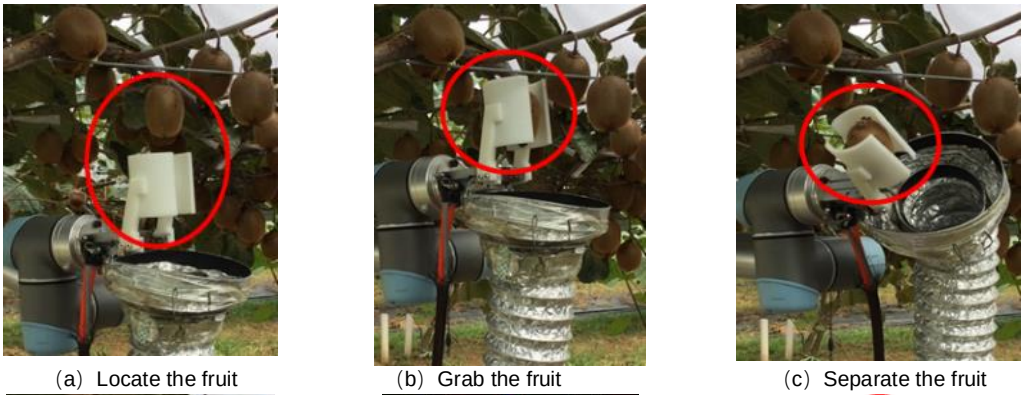
$$\begin{cases} \max Y_1(X_1, X_2, X_3) \\ \min Y_2(X_1, X_2, X_3) \\ \min Y_3(X_1, X_2, X_3) \\ s.t. \begin{cases} -1 \le X_1 \le 1 \\ -1 \le X_2 \le 1 \\ -1 \le X_3 \le 1 \end{cases} \end{cases}$$

The optimal value occurs when the clamping force level is -0.027, the rotation angle level is -0.045, and the rotation speed level is 0.001. The corresponding working parameters are 3.05 N, the rotation angle is 65.75°, the rotation speed is 60.03°/s, the separation success rate is 84.253%, the separation time is 1.866 s, and the damage rate is 7.077%.

Validation test

Experiments are carried out to verify that the obtained combination of picking parameters is optimal. The picking process is shown in Figure 10, the robotic arm moves to the picking position of the fruit to be picked according to the planned path, the end effector grabs the fruit and separates the fruit and the stem. After the harvesting is completed, the robotic arm moves to the next picking target for operation. A total of five groups of picking experiments were carried out, and 20 kiwifruits in the selected area were picked and averaged.

The verification results show that under the optimal combination of picking parameters, the separation success rate is 83%, the separation time is 1.95 s, and the damage rate is 8%. The relative error between the experimental value and the optimized value is less than 5%, and the optimization result is significant.



(a) Locate the fruit (b) Grab the fruit (c) Separate the fruit

(d) Unload fruits (e) Move to the next fruit position (f) Pick the next fruit

Fig. 10 – Kiwifruit picking process

CONCLUSIONS

A kiwifruit picking end effector was designed and developed through the basic parameters and bending picking mechanism of kiwifruit. This end effector enables continuous kiwifruit picking.

The response surface method was used to determine the optimal range of picking parameters, where the fruit separation time, damage rate and harvest success rate in the experiment were taken as indicators. The test results show that when the clamping force is 3.05 N, the separation angle is 65.75°, and the separation speed is 60.03°/s, the harvesting robot has the best picking effect.

ACKNOWLEDGEMENT

This research was funded by National Natural Science Foundation of China, grant number 31971805.

REFERENCES

[1] Bu Lingxin, Guangrui Hu, Chengkun Chen et al. (2020) Experimental and simulation analysis of optimum picking patterns for robotic apple harvesting. *Scientia Horticulturae*, 261: 108937.

[2] Fu Longsheng, Elkamil Tola, Ahmad Al-Mallahi, et al. (2019) A novel image processing algorithm to separate linearly clustered kiwifruits. *Biosystems Engineering*, 183: 184-195.

[3] Fu L.S., Wang B., Cui Y.J. (2015) Kiwifruit recognition at night-time using artificial lighting based on machine vision. *Int. J. Agric & Biol. Eng*, 8(4): 52-59

[4] Fu Longsheng, Yali Feng, Jingzhu Wu, et al. (2020) Fast and accurate detection of kiwifruit in orchard using improved YOLOv3-tiny model. *Precision Agriculture*, 1-23.

[5] Li Kai Yujia Huo YinanLiu, et al. (2020) Design of a lightweight robotic arm for kiwifruit pollinatio，g. *Computers and Electronics in Agriculture*, 198:107114

[6] Li Guoli, Ji Changying, Gu Baoxing, et al. (2016) Kinematics Analysis and Experiment of Apple Harvesting Robot Manipulator with Multiple End-effectors (多末端苹果采摘机器人机械手运动学分析与试验). *Transactions of the Chinese Society for Agricultural Machinery*, 47(12): 14-21+29.

[7] Liu J., Peng Y., Faheem M. (2020) Experimental and theoretical analysis of fruit plucking patterns for robotic tomato harvesting. *Computers and Electronics in Agriculture*, 173:105-121.

[8] Liu Fang, Liu Yukun, Lin Sen, et al. (2020) Fast Recognition Method for Tomatoes under Complex Environments Based on Improved YOLO (基于改进型 YOLO 的复杂环境下番茄果实快速识别方法). *Transactions of the Chinese Society for Agricultural Machinery*, 51(06): 229-237.

[9] Mu Longtao, Liu Haozhou, Cui Yongjie, et al. (2018) Mechanized technologies for scaffolding cultivation in the kiwifruit industry: a review. *Information Processing in Agriculture*, 5(4): 401-410.

[10] Mu Longtao, Gao Zongbin, Cui Yongjie, et al. (2019) Kiwifruit Detection of Far-view and Occluded Fruit Based on Improved AlexNet (基于改进 AlexNet 的广域复杂环境下遮挡猕猴桃目标识别). *Transactions of the Chinese Society for Agricultural Machinery*, 50(10): 24-34.

[11] Mu L., Cui G., Liu Y. et al. (2020) Design and simulation of an integrated end-effector for picking kiwifruit by robot. *Information Processing in Agriculture*, 7(1), 21-32.

[12] Rui Suo, Fg A, Zz A, et al. (2020) Improved multi-classes kiwifruit detection in orchard to avoid collisions during robotic picking. *Computers and Electronics in Agriculture*, 182: 106052.

[13] Williams H., Ting C., Nejati M. et al. (2020) Improvements to and large-scale evaluation of a robotic kiwifruit harvester. *Journal of Field Robotics*, 37(2): 187-201.

[14] Yuan Jin. (2020) Research Progress Analysis of Robotics Selective Harvesting Technologies (选择性收获机器人技术研究进展与分析). *Transactions of the Chinese Society for Agricultural Machinery*, 51(09): 1-17.

[15] Zhongxian Zhou, Zhenzhen Song, Fu Longsheng et al. (2020) Real-time kiwifruit detection in orchard using deep learning on Android™ smartphones for yield estimation. *Computers and Electronics in Agriculture*, 179: 10585

RICE MECHANIZATION IN ETHIOPIA: TRENDS, AND PROSPECTS
/
በኢትዮጵያ የሩዝ ሜካናይዜሽን: አዝማሚያዎች እና ተስፋዎች

Tikuneh DESSYE *[1)], Woldesenbet LAIKE[2)]
[1)]Ethiopian Institute of Agricultural Research, Fogera National Rice Research, and Training Center, P.O.Box: 1937, Wereta, Ethiopia
[2)] Ethiopian Institute of Agricultural Research, P.O.Box: 2003, Addis Ababa, Ethiopia
Tel: +251910419743; E-mail: Dessyebelay20@gmail.com
DOI: https://doi.org/10.35633/inmateh-69-31

***Keywords**: Agriculture, Research, Development, Challenge, Opportunity, Drudgery*

ABSTRACT
The domestic rice industry of Ethiopia is constrained by low productivity, poor quality, and old processing machines. The rice production system is done by hand or with rudimentary tools, and only 2% of households have access to tractors. It takes 175 labor days to weed and 66% of the total farm operations. Rice harvesting and threshing are done manually using a serrated sickle and animal trembling respectively. Farmers are responsible for most of the pre-milling operations and store paddy for household consumption in local stores. Challenges include fragmented farm holdings, poor marketing channels, and a lack of awareness of post-harvest utilization. The prospects for rice mechanization development include improving the rice mechanization research system, training local entrepreneurs, providing repair and maintenance services, promoting custom hiring centers, local manufacturing of farm implements, organizing agricultural cooperatives, landholding, and land ownership structures, assessing foreign experience, linking importers and service providers, and encouraging investments in the rural infrastructure.

አህፅርአት
የኢትዮጵያ የሩዝ ምርት በዝቅተኛ የምርታማነት ፣ በጥራት ጉድለት እና በጎላቀር ማቀነባበሪያ ማሽኖች የተገደበ ነው።የሩዝ አመራረት ሂደት በእጅ ወይም በቀላል የግብርና መሳሪያዎች የሚከናወን ሲሆን 2 በመቶ የሚሆኑት አምራቾች ብቻ ትራክተር ተጠቃሚ ናቸው። አረም ማረም በእጅ በመንቀል የሚተገበር፣ብዙ ጉልበት የሚጠይቅና አንድ ሰው አንድ ሄክታር ለማረምነ 75 የስራ ቀናት የሚጨርስበት ሲሆን ይህም ከጠቅላላው የእርሻ ስራ 66 በመቶውን ይይዛል። የሩዝ ሰብል የማጨድና መውቃት ስራ የሚከናወነው እንደቅደም ተከተላቸው በእጅ በተሰራ ማጭድና የእንሰሳ ትጉልበትን በመጠቀም ነው።አብዛኛዎቹ ገበሬዎች ጀንፈል ሩዝን ለቤተሰብ ፍጆታ የሚያከማቹት ደግሞ በየአካባቢው በተለመዱ የባህላዊ የምርት ማስቀመጫ ቃዎችን በመጠቀም በቤታቸው ውስጥ ነው። ከዋና ዋና የሩዝ ሜካናይዜሽን ተግዳሮቶች መካከል የተበታተኑ የእርሻ ማሳ ይዞታዎች፣ደካማ የግብይት አሰራሮች እና የድህረምርት አጠቃቀም ግንዛቤ ማነስ ጥቂቶቹ ናቸው።የሩዝ ሜካናይዜሽን እድገትን ለማሻሻል ከሚያግዙ ዕድሎች ውስጥ ደግም የሩዝ ሜካናይዜሽን የምርምር ሥርዓትን ማሻሻል፣ የአገር ውስጥ ቴክኖሎጅ አምራቾችን ማብቃት፣ የግብርና ማሽነሪዎች ጥገናና የመገጣጠም አገልግሎት ሰጪ ተቋማትን ማጠናከር፣ የግብርና ማሽነሪ አገልግሎት ሰጪ ማዕከላት ንማስፋፋት፣ የእርሻ መሣሪያዎችን በአገር ውስጥ ማምረት፣የግብርና ጎብረት ሥራ ማኅበራትን ማደራጀት፣ የመሬት ይዞታና የመሬት ባለቤትነት መዋቅሮችን ማሻሻል፣ የተሻሻሉ የሌሎችን ሀገራትን ልምድ በመገምገም መቅሰም፣አስመጪ እና አገልግሎት ሰጪዎችን ማጠናከር እና በጠር መሠረተ ልማት ኢንቨስትመንቶችን ማበረታታት ይገኙበታል።

INTRODUCTION
Rice *(Oryza sativa L.)* is an essential food crop for more than half of the population worldwide *(Ashtiani-Araghi H., et al., 2010).* It was introduced recently in Ethiopia and has been identified as "the new millennium crop of Ethiopia". It has been increasing at a rapid rate in both area coverage and farmers' involvement, reaching 121,000 tons in 2013 and 171,854 tons in 2019 *(Bekele, 2017; CSA, 2019; MoA, 2020)*. However, productivity is low compared to the potential of not suitable, marginally suitable, moderately suitable, and highly suitable areas with 39,931 ha, 312,135 ha, 629,320 ha, and 295,547 ha, respectively throughout the country or from rice hub areas *(Getachew et al., 2015).* There are seven major rice-producing areas, often named rice hubs, which are Fogera in Amhara, Pawi in Benishangul Gumuz, Abobo in Gambella, Chewaka in Oromia, GuraFerda in the Southern Nations, Nationalities, and Peoples' Region (SNNPR), May-Tsebri in Tigray, and Gode in Somali Regions *(Alemu and Assaye, 2021).* The current production is 81.2%, 18.6%, and 0.2% are rain-fed lowland, rain-fed upland, and irrigated accordingly *(Tefera, et al., 2011).*

Ethiopia's rice consumption is rapidly growing, mainly through imported rice *(Bekele, 2017).* This indicates that domestic supply is not satisfying consumer demand. Imports are increasing at an alarming rate, adding to the pressure on the country's inadequate foreign currency reserves *(Merkine, 2022).* Imports expanded from 22,500 t to 533,620 t with foreign currency payments of $12.07 million to $186.2 million between 2008 and 2019 *(Assaye and Alemu, 2020).*

The rice industry is an important source of revenue, and livelihood, which is utilized for both consumption and income to purchase household consumables. The crop has made its way into the local diet and is seen as compatible with traditional foods as well as drink-making. *Injera* (traditional flatbread) is now prepared by mixing a small amount of rice flour with Tef flour (a ratio of roughly one to five). This mixing is liked by customers because of their rising desire for the whiter-colored *Injera* that rice delivers*(Alemu, D., and Thompson, 2020).*

Rice production in Ethiopia is a labor-intensive crop, and all household members play important roles *(Kebede and Getnet, 2020).* Mechanization has the potential to save labor, increase productivity, reduce post-harvest loss, and raise the quality of rice processing. However, labor scarcity during the crop setup period prolongs the age of seedlings, and transplanting old seedlings affects rice yield *(Liu et al., 2017)*. Therefore, it is important to analyze the mechanization trends, challenges, opportunities, and prospects in rice production. This review is intended to provide a better knowledge of status and trends, as well as identify challenges and prospects. Hence, it examines the status, challenges, opportunities, and prospects of rice mechanization research and development in Ethiopia, using both academic and popular findings.

REVIEW METHODS

The review research method was divided into three phases: keyword searches were conducted using TEEAL, PubAG, JSTOR, AGRIS, local hard copies, and gray literature. Resources related to rice mechanization were also sorted sequentially in the Google and Google Scholar databases, chosen publications were evaluated and analyzed in greater depth, and research outputs from other countries were reviewed. The review is meant to be an updated version that can provide insight into research and development, as well as some early possibilities. This fast evidence evaluation was created by searching for relevant publications on the status, difficulties, possibilities, and prospects of rice mechanization both internationally and locally. It was arranged in portions step by step to provide an overview of rice cultivation and processing, including the current status, difficulties, possibilities, and threats.

RESULTS AND DISCUSSIONS

About 51 relevant documents were found in this review by assessing major databases and complementing them with gray literature. As a result, a good deal of pertinent research was discovered, such as peer-reviewed journal articles, literature reviews, forum proceedings, and conferences that give information concerning the trends and prospects of rice mechanization in Ethiopia. The methodological quality of the included studies was also examined through all sorts of investigations was included. Various trends and chances for rice mechanization in Ethiopia were discovered and thoroughly examined. As a result, the paper's conclusions are summarized into four categories: the status, obstacles, possibilities, and challenges of rice mechanization in an Ethiopian environment. The important findings on existing rice mechanization technologies in the country are discussed in detail in each chapter.

1. TRENDS OF RICE MECHANIZATION IN ETHIOPIAN

1.1. Status of Rice Mechanization

Ethiopia's rice farming practice is traditional, with small-scale producers with small farm sizes employed for land preparation, harvesting, threshing, storage, and processing *(MoA, 2020).* The status of agricultural mechanization in soil preparation, rice establishment, crop management, harvesting, cutting, collecting, threshing or winnowing, drying, and storage is backward. In the last two decades, different governmental and non-governmental organizations have tried to assess agricultural mechanized technologies in rice production, which will be discussed section by section.

1.1.1. Pre-Harvest Practices

Ethiopian agriculture is mainly smallholder farming, with 90% of farmers holding less than 2 ha per household. Oxen draft, besides human muscles, is the primary source of agricultural power for land preparation and planting *(FACASI, 2014).* The power provided by animals and people is utilized for all operations with conventional tools and implements, such as an animal-drawn "*ard-plough*" known as *"Maresha"(Kebede and Getnet, 2020).*In normal agricultural conditions, a pair of indigenous oxen is utilized to till with a draft force requirement of around 1.0 kN*(Gebreslasie et al., 2004).* The average working speed of oxen is 0.894 m/s, but the typical rate of utilizing horses is 0.75-1.07 m/s *(Geza, 1999; Gebreslasie et al., 2004).* Pre-harvest technology such as ploughs, harrows, planters, and weeders have been developed and imported from abroad, but effective implementation has been limited.

Some parts of Ethiopia, including Fogera, Gambella, and Pawe, have poorly drained Vertisol soil, making it difficult for farmers to prepare hard soil before the rainy season begins. This sticky quality of the moist soil following the onset of the rainy season creates difficulty in the timely seeding and maintenance of crops using draft animals *(Johansen et al., 2012).* All family members play a vital role in land preparation, including seed cleaning, seed drilling, and weeding *(Kebede and Getnet, 2020).* A precisely leveled field is a prerequisite for effective surface irrigation, sowing, transplanting, and harvesting operations. However, there is a challenge in developing and deploying land-leveling technology for rice production *(Getnet et al., 2019).* A household survey in the Gurafarda and Fogera plains reported that nearly insignificant farmers possess modern mechanized technology other than traditional farm tools as shown in Table 1*(Deribe et al., 2019).*

Table 1

Ownership of farm machinery and farm tools

Type of machine or tool	Ownership (%)			Maximum
	Fogera (N=278)	Gurafarda (N=65)	Total (N=343)	
Engine and manual or tool				
Two-wheel tractors	-	1.54	0.29	1
Harrow	-	1.54	0.29	1
Cultivator	-	1.54	0.29	2
Trailer	-	1.54	0.29	1
Water pump	19.06	7.69	16.91	5
Motorized water pump	14.39	1.54	11.95	2
Animal cart	3.24	-	2.62	2
Sprayer	66.55	50.77	63.56	3
Ordinary farm tools				
Plough (set) ("*Maresha"*)	91.01	86.15	89.80	5
Saw	23.02	15.38	21.57	4
Sickle and forage cutting	95.32	86.15	93.59	13
Machete	1.80	61.54	13.70	6
Hand hoe	31.29	72.31	39.07	10
Spade	46.04	50.77	46.94	3
Mattock	12.95	18.46	13.99	5
Axe	85.25	86.15	85.42	6
Fork	9.71	7.69	9.33	7

Sources: A household survey (Deribe et al., 2019).

A household survey revealed that only 2% of rice farmers had access to tractors, with 1.8% in Fogera and 3.1% in Gurafarda. Tractors are used for initial ploughing before rain when soils are hard and animal traction for the second and third times *(Ayele, 2021).* Draft power users cultivate 0.81 hectares per household *(Deribe et al., 2019).*

Table 2

The use of mechanization by sample HH (%)

Type of operation	Fogera (N=278)	Gurafarda (N=65)	Total (N=343)
Tractor ploughing	1.80	3.07	2.04
Row planting	-	1.54	0.29
Chemical spray (manual)	5.03	6.15	6.48
Harvesting/threshing	0.72	-	0.58
Polishing	28.06	-	22.74
Grain grading	0.36	-	0.29
Improved storage	-	1.54	0.29

Sources: A household survey (Deribe et al., 2019).

Rice weeding requires 175 work days and 66% of all effort for various activities, making it a labor-intensive process. Moreover, weeding requires more work than harvesting and threshing. Women contribute to farm work in other ways as well; 75% of first-time weeding is done by women. The majority of the labor used on farms is hired labor, with male labor playing the dominant role and most farm households relying on family members*(Deribe et al., 2019).*

Table 3

Total labor used by the farm operation and locations (labor days)

Farm operation	Fogera (N = 278)	Gurafarda (N =65)	Total (N =345)
Primary tillage	7.79	8.08	7.36
Secondary tillage	7.57	7.67	6.83
Tertiary tillage	3.90	3.85	4.37
Row planting	14.34	15.97	8.08
1st weeding	76.08	79.91	68.08
2nd weeding	65.44	65.87	64.42
3rd weeding	33.29	27.20	55.79
Transport of harvest	11.88	9.29	15.96
Harvesting	27.34	30.60	20.08
Threshing	17.14	18.35	13.99

Source: A household survey (Deribe et al., 2019).

Research advances have been also made in manual 4-row rice transplanters, hand-pulled 8-row IRRI seeders, and animal-drawn four-row seeders *(Getnet et al., 2019).*In this regard, the rotary and push-pull type weeders were tested and demonstrated by NRRTC in collaboration with the Africa Rice project, with the rotary weeders alone increasing the grain yield of rice by 10.9%. Puddling after 10–15 days of flooding, combined with three times weeding with a small hand weeding supplement, plays a critical role in increasing yield *(Tadesse et al., 2019).* Farmers still use the *"Maresha"* plough for pre-harvest activities, requiring the introduction of mechanization technologies such as single axle and small horsepower tractors for land leveling, puddling, seeding, transplanting, water lifting, weeding, and chemical application *(Getnet et al., 2019).*

1.1.2. Harvesting Trends

In Ethiopia, rice harvesting is done manually using a serrated sickle at a rate of 200 to 240 man-hours/ha for cutting the standing crop and 20 man-hours per hectare for collection and piling *(Kebede et al., 2019).*

As shown in Table 3, the total labor and cost used by rice farmers during harvesting, primarily in the Gurafarda and Fogera plains, were 27.66 labor days per season, respectively, with 42% of households relying on shared labor to accomplish it *(Deribe et al., 2019).* Harvesting with a sickle has a working capacity of only 0.01 ha/h, which is why labor shortages during crop harvesting are a regular problem in Ethiopia *(Islam, 2009).* The lack of mechanized harvesters is the major cause of delays and significant losses due to it, with manual harvesting taking 3–5 days per hectare and incurring losses of 2-7% *(Toquero and Duff, 1974).*

Vertical conveying reapers (VCRs) have been introduced to address the challenge of shattering during the harvesting process. The Melkassa Agricultural Research Center acquired the technologies and evaluated them on the X-Jigna rice crop variety in the Fogera area, which had a 7.1% harvesting loss at 17% grain moisture content *(Kebede et al., 2019).* The Fogera National Rice Research and Training Center (FNRRTC) has introduced and promoted different-sized VCRs, which revealed that a VCR with 4.7 hp cannot perform well. 2WT attached reaper harvesters were harvesting efficiently, even though the adoption of those technologies was not adequately conducted. However, farmers, development agents, and government officials are challenged by the cost, supply, and access to maintenance and assembly services of the technology *(Kebede et al., 2019).*

1.1.3. Post-Harvest Operations

1.1.3.1. Rice Threshing Trends

Rice threshing is typically accomplished by oxen trampling on a layer of 15-20 cm thick harvested rice stalks spread on well-compacted and plastered hard surfaces, followed by manual sweeping and gathering of the grains. It takes two people with five oxen for 10 hours to produce one ton of fairly dried rice, but it is time-consuming, drudgery, and causes huge losses due to spreading fractures and a mix-up with soil impurities *(Amare et al., 2015).* Rural networks have an important contribution, in which 33% of households rely on shared labor for threshing operations. In some places, rice is threshed by beating bunches of panicles with sticks or on small straw-prepared fields without the use of tarpaulins, plastic, or canvasses *(Mutai et al., 2018).* The threshed paddy is then cleaned by tossing it into the air and blowing off most of the light chaff and other impurities that were removed during the field winnowing and de-stoning. Grains are then lost as spillage during this operation, and losses during winnowing can be as high as 4% of the total production. Currently, some communities utilize antiquated winnowing baskets, which depend heavily on natural wind for cleaning, but have limited efficiency in separating rice from debris *(Nath et al., 2017).*

Rice threshers have been developed and evaluated in Fogera. Bahir Dar Agricultural Mechanization and Food Science Research Center developed a hold-on pedal-operated rice thresher that consists of an open rotating drum with wire loops *(Amare et al., 2015).* The Fogera Rice Research and Training Center evaluated three types of engine-driven threshers using Edget and Nerica-4 rice varieties. The *"Selam"* thresher was manufactured by the *Selam*Technical and vocational training center, while the other two were imported from Indonesia and China as shown in Table 4 *(Kebede et al., 2019).*

Table 4

Main operating performances of the three rice threshers

Parameter	Ediget Variety			Nerica-4 Variety		
	Indonesian	China	*Selam*	Indonesian	China	*Selam*
The moisture content of the crop	9.5	9.5	9.5	13.87	13.87	13.87
Threshing capacity (kg/hr.)	606.06	500	416.67	632.9	606.06	588.23
Threshing efficiency (%)	98.2	99.5	97.3	98.5	99.75	96.5
Cleaning efficiency (%)	85.34	99.21	70	86.48	97.33	74.32
Total loss (%	1.05	0.71	3.15	0.845	0.465	3.985

Source: Field performance of rice threshers(Kebede et al., 2019)

FNRRTC introduced the PKG65 model, a rubber crawler-type axial feeding rice thresher machine used to harvest irrigated and muddy paddy fields. It can move throughout the field and thresh bundles, reducing extra time loss and drudgery for collection and pile-up. Farmers preferred it during a demonstration in Fogera Plain because it was easier to manage and less oppressive of the straw. It is recommended to be scaled up and further adopted for small-scale rice farmers.

1.1.3.2. Rice Processing Trends

Rice processing is a critical stage in the rice value chain, with farmers taking their paddy to urban commercial rice processors. Farmers are responsible for most of the pre-milling operations, but only a limited number of farmers are aware of the rice polishing practice *(Deribe et al., 2019).* Due to limited knowledge of the drying process, a significant amount of rice breakage occurs during the milling process *(Kebede et al., 2019).*

Rice processing in the Fogera plain has developed remarkably, with 123 registered and licensed rice processors, with an average annual growth estimated at 34%. Nationally, the number of registered rice processors has increased from 10 in 2009 to over 150 in 2018, and a modern large-scale rice-milling factory has also started *(MoA, 2020).*

The majority of milling machine types used in the Fogera and Gurafarda areas are single-pass Engelberg types with Nx-110, N-90, and N-70 models. However, limited numbers of double-pass SB milling machines with SB10, SB30, and SB50 models are also used, with milling recovery above 60% *(Kebed et al., 2019).* Recently, some processors have purchased new combined multi-level processing machines, but they are not functional due to limited access to infrastructure and working space. Multi-level machines are also common in Gambella areas, with good quality but higher prices in the market *(Assaye and Alemu, 2020).* Table 5, below shows various machine types with different processing capacities *(APRA, 2018).*

Table 5

Common rice processing machines models with their milling capacity in Fogera plain

Machine type in the model	Processing capacity (t/hr.)
N–90	0.8-1.3
N–70	0.9-1.5
Nx–110	1.0-1.2
SB–10	0.05-0.075
SB–30	1.0-1.5
SB–50	1.8-2.3
Multi-level processing	2.5

Source: Milling machine assessment report in the Fogera Plain (APRA, 2018)

Processors are buyers and sellers of rice in Ethiopia, and have incentives to process poorly to increase the volume of by-products and sell them for livestock feed for 1 Birr to 3.5 Birr (US$0.03 to US$0.10) per kg. As grazing lands were reduced in the Fogera Plain due to the expansion of rice, stall feeding became more common *(MEDA, 2019).* Locally milled rice is poor in quality, usually consumed locally, and cannot compete with imported ones in both price and quality. Improvement of the quality of locally produced rice in terms of the physical and cooking attributes of the grain is necessary to make it competitive *(Halos-Kim, 2014).* Business relations between farmers and processors or millers and other supporting agencies are fragile, with farmers claiming that the processors and millers do not reward them for their production investments and rice buyers regretting that the farmers fail to supply quality products in sufficient quantities. Rice processors continued using older processing machines with limited ownership of other required facilities for producing quality rice *(Assaye and Alemu, 2020).*

Parboiling is the other rice processing procedure in which the paddy is soaked in warm or cold water followed by steaming and drying before milling *(Kebede et al., 2019).* It is new and domestic marketing is underdeveloped in Ethiopia, but some processors access electric rice parboiling machines through matching grants with MEDA. The FNRRTC has introduced GEM (Grain Quality Enhancer, Energy-efficient, and Durable Material) parboiling technology, and some youth groups have started to make money through parboiling and byproduct processing. Continuous training and capacity building of processors and farmers are essential for the sustainable quality improvement of the rice processing industry *(Assaye and Alemu, 2020).*

1.1.3.3. Rice Grain Storage and Packaging

Rice post-harvest losses in Ethiopia are estimated to be 10-22%, with qualitative losses as high as 50%. Sun drying is the common drying method in the value chain before storage and processing *(Kebede et al., 2019).* Most Ethiopian farmers store paddy for household consumption in local stores, with Gotera, gotta, keffo, golota, meaqen, walla, jute or Hessian sacks, skin bags (aqomada/loqota, aybet), clay jars, gourds, wooden boxes, metal drums or barrels, and underground pits *(Tadesse et al., 2008).*

On the other hand, processors, and assemblers in small towns store their goods in 50-100 kg plastic or polythene bags that are sewed with a nylon string using a hand sewing tool *(Kebede et al., 2019).* Domestic rice packaging at the retailer's level is also at 0.25, 0.5, and 1 kg using plastic bags. These packaging methods expose the stored grains to different deterioration agents, while the appropriate management and monitoring of the entire set of influencing factors haven't been considered.

Pest infestation due to insects and rodents causes huge losses and is incapable of protecting long-term storage; the grain is periodically fumigated to control insect infestation but may cause long-term health cases.

The FNRRTC has demonstrated rice-sealed storage units of metal silos and PICS bags in the Fogera plain *(Kebede et al., 2019).* These technologies are used on sorghum, maize, and soybean crops in Ethiopia's four major regions to reduce stored grain losses for at least six months *(Obeng-Ofori, 2011).* A metal silo storage facility is a cylindrical structure with a capacity of 300-1000 kg made of 0.5 mm thick galvanized iron sheet. PICS bags are made up of three nested plastic bags and are suitable for the hermetic storage of dry grains. Metal silo and PICS bag storage methods offer economic impact by facilitating storage and sale later in the season when grain prices are higher *(Kebede et al., 2019).*

The collaboration of the Melkassa agricultural research center around grain storage technologies, specifically metal silos, was distributed and adopted in 2017, depending on the interest of rice farmers. About 150 silos were produced and distributed to farmers through a cost-sharing approach by the MEDA project. Six local manufacturers from Fogera, Dera, and Libokemkim were selected, trained, and certified.

1.2. Challenges in the rice mechanization

Despite increased rice production and area coverage in several sub-districts, rice mechanization remains limited and falls short of potential due to a lack of skilled manpower, credit, policy support, land fragmentation, lack of customized tools, farm machinery access, legislation, and other related issues *(Bekele, 2017).* Land size, cropping pattern, and market price are the major factors determining agricultural mechanization, and the average farm size per household in the main rice production plains of Gurafarda and Fogera is 2.40 ha and 0.89 ha, respectively *(Deribe et al., 2019).* Mechanizing small and non-contiguous groups of small farms is against economies of scale because the continued shrinkage in average farm size will make it difficult for individual ownership of agricultural machinery and progressively more uneconomical *(Sims and Kienzle, 2017; Mehta et al., 2014).* Small and fragmented land holdings or subsistence agriculture are the main impediments to the promotion of agricultural mechanization in the country, with similar conditions in other countries like Nepal *(Shrestha, 2011).*

The most important details in this document are that the country's mechanization development is hindered by a poor marketing channel and a lack of knowledge about mechanization management and utilization. Despite the existing demand for tractors, harvesters, and rice processing machines, farmers had poor access to services, such as a lack of credit to pay for hiring services and limited access to credit for the purchase and ownership of machines. Additionally, the country was importing tractors and other farm implements mainly from China, which was not up to the desired standard, resulting in poor quality of work, longer downtime, low output, and high operational costs. Besides, due to the country's lack of foreign currency, the prices of imported machinery are very high and out of reach for poor farmers. As a result, some farmers and processors have lost faith in mechanization technologies *(Derbe et al., 2019).*

The existing imported agricultural machinery, spare parts, and workshops in Ethiopia do not have standardized quality control facilities to ensure their quality. There should be a common facility center for agricultural machinery and spare parts production, and agricultural machinery testing and certification. Implementation of appropriate-scale agricultural mechanization would be a solution for sustaining the development and growth of the sector. Advisory, training, and technical services should work in collaboration with the BoA, suppliers, and dealers, and an adequate skilled workforce in the agricultural engineering field of study is critical. Private and governmental training centers are not efficiently available in rice-based farming, and the sub-sector is lacking at almost all levels of repair, maintenance, and management of farm machinery.

The other essential concepts in this text are the low access to research facilities on rice-based mechanization technology in Ethiopia. National rice research and development is mandated under the FNRRTC, but the agricultural mechanization workshop and laboratory facilities are not sufficiently organized.

Day-to-day research is conducted through the introduction of technologies from abroad, followed by validation and participatory evaluation for further adoption. External support and cooperation are inadequate, and the annual budget allocation for research is limited. Domestic capital expenditure on agriculture has shown a sharp decline recently, and neither loan-based nor assistance-based financing of the sector seems to be sustainable. The government allocated more than 10% of its budget to agricultural development, but agricultural mechanization and its development plans should have received more attention *(Alemayehu, 2002).*

In Ethiopia, there is no comprehensive policy or actionable plan for agricultural mechanization *(Tamrat, 2016).* In recent years, the Ministry of Agriculture and the Ethiopian Agricultural Transformation Agency (ATA) initiated the "Ethiopian National Agricultural Mechanization Strategy" in 2014, but it has not made any deals about the rice mechanization sector. This gap could be a sign of the slow expansion and development of agricultural mechanization in the country. Farmers in rural areas are characterized by poor road infrastructure and quality, isolation from markets, a lack of vehicles, and inefficient truck logistics, further increasing transport costs and discouraging them from commercializing their production. Mechanized farming needs access from farm machinery to the crop field, but most rural areas do not have adequate farm roads *(Alam and Khan, 2017; Islam, 2018).*

The public sector should have the role of putting in place policies to enable farmers to supply, assemble, maintain, and service farm machinery *(FAO, 2014).* Private repair and maintenance workshops are mostly equipped with repairing parts, but operators are not readily available at the district level. After-sales service of farm machinery is also a concern, as the majority of farmers are cost-conscious. Ethiopia's government offers free credit to farmers and local service providers, but it is not well organized and utilized in the Fogera and GuraFarada areas of the Amhara and SNNP regions respectively.

1.3. Opportunities for Rice Mechanization Development

Ethiopia has the potential to develop rice mechanization due to its 30 million ha of rain-fed rice production and ten river basins with the potential for irrigated rice *(MoA, 2010).* The vast potential area suitable for rice farm topography, especially in Fogera and Gurafarda, is the flat to moderate slope, making it less likely to affect the use of agricultural machinery. Demand factors have driven Ethiopian smallholder farmers to start rice production, and market-related opportunities include higher price value of rice grains and increased rice consumption habits *(Alemu, 2015).*

The MoA with ATA initiated the establishment of the Agricultural Mechanization Strategy, which aims to increase national productivity through enhanced and sustainable use of agricultural mechanization technologies to support Ethiopia's middle-income country by 2025. It aims to raise all levels of Ethiopian agricultural mechanization from 0.1 kW/ha to 1 kW/ha, reduce the use of animal power by 50%, promote the usage of agricultural mechanization technologies that can be used by female farmers, mitigate environmental degradation, and address at least 50% of the needs of pastoralists and agro-pastoralists through mechanization inputs *(MoA, and ATA, 2014).* The National Rice Research and Development Strategy has been developed by MoA with the close collaboration of the different organizations that compile overall rice research and development direction in the country. The research side of the strategy is intended to be implemented by FNRRTC and other research centers, but they need to build capacities such as agricultural machinery workshops and laboratories.

The increase in production, import, and consumption of rice has received attention from the government and development partners *(Alemu and Assaye, 2021).* Relevant stakeholders have shown their interest in playing their roles to realize the introduction and utilization of farm mechanization technologies through on-farm demos and partnerships with all national and international stakeholders *(Belete, 2019).* Free taxes and duties on imported agricultural machinery have made the import of agricultural machinery cheaper, motivating local importers to supply at cheap prices. Both governmental and private financial institutions and credit centers are available in the Ethiopian economy, but special attention should be given to collateral *(Kamruzzaman et al., 2009).* Banks now offer hire-purchase loans for agricultural machinery but are dominated by government banks. The motivations of farmers for agricultural mechanization technology will also be an opportunity to motivate the speed of technology adoption.

1.4. PROSPECTS OF RICE MECHANIZATION IN ETHIOPIA

Ethiopian smallholder farms need to shift to labor-saving devices and products to increase agricultural productivity, and appropriate mechanization technologies should be available to reduce drudgery and increase productivity *(Ayele, 2021; Diao et al., 2016).* Based on a review of various studies, recommendations are drawn for the development of rice mechanization in Ethiopia.

1.4.1. Institutional Strengthening

The Rice Mechanization Research System should focus on the physical capacity building of workshop machines, laboratory instruments, and on-farm test sites to promote farm mechanization. Establishing maintenance and assembly centers with adequately trained agro-mechanics and workshop technicians is needed for the promotion of mechanization extension programs. Capacity building of indigenous entrepreneurs is essential for the production of farm machinery prototypes that are adapted to fragmented lands and small holdings. Large-scale demonstrations are required to conduct research and development institutions, and feedback collection on the technologies' usage by end-users is essential. Farmers cannot learn overnight, and they need regularly updated processes of lifelong learning.

1.4.2. Facilitate Corporate Farms

Organizing agricultural cooperatives would be better because they could buy their inputs and sell their total produce together. Various joint farming ventures are profitable experiences in New Zealand, Canada, Portugal, Denmark, Norway, the Netherlands, France, and the UK *(Macken-Walsh and Roche, 2012).* The average farm landholding in Ethiopia is less than 2 ha and is decreasing due to the increasing population. Land holdings need to be consolidated to give their owners access to the benefits of agricultural mechanization. Ethiopia's mountainous terrain and fragmented land holdings mean that promoting small-scale machinery can be suited to Ethiopian conditions. Small-scale mechanization can be suitably used for highly fragmented land with a vibrant private sector, academic engagement in policy processes, and localized technology interventions.

1.4.3. Integrating Public-Private Partnership

Ethiopian researchers and higher learning institutions have a critical role to play in investigating mechanization options. There is a need for a clear division of roles between the public and private sectors. The public sector is best suited to providing subsidies, reducing transaction costs, and promoting the use of new technology *(Atilaw et al., 2017).* Experiences from African and Asian countries suggest that public-sector-supported private-sector mechanization is the best model *(Agricultural Mechanization Forum of Ethiopia, 2018).* Sales outlets that are within easy reach of farmers are essential to the development of a successful and sustainable private farming system *(Clarke, 2000).* Special attention is needed to create conditions so that importers, distributors, and small retail outlets can develop. These commercial units may range from a small, one-family shop in a village to a large national distributor for domestically produced and imported machinery.

1.4.4. Improve the Rice Value Chain

The supply chain approach to analyzing mechanization is a useful framework to describe the extent and typology of mechanization processes taking place in Ethiopia. The supply chains for mechanization cover the manufacturing and importation of machines, mechanized service provision, and spare parts and repair services for machinery maintenance *(Diao et al., 2016).* Ethiopia's Ministry of Agriculture needs to promote an improved paddy and milled rice marketing system, with the possibility of incorporating rice into the Ethiopian commodity exchange trading platform *(Assaye and Alemu, 2020).* The government of Ethiopia must prioritize mechanization throughout the entire rice value chain, not just at the production level. More focus should be placed on post-harvest and processing technologies that assist in boosting the commercialization of farmers' production *(A Malabo Montpellier Panel, 2018).*

Local manufacturers should be supported wherever possible to create implements and equipment adapted to local circumstances. Lessons to be adopted from the Chinese experience in making mechanization accessible to smallholder farmers are subsidies, strong extension services, and infrastructure development *(Sims and Kienzle, 2016).*

1.4.5. Strengthening the Local Manufacturers

Training of local manufacturers and maintenance personals on small-scale mechanization

technologies should be conducted on the operation, maintenance, assembly, and management of agricultural machinery. Experiences from emerging countries like India, China, Brazil, Thailand, Bangladesh, Nepal, the Philippines, Myanmar, etc. showed that the rapid expansion in farm machinery demand has stimulated the growth of local machinery manufacturing. Local manufacturing of farm tools and implements is another crucial factor for the sustainable development of agricultural mechanization in Ethiopia *(FAO and UNIDO, 2008).* The fabrication of metal silos is a good example of what can be done to increase their market locally and is an opportunity for the local manufacturing industry *(Singh, 2015).* Private sector-led mechanization has been growing, with improvements in two-wheel tractors. The Nazareth Tractor Assembly Plant in Ethiopia assembles roughly 300 tractors per year, which accounted for 46% of tractors entering the Ethiopian market between 2005 and 2010 *(World Bank, 2012).*

1.4.6. Infrastructure Investments

Promoting rural infrastructure investment attracts investment in agricultural infrastructure, particularly irrigation, and roads, and adds value to farm outputs through agro-processing at the community level *(FAO and UNIDO, 2008).* Roads should be constructed in rural areas for the movement of tractors, bulldozers, combines, and other heavy farm implements and machinery. Farmers must have local access to the inputs they need, including seeds and fertilizers, electricity, and water, as well as machinery and the supporting infrastructure that mechanization requires. Despite local government pledges to guarantee the availability of electricity and access to reliable power for industrial purposes, rice processing is still challenged by it and needs to be overcome before processing expansion can be realized. Proposals to professionalize rice processing in Ethiopia include providing formal training for the operation and maintenance of rice processing facilities and increasing the availability of agricultural machinery and equipment *(Assaye and Alemu, 2020).*

1.4.7. Finance and Credit Facility

Increased capitalization of agriculture needs sources of finance on favorable terms, whether from the private sector alone or a blend of private and public capital. The financial sector should work with commercially oriented farmers and entrepreneurs to strike the necessary financial deals that are required for increasingly commercialized farming *(FAO and UNIDO, 2008).* Enabling smallholder farmers' access to credit is part of the policies and strategies to improve the productivity of farmers. Commercial banks should be available to farmers at lower interest rates, and co-operatives and microcredit institutions should serve as intermediaries between formal banks and smallholder farmers *(Clarke, 2000).* Microfinance institutions should offer a basic credit facility for both low-cost and motorized equipment including crop protection and irrigation tools.

1.4.8. Safe and Friendly Mechanization Technology

Ethiopia could continue to use animal traction in a combination with engine power by making significant innovations in the implements and by improving the oxen's body condition. The progressive farmers in the hills are in search of appropriate agricultural tools and machinery, but they fail to get into the local markets. Experience shows that for small farmers, the pathways for mechanization technology, especially tractor adoption, are between two-wheel tractors (2WTs) and four-wheel tractors (4WTs). Ethiopia's government has a lot to learn from Asian and African experiences, as well as from its own experience. In Ghana, promoting affordable, smaller tractors suitable for local soil and farming conditions is a key part of the agricultural development strategy. In Thailand, 2WTs have been increasingly adopted, substituting for the use of draft animals, while 4WTs are dominant in India and Nepal *(Agricultural Mechanization Forum of Ethiopia, 2018).* Strategically selecting appropriate technologies and practices from other rice-producing countries in Africa and Asia and adapting them to Ethiopian conditions is also a critical recommendation. Policymakers need clear options backed by evidence. Research reports recommended that strategizing the training and outreach activities of NRRTC is essential to strengthening the capacity for research-based selection of safe and friendly mechanization technologies in all value chain actors and stakeholders of the national rice mechanization system *(Alemu and Thompson, 2020).*

1.4.9. Policy Recommendations

The most important concepts in this section are the structures of landholding, incentives and support measures for mechanization, preferential treatment on capital machinery importation, and multiple value-added taxes on imported raw materials.

Land consolidation is the most important policy instrument, and legislation on land leasing, contract farming, and land banking are suggested options for promoting the mechanization and commercialization of agriculture *(Clarke, 2000).* Tax and subsidy rationalization is needed to promote the use of farm machinery without distorting the market. An immediate work plan is needed for the development of strategies and action plans for the implementation of the new Agriculture Mechanization Promotion Policy. Other critical issues to be considered are custom hiring support of a mechanization service provision through private and cooperative agents, improving smallholder access to mechanization, and unleashing human energy. Mechanization should be part of the government's long-term economic development strategy. This review was developed to help entrepreneurs and advocacy groups involved not only in rice but also in agricultural mechanization in the general start or continue a dialogue with policymakers and major donors to develop policies and programs that will allow the nexus to grow and provide transformative services to communities.

CONCLUSIONS AND RECOMMENDATIONS

Ethiopia is importing rice at more than three times the amount it is producing domestically. Rice mechanization has the potential to increase productivity by saving labor, minimizing drudgery, reducing post-harvest loss, and increasing rice quality. In the last two decades, different governmental and non-governmental organizations and the private sector have been involved in accessing rice mechanization technologies. However, the status of agricultural mechanization indicated that each rice production system was done by hand or with rudimentary tools or types of equipment, as well as traditional animal-drawn implements. Draft power is so important for primary tillage that 93% of households rely on livestock, primarily oxen.

Rice harvesting is done manually using a serrated sickle for cutting the standing crop and a further 20 man-hours/ha for collection and piling. Farmers are responsible for most of the pre-milling operations, with 78.8% of the farmers selling unprocessed rice. Processors and assemblers are also in small towns and are stored in their homes, mill houses, or small storage rooms using 50 to 100 kg plastic bags. The major challenges and constraints to this low level of rice mechanization are fragmented farm holdings, poor marketing channels, a lack of awareness of pre-harvest management and utilization, a scarcity of pre-and post-harvesting technologies, lack of finance and a lack of hiring service providers, an intensive cropping pattern, a supply of poor quality machines, an inadequately skilled workforce, and limited research facilities.

However, Ethiopia has some opportunities for rice mechanization research and development, such as the development of a mechanization strategy, free taxes and duties on imported agricultural machinery, suitable rice farm topography, farmer motivation and awareness of agricultural mechanization technology, and the establishment of a national rice research and training center (NRRTC). Hence, the way forward for this low level of rice mechanization is improving the research system, training local entrepreneurs, repair and maintenance services, promoting custom hiring centers, local manufacturing of farm tools and implements, organizing agricultural cooperatives, improving landholding and landownership structures, assessing foreign experiences, linking machine importers and service providers, and encouraging investments in the rural infrastructure.

ACKNOWLEDGMENTS

The authors would like to acknowledge Dr. Tilahun Tadesse for revising critically this review and giving final technical support during manuscript development. The authors would like to thank MEDA and AfricaRice projects for their technical and financial support of the mechanization research system in FNRRTC.

REFERENCES

[1] A Malabo Montpellier Panel. (2018). Mechanized: Transforming Africa's agriculture value chains (A Malabo Montpellier Panel Report 2018).

[2] Agricultural Mechanization Forum of Ethiopia. (2018). *Agricultural Mechanization Technical Brief A Publication of the Agricultural Mechanization Forum – Ethiopia, Addis Ababa, Ethiopia,*

[3] Agricultural Policy Research in Africa (APRA). (2018) Rice Processors' Survey, Unpublished, Future Agricultures Consortium.

[4] Alam M. and Khan I. N. (2017). Agricultural Mechanization: Status, Challenges, and Opportunities in Bangladesh. In: Gurung, T.R., Kabir, W., and Bokhtiar, S.M. (eds.). 2017. *Mechanization for Sustainable Agricultural Intensification in SAARC Region*. SAARC Agriculture Centre, Dhaka, Bangladesh,pp41- 70.

[5] Alemayehu, G. (2002). Macro-policy and Agricultural Development in Ethiopia. Geberehiwot et al. (eds). *Proceedings of the 11th Annual Conference of the Ethiopian Economy*, Nov. 2 – 4, 2001.Ethiopia.

[6] Alemu, D. (2015). Rice in Ethiopia: Progress in Production Increase and Success Factors. *6th CARD General Meeting*.

[7] Alemu, D. and Thompson, J. (2020). *The Emerging Importance of Rice as a Strategic Crop in Ethiopia, Working Paper 44*, Brighton: Future Agricultures Consortium

[8] Alemu, D., and Assaye, A. (2021). *The Political Economy of the Rice Value Chain in Ethiopia : Actors, Performance, and Discourses Working Paper*No. 051; Issue 051.

[9] Ashtiani-Araghi H., Sadeghi M., Hemmat A. (2010). Physical properties of two rough rice varieties affected by moisture content. *International Agrophysics*. 24: 205-207.

[10] Assaye, A., and Alemu, D. (2020). *Enhancing production of quality rice in Ethiopia* : *Dis/incentives for rice processors* (22).

[11] Atilaw, A., Alemu, D., Bishaw, Z., Kifle, T., and Kaske, K. (2017). Early Generation Seed Production and Supply in Ethiopia: Status, Challenges, and Opportunities. *Ethiop. J. Agric. Sci*, 27(1), 99–119.

[12] Ayele, S. (2021). The resurgence of agricultural mechanization in Ethiopia : rhetoric or real commitment ? *The Journal of Peasant Studies*. https://doi.org/10.1080/03066150.2020.1847091

[13] Bekele, M. (2017). *Agricultural Water Management and Smallholder Rice Production in Ethiopia (EDRI Research Report 30).*

[14] Clarke L.J. (2000). *Strategies for agricultural mechanization development, the roles of the private sector and the government*. Rome, Italy.

[15] CSA (Central Statistical Agency). (2021). Agricultural Sample Survey, Report on Farm Management Practices (Private Peasant Holdings, *Meher* Season). *Statistical Bulletin*, Volume III. Central Statistical Agency (CSA), Addis Ababa, Ethiopia.

[16] Amare D., Yayu N., and Endeblihatu A. (2015). Development and Evaluation of Pedal Thresher for Threshing of Rice. *American Journal of Mechanics and Applications*. Retrieved on 10/23/2018 at http://www.sciencepublishinggroup.com/j/ajma

[17] Deribe, Y., Solomon, A., and Getnet, B. (2019). Diagnosis of Farm Power Sources and Mechanization in Major Rice Producing Areas in Ethiopia. *Proceeding of the National Conference on Completed Agricultural Economics Research Activities*, 1–27.

[18] Diao, X., Silver, J., and Takeshima, H. (2016). *Agricultural Mechanization and Agricultural Transformation: African Transformation Report 2016: Transforming Africa's Agriculture* (Issue February).

[19] Farm Mechanization and Conservation Agriculture for Sustainable Intensification (FACASI) (2014). Development of Agricultural Mechanization in Ethiopia and the Role of National Policies. In *FACASI Project*, First Draft Version (Vol. 1), Addis Ababa, Ethiopia.

[20] Food and Agriculture Organization (FAO) and United Nations Industrial Development Organization (UNIDO). (2008). *Agricultural Mechanization in Africa. Time for Action*. Vialedelle Terme di Caracalla, 00153 Rome, Italy, http://www.fao.org/3/k2584e/k2584e.pdf.

[21] Food and Agriculture Organization (FAO). (2014). *The State of Food and Agriculture: Innovation in family farming*, Rome, Italy.

[22] Gebreslasie, M., Gebregziabher, S., Mouazen, A.M., De Baerdemae- ker, J., Deckers, J., Nyssen, J., Hubert, V., (2004). Soil-tillage tool interaction for the vertisols of the Ethiopian highlands: a review (Poster). In: *Proceeding of the European Agricultural Engineering*. AgEng Leuven 2004. The conference, 12–16 September, Leuven, Belgium, pp. 830–831.

[23] Getachew T. A. and Solomon A. B. (2015). Land Suitability Analysis for Rice Production: A GIS-Based Multi-Criteria Decision Approach. *American Journal of Geographic Information System* 4(3): 95-104. DOI: 10.5923/j.ajgis. 20150403.02

[24] Getnet, B., Alebachew, M., and Ageze, M. (2019). Research on Pre-harvest Technologies for Rice Production in Ethiopia. In T. Tadesse, M. Atnaf, D. Alemu, T. Tadesse, & K. Shiratori (Eds.), *Advances in Rice Research and Development in Ethiopia*. EIAR, Addis Ababa, Ethiopia.

[25] Geza, M., (1999). Harnessing techniques and work performance of the draft horse in Ethiopia. In: Starkey, P., Kaumbutho, P. (Eds.), Meeting the Challenges of Animal Traction. A Resource Book of the Animal Traction Network for Eastern Africa (ATNESA), Harare, Zimbabwe. *Intermediate Technology Publications*, London, p. 326.

[26] Halos-Kim L. (2014). Promoting Rice Post-harvest Handling and Processing Technologies in Ethiopia. Experience in Rice Mechanization. FRG II project, *Empowering Farmers' Innovation*, Series No. 6. Ethiopian Institute of Agricultural Research.

[27] Islam, A. K. M. S. (2018). Status of rice farming mechanization in Bangladesh. *Journal of Bioscience and Agriculture Research*, 17(01), 1386-1395. https://doi.org/10.18801/jbar.170118.171

[28] Islam, D. M. S. (2009). Farm Mechanization for Sustainable Agriculture in Bangladesh: Problems and Prospects. Farm Mech. Sustain. Agric. Bangladesh Probl. Prospect. *5th APCAEM Tech. Comm. Meet. Expert Gr. Meet. Appl. Agric Mach. Sustain. Agric*.pp.14- 16. United Nations Asian Pac 2007.Journal of Development Studies, 53:1502-1517.

[29] Johansen, C., Haque, M. E., Bell, R. W., Thierfelder, C., & Esdaile, R. J. (2012). Conservation agriculture for small holder rainfed farming: Opportunities and constraints of new mechanized seeding systems. *Field Crops Research*, 132, 18-32.

[30] Kamruzzaman, M., Mannan, M. A., Mohanta, U., Hossain, M., and Sarkar, T. (2009). Scope of Mechanization in Rice Cultivation : A Case Study ina Village "Joshpur" Under Comilla District of Bangladesh. *Intl. J. BioRes*., 7(1).

[31] Kebede, L., and Getnet, B. (2020). *Promotion of Rice Mechanization in Ethiopia: Concept Note*. Addis Ababa, Ethiopia.

[32] Kebede L., Getnet B., Lema Y., Alebachew M. and Ageze M. (2019). Post-harvest Processes and Advances to Introduce Loss-reducing Technologies for Rice. In T. Tadesse, M. Atnaf, D. Alemu, T. Tadesse, and K. Shiratori (Eds.), *Advances in Rice Research and Development in Ethiopi*a. EIAR.

[33] Liu, Q., Zhou, X., Li, J., Xin, C., (2017). Effects of seedling age and cultivation density on agronomic characteristics and grain yield of mechanically transplanted rice. *Sci. Rep.* 7, 1–10.

[34] Macken-Walsh, Á., and Roche, B. (2012). *Facilitating farmers' establishment of farm partnerships: A participatory template*. In Teagasc. Carlow, Ireland. https://www.teagasc.ie/media/website/publications/2012/Facilitating_Farmers_Establishment_of_Farm_Partnerships-a_Participatory_Template.pdf

[35] Mehta, C.R., Chandel, N.S., and Senthilkumar, T. (2014). Status, Challenges, and Strategies for Farm Mechanization in India. *Agricultural Mechanization in Asia, Africa and Latin America*, 45(4), 43–50.

[36] Merkine-Mogiso. (2022). On-farm Evaluation of Agronomic Management Practices on Yield of Upland Rice in Kaffa zone. *Journal of Agriculture and Aquaculture*, 4(3). https://zenodo.org/record/6652025#.Y1p5P2dBzb0

[37] MoA (Ministry of Agriculture). (2020) *National Rice Development Strategy-II (2020 – 2030). Addis Ababa: Ministry of Agriculture*. https://riceforafrica.net/images/countries/NRDS_rev/ethiopia_nrds2.pdf

[38] MoA, and ATA. (2014). *Ethiopian National Agricultural Mechanization Strategy: Vision, Systemic Challenges and Strategic Interventions*.

[39] Mutai, E. B. K., Ochieng, M., and Swaleh, M. (2018). Design and Fabrication of a Pedal Powered Paddy Rice Thresher. *International Journal of Innovative Research in Engineering and Management (IJIREM)*, 5(6).

[40] Nath, B.C., Nam, Y.-S., Huda, Md.D., Rahman, Md.M., Ali, P. and Paul, S. (2017) Status and Constrain for Mechanization of Rice Harvesting System in Bangladesh. *Agricultural Sciences*, 8, 492-506. https://doi.org/10.4236/as.2017.86037

[41] Obeng-Ofori, D. (2011). Protecting grain from insect pest infestations in Africa: producer perceptions and practices. *Stewart Postharvest Rev*, *3*(10).

[42] Shrestha, S. (2011). *Status of Agricultural Mechanization in Nepal.*(Vol. 4. www.unapcaem.org

[43] Sims, B., and Kienzle, J. (2017). Sustainable agricultural mechanization for smallholders: what is it and how can we implement it? *Agriculture*, *7*(6), 50.
[44] Sims, B., and Kienzle, J. (2016). Review: Making Mechanization Accessible to Smallholder Farmers in Sub-Saharan Africa. *MDPI: Environments*, 3(11), 1–18. https://doi.org/10.3390/environments3020011
[45] Singh, G. (2015). Agricultural Mechanization Development in India. *Ind. Jn. of Agri. Econ.,* 70(1).
[46] Tadesse, A. A. Ayalew, E. Getu, and Tefera T. (2008). Review of research on postharvest pests. In Increasing crop production through improved plant protection, volume I, ed. A. Tadesse, 475–562. *Plant Protection Society of Ethiopia and EIAR*, Addis Ababa, Ethiopia.
[47] Tadesse, Z., TilahunTadesse, Dejen, T., and Molla, T. (2019). Research on Rice Cultural Practices in Ethiopia. In T. Tadesse, M. Atnaf, D. Alemu, T. Tadesse, and K. Shiratori (Eds.), *Advances in Rice Research and Development in Ethiopia*. pp.1–311. Ethiopian Institute of Agricultural Research. https://www.researchgate.net/profile/Dawit_Alemu/publication/339042455_Advances_in_Rice_Research_and_Development_in_Ethiopia/links/5e3a7533458515072d80278c/Advances-in-Rice-Research-and-Development-in-Ethiopia.pdf#page=13
[48] Tamrat Gebiso Challa. (2016). Prospects and Challenges of Agricultural Mechanization in Oromia Regional State-Ethiopia, Policy Perspectives. *American Journal of Agriculture and Forestry*. 4(5):118-127. DOI: 10.11648/j.ajaf.20160405.12
[49] Tariku, S. (2011). An Overview of Rice Research in Ethiopia. In K. Assefa, D. Alemu, K. Shiratori, and A. Kirub (Eds.), *Challenges and Opportunities of Rice in Ethiopian Agricultural Development* (Issue 2). Ethiopian Institute of Agricultural Research.
[50] Toquero, Z. F. and Duff, B. (1974). *Survey of Post Production Practices among rice farmers in Central Luzon*, Los Banos, Philippines. IRRI.
[51] World Bank. (2012). *Agribusiness Indicators*: Ethiopia. Report no. 68237-ET. Washington DC: World Bank.

EFFECT OF AGING TIME AND VACUUM DRYING ON PROXIMATE ANALYSIS AND AMINO ACID LEVELS OF GOAT MILK KEFIR
/
EFEK WAKTU AGING DAN PENGERINGAN VAKUM PADA ANALISIS PROKSIMAT DAN TINGKAT ASAM AMINO DARI KEFIR SUSU KAMBING

Aman SANTOSO*[1)], Lilik Eka RADIATI[2)], Evi DAMAYANTI[3)], Armaini ARMAINI[4)], Amiroh NABILAH-MUJAHIDAH[1)], Eli Hendrik SANJAYA[1)], Muntholib MUNTHOLIB[1)]; Muhammad Roy ASRORI[1)]

[1)] Department of Chemistry, Faculty of Mathematics and Natural Sciences, Universitas Negeri Malang/ Indonesia;
[2)] Department of Animal Product Technology, Faculty of Animal Science, Universitas Brawijaya/ Indonesia;
[3)] Faculty of Human Ecology, IPB University;
[4)] Department of Chemistry, Faculty of Mathematics and Natural Sciences, Universitas Andalas/ Indonesia.
Tel: +62815599559691; E-mail: aman.santoso.fmipa@um.ac.id
DOI: https://doi.org/10.35633/inmateh-69-32

Keywords: *milk product, fermentation, drying method, chemical characteristics*

ABSTRACT
Goat milk kefir has high nutritional value, especially in protein and calcium content and has a low lactose content. Vacuum drying is an alternative to remove the water content in kefir so that it can extend the shelf life because it inhibits bacterial growth. This study determines the effect of aging time and drying time using vacuum drying method on the characteristics and amino acid composition of goat milk kefir (kefir and powder kefir). Fermented goat milk (24 hours) use kefir grains without aging and with aging times of 1, 2, 3, 4 (week). The total titrated acid and fat content were significantly different in kefir, but it is not significantly different in powder kefir. The yield, moisture, ash, protein, fiber, and fat in both kefir and powder kefir did not show significant differences. The best treatment based on the exponential comparison method for both powder kefir and kefir was 3 weeks of aging time. Therefore, the amino acid components in powder kefir and kefir underwent changes. The highest total amino acids in kefir was kefir without aging. The highest amino acid of powder kefir was obtained after 2 weeks of aging time.

ABSTRAK
Kefir susu kambing memiliki nilai gizi tinggi terutama pada kandungan protein dan kalsium serta memiliki kandungan laktosa rendah. Pengeringan vacuum drying merupakan salah satu alternatif untuk menghilangkan kadar air pada kefir sehingga dapat memperpanjang lama waktu simpan karena mampu menghambat pertumbuhan bakteri. Penelitian ini bertujuan untuk mengetahui pengaruh waktu aging dan waktu pengeringan dengan metode pengeringan vakum terhadap karakteristik dan komposisi asam amino kefir susu kambing (kefir dan kefir bubuk). Susu kambing fermentasi (24 jam) menggunakan butiran kefir tanpa waktu aging dan dengan waktu aging 1, 2, 3, 4 (minggu). Kandungan total asam dan lemak yang dititrasi berbeda nyata pada kefir, namun tidak berbeda nyata pada kefir bubuk. Rendemen, kadar air, abu, protein, serat, dan lemak baik pada kefir maupun kefir bubuk tidak menunjukkan perbedaan yang nyata. Perlakuan terbaik berdasarkan metode perbandingan eksponensial untuk kefir bubuk dan kefir bubuk adalah waktu aging 3 minggu. Oleh karena itu, komponen asam amino pada kefir bubuk dan kefir mengalami perubahan. Total asam amino tertinggi pada kefir tanpa aging. Komponen asam amino bubuk kefir tertinggi diperoleh setelah waktu aging 2 minggu.

INTRODUCTION
Milk is a food with high nutritional content. Milk has a very high-water content, which is around 87.5% and is equipped with 5% sugar (lactose) content, 3.5% protein and 3-4% fat (*Suhartanti & Septian, 2014*). The protein content in milk is very rich in lysine, which is an important amino acid that cannot be produced by the human body (*Nyakayiru et al., 2020*). In addition, milk also contains calcium, phosphorus and vitamin A which are very beneficial for the body (*Woźniak et al., 2022*).

Among the various types of milk, goat milk can be consumed directly (*Nayik et al., 2021*). Every 100 g of goat milk contains higher essential and non-essential amino acids than cow's milk, namely Thr, Ileu, Leu, Lys, Met, Cys, Phe, Tyr, Val, Arg, His, Ala, His, Asp, Glu, Gly, and Pro (*Raynal-Ljutovac et al., 2008*). Goat milk has natural antiseptic properties, has a mild laxative effect and contains easily digestible fat (*Clark & Mora García, 2017*). Even though it has many health benefits, goat milk is less desirable because of the distinctive bad aroma and the goaty flavor it has (*Nayik et al., 2021*).

Even though milk has excellent nutritional content, not everyone can get the good benefits from milk (*Santoso et al., 2020*). This is caused by lactose intolerance and protein intolerance. In addition, the durability of milk is very limited or easily damaged at room temperature (*Santoso et al., 2021*). To extend the shelf life, usability and increase the economic value of milk, it is necessary to apply a processing technique, one of which is through the fermentation process (*Santoso et al., 2023*). The fermentation process can lower the lactose content by hydrolyzing lactose to galactose and lactose (*Yamamoto et al., 2021*).

In the post-Covid-19 pandemic era, people tend to pay more attention to a healthy lifestyle, including the consumption of healthy foods (*Timpanaro & Cascone, 2022*). The shift in the paradigm of this society causes the need for functional food ingredients to increase. Functional food ingredients are food products that not only have nutritional value, but also provide health benefits. One of the functional food products is kefir (*Sulmiyati et al., 2019*). Kefir is a dairy product produced from the alcoholic acid fermentation of milk using kefir seeds (*Kesenkaş et al., 2017*). Kefir has many health benefits such as increasing body immunity and overcoming various diseases (*Aryanta, 2021*). In addition, kefir-derived exopolysaccharides have significant anti-obesity effects which may be due to their involvement in changes in the gut microbiota (*Lim et al., 2017*).

Based on previous research (*Sulmiyati et al., 2018*), it showed that goat milk kefir has better quality compared to kefir made from cow's milk. Goat milk kefir has high nutritional value, especially in protein and calcium content and has a low lactose content (*Satir & Guzel-Seydim, 2023*). The superiority of goat milk which contains short-chain fatty acids and easily digestible protein makes the quality of goat milk kefir also better. In addition, yeast in kefir has proteolytic activity which is used to support the growth of lactic acid bacteria by releasing peptides and amino acids (*Ferreira et al., 2010*).

Kefir amino acid levels are affected by the milk used (*Nurliyani et al., 2014*). The fact that the total amino acid content of goat milk was higher when compared to cow's milk, especially in the levels of valine, isoleucine, leucine and lysine (*Nayik et al., 2022*).

Long shelf life is one of the important factors in the provisions of production standards. Based on previous research (*Putri et al., 2020*), at cold temperatures (5-10°C) kefir can be stored for up to 24 days without damage to kefir. The aging requires low temperatures so the consistency of kefir quality can be maintained. Based on these problems, powder kefir was developed to extend the shelf life of kefir at room temperature.

Powder kefir can be produced through several methods. Previous research *(Nurwantoro et al., 2020)* has carried out kefir drying using the freeze drying, spray drying, and cabinet drying methods with the best treatment obtained by using spray drying method. However, spray drying method still requires a relatively long time (36 hours) and is carried out at high temperatures, so it can cause denaturation of protein compounds and reduce protein levels. Besides, spray drying method is less economic. As an alternative, vacuum drying method is a potential method which is mild operation temperature and takes less time than conventional drying (*Kresnowati et al., 2018*). Vacuum drying promotes a hermetic seal to prevent leakage, so external contamination is prevented from penetrating into the oven. Previous studies, vacuum drying was applied for production of fermented cassava flour (*Kresnowati et al., 2018*). Vacuum drying also used to get butterfly-pea milk powder (*Hariadi et al., 2023*). The studies reveal that vacuum drying does not significantly remove the valuable content of the products.

This study aims to determine the chemical characteristics and composition of amino acids with different aging times and to determine the effect after being dried using vacuum drying method. The effect of aging time and using vacuum drying is evaluated for improving the product value. Determination of amino acid composition is carried out in order to evaluate the change of amino acid contents.

MATERIALS AND METHODS

The used materials were goat milk kefir, gum arabic, NaOH 0.1 N, phenolphthalein indicator, methylene blue indicator, methylene red indicator, selenium mixture, H_2SO_4 p.a. (Sigma Aldrich), aquades, NaOH p.a. (Sigma Aldrich), H_2SO_4 0.1 N, H_2SO_4 0.3 N, NaOH 1.5 N, filter paper, and acetone. The used tools were Erlenmeyer, Biuret, clamp, stative, pipette, measuring cup, digital balance, petri dish, porcelain cup, glass stir bar, vacuum drying, oven, desiccator, exicator, hotplate, chemical glass, heather extract, Buchner funnel, Fatex-S, and Liquid Chromatography Tandem Mass Spectrometry (LC-MS/MS) (of LPPT II UGM). Waters AcquityH UPLC® Class Quaternary Solvent Manager and Xevo TQD MS (Waters, USA) were employed for analysis.

Producing Goat Milk Kefir

Pure goat milk 1 L was pasteurized at 70 ℃ for 15 seconds (steam sterilizer, Tomy S-500). It was cooled down to 40 ℃ then mixed with 3% kefir grain. As incubation, goat milk was fermented at room temperature for 24 hours (Incucell). It was then followed by the aging process at 4 ℃ in refrigerator. Two methods of milk treatment were used, the first included an aging stage of 1-4 weeks, while the second involved processing without aging. The kefir was then mixed with 5% (w/v) gum arabic, stirred until it became homogeneous, and then vacuum-dried at 65 °C for 4 hours. The processes of aging and drying of goat milk kefir are shown in Figure 1.

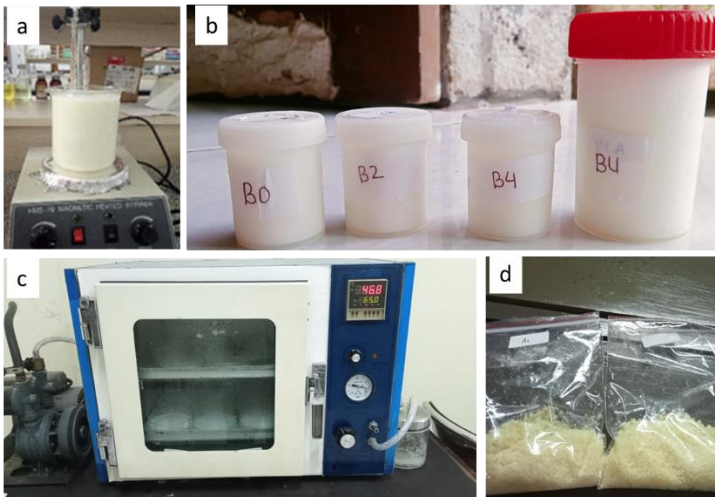


Fig. 1 - Producing of goat milk kefir
a – local goat milk, b – mixing kefir, c – vacuum drying, d – powder kefir

Proximate Analysis of Kefir and Powder Kefir

After producing, kefir and powder kefir were characterized as below. All data in this characterization was processed using the Statistical Package for the Social Science (SPSS) application.

Calculation of Total Titrated Acid Content

1 mL of kefir and powder kefir sample were each put into Erlenmeyer and added 2-3 drops of phenolphthalein indicator. Then the sample was titrated using 0.1 N NaOH solution until it turned pink.

Moisture content test

The sample was weighed and then dried for 24-48 hours at 40 – 60 ℃. After drying, the sample was weighed again as much as 5 grams. The cup was heated in an oven at 105 ℃ for ± 1 hour and cooled in a desiccator and then weighed. The sample was placed into the cup. Samples were put in an oven at 105 ℃ for ± 4-6 hours. The sample was then cooled in desiccator and weighed.

Ash Content Analysis

The crucible was heated in a furnace at 400-600 ℃ and cooled in a desiccator. Weigh the cup (X). 5 grams of sample was weighed and put in a cup and weighed (Y). The sample was burned on a hot plate until it is not smoking. It was put in the furnace and then cooled. It was then weighed (Z).

$$\%A = \frac{Z - X}{Y} \times 100\% \quad (1)$$

where:

$\%A$ - ash content; Z - weigh of cup + final sample; X - cup weight; Y - weigh of cup + initial sample

Analysis of Crude Protein Levels

0.3 grams sample was added with 1.5 grams of selenium mixture catalyst. It was then put in a Kjeldahl flask and added 20 ml of concentrated H_2SO_4. The destruction was carried out until the color of the solution became yellowish green – clear and then cooled for ± 15 minutes. 300 ml of distilled water was added and then cooled again. After adding 100 ml of 40% NaOH (technical), distillation was carried out. The distillation results were collected with 10 ml of H_2SO_4 which had been added with 3 drops of mixed indicators, namely methylene blue and methylene red. It was then titrated with 0.1 N NaOH until the color changes from purple to blue-green. The blank was determined as follows: 10 ml of 0.1 N H_2SO_4 was added to 2 drops of phenolphthalein indicator and then titrated with 0.1 N NaOH. The crude protein content was calculated as follows:

$$\%CP = \frac{V_b - V_s \times N \times 14 \times 6.25}{g} \times 100\% \quad (2)$$

where: $\%CP$ - crude protein; V_b - volume of blank (mL); V_s - volume of sample (mL); g - sample weigh (mg).

Analysis of Crude Fiber Content

1 gram sample (x) was put into the heather extract tool. Then, it was added 50 ml of 0.3 N H_2SO_4, boiled for 30 minutes. Then, it was added 25 ml of 1.5 N NaOH, boiled for 30 minutes. The filter paper that has been heated in an oven at 105 ℃ for 1 hour was weighed on a digital balance (a). The mixture was filtered using a Buchner funnel. Filtering was carried out with a suction flask connected to a vacuum pump. It was then washed using 50 ml of hot water, 50 ml of 0.3 N H_2SO_4, 50 ml of hot water and 25 ml of acetone. The filter paper and its contents were dried in an oven at 105 ℃ for 1 hour. The sample was then cooled using a desiccator and weighed (Y). After cooling, the cup was put into the furnace (400-600 ℃). Furthermore, the cup was cooled and then weighed (Z). The calculation of crude fiber content was as follows:

$$\%CF = \frac{Y - Z - a}{x} \times 100\% \quad (3)$$

where: $\%CF$: crude fiber, Y: weigh of cup + initial sample, Z: weigh of cup + final sample, a: filter paper weigh, x: sample weigh.

Analysis of Crude Fat Content

The filter flask filled with boiling stones was heated at 105-110 ℃ and then cooled in a desiccator. The filter flask (a) was weighed. 1 gram sample (x) was weighed. It was put in a filter sleeve and covered with non-fat cotton. The filter sleeve was inserted into the Soxhlet and filtered using petroleum benzene. The extractor was connected to the condenser. This process was performed using the FATEX-S. The filter flask was removed from the FATEX-S apparatus and then dried in an oven at 105-110 ℃ for 4-6 hours. The sample was cooled and weighed the final weight (b). Crude fat content was calculated as follows:

$$\%CL = \frac{b - a}{x} \times 100\% \quad (3)$$

where: $\%CL$: Crude Fat, b: weigh of flask + final weigh, a: weigh of flask + initial sample, and x: sample weigh.

Determination of amino acid composition

Samples of powder kefir ± 2 g and kefir ± 4 g were taken. The sample was put in a 50 mL screw tube. 20 mL of 6N HCl was added. It was then hydrolyzed in an autoclave at 110 ℃ for 12 hours. Next, it was neutralized with 6N NaOH. With 100 mL, it was filtered with a 0.22 µm filter. Finally, 5 µL sample was injected in LC-MS. The LC-MS was carried out at condition: capillary of 3.5kV, desolvation temperature of 500℃, dissolvation of 1000 L/h and collision energy of 15V. The used mobile phases were 0.1% PDFOA (pentadecafluorooctanoic acid) of 99.5 % : 0.5 % water/CH_3CN with 0.1 % formic acid and 0.1% PDFOA, 10%: 90 % water/CH3CN with 0.1 % formic acid by the flow of 0.6 mL/min (*Puspita et al., 2020*). The obtained data was analyzed by MassLynx V4.1 software. The obtained data were compared with the library of the software.

RESULTS

Yield of goat milk kefir

The yield of goat milk kefir from the initial treatment until 2 weeks increased with the length of aging time. However, the aging time did not show a significant difference (P>0.05) to the amount of yield produced. Based on Figure 2, it can be seen that the highest yield is after 2 weeks of aging time. The lowest yield value is treatment without aging.

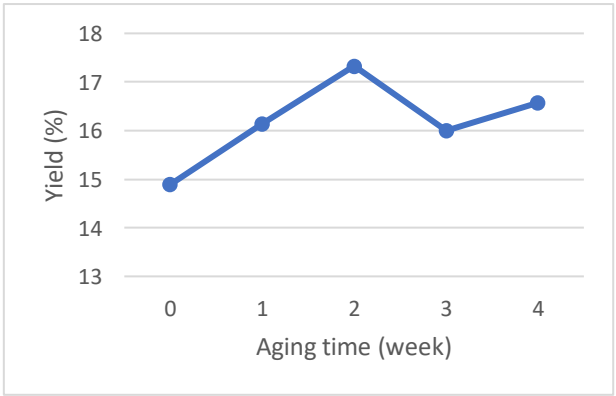


Fig. 2 - Yield of goat milk kefir toward aging time (zero (0) of aging time equals to "without aging")

The higher yield value was affected by the addition of gum arabic as filler. Fillers added in the manufacture of instant beverage products will cause a larger volume and increase the total solids, so the yield will also increase (*Yuliwaty & Susanto, 2015*). The higher the yield, the higher the economic value. Next, proximate analysis was carried out as listed in Table 1.

Table 1

Proximate analysis of goat milk kefir based on aging time

Kefir Type	Aging time	Total of titrated acid	Moisture	Ash	Protein	Fiber	Fat
	Week	%	%	%	%	%	%
kefir	Without aging	1.55	87.93	6.47	19.92	3.23	38.30
	1	1.73	87.73	6.25	19.32	2.81	38.53
	2	1.89	87.93	5.83	16.86	4.33	40.79
	3	2.18	87.66	6.24	19.36	5.98	44.65
	4	2.00	87.57	6.09	19.06	4.26	42.14
Powder kefir	Without aging	1.10	10.27	5.69	18.07	2.01	28.60
	1	1.11	11.68	5.64	18.94	1.45	26.86
	2	1.10	12.01	5.87	18.29	1.42	25.20
	3	1.03	9.34	5.48	17.40	1.84	27.66
	4	1.05	10.57	5.55	16.90	0.89	28.30

Based on Table 1 of total titrated lactic acid, lactic acid levels have increased, with the highest lactic acid levels shown by kefir after 3 weeks of aging time, i.e.: 2.18%. However, powder kefir after 3 weeks of aging time obtained the lowest lactic acid content, i.e.: 1.03%. So, powder kefir has lower levels of lactic acid when compared to kefir (*Zakaria et al., 2013*).

The total lactic acid in kefir showed a significant difference ($P<0.01$) to the length of time it was stored at refrigerator temperature. However, the lactic acid content of kefir only meets the SNI standard until 2 weeks of aging time, where the SNI for yogurt which is also set for kefir standardization is between 0.5 – 2.0%. The longer the aging, the more decreased the pH of kefir. Low pH is a good environment for the growth of lactic acid bacteria (*Mal et al., 2013*). After the vacuum drying process, the total lactic acid in powder kefir did not show a significant difference ($P>0.05$) to the length of aging time. Total acid depends on the supply of nutrients, temperature, time, water and oxygen availability (*Setiawati & Yunianta, 2018*). However, the lactic acid content during aging complies with SNI standards.

Based on Table 1 of moisture content, powder kefir after 3 weeks of aging time showed the lowest moisture content, i.e.: 9.34%. Kefir with the highest moisture content was shown by treatment without aging, which was 87.93%. Then, the moisture content of kefir is much higher than powder kefir. The uses drying method causes a decrease in moisture content due to the evaporation of water in kefir (*Atalar & Dervisoglu, 2015*).

Statistical analysis of kefir and powder kefir was not significantly different ($P>0.05$) toward aging time. Based on the highest moisture content, kefir in this study was not much different from other study (*Setyawardani & Sumarmono, 2015*) where the moisture content in goat milk kefir stored at 6 – 10 ℃ for 30 days ranged from 87.572% to 88.108% . In food, moisture content is an important component that can affect appearance, texture and taste (*Pandiselvam et al., 2022*). The moisture content in yogurt according to SNI 2981:2009 is between 83% -84%. So, the texture of kefir is thinner than a yogurt. The different textures are made possible by different starters, where the kefir grains convert milk lactose into lactic acid, causing kefir to be thinner. Powder kefir has a higher moisture content than other study (*Rizqiati et al., 2021*), but does not meet SNI 01-2970-2006 (maximum 5%). High moisture content makes it easier for microbial growth to occur (*Rizqiati et al., 2020*).

Based on Table 1 of ash content, the ash content after 2 weeks of aging time showed opposite results. On 2 weeks of aging time, ash content of kefir showed the lowest levels. However, ash content of powder kefir showed the highest levels. Therefore, the average, ash content in kefir was higher than powder kefir.

Aging time had no significant effect (P>0.05) on the ash content of powder kefir or kefir. Kefir consisting of protein, fat and ash has relatively small variations during the aging period (*Setyawardani et al., 2017*). The average ash content of kefir was 6.18% and the average ash content of powder kefir was 5.64%.

In this study the ash content produced did not meet SNI 7552:2009, which is a maximum of 1.0%. On the other hand, this study shows that the used drying method can reduce the ash content of kefir.

Based on Table 1 on protein content, the average protein content of goat milk kefir is higher than powder kefir for treatment without aging, which was 19.92%. In this study, processing milk at high temperatures can cause protein denaturation resulting in a decrease in protein content (*Nurwantoro et al., 2020*). However, the difference in the levels of kefir and powder kefir in this study was not significantly different (P>0.05).

The results of statistical analysis showed that aging time had no significant effect (P>0.05) on the protein content of goat milk kefir and powder kefir, as an obtained result of other study (*Sarica & Coşkun, 2021*) where protein levels during 1–35 days of aging time ranged from 3.06 ± 0.003% to 3.10 ± 0.009%. When fermented for 24 hours, kefir microbes produce optimal biomass and increase protein availability (*Susanti & Utami, 2014*). The protein content of kefir up to 4 weeks of aging time still meets the international standard Codex Stand 243-2003, which is at least 2.7%. However, the protein content in powder kefir does not meet SNI 01-2970-2006 regarding powder milk, which is at least 23%.

Based on Table 1 of fat content, the fat content in kefir showed a significant difference (P<0.05). The highest fat content of kefir was obtained after 3 weeks of aging time. However, the fat content of powder kefir did not show a significant difference (P>0.05) toward aging time, where the highest fat content was obtained for treatment without aging. So, the fat content of powder kefir is lower than kefir.

The results of fat contents are in accordance with the international standards codex booth 243-2003 for fermented milk and SNI 01-2970-2006 regarding powder milk. The activity of lactic acid bacteria from kefir seeds will produce lipase enzymes which will affect the fat content. When lactic acid bacteria increase and produce more lipase enzymes, the hydrolyzed fat also increases, so the fat content decreases (*Dewi et al., 2020*). However, in this study, the lactic acid level is directly proportional to the fat level produced. It is possible that, during aging time, the release of lipase enzymes by lactic acid bacteria does not occur, so the fat content of kefir does not decrease (*Setyawardani et al., 2017*).

Fiber content is a compound that cannot be hydrolyzed by acids or bases and can be used as an index of dietary fiber content, because it usually contains 0.2–0.5 parts of dietary fiber (*Korompot et al., 2018*). From Table 1 of Fiber content, the highest fiber content in goat milk kefir was shown by kefir after 3 weeks of aging time, i.e.: 5.98%. In this study, the lowest fiber content was on powder kefir after 4 weeks of aging time, i.e.: 0.89%. So, powder kefir has a lower fiber content than kefir.

The reduction of fiber content is made possible by the use of fiber to support the goat milk kefir fermentation process (*Mumpuni et al., 2020*). The increasing fiber content during 1 week until 3 weeks was caused by the 24-hour fermentation time which caused bacteria to grow optimally, so the decomposition of sucrose into cellulose increased the fiber content (*Wasilu et.al., 2021*).

The best treatment of goat milk kefir dried by vacuum drying method

Selection of the best treatment on kefir and powder goat milk kefir products based on aging time using the Exponential Comparison Method (MPE). The Exponential Comparison Method is a method in a decision support system by ranking decision priorities based on several criteria (*Napian & Meiriza, 2020*).

With this method, the value of the difference between each criterion can be distinguished (*Suranti, 2018*). Based on the results of the calculation for the characterization results of goat milk kefir, the best treatment is 3 week of aging time, both for kefir and powder kefir. Based on the results of statistical analysis, it was found that the characteristics of kefir were very significantly different (P>0.05). The nutritional content of kefir is significantly different after drying using vacuum drying at 65 °C for 4 hours.

Amino acid components of the produced goat milk kefir

Kefir contains vitamins of B1, B2, B5 and C, minerals and essential amino acids which are beneficial in improving fitness, healing processes and homeostasis (*Farag et al., 2020*). The amino acid profile of fermented milk and kefir has higher levels than milk, namely threonine, serine, alanine, lysine and ammonia (*Arslan, 2015*). Goat milk kefir in this study based on Table 2 contains amino acids, such as arginine, histidine, lysine, phenylalanine, isoleucine, leucine, tyrosine, methionine, valine, proline, glutamic acid, aspartic acid, cysteine, threonine, serine and glycine. In this study, the amino acid component with the highest levels was lysine. Lysine is an essential amino acid for humans which is needed for health and can play a role in immune therapy to accelerate wound recovery (*Datta et al., 2001*).

Table 2

Amino acid components of goat milk kefir toward aging time

compound	Powder kefir (%)			Kefir (%)		
	Without aging	2 weeks	4 weeks	Without aging	2 weeks	4 weeks
L-Arginine	0.86	1.02	1.04	0.63	0.48	0.68
L-Histidine	0.56	0.61	0.58	0.31	0.23	0.28
L-Lysine	2.00	2.01	2.12	0.89	0.71	0.81
L-Phenylalanine	0.65	0.65	0.59	0,29	0,24	0,30
L-Isoleucine	0.74	0.73	0.70	0.32	0.26	0.31
L-Leucine	0.98	1.02	0.98	0.47	0.41	0.44
L-Tyrosine	0.11	0.13	0.11	0.12	0.09	0.12
L-Methionine	0.13	0.16	0.15	0.23	0.14	0.17
L-Valine	1.03	1.02	1.01	0.41	0.33	0.38
L-Proline	0.05	0.07	0.05	0.04	0.03	0.03
L-Glutamic Acid	0.98	1.03	0.96	0.48	0.41	0.46
L-Aspartic Acid	1.07	1.04	1.08	0.52	0.42	0.55
L-Threonine	0.60	0.59	0.55	0.30	0.24	0.29
L-Serine	0.83	0.87	0.86	0.42	0.35	0.44
L-Glycine	0.07	0.31	0.22	0.17	0.05	0.11

Powder kefir with different aging times contains different amounts of amino acids. Total amino acids of powder kefir based on aging treatments were 10.67% (without aging), 11.27% (2 weeks of aging time) and 11.00% (4 weeks of aging time). Based on these results, powder kefir was higher after 2 weeks of aging time, especially the components histidine, leucine, tyrosine, methionine, proline, glutamic acid and serine.

Based on Figure 3, kefir has different total amino acid content. Total amino acids of kefir with aging treatments were 5.61% (without aging), 4.39% (2 weeks of aging time) and 5.37% (4 weeks of aging time). Kefir without aging had higher total amino acids, especially in the components of histidine, lysine, leucine, methionine and glycine. The highest amino acid component of kefir in this study was lysine, and the lowest amino acid component was proline. The amino acid component in this study was much higher than other study (*Nurliyani et al., 2014*). The essential amino acids found in kefir play a significant role in regulating protein, glucose and lipid metabolism and have a positive effect on weight management, maintenance of immune response, and energy balance (*Farag et al., 2020*).

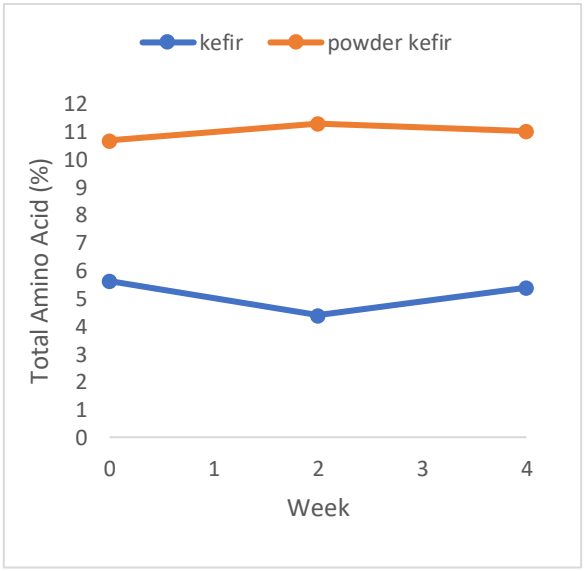


Fig. 3 - Changes in amino acid components after various aging time of kefir and powder goat milk kefir (zero (0) of aging time equals to "without aging")

CONCLUSIONS

This study showed that the total titrated acid and fat content of kefir were significantly different, but powder kefir was not significantly different based on all aging treatments. Yield, and proximate analysis (moisture content, ash content, protein content and fiber content) did not differ significantly with specified aging time. The best treatment based on the exponential comparison method for both powder kefir and kefir is kefir with an aging time of 3 weeks. Based on specified aging time, the amino acid components in powder kefir and kefir underwent changes. The highest total amino acids were in kefir without aging. The highest amino acid component of kefir powder was obtained at 2 weeks of aging time. Based SNI, the both kefir (kefir and powder kefir) have slightly enough quality, but moisture of powder kefir is much lower than the moisture of kefir. The future prospects were sensory and microbiology analysis for evaluating the taste and human health.

ACKNOWLEDGEMENT

The author would like to thank LPPM Universitas Negeri Malang, which provided the research funds for this study.

REFERENCES

[1] Arslan, S. (2015). A review: chemical, microbiological and nutritional characteristics of kefir. *CyTA - Journal of Food*, *13*(3), 340–345. https://doi.org/10.1080/19476337.2014.981588

[2] Aryanta, I. W. R. (2021). Kefir dan Manfaatnya Bagi Kesehatan. *Widya Kesehatan*, *3*(1), 35–38. https://doi.org/10.32795/widyakesehatan.v3i1.1657

[3] Atalar, I., & Dervisoglu, M. (2015). Optimization of spray drying process parameters for kefir powder using response surface methodology. *LWT - Food Science and Technology*, *60*(2, Part 1), 751–757. https://doi.org/10.1016/j.lwt.2014.10.023

[4] Clark, S., & Mora García, M. B. (2017). A 100-Year Review: Advances in goat milk research. *Journal of Dairy Science*, *100*(12), 10026–10044. https://doi.org/10.3168/jds.2017-13287

[5] Datta, D., Bhinge, A., & Chandran, V. (2001). Lysine: Is it worth more? *Cytotechnology*, *36*(1), 3–32. https://doi.org/10.1023/A:1014097121364

[6] Dewi, A. C., Rahardjo, A. H. D., Setyawardani, T., & Subagja, H. (2020). Study on kefir grain concentration and the different length of storage on the physicochemical of goat milk kefir. *Journal of Physics: Conference Series*, *1569*(3), 32001. https://doi.org/10.1088/1742-6596/1569/3/032001

[7] Farag, M. A., Jomaa, S. A., Abd El-Wahed, A., & R. El-Seedi, H. (2020). The Many Faces of Kefir Fermented Dairy Products: Quality Characteristics, Flavour Chemistry, Nutritional Value, Health Benefits, and Safety. *Nutrients*, *12*(2), 346. https://doi.org/10.3390/nu12020346

[8] Ferreira, I. M. P. L. V. O., Pinho, O., Monteiro, D., Faria, S., Cruz, S., Perreira, A., … Tavares, P. (2010). Short communication: effect of kefir grains on proteolysis of major milk proteins. *Journal of Dairy Science*, *93*(1), 27–31. https://doi.org/10.3168/jds.2009-2501

[9] Hariadi, H., Karim, M. A., Hanifah, U., Haryanto, A., Novrinaldi, Surahman, D. N., … Lubis, R. F. L. (2023). Effect of butterfly-pea powder (Clitoria ternatea L.) and drying temperature towards physicochemical characteristics of butterfly-pea milk powder with vacuum drying method. *Food Science and Technology*, *43*, e109622.

[10] Kesenkaş, H., Gürsoy, O., & Özbaş, H. (2017). Chapter 14 - Kefir. In J. Frias, C. Martinez-Villaluenga, & E. B. T.-F. F. in H. and D. P. Peñas (Eds.), *Fermented Foods in Health and Disease Prevention* (pp. 339–361). Boston: Academic Press. https://doi.org/10.1016/B978-0-12-802309-9.00014-5

[11] Korompot, A. R. H., Fatimah, F., & Wuntu, A. D. (2018). Kandungan Serat Kasar Dari Bakasang Ikan Tuna (Thunnus Sp.) Pada Berbagai Kadar Garam, Suhu Dan Waktu Fermentasi. *Jurnal Ilmiah Sains*, *18*(1), 31–34. https://doi.org/10.35799/jis.18.1.2018.19455

[12] Kresnowati, M. T. A. P., Bindar, Y., & Rahmina, F. (2018). Development of Instant Microbial Starter for Production of Fermented Cassava Flour: Effect of Vacuum Drying Temperature, Carrier Media, and Storage Temperature. *Journal of Engineering and Technological Sciences*, *50*(6), 832–840. https://doi.org/10.5614/j.eng.technol.sci.2018.50.6.6

[13] Lim, J., Kale, M., Kim, D.-H., Kim, H.-S., Chon, J.-W., Seo, K.-H., … Kim, H. (2017). Antiobesity Effect of Exopolysaccharides Isolated from Kefir Grains. *Journal of Agricultural and Food Chemistry*, *65*(46), 10011–10019. https://doi.org/10.1021/acs.jafc.7b03764

[14] Mumpuni, O. F., Maulana, R. A., Ayustaningwarno, F., Panunggal, B., & Anjani, G. (2020). Pengaruh Waktu Fortifikasi Vitamin B12 (Sianokobalamin) Dan Vitamin D3 (Kalsiferol) Terhadap Mutu Gizi Kefir Susu Kambing. *Journal Of Nutrition College*, *9*(2), 147–153. https://doi.org/10.14710/jnc.v9i2.27514

[15] Napian, S. D. R., & Meiriza, A. (2020). Implementation of Exponential Comparison Method in Performance Evaluation of Temporary Employees in District Court of Prabumulih. *Proceedings of the Sriwijaya International Conference on Information Technology and Its Applications (SICONIAN 2019)*, 527–531. Atlantis Press. https://doi.org/10.2991/aisr.k.200424.081

[16] Nayik, Gulzar A, Jagdale, Y. D., Gaikwad, S. A., Devkatte, A. N., Dar, A. H., & Ansari, M. J. (2022). Nutritional Profile, Processing and Potential Products: A Comparative Review of Goat Milk. *Dairy*, *3*(3), 622–647. https://doi.org/10.3390/dairy3030044

[17] Nayik, Gulzar Ahmad, Jagdale, Y. D., Gaikwad, S. A., Devkatte, A. N., Dar, A. H., Dezmirean, D. S., … Alotaibi, S. S. (2021). Recent Insights Into Processing Approaches and Potential Health Benefits of Goat Milk and Its Products: A Review. *Frontiers in Nutrition*, Vol. 8, p. 789117. https://doi.org/10.3389/fnut.2021.789117

[18] Nurliyani, Harmayani, E., & Sunarti. (2014). Microbiological Quality, Fatty Acid and Amino Acid Profiles of Kefir Produced from Combination of Goat and Soy Milk. *Pakistan Journal of Nutrition*, *13*(2), 107–115. https://doi.org/10.3923/pjn.2014.107.115

[19] Nurwantoro, N., Susanti, S., & Rizqiati, H. (2020). The Effect of Different Type Drying Methods on Chemical Characteristics and Microbiology of Goat Milk Powder Kefir. *Journal of Applied Food Technology*, *7*(1), 19–24. https://doi.org/10.17728/jaft.6699

[20] Nyakayiru, J., van Lieshout, G. A. A., Trommelen, J., van Kranenburg, J., Verdijk, L. B., Bragt, M. C. E., & van Loon, L. J. C. (2020). The glycation level of milk protein strongly modulates post-prandial lysine availability in humans. *British Journal of Nutrition*, *123*(5), 545–552. https://doi.org/10.1017/S0007114519002927

[21] Pandiselvam, R., Tak, Y., Olum, E., Sujayasree, O. J., Tekgül, Y., Çalışkan Koç, G., … Kumar, M. (2022). Advanced osmotic dehydration techniques combined with emerging drying methods for sustainable food production: Impact on bioactive components, texture, color, and sensory properties of food. *Journal of Texture Studies*, *53*(6), 737–762. https://doi.org/10.1111/jtxs.12643

[22] Puspita, S., Sunarintyas, S., Anwar, C., Mulyawati, E., & HNE Soesatyo, M. (2020). Amino acid identification of Bombyx mori fibroin cocoon as biomaterial using liquid chromatography/mass spectrometry. *BIO Web Conf.*, *28*, 02001. https://doi.org/10.1051/bioconf/20202802001

[23] Putri, Y. D., Setiani, N. A., & Warya, S. (2020). The Effect Of Temperature, Incubation And Storage Time On Lactic Acid Content, Ph, And Viscosity Of Goat Milk Kefir. *Current Research On Biosciences And Biotechnology*, *2*(1), 101–104. https://doi.org/10.5614/Crbb.2020.2.1/Hpmq5042

[24] Raynal-Ljutovac, K., Lagriffoul, G., Paccard, P., Guillet, I., & Chilliard, Y. (2008). Composition of goat and sheep milk products: An update. *Small Ruminant Research*, *79*(1), 57–72. https://doi.org/10.1016/j.smallrumres.2008.07.009

[25] Rizqiati, H., Nurwantoro, N., Febrisiantosa, A., Shauma, C. A., & Khasanah, R. (2020). Pengaruh Isolat Protein Kedelai Terhadap Karakteristik Fisik Dan Kimia Kefir Bubuk. *Jurnal Pangan Dan Agroindustri*, *8*(3), 111–121. https://doi.org/10.21776/Ub.Jpa.2020.008.03.1

[26] Rizqiati, H., Nurwantoro, N., Susanti, S., & Prayoga, M. I. Y. (2021). The effects of dextrin concentration as filler on physical, chemical, and microbiology properties of powdered goat milk kefir. *Journal of the Indonesian Tropical Animal Agriculture*, *46*(2), 145–153. https://doi.org/10.14710/jitaa.46.2.145-153

[27] Santoso, A., Retnosari, R., Pramudita, V., Wijaya, A. R., Anisa, T. N., & Sanjaya, E. H. (2021). The Effect of Starter Concentration and Incubation Time on Yogurt Characteristics. *AIP Conference Proceedings*, *2353*(1), 30080. https://doi.org/10.1063/5.0052694

[28] Santoso, A., Wijaya, A. R., Permatasari, Y., Anisa, T. N., & Sumari. (2020). The effect of starter concentration variations and rennet on cheese characteristics of cow milk. *AIP Conference Proceedings*, *2231*(1), 40042. https://doi.org/10.1063/5.0002557

[29] Santoso, A., Yulianti, V. E. N., Retnosari, R., Asrori, M. R., Sanjaya, E. H., & Marfuah, S. (2023). Effect of preservatives and ultrasonic waves on organoleptic preference levels of milk yogurt respondents in Malang. *AIP Conference Proceedings*, *2634*(1), 20022. https://doi.org/10.1063/5.0111477

[30] Sarica, E., & Coşkun, H. (2021). Effect of frozen storage on some characteristics of kefir samples made from cow's and goat's milk. *Food Science and Technology International*, *28*(2), 157–168. https://doi.org/10.1177/10820132211003710

[31] Satir, G., & Guzel-Seydim, Z. B. (2023). The effect of kefir fermentation on the protein profile and the monoterpenic bioactive compounds in goat milk. *International Dairy Journal*, *137*, 105532. https://doi.org/10.1016/j.idairyj.2022.105532

[32] Setiawati, A. E., & Yunianta, Y. (2018). Kajian Analisis Suhu Dan Lama Penyimpanan Terhadap Karakteristik Kadar Alkohol Kefir Susu Sapi. *Jurnal Pangan Dan Agroindustri*, *6*(4), 77–86. https://doi.org/10.21776/Ub.Jpa.2018.006.04.9

[33] Setyawardani, T. Sumarmono, J., Rahardjo, A. H. D., Sulistyowati, M., & Widayaka, K. (2017). Kualitas Kimia, Fisik Dan Sensori Kefir Susu Kambing Yang Disimpan Pada Suhu Dan Lama Penyimpanan Berbeda. *Buletin Peternakan*, *41*(3), 298–306. https://doi.org/10.21059/buletinpeternak.v41i3.18266

[34] Setyawardani, T., & Sumarmono, J. (2015). Chemical And Microbiological Characteristics Of Goat Milk Kefir During Storage Under Different Temperatures. *Journal Of The Indonesian Tropical Animal Agriculture*, *40*(3), 183–188. https://doi.org/10.14710/jitaa.40.3.183-188

[35] Suhartanti, D., & Septian, R. (2014). Comparison of the Antibacterial Activity of Cow Milk Kefir and Goat Milk Kefir Against Bacteria Bacillus cereus. *Kesmas, Jurnal Kesehatan Masyarakat NasionalA*, *8*(2), 71–76. Retrieved from https://media.neliti.com/media/publications/24991-EN-comparison-of-the-antibacterial-activity-of-cow-milk-kefir-and-goat-milk-kefir-a.pdf

[36] Sulmiyati, S., Said, N. S., Fahrodi, D. U., Malaka, R., & Fatma, F. (2018). Perbandingan Kualitas Fisiokimia Kefir Susu Kambing Dengan Kefir Susu Sapi (Comparison Of Physiochemical Quality Of Goat Milk Kefir With Cow Milk Kefir). *Jurnal Veteriner*, *19*(2), 263–268. https://doi.org/10.19087/jveteriner.2018.19.2.263

[37] Sulmiyati, Sulmiyati, Said, N. S., Fahrodi, D. U., Malaka, R., & Maruddin, F. (2019). The Physicochemical, Microbiology, and Sensory Characteristics of Kefir Goat Milk with Different Levels of Kefir Grain. *Tropical Animal Science Journal*, *42*(2), 152–158. https://doi.org/10.5398/tasj.2019.42.2.152

[38] Suranti, D. (2018). Application of Exponential Comparison Method and Simple Additive Weighting Method in Assessment of Agricultural Extension Performance. *Scientific Journal Of Informatics*, *5*(2), 128–137. https://doi.org/10.15294/sji.v5i2.16128

[39] Susanti, S., & Utami, S. (2014). Pengaruh Lama Fermentasi Terhadap Kandungan Protein Susu Kefir Sebagai Bahan Penyusun Petunjuk Praktikum Mata Kuliah Biokimia. *Florea : Jurnal Biologi Dan Pembelajarannya*, *1*(1), 41–46. https://doi.org/10.25273/florea.v1i1.371

[40] Timpanaro, G., & Cascone, G. (2022). Food consumption and the Covid-19 pandemic: The role of sustainability in purchasing choices. *Journal of Agriculture and Food Research*, *10*, 100385. https://doi.org/10.1016/j.jafr.2022.100385

[41] Wasilu, R. P., Une, S., & Liputo, S. A. (2021). Karakteristik Kimia, Mikrobiologi, Dan Organoleptik Water Kefir Sari Buah Pepaya (Carica Papaya L.) Berdasarkan Lama Fermentasi Dan Konsentrasi Sukrosa. *Jambura Journal of Foof Technology*, *3*(2), 13–26. https://doi.org/10.37905/jjft.v3i2.9769

[42] Woźniak, D., Cichy, W., Dobrzyńska, M., Przysławski, J., & Drzymała-Czyż, S. (2022). Reasonableness of Enriching Cow's Milk with Vitamins and Minerals. *Foods*, Vol. 11. https://doi.org/10.3390/foods11081079

[43] Yamamoto, E., Watanabe, R., Ichimura, T., Ishida, T., & Kimura, K. (2021). Effect of lactose hydrolysis on the milk-fermenting properties of Lactobacillus delbrueckii ssp. bulgaricus 2038 and Streptococcus thermophilus 1131. *Journal of Dairy Science*, *104*(2), 1454–1464. https://doi.org/10.3168/jds.2020-19244

[44] Yuliwaty, S. T., & Susanto, W. H. (2015). Pengaruh Lama Pengeringan Dan Konsentrasi Maltodekstrin Terhadap Karakteristik Fisik Kimia dan Organoleptik Minuman Instan Daun Mengkudu (Morinda Citrifolial). *Jurnal Pangan Dan Agroindustri*, *3*(1), 41–52. Retrieved from https://jpa.ub.ac.id/index.php/jpa/article/view/108

[45] Zakaria, Y., Yurliasni, Y., Delima, M., & Diana, E. (2013). Analisa Keasaman dan Total Bakteri Asam Laktat Yogurt Akibat Bahan Baku dan Persentase Lactobacillus casei yang Berbeda. *Jurnal Agripet*, *13*(2), 31–35. https://doi.org/10.17969/agripet.v13i2.817

DEVELOPMENT AND PERFORMANCE EVALUATION OF A LIQUEFIED PETROLEUM GAS-POWERED FLUIDIZED COFFEE ROASTER

/

PENGEMBANGAN DAN EVALUASI KINERJA PENYANGRAI KOPI FLUIDISASI BERTENAGA LIQUEFIED PETROLEUM GAS

Dadang Dayat HIDAYAT[1)], Ari RAHAYUNINGTYAS[1)], Diang SAGITA*[1)], Maulana FURQON[1)], Arie SUDARYANTO[1)], Dadang GANDARA[1)], Taufik YUDHI[1)], Nandang JAENUDIN[1)]

[1)]Research Centre for Appropriate Technology, National Research and Innovation Agency

Tel: 6285719002251; E-mail: diang.sagita@gmail.com

DOI: ……

Keywords: *fluidized, roaster, coffee, heat exchanger, cyclone*

ABSTRACT

In this study, a fluidized coffee roaster has been successfully designed, constructed, and tested. This prototype has a capacity of 500 grammes per batch to aid small-scale coffee shops in roasting coffee beans. This fluidized coffee roaster is easy to use, cheap and has an appropriate capacity for the small business requirements. The coffee roasting components of the machine consisted of a blower (600 watts), a heat exchanger, a jet burner, a cylindrical roasting chamber, a chaff and dust collector, and a frame. At a range of airflow of 4-6 m/sec, the average temperature increase in the furnace and roasting chamber was 26 °C and 7.8 °C per minute, respectively. Performance tests revealed that the developed fluidized coffee roaster had been able to roast Robusta and Arabica coffee to light, medium, and dark roasting levels. For Robusta coffee, the time required to achieve light, medium, and dark levels were 8.18, 9.85, and 12.03 minutes, respectively, with final roasting temperatures for each level of 209 °C, 220 °C, and 248°C. For Arabica coffee, the time required was 5.32, 7.67, and 11.72 minutes, respectively with the final roasting temperatures of 207 °C, 210 °C, and 218 °C.

ABSTRAK

Dalam penelitian ini, fluidized coffee roaster telah berhasil dirancang, dibangun, dan diuji. Prototipe ini berkapasitas 500 gram per batch untuk membantu kedai kopi skala kecil dalam memanggang biji kopi. Penyangrai kopi terfluidisasi ini mudah digunakan, murah, dan memiliki kapasitas yang sesuai untuk kebutuhan usaha kecil. Komponen mesin sangrai kopi terdiri dari blower (600 watt), penukar panas, pembakar jet, ruang sangrai silinder, pengumpul kulit ari dan debu, dan rangka. Pada kisaran aliran udara 4-6 m/detik, kenaikan suhu rata-rata di dalam tungku dan ruang pemanggangan berturut-turut adalah 26 °C dan 7,8 °C per menit. Uji kinerja menunjukkan bahwa fluidized coffee roaster yang dikembangkan telah mampu menyangrai kopi Robusta dan Arabika hingga tingkat penyangraian ringan, sedang, dan gelap. Untuk kopi Robusta, waktu yang dibutuhkan untuk mencapai level light, medium, dan dark masing-masing adalah 8,18, 9,85, dan 12,03 menit, dengan suhu akhir penyangraian masing-masing level 209 °C, 220 °C, dan 248 °C. Untuk kopi arabika, waktu yang dibutuhkan masing-masing adalah 5,32, 7,67, dan 11,72 menit dengan suhu akhir penyangraian 207 °C, 210 °C, dan 218 °C.

INTRODUCTION

Coffee is one of popular beverages that have been consumed in more than 70 countries *(Kristanti et al., 2022; Sagita et al., 2022; Velasquez et al., 2018)*. Coffee roasting is the final stage in preparing green bean coffee before grinding, brewing, and consumption. *Green beans* coffee is ripe coffee cherries that have been pulped, hulled, and dried. Before roasting, green beans are green in colour, dense, practically flavourless, and have a beany and grassy aroma. Also, green beans do not smell like coffee. Coffee roasting is a chemically complex process *(Baggenstoss et al., 2008; Chandrasekar & Viswanathan, 1999; Clarke, 1987; Petracco & Viani, 2005; Schenker & Rothgeb, 2017; Zimmermann et al., 1996)*.

Dadang D. Hidayat, M.Eng.Sc.; Ari Rahayuningtyas, M.Sc; Diang Sagita, M.Sc.; Maulana Furqon M.Eng.; Arie Sudaryanto, M.Agr.; Dadang Gandara; Taufik Yudhi; Nandang Jaenudin.

Coffee roasting is a complex heat transfer process responsible for chemical, structural, physical and sensory changes (Darmajana, Hidayat, et al., 2022). The coffee bean undergoes numerous chemicals and physical changes during roasting process *(Baggenstoss et al., 2008; Petracco & Viani, 2005)*. The bean changes in size and colour, produces and loses different volatiles, and produces the well-known coffee flavour *(Dorfner et al., 2004; Hernández et al., 2008; Schenker & Rothgeb, 2017)*. The roasting process aims to augment aroma and flavour; it develops about 800 to 1000 aroma compounds. Roasting can also most significantly increase solubility *(Pérez-Martínez et al., 2008)*. The roasting procedure affects the sensory properties of brewed coffee based on panellist preferences *(Darmajana, Wulandari, et al., 2022*).

There are three main stages in roasting, i.e., drying, browning, and development. The drying stage typically lasts 4–8 minutes. It ends at the temperature of 160 °C with the traditional drum. The drying stage is essential for the bean to get energy because the last roasting stage is exothermic, producing heat. At this point, the coffee begins to smell like toasted bread and hay. This is when the smell-making chemicals start to convert into aroma compounds. Browning occurs as the impact of the Maillard reaction. In the Maillard reaction, reducing sugars and amino acids react to make hundreds of different aromas and colour compounds known as melanoidin. At this point, the roast slows down on its own, and flavour development occurs. When the browning process is complete, the coffee starts to pop. This is called the first crack, which means the development stage has begun. During the development stage, the reaction releases heat, and the coffee starts to crack. The energy built up during the drying and browning stages can cause cracks. Development time is when the desired aroma compounds are developing. At the development stage, the roast must slow down; otherwise, the roasted coffee will be smoky. Depending on the desired flavour profile and roast degree, the development stage usually takes 15–25% of the roasting time *(Latvakangas, 2022)*.

There are different roaster configurations, such as fluidized beds and drum roasters. Usually, drum roasters are used for small roasters *(Hidayat et al., 2020)*, while fluidized bed roasters are used for large roasters. Fluidized bed roasters keep the beans in the air using a blower and roast them inside the roasting chamber, while drum roasters heat beans with hot gas in horizontal or vertical drums with paddles *(Wang & Lim, 2015)*. The roasting procedure most significantly influences the formation of coffee flavour. Subpar roasting techniques can ruin even the highest-quality green coffee beans. There are no guidelines for creating a specific roast of coffee, and each roaster uses a different set of roasting techniques.

Baggenstoss et al. (2008) stated that convection is essential for heat to move when roasting coffee beans because it controls how fast and evenly the beans roast. Fluidized-bed roasters, which use convective heating almost exclusively, can make coffee with a low density and a high yield *(Eggers & Pietsch, 2001)*. On the other hand, coffees roasted in drum roasters mainly use conductive heat transfer and have less soluble solids, more burnt flavour, and more volatile loss than coffees roasted in fluidized bed roasters *(Nagaraju et al., 1997)*. Roasting beans requires a high temperature/long time (HTLT) combination. Because of the high temperatures and longer roasting time (15–18 minutes), some beans get burned, oil and char build up on the walls of the cylinder, and fires happen. Also, the equipment is hard to clean after it has been used, which gives the roasted beans an unpleasant, smoky taste.

Several patents for high temperature/short time (HTST) roasting have been disclosed. The fluidized bed roaster is one of these and is used for extensive roasting of beans used to make instant coffee. The coffee beans in an air roaster float on a bed of hot air in the roasting chamber, keeping the temperature steady throughout the process. A separate section in air roasters captures the chaff, preventing the material from smoking and altering the flavour of the batch. A typical air roaster can roast a batch of green coffee beans in six to eight minutes, whereas the drum method can take up to fifteen. Due to their short time of roasting, air-roasted beans have a purer flavour than drum-roasted beans. Air-roasted beans are roasted "to temperature," a far more exact method for determining when a batch is done roasting. Thus, the roaster can simply replicate batches of coffee beans, recreating the same colour, flavour profile, and aroma *(Latvakangas, 2022)*. Product consistency and improved process parameter control are benefits of fluidized bed roasters. However, handling medium and small batches might be challenging with these devices. In addition, most coffee roasters using hot air use more electricity than the average residential capacity of 900 watts. Therefore, for this study, a fluidized coffee roaster that can hold 500 grammes and runs on liquefied petroleum gas was designed and constructed to support small and medium-sized enterprises.

MATERIALS AND METHODS

The stage for the development of fluidized coffee roaster was carried out by design and prototyping method as also used by many previous publications *(Hidayat et al., 2020, 2021; Sagita et al., 2021)*.

These methods consisted of a general description, sizing and determining the main components, creating technical drawings, manufacturing, and performing the functional test.

Design of the machine

The primary considerations in developing this fluidization-type roaster were a simple design, locally necessary materials, and ease of operation and maintenance. The amount of electricity needed is less than 900 watts, which is about the same as the average amount of electricity used in the community. This coffee roaster is designed for a batch size of 500 grammes. The blower and heat source that use liquefied petroleum gas need 600 watts of electricity. This coffee roaster has a cyclone system for collecting chaff and dust. Figure 1 depicts an illustration of the equipment design.

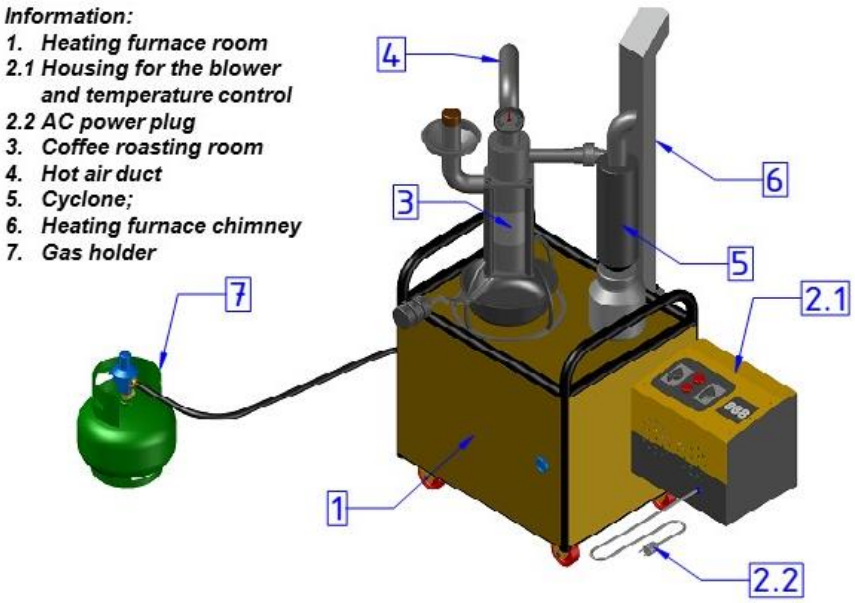


Fig. 1 - An isometric view of a fluidized coffee roaster design

Principle of operation

The blower forces air through a heat exchanger into a pipe inside the roasting chamber to the bottom of the roasting chamber as shown in figure 2.

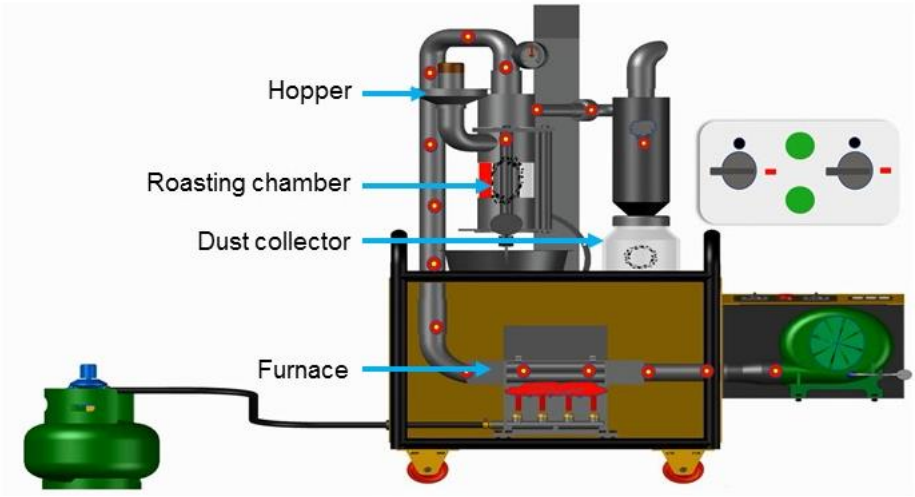


Fig. 2 - Schematic diagram of the roasting principle in the machine

After hitting the bottom of the roasting chamber, the hot air flows back into the chamber to blow the coffee. The hot air that enters the roasting chamber heats the beans through convection, while the evacuated air pressure allows the beans to circulate throughout the chamber, resulting in a uniform mixing and roasting. The temperature of the beans is measured using a thermocouple and digital thermometer. A chaff and dust collector is located in the upper portion of the chamber to collect the chaff and dust that are expelled from the roasting chamber during the roasting process.

Compared to the beans, the chaff and dust of the beans are light enough to rise into the collector. A separator member separates the chaff and dust from the evacuating air, and a cover member directs the chaff and dust into the glass collector and permits further air evacuation from the coffee roaster. At the end of the roasting process, the gas line is shut off to prevent further heating, and the roasted beans are removed from the roasting chamber.

Design consideration

Some considerations taken into account in designing a fluidized roaster system are the type of material used for tool construction, some physical characteristics of green bean coffee, the ratio of the volume of the green bean coffee chamber to the volume of the roasting chamber, the roasting capacity, the temperature of the roasting chamber, the temperature of the heat source, and the necessary electrical power

Heating furnace and blower room

The design of heating furnace room and the blower housing is presented in figure 3. It was made from an iron plate with a thickness of 1.8 mm. The frame was made from an iron pipe with a diameter of 32 mm; the length, width, and height of the heating furnace room were 616 mm, 500 mm, and 503 mm, respectively; and the length, width, and height of the blower room were 350 mm, 263 mm, and 300 mm, respectively. The dimensions of the frame were 632 mm in length, 512 mm in width, and 630 mm in height. The turning radius at the end of the top frame was 63.5 mm.

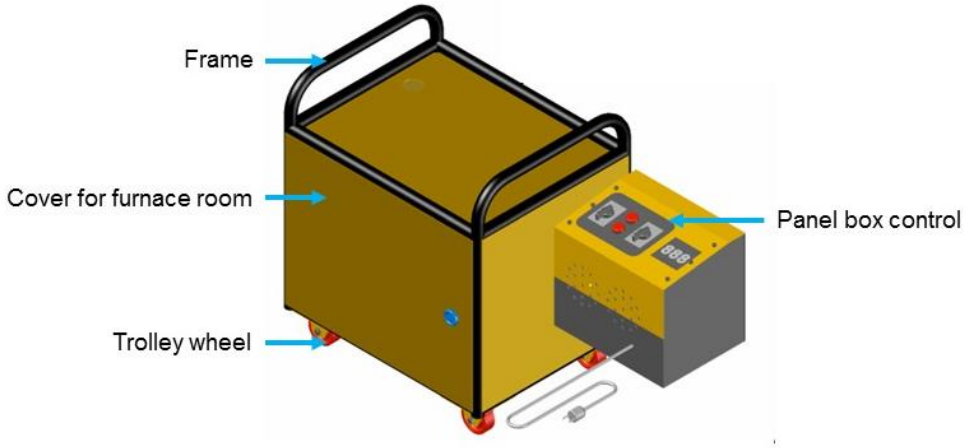


Fig. 3 – Design of heating furnace and blower rooms

Coffee roasting room and hot air duct

The frame of the roasting chamber design is shown in figure 4. This part was constructed from stainless steel 304. The roasting chamber comprises a 110 mm diameter 304 stainless steel pipe and a 110 mm diameter glass globe of a kerosene lamp (Petromax). The diameter of the base of the frame was 300 mm. The hot air supply pipe was made of stainless steel and had a 51 mm diameter.

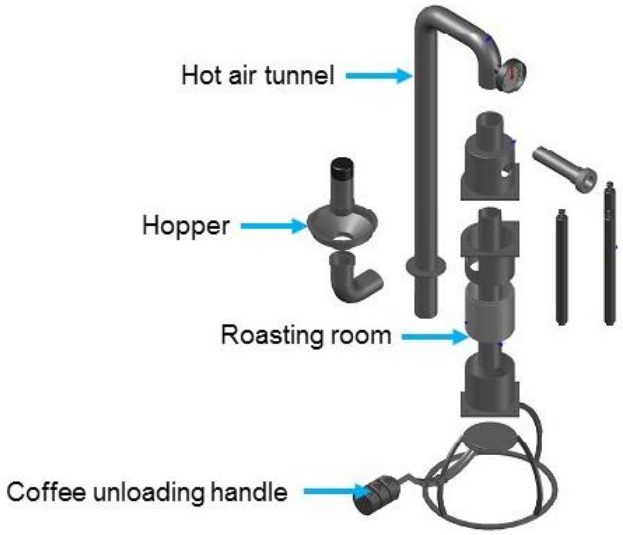


Fig. 4 - Coffee roasting room and hot air duct

Chaffs and dust collector

Material components for the chaff and dust container comprises a stainless-steel pipe with a diameter of 110 mm and a length of 300 mm, as well as a stainless-steel pipe with a diameter of 51 mm and a length of 87 mm. The chaff and dust collection container is a mason jar with a 110 mm top diameter, a 150 mm bottom diameter, and a 190 mm height. The design of this part is presented in figure 5.



Fig. 5 - Chaff and dust collector

Heating furnace and chimney

The heating furnace comprises a heat exchanger heated by a jet burner fuelled by liquefied petroleum gas. The heat exchanger was constructed from five pieces of iron pipes with threaded iron axles; each iron pipe had a diameter of 25.4 mm and a length of 250 mm. The screw configuration of the heat exchanger was intended to increase the heated surface area to create sufficient heat for the roasting process. The higher the heat transfer efficiency, the greater the overall contact area of the heat exchanger. The chimney had a height of 750 mm and was built of 100x40 mm hollow iron. The exploded view of the heat exchanger and jet burner is shown in figure 6.

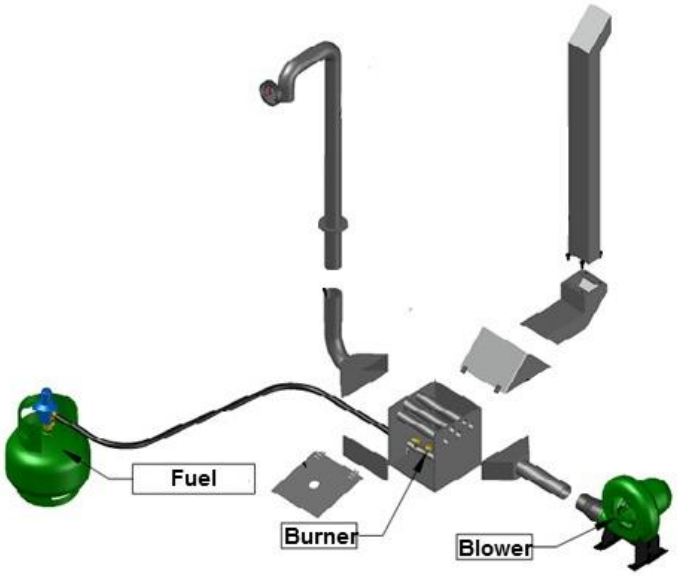


Fig. 6 - Heat exchanger and jet burner

Roasting chamber design

The roasting drum had a capacity of 500 grammes per batch, a bulk density of 0.72 g/mL for green beans, a 50% increase in volume for roasted beans, and a 20% decrease in mass for roasted beans.

Bulk density and percentage of volume growth are required so that the roasting chamber can handle coffee beans whose volume will increase as a result of the roasting process.

Heat exchanger design

The screw type heat exchanger consists of five units of steel pipes with an inside diameter of 25.4 mm, a length of 250 mm and a thickness of 3 mm. Each pipe has a worm screw inside to ensure air can receive more heat as it passes through this pipe. The worm screw inside the steel pipe is made of solid steel with a shaft diameter of 10 mm and a length of 250 mm. The helical spiral's thickness is 2 mm. The illustration of the heat exchanger is shown in figure 7.



Fig. 7 - Heat exchanger design

Evaluation of the fluidized coffee roaster

The evaluation of the prototype was performed under two conditions (with and without loads). Tests under no-load conditions were carried out to investigate air flow and temperature in the heat exchanger and roasting chamber during heating in the absence of coffee beans. Tools used for observing the temperature was Arduino-based data logger with thermocouple type K (accuracy of 0.5 °C).

Performance tests with load condition were conducted using two types of green coffee beans i.e., Robusta and Arabica coffee. The initial moisture water content of the sample coffee beans ranged between 10-12% wet basis. The evaluation was performed to evaluate the coffee roaster in the context of producing the three levels of roasted coffee (light, medium, and dark). The parameters observed consisted of the time required to reach each level, cracking time, cracking temperature, and final temperature (after the desired roasting level was achieved). Based on the preliminary studies, light levels were obtained 1 minute after 1st crack, the medium was obtained 3 minutes after 1st crack and dark levels were obtained 5 minutes after 1st crack. Each level has been validated by comparing it to L* a* b* colour standard for each level in the preliminary studies.

The coffee roasting procedure for each treatment was started under the same conditions, where the temperature in the roasting room reached 180 °C. After that, the green coffee beans (temperature 30 °C) were added and consequently, the temperature in the roasting chamber dropped below 110 °C. Then the temperature in the roasting room rose again over time.

RESULTS

The prototype of fluidized coffee roasting machine

The prototype of fluidized coffee roasting machine developed in this study is shown in figure 8, and the specifications of the machine are presented in table 1.



Fig. 8 - The prototype of a fluidized coffee roaster

Table 1

The specifications of a fluidized coffee roaster prototype

Parameters	Value/type	Unit
Overall dimensions	982 x 500 x 1390	mm
Roasting Chamber	1948	mm^3
Chaff and dust collector	Ø 60 x 110	mm
Blower	220-380 V, 50-60 Hz, 600 watt, 16000 rpm	-
Burner	Jet burner	-
Fuel	LPG	-
Temperature sensors	Roasting chamber and bean	-
Roasting capacity	500	g

According to a calculation based on the size of the planned roaster and the volume and mass and shape of the coffee bean, the space taken up by the roasted green coffee bean was 28.23% of the total volume of the roasting chamber. Previous publications *(Hadzich et al., 2014)* claimed that the green bean to roasting chamber volume ratio was between 24 and 32%; the current findings of the study demonstrated that the proportion fell within this range. According to another source *(Nagaraju et al., 1997)*, the ratio of green bean to roasting chamber capacity can reach up to 40%. The relationship between the volume of green beans and that of the roasting chamber ensures that the roasted green beans receive sufficient heat and that the coffee roasting process is not interrupted. The mass reduction percentage for roasted beans regulates airflow, so that roasted beans are not transported to the chaff and dust collector.

The heat exchanger consisted of five cylinders, each containing a screw, and had an area of 105 mm2 iron plate with a thickness of 2 mm, a 3.89 x 10^4 mm^2 iron plate with a thickness of 3 mm, and a 78.5 mm^2 iron shaft with a length of 1250 mm; The temperature generated in the heat exchanger reached 650 °C, and 220 °C in the roasting chamber.

Fluidized coffee roasting performance

Figure 9 depicts the performance of a fluidized roaster manufactured under no-load conditions. It was shown that the temperature in the heat exchanger and roasting chamber increased with the time. The temperature in the heat exchanger achieved the temperature of about 650 °C, while the temperature in the roasting chamber was about 200 °C. Generally, the coffee beans were fed into the roasting chamber when the temperature was about 180 °C. By using this fluidized roaster, the targeted temperature value could be reached only in 12 minutes, about 6 minutes faster than using the drum type coffee roaster developed by *Hidayat et al. (2020)*.

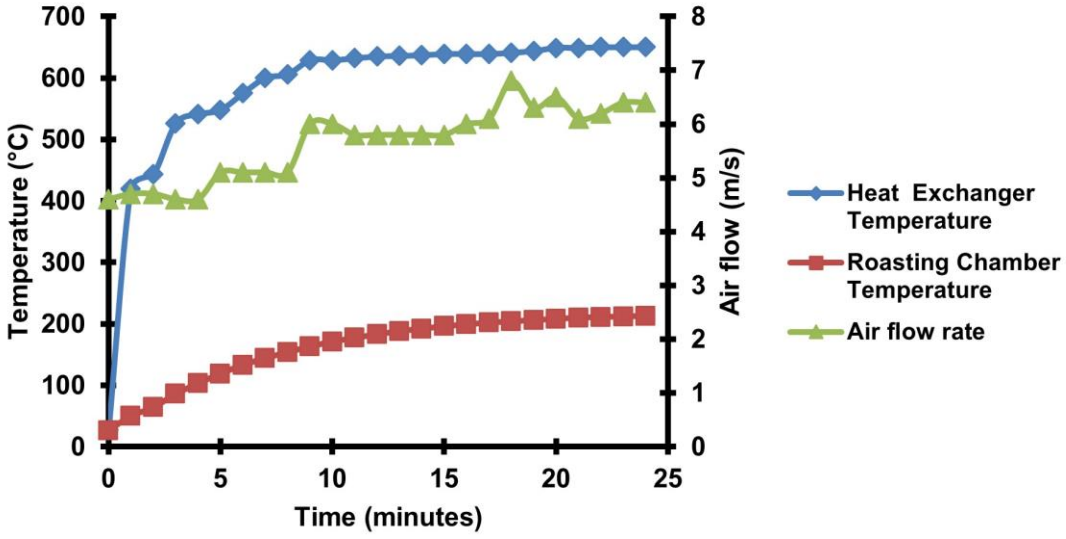


Fig. 9 - Performance of a fluidized roaster fabricated under no-load conditions

Figure 10 present the performance of fluidized coffee roaster using two different type of coffee beans (Robusta and Arabica). At a range of air flow 4-6 m/sec, the average temperature rise in the furnace and roasting chamber was 26 °C and 7.8 °C per minute, respectively.

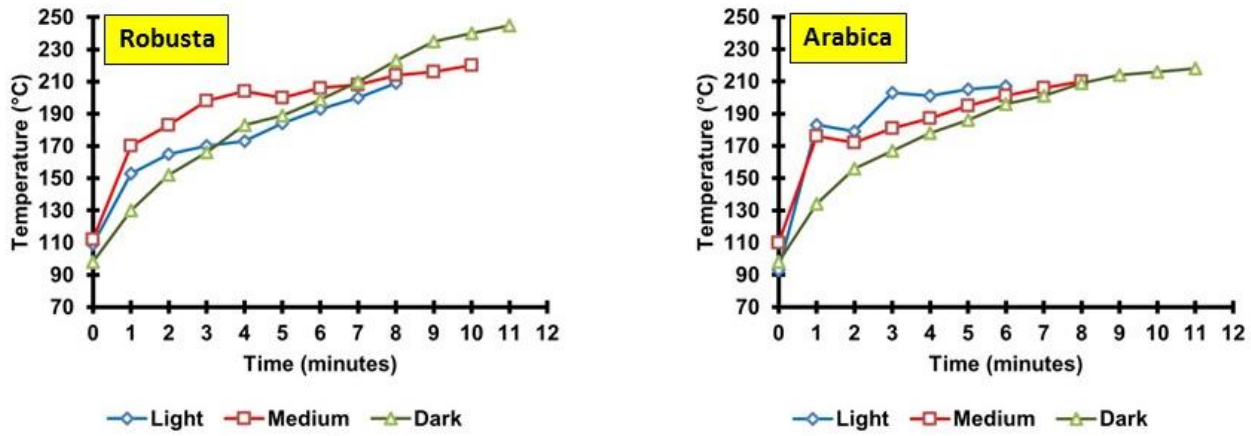


Fig. 10 - Performance of fluidized coffee roaster during roasting process

At all roasting degrees (light, medium, and dark), the cracking time of Robusta coffee during roasting was longer than that of Arabica coffee.

Table 2 shows that the temperature at which Robusta coffee cracked was higher than that of Arabica coffee. The only time Arabica coffee cracked at a higher temperature was when it was lightly roasted.

Table 2

Performance of fluidized roaster on Robusta and Arabica Coffee at various roasting degree

Description	Robusta			Arabica		
	light	medium	dark	light	medium	dark
Cracking time, minute-second	7'11"	6'51"	7'2"	4'19"	4'40"	6'43"
Cracking temperature, °C	201	208	210	205	195	201
Total time required, minute-second	8'11"	9'51"	12'2"	5'19"	7'40"	11'43"
Final roasting temperature, °C	209	220	248	207	210	218

Total time required to achieve the desired roasting level was different between Robusta and Arabica. Robusta coffee required longer time to reach the desired level of roasting compared to Arabica coffee. This was due to the difference in cracking time, where the faster the cracking time was achieved, the faster the desired roasting level was obtained. This result was in line with previous studies which use drum-type coffee roasters, where it was found that the cracking time and total roasting time of Arabica coffee beans were relatively shorter compared to Robusta coffee beans (*Hidayat et al., 2020)*. According to *Hidayat et al. (2020)*, this occurred due to the difference in hardness, where the green Robusta bean was harder than the green Arabica bean. The final coffee beans temperature for both varieties increased from light to dark. Furthermore, Robusta coffee reached a greater final roasting temperature at light, medium, and dark roasting degrees.

From the data, it was also found that roasting process using this fluidized coffee roaster gave shorter total time compared to the roasting process using drum type coffee roaster developed by *Hidayat et al. (2020)*. This happens because in the fluidized type, the coffee beans receive heat evenly over their entire surface due to the exhaled hot air. Heat is also transmitted by convection to all coffee beans, where in the drum type roaster, coffee receives most of the heat by conduction from the drum.

CONCLUSIONS

The fluidized coffee roaster was developed and constructed for small-scale farmers as an economical, simple, and easy-to-operate machine with the capacity to roast 500 grammes of coffee beans. This fluidized roaster consisted of heating furnace room, housing for the blower and temperature control, coffee roasting room, hot air duct, cyclone, heating furnace chimney, and gas holder. At a range of airflow of 4-6 m/sec, the average temperature increase in the furnace and roasting chamber was 26°C and 7.8°C per minute, respectively. The time and temperature of cracking of Robusta coffee were 7'11'', 6'51'', and 7'2" at temperature of 201°C, 208°C and 210°C, respectively, and for Arabica were 4'19", 4'40", and 6'43", at temperature of 205°C, 195°C, and 201°C.

This fluidized roaster was able to roast Robusta coffee beans to a light, medium and dark roast in 8'11", 9'51", and 12'2" minutes with final roasting temperature of 209°C, 220°C, and 248°C, while for Arabica coffee, the time required was 5'19", 7'40", and 11'43" minutes with final roasting temperature 207°C, 210 °C, and 218°C, respectively. This fluidized coffee roaster can be used by the small coffee shop business with appropriate capacity.

ACKNOWLEDGEMENT

The authors would like to thank colleagues at the metal mechanics workshop of Research Centre for Appropriate Technology for their contributions to the production of fluidized roasters and the preparation of test materials.

REFERENCES

[1] Baggenstoss, J., Poisson, L., Kaegi, R., Perren, R., & Escher, F. (2008). Coffee Roasting and Aroma Formation: Application of Different Time−Temperature Conditions. *Journal of Agricultural and Food Chemistry*, *56*(14), 5836–5846. https://doi.org/10.1021/jf800327j

[2] Chandrasekar, V., & Viswanathan, R. (1999). Physical and Thermal Properties of Coffee. *Journal of Agricultural Engineering Research*, *73*(3), 227–234. https://doi.org/10.1006/jaer.1999.0411

[3] Clarke, R. J. (1987). Roasting and Grinding. In R. J. Clarke & R. Macrae (Eds.), Coffee: Volume 2*: Technology* (pp. 73–107). Springer Netherlands. https://doi.org/10.1007/978-94-009-3417-7_4

[4] Darmajana, D. A., Hidayat, D. D., Indriati, A., Sagita, D., Rahayuningtyas, A., & Sudaryanto, A. (2022). *Comparative study of changes in physical, mechanical, and colour properties between Arabica and Robusta coffee beans prior to and after roasting*. *2493*, 040008. https://doi.org/10.1063/5.0109975

[5] Darmajana, D. A., Wulandari, R., & Sagita, D. (2022). Characteristics of cold brewed Arabica coffee from Gunung Karamat village Subang Regency as a result of different temperatures and roasting time. *Inmateh - Agricultural Engineering*, *68*(3), 836–843.

[6] Dorfner, R., Ferge, T., Yeretzian, C., Kettrup, A., & Zimmermann, R. (2004). Laser Mass Spectrometry as On-Line Sensor for Industrial Process Analysis: Process Control of Coffee Roasting. *Analytical Chemistry*, *76*(5), 1386–1402. https://doi.org/10.1021/ac034758n

[7] Eggers, R., & Pietsch, A. (2001). Technology I: Roasting. In *Coffee* (pp. 90–107). https://doi.org/10.1002/9780470690499.ch4

[8] Hadzich, M., Veynandt, F., Delcol, J., Hadzich, L. M., Pérez, J. P., & Vergara, S. (2014). Design of a Solar Coffee Roaster for Rural Areas. *Energy Procedia*, *57*, 3215–3224. https://doi.org/10.1016/j.egypro.2015.06.071

[9] Hernández, J. A., Heyd, B., & Trystram, G. (2008). On-line assessment of brightness and surface kinetics during coffee roasting. *Journal of Food Engineering*, *87*(3), 314–322. https://doi.org/10.1016/j.jfoodeng.2007.12.009

[10] Hidayat, D. D., Sagita, D., Darmajana, D. A., Indriati, A., Rahayuningtyas, A., Sudaryanto, A., Kurniawan, Y. R., & Nugroho, P. (2021). Development and thermal evaluation of double drum dryer for ready-to-eat food products to support stunting prevention. *INMATEH-Agricultural Engineering*, *64*(2).

[11] Hidayat, D. D., Sudaryanto, A., Kurniawan, Y. R., Indriati, A., & Sagita, D. (2020). Development and Evaluation of Drum Coffee Roasting Machine for Small-Scale Enterprises. *INMATEH Agricultural Engineering*, *60*(1), 79–88. https://doi.org/10.35633/inmateh-60-09

[12] Kristanti, D., Setiaboma, W., Ratnawati, L., & Sagita, D. (2022). Robusta coffee cherry fermentation: Physicochemical and sensory evaluation of fermented cascara tea. *Journal of Food Processing and Preservation*. https://doi.org/10.1111/jfpp.17054

[13] Latvakangas, S. (2022). Coffee Roasting Basics: Developing Flavour by Roasting. *Paulig Barista Institute*. https://www.baristainstitute.com/blog/sampo-latvakangas/april-2022/coffee-roasting-basics-developing-flavour-roasting

[14] Nagaraju, V. D., Murthy, C. T., Ramalakshmi, K., & Srinivasa Rao, P. N. (1997). Studies on roasting of coffee beans in a spouted bed. *Journal of Food Engineering*, *31*(2), 263–270. https://doi.org/10.1016/s0260-8774(96)00026-x

[15] Pérez-Martínez, M., Sopelana, P., de Peña, M. P., & Cid, C. (2008). Changes in Volatile Compounds and Overall Aroma Profile during Storage of Coffee Brews at 4 and 25 °C. *Journal of Agricultural and Food Chemistry*, *56*(9), 3145–3154. https://doi.org/10.1021/jf703731x

[16] Petracco, M., & Viani, R. (2005). Coffee consumption and health. *Espresso Coffee*, 352–383. https://doi.org/10.1016/b978-012370371-2/50011-1

[17] Sagita, D., Rahayuningtyas, A., & Kurniawan, Y. R. (2021). Design, fabrication and thermal evaluation of lemang (rice bamboo) cooking device integrated with continuous rotating system. *Agricultural Engineering International: CIGR Journal*, *23*(4), 13.

[18] Sagita, D., Setiaboma, W., Kristanti, D., Kurniawan, Y. R., Hidayat, D. D., Darmajana, D. A., Sudaryanto, A., & Nugroho, P. (2022). Experimental investigation of heating pattern, energy requirement and electrical conductivity in a batch ohmic heating system for coffee fermentation. *Innovative Food Science & Emerging Technologies*, *76*, 102946. https://doi.org/10.1016/j.ifset.2022.102946

[19] Schenker, S., & Rothgeb, T. (2017). The Roast—Creating the Beans' Signature. *The Craft and Science of Coffee*, 245–271. https://doi.org/10.1016/b978-0-12-803520-7.00011-6

[20] Velasquez, S., Peña, N., Bohórquez, J. C., & Gutiérrez, N. (2018). Determination of the complex permittivity of cherry, pulped, green, and roasted coffee using a planar dielectric platform and a coaxial probe between 0.3 and 6 GHz. *International Journal of Food Properties*, *21*(1), 1332–1343. https://doi.org/10.1080/10942912.2018.1490320

[21] Wang, X., & Lim, L.-T. (2015). Chapter 27—Physicochemical Characteristics of Roasted Coffee. In V. R. Preedy (Ed.), *Coffee in Health and Disease Prevention* (pp. 247–254). Academic Press. https://doi.org/10.1016/B978-0-12-409517-5.00027-9

[22] Zimmermann, R., Heger, H. J., Yeretzian, C., Nagel, H., & Boesl, U. (1996). Application of Laser Ionization Mass Spectrometry for On-line Monitoring of Volatiles in the Headspace of Food Products: Roasting and Brewing of Coffee. *Rapid Communications in Mass Spectrometry*, *10*(15), 1975–1979. https://doi.org/10.1002/(sici)1097-0231(199612)10:15<1975::aid-rcm786>3.0.co;2-x

MODELING OF THE RUNNING SYSTEM PRESSURE ON THE SOIL DEPENDING ON THE STRUCTURAL PARAMETERS OF THE TRACTORS
/
МОДЕЛЮВАННЯ ТИСКУ ХОДОВОЇ СИСТЕМИ НА ГРУНТ В ЗАЛЕЖНОСТІ ВІД КОНСТРУКТИВНИХ ПАРАМЕТРОВ ТРАКТОРІВ

Gennadii GOLUB*[1)], Viacheslav CHUBA[2)], Vasyl ACHKEVYCH[1)], Victor KRUSHELNYTSKYI[1)], Nataliya TSYVENKOVA[1)]
[1)] National University of Life and Environmental Sciences of Ukraine / Ukraine;
[2)] Bila Tserkva National Agrarian University / Ukraine;
Tel: +380953115050; E-mail: gagolub@ukr.net
DOI: https://doi.org/10.35633/inmateh-69-34

Keywords: *soil, resistance force, tractor weight, soil reactions*

ABSTRACT
The article defines the influence of the traction resistance of the machine-tractor unit working tool on the weight distribution of the tractor along the running system axles. Depending on the type of field work, the resistance force of tools aggregated with a tractor has a different value, accordingly, the tractor has a different weight distribution along the axles and, thus, different ground pressure. An increase in pressure on the soil leads to additional costs for tillage, and in the future to a decrease in agricultural production efficiency. The article presents a mathematical model for determining the reactions of the soil, and, accordingly, the pressure of tractor engines on the ground, depending on the structural parameters of the tractor, its adequacy estimation, and an example of calculating the weight distribution along the tractor axles.

РЕЗЮМЕ
У статті визначено вплив тягового опору робочого знаряддя машинно-тракторного агрегату на розподіл ваги трактора по осям ходової системи. У залежності від виду польових робіт, сила опору знарядь, що агрегатуються із трактором має різне значення, а відповідно і трактор має різний розподіл ваги по осям та відповідно різний тиск на ґрунт. Збільшення тиску на ґрунт призводить до додаткових витрат на обробіток ґрунту, а у подальшому і до зменшення ефективності аграрного виробництва. У роботі представлена математична модель для визначення реакцій ґрунту, а відповідно і тиску тракторних рушіїв на ґрунт в залежності від конструкційних параметрів трактора, оцінена її адекватність, приведений приклад розрахунку розподілу ваги по осям трактора.

INTRODUCTION

During fieldwork, tractor wheels interact with the fertile soil layer. As a result of the force interaction, the phenomena of soil deformation and compaction are observed *(Golub et al, 2021; Mileusnić et al, 2022)*. Therefore, biological processes in the soil are disrupted *(Keller et al, 2022)*, which leads to a decrease in field crop yields *(Nawaz et al, 2012; Mueller et al., 2010)*.

Taking into account the existing trends towards increasing the productivity of machine-tractor units, as a result of an increase in the traction force and weight of tractors, there is an increase in the negative impact of running systems on the ground *(Keller et al, 2019; Mileusnić et al, 2022)*. In this regard, the problem of minimizing soil compaction is relevant for agricultural production.

The problem of soil compaction is one of the key ones for tractor developers. One of the most effective ways to solve the problem of reducing pressure on the ground is to increase the contact area of running systems with the ground, through the use of double wheels, specially designed tires and specially designed structures of running systems *(Keller et al, 2004; Shaheb et al, 2021; Molari et al, 2012)*.

To ensure the implementation of tractor traction power, it is necessary to provide a certain coupling weight in the contact area of running systems with the ground *(Golub et al, 2017)*. An increase in the resistance of aggregates and tools that are aggregated with the tractor leads to a decrease in pressure on the ground of the front wheels and an increase in pressure on the ground of the rear wheels, which is especially noticeable when working with mounted working machines *(Bauer et al, 2022)*.

It is well known that the most common weight distribution of tractors is as follows: classic row wheel tractor – 60% on the rear axle and 40% on the front axle; articulated frame tractor – 55% on the front axle and

45% on the rear axle; crawler tractor – 60% on the front and 40% on the rear axle. Regardless of the weight distribution of the wheeled tractor along the axles, the ground pressure of the front axle is 10-15% greater than that of the rear axle. The crawler tractor presses on the ground with the front part at a pressure that is 30% greater than the pressure of the tractor rear part.

In the results of field studies regarding ground pressure on wheeled running systems *(Ardvidson and Keller, 2014)*, it is noted that the John Deere tractor on paired wheels in a static state creates pressure at a depth of 15 cm – 150 kPa for the front axle and 145 kPa for the rear; and at a depth of 30 cm – 80 kPa for the front axle and 70 kPa for the rear. However, in this paper there are no dependences of pressure on the soil, taking into account the resistance of tillage or other tools.

Experimental studies of changes in the soil response from changes in the traction load on the hook of a wheeled tractor *(Polcar et al, 2017)* showed that with the traction resistance of the working tool in the range from 55 kPa to 70 kPa, there is a decrease in the pressure on the ground of the front axle and an increase in the pressure of the rear axle by an amount of 6 to 8 %. Similar results of pressure redistribution between the axles of wheeled running systems in the presence of traction load from a working machine are noted in studies *(Patil, 2015; Renčín et al, 2017)*. Analysis of completed studies *(Polcar et al, 2017; Patil, 2015; Renčín et al, 2017)* allows concluding that if there is a traction resistance of a working machine on the tractor hook, the front axle of the tractor is unloaded and the load of the rear axle increases.

Studies of the pressure distribution of crawler running systems of modern tractors *(Keller et al, 2002; Arvidsson et al, 2011; Ardvidson and Keller, 2014)* have shown that in the presence of traction load on the hook in comparison with static load, the load is redistributed, while the front support rollers are unloaded and the load increases in the area of the running systems rear part. The authors *(Keller et al, 2002; Arvidsson et al, 2011)* noted that after appropriate ballasting of the tractor and reducing the height of the working machine attachment point, the maximum vertical load in the tractor rear part was reduced and, accordingly, increased in the front.

The presented research results for different tractors give an idea of the general trends in weight redistribution between the axles and allow stating that the existing traction resistance of the working machine causes a redistribution of tractor weight between the axles. To ensure uniform pressure on the ground and ensure the implementation of engine traction power, the tractor must have an appropriate weight distribution in the contact area of the running systems with the ground under dynamic load during field work. Taking into account the design features of tractors and a variety of working machines, the correct acquisition of machine and tractor units is a rather complex practical task that requires experimental research, taking into account the work in a certain agrotechnological environment.

Polcar et al. obtained a dependence for determining the change in soil response from changes in the load on the tractor hook *(Polcar et al, 2017)*. At the same time, the authors took into account the placement of vectors of tractor traction forces at wheels point of contact with the ground. Since the ground load distribution model is based on the sum of the moments of forces relative to the wheel point of contact with the ground, this arrangement of the traction force vectors excludes their influence on the ground and, in addition, the force applied at the wheel point of contact with the ground cannot be the driving force *(Golub et al, 2017)*.

Wang and Zoerb, (1989), considers the change in axle load during tractor movement. The obtained dependences indicate that the load on the tractor axle depends on the horizontal traction on the hook, the distance of the hook from the rear axle, the height of the hook placement, and the wheelbase of the tractor. The authors obtained a dependence for determining the weight of the tractor front part when driving with a load:

$$W_F = W_{SF} - \frac{D \cdot y}{B} - \frac{D \cdot x}{B}$$

Where W_F – weight of the tractor front part when driving with a load, kg; W_{SF} – weight of the tractor front part without load, kg; D – traction force on the tractor hook, N; y – distance from hook to wheel axis, m; x – hook height above the surface, m; B – tractor wheelbase, m.

From this relationship, it follows that the weight of the tractor front part decreases under the influence of the traction force on the tractor hook. The reduction in the weight of the tractor front part depends proportionally on the coordinates of the hook placement and inversely on the size of the wheelbase.

Kumar et al, (2013), presents a study of changes in the sliding coefficient of the drive wheel depending on the unit speed, the angle of the working bodies' position and the processing depth. The most significant influence on the tractor traction properties was exerted by the processing depth and the angle of the working bodies' position, in contrast to the movement speed. The authors also use a dependency to determine the

weight of the tractor rear axle when driving with a load:

$$W_D = W_S + P\frac{H}{X} \quad (2)$$

Where W_D – weight of the tractor rear part when driving with a load, kg; W_S – weight of the tractor rear part without load, kg; P – thrust force on the hook, N; H – hook height above the surface, m; X – tractor wheelbase, m. From this connection, it also follows that the increase in the weight of the tractor rear part is directly proportional to the height of the hook placement above the surface and inversely proportional to the tractor wheelbase size.

The above dependencies do not take into account the influence on the weight distribution of the tractor along the axles of the application angle of the working machine resistance force, the radii of the tractor wheels, besides, the tractor traction force vector is applied at the contact point of the wheels with the ground *(Wang and Zoerb, 1989; Kumar et al, 2013)*. Also, these dependencies do not take into account the weight of the tractor ballast.

The performed analysis gives an understanding that during operation, the traction resistance of the working machine leads to a redistribution of the tractor weight along the axles of the running systems. Existing dependencies partially take into account the redistribution of tractor weight, but do not fully take into account the design features of the tractor and the effect of forces that occur during its movement. Therefore, the development of refined dependencies for determining tractor weight distribution along the axles of the running system, depending on the traction resistance of the working machine, is an important scientific task.

The purpose of this work is to obtain dependencies for determining tractor weight redistribution, taking into account the action of the working machine resistance forces during field work and the design parameters of the tractor, which will be suitable for determining the weight of the tractor front ballast.

MATERIALS AND METHODS

Determination of the dependence that connects the redistribution of tractor weight and traction resistance on the hook during fieldwork was performed based on the power analysis of the machine-tractor unit, taking into account tractor design features and the resistance force angle of the action.

To check the adequacy of the obtained dependence of the tractor weight redistribution on the action of traction resistance on the hook, a comparison of experimental and theoretical data on the effect of the front load weight on the maximum traction force that the tractor can develop on the hook was performed. The John Deere 7130 wheeled tractor was chosen for experimental research, the main design parameters of which are shown in table 1.

Table 1

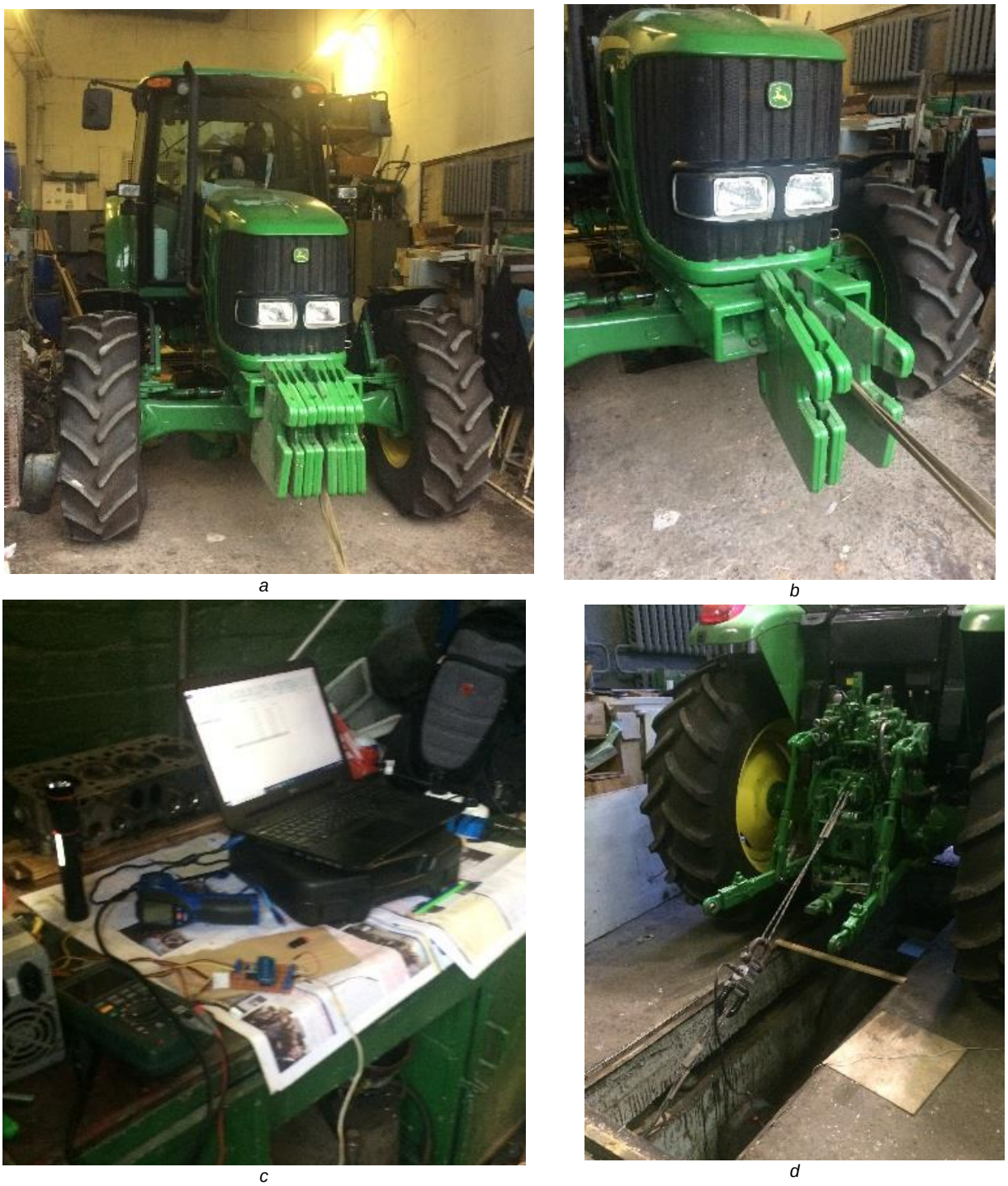
Main design parameters of the John Deere 7130 tractor

Indicator	John Deere 7130
Weight, N	**47,000**
Wheelbase, m	**2.7**
Distance from the front wheel axis to the tractor weight application point, m	**1.832**
Front wheel radius, m	**0.6**
Rear wheel radius, m	**0.9**
Distance from the rear wheel axis to the hook, m	**1.1**
Hook installation height, m	**0.4**

During the research, the tractor was placed on a flat horizontal plane and fixed to prevent horizontal movement. Fixing from horizontal movement was carried out by means of a connecting link, which was rigidly fixed at one end, and attached to the load cell with the other, which was attached to the tractor hook. The connecting link together with the load cell formed the angle of action of the resistance force to moving the tractor. The load cell on the tractor hook measured the resistance to movement that occurred under the traction force action. The maximum traction force on the tractor hook was recorded at the moment when the load from the tractor weight on the front axle was absent and the wheels of the front axle were torn off from the support surface.

When performing experimental studies, the weight of the front ballast load was changed from 0 to 4 kN in increments of 0.5 kN. When applying the torque to the tractor wheels, the separation moment of the front

axle from the horizontal surface and the value of the traction resistance indicator on the load cell were simultaneously recorded. For each value of the ballast load weight, the maximum traction resistance was measured in threefold repetition. The equipment that was used during the research is shown in Fig. 1.



a b c d

Fig. 1 - Equipment used in conducting experimental studies

a – tractor with front load; b – change in the weight of the front load; c – traction load locking system; d – sensor with cables for measuring traction load

When moving evenly from the tractor side, the following factors affect the ground: the weight of the tractor G, the weight of the front G_{FL} and rear G_{BL} load, the resistance of the tool F_{TR}, the traction on the front F_{TF} and rear F_{TB} wheel. This scheme was supplemented with countermeasures from the soil to the front R_F and rear R_B axles. The design diagram of the tractor used during the research is shown in Fig. 2.

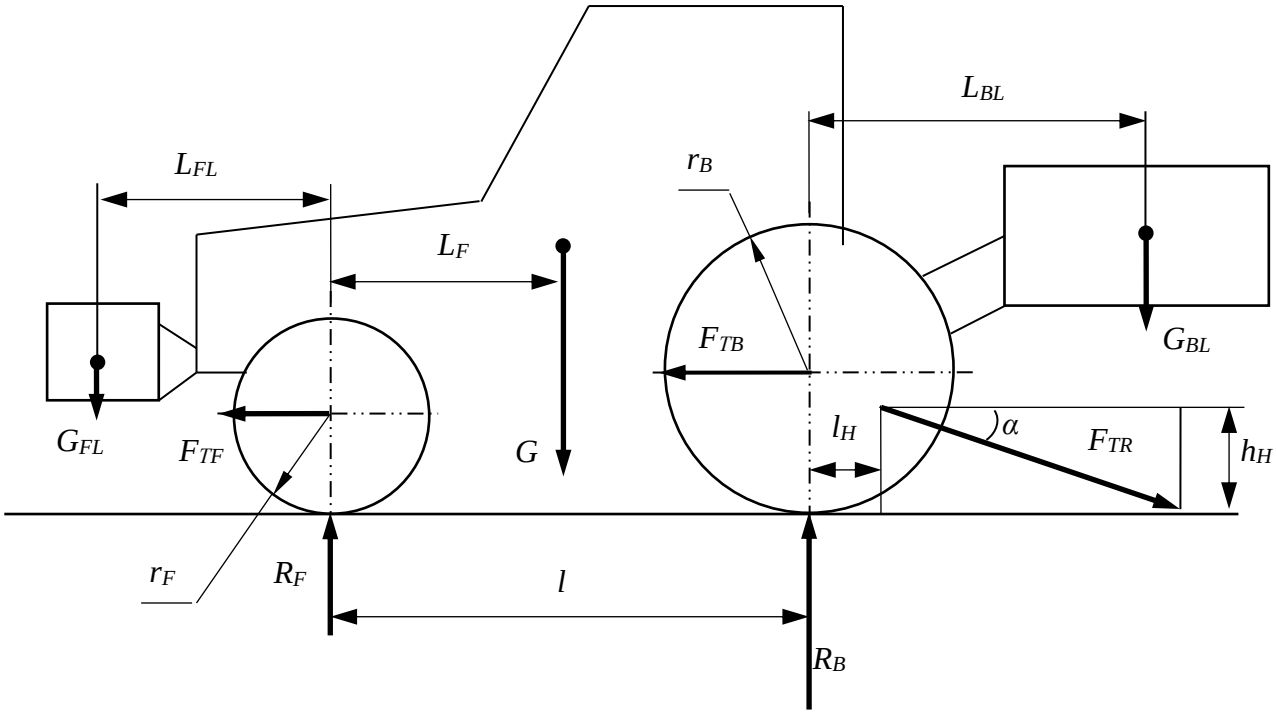


Fig. 2 - Calculation scheme of a wheeled tractor

G – tractor total weight, kN; G_{FL}, G_{BL} – weight of the front and rear loads, kN, respectively; l – distance between tractor wheel axles (tractor base), m; l_F – distance from the front wheel axis to the tractor weight application point, m; l_{FL}, – distance from the front wheel axis to front load center of gravity, m; l_{BL} – distance from the rear wheel axis to rear load center of gravity, m; r_F, r_B – radius of the tractor front and rear wheels, respectively, m; l_H – distance from the rear wheel axis to the hook, m; h_H – hook installation height, m; R_F, R_B – reaction at the tractor front and rear wheels contact point with the ground, kN; F_{TF}, F_{TB} – traction force on the tractor front and rear wheels, respectively, kN; F_{TR} – resistance force of the tillage tool, kN; α – resistance force action angle, rad.

When performing theoretical calculations, the values of the tractor parameters were taken in accordance with those at which experimental studies were performed (Table 1).

RESULTS

By reducing the action of the tractor weight and loads $G = G_{FL} + G_F + G_B + G_{BL}$ to one point and taking into account the distance from the front wheel axis to the application point of the tractor weight l_F, based on the moments from the action of the tractor components weight $G_{FL}(l_{FL} + l_F) + G_F l_F = G_B(l - l_F) + G_{BL}(l_{BL} + l - l_F)$ we will get:

$$l_F = \frac{G_B l - G_{FL} l_{FL} + G_{BL}(l_{BL} + l)}{G_{FL} + G_F + G_B + G_{BL}} \quad (1)$$

In the absence of rear, front, and both loads, this distance will be:

$$l_F^B = \frac{G_B l - G_{FL} l_{FL}}{G_{FL} + G_F + G_B};\ l_F^F = \frac{G_B l + G_{BL}(l_{BL} + l)}{G_F + G_B + G_{BL}};\ l_F^{BF} = \frac{G_B l}{G_F + G_B} \quad (2)$$

Where G_F, G_B – part of the tractor weight transmitted to the front and rear axles of the tractor, kN.

From Fig. 2, the sum of the moments of forces acting on the MTA relative to the wheels points of contact with the ground will be:

$$T_F = R_B l - G l_F + F_{TF} r_F + F_{TB} r_B - F_{TR} h_H \cos\alpha - F_{TR}(l_H + l) sin\alpha = 0 \quad (3)$$

$$T_B = -R_F l + G(l - l_F) + F_{TF} r_F + F_{TB} r_B - F_{TR} h_H \cos\alpha - F_{TR} l_H sin\alpha = 0 \quad (4)$$

Where:

T_F, T_B – the total moment of forces acting on the MTA relative to the front and rear wheels contact point with the ground, respectively, kN m.

The distribution of the traction forces of the front and rear wheels is determined according to the distribution of the tractor weight between the front and rear axles by the expressions: $F_{TF} = \frac{G_F}{G} F_T = k_{TF} F_T$ and

$F_{TB} = \frac{G_B}{G} F_T = k_{TB} F_T$, and taking that the total traction force of the tractor as $F_T = F_{TR} cos\alpha$, the soil reactions to the rear and front axles will have the value:

$$R_B = [G l_F - k_{TF} F_{TR} r_F cos\alpha - k_{TB} F_{TR} r_B cos\alpha + F_{TR} h_H \cos\alpha + F_{TR}(l_H + l) sin\alpha] l^{-1}; \quad (5)$$

$$R_F = [G(l - l_F) + k_{TF} F_{TR} r_F cos\alpha + k_{TB} F_{TR} r_B cos\alpha - F_{TR} h_H \cos\alpha - F_{TR} l_H sin\alpha] l^{-1}, \quad (6)$$

or:

$$R_B = \left[G l_F - F_{TR}\left((k_{TF} r_F + k_{TB} r_B - h_H)\cos\alpha - (l_H + l) sin\alpha\right)\right] l^{-1}; \quad (7)$$

$$R_F = \left[G(l - l_F) + F_{TR}\left((k_{TF} r_F + k_{TB} r_B - h_H)\cos\alpha - l_H sin\alpha\right)\right] l^{-1}, \quad (8)$$

Where k_{TF}, k_{TB} – coefficients of distribution of the tractor total weight between the front and rear axles, respectively, rel. un.

For a crawler tractor that is driven only from the rear axle, using the reaction equations for the wheeled tractor (7) and (8), the soil reaction equations for the front and rear of the crawler tractor will look like:

$$R_B = \left[G l_F - F_{TR}\left((r_C - h_H)\cos\alpha - (l_H + l) sin\alpha\right)\right] l^{-1}; \quad (9)$$

$$R_F = \left[G(l - l_F) + F_{TR}\left((r_C - h_H)\cos\alpha - l_H sin\alpha\right)\right] l^{-1}, \quad (10)$$

Where r_C – radius of the rear drive sprocket of the tractor track, m.

At critical action angles of the drag force (α = 0° and α = 90°) and different conditions of mutual placement of the hook relative to the wheels, the ground reactions to the front and rear axles will have the values shown in table 2.

Table 2

Values of soil reactions to the front and rear axles of the tractor with the same radii of the front and rear wheels ($r_F = r_B = r_W$)

α = 0°, $r_W = h_H$	α = 0°, $r_W > h_H$
$R_B = G\frac{l_F}{l}$; $R_F = G\frac{l - l_F}{l}$	$R_B = G\frac{l_F}{l} - F_{TR}\frac{r_W - h_H}{l}$; $R_F = G\frac{l - l_F}{l} + F_{TR}\frac{r_W - h_H}{l}$
α = 0°, $r_W < h_H$	α = 90°, $r_W = h_H$; $r_W > h_H$; $r_W < h_H$
$R_B = G\frac{l_F}{l} + F_{TR}\frac{h_H - r_W}{l}$; $R_F = G\frac{l - l_F}{l} - F_{TR}\frac{h_H - r_W}{l}$	$R_B = G\frac{l_F}{l} + F_{TR}\frac{l_H + l}{l}$; $R_F = G\frac{l - l_F}{l} - F_{TR}\frac{l_H}{l}$

From the above formulas, it is possible to draw several conclusions: at zero action angle of the resistance force on the tractor hook, the pressure forces of the wheels on the ground do not depend on the resistance force on the tractor hook, but depend only on the distribution of the tractor weight between the axles; if the tractor hook is installed above the wheel axles, then with an increase in the resistance force on the tractor hook, the pressure force of the front wheels on the ground decreases (the tractor can turn around the rear axle), and the pressure force of the rear wheels increases; if the tractor hook is installed below the wheel axles, then when the drag force on the tractor hook increases, the pressure force of the front wheels on the ground, on the contrary, increases, and the pressure force of the rear wheels decreases.

To check the obtained dependences (7 and 8) by conducting experimental studies, from the reaction equation of the front wheels, in the absence of a rear load, it is necessary to determine the conditions under which the pressure of the front wheels on the ground will be absent $(R_F = 0)$:

$$R_F = \left[G(l - l_F) + F_{TR}\left((k_{TF} r_F + k_{TB} r_B - h_H)\cos\alpha - l_H sin\alpha\right)\right] l^{-1} = 0. \quad (9)$$

Therefore, the value of the resistance force at which this condition will be met is:

$$F_{TR} = -\frac{G(l - l_F)}{(k_{TF} r_F + k_{TB} r_B - h_H)\cos\alpha - l_H sin\alpha} = -\frac{(G_{FL} + G_F + G_B + G_{BL})\left(l - \frac{G_B l - G_{FL} l_{FL} + G_{BL}(l_{BL} + l)}{G_{FL} + G_F + G_B + G_{BL}}\right)}{(k_{TF} r_F + k_{TB} r_B - h_H)\cos\alpha - l_H sin\alpha} =$$

$$= -\frac{G_{FL} l + G_F l + G_B l + G_{BL} l - G_B l + G_{FL} l_{FL} - G_{BL}(l_{BL} + l)}{(k_{TF} r_F + k_{TB} r_B - h_H)\cos\alpha - l_H sin\alpha} = -\frac{(G_{FL} + G_F) l + G_{FL} l_{FL} - G_{BL} l_{BL}}{(k_{TF} r_F + k_{TB} r_B - h_H)\cos\alpha - l_H sin\alpha} \quad (10)$$

The drag forces at which the pressure of the front wheels on the ground will be absent in the absence of rear, front and both loads, respectively, will be:

$$F_{TR}^B = -\frac{(G_{FL} + G_F) l + G_{FL} l_{FL}}{(k_{TF} r_F + k_{TB} r_B - h_H)\cos\alpha - l_H sin\alpha}; \; F_{TR}^F = -\frac{G_F l - G_{BL} l_{BL}}{(k_{TF} r_F + k_{TB} r_B - h_H)\cos\alpha - l_H sin\alpha}; \; F_{TR}^{BF} = -\frac{G_F l}{(k_{TF} r_F + k_{TB} r_B - h_H)\cos\alpha - l_H sin\alpha} \quad (11)$$

To check the adequacy of the obtained theoretical dependence (10), a comparison of theoretical and experimental data was performed. As a result of comparative studies, experimental and calculated graphical dependences of the effect of the front ballast load weight on the value of traction resistance on the tractor hook were obtained (Fig. 3).

Studies have shown that when the front ballast weight of the tractor changes in the range from 0 to 4kN, the maximum traction force of the tractor increases by 34.8 %. It should be noted a proportional increase in the maximum traction force with an increase in the mass of the ballast load. The index of determination of the calculated values and experimental data of changes in the traction force on the hook from changes in the weight of the front ballast load is calculated according to the method of *Dospehov, (1985)* and is $\eta^2 = 0.74$.

The specified value of the index of determination allows asserting the adequacy of the obtained calculated dependence (10) on experimental data, and also allows recommending the obtained models (7) and (8) for modeling the influence of tractor traction resistance on the weight redistribution between the axles of running systems when performing machine and tractor units of field work.

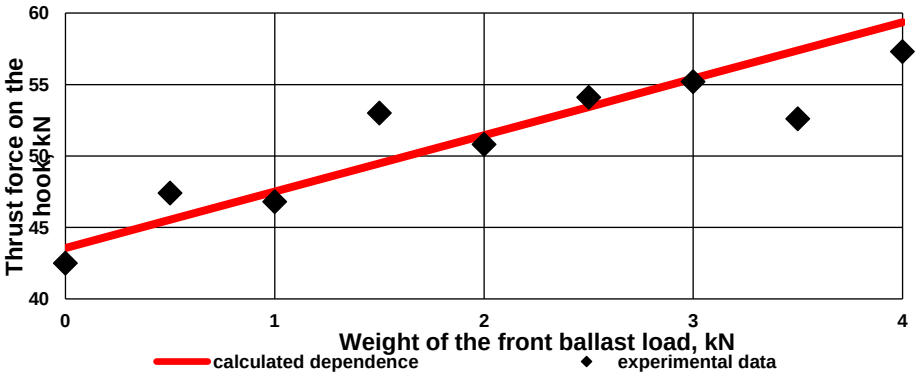


Fig. 3 - Dependence of the traction resistance of the tractor hook on the weight of the front ballast load

Expressions (7) and (8) were used to calculate the dependence of soil reactions (or ground pressure forces) on the front and rear axles as a function of the drag force action angle for the John Deere 7130 tractor when working with a Lemken five-body plow with a resistance of 30,000 N. The weight distribution of the tractor was as follows: the front axle was 15,118 N, the rear axle was 31,882 N. The calculation results are shown in Fig. 4.

Analysis of Fig 4 shows that the addition of a front load weighing 4 kN with a traction resistance of the working machine of 30 kN leads to a decrease in the load on the rear axle by 4.8% and an increase in the load on the front axle – by 29.7% with zero value of the resistance force action angle of the working machine. An increase in the resistance force action angle of the working machine from 0 to 15 degrees with the specified traction resistance leads to an increase in the load of the rear axle by 19.2% and a decrease in the load of the front axle – by 11.9%. Adding a 4 kg front load with a drag force angle of 15 degrees, reduces the load on the rear axle by 3.9% and increases the load on the front axle by 37.7%.

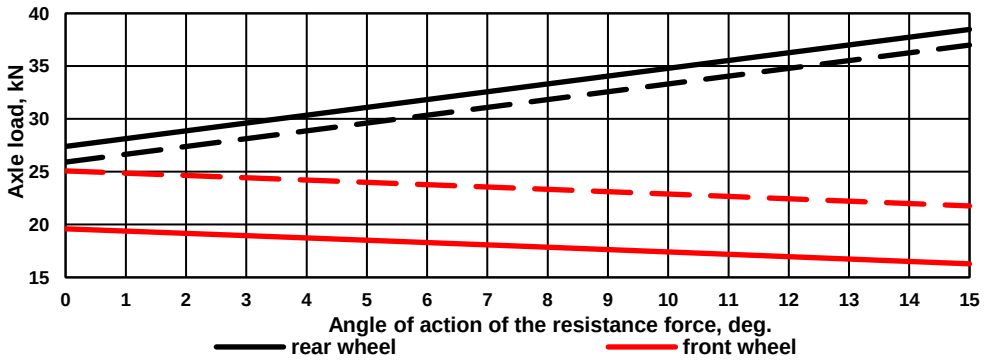


Fig. 4 - Dependence of soil reactions (or ground pressure forces) on the front and rear axles depending on the drag force action angle in the presence of a front load weighing 4 kN and without it

Expressions (9) and (10) were used to calculate the dependence of soil reactions (or ground pressure forces) on the front and rear axles as a function of the drag force action angle for the Challenger MT 845C crawler tractor when working with a Lemken seven-body mounted plow with a resistance of 45,000.

The weight distribution of the tractor was as follows: the front axle was 113,865 N, the rear axle was 75,904 N. The wheelbase of the tractor was 3 m, the radius of the front and rear sprockets was 0.47 m and 0.775 m. The calculation results are shown in Fig. 5 and 6.

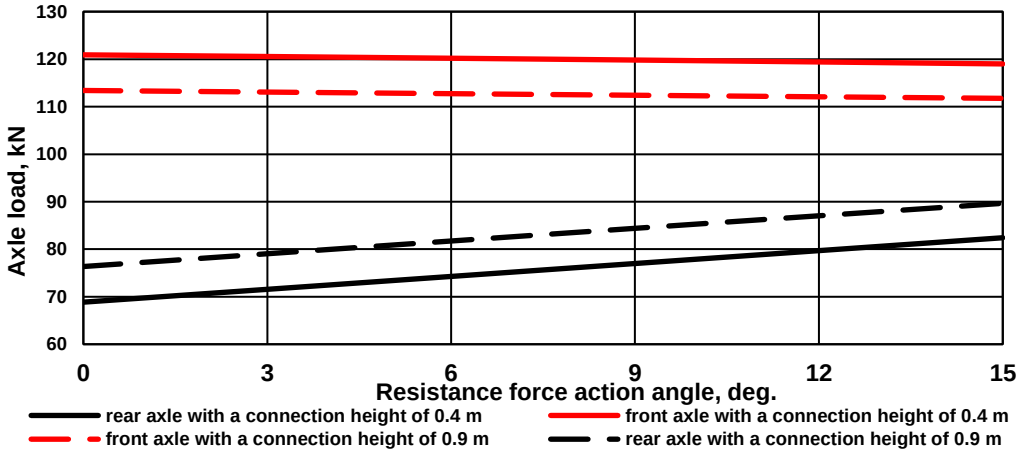


Fig. 5 - Dependence of soil reactions (or ground pressure forces) on the front and rear of the crawler tractor, depending on the drag force action angle and the height of the plow connection

Analysis of the obtained dependencies shown in Fig. 5 demonstrates that for a crawler tractor, when the connection height of the working machine increases, there is an increase in the load on the track rear part and unloading of the track front part. With a traction resistance of the working machine of 45 kN and an angle of action of resistance forces of 0 deg., an increase in the connection height of the working machine from 0.4 to 0.9 m, there is an increase in the load on the rear of the track by 10.9% and unloading by 6.2% of the front of the track. An increase in the drag force action angle of the working machine from 0 to 15 degrees at the specified traction resistance leads to an increase in the load on the rear part of the track by 19.7% and a decrease in the load on the front part of the track by 1.6%. At the same time, there is a slight decrease in the influence of the attachment height of the working machine on the load change. Thus, when the resistance angle of the working machine is 15 degrees, increasing the mounting height from 0.4 to 0.9 m leads to an 8.8% increase in the load on the rear of the track and unloading by 6.1% of the front of the track.

The dependencies shown in Fig. 6 demonstrate the influence of the working machine resistance angle and the height of its connection on the change in the ratio between the load on the front and rear axles of the Challenger MT 845C crawler tractor. The analysis of the obtained dependencies allows stating that by increasing the height of the working machine connection with a traction resistance of 45 kN, it is possible to reduce the ratio between loads between the front and rear axles in the range from 13.2% to 15.43%. It should be noted that a higher value of reducing the ratio corresponds to the resistance force action angle of the working machine at 0 degrees. With an increase in the working machine resistance angle, there is a decrease in the ratio between the loads on the front and rear axles. Thus, an increase in the action angle of the working machine resistance from 0 to 15 at the connection height of the working machine 0.4 m leads to a decrease in the ratio between the loads on the front and rear axles by 17.71%, and by 15.54% at the connection height of 0.9 m. In general, the analysis shows that by increasing the connection height and the action angle of the working machine resistance force, it is possible to reduce the ratio between the loads on the axles from 1.75 to 1.25 rel. units. The results show that due to the change in the connection height of the working machine, it is possible to slightly change the weight balance between the front and rear parts of the track, and by changing the action angle of the working unit resistance, it is possible to significantly load the rear part of the track.

Taking into account the trends in the development of modern crawler tractors, which have a sufficiently large power and a specific weight distribution between the front and rear of the track, manufacturers should develop recommendations in advance on how and with what working units of their machines can work to reduce the negative impact on the soil. To load the crawler tractor, it was chosen a swing mounted unit with a resistance of 45 kN, but it was not possible to ensure the same weight distribution between the front and rear parts of the track when working with it. As a rule, powerful tracked vehicles work with wide-range trailed or semi-trailed working units. However, when working with such units, the connection height and the action angle of the working machine resistance either do not change, or change in a rather insignificant range.

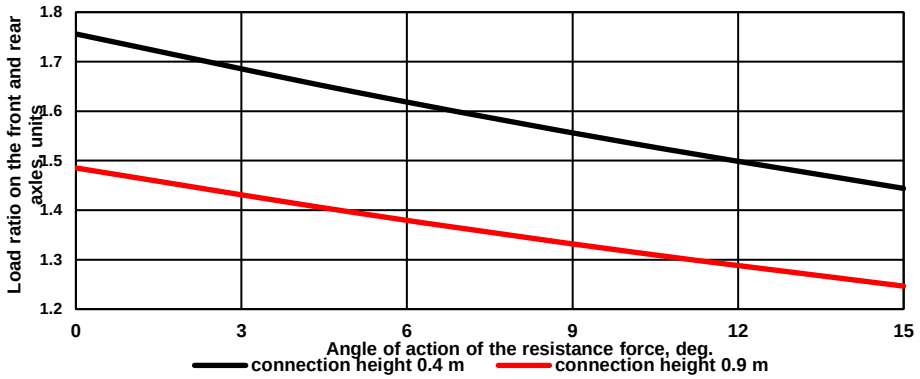


Fig. 6 - Dependence of the load ratio on the front and rear axles depending on the action angle of the resistance force and the height of the plow connection

The obtained dependencies give an understanding of the redistribution of weight between the tractor axles when performing technological operations, allow modeling the influence of structural and technological parameters of machine and tractor units on the distribution of weight between the axles of running systems, predict the further impact of running systems on the fertile soil layer and achieve minimum sliding values of running systems due to the redistribution of tractor weight.

The obtained research results allow checking the efficiency of completing tractors with a working machine, as well as checking the effectiveness of design solutions in the development of new tractors at the design stage.

Further development of the obtained dependencies application will be aimed at solving the consistency issues of the design and parameters of the working machine and tractor to ensure minimal negative impact on the soil. When conducting further research, it is advisable to improve the obtained mathematical model by finding out the influence of the agrotechnological environment properties and driving modes on the weight distribution of the tractor. Also, based on the obtained data, it is advisable to implement an automatic control system for the weight distribution of the tractor when performing technological operations.

CONCLUSIONS

✓ According to the research, the weight distribution of the tractor along the running system axles is established depending on the action angle of the working machine resistance force and its traction resistance. The obtained mathematical model allows, based on the height of the trailer hook installation, the action angle of the working machine resistance force, tractor wheelbase, ballast load mass, the distribution of the tractor weight in a static position, the traction resistance of the working machine, determining the weight distribution of the tractor along the running system axles. The obtained dependence makes it possible to simulate the influence of these factors on the contact load in the running systems contact zone with the soil to minimize the harmful impact on it.

✓ Modeling of the effect of the front ballast load value on the traction force showed that an increase in the front ballast load by 8.5% of the weight of a wheeled tractor leads to an increase by 34.8% of the maximum possible traction force on the tractor hook.

✓ It was established that for a wheeled tractor with a working machine traction resistance of 30 kN, the presence of a front load weighing 4 kN leads to a decrease in the load on the rear axle by 4.8% and an increase in the load on the front axle by 29.7%. An increase in the action angle of the working machine drag force from 0 to 15 degrees with a traction resistance of 30 kN leads to an increase in the load of the rear axle by 19.2% and a decrease in the load of the front axle by 11.9%. The obtained results make it possible to adjust the machine and tractor unit during field work in order to reduce the negative impact of running systems on the soil.

✓ The results of research on the weight distribution of a tracked tractor showed that the use of a mounted tillage tool with a traction resistance of 45kN, as well as design settings, do not allow equalizing the weight distribution between the front and rear parts of the track. According to the simulation performed, when the connection height of the working machine changes from 0.4 to 0.9 m, the load on the rear part of the track increases by 10.88% and the front part of the track is unloaded by 6.2%. By increasing the action angle of the working machine drag force from 0 to 15 degrees, it is possible to increase the load of the track rear part by 19.6% and reduce the load of the track front part by 1.6%. Increasing the connection height of the working

machine allows balancing the weight between the front and rear of the track. By changing the action angle of the working unit resistance, one can significantly load the track rear part. Analysis of the weight distribution of a tracked tractor indicates the need at the design stage to coordinate its power with the parameters of the working machines with which it will work.

REFERENCES

[1] Ardvidson J., Keller T., Soil stresses under tracks and tyres – measurements and model development. *Proceedings International Conference of Agricultural Engineering*, Zurich, 06-10.07. 2014.

[2] Arvidsson J., Westlin H., Keller T., Gilbertssonb M. (2011). Rubber track systems for conventional tractors – Effects on soil compaction and traction. *Soil and Tillage Research*, 117, 103–109.

[3] Bauer F., Porteš P., Polcar A., Čupera J., Fajman M. (2022). Differences in the wheel loads and contact pressure of the in-furrow and on-land rear tractor tyres with mounted and semi-mounted ploughs. *Soil and Tillage Research*, 215. https://doi.org/10.1016/j.still.2021.105190

[4] Dospehov B. A. (1985). *Metodika polevogo opyita (s osnovami statisticheskoy obrabotki rezultatov issledovaniy)*. M.: Agropromizdat, 351p.

[5] Golub G., Chuba V. & Kukharets, S. (2017). Determining the magnitude of traction force on the axes of drive wheels of self-propelled machines. *Eastern European Journal of Enterprise Technologies*, 4 (7), 50–56. https://doi.org/10.15587/1729-4061.2017.107192

[6] Golub G., Chuba V., Yarosh Y., Solarov A. & Tsyvenkova N. (2021). Experimental studies of the interaction of tractor drive wheels with the soil in the plowed field. *INMATEH Agricultural Engineering,* 65 (3), 430–440. https://doi.org/10.35633/inmateh-65-45

[7] Keller T., Lamandé M., Naderi-Boldaji, M., de Lima R.P. (2022). Soil Compaction Due to Agricultural Field Traffic: An Overview of Current Knowledge and Techniques for Compaction Quantification and Mapping. https://doi.org/10.1007/978-3-030-85682-3_13

[8] Keller T., Sandin M., Colombi T., Horn R., Or D. (2019). Historical increase in agricultural machinery weights enhanced soil stress levels and adversely affected soil functioning. *Soil and Tillage Research*, 194. https://doi.org/10.1016/j.still.2019.104293

[9] Keller T., Trautner A., Arvidsson J. (2002). Stress distribution and soil displacement under a rubber-tracked and a wheeled tractor during ploughing, both on-land and within furrows. *Soil and Tillage Research*, 68 (1), 39-47.

[10] Kumar A., Pandey K., Kumar R. (2013). Longitudinal stability indication for 2WD tractors working in different field operations. *International Journal of Advance Agricultural Research*, 1– 6.

[11] Mileusnić Z.I., Saljnikov E., Radojević R.L., Petrović D.V. (2022). Soil compaction due to agricultural machinery impact, *Journal of Terramechanics*, 100, 51-60, https://doi.org/10.1016/j.jterra.2021.12.002

[12] Molari G., Bellentani L., Guarnieri A., Walker M., Sedoni E. (2012). Performance of an agricultural tractor fitted with rubber tracks. *Biosystems Engineering*, 111. https://doi.org/10.1016/j.biosystemseng.2011.10.008

[13] Mueller L., Schindler U., Mirschel W., Shepherd T. G., Ball B. C., Helming K., Rogasik J., Eulenstein F. & . Wiggering H. (2010). Assessing the productivity function of soils: a review. *Agronomy for sustainable development*, 30 (3), 601–614, France. https://doi.org/10.1051/agro/2009057

[14] Nawaz M., Bourrié G., Trolard F. (2012). Soil compaction impact and modelling. A review. *Agronomy for Sustainable Development*, 33. https://doi.org/10.1007/s13593-011-0071-8

[15] Patil M.R. (2015). Measurement of weight transfer in two-wheel drive tractor by developed ring transducer. *International Journal of Agricultural Engineering*, 8 (2), 181–189.

[16] Polcar A., Renčin L., Votava J. (2017) Drawbar pull and its effect on the weight distribution of a tractor. Acta Universitatis Agriculturae *Et Silviculturae Mendelianae Brunensis*, 65 (1), 145–150. https://doi.org/10.11118/actaun201765010145

[17] Renčín L., Polcar A., Bauer F. (2017). The effect of the tractor tires load on the ground loading pressure. *Acta universitatis agriculturae et silviculturae mendelianae brunensis*, 65 (5), 1606–1614.

[18] Shaheb M.R., Klopfenstein A., Tietje R.W., Wiegman C.R., Dio C.D., Alberto S., Herink K., Herbener N., Shearer S.A. (2021). Evaluation of soil-tire interface pressure distributions and areas resulting from various tire and track technologies and configurations. https://doi.org/10.13031/aim.202100889

[19] Wang G., Zoerb C. (1989). Indirect determination of tractor tractive efficiency. Agricultural Engineering Department. University of Saskatchewan, Saskatoon, Canada, 243–248.

MANUFACTURE OF A DEVICE FOR PRUNING FRUIT BRANCHES
/
تصنيع جهاز لتقليم الأفرع الثمرية

Adel AL-GEZAWE, Mokhtar COTTB, Fatma ABD EL GAWAD, Mahmoud AWAD, Osama FOUDA, Mahmoud OKASHA[*1]
Agricultural Engineering Research Institute (AEnRI), Agricultural Research Center (ARC), Giza 12611/ Egypt
Tel: +20-1003133841; E-mail: mahmoudokasha1988@yahoo.com
Corresponding author: Mahmoud Okasha
DOI: https://doi.org/10.35633/inmateh-69-35

Keywords: *Pruning disc; Branches; Pruning damage; Power requirements; Operating cost*

ABSTRACT

Fruit branch pruning is still done manually, resulting in high labor costs, ergonomic hazards, and low efficiency and productivity. Furthermore, there are some limitations with imported agricultural machines because of their high prices and inappropriate local conditions. Hence, the present study aims to manufacture a local device for fruit branch pruning based on validating the correct stem-cutting position using a branch guide. The manufactured device comprises a 60 W electric motor, a formed base, a teethed pruning disc, a telescopic tube made up of the picker-cutting mechanism of the device, and a 12–Volt rechargeable dry battery. The device was made from local and light materials to allow a telescopic tube to reach the high position of the citrus fruit branches and consider ergonomic aspects. Field trials were executed on sour oranges trees to assess the pruning device's performance as a function of change in peripheral speeds of cutting disc (9.81, 13.74, 17.66, and 21.59 m/s), cutting disc teeth numbers (60, 80, and 100 teeth), different groups of branches diameters {A (from 5 mm to less than 10 mm), B (10 mm to less than 20 mm), C (from 20 mm to less than 30 mm) and D (from 30 mm to less than 40 mm)}. The manufactured device was assessed in terms of device productivity, pruning efficiency, pruning damage, power requirements, specific energy, and operating cost. The results indicated that the highest device productivity and pruning efficiency were 780, 218, 100 and 65 branch/h; and 96.0, 94.0, 92.0 and 90.5%, while the lowest pruning branch damage were 4.0, 6.0, 8.0 and 9.5%, specific energy were 0.0447, 0.1645, 0.4050 and 0.700 Wh per branch, for the groups of branches diameters A, B, C, and D respectively. The current investigation recommended that the optimal operational conditions were using the manufactured device for pruning citrus trees at 17.66 m/s pruning disc speed with a pruning disc teeth number of 60 teeth.

الملخص

لا يزال تقليم أغصان الفاكهة يتم بالصورة اليدوية، والذي ينتج عنه ارتفاع تكاليف العمالة والمخاطر الجسدية للعامل وانخفاض كفاءة وانتاجية العامل لعملية التقليم. علاوة على ذلك، هناك بعض القيود بالنسبة لاستيراد الآلات الزراعية بسبب ارتفاع أسعارها وعدم ملاءمتها للظروف المحلية. ومن ثم، تهدف الدراسة الحالية إلى تصنيع جهاز محلي لتقليم أغصان الفاكهة حيث يعتمد في تصميمه على التحقق من صحة موضع قطع الساق الصحيح باستخدام دليل الفرع. ويتكون الجهاز من موتور كهربي بقدرة 60 وات، وقاعدة مشكلة، وقرص تقليم مسنن وأنبوب تلسكوبي وبطارية جافة 12 فولت. تم تصنيع الجهاز من خامات محلية وخفيفة الوزن للسماح لأنبوب تلسكوبي بالوصول إلى الموضع المرتفع لأغصان الشجرة وأيضا لمراعاة بيئة عمل مريحة للعامل. وأجريت التجارب على أشجار النارنج لتقييم أداء جهاز التقليم عند استخدام أربع سرعات محيطية لقرص القطع (9.81، 13.74، 17.66 و21.59 م/ث)، عدد أسنان قرص القطع (60، 80، 100 سن)، أربع مجموعات مختلفة لأقطار الفروع {A (من 5 مم إلى أقل من 10 مم)، B (10مم إلى أقل من 20 مم)، C (من 20 مم إلى أقل من 30 مم) و D (من 30 مم إلى أقل من 40 مم)}. وتم تقييم أداء الجهاز المصنع من حيث إنتاجية الجهاز وكفاءة التقليم ونسبة تلف الناتج عن التقليم ومتطلبات القدرة والطاقة والتكلفة التشغيلية. وأظهرت النتائج أن أعلى قيم إنتاجية للجهاز وكفاءة التقليم كانت 780 و218 و100 و65 فرعًا في الساعة؛ و96.0 و94.0 و92.0 و90.5٪ بينما كانت أقل قيم تلف فرع التقليم 4.0 و6.0 و8.0 و9.5٪ ومتطلبات الطاقة 0.0447 و0.1645 و0.4050 و0.700 وات ساعة لكل فرع لمجموعات الفروع بأقطار A و B و C و D على التوالي. وأوصت الدراسة الحالية بان ظروف التشغيل المثلى هي باستخدام جهاز التقليم المصنع عند سرعة تقليم 17.66 م/ث مع قرص القطع بعدد أسنان 60 سن لتقليم أشجار الحمضيات.

INTRODUCTION

Fruit and citrus trees are a major source of income for the country. Fruit trees are extremely important in the production of food. Egypt's total cultivated fruit trees area was 420,000 ha, 150,000 ha of which are citrus (about 12,300 million trees).

[1] *Adel Al-Gezawe, Senior Researcher; Mokhtar Cottb, Senior Researcher; Fatma Abd El Gawad, Senior Researcher; Mahmoud Awad, Senior Researcher; Osama Fouda, Senior Researcher; Mahmoud Okasha, Researcher*

The most important citrus cultivars are sweet orange (approximately 65%), followed by local mandarin (25%) and lemon (10%). The average production ranges between 15–17 tons/ha, with total citrus production of 3,240,000 tons in 2020 (*MALR, 2020*). Pruning is a crucial canopy managing strategy for achieving and sustaining optimal yield with profitable fruit size plus quality (*Krajewski et al., 2021*). Pruning methods in citriculture are crucial in keeping plant health to achieve a satisfactory symmetry between reproductive and vegetative growth, which is an essential aspect of citrus crop development (*Intrigliolo and Roccuzzo, 2011*). Pruning eliminates ineffective and/or damaged branches, diminishes excess fruit on the tree, plus improves nutrient distribution, thus resulting in larger fruits. Generally, the tree's response to pruning relies on many aspects, including tree variety, tree age, rootstock, growing circumstances, production practices, and pruning time during the growing period (*Kadlec et al., 2022; Vashisth et al., 2022*).

Furthermore, pruning can lessen competition for assimilates, thereby maximizing assimilate distribution, and it is an eco-friendly aspect of diminishing crop load (*Bound, 2021*). Pruning is the second greatest labor expense after harvesting expenses in tree fruit production, representing approximately 20% or over of the entire pre-harvest production cost (*Gallardo et al. 2009; Hansen 2011*). Also, Chueca et al. (2021) and Martin-Gorriz et al. (2021) reported that pruning is the second most costly mission in citrus production after harvesting. General, manual pruning costs account for between 10% and 15% of entire citrus production costs and 30% to 50% of entire labor costs. In a similar vein, Fonte *et al.* (2022) stated that pruning is regarded as one of the most costly and laborious tasks of citrus production, and its mechanization could boost citrus farms' efficiency and competitiveness. The influence of mechanical pruning on yield relies on the variety, location, and crop condition, among further aspects. Pruning can be done manually or mechanically, utilizing pruning tools (*Abbood et al., 2019*). Manual citrus pruning is performed mostly with hand scissors and saws. This practice has disadvantages and causes considerable problems, including but not limited to being slow, costly, and requires skilled laborers that know how to prune appropriately (*Intrigliolo and Roccuzzo, 2011; Liu et al., 2018; Zhang et al.,2020)*. On the other side, mechanical pruning chiefly uses a machine to prune and shape on a vast scale and in orchards with standardized planting arrangements (*Chueca et al., 2021*). Common fruit tree pruning machines consist of a pruning device, a power system, a frame, and additional key parts (*Ottanelli et al., 2019*). Mechanical pruning primarily involves hedging, and only some pruning machines, such as teeth-type and disc-type cutters, are available for tree fruit harvests, depending upon the requirements. Mechanical pruning could be implemented by hedging on both sides of the canopy and/or topping the canopy parallel to the ground (*Dias et al., 2014*). Rubin *et al*. (2019) designed and manufactured a tree-pruning device. The device comprises a rectangular frame of mild steel that supports all the parts to be built upon. It has four wooden rollers with rubber grippers and two drilling machine motors. A stationary blade made of stainless steel is mounted on the frame. The motors are electrically supplied, and a relay controller comprises a remotely operable electromagnetic switch that regulates their motion. The device is equipped with a spring-loaded mechanism to provide flexibility during climbing the tree. The device has been evaluated and proven safe, dependable, and effective. Therefore, it minimizes the difficulty of climbing trees and cutting branches.

As the cultivation of fruit trees grew, it was imperative to develop pruning methods for completing the pruning process quickly, easily, and with high quality so as not to break the fruit branches or scratch the fruits, causing them to rot. Therefore, the present study aims to manufacture a device with a branch guide for fruit branch pruning and determine the best operating parameters for the fruit pruning device.

MATERIALS AND METHODS

The manufactured tree-pruning device

The pruning device was manufactured at a private workshop in Sharkia Governorate, Egypt. The manufactured citrus tree pruning device comprises three main parts (i.e., telescopic tubes, pruning unit, and battery), as shown in Fig. 1. The pruning device was made from light materials to allow a telescopic tube to reach the high positions on the tree, in addition to ergonomic considerations. The manufactured device was based on validating the correct stem-cutting position, safeguarding the branch from harm. The first part comprises six telescopic tubes made of plastic with a thickness of 1 mm were used to carry the pruning unit on its top. Each tube has a length of 500 mm and edges diameters of 36 and 32 mm. Second, the pruning unit comprises a teethed pruning disc, a power source, a formed base, a pruning disc house, and a branch guide.

The teethed pruning disc was made of alloy steel with 1 mm thickness and 125 mm diameter. Three teethed pruning discs with teeth numbers 60, 80, and 100 were tested, as shown in Fig. 2. A 60-watt electric motor was used to operate the pruning unit.

The motor specifications are Buhler Motor GmbH Germany, brushed type, voltage 12, torque 0.18 Nm, power 60 W (0.082 HP), rotational speed 3,300 rpm, and 39 mm shaft diameter. The motor shaft interfered with a threaded plate of 18 mm diameter and 6.5 mm thickness. The pruning disc was connected with a threaded plate by a nut with an inside diameter of 18 mm. There is a formed base underneath the threaded plate. This base was bolted with the motor by three bolts of 3 mm diameter. The base has a U-shaped guide, and its other side has a bent bracket bolted with the telescopic tube. The pruning disc housing consists of two plastic covers with a 156 mm diameter, 17 mm height, and 1.5 mm thickness. Each cover was bolted with the formed base by bolts with a diameter of 3 mm. The branch guide is located on the U-shaped formed base. The distance between the sides is 50 mm, and its length is 60 mm until the beginning of the pruning disc with a width of 15 mm. The branch guide was used to control the branches during the pruning process.

The pruning-device base was fastened with the top of the telescopic tube by two iron brackets with 1.5 mm thickness, 100 mm length, and 25 mm width. The two brackets were bolted with the end of the telescopic tube by two bolts with a 5 mm diameter. The total mass of the pruning device with telescoping tubes is 1400 g. Third, a 12-Volt rechargeable dry battery is connected by an electric cable with a 2 mm thickness. Each telescopic tube has an electric cable passed through, and the operator carries the battery bag by belt. The total mass of the bag with the battery is 3180 g. An adjustable voltage regulator was used to allow the operator to control and adjust the electric motor's rotational speed by altering the voltage's control switch to achieve the required speeds.

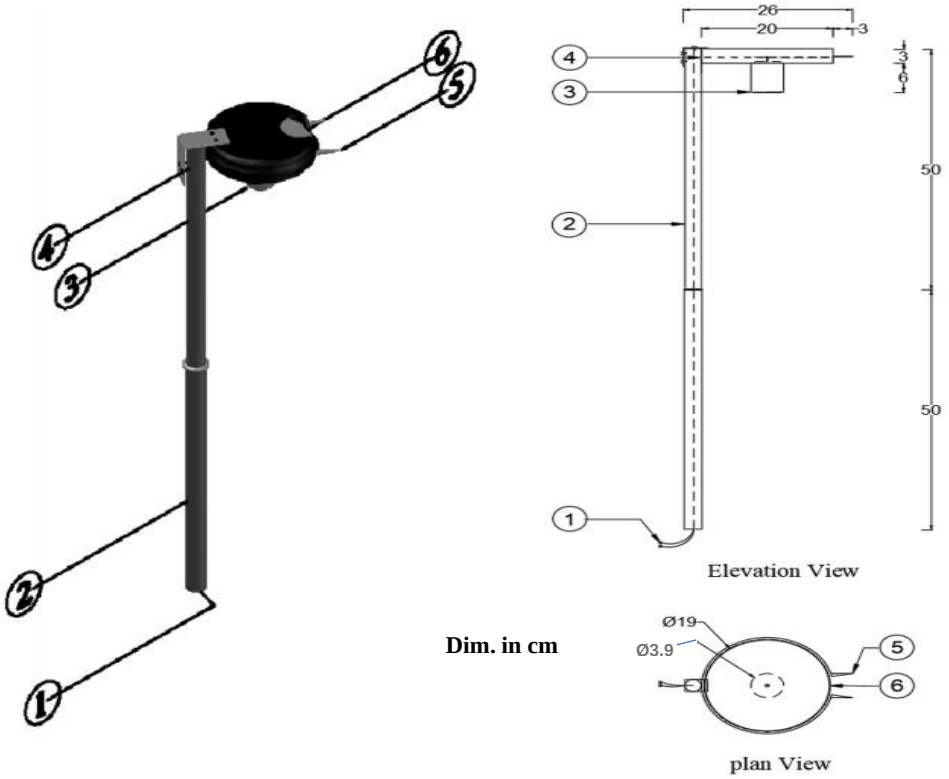
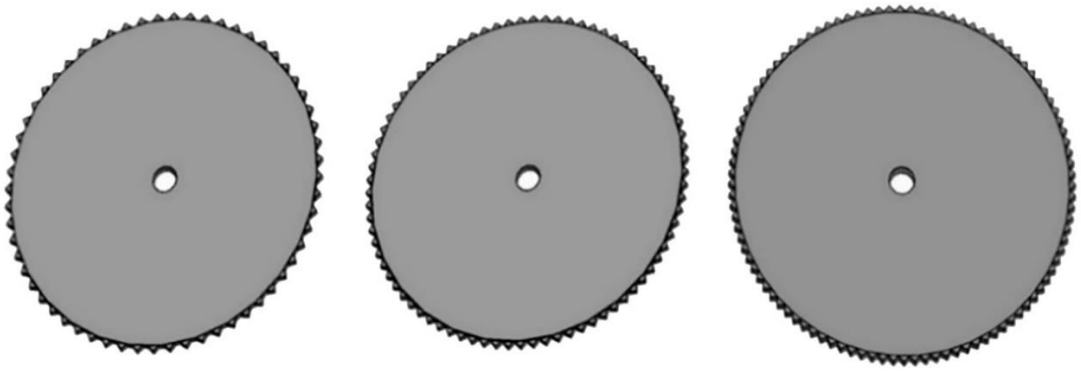


Fig. 1 – Views of the manufactured pruning device for citrus trees

1 – Electrical cable; 2 – Telescopic tube; 3 – DC-motor; 4 – Disc housing; 5 – Branch guide; 6 – Pruning disc



60 teeth pruning disc **80 teeth pruning disc** **100 teeth pruning disc**

Fig. 2 – Three different numbers of pruning disc teeth

The citrus trees

Citrus orange trees (sour orange) were selected to evaluate the manufactured pruning device's performance because its branches contain thistle, which is difficult to perform manually, as shown in Fig. 3.



Fig. 3 – Image of the pruning device during pruning citrus trees

Parameters and measurements

The manufactured pruning device was evaluated under four different peripheral speeds of pruning disc (9.81, 13.74, 17.66, and 21.59 m/s), three different numbers of pruning disc teeth (60, 80, and 100 teeth), four groups of the sour orange trees branches diameters "A – B – C – D" (i.e., "A" branches with diameters from 5 mm to less than 10 mm, "B" branches with diameters from 10 mm to less than 20 mm, "C" branches with diameters from 20 mm to less than 30 mm, and "D" branches with diameters from 30 mm to less than 40 mm. The manufactured device was assessed for its performance in terms of pruning productivity, efficiency, damage, power requirements, specific energy, and operational cost.

The pruning device productivity was determined in terms of the number of pruned branches per hour. The pruning device productivity was determined according to Eq. (1) as follows:

$$PDP = \frac{Q}{t} \quad (1)$$

where PDP is the pruning device productivity [branch/h], Q is the number of pruned branches after pruning [branch], and t is the time required for pruning branches of the citrus trees [h].

The pruning efficiency was determined according to Eq. (2) as follows:

$$PE = \frac{Q}{M_{mb}} \times 100 \quad (2)$$

where PE is the pruning efficiency [%], Q is the number of pruned branches after pruning [branch], and M_{mb} is the number of mature branches needed for pruning on the tree before pruning [branch].

The pruning branches damage was calculated according to Eq. (3) as follows:

$$PBD = \frac{M_{da}}{M_{mb}} \times 100 \quad (3)$$

where PBD is the pruning branches damage [%], M_{da} is the number of damaged branches after pruning [branch], and M_{mb} is the number of mature branches needed for pruning on the tree before pruning [branch].

The power requirements for the pruning device in this study were calculated according to Eq. (4) as follows:

$$PR = \frac{I \times V \times cos\theta}{1000} \quad (4)$$

where PR is the power requirements [kW], I is the line current strength [Amperes], V is the potential difference [Voltage], and $cos\theta$ is the power factor ≈ 0.85.

The specific energy for the pruning device was determined according to Eq. (5) as follows:

$$SE = \frac{PR}{PDP} \quad (5)$$

where SE is the specific energy [kWh/branch], PR is the power requirements [kW], and PDP is the pruning device productivity [branch/h].

The pruning device hourly cost was estimated according to (*Awady et al., 1978),* as follows in Eq. (6):

$$C = \frac{p}{h}\left(\frac{1}{l} + \frac{i}{2} + t + r\right) + (PR \times e) + \left(\frac{m}{144}\right) \quad (6)$$

where C is the pruning device hourly cost [EGP/h], p is the pruning device price [EGP], h is the pruning device yearly operating hours [h/year], l is the pruning device life expectancy [h], i is the interest rate per year [%], t is the taxes rate [%], r is the repair and maintenance ratio [%], PR is the power requirements [kW], e is the hourly electricity cost [EGP/kWh], m is the operator's monthly wage [EGP], and 144 is the monthly working hours.

The operational cost per branch was estimated according to Eq. (7) as follows:

$$OCPB = \frac{C}{PDP} \quad (7)$$

where $OCPB$ is the operational cost per branch [EGP/branch], C is the pruning device hourly cost [EGP/h], and PDP is the pruning device productivity [branch/h].

The operational cost per tree was estimated according to Eq. (8) as follows:

$$OCPT = OCPB \times NBPT \quad (8)$$

where $OCPT$ is the operational cost per tree [EGP/tree], $OCPB$ is the operational cost per branch [EGP/branch], $NBPT$ is the number of branches per tree [branch/tree].

RESULTS AND DISCUSSION

Influence of operating parameters on the manufactured device productivity

Fig. 4 presents the influence of the peripheral speed of the pruning disc, pruning disc teeth number and branches diameter on the device productivity. Concerning the influence of the peripheral speed of the pruning disc on the manufactured device productivity, the results reveal that increasing the peripheral speed of the pruning disc increased the device productivity at any pruning disc teeth number and branch diameter. The obtained results indicate that increasing the peripheral speed of the pruning disc from 9.81 to 21.59 m/s at a constant pruning disc teeth number of 60 teeth increased device productivity from 530 to 850, from 165 to 260, from 64 to 120, and from 40 to 88 branch/h, under sour orange branches diameters A, B, C, and D, respectively. This may be because increasing the peripheral speed of the pruning disc decreases the required cutting force, accelerating the pruning period and thus increasing productivity. These results are in line with *Abdallah et al. (2014)* and *Moradpour et al. (2016)*.

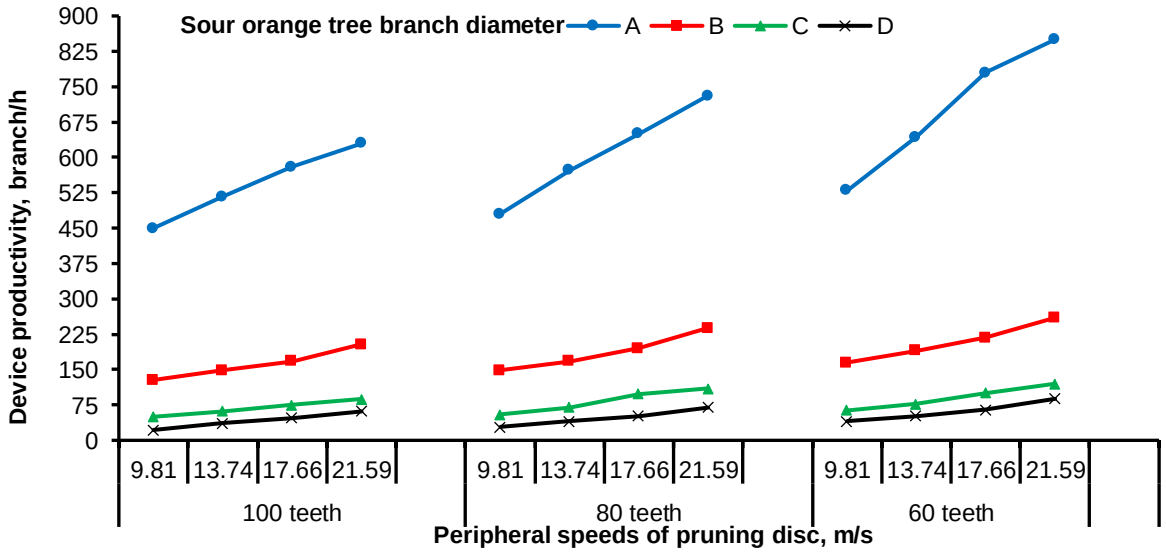


Fig. 4 – Influence of operating parameters on the manufactured pruning device productivity

Regarding the influence of the pruning disc teeth number on the device productivity, the results show that decreasing pruning disc teeth number increased device productivity at any peripheral speed of the pruning disc and branch diameter. The obtained results reveal that decreasing the pruning disc teeth number from 100 to 60 teeth at a constant peripheral speed of the pruning disc of 21.59 m/s increased device productivity from 630 to 850, from 203 to 260, from 87 to 120, and from 62 to 88 branch/h, under sour orange branches diameters A, B, C, and D, respectively.

Relating the influence of branch diameter on the device productivity, the results demonstrate that increasing branch diameter decreased the device productivity at any peripheral speed of the pruning disc and pruning disc teeth number. The obtained results show that increasing branch diameter from A to D at a constant peripheral speed of the pruning disc of 21.59 m/s decreased the device productivity by a percentage of 89.65, 90.42, and 90.16% at pruning disc teeth number 60, 80, and 100 teeth, respectively. This may be ascribed to the fact that increasing branch diameter caused an increase in branch resistance for cutting, which increases the required time for pruning, hence decreasing productivity. These results are in agreement with *Esgici et al. (2019), Kang et al. (2020)*, and *Li et al. (2022)*.

Regarding the influence of the pruning disc teeth number on the device productivity, the results show that decreasing pruning disc teeth number increased device productivity at any peripheral speed of the pruning disc and branch diameter. The obtained results reveal that decreasing the pruning disc teeth number from 100 to 60 teeth at a constant peripheral speed of the pruning disc of 21.59 m/s increased device productivity from 630 to 850, from 203 to 260, from 87 to 120, and from 62 to 88 branch/h, under sour orange branches diameters A, B, C, and D, respectively.

Relating the influence of branch diameter on the device productivity, the results demonstrate that increasing branch diameter decreased the device productivity at any peripheral speed of the pruning disc and pruning disc teeth number. The obtained results show that increasing branch diameter from A to D at a constant peripheral speed of the pruning disc of 21.59 m/s decreased the device productivity by a percentage of 89.65, 90.42, and 90.16% at pruning disc teeth number 60, 80, and 100 teeth, respectively. This may be ascribed to the fact that increasing branch diameter caused an increase in branch resistance for cutting, which increases the required time for pruning, hence decreasing productivity. These results are in agreement with *Esgici et al. (2019), Kang et al. (2020),* and *Li et al. (2022)*.

Influence of operating parameters on pruning efficiency

Fig. 5 illustrates the effect of the peripheral speed of the pruning disc, pruning disc teeth number and branch diameter on pruning efficiency. Regarding the effect of the peripheral speed of the pruning disc on pruning efficiency, the results declare that increasing the peripheral speed of the pruning disc up to 17.66 m/s increased the pruning efficiency at any pruning disc teeth number and branch diameter. Furthermore, increasing the peripheral speed of the pruning disc from 17.66 to 21.59 m/s tends to decrease the pruning efficiency. The attained results reveal that increasing the peripheral speed of the pruning disc from 9.81m/s to 17.66 m/s at a constant pruning disc teeth number of 60 teeth increased pruning efficiency from 93.0 to 96.0%, from 90.0 to 94.0%, from 87.0 to 92.0%, and from 85.0 to 90.5%, under sour orange branches diameters A, B, C, and D, respectively. This may be due to the increased impact forces applied to the branch, which improve pruning operation and hence pruning efficiency.

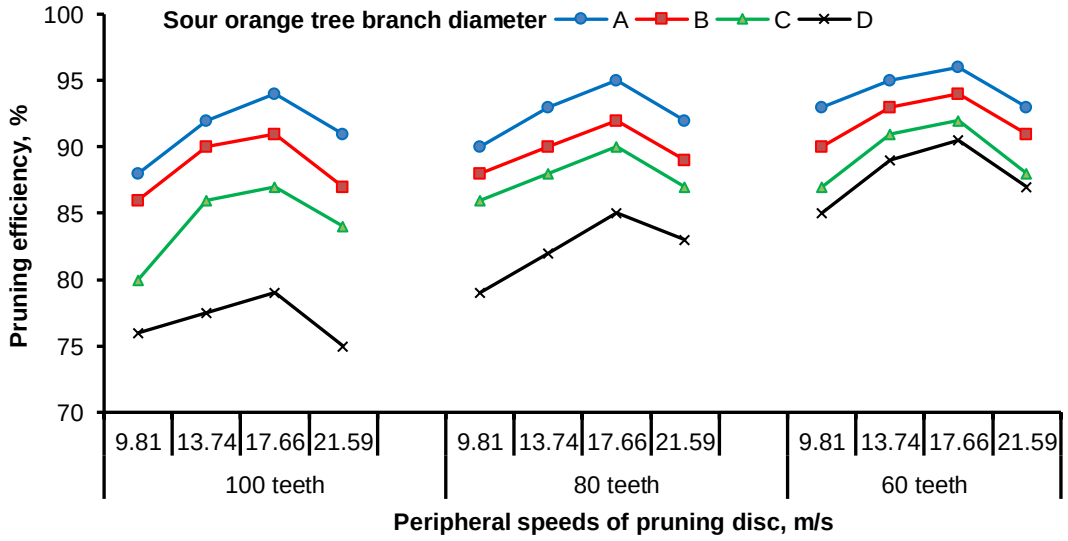


Fig. 5 – Influence of operating parameters on pruning efficiency

Concerning the influence of pruning disc teeth number on pruning efficiency, the results show that decreasing pruning disc teeth number from 100 to 60 teeth at a constant peripheral speed of the pruning disc

of 17.66 m/s increased the pruning efficiency from 94.0 to 96.0%, from 91.0 to 94.0%, from 87.0 to 92.0%, and from 79.0 to 90.5%, under branches diameters A, B, C, and D, respectively.

Regarding the impact of branch diameter on pruning efficiency, the results illustrate that increasing the branch diameter decreased pruning efficiency at any peripheral speed of the pruning disc and pruning disc teeth number, as shown in Fig. 5, where increasing branch diameter from A to D at a constant peripheral speed of the pruning disc of 17.66 m/s decreased the pruning efficiency by a percentage of 5.73%, 10.53%, and 15.95%, at pruning disc teeth number of 60, 80, and 100 teeth, respectively. This may be attributed to the increase in branch diameter, causing an increase in branch resistance for cutting, which increases the required cutting force for pruning, accordingly decreasing pruning's efficiency. These results are in line with *Li et al. (2022).*

Influence of operating parameters on the pruning branch damage

The pruning branch damage is greatly affected by the peripheral speed of the pruning disc, pruning disc teeth number and branch diameter, as shown in Fig. 6. Regarding the effect of the peripheral speed of the pruning disc on the pruning branch damage, increasing peripheral speed of the pruning disc from 9.81 to 17.66 m/s at a constant pruning disc teeth number of 60 teeth decreased pruning branch damage from 7.0 to 4.0%, from 10.0 to 6.0%, from 13.0 to 8.0%, and from 15.0 to 9.5%, under sour orange branches diameters A, B, C, and D, respectively. This may be due to increasing the peripheral speed of the pruning disc accelerating the pruning process; thus, fewer times are required to use the pruning disc to prune one branch, consequently decreasing the pruning damage. Any increase in the peripheral speed of the pruning disc of over 17.66 m/s up to 21.59 m/s increased the pruning branch damage from 4.0 to 7.0%, from 6.0 to 8.0%, from 8.0 to 12.0%, and from 9.5 to 13.0% under the same previous conditions.

Fig. 6 presents the influence of the pruning disc teeth number on the pruning damage. The results demonstrate that increasing the pruning disc teeth number from 60 to 100 teeth at a constant peripheral speed of the pruning disc of 17.66 m/s, increased the pruning damage from 4.0 to 6.0%, from 6.0 to 8.0%, from 8.0 to 13.0%, and from 9.5 to 21.0% under branches diameters A, B, C, and D, respectively.

Concerning the influence of branch diameter on pruning damage percentage, it was clear that increasing branch diameter from A to D at a constant peripheral speed of the pruning disc of 17.66 m/s increased pruning damage percentage by a percentage of 57.89, 66.66, and 71.43%, at pruning disc teeth number of 60, 80, and 100 teeth, respectively. This may be because the increase in the branch's diameter led to increased resistance of the branches to pruning, which in turn required several times the use of the pruning disc to prune one branch, thus increasing the pruning damage.

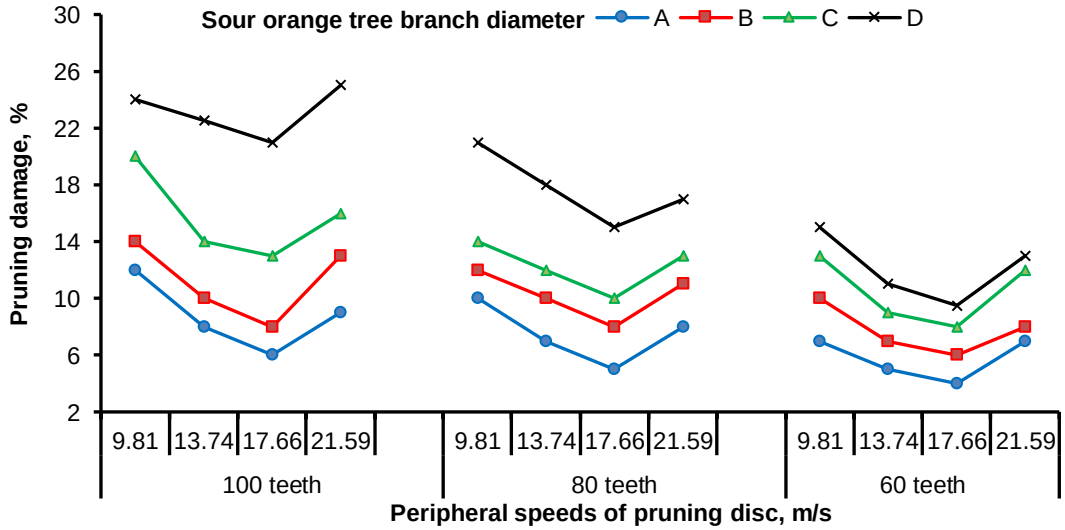


Fig. 6 – Influence of operating parameters on the pruning branch damage

Influence of operating parameters on the power requirements and specific energy

Figs. 7 and 8 show the influence of the peripheral speed of the pruning disc, pruning disc teeth number and branch diameter on power requirements and specific energy. Concerning the influence of the peripheral speed of the pruning disc on power requirements and specific energy, the results illustrate that increasing peripheral speed of the pruning disc from 9.81 m/s to 21.59 m/s at a constant pruning disc teeth number of 60

teeth increased power requirements from 29.55 W to 36.33 W, from 30.72 W to 39.50 W, from 35.45 W to 43.35 W, and from 40.33 to 48.10 W, under branches diameters A, B, C, and D, respectively.

These results are in harmony with *Hegazy et al. (2021).* In contrast, the specific energy decreased by a percentage of 22.46, 18.42, 34.80, and 45.79% under the same conditions. These results are in line with *Awad et al. (2022).*

Regarding the effect of pruning disc teeth number on power requirements and specific energy, the results reveal that increasing pruning disc teeth number from 60 to 100 teeth at a constant peripheral speed of the pruning disc of 21.59 m/s increased power requirements from 36.33 W to 39.35 W, from 39.50 W to 42.78 W, from 43.35W to 50.25 W, and from 48.10 W to 58.62 W, under branches diameters A, B, C, and D respectively. In the same vein, the specific energy increased by a percentage of 31.41%, 27.91%, 37.46%, and 42.19% under the same conditions.

Relating the influence of branch diameter on power requirements and specific energy, it was clear that increasing branch diameter from A to D at a constant peripheral speed of the pruning disc of 21.59 m/s increased power requirements from 36.33 W to 48.10 W, from 38.22 W to 55.35 W, and from 39.35 to 58.62 W, at pruning disc teeth number of 60, 80, and 100 teeth, respectively. This may be attributed to the increasing branch diameter, increasing the branch resistance for pruning, hence increasing the required power. These results are in agreement with *Li et al. (2022).* In the same vein, the specific energy increased by a percentage of 92.17%, 93.38%, and 93.40% under the same conditions.

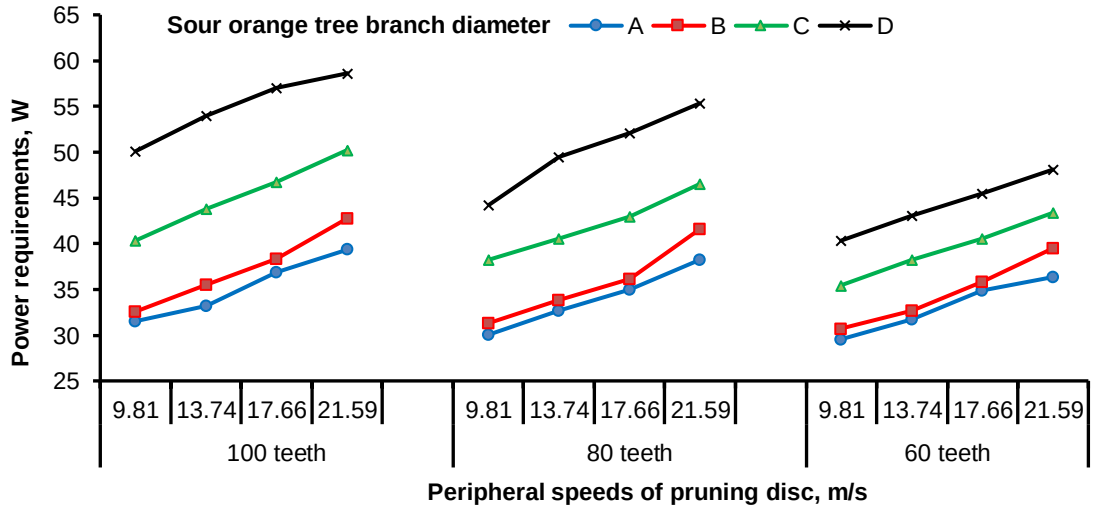


Fig. 7 – Influence of operating parameters on the power requirements

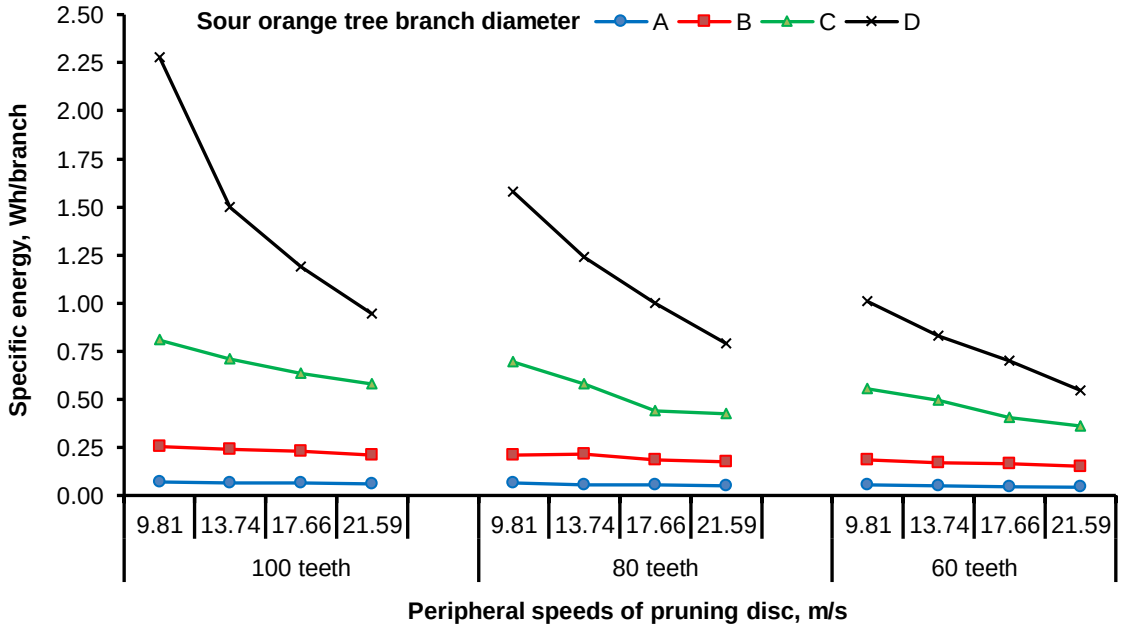


Fig. 8 – Influence of operating parameters on specific energy

Influence of operating parameters on operational costs

A cost analysis was performed for the manufactured device under different operating conditions related to the productivity of the pruning device. The total manufacturing cost of the device was 2000 EGP, according to the 2022 prices. The device's life expectancy is five years.

The results demonstrate that the operational cost per tree was affected by the peripheral speed of the pruning disc, pruning disc teeth number, and power. Fig. 9 presents the representative values of operational cost per tree versus peripheral speed of the pruning disc and pruning disc teeth number for the different groups of sour orange branch diameters.

Concerning the effect of pruning disc teeth number on the operational cost, the results show that increasing the number of disc teeth at any peripheral speed of the pruning disc increased the operational cost. With the increasing pruning disc teeth number from 60 to 100, at a constant peripheral speed of the pruning disc of 17.66 m/s, the operating cost increased from 4.07 to 5.45 EGP/tree. The increase in operational cost of pruning disc teeth is attributed to the decrease in device productivity with discs with higher teeth numbers.

Relating the effect of the peripheral speed of the pruning disc on the operational cost, the results show that increasing the peripheral speed of the pruning disc decreased the operational cost at any pruning disc teeth number. Increasing the peripheral speed of the pruning disc from 9.81 to 21.59 m/s decreased the operational cost from 6.2 to 3.9 EGP/tree. The decrease in operational cost by increasing the peripheral speed of the pruning disc is attributed to the increase in device productivity accompanied by the high disc speed.

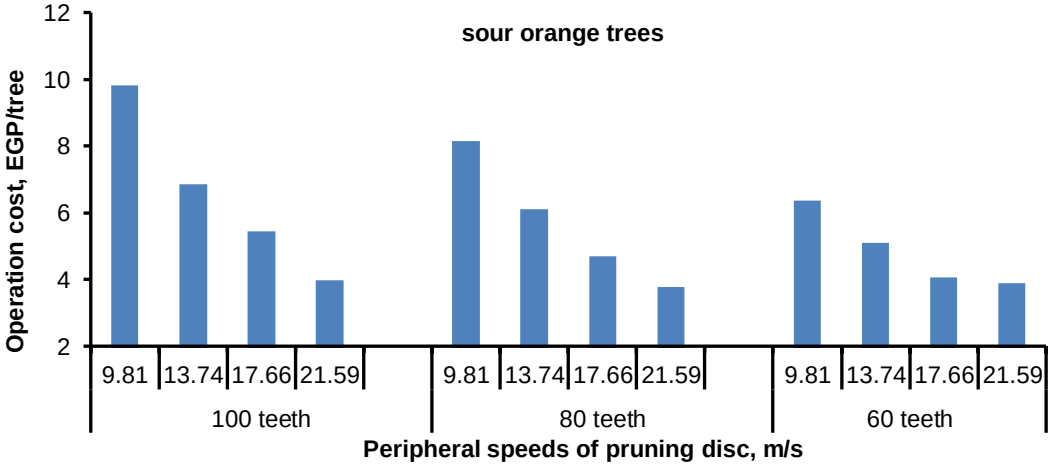


Fig. 9 – Effect of operating parameters on operational costs

CONCLUSIONS

The findings in the current research confirmed the effectiveness of using the manufactured pruning device for pruning citrus trees. Therefore, using the manufactured pruning device for pruning citrus trees under 17.66 m/s peripheral speed of the pruning disc with a pruning disc of 60 teeth can be recommended. Under these conditions, the following data were achieved, the highest values of pruning device productivity and pruning efficiency were 780, 218, 100, and 65 branch/h; and 96.0, 94, 92, and 90.5% for the groups of sour orange branches diameters A, B, C, and D respectively. The lowest values of pruning damage were 4.0, 6.0, 8.0, and 9.5%, and energy requirements were 0.0447,0.1645, 0.4050, and 0.700 Wh/branch for the groups of sour orange branches diameters A, B, C, and D respectively. The operational costs were 4.07, 4.70, and 5.45 EGP/tree when using pruning discs 60, 80, and 100 teeth at a constant peripheral speed of the pruning disc of 17.66 m/s for the sour orange trees, respectively.

ACKNOWLEDGEMENT

The authors would like to thank the Agricultural Engineering Research Institute (AEnRI), Agricultural Research Center (ARC), Giza, Egypt.

REFERENCES

[1] Abbood, S., Abbood, M., Jasim, A., Lect, A., & Aldafar, S. (2019). Manufacturing and testing of date palm vibration motorized fronds cutter. *Iraqi Journal of Agricultural Sciences*, *49*(3), 763–773. https://doi.org/10.36103/ijas.v49i3.106

[2] Abdallah, R., Auchet, S., & Méausoone, P. (2014). A dynamic measurement of a disc chipper cutting forces. *Biomass Bioenergy*, *64*, 269–275. https://doi.org/10.1016/j.biombioe.2014.02.033

[3] Awad, M., Fouda, O., Fathy, W., El Balkemy, W., Egela, M., El-Fakhrany, W., & Okasha, M. (2022). *A combined machine for collecting and chopping rice straw. Heliyon*, 8, e10412. https://doi.org/10.1016/j.heliyon.2022.e10412
[4] Awady, M. N. (1978). *Tractor and farm machinery*. Text Book, Faculty of Agriculture, Ain–shams Univ., 164–167.
[5] Bound, S. A. (2021). Managing Crop Load in European Pear (Pyrus communis L.) – A Review. *Agriculture*, *11*(7), 637. https://doi.org/10.3390/agriculture11070637
[6] Chueca, P., Mateu, G., Garcerá, C., Fonte, A., Ortiz, C., & Torregrosa, A. (2021). Yield and Economic Results of Different Mechanical Pruning Strategies on "Navel Foyos" Oranges in the Mediterranean Area. *Agriculture*, *11*(1), 82. https://doi.org/10.3390/agriculture11010082
[7] Dias, A. B., Patrocinio, S., Pereira, S., Brites, T., Pita, V., & Mota Barroso, J. M. (2014). Evaluation of the use of a disc-saw machine in winter pruning 'Rocha' pears orchard-An account of five years. XII Int. Pear Symp. (1094): 281–288. https://doi.org/10.17660/ActaHortic.2015.1094.36
[8] Esgici, R., Pekitkan, F., Ozdemir, G., Güzel, E., & Sessiz, A. (2019). Cutting parameters of some grape varieties subject to the diameter and age of canes. *Fresenius Environmental Bulletin*, *28*, 167–170.
[9] Fonte, A., Torregrosa, A., Garcerá, C., Mateu, G., & Chueca, P. (2022). Mechanical Pruning of 'Clemenules' Mandarins in Spain: Yield Effects and Economic Analysis. *Agronomy*, *12*(4):761. https://doi.org/10.3390/agronomy12040761
[10] Gallardo, K., Taylor, M., & Hinman, H. (2009). Cost Estimates of Establishing and Producing Gala Apples in Washington; Washington State University: Washington, DC, USA, 2011; FS005E.
[11] Hansen, M. (2011). Fruiting Walls Suit Machinery. Good Fruit Grow. (62): 24–25.
[12] Hegazy, R.A., Moussa, W.M., El-Nagar, A.B., Abdelmotaleb, I. A. (2021). Modification and Performance Evaluation of Industrial Fodder Chopping Machine. *Fresenius Environmental Bulletin*, *30*, 10782–10789.
[13] Intrigliolo, F., & Roccuzzo, G. (2011). Modern trends of citrus pruning in Italy. *Advances in Horticultural Science*, *25*(3), 187–192. http://www.jstor.org/stable/42882836
[14] Kadlec, J., Novosadová, K., & Pokorný, R. (2022). Impact of Different Pruning Practices on Height Growth of Paulownia Clon in Vitro 112®. *Forests*, *13*(2), 317. https://doi.org/10.3390/f13020317
[15] Kang, F., Tong, S., Zhang, H., Li, W., Chen, Z., & Zheng, Y. (2020). Analysis and experiments of reciprocating cutting parameters for apple tree branches. *Transactions of the Chinese Society of Agricultural Engineering*, *36*(16), 9–16.
[16] Krajewski, A., Schumann, A., Ebert, T., Oswalt, C., Ferrarezi, R. S., & Waldo, L. (2021). Management of citrus tree canopies for fresh-fruit production. Dept. Soil Water Sci. UF/IFAS Extension, document SL485/SS698, 1/2021. https://doi.org/10.32473/edis-ss698-2021
[17] Li, C., Zhang, H., Wang, Q., & Chen, Z. (2022). Influencing Factors of Cutting Force for Apple Tree Branch Pruning. *Agriculture*, *12*(2), 312. https://doi.org/10.3390/agriculture12020312
[18] Liu, Y. D., Pan, J. B., Chen, Y. Y., Zhang, Z. Y., & Fu, W. (2018). Design and Finite Element Analysis of the Connecting Seat Jujube Pruning Machine. *Journal of Chinese Agricultural Mechanization*, *40*, 29–33.
[19] MALR. (2020). Ministry of Agricultural and Land Reclamation, Economic Affairs Sector, *Agricultural statistics crops*. Accessed 3 January 2023.
[20] Martin-Gorriz, B., Martínez-Barba, C., & Torregrosa, A. (2021). Lemon trees response to different long-term mechanical and manual pruning practices. *Scientia Horticulturae*, *275*, 109700. https://doi.org/10.1016/j.scienta.2020.109700
[21] Moradpour, P., Scholz, F., Doosthoseini, K., & Tarmian, A. (2016). Measurement of Wood Cutting Forces during Bandsawing Using Piezoelectric Dynamometer. *Drvna industrija*, *67*(1), 79–84. http://dx.doi.org/10.5552/drind.2016.1433
[22] Ottanelli, A., Marone, E., & Fiorino, P. (2019). A new device to improve the mechanical winter pruning in olive trees hedgerows. *Advances in Horticultural Science*, *33*(1), 113–122. https://doi.org/10.13128/ahs-24787
[23] Rubin, M. R., Chacko, G., Sunil, G., Johnson, J., & Felix, F. (2019). Design and Fabrication of Tree Pruning Machine. *International Journal of Applied Engineering Research*. *14*(14): 106–109.
[24] Vashisth, T., Zekri, M., & Alferez, F. (2022). Florida Citrus Production Guide: Canopy Management: Chapter 19, CMG16/HS1303, Rev. 4/2021. EDIS 2022, 4. Available online: https://edis.ifas.ufl.edu/pdf/HS/HS1303/HS1303-Dxj7z1csni.pdf. Accessed 3 January 2023.
[25] Zhang, B., Fu, W., Wang, X.F., Lou, Z.X., Liu, Y.D., Fu, Y.X., Chen, Y.Y. (2020). Bench test and parameter optimization of jujube pruning tools. *International Agricultural Engineering Journal*, *29*, 58–68.

GRAIN MOISTURE MEASUREMENT SYSTEM WITH ROBUST TRANSFER FUNCTION, INVARIANT TO THE CHANGE OF A PHYSICO-CHEMICAL GRAIN COMPOSITION
/
СИСТЕМА ВИМІРЮВАННЯ ВМІСТУ ВОЛОГИ ЗЕРНА З РОБАСТНОЮ ФУНКЦІЄЮ ПЕРЕТВОРЕННЯ, ІНВАРІАНТНОЮ ДО ЗМІНИ ФІЗИКО-ХІМІЧНОГО СКЛАДУ ЗЕРНА

Oleksandr ZABOLOTNYI [1)], Vitalii ZABOLOTNYI [1)], Nicolay KOSHEVOY [1)]
[1)] National Aerospace University «Kharkiv Aviation Institute» / Ukraine
E-mail: o.zabolotnyi@khai.edu
DOI: https://doi.org/10.35633/inmateh-69-36

Keywords: *moisture measurement, capacitive sensor, direct comparison, robust transfer function, general linear regression, dispersion analysis*

ABSTRACT
The main task was to receive a robust transfer function for the capacitive grain moisture measurement system. It was estimated how the new transfer function compensates for the type uncertainty and how close it is to the nominal values of moisture content. Dispersions of adequacy and repeatability of the new transfer function, which describe possible variation in the measured moisture values and the correspondence of the new transfer function with the nominal linear transfer function of a moisture meter respectively, were calculated for five chosen substances. It was proved that the new transfer function has lower sensitivity to grain type and better adequacy to the ideal transfer function than the closest analog.

АНОТАЦІЯ
Головним завданням був синтез робастної функції перетворення для ємнісної системи вимірювання вмісту вологи зерна. Було оцінено здатність запропонованої функції перетворення компенсувати сортову невизначеність і ступінь її наближеності до номінальних значень вмісту вологи. Для запропонованої функції перетворення було обчислено дисперсії адекватності і відтворюваності для п'яти обраних речовин, які описують можливу варіацію результатів вимірювання вмісту вологи і відповідність нової функції перетворення з номінальною лінійною функцією перетворення вологоміра. Було доведено, що нова функція перетворення має нижчу чутливість до типу зерна і кращу адекватність із ідеальною функцією перетворення у порівнянні з найближчим аналогом.

INTRODUCTION

It is necessary to emphasize that Ukraine is among the top 10 world grain producers, according to FAOSTAT. Ukrainian grain belongs to a relatively short list of products that benefit the internal market and can be competitive abroad. Local grain farming produces approximately 25 million tons of grain and demonstrates stable growth of the grain production index. The structure of local grain production is relatively stable: the most significant part traditionally belongs to the hard, red variant of winter wheat used in bread making (up to 90 %). On the other hand, modern performance indexes of grain are regulated with national and international standards. It is mentioned that grain moisture content should not be more than 14,5…15,5 % (in general) to provide its long-term storage. Grain moisture is one of the main factors affecting the duration of storage without possible damage and loss (*Jones and Shelton, 1994; Tahir et al., 2007; Pathaveerat and Pruengam, 2020; Beficadu, 2014; Mhiko, 2012; Hassoon and Dziki, 2018*).

The excess or absence of moisture in food products is reflected in physical-chemical, physical-mechanical, and functional properties, as well as natural quality indicators (Nielsen, 2010). The grain drying process is one of the most energy-intensive and responsible for the entire grain storage and processing cycle (*Rolle et al., 2015; Amit et al, 2017*).

It is reasonable that grain producers always try to use its food potential most fully, especially peripheral components and fetuses, as a source of valuable nutrients. The grain processing industry implements a list of technologies for that purpose. Among them, we have long-term hydrothermal grain treatment with further sprouting and its usage as basic foodstuffs *(Lupu et al., 2016; Morishita et al., 2020; Hassoon et al., 2021)*. It is possible to use one or two times humidification with further binning, steaming with humid saturated steam for 20 – 30 sec, and 44 – 46 °C temperature control for 20 minutes for grain with weak gluten to improve its bakery properties. *(Jung et al., 2018; Probst et al., 2013; Dabbour et al., 2015)*.

Most European countries have already changed their local standards for moisture meters following international recommendation OIML R59 "Moisture Meters for Cereal Grain and Oilseeds" (*OIML R59*), which restricts the maximal permissible value of moisture content uncertainty to not more than 3% of relative full-scale error. However, even the most popular laboratory moisture meters like Kett, AgraTronix, Isoelectric, and Next Instruments series have a significant accuracy decrease when determining moisture in different kinds of grains of the same type, for example, in different kinds of wheat. An extensive list of factors influences the accuracy of current moisture meters in different bulk substances *(Wu et al., 2018; Wanga and Wang, 2012)*. In addition, it can be said that grain products' physical and chemical composition depends not only on the grains' type but the origin and ways of cultivation, storage, and processing – factors that can hardly be predicted *(Thakur et al., 2015)*.

Currently, a significant part of the means of measurement, which control substances' properties and composition, is occupied with measuring instruments that use capacitive sensors *(Zambrano et al., 2019; Flor et al., 2022)*. It is pretty evident that the widespread introduction of versatile and accurate grain moisture meters and their proper operation will have a tangible technical and economic effect *(Casada and Armstrong, 2009; Song et al., 2020; Li et al., 2021; Klomklao et al., 2017)*. 'Successful' modifications of capacitive sensors appeared years ago *(Hegg and Mamishev, 2004)*. The main idea was to fulfil capacitive measurements using two or several positions for one of the capacitor plates with further direct comparison method application. It helps to eliminate parasitic capacitances, compensate leakage currents and reduce the influence of fringe electric fields. However, for the process of moisture measurement in different types of bulks, 'type uncertainty' error can strongly influence the moisture measurement result *(Shi et al., 2015)*. Its value depends explicitly on the dielectric permittivity of a substance, which is under research (grain type, for example), and needs to be compensated *(Wanga and Wang, 2012; Bessa et al., 2013)*. This compensation is traditionally performed in a secondary measuring transducer using complementary reference capacitors, particular analytic calculations, reference calibration curves stored in the secondary measuring transducers' memory, etc. *(Wu et al., 2018; Jafari et al., 2020)*. Traditional ways of 'type uncertainty' compensation can be used only when it is possible to get an analytic forecast of chemical composition and different features of all the materials, which list is usually limited to a few grain types. The main task of the research is to receive a grain moisture measurement system with robust transfer function, invariant to the change of a physico-chemical grain composition, as described in *(Zabolotnyi and Koshevoi, 2020)*.

MATERIALS AND METHODS

The suggested design of the grain moisture measurement system is described below (Fig. 1). Both of its' sensors consist of a system of flat plates 1, where two pairs of flat plates belong to measuring capacitors C_1 and C_4, and the rest of flat plates create another pair of measuring capacitors C_2 and C_3. All flat plates of equal length l are assembled inside two fluoroplastic rings 2 at an equal gap, designated as *Z*.

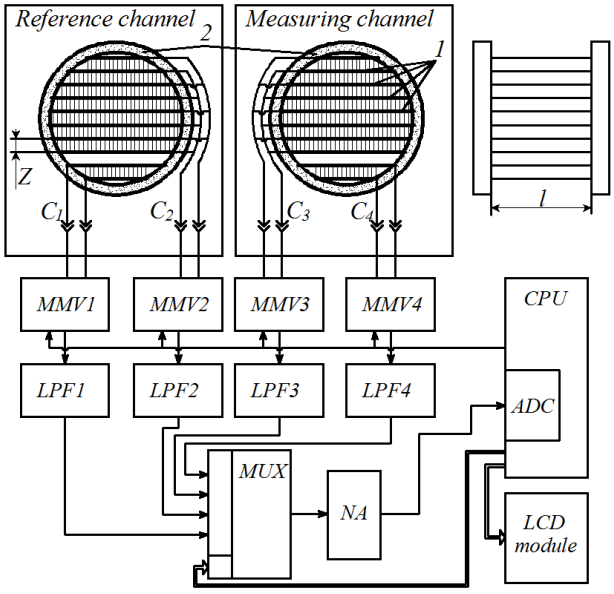


Fig. 1 - Functional electrical circuit of the moisture measurement system
MO1…MO4 – monostable oscillators; LPF1…LPF4 – low-pass filters; MUX – multiplexer; NA – normalizing amplifier; ADC – analog to digital converter

The process of moisture measurement can be performed as described below. The instrument measuring transducer of the moisture measurement system consists of four capacitive sensors C_1, C_2, C_3, and C_4. Two of them (C_3 and C_4) should be filled with a probe of bulk substance in which moisture is going to be measured. Another two (C_1 and C_2) should be filled with a similar probe but previously dehydrated. After the values of C_1, C_2, C_3, and C_4 were measured, we should calculate the relation $(C_3 – C_4)/(C_2 – C_1)$.

A structure of the moisture measurement system is given in Fig.1. Four capacitive sensors C_1, C_2, C_3, and C_4 are connected to the inputs of corresponding monostable oscillators MO_1…MO_4. They act as capacitance into pulse duration secondary transducers. The duration of the sequence of rectangular pulses, taken from the corresponding monostable oscillators' output, is proportional to the capacitance value. Central processing unit *CPU* launches monostable oscillators MO_1…MO_4 and controls their work by sending the sequence of rectangular pulses of a stable frequency to their corresponding inputs. Low-pass filters convert pulse duration into DC voltage with an amplitude proportional to the pulse duration. Multiplexer *MUX*, controlled by *CPU*, connects the low-pass filters *LPF1…LPF4* outputs with the input of normalizing amplifier *NA*, which, in turn, provides DC voltage levels compatible with measuring range of embedded in *CPU* analog-to-digital converter *ADC*. As soon as four capacitance values are converted into four DC voltage values and passed to the *ADC* input, *CPU* can calculate the value of moisture content and displays it on the *LCD* screen.

As mentioned, moisture content of a substance can be calculated using formula:

$$W = K \cdot \left(\frac{C_3 - C_4}{C_2 - C_1} \right), \tag{1}$$

where K is a normalizing coefficient.

If the values of electric capacitances are considered (not filled with a substance), equal to 15 pF for C_1, C_4 and 50 pF for C_2, C_3, normalized equation (2) of a moisture meter transfer function is obtained.

$$W = 28.599 \cdot \left(\frac{C_3 - C_4}{C_2 - C_1} \right). \tag{2}$$

To conduct experimental research it was necessary to get reference samples for chosen grain types with different dielectric permittivity values and prepare necessary laboratory setup.

Unfortunately, the local industry produces stable polymer-based reference samples with controlled values of moisture equal to 12 % and 13 % only. So, necessary grain samples were prepared by grain drying (dehydration) following international standards (*Diane Lee and Harris, 2016; ISO 712:2009*), and subsequent addition of water into dehydrated samples *(ISO 835:2007)*.

A list of grain types to be examined includes: wheat cereals (ε = 2.55), pea (ε = 2.97), millet (ε = 3.17), poppy (ε = 3.56), pearl barley (ε = 3,68), and, following the standards for grain samples dehydration, 20 g weights are necessary. They should be placed in a drying oven with 130°C temperature for 120 minutes (fig. 2) *(Zabolotnyi and Koshevoi, 2020; Zabolotnyi, 2019)*.



Fig. 2 - Preparation of 30 aluminium containers with 20 g weights of poppy seed, further drying and cooling in desiccators

After drying, moistening and holding in desiccators for an hour, such grain moisture samples can be used to verify any capacitive grain moisture meter.

The connection scheme of the laboratory setup used in the process of moisture measurement is given in Fig.3. It includes four capacitive sensors C_1, C_2, C_3, and C_4, one channeled capacitance into a DC-voltage transducer which performs the sequence of transformations 'capacitance – pulse duration – DC voltage', variable air capacitor (reference capacitor), oscilloscope, digital voltmeter and RLC meter.

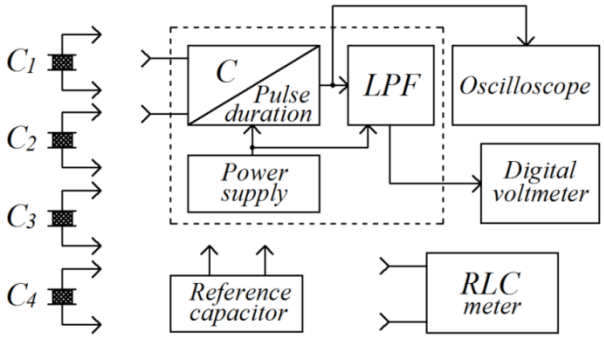


Fig. 3 - Connection scheme of the laboratory setup

Measurement procedure consisted of several steps. Firstly, capacitive sensors of the reference channel were filled with dehydrated sample of grain. Both of C_1 and C_2 capacitive sensors were one by one connected to the input of *C*/*Pulse duration*/DC voltage secondary transducer. Corresponding values of DC voltages were taken from the screen of a digital voltmeter and remembered.

After that, the appropriate capacitive sensor (let it be C_1) was disconnected from the secondary transducers' input, and the variable air capacitor (reference capacitor) was connected to its input. The capacitance of a variable reference capacitor had been slowly increased until the voltage value on the digital voltmeters' screen reached the value previously remembered by the operator. As soon as it happened, the reference capacitor was disconnected from the input of a secondary transducer, and the value of its capacitance was measured with the help of an accurate RLC meter at a 10 kHz frequency. The same substitution measurement procedure was applied to C_2, C_3, and C_4 capacitive sensors ten times each. As a result, ten measurements of electric capacitance were received from each capacitive sensor and the value of capacitance was calculated as an arithmetic mean value for ten separate measurements.

The sensors of an instrument measuring transducer were assembled from four identical rings with slots to insert flat stainless steel plates carved out from fluoroplast-4. Stainless steel plates were glued to the internal surface of appropriate pair of fluoroplastic rings with the help of superglue gel and soldered with wires to create four capacitive sensors. Both halves of an instrument measuring transducer (first pair with sensors C_1 and C_2 and second pair with sensors C_3 and C_4) consist of two capacitors with capacitance values of 47 pF for C_2 and C_3 and 15 pF for C_1 and C_4 in the empty state (Fig. 4, a).

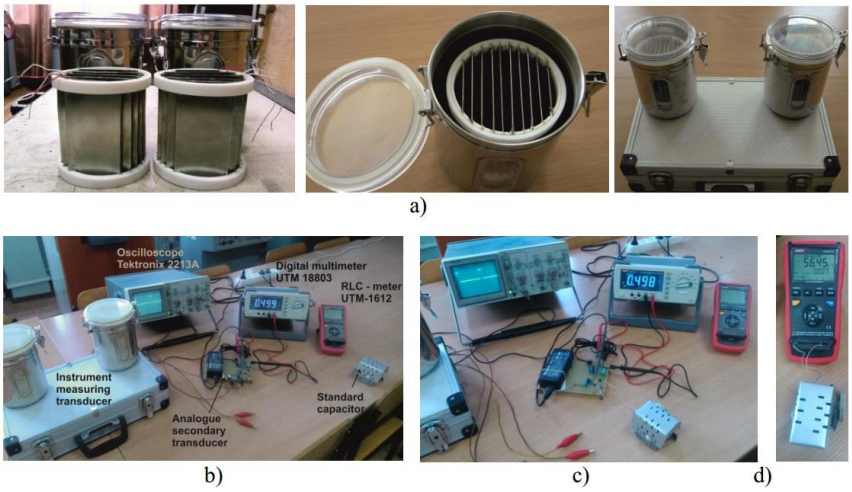


Fig. 4 - Experimental setup for moisture measurement

a – components of the moisture content instrument measuring transducer; b – one of capacitive sensors is connected to secondary transducer; c – standard variable capacitor is connected instead of capacitive sensor; d – capacitance of standard variable capacitor is measured with high accuracy

Each pair with two sensors was placed in its personal container, which, in its turn, was assembled on the front panel of the aluminium case. Images of the moisture measurement process and experimental setup can be found in fig 4, b, c, and d. To check the ability of equation (2) to retain invariance when working with different types of grain, we took four imaginary values of dielectric permittivity (to simulate different types of grain matrix): $\varepsilon_n = 2.0$; $\varepsilon_n = 2.5$; $\varepsilon_n = 3.0$; $\varepsilon_n = 3.5$. Besides, we set four different values of moisture content for that purpose ($W = 0$ %; $W = 10$ %; $W = 20$ %; $W = 30$ %). Dielectric permittivity of moist grain samples was calculated with application of universal Wiener equation *(Zabolotnyi et al., 2022)*. The values of C_1, C_2, C_3, and C_4 together with the values of theoretical moisture content are given in Table 1.

Table 1

Calculated values of sensors' capacitances and moisture content for the transfer function (1)

W, %	ε_n	2.0	2.5	3.0	3.5	W, %	ε_n	2.614	3.252	3.885	4.512
0	C_1, pF	30	37.5	45	52.5	10	C_1, pF	30	37.5	45	52.5
	C_2, pF	100	125	150	175		C_2, pF	100	125	150	175
	C_3, pF	100	125	150	175		C_3, pF	130.7	162.6	194.25	225.6
	C_4, pF	30	37.5	45	52.5		C_4, pF	39.21	48.78	58.28	67.68
	W_{calc}	0	0	0	0		W_{calc}	8.78	8.60	8.44	8.23
20	ε_n	3.368	4.317	4.963	5.741	30	ε_n	4.317	5.324	6.305	7.262
	C_1, pF	30	37.5	45	52.5		C_1, pF	30	37.5	45	52.5
	C_2, pF	100	125	150	175		C_2, pF	100	125	150	175
	C_3, pF	168.4	215.85	248.15	287.05		C_3, pF	215.85	266.2	315.25	363.1
	C_4, pF	50.52	64.76	74.45	86.12		C_4, pF	64.76	79.86	94.58	108.93
	W_{calc}	19.56	20.78	18.71	18.31		W_{calc}	33.13	32.31	31.51	30.74

As can be seen, theoretical values of moisture content do not correspond with nominal in all points, except for $W = 0$ %. It can be concluded that the transfer function (2) should be close to linear.

To receive the near linear function for moisture content W and $(C_3 - C_4)/(C_2 - C_1)$ relation, the method of Least Squares was used:

$$a + b \cdot W = (C_3 - C_4)/(C_2 - C_1), \tag{3}$$

where a and b – coefficients needed to be calculated.

For the system of equations (4) average values were taken for $(C_3 - C_4)/(C_2 - C_1)$ relation (table 2).

Table 2

Average values for the relation $(C_3 - C_4)/(C_2 - C_1)$

W, %	$(C_3 - C_4)/(C_2 - C_1)$				
	$\varepsilon_n = 2.0$	$\varepsilon_n = 2.5$	$\varepsilon_n = 3.0$	$\varepsilon_n = 3.5$	Average
0	1	1	1	1	1
10	1.307	1.301	1.295	1.289	1.298
20	1.684	1.669	1.654	1.640	1.662
30	2.158	2.130	2.102	2.075	2.116

$$\begin{cases} a + b \cdot 0 = 1, \\ a + b \cdot 10 = 1.298, \\ a + b \cdot 20 = 1.662, \\ a + b \cdot 30 = 2.116. \end{cases} \tag{4}$$

Solution for the system (4) was obtained in a traditional way:

$$[XX] = 4,\ [XY] = [YX] = 60,\ [YY] = 1400,\ [XL] = 6.076,\ [YL] = 109.7$$

$$Q = \begin{vmatrix} [XX] & [XY] \\ [YX] & [YY] \end{vmatrix} = \begin{vmatrix} 4 & 60 \\ 60 & 1400 \end{vmatrix} = 2000,\ Q_a = \begin{vmatrix} [XL] & [XY] \\ [YL] & [YY] \end{vmatrix} = \begin{vmatrix} 6.076 & 60 \\ 109.7 & 1400 \end{vmatrix} = 1924.4$$

$$Q_b = \begin{vmatrix} [XX] & [XL] \\ [YX] & [YL] \end{vmatrix} = \begin{vmatrix} 4 & 6.076 \\ 60 & 109.7 \end{vmatrix} = 74.24,\ a = \frac{Q_a}{Q} = \frac{1924.4}{2000} = 0.9622,\ b = \frac{Q_b}{Q} = \frac{74.24}{2000} = 0.0371$$

Calculated values of moisture content W', received from the equation (3), can be found in Table 3:

$$0.9622 + 0.0371 \cdot W' = (C_3 - C_4)/(C_2 - C_1),\quad W' = \frac{\left((C_3 - C_4)/(C_2 - C_1)\right) - 0.9622}{0.0371}$$

Table 3

Values of moisture content *W'*

W, %	ε_n = 2.0	ε_n = 2.5	ε_n = 3.0 (*W'*)	ε_n = 3.5	Δ*W*	Δ*W'*
	Values of *W'*, received from a first-order polynomial (2)					
1	2	3	4	5	6	7
0	1.019	1.019	**1.019**	1.019	1.019	1.019
10	9.294	9.132	**8.970**	8.809	-1.030	-1.030
20	19.456	19.051	**18.647**	18.270	-1.353	-1.353
30	32.232	31.477	**30.722**	29.995	0.722	0.722
	Values of W_m, calculated with the help of transfer function (6)					
0	0.268	0.268	0.268	0.268		
10	10.230	10.045	9.859	9.674		
20	20.850	20.470	20.085	19.723		
30	30.658	30.211	29.476	29.280		

Analysing the data in table 3, we can see that LS method happened to be not as effective as it was expected because of poor linearity of the moisture meters' transfer function. A step forward was to calculate discrepancies Δ*W* between nominal points of moisture content and values of the equation (3), and approximate Δ*W* values by applying instruments of general linear regression *(Zabolotnyi, 2021)*. Discrepancies $\Delta W = W' - W_{nominal}$ between nominal points of moisture content (Table 3, column 1) and moisture values, taken for ε_n = 3.0 (Table 3, column 4, bold), are given in column 6 of Table 3. To approximate the values of Δ*W*, a sum of four functions (1, *W*, W^2, and W^3) was taken with appropriate coefficients, defined with the help of Mathcad software (function linfit(x, y, Y)).

$$\Delta W' = 1.019 - 0.269 \cdot W + 0.00527 \cdot W^2 + 0.000112 \cdot W^3$$

$$\Delta W' = 1.019 - 0.269 \cdot \frac{\left(\frac{C_3 - C_4}{C_2 - C_1} - a\right)}{b} + 0.00527 \cdot \frac{\left(\frac{C_3 - C_4}{C_2 - C_1} - a\right)^2}{b^2} + 0.000112 \cdot \frac{\left(\frac{C_3 - C_4}{C_2 - C_1} - a\right)^3}{b^3} \quad (5)$$

Formula (5) provides an ideal approximation of the discrepancies Δ*W*, as can be seen from table 3, columns 6 and 7. Taking formula (5) into account, a new transfer function for a moisture meter can be built:

$$W_m = W' - \Delta W' = \frac{\left(\frac{C_3 - C_4}{C_2 - C_1} - a\right)}{b} - 1.019 + 0.269 \cdot \frac{\left(\frac{C_3 - C_4}{C_2 - C_1} - a\right)}{b} - 0.00527 \cdot \frac{\left(\frac{C_3 - C_4}{C_2 - C_1} - a\right)^2}{b^2} - 0.000112 \cdot \frac{\left(\frac{C_3 - C_4}{C_2 - C_1} - a\right)^3}{b^3}$$

$$W_m = -1.019 + 1.269 \cdot \frac{\left(\frac{C_3 - C_4}{C_2 - C_1} - a\right)}{b} - 0.00527 \cdot \frac{\left(\frac{C_3 - C_4}{C_2 - C_1} - a\right)^2}{b^2} - 0.000112 \cdot \frac{\left(\frac{C_3 - C_4}{C_2 - C_1} - a\right)^3}{b^3} \quad (6)$$

Near linear values of moisture content, calculated with the help of formula (6), are given in table 3. If we compare the values of moisture content *W'*, received from a first-order polynomial (2) and modified transfer function (6), it can be concluded that the transfer function (6) is far more close to linear than the initial transfer function (2) and transfer function received from a first-order polynomial (3).

RESULTS

The results of multiple measurements for capacitive sensors C_1, C_2, C_3 and C_4 are given in table 4. After having these results, the robustness of a static function (6) can be checked with mean values or medians. Calculated values of moisture content with mean and median values of sensors' capacitances can be found in tables 5 and 6.

Table 4

Multiple measurements of sensors' capacitance

№	*W* = 0 %		*W* = 10 %		*W* = 20 %		*W* = 30 %	
	C_1, pF	C_2, pF	C_3, pF	C_4, pF	C_3, pF	C_4, pF	C_3, pF	C_4, pF
	Pearl barley							
1	57.05	189.95	250.99	76.38	322.60	104.27	418.46	136.46
2	56.74	189.70	251.64	77.21	323.03	103.50	419.37	135.64
3	56.78	189.42	251.56	76.82	322.30	103.93	418.75	136.12
4	56.45	189.92	251.05	76.61	322.45	104.04	418.93	135.72

5	56.63	189.56	251.27	76.78	322.61	104.30	419.44	135.51
6	57.00	189.43	251.41	76.84	323.10	104.23	419.45	135.98
7	56.94	189.44	251.44	76.59	322.50	103.74	418.88	136.14
8	56.49	189.56	251.55	77.01	322.65	103.86	418.96	136.21
9	56.52	189.58	251.14	77.54	322.80	104.15	419.10	135.84
10	56.69	189.51	251.31	77.12	322.98	103.88	419.29	135.89
	Mean values (Pearl barley)							
	56.73	189.58	251.34	76.87	322.70	103.99	419.16	135.95
	Values of median (Pearl barley)							
	56.72	189.56	251.36	76.83	322.63	103.99	419.03	135.94
	Mean values (Poppy)							
	53.42	178.40	230.20	69.32	293.69	88.35	370.47	112.74
	Values of median (Poppy)							
	53.42	178.47	230.23	69.46	293.62	88.42	370.55	112.77
	Mean values (Millet)							
	47.46	158.90	210.34	64.95	266.48	79.93	335.26	103.12
	Values of median (Millet)							
	47.46	158.92	210.31	64.97	266.44	79.93	335.30	103.13
	Mean values (Pea)							
	44.51	150.05	195.19	58.54	249.81	75.49	316.96	96.61
	Values of median (Pea)							
	44.57	150.06	195.22	58.58	249.81	75.44	316.89	96.66
	Mean values (Wheat cereals)							
	38.10	127.85	166.47	48.26	217.29	67.13	274.44	84.51
	Values of median (Wheat cereals)							
	38.02	127.86	166.38	48.26	217.31	67.12	274.49	84.48

Table 5

Calculated values of a transfer function (6) with mean values

$W_{nominal}$, %	$W_{calculated}$, %				
	Pearl barley	**Poppy**	**Millet**	**Pea**	**Wheat cereals**
0	0.268	0.268	0.268	0.268	0.268
10	10.423	9.575	10.157	9.852	10.540
20	19.886	19.678	20.597	20.026	20.574
30	30.240	29.013	29.422	29.504	29.984

Table 6

Calculated values of a transfer function (6) with median values

$W_{nominal}$, %	$W_{calculated}$, %				
	Pearl barley	**Poppy**	**Millet**	**Pea**	**Wheat cereals**
0	0.268	0.268	0.268	0.268	0.268
10	10.440	9.570	10.136	9.868	10.469
20	19.876	19.748	20.580	20.058	20.540
30	30.228	29.040	29.420	29.501	29.964

For the initial transfer function (2) calculated values of moisture content for the same mean and median capacitance values can be found in tables 7 and 8.

Table 7

Calculated values of a transfer function (2) with mean values

$W_{nominal}$, %	$W_{calculated}$, %				
	Pearl barley	**Poppy**	**Millet**	**Pea**	**Wheat cereals**
0	0.268	0.268	0.268	0.268	0.268
10	8.960	8.215	8.708	8.430	9.069
20	18.483	18.389	19.276	18.638	19.250
30	32.368	30.377	30.975	31.111	32.878

Table 8

Calculated values of a transfer function (2) with median values

$W_{nominal}$, %	$W_{calculated}$, %				
	Pearl barley	**Poppy**	**Millet**	**Pea**	**Wheat cereals**
0	0.268	0.268	0.268	0.268	0.268
10	8.975	8.169	8.693	8.445	9.002
20	18.472	18.330	19.257	18.674	19.211
30	32.347	30.355	30.972	31.107	31.887

To compare the robustness of the data, given in tables 5 – 8 we used the instruments of dispersion analysis. At first, four dispersions of repeatability and four dispersions of adequacy (for data in tables 5 – 8) were calculated. Dispersions of adequacy were compared with the dispersions of repeatability by using F-test. All calculations for the results, given in tables 5 – 8 can be found in table 9.

Table 9

Results of robustness verification for the transfer functions (6) and (2)

Data source	S^2_{rep}	S^2_{ad}	F
Table 5	0.09344	0.0161	0.172
Table 6	0.10775	0.0162	0.150
Table 7	0.29244	0.3750	1.282
Table 8	0.30436	0.3401	1.117

Possible accuracy of moisture measurements can be estimated by using the method of mathematical programming. If some function $f(x)$ is continuous, it's possible to find maximal and minimal values of $f(x)$ inside the limit value of the function's argument error. Absolute uncertainty of moisture measurement can be calculated as a half difference $\Delta f = (f_{max}(x) - f_{min}(x))/2$. Maximal and minimal capacitance values were taken from the results of ten random measurements in pearl barley with 30 % of moisture content (table 10).

Table 10

Maximal and minimal values of electric capacitance

Pearl barley		Electric capacitance value, pF			
W, %		C_1	C_2	C_3	C_4
30	max	57.05	189.95	419.45	136.46
	min	56.45	189.42	418.46	135.51

After substituting the values from table 10 into the transfer function (6), maximal and minimal values of moisture content are obtained: $W_{\max}$ = 30.45 %, $W_{\min}$ = 29.92 %. The value of an absolute moisture measurement extended uncertainty would be equal to $U(W_m)$ = (30.45 – 29.92)/2 = 0,27 %, which is very good for a capacitive grain moisture meter. The same operations had been done for the initial transfer function (2): $W_{\max}$ = 32.75 %, $W_{\min}$ = 31.81 %, $U(W_m)$ = (32.75 – 31.81)/2 = 0,47 %. As it can be seen, moisture measurement extended uncertainty of the modified transfer function (6) is approximately two times smaller in comparison with the uncertainty of initial transfer function (2).

CONCLUSIONS

After checking the workability of the equation (6) for different moist substances, it was possible to say that it happened to be far more robust to grain type variation than the initial transfer function, suggested in *(Zabolotnyi and Koshevoi, 2020)* and equation (3), received from a first-order polynomial after LS method implementation.

During the meter's transfer functions (2) and (6) comparative analysis, it was necessary to estimate how both of them compensated for the type uncertainty, and how close both of them were to the nominal linear transfer function. Dispersions of repeatability, calculated for transfer function (2) and transfer function (6) with mean and median values, describe a possible variation in the measured moisture values for five chosen substances (wheat cereals, pea, millet, poppy, and pearl barley).

It was demonstrated that the values of the dispersions of repeatability of S^2_{rep1} and S^2_{rep2} are approximately 3 times smaller compared with S^2_{rep3} and S^2_{rep4}.

This means that the transfer function (6) is not as sensitive to grain type as an equation (2). Dispersions of adequacy describe the correspondence of experimental transfer functions (6) and (2) (taken for different grain types as dielectric substances with a significant difference in relative permittivity) with the nominal linear transfer function of a moisture meter. Again, we can see that the dispersions of adequacy calculated for the transfer function (6) give values that are much smaller in comparison with the dispersions of transfer function (2). This means that transfer function (6) provides better adequacy to the ideal than transfer function (2). As a general result, it can be concluded that it would be rational to apply transfer function (6) with median values of moisture content as a nominal transfer function of the grain moisture measurement system.

REFERENCES

[1] Amit, S.K., Uddin, Md.M., Rahman, R., Rezwanul Islam, S.M., Khan, M.S., (2017), A review on mechanisms and commercial aspects of food preservation and processing. *Agriculture & Food Security,* vol. 6, 51. https://doi.org/10.1186/s40066-017-0130-8

[2] Befikadu, D., (2014), Factors affecting quality of grain stored in Ethiopian traditional storage structures and opportunities for improvement. *International Journal of Sciences: Basic and Applied Research (IJSBAR)*, vol. 18, no. 1, pp. 235-257.

[3] Bessa, W.S., Ribeiro, E.P., Bonfim, M.C., Leandro, G.V., Errera, M.R., (2013), Analysis of capacitive measurements at low frequencies for moisture content determination in soybeans. *Brazilian Journal of Instrumentation and Control,* vol. 1, no. 1, 29–34. https://doi.org/10.3895/S2318-45312013000100005

[4] Casada, M. E., Armstrong P. R., (2009), Wheat moisture measurement with a fringing field capacitive sensor. *Transactions of the ASABE*, vol. 52, no. 5, pp. 1785-1791.

[5] Dabbour, M., Bahnasawy, A., Ali, S., El-Haddad, Z., (2015), Grinding parameters and their effects on the quality of corn for feed processing. *Journal of food processing & technology,* vol. 6, no. 9, 482. https://doi.org/10.4172/2157-7110.1000482

[6] Diane Lee, G., Harris, G., (2016), Examination of Grain Moisture Meters Using Air-Oven Reference Method Transfer Standards. National Institute of Standards and Technology, Maryland, U.S.

[7] Flor, O., Palacios, H., Suárez, F., Salazar, K., Reyes, L., González, M., Jiménez, K., (2022), New Sensing Technologies for Grain Moisture. *Agriculture*, vol. 12, 386. https://doi.org/10.3390/agri-culture12030386

[8] Goncharenko A.V., Lozovski, V.Z., Venger, E.F., (2000), Lichtenecker's equation: applicability and limitations. *Optics Communications,* vol. 174, pp. 19-32.

[9] Hassoon, W., Dziki, D., (2018), The effect of seed moisture and temperature on grinding characteristics of quinoa (Chenopodium quinoa Willd.). *BIO Web of Conferences,* vol. 10, 01006. https://doi.org/10.1051/bioconf/20181001006

[10] Hassoon, W.H., Dziki, D., Mi´s, A., Biernacka, B., (2021), Wheat Grinding Process with Low Moisture Content: A New Approach for Wholemeal Flour Production. *Processes*, vol. 9, 32. https://doi.org/10.3390/pr9010032

[11] Hegg, M.C., Mamishev, A.V., (2004), Influence of variable plate separation on fringing electric fields in parallel-plate capacitors. *2004 IEEE International Symposium on Electrical Insulation*, Indianapolis, IN, USA, pp. 384-387. https://doi.org/10.1109/ELINSL.2004. 1380606

[12] Jafari, M., Chegini, G.R., Rezaeealam, B., Shaygani Akmal, A.A., (2020), Experimental determination of the dielectric constant of wheat grain and cluster straw in different moisture contents. *Food Science & Nutrition,* vol. 8, pp. 629-635. https://doi.org/10.1002/fsn3.1350

[13] Jones, D., Shelton, P., (1994), G94-1199 Management to Maintain Stored Grain Quality. *Historical Materials from University of Nebraska-Lincoln Extension*. Paper 595. http://digitalcommons.unl.edu/ extensionhist/595

[14] Jung, H., Lee, Y.J., Yoon, W.B., (2018), Effect of Moisture Content on the Grinding Process and Powder Properties in Food: A Review. *Processes,* vol. 6, no. 69. https://doi.org/10.3390/pr6060069

[15] International Organization of Legal Metrology. (2006), *Moisture Meters for Cereal Grain and Oilseeds*. (International recommendation OIML R59). https://www.oiml.org/en/tc-sc-pg/committee-drafts/files/tc17-sc1-r59-4cd.pdf

[16] International Organization for Standardization. (2009), *Cereals and Cereal products – Determination of moisture content – Reference method* (ISO Standard No. 712:2009). https://www.iso.org/ standard/44807.html

[17] International Organization for Standardization. (2007), *Laboratory glassware – Graduated pipettes* (ISO Standard No. 835:2007). https://www.iso.org/standard/41794.html

[18] Klomklao, P., Kuntinugunetanon, S., Wongkokua, W., (2017), Moisture content measurement in paddy. IOP Conf. Series. *Journal of Physics,* vol. 901, 012068. https://doi.org/10.1088/1742-6596/901/1/012068

[19] Li, C., Zhang, X., Meng, M., Li, B., Li, C., (2021), Capacitive Online Corn Moisture Content Sensor Considering Porosity Distributions: Modeling, Design, and Experiments. *Applied Sciences,* vol. 11, 7655. https://doi.org/10.3390/app11167655

[20] Lupu, M.I., Pădureanu, V., Canja, C.M., Măzărel, A., (2016), The effect of moisture content on grinding process of wheat and maize single kernel. *IOP Conf. Series: Materials Science and Engineering*, vol. 145, 022024. https://doi.org/10.1088/ 1757-899X/145/2/022024

[21] Mhiko, T., (2012), Determination of the causes and the effects of storage conditions on the quality of silo stored wheat (Triticum aestivum) in Zimbabwe. *Natural Products and Bioprospecting*, vol. 2, pp. 21-28. https://doi.org/10.1007/s13659-012-0004-5

[22] Morishita, T., Ishiguro, K., Noda, T., Suzuki, T., (2020), The effect of grain moisture contents on the roll milling characteristics of Tartary buckwheat cultivar 'Manten-Kirari'. *Plant Production Science*, vol. 23, no. 4, pp. 539-546. https://doi.org/10.1080/1343943X.2020.1747358

[23] Nielsen, S.S., (2010), *Food Analysis, Food Science Texts Series.* Springer New York, NY. 602 pp. https://doi.org/10.1007/978-1-4419-1478-1

[24] Pathaveerat, S., Pruengam, P., (2020), Low cost measurement of moisture content in long grain paddy. *Journal of Stored Products Research*, vol. 89. 101728. https://doi.org/10.1016/j.jspr.2020.101728

[25] Probst, K.V., Kingsly Ambrose, R.P., Pinto, R.L., Bali, R., Krishnakumar, P., Ileleji, K.E., (2013), The effect of moisture content on the grinding performance of corn and corncobs by hammer milling. *Transactions of the ASABE*, vol. 56, no. 3, pp. 1025-1033.

[26] Rolle, F., Beltramino, G., Fernicola, V., Sega, M., Verdoja, A., (2015), Moisture determination for food quality assessment. *17 International Congress of Metrology*, 15006. EDP Sciences, Les Ulis, France. https://doi.org/10.1051/metrology/201515006

[27] Shi, Q., Liu, Y., Zhang, W., (2015), Design of High-Frequency Based Measuring Sensor for Grain Moisture Content. *9th International Conference on Computer and Computing Technologies in Agriculture (CCTA)*, Beijing, China, pp.197-207. https://doi.org/10.1007/978-3-319-48357-3_19

[28] Song, Q., Wei, X., Sun, W., Lu, Z., Tao, T., (2020), Design of Capacitive Paddy Moisture Sensor Based on Electrical Impedance Spectroscopy Analysis. *Applied Sciences*, vol. 10, 3968. https://doi.org/10.3390/app10113968

[29] Tahir, A.R., Neethirajan, S., Jayas, D.S., Shahin, M.A., Symons, S.J., White, N.D.G., (2007), Evaluation of the effect of moisture content on cereal grains by digital image analysis. *Food Research International,* vol. 40, no. 9, pp. 1140-1145. https://doi.org/10.1016/j.foodres.2007.06.009

[30] Thakur, R., Chatterji, S., Kumar, A., Bansod, B.S., (2015), Development of multi-grain capacitive sensor for determination of moisture content in grains. *Quality Assurance and Safety of Crops & Foods,* vol. 7, no. 2, pp. 201-206. https://doi.org/10.3920/QAS2013.0285

[31] Wanga, W.C., Wang, L., (2012), Design of Moisture Content Detection System. *Physics Procedia,* vol. 33, pp. 1408-1411. https://doi.org/10.1016/j.phpro.2012.05.230

[32] Wu, S., Zhang, B., Tian, Y., Zhou S., Ma, H., (2018), A grain moisture model based on capacitive sensor. *Journal of Physics: Conference Series*, vol. 1074, 012120. https://doi.org/10.1088/1742-6596/1074/1/012120

[33] Zabolotnyi, O.V., (2019), Proximate testing method of moisture measurement for substances of dielectric nature. *Radio Electronics, Computer Science, Control*, vol. 1, pp. 7-17. https://doi.org/10.15588/1607-3274-2019-1-1

[34] Zabolotnyi, O., Koshevoi, M., (2020), An effective method of bulk materials moisture measurement using capacitive sensors. *Journal of Stored Products Research*, vol. 89, 101733. https://doi.org/10.1016/ j.jspr.2020.101733

[35] Zabolotnyi, O., (2021), Moisture content control in heavy fuel during the process of emulsification with a help of capacitive sensors, *Proceedings of the 25th International Scientific Conference "Transport Means 2021", Kaunas / Lithuania,* ISSN 2351-7034, pp. 215-221.

[36] Zabolotnyi, O.; Zabolotnyi, V.; Koshevoy, N., (2022), Capacitive Water-Cut Meter with Robust Near-Linear Transfer Function. *Computation*, vol. 10, 115. http://doi.org/10.3390/computation10070115

[37] Zambrano, M.V., Duttaa, B., Mercerb, D.G., MacLeana, H.L., Touchie M.F., (2019), Assessment of moisture content measurement methods of dried food products in small-scale operations in developing countries: A review. *Trends in Food Science & Technology,* vol. 88, pp. 484-496. https://doi.org/10.1016/j.tifs.2019.04.006

PARAMETERS CALIBRATION OF DISCRETE ELEMENT MODEL FOR CRUSHED CORN STALKS
/
碎玉米秸秆离散元模型参数标定

Min FU*, Xiaoqing CHEN, Zefei GAO, Chengmeng WANG, Bing XU, Yilin HAO[1]
Northeast Forestry University, College of Mechanical and Electrical Engineering, Harbin / China
Tel: +86 15663688203; E-mail: fumin1996@163.com
DOI: https://doi.org/10.35633/inmateh-69-37

Keywords: *crushed corn stalk, angle of repose, discrete element simulation, parameter calibration*

ABSTRACT
For the problem of lacking reliable parameters during simulation analysis of the crushed corn stalk (CCS) micro-comminution process with gas-solid coupling method, the simulation parameters are calibrated using a combination of physical measurements and virtual experiments with CCS as the research object. The intrinsic parameters of CCS are obtained by physical experiment, and the stacking test is carried out by cylinder lifting method, and the actual angle of repose(AoR) is obtained as 44.12° by fitting the boundary line with Matlab software; the discrete element model of CCS is established, and the virtual stacking test is carried out by EDEM software; CCS-CCS dynamic friction coefficient, CCS-CCS static friction coefficient and JKR (Johnson-Kendall-Roberts) surface energy are identified as the parameters with significant effects on the AoR by Plackett-Burman test; the steepest climb test is leveraged to determine the center of response surface analysis; the quadratic polynomial regression model of the simulation parameters and the AoR is established by the Box-Behnken test using the AoR as the evaluation index, and the optimal combination of the significant parameters are obtained as follows: the CCS-CCS dynamic friction coefficient is 0.55, the CCS-CCS static friction coefficient is 0.14, and the JKR surface energy is 0.12; the AoR verification test is conducted based on the optimal combination of the significant parameters. The results show that the AoR of the CCS is 43.82°, which is 0.68% of the actual AoR, indicating that the parameter combination is reliable. The data obtained in this research can provide corresponding simulation parameters for CCS discrete element simulation and the development of straw micro-crushing equipment.

摘要
针对采用气固耦合法对碎玉米秸秆微粉碎过程仿真分析时，所需的仿真参数缺乏可靠数值的问题，以碎玉米秸秆为研究对象，采用物理测定与虚拟试验相结合的方法对仿真参数进行标定。通过物理试验获取碎玉米秸秆的本征参数，采用圆筒提升法进行堆积试验，并利用 Matlab 软件拟合边界线得到实际休止角为 44.12°；建立碎玉米秸秆离散元模型，利用 EDEM 软件进行虚拟堆积试验；通过 Plackett-Burman 试验，确定对休止角影响显著的参数为碎玉米秸秆间滚动摩擦因数、碎玉米秸秆间静摩擦因数和 JKR（Johnson-Kendall-Roberts）表面能；利用最陡爬坡试验，确定响应面分析的中心；以休止角为评价指标，通过 Box-Behnken 试验建立显著参数与碎秸秆休止角的二次多项式回归模型，对显著参数的取值进行寻优，得到较优的显著参数组合为：碎玉米秸秆间滚动摩擦因数为 0.55、碎玉米秸秆间静摩擦因数为 0.14、JKR 表面能为 0.12；基于最优参数组合进行休止角验证试验，试验结果表明，该参数组合下碎玉米秸秆的休止角为 43.82°，与实际休止角误差为 0.68%，表明该参数组合具有可靠性。本文得到的数据可为碎玉米秸秆离散元仿真以及秸秆微粉碎设备的研发提供相应的仿真参数。

INTRODUCTION
Corn stalk can be used as a new energy saving and environmental protection raw material after micro-grinding to achieve fine and high value utilization, so that it is no longer limited to low value-added fields such as heating and feeding, and could also save resources and protect the environment (*Koul et al., 2021*). At present, stalk powder is used in many fields such as composite materials, biodegradable plastics, hydrogen production and battery materials, and with increasing market demand. (*Mustafa* et *al., 2022; Cindradewi et al., 2021; Gao et al., 2022; Nita et al., 2021*). But existing stalk micro-crushing equipment can hardly support the demand of stalk powder scale up and industrialization.

[1] *Min Fu, Prof.; Xiaoqing Chen, M.S.Stud.Eng; Zefei Gao, M.S.Stud.Eng; Chengmeng Wang, M.S.Stud.Eng; Bing Xu, M.S.Stud.Eng; Yilin Hao, M.S. Stud.Eng.*

It is necessary to research and develop the micro-crushing equipment. The movement process of stalk powder is studied by using DEM, and further the grinding mechanism of straw is studied, which provides a new idea for the research of micro-crushing equipment.

In order to improve the accuracy of simulation test, many scholars have calibrated discrete element parameters of different materials based on Angle of repose (AoR) test. *Mu et al., (2021),* studied the discrete element model parameters of the stem and leaf of smashed sweet potatoes by combining physical experiments and virtual calibration. *Huan et al., (2022*), measured the intrinsic parameters of king grass stalks by physical experiments, using the index of AoR, the discrete element parameters of king grass stalks were calibrated using response surface optimization method, and the calibration results were verified by throwing trajectory tests; *Wang et al., (2021),* conducted parameter calibration tests using straw powder as homogeneous material in the mechanical properties test of corn straw powder. However, there is no study on calibration for discrete element parameterization of the crushed corn stalk (CCS). In this paper, the range of CCS characteristic parameters, CCS-CCS and CCS-65Mn steel plate (65Mn SP) contact parameters are measured by physical experiments, and a multisphere model of CCS is created based on EDEM software. By means of the actual AoR measured by stacking test, using the Plackett-Burman test, the steepest climb test and the Box-Behnken test, the discrete element model of CCS is calibrated to obtain the parameters of CCS which could be used in discrete element simulation. It is supposed to provide reliable discrete element basic parameters for the research and development simulation of straw micro-grinding equipment.

MATERIALS AND METHODS

Test material

The experimental materials are obtained from Donghai County, Lianyungang City, Jiangsu Province, China. The corn stalks are crushed using a Konnon straw crusher, and the crushed corn stalks (CCS) are sieved through a 20-mesh screen using a ZFJ-Ⅱ standard inspection sifter. The average length of the CCS is 10 mm and the diameter is 4 mm measured by the vernier caliper, and the moisture content of the CCS is 11.63% evaluated by rapid moisture tester.

CCS feature parameter measurement

Since the shape of CCS varies in size, the overflow method is leveraged to measure the volume of CCS (*Mu et al.,2021*). The paper cup is filled with pure water and put into the sink, 5g of CCS is weighed using a high-precision electronic scale (error ±0.05g), and the weighed CCS is put into the paper cup, then the pure water will overflow. Because the density of CCS is smaller than water, therefore, pressure the cover plate on the paper cup, so that the CCS is submerged in water, as shown in Figure 1.

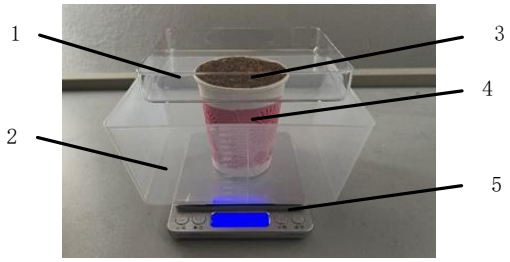


Fig. 1 - Measurement of CCS density

1-Cover plate; 2-Sink; 3-CCS; 4-Paper cup; 5-Electronic scale;

When the water no longer overflows, the paper cup will be removed from the sink. At this time, the volume of overflowing water is known as the volume of CCS. The obtained value is substituted into formula (1), and the density of CCS can be obtained.

$$\rho = \frac{m}{v} \tag{1}$$

where: ρ - density of CCS, kg/m^3;

m - mass of CCS，kg;

v – volume of CCS, m^3.

Repeating the above operations five times, the density of CCS is obtained as: 116.15 kg/m^3, 126.14 kg/m^3, 101.42 kg/m^3, 112.35 kg/m^3, 115.74 kg/m^3, with an average density of 114.36 kg/m^3.

The stalk compression test is carried out using the universal testing machine (WDW-100 type, China Changchun Kexin test apparatus Co., Ltd. production, see Figure 2), with the test loading speed of 5 mm/min. According to the change of straw diameter and height after the test, the shear modulus of stalk is obtained as 2.5 MPa, Poisson's ratio as 0.3. The relationship between shear modulus, elastic modulus and Poisson's ratio is shown in Equation 2.

$$G = \frac{E}{2(1+\mu)} \tag{2}$$

where: μ - Poisson's ratio;

E - Elastic modulus, GPa;

G - Shear modulus, MPa.



Fig. 2 - Radial global compression test of CCS

1-CCS; 2- WDW-100 universal tester; 3- Indenter;

Since 65Mn is commonly used as cutting tool material in straw micro-crushing equipment, 65Mn is selected as the test steel. The sliding method is used to measure the static friction coefficient of CCS-CCS and CCS-65Mn SP. The experimental apparatus consists of an angle digital display instrument and homemade test bench (see Figure 3). When the test begins, the digital display inclinometer and 65Mn SP are fastened horizontally on the test bench. Because the rolling of CCS will increase the test error, the CCS is glued together and placed on the steel plate. One end of the test bench is slowly lifted, when the first CCS particle begins to slide, stop lifting at the same time, and record the value on the inclinometer (*Huan et al., 2022; Fang et al., 2022*).

The above operations are repeated 10 times and the values of the inclination angle are between 21° and 35°. The CCS-65Mn SP static friction coefficient ranges from 0.35 to 0.75 by substituting the values into formula (3).

$$\mu = \tan\alpha \tag{3}$$

where: μ - static friction coefficient;

α - inclination angle.



Fig. 3 -Static friction coefficient measurement device

1-Angle digital display instrument; 2-CCS; 3-homemade test stand; 4-65Mn SP;

The inclined plane method is also used to measure the CCS-CCS static friction coefficient. Because the shape of the CCS is irregular, it is difficult to directly measure the static friction coefficient between the CCS, so the CCS is laid flat on the steel plate to form a material board, and then the CCS is placed on the material board. One end of the test stand is slowly lifted, when the first CCS particle begins to slide, stop lifting and record the value on the inclinometer. The above operations are repeated 10 times and the values of the inclination angle are between 20° and 37°. The values are substituted into formula 3 to obtain the CCS-CCS static friction coefficient in the range of 0.35~0.75. Based on the preliminary experimental measurements and review of relevant literature, the range of values for the parameters of AoR simulation model for CCS is determined, as illustrated in Table 1 (*Zhang et al., 2018; Song et al., 2022*).

Table 1

Parameters of AoR simulation model for CCS

Parameters	Numerical value
Poisson's ratio of CCS x_1	0.2~0.4
Shear modulus of CCS G_1 / MPa	2.5
CCS density ρ_1 /(kg·m^{-3})	114.36
Poisson's ratio of 65Mn SP v_2	0.3
Shear modulus of 65Mn SP G_2 / MPa	79000
65Mn SP density ρ_2 / (kg·m^{-3})	7865
CCS-CCS Coefficient of restitution x_2	0.2~0.4
CCS-CCS static friction coefficient x_3	0.35~0.75
CCS-CCS dynamic friction coefficient x_4	0.03~0.15
CCS-65Mn SP Coefficient of restitution x_5	0.3~0.6
CCS-65Mn SP static friction coefficient x_6	0.4~0.7
CCS-65Mn SP dynamic friction coefficient x_7	0.01~0.3
CCS-CCS JKR surface energy x_8/(J·m^{-2})	0.04~0.12

Physical test on the AoR of CCS

The cylinder lifting method is used to calculate the AoR of the CCS (*Jia et al., 2021*). The material's size determines the size of the cylinder, which has a diameter more than four to five times the material's maximum length and a height to diameter ratio of three to one (*Zhang et al., 2022*). Because the average length of the CCS is 10 mm, the diameter of the cylinder used in this test is 50 mm, the height is 150 mm, and the size of the test steel plate is 300×300×5 mm. The CCS screened by ZFJ-II standard inspection screening machine is used as the test material. After the cylinder is placed vertically on the 65Mn SP, the CCS is filled with the cylinder, and the cylinder is constantly lifted at the speed of 0.05 m/s using WDW-100 universal testing machine, and the CCS will form a pile on the 65Mn SP through the bottom of the cylinder, as shown in Figure 4. A vertical picture of the front of the CCS pile is photographed by a camera after the straw pile is stable.

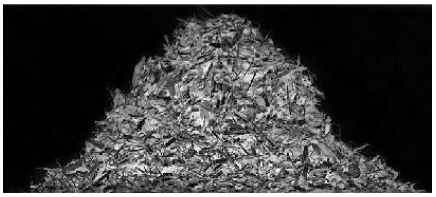


Fig. 4 - AoR physical test

1-WDW-100 universal tester; 2-65Mn SP; 3-Cylinder; 4-CCS pile

The frontal image is successively processed by grayscale processing, binarization processing and edge contour extraction by using Matlab software (see Figure 5), and then linear fitting is carried out on the edge contour, and the slope obtained by linear fitting is read, so as to obtain the AoR of the frontal image (*Chen et al., 2022*). The above steps are retested 5 times, and the test results are exhibited in Table 2.


(a) Original image


(b) Grayscale images


(c) Binarized images

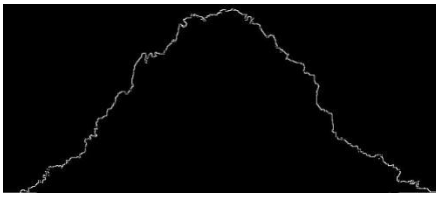

(d) Edge contour

Fig. 5 – AoR image processing

Table 2

AoR measurement

Number	AoR θ / (°)
1	44.62
2	45.21
3	46.09
4	41.89
5	42.77
average value	44.12

Establishment of the simulation model

Contact model selection

The commonly used Hertz-Mindlin contact model only calculates the elastic deformation of the material without considering the adhesive force between the materials (*Qu et al., 2020*). The Hertz-Mindlin with JKR contact model considers the adhesion force-JKR (Johnson-Kendall-Roberts) on the basis of Hertz theory. JKR can reflect the adhesion force between materials, and the influence of adhesion force on material motion can be obtained by calculation (*Wang et al., 2022; Tian et al., 2021; Dong et al., 2022*). Since the CCS has a certain bonding property, Hertz-Mindlin with JKR contact model is chosen for simulation calculation. The magnitude of the normal elastic force in the model is based on the normal overlap and surface energy, and the calculation equation is:

$$F_{JKR} = -4\sqrt{\pi\gamma E^*}\alpha^{\frac{3}{2}} + \frac{4E^*}{3R^*}\alpha^3 \quad (4)$$

$$\delta = \frac{\alpha^2}{R^*} - \sqrt{\frac{4\pi\gamma\alpha}{E^*}} \quad (5)$$

There into

$$\frac{1}{E^*} = \frac{1-\nu_1^2}{E_1} + \frac{1-\nu_2^2}{E_2} \quad (6)$$

$$\frac{1}{R^*} = \frac{1}{R_1} + \frac{1}{R_2} \quad (7)$$

where: F_{JKR} - JKR normal elastic force, N;

E^* - Equivalent modulus of elasticity, Pa;

δ - Normal overlap between two contacting particles, m;

α - Radius of the contact circle between two contacting particles, m;

γ - Surface energy, N/m;

R^* - Equivalent contact radius, m;

R_1, R_2 - Radius of contact of two particles, m;

ν_1, ν_2 - Poisson's ratio of two contact particles;

E_1, E_2 - Modulus of elasticity of two contact particles, Pa.

Simulation model building

Because of the small diameter of the CCS, multiple particles are needed to form the CCS model, which will increase the computer processing time, so the CCS is simplified into a cylinder with the same size. The average length of the CCS is measured as 10 mm and the diameter as 4 mm using vernier calipers. Then, the model is generated at the same size in EDEM and the geometric model of the CCS is illustrated in Figure 6.

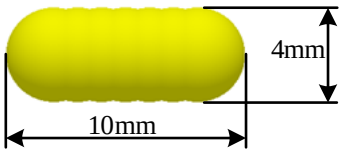


Fig. 6 - Geometric model of CCS

The models of the 65Mn cylinder (used to hold the CCS) and the steel plate are generated in EDEM, the length of the 65Mn cylinder is 150 mm and the diameter is 30 mm, the length and width of the 65Mn SP are both 300 mm.

Simulation of the AoR of CCS

The pellet plant is a circular plane with a diameter of 50 mm, which is dropped from the top of the cylinder, and the radius of the produced pellets is between 0.75 and 1.25 of the prototype radius. Dynamic random generation is used, with a generation rate of 5000 pcs/s and a uniform drop speed of 1m/s and a filling time of 0.6 s. The simulation fixed time step is 20% of the Rayleigh time step and the grid size is 2.5R. After the particles are filled, the cylinder is lifted at a uniform speed of 0.05 m/s and the particles fall on the 65Mn SP by gravity to form a particle pile (*Zhang et al., 2022; Coerzee, et al., 2022;*), as shown in Figure 7, and the AoR of the pile is read by Matlab software after the pile is stabilized.

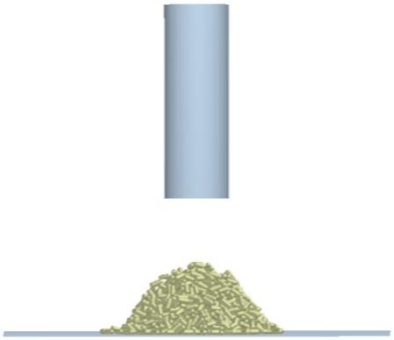


Fig. 7 - Simulation test of AoR

RESULTS

Plackett-Burman screening test and significance analysis

The Plackett-Burman test can be used to screen out the parameters that significantly affect the AoR. In order to simplify the test process, the high-level parameter is set as twice the low-level parameter, as shown in Table 3. Design-expert 8.0.6 software is used to design the experiment, and a total of 12 groups of simulation tests are performed. The testing program and simulation results are shown in Table 4.

Table 3

The parameters of Plackett Burman test

Symbol	Parameters	Level	
		low-level	high-level
X_1	Poisson's ratio of CCS	0.2	0.4
X_2	CCS-CCS restitution coefficient	0.25	0.5
X_3	CCS-CCS static friction coefficient	0.35	0.7
X_4	CCS-CCS dynamic friction coefficient	0.01	0.02
X_5	CCS-65Mn SP restitution coefficient	0.3	0.6
X_6	CCS-65Mn SP static friction coefficient	0.4	0.8
X_7	CCS-65Mn SP dynamic friction coefficient	0.01	0.02
X_8	CCS JKR surface energy / $(J \cdot m^{-2})$	0.01	0.02

Plackett-Burman Test scheme and results Table 4

Number	x_1	x_2	x_3	x_4	x_5	x_6	x_7	x_8	AoR θ / (°)
1	1	1	-1	1	1	1	-1	-1	30.27
2	-1	1	1	-1	1	1	1	-1	27.42
3	1	-1	1	1	-1	1	1	1	37.07
4	-1	1	-1	1	1	-1	1	1	32.23
5	-1	-1	1	-1	1	1	-1	1	31.34
6	-1	-1	-1	1	-1	1	1	-1	28.07
7	1	-1	-1	-1	1	-1	1	1	29.56
8	1	1	-1	-1	-1	1	-1	1	30.34
9	1	1	1	-1	-1	-1	1	-1	28.55
10	-1	1	1	1	-1	-1	-1	1	36.53
11	1	-1	1	1	1	-1	-1	-1	30.55
12	-1	-1	-1	-1	-1	-1	-1	-1	25.54

Design-Expert 8.0.6 is used to analyze the data in Table 4, and the variance analysis of test results is shown in Table 5. As can be seen from Table 5, P=0.0277<0.5 of Plackett-Burman test model indicates that this regression model is significant. The *p*-values of each parameter are ranked and three parameters are found to have $p<0.5$, among which, $p<0.01$ for the CCS-CCS dynamic friction coefficient x_4 and CCS JKR surface energy x_8, which are extremely significant parameters, and $p<0.05$ for the CCS-CCS static friction coefficient x_3, which are significant parameters. Therefore, the steepest climb test is conducted for x_3, x_4 and x_8.

Significance analysis of Plackett-Burman test parameters Table 5

Parameters	Sum of squares	df	F-value	p-value	Significance ranking
Model	124.61	8	15.55	0.0227*	
x_1	2.26	1	2.26	0.2302	4
x_2	0.86	1	0.86	0.4225	6
x_3	19.84	1	19.80	0.0211*	3
x_4	40.18	1	40.10	0.0080**	2
x_5	1.87	1	1.87	0.2648	5
x_6	0.20	1	0.20	0.6848	8
x_7	0.23	1	0.23	0.6629	7
x_8	59.116	1	59.04	0.0046**	1

*Note: ** Indicates that the influence is very significant (P<0.01), * the effect is significant (P<0.05).*

Analysis of the steepest climbing test

According to the screening results of the above tests, the steepest climb test is conducted for x_3, x_4 and x_8. The relative error between the actual AoR and the simulation AoR is calculated to determine the optimal range of simulation parameters. The CCS-CCS dynamic friction coefficient is taken as 0.01-0.13, the CCS JKR surface energy is taken as 0.03-0.15, the CCS-CCS static friction coefficient is taken as 0.35-0.75, and the remaining parameters are selected in the middle level for 5 sets of tests, and the test protocol and results are shown in Table 6. Table 6 shows that 4th group of tests has relatively small errors, so the optimal parameter range is around the 4th group of parameter values. Therefore the 4th group of parameter values are taken as the central point of the follow-up test and the 3rd and 5th group of parameter values are used as low level and high level, respectively.

Test design scheme and results of path of steepest ascent method Table 6

Number	x_3	x_4	x_8	AoR / (°)	Relative errors φ /%
1	0.35	0.03	0.04	32.43	26.45
2	0.45	0.06	0.06	35.22	20.17
3	0.55	0.09	0.08	37.16	15.78
4	0.65	0.12	0.10	41.91	5.01
5	0.75	0.15	0.12	48.30	9.47

Box-Behnken test analysis

Design-Expert 8.0.6 is used to design the Box-Behnken test, with center point per block adjusted to 3. A total of 15 groups of tests are carried out. The test scheme and results are shown in Table 7. Multiple regression fitting is performed on the test results, and the regression equation of the AoR is obtained as:

$$AoR = 41.77+2.43x_3+1.48x_4+3.18x_8-0.69x_3x_4-0.40x_3x_8+0.19x_4x_8+1.25x_3^2+0.37x_4^2-1.22x_8^2 \quad (9)$$

Box-Behnken test scheme and results **Table 7**

Number	x_3	x_4	x_8	AoR θ / (°)
1	-1	-1	0	38.32
2	0	-1	1	42.40
3	0	0	0	41.65
4	-1	0	-1	35.87
5	-1	1	0	43.03
6	0	-1	-1	36.82
7	1	0	1	46.91
8	0	1	1	45.39
9	1	-1	0	45.13
10	-1	0	1	43.42
11	0	1	-1	39.05
12	0	0	0	41.58
13	1	0	-1	40.97
14	0	0	0	42.07
15	1	1	0	47.06

According to the results of variance analysis of the model (see Table 8), the model's p=0.0001, determination coefficient R^2=0.9918, and correction determination coefficient R_{adj}^2=0.9770, both of which are close to 1, indicating that the regression equation fits well. The coefficient of variation is 1.23%, which indicates that the experiment is reliable. The precision (Adeq Precision) is 26.586, which indicates that the model can predict the AoR of CCS better. x_3, x_4, x_8, x_3^2 and x_8^2 have highly significant effects on the AoR of CCS, and x_3x_4 has significant effects on the AoR of CCS.

Table 8

Variance analysis of Box-Behnken quadratic model

Source of variance	Sum of Square	Degree of freedom	Mean Square	p-value
Model	160.92	9	17.88	0.0001**
x_3	47.19	1	47.19	<0.0001**
x_4	17.58	1	17.58	0.0005**
x_8	80.71	1	80.71	<0.0001**
x_3x_4	1.93	1	1.93	0.0432*
x_3x_8	0.65	1	0.65	0.1798
x_4x_8	0.14	1	0.14	0.4949
x_3^2	5.75	1	5.57	0.0056**
x_4^2	0.51	1	0.51	0.2266
x_8^2	5.51	1	5.51	0.0061**
Residual	1.33	5	0.27	
Lack of Fit	1.19	3	0.40	0.1538
Pure Error	0.14	2	0.07	

Based on the results of ANOVA, it can be seen that x_3x_4 interaction terms have a significant effect on the AoR of the CCS, and the corresponding surface of the interaction is plotted using Design-Expert 8.0.6 software in Fig. 8. From Fig. 8, it can be seen that when the value of x_4 is fixed, the AoR increases with the increase of x_3, and the variation tendency is obvious, so x_3 has significant effect on the AoR of CCS.

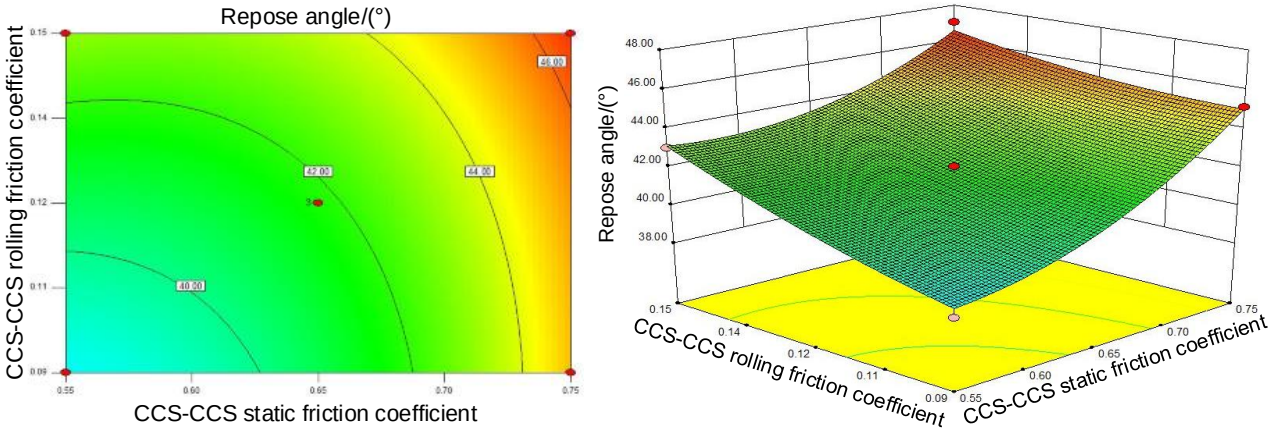


Fig. 8 - Interaction response surface diagrams

Taking the AoR of the physical experiment of CCS as target value, formula (9) is optimized and solved by Design-Expert 8.0.6, and the optimal combination of parameters is obtained as follows: x_3 is 0.55、x_4 is 0.14 and x_8 is 0.12. Other parameters are taken as intermediate values.

In order to verify the accuracy of the above parameters, they are substituted into EDEM for 5 times of simulation tests. The mean value of the measured AoR is 43.82°, and the relative error between the measured AoR and the AoR of physical experiment (44.12°) is 0.68%, which verifies the authenticity and reliability of the simulation test.



(a)Physical tests (b) Simulation test

Fig.9 - Comparison of physical test and simulation test

CONCLUSIONS

The measurement of CCS-related parameters is carried out based on the physical experiment method. The average length of CCS is 10 mm and the diameter is 4 mm using vernier calipers; the moisture content of CCS is 11.63% using a rapid moisture tester; the density of CCS is 114.36 kg/m3 using the overflow method; Through compression test with a universal testing machine, the shear modulus of CCS is 2.5 MPa and Poisson's ratio is 0.3; The range of static friction coefficient of CCS-CCS and CCS-65Mn SP measured by sliding method is 0.35-0.75 and 0.03-0.15 respectively.

According to the stacking test of CCS by cylinder lifting method, a vertical picture of the front of the CCS pile is photographed by camera, and the edge profile of the image is linearly fitted by Matlab software, and the AoR of the CCS pile is obtained as 44.12°. The Hertz-Mindlin with JKR contact model is adopted to establish the simulation model of CCS in EDEM. The model is a cylinder with length of 10 mm and diameter of 4 mm, which is composed of 7 spheres with diameter of 4 mm.

Plackett-Burman test shows that the effects of rolling friction coefficient of CCS-CCS, JKR surface energy and static friction coefficient of CCS on the AoR of CCS are more significant. The simulation parameters of CCS are optimized by taking the AoR of CCS is 44.12° as the test target. According to the results of Box-Behnken test, a set of solutions which are close to the results of physical experiment are obtained: the CCS-CCS static friction coefficient is 0.55, the CCS-CCS rolling friction coefficient is 0.14, and the JKR surface energy is 0.12. According to the simulation parameters obtained, five stacking tests are carried out in EDEM, and the average AoR is obtained as 43.68°, with a relative error of 0.68% compared to the actual experiment results. The calibration results are authentic and trustworthy on the basis of the verification test results, and it can provide basic parameters for the simulation of the mechanized operation of CCS in the stages of micro-crushing and collecting.

ACKNOWLEDGEMENT

This paper was funded by the National Natural Science Foundation of China (Grant No.51975114).

REFERENCES

[1] Chen B., Liu Y., Yu Q.X., Chen X.B., (2022), Calibration of soil discrete element contact parameter in rhizome medicinal materials planting area in hilly region. *INMATEH Agricultural Engineering*, Vol.68, Issue 03, pp.512-532.

[2] Cindradewi A.W., Bandi R., Park C.W., (2021), Preparation and Characterization of Polybutylene Succinate Reinforced with Pure Cellulose Nanofibril and Lignocellulose Nanofibril Using Two-Step Process. *Polymers*, Vol.13, Issue 22, pp.3945-3945.

[3] Coerzee C.J., Scheffler O.C., (2022), Review: The Calibration of DEM Parameters for the Bulk Modelling of Cohesive Materials. *Processes,* Vol.11, Issue 01, pp.5.

[4] Dong X.Q., Zheng H.N., Jia X., Li Y.L., Song J.N., Wang J.C., (2022), Calibration and experiments of the discrete element simulation parameters for rice bud damage. *INMATEH Agricultural Engineering*, Vol.68, Issue 03, pp.659-668.

[5] Fang W.Q., Wang X.Z., Han D.L., Chen X.G., (2022), Review of material parameter calibration method. *Agriculture*, Vol.12, Issue 05, pp.706.

[6] Gao Z.H., Shang S.Q., Xu N., Wang D.W., (2022), Parameter calibration of discrete element simulation model of wheat straw-soil mixture in Huang Huai Hai production area. *INMATEH Agricultural Engineering*, Vol.66, Issue 01, pp.201-210. Romania.

[7] Huan X.L., Wang D.C., You Y., Ma W.P., Zhu L., Li S.B., (2022), Establishment and calibration of discrete element model of king grass stalk based on throwing test. *INMATEH Agricultural Engineering*, Vol.66, Issue 01, pp.19-30.

[8] Jia H., Deng J., Deng Y., (2021), Contact parameter analysis and calibration in discrete element simulation of rice straw. *J. Agric. & Biol. Eng*, Vol.14, Issue.04, pp.72-81.

[9] Koul B., Yakoob M., Shah M.P., (2021), Agricultural waste management strategies for environmental s ustainability. *Environmental Research,* Vol.206, Issue.4, pp.112285.

[10] Mu G.Z., Qi X.T., Zhang W.Z., Lv Z.Q., Zhang T.T., Wang S.W., (2021), Parameter Measurement and Calibration in Discrete Element Simulation of Broken Sweet Potato Seedlings. American Journal of Bio chemistry and Biotechnology, Vol.17, Issue.02, pp.256-266.

[11] Mustafa M.S., Muneer M.A., Zafar M.Q., et al. (2022), Process parameter optimization for Fused Filam ent Fabrication additive manufacturing of PLA/PHA biodegradable polymer blend. *International Polyme r Processing*, Vol.37, Issue.1, pp.1-14.

[12] Nita C., Zhang B., Dentzer J., (2021), Hard carbon derived from coconut shells, walnut shells, and corn silk biomass waste exhibiting high capacity for Na-ion batteries. *Journal of Energy Chemistry*, Vol.58, Issue 07, pp.207-218.

[13] Qu T.M., Feng Y.T., Zhao T.T., Wang M., (2020), A hybrid calibration approach to Hertz–type contact parameters for discrete element models. *International Journal for Numerical and Analytical Methods in Geomechanics*, Vol.44, Issue 09, pp.1281-1300.

[14] Song Z.H., Li H., Yan Y.F., Tian F.Y., (2022), Calibration Method of Contact Characteristic Parameters of Soil in Mulberry Field Based on Unequal-diameter Particles DEM Theory (桑园土壤非等径颗粒离散元仿真模型参数标定与试验). *Transactions of the Chinese Society for Agricultural Machinery*, Vol.53, Issue 06, pp.21-33.

[15] Tian X.L., Cong X., Qi J.T., Guo H., Li M., Fan X.H., (2021), Parameter Calibration of Discrete Element Model for Corn Straw – Soil Mixture in Black Soil Areas (黑土区玉米秸秆-土壤混料离散元模型参数标定). *Transactions of the Chinese Society for Agricultural Machinery*, Vol.52, Issue 10, pp.100-108+242.

[16] Wang W.W., Cai D.Y., Xie J.J., (2021), Parameters calibration of discrete element model for corn stalk powder compression simulation（玉米秸秆粉料致密成型离散元模型参数标定）. *Transactions of the Chinese Society for Agricultural Machinery*, Vol.52, Issue 03, pp.127-134.

[17] Zhang P., Zhang H., Li J.M., Tan C.L., Zhang J.X., (2022), Parametric calibration of cotton straw parameters in Xinjiang based on discrete elements. *INMATEH Agricultural Engineering*, Vol.67(2), pp.314-322.

[18] Zhang T., Liu F., Zhao M.Q., Wang W., (2018), Determination of corn stalk contact parameters and calibration of discrete element method simulation（玉米秸秆接触物理参数测定与离散元仿真标定）. *Journal of China Agricultural University*, Vol.23, Issue.04, pp.120-127.

Zhang W., Wang F., (2022), Parameter calibration of American ginseng seeds for discrete element. *International Journal of Agricultural and Biological Engineering*, Vol.15, Issue 06, pp.16-22.

SIMULATION RESEARCH ON THE INFLUENCE OF INCLINATION ANGLE OF LINEAR VIBRATING SCREEN ON BUCKWHEAT SIZING EFFECT
/
直线振动筛筛面倾角对荞麦分级效果影响的模拟研究

Bing XU[1,2], Decong ZHENG *[1,2,3], Qingliang CUI [1,2],Hanqing YAO[1]
[1] College of Agricultural Engineering, Shanxi Agricultural University, Taigu 030801 / China;
[2] Dryland Farm Machinery Key Technology and Equipment Key Laboratory of Shanxi Province, Taigu 030801 / China
[3] Research centre of Shanxi modern agricultural facilities and equipment, Taiyuan 030031 / China
Tel: +86-0354-6288339; E-mail: zhengdecong@126.com
DOI: https://doi.org/10.35633/inmateh-69-38

Keywords: *buckwheat grains, vibrating screen, inclination angle of the screen, discrete element*

ABSTRACT
In the buckwheat industry, buckwheat sizing effect has played a significant role in the subsequent hulling effect and food quality in its deep processing. In order to study the influence of inclination angle of linear vibrating screen on buckwheat sizing effect, EDEM was used for numerical simulation of sizing process with the inclination angle of the screen separately at 2º, 3º, 4º, and 5º. By observing particle distribution on the screen deck and calculating the different types of particles in various statistical areas, qualitative comparison and quantitative analysis on the conveying capability of the screen and the penetrating capability of particles at different inclination angles were made, and the results revealed that with the increase in the inclination angle of the screen, the conveying capability of the screen was enhanced, while particles became less capable of penetrating through the sieve. When the inclination angle was increased from 2º to 3º, the conveying capability of the screen was significantly improved, while the penetrating capability of particles on both screen decks was slightly reduced. By taking the penetrating capability of particles and the conveying capability of the screen into comprehensive consideration, it turned out that better sizing effect would be achieved at the inclination angle of 3º. Our research will provide a reference for optimizing the processing parameters during the vibrating separation of buckwheat.

摘要
荞麦产业精深加工过程中，荞麦分级效果对后续脱壳效果乃至食品品质都有重要的影响，为探究直线振动筛筛面倾角对荞麦分级效果的影响，利用 EDEM 软件对筛面倾角为 2°、3°、4°、5°时的分级过程进行了数值模拟，通过观察筛面颗粒分布及对各统计区不同类型颗粒的统计，对不同筛面倾角下筛面输送能力、颗粒透筛能力进行定性比较和定量分析，结果表明：随着筛面倾角增大筛面输送能力增强，而颗粒透筛能力降低，当筛面倾角由 2°增加到 3°时，两层筛面颗粒透筛能力略有降低的情况下，筛面输送能力显著提高，综合颗粒透筛能力及筛面输送能力两项指标，筛面倾角为 3°时分级效果较好。本研究可为荞麦振动分级过程中工艺参数的优化提供参考。

INTRODUCTION
Rich in multiple functional factors, such as bioflavonoid and dietary fibre, buckwheat has become an ideal raw material in health care and nutrition products *(Cheng et al., 2021; Nešović et al., 2021; Sinkovič et al., 2021)*. Also as coarse food grain, buckwheat is highly complementary to wheat and rice in terms of nutritional ingredient. In recent years, buckwheat has been a basic ingredient in more and more products, such as buckwheat noodle, buckwheat biscuit, and buckwheat tea, all of which have attracted wide attention from the healthy consumption market, leading to the increasing yield of buckwheat in the world *(Cheng et al., 2021; Hou et al., 2022)*.

Due to the small gap between buckwheat hull and kernel, shell breakage rate is very high although buckwheat hull is rich in lignin and cellulose, and it has become one of the main factors restricting the scale production of buckwheat and the development of its processing industry *(Ma et al., 2022)*. Research has proved that improved sizing effect will increase the whole rice yield in the shelling process *(Quan et al., 2014)*.

In recent years, numerous studies on vibratory screening of agricultural materials have been made by many scholars at home and abroad.

---

[1] *As Lec.M.S.Eng. Bing XU; Decong ZHENG, Prof. Eng.;Qingliang CUI, Prof. Ph.D. Eng.*

[2] *Decong ZHENG, Prof. Eng. Chief of Research Centre*

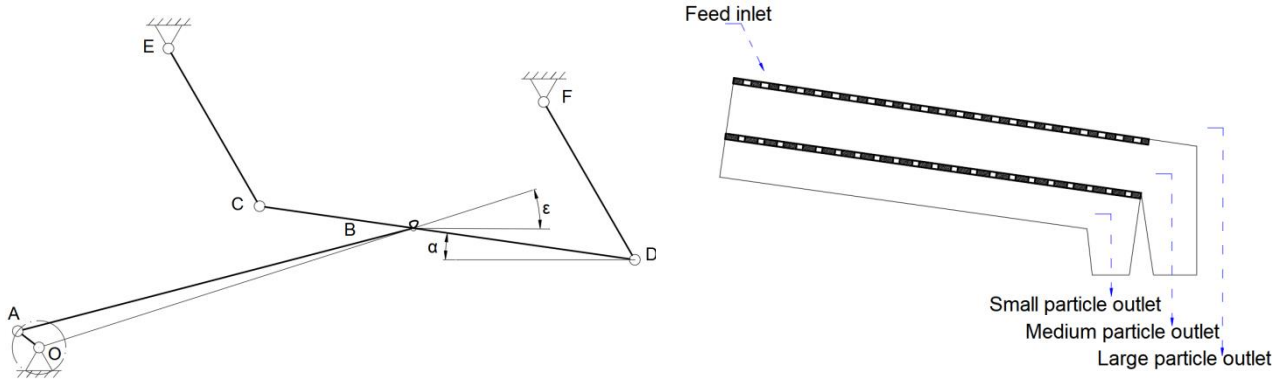
Fan et al. used QXS-3.0 air-and-screen cleaning testing platform for buckwheat cleaning test to analyse the distribution rule of screen underflow at different fan speeds, wind directions, rotation speeds of crank, and diameters of crank *(Fan et al., 2023)*. Jia et al. proposed a double-layer screening method to establish the relationship between the screening efficiency of a double-layer vibrating screen and the elements in screening process with screening parameters according to the discrete element method *(Jia et al., 2022)*. Hu et al. performed simulation analysis on the vibrating separation effect based on the discrete element method under different processing parameters by taking the mixed materials of buckwheat hull and kernel as research objects *(Hu et al., 2023)*. In 2019, A. Davoodi et al. discovered the better screening performance by determining the optimal shape of mesh after contrastive analysis was made on the screening performance of screens in different shapes and different mesh sizes based on DEM *(Davoodi et al., 2019)*. Xu et al. used automatic filling method to establish a DEM for buckwheat grains, where all of the contact parameters were calibrated. It laid a foundation for the application of DEM to the production of buckwheat and the development of processing equipment *(Xu et al., 2021)*. Also, they made simulation analysis on the sizing process under different amplitudes by designing a three-stage sizing device for the separation of buckwheat *(Xu et al., 2022)*.

Buckwheat is a kind of minor coarse cereal, and generally there are few studies on its sizing devices and processes. Based on the previously designed three-stage sizing device, this study explores the influence of inclination angle of the screen on the separation effect of buckwheat. The simulation on various sizing processes at different inclination angles based on DEM will provide a reference for optimizing the vibrating separation process of buckwheat.

MATERIALS AND METHODS

Principle of buckwheat vibration sizing screen

When linear vibrating screen was adopted to separate buckwheat grains, the vibration of screen box would be made by vibrating screen via the crank-link mechanism to loosen, stratify, or sift out buckwheat materials, which will then be conveyed for screening. The connection between crank centre and the hinged joint of connecting rod on the screen box is also the vibrating direction of the screen. The angle ε between this direction and the horizon is the vibrating direction angle, and the angle α between screen box and the horizon is the inclination angle of the screen *(Geng et al., 2011; China Academy of Agricultural Mechanization Sciences, 2007)*. The schematic diagram for the mechanism of vibrating screen is indicated in Figure 1 (a), where the screen box consists of two parallel screen decks, which have meshes in different sizes to separate buckwheat grains into three sizes as shown in Figure 1(b).



(a) Schematic diagram of vibrating screen mechanism (b) Schematic diagram of classification process

Fig. 1 - Schematic diagram of vibrating sizing screen

DEM for three-stage buckwheat vibrating screen

Buckwheat grains vary very much in size during the harvesting time with the real picture shown in Figure 2. According to the different sizes of buckwheat grains, discrete element models for buckwheat grains in large, medium, and small size were separately built in EDEM. In the vibration screening process, the motion of particles must take the process of mutual contact between different particles or between particles and the surface of sizing screen into account *(Hu et al., 2023)*. In this paper, Hertz-Mindlin no-slip contact model was adopted *(Wang et al., 2010)*, where the intrinsic and contact parameters of the materials required in buckwheat vibration screening process and determined according to the relevant references (*Zhang et al., 2020; Hou et al., 2019; Xu et al., 2021; Fan et al., 2022; Xu et al., 2022*) were provided in Table 1 and Table 2, respectively.



Fig. 2 - Buckwheat grains in different sizes

Table 1

Material intrinsic parameters

Material	Poisson's ratio	Shear modulus / Pa	Density / (kg·m^{-3})
Buckwheat	0.30	3.43×10^{7}	2.54×10^{3}
Vibrating screen	0.29	7.00×10^{10}	8.00×10^{3}

Table 2

Material contact parameters

Material	Restore collision coefficient	Static friction coefficient	Rolling friction coefficient
Buckwheat-buckwheat	0.200	0.532	0.010
Buckwheat-Vibrating screen	0.508	0.700	0.043

The common feeding methods include continuous feeding and fixed time feeding *(Jia et al., 2022)*. In order to be closer to the real situation during the simulation, continuous feeding method was used for simulation in our research. It means that particles in three different sizes have been uniformly produced by the particle factory at the front end of screen box from the beginning to the end of simulation at a speed of 1,200 pcs/s with the simulation time set as 16 s.

Design of experiments

In order to explore the influence of inclination angle of the screen on the buckwheat vibration screening effect, single factor experiments were designed based on the previous research after vibration frequency, vibrating direction angle, and amplitude were determined, as indicated in Table 3.

Table 3

Design of experiments

Number	Inclination angle of screen surface / (°)	Vibrational frequency / (HZ)	Vibrational direction angle / (°)	Amplitude / (mm)
1	2	4.5	30	28
2	3	4.5	30	28
3	4	4.5	30	28
4	5	4.5	30	28

In order to facilitate the processing and analysis of simulation results, statistical areas were built on the constructed buckwheat vibration screening model.

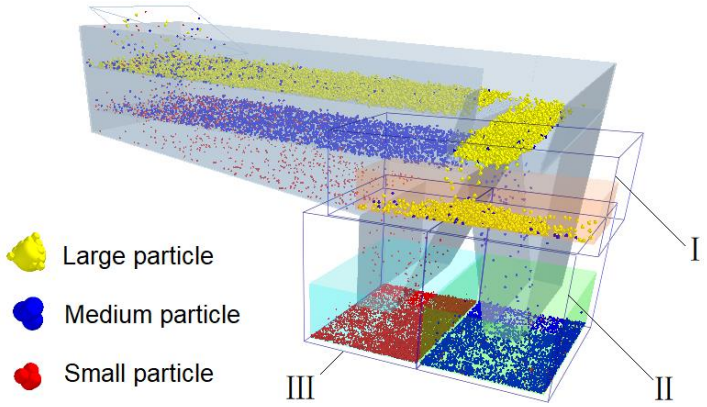


Fig. 3 - Division of statistical domains

As indicated in Figure 3, Area I, II, and III were the statistical areas for screen overflow, screen residue, and screen underflow, respectively. In each area, the number of large, medium and small-size particles simulated at any time could be separately calculated. Moreover, with the adoption of observation method in our research, particle distribution on two screen decks at different inclination angles was simultaneously observed to compare the particle penetration.

RESULTS

Figure 4 shows the particle distribution on the first screen deck at different inclination angles of the screen at 16 s after the simulation.

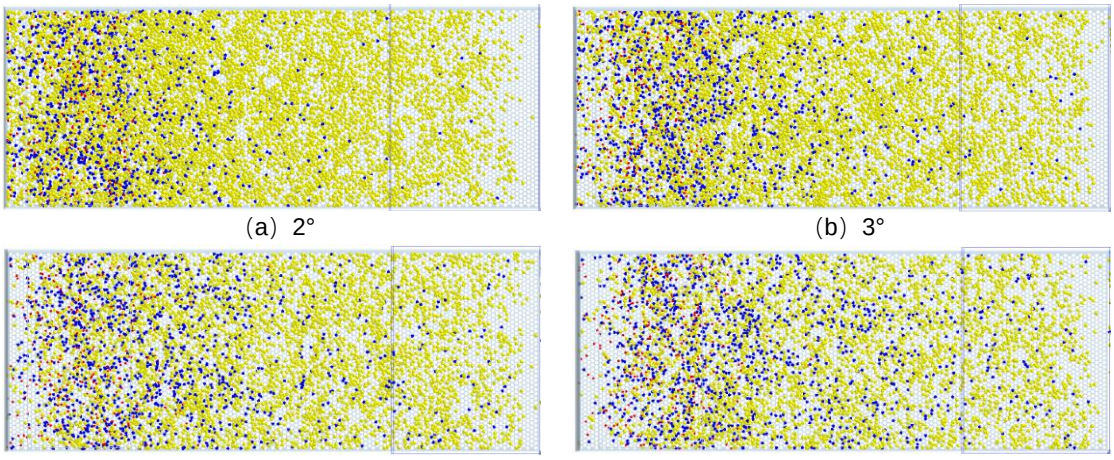


Fig. 4 - Particle distribution on the first screen deck at 16 s

It can be seen from Figure 4 that in the process of conveying materials from the front end of the screen to the tail on the first screen deck, most of the small particles penetrated through the sieve within the length that was 2/3 of the total in the front of sieve plate at the four inclination angles, suggesting strong penetrating capability. However, it varied very much regarding the penetrating capability of medium-size particles. With the increase in the inclination angle of the screen, more medium-size particles were conveyed to the tail area, indicating that medium-size particles are less capable of penetrating through the sieve with the increase in the inclination angle of the screen. To facilitate the quantitative analysis of the conveying and penetrating capabilities on the first screen deck, the number of different types of particles in the statistical area for screen overflow at 16 s was calculated, as indicated in Table 4.

Table 4

Number of particles in the statistical area for screen overflow at 16 s

Inclination angle of screen surface/ (°)	Number of large particles/pcs	Number of medium particles/pcs	Number of small particles/pcs	Total number of particles/pcs
2	677	60	0	737
3	1278	118	0	1396
4	1893	213	0	2103
5	2403	383	7	2793

It can be known from Table 4 that the number of large-size particles in the statistical area for screen overflow at the four inclination angles was separately 677, 1,278, 1,893, and 2,403 at the end of simulation, proving that with the increase in the inclination angle of the screen, the conveying capability of the first screen deck was enhanced.

According to Table 4, the distribution of different types of particles in the statistical area for screen overflow at different inclination angles was shown with a pie chart, as indicated in Figure 5.

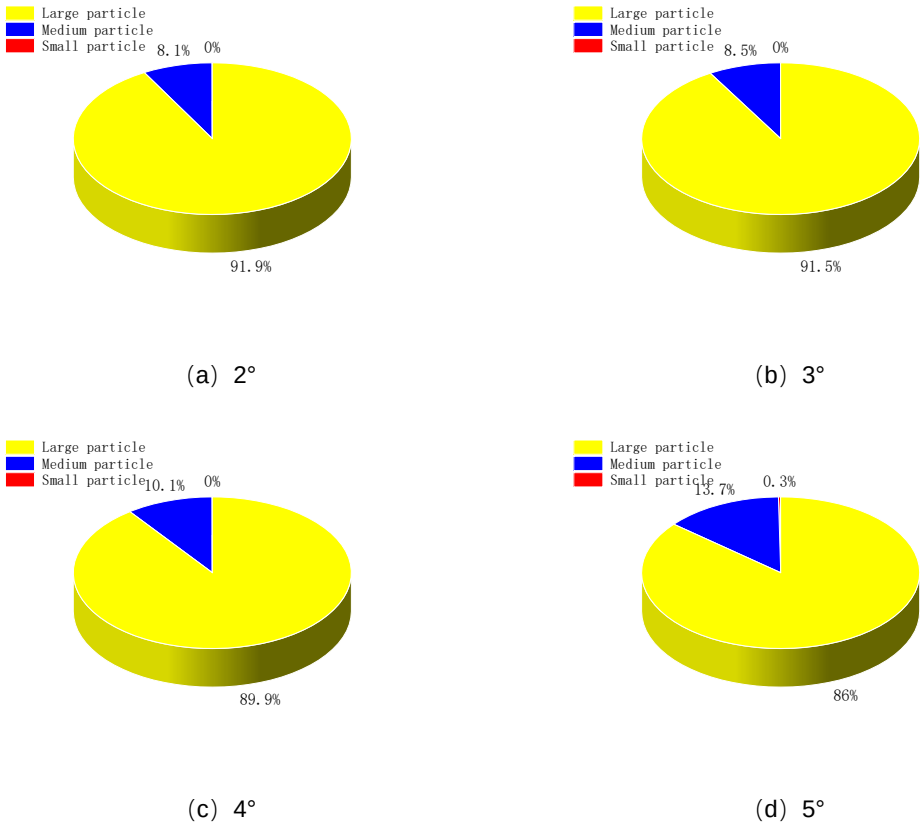


Fig. 5 - Proportion of different types of particles in the statistical area for screen overflow

The medium and small-size particles that failed to penetrate through the first screen deck were conveyed along with the large-size particles to the statistical area for screen overflow. According to Figure 5, at the four inclination angles of the screen, the percentage of medium-size particles in the statistical area for screen overflow was separately 8.1%, 8.5%, 10.1%, and 13.7%. On the first screen deck, medium-size particles were slightly less capable of penetrating through the sieve with the increase of the inclination angle from 2° to 3°. However, the penetrating capability of medium-size particles was significantly reduced when the inclination angle varied between 3°~5°.

Figure 6 shows the distribution of particles on the second screen deck at 16 s.

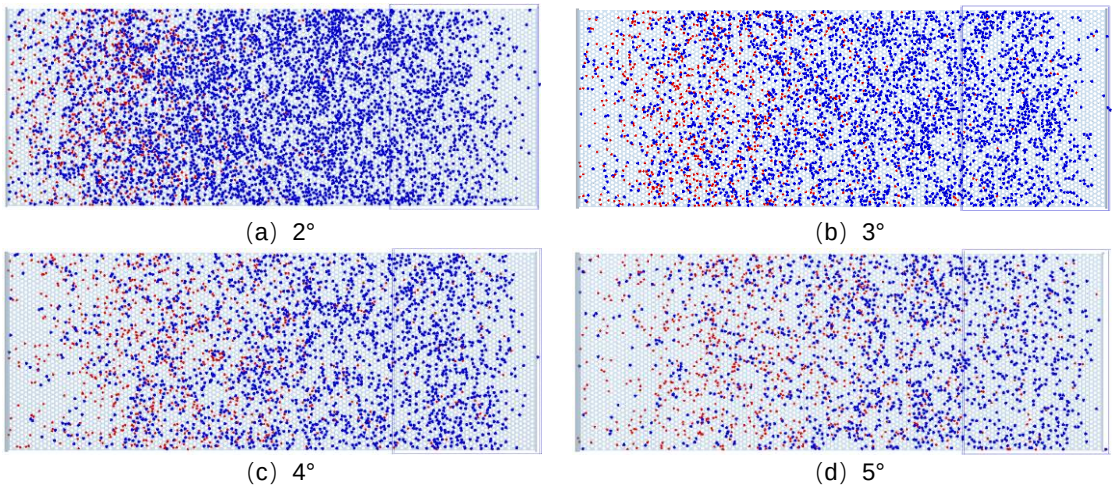


Fig. 6 - Particle distribution on the second screen deck at 16 s

As shown in Figure 6, small particles varied in penetrating capability in the process of conveying materials from the front end of the screen to the tail on the second screen deck. More small particles were conveyed into the tail area with the increase in the inclination angle of the screen, suggesting that the penetrating capability of small particles was reduced with the increase in the inclination angle of the screen. To facilitate the quantitative analysis of the conveying and penetrating capabilities on the second screen deck, the number of different types of particles in the statistical area for screen residue at 16 s was calculated, as indicated in Table 5.

Table 5

Number of particles in the statistical area for screen residue at 16 s

Inclination angle of screen surface / (°)	Number of large particles/pcs	Number of medium particles/pcs	Number of small particles/pcs	Total number of particles/pcs
2	0	1189	56	1245
3	0	2240	141	2381
4	0	2886	289	3175
5	0	3260	529	3789

It can be seen from Table 5 that the number of medium-size particles in the statistical area for screen residue at the four inclination angles was separately 1,189, 2,240, 2,886, and 3,260 at the end of simulation, indicating that with the increase in the inclination angle of the screen, the conveying capability of the second screen deck was enhanced. According to Table 5, the distribution of different types of particles in the statistical area for screen residue at different inclination angles was shown with a pie chart, as indicated in Figure 7.

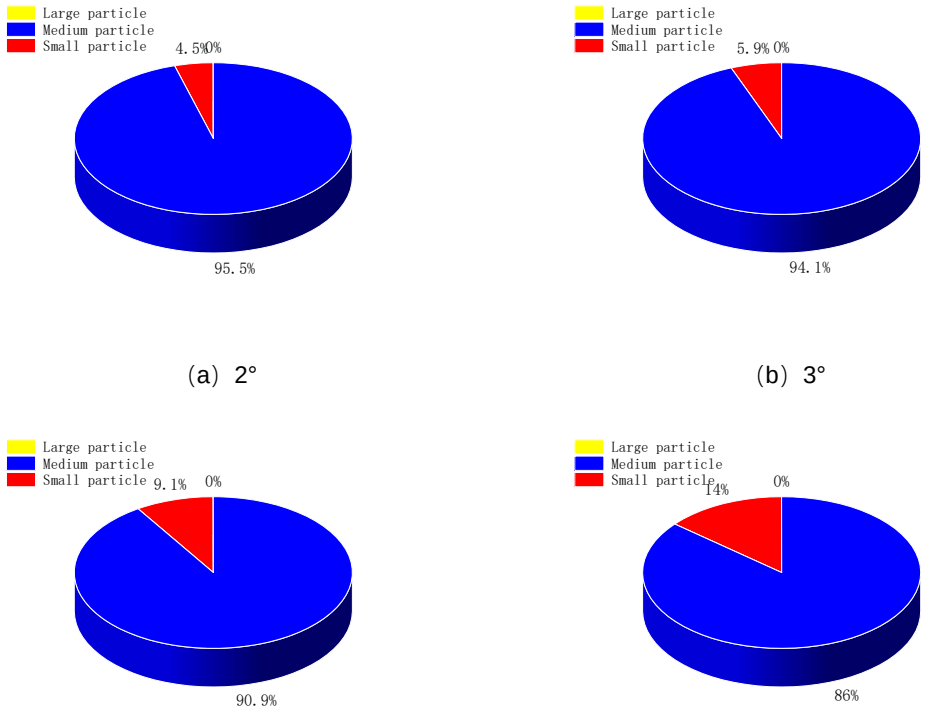


Fig. 7 - Proportion of different types of particles in the statistical area for screen residue

Small particles that failed to penetrate through the second screen deck were conveyed along with the medium-size particles to the statistical area for screen residue. Figure 7 shows that at the four inclination angles of the screen, the percentage of small particles in the statistical area for screen residue was separately 4.5%, 5.9%, 9.1%, and 14%. On the second screen deck, small particles were slightly less capable of penetrating through the sieve with the increase in the inclination angle of the screen from 2° to 3°. However, the penetrating capability of small particles was significantly reduced when the inclination angle varied between 3°~5°.

Comprehensive analysis on the conveying and penetrating capabilities on both screen decks revealed that when the inclination angle of the screen was increased from 2° to 3°, the conveying capability could be enhanced significantly, while the penetrating capability of particles on both screen decks was slightly reduced.

CONCLUSIONS

(1) Based on the previously designed three-stage vibration screening device, a three-stage vibration screening model at different inclination angle was constructed in this paper.

(2) Numerical simulation on buckwheat sizing processes was performed separately at the inclination angles of 2°, 3°, 4°, and 5°. Through visual observation, the distribution of particles simulated at the same time on both screen decks at different inclination angles revealed that small particles had strong penetrating capability on the first screen deck when the inclination angle varied between 2°~5°. However, medium-size particles on the first screen deck and small particles on the second screen deck were less capable of penetrating through the sieve with the increase in the inclination angle of the screen.

(3) At the end of the simulation, quantitative analysis on the proportion of different types of particles in various statistical areas at different inclination angles revealed that with the increase in the inclination angle from 2° to 3°, the conveying capability could be significantly improved, while particles on both screen decks became slightly less capable of penetrating through the sieve. By taking the penetrating capability of particles and the conveying capability of the screen into comprehensive consideration, it turned out that better sizing effect would be achieved at the inclination angle of 3°.

ACKNOWLEDGEMENT

This research, titled “Simulation Research on Influence of Leaning Angle of Linear Vibrating Screen on Buckwheat Sizing Effect”, was supported by Fundamental Research Program of Shanxi Province (202203021222141), by project: “Major Special Projects for the Construction of China Modern Agricultural Industrial Technology System (Grant No. CARS-07-D-2)”.

REFERENCES

[1] Cheng J.L., Liu J., Mao J.Q., et al., (2021). Effects of Different Illumination Treatments on Flavonoids and Gene Expression of Related Metabolic Enzymes in Buckwheat Sprouts *(不同光照对荞麦芽黄酮类化合物及相关代谢酶基因表达的影响)*. *Food Science,* Vol.42, Issue 23, pp.72-79, Beijing/China;

[2] Davoodi A., Bengtsson M., Hulthén E., et al., (2019), Effects of screen decks' aperture shapes and materials on screening efficiency. Minerals Engineering, Vol.139,105699. Ed. Elsevier, London/England;

[3] Fan R., Cui Q.L., Lu Q., et al., (2022), Experimental study on non-planar screening device for buckwheat threshing material[J]. *INMATEH Agricultural Engineering*, Vol.66, Issue 1, pp.73-80. Bucharest/Romania. DOI: https://doi.org/10.35633/inmateh-66-07

[4] Fan R., Cui Q.L., Lu Q., et al. (2023), Study on the distribution law of materials under sieve in air-and-screen cleaning device *(风筛式清选装置筛下物料分布规律研究)*. Journal of Chinese Agricultural Mechanization, Vol.44, Issue 01, pp.142-151, Nanjing/China;

[5] Geng D.Y., Zhang D.L., Wang X.Y., et al., (2011), *Agricultural Mechanics (新编农业机械学),* ISBN 9787118075281, National Defence Industry Press, Beijing/China.

[6] Hou H.M., (2019), *Experimental study on cleaning dynamic characteristics of coarse cereals crops harvested by machinery (杂粮作物机械收获清选动力学特性研究)*. PhD Dissertation. Shanxi Agricultural University, Taiyuan/China.

[7] Hou H.H., Liu R., Sun Y.L. et al. (2022), Optimization of the Preparation Process of Buckwheat Noodles Based on Response Surface Analysis *(基于响应面分析优化荞麦面条制备工艺)*. Food Research and Development, Vol.43, Issue 2, pp.63-70, Tianjin / China;

[8] Hu G.Y., Chen X.D., Zhao T.F., et al., (2023), Study on grading technology of walnut shell and kernel mixture vibrating screen based on EDEM *(基于 EDEM 的核桃壳仁混合物振动筛分级工艺研究)*. *China Oils and Fats*, [J/OL].1-8. DOI: 10.19902/j.cnki.zgyz.1003-7969.220419, Xi’an / China;

[9] Jia P.Y., (2022), *Parameter Optimization and Mechanism Research of Double-Layer Variable Screen Surface Vibrating Screen (双层变筛面振动筛参数优化及筛分机理研究)*. Master thesis. Fujian University of Technology, Fuzhou/China;

[10] Ma G.F., Xin H.B., Xiu L. et al., (2022), Buckwheat Seed Shelling Characters: A Review *(荞麦脱壳性状的研究进展)*. *Chinese Agricultural Science Bulletin*, Vol.38, Issue 24, pp.19-27, Beijing / China;

[11] Nešović M., Gašić U., Tosti T. et al., (2021), Distribution of polyphenolic and sugar compounds in different buckwheat plant parts. RSC Advances, Vol.11, Issue 42, pp.25816-25829. London/England;
[12] Quan Y.J., Du W.L., Liu C.et al., (2014), The Research on the Influence of Elongated Apertures with Round Screens Grading to Buckwheat Shelling Effect *(长圆孔筛分级对荞麦剥壳效果的影响试验)*. *The Food Industry*, Vol.35, Issue 10, pp.205-208, Shanghai/China.
[13] Sinkovič, L., Kokalj S.D., Meglič V., Milling Fractions Composition of Common (Fagopyrum esculentum Moench) and Tartary (Fagopyrum tataricum (L.) Gaertn.) Buckwheat, Food Chemistry (2021), DOI: https://doi.org/10.1016/j.foodchem.2021.130459.Ed. Elsevier, London/England;
[14] Wang G.Q., (2010), *Discrete element method and its application in EDEM (离散单元法及其在 EDEM 上的实践)*, ISBN 9787561227978, Northwestern Polytechnic University Press, Xi'an/China.
[15] Xu B., (2021). Construction of a discrete element model of buckwheat grain and calibration of parameters. *INMATEH-Agricultural Engineering*, Vol.64, Issue 2, pp.175-184, Bucharest / Romania;
[16] Xu B., (2022). Experimental Research on Three-Level Vibrating Screening of Buckwheat Based on Discrete Element Method. *INMATEH-Agricultural Engineering*, Vol.68, Issue 3, pp.191-200, Bucharest / Romania; DOI: https://doi.org/10.35633/inmateh-68-19
[17] Zhang L.X., (2020), *Research and Design of Buckwheat Harvester Cleaning Device Based on FLUENT-EDEM Coupling (基于 FLUENT-EDEM 耦合的荞麦收获机清选装置研究设计).* PhD Dissertation. Cheng du University, Chengdu / China.
[18] Zhou Y., Qin D.L., Li Q.Q., et al., (2022), *Optimization design of coix vibrating screen cleaning device based on EDEM (基于 EDEM 薏苡振动筛清选装置优化设计与试验)*. Journal of Northeast Agricultural University, Vol.53, Issue 11, pp.68-76, Harbin / China;
[19] ***China Academy of Agricultural Mechanization Sciences, (2007), *Agricultural Machinery Design Manual (农业机械设计手册)*. ISBN 9787802333352, China Agricultural Science and Technology Press, Beijing / China.

AN IoT-ENABLED DESIGN FOR REAL-TIME WATER QUALITY MONITORING AND CONTROL OF GREENHOUSE IRRIGATION SYSTEMS
/
DESAIN PERANGKAT BERBASIS IoT UNTUK PEMANTAUAN DAN PENGENDALIAN KUALITAS AIR PADA SISTEM IRIGASI RUMAH KACA

Irfan ARDIANSAH[1*)], Ryan Ganesha CALIBRA[1)], Nurpilihan BAFDAL[2)], Awang BONO[3)], Edy SURYADI[2)], Siti NURHASANAH[4)]

[1)] Department of Agroindustrial Technology, Faculty of Agroindustrial Technology, Universitas Padjadjaran, Indonesia
[2)] Department of Agriculture Engineering and Biosystem, Faculty of Agroindustrial Technology, Universitas Padjadjaran, Indonesia
[3)] Department of Chemical Engineering, Faculty of Engineering, Universiti Malaysia Sabah, Malaysia
[4)] Department of Food Industrial Technology, Faculty of Agroindustrial Technology, Universitas Padjadjaran, Indonesia
E-mail: irfan@unpad.ac.id
DOI: https://doi.org/10.35633/inmateh-69-39

Keywords: *greenhouse, internet of things, water quality, irrigation system, automation*

ABSTRACT

Because hydroponic plant nutrients are dissolved in the water, water quality management is essential for growing healthy plants. Taking care of the total dissolved solids (TDS) and the pH (water acidity) is essential. The purpose of this research is to create an IoT-based water quality monitoring device. The average TDS after 30 days of automation with an Arduino UNO was 1162.82 ppm, and the gadget kicked on the nutrient pump whenever the TDS fell below 1000 ppm or the EC fell below 2. The mechanism self-adjusts the pH when it falls below 5.5 or rises above 6.5, with a mean of 6.17.

ABSTRAK

Karena nutrisi tanaman hidroponik terlarut di dalam air, manajemen kualitas air sangat penting untuk menanam tanaman yang sehat. Menjaga total dissolved solid (TDS) dan pH (keasaman air) sangat penting. Tujuan dari penelitian ini adalah untuk membangun perangkat pemantauan kualitas air berbasis IoT. Rata-rata TDS setelah 30 hari otomatisasi dengan Arduino UNO adalah 1162.82 ppm, dan alat ini akan menyalakan pompa nutrisi setiap kali TDS turun di bawah 1000 ppm atau EC turun di bawah 2. Mekanisme ini akan menyesuaikan pH ketika turun di bawah 5.5 atau naik di atas 6.5, dengan rata-rata 6.17.

INTRODUCTION

Smart farming, which is also called intelligent agriculture, is a way of managing farms that uses information technology like the Internet of Things (IoT), robotics, drones, and artificial intelligence to improve the quantity and quality of agricultural products while reducing the amount of labor needed for farming *(Raj, Appadurai, & Athiappan, 2022).* Producers and decision-makers will be able to evaluate and protect the agricultural sector. They will also be able to fight climate change and improve production with these tools. Through the integration of Internet of Things (IoT), it is expected that farmers can minimize crop failure and increase the quantity and quality of production by measuring environmental conditions on agricultural land by empowering precision agriculture which hopes to optimize, for example, irrigation techniques that are efficient, targeted and have nutrient levels that are in accordance with the needs of plants or feeding that adjusts to the age of livestock and their nutritional needs *(Bodirsky et al., 2022; Pachayappan, Ganeshkumar, & Sugundan, 2020)*. The application of IoT enables the development of smart agriculture that has the vision to collect, process and analyze data at the same time, automate various steps of agricultural procedures and allow for the improvement of overall farm operations and management, so that farmers can make more informed and faster decisions *(Trilles, González-Pérez, & Huerta, 2020)*.

One of the most promising ways to use IoT is to add automation and information technology to a greenhouse. This would allow the greenhouse's condition to be constantly monitored and recorded. The goal is to track and analyze data about plant growth, irrigation, environmental conditions, climate changes, and pest infestations. This data can be easily stored on a server and shared through different channels, like social media or websites *(Ardiansah, Bafdal, Bono, Suryadi, & Husnuzhan, 2021)*. To do this, the IoT application needs to have a constant internet connection in the greenhouse, use microcontrollers and sensors to replace human senses, and record data in real time so that it can be used for further development *(Gondchawar & Kawitkar, 2016)*. Using a greenhouse gives you the chance to control all of the things that affect how plants grow, both

by hand and automatically. Automated control can change things like temperature, humidity, air flow, how much light a plant gets, how much food and water it gets, and even the quality of the water *(Bhosure, Bhosure, & Sharma, 2016; Khoa, Man, Nguyen, Nguyen, & Nam, 2019).* Through automation, the data that is collected and stored can be used to predict future trends. This lets the automation device figure out the best way to proceed based on calculations from the past. For plants to grow better and crop yields to be as high as they can be, Indonesia needs to come up with smart agricultural practices to monitor and control the microclimate inside greenhouses and to control the quality of irrigation water before it is delivered *(Bersani, Ruggiero, Sacile, Soussi, & Zero, 2022)*. Because there isn't a good way to monitor and control the water quality in greenhouses, plants get water that hasn't been cleaned. So, the goal of this study is to come up with and implement an automated system that uses the Internet of Things to check and control the quality of irrigation water before it is given to plants in greenhouses.

MATERIALS AND METHODS

When it comes to measuring water, keeping the temperature stable is the most important thing because of how it affects pH and DO measurements. In this situation, the waterproof DS18B20 sensor stands out as a very reliable way to measure the temperature of water. The error rate of this high-tech sensor is well below 2%, which is a very good thing *(Agustin et al., 2022)*. It is especially impressive how accurate it is at normal temperatures. The DS18B20 temperature sensor has a digital sensor with a sophisticated silicon-based internal circuit. It also has a temperature sensor, an analog-to-digital converter, and a place to store data. Because of these technical details, the sensor can do complicated calculations and give accurate readings in the form of actual water temperature values. A pH sensor is used to measure the amount of acidity in water. Its main jobs are to keep an eye on the quality of the water and help aquatic organisms grow. A pH meter's main job, based on a comparison to pure water with a neutral pH, is to measure the amount of hydrogen ions in a solution. On a scale from 0 to 14, the pH value shows how acidic or alkaline something is, with 0 meaning very acidic and 14 meaning very alkaline *(Egbueri, Mgbenu, Digwo, & Nnyigide, 2021)*.

In order to foster optimal growth, nutrient concentration and pH levels must be harmoniously balanced and remain stable over a duration of time, ensuring that the plant consistently receives the requisite amount of nutrients *(Selim, 2021)*. In hydroponic systems, the amount of nutrients in the water decreases over time as the roots use up the nutrients in the water. One such method of measuring nutrients involves gauging PPM (Part per million) or TDS (total dissolved solid), which can be achieved using a Gravity TDS meter. In this instance, the measurement hinges on the electroconductivity of the solution and the calibration of the device *(Hasan, Khandaker, Iqbal, & Kabir, 2020)*. The turbidity is used to measure the level of turbidity in water by looking at how the water looks. It works by measuring the amount of light between two probes and figuring out how much light was picked up by the reader probe. When the light hits particles that are floating in the water, it spreads out, which changes the intensity reading. So, the output voltage of the sensor changes based on how cloudy the water *is (Rafid, Redwan, Abrar, Ahmed, & Pathik, 2019)*.

Methodology

The inputs of the device are measured water quality values from sensors at the top of the tank. The monitoring function of the device is turned on when the water level in the tank reaches a certain level. During the mixing of the solution, the device checks to see if the results of the measurements are still within or outside the pre-set threshold. In the end, the output is used to check the quality of the monitored water by adding the solution until the values match the set point. An Arduino UNO is used to carry out these three steps. The Raspberry Pi SBC also acts as a server that controls the data sent by the microcontroller. This lets users access the monitoring and control data for water quality. The program algorithm starts when water is put into the storage tank and stops when the water reaches a certain level. At that point, the sensor system takes readings to see if the set point has been met or if more treatment is needed. If more treatment is needed, the water is moved to the next storage tank so that the quality can be changed until the water meets the set point. When the TDS value is less than 1000 ppm, an AB Mix solution is added to reach the required TDS value *(Setyawan, Nugrohoa, Febyana, & Pramono, 2022)*. When the pH level is outside of the range of 5.5 to 6.5, an alternative solution is used for the best control *(Ardiansah, Bafdal, Bono, Suryad, & Nurhasanah, 2022)*. As soon as the water quality is good enough for greenhouse plants, it is let out until the storage tank is empty.

The used equipment has a data management server, an automation process device, and four different sensors, including the TDS and EC Sensor (Gravity TDS Meter 1.0), pH Sensor (pH-4502C), Water temperature sensor (DS18B20), and Turbidity sensor. In addition to these, a relay unit is incorporated as a

switch, to enable activation or deactivation of the DC motor. The DC motor's primary purpose is to energize the AB Mix solution pump and pH solution. It is important to use a relay because the motor needs a 12v voltage from an extra DC power source to move. When a reading from the TDS sensor or pH sensor doesn't match the set point, the relay gets turned on. This turns on the DC motor connected to the peristaltic pump, which mixes the control solution with the water to reach the set point. Through a serial port, the automation system device connects to the SBC, which acts as a server, and sends water quality monitoring results, the status of the automation system, and the processing time.

Design

The Single Board Computer (SBC) works as a server because it has multiple ways to connect to a communication network. It can connect to a Local Area Network (LAN) using RJ45 or LAN cables, or it can connect wirelessly using WiFi or Bluetooth, giving users a variety of ways to get to their data. MicroSD-based storage media can be used by automation systems to handle large amounts of data in an efficient way.

The TDS and pH sensors used in the experiment can only have analog pins, so they have to be hooked up to a microcontroller. If both sensors are turned on at the same time, there might not be enough DC power, which could cause inaccurate data readings. This lack of power can also happen when the relay is turned on. Since the peristaltic pumps need a voltage of 12V, the relay used cannot make them work. To solve this problem, a step-up converter is built into the system to connect the switching relays to the voltage supply for the pump. With this setup, the pump can move the AB Mix solution and the pH solution into the storage tank.

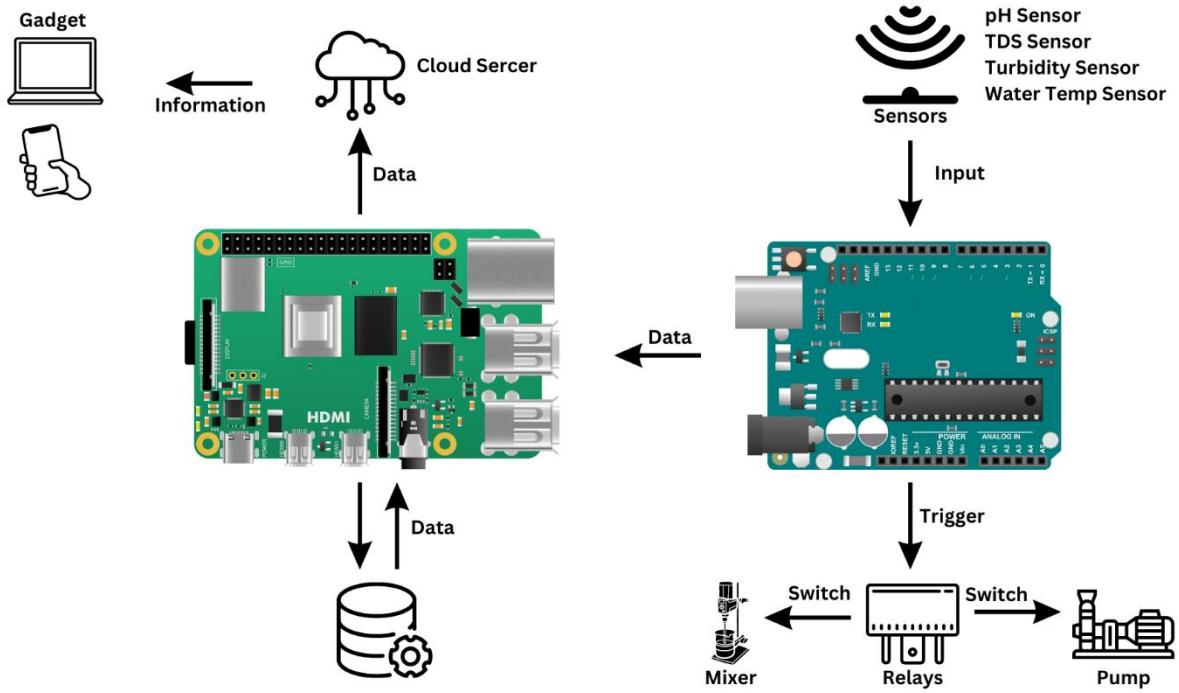


Fig. 1 - Water quality monitoring and control automation system architecture

Design shown in Figure 1 is used to build the water quality automation system. This involves changing the design of the nutrient solution reservoir that is already available in the Unpad ALG Greenhouse. This is done by moving the reservoir lower so that water from the main source of water storage can flow into the system storage tank. On the side of the storage tank are the microcontroller, SBC, and all of the sensors and parts that go with them. Since the two are connected by a USB cable, they are close to each other. The sensor probe, which is used to measure water quality, is in the storage tank. When the water in the tank stops moving, the probe automatically takes measurements. The peristaltic pump, which is an actuator, is placed close to the relay so that it can be fixed faster if there is a problem with how the two are connected. The data about the water quality will be sent through a serial connection in the form of an array. The SBC will receive the data and translate it before putting it in the database. As soon as the data shows that the water is no longer of the right quality, the microcontroller will change the pH and TDS values of the water. The control system will work every six hours. First, water will flow into the storage tank. Then, the water will be checked to make sure it's at the right quality level before it's used for irrigation.

The amount of data that comes out of each iteration depends on the initial measurement of water quality. The bigger the difference between the measurement and the set value, the more procedures are run, which means more data is sent to the database and stored there. In this research, the TDS and pH levels of the water are the most important data points. Other data points, such as temperature and turbidity, add to and strengthen the monitoring results. The pump is set up to dispense the AB Mix, pH Up, or pH Down solutions depending on what is needed. When the set value is reached, the microcontroller tells the relay to change its state, which stops the pump from working. Since the pH sensor used in this study is analog and sends the pH value as a voltage between 0 and 5v, but the pH value is between 0 (extreme acidity) and 14 (extreme alkalinity), it is important to convert the voltage readings sent by the sensor into pH units to make sure the SBC gets the right values *(Mwemezi & Sam, 2019)*. Table 1 shows the algorithm that is used for the conversion process.

Table 1

Pseudocode for checking water ph value

```
load ph library
connect to ph sensor
if (serial port) ≠ ready
 recheck
end if

while (true)
 while (samples <= 10)
  read bitvalue from water
 end while

 voltage = 5 / (1024.0 * (bitvalue/samples))
 ph = -5.7 * voltage + 22.74

 if (pH < 5.5)
  pHUp Pump ON
 else if (pH > 6.5)
  pHDown Pump ON
 else
  pHUP Pump OFF
  phDown Pump OFF
 end if
 read DHT11 humidity in Percent

 send pH data using serial connection
 delay for 60 seconds before continue reading
end while
```

The nutrient content has to be controlled over and over again, just like the pH level, until the TDS value goes over 1000ppm. Before turning on the TDS sensor, all relays must be turned off to make sure that the measurements are accurate and that the data sent to the database isn't messed up. One sign of a drop in voltage is that the indicator light on the automation system is not as bright as it should be.

Table 2

Pseudocode of Nutrient Addition in Water

```
load tds library
get datetime now

if (serial port) ≠ ready
 recheck
end if

while (true)
 water_level = duration * (0.034 / 2)
 if (water_level < 15)
  water pump ON
 else if (water_level > 15)
  water pump OFF
 end if

 get water temp
 get voltage
```

```
tds = (voltage – 55) / 1.75
ec = tds – 500

if (tds < 1000)
 nutrition pump on
 stir water ON
else
 nutrition pump off
 stir water OFF
end if
```

Table 2 shows how the AB Mix nutrient solution is used to control the amount of nutrients in the water reservoir. When the TDS value is different from the set point, the automation system will turn on both nutrient solution pumps A and B. Once the flow of nutrient solution is done, the automation system will turn off the relay connected to the nutrient pump and turn on the relay connected to the DC Fan for 1 minute. This will make sure that the AB Mix nutrient solution and the water in the reservoir are thoroughly mixed. To connect the relay to the DC Fan, which runs on a voltage of 12v, you need a 12v voltage adapter. Also, the water quality monitoring and control automation system can collect sensor data like pH, TDS, water temperature, turbidity, and monitoring time. By adding the Real Time Clock (RTC) module, the automation system can get measurement time data, which makes it easier to plan when to supply water. Adding the RTC module to the automation system gives it an extra benefit, making it better for controlling when water is supplied.

Construction

The microcontroller sends data to the serial port in the form of an array, which is easy for the application to understand and decode. This includes readings of the water tank level, TDS value regulation (if the value is outside the set-point), pH value regulation (if the value is outside the set-point), and a final reading when all stages are finished. The reason for sending data one at a time is to speed up the process of reading data from the microcontroller and entering it into the right database column. Through the serial port, the data is sent in this order: Water Temperature, TDS, EC, pH, and Turbidity. If the water meets the parameters that have been set, it goes to the plant. If it doesn't, it goes to a secondary storage tank for more testing. If the TDS value is wrong, the AB Mix solution pump starts working. If the pH value is wrong, either the pH Up or pH Down pump starts working. If the TDS and pH values don't match the set points, the system will first turn on the AB Mix solution pump until the values match, and then it will turn on the pH solution pump. A 12v DC Fan is built in to make sure that the added solution and the water in the storage tank mix evenly. Once the mixing is done, the system will use the sensor to take another reading of the TDS and pH levels of the water to see if they match the set-points. If the set points don't match up with the parameters, the control process will start over and end with the last reading.

RESULTS AND DISCUSSIONS

Study by *(Soerya, Bafdal, & Kendarto, 2020)* on how rainwater fertigation technology and hydroponics can be used in a greenhouse, a system has been made to monitor and control the quality of irrigation water. The study showed that watering tomato plants with rainwater can lead to a harvest weight of 2.45 KG per plant, with 19.01 liters of water used and an impressive efficiency of 94.07 KG/m^3. These results show that crop yields could be increased by making sure that the quality of the water matches the needs of the plant *(Shah & Wu, 2019)*.

Evaluation of TDS Sensors

In the experiment, the TDS sensor was put through ten tests with different TDS values. The TDS sensor was used to measure the TDS value of the water. Then, the results from the TDS-3 Handheld Meter, a measuring device with an accuracy of 2.00%, were compared to those from the TDS sensor. The datasheet for the TDS Gravity sensor says that the maximum reading is 1000ppm, but during testing, the TDS sensor was able to measure TDS values of up to about 1200ppm. When compared to the measuring instrument, the TDS values from the sensor were wrong for measurements above 1200ppm. Table 3 shows the test results for the TDS sensor, which had a measurement error of 5.02% when compared to the measuring tool. From these results, we can conclude that the TDS sensor is a reliable and accurate way to measure the TDS value in this research. In ten tests, the difference between measurements was only 70.00ppm, and the average error was 30.30ppm. This shows that the sensor works well, as it is on par with the TDS-3 Handheld Meter, a measuring device made specifically for measuring TDS values in water.

Table 3

Testing results of TDS sensor

No	TDS meter	TDS Sensor	Difference	Percentage Error
1	324.00	304.00	20.00	6.10%
2	414.00	380.00	34.00	8.20%
3	482.00	452.00	30.00	6.10%
4	536.00	536.00	0.00	0.00%
5	579.00	605.00	26.00	4.40%
7	650.00	715.00	65.00	10.00%
8	721.00	791.00	70.00	9.40%
9	936.00	986.00	50.00	5.30%
10	1020.00	1028.00	8.00	0.70%
		Mean	30.30	5.02%

During the evaluation process, the same steps are used to automatically measure TDS levels. First, a peristaltic pump moves water into the holding tank until it's full. Then, a TDS sensor and instrument are used to measure how much TDS is in the water. After the initial readings are taken, the AB Mix solution is poured into the water reservoir and stirred well. This process of mixing and stirring is done nine times, and after each time, the TDS level is measured again.

Putting the pH Monitor to the Test

The pH sensor goes through a similar process in which the measurement results are looked at ten times with different pH values. The pH-009i Handheld Meter, which has an accuracy of 0.1, is used to compare the pH4502c sensor with the pH-009i Handheld Meter. Even though litmus paper is an alternative way to test, it is not very accurate at 1. The datasheet says that the pH4502c sensor has a level of accuracy of 0.50. By looking at the test results in Table 4, we can see that the pH sensor can give accurate measurements with a measurement error of only 4% when compared to the measuring instrument. This proves that it could be used in this study. Also, the difference between the ten tests was no more than 0.41, and the average measurement error was 0.25. This shows that the pH sensor's performance is very close to that of the pH-009i Handheld Meter, which is used to measure the pH of water.

Table 4

Testing results of pH sensor

No	pH meter	pH4502C Sensor	Difference	Percentage Error
1	7.2	7.39	0.19	2.60%
2	7.1	6.85	0.25	3.50%
3	4.2	4.03	0.17	4.00%
4	4.5	4.09	0.41	9.10%
5	8.1	7.84	0.26	3.20%
7	8.2	8.57	0.37	4.50%
8	8	7.93	0.07	0.90%
9	7	7.28	0.28	4.00%
10	6.7	6.42	0.28	4.20%
		Mean	0.25	4.00%

In the evaluation process, the same method is used over and over to automatically measure the pH level of the storage tank. A peristaltic pump fills the tank with water until it is full, and then a pH sensor and measuring device are used to measure the pH. After the measurements are written down, the pH Up or pH Down solution is added to the water tank and the water is stirred very hard nine times to make sure it is all the same. After that, pH values are measured again.

Irrigation Water Quality Monitoring Automation Data: A Descriptive Statistical Study

The effectiveness of an automation system can be judged by how well it can control a number of parameters, such as the TDS and pH values of water, based on pre-set points. The monitoring and control automation system for water quality was built, and its performance was measured over the course of a month.

Every six hours, data was collected and put in a database so that it could be used later for statistical analysis. Also, descriptive statistical analysis was done on the data collected about the quality of the water when it went into the tank. The results are shown in Table 5.

Table 5

Descriptive statistics when water enters the tank

	Temperature	TDS	EC	pH
Total	3209.00	49937.00	23.00	807.72
Mean	27.15	423.15	0.20	6.84
Median	27.00	398.00	0.00	6.72
Modus	27.00	409.00	0.00	6.48
STDev	0.82	212.22	0.52	0.68
Max	29.00	1662.00	3.00	10.44
Min	25.00	103.00	0.00	5.03
Range	4.00	1559.00	3.00	5.41

Table 5 shows that when water is put into the tank, the average TDS value is 423.15 ppm, which is not enough to meet the plant's requirement of 1000ppm, and the standard deviation is 212.22. This means that the water's electrical conductivity and TDS level aren't good enough, so AB Mix liquid fertilizer needs to be used to raise the TDS level. On the other hand, the average pH value of the water going into the tank was found to be 6.84 0.68. This means that the pH level is still higher than the expected range of 5.50 to 6.50. As a result, the pH Down pump runs more often than the pH Up pump. Still, as the table shows, the pH value of 6.48 is the one that is seen most of the time.

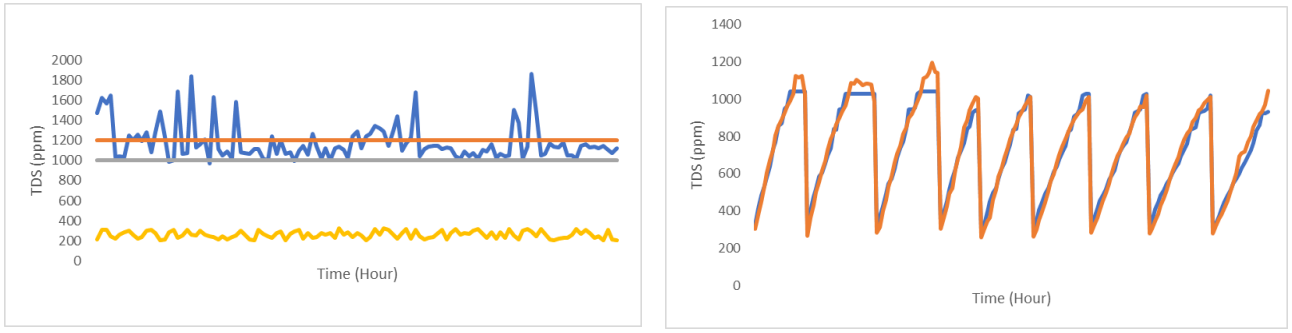
Based on the calculations shown in Table 6, descriptive statistics were used to look at the TDS and pH levels after the automation system had finished controlling them. The average TDS value of 1181.30 183.68 ppm is higher than the goal of 1000 ppm, so the expected goal was met. But because several sensors were being used at the same time and there were problems with the power supply, the maximum TDS value of 1870.00ppm was reached, which caused sensor readings to be wrong. This problem could be solved by connecting only one sensor to the microcontroller, which would eliminate worries about running out of power. Regarding the pH control, the average value of 6.17 0.30 shows that the pH control did not produce the expected results. This could be due to a less-than-ideal pH solution, an uneven mix of water and pH solution, or the effect of the AB Mix solution on the pH value. In the future, research will be done to find out what effect AB Mix solution has on pH. Also, the maximum pH value of 7.21 is lower than the value of 10.44 that was seen when water was put into the tank. This shows that the pH solution can lower pH, but has not yet reached the set point of 5.5 to 6.5.

Table 6

Descriptive statistics when control is complete

	Temperature	TDS	EC	pH
Total	3180.00	138211.00	238.00	722.44
Mean	27.18	1181.30	2.03	6.17
Median	27.00	1127.00	2.00	6.18
Modus	27.00	1046.00	2.00	6.12
STDev	0.79	183.68	0.29	0.30
Max	29.00	1870.00	3.00	7.21
Min	25.00	973.00	1.00	5.11
Range	4.00	897.00	2.00	2.10

Based on all of the TDS measurement data, the results show that the automation system is able to raise the TDS value until it reaches the set point of 1000 ppm. The automated system for adding nutrients has shown that it can raise the levels of nutrients up to the limit that was set. It's important to remember that the 1000ppm threshold was set based on the sensor's ability to measure TDS, which can only read up to 1000ppm with a 10% tolerance, according to the datasheet for the sensor. But a look at the sensor reading after the experiment has shown that it has reached 1100ppm. Figure 2a shows that out of the 118 processes that were run, 36 had measurement values that were higher than 1200ppm. This shows that the automation system is good at measuring and controlling the TDS and pH of water. But it's important to know that high-value spikes can happen because of sensor interference, like a drop in voltage or dirty sensors.

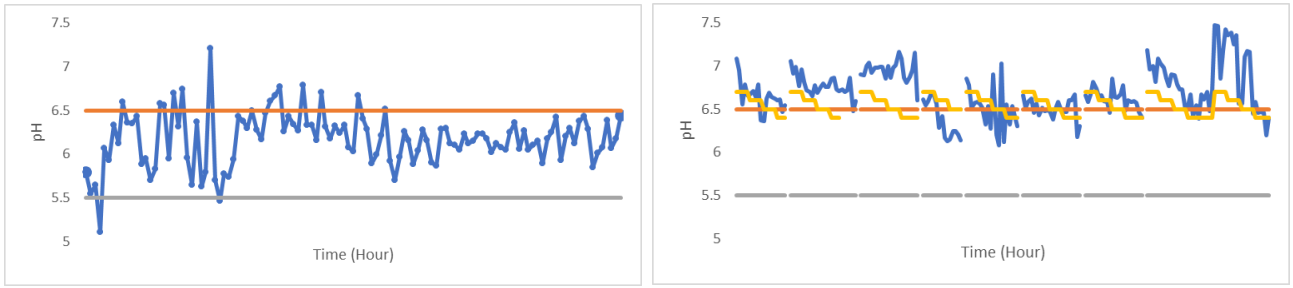


(a) (b)

Fig. 2 – (a) Results of TDS control automation (b) Movement of TDS value from flow to process completion

Figure 2a shows that there was a sharp surge in the measurements results, with a worrying high of 1800ppm. Such wrong readings shouldn't have happened, but our thorough analysis has found several reasons why they did: (1) Sensor readings that change like the voltage, (2) Errors caused by loosely connected jumper cables that lead to intermittent power supply and, as a result, less accurate measurements, and (3) DC fans that don't work right and don't mix the solution well, which leads to inaccurate readings of TDS and pH values. It is important to remember that if you don't mix the AB Mix nutrient solution with water well enough, the solution can settle in the water, which causes the TDS values of the next nutrients to be high.

Figure 2b portrays the automation process of infusing AB Mix nutrients and gauging the TDS value, commencing from the water's entry into the system until the culmination of the control process. The precision of the TDS sensor measurements is demonstrated through a comparison with data collected from the TDS-3 Handheld Meter, encompassing the period from water entry into the storage tank to the completion of the control process. A peristaltic pump flows AB Mix nutrient solution for a trifling three seconds, after which a DC Fan blends the solution homogeneously. The ensuing measurements are methodically translated into a graph showcasing the meticulous course of AB Mix nutrient solution infusion, culminating at the desirable 1000ppm concentration, with the concurrent pH control process concluding after a 12-minute runtime.



(a) (b)

Fig. 3 – (a) Results of pH control automation (b) Movement of pH value from flow to process completion

Figure 3a depicts the procedural steps taken post the completion of water pH control. As the AB Mix nutrient solution is gradually introduced, the pH measurement records a corresponding decline. In the event that the water pH falls beyond the predetermined set-point, the pH Down pump is initiated to initiate the water pH control procedure. Although the pH sensor probe is capable of determining the acidity of the water, it necessitates calibration before use. Upon conducting several experiments, a pH value of 6.70 is recorded for the water in the holding tank using a Handheld Meter pH measuring device, which decreases to 6.40 after the incorporation of AB Mix nutrient solution.

Graph at Figure 3b does a good job of showing the changes that happen during the control process. This happens because the pH sensor reading is messed up when the TDS sensor is working at the same time. Along with interference from the TDS sensor, changes in pH values can be caused by: 1) Probes that get dirty over time, 2) putting a pH probe next to a TDS sensor, which causes a voltage drop in the pH sensor, 3) putting pH probes above the surface of the water while measuring, and 4) other things *(Rastegari et al., 2023).*

CONCLUSIONS

The findings of this study led the researchers to the conclusion that the instrument that was developed has the capability of automatically reading water quality and updating data on a database. This data includes information on parameters such as temperature, total dissolved solids (TDS), electrical conductivity (EC), pH, and turbidity, as well as the process that was carried out. The automation device for adjusting TDS and pH can function based on predetermined setpoints if those points are used. With an average TDS result of 1162.86 ppm and an average pH value of 6.174 when the process is complete, the nutrient pump will turn on automatically when the TDS value drops below 1000 ppm, and the pH balancing pump will turn on when the pH rises above 6.5. In total, the process will produce an average TDS result of 1162.86 ppm and an average pH value of 6.174.

ACKNOWLEDGEMENT

We would like to take this opportunity to thank the Rector of Universitas Padjadjaran, the Directorate of Research and Community Service, and the Directorate of Finance and Treasury of Universitas Padjadjaran for granting me the chance to receive a scholarship and carry out research as part of the Unpad Doctoral Dissertation Research scheme with contract number 1595/UN6.3.1/PT.00/2021. I am extremely grateful for this opportunity.

REFERENCES

[1] Agustin, M., Zain, A. R., Soelaiman, N. F., Oktivasari, P., Bohan, J. R., Karim, M. A., … Fahroji, M. F. (2022). The Aquarium Monitoring System Design and Prototype for Ornamental Fish Farmers using NodeMCU with Telegram Data Notifications. In *2022 5th International Conference of Computer and Informatics Engineering (IC2IE)* (pp. 162–166). IEEE.

[2] Ardiansah, I., Bafdal, N., Bono, A., Suryad, E., & Nurhasanah, S. (2022). An overview of IoT based intelligent irrigation systems for greenhouse: Recent trends and challenges. *Journal of Applied Engineering Science*, *20*(3), 657–672. https://doi.org/10.5937/jaes0-35224

[3] Ardiansah, I., Bafdal, N., Bono, A., Suryadi, E., & Husnuzhan, R. (2021). Impact Of Ventilations In Electronic Device Shield On Micro-climate Data Acquired In A Tropical Greenhouse. *INMATEH - Agricultural Engineering*, *63*(1), 397–404. https://doi.org/10.35633/INMATEH-63-40

[4] Bersani, C., Ruggiero, C., Sacile, R., Soussi, A., & Zero, E. (2022). Internet of Things Approaches for Monitoring and Control of Smart Greenhouses in Industry 4.0. *Energies*, *15*(10), 3834.

[5] Bhosure, A., Bhosure, M., & Sharma, R. (2016). Web Based Greenhouse Environment Monitoring and Controlling System using Arduino Platform. *International Journal of Scientific Engineering and Applied Science*, 22, 2395–3470. Retrieved from www.ijseas.com

[6] Bodirsky, B. L., Chen, D. M.-C., Weindl, I., Soergel, B., Beier, F., Molina Bacca, E. J., … Lotze-Campen, H. (2022). Integrating degrowth and efficiency perspectives enables an emission-neutral food system by 2100. *Nature Food*, *3*(5), 341–348.

[7] Egbueri, J. C., Mgbenu, C. N., Digwo, D. C., & Nnyigide, C. S. (2021). A multi-criteria water quality evaluation for human consumption, irrigation and industrial purposes in Umunya area, southeastern Nigeria. *International Journal of Environmental Analytical Chemistry*, 1–25.

[8] Gondchawar, N., & Kawitkar, R. S. (2016). IoT based Smart Agriculture. *International Journal of Advanced Research in Computer and Communication Engineering*, *5*(6), 838–842. https://doi.org/10.17148/IJARCCE.2016.56188

[9] Hasan, M. S., Khandaker, S., Iqbal, M. S., & Kabir, M. M. (2020). A real-time smart wastewater monitoring system using IoT: Perspective of Bangladesh. In *2020 2nd International Conference on Sustainable Technologies for Industry 4.0 (STI)* (pp. 1–6). IEEE.

[10] Khoa, T. A., Man, M. M., Nguyen, T. Y., Nguyen, V. D., & Nam, N. H. (2019). Smart agriculture using IoT multi-sensors: A novel watering management system. *Journal of Sensor and Actuator Networks*, *8*(3). https://doi.org/10.3390/jsan8030045

[11] Mwemezi, K., & Sam, A. (2019). Development of innovative secured remote sensor water quality monitoring & management system: case of Pangani water basin.

[12] Pachayappan, M., Ganeshkumar, C., & Sugundan, N. (2020). Technological implication and its impact in agricultural sector: An IoT Based Collaboration framework. *Procedia Computer Science*, *171*, 1166–1173.

[13] Rafid, S., Redwan, F., Abrar, A. H., Ahmed, S. N. U., & Pathik, B. B. (2019). Water Quality Monitoring System: A Sustainable Design. In *2019 6th International Conference on Signal Processing and Integrated Networks (SPIN)* (pp. 414–419). IEEE.

[14] Raj, E. F. I., Appadurai, M., & Athiappan, K. (2022). Precision farming in modern agriculture. In *Smart Agriculture Automation Using Advanced Technologies: Data Analytics and Machine Learning, Cloud Architecture, Automation and IoT* (pp. 61–87). Springer.

[15] Rastegari, H., Nadi, F., Lam, S. S., Abdullah, M. I., Kasan, N. A., Rahmat, R. F., & Mahari, W. A. W. (2023). Internet of Things in aquaculture: A review of the challenges and potential solutions based on current and future trends. *Smart Agricultural Technology*, 100187.

[16] Selim, M. M. (2021). Introduction to the integrated nutrient management strategies, and contribution on yield and soil properties. *Journal of Plant Sciences*, *9*(4), 139–150.

[17] Setyawan, T. A., Nugrohoa, A. R. I. S., Febyana, A., & Pramono, S. (2022). Multiple linear regression method used to control nutrient solution on hydroponic cultivation. *Journal of Engineering Science and Technology*, *17*(5), 3460–3474.

[18] Shah, F., & Wu, W. (2019). Soil and crop management strategies to ensure higher crop productivity within sustainable environments. *Sustainability*, *11*(5), 1485.

[19] Soerya, S. F., Bafdal, N., & Kendarto, D. R. (2020). Kajian Kualitas Air Hujan dan NPK Budidaya Tomat (Mill. var. pyriforme) Apel dengan Cocopeat dan Kompos. *Jurnal Keteknikan Pertanian Tropis Dan Biosistem*, *8*(2), 135–142. https://doi.org/10.21776/ub.jkptb.2020.008.02.03

[20] Trilles, S., González-Pérez, A., & Huerta, J. (2020). An IoT platform based on microservices and serverless paradigms for smart farming purposes. *Sensors*, *20*(8), 2418.

AGRICULTURAL PLATFORM EQUIPPED WITH A HYDROSTATIC TRANSMISSION CAPABLE OF CONTINUOUSLY ADJUSTABLE TRAVEL VELOCITY AND NON-LINEAR DISTURBANCE COMPENSATION CAPABILITIES
/
PLATFORMĂ AGRICOLĂ DOTATĂ CU O TRANSMISIE HIDROSTATICĂ CAPABILĂ SĂ REALIZEZE VITEZE DE DEPLASARE CONTINUU VARIABILE ȘI CAPABILITĂȚI DE COMPENSARE A PERTURBAȚIILOR NELINIARE

Alexandru-Polifron CHIRIȚĂ*[1),2)] [1]; Cristian PAVEL[2)]
[1)] INOE 2000 - Subsidiary Hydraulics and Pneumatics Research Institute / Romania;
[2)] Faculty of Mechanical Engineering and Robotics in Construction, Technical University of Civil Engineering Bucharest / Romania
** E-mail: chirita.ihp@fluidas.ro*
DOI: https://doi.org/10.35633/inmateh-69-40

Keywords: *precision agriculture platform, continuously variable velocity, feedforward*

ABSTRACT
Both in the case of precision agriculture and in the case of some agricultural works, in which the technological process is dependent on the velocity of displacement of the platform carrying the agricultural equipment, it is necessary to precisely adjust or even continuously adjust the velocity of displacement. This article presents the capabilities of continuously regulating the travel velocity of an agricultural platform equipped with a hydrostatic transmission and a PID controller with feedback, feedforward, as well as nonlinear disturbance compensation capabilities; such a platform can be fitted with various agricultural equipment.

REZUMAT
Atât în cazul agriculturii de precizie, cât și în cazul unor lucrări agricole în care procesul tehnologic este dependent de viteza de deplasare a platformei purtătoare de echipamente agricole, este necesară reglarea cu precizie sau chiar reglarea continuă a vitezei de deplasare. Acest articol prezintă capabilitățile de reglare continuă a vitezei de deplasare a unei platforme agricole dotată cu o transmisie hidrostatică și un regulator PID cu feedback, feedforward, precum și capabilități de compensare a perturbațiilor neliniare, platformă ce poate fi dotată cu diverse echipamente agricole.

INTRODUCTION

Studies on the mechanics of agricultural machinery, such as tractors, are getting better and better as agricultural modernization and intelligence levels continue to advance *(Cheng and Lu, 2021; Balafoutis et al., 2017)*. Precision agriculture is the use of information and communications technologies to control the spatial and temporal variation in the fields related to the soil, atmosphere, and plants *(Zhang, 2015)*. Agricultural vehicles frequently use hydrostatic transmissions, which are continuously variable transmissions that vary steplessly across an infinite range of effective transmission ratios *(Guo and Hu, 2014; Warring, 2014)*. The power given to the driving wheels from the engine, the tire pressure and the state of the field's terrain all affect the travel velocity, so in order to carry out the whole process in an optimized manner and prevent possible damage to the crops a precise continuously performed velocity control is needed. It is challenging to develop an appropriate mathematical model for this process since it is a complicated, multi-variable, nonlinear, time-varying system.

In their study, *Li et al. (2021)* aimed to design a hydraulic drive system for an orchard conveyor that addresses the issues and complexity of traditional transmission systems. The new system they propose allows for quick reversal, stepless speed regulation, and instantaneous braking. To test the feasibility of this system, they used simulations to mimic the operation of an orchard conveyor under different load states. Another study - *(Hu et al., 2021)* - has proposed a technical solution of a fully hydraulic chassis drive system for tractors in hilly and mountainous areas in order to address the adaptation problem of traditional tractors in these areas. The results show that the motor performance must meet demanding requirements in terms of working pressure, output torque, and output velocity. *Cheng and Lu, (2022),* have developed a hydro-mechanical continuously variable transmission with optimized speed-regulating characteristics for use in precision agriculture with tractors.

[1] *Alexandru-Polifron Chiriță, PhD. Stud. Eng.; Cristian Pavel, Prof. PhD. Eng.*

The transmission uses eight gear pairs, two planetary rows, three wet clutches, a variable-pump and a constant speed motor. *Guo et al., (2013)* developed a GPS-based intelligent operation control system for rice transplanters in order to regulate travel speed in accordance with the prescribed map.

MATERIALS AND METHODS

Since the velocity of displacement of the platforms carrying various agricultural technological equipment is in some cases dependent on the technological process, with the help of the AMESim (**A**dvanced **M**odeling **E**nvironment for performing **Sim**ulations of engineering systems), the dynamic parameters of these platforms have been optimized. Because the technological processes in the agricultural field do not require travel speeds higher than 12 km/h and because it is necessary to continuously adjust the travel velocity to improve productivity or because the technological process requires it, it has been chosen for the agricultural platform to be equipped with a closed-loop hydrostatic transmission, with primary control *(Tecușan and Ionescu, 1982)*.

Fig. 1 shows the simulation network of the agricultural platform equipped with a closed-loop primary regulation hydrostatic transmission. The simulation model shown in Fig. 1 comprises a hydrostatic transmission, a prime mover that can be a thermal engine or an electric one powered by batteries and the agricultural platform with all-wheel drive. The platform tows technological equipment that performs a technological operation simultaneously with the measurement of the travel speed; that travel speed is transmitted to the comparator element of the PID (**P**roportional **I**ntegral **D**erivative) controller with feedback, feedforward and capabilities for compensation of non-linear phenomena.

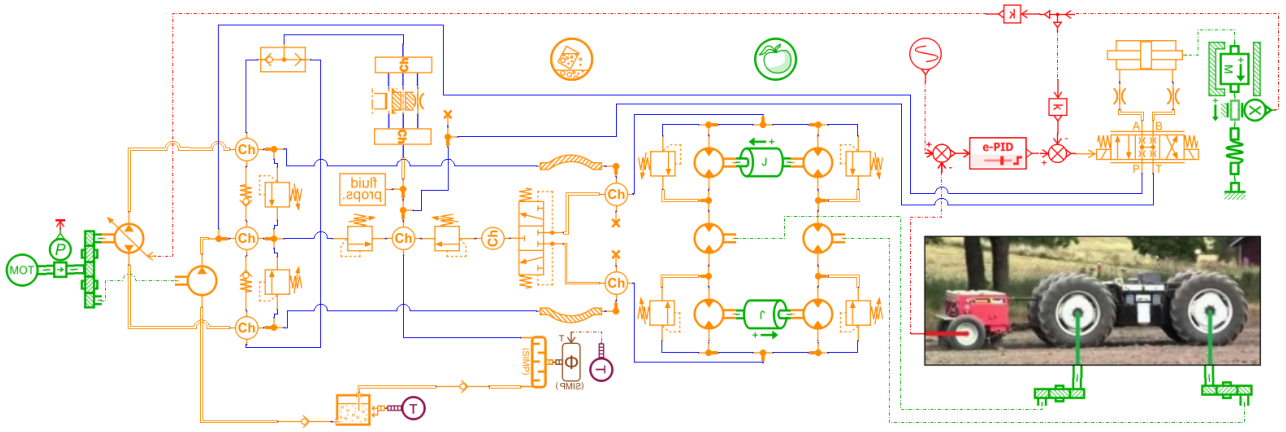


Fig. 1 - The simulation network of the agricultural platform

The hydrostatic transmission is composed of a servo-pump whose main pump has a displacement of 210 cm^3/rev; a compensation pump with a displacement of 32 cm^3/rev; the relief valves acting as safety valves in the closed-loop circuit are set at 350 bar, and the compensation pump relief valve is set at 25 bar; the check valves open at 0.5 bar. The simulation model also takes into account the volumetric losses of the transmission; they are modeled in detail, through three interstices of different shapes and sections because the results should be as close to reality as possible. Also, in the structure of the servo-pump there is the servo-mechanism for regulating the pump displacement; the numerical simulation model of that servo-mechanism has been experimentally validated by *Chiriță and Pavel, (2022)*. As part of the hydrostatic transmission structure, there are also two hydrostatic motors with a displacement of 300 cm^3/rev and a maximum pressure of 450 bar. They are connected to the two axles of the agricultural platform that have the transmission ratio i = 4; since the load on the two motor axles of the platform is 60% (rear) and 40% (front), it was necessary to use flow rate dividers, which divide the flow rate of the servo-pump equally, regardless of the load (torque or pressure); the two flow dividers fulfil the role of a lockable differential; each of these is composed of two hydraulic motors with gears that have a displacement of 52.5 cm^3/rev and two pressure relief valves that have the role of bypassing the motors if the pressure exceeds 300 bar. In close proximity to the hydrostatic motors, there is also connected a flushing valve whose relief valve is set at 20 bar. The numerical simulation model also includes a heat exchanger with a volume of 10 L, which has the role of maintaining the hydraulic fluid at an optimal temperature and viscosity, together with a hydraulic fluid tank model with a volume of 35 L and variable height of fluid level.

All hydraulic components of the transmission, those coloured in orange in the simulation network, take into account the effects of temperature on the hydraulic fluid and hydraulic components.

Fig. 2 presents the parameters of the PID controller for the case of its manual tuning and the linearization of the physical process required for automatic tuning (on the gain curve); in the same figure one can notice that the physical process corresponds to one of a 2nd order system with a 99.5% match and a natural frequency of 4.5 Hz.

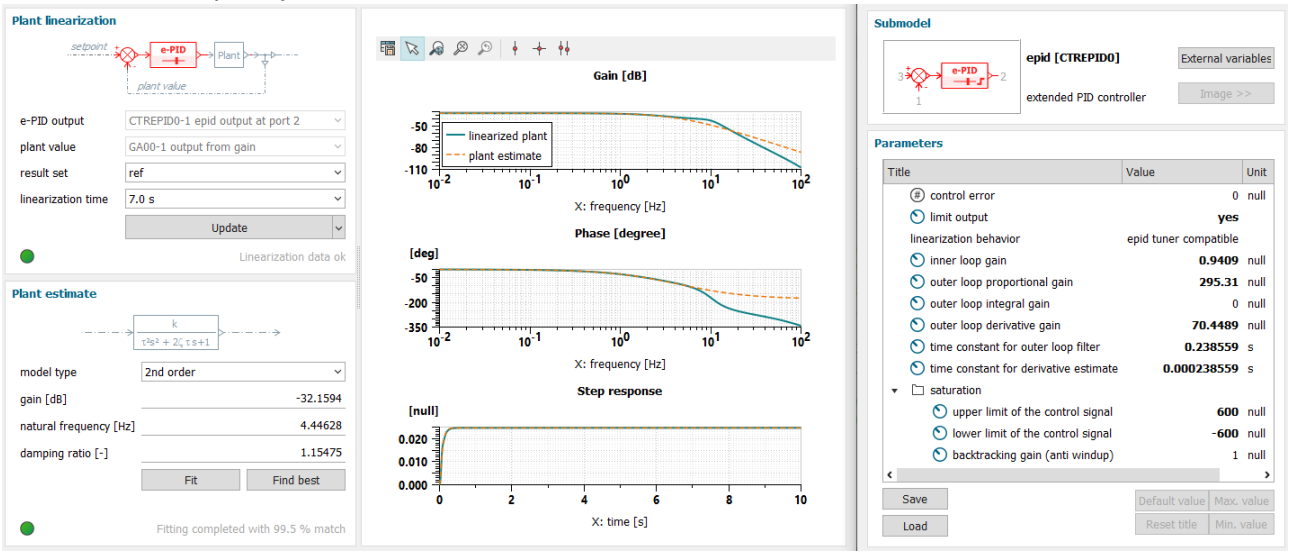


Fig. 2 - Plant linearization for automatic PID controller tuning and controller parameters for manual tuning

Because closed-loop hydrostatic transmissions whose parameters are not well optimized suffer from overheating and the servo-pumps equipping them face premature wearing out due to the cavitation that occurs on the suction port of the pump, an advanced fluid model that takes into account the influence of temperature and advanced laws for cavitation has been used. The fluid parameters can be consulted in Fig. 3 below.

Title	Value	Unit
index of thermal hydraulic fluid	**0**	
fluid type	**advanced**	
cavitation and aeration model	**... cavitation with advanced laws for Pvap(T)**	
reference database	**ISO VG 46 oil - Mobil DTE Medium**	
polytropic index for air/gas vapor content	1.4	null
▸ equation of state parameters		
▸ caloric properties (specific heat or speed of sound)		
▸ liquid viscosity and thermal conductivity		
▾ aeration		
default gas content	0.1	%
aeration/dissolution	constant gas content	
saturation pressure (for dissolved gas)	2500	barA
▾ gas properties		
density of gas	1.2	kg/m**3
absolute viscosity of gas	0.02	cP
constant-pressure specific heat of gas	1004	J/kg/K
thermal conductivity of gas	0.026	W/m/K
▾ cavitation		
filename or expression for high saturated vapor pressure in cavitation[barA] = f(T[degC])	10^(6.20963-2354.731/(280.709+T))+0.02	
filename or expression for low saturated vapor pressure in cavitation[barA] = f(T[degC])	10^(6.20963-2354.731/(280.709+T))	
absolute viscosity of vapor	0.02	cP
effective molecular mass of vapor	200	g/mol
constant-pressure specific heat of vapor	1850	J/kg/K
thermal conductivity of vapor	0.017	W/m/K
▾ fluid temperature computation		
assumption level	full energy balance (thermal-hydraulics)	
▾ reference state definition		
reference state pressure	1.013	barA
reference state temperature	20	degC

Fig. 3 - Parameters of the advanced hydraulic fluid model

RESULTS

Running the numerical simulation model for a 10-second period, in which the agricultural platform moves on rough terrain with a 45% slope (the first 5 seconds for ascending the slope with variable velocity and the other 5 seconds for descending the slope, also with variable velocity), results in the graphs that will be presented below.

The speed of the shaft of the servo-pump together with the time-variation of the resistant torque to the shaft of the same pump and the power consumed by it can be seen in Fig. 4. In the same figure one can see that the speed is constant and has a value of 1000 rev/min for the servo-pump to work with maximum efficiency; the necessary speed and torque can be provided by both a thermal engine or electric motor.

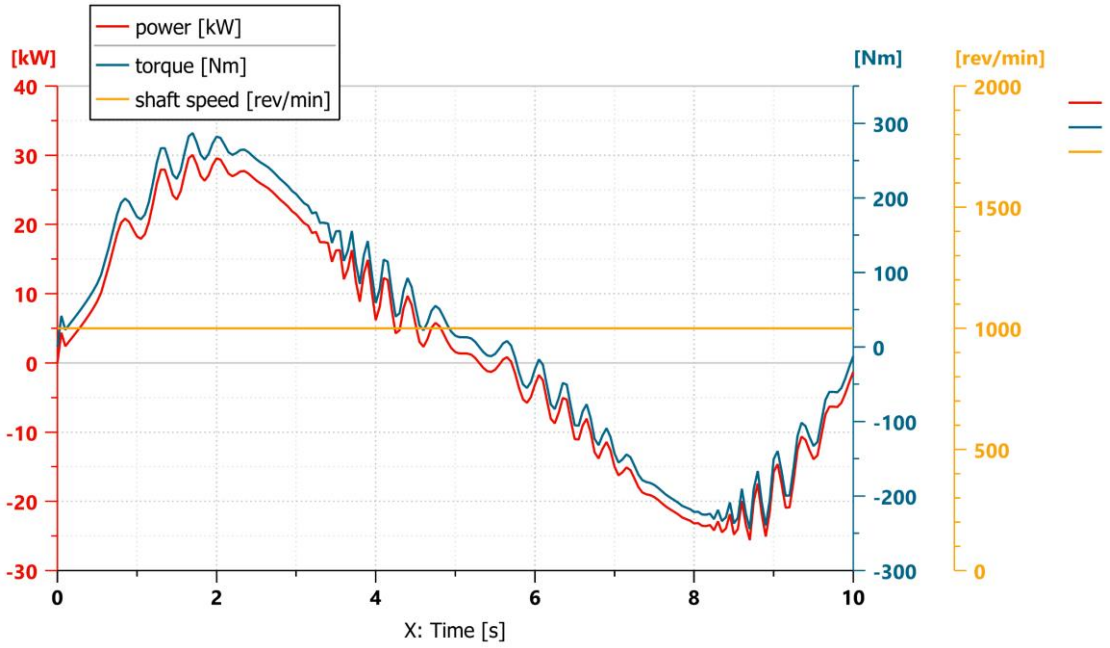


Fig. 4 - The speed, torque and power used by the servo-pump

The time-variation of the pressures on the two sides of the closed-loop hydrostatic transmission and the flow rate of the servo-pump are shown in Fig, 5; on this graph, one can see that the maximum pressure reached on one of the sides has the value of 170 bar, and on the other the pressure does not drop below the value of 20 bar, which means that cavitation does not occur on the pump suction port. The flow rate takes positive and negative values because it is measured at the same port and the sign shows the flow rate direction.

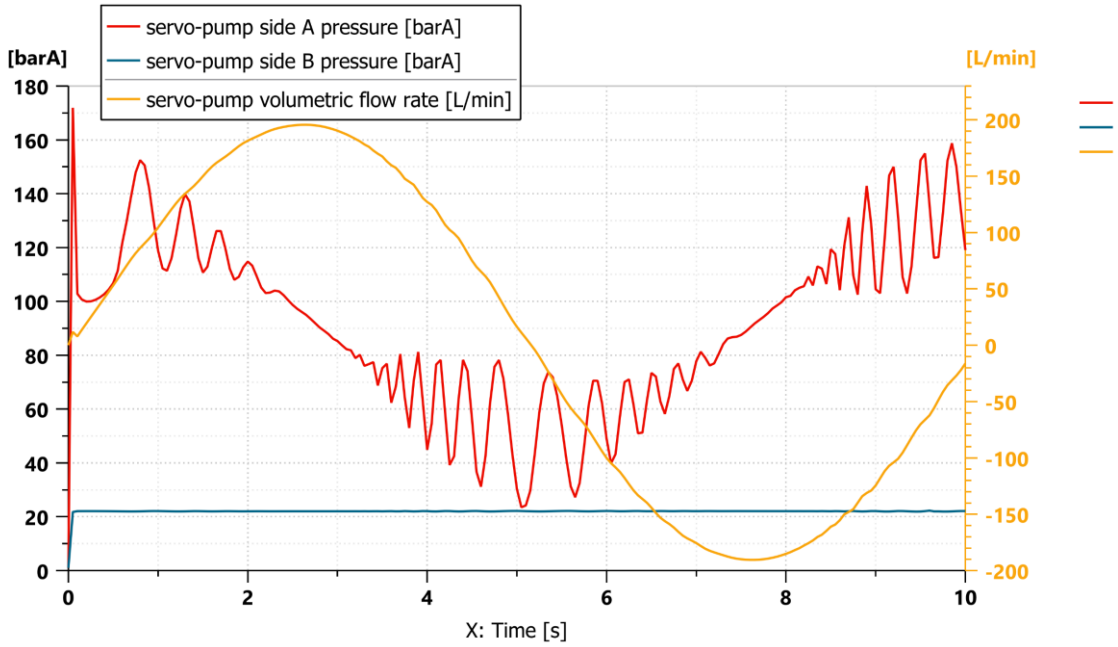


Fig. 5 - The pressures on the two sides of the closed-loop hydrostatic transmission and the flow rate of the servo pump

In the graph in Fig. 6, one can notice the variation over time of the various flow rates that pass through various components of the transmission; among them, the variation over time of the volumetric losses of the transmission can be noticed; those losses are proportional to the pressure in the system. Another curve of interest is that of the flow rate sent to the tank by the flush valve to be cooled and filtered and together with the volumetric losses, these two flow rates must have a value equal to that of the compensation pump that introduces cooled oil on the suction port of the main pump.

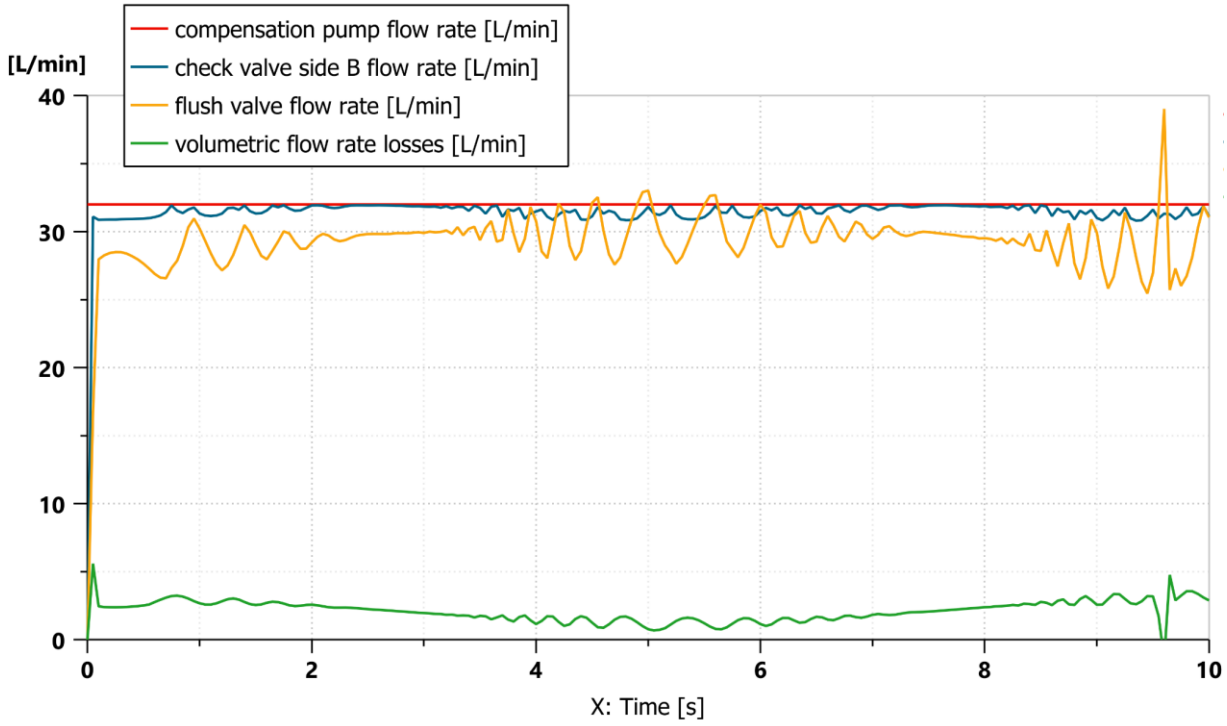


Fig. 6 - The flow rates through various components of the transmission and the amount of volumetric losses of the transmission

Fig. 7 shows the time-variation of hydraulic fluid parameters such as temperature, kinematic viscosity and undissolved gases.

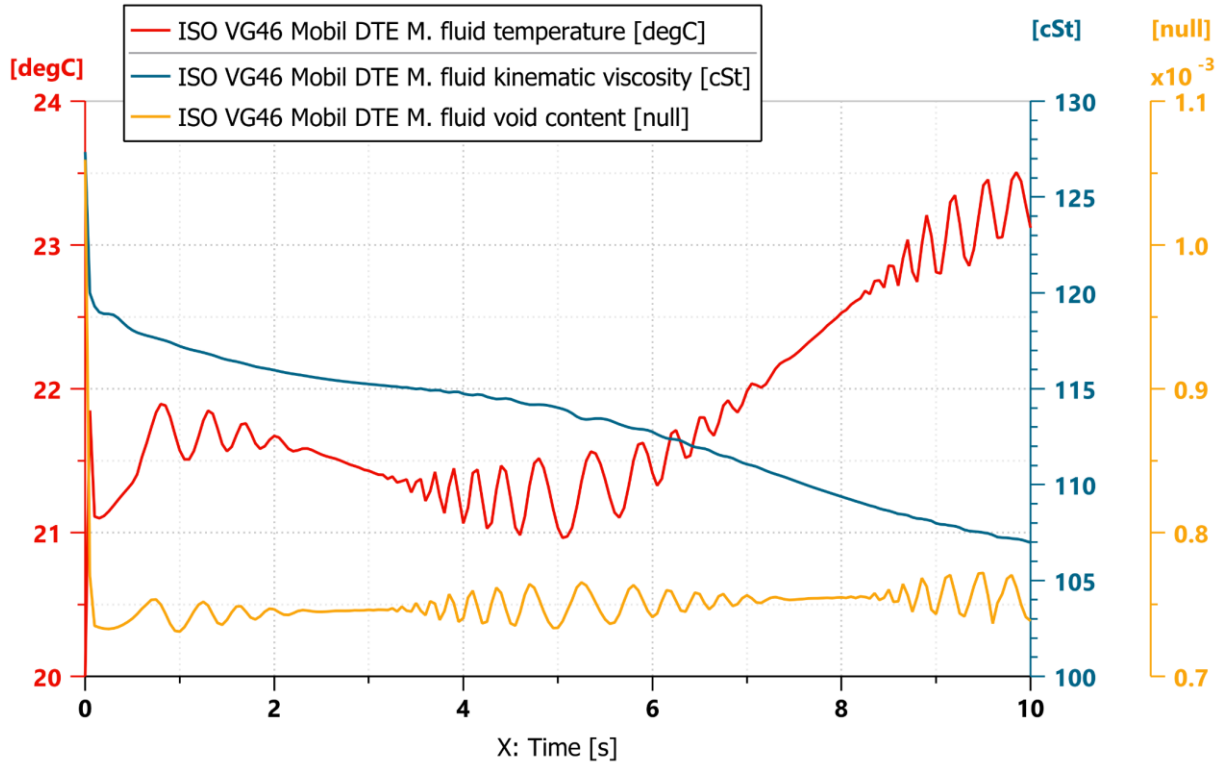


Fig. 7 - Hydraulic fluid parameters

In Fig. 8 one can see the time-variation of the flow rates and pressures at the ports of the two hydrostatic motors; in the same figure one can see how the flow divider divides the flow equally regardless of the pressure at the ports of the two hydrostatic motors.

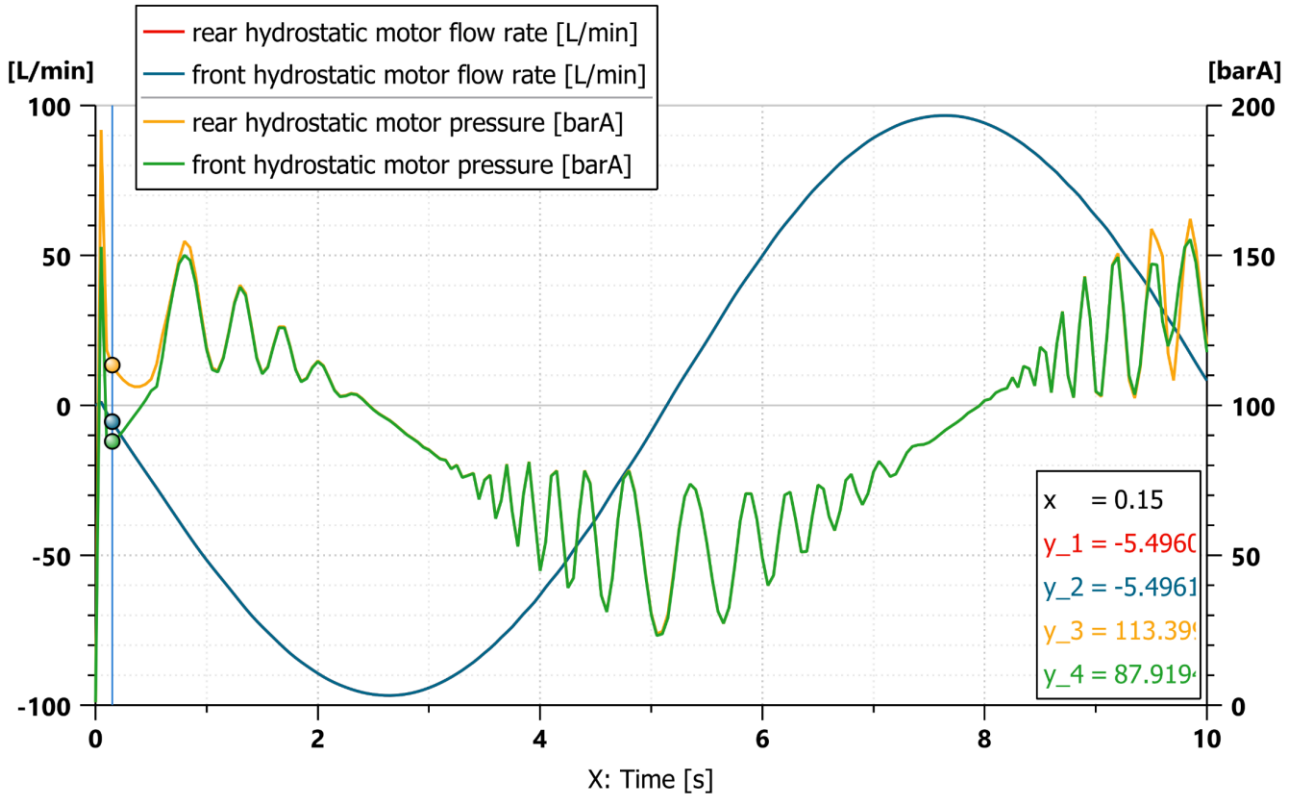


Fig. 8 – Flow rates and pressures at the ports of the two hydrostatic motors

The total mass of the platform and its payload, the slope of the ground as well as the variation over time of its profile can be seen in Fig. 9. On the same graph, it can be seen that the platform moves on rough terrain with unevenness of up to 0.025 m.

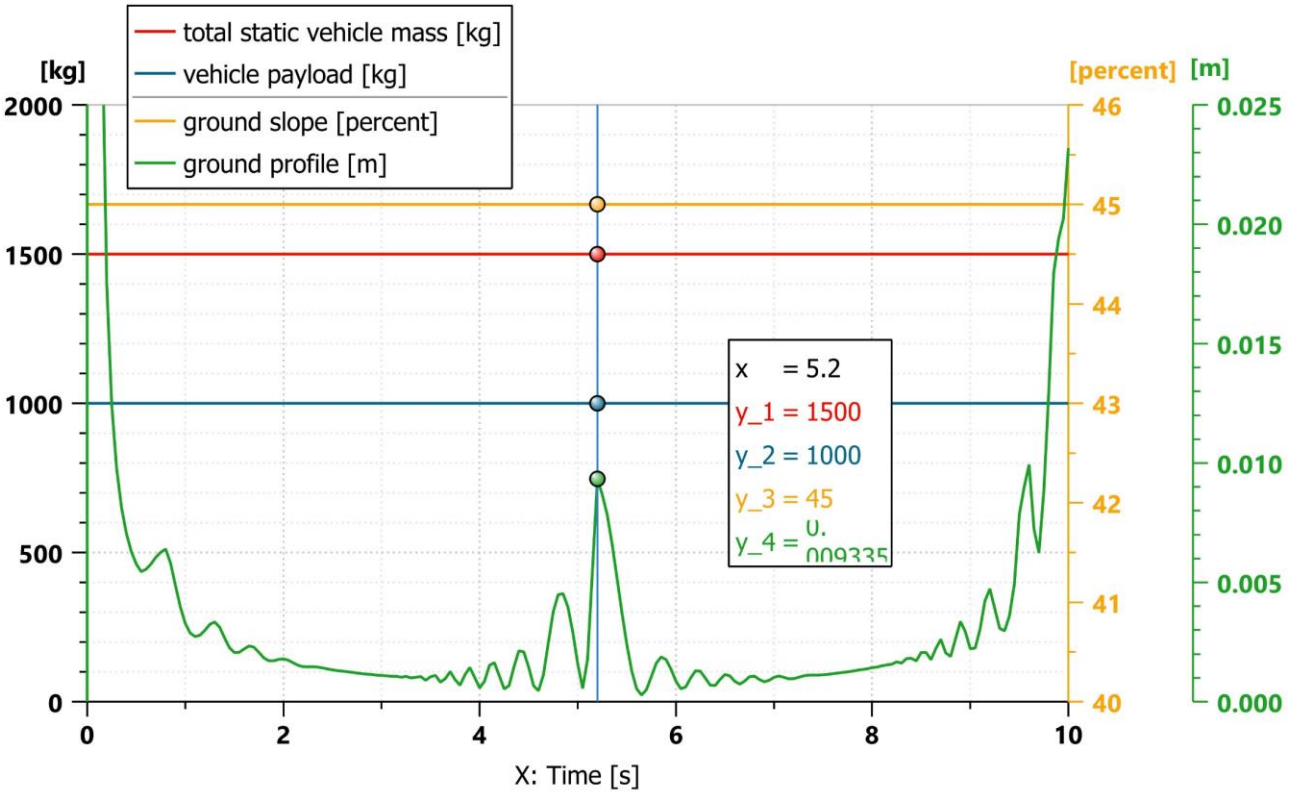


Fig. 9 – The total mass of the platform and its payload, the slope of the ground as well as its profile

The variation over time of the traction parameters of the agricultural platform are presented in Fig. 10; on this figure one can see how driving force is proportional to the acceleration of the platform.

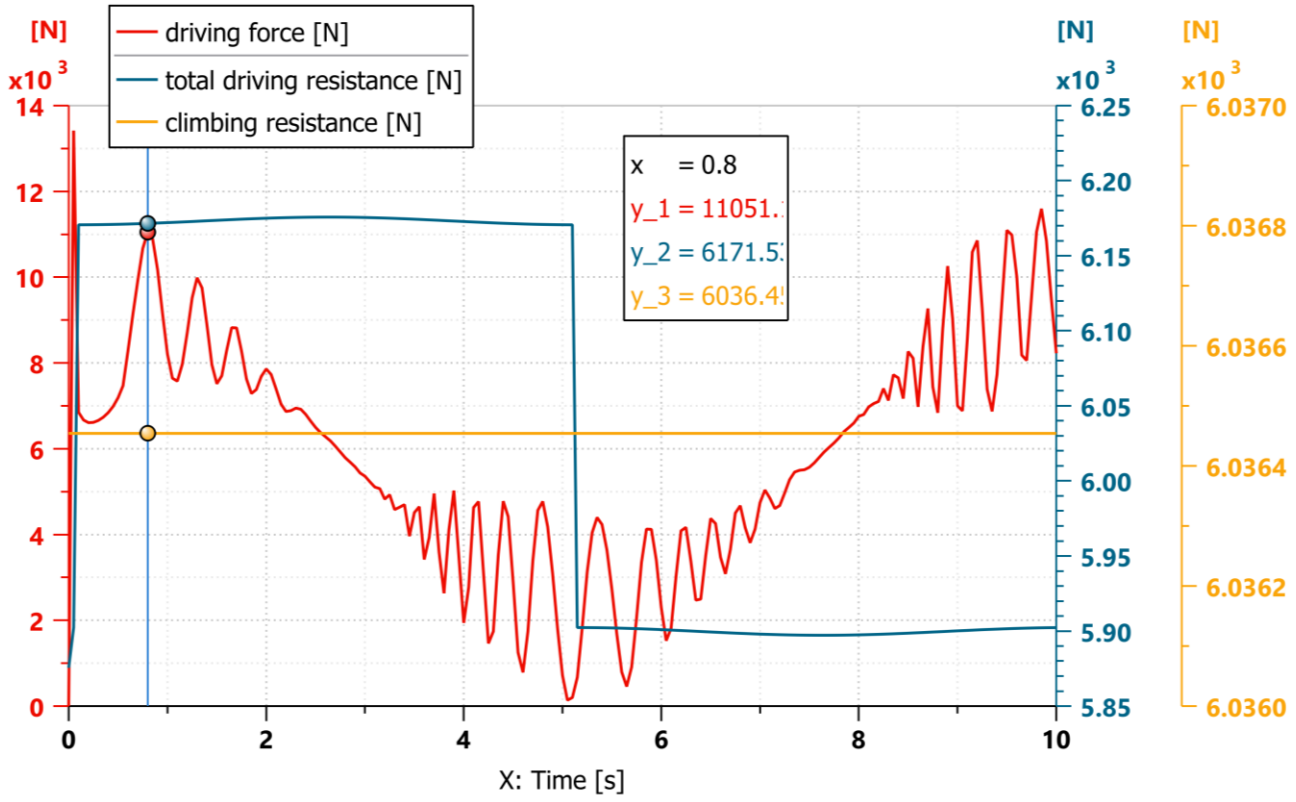


Fig. 10 – Driving force, total driving resistance and climbing resistance

Fig. 11 shows the torque variation over time of the wheels of the two driving axles, as well as their rotation speed, which is identical even if the torque of the two axles is different due to the uneven distribution of the mass of the platform on the two axles. The flow divider performs the role of a lockable differential.

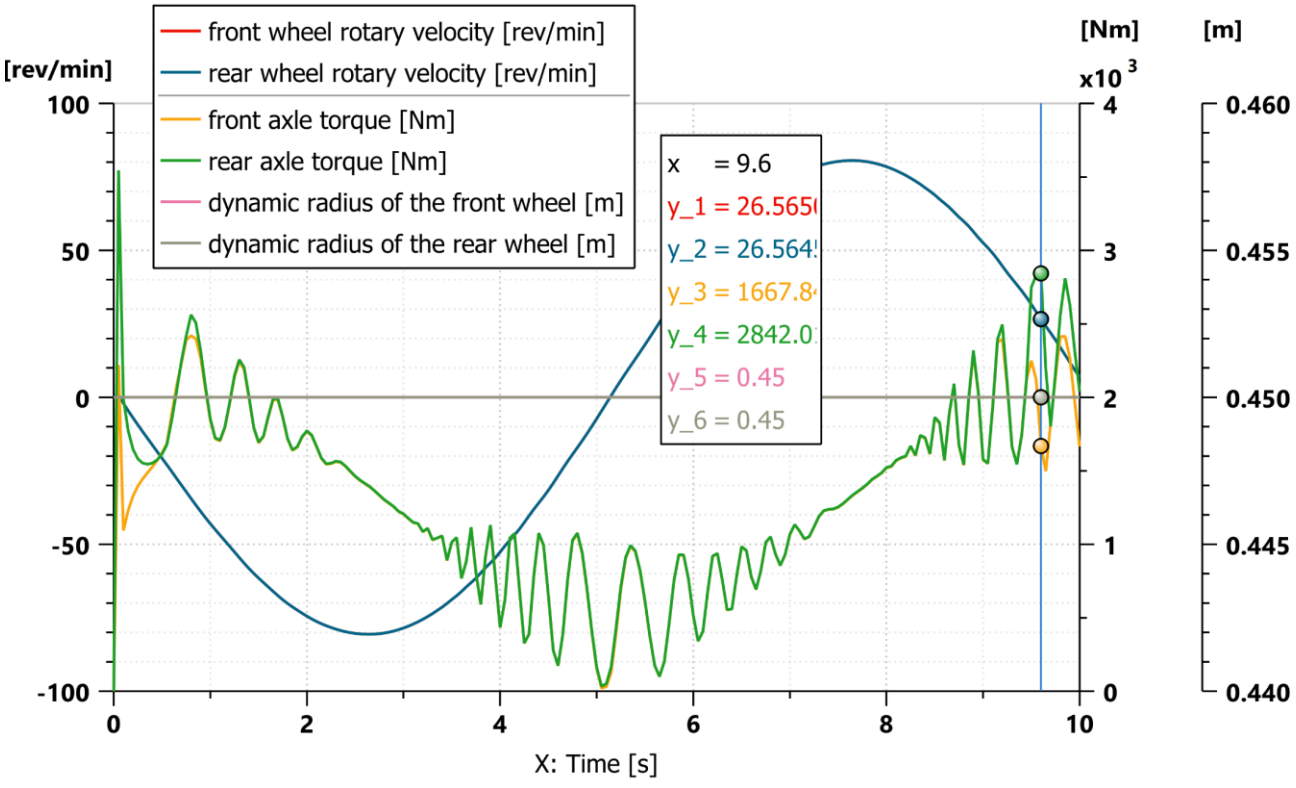


Fig. 11 – Platform wheels' velocity, torque and their dynamic radius

Fig. 12 shows the variation over time of the longitudinal slip expressed as a percentage of the driving axles of the agricultural platform; the values are different because the mass distribution on the two driving axles is different.

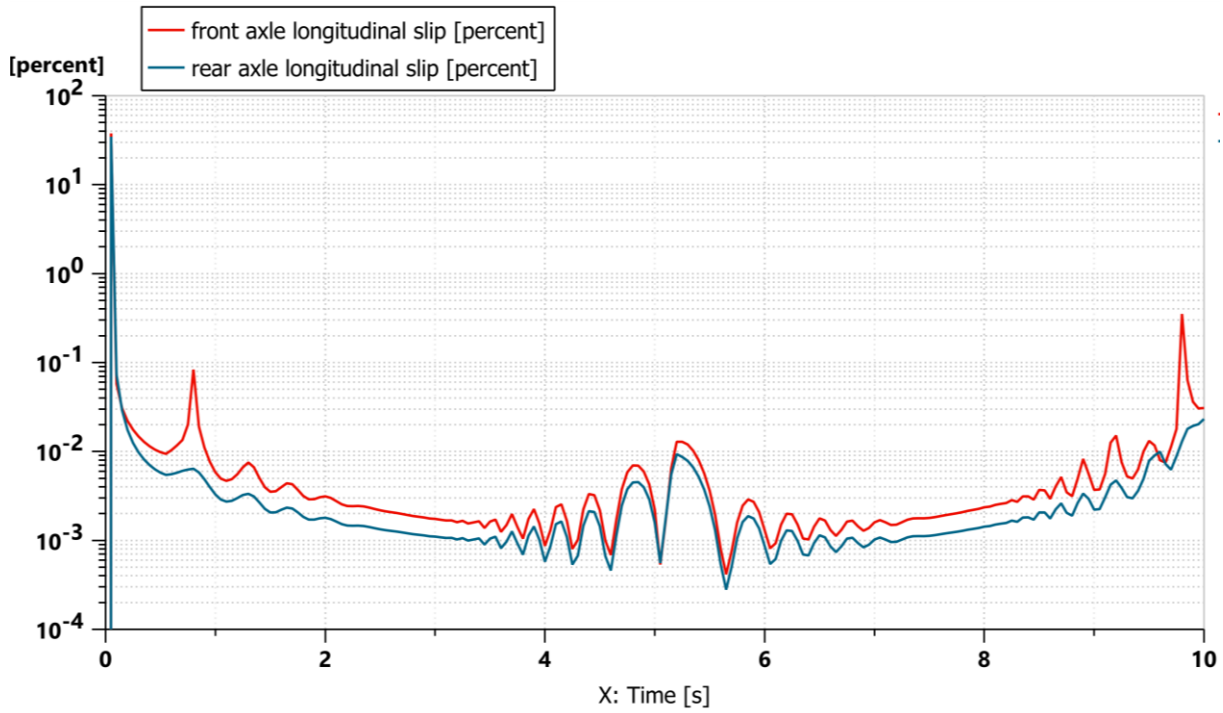


Fig. 12 – Longitudinal slip of the platform wheels (tires)

The time-variation of the dynamic parameters of the agricultural platform - linear displacement, linear velocity and linear acceleration - are presented in Fig. 13. On this figure, one can see the agricultural platform going up and down a slope, and reaching a certain altitude.

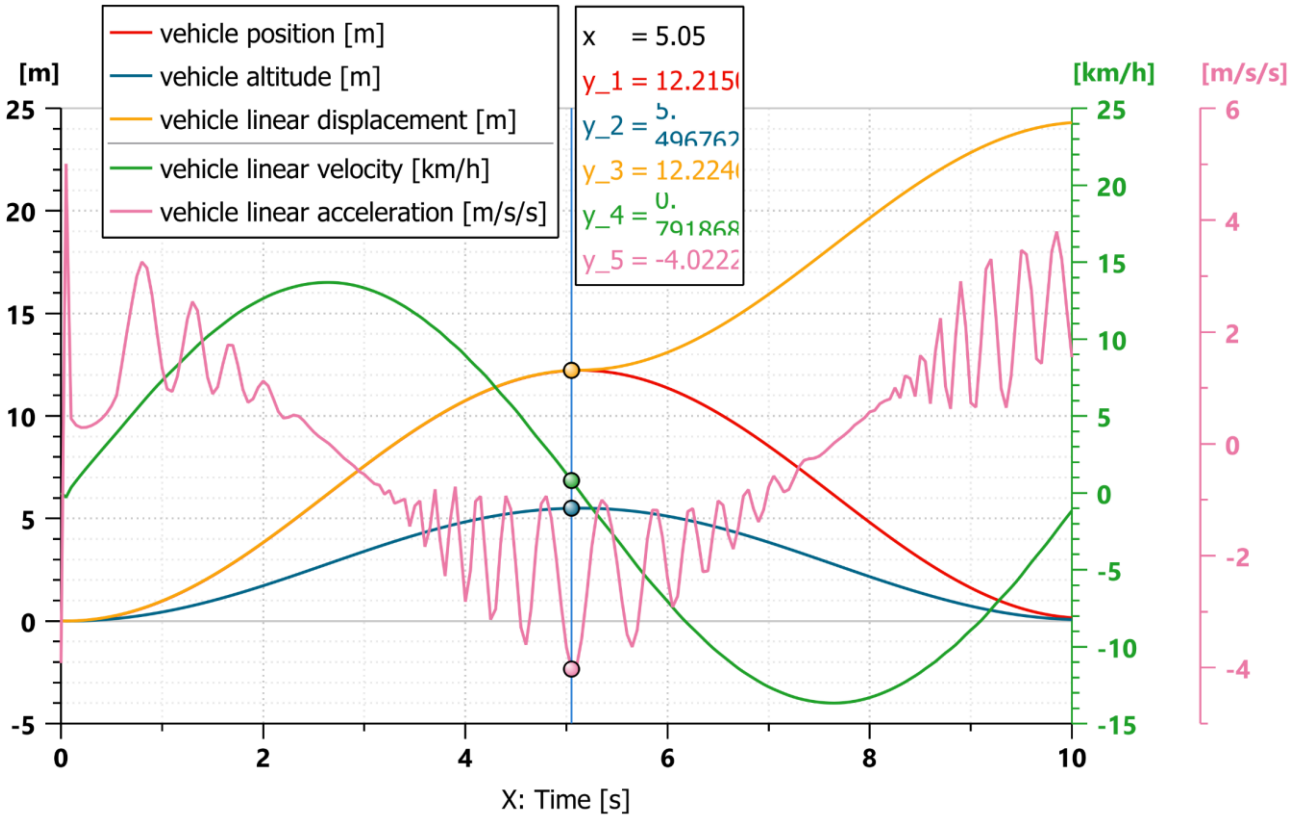


Fig. 13 - The dynamic parameters of the agricultural platform: linear displacement, linear velocity, linear acceleration and altitude

The time-variation of the control setpoint, plant value and instantaneous control error are shown in Fig. 14. In the same figure, it can be seen that the platform can achieve a continuously adjustable travel velocity of more than 12 km/h, which is the maximum velocity required for various technological works; the instantaneous adjustment error is small and is mainly due to the delay caused by the longitudinal slip of the wheels on the ground. It should be noted that the travel velocity is uniform and steady.

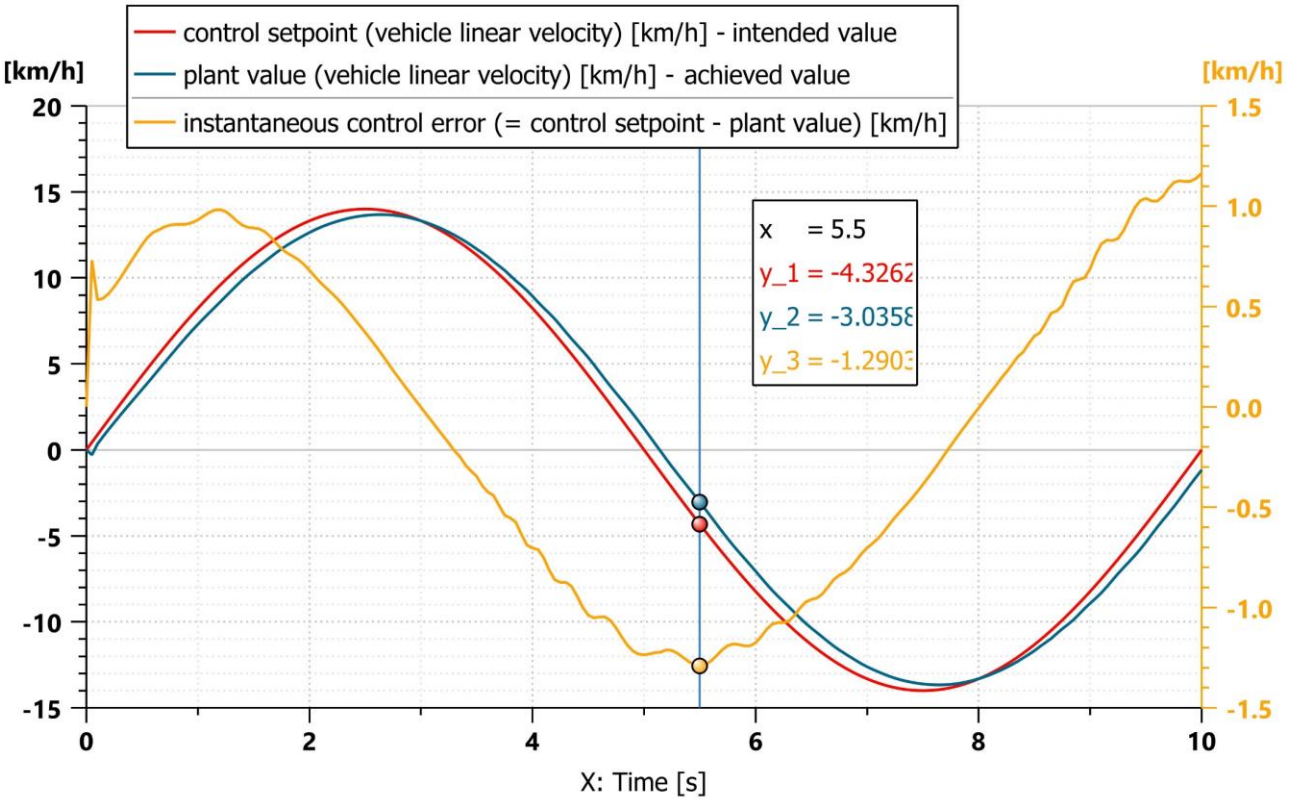


Fig. 14 - The performance of adjusting the travel speed of the agricultural platform

Since all the points in the graph in Fig. 15 are located to the left of the imaginary axis and in close proximity to the axis of real numbers or even on it, it follows that the system is stable and well damped.

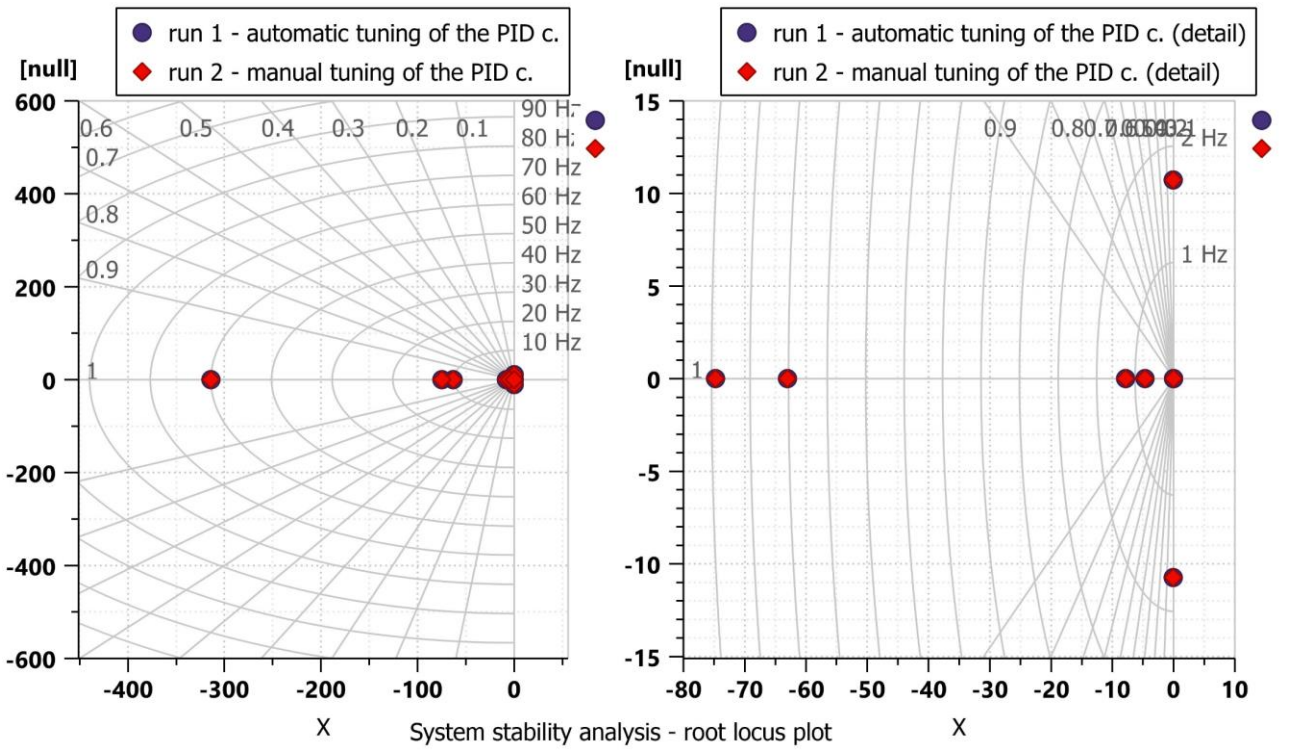


Fig. 15 - The plot of the stability analysis of the automatic adjustment system

CONCLUSIONS

The numerical simulation model is a scalable one and it can be used to study and optimize the dynamic parameters of closed-loop hydrostatic transmissions of various agricultural platforms.

Since the numerical simulation model is an advanced one that takes into account the influence of temperature on the hydraulic components, it can also be used for the precise sizing of the power required for the oil heat exchanger. The parameters of the hydraulic components in the simulation have been chosen in such a way that regardless of the operating conditions of the agricultural platform, it would work optimally in safe conditions.

Although the numerical simulation takes into account a terrain slope of 45%, for which the fluid pressure reaches max. 170 bar when the platform accelerates, the remaining pressure margin up to the nominal pressure of 300 bar would allow the platform to climb an even steeper slope or to tow heavy equipment.

Following the optimization of the dynamic parameters of the agricultural platform, one can notice that it is possible to achieve a continuous adjustment of the travel velocity, with a response time of max. 0.15 seconds, despite the non-linear disturbances of the physical process, which means that the platform can be used even for agricultural works that require high precision in velocity regulation and a fast response time.

ACKNOWLEDGEMENT

This paper has been financed under a project funded by the Ministry of Research, Innovation and Digitalization through Programme 1- Development of the national research & development system, Sub-programme 1.2 - Institutional performance - Projects financing the RDI excellence, Financial Agreement no. 18PFE/30.12.2021.

REFERENCES

[1] Balafoutis, A., Beck, B., Fountas, S., Tsiropoulos, Z., Vangeyte, J., van der Wal, T., Soto-Embodas, I., Gómez-Barbero, M., & and Pedersen, S. M., (2017), Smart Farming Technologies – Description, Taxonomy and Economic Impact, In: Pedersen, S., & Lind, K. (eds.) *Progress in Precision Agriculture*, Springer, Cham, ISBN 978-3-319-68713-1, pp. 21–77. https://doi.org/10.1007/978-3-319-68715-5_2;

[2] Cheng, Z., & Lu, Z., (2021), Research on Load Disturbance Based Variable Speed PID Control and a Novel Denoising Method Based Effect Evaluation of HST for Agricultural Machinery, *Agriculture*, vol. 11, no. 10, MDPI, ISSN 2077-0472, ID 960. https://doi.org/10.3390/agriculture11100960;

[3] Cheng, Z., & Lu, Z., (2022), Regression-Based Correction and I-PSO-Based Optimization of HMCVT's Speed Regulating Characteristics for Agricultural Machinery, *Agriculture*, vol. 12, no. 5, MDPI, ISSN 2077-0472, ID 580. https://doi.org/10.3390/agriculture12050580;

[4] Chiriță, Al.-P., & Pavel, C., (2022), Mathematical Modeling, Laboratory Testing and Numerical Simulation of a Servo-Pump as Part of a Closed Circuit Primary Control Hydrostatic Transmission for Multi-Purpose Trucks, *Hidraulica Magazine*, no. 4, Bucharest, ISSN 1453 – 7303, pp. 7-18;

[5] Guo, N., & Hu, J., (2014), Velocity Control System with Variable Universe Adaptive Fuzzy-PD Method for Agricultural Vehicles. *Proceeding of the 11th World Congress on Intelligent Control and Automation*, Shenyang / China, pp. 2148-2154. https://doi.org/10.1109/wcica.2014.7053054;

[6] Guo, N., Hu, J., & Wang, H., (2013), Intelligent operation control system for rice transplanter based on GPS navigation. *Nongye Jixie Xuebao/Transactions of the Chinese Society for Agricultural Machinery*, vol. 44, no. 1, ISSN 1000-1298, pp. 200-204. https://doi.org/10.6041/j.issn.1000-1298.2013.01.038;

[7] Hu, K., Zhang, W., Liu, H., & Li, K, (2021), Design and Simulation of the Hydraulic Driving System of Hilly Tractors, *Machine Tool & Hydraulics*, vol. 49, no. 16, ISSN 1001-3881, pp. 93–97. https://doi.org/10.3969/j.issn.1001-3881.2021.16.019;

[8] Li, J., Li, S., Zhang, Y., Wu, H., Liu, M., & Gao, Z., (2021), Design of hydraulic drive system for mountain orchard transporter, *J. Anhui Agric. Univ.*, vol. 48, no. 1, ISSN 1672-352X, pp. 143–149;

[9] Tecușan, N., & Ionescu, E., (1982), *Tractors and automobiles (Tractoare și automobile)*. Bucharest/Romania, Didactic and Pedagogical Publishing House;

[10] Warring, R. H., (2014), *Some Aspects of Hydraulics in Mechanical Handling and Mobile Equipment*. Morden, Elsevier, ISBN 9781483296104;

[11] Zhang, Q. (ed.), (2015), *Precision Agriculture Technology for Crop Farming*. Boca Raton, CRC Press, ISBN 9781482251081.

EFFECTS OF WATER-SAVING IRRIGATION COMBINED WITH CONDITIONER ON YIELD, NUTRIENT ABSORPTION AND QUALITY OF DRY DIRECT SEEDING RICE [1]

节水灌溉与调理剂结合对旱直播稻产量、养分吸收及品质影响

Shuchang LU *), Xiawen LI
College of Agronomy and Resources and Environment, Tianjin Agricultural University, Tianjin, 300392, China
E-mail: lsc9707@163.com

DOI: https://doi.org/10.35633/inmateh-69-41

Keywords: *Water saving irrigation, Dry direct seeding, Growth, Output, Nutrient absorption, Quality*

ABSTRACT

Dry direct seeding cultivation technology of rice is an important aspect of rice production and management. Six treatments were designed in this paper, and that is, T1 (conventional irrigation), T2 (conventional irrigation + conditioner), T3 (30% water-saving irrigation), T4 (30% water-saving irrigation + conditioner), T5 (50% water-saving irrigation), T6 (50% water-saving irrigation + conditioner). The results showed that in the three separate irrigation treatments, 30% water-saving irrigation was conducive to the growth of dry direct seeding rice at the tillering stage, jointing and booting stage, and 50% water-saving irrigation was more conducive to the growth of rice at grain filling stage. Compared with no application of amendments, all kinds of treatments could significantly promote the growth of dry direct seeding rice. Under the condition of water-saving irrigation of 30%, higher dry matter quality, yield and nutrient absorption can be obtained. The total dry matter quality and rice yield of T4 treatment with 30% water-saving irrigation and conditioner were the highest, which were 99.90 g/pot and 37.76 g/pot respectively, compared with conventional treatment (T1) was 37.60% and 45.96% higher, and this treatment had obvious effect on nitrogen and potassium absorption. In terms of quality impact, water saving was 30%. Irrigation conditions are conducive to the improvement of rice processing quality, appearance quality and nutritional quality, especially after the application of conditioner, the overall rice quality is improved. This study has a certain reference value for water-saving irrigation, promoting nutrient utilization, stable yield and high quality of dry direct seeding rice.

摘要

水稻旱直播栽培技术是水稻生产管理中重要方面。本文设计了 6 个处理，即 T1（常规灌溉）、T2（常规灌溉+调理剂）、T3（节水 30%灌溉）、T4（节水 30%灌溉+调理剂）、T5（节水 50%灌溉）、T6（节水 50%灌溉+调理剂）。结果表明：单独三种灌溉方式处理中，节水 30%灌溉有利于旱直播稻分蘖期和拔节孕穗期的生长，节水 50%灌溉更有利于灌浆期水稻生长。相对未施调理剂处理，各种施用调理剂处理均可显著促进旱直播稻长势。节水 30%灌溉条件下能够获得较高干物质量、产量与养分吸收量，其中节水 30%灌溉与调理剂结合的 T4 处理总干物质量和稻谷产量最高，分别为 99.90 g/盆、37.76 g/盆，分别较常规处理（T1）高出 37.60%、45.96%，并且该处理在氮钾吸收方面均作用明显。在品质影响方面，节水 30%灌溉条件有利于稻谷加工品质、外观品质与营养品质提升，尤其施用调理剂后总体稻谷品质有所改善。该研究对旱直播稻节水灌溉、促进养分利用、稳产优质具有一定参考价值。

INTRODUCTION

Rice is one of the most important food crops for mankind and plays a decisive role in global food security *(Peng and Khush, 2003; Nguyen and Ferrero, 2006).* In China's conventional rice production, excessive water input and low fertilizer utilization rate are caused by leaching under heavy water irrigation and surface evaporation, which seriously restricts the production efficiency and sustainable development of China's rice production system, especially in the production areas with tight water resources in North China. Dry direct seeding water-saving technology is a light and simple rice cultivation technology that saves water, labor and cost without seedling raising and transplanting and directly planting seeds in the field *(Kuma and Ladha, 2011).*

[1] *Shuchang LU, Professor; Xiawen LI, Research Assistant.*

Some scholars have found that compared with conventional flooding irrigation, drip irrigation and dry direct seeding can save 63.88% of irrigation water in the whole growth period, and the water use efficiency of leaves and yield can be increased by 31.5% and 2.7 times respectively, which is conducive to promoting the growth, development and yield formation of rice *(Wei et al., 2018). Bi et al. (2019)* also pointed out that under the water-saving irrigation of 80% and 60% of the traditional irrigation, the water use efficiency increased significantly, and the yield did not decrease significantly. In addition, intermittent irrigation in paddy field can reduce irrigation water consumption, reduce nitrogen and phosphorus leakage and surface loss, and improve the utilization of soil nitrogen and phosphorus. *Peng et al. (2011)* found in the study on nitrogen and phosphorus leaching loss of the paddy field that compared with flooding irrigation, the leaching loss of N and P under controlled irrigation was significantly reduced.

There are significant differences in the needs of soil physical and chemical properties between dry direct seeding rice and conventional rice, and the application of soil conditioner can improve soil properties and significantly promote the growth and development of rice. According to the relationship between soil, crop and environment and the action mechanism of conditioner, some scholars divide soil conditioner into three types: nutrient type, passivation type and coordinated type. Among them, nutrient type and coordinated type conditioner play a more prominent role in improving soil properties and promoting rice growth. As a coordinated conditioner, such as biochar, it has the characteristics of rich micropore structure and large specific surface area and has a good improvement effect on soil structure, permeability, nutrient absorption and utilization *(Steiner et al., 2008; Novak et al., 2009; Masulili et al., 2010)*. The study further shows that the application of biochar can significantly improve rice yield and nitrogen absorption, so as to improve nitrogen utilization. As a nutritional conditioner, humic acid has strong adsorption capacity and complexation due to its containing a variety of active groups. It can improve the content of soil available nutrients, and then has a significant effect on improving root activity and promoting crop root development, which is conducive to crop growth. In addition, rice is a typical silicon loving crop. As a nutritional conditioner, silicon residue material can promote the absorption of nutrient elements by plants, which is conducive to the growth and development of rice and improve rice quality *(Ma and Takahashi, 1990; Hou, 2020; Salisbury and Ross, 1992).*

Purpose of this paper: (i) Deeply study the effects of water-saving irrigation and conditioner application on growth, yield, nitrogen, phosphorus and potassium absorption and quality of dry direct seeding rice; (ii) Deeply study the comprehensive effects of water management and Regulator Application in the cultivation technology of dry direct seeding rice; (iii) The purpose is to provide theoretical reference for the development of water-saving cultivation of dry direct seeding rice in production areas with large water constraints.

MATERIALS AND METHODS

Test soil properties

The experiment was carried out in the greenhouse of the West Campus of Tianjin Agricultural University. The soil used for the experiment was collected from 0-20 cm topsoil of grain field in Houyou Town, Dameng Village, Wuqing District, Tianjin. The test soil type was light meadow soil with light soil texture, not saline soil. Specific soil physical and chemical properties are shown in Table 1.

Table 1

Soil Physical and chemical properties

Index	Index value	Index	Index value
Organic matter (g kg^{-1})	21.21±1.55	CEC (cmol kg^{-1})	15.54±0.02
Total nitrogen (g kg^{-1})	1.86±0.078	Available potassium (mg kg^{-1})	212.37±0.05
Available phosphorus (mg kg^{-1})	34.56±7.85	Nitrate nitrogen (mg kg^{-1})	10.51.±0.02

Test crop

Early rice, variety is Jinyuan E28. The variety is a japonica conventional rice, with an average growth period of 170 ~ 180 d in Beijing, Tianjin and Tangshan.

Test materials

The comprehensive conditioner is composed of biochar, silicon slag material and humic acid. 30% of the conventional application amount of each conditioner material is prepared respectively, that is, biochar 2,4000 kg/hm^2 + silicon slag material 225 kg/hm^2 + humic acid 1500 kg/hm^2.

Rice husk biochar: purchased from Tianjin Adel Biomass Technology Co., Ltd. and made of rice husk materials, with organic carbon content of 450 g/kg, pH 10.5 and specific surface area of 292 m^2/g. Silicon slag material: it is purchased from Zhejiang Yinyi Group Co., Ltd. and is solid powder. After testing, the main component is porous active silica, with silica content of 84%, organic carbon content of 7.19 g/kg, pH 2.4 and specific surface area of 80-97 m^2/g. Humic acid: purchased from Tianjin X- humate International Trade Co., Ltd., solid powder, pH 5.3, specific surface area 2000 m^2/g.

Test treatment and management

The test time is from June to November 2020. Six treatments are designed, namely T1 (conventional irrigation), T2 (conventional irrigation + conditioner), T3 (30% water-saving irrigation), T4 (30% water-saving irrigation + conditioner), T5 (50% water-saving irrigation) and T6 (50% water-saving irrigation + conditioner). They are repeated for three times, with a total of 18 pots (the specification of the test pot is 40 cm high, 38 cm diameter and 35L total volume), and each basin contains 20 kg of soil. The sowing amount is 6 kg / 667 m^2, i.e. 1.25 g/pot, the sowing depth is 3 cm, the row spacing is 10 cm, and each pot is planted longitudinally in 3 rows. The irrigation volume of conventional flooding irrigation in the whole growth period is 700 m^3 / 667 m^2; moist irrigation is used to irrigate small water and keep the soil moist. The irrigation amount in the whole growth period is 500 m^3 / 667 m^2, which is 70% of the conventional irrigation amount, each irrigation in key water demand period ensures the physiological water demand of rice at the tillering stage, booting and heading stage and grain filling stage, timely replenish water. The irrigation amount in the whole growth period is 350 m^3 / 667 m^2, which is 50% of the conventional irrigation amount. The total irrigation amount of each basin shall be converted according to the proportion of soil weight of each basin to the weight of arable soil per mu of farmland (160000 kg). Conditioner refers to the application of 66.67 g biochar + 30.62 g silicon conditioner + 4.17 g humic acid in each basin.

Water and fertilizer management: after seedling emergence, the summer high temperature period is from June to August, and irrigation is conducted each 3-4 d. Each irrigation amount is 4L for conventional flooding irrigation, 3L for 30% water-saving irrigation and 2L for key water demand period; during booting and grain filling period from September to November, water shall be irrigated each 7-8 d. Each irrigation amount is 3L for conventional flooding irrigation, 2L for moist irrigation and 1.5L for key water demand period. Water shall be cut off 7 d before harvest. In the whole growth period, pure N 20 kg / 667m^2, P_2O_5 6 kg / 667 m^2 and K_2O 5 kg / 667 m^2 were applied. Nitrogen fertilizer is applied four times: base fertilizer (1 g/pot), tillering stage (0.5 g/pot), jointing and booting stage (0.5 g/pot) and grain filling and fruiting stage (0.5 g/pot), which are applied at 40%, 20%, 20% and 20% respectively, that is, the base topdressing ratio is 4:6, which is provided in the form of urea. Phosphorus and potassium are applied as base fertilizer at one time, with 0.75 g P_2O_5 and 0.625 g K_2O applied in each pot in the form of diammonium and potassium sulfate. The nitrogen in diammonium phosphate needs to be deducted in the calculation of urea application rate of base fertilizer.

Test methods

Tillering stage, jointing booting stage and grain filling stage are important growth stages affecting rice growth, grain filling and yield. This experiment investigated the growth of dry direct seeding rice in these three key periods.

Plant height: the height from stem base to spike tip, measured with a tape measure; Chlorophyll: the top three leaves, take the average value of the front, middle and rear parts, and measure it with chlorophyll meter (SPAD-502); Photosynthetic rate: the top three leaves were measured by photosynthetic rate meter (CI-340). Leaf area: the top three leaves are inverted, the leaf length and width are measured with a tape measure, and the correction coefficient method (leaf length) is adopted × Leaf width × 0.7348) calculated leaf area *(Yu et al., 2007).*

At maturity, all dry direct seeding rice in each basin shall be harvested as a whole. After natural air drying, the stem, leaf, root and ear of dry direct seeding rice shall be separated, and each part shall be weighed respectively to calculate the dry matter mass.

Brown rice rate and milled rice rate are the evaluation indexes of rice grading. Brown rice rate refers to the percentage of the weight of brown rice processed by ridge rice machine to the weight of total rice. Milled rice rate refers to the percentage of the weight of milled rice after removing the husk of brown rice to the weight of total rice. Chalkiness is the main character to measure the appearance quality of rice; Chalky grain rate refers to the percentage of chalky rice grains in the whole rice sample *(Zhou et al, 2021).*

The rice is milled into brown rice by ridge rice mill (Korean Shuanglong Company, Model SY88-TH), and then milled into milled rice by rice mill (Japan Sasaki Company, Model CBS300AS (1)). The rate of brown rice, milled rice and chalkiness are determined according to GB/T 17891—1999: high quality rice and NY/T 83—2017: Method for determination of rice quality. The particle length, particle width and surface area shall be measured by the particle evaluator (Model: RGQI20) produced by Sasaki Company of Japan. Nutrition and taste quality are mainly reflected by protein content, amylose content, fatty acid content and taste value, in which taste is an important index to measure rice quality. Japan Sasaki Company has established and developed rice taste evaluation system and taste detection instrument, which can scientifically reflect taste quality. The protein content, amylose content, fatty acid content and taste value are measured by the taste analyzer (Model RLTA10B) produced by Sasaki Company in Japan. The taste value is calculated by the near-infrared spectroscopic analysis method by measuring the protein, amylose and fatty acid content of granular rice.

After the plant samples were digested with concentrated sulfuric acid-H_2O_2, the contents of total nitrogen, total phosphorus and total potassium in each part were determined by Kjeldahl method, vanadium molybdenum yellow colorimetry and flame photometry *(Michalowski et al., 2013).*

The nitrogen absorption of each part was calculated:

$$Nitrogen\ absorption = dry\ matter\ mass \times nitrogen\ content \quad (1)$$

The phosphorus absorption of each part was calculated:

$$Phosphorus\ absorption = dry\ matter\ mass \times phosphorus\ content \quad (2)$$

The potassium absorption of each part was calculated:

$$Potassium\ absorption = dry\ matter\ mass \times potassium\ content \quad (3)$$

Data processing and analysis

The data were processed by Excel 2010, analyzed by One-way ANOVA with SAS 9.4 software, and tested by Duncan method and LSD method.

RESULTS

Growth statuses of dry direct seeding rice under different treatments

As shown in Table 2, at the tillering stage, under the same water irrigation conditions, the plant height, leaf color value, leaf area and photosynthetic rate of dry direct seeding rice treated with conditioner were better than those without application, among which T4 was the best. Compared with T3, the plant height was significantly higher by 3.75%, and the leaf area, leaf color value and photosynthetic rate were higher by 61.87%, 9.37% and 13.21% respectively. From different irrigation conditions, under the condition of wetting irrigation, the growth condition was obvious. Except plant height, other indexes were significantly higher than conventional irrigation and critical water requirement irrigation. Among them, the growth of T4 was the best by combination of conditioner and 30% water-saving irrigation, and plant height, leaf color value, leaf area and photosynthetic rate were significantly higher than those of conventional treatment T1 by 4.92%, 28.79%, 2.33% and 9.53% respectively.

As shown in Table 3 and Table 4, in jointing booting stage and filling stage, under the same water irrigation conditions, the growth status of each treatment shows the same law as that in tillering stage, that is, T2, T4 and T6 are significantly better than T1, T3 and T5. From different water irrigation conditions, the jointing booting stage is the same as the tillering stage. Under 30% water-saving irrigation, the growth advantage is obvious. Among all treatments, T4 has the best growth, and its plant height, leaf color value, leaf area and photosynthetic rate are 6.34%, 23.84%, 22.20% and 11.90% higher than T1 respectively; the leaf color value and photosynthetic rate in the filling stage were different from those in the first two stages. It was better under irrigation in the key water demand stage. Compared with the conventional treatment T1, T6 was significantly higher by 75.68% and 87.50% respectively.

In conclusion, the application of conditioner can significantly promote the growth of dry direct seeding rice. In tillering stage and jointing booting stage, 30% water-saving irrigation is obviously conducive to the growth of dry direct seeding rice, while in grain filling stage, the irrigation management mode in key water demand stage is more conducive to the growth and development of dry direct seeding rice and promote ripening. The combination of 30% water-saving irrigation and conditioner T4 grows better in the early stage of growth, T6 has advantages in the middle and late stage.

Table 2

Growth status of dry direct seeding rice at tillering stage under different treatments

Treatment	Plant height (cm)	Leaf area (cm^2)	Leaf color (SPAD value)	Photosynthetic rate ($\mu mol/(m^2 \cdot s)$)
T1	66.00±2.55b	29.70±1.83c	37.30±2.34b	24.65±3.68c
T2	68.25±2.17a	32.63±1.50b	37.57±0.77b	26.75±2.23b
T3	66.75±3.90b	23.63±1.17d	34.90±4.14c	23.85±1.25c
T4	69.25±2.28a	38.25±1.60a	38.17±278a	27.00±1.90a
T5	48.50±5.02d	21.49±0.86e	26.87±1.73d	19.60±3.25d
T6	52.00±1.22c	22.95±1.14d	27.73±1.27d	21.45±1.13d

Note: Different small letters in the same column represent significant differences between treatments ($P < 0.05$). The same below.

Table 3

Growth status of dry direct seeding rice at jointing booting stage under different treatments

Treatment	Plant height (cm)	Leaf area (cm^2)	Leaf color (SPAD value)	Photosynthetic rate ($\mu mol/(m^2 \cdot s)$)
T1	82.75±2.77b	38.55±2.02c	31.53±1.77c	21.00±2.23b
T2	88.75±2.55a	45.23±1.65b	33.53±234b	21.15±1.90b
T3	81.50±3.77b	46.06±1.14b	33.90±2.85b	19.60±3.25c
T4	88.00±3.02a	47.74±1.46a	38.53±4.14a	23.50±1.25a
T5	51.50±1.12d	29.76±1.06e	21.67±1.73d	17.75±3.68d
T6	71.00±2.45c	38.78±1.24d	32.73±1.27c	18.25±1.13c

Table 4

Growth status of dry direct seeding rice at filling stage under different treatment

Treatment	Plant height (cm)	Leaf area (cm^2)	Leaf color (SPAD value)	Photosynthetic rate ($\mu mol/(m^2 \cdot s)$)
T1	82.75±1.92b	41.66±2.02b	14.97±0.95e	3.60±0.25c
T2	86.25±2.17a	48.28±1.80a	16.93±234d	2.45±0.88d
T3	84.50±1.66c	37.63±1.58c	15.93±278e	3.85±0.45c
T4	88.25±3.11a	38.25±1.60c	18.93±4.14c	4.00±0.90b
T5	51.50±2.06d	28.43±1.86e	22.27±1.27b	4.65±0.96b
T6	69.50±2.29c	30.95±1.14d	26.30±1.73a	6.75±1.23a

Dry matter quality and yield of dry direct seeding rice under different treatments

It can be seen from Figure 1 that the dry matter quality of each treatment of dry direct seeding rice is stem and leaf > rice > root, in which the proportion of stem and leaf is 40.1%-54.1%, and the proportion of rice is 24.0%-41.4%. The total dry matter mass of each treatment T4 > T2 > T1 > T3 > T6 > T5. Under the same water irrigation conditions, the treatment with conditioner can obtain higher dry matter mass. The total dry matter mass of T4 of each treatment is the largest, which is 99.90 g/pot, 21.68% higher than that of T3 without treatment. Among the three water irrigation methods, the total dry matter quality of 30% water-saving irrigation is better than that of conventional irrigation and irrigation in key water demand period. T3 in the treatment without conditioner is significantly better than T1 and T5, and T4 and T2 in the treatment with conditioner are not significantly different, which is 24.25% higher than T6. The total dry matter quality of T4 was significantly better than that of T1, which was 37.60% higher. The rice yield and total dry matter quality showed the same law. The maximum rice yield of T4 was 37.76 g/pot, which was significantly better than that of other treatments, followed by T2 which was 35.86 g/pot, and there was no significant difference between them. T4 was 11.06% and 14.32% higher than T3 and T6, and 45.96% higher than that of conventional treatment T1.

In conclusion, the application of soil conditioner can significantly promote the dry matter accumulation of dry direct seeding rice and have a significant effect on the improvement of rice yield. Under 30% water-saving irrigation, dry direct seeding rice can obtain higher dry matter quality and yield, which is not significantly different from conventional irrigation. The combination of 30% water-saving irrigation and conditioner is the best for T4 biomass accumulation.

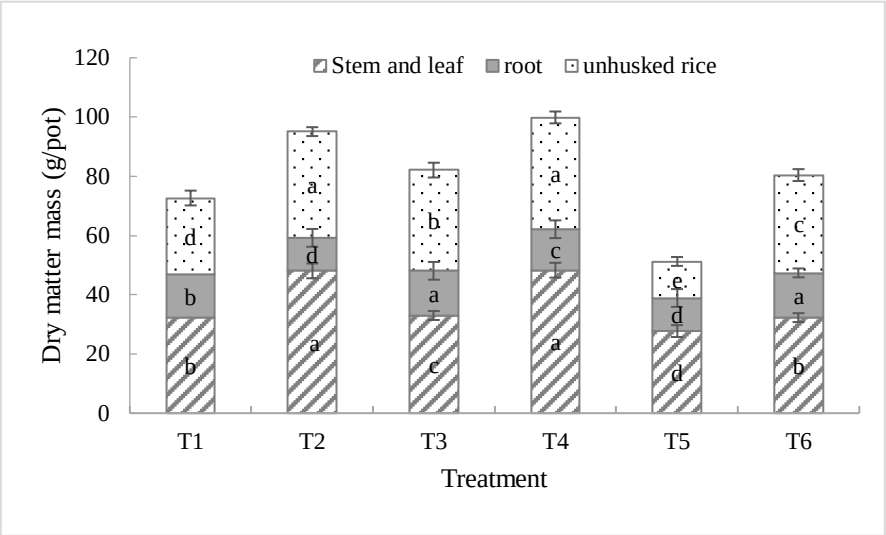


Fig. 1 - Dry matter quality of dry direct seeding rice under different treatments

Note: Different upper and lower case letters represent significant differences among treatments ($P < 0.05$). The same below.

Nitrogen uptake of dry direct seeding rice under different treatments

As shown in Figure 2, under the same water irrigation conditions, the total nitrogen absorption is T2 > T4 > T1 > T3 > T6 > T5, that is, the nitrogen absorption of the treatment with conditioner is significantly better than that without treatment, and the stem, leaf and rice parts also show the same law. Among the three water irrigation methods, the nitrogen uptake under 30% water-saving irrigation (T3, T4) is not different from that under conventional irrigation (T1, T2), but significantly better than that in key water demand period (T5, T6). The total nitrogen uptake of T2 combined with conventional irrigation and conditioner was the largest, which was 0.84 g/pot, followed by T4 combined with 30% water-saving irrigation and conditioner, which was 0.80 g/pot. The maximum nitrogen uptake of rice T2 was 0.44 g/pot, followed by T4 which was 0.41 g/pot. The two treatments did not reach significant difference, but were significantly higher than other treatments. Compared with T1 and T3 without conditioner, T2 and T4 were 42.45% and 37.71% higher respectively. In conclusion, the application of conditioner can promote the nitrogen absorption of dry direct seeding rice and promote the nitrogen absorption and transformation of rice and stem and leaf, so as to improve the yield; the nitrogen absorption of dry direct seeding rice under 30% water-saving irrigation was significantly better than that in the key water demand period, but there was little difference with conventional irrigation, indicating that water-saving irrigation had no significant effect on nitrogen absorption at 70%.

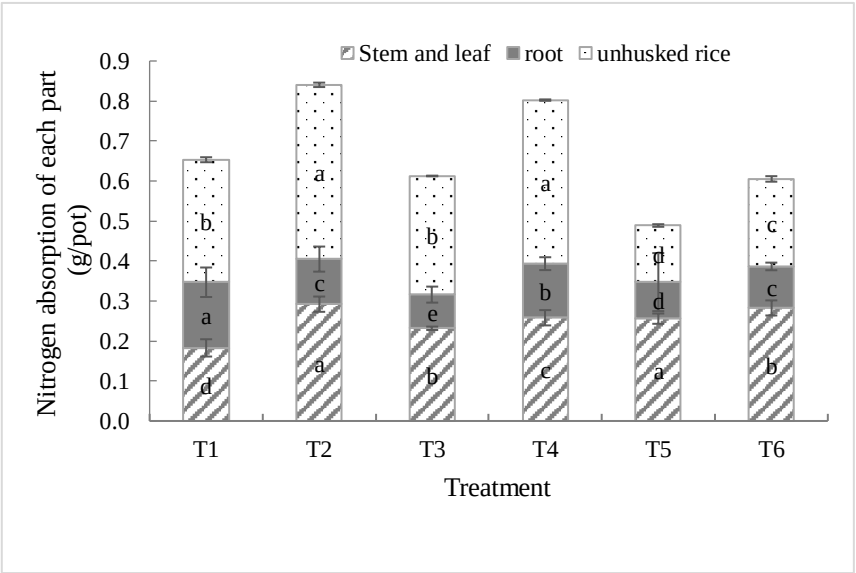


Fig. 2 - Nitrogen uptake in different parts of dry direct seeding rice

Phosphorus uptake by dry direct seeding rice under different treatments

As shown in Figure 3, the phosphorus uptake of different parts of each treatment showed that stem and leaf > rice > root. Under the same water irrigation conditions, the overall phosphorus absorption was T2 > T6 > T1 > T5 > T4 > T3. The effect of regulator application was the same as that of nitrogen absorption. Among the three water irrigation methods, the key water demand period irrigation is significantly higher than 30% water-saving irrigation, and there is little difference from conventional irrigation. The maximum total phosphorus uptake of each treatment T2 is 0.25 g/pot, followed by T6 which is 0.24 g/pot. The rules of rice parts are the same. The combination of conventional irrigation and conditioner T2 and the combination of irrigation and conditioner T6 in key water demand period are significantly better than other treatments, which are 0.10 g/pot and 0.11 g/pot respectively. There is no significant difference between them.

Compared with T1 and T3 without conditioner under the same irrigation conditions, T2 and T6 are 25.00% and 47.89% higher respectively. In conclusion, the application of conditioner can promote the phosphorus absorption of dry direct seeding rice. Conventional irrigation and irrigation in key water demand period are conducive to the phosphorus absorption of dry direct seeding rice and its stems and leaves.

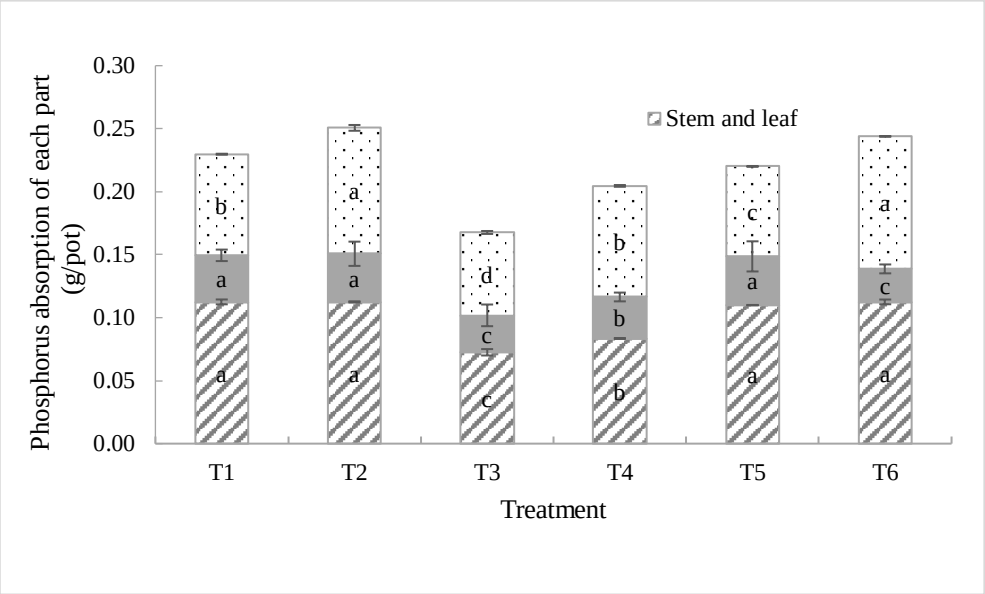


Fig. 3 - Phosphorus absorption in different parts of dry direct seeding rice

Potassium uptake by dry direct seeding rice under different treatments

As shown in Figure 4, the proportion of potassium uptake by stem and leaf parts of each treatment is the largest. Under the same water irrigation conditions, the overall performance is T2 > T4 > T1 > T3 > T6 > T5. After the application of conditioner, the potassium uptake is significantly higher than that of no treatment; among the three water irrigation methods, 30% water-saving irrigation is significantly higher than that in the key water demand period, and has little difference from conventional irrigation. In each treatment, the maximum total potassium uptake of T2 was 1.649 g/pot, followed by T4, which was 1.483 g/pot; the potassium uptake of T2 and T4 was 0.947 g/pot and 0.923 g/pot respectively, which was significantly better than other treatments. There was no significant difference between the two treatments.

Compared with T1 and T3 without conditioner, T2 and T4 were 22.93% and 17.35% higher respectively.

In conclusion, stem and leaf are the main parts of dry direct seeding rice to absorb potassium. The application of conditioner is conducive to the absorption and operation of Assimilates in stem and leaf of dry direct seeding rice, and can significantly improve potassium absorption. Among the three water management methods, conventional irrigation and 30% water-saving irrigation are more conducive to promote potassium absorption.

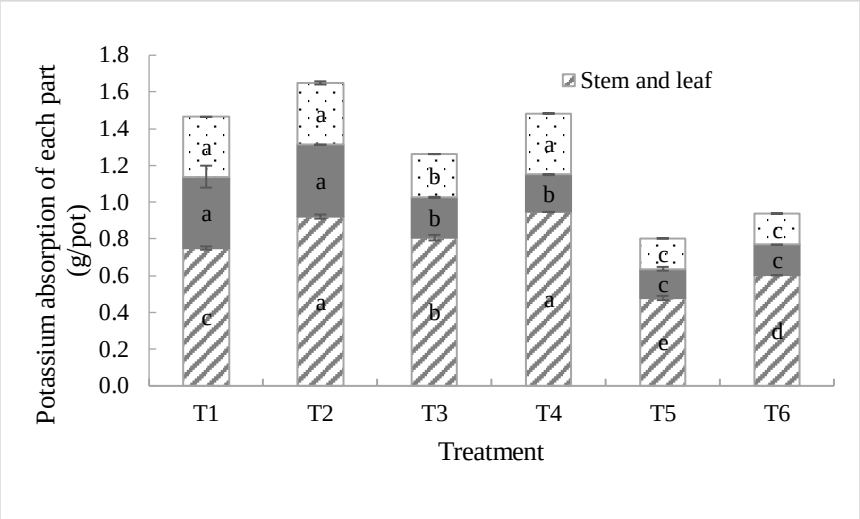


Fig. 4 - Potassium uptake in different parts of dry direct seeding rice

Processing and appearance quality of dry direct seeding rice under different treatments

It can be seen from Table 5 that the conditioner and moisture have certain effects on the processing and appearance quality of dry direct seeding rice. Under the same water irrigation conditions, the processing quality and appearance quality of the treatment with conditioner were better than those without treatment. The brown rice rate and milled rice rate of T4 treatment were the best, which were 30.64% and 1.46% higher than those of T3 without conditioner, respectively; In terms of appearance quality, the chalky grain rate of T4 was the smallest, 12.50%, 30.56% lower than T3, followed by T2 treatment, 16.50%, 25.00% lower than T1. T4 had the best overall performance in grain shape.

Among the three water irrigation methods, the brown rice rate and milled rice rate are T3 > T1 > T5, T4 > T2 > T6, and the chalky grain rate is T3 and T4, that is, 30% water-saving irrigation is conducive to improving rice processing quality, reducing chalky grain rate and improving appearance quality.

Table 5

Processing and appearance quality of dry direct seeding rice under different treatments

Treatment	Brown rice rate (%)	Milled rice rate (%)	Chalky grain rate (%)	Grain length (mm)	Grain width (mm)	Surface area (mm^2)
T1	90.02b	74.61cd	22.12b	4.37±1.09bc	2.34±0.30bc	8.49±2.64b
T2	92.07a	77.40b	16.50c	4.51±0.94ab	2.36±0.31b	8.56±2.16b
T3	91.69a	75.48c	22.00b	4.38±1.03bc	2.34±0.28bc	8.53±2.57b
T4	95.03a	79.61a	12.50d	4.55±1.01a	2.46±0.29a	9.40±2.65a
T5	86.69c	72.75e	23.00a	4.27±0.99cd	2.25±0.30cd	8.28±2.31b
T6	87.58c	73.78de	18.00c	4.33±1.05cd	2.32±0.30bcd	8.47±2.48b

Nutrition and taste quality of dry direct seeding rice under different treatments

Amylose content directly affects the physicochemical properties and taste of rice. It is an important index to evaluate the cooking and eating quality. If the protein content exceeds 9%, it will affect the taste value, and there is a significant negative correlation between gliadin and taste value. It can be seen from Table 6 that under the same water irrigation conditions, the nutritional quality of rice increased significantly after the application of conditioner, while the eating quality was significantly lower than that without application treatment.

Among the three water irrigation methods, the nutrient quality was the highest under 30% water-saving irrigation and the next under conventional irrigation. The contents of protein, amylose and fatty acid in T4 treatment were higher, which were 49.38%, 7.42% and 27.85% higher than those in T1 treatment. In terms of taste quality, the application of conditioner reduced the taste value, and the three irrigation methods had no significant effect on the taste quality of dry direct seeding rice under the same conditions.

Table 6

Nutrition and taste quality of dry direct seeding rice under different treatments

Treatment	Protein/%	Amylose/%	Fatty acid/(mg/100g)	Taste value
T1	8.00d	20.90b	22.84c	55.0a
T2	11.50b	22.12a	29.10a	49.0b
T3	8.80d	20.95b	23.85b	56.0a
T4	11.95a	22.45a	29.20a	49.5b
T5	8.00d	20.80b	22.95c	56.5a
T6	10.70c	22.45a	29.15a	49.0b

DISCUSSION

Different water irrigation methods have different effects on rice growth, yield and quality. In the results of this study, under the irrigation management in the key water demand period (T6 and T5), the plant height is low in the early stage of growth, and the chlorophyll content and photosynthetic rate of leaves are increased in the middle and late stage.

In this study, the photosynthetic rate of T6 was lower at the tillering stage and 68.75% higher than that of T4 in the middle and late growth stage, which was consistent with the research results of *Yu (2017).* Drought control caused the decrease of leaf water content and the intensification of leaf transpiration, and the accumulation of organic matter increased under the condition of consuming unit water. In addition, water stress developed the roots of dry direct seeding rice in the middle and late growth stage, The photosynthetic rate under irrigation in the key water demand period of grain filling period is significantly higher than that under 30% water-saving irrigation, indicating that moderate water-saving irrigation according to the law of crop water demand can also promote the normal growth of dry direct seeding rice.

LV et al. (2016) showed that the dry matter quality of dry wet alternate irrigation was 9.15% and 13.45% higher than that of conventional irrigation and wet irrigation respectively, and the irrigation yield and nitrogen absorption in the key water demand period of this experiment were lower than that of 30% water-saving irrigation, which may be due to the high root shoot ratio of dry direct seeding rice under severe dry wet alternate irrigation in the key water demand period, and the increase of dry matter accumulation rate was concentrated in the root, In the late heading stage, they compete for photosynthetic products with grains, resulting in low yield. Under 30% water-saving irrigation, the water is relatively sufficient, and the root vitality will not be too vigorous. In terms of phosphorus absorption, the phosphorus absorption of irrigated rice in the key water demand period is significantly higher than that of 30% water-saving irrigation, which may be due to the accelerated internal operation of crops under moderate drought, which promotes the transportation of phosphorus from the stem and leaf to rice.

He and Tian (2015) also showed in the study that appropriate water stress slows down the filling speed, is conducive to the accumulation of nutrients, makes the grains plumper, and is conducive to the reduction of rice chalkiness. At the same time, the contents of protein and amylose are also increased, but serious water deficit will reduce rice quality. The results also confirmed this point. The processing and appearance quality under 30% water-saving irrigation were better than that under conventional irrigation, the nutritional quality was also significantly improved, and the rice quality was lower under irrigation in the key water demand period.

The application of conditioner can obtain higher total dry matter mass and nutrient absorption. *Hardy et al. (2017)* found that biochar treatment significantly improved the potassium absorption of double cropping rice, which was conducive to the transport of assimilates from rice stems and leaves to grains, and finally increased the yield. Biochar combined with nitrogen fertilizer significantly increased rice grain yield by 44.89%, increased aboveground nitrogen absorption by 66.27 kg/hm^2, and greatly improved nitrogen absorption. In this experiment, the conditioner treatment (T2, T4 and T6) has obvious advantages in biomass and nutrient absorption, which may be due to the strong adsorption of biochar surface, which can adsorb a large number of polyphenol compounds, provide carbon source for microorganisms, improve microbial activity and promote mineralization, so as to promote nitrogen fixation. On the other hand, biochar has developed pore structure and high stability. Nutrient retention can be achieved by retaining water in soil micro- and mesopores, so as to enhance the absorption capacity of nitrogen *(Lu et al., 2021)* and promote the upward absorption of nitrogen in soil. The application of silicon can significantly improve the content of grain nitrogen and phosphorus, while humic acid can strengthen nitrogen absorption and promote the development of roots.

The application of conditioner can improve rice quality. The study of *Shi et al., (2021)* shows that the combined application of biochar and nitrogen fertilizer can improve the appearance quality of rice such as milled rice rate, chalkiness and grain length, as well as the nutritional quality such as amylose and protein. The study of *Yang et al., (2021)* shows that silicon application has a significant effect on the improvement of rice quality. The content of protein and amylose is high, which has a negative effect on eating quality. In this experiment, the content of protein, amylose and fatty acid in T4 treated with conditioner is significantly higher than that in untreated treatment, which is consistent with the study of *Khan et al., (2008).* Biochar contains high potassium and many trace elements such as Ca, Mn and Zn, which can promote the synthesis of related enzymes in plants. The application of silicon conditioner balanced the content of nitrogen, phosphorus and potassium, while humic acid could accelerate the absorption and operation of nutrient elements. The combination of the three had a good effect on improving rice quality.

The optimal combination of soil conditioner and water has a positive effect on crop yield and nutrient absorption. *Cao et al., (2021)* showed that under the dry wet alternative irrigation mode, biochar combined with slow-release/stable compound fertilizer can synergistically promote the smooth nitrogen absorption, distribution and operation of rice, and significantly improve the population quality, nitrogen utilization and nitrogen availability of rice field. The application of soil modifier clinoptilolite under energy regulated irrigation significantly improved rice yield, nitrogen utilization and rice quality. The combination of soil conditioner and drip irrigation improved the yield and quality of apple, and the contents of total nitrogen and total potassium in leaves and fruits increased significantly, with significant positive interaction. The results showed that under the combination of 30% water-saving irrigation and conditioner, the biomass and nutrient absorption of dry direct seeding rice were not lower or even higher than those of conventional treatment, indicating that the interaction between conditioner and water had a significant positive effect on dry direct seeding cultivation technology.

CONCLUSIONS

Among the three irrigation methods, in terms of growth, 30% water-saving irrigation can promote the growth of dry direct seeding rice at tillering stage and jointing booting stage, and irrigation in key water demand stage is more conducive to the growth of rice at grain filling stage. In terms of biomass and nutrient absorption, 30% water-saving irrigation can obtain higher dry matter quality, yield and nitrogen and potassium nutrient absorption, and there is no significant difference with conventional irrigation, but it has no obvious effect on phosphorus absorption. In terms of quality, 30% water-saving irrigation conditions are conducive to the improvement of rice processing quality, appearance quality and nutritional quality, followed by conventional irrigation conditions. The irrigation conditions in the key water demand period are general. The three irrigation methods have no significant impact on rice eating quality under the same conditions.

The application of soil conditioner can significantly promote the growth and development of dry direct seeding rice. In terms of growth, the treatment with conditioner (T2, T4 and T6) is significantly better than the treatment without conditioner (T1, T3 and T5).

Among all treatments, T4 (30% water-saving irrigation + conditioner) has the best growth in the early growth stage of dry direct seeding rice, and T6 (irrigation in key water demand period + conditioner) has obvious growth advantages in the middle and late growth stage. In terms of biomass, yield and nutrient absorption, the dry matter quality of each treatment was stem and leaf > rice > root, of which rice accounted for 24.0%-37.8%.

The total dry matter quality and rice yield of T4 combined with 30% water-saving irrigation and conditioner were the highest, 99.90 g/pot and 37.76 g/pot respectively, 37.60% and 45.96% higher than those of conventional treatment (T1), which played an obvious role in nitrogen and potassium absorption. The absorption of phosphorus was 13% lower than that of conventional treatment.

The total dry matter mass and rice yield of T2 combined with conventional irrigation and conditioner were slightly lower than those of T4, the difference was not significant, and there was no difference in nitrogen and potassium absorption between the two treatments, but the phosphorus absorption of T2 was significantly higher than that of T4 by 22.4%. In terms of quality, the overall rice quality was improved after the application of conditioner. Among them, the brown rice rate and milled rice rate of T4 treatment were the highest, the chalky grain rate was lower, and the nutritional qualities such as protein, amylose and fatty acid content were higher, 49.38%, 7.42% and 27.85% higher than that of conventional treatment (T1), respectively. However, the eating quality of T4 treatment was significantly lower than that of no conditioner treatment.

In conclusion, the application of soil conditioner can significantly promote the growth, nutrient absorption and yield of dry direct seeding rice and is conducive to the improvement of rice processing, appearance quality and nutritional quality. 30% water saving irrigation combined with conditioner (T4) is conducive to early growth, higher dry matter quality and yield, and improves nitrogen and potassium absorption and rice processing, appearance quality and nutritional quality of dry direct seeding rice. 50% water saving irrigation combined with conditioner (T6) is conducive to late growth and obvious effect of promoting phosphorus absorption.

ACKNOWLEDGEMENTS

This study was financially supported by the Chinese soil as a Fund Project: Key Scientific and Technological Support Project of Tianjin Key R & D plan (19YFZCSN00290), National Key R & D Plan Project (2016YFD0801006) and Tianjin University "Discipline Leading Talent Training Plan" Project (J01009030705). We thank our team members Wang Dafeng, Wang Wei, Xia Yujing and Zhang YingKe for helpful discussions.

REFERENCES

[1] Bi, J. G., Tan, J. S., Zhang, A. N., Wang, F. M., Liu, Y., Yu, X. Q., Liu, G. L., Luo, L. J. (2019). Effects of irrigation on Yield and water use efficiency of water-saving and drought resistant rice (灌溉量对节水抗旱稻产量及水分利用效率的影响). *Shanghai Journal of Agriculture*, Vol. 39, 7-10. Shanghai/China

[2] Cao, X. C., Wu, L. L., Zhu, C. Q., Zhu, L. F., Kong, Y. L., Lu, R. H., Kong, H. M., Hu, Z. P., Dai, F., Zhang, J. Ha., Jin, Q. Y. (2021). Effects of different irrigation and fertilization modes on rice yield, nitrogen utilization and nitrogen transformation characteristics in paddy fields. *China Agricultural Sciences*, Vol. 39, 1482-1498. Beijing/China.

[3] Hardy, B., Cornelis, J. T., Houben, D., Leifeld, J., Lambert, R., Dufey, J. (2017). Evaluation of the long-term effect of biochar on properties of temperate agricultural soil at preindustrial charcoal kiln sites in Wallonia, Belgium. *Eur J Soil Sci*, Vol. 68, 80-89. England.

[4] He, J. Y., Tian, J. C. (2015). Effects of different water conditions on grain quality of dryland rice under drip irrigation under film (不同水分条件对膜下滴灌旱作水稻稻谷品质的影响). *Water saving irrigation*, Vol. 8, 8-10. Hubei/China.

[5] Hou, K. (2020). *Effects of combined application of nitrogen and silicon on rice growth, nutrient absorption and quality under dry direct seeding cultivation (旱直播栽培方式下氮硅配施对水稻生长、养分吸收及品质影响研究).* Tianjin Agricultural University. Tianjin/China.

[6] Khan, M. A., Kim, K.-W., Mingzhi, W., Lim, B.-K., Lee, W.-H., Lee, J.-Y. (2008). Nutrient-impregnated charcoal: an environmentally friendly slow-release fertilizer. *The Environmentalist*, Vol. 28, 231-235. United States.

[7] Kuma, V., Ladha, J. K. (2011). Chapter Six - Direct Seeding of Rice: Recent Developments and Future Research Needs. *Advances in Agronomy*, Vol. 111, 297-413. United States

[8] Lu, H. Y., Du, W. T., Zhang, H. Z., Ayaz, M., Xu, J. X., Wang, R. J., Li, R. N., Yang, X. Y., Zhang, S. L. (2021). Effects of water and fertilizer management and biochar on crop yield, nitrogen efficiency and nitrogen leaching (水肥管理与生物炭对作物产量和氮效率及氮淋失的影响). *Journal of Northwest University of Agriculture and Forestry Science and Technology (NATURAL SCIENCE EDITION)*, Vol. 49, 75-85. Shaanxi/China.

[9] LV, Y. F., Ren, Y. Y., Liu, D., Zhang, Y. C., He, J. Y. (2016). Effects of different water management methods on rice growth, yield and quality (不同水分管理方式对水稻生长、产量及品质的影响). *Tianjin Agricultural Science*, Vol. 22, 106-110. Tianjin/China.

[10] Ma, J., Takahashi, E. (1990). Effect of silicon on the growth and phosphorus uptake of rice. *Plant and Soil*, Vol.126, 115-119. Netherlands.

[11] Masulili, A., Utomo, W. H., Syechfani, M. S. (2010). The characteristics of rice husk biochar and its influence on the properties of acid sulfate soils and rice growth in west Kalimantan, Indonesia. *Journal of Agricultural Science*, Vol. 2, 39-47. England.

[12] Novak, J. M., Busscher, W. J., Laird, D. L., Ahmedna, M., Watts, D. W., Niandou, M. A. S. (2009). Impact of Biochar amendment on fertility of a southeastern coastal plain soil. *Soil Science*, Vol. 174, 105-112. United States.

[13] Peng, S., Khush, G. (2003). Four decades of breeding for varietal improvement of irrigated lowland rice in the International Rice Research Institute. *Plant Prod Sci*, Vol. 6, 157-64. Japan.

[14] Peng, S. Z., Yang, S. H., Xu, Z., Luo, Y. F., Hou, H. J. (2011). Nitrogen and phosphorus leaching losses from paddy fields with different water and nitrogen managements. *Paddy Water Environ*. Vol. 9, 333-342. Germany.

[15] Salisbury, F. B., Ross, C. W. (1992). *Plant Physiology* (4th Ed). Belmont, CA: Wadsworth Publishing Company. Springer.

[16] Michalowski, T., Asuero, A. G., Wybraniec, S. A. (2013). The titration in the Kjeldahl method of nitrogen determination: Base or acid as titrant. *J. Chem. Educ.*, Vol. 90, 191-197. United States.

[17] Shi, D. L., Wang, X. L., Liu, A. K., Hou, Z. F., Liang, G. T. (2021). Response of soil microbial biomass carbon and nitrogen and rice quality to biochar combined with nitrogen fertilizer in yellow soil paddy field (黄壤稻田土壤微生物量碳氮及水稻品质对生物炭配施氮肥的响应). *Environmental Science*, Vol. 901, 443-449. Beijing/China.

[18] Steiner, C., Glaser, B., Teixeira, W. G., Lehmann, J., Blum, W. E. H, Zech, W. (2008). Nitrogen retention and plant uptake on a highly weathered central Amazonian Ferralsol amended with compost and charcoal. *Journal of Soil Science and Plant Nutrition*, Vol. 171, 893-899. Germany.

[19] Nguyen, N. V, Ferrero, A. (2006). Meeting the challenges of global rice production. *Paddy Water Environ*, Vol. 4, 1-9. Germany.

[20] Wei, Y. X., Hou, J. X., Wu, Y., Liu, H., Ru, C., Yang, J. M. (2018). Growth physiology and water saving effects of dry direct seeding rice under different water management (不同水分管理旱直播水稻生长生理与节水效应). *Journal of Agricultural Machinery*, Vol. 49, 253-264. Beijing/China.

[21] Yang, G. Y., Guo, Z., Sheng, J., Wang, G. D., Wang, X., Chen, L. G. (2021). Effects of silicon fertilizer application at different growth stages on Yield and quality of high-quality edible japonica rice (不同生育时期施用硅肥对优质食味粳稻产量和品质的影响). *China rice*, Vol. 27, 68-74 + 79. Zhejiang/China.

[22] Yu, J. Y., He, Y., Zhao, Z. F., Wang, D. (2007). Study on correction coefficient for measuring crop leaf area by length width method (长宽法测定作物叶面积的校正系数研究). *Jiangsu Agricultural Science*, Vol. 2, 37-39. Jiangsu/China.

[23] Yu, M. F. (2017). *Effects of drought stress at tillering stage on yield formation of Japonica Rice in cold region (分蘖期干旱胁迫对寒地粳稻产量形成的影响).* Harbin: Northeast Agricultural University. Heilongjiang/China.

[24] Zhou, X. Q., Fu, S. S., Zhang, Y. R., Zhang, Y. R., Li, R. L., Wu, F. (2021). Analysis of processing quality, appearance quality and cooking characteristics of steamed rice prepared from rice with different storage years (不同储藏年限稻谷制备的蒸谷米加工品质、外观品质及蒸煮特性分析). *Journal of Henan University of Technology (NATURAL SCIENCE EDITION)*, Vol. 42, 75-81. Henan/China.

RESEARCH ON SOIL MOISTURE DETECTION AND REMOTE PRECISION IRRIGATION OF SEEDLINGS BASED ON INTERNET OF THINGS

/

基于物联网的苗木土壤墒情检测与远程精准灌溉研究

Yakun ZHANG*), Zihua FENG, Yalin HUANG, Tingting LI, Xingyang YANG, Hangxing ZHANG, Libo WANG [1]

College of Agricultural Equipment Engineering, Henan University of Science and Technology, Luoyang, 471023, China;

**Corresponding authors Email: zhangyakun2011@163.com*

DOI: https://doi.org/10.35633/inmateh-69-42

***Keywords**: Internet of Things, Smart Agriculture, Single Chip Microcomputer, Precision Irrigation.*

ABSTRACT

Smart agriculture, which combines the Internet of Things (IoT) with agriculture, is the future of agricultural development. In China, manual irrigation is currently the dominant method for seedling irrigation management, but it is inefficient and can lead to water waste. To improve seedling quality and output, reduce labor costs, and conserve water resources, this paper presents a design for an IoT system that uses soil moisture detection and remote precision irrigation for seedlings. The system includes a STC12C5A60S2 microcontroller, an ESP8266-01S communication module, a PRISON PR-3000-ECTH-N01 soil temperature and humidity module, and a 12V water pump. The system is connected to the OneNET platform via the MQTT protocol of the Wi-Fi module and includes software modules for data processing, Wi-Fi communication, and relay control. The OneNET platform allows users to monitor and record real-time temperature and humidity data and switch between automatic and manual modes and seedling threshold types. The system was tested for 24 hours and collected 28,000 temperature and humidity data points every 3 seconds with a packet loss rate of less than 5%. The results show that the system is stable and reliable.

摘要

目前我国大部分地区对苗木的灌溉管理多采用人工灌溉，需要进行实地测试和勘察，且对量和时的把握不够科学，容易造成水资源浪费。为极大地减少人工劳动力的成本，合理并高效地利用水资源以及为苗木的生长环境进行控制，进而提高苗木的品质和产出，实现智能化和高收益化。本文研究了基于物联网的苗木土壤墒情检测与远程精准灌溉的实现，并设计了一套采集土壤温湿度并上传至 OneNET 云平台进行实时监控记录，并且可以从客户端进行指令操作进行精准灌溉以及切换工作模式的一套物联网系统。实现温湿度数据采集、数据处理、数据上传、指令下发以及水泵灌溉的功能。系统以 STC12C5A60S2 单片机为驱动芯片，ESP8266-01S 为通信模块，普瑞森社的 PR-3000-ECTH-N01 土壤温湿度模块为采集模块，12V 水泵作为受控模块进行温湿度调节。整个系统通过 Wi-Fi 模组内置的 MQTT 协议便捷地接入 OneNET 平台。对 OneNET 数据可视化进行设计，包括温湿度数据、自动手动模式切换以及苗木阈值类型切换功能，使得客户端界面清晰直观，便于使用者准确了解实时状况并进行精准灌溉。在设计和调试完成后，对系统进行了 24 小时稳定性测试，以每 3 秒采集一次数据，共采集温湿度数据各 28,000 个左右，丢包率低于 5%。结论为系统稳定性准确可靠。

INTRODUCTION

As a large agricultural country, the application of water resources has a fundamental impact on agriculture, even the lifeblood of the country and agricultural industry. China's water resources are relatively poor, lower than the global average precipitation. It has 2.8 trillion cubic meters of fresh water resources every year, with an average per capita water volume of less than 2300 cubic meters, ranking 109th in the world, and accounting for only 1/4 of the world's per capita level *(Liu and Chen, 2022).* One of the objectives of the irrigation system is to track the water demand of crops based on the collected data and drive the water flow according to the expected set demand without the participation of operators *(Sinha and Dhanalakshmi, 2022).*

[1]*Zhang Yakun, Lecturer; Feng Zihua, Master; Huang Yalin, Bachelor; Li Tingting, Bachelor; Yang Xingyang, Bachelor; Zhang Hangxing, Bachelor; Wang Libo, Lecturer.*

As a large agricultural production country, China's agricultural irrigation water accounts for 70% - 80% of the total water consumption. However, the utilization rate of agricultural water is only about 40%, which is far from that of developed countries *(Shen, 2021*).

There are many problems in China's smart agriculture development, such as lack of overall planning, difficulties in data collection and application, low level of scientific and technological investment and informatization, large impact of factor resources on smart agriculture development, and lack of innovative agricultural business models. These should be solved from the top design arrangement, scientific and technological research and development investment, professional talent training, and policy system construction *(Song, 2020)*. The development of smart agriculture is an important part of China's high-quality agricultural development during the 14th Five-Year Plan period and even in 2035. The development of smart agriculture in the future urgently needs to work together in technology development, application demonstration, policy experiment and social experiment *(Zhao, 2021).*

Agricultural digitalization has improved the efficiency and productivity of the industry, and the agricultural IoT is a promising direction for the technological breakthrough of rational resource-saving Agriculture 4.0 *(Solodovnik et al., 2021)*. A UAV part was introduced to collect these environmental data from different areas of the farm, and the developed system can monitor water demand to guide farmers *(Karar et al., 2021).* The form of agricultural IoT is also constantly innovating. The Internet of Underground Things (IoUT) is a new view of IoT. Through testing, ESP8266 nodes were buried in fields of 10 cm, 20 cm, 30 cm and 40 cm, and the nodes programmed by AP (access point) were placed at several distances of 50 cm high. The results showed that the coverage effect of nodes with a depth of 20 cm was better *(García et al., 2019)*. The IoUT consists of sensors and communication equipment, partially or completely buried underground for real-time perception and monitoring *(Vuran et al., 2018).* It is particularly suitable for the IoT systems of irrigation and precision agriculture. Because these devices will not hinder the work of machines and farmers, and will also reduce the physical damage that nodes deployed on the field may suffer, while Wi-Fi allows underground and aboveground communication to provide communication protection *(Garcia et al., 2020).*

IoT is one of the key technologies of Agriculture 4.0. Agriculture 4.0 is still limited in theory and has been shelved for a long time *(Monteleone et al., 2020)*. In smart agriculture, IoT equipment is installed in an open field under harsh environmental conditions, and it may not be able to communicate in time and transmit the acquired data to the server or cloud *(Gzar et al., 2022).* Currently, the main research objects of smart agriculture and agricultural IoT are greenhouse crops, and there is little intelligent system design on seedlings. There are many high-value and high-income seedlings in China, such as camphor, yew and ginkgo, which lack intelligent irrigation systems, have high cultivation costs and poor manual cultivation, and urgently need the input of freshwater intelligent management systems for agricultural precision irrigation, which is essential to improve crop yields and reduce costs, while contributing to environmental sustainability *(Boursianis et al., 2021).* This paper aims to research and design for the defects of the current irrigation mode of seedling class, and build a simple, efficient as well as low-cost intelligent irrigation system with STC12C5A60S2 microcontroller as the core, while compared to the current widely practical STM32 chip-based irrigation system *(Zhang and Guo, 2022).* This system has much lower cost and power consumption, more consideration of economic practicality, and is also more suitable for application scenarios that need to run for a long time, especially seedlings class perennial needs to monitor the soil moisture and irrigation, which can guide the current situation.

The current IoT irrigation system is generally a single operating platform, such as in the Android mobile terminal, IOS system terminal, or computer terminal for terminal monitoring and remote operation, such as “IoT-based automatic irrigation system design and implementation of the system” *(Xia and Wu, 2022),* and “A distributed system for supporting smart irrigation using Internet of Things technology” *(Ahmed et al., 2021)*. Their terminal platforms are the Android cell phone platform, which is limited and lacks flexibility. This system uses the online OneNET platform as the terminal, which is very flexible and convenient as it can be transplanted and practiced on any operating platform. Since the soil environment of seedlings is different in different regions, such as the north is mainly temperate while the south is mostly subtropical, this system has set different seedling thresholds for precise irrigation of seedlings in different regions, which can adapt to different regions and seedling types. Finally, the results show that the paper has the practical reference significance for future research on more diversified intelligent systems of seedlings.

MATERIALS AND METHODS

Overall system design

The Internet of Things is one of the most advanced technologies available, and it can be easily integrated with almost all traditional methods to perform tasks *(Jadon and Singh, 2022)*. The development and integration of sensor technology, high-speed information processing technology, and stable communication technology have provided the foundation for the formation of the Internet of Things *(Seng et al., 2022)*. The soil moisture detection and remote precision irrigation system of seedlings based on IoT is mainly divided into two parts: the client data display instruction control part, and the main control chip MCU part and the controlled end *(Lu et al., 2021)*. For the client part, the system adopts China Mobile's OneNET cloud platform, mainly including the creation of products and equipment, data connection and data visualization interface drawing, to achieve clear and stable display of soil data on the interface. It also includes the buttons, such as system working mode, to ensure that the cloud platform can realize the issuance of data instructions after the user presses a button, thereby realizing information interaction through the Internet and single-chip microcomputer to achieve the cloud control.

For intuitive understanding, the structure diagram Fig. 1 is as follows:

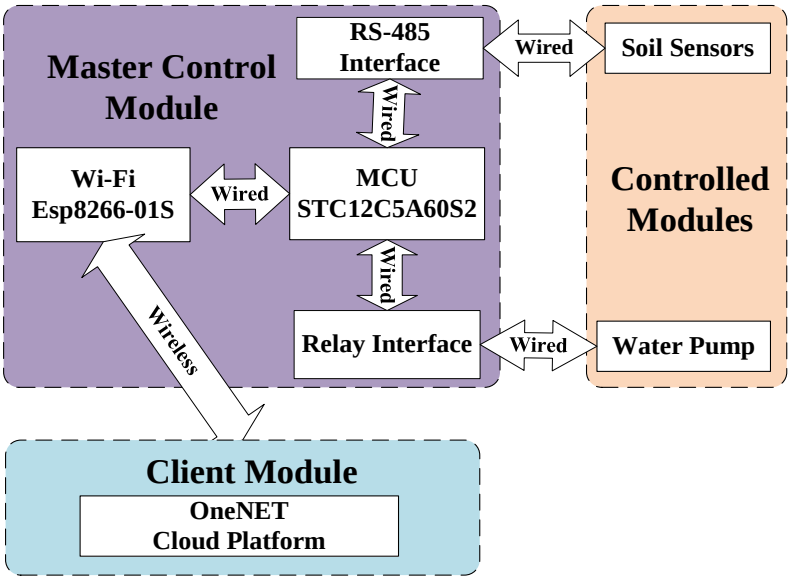


Fig. 1 - System structure diagram

MCU of the main control chip includes the MCU using STC12C5A60S2, the Wi-Fi mode ESP8266-01S chip, the soil data acquisition part of the RS-485 interface and the relay part connecting the water pump for irrigation control. The programming part is mainly to program the STC12C5A60S2 single chip computer to realize the communication and control of the Wi-Fi module, sensor module and relay module, so as to realize the system design. The single chip computer connects the instructions sent by ESP8266-01S through the serial port and connects to the OneNET platform. Through the serial port, the single chip computer sends the data frame request to the RS-485 soil sensor to obtain the real value after the sensor data analysis.

Each module works together to realize the system design. The intelligent irrigation system is generally divided into three parts: client cloud platform, master chip control and terminal execution equipment. The client is the platform module that customers can see and use. The client used in this system design is China Mobile's OneNET cloud platform. The instructions of the OneNET cloud platform are all open sources, and the details of both data upload and instructions can be clear.

The main control module is composed of the single chip MCU, single chip STC12C5A60S2, Wi-Fi module ESP8266-01S, relay interface and RS-485 interface. MCU, as the core, sends commands to each module for communication. The controlled end is the final command realization end. RS-485 sensor is selected for data acquisition according to the requirements in this design. The sensor can sense and will detect the sensed information and output regular signals to achieve stable transmission and convenient processing of information.

System hardware design

The hardware is mainly the main control module and the controlled module, including the physical connection and working principle of the MCU STC12C5A60S2, the Wi-Fi module ESP8266-01S, the relay pump, the sensor and more.

Selecting a single chip computer is the first and one of the most important steps in system design. To meet the design requirements, the main selection indicators are RAM, ROM and serial port. The system needs a set of serial ports to communicate with each other in order to realize the data collected by RS-485 soil sensor and sent to the single-chip microcomputer; then the network transmission is carried out through the Wi-Fi module. The single chip also needs to communicate with the Esp8266-01S and a set of serial ports for communication. As a result, at least two sets of serial ports are required for independent communication, and STC12C5A60S2 dual-serial port single chip microcomputer is selected to enhance its performance. On a single chip, STC12C5A60S2 provides flexible and effective solutions for many embedded control application systems with a smart 8-bit CPU and in-system programmable Flash.

The soil sensor data communication adopted by this system is based on the RS-485 protocol. The main control chip of RS-485 module is MAX485 chip, which mainly realizes signal conversion. Through MAX485 chip, TTL-signal and RS-485-signal can be stably converted to achieve data transmission. RS-485 communication has many advantages. When a specific RS-485 device exchanges data with a single chip computer through an interface, it first converts the TTL and RS-485 signals in two directions through the MAX485 chip. The interface at both ends of the chip is the standard RS-485 interface A/B interface, which connects the A/B line of the sensor respectively. The other end of the chip is the RS-485 communication direction control terminal used to control the data transmission direction and the RX/TX terminal used to communicate with the single-chip computer. Of course, the soil sensor needs to share power and ground with the SCM, and can use the power and ground of the SCM power module to achieve stable work, as shown in Fig. 2.

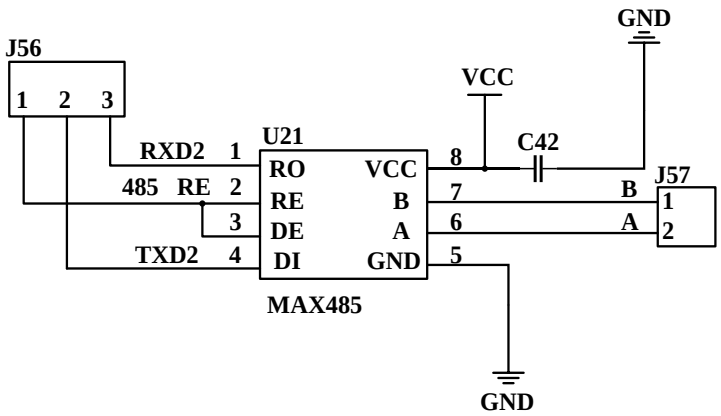


Fig. 2– RS-485 interface schematic

The system uses the PR-3000-ECTH-N01Ver 2.0 model RS-485-soil temperature and humidity sensor of Prison, with stable working performance and high sensitivity and accuracy. Through measuring the dielectric constant of the soil, the moisture content and temperature value of the soil can be directly obtained, which conforms to the international standard measurement method. The working voltage of the sensor is 4.5V-30V DC; the working temperature is -40°C~+60°C, and the protection grade is IP68. The product specification is 45*15*123 mm, and the output signal is RS-485 signal, as shown in Fig. 3.



Fig. 3 – RS-485 soil temperature and humidity sensor

The baud rate it supports is 9600 bit/s, 2400 bit/s and 4800 bit/s. Modbus protocol is a serial communication protocol, and the data is sent and received in the form of data frame. A frame message of Modbus protocol includes address code, function code, data and CRC check code. When there are multiple devices, the communication device can be determined according to the address code; the function code indicates the function of sending instructions to the host, and the device only uses the function 0x03 to read register data.

Wi-Fi serves as the foundation and hub of Internet of Things (IoT) implementations, due to the increasing popularity of smart products, rapid advancements in wireless technology, and upgrades to various communication interfaces. The use of WI-FI technology and wired network for integration and networking to realize IOT can greatly reduce costs *(Qiu, 2017).* The design of this system uses the chip ESP8266-01S as the Wi-Fi module. It is developed and manufactured by the Ai-Thinker company, and the main frequency supports 80 MHz and 160 MHz. The built-in TCP/IP protocol stack can realize TCP transparent transmission. It supports local firmware upgrade and cloud OTA upgrade, and local firmware burning and upgrading have been performed for ESP8266-01S in the design of this system. ESP8266-01S has three working modes, STA, AP and STA+AP, for selection. The working voltage is 3.0-3.6 V, and the typical value of 3.3 V is generally used for power supply. The ESP8266-01S firmware of this system needs to be burned, and the firmware burning needs to use the Download Tool GUI instruction software. After entering the software, ESP8266 Download Tool is selected to choose the bin file to be burned at the corresponding address, and then some indicators corresponding to the ESP8266-01S to be burned are set. SPI SPEED selects 40MHz; SPI MODE selects DOUT mode; FLASH SIZE selects 8Mbit, and then the baud rate setting. The default baud rate of ESP8266-01S is 115200. If the baud rate of ESP8266-01S has been set previously, the set will be changed. The pins of ESP8066-01S are shown in Fig. 4.

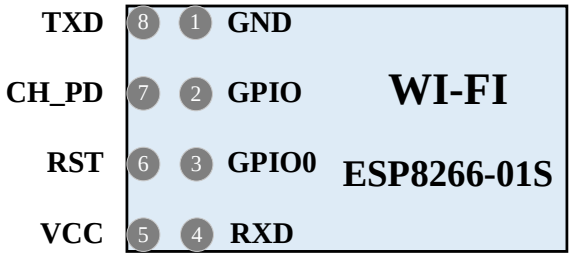


Fig. 4 - ESP8266-01S pinout

Relay is an electrical controller with two parts: control system and controlled system. It uses weak control voltage to control high voltage and high current equipment when working and is widely used in automatic control circuits. As shown in Fig. 5, P1 has three ports: NC normally closed end, COM common end and NO normally open end. It is only necessary to connect the positive and negative poles of electrical equipment such as water pump to COM end and NO end to realize on-off control. J15 terminal is the trigger signal terminal, which can be connected to any I/O port on the single chip computer to realize the high- and low-level control of power-on or not. The schematic diagram of relay is shown in Fig. 5:

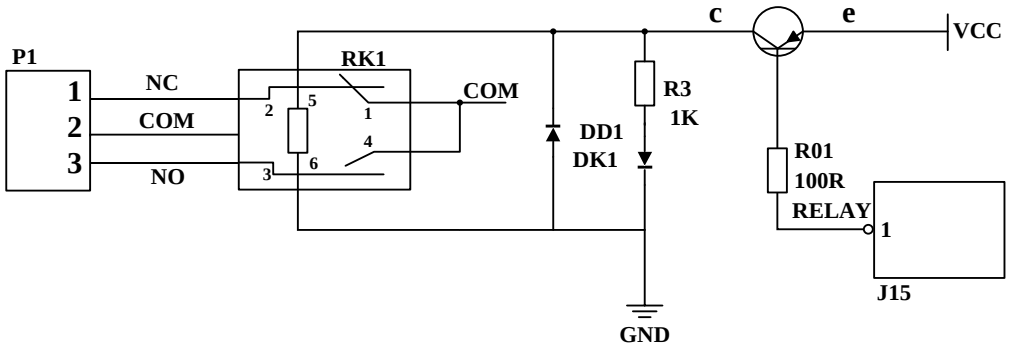


Fig. 5 - Relay schematic

System software design

The software design and programming of this system are all implemented in Keil uVision5 software, using C51 programming language. The program is mainly divided into main function module, serial port 1 module, RS-485 module, serial port 2-module, timer module and delay function module.

The total function of the code is that the microcontroller obtains the soil temperature and humidity data collected by RS-485 sensor through serial port 2 module, and sends it to OneNET cloud server through serial port 2 and displays it through data visualization. The client can control the irrigation system by issuing commands based on real-time soil data to achieve remote control of IoT.

The general structure of the program is shown in Fig. 6. The main function module is used to call other module functions to realize the design: serial port 2 module code part, serial port 2 and RS-485 soil sensor are connected through MAX485 chip interface, so the function of serial port 2 is to obtain the data of soil sensor. The program includes serial port initialization; serial port sending function and serial port interrupt function. When the serial port receives the data, it will have an interrupt request and enter the interrupt. The serial port sending data function should meet the requirements of RS-485 to send the inquiry frame. One frame of data is 8 bytes and needs to control the direction. The interrupt service function is called when receiving the data sent by the sensor, and uses the judgment method of timeout reception to determine whether a frame of data has been received. After acceptance, it will be stored in a register to wait for decoding.

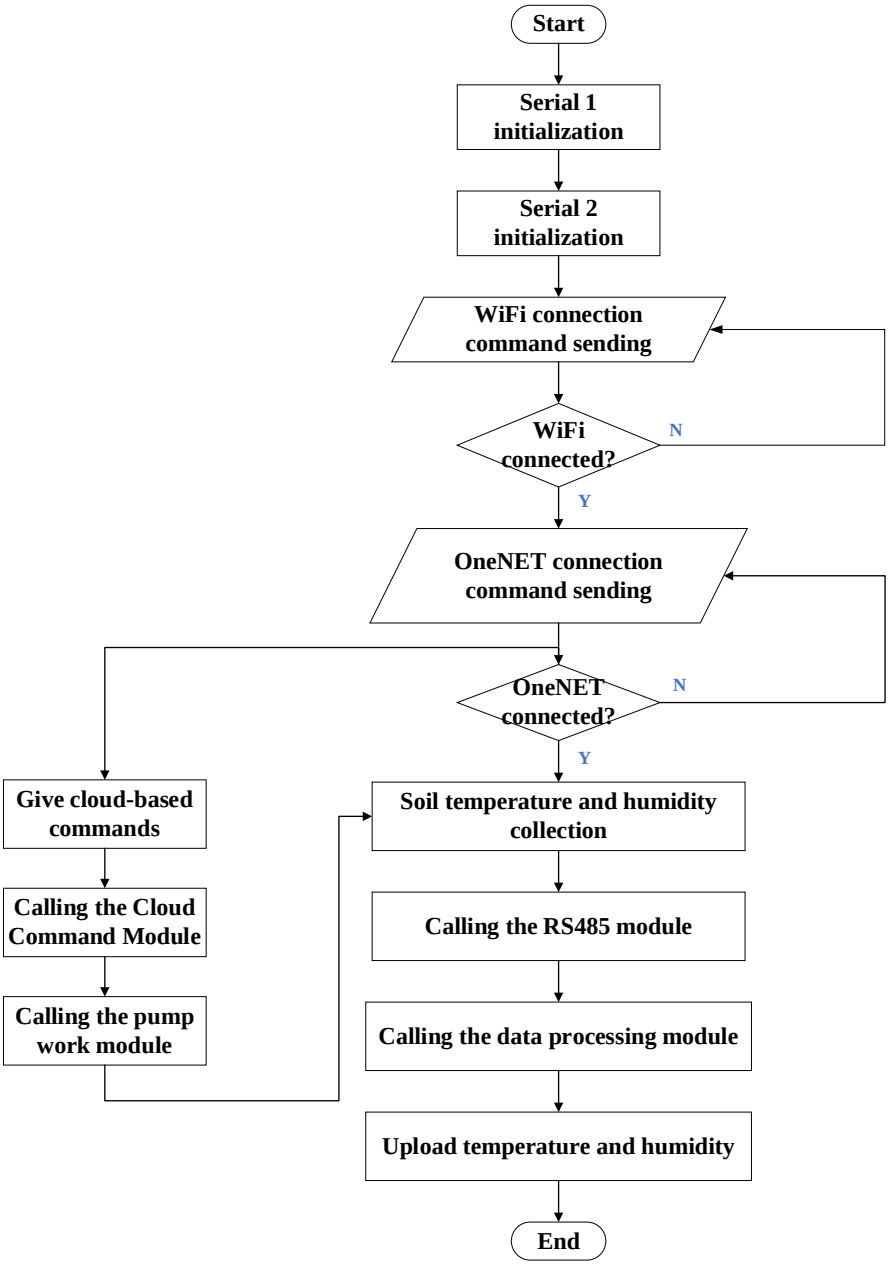


Fig. 6 - Data receiving and processing structure

Designing a data decoding program is a guarantee of data accuracy. Modbus data processing function, whose main function is to calibrate the data read from the sensor by the single chip computer and converts it

to the decimal real value. The data obtained from the sensor is hexadecimal, and the first step is to convert it to decimal, for example, for the hexadecimal data $abcd(H)$, the humidity decimal value is:

$$H = abcd(H) = a \times 16^0 + b \times 16^1 + c \times 16^2 + d \times 16^3 \quad (1)$$

The true value of humidity data h is:

$$h = H/1000 \quad (2)$$

The temperature data also needs to be converted from hexadecimal to decimal first, and when the temperature is positive, the data is transmitted in the true form as follows:

$$T_p = abcd(H) = a \times 16^0 + b \times 16^1 + c \times 16^2 + d \times 16^3 \quad (3)$$

When the temperature data is negative, the data is transmitted in two's complement, as follows:

$$T_n = -(2^k - T_p) \quad (4)$$

K is the data length in binary, and the data length in this system is 16, so k is 16. The true temperature value conversion formula is as follows:

$$t = T/10 \quad (5)$$

H and T are the byte values after processing in the data processing program. The flowchart is shown in Fig. 7.

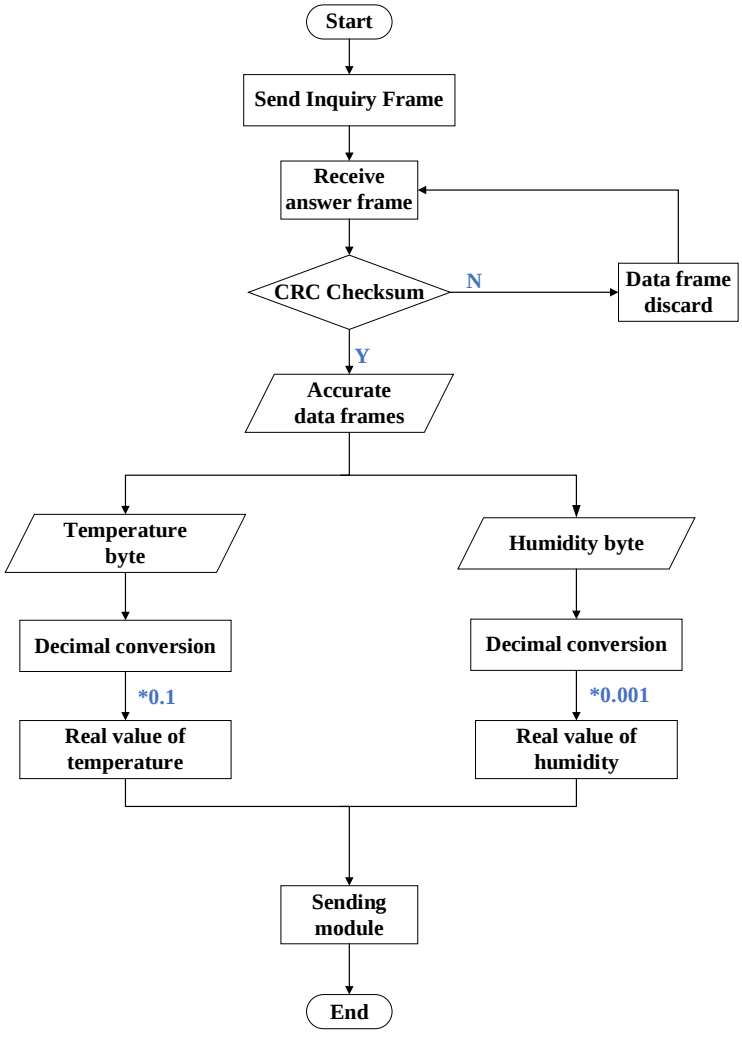


Fig. 7 - Data receiving and processing structure

The CRC checksum used in the figure is calculated as follows. The data byte is divided into an information segment and a check segment, and the length of the code word is set to N, the information field is L bits, and the check field is R bits $(N=L+R)$. There exists and only exists a polynomial of order R $g(x)$.

$$V(x) = A(x)g(x) = xRm(x) + r(x) \quad (6)$$

where $m(x)$ is the original information polynomial of order L, $r(x)$ is the checksum polynomial of order R-1 and $g(x)$ is called the generating polynomial.

$$g(x) = g0 + g1 \times 1 + g2 \times 2 + \ldots + g(R-1) \times (R-1) + g(R) \times R \quad (7)$$

The sender generates the CRC code word by the specified g(x), and the receiver verifies the received CRC code word by this g(x). With this calculated checksum, abnormal transmission data can be discarded.

The system has two working modes: automatic mode and manual mode. Taking the variable Mode as the flag bit, it is automatic mode when Mode=0, and the default is automatic mode; when Mode=1, it is manual mode. When the temperature is greater than the set threshold Value_Temp_H or the humidity is less than the set threshold Value_Humb_L, the water pump working flag Water_pin will be triggered to achieve automatic irrigation. When the temperature is less than the set threshold value_ Temp_ L and the humidity is greater than the set threshold Value_Humb_H, it will be set to zero and the irrigation will be stopped. In this design, four seedling thresholds, yew, ginkgo, poplar and sandalwood are set. When instructions are sent on the OneNET client, it will judge and accept the instructions and assign the threshold of temperature and humidity to switch different seedling thresholds. At startup, the default threshold value is set such that the pump will automatically start pumping water when the humidity is less than 40% or the temperature is greater than 25°C. Conversely, the pump will automatically stop pumping water when the humidity is more than 50% and the temperature is less than 21°C. In manual mode=1, only the two control commands OPEN and CLOS are the instructions for pump on/off respectively. The flowchart in automatic mode is shown in Fig. 8:

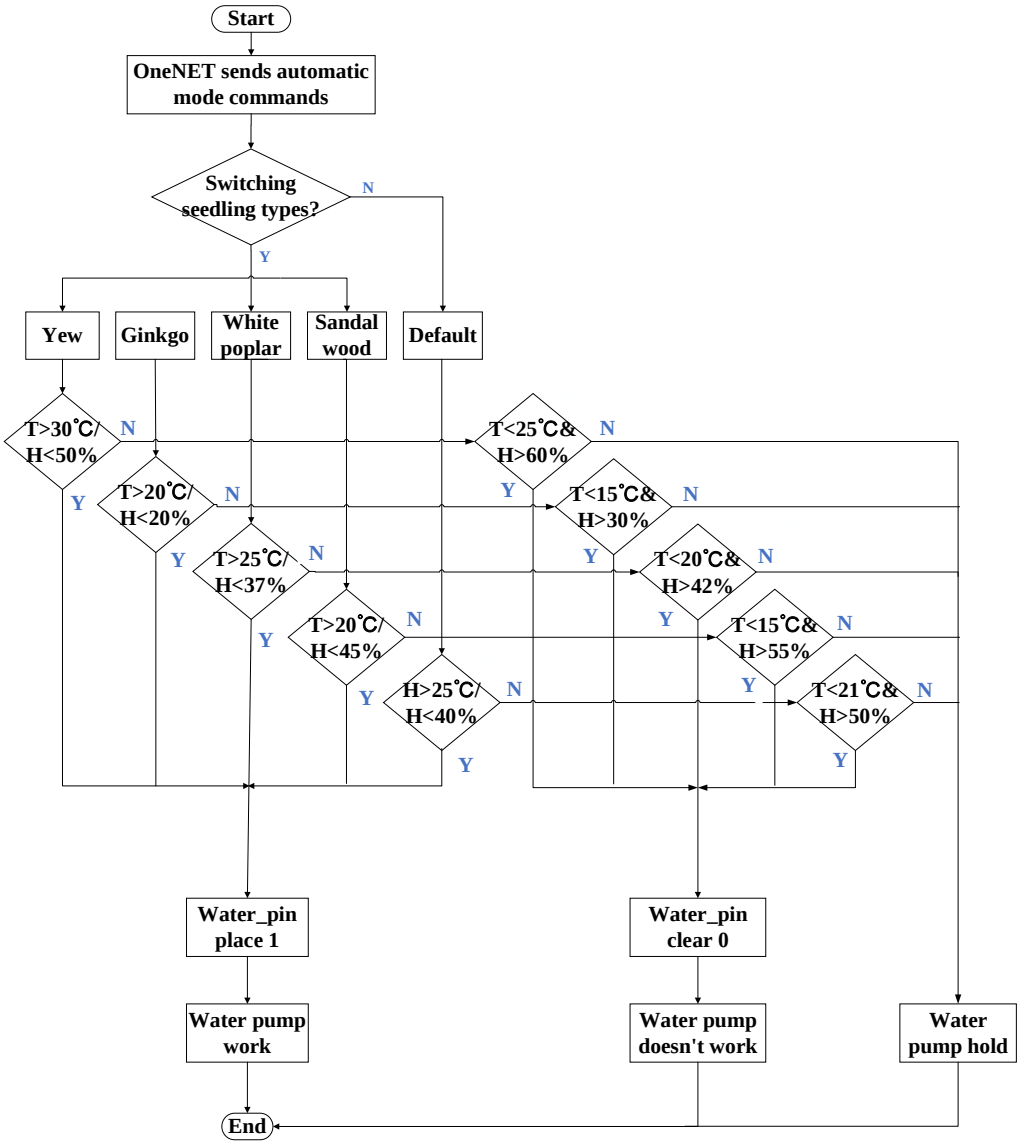


Fig. 8 - Automatic mode flowchart

The client adopts the OneNET platform and carries out visual design. OneNET provides a wealth of data visualization tools, including drag-and-drop editing, 3D project support, various industry templates, and multi-data source docking, which can greatly facilitate and beautify the design interface, and be applied in smart furniture, smart agriculture, water conservancy and hydropower. The open OneNET as an open service platform is used to reduce the development difficulty, save the development cost and shorten the development cycle *(Zhang and Chen, 2020)*. To make the data display and command control more humanized, a data visualization interface with some components and data interface connectivity is designed. The components mainly use control switches, instrument panels and line diagrams. Data filtering is required in data connection, and the filter functions of temperature and humidity instrument panel and line chart are shown in Fig. 9:

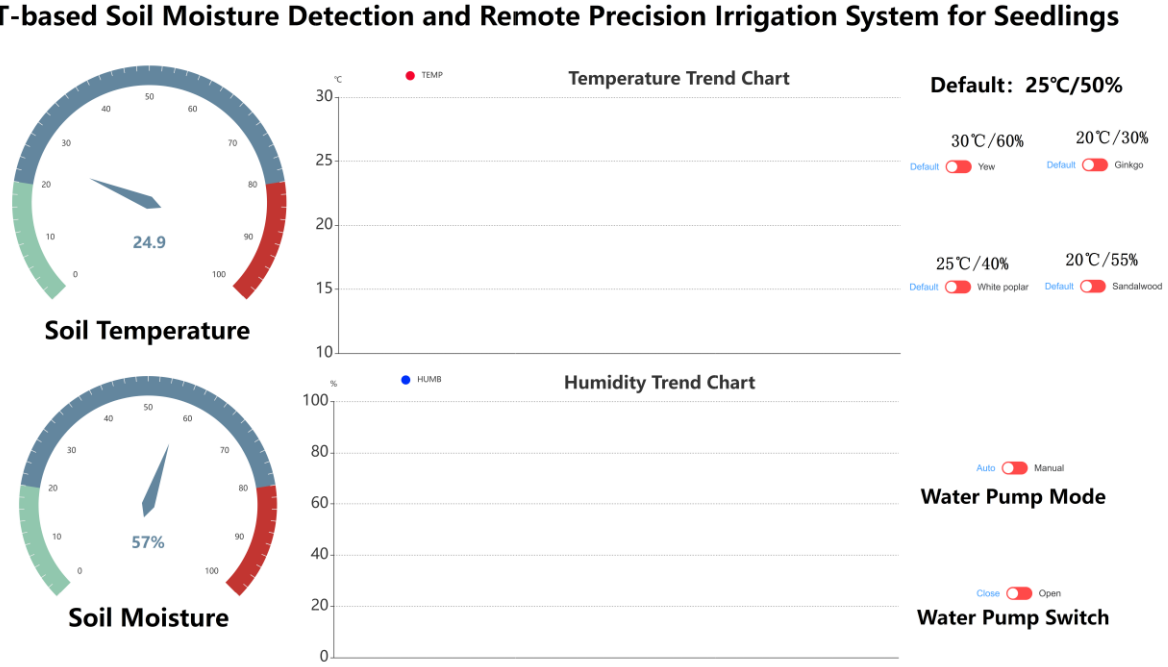


Fig. 9 - OneNET client data visualization interface

RESULTS

After the system design is completed, the function and stability of the whole system are tested to determine whether the system can meet the requirements of the actual working environment. According to the 24-hour test, it mainly tests the ability of the system to work for a long time and the ability of data control accuracy. According to the 24-hour records, the temperature and humidity data are exported to the EXCEL file. The data is updated every three seconds, and the sampling test is selected due to the huge data. The data are shown in Table 1, Table 2 and Table 3, respectively:

Table 1

Test data 1

Time	2022-05-13 00:00	2022-05-13 02:00	2022-05-13 04:00	2022-05-13 06:00
Temperature / °C	17.8	17.5	17.2	17.5
Humidity / %	55.0	54.4	54.0	53.3
Water Pump	Off	Off	Off	Off

Table 2

Test data 2

Time	2022-05-13 08:00	2022-05-13 10:00	2022-05-13 12:00	2022-05-13 14:00
Temperature /°C	18.0	19.0	20.1	20.2
Humidity /%	53.0	38.0	58.0	57.6
Water Pump	Off	On	Off	Off

Table 3

Test data 3

Time	2022-05-13 16:00	2022-05-13 18:00	2022-05-13 20:00	2022-05-13 22:00
Temperature /°C	27.0	19.6	18.3	18.0
Humidity %	56.5	56.0	55.8	55.4
Water Pump	On	Off	Off	Off

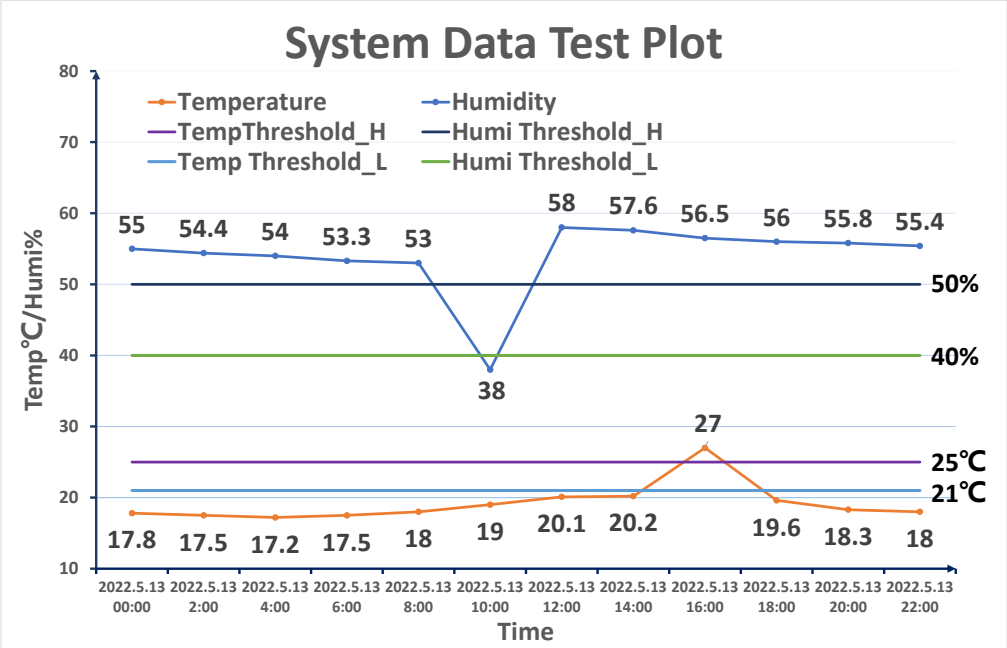


Fig. 10- System test data line chart

In addition, to visually display the changes of each data, the corresponding data line chart is made as shown in Fig. 10. At 10:00 on May 13, human intervention reduced the soil humidity to 38%, and the default automatic mode was automatic watering when the temperature was higher than 25°C or the humidity was less than 40%. When the temperature was lower than 30°C or the humidity was higher than 50%, the watering would be stopped. Therefore, it can be seen from the data that the system has completed the set function. The same intervention was also carried out at 16:00 on May 13. The sensor was pulled out of the soil and held by hand to make the temperature rise to 27°C, and then inserted into the soil, which also triggered the water pump to work and raised the humidity to 70.5% and reduced the temperature to 19.6°C. The system stability was tested for 24 hours, and the data was collected every 3 seconds. A total of 28000 temperature and humidity data were collected, and the packet loss rate was less than 5%. The conclusion is that the system is stable, accurate and reliable without obvious deviation of data, and the system can work stably for a long time and meet the test requirements.

Compared to the study on the precise irrigation system of a blueberry garden based on LoRa and SVM-Markov *(Wu et al., 2022)*, which requires the purchase of corresponding hardware equipment that uses LoRa technology, and has a high computational complexity in the SVM-Markov algorithm that necessitates high-performance computers, this system uses ESP8266-01S as the basis for IOT implementation. It utilizes the STC12C5A60S2 microcontroller as the main control chip, and is easy to operate. In terms of management and maintenance complexity, the LoRa and SVM-Markov system orchards requires regular maintenance and management, and requires technicians to monitor and maintain the system. Our system is very simple and efficient in maintenance due to its simple structure and easy operation. Limited scope of application: The LoRa and SVM-Markov system orchards has a limited scope of application and cannot meet all irrigation needs; Our system is designed with automatic and manual modes for various seedling types and can be programmed to modify the optimal irrigation thresholds for various seedlings and realize the irrigation needs of different seedlings.

Compared with the design of smart planter remote control system based on STM32 and OneNET cloud platform *(Zhang and Guo, 2022)*, the use of STM32 chip is more costly and not suitable for low-cost application scenarios; at the same time, the power consumption is not suitable for application scenarios that need to run for a long time. This system adopts STC12C5A60S2, which has lower cost and is suitable for low-cost application scenarios, especially for seedlings, which need to be applied in large quantities, and cost control is an important factor. The STC12C5A60S2 also has higher operating frequency and faster digital input/output response time. The STC12C5A60S2 also has a more flexible way to build the system, supporting multiple programming modes, such as assembly language and C Programming Language, for more diversity in system programming to suit different conditions.

CONCLUSIONS

1) A seedling soil moisture detection and irrigation system based on WI-FI and OneNET cloud platform is proposed and designed. The system can update soil data in real time with high accuracy and convenient operation. It is applicable to many different seedlings and can be switched between manual and automatic modes. The user is simple to operate, and the operation can be synchronized at the computer end, tablet end and mobile phone end.

2) Taking ESP8266-01S as the basis for the implementation of IoT, STC12C5A60S2 single chip microcomputer as the main control chip to make each module communicate with each other, the soil temperature and humidity detection and remote precision irrigation system based on IoT are realized. The system design structure is reasonable, and the data packet loss rate is less than 5% with certain promotion and application value.

3) Taking the OneNET platform as the client, the data visualization interface is designed to accurately display real-time data and issue commands, and realize wireless, long-distance and real-time monitoring of seedling soil. The intelligent level of soil environment monitoring is improved, and intelligent irrigation of other types of crops also has certain reference significance.

ACKNOWLEDGEMENT

This research was funded by the Henan Provincial Science and Technology Research Project (No. 212102110207), 2021 Henan Science and Technology Commissioner Project, Collaborative Education Project of Ministry of Education (No.220505078205656, No.220503880205011), and the National Natural Science Foundation of China (No.32202096) . We were very grateful to General Manager Ma Junpeng (Hele Nursery Field, Mangshan Town, Yanshi City) for the experimental site provided.

REFERENCES

[1] Ahmed, A. A., Omari, S. A., Awal, R., Fares, A., Chouikha, M. (2021). A distributed system for supporting smart irrigation using Internet of Things technology. *Engineering Reports*, Volume3, Issue7 (e12352), United Kingdom.

[2] Boursianis, A., Papadopoulou, M. S., Gotsis, A., Wan, S., Sarigiannidis, P. G., Nikolaidis, S., Goudos, S. K. (2021). Smart Irrigation System for Precision Agriculture-The ARETHOU5A IoT Platform. *IEEE Sensors Journal*, Vol. 21, pp. 17539-17547. United States.

[3] Garcia, L., Parra, L., Jimenez, J. M., Lloret, J., Lorenz, P. (2020). IoT-Based Smart Irrigation Systems: An Overview on the Recent Trends on Sensors and IoT Systems for Irrigation in Precision Agriculture. *Sensors*, Vol. 20, Switzerland.

[4] García, L., Parra-Boronat, L., Jimenez, J. M., Lloret, J., Abouaissa, A., Lorenz, P. (2019). Internet of Underground Things ESP8266 WiFi Coverage Study. *The Eighth International Conference on Communications, Computation, Networks and Technologies*. pp. 1-6. United States.

[5] Gzar, D. A., Mahmood, A. M., Al-Adilee, M. K. (2022). Recent trends of smart agricultural systems based on Internet of Things technology: A survey. *Computers and Electrical Engineering*, Vol. 104, pp. 108453. England.

[6] Jadon, J. K. S., Singh, R. (2022). Challenges and Opportunities of Internet of Things in Smart Agriculture: A Review. *The 2nd International Conference on Electronic Systems and Intelligent Computing*, Vol. 860, pp. 653-662. Singapore.

[7] Karar, M. E., Alotaibi, F., AL Rasheed, A., Reyad, O. (2021). A Pilot Study of Smart Agricultural Irrigation using Unmanned Aerial Vehicles and IoT-Based Cloud System. *Information Sciences Letters*. Vol. 1, pp. 131-140. United States.

[8] Liu, L. M., Chen, J. F. (2022). Research on Industrial and Agricultural Water Saving Potential in China Provincial Region Based on Meta Frontier DEA Model (基于共同前沿 DEA 的中国省域工农业节水潜力分析). *Water Resources and Power*, Vol. 40, pp. 94-97+111. Hubei/China.

[9] Lu, X. T., Zhang, L. N., Liu, H., Zhi, C. Q., Li, J. (2021). Design of the Networked Precision Irrigation System for Paddy Field Crops in Intelligent Agriculture (智慧农业水田作物网络化精准灌溉系统设计). *Transactions of the Chinese Society of Agricultural Engineering*, Vol. 37, pp. 71-81. Beijing/China.

[10] Monteleone, S., de Moraes, E. A., de Faria, B. T., Aquino, P. T., Maia, R. F., Neto, A. T., Toscano, A. (2020). Exploring the Adoption of Precision Agriculture for Irrigation in the Context of Agriculture 4.0: The Key Role of Internet of Things. *Sensors*, Vol. 20, Switzerland.

[11] Qiu, H. B. (2017). An IoT Design Idea Based on ESP8266 Module (一种基于 ESP8266 模块的物联网设计思路). *Electronics World*, Vol. pp. 157. Beijing/China.

[12] Seng, K. P., Ang, L. M., Ngharamike, E. (2022). Artificial intelligence Internet of Things: A new paradigm of distributed sensor networks. *International Journal of Distributed Sensor Networks*, Vol. 18, United States.

[13] Shen, K. (2021). How to Achieve Water-saving Development in China's Agriculture - Review of "Water-saving agriculture in China" (中国农业如何实现节水发展——评《节水农业在中国》). *Journal of Irrigation and Drainage*, Vol. 40, pp. 159. Henan/China.

[14] Sinha, B. B., Dhanalakshmi, R. (2022). Recent advancements and challenges of Internet of Things in smart agriculture: A survey. *Future Generation Computer Systems*, Vol. 126, pp. 169-184. Netherlands.

[15] Solodovnik, A. I., Savkin, V. I., Amelina, A. V. (2021). The role of the Internet of Things as direction for the development of agriculture 4.0 for rural areas. *IOP Conference Series: Earth and Environmental Science*, Vol. 839. England.

[16] Song, H. Y. (2020). The Status and Problems of Smart Agriculture Development and Responses (智慧农业发展的状况、面临的问题及对策建议). *Frontiers*, Vol. 24, pp. 62-69. Beijing/China.

[17] Vuran, M. C., Salam, A., Wong, R., Irmak, S. (2018). Internet of Underground Things: Sensing and Communications on the Field for Precision Agriculture. *The 4th IEEE World Forum on Internet of Things (WF-IoT)*, Vol. 2018, pp. 586-591. United States.

[18] Wu, D., Liu, Y. H., Luo, Y. J. (2022). Research on precision irrigation system of blueberry orchard based on LoRa and SVM-Markov (基于 LoRa 和 SVM-Markov 的蓝莓园精准灌溉系统研究). *Journal of Chinese Agricultural Mechanization*, Vol. 43, pp. 203-208+215. Jiangsu/China.

[19] Xia, S. F., Wu, J. Y. (2022). Design and Implementation of Automatic Irrigation System Based on Internet of Things (基于物联网的自动灌溉系统设计与实现). *Modern Information Technology*, Vol. 6, pp. 192-194+198. Guangdong/China.

[20] Zhang, Q. L., Chen, X. P. (2020). WiFi Remote Control Smart Home System Based on OneNET Cloud Platform. *Modern Electronics Technique*, Vol. 43, pp. 25-29. Shannxi/China.

[21] Zhang, Y. F., Guo, X. Y. (2022). Design of Intelligent Flowerpot Remote Control System Based on STM32 and OneNET Cloud Platform (基于 STM32 和 OneNET 云平台的智能花盆远程操控系统设计). *Industrial Control Computer*, Vol. 35, pp. 151-152+155. Jiangsu/Nanjing.

[22] Zhao, C. J. (2021). Current Situations and Prospects of Smart Agriculture (智慧农业的发展现状与未来展望). *Journal of South China Agricultural University*, Vol. 42, pp. 1-7. Guangdong/China.

DESIGN AND EXPERIMENT OF TRANSVERSE AXIAL FLOW CORN FLEXIBLE THRESHING DEVICE

/

横轴流玉米柔性脱粒元件的设计与试验

Huabiao LI, Qihuan WANG, Jie MA, Yanan WANG, Dong YUE, Duanyang GENG*)
School of Agricultural and Food Engineering, Shandong University of Technology, Zibo, 255000, China
E-mail: dygxt@sdut.edu.cn

DOI: https://doi.org/10.35633/inmateh-69-43

***Keywords**: Corn, grain direct harvest, flexible threshing, broken rate, impurity rate.*

ABSTRACT

In order to solve the problem of high broken rate and impurity rate in the direct harvesting of corn kernels in China, a flexible threshing element with variable stiffness consisting of a conical spring and rasp bar was developed on the basis of the existing horizontal axial-flow corn threshing cylinder structure to achieve low loss harvesting of corn kernels. Through mechanical analysis of the key components of the threshing element, its structure and operating parameters were determined. Then, orthogonal tests were carried out using the feed amount, threshing clearance and cylinder speed as the test factors, and the broken rate and impurity rate of the corn kernels as the test indicators. The results showed that the feed amount, threshing clearance and cylinder speed had a significant effect on the broken rate and impurity rate of corn kernels; the optimum parameters for the corn variable stiffness flexible threshing device were feed amount 6.1 kg·s^{-1}, threshing clearance 40 mm and cylinder speed 392 r·min^{-1}. The broken rate of corn kernels was 1.67% and impurity rate 1.03%. The test results fully met the requirements of the national standards for corn harvesting operations. This study provides a technical basis for the application of the axial flow corn flexible threshing device in the corn direct harvesting combine.

摘要

为了解决我国玉米籽粒直收过程中籽粒破碎率和含杂率高的问题，在现有横轴流玉米脱粒滚筒结构的基础上，研制了一种锥形弹簧和短纹杆组成的变刚度玉米柔性脱粒元件，实现了玉米籽粒的低损收获。通过对脱粒元件关键部件的力学分析，确定了其结构和工作参数。以玉米果穗喂入量、脱粒间隙和滚筒速度为试验因素，以玉米籽粒的破碎率和含杂率作为试验指标，进行了正交试验。结果表明：果穗喂入量、脱粒间隙和滚筒速度对玉米籽粒破碎率与含杂率均有显著影响；玉米变刚度柔性脱粒装置的最佳参数喂入量 6.1kg·s^{-1}，脱粒间隙 40mm，滚筒速度 392r·min^{-1}。此时，玉米籽粒的破碎率为 1.67%，含杂率为 1.03%。试验结果完全符合玉米收获作业的国家标准要求。本研究为轴流玉米柔性脱粒装置在玉米籽粒直收联合收获机中的应用提供了技术依据。

INTRODUCTION

Corn is not only an important food crop in China, but also has important application value in feed, chemical, energy and other fields *(Srison et al., 2016; Yang et al., 2021)*. In recent years, with the large-scale development of corn planting, labor shortage during the corn harvest season has become an increasingly prominent problem. The direct harvest of corn kernels can complete ear picking, threshing, separation and cleaning operations at one time, which greatly shortens the harvest cycle, effectively saves labor costs and solves the problem of labor shortage *(Li et al., 2020; Yang et al., 2021)*. Therefore, direct harvesting of corn kernels is of great significance for shortening the corn harvest cycle, saving production costs, and promoting the mechanization of corn agriculture *(Akubuo, 2002; Bratan et al., 2019; Chai et al., 2020).*

[1] *Huabiao LI, Postgraduate; Qihuan WANG, Postgraduate; Jie MA, Postgraduate; Yanan WANG, Postgraduate; Dong YUE, Postgraduate; Duanyang GENG, Professor.*

Threshing is a key part of the corn direct harvesting, which directly affects the quality and performance of the entire corn harvest *(Yang et al., 2021)*. Broken rate and impurity rate are important indicators to evaluate the quality of threshing operations *(Shahbazi and Shahbazi, 2018; Su et al., 2020)*. Countries represented by Germany, the United States and other countries usually use combine harvesting machines to directly harvest corn. Large-scale corn harvesters developed by well-known agricultural machinery brands such as John Deere, CASE, and CLASS have high efficiency and degree of mechanization *(Fu et al., 2019)*. In China, scientific research institutions and related enterprises, such as Foton Lovol, Wuzheng Group, and Yongmeng Company, have done a lot of research on corn grain combine harvesters, and have had good field test results in various provinces. However, due to the high grain moisture content of corn harvested in my country, there is still serious kernel damage *(Feng et al., 2019, Chen, 2020, Wang, 2021).*

In order to reduce the rate of corn kernel broken, Chinese scholars have carried out a lot of research. In terms of threshing device, *Srison et al.* explored the effects of threshing cylinder structural parameters and corn characteristics on corn threshing damage and power consumption *(Srison et al., 2016)*. Pužauskas and other studies found that the concave plate structure is an important factor affecting the separation rate of grains, as well as the breakage rate and loss rate of grains *(Pužauskas et al., 2017)*. *Xie et al, (2019),* designed a flexible rod-tooth-type threshing cylinder. Compared with rigid rod-tooth, the flexible rod-tooth can greatly reduce the broken rate of grains. However, most of the current research is the experimental study of the threshing process and technical parameters of the threshing device on the damage to the grain, and there is a lack of innovation and research on the threshing element of the large-scale threshing device of the corn kernel harvester.

In order to solve the above problems, on the basis of the characteristics of the existing threshing cylinder, combined with the characteristics of corn in China, a flexible threshing device with variable stiffness was designed. Through multi-factor orthogonal test, the factors affecting the broken rate and impurity rate of grains were analyzed, and the optimal working parameters were determined. It is hoped that this study can solve the problem of high loss rate and impurity rate in the process of direct harvesting of corn kernels, and improve the quality of corn combine harvesters.

MATERIAL AND METHODS

Overall Structure and Working Principle

The whole structure of the corn variable stiffness flexible threshing device is shown in Fig. 1. It mainly consists of threshing cylinder, upper cover, the guide plate, frame, adjusting concave plate, and screw conveyor, feeding port, blanking plate, grain box, motor and other components.

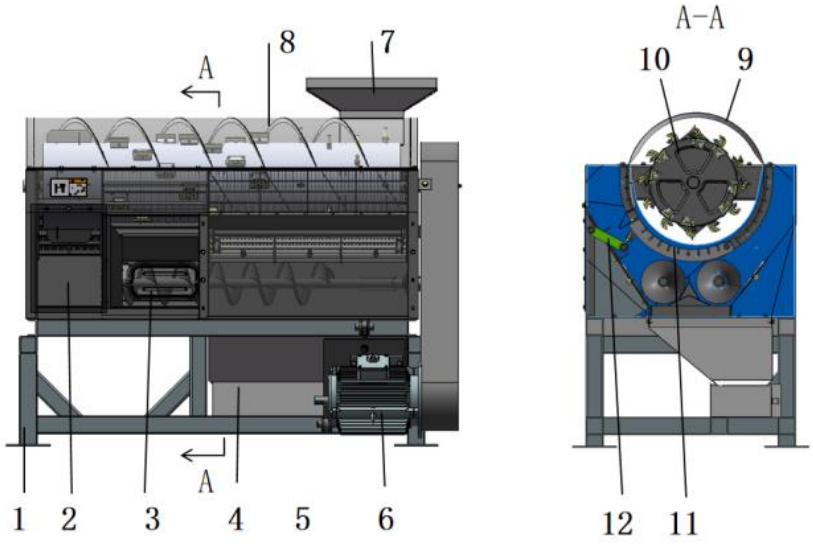


Fig. 1 - Overall structure diagram of flexible threshing device with variable stiffness

1. Frame; 2. Cob outlet; 3. Grain screw conveyor; 4 Grain box; 5. Adjustable concave plate; 6. Electric motor; 7. Corn inlet; 8. Upper cover; 9. The guide plate; 10. Threshing cylinder; 11. Concave; 12. Adjustment device

The corn flexible threshing device adopts the principle of radial feeding and axial flow threshing. When the threshing device is working, the cylinder is driven by the motor, and the corn ears continuously enter the threshing device from the feeding inlet. The ears are forced by the spiral of spike tooth at the front of the cylinder to the threshing section, where they are subjected to the blows of the threshing tooth and striker, the squeezing and friction between the threshing concave plates and the impact between the ears to complete the threshing. Finally, the threshed grains are transported to the grain box through the screw conveyor, and the corncob is discharged from the outlet to complete the whole process.

Design of Threshing Elements

The structure of the threshing element will have a large effect on the kernel broken rate and impurity rate *(Kiniulis et al., 2017; Bratan et al., 2019).* The variable stiffness flexible threshing element designed in this study is shown in Fig. 2. It mainly consists of conical spring seat, cover plate, conical spring, striker block, tension bolt and connecting shaft. The connecting shaft acts on the conical spring seat and the striker block, and the back of the striker block is in contact with the conical spring by the preload of the bolt, and the variable stiffness flexible threshing of the striker block is realized by the variable stiffness characteristic of the conical spring.

The force analysis of the corn cob and threshing element is shown in Fig. 3.

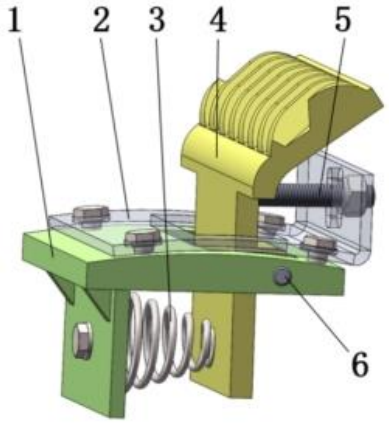


Fig. 2 - The structure of the threshing element
1. Conical spring seat; 2. Cover plate; 3. Conical spring; 4. Grain bar block; 5. Tension bolt; 6. Connecting shaft

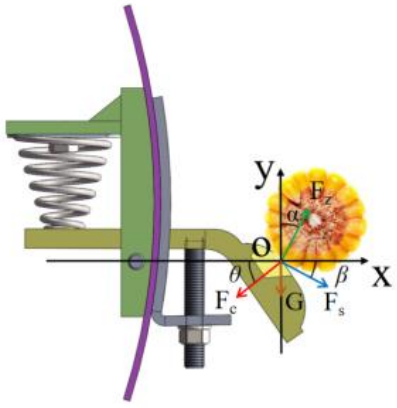


Fig. 3 - Analysis of the threshing force

Take a point of the corn cob impact threshing element, cross the connecting axis horizontal line direction at the point O to establish a coordinate OXY. When the threshing element is working, if the force F_c of the corn cob on the striker is sufficient to turn the striker block backward around the connecting axis as a circle, then the angle α and β will increase, and θ is constant. When the corn cob is in contact with the threshing element, the force in the direction of F_s is:

$$F_s = G\sin\beta - F_c\cos(\beta+\theta)\ [N] \quad (1)$$

Where: G is the gravity, N.

From the above equation (1), it can be obtained:

$$F_c = \frac{G\sin\beta - F_s}{\cos(\beta+\theta)}\ [N] \quad (2)$$

From the above equation, it can be seen that β increases the impact force F_c of the thresher on the cob. Then the threshing force on the cob also increases, which makes the corn cob easier to be threshed. At the same time, the conical spring under the threshing element is compressed, which acts as a cushion and reduces the impact of the thresher on the corn cob, which can reduce the broken rate of the corn kernels. Therefore, the conical spring as a flexible mechanism of the thresher work can greatly reduce the breaking of corn kernels when threshing.

Test Conditions and Instruments

In October 2021, the tests were carried out in the Agricultural Machinery Performance Laboratory of Shandong University of Science and Technology with the self-made variable stiffness threshing cylinder test bench. The test apparatus included a scraper-type cob lifter, an LDS-1G grain moisture meter (Ningbo Comet Instrument Co., Ltd.), a TESTO 465 digital tachometer (Detu Instruments International Trade Co., Ltd.), an ACS20 small electronic scale (Shanghai Huachao Electric Co., Ltd.), an 11kw three-phase asynchronous motor (Taizhou Yinniu Mechanical and Electrical Co., Ltd.) and a SAJ8000 series inverter (Guangzhou Sanjing Electric Co., Ltd.), etc. The test process is shown in Fig. 4.



Fig. 4 - Experimental process

The test material was selected from Zhengdan 958, and the basic characteristics of 50 corn ears were measured randomly using vernier calipers and LDS-1G grain moisture meter before the start of the test, and the values of the basic characteristics of corn ears are shown in Table 1.

Table 1

Corn parameters in experiment

Parameters	Value
Average ear length / mm	145.6
Average large end diameter / mm	50.2
Average small end diameter / mm	45.6
Kernel moisture content / %	27.6~28.5

Test Factors, Indicators and Methods

The corn threshing mechanism relies on the active rotation of the threshing element and the cob, the cob and the cob, the cob and the grating to generate force, ultimately achieving the threshing function *(Pužauskas et al., 2017).* Therefore, the threshing element and concave plate is the key components of the threshing device, its threshing element movement speed, concave clearance and feeding amount are the main factors affecting the threshing performance and kernel breakage.

After the experiment, the test results were measured in accordance with GB/T 21961-2008 "Test Methods for Corn Harvesting Machinery" and GB/T 21962-2020 "Corn Harvesting Machinery". At the end of each test, 2000 g of corn kernels were randomly selected from the kernel collection box, from which corn kernels with obvious cracks, damage, and broken skins were selected and weighed out to calculate the kernel breakage rate according to the following equation (3). During the measurement time, 2000 g of mixed kernels were taken from the kernel collection box, from which the mass of impurities was selected and weighed out to calculate the mass of mixed kernels and the impurity. The impurity rate was calculated according to equation (4).

Broken rate:

$$Z_s = \frac{m_s}{m_i} \times 100\ [\%] \quad (1)$$

Where: m_s is the mass of broken kernels sample, g; m_i is the mass of sample kernels; Z_s is the broken rate, %.

Impurity rate:

$$Z_z = \frac{m_{za}}{m_h} \times 100\ [\%] \quad (4)$$

Where m_{za} is the impurity quality, g; m_h is the mass of mixed grain, g; Z_z is the impurities rate, %.

RESULTS AND DISCUSSION

Orthogonal Test

Based on the results of the single-factor test, the regression analysis was performed on the data using Design-Expert 10.0.3 statistical software with cylinder speed (X_1), concave clearance (X_2) and feeding amount (X_3) as independent variables and the response values of the broken rate Y1 and impurity rate Y_2 of corn kernels, and the regression models of BR and IR were analyzed, and the experimental factor levels were arranged as shown in Table 2.

Table 2

Levels of parameters

Levels	Factors		
	Cylinder speed X_1 / ($r \cdot min^{-1}$)	Concave clearance X_2 / mm	Feed amount X_3 / ($kg \cdot s^{-1}$)
-1	350	35	6
0	400	40	7
1	450	45	8

Multi-factor Test Analysis

The test used the broken rate Y_1 and the impurity rate Y_2 as evaluation indices. Each test group was conducted three times in order to determine the mean value. The experimental design and outcomes are shown in Table 3.

Table 3

Results of multi-factorial tests

Test Number	X_1 ($r \cdot min^{-1}$)	X_2 (mm)	X_3 ($kg \cdot s^{-1}$)	BR (%)	IR (%)
1	-1	-1	0	3.75	6.25
2	1	-1	0	6.05	2.25
3	-1	1	0	2.15	5.07
4	1	1	0	4.75	4.11
5	-1	0	-1	2.16	4.05
6	1	0	-1	5.79	0.99
7	-1	0	1	3.01	4.02
8	1	0	1	6.13	2.15
9	0	-1	-1	3.82	0.83
10	0	1	-1	2.99	2.49
11	0	-1	1	4.45	2.59
12	0	1	1	3.88	3.15
13	0	0	0	3.21	1.33
14	0	0	0	2.86	1.05
15	0	0	0	2.34	1.86
16	0	0	0	2.66	1.15
17	0	0	0	2.88	1.52

The experimental data from Table 4 were subjected to an ANOVA with kernel broken rate and impurity rate as response values; the results are presented in Table 5.

The p value was used to determine the significance of the coefficients and also to test the interaction of the combined factors. As can be seen from the analysis in Table 4, for corn kernel broken rate, the model $p = 0.0005 < 0.001$, indicating that the fitted model reached a highly significant level; the out-of-fit term $p = 0.2129 > 0.05$, the out-of-fit term was not significant, indicating that the regression mathematical model fitted the actual results with high accuracy.

As can be seen from Table 4, ANOVA was performed on the kernel broken rate. the linear term of X_3 and the quadratic term of X_3 were both significant for the broken rate of kernels; the linear term of X_2 and the quadratic term of X_1 were both highly significant for the broken rate of kernels; and the linear term of X_1 was highly significant for the broken rate of kernels. Therefore, the order of the factors affecting the kernel broken rate was as follows: $X_1 > X_2 > X_3$. Since the smaller the broken rate of threshing, the better the quality of threshing.

Table 4

Analysis of variance for kernel broken rate

Variance Source	Sum of Squares of Deviations	Freedom *f*	*F* Value	*p*-Value	Significance Marker
Model	26.68	9	18.34	0.0005	***
X_1	16.97	1	104.96	< 0.0001	***
X_2	2.31	1	14.3	0.0069	**
X_3	0.92	1	5.68	0.0487	*
X_1X_2	0.023	1	0.14	0.7201	
X_1X_3	0.065	1	0.4	0.5461	
X_2X_3	0.017	1	0.1	0.7559	
X_1^2	3.69	1	22.83	0.002	**
X_2^2	0.85	1	5.25	0.0558	
X_3^2	1.26	1	7.77	0.027	*
Residual	1.13	7			
Lack of Fit	0.72	3	2.36	0.2129	not significant
Pure Error	0.41	4			
Cor Total	27.81	16			

Note: X_1 is cylinder speed / ($r \cdot min^{-1}$); X_2 is clearance between concave and cylinder/mm; X_3 is feed amount / ($kg \cdot s^{-1}$); * is significant ($p < 0.05$); ** is very significant ($p < 0.01$); *** is extremely significant ($p < 0.001$); *F* is Fischer's variance ratio; *p* is probability value.

As shown in Table 5, the impurity rate analysis was targeted and the linear terms of X_2 and X_3 and the quadratic terms of X_3 were significant for the impurity rate of the kernels; the interaction of X_1X_2 was highly significant for the impurity rate of the kernels; the linear terms of X1 and the quadratic terms of X_1 and X_2 were highly significant for the impurity rate of the kernels.

Table 5

Analysis of variance (ANOVA) for kernel impurity rate

Variance Source	Sum of Squares of Deviations	Freedom *f*	*F* Value	*p*-Value	Significance Marker
Model	39.07	9	33.08	< 0.0001	***
X_1	12.23	1	93.14	< 0.0001	***
X_2	1.05	1	8.01	0.0254	*
X_3	1.58	1	12	0.0105	*
X_1X_2	2.31	1	17.6	0.0041	**
X_1X_3	0.35	1	2.7	0.1445	
X_2X_3	0.3	1	2.3	0.1728	
X_1^2	13.46	1	102.52	< 0.0001	***
X_2^2	6.58	1	50.14	0.0002	***
X_3^2	0.57	1	4.33	0.0761	*

Variance Source	Sum of Squares of Deviations	Freedom *f*	*F* Value	*p*-Value	Significance Marker
Residual	0.92	7			
Lack of Fit	0.5	3	1.62	0.3179	not significant
Pure Error	0.41	4			
Cor Total	39.99	16			

Note: X_1 is cylinder speed/ (r·min^{-1}); X_2 is clearance between concave and cylinder/mm; X_3 is feed amount/ (kg·s^{-1}); * is significant ($p < 0.05$); ** is very significant ($p < 0.01$); *** is extremely significant ($p < 0.001$); *F* is Fischer's variance ratio; *p* is probability value.

Response Surface Analysis

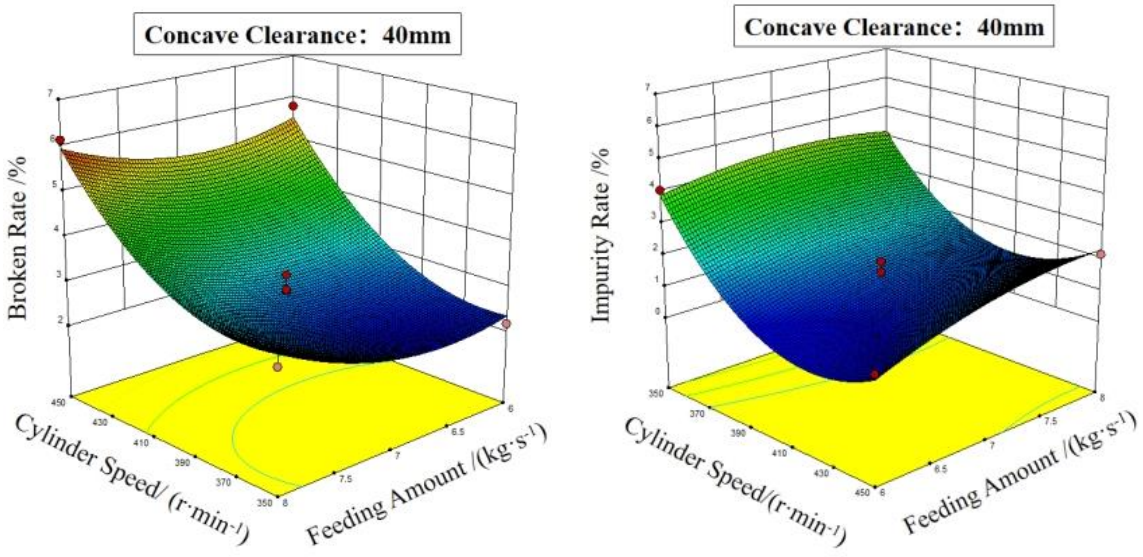
To obtain the influence law of the experimental factors on each test index in a more intuitive manner, study the interaction effect of the other two factors by fixing one factor at zero levels, and transform the regression equation into a three-dimensional contour map using Design Expert10, as depicted in Fig. 5, Fig. 6 & Fig. 7.

$$BR = 1.79 + 1.48X_1 - 0.54X_2 + 0.32X_3 + 0.08X_1X_2 - 0.17X_1X_3 + 0.07X_2X_3 + 0.96X_1^2 + 0.43X_2^2 + 0.57X_3^2 \quad (5)$$

$$IR = 1.38 - 1.24X_1 + 0.36X_2 + 0.44X_3 + 0.76X_1X_2 + 0.29X_1X_3 - 0.27X_2X_3 + 1.79X_1^2 + 1.25X_2^2 - 0.37X_3^2 \quad (6)$$

From Fig. 5(a), it can be seen that when the concave clearance is 40 mm. At a particular cylinder speed, the kernel broken rate falls and then increases as the feeding amount increases. When the feeding amount increases to approximately 7 kg/s, as depicted in figure 5a, the threshing mode changes from striking to rubbing and threshing of corn, which decreases the breaking rate due to an increase in the amount of corn cob in the concave clearance.

As shown in Fig. 5(b), the impurity rate of kernels increased and then decreased with the increase of feeding amount. When the feeding amount is low, the spike tooth inside the cylinder has less impact on the cob and the mutual rubbing effect between the cob and the cob is weak, which is not conducive to the separation of the kernels and the cob, so the impurity rate is larger.

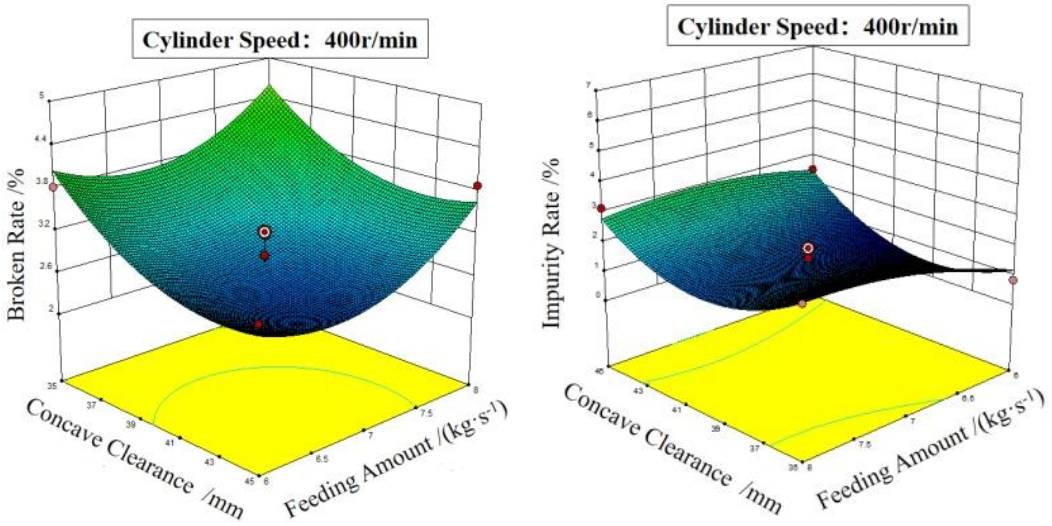


(a) (b)

Fig. 5 - Response surface diagrams of interaction

(a) Interaction of the cylinder speed and feeding amount on broken rate;
(b) Interaction of the cylinder speed and feeding amount on the impurity rate.

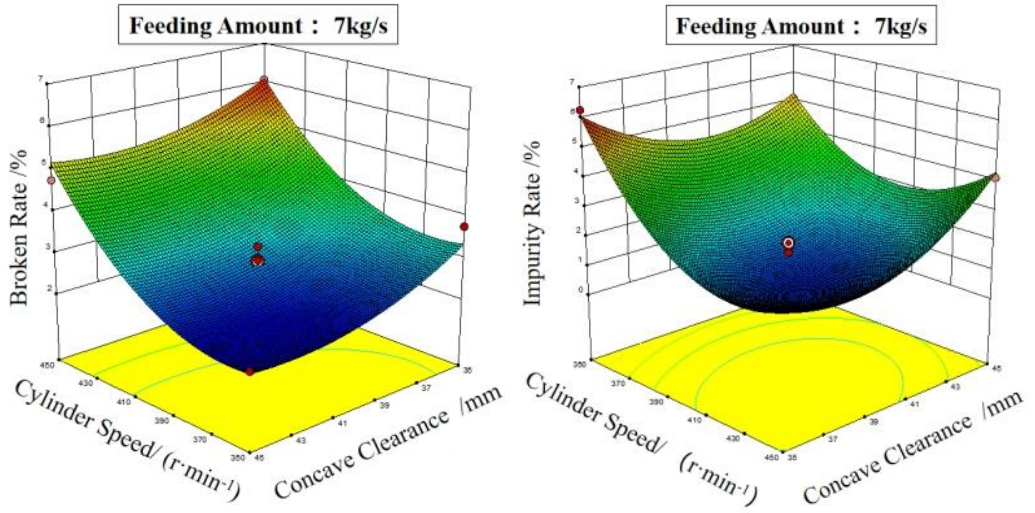
From Fig. 6(a), it can be seen that the increase of concave clearance leads to a slight decrease and then an increase of kernel broken first. It may be because when the feeding amount is small, the threshing space is relatively sufficient, and the change of the concave clearance has less influence on the degree of material filling. From Fig. 6(b), it can be seen that the first reduction in impurity rate gradually increases with the increase in the concave clearance. This is because as the concave clearance increases, the influence of the threshing element on the cob diminishes and the mutual squeezing and friction effects between the cobs diminish, leading to an increase in the impurity rate.



(a) (b)

Fig. 6 - Response surface diagrams of interaction

(a) Interaction of the concave clearance and feeding amount on broken rate;
(b) Interaction of the concave clearance and feeding amount on the impurity rate.



(a) (b)

Fig. 7 - Response surface diagrams of interaction

(a) Interaction of the cylinder speed and concave clearance on broken rate;
(b) Interaction of the cylinder speed and concave clearance on the impurity rate.

From Fig. 7(a), it can be seen that as the cylinder speed increases, the kernel broken rate increases; and as the concave clearance increases, the kernel broken rate shows a decreasing trend. When the cylinder speed increased, the linear velocity of the spike teeth striking the corn increased, which then led to an increase in the collision velocity and a higher broken rate. When the concave clearance increased, the broken rate decreases because the crushing effect of the nail tooth and the concave clearance on the corn cob is reduced.

Fig. 7(b) shows that as the cylinder speed increases, the impurity rate decreases, and as the gap between the concave plate's increases, the impurity rate increases. When the cylinder speed increases, the impact of the spike tooth on the corn cob is enhanced, and the corn kernels are more easily dislodged from the cob, so the impurity rate decreases. When the concave clearance increases, the extrusion of the threshing cylinder to the corn cob and the kneading effect between the corn and the corn are weakened, and the kernels are not easy to come off from the cob, so the rate of impurity increases.

Verification Experiment

The regression equation was solved by Design-Expert software and the optimal operating parameters (decimals rounded) for the results averaged over the variable stiffness corn flexible threshing device was: cylinder speed 392 r·min^{-1}, concave clearance 40 mm, and feeding rate 6.1 kg·s^{-1}. Under these conditions: broken rate 1.67 % and impurity rate 1.03 %.

$$\begin{cases} \mathrm{BR} = \text{minimize} \\ \mathrm{IR} = \text{minimize} \\ 350 < \mathrm{X}_1 < 450 \\ 35 < \mathrm{X}_2 < 45 \\ 6 < \mathrm{X}_3 < 8 \end{cases} \quad (7)$$

To verify the reliability of the regression model, the results were averaged over three trials of the above optimal threshing operation parameters, and the test results showed that the mean value of the broken rate was 1.74% and the mean value of the impurity rate was 0.98%. The relative error with the predicted value is less than 5%, which indicates that the accuracy of the regression model is high. The test results still meet the requirements of the national standard.

CONCLUSIONS

(1) The variable stiffness corn threshing element is designed to reduce the impact on the corn kernels, which can reduce the kernel broken rate.

(2) The optimum values of the operating parameters of the corn threshing unit were determined by multi-factor tests. The ANOVA of the test results showed that the cylinder speed was 392 r·min^{-1}, the concave clearance was 40 mm, and the feed amount was 6.1 kg·s^{-1}. The BR was 1.47% and the IR was 1.03%.

(3) Threshing cylinder speed, concave clearance and feeding amount had significant effects on corn kernel broken rate and impurity rate.

Currently, only one variety of corn has been tested in this study. The team will continue to test different varieties of corn in the field to further validate the threshing performance and adaptability of the designed threshing device.

ACKNOWLEDGEMENT

This research was funded by the National Key R&D Program of China, grant number 2021YFD2000502, the Natural Science Foundation of Shandong Province, grant number ZR202111290044.

REFERENCES

[1] Akubuo, C. O. (2002). PH—Pastharvest Technology: Performance Evaluation of a Local Maize Sheller. *Biosystems Engineering*, Vol. 83, 77-83. England. https://doi.org/10.1006/bioe.2002.0095

[2] Bratan, S., Safonov, V., Zhalnin, E., Lapa, M., & Bordan, D. (2019). Use of vortex flows for aerodynamic threshing of agricultural crops. *E3S Web of Conferences*, Vol. 126. Russia. https://doi.org/10.1051/e3sconf/201912600004

[3] Chai, X., Zhou, Y., Xu, L., Li, Y., Li, Y., & Lv, L. (2020). Effect of guide strips on the distribution of threshed outputs and cleaning losses for a tangential-longitudinal flow rice combine harvester. *Biosystems Engineering*, Vol. 198, 223-234. England. https://doi.org/10.1016/j.biosystemseng.2020.08.009

[4] Chen, Z., Wassgren, C., & Ambrose, K. (2020). A Review of Grain Kernel Damage: Mechanisms, Modeling, and Testing Procedures. *Transactions of the ASABE*, 63(2), 455-475. https://doi.org/10.13031/trans.13643

[5] Feng, J., Wu, Z., Qi, D., Jin, Y., & Wu, W. (2019). Accurate measurements and establishment of a model of the mechanical properties of dried corn kernels. *International Agrophysics*, Vol. 33, 373-381. Poland. https://doi.org/10.31545/intagr/110845

[6] Fu, Q., Fu, J., Chen, Z., Han, L., & Ren, L. (2019). Effect of impact parameters and moisture content on kernel loss during corn snapping. *International Agrophysics*, Vol. 33, 493-502. Poland. https://doi.org/10.31545/intagr/113490

[7] Kiniulis, V., SteponaviČIus, D., KemzŪRaitĖ, A., AndriuŠIs, A., JukneviČIus, D. (2018). Dynamic Indicators of a Corn Ear Threshing Process Influenced by the Threshing-Separation Unit Load. *Mechanics*, Vol. 24, 412-421. Lithuania. https://doi.org/10.5755/j01.mech.4.24.20721

[8] Li, X., Du, Y., Guo, J., Mao, E. (2020). Design, Simulation, and Test of a New Threshing Cylinder for High Moisture Content Corn. *Applied Sciences*, Vol. 10, 4925. Switzerland. https://doi.org/10.3390/app10144925

[9] Pakhomov, V. I., Braginets, S. V., Bakhchevnikov, O. N., Benova, E. V., Rukhlyada, A. I. (2020). Experimental Data of the Ear Threshing Process in a Pneumatic Device. *Engineering Technologies and Systems*, Vol. 30, 111-132. Russian Federation. https://doi.org/10.15507/2658-4123.030.202001.111-132

[10] Pužauskas, E., Steponavičius, D., Jotautienė, E., Petkevičius, S., & Kemzūraitė, A. (2017). Substantiation of concave crossbar shape for corn ear threshing. *Mechanics*, 22(6). https://doi.org/10.5755/j01.mech.22.6.16370

[11] Wang, B., Wang, J. (2019). Mechanical properties of maize kernel horny endosperm, floury endosperm and germ. *International Journal of Food Properties*, Vol. 22, 863-877. United States. https://doi.org/10.1080/10942912.2019.1614050

[12] Wang, D., Tian, H., Zhang, T., He, C., & Liu, F. (2021). Dem Simulation and Experiment of Corn Grain Grinding Process. *Engenharia Agricola*, 41(5), 559-566. https://doi.org/10.1590/1809-4430-eng.agric.v41n5p559-566/2021

[13] Shahbazi, F., Shahbazi, R. (2018). Mechanical Damage to Corn Seeds. *Cercetari Agronomice in Moldova*, Vol. 51, 1-12. Poland. https://doi.org/10.2478/cerce-2018-0021

[14] Srison, W., Chuan-Udom, S., Saengprachatanarak, K. (2016). Effects of operating factors for an axial-flow corn shelling unit on losses and power consumption. *Agriculture and Natural Resources*, Vol. 50, 421-425. Thailand. https://doi.org/10.1016/j.anres.2016.05.002

[15] Su, Z., Li, Y., Dong, Y., Tang, Z., Liang, Z. (2020). Simulation of rice threshing performance with concentric and non-concentric threshing gaps. *Biosystems Engineering*, Vol. 197, 270-284. England. https://doi.org/10.1016/j.biosystemseng.2020.05.020

[16] Xie, F., Luo, X., Lu, X., Sun, S., Tang, C. (2009). Experiment on the influence of flexible drum structure parameters on rice threshing effect (柔性滚筒结构参数对水稻脱粒效果的影响试验). *Research on Agricultural Mechanization*, Vol. 31, 147-151. Heilongjiang/China.

[17] Yang, R., Chen, D., Zha, X., Pan, Z., Shang, S. (2021). Optimization Design and Experiment of Ear-Picking and Threshing Devices of Corn Plot Kernel Harvester. *Agriculture*, Vol. 11, 904. Switzerland. https://doi.org/10.3390/agriculture11090904

[18] Yang, H., Cao, M., Wang, B., Hu, Z., Xu, H., Wang, S., Yu, Z. (2022). Design and Test of a Tangential-Axial Flow Picking Device for Peanut Combine Harvesting. *Agriculture*, Vol. 12, 179. Switzerland. https://doi.org/10.3390/agriculture12020179

STUDY ON THE LOSS CONTROL SYSTEM OF WHEAT COMBINE HARVESTER
/
小麦联合收获机损失控制系统研究

Jizhong WANG[1)], Xianfa FANG[1,*)], Fengzhu WANG[1)], Yangchun LIU[1)], Bo ZHAO[1)]
[1)] National Key Laboratory of Agricultural Equipment Technology,
Chinese Academy of Agricultural Mechanization Sciences, Beijing, 100083, China
[*]E-mail: 780227311@qq.com
DOI: https://doi.org/10.35633/inmateh-69-44

Keywords: *Feeding quantity; drum speed; harvest loss; walking speed; automatic control system*

ABSTRACT
In order to reduce the harvest loss and optimize and improve the comprehensive performance of the combine harvester, the relationship between the feeding quantity, drum torque, drum speed, harvest loss, and other factors of the wheat combine harvester is studied, and the functional relationship between the loss, feeding quantity and speed is determined. According to the test data, the relationship model between the feeding quantity of the harvester and the drum torque is a quadratic function. For the land with uniform growth, the size of feeding quantity is mainly affected by the forward speed of the harvester. In this way, this paper indirectly achieves the purpose of controlling the feeding quantity by controlling the speed of the harvesting machinery. The control system designed in this paper uses the compensated fuzzy PID to control the walking speed of the vehicle through real-time detection of the drum torque, drum speed and loss of the harvester, so as to comprehensively control the working speed of the harvester and effectively control the harvest loss. The test results show that the control system can effectively reduce the harvest loss and improve the harvest efficiency compared with the manual harvest of the wheat.

摘要
为减少小麦联合收获机收获过程中的收获损失，优化提升联合收获机工作综合性能，本文对小麦联合收获机的喂入量、滚筒转矩、滚筒转速、收获损失等因素间的相互关系进行研究，并确定了损失与喂入量、车速等之间的函数关系。根据试验数据分析得到收获机的喂入量与滚筒转矩呈一次函数关系模型；喂入量与收获损失呈二次函数关系模型。由分析数据模型可知，通过改变收获机械喂入量，可实现低损失控制；喂入量的大小对于长势均匀的地块而言，其主要受收获机械前进速度影响，因此本文通过控制收获机械的车速间接达到控制喂入量的目的。本文所设计的控制系统，通过实时检测收获机的滚筒转矩和滚筒转速及损失等数据，使用补偿式模糊 PID 控制车辆的行走速度，实现综合控制收获机械的工作速度进而达到有效控制收获损失。试验结果表明，该控制系统与人工操作收割小麦相比，有效降低了收获损失，提高了收获效率。

INTRODUCTION
During the working process of the combine harvester, there will be different harvest losses due to the influence of harvesting time and harvesting method, among which the harvest losses mainly include pre-harvest losses, header losses and harvest process losses *(Cujbescu et al., 2021)*. Pre-harvest loss refers to the loss of grain falling caused by natural factors such as wind, rain and maturity before harvest. This loss is natural loss and is affected by uncontrollable factors of natural attributes. The header loss is mainly composed of missed cutting, grain falling and ear loss, which is affected by grain maturity, operation route, and the reel position and rotation speed *(Vlăduț et al., 2022)*. In addition to the natural properties of grains, the harvest loss is also mainly affected by the harvest parameters such as the feeding quantity, and the ratio of grass to grain. This loss directly affects the efficiency and operation quality of the harvester *(Sessiz and Ulger, 2003; Bhardwaj et al., 2021; Ivan et al., 2015)*. The losses in harvesting process mainly include threshing loss, separation loss and cleaning loss, which are caused by threshing, separation and cleaning devices of the combine harvester respectively.

To reduce the harvest loss of the combine harvester, many scholars have conducted a lot of researches on the factors related to the harvest loss and structural control. According to detecting the load of the inclined conveying feeding roller, *Coers and Burke, (2004),* indirectly measured the feed in quantity of the harvester and controlled the speed of the harvester according to the feeding quantity, so as to improve the efficiency.

[1]*Jizhong WANG, Dr., Xianfa FANG, Dr., Fengzhu WANG Dr., Yangchun LIU Dr., Bo ZHAO, Dr.*

Staiert and Krukow (1982) designed a control structure for the feeding roller and tried to achieve the purpose of uniform grain feeding by changing the speed of the feeding roller. Through analyzing the relevant structure of the harvester and the relationship between the feeding quantity and the threshing drum, *Budzich(1964)* designed a measurement system to detect the feeding quantity of the measurement system by detecting the torque of the threshing drum, so as to realize the control of the working speed. Based on the experiments of 3 models, *Chen et al. (2011)* studied the relationship between the feeding quantity and harvest loss. A relationship model based on power function, exponential function and quadratic function was established, in which the quadratic function model had high accuracy *(Chen et al., 2020)*. According to the detection of the feeding quantity through the pressure sensor installed on the tilt conveyor, many tests were carried out. Finally, a feeding quantity model based on the pressure of grains on the bottom plate of the tilt conveyor was established for the feedback of the working speed and the control of the feeding quantity *(Chen et al., 2020)*.

Most scholars obtain the feeding information by detecting different parts of the harvester to control the speed and improve the efficiency of the vehicle, but ignore the harvest loss *(Wang et al., 2018; Mu et al., 2018; Marjanović et al., 2018; Madhusudana et al., 2018; Chai et al., 2020; Galluzzi et al., 2018)*. It is necessary to reduce harvest loss while improving the efficiency. Based on the feeding quantity, the harvest loss of the combine harvester is studied and a compensation fuzzy PID automatic walking control system based on the drum torque and drum speed is proposed.

MATERIALS AND METHODS

Sample acquisition

The RevoGushen GE80-H wheeled grain combine harvester (rated feeding quantity 8.0 kg/s, cutting range 2.65 m, productivity 0.6-1.3 hm2/h) was used as the test prototype, as shown in Fig.1. A field harvesting experiment of wheat was carried out in Jimo District, Qingdao, Shandong Province to obtain a large amount of experimental data. The test field was divided into small plots with a width of 2.75m and a length of 26m, and 24 small plots in all. For each small plot, the four-point sampling method was used to collect four corners of the plot as test samples. The side length of the collected sample was 0.5m, and the area was 0.25m^2. The average value of the four groups of data was calculated to obtain the wheat planting density, the ratio of grain to grass and other information of the test plot. After removing 0.5m from both ends of the small plot, the remaining plot will be used as the plot for harvest test. In the test, the plots were harvested at different speeds. GPS was used to record the real-time track information and speed information to obtain the working condition of the drum torque and drum speed of the combine harvester under different feeding quantities.

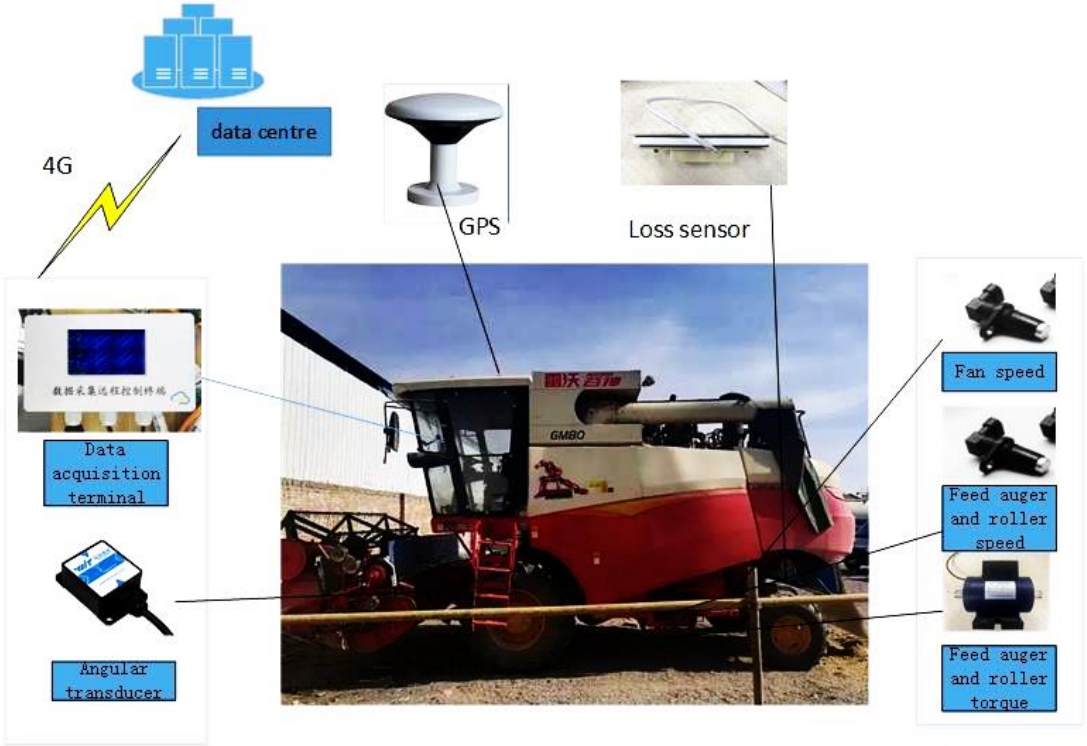


Fig. 1-Test prototype

Test principle

In addition to being related to the structure of the vehicle, the harvest loss generated in the harvesting process of the combine harvester will also be greatly related to the feeding quantity *(Pokojski et al., 2019)*. Among them, the influencing factors of the feeding quantity q_i per unit time of the header mainly includes the cutting width B, the working speed v, the grain density W and the grain-grass ratio γ. The mathematical relationship model of the feeding quantity per unit time of the header is as follows:

$$q_i = \frac{B\ v\ W}{10000}\left(1 + \frac{1}{\gamma}\right) \quad (1)$$

For a specific combine harvester, the cutting width B is a constant. During the harvesting, the header height of the combine harvester is almost constant, and the grain-straw ratio γ isalmost unchanged. The grain density W fluctuates greatly in the field, which is not only related to the number of plants per unit area and growth potential, but also related to the moisture content of straw *(Li et al., 2019)*. The operation speed v is the working speed of the vehicle, which will vary due to the influence of the ground and the driver. When the working speed increases, the feeding quantity will also increase *(Reddy and Rangadu, 2018*). To this end, it is necessary to control the operating speed v of the harvester to control the feeding quantity of the harvester.

The crop is transported from the header to the threshing drum through the conveyor. The feeding quantity of the conveyor is the same as the harvest of the header at unit time. The feeding quantity flowing into the threshing drum can be obtained as follows:

$$q_r = q_i * \delta(t - t_s) \quad (2)$$

where:

q_r is the feeding quantity of the threshing drum; *t* is the feeding time, and t_s is the transfer delay time from the header to the threshing drum.

In addition to providing no-load load moment and inertia moment for itself, the threshing drum also needs to provide kinetic energy moment for the input grain. When the drum is unloaded, it is necessary to overcome the mechanical friction resistance during rotation and the blowing resistance of the drum. According to the drum theory, the no-load torque of the threshing drum can be obtained as follows:

$$\mathrm{M_{rk}} = \mathrm{A} + \mathrm{B}\omega^2 \quad (3)$$

where"

ω is the angular velocity of the threshing drum; A is the torque generated by mechanical friction, and B is the blower torque coefficient of the drum. The moment of inertia of the threshing drum is as follows:

$$\mathrm{M_{rg}} = \mathrm{J}\frac{\mathrm{d}\omega}{\mathrm{dt}} \quad (4)$$

where:

J is the moment of inertia of the threshing drum, and ω is the angular velocity of the threshing drum.

During the harvesting, the grain fed into the drum is set to be evenly feeding and the threshing space is constantly flowing, then the overall power consumption of the threshing drum is as follows:

$$\mathrm{P_c} = \zeta\frac{\mathrm{q_r}}{1-\mathrm{f}}\mathrm{R}^2\omega^2 \quad (5)$$

Where:

ζ is the correction coefficient;f is the comprehensive kneading friction coefficient when the grain passes through the threshing drum gap, and R is the drum radius.

The torque $\mathrm{M_{rc}}$of the drum threshing at this time is as follows:

$$\mathrm{M_{rc}} = \zeta\frac{\mathrm{q_r}}{1-\mathrm{f}}\mathrm{R}^2\omega \quad (6)$$

The total torque of the threshing drum is as follows:

$$\mathrm{M} = (\mathrm{A} + \mathrm{B}\omega^2) + \mathrm{J}\frac{\mathrm{d}\omega}{\mathrm{dt}} + \zeta\frac{\mathrm{q_r}}{1-\mathrm{f}}\mathrm{R}^2\omega^2 \quad (7)$$

From the above, when the threshing drum rotates at a constant speed (ω is a fixed value), the torque and the feeding quantity of the threshing drum are a function relationship, which can better reflect the size of the feeding quantity.

In the actual harvesting process, when the feeding quantity of the threshing drum of the combine harvester is too small, the kneading between the threshing drum and the grain is not sufficient, resulting in unclean threshing and increasing losses. If the feeding quantity of the threshing drum is too high, the separation and cleaning system will not be able to fully separate and clean the threshed materials, resulting in an increase in the loss rate of the harvest. To reduce the loss rate of the harvester, it is necessary to effectively control the feed rate of the harvester.

Scheme design of the speed control system

The aim of the control system of the combine harvester is to reduce the harvest loss. A complementary PID control system scheme is thus designed to control the walking speed of the harvester, and then indirectly control the feeding quantity to reduce the harvest loss. The sensors used in the system include torque sensor, speed sensor and GPS. The torque sensor installing on the rotating shaft of the threshing drum is used to detect the torque of the threshing drum, so as to detect and obtain the feeding information of the vehicle. The speed sensor is installed on the axis of the threshing drum to detect the speed of the threshing drum. GPS is used to detect the driving track and speed of the vehicle.

PID control is a widely used control method for control system, and its control system expression is as follows:

$$\mathrm{u}(t) = \mathrm{K_p} e(t) + \mathrm{K_i} \int_0^{\mathrm{k}} e(k) + \mathrm{K_d} \frac{\mathrm{de(t)}}{\mathrm{dt}} \quad (8)$$

In practical applications, signal acquisition is generally discrete, and the discrete PID is used commonly. Its discrete PID control expression is as follows:

$$\mathrm{u}(k) = \mathrm{K_p} e(k) + \mathrm{K_i} \sum e(k) + \mathrm{K_d}(e(k) - e(k-1) \quad (9)$$

In order to reduce the impact of cumulative error, the incremental PID can be used for control, and its formula is as follows:

$$\Delta \mathrm{u}(k) = \mathrm{u}(k) - \mathrm{u}(k-1) = \mathrm{K_p}(e(k) - e(k-1)) + \mathrm{K_i} e(k) + \mathrm{K_d}(e(k) - 2e(k-1) + e(k-2) \quad (10)$$

In PID control, $\mathrm{K_p}$is the proportional control coefficient that is used to reflect the deviation signal of the control system proportionally and make the system immediately produce control effect to reduce the deviation.The output u(t)of the proportional controller is proportional to the input deviation e(t), which can quickly reflect the deviation to reduce the deviation, but cannot eliminate the static error. $\mathrm{K_i}$is the integral control coefficient, which is mainly used to eliminate the static error and improve the error-free degree of the system. However, if the integral coefficient is too large, the integral effect will be too strong, resulting in the increase of system overshoot and even the oscillation of the system.$\mathrm{K_d}$isa differential control coefficient that is used to reflect the change trend of the deviation signal *(Lopez and Rubio, 2018).* It can introduce an effective early correction signal into the system before the value of the deviation signal becomes too large, so as to speed up the action speed of the system and reduce the adjustment time. If the differential time constant is too large, it will make the system unstable and easy to introduce high-frequency noise.

To effectively control the system, the fuzzy PID control is introduced based on PID control. Through fuzzy reasoning, the three parameters Kp, Ki and Kd are effectively controlled, so that it can control and use different PID parameters under different deviations to quickly and stably achieve the control goal*(Sun et al., 2021)*.

This design uses the compensation fuzzy PID control algorithm. This algorithm uses the fuzzy PID to change the three parameters, Kp, Ki and Kd, of the incremental PID through the error $\mathrm{e_1}$ and the error variation$\mathrm{e_1}'$ to obtain the speed control. Its control diagram is shown in Fig. 2.To improve the response speed of the system when the feeding quantity is too large, the system will make fuzzy prediction to the drum speed error and amplify the output of fuzzy PID in different proportions *(Wu et al., 2018)*, so as to compensate the sensitivity of the fuzzy PID control for large feeding quantity, and finally obtain the vehicle speed to be controlled.The control process is shown in Fig. 2.*(Aulin et al., 2019).*

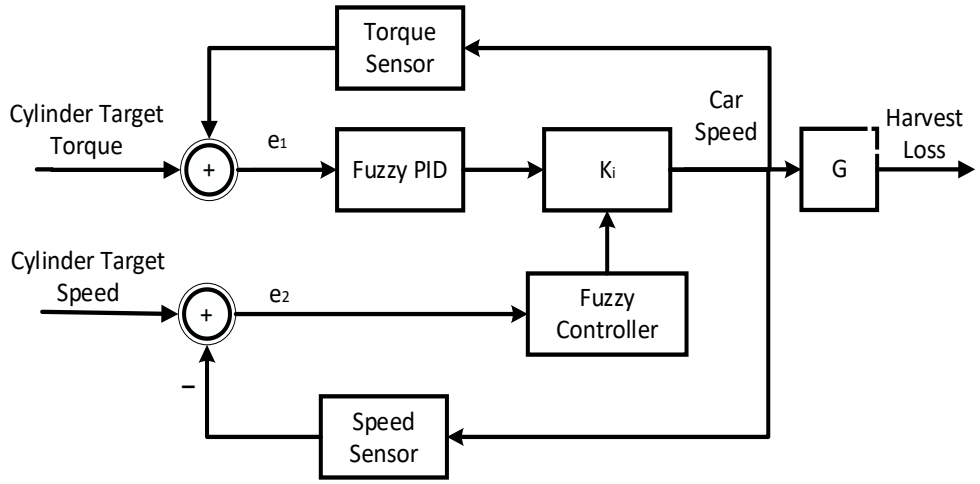


Fig. 2 - Flow of combine loss control system

RESULTS AND ANALYSIS

Data analysis

The data of 24 test plots obtained through the test are shown in Table 1.

Table 1

Data sheet of the test plot

Plot No.	Feeding quantity (kg/s)	Operating speed (m/s)	Drum torque (Nm)	Drum speed (r/min)	Loss rate (%)
0	0	0	28.63	1184	
1	1.46	0.76	55.32	1184	2.32
2	1.71	0.95	55.38	1183	2.43
3	1.74	1.02	53.8	1183	2.22
4	1.85	0.89	63.65	1182	1.77
5	2.16	0.99	78.6	1183	2.05
6	2.66	1.45	96.51	1182	1.59
7	3.06	1.43	100.09	1182	1.27
8	3.16	1.26	98.63	1180	1.20
9	3.52	1.33	109.35	1179	1.22
10	3.57	1.56	112.25	1180	1.24
11	3.59	1.85	118.23	1181	1.23
12	3.86	1.82	115.23	1178	1.32
13	3.91	1.71	121.65	1175	1.27
14	4.09	1.84	131.34	1169	1.32
15	4.56	1.86	132.65	1163	1.48
16	4.91	2.01	147.06	1168	1.89
17	5.15	2.05	156.21	1160	2.27
18	5.56	2.06	142.92	1157	2.38
19	5.66	2.05	163.51	1156	2.21
20	5.69	2.46	156.38	1158	2.24
21	5.85	2.16	166.85	1144	2.48
22	6.55	2.55	172.69	1139	2.68
23	6.56	2.90	160.84	1141	2.45
24	6.66	2.50	173.09	1138	2.72

Note: The plot with label 0 is the operating condition of the vehicle when the combine harvester runs without load.

According to the test data, the relationship curve between the feeding quantity and rotation speed is shown in Fig. 3.

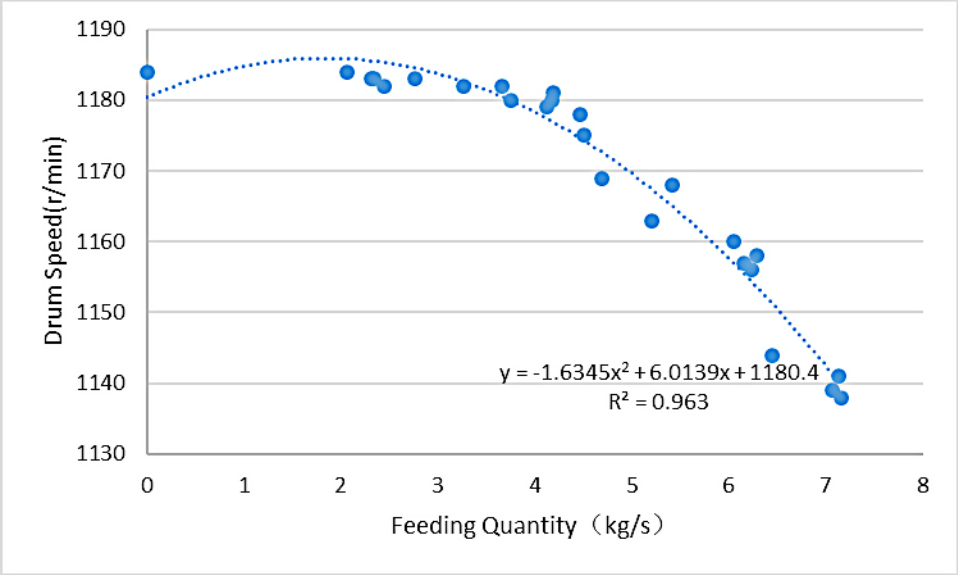


Fig. 3 - Relation curve between the feeding quantity and rotation speed

As shown in Fig. 3, when the feeding quantity is lower than 3.76kg/s, the rotation speed of the threshing drum is relatively stable and will not change with the feeding quantity. When the speed is greater than 3.76kg/s, the speed of the threshing drum will decrease with the increase of feeding quantity due to the large load. The numerical relationship between the feeding quantity and the drum torque obtained from the test is shown in Fig. 4.

According to Fig. 4, there is a functional relationship between the feeding quantity and torque of the combine harvester. R^2 is 0.9673, and the greater the feeding quantity, the greater the torque. The numerical relationship between the feeding quantity and the harvest loss obtained from the test is shown in Fig. 5.

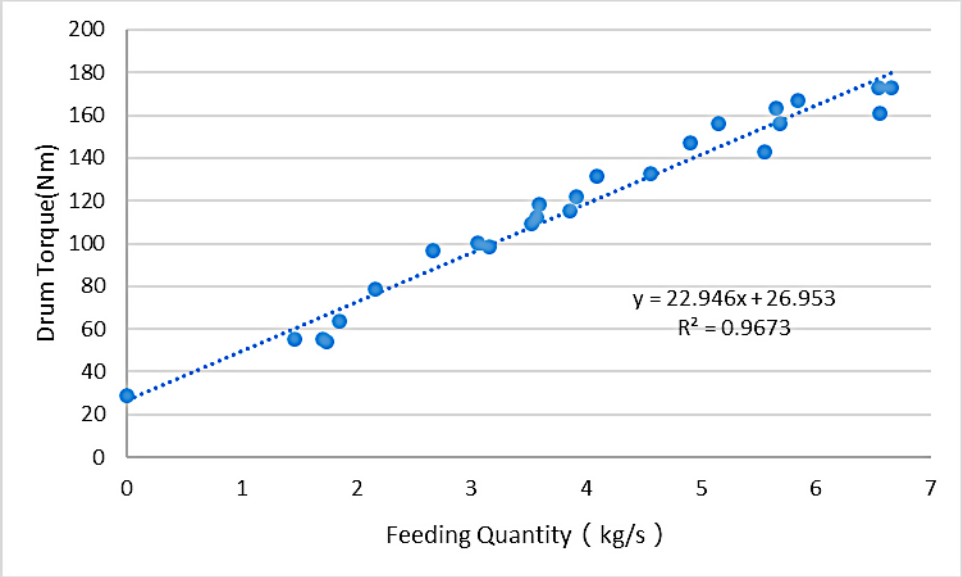


Fig. 4 - Relation curve between the feeding quantity and the drum torque

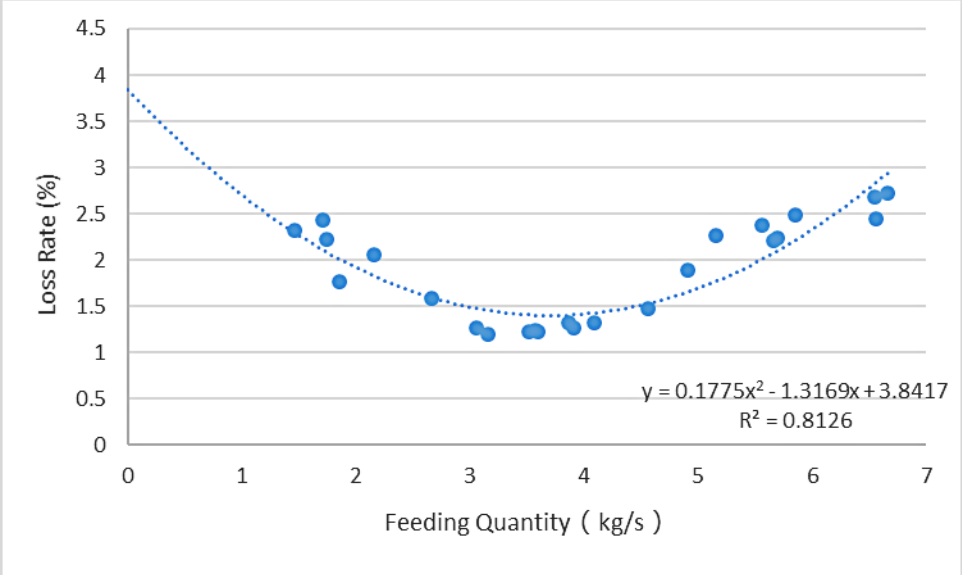


Fig. 5 - Relation between the feeding quantity and the harvest loss

According to the fitting curve between the feeding quantity and the harvest loss in Fig. 5, the quadratic function relationship model is higher than the primary function relationship and the power exponential relationship, which can better reflect the relationship between the two, and its R^2 is 0.8126.The relationship obtained from this model is as follows:

$$Y=0.1775X2-1.3943X+4.1224 \quad (11)$$

From this relationship curve, the lowest point is X=3.71kg/s. When the feeding quantity is 3.71kg/m, the harvest loss of the combine harvester can reach the minimum. In this way, taking this point as the target point of the feeding quantity of the control system can minimize the harvest loss. Since the feeding quantity is difficult

to measure directly, it can be reflected by the drum torque and drum speed at this time. According to the above data model, it can be concluded that the drum torque corresponding to the feeding control target at this time is 112.08Nm and the drum speed is 1180r/min.

Control system result analysis

According to the above results, the torque error of the drum is set to [-20Nm, 20Nm] and is divided into 7 levels using the triangular membership algorithm; the change rate of the drum torque error is set to [-10Nm, 10Nm]and is divided into 7 levels using the triangular membership algorithm; the speed error of the drum is set to [-25r/min, 25r/min]and is divided into five levels using the triangular membership algorithm; the error change rate of the drum speed is set to [10r/min, 10r/min] and divided into five levels using the triangular membership algorithm. The fuzzy control rules and tables, and a complete combine harvester control system are designed.

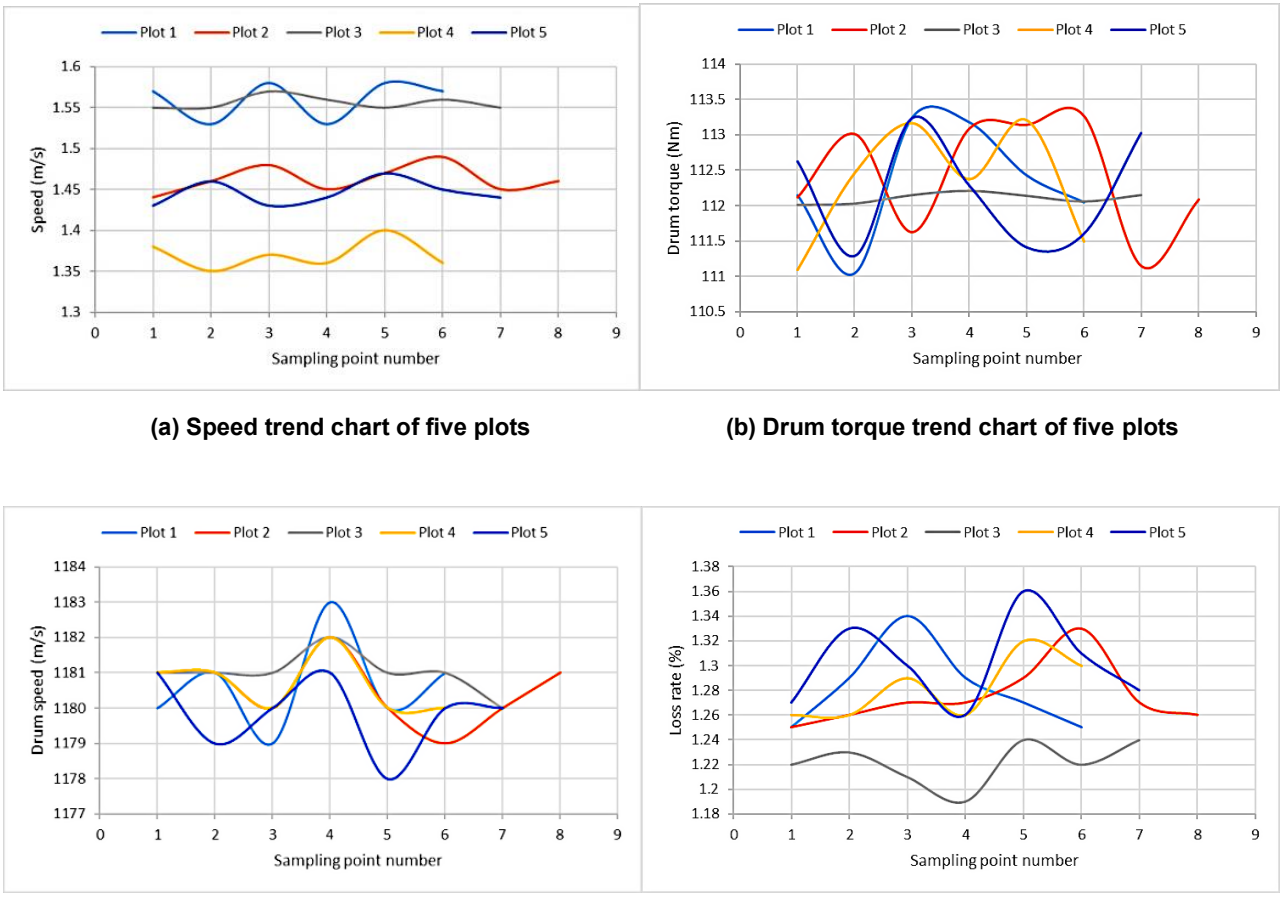
The actual harvest test was carried out on the designed control system, and the relevant verification test was carried out in Rizhao, Shandong Province. A total of 5 different plots were selected in the experiment, and the automatic control system was used to harvest wheat on the plots. During the harvesting process, GPS was used to obtain the real-time positioning and speed of the vehicle. During the walking process, the sampling points were randomly selected, each with a length of 10m and a width of 2.75m. The central axis was symmetrical with the track of the vehicle. The wheat harvest losses were collected manually, and the data after the test is shown in Table 2 as follows.

Table 2

Experimental data of the control system

Plots	Sampling point label	Speed (m/s)	Drum torque (Nm)	Drum speed (r/min)	Loss rate (%)
Plot 1	1-1	1.57	112.15	1180	1.25
	1-2	1.53	111.05	1181	1.29
	1-3	1.58	113.25	1179	1.34
	1-4	1.53	113.18	1183	1.29
	1-5	1.58	112.43	1180	1.27
	1-6	1.57	112.05	1181	1.25
Plot 2	2-1	1.44	112.12	1181	1.25
	2-2	1.46	113.01	1181	1.26
	2-3	1.48	111.63	1180	1.27
	2-4	1.45	113.09	1182	1.27
	2-5	1.47	113.14	1180	1.29
	2-6	1.49	113.26	1179	1.33
	2-7	1.45	111.15	1180	1.27
	2-8	1.46	112.09	1181	1.26
Plot 3	3-1	1.55	112.01	1181	1.22
	3-2	1.55	112.03	1181	1.23
	3-3	1.57	112.15	1181	1.21
	3-4	1.56	112.21	1182	1.19
	3-5	1.55	112.14	1181	1.24
	3-6	1.56	112.06	1181	1.22
	3-7	1.55	112.15	1180	1.24
Plot 4	4-1	1.38	111.09	1181	1.26
	4-2	1.35	112.46	1181	1.26
	4-3	1.37	113.16	1180	1.29
	4-4	1.36	112.37	1182	1.26
	4-5	1.40	113.20	1180	1.32
	4-6	1.36	111.49	1180	1.30
Plot 5	5-1	1.43	112.62	1181	1.27
	5-2	1.46	111.29	1179	1.33
	5-3	1.43	113.23	1180	1.30
	5-4	1.44	112.28	1181	1.26
	5-5	1.47	111.41	1178	1.36
	5-6	1.45	111.60	1180	1.31
	5-7	1.44	113.02	1180	1.28

The curves of vehicle speed, drum torque, drum speed and loss rate of the five blocks are drawn respectively, as shown in Fig. 6.



(a) Speed trend chart of five plots

(b) Drum torque trend chart of five plots

(c)Drum speed trend chart of five plots

(d) Loss rate trend chart of five plots

Fig. 6 - Trend chart of five-plot test data

According to the results, the drum torque harvested by the control system is relatively stable. The threshing drum torque can be controlled within 111r/min-113.5r/min, and the loss rate can be effectively controlled within 1.4%. The control system not only improves the working efficiency, but also achieves the effect of reducing the loss rate.

CONCLUSION

After field experiment and analysis of experimental data, the following conclusions are drawn:

(1) Analyzing the relationship between the feeding quantity of the harvester and the operating parameters and loss rate of its key working parts, it is found that the loss rate of the combine harvester is mainly affected by the feeding quantity. At the beginning, the combine harvester cannot reach the optimal working state due to the small feeding quantity, and its loss is large. As the feeding quantity increases, the minimum loss rate occurs when the feed rate is about 3.71kg/s, and the working state of the harvester reaches the optimum. Then the loss rate gradually increases with the increase of the feeding quantity.

(2) The control system uses the compensated fuzzy PID algorithm to combine the drum speed control and the drum torque control to jointly realize the speed control of the combine harvester, and then realize the effective control of the feeding quantity. According to the analysis of the verification test data, the control system designed in this paper can effectively reduce the harvest loss and improve the work efficiency.

ACKNOWLEDGEMENT

This work was financially supported by the National Key Research and Development Program of China Subproject (No. 2021YFD2000600)

REFERENCES

[1] Aulin, V. V., Pankov, A. O., Zamota, T. M., Lyashuk, O. L., Hrynkiv A. V., Tykhyi A. A., Kuzyk, A. V.(2019). Development of mechatronic module for the seeding control system. *INMATEH - Agricultural Engineering*, Vol. 59, pp. 181-188. https://doi.org/10.35633/inmateh-59-20

[2] Bhardwaj, M., Dogra, R.,Javed, M., Singh, M., Dogra, B. (2021).Optimization of conventional combine harvester to reduce combine losses for basmati rice (Oryza Sativa). *Agricultural Sciences,* Vol.12, pp.259-272. https://doi.org/10.4236/as.2021.123017

[3] Budzich, T. (1964). *Control in harvester machine*, USA: 3138908.

[4] Chai, X., Zhou, Y., Xu, L., Li, Y., Li, Y., &Lv, L. (2020). Effect of guide strips on the distribution of threshed outputs and cleaning losses for a tangential-longitudinal flow rice combine harvester. *Biosystems Engineering*, Vol. 198, pp. 223-234. https://doi.org/10.1016/j.biosystemseng.2020.08.009

[5] Chen, D., Wang, S.M., Kang, F., Zhu, Q.Y., Li, X.H. (2011). Mathematical model of feeding rate and processing loss for combine harvester(联合收割机喂入量与收获过程损失模型). *Transactions of the Chinese Society of Agricultural Engineering*, Vol. 27, pp. 18-21. Beijing/China.

[6] Chen, J., Lian, Y., & Li, Y. (2020). Real-time grain impurity sensing for rice combine harvesters using image processing and decision-tree algorithm. *Computers and Electronics in Agriculture*, Vol. 175, pp. 105591. https://doi.org/10.1016/j.compag

[7] Coers, B.A., Burke, D. J. (2004). *Automatic control initiation for a harvester*, USA: 6834484.

[8] Cujbescu, D., Găgeanu, I., Iosif, A. (2021). Mathematical modeling of ear grain separation process depending on the length of the axial low threshing apparatus. *INMATEH-Agricultural Engineering,* Vol.65, pp. 101-110. https://doi.org/10.35633/inmateh-65-11

[9] Galluzzi, R., Xu, Y., Amati, N., &Tonoli, A. (2018). Optimized design and characterization of motor-pump unit for energy-regenerative shock absorbers. *Applied Energy*, Vol. 210, pp. 16-27. https://doi.org/10.1016/j.apenergy.2017.10.100

[10] Ivan, G., Vlăduţ, V., Ganea-Christu, I. (2015). Improving threshing system feeding of conventional cereal harvesting combine, *Proceedings of the 43rd international symposium on agricultural engineering* "*Actual Tasks on Agricultural Engineering*", pp. 431 440. Opatija/Croatia.

[11] Li, X., Qiu, S., & Ming, H. X. (2019.). An integrated module-based reasoning and axiomatic design approach for new product design under incomplete information environment. *Computers & Industrial Engineering*, Vol. 127, pp. 63-73.https://doi.org/10.1016/j.cie.2018.11.057

[12] Lopez, J., & Rubio, J. E. (2018). Access control for cyber-physical systems interconnected to the cloud. *Computer Networks*, Vol. 134, pp. 46-54. https://doi.org/10.1016/j.comnet.2018.01.037

[13] Madhusudana, C. K., Kumar, H., Narendranath, S. (2018). Fault Diagnosis of Face Milling Tool using Decision Tree and Sound Signal. *Materials Today: Proceedings*, Vol. 5, pp. 12035-12044. https://doi.org/10.1016/j.matpr.2018.02.178

[14] Marjanović, M., Krautblatter, M., Abolmasov, B., Đurić, U., Sandić, C., &Nikolić, V. (2018). The rainfall-induced landsliding in Western Serbia: A temporal prediction approach using Decision Tree technique. *Engineering Geology*, Vol. 232, pp. 147-159. https://doi.org/10.1016/j.enggeo.2017.11.021

[15] Mu, Y., Liu, X., & Wang, L. (2018). A Pearson's correlation coefficient based decision tree and its parallel implementation. *Information Sciences*, Vol. 435, pp. 40-58, https://doi.org/10.1016/j.ins.2017.12.059

[16] Pokojski, J., Oleksiński, K., Pruszyński, J. (2019). Knowledge based processes in the context of conceptual design. *Journal of Industrial Information Integration*, Vol. 15, pp. 219-238. https://doi.org/10.1016/j.jii.2018.07.002

[17] Reddy, E. J., &Rangadu, V. P. (2018). Development of knowledge based parametric CAD modeling system for spur gear: An approach. *Alexandria Engineering Journal*, Vol. 57, pp. 3139-3149. https://doi.org/10.1016/j.aej.2018.07.010

[18] Sessiz, A., Ulger, P. (2003). Determination of threshing losses with a raspbar type axial flow threshing unit. *Journal of Agricultural Engineering.* Vol. 40. pp. 1-8. Italy.

[19] Staiert, R.W., Krukow, E.T. (1982). *Combine feeder drive control,* USA: 4332127.

[20] Sun, J., Yang, L., Xu, B., Guo, Y., Cui, Q. Zhang, Y. (2021). Design and experiment of centrifugal collision test device for millet and sweet buckwheat grain. *INMATEH - Agricultural Engineering*, Vol. 65, pp. 193-202. https://doi.org/10.35633/inmateh-65-20

[21] Vlăduț, N.-V., Biriş, S.Ş., Cârdei, P., Găgeanu, I., Cujbescu, D.,Ungureanu, N., Popa, L.D., Perişoară, L., Matei, G., Teliban, G.-C. (2022). Contributions to the mathematical modeling of the threshing and separation process in an axial flow combine. *Agriculture,* Vol.12, pp. 1520. https://doi.org/10.3390/agriculture12101520

[22] Wang, L., Zhi, K., Li, B., & Zhang, Y. (2018). Dynamically Adjusting Filter Gain Method for Suppressing GNSS Observation Outliers in Integrated Navigation. *Journal of Navigation*, Vol. 71, pp. 1396-1412. https://doi.org/10.1017/S0373463318000334

[23] Wu, Z., Liao, J., Song, W., Mao, H., Huang, Z., Li, X., & Mao, H. (2018). Semantic hyper-graph-based knowledge representation architecture for complex product development. *Computers in Industry*, Vol. 100, pp. 43-56. https://doi.org/10.1016/j.compind.2018.04.008

OPTIMIZATION AND APPLICATION OF IRRIGATION SCHEDULING BASED ON HYDRUS-2D AND STEWART MODEL IN A SEMI-ARID AREA OF CHINA
/
基于Hdyrus-2D 和Stewart 模型的半干旱区灌溉制度优化及其应用

Haihua JING, Jing ZHANG, Kebao DONG*), Jiaqi MA, Zexu JIN
College of Water Conservancy, Shenyang Agricultural University, Shenyang, 110866, China
Tel: +8613624012571; E-mail: dongkebao@126.com
DOI: https://doi.org/10.35633/inmateh-69-45

Keywords: *Irrigation scheduling; Deficit irrigation; Hydrus-2D; Water-saving irrigation; Water management*

ABSTRACT
Water scarcity has been a critical constraint to economic development in semi-arid areas of China, so optimizing irrigation scheduling has become essential. This study obtained quantitative relationships between crop yield, crop water consumption, and irrigation quantity based on the Hydrus-2D and Stewart models. Different irrigation scheduling scenarios were evaluated to obtain the best irrigation scheduling based on the principle of simultaneous water conservation and crop productivity improvement with the evaluation indicators of crop yield, water use efficiency (WUE), irrigation water use efficiency (IWUE), and Critic-Topsis method. Taking drip irrigation under mulch as an example, the problem of optimizing the irrigation scheduling for different typical years was calculated. The optimization results showed that in the wet, normal, dry, and very dry years the annual irrigation quantity should be 49.68 mm, 49.68 mm, 85.38 mm, and 123.72 mm, when the WUE as well as IWUE, increases significantly, which had less impact on the crop yield and can save irrigation quantity by 30.00%, 30.00%, 35.00%, 27.00%. This study used Hydrus-2D to make a new attempt in irrigation scheduling optimization, giving full play to the model's high accuracy in soil water transport simulation and flexibility in boundary condition simulation. The optimization results can provide a reference for achieving accurate control of irrigation quantity during the crop growth period and reasonable irrigation scheduling formulation for regional crops.

摘要
在中国半干旱农灌区水资源短缺一直是制约经济发展的关键因素，因此对灌溉制度进行优化变的十分重要。本文基于 Hydrus-2D 和 Stewart 模型，得到作物产量-耗水量-灌溉量的定量关系，利用 Critic-Topsis 法，以水资源节约和作物生产力同步提高为原则，将作物产量、水分生产率、灌溉水利用效率作为评价指标对不同情景方案下的灌溉制度进行评价，优选得到最佳灌溉制度。以膜下滴灌为例，求解了不同水平年的灌溉制度优化问题，优化结果表明，在丰水年、平水年、枯水年、干旱年的年灌水量应为 49.68mm，49.68mm，85.38mm，123.72mm，水分利用效率以及灌溉水利用效率增加显著，对作物产量的影响较小的情况下，节约灌溉用水 30.00%，30.00%，35.00%，27.00%。本文利用 Hydrus-2D 在灌溉制度优化方面进行了新的尝试，充分发挥模型对土壤水运移模拟的高精度性及对边界条件模拟的灵活性，优化结果可为实现作物生育期内灌水量的精准控制，地区作物的合理的灌水方案制定提供参考。

INTRODUCTION
Agriculture water accounts for approximately 70% of global water resources and is the number one water user. China's arid and semi-arid areas, mainly located in the water-scarce north, account for an even higher proportion of agricultural water, making water scarcity even more of a problem for these areas, which are highly dependent on irrigation and also bear the brunt of agricultural production (*Soltani L. et al., 2022; Li M. et al., 2019*). Irrigation scheduling is the key and scientific basis for rational water use. Regulated deficit irrigation can reduce irrigation quantity and improve water use efficiency (WUE) while ensuring crop yields (*Cui J. et al., 2019; Ors S. et al., 2015*). Therefore, optimizing the existing irrigation scheduling and formulating a more reasonable irrigation scheduling to improve the water resources management level is necessary.

Irrigation scheduling optimization is an essential tool for regional water management and has been the subject of much research by scholars. There are currently two main ways of using models for irrigation scheduling optimization: (1) Use the model of crop response to water (Jensen model, Stewart model, etc.) to describe the relationship between water deficit and yield at different periods of crop growth through the analysis and fitting of experimental data, and carry out irrigation scheduling optimization. (2) Crop growth models (DSSAT model, AquaCrop model, etc.) (*Mubeen M. et al., 2016; Zhao Y. et al., 2021; Han C. et al., 2020*) are used to describe the relationship between soil moisture changes and crop growth and development for irrigation scheduling optimization.

The core objectives of irrigation scheduling optimization are to maximize crop yield and minimize irrigation water, however, the current approach to irrigation scheduling optimization is basically to use models to establish a relationship between crop yield and crop water consumption, based on which irrigation decisions can be further optimized. If the relationship between crop yield and irrigation quantity are established directly, it would provide greater convenience to irrigation decision-makers. In addition, when models are used to optimize irrigation scheduling, the study's environment is often idealized to a certain extent (*Araya A. et al., 2010; Salemi H. et al., 2011*). For example, the DSSAT model simplified the soil water transport to a one-dimensional model, and cannot simulate well the boundary conditions and the resulting lateral transport of soil water under irrigation methods such as drip irrigation under mulch and furrow irrigation, which will have a certain impact on the optimization effect.

Effective rainfall is one of the sources of soil moisture and has positive implications for improving irrigation water use efficiency when optimizing irrigation scheduling, yet many models do not consider rainfall comprehensively (*Xie Y. L. et al., 2018*). In addition, in areas with shallow groundwater depths, crop roots can access a certain amount of water through groundwater under the influence of capillary-effect, thus reducing irrigation water, but it is difficult to quantify groundwater recharge to crops when existing crop models are optimized for irrigation scheduling (*Peng Z. et al., 2019*). All of the above hurt optimization results.

The Hydrus-2D model is a finite element computational model for simulating water, solute, and heat transport in saturated-unsaturated porous media. The model allows a better and more flexible description of various boundary conditions, enables two-dimensional simulation of soil hydrothermal transport with high accuracy and enables simulation of transport fluxes, quantifies deep percolation and groundwater recharge to crops, and is now widely used to simulate soil moisture movement (*Shan G. et al., 2019; Karandish F. et al., 2019*). Given the advantages of the Hydrus-2D model in the simulation of soil water transport, it is necessary to use Hydrus-2D to study the optimization of irrigation scheduling (*Er-Raki S. et al., 2021*).

When using Hydrus-2D to optimize irrigation scheduling, the selection of optimization objectives was often directed at the water and solute processes, such as seeking to reduce crop water consumption (*Er-Raki S. et al., 2021*), reduce deep percolation (*Egea G. et al., 2016*) or optimize solute transport processes (*Shekhar S. et al., 2021; Zeng W. et al., 2014*). Crop yield is often a priority when optimizing irrigation scheduling, but the Hydrus-2D model does not simulate crop yield, so we combined the Hydrus-2D model with the Stewart water production function to optimize irrigation scheduling (*Wang D. et al., 2017; Cheng W. et al., 2016*), which took advantage of the Hydrus-2D model's strengths in soil water transport simulation while taking crop yield into account.

This paper presented a new attempt at optimizing irrigation scheduling using the Hydrus-2D model, combining Hydrus-2D and Stewart models to establish a quantitative crop yield-crop water consumption-irrigation quantity relationship under different meteorological conditions (typical years). We proposed an irrigation scheduling optimization method using Hydrus-2D and Stewart models based on the principle of simultaneous improvement of water conservation and crop productivity and applied it in the experimental area.

MATERIALS AND METHODS

Hydrus-2D model

The Hydrus-2D model is a finite element computational model developed by the US Salinity Laboratory to simulate the two-dimensional movement of water, heat, and solutes in saturated-unsaturated porous media. Hydrus-2D has the advantage of high simulation accuracy and a wide range of algorithms for arbitrarily complex terrain conditions and is now widely used to simulate soil moisture movement processes in the field. The Hydrus-2D soil water movement model consists of the Richard equation, the Van Genuchten-Mualem hydraulic model, crop root uptake, and evapotranspiration modules, where evapotranspiration is calculated using the Penman-Monteith model recommended by FAO-56.

The irrigation scheduling should be optimized by using Hydrus-2D to establish an in-situ soil water transport model in the field so that the effects of meteorological factors, ineffective deep percolation, and groundwater recharge to the crop on the irrigation quantity can be fully taken into account and the irrigation quantity can be accurately controlled during the crop growth period.

Stewart model

The crop water production function is an effective method for determining the quantitative relationship between crop water consumption and yield, and numerous experiments have established the applicability of the Stewart model in semi-arid areas (*Wang D. et al., 2017; Cheng W. et al., 2016*). The Stewart model reflects the effect of water stress on crop growth at different growth stages, using the relative water deficit as the independent variable, multiplied by the corresponding stage sensitivity coefficient to represent the water production function in the form shown in Equation 1. The model weakens the influence of climate and crop variety on the relationship between crop yield and crop water consumption. Compared with the crop growth model, it has the advantage of being simpler to calculate, requires fewer types of data, and can reflect the response of crop yield to moisture factors more accurately in the same region.

$$1-\frac{Y_a}{Y_m}=\sum_{i=1}^{n} Bi\left[\frac{\left(ET_{m_i}-ET_{ai}\right)}{ET_{m_i}}\right] \quad (1)$$

where: Y_a is the measured yield of the crop (kg/hm^2);

Y_m - the maximum yield of the crop (kg/hm^2);

ET_{ai} - the measured water requirement of the crop at each growth period (mm);

ET_{mi} - the crop water requirement under full irrigation treatment (mm);

B_i is the sensitivity coefficient of water deficit on yield at different growth period of the crop;

i = 1, 2, …, n is the serial number of the crop at each period of growth.

As a statistical model, the Stewart water production function is based on a large amount of field experiment data. Therefore, crop deficit irrigation experiments are required for irrigation scheduling optimization. The experiment is carried out in the field of the experimental area using the comparative method and the experimental treatments are designed according to different combinations of water deficit levels at each period of growth. Considering the influence of rainfall on irrigation, a movable rain shelter should be set up in the experimental plot and used during rainfall.

Critic-Topsis method

The evaluation indicators of irrigation scheduling involve various factors such as resources, economy, and ecological environment. For the multi-attribute and multi-objective characteristics of irrigation scheduling evaluation, Critic-Topsis can be used to evaluate the irrigation scheduling and preferably select the optimal irrigation scheduling. The Topsis method eliminates the influence of different indicator scales, makes full use of the information in the raw data, reflects the gaps between scenarios, and is universally applicable. The Critic weighting method takes into account the differences and correlations of each indicator, resulting in more objective and accurate weights (*Liu, X. et al., 2018; Liu X. et al., 2021*).

This paper is based on the principle of simultaneous improvement of water conservation and crop productivity, taking into account a combination of indexes of economic yield size (crop yield Y) and effectiveness indexes of water resources utilization (water use efficiency WUE and irrigation water use efficiency $IWUE$). WUE and $IWUE$ are calculated using equations 2,3 respectively.

$$WUE=\frac{Y}{ET} \quad (2)$$

$$IWUE=\frac{Y}{I} \quad (3)$$

where: Y is the crop yield (kg·hm^{-2});

WUE - water use efficiency (kg/m^3); and

IWUE - irrigation water use efficiency (kg/m^3);

ET - crop water consumption (mm);

I - irrigation quantity (mm).

The above three indicators (Y, WUE, $IWUE$) constitute the pool of factors for the comprehensive evaluation of irrigation scheduling optimization in this study, with higher scores on the index Ci for Topsis indicating that the subject is closer to the optimal level.

Optimization process

The optimization process is shown in Fig.1.

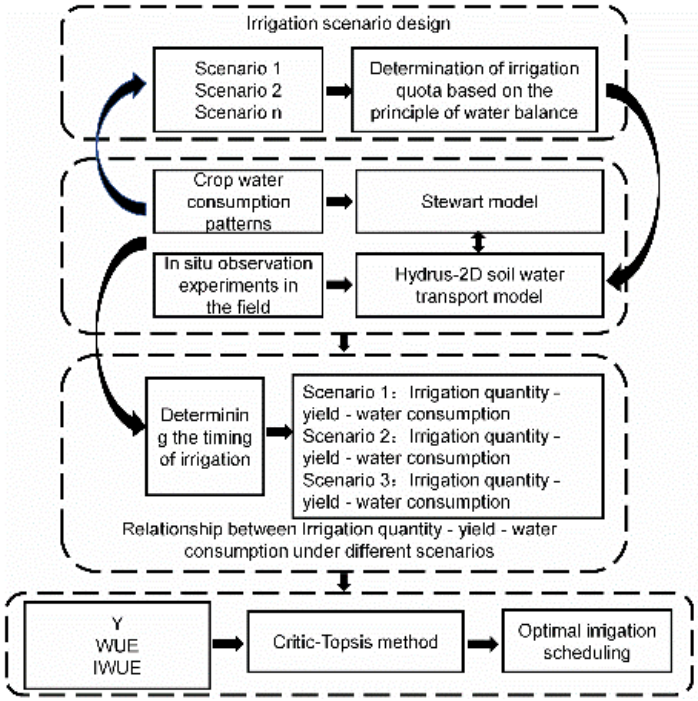


Fig. 1 - Optimization process

The first step is the establishment of the soil water model: Hdyrus-2D is used to establish the soil water transport model, the model parameters are calibrated and the simulation results are validated using in situ soil water transport monitoring experimental data in the field. The second step is the establishment of the crop water model: using the Stewart model, the yield-evapotranspiration (crop water consumption) relationship is fitted using the standardized and weakened dispersion of deficit irrigated crop data in the field. The third step is the design of scenarios for irrigation scheduling optimization: the design of scenarios for irrigation scheduling optimization at different combinations of water deficit levels for a growth period with a low water sensitivity coefficient. The fourth step is the simulation of the irrigation scheduling: the irrigation quota is determined according to the design scenario, based on the water balance method. Using the Subregions and Cumulative Fluxes modules in Hydrus-2D, iterative calculations are carried out to determine the irrigation time points and output the water consumption for different crop growth periods associated with irrigation quotas and meteorological data. Combined with the water production function, the relationship between crop yield - crop water consumption – irrigation quantity is obtained for different scenarios. The fifth step is irrigation scheduling optimal selection: considering crop yield, WUE, and $IWUE$, the Critic-Topsis method is used to evaluate the irrigation scheduling under different scenarios to obtain the optimal irrigation scheduling.

OPTIMIZATION OF DRIP IRRIGATION UNDER MULCH IRRIGATION SCHEDULING FOR MAIZE

Experimental design and data collection

The experiment was carried out at Jianping Irrigation Experimental Station in Chaoyang City, Liaoning Province, China, which is located at 119°18′ E, 41°47′ N, and 461 m above sea level. The average annual temperature is 5-6°C, the average annual precipitation is 440 mm and the average annual evapotranspiration is 1800-2100 mm. It has a typical semi-arid monsoon climate with low rainfall and high evaporation. The local irrigation method is drip irrigation under mulch, and the main crop is maize. The experiment started in April 2019 - ended in October 2019 and started in April 2021 - ended in October 2021. The average depth of groundwater in the study area during the test was 300 cm.

In-situ soil water transport monitoring experimental

Two monitoring sections were set up in the middle of the furrow (MFD) and the middle of the mulch (MMD). Three sets of 1 m deep trim tubes were set up at each monitoring section to monitor soil water content using TDR. The maximum monitoring depth was 80 cm. The monitoring section settings are shown in Fig.2.

Meteorological data on rainfall, temperature, humidity and wind speed were obtained from nearby weather station during the experiment (http://data.cma.cn, Station No. 54326).

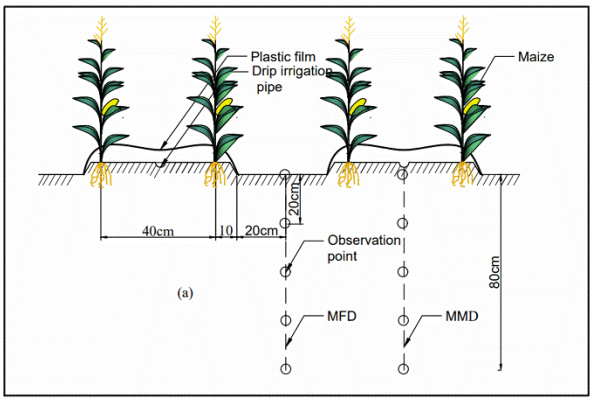


Fig. 2 - Settings of monitoring sections.

Deficit irrigation experiment

Considering the depth of groundwater in the study area, the experiment was carried out in a bottomed soil pit (2 m x 3.3 m). The experiment was set up according to the lower limit of irrigation for each growth stage of maize, dividing the entire growth period into seedling, jointing, tasseling, and filling stages. The experiment used 60% and 50% of the soil field capacity (θ_{fc}) as the lower limit of irrigation, eight experimental treatments, and one control group (the lower limit of irrigation was 70% θ_{fc}), the upper limit of irrigation was all soil field capacity, and three replications were set up for each treatment. The monitoring sections were set up in the same way as the in-situ soil water transport monitoring experimental data in the field. Five crops were selected for each treatment and the number of plants and spikes were counted for each treatment before harvest and the yield of the plants was measured.

Hydrus-2D model calibration and validation

Hydraulic parameters were initially predicted from the proportion of the soil particle size and soil water retention curve using the Rosetta program. The inverse module and the experimental data from 2019 were used to optimize the hydraulic parameters. The optimized Soil hydraulic parameters are shown in table 1.

Table 1

Soil hydraulic parameters

Depth (cm)	θ_r ($cm^3 \cdot cm^{-3}$)	θ_s ($cm^3 \cdot cm^{-3}$)	α (cm^{-1})	n (-)	Ks ($cm^3 \cdot day^{-1}$)	I (-)
0-40	0.065	0.44	0.114	1.53	348.00	0.5
40-70	0.057	0.44	0.106	1.38	41.10	0.5
70-80	0.025	0.43	0.124	1.27	435.07	0.5

The model was validated using experimental data from 2021. The performance of the model was evaluated using the following three statistical indicators: mean absolute error (MAE), root mean square error (RMSE), and coefficient of determination (R^2). The results are shown in Fig.3, and Table 2.

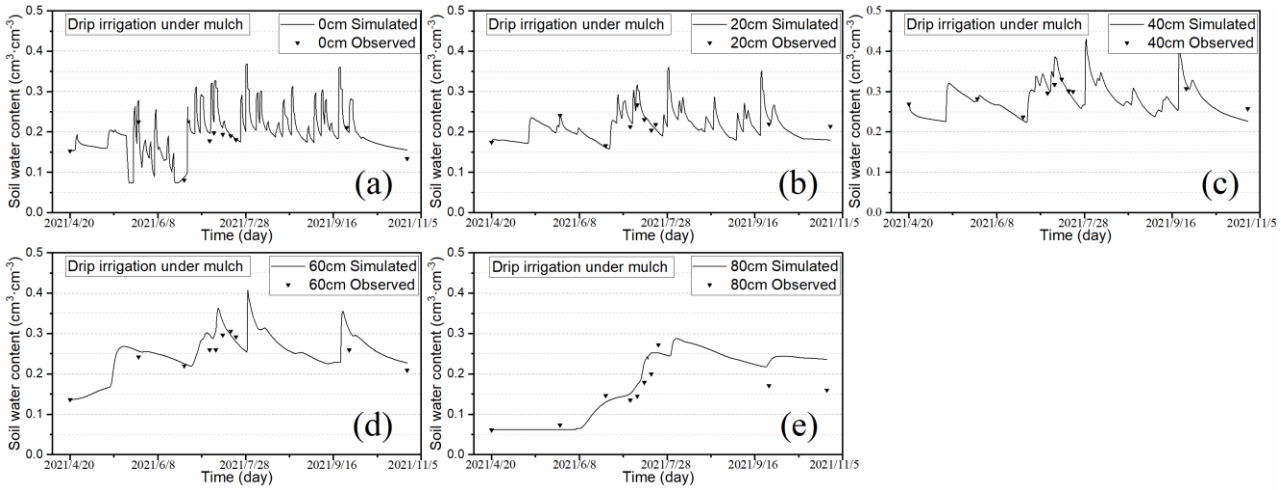


Fig. 3 - Simulated and measured soil water contents at different soil depths

(a), (b), (c), (d), and (e) are Simulated and measured soil water contents at 0, 20, 40, 60, and 80 cm soil depth respectively

Table 2

The error analysis of soil water contents

Depth (cm)	MAE (cm^3/cm^3)	R^2	RMSE (cm^3/cm^3)
0	0.017	0.87	0.025
20	0.015	0.79	0.021
40	0.015	0.78	0.024
60	0.023	0.85	0.028
80	0.033	0.79	0.040

The graphical and statistical results show that the trend of the simulated soil moisture content is consistent with the measured values, with R^2 of 0.78-0.87, RMSE of 0.021-0.040, and MAE of 0.015-0.033 at 0-80 cm. The model simulation accuracy is high and the simulated and measured soil moisture contents show a good agreement. Considering the complexity of the in situ field experiments, many disturbing factors (e.g., soil spatial variability, uneven distribution of rainfall and irrigation, the effects of uneven distribution of crop roots, etc.) might be encountered. Still, the model met the accuracy criteria and could simulate soil moisture movement better.

Stewart model calibration and validation

The Stewart water production function was fitted and optimized using the crop yield-crop water consumption relationship obtained from the deficit irrigation experiment, and the optimized parameters are shown in Table 3.

Water sensitivity coefficient Table 3

Water sensitivity coefficient	Seedling	Jointing	Tasseling	Filling
Bi	0.6854	0.1648	0.1002	0.2937

The simulation of the model was evaluated using three statistical indicators: mean absolute error (MAE), root mean square error (RMSE), and coefficient of determination (R^2). The R^2 of the water production function is 0.99, the MAE is 66.543 and the RMSE is 75.199. The accuracy of the simulation of the Stewart model is high and met the accuracy criteria, which could better reflect the relationship between crop water consumption and crop yield.

Scenario design

To ensure maize yield, was selected the growth period that had a relatively low impact on the yield of the crop (filling and pulling stage) for deficit irrigation. Typical years were determined using the curve-fitting method, as shown in the table 4.

Typical year selection Table 4

Typical year	Rainfall (mm)	Frequency	Year
Wet year(W)	530.7	25%	1995
Normal year (N)	471.0	50%	2019
Dry year (D)	386.7	75%	1997
Very Dry year (VD)	333.9	90%	1992

Nine scenarios were designed using $70\%\theta_{fc}$, $60\%\theta_{fc}$, and $50\%\theta_{fc}$ as the lower limit of irrigation at the filling and pulling. The scenarios for the wet year are shown in table 5, where W1 is fully irrigated and W2-W9 is irrigated with varying degrees of deficit regulation. The scenario design for normal, dry, and very dry years is the same as for wet years.

Wet year scenario design Table 5

Wet year (W)	Seedling	Jointing	Tasseling	Filling
W1	$70\%\theta_{fc}$	$70\%\theta_{fc}$	$70\%\theta_{fc}$	$70\%\theta_{fc}$
W2	$70\%\theta_{fc}$	$70\%\theta_{fc}$	$60\%\theta_{fc}$	$70\%\theta_{fc}$
W3	$70\%\theta_{fc}$	$70\%\theta_{fc}$	$50\%\theta_{fc}$	$70\%\theta_{fc}$
W4	$70\%\theta_{fc}$	$60\%\theta_{fc}$	$70\%\theta_{fc}$	$70\%\theta_{fc}$
W5	$70\%\theta_{fc}$	$60\%\theta_{fc}$	$60\%\theta_{fc}$	$70\%\theta_{fc}$
W6	$70\%\theta_{fc}$	$60\%\theta_{fc}$	$50\%\theta_{fc}$	$70\%\theta_{fc}$
W7	$70\%\theta_{fc}$	$50\%\theta_{fc}$	$70\%\theta_{fc}$	$70\%\theta_{fc}$
W8	$70\%\theta_{fc}$	$50\%\theta_{fc}$	$60\%\theta_{fc}$	$70\%\theta_{fc}$
W9	$70\%\theta_{fc}$	$50\%\theta_{fc}$	$50\%\theta_{fc}$	$70\%\theta_{fc}$

Irrigation scheduling simulation

The Hydrus-2D model was used to simulate irrigation regimes for nine irrigation scenarios at different typical years. The results obtained are shown in Fig. 4 below.

As can be seen from Fig. 4, there is little change in irrigation scheduling for some scenarios, such as W1, W2, and W3 versus N1, N2, and N3. The reason for this might be related to the interannual distribution of rainfall in the year. In the case of W1, W2, and W3, all three scenarios are irrigated for deficits during the tasseling period, when rainfall is more frequently distributed to meet the normal water requirements of the crop, resulting in no need for irrigation during this period, thus resulting in little difference between the irrigation scheduling of the three scenarios. As the typical annual rainfall decreased, the irrigation scheduling varied increasingly across the typical years.

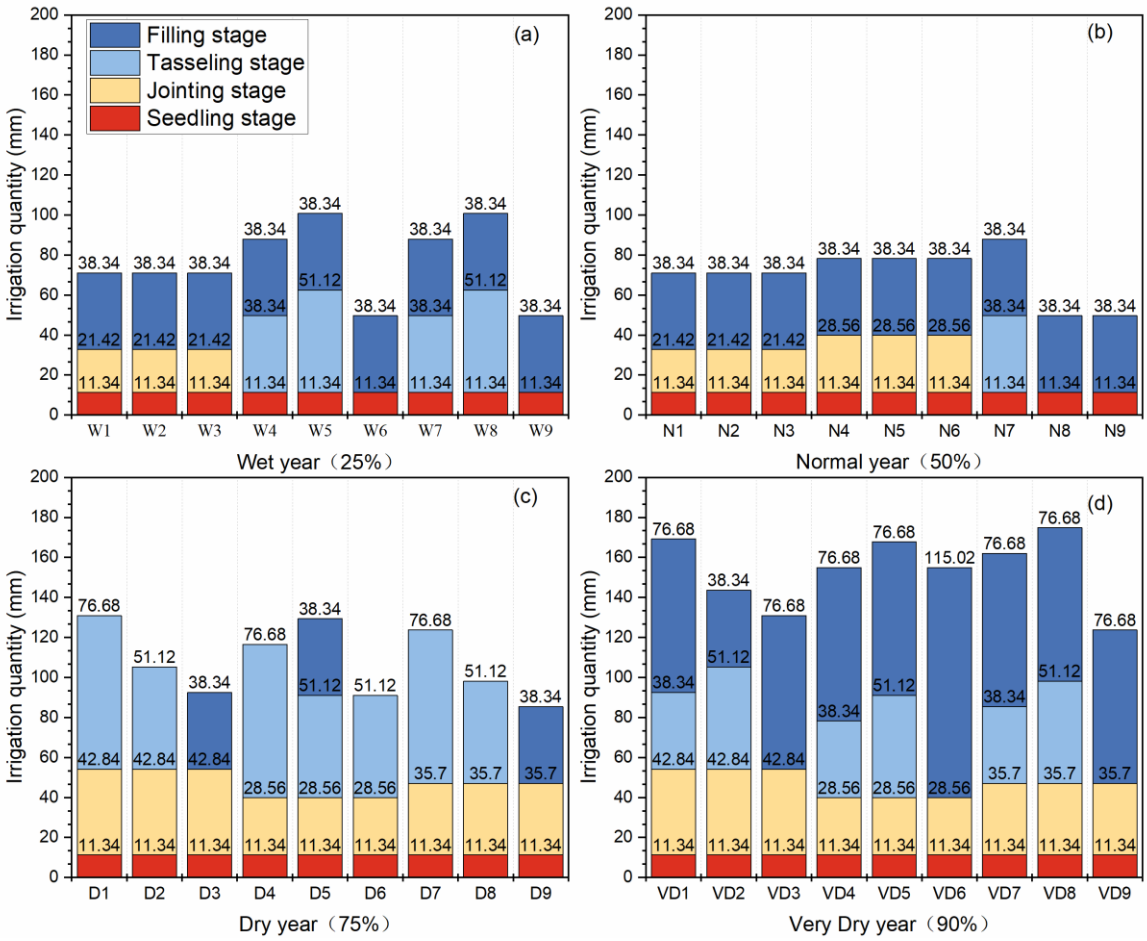


Fig. 4 - Irrigation scheduling simulation

(a) is wet year, (b) is normal year, (c) is dry year, and (d) is very dry year.

Optimal irrigation scheduling

The Hydrus-2D and Stewart models were used jointly to output the crop yield-crop water consumption-irrigation quantity relationship for different scenarios and to calculate WUE and IWUE. The Critic weighting method was used to calculate the weight values for the three indicators (yield, WUE, IWUE) for the years of wet (0.4458, 0.3234, 0.2308), normal (0.4799, 0.2995, 0.2207), dry (0.4409, 0.2792, 0.2800) and very dry (0.4021, 0.3428, 0.2551). The data was standardized and orthogonalized using the Topsis method to calculate Ci values. The results are shown in Fig.5.

As can be seen in Fig.5, W9, N9, D9, and VD9 are the optimal irrigation scheduling for the corresponding typical years, with Ci values of 0.5658, 0.5299, 0.5100, and 0.5515 respectively. The lower limit of irrigation for W9, N9, D9, and VD9 is 50% of θ_{fc} at the time of jointing and tasseling, which means that irrigation with 50% of θ_{fc} at the time of jointing and tasseling will result in better performance in terms for yield, WUE, and IWUE. The Ci values for W6 and W9 are the same in the wet year, which is related to the inter-annual distribution of rainfall for the reasons explained in section 3.5. The choice of W6 or W9 does not affect crop yield, WUE, and IWUE. For the sake of simplicity and practicality of the conclusions, W9 is chosen as the optimal irrigation scheduling in the wet year, and the same applies to N8 and N9 in the normal year.

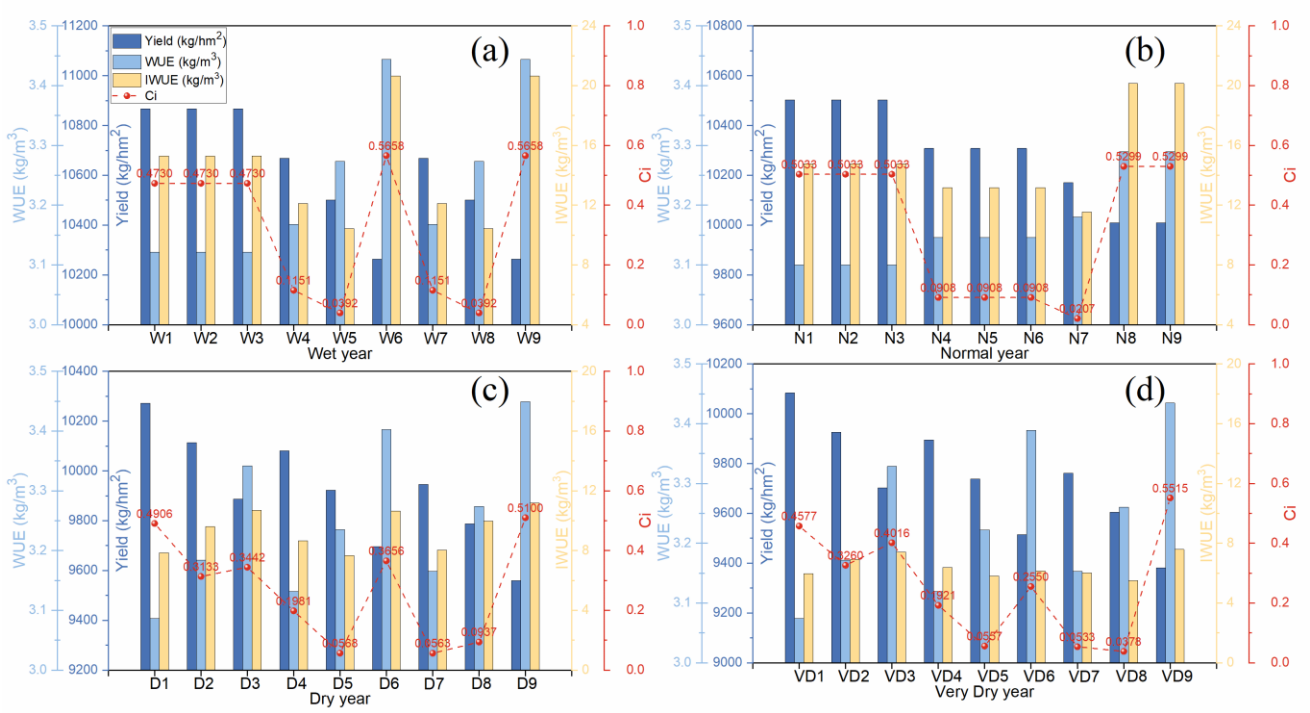


Fig. 5 - Irrigation scheduling simulation

(a) is wet year, (b) is normal year, (c) is dry year, and (d) is very dry year.

RESULTS

The semi-arid areas are located on a plain, with gentle topography, few rivers, active infiltration of precipitation, and almost no surface runoff. The hydrological cycle is characterized by predominantly groundwater recharge-discharge, with the main processes of the hydrological cycle being: precipitation-evaporation-infiltration to recharge groundwater-transpiration (*Wang Y. et al., 2021*). The Hydrus-2D model can simulate soil evaporation, crop transpiration, deep seepage, and groundwater recharge to crops in agricultural fields, and the entire hydrological element of semi-arid agricultural fields can be simulated using this model alone. The model is suitable for complex subsurface conditions and can better and more flexibly describe various boundary conditions. The boundary conditions under irrigation methods such as drip irrigation under mulch and furrow irrigation and the resulting lateral migration of soil water can be well simulated, the simulation accuracy is high, and the simulated and measured soil water content shows good agreement.

The combined use of Hydrus-2D and Stewart models enables the quantitative relationship between crop yield - crop water consumption - irrigation quantity to be obtained, bringing greater convenience to the multi-objective optimization of irrigation scheduling and the decision-making of irrigation strategies.

By optimizing the irrigation scheduling for maize drip irrigation under mulch, the optimum irrigation system was obtained for wet years, normal years, dry years, and very dry years. The irrigation scheduling is shown in Table 6 below. Compared to the initial irrigation scheduling with full irrigation, the yield of optimized irrigation scheduling decreased 603.88, 493.77, 712.51, and 702.08 kg/hm^2, accounting for 5.55%, 4.67%, 6.86%, and 6.86% of the yield of initial irrigation system, whereas the WUE increased by 10.33%, 6.13%, 11.84%, and 11.84%, respectively, and the IWUE increased by 35.16%, 36.43%, 42.76%, and 27.38%, respectively. It can be seen that the optimized irrigation scheduling has a significant increase in WUE as well as IWUE with less impact on crop yield, saving irrigation water by 30.00%, 30.00%, 35.00%, and 27.00%, respectively.

Table 6

Optimal irrigation scheduling

Typical year	Seedling(mm)	Jointing(mm)	Tasseling(mm)	Filling(mm)	Annual irrigation quantity(mm)
Wet year	11.34	0	0	38.34	49.68
Normal year	11.34	0	0	38.34	49.68
Dry year	11.34	35.7	0	38.34	85.38
Very Dry year	11.34	35.7	0	76.68	123.72

In this paper, the Stewart model was used to establish the crop water production function, but the choice of crop water production function is related to the irrigation method, crop type, location of the experimental area, etc. Therefore, the water sensitivity coefficient in Stewart also varies across areas (*Cheng W. et al., 2016; Saseendran S.A. et al., 2015*). To better optimize the irrigation scheduling and reduce the model error, an appropriate water production model should be chosen when establishing the water consumption-yield relationship (*Mukherjee D., 2021; Cheng W. et al., 2016*).

Maize water sensitivity coefficient values in the experimental area were seedling stage (0.6854) > filling stage (0.2937) > jointing stage (0.1648) > tasseling stage (0.1002). This suggested that rewatering after water deficits at the jointing stage and the tasseling stage could produce a compensation or overcompensation effect on plant growth and development (*Liu H. et al. 2017*). In addition, the experimental area receives sufficient rainfall at the jointing stage as well as at the tasseling stage, with about 70% of the annual rainfall falling between June and August, which provides a certain source of water for the crop.

The setting of the irrigation scenario may have an impact on the optimization results, as the lower limit of irrigation for the optimum irrigation scheduling may occur between$70\%\theta_{fc}$ - $60\%\theta_{fc}$ or $60\%\theta_{fc}$ - $50\%\theta_{fc}$, but the water sensitivity coefficient values are lower at the jointing stage and the tasseling stage, when deficit irrigation has less impact on yield and can increase WUE and $IWUE$ to a greater extent (*Yang X. et al., 2016*), so the conclusions are considered reliable. In the actual process of irrigation system optimization, irrigation scenarios should be designed to set more gradients and consider more growth periods to obtain better irrigation scheduling.

CONCLUSIONS

This paper proposed a method for optimizing irrigation scheduling in semi-arid areas based on the Hydrus-2D and Stewart models, with the principle of simultaneous water conservation and crop productivity improvement. The optimization process mainly included (1) the establishment of the soil water model; (2) the establishment of the crop water model; (3) the design of scenarios for irrigation scheduling optimization; (4) the simulation of the irrigation system; and (5) irrigation scheduling optimal selection.

The method is suitable for the characteristics of the hydrological cycle in semi-arid areas and takes full account of the influence of meteorological factors on the optimization of irrigation scheduling. The method allows for a better and more flexible description of the various boundary conditions and applies to irrigation scheduling optimization problems under various irrigation methods. Through the combined use of Hydrus-2D and Stewart models, a quantitative crop yield-crop water consumption-irrigation quantity relationship is obtained, bringing greater convenience to the multi-objective optimization of scheduling and the decision-making of irrigation strategies.

By optimizing the irrigation scheduling of maize drip irrigation under mulch in different typical years, the optimal annual irrigation quantity should be 49.68 mm, 49.68 mm, 85.38 mm, 123.72 mm for the wet year, normal year, dry year, and very dry year, and the lower limit of irrigation should be 50% θ_{fc} for jointing stage and tasseling stage. The WUE, as well as the $IWUE$, increased significantly at this time, saving 30.00%, 30.00%, 35.00%, and 27.00% of irrigation quantity respectively, with less impact on crop yield.

This paper used Hydrus-2D to optimize the irrigation system, the results of which could provide a reference for the precise control of irrigation water during the crop reproductive period and the development of a reasonable irrigation plan for regional crops. In practical application, attention should be paid to the choice of the water production function, the setting of irrigation scenarios, and the influence of the spatial and temporal distribution of rainfall on the optimization effect.

ACKNOWLEDGEMENT

The authors acknowledge the public science and technology research funds project of the National Ministry of Water Resources. The granted research is titled “Study of key technology of hydrologic cycle and aquatic safety in the semi-arid region (201501031)”. The authors would like to thank the anonymous reviewer for the helpful comments, which improved the quality of the manuscript.

REFERENCES

[1] Araya, A., Keesstra, S. D., & Stroosnijder, L. (2010). Simulating yield response to water of Teff (Eragrostis tef) with FAO's AquaCrop model. *Field Crops Research*, Vol. 116, Issues 1–2, pp. 196-204, Netherlands;

[2] Cheng, W., Lu, W., Xin, X., Zhang, Z., & Chu, H. (2016). Adaptability of various models of the water production function for rice in Jilin Province, China. *Paddy and water environment*, Vol. 14, pp. 355-365. Germany;
[3] Cui, J., Shao, G., Lu, J., Keabetswe, L., & Hoogenboom, G. (2019). Yield, quality and drought sensitivity of tomato to water deficit during different growth stages. *Scientia agrícola*, Vol. 77. Brazil;
[4] Egea, G., Diaz-Espejo, A., & Fernandez, J. E. (2016). Soil moisture dynamics in a hedgerow olive orchard under well-watered and deficit irrigation regimes: Assessment, prediction and scenario analysis. *Agricultural Water Management*, Vol.164, pp.197-211, Netherlands;
[5] Er-Raki, S., Ezzahar, J., Merlin, O., Amazirh, A., Hssaine, B. A., Kharrou, M. H., ... & Chehbouni, A. (2021). Performance of the HYDRUS-1D model for water balance components assessment of irrigated winter wheat under different water managements in semi-arid region of Morocco. *Agricultural Water Management*, Vol.244, pp. 106546, Netherlands;
[6] Han, C., Zhang, B., & Liu, Y. (2020). Efficient water-saving irrigation based on regional irrigation schedule optimization. *DESALINATION AND WATER TREATMENT*, Vol.187, pp. 30-41, Italy;
[7] Karandish, F., & Šimůnek, J. (2019). A comparison of the HYDRUS (2D/3D) and SALTMED models to investigate the influence of various water-saving irrigation strategies on the maize water footprint. *Agricultural Water Management*, Vol.213, pp. 809-820, Netherlands;
[8] Li, M., Fu, Q., Singh, V. P., Liu, D., & Li, T. (2019). Stochastic multi-objective modeling for optimization of water-food-energy nexus of irrigated agriculture. *Advances in water resources*, Vol. 127, pp. 209-224, England;
[9] Liu, H., Wang, X., Zhang, X., Zhang, L., Li, Y., & Huang, G. (2017). Evaluation on the responses of maize (Zea mays L.) growth, yield and water use efficiency to drip irrigation water under mulch condition in the Hetao irrigation District of China. *Agricultural Water Management*, Vol. 179, pp. 144-157, Netherlands;
[10] Liu, X., Peng, Y., Yang, Q., Wang, X., & Cui, N. (2021). Determining optimal deficit irrigation and fertilization to increase mango yield, quality, and WUE in a dry hot environment based on TOPSIS. *Agricultural Water Management*, Vol. 245, pp.106650, Netherlands;
[11] Liu, X., Qi, Y., Li, F., Yang, Q., & Yu, L. (2018). Impacts of regulated deficit irrigation on yield, quality and water use efficiency of Arabica coffee under different shading levels in dry and hot regions of southwest China. *Agricultural water management*, Vol. 204, pp.292-300, Netherlands;
[12] Mubeen, M., Ahmad, A., Wajid, A., Khaliq, T., Hammad, H. M., Sultana, S. R., ... & Nasim, W. (2016). Application of CSM-CERES-Maize model in optimizing irrigated conditions. *Outlook on Agriculture*, Vol. 45, Issues 3, pp.173-184, England;
[13] Mukherjee, D. (2021). Optimizing Water Production Function and Deficit Irrigation Scheduling during Extreme Dry Periods. *Journal of Irrigation and Drainage Engineering*, Vol.147(12), pp.04021060, USA;
[14] Ors, S., Sahİn, U., & Kİzİloglu, F. M. (2015). Yield, quality and irrigation water use of drip-irrigated silage maize with different irrigation techniques. *Pakistan Journal of Agricultural Sciences*, Vol. 52, Issues 3, pp.595-607;
[15] Peng, Z., Zhang, B., Cai, J., Wei, Z., Chen, H., & Liu, Y. (2019). Optimization of spring wheat irrigation schedule in shallow groundwater area of Jiefangzha region in Hetao irrigation district. *Water*, Vol.11, Issues 12, pp.2627, Switzerland;
[16] Salemi, H., Soom, M. A. M., Mousavi, S. F., Ganji, A., Lee, T. S., Yusoff, M. K., & Verdinejad, V. R. (2011). Irrigated silage maize yield and water productivity response to deficit irrigation in an arid region. *Polish Journal of Environmental Studies*, Vol. 20, Issues 5, pp.1295-1303, Poland;
[17] Saseendran, S. A., Ahuja, L. R., Ma, L., Trout, T. J., McMaster, G. S., Nielsen, D. C., ... & Fang, Q. X. (2015). Developing and normalizing average corn crop water production functions across years and locations using a system model. *Agricultural Water Management*, Vol.157, pp.65-77, Netherlands;
[18] Shan, G., Sun, Y., Zhou, H., Lammers, P. S., Grantz, D. A., Xue, X., & Wang, Z. (2019). A horizontal mobile dielectric sensor to assess dynamic soil water content and flows: Direct measurements under drip irrigation compared with HYDRUS-2D model simulation. *Biosystems Engineering*, Vol.179, pp.13-21, England.
[19] Shekhar, S., Mailapalli, D. R., & Raghuwanshi, N. S. (2021). Simulating nitrogen transport in paddy crop irrigated with alternate wetting and drying practice. *Paddy and Water Environment*, Vol.19, Issues 3, pp.499-513, Germany;

[20] Soltani, L., & Mellah, T. (2022). Exploring farmers' adaptation strategies to water shortage under climate change in the Tunisian semi-arid region. *Environmental Management*, Vol.71, pp.74-86, USA;
[21] Wang, D., Li, F., & Nong, M. (2017). Response of yield and water use efficiency to different irrigation levels at different growth stages of Kenaf and crop water production function. *Agricultural Water Management*, Vol.179, pp. 177-183, Netherlands;
[22] Wang, Y., Chen, M., Yan, L., Zhao, Y., & Deng, W. (2021). A new method for quantifying threshold water tables in a phreatic aquifer feeding an irrigation district in northwestern China. *Agricultural Water Management*, Vol.244, pp. 106595, Netherlands;
[23] Xie, Y. L., Xia, D. X., Ji, L., & Huang, G. H. (2018). An inexact stochastic-fuzzy optimization model for agricultural water allocation and land resources utilization management under considering effective rainfall. *Ecological indicators*, Vol. 92, pp.301-311, Netherlands;
[24] Yang, X., He, J., FU, Y., Dong, K., & Yang., Q. (2016). Water Consumption Characteristics of Maize under Different Irrigation Methods in Western Liaoning. *Journal of Irrigation and Drainage*, 35(04), 59-64.
[25] Zeng, W., Xu, C., Wu, J., & Huang, J. (2014). Soil salt leaching under different irrigation regimes: HYDRUS-1D modelling and analysis. *Journal of Arid Land*, Vol.6, Issues 1, pp.44-58, China
[26] Zhao, Y., Li, F., & Jiang, R. (2021). Irrigation schedule optimization based on the combination of an economic irrigation quota and the AquaCrop model. *Irrigation and Drainage*, Vol.70, Issues 4, pp. 773-785, England.

HYPERSPECTRAL IMAGE CLASSIFICATION IN DESERT GRASSLAND BASED ON THREE-DIMENSIONAL DEEP LEARNING MODEL

基于 3D 深度学习模型的荒漠草原高光谱图像分类

Ronghua WANG [1], Yanbin ZHANG [2]*, Jianmin DU [2], Yuge BI[2]
[1] Inner Mongolia Technical College of Mechanics and Electrics, Hohhot, China
[2] Inner Mongolia Agricultural University, Hohhot, China
Tel: +86 13214055530; E-mail: zyb359@126.com
Corresponding author: Yanbin ZHANG
DOI: https://doi.org/10.35633/inmateh-69-46

Keywords: *hyperspectral remote sensing, unmanned aerial vehicle, deep learning, classification, desert grassland*

ABSTRACT

Identification and classification of vegetation are the basis for grassland degradation monitoring, classification and quantification studies. Here, four deep learning models were used to classify the unmanned aerial vehicle *(UAV) hyperspectral remote sensing images of desert grassland. VGG16 and ResNet18 achieved better image classification results for vegetation and bare soil, whereas three-dimensional (3D)-VGG16 and 3D-ResNet18, improved by 3D convolutional kernels, achieved better classification for vegetation, bare soil and small sample features in the images. The number of convolutional kernels, its size and batch size parameters of each model were optimised, and 3D-ResNet18-J had the best classification performance, with an overall classification accuracy of 97.74%. It achieved high precision and efficiency in classifying UAV hyperspectral remote sensing images of desert grassland.*

摘要

对植被进行识别与分类是草原退化监测、分级和定量化研究的基础。通过四种深度学习模型对荒漠草原无人机高光谱遥感图像进行分类，VGG16 和 ResNet18 对图像中的植被和裸土取得了较好的分类结果，而经过 3D 卷积核改进的 3D-VGG16 和 3D-ResNet18 模型对图像中植被、裸土和小样本地物均取得了较好的分类潜力。对各模型的卷积核数量、卷积核尺寸和 Batch size 参数优化，发现分类性能最佳的模型为 3D-ResNet18-J，总体分类精度达到 97.74%。实现了对荒漠草原无人机高光谱遥感图像的高精度和高效率分类。

INTRODUCTION

With the rapid development of computer hardware, computer vision and deep learning have made considerable progress *(Khekare et al., 2022)*. Computer vision has been used in many applications, including object detection, target localisation, target detection and scene classification *(Luca et al., 2022)*. Its misclassification rate for some datasets is lower than that of human eyes. *(Xu et al., 2021)*. Subsequently, deep learning classification methods were gradually introduced into remote sensing image classification, and the early classification stage was mainly based on the spectral feature classification model of remote sensing data with less dimensionality. As the sensor performance improved and the data dimensionality increased substantially, researchers began to explore the classification model using spatial information features. Recently, inspired by video sequence target detection, classification models with joint spectral–spatial feature information were gradually developed for the analysis of high-dimensional remote sensing data *(Zhang et al., 2020)*. Three-dimensional (3D) convolution can extract spectral–spatial feature information simultaneously, which is a powerful tool for extracting detailed features. Deep learning models based on 3D convolution have been successfully applied to the feature classification of widely used remote sensing datasets such as Pavia University, Indian Pines and Botswana *(Liang et al., 2021)*, while researchers have developed and optimised 3D convolution models for the data characteristics and feature characteristics of widely used remote sensing datasets *(Xiao et al., 2019)*.

The remote sensing monitoring of grassland degradation is mainly based on vegetation community characteristics, cover, biomass and soil properties to identify the degradation degree *(Zhou et al., 2019*; *Esteves de Oliveira et al., 2017)*, while the low-altitude remote sensing platform formed by "Unmanned aerial vehicle (UAV) + hyperspectral remote sensing" has the advantages of abundant data sources, wide coverage, time and effort saving and rapid and repeated deployment *(Liu et al., 2018)*. The obtained hyperspectral images have rich spectral dimensional information and high spatial–spectral resolution, which makes them high-quality data sources for studying the composition of target features at a microscopic scale *(Paoletti et al., 2019)*. Presently, the following bottlenecks exist in grassland vegetation classification. For data acquisition, satellite data, UAV + camera, and UAV + multispectrometer are commonly used, and their spatial resolution is limited. For data classification methods, most of the features are classified by calculus operation, vegetation index operation, threshold difference calculations, etc. The desertified grassland land has high similarity among species groups and sparse and low vegetation. This high similarity among species groups, low vegetation sparseness and fragmented patchy distribution in desertified grassland makes identification and classification extremely difficult and requires high-quality data and classification methods.

The spatial resolution of the UAV hyperspectral remote sensing images collected in this research is up to the centimetre level, which is quantitatively different from the widely used remote sensing datasets, and the features are small, fragmented and sparse. Thus, we fully use the spectral–spatial characteristics of the data to further explore, establish and optimise the deep learning streamlined model applicable to the characteristics of the hyperspectral datasets of desert grassland features to realise the efficient, high precision and intelligent classification and statistics of desert grassland features.

MATERIALS AND METHODS

Data acquisition

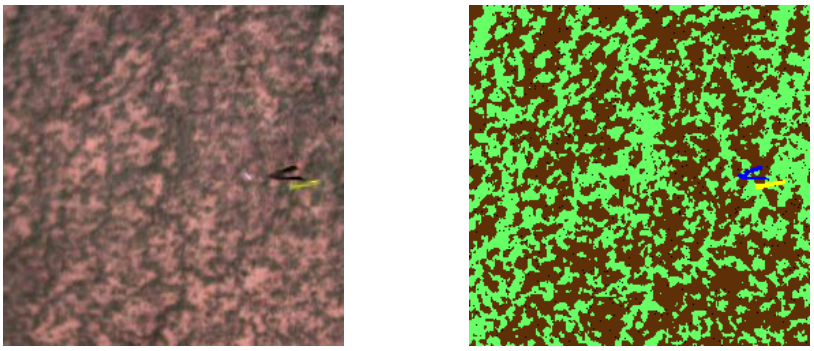
The test area is located in Gegentara Grassland, Siziwang Banner, Ulanqab city (41.78°N, 111.88°E), and a MATRICE 600 PRO six-rotor UAV with a Gaiasky-mini-VN hyperspectral instrument was used to collect hyperspectral remote sensing images of the interior of the test area in hovering mode. The data were collected from July 27 to August 8 during the mushrooming period of forage grass in 2021. To ensure acquisition quality, clear, cloudless days with good light conditions and low wind conditions were selected for the measurement, and the acquisition time was from 10:00 to 14:00. A calibration was required every 10–20 min using a standard whiteboard to eliminate the influence of light intensity changes on the UAV hyperspectral images. The UAV was equipped with a hyperspectral instrument to measure the hyperspectral data of the canopy and the vegetation community in the test area at the height of 30 m perpendicular to the ground directly, and 2–3 hyperspectral remote sensing images were collected at each hovering point. The ground survey included recording GPS information, vegetation species in the occupied area and the bare soil area to obtain accurate ground verification values.

Data processing

The raw hyperspectral image data captured by Gaiasky -mini-VN were pre-processed in three steps. The first step is image quality evaluation, where the remote sensing images with the best image quality were selected by manually checking to remove overexposed, underexposed, bent and littered images. The second step is radiometric calibration, wherein the original DN values were converted into reflectance using the professional spectral software SpecView. The third step is smoothing and noise reduction, for which the classical Frobenius norm^2 method was used to retain the complete spectral space information and achieve data dimensionality reduction *(Wang et al., 2019)*.

Ground truth value

To improve the calculation efficiency of the four-network model, the collected T1 images of the desert grassland were cropped to a size of 250 rows × 250 columns, with a total of 62,500 image elements to make a hyperspectral dataset, as shown in Figure 1a. The four grassland features in the dataset were labelled as vegetation, bare soil, shadow and others, as shown in Figure 1b. The colour coding and the number of samples are listed in Table 1. Among the labelled samples, 60% were randomly selected as training data, and 40% were test data to identify the features.



a. False colour composite *b. Ground truth value*

Fig. 1 - T1 image false colour composite and the ground truth

Table 1

Colour coding and sample number of T1 images

Class	Colour coding	Number of test samples	Number of training samples	Total
Vegetation		10582	15874	26456
Bare soil		14348	21524	35872
Shadow		38	57	95
Others		30	47	77
Total		24998	37502	62500

VGG16 Network model

Proposed by the Oxford Visual Geometry team, the VGG16 model is a classical neural network model. It is essentially a deep learning approach to improving image recognition and classification accuracy by minimising the loss function in the network by gradient descent and continuously optimising it after several iterations of training *(Zhang et al., 2022).* This model replaces the original 5 × 5 and 11 × 11 convolutional kernels in AlexNet with 3 × 3 convolutional kernels, and the study proves that the 3 × 3 convolutional kernels can reduce the computational complexity, effectively reduce the parameters and improve the training efficiency. The VGG model achieves good results in image classification and image localisation and can effectively extract deep features. In this study, the VGG16 convolutional neural network is built based on the VGG model proposed by Simonyan *(Simonyan et al., 2014)* using the Pytorch module, which has 22 layers, including 13 convolutional layers, five pooling layers, three fully connected layers, and one Softmax layer. The 13 convolutional layers are divided into five convolutional blocks, and a pooling layer is placed after each convolutional block. The minimum number of cores for the convolutional layers is 32, and the maximum number is 1024.

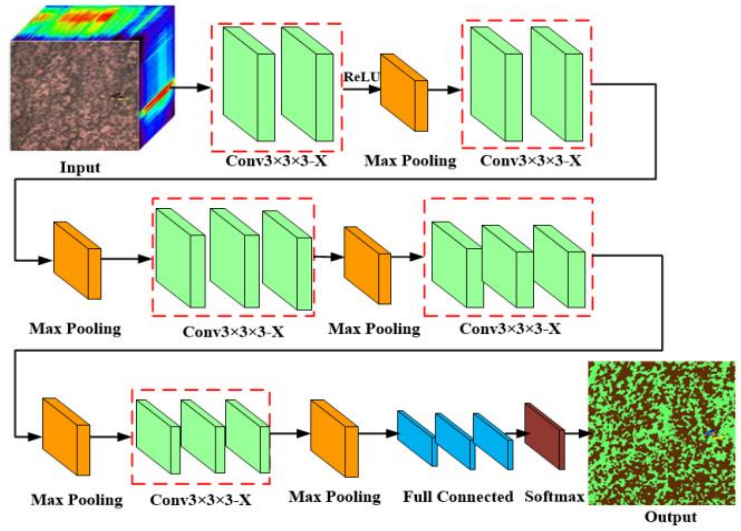
ResNet18 Network model

Proposed by engineers such as He of Microsoft *(He et al., 2015)*, ResNet18 is a classical neural network model. This model introduces the idea of residual learning into the network structure, superimposes the input and output of the residual block (Residual Block) and sums them through the Skip Connection. This operation improves the efficiency of backpropagation, effectively solves the gradient disappearance and gradient explosion problems that occur in deep networks, accelerates neural network training and realises the use of a deep network structure to extract detailed features *(Zhang et al., 2019)*. The ResNet18 convolutional neural network is built based on the ResNet model proposed by *He et al.* using the Pytorch module, which has 21 layers, including 17 convolutional layers, two pooling layers, one fully connected layer, and one Softmax layer. The 17 convolutional layers are divided into one convolutional layer and eight residual blocks. Two convolutional layer operations are performed in each residual block and superimposed with the parameters before convolution, followed by activation into the next residual block using the activation function ReLU. The minimum number of convolutional layers is 32, and the maximum number is 1024 kernels.

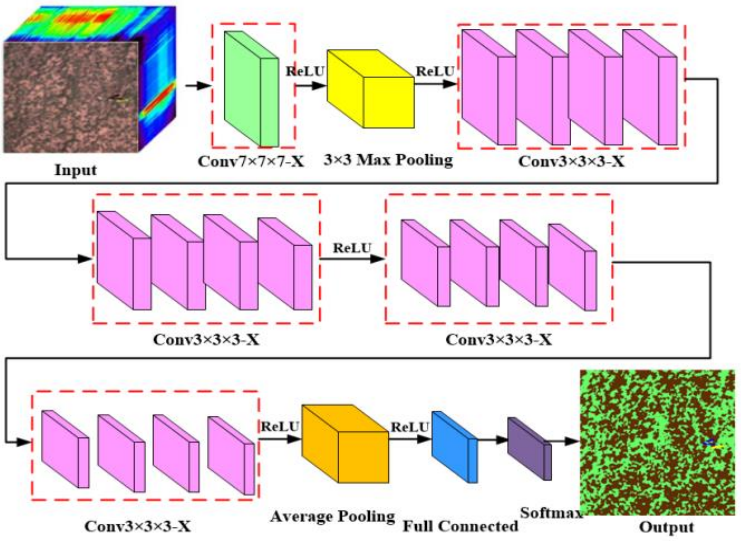
3D model based on VGG16 and ResNet18

Based on the Pytorch module, the two-dimensional (2D) convolutional kernels of two typical deep learning models, VGG16 and ResNet18 (hereafter referred to as VGG and ResNet, respectively), were replaced by 3D convolutional kernels to build the 3D-VGG16 model and the 3D-ResNet18 model (hereafter referred to as the 3D-VGG model and the 3D-ResNet model, respectively). Because of the numerous parameters involved in the 3D convolutional operations, the models on a DELL Precision 7920 workstation were trained with the following main parameters: a Xeon Gold CPU containing 16 cores and 32 threads; an NVIDIA Quadro P4000 graphics card with 24 GB of video memory, containing 3840 CUDA cores; and 256 GB of RAM.

3D-VGG comprises 13 convolutional layers (convolutional cores are denoted as Conv1×1×1-X, Conv3×3×3-X, where X is the number of convolutional cores), three fully connected layers (denoted as Fc-x, where x is the fully connected layer level), and five pooling layers (denoted as Max Pooling). 3D-ResNet18 comprises 17 convolutional layers (denoted as Conv3×3×3-X, Conv7×7×7-X, X being the number of convolutional kernels), one fully connected layer (denoted as Fc) and two pooling layers (denoted as Pooling). Two convolutional layer operations are performed in each residual block and superimposed with the parameters before convolution, followed by activation into the next residual block using the activation function ReLU. The 3D-VGG and 3D-ResNet18 deep learning models are structured as shown in Figure 2.



a. 3D-VGG



b. 3D-ResNet

Fig. 2 - Structure diagram of the 3D-VGG and 3D-ResNet deep learning models

Evaluation indices

Overall classification accuracy (OA) and producer accuracy (PA) will be used to evaluate the classification accuracy.

(1) The OA refers to the ratio of the number of correctly classified pixels in a random sample to the total number of pixels in the sample, which can reflect the accuracy of hyperspectral remote sensing classification results more intuitively. The formula for OA is shown in equation (1).

$$\mathrm{OA} = \frac{\sum_{i=1}^{k} x_{ii}}{N}, \quad (1)$$

Where:

N represents the number of sample pixels, k represents the number of categories, and x_{ii} represents the composition of class i of the classification result with respect to class i of the reference type data.

(2) The PA refers to the ratio of the number of pixels that correctly classify the entire image into a certain class to the total number of such real samples. The formula for PA is shown in equation (2).

$$\mathrm{PA} = \frac{P_i}{R_i}, \quad (2)$$

Where:

P_i represents the number of samples whose type i is correctly classified in the classification result, and R_i represents the true value of the image element of type i.

RESULTS AND DISCUSSION

The main parameters of the four deep learning models, such as the number of convolutional kernels, kernel size and batch size, were optimised, and the influence of each parameter on the 3D convolutional neural network model was analysed to further improve the accuracy and efficiency of the 3D convolutional neural network model for feature classification.

Optimisation of the number of convolutional kernels

The classification performances are compared based on the VGG and 3D-VGG network models with three numbers of convolutional kernels, A, B and C. The corresponding numbers of convolutional kernels are shown in Table 2. The label Conv3×3(×3)-32 represents that 32 convolutional kernels of size 3 × 3 are in the Block_1 layer of VGG-A, 32 convolutional kernels of size 3 × 3 × 3 are in the Block_1 layer of 3D-VGG-A, and so on. The classification performance comparison is based on ResNet and 3D-ResNet network models with three convolutional kernels, A, B and C. The corresponding convolutional kernels are shown in Table 2. In this table, Conv7×7(×7)-32 represents that 32 convolutional kernels of size 7 × 7 are in the Block_1 layer of ResNet-A, 32 convolutional kernels of size 7 × 7 × 7 are in the Block_1 layer of 3D-ResNet-A, and so on.

Table 2

Number of different convolutional kernels for the four models

Model	Block_1	Block_2	Block_3	Block_4	Block_5
VGG-A(3D-VGG-A)	Conv3×3(×3)-32	Conv3×3(×3)-64	Conv3×3(×3)-128	Conv3×3(×3)-256	Conv3×3(×3)-256
VGG-B(3D-VGG-B)	Conv3×3(×3)-64	Conv3×3(×3)-128	Conv3×3(×3)-256	Conv3×3(×3)-512	Conv3×3(×3)-512
VGG-C(3D-VGG-C)	Conv3×3(×3)-128	Conv3×3(×3)-256	Conv3×3(×3)-512	Conv3×3(×3)-1024	Conv3×3(×3)-1024
ResNet-A(3D-ResNet-	Conv7×7(×7)-32	Conv3×3(×3)-32	Conv3×3(×3)-64	Conv3×3(×3)-128	Conv3×3(×3)-256
ResNet-B(3D-ResNet-	Conv7×7(×7)-64	Conv3×3(×3)-64	Conv3×3(×3)-128	Conv3×3(×3)-256	Conv3×3(×3)-512
ResNet-C(3D-ResNet-	Conv7×7(×7)-128	Conv3×3(×3)-128	Conv3×3(×3)-256	Conv3×3(×3)-512	Conv3×3(×3)-1024

Figure 3 shows that the PA of the VGG model increases with the number of convolutional kernels. The increasing trend in diverse native vegetation and bare soil is more obvious, while the small sample features-

shadow performs best in the VGG-B model. All three models cannot classify the small sample features-other, and the VGG-B model has the best OA.

The 3D-VGG-B model has the best OA at 96.98%, which is 0.52 percentage points better than that of the VGG-B model. 3D-ResNet has better classification performance than ResNet. The PA of the ResNet model increases with the number of convolutional kernels, while the increasing trend in diverse native vegetation and bare soil is smaller. The increasing trend in small sample features-other is more obvious, while the highest accuracy in small sample features-shadow is achieved by the ResNet-B model. The difference in the PA of diverse natives in the 3D-ResNet model is smaller. The best PA was obtained by the 3D-ResNet-B model.

The highest OA, 97.14%, was obtained by the 3D-ResNet-B model and was 2.02% higher than that of the ResNet-B model.

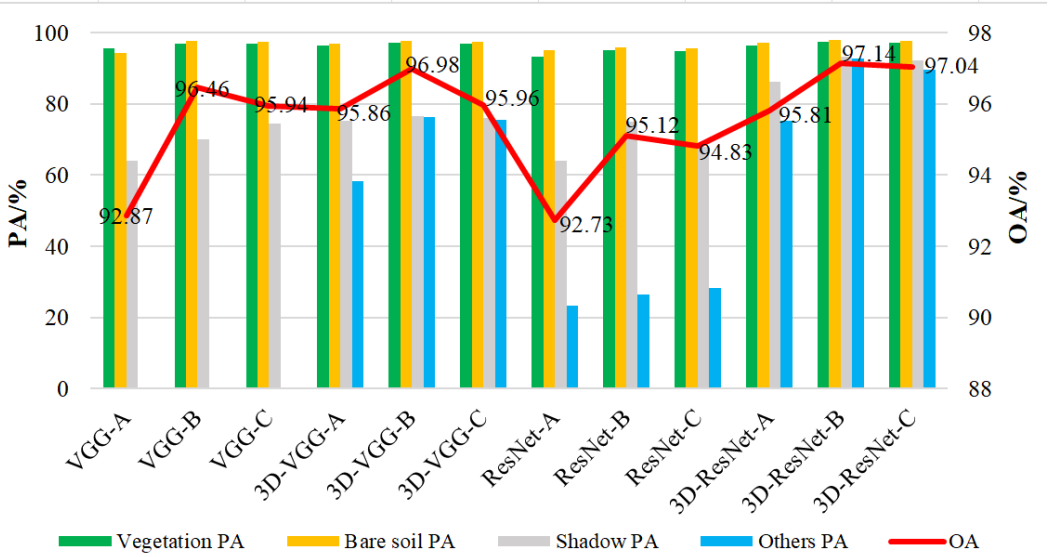


Fig. 3 - Comparison of the classification performances of models with different numbers of convolutional kernels

Convolutional kernel size optimisation

The three convolutional kernel sizes based on the VGG and 3D-VGG network models, identified as D, E and F, are compared in terms of classification performance. The corresponding number of convolutional kernels is shown in Table 3, and the label Conv3×3(×3)-64 represents that 64 convolutional kernels of size 3 × 3 are in the Block_1 layer of VGG-D, 64 convolutional kernels of size 3 × 3 × 3 are in the Block_1 layer of 3D-VGG-D, and so on. The classification performance comparison based on ResNet and 3D-ResNet network models with three convolutional kernel sizes, D, E, and F, and the corresponding number of convolutional kernels are shown in Table 3. Conv7×7(×7)-64 in this table represents that 64 convolutional kernels of size 7 × 7 are in the Block_1 layer of ResNet-D, 64 convolutional kernels of size 7 × 7 × 7 are in the Block_1 layer of 3D-ResNet-D, and so on.

Table 3

Convolutional kernel sizes for the four models

Model	Block_1	Block_2	Block_3	Block_4	Block_5
VGG-D(3D-VGG-D)	Conv3×3(×3)-64	Conv3×3(×3)-128	Conv3×3(×3)-256	Conv3×3(×3)-512	Conv3×3(×3)-512
VGG-E(3D-VGG-E)	Conv5×5(×5)-64	Conv5×5(×5)-128	Conv5×5(×5)-256	Conv5×5(×5)-512	Conv5×5(×5)-512
VGG-F(3D-VGG-F)	Conv7×7(×7)-64	Conv7×7(×7)-128	Conv7×7(×7)-256	Conv7×7(×7)-512	Conv7×7(×7)-512
ResNet-D(3D-ResNet-D)	Conv7×7(×7)-64	Conv3×3(×3)-64	Conv3×3(×3)-128	Conv3×3(×3)-256	Conv3×3(×3)-512
ResNet-E(3D-ResNet-E)	Conv7×7(×7)-64	Conv5×5(×5)-64	Conv5×5(×5)-128	Conv5×5(×5)-256	Conv5×5(×5)-512
ResNet-F(3D-ResNet-F)	Conv7×7(×7)-64	Conv7×7(×7)-64	Conv7×7(×7)-128	Conv7×7(×7)-256	Conv7×7(×7)-512

The classification performance of the 3D-VGG model with different convolutional kernel sizes is better than that of the VGG model, and all models reach the best classification performance in the F model. The PA of the VGG model is positively correlated with the convolutional kernel size, among which the increasing trend in diverse native vegetation and bare soil and small sample features-shadow is more obvious. In contrast, all three models cannot classify small sample features-other, and the highest OA is that of the VGG-F model. The 3D-VGG model has the highest OA at 97.29%, which is 0.51 percentage points higher than that of the VGG-F model. The 3D-VGG model is positively correlated with the size of the convolutional kernel, and the increasing trend in the small sample features-other is the most obvious.

In terms of classification performance, the ResNet model outperformed the ResNet model, and both models reached their best classification performance in the F model. The PA of the ResNet model was positively correlated with the number of convolutional kernels and showed less increase for diverse features of vegetation and bare soil. In contrast, the PA of small sample features-other increased more, and the ResNet-F model had the highest OA. The PA of the 3D-ResNet model is positively correlated with the number of convolutional kernels, smaller for two diverse natives and larger for two small sample features.

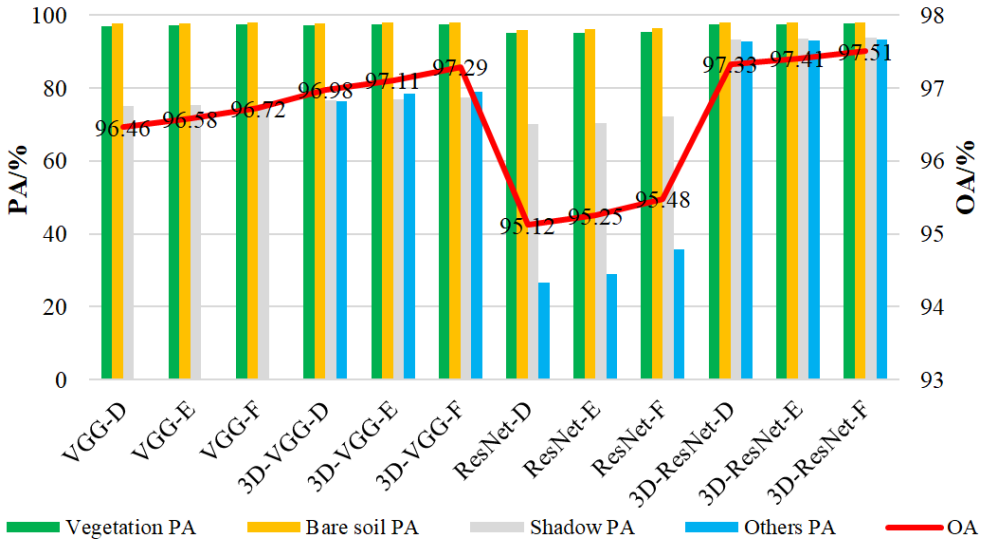


Fig. 4 - Comparison of classification performances under different convolutional kernel sizes

Batch size optimisation

The classification performances of different batch size models on the dataset were investigated for the batch sizes 32, 64, 128 and 256, identified as G, H, I and J, respectively. The corresponding names of the batch size models are shown in Table 4.

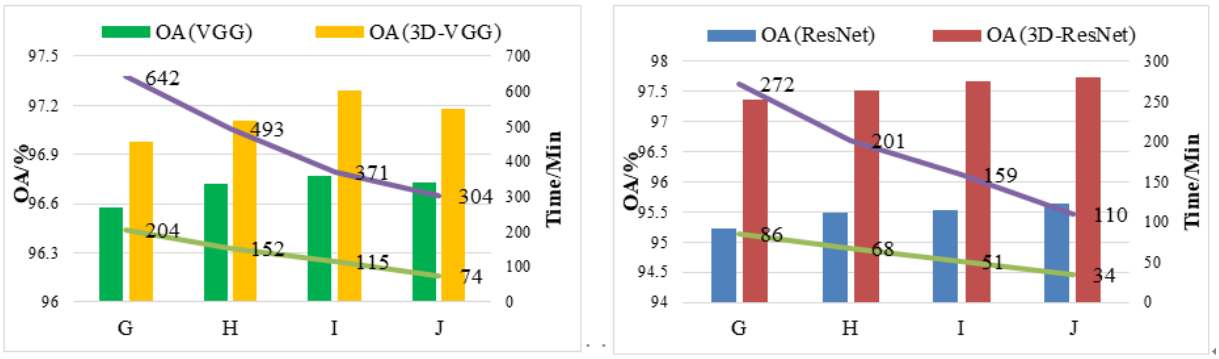
Table 4

Different batch sizes for the four models

Batch Size	32	64	128	256
VGG	VGG-G	VGG-H	VGG-I	VGG-J
3D-VGG	3D-VGG-G	3D-VGG-H	3D-VGG-I	3D-VGG-J
ResNet	ResNet-G	ResNet-H	ResNet-I	ResNet-J
3D-ResNet	3D-ResNet-G	3D-ResNet-H	3D-ResNet-I	3D-ResNet-J

Figure. 5a shows that as the batch size gradually increases, the time to reach convergence and the overall classification accuracy show decreasing and increasing trends, respectively, for the VGG model, and the highest OA is obtained at a batch size of 128 (VGG-I). The 3D-VGG model with four batch sizes shows a decreasing trend in convergence time, and an increasing trend in OA as the batch size gradually increases. The highest OA was obtained at a batch size of 128 (3D-VGG-I). A comparison of the performances of the VGG and 3D-VGG models with four batch sizes shows that the VGG model converges sooner and has lower accuracy. The VGG-I model with the best classification accuracy of 96.85% converges in 115 min, while the 3D-VGG-I model with the best classification accuracy of 97.38% converges in 371 min.

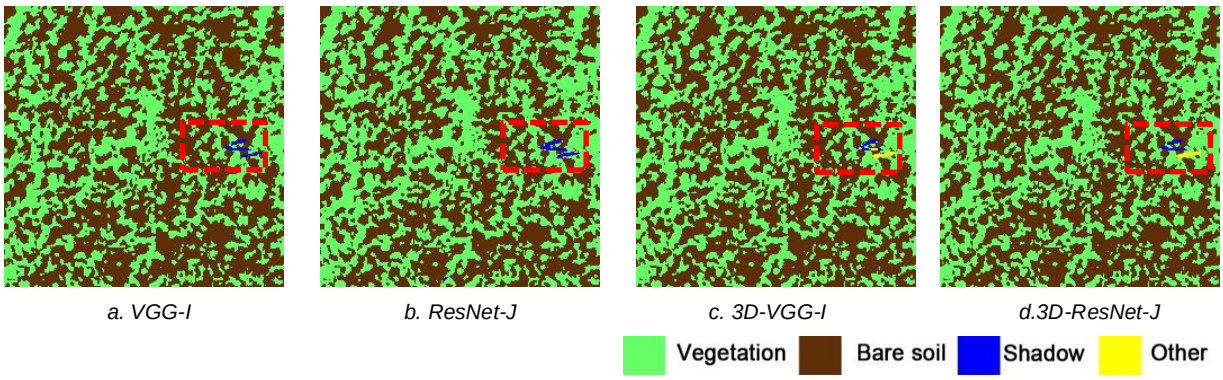
As shown in Figure 5b, as the batch size gradually increases, the convergence times and overall accuracies of the four batch size ResNet models tend to decrease and increase, respectively, and the highest OA is obtained at a batch size of 256 (ResNet-J). The 3D-ResNet models with four batch sizes show a decreasing trend in convergence time and an increasing trend in OA with increasing batch size. The highest OA was obtained at a batch size of 256 (3D-ResNet -J). Comparing the performance of the ResNet and 3D-ResNet models with four batch sizes, it is observed that the ResNet model converges faster and has lower accuracy. The ResNet-J model with the best accuracy of 95.64% converges in 34 min, while the 3D-ResNet-J model with the best accuracy of 97.74% converges in 110 min.



a. VGG and 3D-VGG *b. ResNet and 3D-ResNet*

Fig. 5 - Classification performances of the four models with different batch sizes

After optimisation, the visualisation results of the best classification effect of the four types of deep learning models are shown in Figure 6.



a. VGG-I *b. ResNet-J* *c. 3D-VGG-I* *d.3D-ResNet-J*

Fig. 6 - Classification visualisation results of the four models

CONCLUSIONS

The main conclusions of this study are as follows:

(1) Optimising the model structure and the hyperparameters of the number of convolutional kernels, their size and batch size improves the accuracy of the 2D convolutional model substantially, indicating that the initial 2D model has a considerable improvement space for the feature extraction of small sized features in a dataset. The initial 3D model performs better than the 2D model at dataset feature extraction with less improvement space.

(2) The study found that the 3D convolutional network model has better dataset classification performance than the 2D model. Compared with 2D convolution, which can only extract 2D spectral information in the dataset, 3D convolution can extract combined spectral–spatial information simultaneously, making full use of the data characteristics of hyperspectral datasets and showing good potential for the extraction of vegetation and other features. This potential exists because the 3D convolutional kernel can simultaneously extract spectral information of fine features in the three dimensions of the hyperspectral data than the 2D convolutional kernel that simultaneously extracts spectral information only in two dimensions.

(3) The model performance is gradually improved by optimising the model structure and hyperparameters, and the 3D-ResNet model with a deeper convolutional structure shows better performance. Its producer accuracy and OA are higher than those of the 3D-VGG model. The overall accuracy of the optimised 3D-ResNet-J model reaches up to 97.74%, which is 2–5% higher than the other ResNet models. It achieves high precision, efficiency and intelligent classification of features in the dataset, laying the foundation for fast, efficient and accurate statistics of different vegetation communities in desert grasslands based on UAV hyperspectral remote sensing.

ACKNOWLEDGEMENT

The paper has been funded by the National Natural Science Foundation of China (NSFC) (No.31660137) and the Scientific Research Project of the Inner Mongolia Autonomous Region (No. NJZY21518) and special fund support for basic scientific research business expenses of Inner Mongolia Agricultural University (No. BR220152).

REFERENCES

[1] He, K., Zhang, X., Ren, S. (2015). Deep residual learning for image recognition. *IEEE*, Vol. 12, pp.1-12.

[2] Khekare, P., Bonthu, S., Hunt, V., Helmicki, A., & Lee, K. (2022). A case study on multilane roundabout capacity evaluation using computer vision and deep learning. *Journal of computing in civil engineering* (3), 36.

[3] Liang, L.H., Li, J., &Zhang, S.Q. (2021). Hyperspectral images classification method based on 3D Octave Convolution and Bi-RNN Attention Network (基于 3D Octave 卷积和 Bi-RNN 注意力网络的高光谱图像分类方法). *Acta Photonica Sinica*, Vol. 50, pp.284-296.

[4] Liu, Z., Wan, W., Huang, J.Y. (2018). Progress on key parameters inversion of crop growth based on unmanned aerial vehicle remote sensing (基于无人机遥感的农作物长势关键参数反演研究进展). *Transactions of the Chinese Society of Agricultural Engineering*, Vol.34, pp.60-71.

[5] Luca, B., Alberto, F., Mauro, J. (2022). Precise Agriculture: Effective Deep Learning Strategies to Detect Pest Insects. *IEEE/CAA Journal of Automatica Sinica*, Vol. 9, pp.246-258.

[6] Paoletti, M.E., Haut, J.M., Plaza, J. (2019). Deep learning classifiers for hyperspectral imaging: A review. *ISPRS Journal of Photogrammetry and Remote Sensing*, Vol. 158, pp.279-317.

[7] Simonyan, K., Zisserman, A. (2014). Very deep convolutional networks for large-scale image recognition. *Computer Vision and Pattern Recognition*, Vol. 9, pp. 22-28.

[8] Esteves de Oliveira, T., David, Santos de Freitas, D., Gianezini, M., Ruviaro, C.F., Zago, D., Mercio, T.Z., Dias, E.A., Lampert, V., Barcellos, J. (2017). Agricultural land use change in the Brazilian Pampa Biome: The reduction of natural grasslands. *Land Use Policy*, Vol. 63, pp.394–400.

[9] Wang, W.G., Song, W., Wang, G.Y. (2019). Image recovery and recognition: A combining method of matrix norm regularization. *IET Image Processing*, Vol.13, pp.1246-1253.

[10] Xu, D., Wang, L., & Li, F. (2021). Review of typical object detection algorithms for deep learning (深度学习的典型目标检测算法研究综述). *Computer Engineering and Applications*, Vol. 57, pp.10-25.

[11] Xiao, Z., Jiang, J., & Ni, C. (2019). Spectral-spatial classification of hyperspectral image based on self-adaptive deep residual 3D convolutional neural network. *Journal of Computer-Aided Design & Computer Graphics*.

[12] Zhang, B., Zhao, L., & Zhang, X. L. (2020). Three-dimensional convolutional neural network model for tree species classification using airborne hyperspectral images. *Remote Sensing of Environment*, Vol.247, pp.1-16.

[13] Zhou, L., Xin, X.P., Li, G. (2019). Application progress on hyperspectral remote sensing in grassland monitoring (高光谱遥感在草原监测中的应用). *Pratacultural Science*, Vol.26, pp.20-27.

[14] Zhang, X.L., Peng, Y. (2019). An audio recognition method based on residual network and random forest (基于残差网络和随机森林的音频识别方法). *Computer Engineering & Science*, Vol.41, pp.727-732.

[15] Zhang, Y.B., Du, J.M., Pi, W.Q., Wang, Y., Gao, X. C. (2022). Deep learning classification of grassland desertification in China via low-altitude UAV hyperspectral remote sensing. *Spectroscopy*, Vol.37, pp.28-35.

RESEARCH ON KINEMATICS SIMULATION AND DYNAMIC ANALYSIS OF THE COLLECTION MECHANISM OF ORCHARD BRANCHES
/
果园枝条收集机构的运动学仿真与动力学分析研究

Hui LI[1)], Xin YANG[2*)], Aiqian YANG[1)]
[1)]Hengshui University, Hengshui, 053000 / China;
[2)]College of Mechanical and Electrical Engineering, Hebei Agricultural University, Baoding, 071000 / China;
E-mail: yangxin@hebau.edu.cn
DOI: https://doi.org/10.35633/inmateh-69-47

Keywords: *branch pruning residue, spring finger, collection mechanism, dynamic, simulation*

ABSTRACT
The spring finger collection mechanism is a core component of balers. It is usually used to collect soft straw crops (corn straw, wheat straw, green forage), and rarely used for hard stem crops (such as branch pruning residues). Due to different biophysical characteristics of hard stem crops and soft straw crops, the collection mechanisms are also different. In China, branch pruning residues in apple orchards are collected manually. It is a heavy labor task. To this end, this article uses an improved spring finger mechanism to collect pruning residues in apple orchard branches, effectively replacing manual collection operations. A dynamic motion trajectory simulation platform is developed by analyzing each action using pitchforks or other agricultural tools throughout the entire collection process, and combined with the structure of the spring finger collection mechanism. The platform of the spring finger collection mechanism is improved to collect orchard branches, and redesign and manufacture the core components of the collection mechanism. In addition, comparative tests were performed on4 different placement orientation sunder the conditions of R=40±2 r/min and V=0.9-1.1 m/s. That is, 1) messy, 2) transverse, 3) portrait orientation (the treetop firstly contacts the collection device), and 4) portrait orientation (the thick stems of the branches first touch the collection device). The results indicate that 1) and 2) have similar success rates in picking branches, while 3) and 4) have lower success rates, especially with 4) being the lowest). The analysis found that some branches were directly inserted into the spring finger gap and moved under the machine, resulting in a large amount of losses. This study aims to improve the success rate of picking branches in the bundling machine and verify the relationship between different placement directions and the success rate of picking branches.

摘要
弹簧指型收集机构是打捆机的核心部件，通常用于收集软秸秆作物（玉米秸秆、小麦秸秆、绿色牧草），而很少用于硬秸秆作物（树枝修剪残留物）。由于硬秸秆作物和软秸秆作物的生物物理特性不同，两者的收集机制也有所不同。在中国，苹果园的树枝修剪残留物是人工收集的。这是一项繁重的劳动任务。本文采用一种改进的弹簧指式机构收集苹果园枝条修剪残余物，以有效代替人工收集作业。通过分析在整个收集过程中使用干草叉或其它农具的每个动作，并结合弹簧指型收集机构本身的结构，开发了一个动态运动轨迹仿真平台。该平台对弹簧指型收集机构进行了改进以适应收集果园枝条，并对收集机构的核心部件进行了重新设计和制造。此外，在 R=40±2 R/min 和 V=0.9~1.1 m/s 的条件下，对 4 种不同的摆放位置进行了对比试验，即 1）杂乱、2）横向、3）纵向（树梢首先接触收集装置）和 4）纵向（树枝的粗茎首先接触收集装置）。结果表明，1）和 2）拾取树枝的成功率相似，而 3）和 4）的成功率较低，尤其是 4 最低），分析原因发现一些树枝直接插入弹簧指间隙并移动到机器下方，从而导致大量损失。本研究的目的是提高打捆机的拾取枝条成功率，并验证不同放置方向对拾取成功率的影响关系。

Hui Li, Lecturer. Ph.D.; Xin Yang, Prof. Ph.D.; Aiqian Yang, Lecturer;

INTRODUCTION

In recent years, the development and utilization of renewable energy has received more and more attention *(Romański et al., 2014).* In Poland, statistic results show that 60% of orchard farms are planted on an area greater than 5 hectares, and up to 71% are covered by apple orchards *(Adamczyk et al., 2014). A* large number of apple branch pruning residues are produced annually. *Spinelli and Picchi, (2010),* confirmed that the potential supply of wood from orchards ranged from 0.6 to 20 million m^3/year. For many years, most growers have treated the apple branch pruning residues by either stacking them together and burning them, or directly smashing them by a shredder to cover the soil *(Popa et al., 2022)*. Obviously, these methods do not bring economic benefits to growers and may pollute air quality and the environment.

In the last few years, some growers proposed to collect the scattered branch pruning residues from apple orchards using the collection mechanism of a baler, and then store the apple branch residues in baled form to replace wood as a fuel energy source *(Arkadiusz, 2019; Adamczyk et al., 2014)*. They conducted a feasibility assessment of using apple tree pruning residues in bales for energetic purposes, and suggested that the annual harvest of pruned biomass could be considered a good energy source for local heating systems *(Arkadiusz, 2018)*.

Ntalos and Grigoriou (2002) also stated that vineyard pruning residues could partly replace the traditional wood assortments for energy and industrial use. These pruning residues play an important subsidiary role in supplying bio-energy plants with renewable fuel *(Bernetti et al., 2006)*. Clearly, pruning residues are an important renewable biomass energy source that could bring some economic benefits if they could be conveniently collected and stored from orchards *(Arkadiusz, 2019).*

Currently, New Holland Company has developed and tested a round branch baler, demonstrating the feasibility of using a baler to collect branch pruning residues.

Fŕckowiak et al. (2016) reported that the Poznan Institute of Agricultural Engineering Industry developed a new machine for compressing branch pruning residues in orchards into round bales, and modified and reinforced the picking system of the branch baler.

Raffaele et al., (2012) reported that a new mini-baler system was designed and tested to recover pruning residues from vineyards where conventional tractors could not be used. But all of these rarely mention the pickup system of the machine.

In China, the spring finger collection mechanism is usually used to collect soft straw crops, and rarely for hard stem crops (such as apples, vineyards and olives). Since these branch pruning residues have biophysical properties with high wood fiber content, a relatively harder surface, less elasticity and resistance to deformation, they are different from soft straw crops. Therefore, the collection mechanism of soft straw crops is not suitable for hard stem crops.

Fu (2015) performed the structure design of the spring finger collection mechanism for collecting green forage and corn straws.

Xu et al., (2016), optimized the primary parameters of the spring finger collection mechanism for the two-stage harvest peanut straws. However, all reports have rarely investigated the spring finger collection mechanism used to collect hard stem crops.

The main objective of this study is to develop a hard stem crop collection mechanism for balers, considering picking height, picking angle, picking dynamic motion trajectory, picking speed and dynamic analysis. The purpose is to enhance the picking performance of the collection mechanism for hard stem crops, and to verify the optimal orientations of branches laid on the ground, so as to achieve better collection results.

MATERIALS AND METHODS

Process for collecting branch residues using farm implements

In a survey, in dwarfed and high-density planted apple orchards, most apple branches will be pruned and a new cycle of young branches will be created within 3-4 years to replace the old branches. *Zhen, (2017),* reported that the branches less than 35mm in diameter account for more than 90% of the pruning residues, and most of branch pruning residues end up close to the ground (Fig 1).

Some workers use a rake to pile branches and leave them in a swath on the ground. It is found that the rod of the rake forms a series of angles with the ground during collection. When these branch residues move next to the rake, the angle of the rake rod changes, and the angle changes in the range of 40°-70°. Other workers use a large pitchfork to lift the branch residues off the ground. Through the branch lifting process, the first insert angle into the piled branches is about 25°- 40°, and then the branches are lifted until the rod of the tool is horizontal to the ground.

The next step is to transport the branch residues to the entrance of the vehicle or shredder. Due to the high position of the entrance to the vehicle or the shredder, people stand on the side of the vehicle and the branches are lifted, and then the pitchfork moves in an arc to the entrance of the vehicle in the space. Finally, the pitchfork quickly breaks off from a set of branch residues to start a new cycle.



Fig. 1 - Distribution of branch pruning residues in an apple orchard

Kinetic analysis of the spring finger collection mechanism

To improve the branch picking performance of the baler, the spring finger collection mechanism is improved. The collection mechanism is a core component of the baler, which determines the percentage of retrieved branches relative to the total amount, directly influencing the baler collection performance. According to investigators who have demonstrated the use of agricultural tools to collect branches, the changes in the use of agricultural tools mainly involves angles, postures, and trajectories. Based on various crop straw collection devices, a spring finger collection mechanism is selected.

There are two reasons, that is, the trajectory and attitude are the key factors of the picking process, and the cam disk is the core component of the spring finger collection mechanism, which directly determines the trajectory and angle of the spring finger. The shape of the cam disk is improved to meet the collection requirements. The methods of separating branches preserve their integrity and allow them to be stored in bales.

Wang, (2012), reported the working principle of the spring finger cylinder collection device, which is mainly composed of spring fingers_ (1), crank_(2), link_(3), central axis_(4), cam disk_(5) and guard plate_(6), as shown in Fig. 2.

According to the angle of the spring finger in space, the entire cycle of the collection is divided into about five phases (gathering, lifting, transporting, feeding, separating and recovering). When using farm machinery, each stage of the collection mechanism will be matched with an operation. During the collection process of branches, Fig. 2 shows the force of branches. Force F is divided into F_1 (force in the horizontal direction) and F_2 (force in the vertical direction). α_1, α_2, α_3, $\alpha_4$and α_5 are the rotation angles of the central axis in the gathering, lifting, transporting, feeding, separating and recovering phases, respectively.

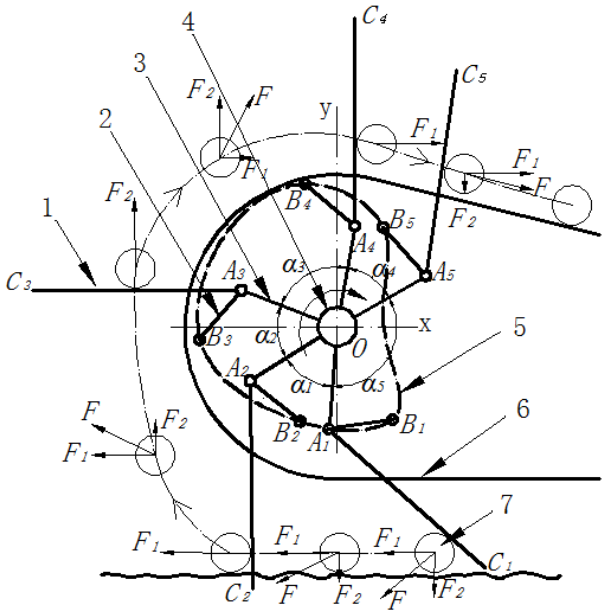


Fig. 2 - Kinetic analysis of the spring finger collection mechanism

The collection device mainly consists of spring fingers_ (1), crank_(2), link_(3), central axis_(4), cam disk_(5) and guard plate_(6), branch pruning residues_ (7). $\Delta A_1B_1C_1$, $\Delta A_2B_2C_2$, $\Delta A_3B_3C_3$, $\Delta A_4B_4C_4$ and $\Delta A_5B_5C_5$ are the collection mechanisms for different positions.

In Fig. 2, during the gathering phase_ (A_1C_1-A_2C_2), the spring fingers start to contact the branches and push them ahead, and then pile them together. F_1 has a critical influence on the branches laid on the ground during this phase. During the lifting phase_ (A_2C_2-A_3C_3), F_2 will increase gradually, and it will play a key role in taking branches off the ground. During the transporting phase_ (A_3C_3-A_4C_4), F_1 will change its direction compared with the above phases, and help the branches to move into the cavity of the baler. During the feeding phase_ (A_4C_4-A_5C_5), F will force the branches to follow the top side of the guard plate and slide into the cavity of the baler. During the separating and recovering phase_ (A_5C_5-A_1C_1), it will complete the separation between the spring finger and branches, and then recovery the original state. The data analysis and process are shown in Table 1.

Table 1

Kinetic analysis in each phase of periodic collection

Each phase of collection	Stress on branches		α	β		The moving position of the spring finger in space
	F_1	F_2		Start	End	
Gathering	-↑	-↓	α_1	The far end of the spring finger touches the ground	90°	A_1C_1-A_2C_2
Lifting	-↓	+↑	α_2	90°	180°	A_2C_2-A_3C_3
Transporting	+↑	+↓	α_3	180°	270°	A_3C_3-A_4C_4
Feeding	+↓	-↑	α_4	270°	Vertical between the spring finger and the top side of the guard plate	A_4C_4-A_5C_5
Separating and recovering	0	0	α_5	The spring finger withdraws to the inner of the guard plate	The far end of the spring finger contacts the ground	A_5C_5-A_1C_1

Note that the collection mechanism rotates clockwise as the positive direction. α is the rotation angle of the middle center axis; β is the angle between the spring finger and the horizontal coordinate axis in the coordinate system; '↑' is the gradual increase; '↓'is the gradual decrease. '+' is the positive direction in the coordinate system, and '-' is the negative direction in the coordinate system.

Optimization objectives

In the collection cycle, point *O* acts as the rotation center of the coordinate systemin Fig. 2. The collection mechanism rotates clockwise.

(1) During the gathering phase, if the angle of the spring finger is over-inclined, the effective length of the spring finger would be affected, resulting in the reduced storage space, which may lead to "congestion" or "overload" phenomena. The spring finger should thus remain at an angle of 45°-55° in contact with the branches laid on the ground.

(2) To obtain the lower picking height of the collection mechanism (the shortest distance between A_3C_3 and the ground in Fig. 2), the spring finger should contact the branches as early as possible, and the angle(α_1) of the gathering phase should be reduced to meet the demand.

(3) According to the kinetic analysis of the lifting phase, F_1 has an adverse influence on the branches. The angle_(α_2) of the lifting phase being reduced as soon as possible to prevent the branches from flying out after collision with the spring finger. The optimal solution is to lower the picking height of the collection mechanism to keep the collection system stable.

(4) During the transporting and feeding phases, the spring finger changes its angle as soon as possible and the angle_(α_3) of the central axis is reduced as much as possible to reach the vertical angle sooner. This generates a stronger pull force on the branches, and then the spring finger will form a favorable angle to strengthen the feeding performance of the collection mechanism.

(5) During the feeding phase, the rotation angle_(α_4) of the central axis is increased as much as possible to prolong the feeding distance. The vertical angle of the spring finger is positioned to meet the tensile force needs of the branch group.

(6) During the separation and recovery phase, the spring finger will gradually retract along the vertical direction at the top of the guard plate to avoid clamping the branches and not being able to separate. The angle of the spring finger should be recovered to the original state as soon as possible in the rotation angle_(α_5) of this phase.

Dynamic simulation of the collection mechanism

A mathematical model is first established based on the structure of the collection mechanism. Then the static and dynamic simulation programs are compiled in MATLAB to optimize these primary parameters of the mathematical model, through the interaction of human-computer *(Wuet al., 2008).* The dynamic simulation (Fig. 5) displays the actual running trajectory and the angle of the collection mechanism. Combined with experts' experience, the optimal angle and trajectory for branch collection are selected. The effective collection distance indicates the running distance of the spring finger on the operation plane.

The effective rate of the collection distance (η_1) is determined using the equation:

$$\eta_1 = \frac{K_2K_1}{K_3K_2 + K_2K_1} \times 100 \quad (1)$$

Where:

η_1 is the effective rate (%) of the collection distance within an entire cycle;

K_2K_1 is the collection distance in the dynamic movement trajectory;

K_3K_2 is the distance of the loss collection in the dynamic movement trajectory.

Prototype open verification

To implement the testing task smoothly, a rectangular baler with a spring finger collection mechanism was selected as the experimental carrier. The focus is on redesigning the picking-up mechanism.

In Table 2, the critical data on the collection mechanism were measured and the optimization process was performed. The center-line data value of the cam disk groove was obtained. *Li et al., (2019)* reported the method of processing the data of the cam disk groove with MATLAB. In accordance with these final data, the shape of the cam disk (Fig. 3) was redesigned, and some relative components (Fig. 4) were improved. The collection system was tested with these improved components. In addition, because the other components of the collection mechanism are unchanged, these original parts no longer require modification.



Fig. 3 - Cam disk



Fig. 4 - Some improved relative components

This experiment was conducted in an open square at an agricultural company located in Shijia Zhuang, China. First, the branch residue was laid on a 15m long and 1.8m wide lane, and then 4 different branch residue orientations, messy, transverse and longitudinal (the treetops first contact the collection device, and the thick stems of the branches contact the collection device first) were set. In addition, a laser tachometer was used to measure the rotation speed and the scales were used to measure the total weight of branch residues before testing and the loss weight of branch residues after testing (Table 2).

Table 2

Prepared tests and parametric condition measurements

Branch pruning residue orientations laid on the ground			Test equipment parameters
Messy branches			Tractor: Dongfanghong-MF604 Scales: Edberg NK/HP (within 5kg) G&G/Shuangjie SW-6234C (5~30 kg) Laser Tachometer: SW-6234C Fig.2, the length of the spring finger_ (1) =120 mm, the length of the crank_ (2) =45 mm, the radius of link_ (3) + the radius of central axis _ (4) =67 mm, ∠B1A1C1=39°.
Transverse orientation			
Portrait orientation	The treetop first contacts the collection device		
	The thick stems of branches first contact the collection device		

Note that the forward direction of the tractor is in portrait, and the vertical is transverse.

The success rate of branch residue collection is defined as the percentage of the successfully collected branch residues against the total weight.

The success rate of the picking system for branch residues is determined by using equation (2):

$$\eta_2 = \frac{W - W_r}{W} \times 100 \tag{2}$$

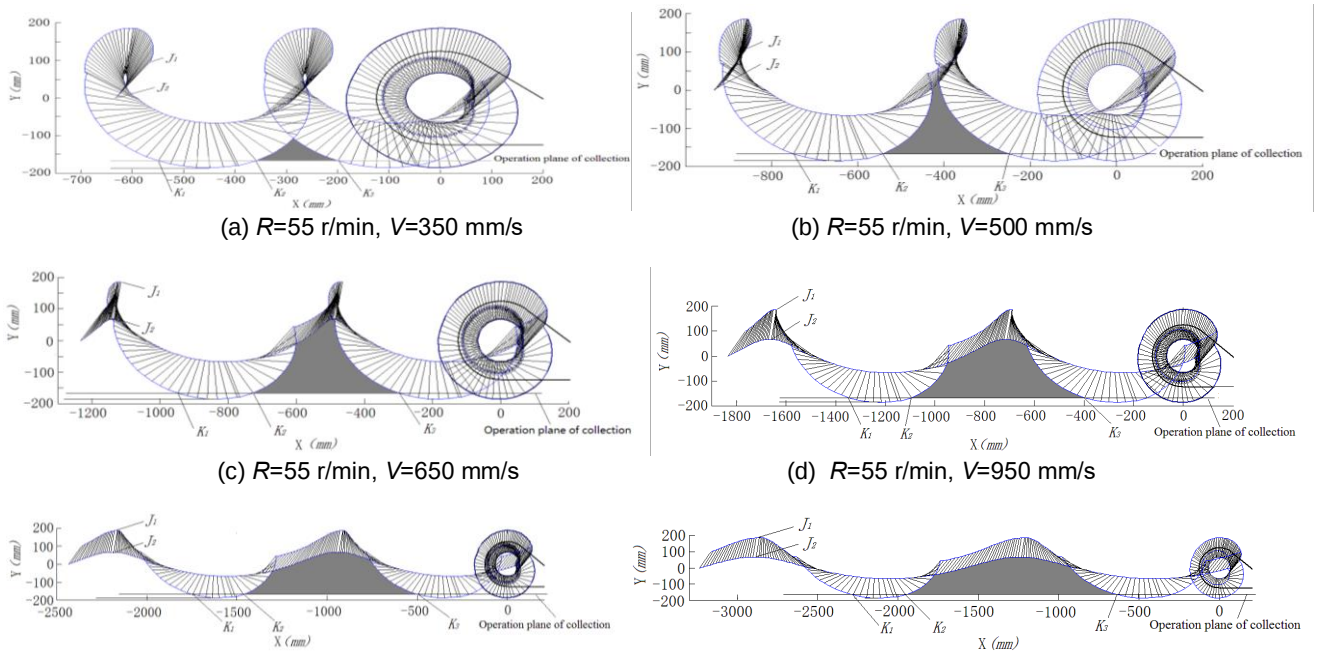
where, η_2 is the success rate (%) of picking; W_r is the loss weight of branch residues, and W is the weight of the total branch residues scattered on the ground in each test.

RESULTS AND DISCUSSION

Dynamic simulation results for the collection mechanism

In Fig. 5, as the tractor moves forward, one of the spring fingers in the collection mechanism is simulated. The dynamic movement trajectory of the collection mechanism clearly shows the position and angle of the spring finger during these two running periods. Suppose the tip of the spring finger is inserted into the soil 10 mm deep to ensure that it touches the branches on the ground. As such, a line is set in the dynamic motion trajectory as the acquisition operation plane.

As shown in Fig. 5, when *V* increases, the ring of the top of the trajectory reduces gradually or even vanishes. The gray area is the loss collection area, gradually expanding, which will obviously be detrimental to collection.



(a) *R*=55 r/min, *V*=350 mm/s (b) *R*=55 r/min, *V*=500 mm/s

(c) *R*=55 r/min, *V*=650 mm/s (d) *R*=55 r/min, *V*=950 mm/s

(e) *R*=55 r/min, *V*=1250 mm/s (f) *R*=55 r/min, *V*=1650 mm/s

Fig. 5- The dynamic simulation trajectory of the collection mechanism at R=55 r/min and different forward speeds

R is the rotation speed of the collection mechanism; V is the velocity of the tractor; K_1 is the end point of effective collection in the operational plane; K_2 is the start point of effective collection in the operational plane, and the end point of loss collection in the operational plane. K_3 is the start point for loss collection in the operational plane; K_3K_2 is the distance of the loss collection; $K_2K_1$is the distance of effective collection; J_1J_2 is the spring finger angle *which shows the minimum angle for feeding the dynamic movement trajectory.*

Note that the minimum feeding angle in the dynamic movement trajectory is an angle between $J_1J_2$and the horizon plane.

Table 3

Parameterdata in the dynamic movement trajectory

R r/min	***V*** mm/s	**Coordinate**			***K_3K_2*** (mm)	***K_2K_1*** (mm)	***η_1*** (%)	**Coordinate**		**Minimum feeding angle**	**Ring trajectory**	
		K_3	***K_2***	***K_1***				***J_1***	***J_2***		**Point C_1**	**Point A_1**
55	350	(-199.3, -167)	(-358, -167)	(-549.3, -167)	158.7	191.3	54.7	(-564.2, 98.3)	(-633,0)	49.01°	Y	Y
	500	(-248.7, -167)	(-542.1, -167)	(-748.7, -167)	293.4	206.6	41.3	(-864.2, 98.3)	(-933,0)	47.99°	Y	N
	650	(-298, -167)	(-726.3, -167)	(-948, -167)	428.3	221.7	34.11	(-1115, 185.2)	(-1135, 67)	80.4°	Y	N
	950	(396.8, -167)	(-1095, -167)	(-1347, -167)	698.2	252	26.53	(-1639, 185.2)	(-1659, 67)	80.4°	N	N
	1250	(-495.5, -167)	(-1463, -167)	(-1745, -167)	967.5	282	22.56	(-2163, 185.2)	(-2184, 67)	79.92°	N	N
	1650	(-627.1, -167)	(-1954, -167)	(-2277, -167)	1326.9	323	19.58	(-2861, 185.2)	(-2882, 67)	79.92°	N	N

Note that 'Y' is the existing ring trajectory and 'N' indicates that it does not exist. Point C1 and A1 are shown in Fig. 2.

The data in Table 3 show that when V increases, the distances of the collection (K_2K_1) and the loss collection (K_3K_2) both enlarge, and the occupying rate (η_1) of the former decreases gradually in the collection cycle. The tractor running speed is too fast under the same rotation speed, which is not conductive to the collection operation. Due to the increase in speed, the top ring trajectory gradually disappears, and the minimum feed angle of the spring finger also changes. When the entire top ring trajectory disappears completely, the minimum feed angle of the spring finger within the dynamic motion trajectory remains unchanged.

Comparing the changes of the minimum feed angle, the results show that when there is a ring trajectory, the minimum feed angle value is greatly reduced relative to the ring trajectory when it disappears.

According to the kinetic analysis of the feeding phase in Table 1, the angle of the spring finger in the range of 40°- 60° will be conducive to the feed action. The minimum feeding angle meets the feeding requirement. The analysis results in Table 3 and Fig. 5 of the ring trajectory will directly affect the feeding of collection. As V increases, the ring trajectory appears, and the collection ability is weakened gradually. When V reaches a certain value, the spring teeth will not provide an effective feeding.

Open validation testing

Comparing 4 different orientations of branch residue collections in Table 4, it is found that Fig. 6 (a) and Fig.6 (b) have similar picking success rates at almost the same tractor velocity and rotation speed of the collection mechanism. Through the collection video_ Fig. 6 (b), it is clear that the spring finger begin to push the branches forward in the lateral direction, and then stack together similar to the messy orientation.

The video of Fig. 6 (c) shows that the branches easily move to two sides of the collection mechanism, resulting in the loss of some branches. The branch orientation of Fig. 6 (d) makes the picking difficult, because the thick stems of some branches are inserted directly into the gap between the spring fingers, which loses its hold on the branches. After the thick branches are sent below the collection mechanism, most of the branches will not be collected. Thereby the orientation in Fig. 6 (d) should be avoided as much as possible when the branch residues are laid on the ground.

The picking data in Table 4 can guide people to arrange the branch residues as close as possible to the orientations of Fig. 6 (a) or Fig. 6 (b), and then the branches can be stacked together, but the height of the piles should be limited.



(a) The messy orientation of branches

(b) The transverse orientation of branches

(c) The treetop orientations first contact the collection device

(d) The thick stems of the branches first contact the collection device

Fig. 6 - The influence of different orientations of branches on the success rate of picking

Table 4

The success rate of picking branches at different orientations

Laid orientations	V (m/s)	R (r/min)	Weight (kg)		η_2 (%)
			W	Wr	
Fig. 6a)	0.9–1.1	40±2	15±0.2	0.84	94.4
Fig. 6b)				1.30	91.3
Fig. 6c)				4.72	68.5
Fig. 6d)				9.22	38.5

CONCLUSIONS

In this study, the collection process of branch residues was simulated on a dynamic basis, with a kinetic analysis for each motion of the entire collection cycle. The angle of the spring finger and the trajectory of the end of the spring finger were determined through the human-computer interaction interface in an entire collection cycle. The core components of the collection mechanism were redesigned, fabricated and tested, and the site evaluation tests were carried out on 4 different orientations of branch residues laid on the ground, from which the following conclusions can be drawn:

(1) The improved spring finger collection mechanism can achieve a satisfactory picking success rate of branch pruning residues, which proves the availability and potential of this method.

(2) The messy and transverse orientations facilitate the collection of branch pruning residues.

(3) The portrait orientation for branches should be avoided, especially when the thick stems of the branches first touch the spring finger. They easily move in the direction of the collection mechanism axis through the gap between the spring fingers, resulting in loss.

Further, different parameters of the spring finger collection mechanism will be studied and different phenomena will be recorded to provide basic data for other researchers and solve the compatibility problem with a baler. In addition, the device is also suitable for the removal of surface wastes.

ACKNOWLEDGMENTS

This work was supported in part by the special project of the funding projects for the introduction of overseas students in Hebei Province (C20200355), the construction of modern agricultural industrial technology system in China (CARS-27), Natural Science Research Project of Colleges and Universities in Hebei Province (ZC2023031), Scientific Research Project of Hengshui University (2022GC09), Scientific Research Project of Hengshui University (2023XJZX21),Scientific Research Project of Hengshui University (2022XJZX23), Hengshui Science and Technology Plan Project(2022014024Z).

REFERENCES

[1] Adamczyk, F., Dyjakon, A., Frąckowiak, P., Romański, L. (2014). Conception of machine for pressing branches with pruning tree fruit. *Journal of Research and Applications in Agricultural Engineering,* Vol. 59, 5-9. Poland.

[2] Arkadiusz, D. (2018). Harvesting and Baling of Pruned Biomass in Apple Orchards for Energy Production. *Energies,* Vol. 11, 1680. Basel, Switzerland.

[3] Arkadiusz, D. (2019). The Influence of Apple Orchard Management on Energy Performance and Pruned Biomass Harvesting for Energetic Applications. *Energies,* Vol. 12, 632. Basel, Switzerland.

[4] Bernetti, I., Fagarazzi, C., Fratini, R. (2006). A methodology to analyze the potential development of biomass energy sector: an application in Tuscany. *Forest Policy and Economics*, Vol. 6, 415-32. United States.

[5] Frąckowiak, P., Adamczyk, F., Wąchalski, G., Szaroleta, M., Dyjakon, A., Pari, L., Suardi, A. (2016). A Prototype Machine for Harvesting and Baling of Pruning Residues in Orchards: First Test on Apple Orchard (Malus Mill.) In Poland. *Journal of Research and Applications in Agricultural Engineering*, Vol. 61, 88-93. Poland.

[6] Fu, W. J. (2015). *Design and Field Experimental Study of pick up roller on corn straw collecting grinder (玉米秸秆捡拾粉碎机设计及田间性能试验研究)*. Xinjiang Agricultural University. China.

[7] Li, H., Yang, A. Q., Li, J. P. (2019). Subsection Curve Fitting Parameter of Spring-finger Cylinder on Branch Pickup Mechanism Calculated by Reverse Method (多段曲线拟合弹齿式枝条捡拾参数反求法求解). *Journal of Agricultural Mechanization Research,* Vol. 41, 34-39. Heilongjiang/China.

[8] Ntalos, G. A., Grigoriou, A. H. (2002). Characterisation and utilisation of vine prunings as a wood substitute for particle board production. *Ind Crop Prod,* Vol.16, 59-68. Netherlands.

[9] Popa, L., Trokhaniak, V, Constantin, A.M. (2022). Experimental research regarding the realization of an equipment intended for chopping woody waste. *INMATEH Agricultural Engineering*, Vol. 68, Issue 3, pp.757-766. https://doi.org/10.35633/inmateh-68-75

[10] Raffaele, S., Carla, N., Luigi, P., Enzo, M., Natascia, M. (2012). Production and quality of biomass fuels from mechanized collection and processing of vineyard pruning residues. *Applied Energy,* Vol.89, 374-379. England.

[11] Repullo, M. A., Carbonell, R., Hidalgo, J., Rodríguez-Lizana, A., Ordóñez R. (2012). Using olive pruning residues to cover soil and improve fertility. *Soil and Tillage Research*, Vol.124, 36-46. Netherlands.

[12] Romański, L., Dyjakon, A., Adamczyk, F., Frąckowiak, P. (2014). Problems With Deriving the Fruit Tree Pruned Biomass for Energy Use. *Agricultural Engineering,* Vol. 3, 157-167. Poland

[13] Spinelli, R., Picchi, G. (2010). Industrial harvesting of olive tree pruning residue for energy biomass. *Bioresource Technology,* Vol.101, 730-735. Netherlands.

[14] Wang, W. (2012). *Parameter analysis and improving design of spring finger cylinder pick up collector (弹齿滚筒式捡拾装置参数分析和改进设计研究).* Inner Mongolia Agricultural University. 19~21. China.

[15] Wu, C. Y., Zhao, Y., and Chen, J. N. (2008). Optimization design of transplanting mechanism of rice transplanter based on visualization human-computer interaction (水稻插秧机分插机构人机交互可视化优化设计). *Transaction of the Chinese Society for Agricultural Machinery*. Vol.39, 46-49. Beijing/China.

[16] Xu, T., Shen, Y. Z., Gao, L. X. (2016). Spring-finger Peanut Pickup Mechanism Based on Two-stage Harvest (基于两段收获的弹齿式花生捡拾机构研究). *Transactions of the Chinese Society for Agricultural Machinery,* Vol.47,90-97. Beijing/China.

[17] Zhen, J. X. (2017). *Research on Fruit Tree Branch Processing Machine Based on Field Return Technology (基于就地还田技术的果树枝条处理机的研究)*. Hebei Agriculture University. China

NUMERICAL SIMULATION AND EXPERIMENT ON AIRFLOW FIELD OF CORN SEED HARVESTER CLEANING DEVICE

/

玉米籽粒收获机清选装置气流场数值模拟与试验

Zedong ZHAO[1)], Hongyong DU[2)], Xiaohui YANG[1)], Guohai ZHANG[1*)]

[1)] College of Agricultural Engineering and Food Science, Shandong University of Technology, Zibo 255091, China

[2)] Shandong Himile Mechanical Manufacturing Co., Ltd., Weifang 261500, China

Tel: +86-15965534882; E-mail: guohaizhang@163.com

DOI: https://doi.org/10.35633/inmateh-69-48

Keywords: *Numerical simulation; airflow field; sieve plate opening scales; cleaning device*

ABSTRACT

To better analyze the distribution law of airflow in the wind sieve type cleaning device, this study took the cleaning device of Yafeng 4YZL-6S corn seed harvester as an example and conducted numerical simulation and comparative analysis of the airflow field inside the cleaning device under the sieve plate opening scales of 12, 16 and 20 mm using CFD software. The numerical simulation showed that the distribution of airflow velocity above the sieve surface was uniform at a sieve plate opening scale of 16 mm. Airflow velocity measurements were performed on the test prototype using an anemometer to verify the accuracy of the numerical simulation results. The simulation test results were supplemented by field trials, which showed that when the speed of the cleaning fan was 1200 r/min and the sieve plate opening scale was 16 mm, the impurity rate in the field harvest of the operating machinery was 1.03% and the loss rate was 1.91%. The operating effect met the standard of mechanized corn grain harvesting. This paper can provide a reference for the design and working mechanism research of corn seed harvester cleaning devices.

摘要

为了更好地分析风筛式清选装置中气流的分布规律，本研究以亚丰 4YZL-6S 玉米籽粒收获机清选装置为例，运用 CFD 软件对筛片开度分别为 12、16 和 20 mm 的清选装置内部气流场进行了数值模拟和对比分析。数值模拟结果表明：当筛片开度为 16 mm 时，筛面上方气流速度分布均匀。使用风速仪在试验样机上进行了气流速度测量，验证了数值模拟结果的准确性。通过田间试验对模拟试验结果进行了补充，田间试验结果表明：当清选风机转速为 1200r/min，筛片开度为 16 mm 时，作业机具田间收获的含杂率为 1.03%、损失率 1.91%，作业效果符合玉米籽粒机械化收获标准。本文可为玉米籽粒收获机清选装置设计和工作机理研究提供参考。

INTRODUCTION

Currently, combine harvesters commonly used wind-sieve-type cleaning devices for corn cleaning operations. The device used the blowing effect of airflow and the vibration effect of the sieve to complete the cleaning work together, which had the advantages of high cleaning efficiency, low grain loss rate and good cleaning effect *(Xu, 2019)*. The airflow distribution in the cleaning chamber can affect the cleaning effect, and the study of it has practical application significance. The traditional cleaning research mainly adopted the method of experiment plus experience, which had the disadvantages of large measurement errors, tedious test processes and inaccurate data, etc. Calculated fluid dynamics CFD numerical simulation software was used to analyze the distribution pattern of the airflow field in the cleaning room, which can save research time and accurately derive the movement pattern of airflow, which had been widely used in recent years *(Mekonnen et al., 2010)*.

Many scholars had conducted numerical simulation analyses of the cleaning device. Some scholars used CFD software to simulate the worm wall of different fans and obtained the conclusion that different positions of the worm wall affect the airflow field inside the fan and change the airflow distribution inside the cleaning chamber *(Casarsa L et al., 2011)*. Some scholars invented a constant pressure concave screen of a combine harvester and modeled the threshing device by using the method of data acquisition and testing *(Alan et al., 2015)*. What's more, some scholars conducted a numerical simulation of the mixed airflow field generated by the fan and detaching drum in the longitudinal axial flow cleaning device, improved the fan structure, compared the airflow field before and after the improvement, and verified the rationality of the improved fan through field tests *(Tong et al., 2016)*. Some scholars used FLUENT software to analyze the

airflow field of four fan models in the cleaning device and studied the transverse airflow distribution law of the four fan models *(Wang et al., 2017)*. In addition, some scholars studied the airflow field distribution and the optimization of fan parameters for the multi-duct cleaning device with the centrifugal fan speed, the number of blades of the impeller, and the fan outlet angle as the research factors *(Ning et al., 2019)*. Some scholars have constructed a mathematical model of the linkage structure of the cleaning system of a grain combine harvester by deriving the coordinates, velocity, and acceleration of each node of the cleaning system *(Badretdinov et al., 2019; Badretdinov et al., 2020)*.

Our team conducted theoretical analysis and optimization of the operation process of the corn seed harvester cleaning device in the early stage *(Zhao et al., 2022)*. To further reveal the influence law of airflow field on the performance of the cleaning device, established CFD mode for the cleaning device of Yafeng 4YZL-6S corn seed harvester. The distribution of the airflow field in the cleaning chamber under different sieve plate opening scales was compared and conducted to check the reliability of the simulation model. This paper can provide a reference for further optimization research of corn seed harvester cleaning devices.

MATERIALS AND METHODS

Overall structure and working principle of cleaning device

As shown in Fig.1, the cleaning device of the corn seed harvester is mainly composed of a shaking plate, crank-link mechanism, fish scale sieve, tail sieve, miscellaneous auger, grain auger, adjustment device of the air-regulating plate, and cleaning fan.

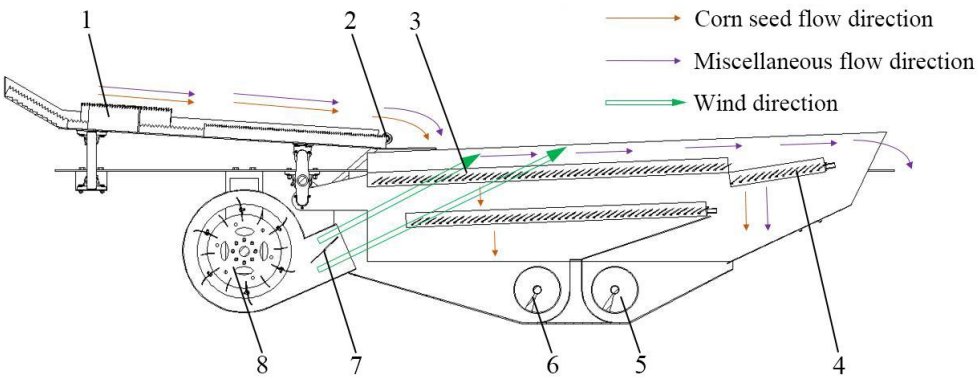


Fig. 1 – Schematic diagram of the structure of the cleaning device

1.Shaking plate; 2. Crank-link mechanism; 3. Fish scale sieve; 4. Tail sieve; 5. Miscellaneous auger ; 6. Grain auger; 7. Adjustment device of the air-regulating plate; 8. Cleaning fan

The working principle of the cleaning device is: after the completed threshing operation, the corn threshed mixture is discharged from the holes of the separation concave plate and falls onto the shaking plate. After shaking and bouncing on the shaking board, it will fall evenly on the upper fish scale screen. Light impurities are distributed in the surface layer of the corn threshed mixture, which is directly discharged from the machine after the action of the centrifugal fan. The remaining corn threshed mixture passes through the upper fish scale sieve and falls into the lower fish scale sieve, where the impurity content is less, and clean corn kernels are obtained after further screening by the lower fish scale sieve. The screened seeds slide down the sloping board into the grain auger. The grain auger first collects the seeds to one side and then transports them to the seed collection device. The unclean material from the tail sieve falls into the miscellaneous auger. It enters the threshing unit for the second threshing and cleaning after the action of the miscellaneous auger and the elevator.

Cleaning fan

The cleaning fan is a worm shell centrifugal fan, mainly by the blade, blade connection seat, fan shaft, volute, adjustment device, and damper adjusting plate. Its structure is shown in Fig.2. Compared to the widely used four-blade agricultural centrifugal fan, the six-blade centrifugal fan can provide higher air velocity, air pressure and gas flow. And it can be used for harvests with high material volumes, high water content and high seed content *(Cheng et al., 2019)*. Its main structural parameters are shown in Table 1.

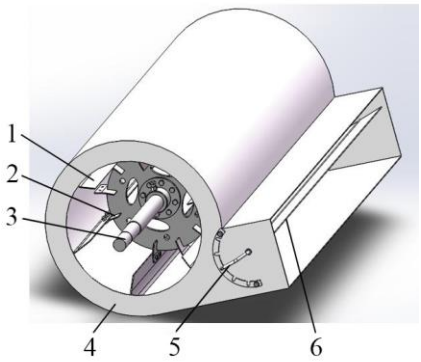


Fig. 2 – Fan structure diagram

1.Blade; 2. Blade connection seat; 3. Fan shaft; 4. Volute； 5. Adjustment device; 6. Damper adjusting plate

Table 1

Centrifugal fan basic parameters

Parameters	Value
Number of blades	6
Outer diameter of impeller /mm	410
Inner diameter of impeller /mm	205
Air inlet diameter/mm	328
Air outlet height/mm	205

Fish scale sieve

As shown in Fig.3, the cleaning sieve is a double-layer fish scale sieve. The fish scale sieve has a similar shape to the fish scale, which has the advantages of strong cleaning ability and high applicability. In addition, the fish scale sieve can well reduce the penetration rate of the threshed mixture and the sieve holes are not easily blocked *(Li, 2012).* Its structural parameters are shown in Table 2.



Fig. 3 – Fish scale sieve structure diagram

1.Fish scale sieves; 2. Fish scale sieve adjustment mechanism

Table 2

Centrifugal fan basic parameters

Parameters	Value
Upper fish scale sieve size (L×W)/mm	1500 × 1250
Lower fish scale sieve size (L×W)/mm	1300 × 1250
Upper fish scale screen tilt angle / (°)	5
Lower fish scale sieve tilt angle / (°)	5

Simulation modeling of cleaning airflow field

Based on the model of the 4YZL-6S corn seed harvester cleaning device, the cleaning device was reasonably simplified while retaining the main working parts *(Jiang, 2015)*. In the width direction, 300 mm were selected for the study, SolidWorks was used to establish a three-dimensional flow channel model, saved in igs format, the established model was shown in Fig.4. The length of the model for setting the flow channel of the cleaning device was 2386 mm, the width was 300 mm and the height was 890 mm. The

distance between the front end of the upper fish scale sieve and the front end of the cleaning chamber was 447 mm, and the distance between the front end and the upper end of the cleaning chamber was 413 mm. The distance between the front end of the lower fish scale sieve and the front end of the cleaning chamber was 717 mm, the distance between the front end and the upper end of the cleaning chamber was 529.5 mm, and the two fish scale sieves are parallel to each other. The angle of inclination of the air inlet of the cleaning device was 20°.

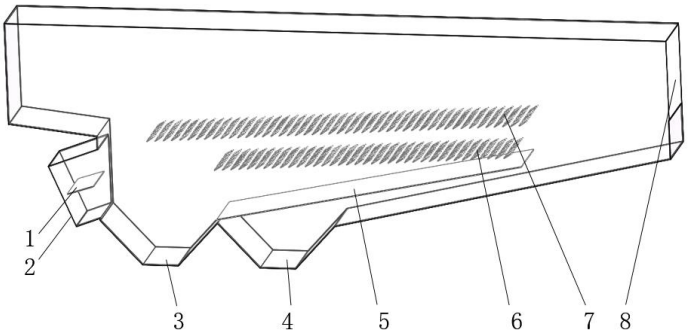


Fig. 4 – Three-dimensional model of cleaning device

1.Damper adjusting plate; 2. Air inlet; 3. Seed auger conveying tank; 4. Miscellaneous auger conveying tank; 5. Grain slide; 6. Lower fish scale sieve; 7. Upper fish scale sieve; 8. Air outlet

The saved .igs file of the cleaning device flow channel model was imported into the Mesh module in Ansys Workbench to divide the mesh. The quality of the mesh division determined the speed and accuracy of the calculation, and a reasonable mesh division was a prerequisite for a successful numerical simulation *(Xu et al., 2014)*. The size of this cleaning device was large, and the flow of internal airflow was complicated, so a tetrahedral unstructured mesh was used for the simulation calculation, and the total number of divided meshes was 6441166. The mesh division was shown in Fig.5.

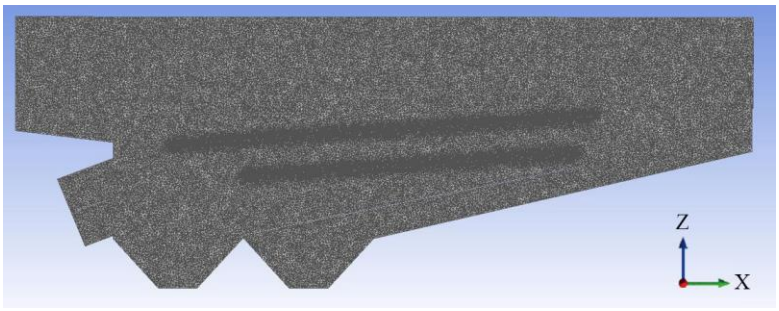


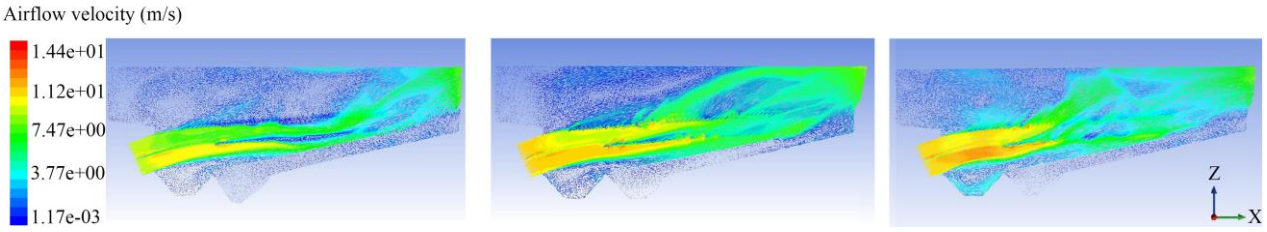
Fig. 5 – Grid division of cleaning device

The divided mesh model was Imported into FLUENT, and it was checked whether the divided mesh met the requirements by the Check command in Setup. And only when the minimum volume was positive, the next step of the solution set could be performed. The dynamic coordinate system method was adopted and the impeller part of the airflow field model was set as the dynamic coordinate system, whose center of rotation was the impeller axis center and the speed was set to 1200 r/min. After setting each boundary condition reasonably, the solution method was set as the pressure-based SIMPLE algorithm, and the model was adopted as the Standard k-ε model. The number of iteration steps was set to 2800, and the convergence residual was 0.001. By varying the tilt angle of the sieve, three airflow field models were established with sieve plate opening scales of 12, 16 and 20 mm, respectively.

RESULTS AND ANALYSIS

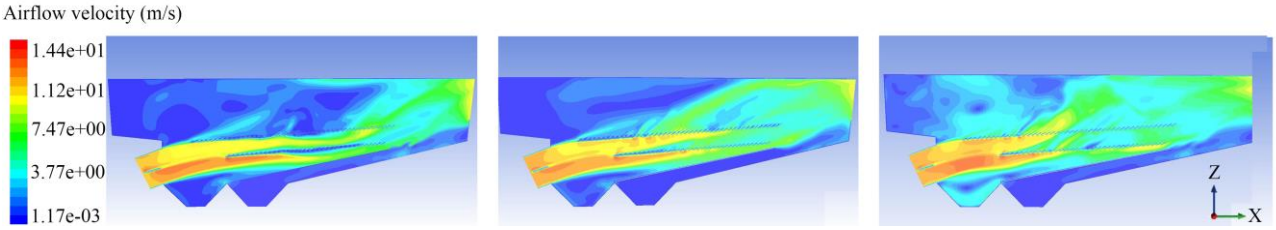
Analysis of numerical simulation results

The monitoring window was set to outlet mass flow rate. When the number of iteration steps was 2,000, the exit mass flow rate reached a steady state, indicating that the variable reached convergence. After the solution was completed, the post-processing was carried out by CFD software, and the plane of z=200 mm in the width direction perpendicular to the sieve plane was selected as the study object, and the velocity vector diagram of the cleaning device was obtained as shown in Fig.6, and the velocity cloud diagram was shown in Figure 7.



(a)12 mm (b)16 mm (c)20 mm

Fig. 6 – Velocity vector diagram



(a)12 mm (b)16 mm (c)20 mm

Fig. 7 – Velocity cloud diagram

Compared with the simulation results under different sieve plate opening scales in the figure, it can be seen that when the sieve plate opening scale was 12 mm, the airflow was obstructed by the fish scale sieve and blown to the rear outlet of the cleaning device, and the airflow direction was almost parallel to the sieve surface. The middle position of the vibrating sieve formed a large area of low air-speed area, the sieve surface airflow speed was low and could not blow the seeds and miscellaneous residues in this area to the back of the cleaning room in time, the airflow was not effectively used and did not meet the actual cleaning needs *(Jiang et al, 2015).*

When the sieve plate opening scale was 16 mm, the sieve had a good inflow effect on the airflow, the gas flow line even ran through the sieve, and there was no vortex between the sieves. The airflow in the middle and rear sections was effectively directed above the sieve surface and high airflow velocity was maintained in these areas. The overall airflow in the cleaning chamber was more uniform, which helped to separate the corn and impurities concentrated in front of the sieve, and the airflow speed at the outlet was increased, which could blow the impurities out of the machine quickly.

When the sieve plate opening scale was 20 mm, because the sieve plate opening scale was too large, it would be made too much high-speed airflow back-guided to the top of the sieve, which could result in the miscellaneous residue being blown to the top of the cleaning room, which could not be effectively excluded, finally causing a decrease in the seed cleaning rate.

Compared with the analysis of the airflow field distribution in the cleaning room under the effect of different sieve plate opening scales, it can be seen that although reducing the sieve plate opening scale could increase the air speed in the X direction, the airflow speed in the Z direction generated by the fan was smaller, which was not conducive to blowing impurities out of the cleaning room. However, when the sieve plate opening scale was too large, it would cause the airflow velocity in the Z direction to become larger. Compared with the simulation results of three different sieve plate opening scales, it can be seen that when the sieve plate opening scale was 16 mm, the air velocity distribution of the airflow field was optimal, which not only produced sufficient airflow in the X direction, but also took into account the airflow in the Z direction, and at the same time, the area of low-speed airflow in the middle of the vibrating sieve was small, which could be met the requirements of the cleaning operation *(Zhu, 2019).*

Airflow field test verification

In order to ensure that the air velocity distribution law obtained from the simulation had a reference value, the air velocity at the inlet cross-section position of the cleaning device was measured using the cloth point method under the condition of no corn threshed mixture *(Ma, 2015)*. The velocity measurement points were shown in Fig.8, with the lower left end of the air inlet section as the coordinate origin, to the right for X-positive, up for Z-positive, and each measurement point was evenly distributed.

Adjusted the speed of the centrifugal fan to 1200 r/min, refer to GB1236-1985 "Ventilator Aerodynamic Performance Test Methods" to the measurement point at the inlet cross-section for speed testing *(Zhang, 2022)*. Each speed measurement point was tested three times and the average value was taken. Since the

results of the numerical simulation were given in the form of the distribution range, but the test was the airflow velocity at a certain point, in order to compare and analyze the simulation results and test results more accurately, after using TECPLOT software to extract the data of each test point in the simulation results, the measured and simulated values of airflow velocity at each test point were shown in Table 3.

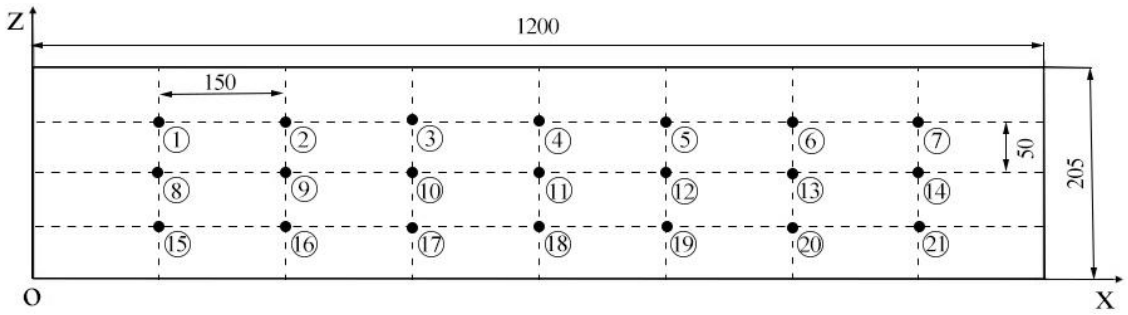


Fig. 8 – Locations of Anemometer Measuring Points at the Wind inlet of cleaning device

Table 3

Airflow speed comparison

No.	Measured value(m/s)	Simulated values(m/s)	No.	Measured value(m/s)	Simulated values(m/s)	No.	Measured value(m/s)	Simulated values(m/s)
1	11.3	11.7	8	10.5	10.7	15	10.8	11.0
2	12.0	12.3	9	12.2	12.6	16	12.8	13.1
3	13.8	14.0	10	14.1	14.2	17	13.2	13.7
4	13.5	13.6	11	13.9	14.0	18	13.5	13.9
5	13.6	14.1	12	14.0	14.3	19	13.7	14.0
6	11.9	12.3	13	12.4	12.6	20	12.3	12.7
7	11.4	11.7	14	10.8	11.0	21	10.5	10.9

As can be seen from Table 3, the simulated values follow the same trend as the measured values, but the simulated values were slightly larger, the experimental results are consistent with the findings of some scholars *(Xu et al., 2010; Wang et al., 2017; Zhu 2019; Ning 2019)*. The main factors that caused the errors were:

1. The interference of machine vibration and other factors that would cause the inaccuracy of the measured values.

2. In the numerical simulation, the model was created on the basis of simplicity and smoothness, and ignored some of the actual working conditions and flow field energy losses, which caused the simulation values to be large.

The error between the simulated and experimental values at each measurement point was less than 5%, and the overall change trend was consistent, which indicated that the numerical simulation of the flow field in the clearing device of the 4YZL-6S corn seed harvester was reasonable.

Field trials

From the previous numerical simulation and verification test of the airflow field of the cleaning device, the distribution law of the airflow velocity under different sieve plate opening scales was obtained, and the sieve plate opening scale that could produce the ideal flow field was determined to be 16 mm. In order to obtain stable data, the analysis of the airflow velocity above the cleaning sieve was carried out in the stationary state of the mechanism, which had certain limitations, so it was necessary to verify the preliminary study by field trials to investigate whether the actual cleaning effect under the mechanism dynamics meets the demand of cleaning operation.

As shown in Fig.9, the field validation trial was conducted from August 23 to 25, 2022, at the experimental field of Shandong University of Technology, Nanding Town, Zibo City, Shandong Province. The harvested corn variety was Dika 517, the length range was 15~18 cm, the radius range was 4.3~4.8 cm, the mass weight of 1000 grains was 409 g, and the average moisture content of harvested seeds was 30.8%. The test was conducted by Chinese National Standard GB/T 21962-2020 "Corn Harvesting Machinery" *(Du et al., 2022)*.



Fig. 8 – Test site

During the test, the forward speed of the harvester was 2.5 km/h, and the end of harvesting in the test area was the signal for the end of the single test. After the end of the single test, the grain mouth discharge of not less than 2000 g of samples was extracted, and measured according to the five-point sampling method, clean sample bags were used for bagging number. The working parameters of the test machine were set according to the working condition of the simulation test, and the electronic scale with an accuracy of 0.001 g was used to measure the results after the completion of multiple operations, and the results were averaged, and the impurity rate Y_1 and loss rate Y_2 of the operating machine were calculated according to the following formula. As shown in Fig.10, the operation inside the cleaning device was observed through a high-speed camera during the test.

Impurity rate Y_1:

$$Y_1 = \frac{m_z}{m} \times 100\% \quad (1)$$

Loss rate Y_2:

$$Y_2 = \frac{m_s}{m} \times 100\% \quad (2)$$

where, m is the total mass of the sample, g; m_z is the mass of impurity in the sample, g; m_s is the mass of corn grains in the sample, g.

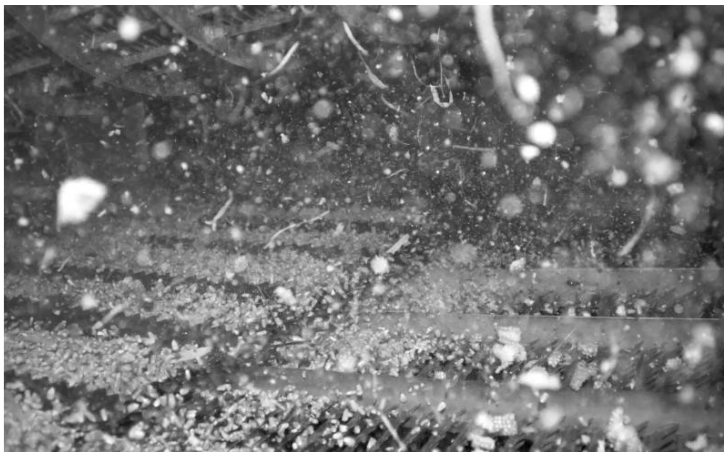


Fig. 10 – Operation inside the cleaning device

According to the test standard, combined with the characteristics of corn cultivation in North China and the requirements of corn mechanized harvesting, the impurity rate in corn seed combine harvester should not exceed 2.5% and the loss rate should not exceed 4%. The values of each index were calculated from equations (1) to (2), and the results were shown in Table 4.

During the test, the machine ran smoothly, the failure rate was zero, the stubble height met the test index. From Table 4, it can be seen that the impurity rate and loss rate were small, and all test indexes had met the requirements of relevant standards.

Table 4

Results of field trials

Test index	Impurity rate/%	Loss rat/%
Standard value	≤2.5	≤4
Test result	1.03	1.91

CONCLUSIONS

Through numerical simulations and validation tests, the following conclusions were drawn:

1. The numerical simulation results of the airflow field of the cleaning device show that when the sieve plate opening scale was 16 mm, the sieve had a better infusion effect on the airflow. The airflow can pass through the sieve coherently, and there was no eddy flow between the sieves. The overall airflow in the cleaning room was more uniform, and the airflow speed at the outlet had increased, so that impurities could be blown out of the machine quickly.

2. By comparing the measured and numerical simulation results, it can be seen that the airflow velocity distribution was consistent under the same working parameters, and the numerical simulation can be verified as real and reliable.

3. The results of the field cleaning performance test showed that under the working conditions of a fan speed of 1200 r/min and a sieve plate opening scale of 16 mm, the impurity rate was 1.03% and the loss rate was 1.91% after the operation of the cleaning device. The cleaning effect had met the standard of corn grain mechanized harvesting.

ACKNOWLEDGEMENT

The work was supported by the High Efficiency and Low Loss Single Longitudinal Axial Flow Threshing and Separation Technology and Development of Intelligent Flexible Threshing Device, (Grant No.2021YFD200050204), and the Development of Intelligent Multifunctional Wheat Corn Grain Combine Harvester, (Grant No.2016YF026).

REFERENCES

[1] Alan R.B., Bernard D.R. (2015). *Constant Pressure Concave Assembly in a Combine Harvester Processing System*. U.S. Patent 9220200B2, 29 December 2015, USA.

[2] Badretdinov I, Mudarisov S, Lukmanov R, et al. (2019). Mathematical modeling and research of the work of the grain combine harvester cleaning system [J]. *Computers and Electronics in Agriculture*, 165:104966, Russia.

[3] Badretdinov I., Mudarisov S., Lukmanov R., Ibragimov R., Permyakov V., Tuktarov M. (2020). Mathematical modeling and study of the grain cleaning machine sieve frame operation [J]. *INMATEH Agricultural Engineering*, vol.60 (1), pp.19-28, Romania. https://doi.org/10.35633/inmateh-60-02

[4] Casarsa L., Giannattasio P. (2011). Experimental study of the three-dimensional flow field in cross-flow fans [J]. *Experimental Thermal and Fluid Science*, 35 (06): 948 - 959, Italy.

[5] Cheng C., Fu J., Chen Z. (2019). Parameter optimization test of corn seed harvester cleaning device (玉米籽粒收获机清选装置参数优化试验), *Transactions of the Chinese Society for Agricultural Machinery*, 50(07): 151-158, China.

[6] Du Y., Zhang L., Mao En, et al. (2022). Design and experiment of combined harvester seed loss monitoring sensor based on EMD (基于EMD的联合收获机籽粒损失监测传感器设计与试验), *Transactions of the Chinese Society for Agricultural Machinery*, 53(S1):158-165, China.

[7] Jiang T. (2015). *Simulation and research on air and screen cleaning of combine harvest based on CFD-DEM* (基于CFD-DEM的联合收获风筛选仿真研究), Anhui Agricultural University, China.

[8] Jiang T., Wu C., Wu D. (2015). Simulation analysis of wind screen flow field for combine harvester based on Fluent (基于Fluent的联合收割机风筛选流场仿真分析), *Journal of Chinese Agricultural Mechanization*, 36 (03): 26 - 29, China.

[9] Li H. (2012). *Research on the design theory and method of wind sieve type cleaning device (风筛式清选装置设计理论与方法研究*), Nanjing Agricultural University, China.

[10] Mekonnen G.G., Josse D.B., Martine B. (2010). Effect of a cross-flow opening on the performance of a centrifugal fan in a combine harvester: Computational and experimental study [J]. *Biosystems Engineering*, 105 (02): 247 - 256, Belgium.

[11] Ma J. (2015). *Study on the model of corn grain traversing the holes of the screen in air-and-screen cleaning device (贯流风筛清选玉米颗粒透筛模型的研究)*, Northeast Agricultural University, China.

[12] Ning X., Xu L., Sun C. (2019). Fan's parameters optimization and internal flow field distribution in multi-duct cleaning device of combine harvester (联合收获机多风道清选装置气流场分布与风机参数优化), *Journal of Agricultural Mechanization Research*, 41 (06): 32 - 37, China.

[13] Tong S., Shen Q, Tang N. (2016). Numerical simulation and optimization experiment of mixed flow field on longitudinal axial flow cleaning device (纵轴流清选装置混合流场数值模拟与优化试验), *Transactions of the Chinese Society for Agricultural Machinery*, 47 (07): 135 - 142, China.

[14] Wang L., Jiao Z., Zhao G. (2017). Simulation analysis of centrifugal fan in air screen type cleaning device (风筛式清选装置离心风机气流场仿真分析), *Agricultural Equipment & Vehicle Engineering*, 55 (08): 10-14, China.

[15] Xu Y. (2018). *Design and test of self-propelled corn kernel harvester cleaning fan of Makin 4YZT-8 type (牧神4YZT-8型自走式玉米籽粒收获机清选风机的设计与试验)*, Xinjiang Agricultural Mechanization, (01): 7-9, China.

[16] Xu L., Yu L., Li Y. (2014). Numerical simulation of internal flow field in centrifugal fan with double outlet and multi-duct (双出风口多风道离心风机内部流场数值模拟), *Transactions of the Chinese Society for Agricultural Machinery*, 45 (10): 78 - 86, China.

[17] Xu X., He M. (2010). *Experimental design with Design-Expert, SPSS application (试验设计与Design-Expert、SPSS应用)*, Science Press, China.

[18] Zhao Z., Yang X., Zhang G. (2022). Analysis and optimization test of operation process of cleaning device of corn seed harvester. *INMATEH–Agricultural Engineering*, Vol.68 (3), pp.211-220, China. https://doi.org/10.35633/inmateh-68-21

[19] Zhu P. (2019). *Simulation research on grain air-and-screen cleaning process and optimization of key parameters (谷物风筛清选仿真研究及关键参数优化设计),* Zhejiang University, China.

[20] Zhang N. (2022). *Analysis of working mechanism and optimization of fish scale sieve cleaning device of corn seed harvester (玉米籽粒收获机鱼鳞筛清选装置工作机理及优化分析)*, Jilin University, China.

MANAGEMENT PRACTICES IN INDUSTRIAL HEMP HARVESTING AND STORAGE
/
PRACTICI DE MANAGEMENT ÎN RECOLTAREA ŞI DEPOZITAREA CÂNEPEI INDUSTRIALE

Dragoș MANEA, Gheorghe STROESCU, Lucreţia POPA*), Alexandru IONESCU, Alexandru ZAICA
National Institute of Research-Development for Machines and Installations designed for Agriculture and Food Industry – INMA / Bucharest, Romania
Tel: 021/269.32.50; Fax: 021/269.32.73; E-mail: manea_dragos_05@yahoo.com
DOI : https://doi.org/10.35633/inmateh-69-49

Keywords: *stalks, harvest, equipment, quality indices.*

ABSTRACT
This paper presents the results obtained by INMA Bucharest, following a research project, in which a technology for harvesting and storing industrial hemp was developed. The equipment for harvesting green hemp stalks intended for this technology was tested in an experimental plot grown with Dacia - Secuieni hemp. Operating indices (actual torque at the power take-off, traction force at drawbar, total effective power to operate the equipment, working speed, effective working capacity) and working qualitative indices (stalk cutting height at lower knife and upper knife, degree of stalk cutting, stalk diameter, the average length of the stalk cut without inflorescence). As a result of the analysis of the values obtained for the operating indices and qualitative working indices, a series of pertinent conclusions and observations resulted, which will help guide harvesting and storage practices to ensure quality requirements for hemp fibre production are met.

REZUMAT
Această lucrare prezintă rezultatele obținute de INMA București, în urma derulării unui proiect de cercetare, în care s-a elaborat o tehnologie de recoltare și depozitare a cânepii industriale. Echipamentul pentru recoltarea tulpinilor de cânepă în verde destinat acestei tehnologii a fost testat într-un lot experimental cultivat cu varietatea de cânepă Dacia - Secuieni. Au fost determinați indicii de operare (momentul real la priza de putere, forța de tracțiune la bara de cuplare, puterea efectivă totală, viteza de lucru, capacitatea efectivă de lucru) și indicii calitativi de lucru (înălțimea de tăiere a tulpinilor la cuțitul inferior și la cuțitul superior, gradul de tăiere a tulpinilor, diametrul tulpinilor, lungimea medie de tăiere a tulpinilor fără inflorescență). În urma analizei valorilor obținute pentru indicii de operare și indicii calitativi de lucru au rezultat o serie de concluzii și observații pertinente, care vor ajuta la ghidarea practicilor de recoltare și depozitare, pentru a asigura satisfacerea cerințelor de calitate pentru producția de fibre de cânepă.

INTRODUCTION

Industrial hemp (*Cannabis sativa L.*) is a crop that provides raw material for the pharmaceutical industry, the industry of concentrates necessary for animal nutrition and last but not least it is used as biomass (obtaining fibres for the textile industry), under development in Romania. Hemp is among the few cultivated plants that can be fully utilized, being at the same time an ecological crop. After its harvest, the field remains clean of weeds, being an excellent precursor for most crops. In addition to these advantages, there is also the fact that the wood produced per hectare of hemp is equivalent to the amount of wood produced by the annual growth of a hectare of mature fir forest.

Currently there is a huge potential for growing hemp for fibre. Also, in recent years, there have been signs of a revival of hemp towards other production niches, such as the production of oil from hemp seeds. Hemp oil contains over 80% polyunsaturated fatty acids (PUFA) and is an exceptionally rich source of the two essential fatty acids (EFAs) linoleic acid (18:2 omega-6) and alpha-linolenic acid (18:3 omega -3) *(Carus et al., 2013)*.

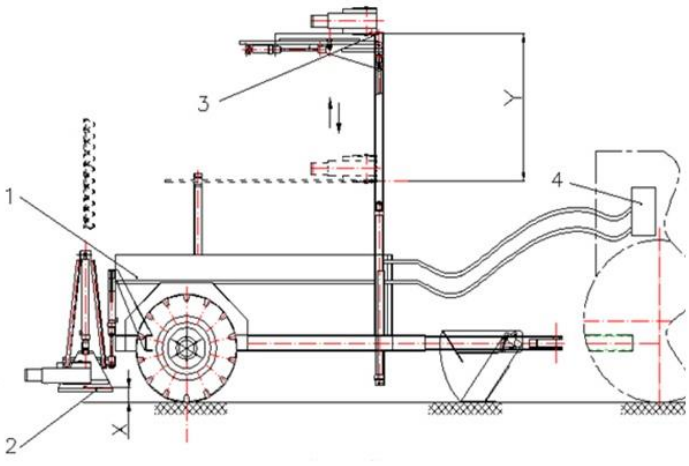
Stalks and seed productivity of diverse commercial cultivars were compared, with the aim of providing novel information to support dual-purpose cultivation of hemp in Europe (*Struik et al., 2016).* Hemp culture can represent circularity and zero waste for a future business model *(European Industrial Hemp Association, 2021).* The quality of the fibres used in the textile industry depends primarily on the efficiency of the hemp harvesting equipment.

Nedelcu et al., (2020), proposed an integrated method for hemp harvesting, which involved the manufacture of equipment to cut the stalks, sheaf-binding and leaving on the ground. *Huang et al, 2017* designed and test a self-propelled hemp harvester which could complete cutting, conveying and loading at a time. *Păun et al. (2020),* shows that when designing and manufacturing the equipment, several requirements imposed on the process of harvesting hemp for fibres must be taken into account (ex. stalk cutting height, damaged stalks etc.)

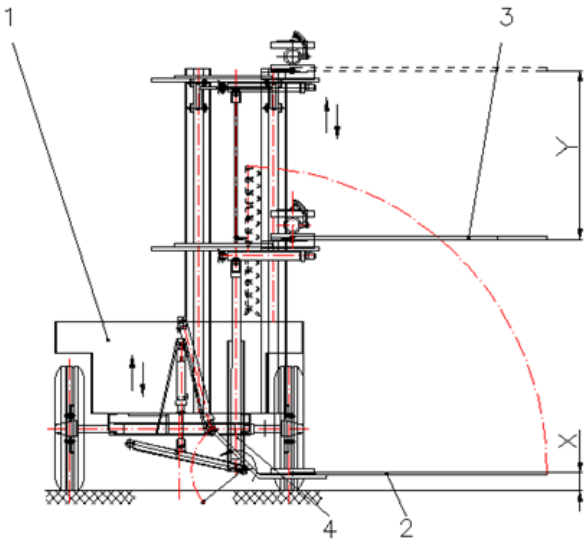
This paper will present the research results obtained by applying hemp harvesting technology with the equipment for harvesting green hemp stalks, designed, manufactured and tested at INMA Bucharest.

MATERIALS AND METHODS

The equipment for harvesting green hemp stalk was the subject of a patent application *(Păun et al., 2019)* and the concept design is presented in figure 1. The equipment was designed to be used in small and medium farms (*Păun et al., 2021).*



a) Side view



b) Rear view

Fig. 1 - Concept design of the harvesting equipment, lateral view (left) and back view (right)

1 - mobile platform; 2 - lower knife; 3 - upper knife 2; 4 - hydraulic system

The main subassemblies of the equipment for harvesting green hemp stalks are: *1*- mobile platform; *2* - lower knife; *3* - upper knife; *4* - hydraulic system. The mobile platform is a semi-mounted type construction, transferring part of the weight to the rear axle of the tractor. On the mobile platform, the following components are mounted: a mobile arm for fixing lower knife, a mobile arm for fixing upper knife and the hydraulic drive system. When moving, the platform rests on two wheels of the drivetrain, and when stationary, with the equipment decoupled from the tractor, a support leg mounted in the front part of the drawbar is used. The drawbar consists of a welded construction and a bolt that secures the coupling to the tractor.

The equipment for harvesting green hemp stalk was included in the harvesting technology, as it is shown in figure 2. The working process of the equipment involves cutting the inflorescences and green stalks and leaving them mixed on the ground.

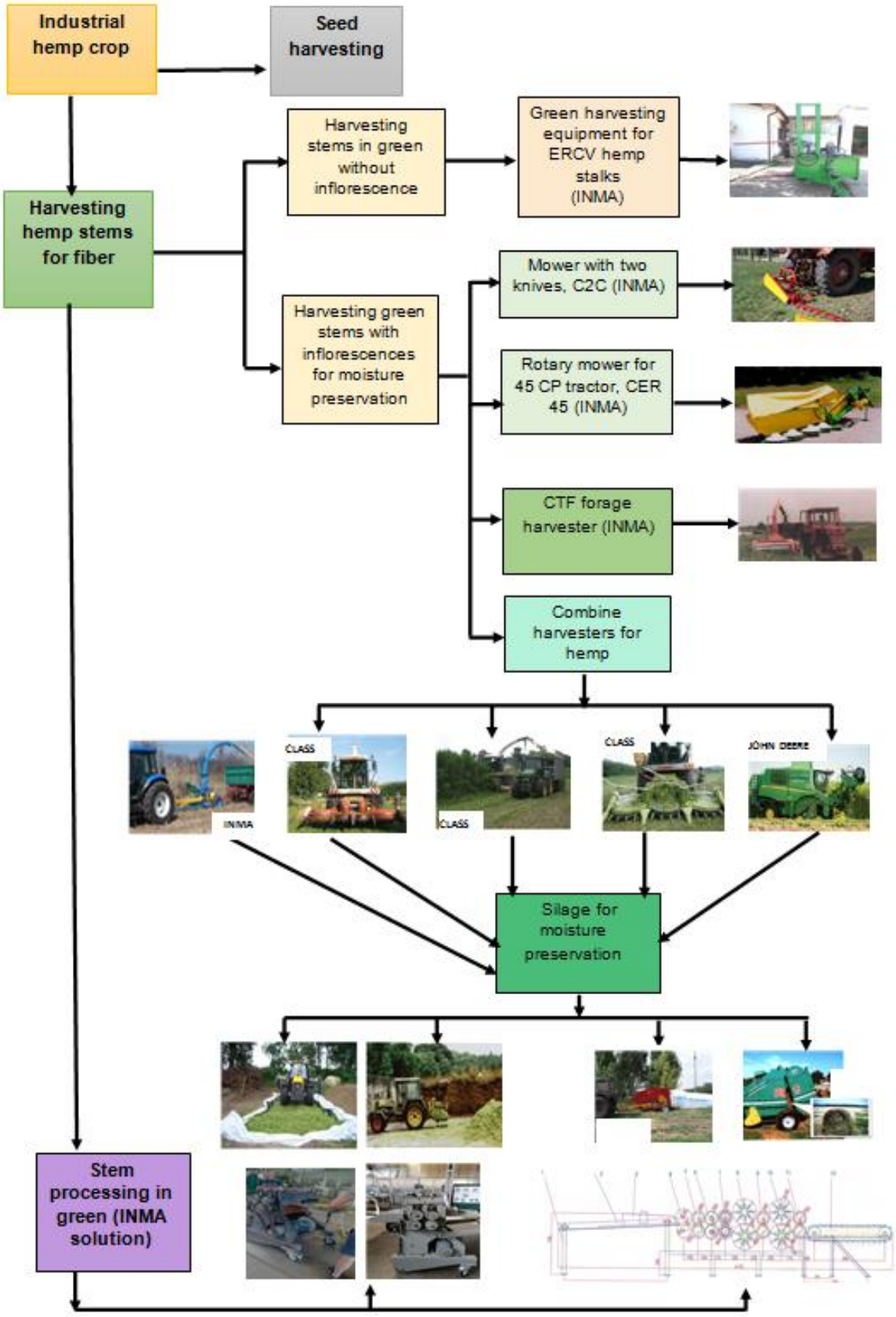


Fig. 2 - Green harvesting technology for hemp stalks

The equipment for harvesting green hemp stalks, was tested at INMA Bucharest. In order to ensure optimal testing conditions, an experimental hemp plot located at INMA Bucharest, with Dacia - Secuieni hemp variety, which is a specific variety for stalks and fibres, was established in the spring of 2021 (figure 3).



Fig. 3 - Experimental plot grown with hemp for fibre at INMA Bucharest location

During the hemp harvesting process, the most important components of the equipment are the lower knife and the upper knife. A T4A type transducer manufactured by HBM (Hottinger Baldwin Messtechnik), which is available at INMA Bucharest, was used to measure the torque at the tractor's PTO shaft.

The power transmitted through the power take-off, P_p, was calculated using formula (1):

$$P_p = M_p \cdot \omega_{p\cdot} \cdot 10^{-3} \text{ [kW]} \quad (1)$$

where:

M_p – is the torque measured at the tractor's PTO shaft, [N·m];

$\omega_p = \frac{\pi \cdot n_p}{30}$ - angular velocity of the PTO shaft, [rad/s];

n_p – the speed of the PTO shaft, [rpm].

The power required to trail the equipment during operation, P_t, was calculated using formula (2):

$$P_t = F_t \cdot V_l \cdot 10^{-3} \text{ [kW]} \quad (2)$$

where:

F_t – is the traction force measured at the drawbar, [N];

V_l – is the working (moving) speed of the aggregate, [m/s].

The total power, P_{tot} , required in the working process consists of the power transmitted through the power take-off and the power required to trail the equipment and was calculated using formula (3):

$$P_{tot} = P_p + P_t = \left(M_p \cdot \frac{\pi \cdot n}{30} + F_t \cdot V_l \right) \cdot 10^{-3} \quad (3)$$

RESULTS

The tests were carried out in August, when the hemp stalks were green, but also in October when they had a high degree of drying (figure 4).



a) b)

Fig. 4 - Aspects during the tests with the equipment for harvesting hemp stalks

a) harvesting green stalks in August; b) harvesting dry stalks in October

Tables 1, 2 and 3 present the results obtained during the tests with the equipment for harvesting hemp stalks, regarding the working conditions, operating indices and work quality indices.

Table 1

Working conditions

Den. no.	Specifications	UM	Values			
			Test I	Test II	Test III	Average
1	Harvested crop		Green hemp stalks of the Dacia - Secuieni variety			
2	Biomass production	t / ha	8.4	8.4	8.4	8.4
3	Vegetation year	-	2021			
4	Vegetation period	days	115-120	115-120	115-120	115-120
5	The appearance of the row	-	Not uniform with plants lying in small numbers			
6	The average height of the row	mm	1600-2300 (~2000)			
7	The average stalk thickness	mm				
	lower knife		10.2	9.9	11.0	10.4
	upper knife		4.2	3.6	5.1	5.3
8	Number of plants per m^2	pc	280-300			
9	Plant moisture at harvest	%	30.2	32.1	31.9	31.4

The working conditions presented in Table 1 provide a clear image of the parameters of the green hemp stalks in the experimental plot, at the time of the tests. The average plant moisture of 31.4% indicates that the time of harvesting was optimally chosen.

Table 2

Operating indices

Parameters	UM	Sample			
		Load drive			
		Test I	Test II	Test III	Average
Engine rotational speed, with power take-off at 540 rpm	rpm	2199	2198	2199	2198
PTO speed, n_p	rpm	540	540	540	540
Actual torque at the power take-off	daNm	42.1	42.1	42.1	42.1
Traction force at drawbar, F_t: - with the equipment trailed	daN	550	550	550	550
Pressure force on the tractor, F_{ap}	daN	355	354	356	355
Effective PTO power, $P_{p\,ef}$	kW [CP]	24.51 32.84	24.51 32.84	24.5 32.86	24.50 32.86
Total effective power to operate the equipment during operation, P_{tot}	kW [CP]	33.52 44.96	33.52 44.96	33.53 44.96	33.52 44.96
Working speed, V_l	km/h	6.1	6.5	5.5	6.03
Degree of pruning (stalks without inflorescence) G_{t2}	%	92.5	93.2	90.2	93.56
Effective working capacity (W_{ef})	t/h	7.5	7.9	7.2	7.6
Useful width (cutting)	mm	1300	1300	1300	1300

The data presented in Table 2 for the traction force at drawbar, the effective PTO power and the total effective power to operate the equipment indicates an optimal exploitation of the power resources of the energy source during operation. The degree of pruning average value of 93.56% was obtained in the conditions where the hemp from the experimental plot was not uniform, with plants lying in small numbers.

Table 3

Qualitative working indices

Den. no.	Specifications	UM	Values			
			Test I	Test II	Test III	Average
1	Cutting machine speed 1	rpm	1000	1000	1000	1000
2	Cutting machine speed 2	rpm	1000	1000	1000	1000
3	Working width	mm	1300	1300	1300	1300
4	Stalks cutting height	mm				
	lower knife		99.5	98.3	98.1	98.60
	upper knife		1550	2100	2400	2016.6
5	Degree of cutting (stalks cut - magnified)	%	92.5	93.2	90.2	91.96
6	Degree of pruning (stalks without inflorescence)	%	89.2	94.3	97.2	93.56
7	Stalks diameter	mm	10.2	9.9	11.0	10.4
	lower knife					
	upper knife		4.2	3.6	5.1	5.3
8	The average length of the stalk cut without inflorescence	m	1.38-1.65			

According to the data presented in Table 3, on the constant working width of 1300 mm, a good uniformity of the stalks cutting height was obtained for the lower knife (98.60 mm) and less good for the upper knife (2016.6 mm), due to the non-uniform development of the plants in height.

In figure 5 is presented the variation of the effective working capacity depending on the harvesting equipment working speed.

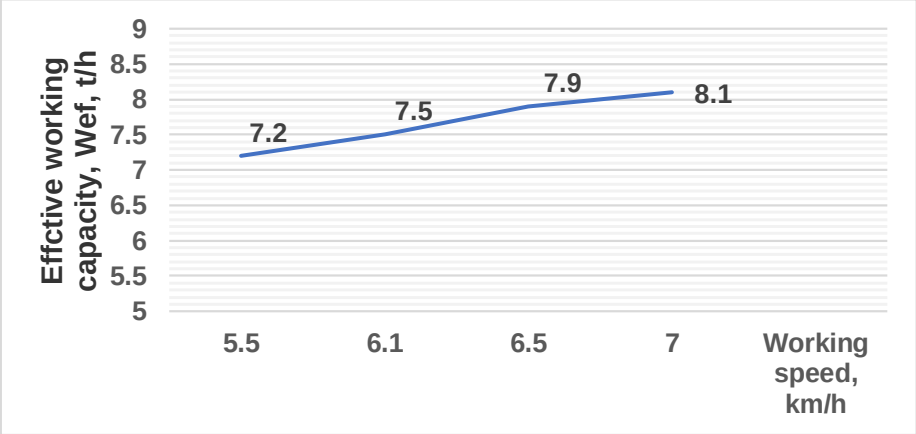


Fig. 5 - Variation of the harvesting equipment effective working capacity

The effective working capacity increases linearly with the increase of the working speed; for the working speed of 6.5 km/h the effective working capacity had the value of 7.9 t/h.

CONCLUSIONS

Following experimental research with the equipment for harvesting green hemp stalks, the results of which are presented in the tables 1, 2 and 3, main conclusions can be drawn:

- Stalks cutting height remained constant on the working width and had the following average values: lower knife - 98.60 mm; upper knife - 2016 mm;
- Stalks degree of cutting for 1 m^2 of cut plants for lower knife was 91.96% and for upper knife was 93.56%;
- During the tests, the hemp harvesting equipment moved with an average speed of 6.03 km/h;
- Actual torque at the power take-off had the value of 42.1 daNm;
- Traction force at the tractor drawbar was 550 daN with the equipment trailed;
- The average pressure force on the tractor had the value of 355 daN under load;

- The pressure force of the drawbar on the tractor (F_{ap}) had the value of 308 daN when empty and 355 daN under load, resulting in the coupling system of the harvesting equipment to the tractor working optimally;
- The average power take-off had the value of 24.5 kW;
- The working speed largely depends on the condition of the plot on which the hemp crop is located; the better the field is levelled and there are not many fallen plants, the faster the work speed increases.

In this paper, the results of the research obtained through the application of management practices in the harvesting and storage of industrial hemp were presented. By using green hemp stalk harvesting equipment in management practices, higher quality indices and quality material for hemp fibre production can be achieved.

ACKNOWLEDGEMENT

This research work was supported by:

- a grant of the Romanian Research, Innovation and Digitalization Ministry, PN 19 10 01 03-Substantion of the technology for harvesting and primary processing green hemp stalks, contract no. 5N/07.02.2019.

- PN 19 10 01 01 - Research on the realization of integrated systems for the field of Bioeconomy according to the concept of intelligent agriculture

REFERENCES

[1] Bogdanof G., Păun A., Brăcăcescu C., Stroescu Gh., (2019), Considerations on the hydraulic installation of the equipment for harvesting green hemp stalks, ISSN 1454 – 8003, *Proceedings of 2019 International Conference on Hydraulics and Pneumatics – HERVEX*;

[2] Carus M., Karst S., Kauffmann A. The European Hemp Industry, (2013), Cultivation, Processing and Applications for Fibres, Shives and Seeds. *Cologne: EIHA*, pp. 1–9;

[3] Huang J., Shen C., Li X., Tian K., Chen Q., Zhang B., (2017), Design and tests of hemp harvester, *International Agricultural Engineering Journal*, Vol. 26, No. 2.

[4] Nedelcu A., Popa L.-D., Zaica Al. Zaica A., Ştefan V., (2020), Considerations regarding technologies for hemp stem harvesting, *ISB-INMA TEH' 2020 International Symposium "Agricultural and Mechanical Engineering"* Jubilee Edition-Bucharest, October 30, 2020, pp. 609-614.

[5] Păun A., Stroescu Gh., Zaica Al., Olan M., Gheorghe G., Zaica A., Anghelache D., Ionescu Al., (2021), Technologies and technical equipment for hemp fibre crop, *Annals of the University of Craiova - Agriculture, Montanology, Cadastre Series* (*Analele Universităţii din Craiova, seria Agricultură – Montanologie – Cadastru*), Vol. 51/2/2021, pp. 426-434;

[6] Păun A., Bogdanof G., Ganea-Christu I., Ciupercă R., Matache M., (2019), *Equipment for harvesting green hemp.* Patent application no. A-00426/04.07.2019 OSIM, Romania;

[7] Păun A., Stroescu Ghe., Bunduchi G., Olan M., Milea D., Epure M., Zaica A., (2021), The influence of morphological particularities of hemp plants on technical equipment during the harvesting process, *Symposium ISB - INMA TEH' 2021, Agricultural and Mechanical Engineering, ISB-INMA TEH' 2021*, pp.652-661;

[8] Păun A., Stroescu Gh., Zaica A., Ciupercă R., Bogdanof C-tin., (2020), Analysis of the process of green hemp stalks sequential harvesting, *TE-RE-RD 2020, 9th International Conference on Thermal Equipment, Renewable Energy and Rural Development*, E3S Web of Conferences 180, 03026, 7, https://doi.org/10.1051/e3sconf/202018003026;

[9] Struik P. C., Yin X., Thouminot C., Bjelková M., Stramkale V., et al. (2016), Comparing hemp (Cannabis sativa L.) cultivars for dual-purpose production under contrasting environments. *Ind. Crops Prod*. 87, pp 33–44;

[10] ***European Industrial Hemp Association, http://eiha.org

MECHANICAL MODEL OF *CERASUS HUMILIS* ESTABLISHED BY UNIAXIAL COMPRESSION PHYSICAL TEST AND VIRTUAL SIMULATION
/
基于单轴压缩物理试验和虚拟仿真的钙果力学模型构建

Shilei KANG[1,2], Jiaxuan LU[1], Huhu YANG[1], Yanxi GUO[1], Junlin HE*[1,2]
[1]College of Agricultural Engineering, Shanxi Agricultural University, Taigu 030801, China;
[2]Dryland Farm Machinery Key Technology and Equipment Key Laboratory of Shanxi Province, Taigu 030801, China
Tel: +86-0354-6288400; E-mail: hejunlin26@126.com
Corresponding author: Junlin HE
DOI:https://doi.org/10.35633/inmateh-69-50

Keywords: *Cerasus humilis*, *uniaxial compression, elastic–plastic model, optimization*

ABSTRACT
The mechanical parameters of Cerasus humilis are the basic data for subsequent studies on fruit deformation, damage, and movement characteristics during harvesting and transportation, but these parameters are rarely reported. Relevant mechanical parameters of whole fruit compression are calculated by comparing physical tests and virtual simulations. The orthogonal rotating combined experimental design was used to arrange the simulation tests, with the elastic modulus (E), yield limit (E_y), and tangent modulus (E_t) as the influence factors and compression force as the result. Response surface optimization was employed to find the closest test point to the force–deformation curve of the physical test. The parameters of the pulp test point are as follows: E = 0.923 MPa, E_y = 0.0897 MPa, and E_t = 0.478 MPa. Results show that the step on the force–deformation curve was not the beginning of the pulp yield, which was substantially earlier than the strain rate at the simulation step. The region of increased stress in the pulp first appeared at the junction with the core due to stress concentration. Combining virtual and physical tests to solve the mechanical parameters of fruits is more suitable than testing the standard pulp sample.

摘要
钙果的力学参数是后续研究果实在采收和运输过程中变形、损伤和运动特性的基础数据，但这些参数的报道很少。通过物理试验和虚拟仿真的结合，计算了全果压缩的相关力学参数。采用正交旋转组合试验设计，以弹性模量(E)、屈服极限(E_y)和切线模量(E_t)为影响因素，压缩力为结果，设计了虚拟试验方案。采用响应面优化方法，寻找最接近物理试验力–变形曲线的试验点。果肉测点参数为:E = 0.923 MPa, E_y = 0.0897 MPa, E_t = 0.478 MPa。结果表明:果肉屈服的起始点并非力–变形曲线上的阶跃点，而是明显早于阶跃点的应变率。由于应力集中，果肉中应力增加的区域首先出现在与果核的交界处。将虚拟试验和物理试验相结合来求解水果的力学参数，比测试标准果肉样品更合适。

INTRODUCTION
Cerasus humilis, a type of tiny fruit, has been selected from wild plums by fruit experts in China in recent decades. In the process of brush harvesting, fruits, branches, and comb teeth contact each other, and these contact behaviours will induce fruit crushing and damage. Moreover, this fruit will also be squeezed until damaged during fruit packaging, transportation, storage, and other links. Therefore, extrusion is an important damage cause, and studying the mechanical behaviour of *Cerasus humilis* under extrusion is necessary.

In the research on the mechanical properties of extrusion contact of fruits, a testing method similar to that of metal materials was used by *Shirvani (2014*), *Alamar (2008), and Celik (2021)* to examine fruits with cut standard shape samples. However, this method ignores that the fruit comprises materials of different properties and disregards the influence of the complex structure of the fruit on its stress and deformation, which is inappropriate for fruit with continuous production links. The uniaxial plate compression test of whole fruit is most suitable to simulate the stress phenomenon during fruit production.

Tian (2017) stated that although physical tests can obtain the relationship between force and deformation of fruit, the distribution of stress inside the fruit is unavailable. By contrast, computer simulation techniques can perform the aforementioned task.

[1] *Shilei KANG,As Lec.PhD. Eng; Jiaxuan LU,M.S. Eng; Huhu YANG,M.S. Eng; Yanxi GUO,M.S. Eng; Junlin HE,Prof.Ph.D.Eng.*

Dintwa (2008) and *Rashvand (2022)* stated that the finite element method was commonly used to calculate the internal stress distribution of complex structures. *Liu (2022)* and *Wang (2006)* indicated that the method can analyse the effects of various fruit parts. The distribution of stress is of considerable importance to the study of fruit damage under the action of external load. At present, the force–deformation curve obtained from the compression of the whole fruit with a rigid flat cannot be converted into the real stress–strain relationship of fruit materials. Therefore, this paper will use the method of combining physical tests and simulations to study the mechanical behaviour of the whole fruit under compression to explore the distribution of stress and strain inside the fruit and the physical properties of related materials.

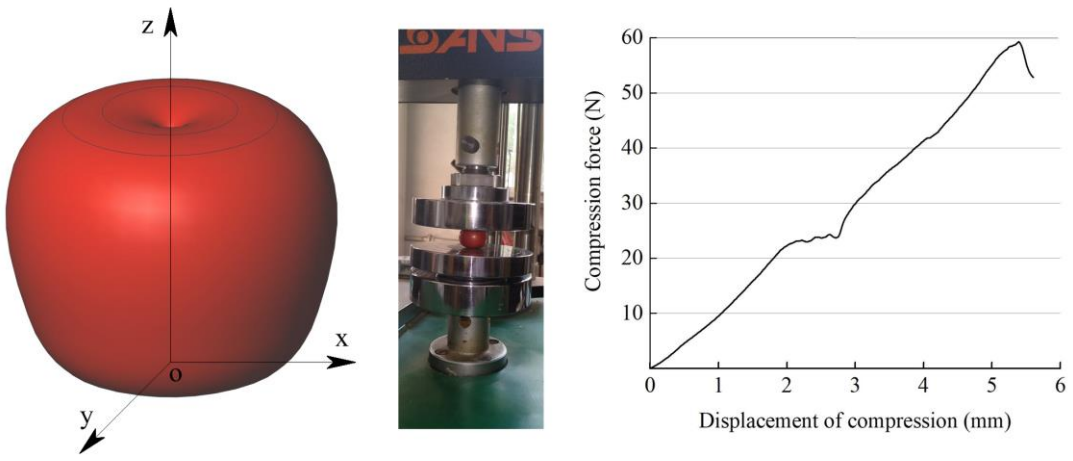
MATERIALS AND METHODS

Physical test of uniaxial compression

In this experiment, *Cerasus humilis* "Nongda No.4", which met the harvest requirement, was collected in Juxin Modern Agriculture Demonstration Park in Shanxi Province in the morning of September 3, 2021, in a sunny day. The entire branch was cut and brought back to the laboratory, the incision was immersed in water to keep the branches active, and all the tests were completed within 4 h. During the experiment, fruits were individually picked from the branches, the stalks were removed, the surfaces were wiped, and the bad fruits with abnormal development and pests were discarded. Fruits with approximate symmetry along the calyx–stalk axis were selected as test samples.

A CMT6104 microcomputer control electronic universal testing machine, which can automatically collect the compression deformation and its corresponding force in the test process, was used. The force sensor with a range of 500 N was chosen, and a circular flat plate indenter with a diameter of 100 mm was selected. The falling speed of the indenter is 5 mm/min, and the data sampling frequency is 15 Hz.

Before the compression test, an electronic vernier calliper was utilized to measure the 3D size of the sample. Measurement results revealed that the fruit was slightly small in the longitudinal (Z) direction and slightly large in the transverse (XOY) direction perpendicular to it, demonstrating a nearly circular cross-section (as shown in Fig. 1a). Many simulation times are needed in this study. The axial compression model can be simplified into a plane one, which can markedly reduce the calculation scale compared with transverse compression. Therefore, only axial compression data are used for research. Fig. 1b shows the physical compression test. At least 20 valid sample data are obtained by compression until the fruit breaks.



(a) (b) (c)

Fig. 1 - 3D model, physical test, and typical force–deformation curve

Fig.1c shows a typical force–deformation curve from the uniaxial compression test. All the sample curves showed a temporary step, which was not accidental; this step was not caused simply by the pulp yield but the macroscopic manifestation of partial separation of pulp and core or the partial rupture and collapse of pulp. According to previous compression tests on standard-shaped pulp samples of *Shirvani (2014)*, the deformation rate of pulp yield is often considerably smaller than that of the step in this paper, and the appearance of step is not the beginning of yield. For the whole fruit comprising multiple materials, the step on the force–deformation curve does not correspond to the yield phenomenon on the stress–strain curve obtained by the test of the standard shape sample made of pulp.

The fruit structure has been destroyed when the internal pulp damage has occurred at the step of the force–deformation curve. In the work on the whole fruit, its deformation rate generally does not reach this step. The deformation rate corresponding to this step is approximately 10% in the force–deformation curves of all samples. Therefore, only the part of the curve before the step is conducted in the simulation test.

Virtual test of uniaxial compression

Virtual geometric model

The typical force–deformation curve of uniaxial compression is taken as the comparison standard. Sample data near the average value were selected to realize representativeness. The fruit of the same size as the sample was measured in 3D and then cut in half along the meridian with a sharp knife and photographed. The shape of this fruit was traced with a pen after the section was attached to the paper (dimensions: longitudinal 16.0 mm, transverse average 19.98 mm). Fig. 2 shows the longitudinal section of *Cerasus humilis*, which comprises three parts, namely core, pulp, and peel. The core is small and ellipsoidal, with long and short semi-axes of approximately 5 and 3 mm, respectively. The peel is thin and dense, and the pulp is carefully scraped off with a knife and the thickness of the peel is about 0.1 mm measured with an electronic vernier calliper. The images were fitted with a spline curve in CAD software to fit the shape and position relationship of each part. These images were then scaled to the measured dimensions to make a 3D compression model (shown in the cross-section in Fig. 2), and the cross-section of the axisymmetric model was extracted as the simulation analysis object.

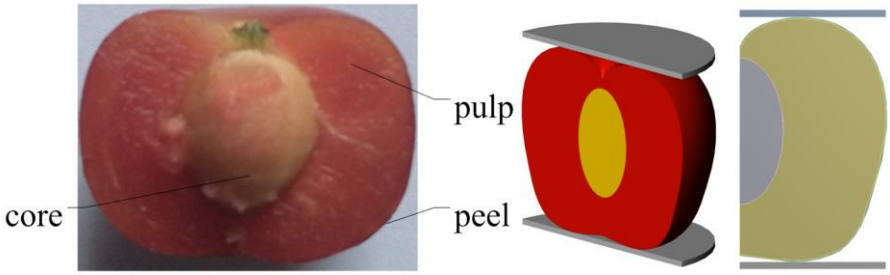


Fig. 2 - Anatomical structure and geometric model

Mechanical properties

The relevant physical parameters of each structure of the model should be generally obtained before the simulation test. The upper and lower plates are stainless steel indenters in physical tests and can be set as rigid bodies in the simulation. The core of the fruit is a wooden structure with a hard texture, and its stiffness is several orders of magnitude larger than that of the pulp. The core can also be set as a rigid body in the simulation.

Most fruit materials demonstrate an elastic behaviour under a small strain. An increase in strain shows elastic–plastic deformation, and a continuous strain increment shows full-plastic deformation. At the macro level, the fruit demonstrates irreversible deformation until rupture. *Kim (2008)* regarded fruits as completely elastic materials and applied Hertz theory to explain mechanical phenomena, which is true under remarkably small strains. However, the strain in this study becomes seriously asynchronous and demonstrates the stress concentration phenomenon due to the existence of a hardcore. Thus, even if the whole fruit has only a small strain, its local strain will be several times that of the whole strain. Alamar *(2008)* stated that the strain was only approximately 5% when the modulus of elasticity was calculated in accordance with the stress–strain curve obtained from the standard cuboid apple pulp sample test. *Cerasus humilis* and “Golden Delicious” apple have a similar texture; thus, the elastic limit strain of *Cerasus humilis* should also be similar. Under the overall strain of 10% in this study, the local stress concentration of pulp facilitated the entrance of part of pulp stress in the plastic stage. Therefore, the completely elastic model was inappropriate. Pulp was not used as a viscoelastic material but as an elastoplastic material because viscoelasticity is unsuitable to express the permanent damage caused by fruits exceeding the yield limit, and the elastoplastic model is simple. *Celik (2017)* stated that fruit materials were assumed to be isotropic elastoplastic materials and are often characterized by bilinear hardening models. Consider the fruit as a multibody system, where each part was regarded as a uniform material by *Li (2013)*.

The pulp comprises cells with sufficient moisture content, which is determined to be more than 90%. Previous researchers used moulds to cut standard samples when testing the modulus of elasticity of large fruits, such as an apple with similar materials to calcium pulp. However, the fruit size in this study is too small to make standard shape samples.

More importantly, a considerable amount of water is lost during compression, and its boundary conditions are completely different from those in the whole fruit tests. As for the modulus of elasticity of fruit peel, *Juxia (2015)* and *Hetzroni (2011)* separated the peel and pulp of apples and tomatoes to make approximately rectangular samples. This method has several disadvantages; fruit peel and pulp are often closely combined, and pulp residue will emerge in the samples. Moreover, spherical fruit peel cannot be expanded into a plane theoretically, and a serious uneven force exists in the cross-section of the sample during the tensile test. Therefore, the value range of the elastic modulus of pulp and peel is estimated in accordance with the order of magnitude of similar fruits. This range is adjusted and optimized in the simulation test, until the force–deformation curve obtained in the simulation and physical tests is consistent.

The fruit was treated as a single completely elastic material, and the calculated apparent elastic modulus of the whole fruit of "Nongda No.4" *Cerasus humilis* by Hertz contact theory is 0.66 MPa according to *Zhibin (2016)*. A total of 0.5–1.5 MPa was taken as the optimal range of the elastic modulus of pulp because of the wide elastic modulus range of biomaterials with different maturities. The yield limit of pulp may also have a certain influence on the mechanical behaviour in compression. The yield limit is usually proportional to the elastic modulus, which is set as 10% of the elastic modulus in a previous study. The tangent modulus is the slope between yield and strength limits on the stress–strain curve of the material. According to previous studies on standard apple samples, it is approximately one-third of elastic modulus *(Zhe, 2016*) and is preset to 0.15–0.5 MPa.

Cerasus humilis and *"Golden Delicious" apple* are all thin-peel fruits. The peel mainly plays the role of preventing water loss, oxidation, and the invasion of outside bacteria. The bearing capacity of fruit peel is limited, and the mechanical parameters of fruit pulp dominate the force–deformation relationship during fruit compression. *Juxia (2015)* stated that the elastic modulus of peel was one order of magnitude higher than that of pulp. The peel possibly remains in the elastic stage under the deformation rate of fruit in this study. Therefore, only the elastic modulus of the peel is considered.

When measuring the Poisson's ratio of pulp, 20 standard-shaped fruits were selected and numbered as samples and fresh weight was measured. The fruits were then naturally air-dried, the dry core was obtained, the powder of pulp and the peel was also acquired. The core and the powder were weighed, and the moisture content of the pulp and the peel mixture was calculated. Separating pulp and peel under dry and wet conditions is difficult, and the calculated moisture content is also the sum of the two. The average moisture content of 20 samples is 93%. The formula (1) was used to calculate the Poisson's ratio by *Ashtiani (2019)*.

$$\mu = 0.1 + 0.4 * M \quad (1)$$

where: M is the average moisture content, [%]; μ is the Poisson's ratio, which is calculated to be 0.47, and it can be approximated as the Poisson's ratio of pulp, because the mass of the peel in the powder is remarkably small.

Finite element model, load, boundary conditions, and meshing

In the uniaxial compression fruit model, the upper and lower plates are round and their connecting line is coaxial with the symmetry axis of the fruit. The fruit surface is tangent to the upper and lower plates. The model is simplified to a 2D axisymmetric plane model because of its axisymmetric characteristics. The contact between pulp and core (Nongda No.4 is adherent stone) and between peel and pulp should be bonded contact. The upper and lower plates comprise stainless steel; therefore, the contact type with the fruit is frictional contact. Except for axial movement, frictionless constraints were applied to the symmetry axes of the upper and lower plates and the fruit to limit their degrees of freedom. The lower plate imposed fixed constraints to limit all degrees of freedom. *Jackson (2005)* stated two load application methods to the upper plate: applying force and displacement loads. The displacement load has a faster convergence rate than the force load. Therefore, 1.6 mm displacement is applied on the upper plate (corresponding to 10% strain) and the compression speed is the same as the physical test (5 mm/min), which is in line with the standard of *ASAE (2022).*

The separate structures of core, pulp, and peel are combined into a whole before mesh division. Therefore, common nodes can be generated on the contact surface during mesh in the later stage, which is conducive to improving the calculation stability. In the meshing, the contact region of each structure is refined to simulate the curve deformation accurately. The mesh size away from the contact area gradually increases with a growth rate of 1.1 times and is dominated by quadrilateral meshes. The specific mesh size is gradually refined until the pulp stress obtained by calculation stabilizes. The corresponding force is equal to the compression reaction force in the simulation when the displacement load is applied to the upper plate.

Simplification of the geometric model

In the simulation, an accurate virtual model is always needed to represent the physical model. Simultaneously, the model should be as simple as possible to reduce the calculation scale. Many assumptions were made in the modelling process, and the material properties of various parts and the connections between them in the model may be different from the real situation. However, the virtual model is considered reasonable as long as the deformation of the simulation model under the same external load is consistent with the real physical test results and the distribution of internal stress conforms to the mechanical law.

Whether the peel and pulp can be considered as a whole is a problem to be discussed when deliberating the distribution and change in stress inside the fruit under a 10% compression rate. Stripping the peel is difficult; therefore, measuring its physical parameters is also difficult. Moreover, only one reference standard is used to verify the virtual model, that is, the force–deformation curve obtained from physical tests. Therefore, if the peel model parameters were added, then the unknown quantity of the virtual model would be excessive and difficult to establish.

A simulation test was then conducted to calculate the stress distribution and change process of pulp in the compression process to determine the retention of fruit peel in the virtual model. The peel is assumed to be a part of the pulp; therefore, only two types of material are left in the fruit model: the core and the pulp. The core is regarded as a rigid body, and the material parameters that must be adjusted and optimized belong to the pulp. The pulp model parameters include elastic modulus E, Poisson's ratio μ, yield strength E_y, and tangent modulus E_t. The elastic modulus is estimated to be approximately 0.9 MPa according to the previous analysis, the yield limit is 10% of the elastic modulus, the Poisson's ratio is 0.47, and the tangent modulus is 0.3 MPa. The meshing, boundary conditions, and load of the model are consistent with those mentioned above. After constant adjustment of the calculation, the distribution and variation trend of stress and strain in the fruit can be considered reasonable until the force–deformation curve obtained from the virtual test is close to the corresponding physical test result.

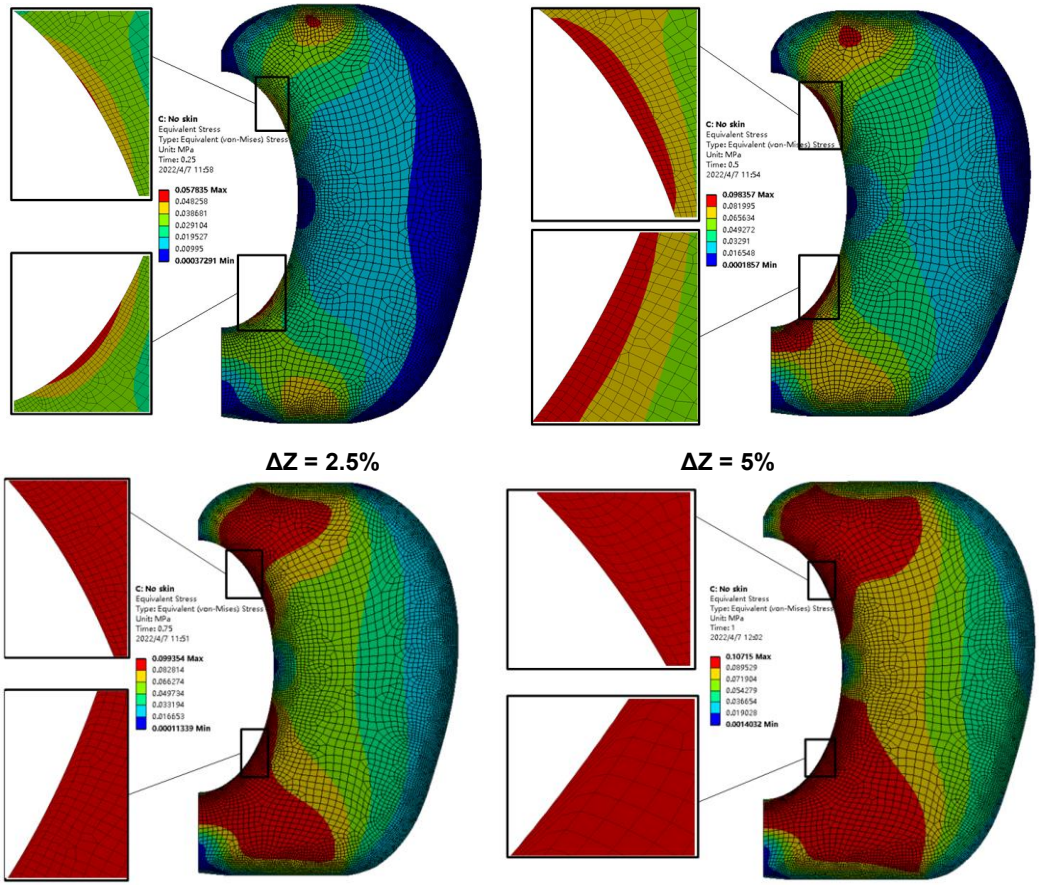


Fig. 3 - Distribution and variation of equivalent stress of pulp

Zulkifli (2020) stated that fruits comprise materials with different properties, and the inhomogeneity of materials and their connections seriously affect the stress distribution of fruit. The peel and core of different fruits have varying effects on the stress distribution of pulp.

Fig. 3 shows the equivalent stress distribution and variation of pulp during virtual compression. The stress increase in pulp starts from two different regions: one is at the junction of the core and the other is at a certain distance under the peel of the part in contact with the flat plate. The equivalent stress gradually increases to the yield limit with the compression ratio, and then the yield region continues to expand. The maximum stress occurs at the junction with the core, followed by a certain depth under the peel of the contact part. This phenomenon is due to the stiffness difference of several orders of magnitude between the pulp and the core, and the strain of the pulp and the core is seriously asynchronous when the fruit is subjected to external compression, resulting in serious asynchronicity at the interface between the pulp and the core and inducing shear stress. However, the increase in stress near the contact region with the upper and lower parts and the flat plate is relatively lagging. The yield region of pulp does not extend to the peel even when the overall compression rate reaches 10%. However, at this time, the mesh of part of the pulp at the junction with the core was considerably distorted, indicating that the shearing stress of this part of the pulp had reached a remarkably serious degree, and some pulp was almost destroyed. This phenomenon did not occur farther away from the pit. This finding is inconsistent with the observed phenomenon in the compression simulation of the apple by *Fenyvesi (2013)*. The apple is a no stone fruit while *Cerasus humilis* is a stone fruit; thus, the difference in the internal structure of the two results in different stress distributions.

This experiment reveals that the stress distribution in the fruit is seriously affected by the wooden core. The region exceeding the yield limit did not extend to the fruit surface until the compression rate in this study according to the stress distribution and its development. Therefore, within the range of compression rate in this study, taking the peel as a part of the pulp without separate modelling is reasonable when investigating the fruit deformation behaviour.

Virtual experiment design

The pulp parameters to be determined in this study include elastic modulus E, yield limit E_y, and tangent modulus E_t, which are respectively represented by codes X_1, X_2, and X_3, and the compression reaction force Y is used as the test index. The rotating centre composite design method was utilized to arrange the test to determine the relationship between the influence factors and the test index. As the number of factors is 3, the number of second-level comprehensive tests is 8, and the number of asterisk tests is 6. The number of zero-level tests is 1 because it is a simulation test. The length of the asterisk arm is calculated from the number of zero- and two-level tests. The level codes and parameter values of each factor are shown in Table 1, and the coded quadratic regression orthogonal rotation combination test sites are shown in Table 2.

Table 1

Factors and levels

Level code	Factor		
	X_1 [MPa]	X_2 [MPa]	X_3 [MPa]
r (1.215)	1.5	0.15	0.5
1	1.3	0.13	0.429
0	1	0.1	0.325
−1	0.7	0.07	0.221
−r (1.215)	0.5	0.05	0.15

Table 2

CCD design scheme and experimental results

Serial number	X_1	X_2	X_3	X_1X_2	X_1X_3	X_2X_3	X_1^2	X_2^2	X_3^2	Y
1	1	1	1	1	1	1	1	1	1	23.6
2	1	1	−1	1	−1	−1	1	1	1	22.9
3	1	−1	1	−1	1	−1	1	1	1	19
4	1	−1	−1	−1	−1	1	1	1	1	17.2
5	−1	1	1	−1	−1	1	1	1	1	14
6	−1	1	−1	−1	1	−1	1	1	1	13.9
7	−1	−1	1	1	−1	−1	1	1	1	13.3
8	−1	−1	−1	1	1	1	1	1	1	12.7
9	r	0	0	0	0	0	r^2	0	0	22.7
10	−r	0	0	0	0	0	r^2	0	0	9.96
11	0	r	0	0	0	0	0	r^2	0	19.4
12	0	-r	0	0	0	0	0	r^2	0	14.2
13	0	0	r	0	0	0	0	0	r^2	18.7
14	0	0	-r	0	0	0	0	0	r^2	17.6
15	0	0	0	0	0	0	0	0	0	18.2

RESULTS

Statistical analysis of experiment results

The experiment results of quasistatic compression simulation were obtained, as shown in Table 2. The analysis of variance (ANOVA) was applied to the experiment results by Design-Expert 8.0.6. All factors and interactions were included in the first ANOVA. The analysis revealed that the F values of interaction terms X_1X_3, X_2X_3, and quadratic term X_3^2 were less than 1, indicating that the influence of these items on the results could be ignored. Therefore, these items were incorporated into the residual term and ANOVA was conducted again, as shown in Table 3.

According to ANOVA, modulus of elasticity E (X_1) had the highest significant level of compression force, sequentially followed by yield limit E_y (X_2) and modulus of tangent E_t (X_3). Simultaneously, the interaction X_1X_2 and quadratic terms X_1^2 and X_2^2 had a certain impact on the compression force.

The post-ANOVA information also provided a prediction of coefficient estimates and their standard errors for a predictive regression model. The quadratic regression between modulus of elasticity (X_1), yield limit (X_2), modulus of tangent(X_3), and compression force(Y) is computed as follows:

$$Y = -1.88 + 16.22X_1 + 39.86\ X_2 + 3.56\ X_3 + 117.84\ X_1\ X_2 - 7.78\ X_1^2 - 531.7\ X_2^2 \quad (2)$$

ANOVA was conducted for the above regression model and a significance test was performed. The results are shown in Table 3. The coefficient of determination of the model is $R^2 = 0.9955$ and F is substantially higher than $F_{0.01}(6,8)$, indicating that the multiple regression model is extremely significant and the regression equation is effective.

Table 3

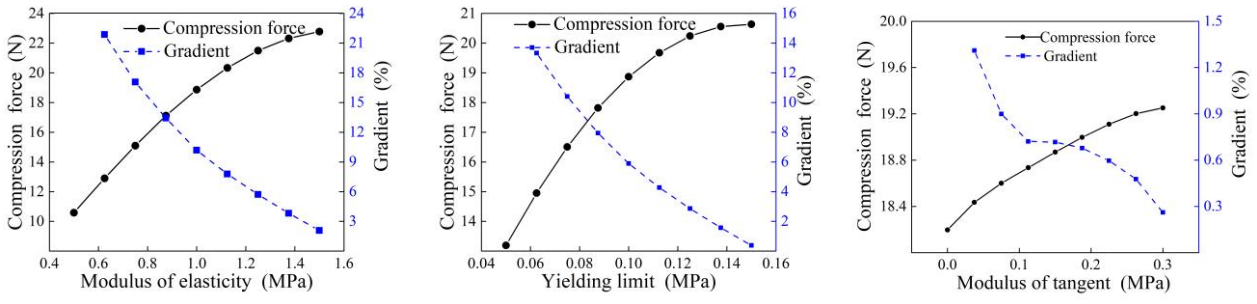
Analysis of variance

Source	SS	DF	MS	F-value	P-value	Sig
X_1	188.45	1	188.45	1400.64	<0.0001	***
X_2	32.12	1	32.12	238.76	<0.0001	***
X_3	1.87	1	1.87	13.88	0.0058	**
X_1 X_2	8.82	1	8.82	65.56	<0.0001	***
X_1^2	4.74	1	4.74	35.21	0.0003	**
X_2^2	2.21	1	2.21	16.46	0.0036	**
Model	236.50	6	39.42	292.96	<0.0001	***
Residual	1.08	8	0.13			

*Notes: SS is the sum of squares, DF is degrees of freedom, MS is mean square, F-value is statistics value, Sig is significance, ***means P < 0.001,** means P < 0.01, $F_{0.01}(1,8) = 11.26$, $F_{0.01}(6,8) = 6.37$.*

Influence of a single factor on the compression reaction force

Fig. 4 was drawn on the basis of simulation test data. Fig. 4a reveals the relationship between the compression force and the gradient of a single factor (the modulus of elasticity). The curve showed an increasing trend with the elastic modulus of pulp, which was consistent with previous cognition. When the elastic modulus increased from 0.5 MPa to 1.5 MPa, the compression force of the whole fruit increased from 9.96 N to 22.75 N and the compression force was highly sensitive to the elastic modulus. ANOVA results also reveal that elastic modulus has a significant influence on compression reaction force. With the increase in elastic modulus, the gradient of compression force decreases from 24% to less than 3% at 1/8 intervals in the range of 0.5–1.5 MPa.



(a) (b) (c)

Fig. 4 - Effects of physical parameters of pulp on fruit compression force

Fig. 4b reveals the relationship between the compression force and the gradient of a single factor (the yield limit). The figure shows that the compression force increases with the yield limit. When the yield limit increases from 0.05 MPa to 0.15 MPa, the compression force rises from 14.2 N to 19.4 N and its sensitivity to the yield limit is also substantially high. ANOVA results also indicate that the yield limit has a remarkably significant influence on the compression force. The increment in compression force gradually decreases with the increase in yield limit. The gradient of compression force decreases from 9.9% to 1.1% at 1/8 intervals under range of 0.05–0.15 MPa.

Fig. 4c reveals the relationship between the compression force and the gradient of a single factor (the tangent modulus). The figure shows that although the compression force also demonstrates an increasing trend with the tangent modulus, its change rate is within 1% in all test levels. The compression force only increases by 5% when the tangent modulus rises from 0.15 MPa to 0.5 MPa. The compression force is insensitive to the change in tangent modulus. ANOVA results also demonstrate that the significance level of tangent modulus is lower than the two other factors.

Influence of interaction on compression force

Fig. 5 shows the response surface and contour to the reaction force of compression as a function of modulus of elasticity (X_1) and yield limit (X_2). The influence factors of X_1 and X_2 were significant at 0.01 probability level by the F test of ANOVA, and their interaction was also significant at 0.01 probability level. The overall effect of the two main influence factors on the reaction force of compression was observed in the response surface. The compression reaction tends to increase with the rise in elastic modulus and yield limit. The interaction terms X_1X_3 and X_2X_3 related to X_3 in the first ANOVA have been excluded. Therefore, analysing the response surfaces of the two interactions is no longer necessary.

The quadratic terms X_1^2 and X_2^2 were also significant at the 0.01 probability level in the ANOVA of the model.

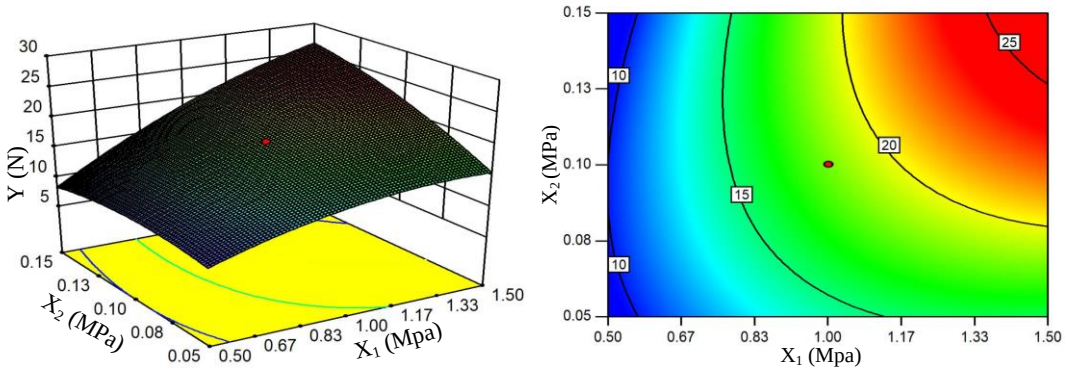


Fig. 5 - Response surface and contour of elastic modulus (X_1) and yielding limit (X_2)

Optimization

The optimization design method is originally used in structural or technological design to find the optimal scheme according to the predetermined objective under certain constraints. The material properties of pulp are inherent and cannot be designed. However, pulp materials are often uneven and anisotropic, and their inherent properties remarkably vary with different positions. A set of simplified equivalent parameters is needed to represent the pulp to study the mechanical behaviour of fruits at the macro scale. Thus, the obtained parameters are not necessarily the real properties of the pulp, but their combination can approximate the physical model. Moreover, measuring the real properties of the pulp of small berries with high moisture content is difficult. Therefore, the specific value of this parameter combination must be determined or designed. Response surface optimization (RSM) can use appropriate strategies to find the optimal parameters for pulp model construction.

Taking the compression force of 17.1 N under 10% strain in the physical test curve as the optimization object, three candidate points were given by the RSM algorithm, as shown in Table 4. The force–deformation curves corresponding to the three points were obtained and plotted on the same coordinate plane as the physical test curve, as shown in Fig. 6. The cubic regression equations of the physical test and three candidate point curves in the figure (intercept was set as 0) are shown in Table 4. The table reveals that the regression equation of candidate Point 1 is closest to the physical test; therefore, its parameter value can be used as the material parameter of the pulp sample studied in this test.

Table 4

Physical test and candidate points

	E (MPa)	E_y (MPa)	E_t (MPa)	Y (N)	Equation of regression
Physical test				17.1	$y = 0.318x^3 + 1.038x^2 + 8.266x$ ($R^2 = 0.997$)
Candidate 1	0.923	0.0897	0.478	17.2	$y = -1.657x^3 + 5.49x^2 + 6.156x$ ($R^2 = 1$)
Candidate 2	1.1	0.0666	0.39	17.0	$y = -2.229x^3 + 5.147x^2 + 8.015x$ ($R^2 = 0.998$)
Candidate 3	0.955	0.0889	0.339	17.1	$y = -2.006x^3 + 5.893x^2 + 6.352x$ ($R^2 = 0.999$)

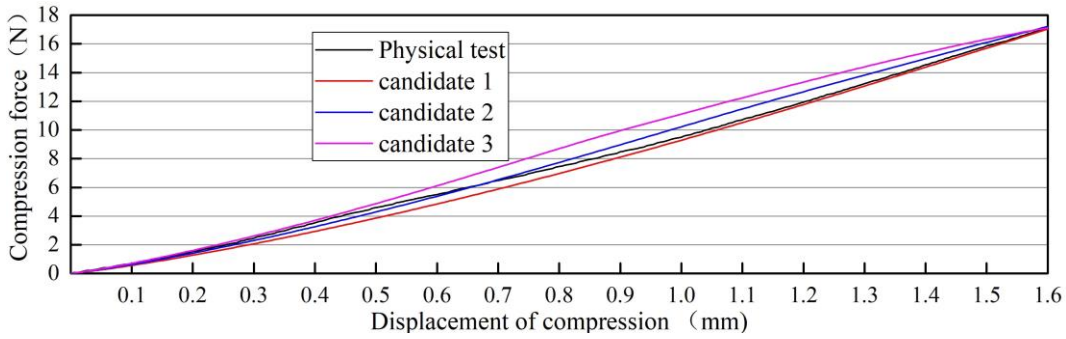


Fig. 6 - Force–deformation curves of physical test and three candidate points

CONCLUSIONS

(1) In the uniaxial compression of the whole "Nongda No.4" *Cerasus Humilis*, the step on the force–deformation curve was not the beginning of pulp yield but the partial tear at the pulp–core junction and the collapse of pulp at a certain distance under the peel of the contact point with the flat plate.

(2) When looking for the combination of parameters in the virtual pulp model, the regression equation between the compression force and each parameter was obtained by the central combination rotation orthogonal test method and the model was remarkably significant.

(3) The parameter value combination, which can represent the physical model of the pulp, can be obtained through the combination of physical and simulation tests and certain optimization strategies. The virtual model constituted by this parameter combination can replace the physical model and the stress distribution and variation inside the fruit, which cannot be observed by the physical test, can also be realized.

ACKNOWLEDGEMENT

This research, titled "Mechanical model of *Cerasus humilis* established by uniaxial compression physical test and virtual simulation", was funded by project: "Science and Technology Innovation Fund of Shanxi Agricultural University (Grant No. 2017017)", and was also supported by "Shanxi Basic Research Program (Grant No. 202203021221174)".

REFERENCES

[1] Alamar M. C., Vanstreels E., Oey M. L., Moltó E., & Nicolai B. M., (2008). Micromechanical behaviour of apple tissue in tensile and compression tests: Storage conditions and cultivar effect. *Journal of Food Engineering*, 86(3), 324-333;

[2] ASAE., (2022), Compression test of food materials of convex shape, ASAE S368.4 DEC2000(R2022);

[3] Ashtiani S.M., Sadrnia H., Mohammadinezhad H., Aghkhani M.H., Khojastehpour M., & Abbaspour-Fard M.H., (2019), Fem-based simulation of the mechanical behaviour of grapefruit under compressive loading, *Scientia Horticulturae,* 245, 39-46;

[4] Celik K. H. (2017), Determination of bruise susceptibility of pears (Ankara variety) to impact load by means of fem-based explicit dynamics simulation. *Postharvest Biology & Technology,* 128:83-97;

[5] Celik H. K., Ustun H., Erkan M., Rennie A. E., & Akinci I., (2021), Effects of bruising of 'Pink Lady' apple under impact loading in drop test on firmness, colour and gas exchange of fruit during long term storage, *Postharvest Biology and Technology*, 179, 111561;

[6] Dintwa E., Zeebroeck M.V., Ramon H., Tijskens E., (2008), Finite element analysis of the dynamic collision of apple fruit. *Postharvest Biology & Technology*, 49(2):260-276;
[7] Fenyvesi L., Fenyvesi D., & Csatár A., (2013), Stress analysis in fruits. *Advances in Mechanical Engineering,* 5, 874673;
[8] Hetzroni A., Vana A., & Mizrach A., (2011), Biomechanical characteristics of tomato fruit peels. *Postharvest Biology & Technology,* 59(1):80-84;
[9] Jackson R. L., & Green I., (2005), A Finite Element Study of Elasto-Plastic Hemispherical Contact Against a Rigid Flat. *Journal of Tribology,* 127(2):343-354;
[10] Juxia W., Qingliang C., Hongbo, L., & Yaping L., (2015), Experimental research on mechanical properties of apple peels. *Journal of Engineering and Technological Sciences,* 47(6):688-705;
[11] Kim G.W., Do G.S., Bae Y., & Sagara Y., (2008), Analysis of mechanical properties of whole apple using finite element method based on three-dimensional real geometry. *Food Science & Technology Research,* 14(4):329-336;
[12] Li Z., Yang H., Li P., Liu J., Wang J., Xu Y., (2013), Fruit biomechanics based on anatomy: a review. *International Agrophysics,* 27(1):97-106;
[13] Liu X., Cao Z., Yang L., Chen H., & Zhang Y., (2022), Research on Damage Properties of Apples Based on Static Compression Combined with the Finite Element Method. *Foods*, 11(13), 1851;
[14] Rashvand M., Altieri G., Genovese F., Li Z., & Di Renzo G. C., (2022), Numerical simulation as a tool for predicting mechanical damage in fresh fruit, *Postharvest Biology and Technology*, 187, 111875;
[15] Shirvani M., Ghanbarian D., & Ghasemi-Varnamkhasti M., (2014), Measurement and evaluation of the apparent modulus of elasticity of apple based on Hooke's, Hertz's and Boussinesq's theories, *Measurement,* 54:133-139;
[16] Tian K., Cheng S., Li X., Huang J., & Zhang B., (2017), Mechanical properties and compression damage simulation by finite element for kiwifruit, *International Agricultural Engineering Journal,* 26(4):191-201;
[17] Wang C.X., Pritchard J., & Thomas C. R., (2006), Investigation of the mechanics of single tomato fruit cells. *Journal of Texture Studies,* 37(5):597-606;
[18] Zhe Feng., (2016), *Measurement of contact pressure of apple under different loads and bruising predication using finite element analysis （苹果不同受载时接触应力测量分析及损伤预测）*, Master Thesis, Shihezi University, China;
[19] Zhibin Sun., (2016), *Experimental Research of Branches Feeding Device of Cerasus humilis (钙果枝条喂入装置的试验研究),* Master Thesis, Shanxi Agricultural University, China;
[20] Zulkifli N., Hashim N., Harith H. H., & Shukery M. F. M., (2020). Finite element modelling for fruit stress analysis-A review. *Trends in Food Science & Technology*, 97, 29-37;

CONFIGURATION OPTIMIZATION METHOD OF AGRICULTURAL MACHINERY CLUSTER OPERATION MAINTENANCE SERVICE VEHICLE
/
农机集群作业维修服务车配置优化方法

Weipeng ZHANG, Bo ZHAO*), Guangrui LI, Liming ZHOU, Kang NIU, Shengbo GAO
National Key Laboratory of Agricultural Equipment Technology, China Academy of Agricultural Mechanization Science Group Co., Ltd. Beijing 100083, China;
Tel: +86-15210666162; E-mail: zhaoboshi@126.com; correspondent author: Bo ZHAO
DOI: https://doi.org/10.35633/inmateh-69-51

Keywords: *Maintenance services, Service car configuration, Improved genetic algorithm, Case application verification, Service platform*

ABSTRACT
In response to the seasonal surge in the number of agricultural machinery failures in the service area caused by cross regional operations of agricultural machinery, agricultural machinery and equipment manufacturing enterprises have established emergency service networks to compensate for the insufficient service capacity of service providers. This paper proposes a method for locating and allocating emergency service vehicles based on a set coverage model, which aims to minimize the total cost of vehicle scheduling schemes and comprehensively consider the service scope and service capabilities of emergency service vehicles. An improved genetic algorithm is designed to solve the emergency service vehicle configuration problem, determine the scheduling location and number of emergency service vehicles, and verify its effectiveness through practical cases, to provide effective protection for agricultural machinery maintenance services in the course of cluster operations and to improve the efficiency of maintenance services.

摘要
为应对农机跨区域作业造成的服务区农机故障数量季节性激增，农机设备制造企业建立了应急服务网络，以弥补服务商服务能力不足的问题。本文提出了一种基于集合覆盖模型的应急服务车辆定位和分配方法，旨在最大限度地降低车辆调度方案的总成本，并综合考虑应急服务车辆的服务范围和服务能力。设计了一种改进的遗传算法来解决应急服务车辆配置问题，确定应急服务车辆的调度位置和数量，并通过实际案例验证其有效性。为农机企业在集群作业过程中，农机维修服务提供有效的保障，提升维修服务效率。

INTRODUCTION
Maintenance service refers to the service provided by relevant maintenance enterprises for repairing, maintaining and repairing faulty equipment *(Husniah et al., 2021; Chen et al., 2023)*. Due to the particularity of agricultural machinery, its dynamic performance lags far behind that of ordinary cars. After the failure of agricultural machinery equipment, it is impossible to go to the 4S service center for maintenance services, but only by manually contacting the service station and sending maintenance personnel to the scene of agricultural machinery failure for troubleshooting (*Li et al., 2019*). Since the 1950s, comprehensive operation and maintenance has been divided into preventive maintenance *(Wang et al., 2020; Classens et al., 2022*), predictive maintenance (*Mourtzis et al., 2022)* and fault maintenance (*Kokieva et al., 2020*). Using big data, artificial intelligence and other technologies to optimize the allocation of equipment maintenance resources has become the focus of current maintenance service research (*Myalo et al., 2020*). Due to the geography, seasons and production environment, the harvest season in China presents seasonality and time phases (*Chen et al., 2022*). At the same time, due to the current agricultural environment such as small land plots owned by farmers and wide distribution of farmland (*Wang and Wang, 2022)*, combine harvesters can not only meet their own needs but also provide services for families without agricultural machinery, bringing economic income to agricultural machinery owners, and providing harvesting tasks for other regions in China. Through this form, agricultural machinery operation teams have been formed continuously. At the same time, agricultural machinery enterprises provide order information for operation team through the management of resources and agricultural machinery *(Han et al., 2020; Hu et al., 2020),* and guarantee the maintenance service of agricultural machinery.

Agriculture 4.0 marks the surge of connection sensing of various information resources across region, resources and systems (*Wysel et al., 2021*). However, agricultural machinery has obvious characteristics of time and space evolution, and the value of agricultural machinery operations is huge, so the maintenance of agricultural machinery failure has strong timeliness and urgent demand. In the actual maintenance service, due to the limitation of service resources and cost, traditional agricultural machinery maintenance services is most based on manual experience. In view of the failure of agricultural machinery, self-maintenance and seeking help from maintenance shops for other machinery and equipment nearby are adopted. However, due to the lack of agricultural machinery background, it is difficult to solve the problem of agricultural machinery failure, and at the same time it affects the efficiency and time of agricultural machinery (*Cao et al., 2022)*. The maintenance service request of cross-regional operation of agricultural machinery is dynamic, that is, the location of faulty agricultural machinery, the demand for maintenance resource, and the change of fault type, etc. directly affect the cooperation mode of harvester maintenance operation service. How to optimize the allocation of service resources and realize the dynamic response and resource supply to the operation and maintenance service of combine harvester is the key to ensure the reliable operation of agricultural machinery, and it is also the core of the research on cross-regional maintenance of harvesters.

MATERIALS AND METHODS

Optimization method of service vehicle configuration considering maintenance needs

Problem analysis

In this study, the maintenance service vehicle configuration was a temporary facility set up after the earthquake. As shown in Figure 1, during the busy farming season, the agricultural machinery moves across a large range. For a low-level agricultural machinery service station, it is necessary to use limited vehicles to provide door-to-door maintenance work within a larger area. At the same time, the low-level service station also needs to take into account other maintenance tasks where the service station is located, and the unreasonable number of maintenance vehicles is easy to increase mileage costs. Therefore, in order to ensure the mobility and flexibility of the service station and reduce the cost of maintenance service, it is necessary to reasonably control the number of maintenance vehicles dispatched. In this part, according to the service demand, the mode of configuring service vehicle in the service area was used to solve the problem of the location and quantity dispatch of the maintenance service vehicle in the after-sales process of agricultural machinery enterprises and to determine the dispatch location and quantity of the service vehicles, so as to achieve the lowest configuration cost of the service vehicles.

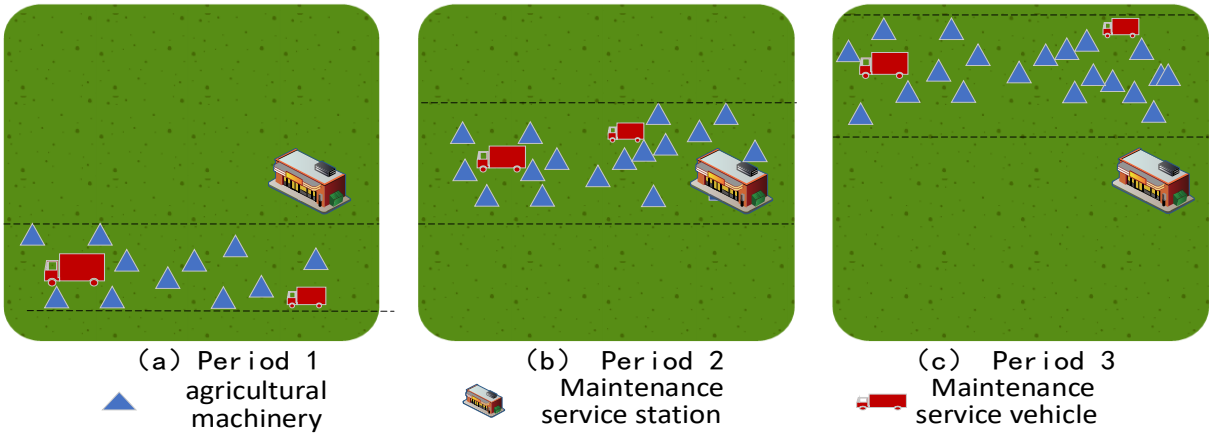


Fig. 1 - Migration and distribution of agricultural machinery working time

The sources of service vehicles in maintenance service stations mainly include fixed maintenance services in maintenance service stations and mobile service vehicles configured by enterprises according to seasonal conditions. The mobile service vehicle is mainly used for enterprises to allocate supplementary maintenance service capacity for a maintenance service station when it is difficult to meet the fault service in the area. Because enterprises will generate configuration costs when allocating maintenance service vehicle, fixed service vehicles will usually be used for maintenance service station. When it is difficult to meet the maintenance demand during the busy farming season, mobile service vehicles will be equipped by the enterprises. During the busy farming season, agricultural machinery maintenance is usually carried out on-site using maintenance service vehicles.

However, due to the surge in faults and the increasing demand for agricultural machinery faults, the maintenance capacity of agricultural machinery in the region is insufficient. Agricultural machinery enterprises usually dispatch additional maintenance service vehicles to solve the problem. The problem of insufficient maintenance and the configuration of service vehicles is shown in Figure 2, and the faulty agricultural machinery sends maintenance requests in the field, The maintenance service station provides maintenance services for faulty agricultural machinery in the field. If the demand is difficult to meet, the enterprise provides mobile service vehicles for the maintenance service station to improve maintenance efficiency.

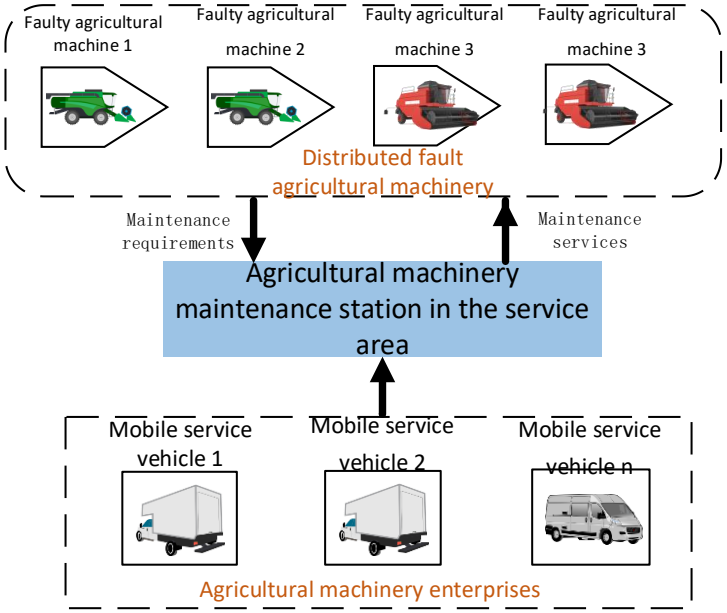


Fig. 2 - Schematic diagram of service vehicle configuration problem

Parameter setting and model building

In order to understand the optimal configuration model of maintenance service vehicle, the parameters are summarized as follows:

(1) Set

i: The number of the repair demand points, $i \in I$, I= {1, 2, n}, where n is the number of repair demand points.

j: The number j represents the central location of the area, j∈J, a collection of maintenance service areas.

(2) Parameters

C_g: The cost of configuration per service vehicle.

C_f: The penalty cost incurred when the agricultural machinery failure point is not met by the service vehicle.

k: The maintenance capacity of each maintenance service vehicle.

F_j: The number of faulty farm machinery contained in area j.

G_f: Agricultural machinery failure rate in the overall service area.

(3) Decision variables

L_j: The number of service vehicles in the candidate area j.

W_j: The selected candidate service area j.

U_{ij}: Demand point i is covered by candidate service area j.

C_j: Penalty costs incurred by region j for not meeting maintenance needs within its scope of service.

According to the objective of minimizing maintenance service vehicles, the following models of location and allocation of maintenance service vehicles are established:

The cost-of-service vehicle dispatch increases linearly with the increase of service vehicles:

$$Z_1 = \sum_{j=1}^{J} L_j C_g \quad (1)$$

The penalty cost incurred when the repair request cannot be met by the service vehicle *u*:

$$Z_2 = \sum_{j=1}^{J} C^j \tag{2}$$

From the above analysis, it can be obtained that the objective function of the minimum configuration cost of vehicles in the region is:

$$\min Z = \sum_{j=1}^{J} L_j C_g + \sum_{j=1}^{J} C_j \tag{3}$$

Constraints

Ensure that every failed farm machine is in at least one service area

$$\sum_{j}^{J} U_{ij} \geq 1 \tag{4}$$

0, 1 variable dimension constraints

$$U_{ij} = 0 \ or \ 1 \tag{5}$$

$$W_j = 0 \ or \ 1 \tag{6}$$

Variable

The penalty cost is equal to the product of the unmet repair need and the unit penalty cost. The formula for calculating the penalty cost incurred if the repair request does not meet it

$$C_j = \begin{cases} C_f\left(F_j G_f - L_j k\right) & F_j G_f - L_j k > 0 \text{（Incur penalty costs）} \\ 0 & F_j G_f - L_j k \leq 0 \text{（No penalty costs incurred）} \end{cases} \tag{7}$$

The number of service vehicles is determined by the demand for maintenance and the capacity of the service vehicles, which is calculated as follows:

$$L_j = F * G_f / K \tag{8}$$

Algorithm design

The emergency configuration optimization and demand allocation model is an NP-Hard problem. In this paper, an improved genetic algorithm was adopted, and chromosome optimization and population elite strategy were added to the traditional genetic algorithm, which can accelerate the convergence of the algorithm, ensure population diversity and improve the computational efficiency.

Coding design

Chromosome coding is the process of converting the solution variables of the model into chromosomes by certain methods. Each chromosome corresponds to the solution result of the model objective function. There are many methods of chromosomes coding, including real number coding, symbol coding, permutation coding, etc. Chromosome coding is the process of converting the solution variables of the model into chromosomes by certain methods. Each chromosome corresponds to the solution result of the objective function of the model. There are many coding methods of chromosomes, including real number coding, symbol coding, permutation coding, etc. In this study, each gene represents a maintenance service station in a region. When the gene value is 1, it represents the solution to select the maintenance service station. If it is 0, it is not selected.

As shown in Figure 3, in the X chromosome, the expression is: [1, 1, 1, 1, 0, 0, 0, 1, 1, 0] and there are 10 genes, that is, there are 10 maintenance service stations, in which the values of the 1st, 2nd, 3rd, 4th, 8th, 9th gene are 1, and the values of the remaining genes are 0, that is, the 1st, 2nd, 3rd, 4th, 8th, 9th maintenance service stations are selected as the locations of the service vehicles requiring supplementary maintenance in this optimization scheme. Matrix A is the relationship matrix between maintenance service stations and agricultural machinery fault points, with each column representing an agricultural machinery maintenance service station and each row representing an agricultural machinery failure point. Matrix A expresses the relationship between 10 and 8 maintenance demand points. For example, a value of 1 in row 1 and column 1 in Matrix A means that the first maintenance demand point can be covered by the first maintenance service station. If the value of a_{ij} in the matrix is 0, it means that the ith agricultural machinery fault point cannot be covered by the j^{th} service station, that is, the service is not satisfied.

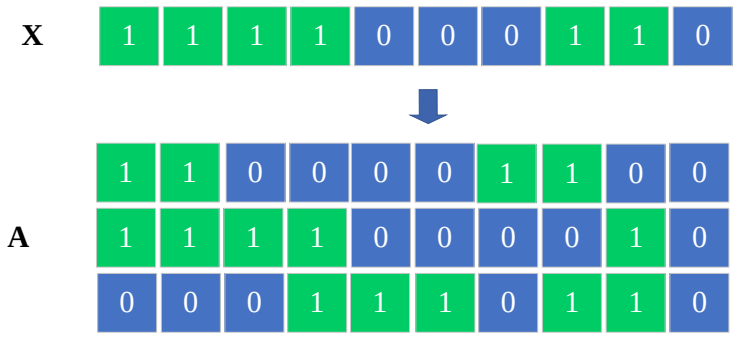


Fig. 3 - Example diagram of the relationship matrix between agricultural machinery failure points and maintenance service stations

Chromosome optimization

There are two factors in the production of chromosomes, one is initially randomly generated, and the other is generated by cross-mutation operations. However, the chromosomes produced in the two cases cannot guarantee that the maintenance needs are covered by the service area, which leads to the deviation of the final optimal solution. Therefore, it is necessary to optimize the chromosomes selection. In this paper, two steps were taken to optimize the selection of chromosomes, so that chromosomes could meet the conditions that all maintenance needs were covered by the service area, and the amount of computation could be reduced and the local search ability of the algorithm could be improved.

Add the genetic method

In this paper, constraints were added to the selection of chromosomes. The candidate emergency service area selected for chromosomes must completely cover all maintenance demand points. If the constraint is not met, new genes will be added to the chromosome until the constraint is met. How to select the genes to be added is based on the performance priority algorithm. Performance priority means that in the chromosome scheme, the number of rows that are not covered by the column corresponding to the selected gene is added in descending order, and the genes with high performance are added first, that is, among the genes with a numerical value of 0 in the chromosome, the genes whose maintenance demand points are not selected for service station are more covered by the region are added first. If the chromosome scheme and relationship matrix are shown in Figure 4, and the 2nd, 3rd, 4th, and 5th maintenance demand points are not covered, and the column covered by the third gene has the largest number of remaining maintenance demand points, the third gene will be added to the chromosome preferentially, and the value of the third gene will become 1.

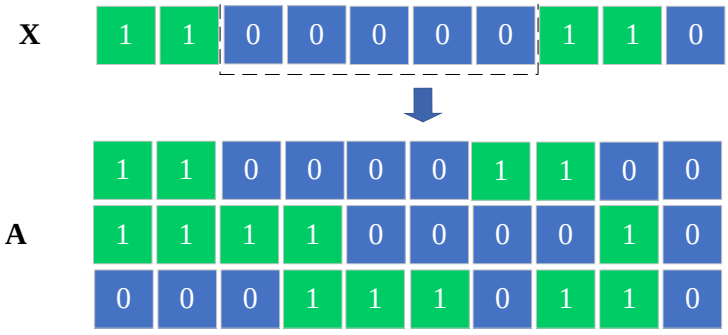


Fig. 4 - Example diagram of the relationship matrix between agricultural machinery failure points and maintenance service stations

Delete redundant genes

If there are too many genes with a value of 1 when the chromosome meets the coverage maintenance demand point, it is also not conducive to the convergence of the algorithm process, so the method of deleting redundant genes was adopted in this paper and redundant gene were deleted when the chromosomes met the coverage maintenance demand points. The genes with a value of 1 in the chromosome are arranged in order of the number of covered demand points from largest to smallest, and genes with a large number of covered demand points are preferentially retained, and the number of remaining uncovered demand points at this time is recorded. According to the performance priority algorithm in the additive gene method, the genes are reserved from the remaining genes until all maintenance demand points are covered, and the genes that have not entered the retention sequence are redundant genes and they will be deleted.

Fitness function design

The fitness function is a standard to judge the quality of each chromosome in the population. According to the fitness value of chromosome, high-quality individuals are determined, and whether the chromosome can be retained from the parent is determined by the fitness function value. Generally speaking, the higher the value of the fitness function, the stronger the individual adaptability, the greater the probability of being retained. Therefore, the fitness function should be set according to the objective function, and the objective function needs to be transformed into an adaptation function through certain rules in order to determine the quality of the solution. The objective function of the vehicle configuration model constructed in this paper was to minimize the total distribution cost. Therefore, fitness function is:

$$fit(x) = \frac{1}{Z(x)} \tag{9}$$

Selection strategy

The purpose of the selection operation is to select individuals with excellent fitness from the current population to enter the next generation, and then produce offspring chromosomes as parents. As shown in Figure 5, under the single roulette wheel mechanism, after turning the wheel, the probability of the pointer pointing to each block is proportional to the size of the area of the block. Correspondingly, in genetic algorithm, the fitness values of all individuals in the population are also very different, and the probability of being selected is determined according to the proportion of their fitness values in the total fitness values of the population. Although every individual in the current population has a chance to be selected, randomness may still lead to the elimination of some outstanding individuals, thus reducing the quality of the next generation population.

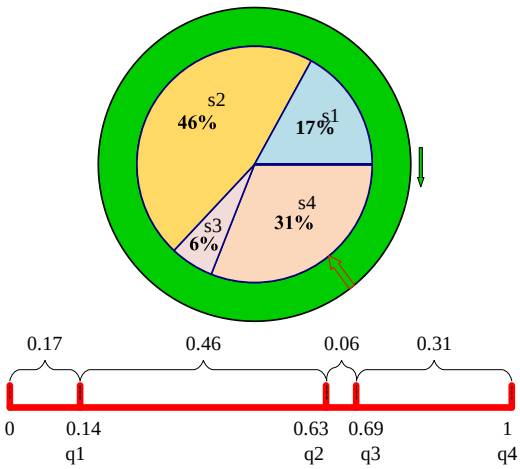


Fig. 5 - Schematic diagram of roulette selection method

Assuming that the initial population size of the algorithm is N and the fitness value of individual i is $fit(x)$, the fitness value of each individual $fit(x)$ is calculated, and then the total fitness value of the population $\sum_{i=1}^{N} fit(x)$ is calculated by summing these total fitness values; Find out the probability of selecting an individual to enter the next generation $p_i = fit(x)/\sum_{i=1}^{N} fit(x)$; The cumulative probability $q_i = \sum_{j=1}^{i} p_j$ of each chromosome i is calculated, and finally, the wheel is simulated to rotate n times. Each time the wheel turns, a chromosomal individual is selected to join the new population, the specific process is: a random floating-point number s between [0,1], compare it with the cumulative probability, if $q_1 \geq s$, select the first individual b1; If $q_1 < s$, select the individual $b_i(i = 2, \cdots, n)$ so that it satisfies $q_{i-1} < s < q_i$.

Although this roulette selection method is simple and easy to use, due to random selection, individuals with high fitness in the group may not be selected, which makes it difficult for the algorithm to converge to the optimal solution. Therefore, a combination of roulette mechanism and elite strategy for selection operations was adopted in this paper, that is, when generating a new generation of populations, all individuals in the current population are sorted according to fitness, and the best individuals are directly copied to the next generation, and then the remaining chromosomes are operated according to the roulette method to determine the selected individuals. This operation is repeated until the offspring and parents have the same population size. The strategy of combining roulette and elite retention can form a stable next generation in the process of evolution, which makes the algorithm converge quickly.

Crossover strategy

Due to these constraints, the traditional single-point or bit-by-bit crossover easily leads to the loss of excellent genes, which leads to the low quality of solution obtained by the algorithm, and even some unfeasible solutions.

To avoid these problems, a crossover method with maximum gene fragment retention was adopted in this paper to ensure the good inheritance of excellent genes. First, two chromosomes are randomly selected, and then a gene fragment is randomly selected from each of these two chromosomes as an object for cross-reservation. In order to avoid the change of carrier configuration and chromosome structure after chromosome crossing, a crossover method with maximum retention of gene segments was used in this paper to ensure good inheritance of excellent genes. Randomly selected gene fragments should contain the same number of "0s", that is, they have the same number of maintenance stations. Finally, after deleting duplicate genes with cross-reserved gene fragments in their respective chromosomes and another chromosome, other genes will cover the genes in the non-reserved region in turn, thus, forming a new pair of chromosomes. The crossover operation process is shown in Figure 6.

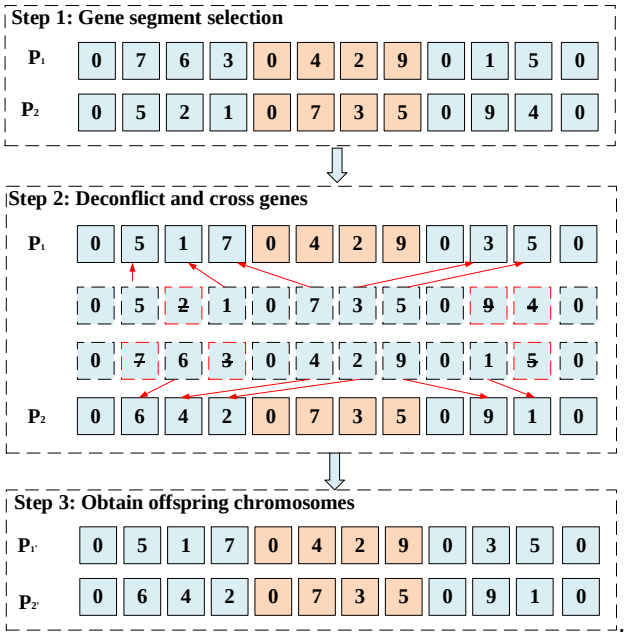


Fig. 6 - Cross diagram

Mutation strategy

In the later stage of the solution, it is difficult for chromosomes to produce new excellent individuals through crossing, and the optimal individual value at this time does not reach the expected value. Therefore, effective mutation operations is used to increase the diversity of the population, so that the algorithm can jump out of the local optimum and find the expected optimal solution. In this paper, a random mutation method is set up: set a chromosomal mutation probability P_m to ensure that the first gene of each natural chromatic body was unchanged, and randomly generate floating-point numbers Z_i between 0 and 1 to determine whether the remaining factors produce mutation in turn. If $Z_i < P_m$, remove it from the chromosome and store it in the base bank Z; If $Z_i > P_m$, the corresponding gene does not produce mutation. When all genes are judged, genes are randomly selected in gene bank Z to insert into any position in the chromosome except the first gene position. When inserting genes, it is necessary to judge whether the corresponding line is overloaded. If it is overloaded, the gene will be inserted into other positions, repeat this operation, and finally complete the allocation of all genes in gene bank Z and complete the mutation operation.

Conditions of Termination

Considering the actual conditions of the model, the maximum number of iterations can be set according to the requirements of the value interval of the number of vehicles when the genetic algorithm is solved, so as to reduce the number of iterations and prevent local convergence. Therefore, the maximum number of iterations is set to 200 in this paper.

Service vehicle configuration verification

Case description

Through the investigation of an enterprise, it was known that each province in China had a business department for agricultural machinery maintenance services. In view of the characteristics that agricultural machinery flows in clusters from south to north in China, the peak season of agricultural machinery operation in Anhui Province is July. As shown in Figure 8, after-sales service data of enterprises from 30 townships under the jurisdiction of Yingshang County of Anhui Province, including the location of agricultural machinery service stations and fault points, were extracted. Table 1 shows the location information of each township, and the maintenance service station of each township are used as the distribution location of the maintenance service vehicle. At the same time, the location information of agricultural machinery fault points in this area is obtained, and Table 2 shows the location information of agricultural machinery fault points.

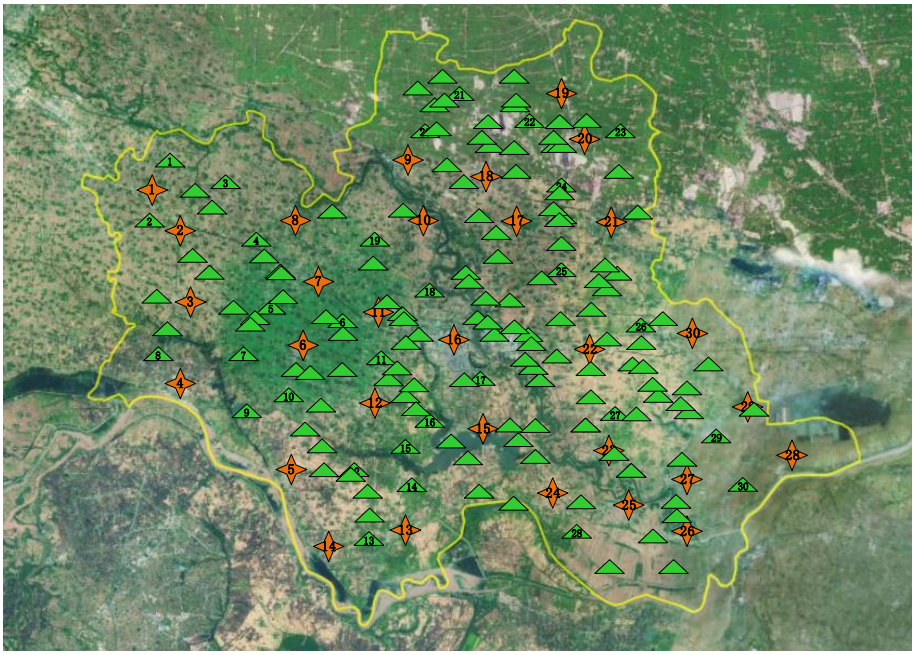


Fig. 8 - Distribution map of agricultural machinery maintenance stations and agricultural machinery failure points in Yingshang County

Table 1

Distribution of regional agricultural machinery maintenance service stations

Agricultural machinery failure point	Coordinate position	Agricultural machinery failure point	Coordinate position
1	115.961, 32.769	16	116.260, 32.643
2	116.005, 32.746	17	116.308, 32.737
3	116.003, 32.683	18	116.057, 32.860
4	116.000, 32.613	19	116.362, 32.837
5	116.106, 32.540	20	116.372, 32.809
6	116.115, 32.642	21	116.366, 32.772
7	116.115, 32.708	22	116.367, 32.644
8	116.110, 32.753	23	116.388, 32.561
9	116.207, 32.790	24	116.336, 32.523
10	116.224, 32.742	25	116.406, 32.522
11	116.182, 32.668	26	116.461, 32.498
12	116.180, 32.600	27	116.461, 32.543
13	116.204, 32.501	28	116.556, 32.550
14	116.139, 32.491	29	116.505, 32.600
15	116.286, 32.575	30	116.456, 32.656

Table 2

Location of agricultural machinery failure point

Agricultural machinery failure point	Coordinate position	Agricultural machinery failure point	Coordinate position
1	115.999, 32.798	…	…
2	115.987, 32.754	…	…
3	116.052, 32.778	…	…
4	116.064, 32.737	…	…
5	116.096, 32.686	194	116.182, 32.552
6	116.159, 32.670	195	116.371, 32.701
7	116.073, 32.646	196	116.437, 32.166
8	115.997, 32.644	197	116.420, 32.590
9	116.199, 32.734	198	116.384, 32.501
10	116.242, 32.816	199	116.505, 32.578
11	116.278, 32.850	200	116.552, 32.545

RESULTS

Parameter settings

The service range of the maintenance service vehicle configured by the agricultural machinery enterprise was defined as 20 kilometers. Considering the requirements of the operation season, the working time of the maintenance service vehicle is 10 hours, and each emergency service vehicle can meet the need of 4 faulty agricultural machinery to provide maintenance services. Among them, the failure rate of agricultural machinery was calculated according to the data of agricultural machinery enterprises in Yingshang County, Anhui Province in July. Set the daily dispatch cost of service vehicle to 1,000 yuan (including the salary of the maintenance engineer, the vehicle is damaged, and the asset conversion of maintenance tools and spare parts). The penalty cost when the maintenance demand point was not met was set to 100 yuan. The improved genetic algorithm was applied to solve the problem in MATLAB R2016a/WIN10. The crossover and mutation parameters in the algorithm were set to 0.9 and 0.05, respectively, and the number of termination iterations was set to 100.

Verification of regional resource configuration algorithm

The coverage of agricultural machinery fault points in each area is shown in Table 3. In agricultural production, crops are sown and harvested according to the season, and there will be busy seasons and leisure seasons in a year. In busy agricultural season, the utilization rate of agricultural machinery is high and the operation intensity is high, so the failure rate of agricultural machinery will increase compared with usual, and the timeliness requirements for agricultural machinery maintenance services will also increase during the busy agricultural season. Therefore, in order to cope with the changes in the failure rate of agricultural machinery, a service vehicle configuration model was established, effectively solving the problem of service vehicle configuration during the failure rate change process.

Table 3

Table of coverage relationship between maintenance service stations and agricultural machinery fault points

Maintenance service station	Agricultural machinery failure point									
1	1	2	3	4	5	6	7	8	9	……
2	4	5	6	7	8	9	10	11	12	……
3	24	25	26	27	28	29	30	31	32	……
4	40	41	42	43	44	45	46	47	48	……
5	50	51	52	53	54	55	56	57	58	……
…	……	……	……	……	……	……	……	……	……	……
27	166	167	168	169	170	171	172	173	174	……
28	172	173	174	175	176	177	178	179	180	……
29	180	181	182	183	184	185	186	187	188	……
30	188	189	190	191	192	193	194	195	196	……

Note: Maintenance service station 1 can cover fault point 1, fault point 2, fault point 3, that is, $a_{11}=1$, $a_{12}=1$, $a_{13}=1$;

The relationship matrix is obtained

As shown in Figure 9, the case is verified through the proposed algorithm. In 30 townships of Yingshang County, according to the regional failure rate and the service capacity of maintenance service vehicles, in the current maintenance service stations in 30 townships, enterprises have provided service vehicles in 26 of them through the optimization of service vehicle configuration.

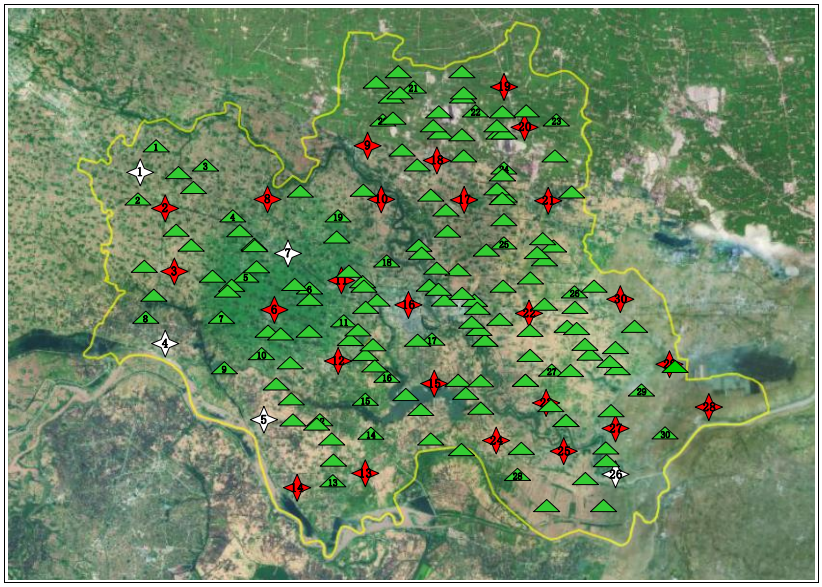


Fig. 9 - Service vehicle optimization configuration scheme diagram

Table 3

Maintenance service vehicle configuration plan

Workshop number	Number of service vehicle configurations	Workshop number	Number of service vehicle configurations
1	0	16	1
2	1	17	1
3	1	18	3
4	0	19	1
5	0	20	5
6	1	21	1
7	0	22	1
8	2	23	1
9	1	24	2
10	5	25	5
11	1	26	0
12	10	27	1
13	1	28	1
14	1	29	1
15	1	30	1

As shown in Table 3, based on the maintenance capacity and regional scope of each maintenance station, by considering minimizing the dispatch cost of service vehicles, the final result is that service stations 1, 4, 5, 7, and 26 do not require the enterprise to dispatch mobile service vehicles to supplement the maintenance service capacity of the area. Among them, the number of service vehicles dispatched by maintenance station 12 is 10, usually due to the large number of agricultural machinery failure points in the area. While considering dispatch costs and penalty costs, a large number of service vehicles were dispatched for them. There are a total of 50 vehicles in the entire area. The final maintenance service vehicle configuration cost is 10364.58 yuan, including vehicle dispatch costs and penalty costs for not meeting the requirements.

Service vehicle configurations with different penalty coefficients

In practice, in the case of different punishment coefficients, compared with the configuration of service vehicles, it is used to formulate different configuration strategies for O&M service providers to provide differences in customer satisfaction. The size of the penalty factor depends on how much the company cares about customer satisfaction. When the penalty factor is large, it is necessary to increase the service cart to reduce the loss caused by the decrease in customer satisfaction. When the penalty factor is small, the number of service vehicles can be appropriately decreased to reduce the fixed cost of configuring service vehicles, and the source of parameter settings can be determined according to the historical data. In this case, it is set to 1000, 500 and 100 respectively.

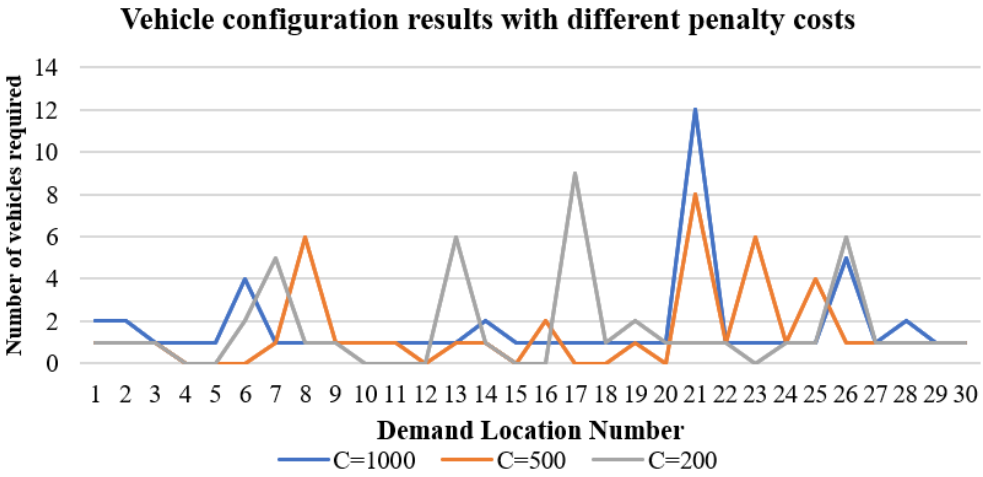


Fig. 10 - Changes in service vehicle configuration under different penalties

Figure 10 shows the comparison of resource allocation under different penalty factors, which can be more intuitively reflected in the differences in service vehicle configuration under different penalty factors. When considering high customer satisfaction requirements, a higher penalty cost was set. By configuring more maintenance service vehicles, the efficiency of maintenance service effects was improved, customer time window requirements were enhanced, and satisfaction was enhanced. When considering lower customer satisfaction and lower dispatch costs, companies provide fewer service vehicles to service stations, with a smaller penalty coefficient and fewer dispatched vehicles. Although there is a significant difference in the number of service vehicles, this difference is limited, which makes it easier for service providers to make decisions when considering different satisfaction levels. Because after a certain number of service vehicles arrive, the effect of increasing service vehicles on improving service efficiency becomes very weak, that is, when the vehicles reach a certain service capacity, the cost is balanced.

CONCLUSIONS

（1）This study considers the service capacity and service scope radius of maintenance service vehicles, and designs a location and allocation model for maintenance service vehicles. The aim is to determine the location and quantity of maintenance service vehicles dispatched by service enterprises to maintenance service stations in different regions during the busy farming season, and to minimize the cost of emergency service vehicle dispatch.

（2）A mathematical model with the goal of minimizing operation and maintenance costs was established to address the issue of dispatch location and quantity of maintenance service vehicles during the busy farming season. An improved genetic algorithm was designed to solve the model. Finally, the feasibility of the algorithm was verified through practical case studies. The impact of cost changes on the number of service vehicles was analyzed by setting different penalty cost coefficients.

ACKNOWLEDGEMENT

The work was sponsored by the National Key R&D Program Project of China (2020YFB1709603).

REFERENCES

[1] Cao, Y., Yi, C., Wan, G., Hu, H., Li, Q., and Wang, S. (2022). An analysis on the role of blockchain-based platforms in agricultural supply chains. *Transportation Research Part E: Logistics and Transportation Review*, Vol. 163, pp. 102731, Hunan/China.

[2] Chen, L.W., Zhang, Z.Y., Li, H.B., and Zhang, X.P. (2023). Maintenance Skill Training Gives Agricultural Socialized Service Providers More Advantages. *Agriculture-Base*, Vol. 13, pp. 135-135, Zhenjiang/China.

[3] Chen, Y., Li, G., Zhang, X., Jia, J., Zhou, K., and Wu, C. (2022). Identifying field and road modes of agricultural Machinery based on GNSS Recordings: A graph convolutional neural network approach. *Computers and Electronics in Agriculture*, Vol. 198, pp. 107082, Beijing/China.

[4] Classens, K., Verbeek, S., Heemels, W.P.M.H., and Oomen, T. (2022). Joint Estimation of Additive and Parametric Faults: A Model-Based Fault Diagnosis Approach towards Predictive Maintenance. *IFAC-PapersOnLine*, Vol. 55, pp. 304-309, Netherlands

[5] Han, J., Hu, Y., Mao, M., and Wan, S. (2020). A multi-objective districting problem applied to agricultural machinery maintenance service network. *European Journal of Operational Research*, Vol. 287, pp. 1120-1130, Jiangxi/China.

[6] Hu, Y., Liu, Y., Wang, Z., Wen, J., Li, J., and Lu, J. (2020). A two-stage dynamic capacity planning approach for agricultural machinery maintenance service with demand uncertainty. *Biosystems Engineering*, Vol. 190, pp. 201-217, Beijing/China.

[7] Husniah, H., Pasaribu, U.S., Wangsaputra, R., and Iskandar, B.P. (2021). Condition-based maintenance policy for a leased reman product. *Heliyon*, Vol. 7, pp. e06494-e06494, Indonesia.

[8] Kokieva, G.E., Voinash, S.A., Maksimovich, K.Y., Sokolova, V.A., Ivanov, A.A., Panov, A.Y. (2020). On calculation and assessment of machine reliability. *Journal of Physics: Conference Series,* Vol. 1679, pp. 042029, Russian Federation.

[9] Li, D., Zheng, Y., and Zhao, W. (2019). Fault Analysis System for Agricultural Machinery Based on Big Data. *Ieee Access*, Vol. 7, pp. 99136-99151, Heilongjiang/China.

[10] Mourtzis, D., Angelopoulos, J., and Panopoulos, N. (2022). Design and Development of an Edge-Computing Platform Towards 5G Technology Adoption for Improving Equipment Predictive Maintenance. *Procedia Computer Science*, Vol. 200, pp. 611-619, Greece.

[11] Myalo, O.V., Prokopov, S.P., Myalo, V.V., Redreev, G.V., Demchuk, E.V. (2021). Feasibility and efficiency of agricultural machinery maintenance. *IOP Conference Series: Earth and Environmental Science, Vol. 659, pp. 012053, Russia.*

[12] Wang, N., Ren, S., Liu, Y., Yang, M., Wang, J., and Huisingh, D. (2020). An active preventive maintenance approach of complex equipment based on a novel product-service system operation mode. *Journal of Cleaner Production*, Vol. 277, pp. 123365, Shanxi/China.

[13] Wang, Y., and Wang, H. (2022). Effects of farmland use rights transfer on collective action in the commons: Evidence from rural China. *Land Use Policy,* Vol. 120, pp. 106262, Beijing/China.

[14] Wysel, M., Baker, D., and Billingsley, W. (2021). Data sharing platforms: How value is created from agricultural data. *Agricultural Systems,* Vol. 193, pp. 103241, Australia.

DETECTION OF FLAXSEED OIL ADULTERATION BASED ON TWO-DIMENSIONAL CORRELATION NEAR-INFRARED SPECTRA

基于二维相关近红外光谱的亚麻籽油掺杂检测

Ning HAN, Tonghui WU, Qian WU, Hongzhi DU, Zhiyong ZHANG*, Yanqing ZHANG
College of Agricultural Engineering, Shanxi Agricultural University, Taigu/China
Tel: +86-0354-6289253; E-mail: zzyzzy1979@163.com
DOI: https://doi.org/10.35633/inmateh-69-52

Keywords: *flaxseed oil, two-dimensional correlation spectroscopy, N-way partial least square, bi-dimensional empirical mode decomposition*

ABSTRACT

Flaxseed oil is rich in α-linolenic acid and other nutrients, and the adulteration happens frequently because of its high price. To detect the adulteration of flaxseed oil quickly and accurately, a method was proposed based on weighted reconstructed two-dimensional correlation near-infrared (NIR) spectra. The near-infrared spectra of 79 adulterated flaxseed oil samples were measured, and the traditional two-dimensional correlation synchronous spectra were calculated. The two-dimensional correlation synchronous spectra of all samples were decomposed into multiple components of different scales by the bi-dimensional empirical mode decomposition algorithm (BEMD). According to the root mean square error (RMSE) values of the adulteration detection sub-models established by each component, the weights of the corresponding components were calculated, and then the two-dimensional correlation spectra of all samples were reconstructed by accumulating the weighted components. A quantitative analysis model of flaxseed oil adulteration was established based on the weighted reconstructed two-dimensional correlation spectra combined with the N-way partial least square (N-PLS) algorithm. Compared with the traditional two-dimensional correlation spectroscopy, the model built by the weighted reconstructed two-dimensional correlation spectra had better performance with the calibration determination coefficient increased by 6.05%, and the prediction determination coefficient increased by 7.5%. The proposed method could effectively enhance the spectral feature information, reduce the spectral noise interference, and hence provide a new idea for the detection of edible oil adulteration.

摘要

亚麻籽油富含 α-亚麻酸等营养成分，市场价格较高，掺假现象频出。为快速、准确检测亚麻籽油掺杂，本文提出一种基于加权重构二维相关近红外光谱的亚麻籽油掺杂检测方法。采集了 79 个掺杂亚麻籽油样本（以菜籽油为掺杂油,掺杂体积比例1%-40%）的近红外光谱，计算各样本的常规二维相关同步光谱；利用二维经验模态分解算法将各样本的二维相关光谱分解为不同尺度的多个分量，以各分量所建立的掺杂检测子模型的均方根误差值为依据，计算相应尺度分量的加权值，然后通过加权分量叠加重构各样本的二维相关光谱；基于加权重构的二维相关光谱结合多维偏最小二乘方法建立了亚麻籽油掺杂的定量分析模型。结果表明：相比于常规二维相关光谱，加权重构二维相关光谱建立的掺杂检测模型性能更佳，模型的校正决定系数提高了 6.05%，预测决定系数提高了 7.5%，该方法可有效增强光谱特征信息，降低光谱噪声干扰，为食用油掺假检测提供了一种新的思路。

INTRODUCTION

Flaxseed oil is a high-quality edible oil obtained from flaxseed, which contains high concentrations of healthy compounds, such as α-linolenic acid and linoleic acid (*Zhou et al., 2018*). Flaxseed oil has various health-related benefits such as lowering blood pressure and lipids, anti-inflammatory and anti-cancer, and improving vision (*Goyal A.et al., 2014; Liao et al., 2021; Xian et al., 2018*). Because of its higher price than other vegetable oils, flaxseed oil can be adulterated with cheaper vegetable oils by some illegal oil suppliers, which will not only damage the legitimate rights and interests of consumers but also disturb the market order.

[1] *Ning Han, M.S. Stud. Eng.; Tonghui Wu, M.S. Stud. Eng.; Qian Wu, M.S. Stud. Eng.; Hongzhi Du, M.S. Stud. Eng.; Zhiyong Zhang*, Assoc Prof. Ph.D. Eng.; Yanqing Zhang, Assoc. Prof. Ph.D. Eng.*

Some analytical methods, such as gas chromatography, gas chromatography-mass spectrometry, liquid chromatography-mass spectrometry, have been reported to be successful (*Sun et al., 2015; Wei et al., 2018; Chen et al., 2012; Liao et al., 2018*); however, these methods are expensive, time-consuming, and laborious, and cannot be used for on-site real-time detection. Therefore, it is of great significance to study the rapid detection method of flaxseed oil adulteration.

Two-dimensional correlation near-infrared spectroscopy provides an attractive technique for the detection of food quality and safety due to its rapidity, simplicity, and low costs (*Chen J.B. et al., 2016; Wang et al., 2018; Yang et al., 2013; Zhang et al., 2010*). Compared with traditional one-dimensional near-infrared spectroscopy, two-dimensional correlation spectroscopy has a higher spectral resolution and better spectral selectivity and can enlarge subtle spectral information of the interested substance by specific external perturbations such as changes in temperature, and concentration (*Park et al., 2016; Yang et al., 2015*). Combined with suitable multivariate calibration methods, two-dimensional correlation spectroscopy has been applied in the detection of adulterated oil (*Zhang et al., 2019; Wang et al., 2020*). However, when the spectral resolution is improved by two-dimensional correlation spectroscopy, the influence of noise also increases, and thus false information caused by noise may appear, which will decrease the signal-to-noise ratio of two-dimensional correlation spectra and bring about the negative influence on the accuracy of the model (*Zhan et al., 2004; Sun et al., 2015*). The spectral signal has multi-scale characteristics and can be decomposed into multiple components of different frequency bands (*Chen D. et al., 2016; Liu et al., 2009*). The high-frequency components contain more noise information, the background interference is mostly concentrated in the low-frequency component, and the spectral characteristic information is mainly located in the middle-frequency components. But if the noise interference and spectral characteristic information are distinguished simply by the frequency, some of the useful spectral information may be lost, which will affect the performance of the spectral analysis model.

Based on the multi-scale characteristics of spectra, this paper presents a new method to detect flaxseed oil adulteration using weighted reconstructed two-dimensional correlation near-infrared spectroscopy. Firstly, the two-dimensional correlation near-infrared spectra of adulterated flaxseed oil samples were decomposed into multiple components by the bi-dimensional empirical mode decomposition algorithm. Then each component was weighted according to the root mean square error of the detection sub-model based on the corresponding component, and the two-dimensional correlation spectrum was reconstructed by the accumulation of weighted components. Finally, the detection model for flaxseed oil adulteration was constructed based on the weighted reconstructed two-dimensional correlation spectra in combination with the N-way partial least squares algorithm. The proposed method can mine the effective spectral information as much as possible, reduce noise and background interference, and enhance the contribution of spectral characteristic information to modeling by the weighted reconstruction of two-dimensional correlation spectra.

MATERIALS AND METHODS

Sample preparation

Pure rapeseed oil (Brand: Golden Arowana) was added to pure flaxseed oil (Brand: Fuyide) according to the adulterating volume ratio of 1%-40% (adulterating gradient: 0.5%) to prepare 79 adulterated flaxseed oil samples. Before spectral collection, all adulterated flaxseed oil samples were manually stirred to ensure homogeneity. The adulterated flaxseed oil samples were divided into the calibration set with 60 samples and the prediction set with 19 samples. The statistical parameters of the calculation set and prediction set are shown in Table 1.

Table 1

Statistics of the calculation set and prediction set

Item	Min.	Max.	Mean	Standard deviation
Calculation set adulterating ratio	1%	40%	20.66%	11.63%
Prediction set adulterating ratio	2%	38%	20%	11.25%

Spectral data acquisition

The near-infrared transmission spectra of all samples were collected using a Field Spec3 spectrometer (ASD company, USA) equipped with the InGaAs detector. The wavelength interval of spectral data is 1 nm, and the wavelength range is from 350 to 2500 nm.

The measurements were undertaken in a quartz cuvette with an optical path length of 10 mm. Taking the blank cuvette as the reference, the transmission spectra of all samples were collected. Fig.1 shows the acquisition system of near-infrared spectra.

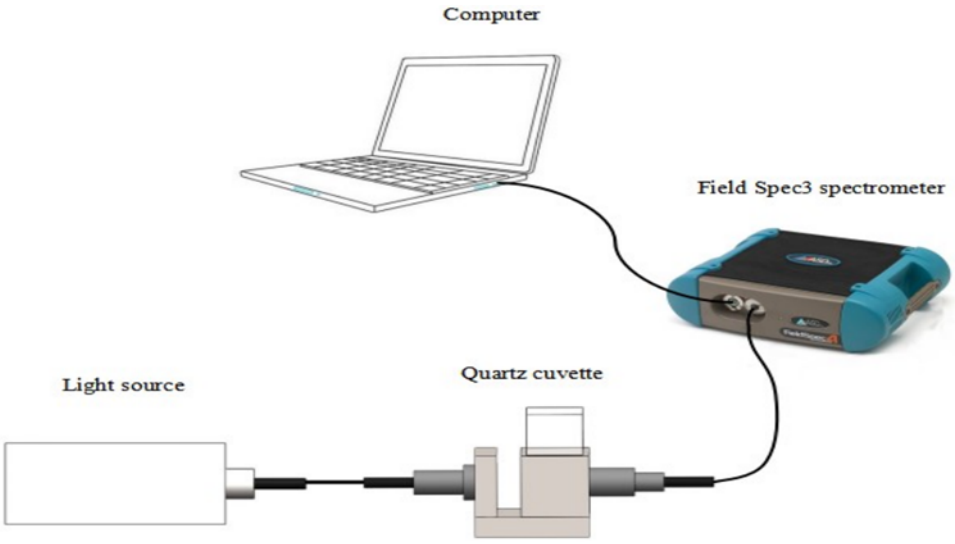


Fig. 1 - The acquisition system of near-infrared spectra

Spectral data processing

(1) Calculation of two-dimensional correlation spectra

The theory of two-dimensional correlation spectroscopy was first proposed by Noda (*Noda,2004*). The near-infrared transmission spectra of samples, which were measured at a specific external disturbance (different adulterating ratios of rapeseed oil), could be formed into a dynamic spectral matrix $A_{m\times n}$ with the *m* spectra (*n* wavelengths).

According to Noda's theory, two-dimensional correlation synchronous spectra of all samples could be calculated as follows:

$$\Phi(v_1, v_2) = \frac{1}{m-1} A^T A \tag{1}$$

where v_1 and v_2 represent two independent spectral wavelengths, T refers to the matrix transpose operation.

Matrix A contains 2 spectra in rows (m=2). The first row of A is the near-infrared transmission spectral data of the pure flaxseed oil sample, while the second row is the spectral data of the i^{th} adulterated flaxseed oil. The two-dimensional correlation near-infrared spectrum of i^{th} adulterated flaxseed oil could be obtained in terms of Eqn. (1) and by the calculation software programmed by ourselves.

(2) Weighted reconstruction of two-dimensional correlation spectra

The bi-dimensional empirical mode decomposition (BEMD) algorithm was proposed by *Nune,* (*2005*), and it can adaptively decompose the two-dimensional signals (such as image signals) into multiple compone nts at different scales. The two-dimensional correlation spectra of all adulterated flaxseed oil samples can be decomposed by the BEMD algorithm into multiple components, which correspond to different frequency ban ds.

Based on the decomposed components, the detection sub-models of flaxseed oil adulteration were established respectively, in combination with the N-way partial least squares algorithm (N-PLS) and the root mean square error (*RMSE*) of each sub-model was calculated as follows:

$$RMSE_i = \sqrt{\frac{1}{m}\sum_{j=1}^{m}(y_j - y_{ij}')^2} \tag{2}$$

where:

$RMSE_i$ is the root mean square error of the sub-model built by the i^{th} component, and m is the total number of samples. y_j is the actual adulterating value of the j^{th} sample, and y_{ij}' is the predicted adulterating ratio of the j^{th} sample by the i^{th} component sub-model.

The N-PLS algorithm is a data analysis method that extends the conventional partial least squares method to high-dimensional data, which can effectively solve the modeling problem of high-dimensional data (*Chu et al, 2006*).

The reconstruction weight of each component is calculated based on the $RMSE$ value of each sub-model as follows:

$$W_i = \frac{n(\frac{1}{RMSE_i})}{\sum_{i=1}^{n}(\frac{1}{RMSE_i})} \quad (3)$$

where: n is the total number of components of the two-dimensional correlation spectra decomposed by BEMD.

Then the two-dimensional correlation spectra of all samples can be reconstructed by accumulating the weighted components.

(3) Quantitative analysis modeling

Based on the weighted reconstructed two-dimensional correlation spectra, the quantitative analysis model of flaxseed oil adulteration was established combined with the N-PLS algorithm. Model performance was evaluated by the calibration determination coefficient (R^2_C), the prediction determination coefficient (R^2_P), the root mean square error of calibration ($RMSEC$), and the root mean square error of prediction ($RMSEP$).

These assessment parameters were calculated as follows:

$$R_c^2 = 1 - \sum_{i=1}^{n}(\hat{y}_i - y_i)^2 / \sum_{i=1}^{n}(\hat{y}_i - y_c)^2 \quad (4)$$

$$R_p^2 = 1 - \sum_{j=1}^{n}(\hat{y}_i - y_i)^2 / \sum_{j=1}^{n}(\hat{y}_i - y_p)^2 \quad (5)$$

$$RMSEC = \sqrt{\frac{1}{n}\sum_{i=1}^{n}(\hat{y}_i - y_i)^2} \quad (6)$$

$$RMSEP = \sqrt{\frac{1}{n}\sum_{j=1}^{n}(\hat{y}_j - y_j)^2} \quad (7)$$

where:

$\hat{y}_i$ and y_i are the predicted and actual adulterating ratios of the i^{th} sample in the calibration set, and y_c is the averaged adulterating ratio of calibration set samples; $\hat{y}_j$ and y_j are the predicted and actual adulterating ratios of the j^{th} sample in the prediction set, and y_p is the averaged adulterating ratio of prediction set samples; n and m are the number of samples in the calibration and prediction set, respectively.

Higher R^2_C and smaller $RMSEC$ correspond to the model's high calibration accuracy, while higher R^2_P and smaller $RMSEP$ correspond to high prediction stability.

All the computations above were performed in MATLAB (*Version R2015a, The Math Works Inc.)* under Windows 10.

RESULTS

Near-infrared spectra

Figure 2 showed the near-infrared spectra of pure flaxseed oil and adulterated flaxseed oil (20% adulteration ratio). Because vegetable oils are mainly composed of triglycerides and similar in chemical composition, it can be seen that the spectral waveform and absorption peak location (at 467 nm, 611 nm, 674 nm, 1208 nm, 1415 nm, 1724 nm, 1763 nm, 2144 nm, 2180 nm) of the two spectra look closely similar except for the subtle difference in absorbance. Therefore, it is difficult to carry out adulteration detection only using traditional one-dimensional spectroscopy. The spectral noise in the 2250-2500 nm band is strong and cannot provide useful information, so the spectral data in the 350-2249 nm band is intercepted for subsequent two-dimensional correlation and quantitative detection analysis.

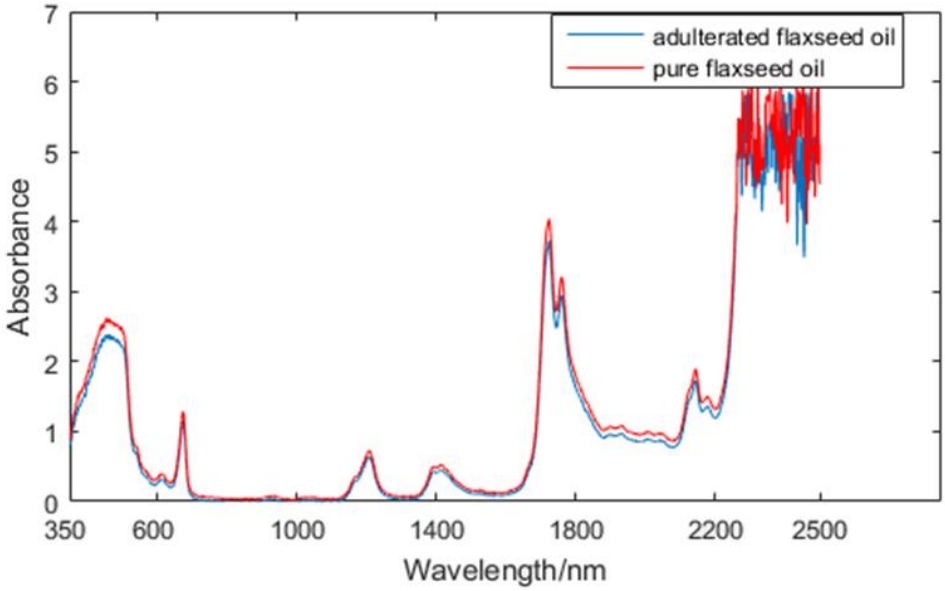


Fig. 2 - Near-infrared spectra of pure and adulterated flaxseed oil

Two-dimensional correlation spectra

Based on the collected near-infrared spectra, the two-dimensional correlation synchronous spectra of all adulterated flaxseed oil samples were calculated in terms of Eq. (1). Figure 3 showed the calculated two-dimensional correlation synchronous spectra of the flaxseed oil sample with the 20% adulterating ratio. To reduce the operation amount, the wavelength interval of the two-dimensional correlation is taken as 3 nm in the region of 350-2249 nm.

As can be seen in Fig.3, the spectral information changes mainly occurred in the two wavelength ranges of 350 nm-675 nm and 1207 nm-2249 nm. Autocorrelation peaks appeared at (467 nm, 467 nm), (674 nm, 674 nm), (1724 nm, 1724 nm), and (2144 nm, 2144 nm) in the main diagonal line, indicating that the relative intensity of these peaks changes significantly with adulteration. Positive cross-peaks appeared at (467 nm, 1724 nm), (674 nm, 1724 nm), (467 nm, 1208 nm), (467 nm, 1415 nm), (467 nm, 2144 nm), (1208 nm, 2144 nm), (1415 nm, 2144 nm) on either side of the main diagonal line, indicating that the spectral information at the autocorrelation peaks may change synergistically due to adulteration.

Two-dimensional correlation spectra can provide detailed spectral information caused by adulteration, but may also amplify the noise and reduce the signal-to-noise ratio of the spectra at the same time. As can be seen in Figure 3, the spectrum had relatively strong burr noise and low smoothness. To weaken the influence of noise interference and fully mine the effective spectral information for modeling, based on the multi-scale characteristics of spectra, BEMD algorithm was used to decompose the two-dimensional correlation synchronization spectra, and then each scale component was weighted reconstructed according to the performance of the sub-model built by the corresponding component.

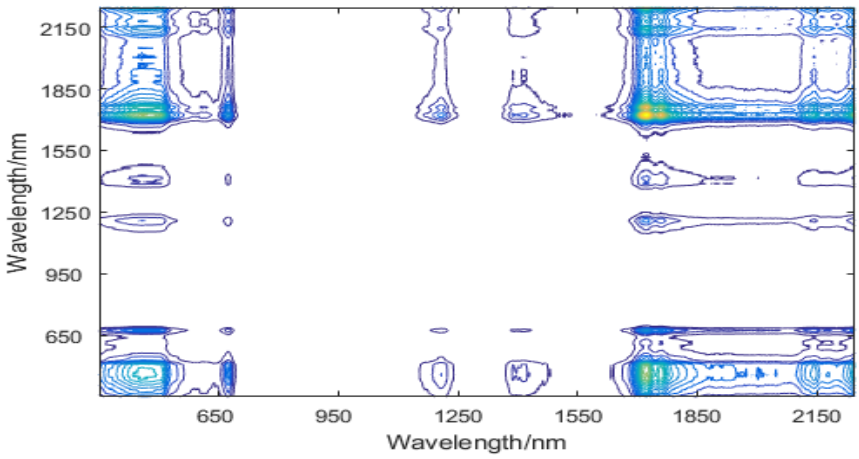


Fig. 3 - Two-dimensional correlation spectra of adulterated flaxseed oil

Weighted reconstruction of two-dimensional correlation spectra

Using the BEMD algorithm to adaptively decompose the two-dimensional correlation spectrum of each sample, six components of different scales were obtained after decomposition. Fig.4 showed the decomposed six components of the two-dimensional correlation spectrum in Fig.3. The frequencies of component 1-component 6 varied from high to low.

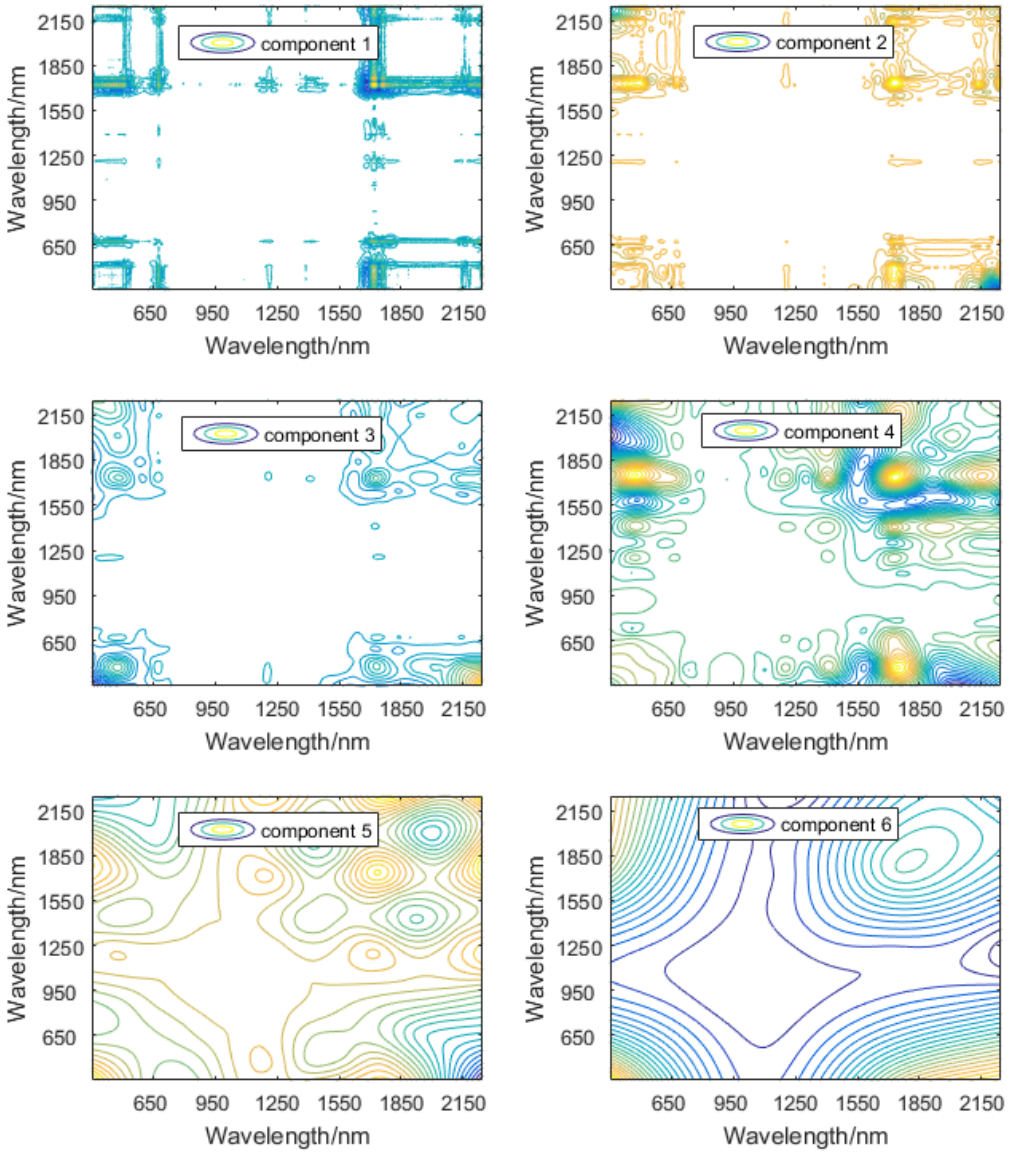


Fig. 4 - Each decomposed component of the two-dimensional correlation spectra

Based on the six components of different scales, the corresponding sub-models for flaxseed oil adulteration detection were established, and the *RMSE* values of each sub-model were calculated in terms of Eq. (2) shown in Fig. 5.

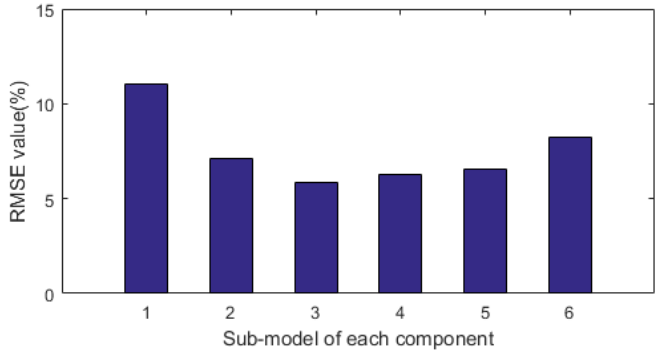


Fig. 5 - RMSE value of each sub-model based on the corresponding component

As can be seen in Figure 5, the RMSE values of the sub-models built by high-frequency component 1 and low-frequency component 6 are larger than those of the other components, because component 1 mainly contains high-frequency noise, while component 6 contains background signals. The RMSE values of the sub-models built by components 2, 3, 4, 5 are relatively smaller because these intermediate-frequency components contain more spectral information, which is in agreement with the multi-scale characteristics of spectra.

The reconstruction weight of each component was calculated in terms of Eq. (3) and shown in Fig. 6. It can be seen that the weights assigned to component 1 and component 6 were relatively smaller, and the weights assigned to component 2, component 3, component 4 and component 5 were relatively larger. The weight reassignment enhanced the intermediate-frequency components and their contribution to the modeling, reduced the proportion of high-frequency and low-frequency components, and hence suppressed spectral noise interference.

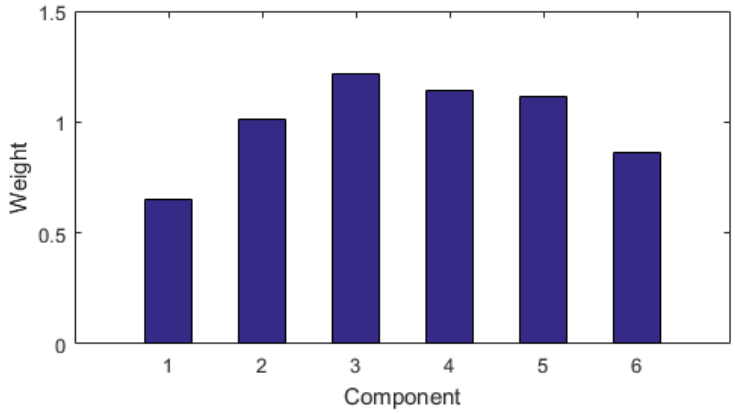


Fig. 6 - The weight assigned to each component

The two-dimensional correlation spectra of all samples were reconstructed by accumulating the weighted components and displayed in Fig.7. It can be seen that the weighted reconstructed two-dimensional correlation spectrum became clearer and smoother, and the burr noise was effectively suppressed. The weak peaks appeared at 1207 nm, 1412 nm in the main diagonal line, indicating that the relative intensity of these peaks was enhanced. The cross-peaks are well separated from the autocorrelation peaks, which improves the resolution of the spectrum.

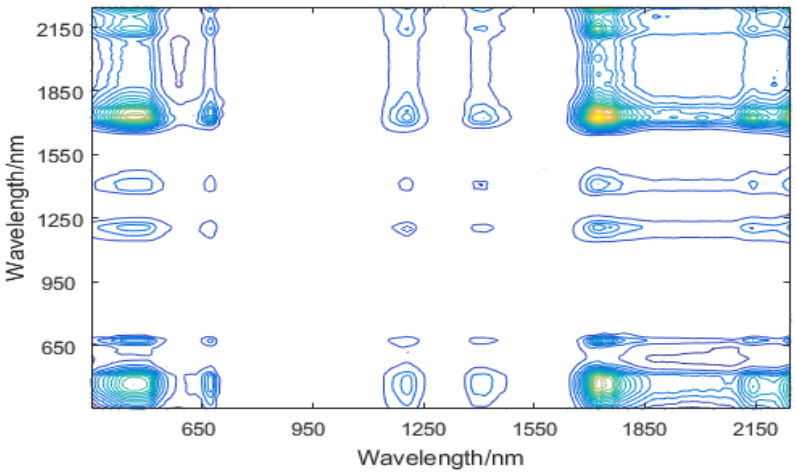


Fig. 7 - The weighted reconstructed two-dimensional correlation spectra

N-PLS model for the detection of adulterated flaxseed oil

The quantitative detection model of flaxseed oil adulteration was established using the weighted reconstructed two-dimensional correlation spectra combined with the N-PLS algorithm. The model's calibration determination coefficient (R^2_C) is 0.9375, and the root mean square error of calibration (*RMSEC*) is 2.8837%; the prediction determination coefficient (R^2_P) is 0.9252, and the root mean square error of prediction (*RMSEP*) is 2.9956%. Fig.8 and Fig.9 showed the model scatter plots of the calibration set and prediction set, respectively. The plots illustrated that the predicted adulterating ratio and actual adulterating ratio were in good agreement and the model provided a good detection precision.

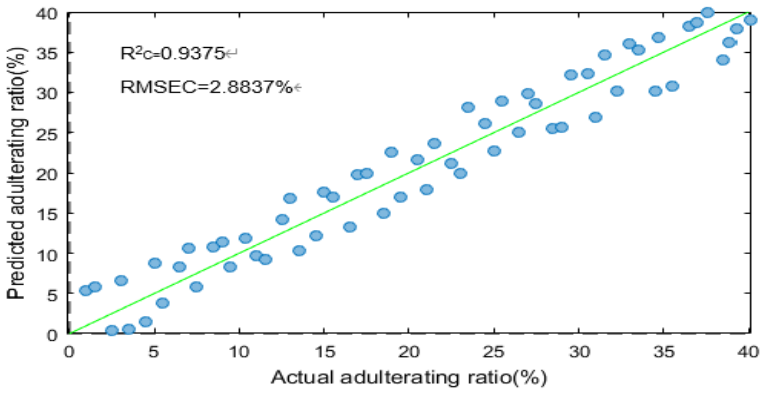


Fig. 8 - The model scatter plot of the calibration set

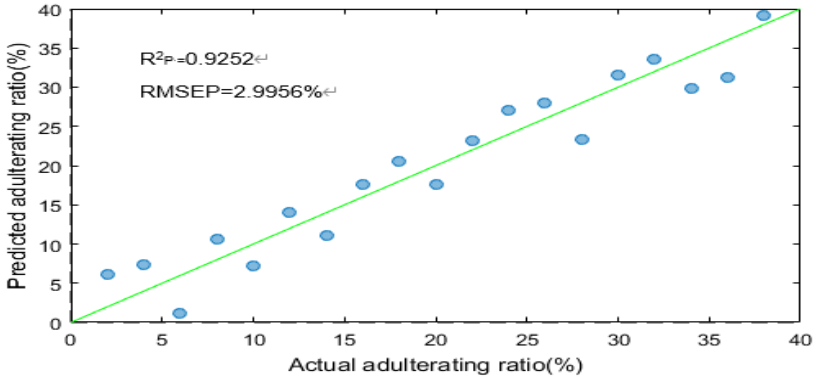


Fig. 9 - The model scatter plot of the prediction set

The average cutting speed and blade. To compare with the traditional two-dimensional correlation spectra (shown in figure 3), the detection model was also built based on the traditional two-dimensional correlation spectra combined with the N-PLS algorithm, and the model results are shown in Table 2.

Table 2

Results of detection model

Item	R^2_C	R^2_P	RMSEC	RMSEP
Traditional two-dimensional correlation spectra	0.8840	0.8606	3.9283%	4.0893%
Weighted reconstructed two-dimensional correlation spectra	0.9375	0.9252	2.8837%	2.9956%

From this table, it is clear that better performance of the model can be obtained using weighted reconstructed two-dimensional correlation spectra, with the R^2_C increased by 6.05% and R^2_P increased by 7.5%, which showed that the detection model based on weighted reconstructed two-dimensional correlation spectra has higher accuracy and better prediction stability.

CONCLUSIONS

In this paper, a method was proposed for the detection of flaxseed oil adulteration based on weighted reconstructed two-dimensional correlation near-infrared spectroscopy. Based on the multi-scale characteristics of the spectra, the two-dimensional correlation near-infrared of the adulterated flaxseed oil samples were decomposed at multiple scales and weighted reconstructed. The quantitative detection model based on the reconstructed two-dimensional correlation spectra can provide better performance than the model based on the traditional two-dimensional correlation spectra with the R^2_C increased by 6.05% and R^2_P increased by 7.5%. The results showed that the weighted reconstructed two-dimensional correlation spectra can effectively reduce the spectral noise interference, enhance the spectral feature information, thereby improving the accuracy and robustness of the adulteration detection model. The proposed method explored a new perspective for the detection of adulterated oil based on two-dimensional correlation near-infrared spectra and it can also be applied to other food adulteration detection areas.

ACKNOWLEDGEMENTS

This research was supported by Applied Basic Research Program of Shanxi Province, China (201701 D121103), and Key Research and Development Program of Shanxi Province, China (202102020101012).

REFERENCES

[1] Bro R., (1996), Multiway calibration. Multilinear PLS, *Journal of Chemometrics*, VOL.10, Issue 1, pp.47-61, Chichester/England;

[2] Chen D., Lu F., Li Q.F., et al., (2016), Development of multi-scale modeling methods for calibration transfer in near infrared spectroscopy, *Nanotechnology and Precision Engineering*, Vol.15, Issue 2. pp.121-126, Tianjin / China;

[3] Chen J. B., Zhou Q., Noda I., et al., (2016), Quantitative classification of two-dimensional correlation spectra, *Applied Spectroscopy*, Vol. 63, Issue 8. pp.920-925, Maryland / USA

[4] Chen Y.X., Ma Y.X., Lu Y., et al., (2012), Detection and identification of characteristic fatty acids in common edible vegetable oil, *Chinese Journal of Food Hygiene*, Vol. 24, Issue 4, pp.301-305, Beijing / China;

[5] Chu X.L., Tian G.Y., Yuan H.F., et al., (2006), Quantitative analysis of near-infrared spectroscopy combination of wavelet analysis and N-way partial least square, *Chinese Journal of Analytical Chemistry*, Vol.34, Issue 9. pp.175-178, Beijing / China;

[6] Goyal A, Sharma V, Upadhyay N, et al., (2014), Flax and flaxseed oil an ancient medicine &modern functional food, *J Food Sci Technol*, Vol.51, Issue 9, pp.1633－1653, Haryana/ India;

[7] Liao L.P., Xiao A.P., Leng J., et al., (2018), GC-MS Analysis of Fatty Acids of Flaxseed Oil Obtained by Cold Pressing Method from Different Districts, *Plant Fiber Sciences in China*, Vol.40, Issue7, pp.234-238, Changsha / China;

[8] Liao Z.L., LI Q.Y., CHEN J.J., et al., (2021), Research progress on the functional activity of flaxseed oil components, *Modern Food Science and Technology*, Vol.37, Issue 11, pp.379-389, Guangzhou/ China;

[9] Liu Z. C., Cai W. S., Shao X G., (2009), A weighted multiscale regression for multivariate calibration of near infrared spectra, *Analyst*, Vol.134, Issue 2. pp.261-266, Cambridge/England;

[10] Noda. I., (2004), Advances in two-dimensional correlation spectroscopy. *Vibrational Spectroscopy*, Vol.36, Issue 2, pp.143-165, Amsterdam/Netherlands;

[11] Nunes J.C., Guyot S., Deléchelle E., (2005), Texture analysis based on local analysis of the bidimensional empirical mode decomposition, *Machine Vision and Applications*, Vol.16, Issue 3, pp. 177-188, New York/USA;

[12] Park Y.; Noda I.; Jung Y. M., et al. (2016), Novel developments and applications of two-dimensional correlation spectroscopy, *Journal of Molecular Structure*, Vol. 1124, pp.11-28, Amsterdam/Netherlands;

[13] Sun X.M., Zhang L.X., Li P.W., et al., (2015), Fatty acid profiles based adulteration detection for flaxseed oil by gas chromatography mass spectrometry, *LWT-Food Science and Technology*, Vol.63, Issue 1, pp.430-436, Amsterdam/Netherlands;

[14] Sun X.S., Yang R.J., Yang Y.R., et al., (2015), Effects of Different Pretreatment Methods on Two-dimensional Correlation Spectroscopy, *Normalization Method Journal of Tianjin Agricultural University*, Vol. 22, Issue 4. pp.13-16, Tianjin / China;

[15] Wang W.X., Peng Y.K., Sun H.W., et al. (2018), Evaluation of pork freshness using two-dimensional correlation visible/near-infrared spectroscopy combined with support vector machine, *Food Science*, Vol. 39, Issue 18, pp.273-279, Beijing / China;

[16] Wang z., Li C.X., Qian R., et al., (2020), Research on vegetable oils classification based on two-dimensional correlation near-infrared spectroscopy, *Spectroscopy and Spectral Analysis*, Vol.40, Issue 10. pp.3230-3234, Beijing / China;

[17] Wei C.Q. Zhou Q. Chen Z., et al., (2018), Construction of Aromatic Fingerprint of Flaxseed Oil in Xinjiang, *Journal of the Chinese Cereals and Oil Association*, Vol. 33, Issue 3, pp.104-111, Beijing/ China;

[18] Xian Y., Zhang L., Liao X., et al., (2018), Clinical research about regulating blood glucose and blood lipids by flaxseed powder in patients with gestational diabetes mellitus, *Chinese Journal of Woman and Child Health Research*, Vol.29, Issue 6, pp. 721-726, Xian/ China;

[19] Yang R. J., Liu R., Xu K.X., et al., (2013), Classification of adulterated milk with the parameterization of two-dimensional correlation spectroscopy and least squares support vector machines, *Analytical Methods*, Vol. 5, Issue 21,pp.5949-5953, Cambridge / England;

[20] Yang R.J., Yang Y.R., Liu H.X., et al., (2015), Progress in application of two-dimensional correlation spectroscopy for detection of food quality, *Spectroscopy and Spectral Analysis*, Vol.35, Issue 8, pp. 2124-2129, Beijing / China;
[21] Zhan D.Q., Sun S.Q., Zhou Q., et al., (2004). Wavelet denoising and optimization of two-dimensional correlation IR spectroscopy, *Spectroscopy and Spectral Analysis*, Vol.24, Issue 12, pp.1549-1552, Beijing / China;
[22] Zhang J., Shan H.Y., Yang R.J., et al., (2019), Discrimination of adulterated sesame oil using fusion of near-mid infrared correlation spectra, *Acta Photonica Sinica*, Vol. 48, Issue 6, pp. 06300031-06300037, Xian/ China;
[23] Zhang, Y.L., Chen J. B.,Y. Zhou L.Q., et al., (2010), Discrimination of different red wine by Fourier-transform infrared and two-dimensional infrared correlation spectroscopy, *Journal of Molecular Structure*, Vol. 974, Issue 1. pp. 144-150, Chichester / England;
[24] Zhou Y., Huang J.H., Jin Q.Z., et al., (2018), Comparison of lipid composition of cold-pressed flaxseed oil from different origins, *China Oils and Fats*, Vol. 43, Issue 9, pp.125-128, Xian/ China.

EXPERIMENT ON SPRAY FLOW FIELD CHARACTERISTICS AND DEPOSITION PERFORMANCE OF CONICAL WIND FIELD ANTI-DRIFT SPRAY
/
锥形风场式防飘喷雾流场特性及沉积性能试验研究

Changxi LIU [1,2,3], Jun HU *[1,2,3], Yufei LI [1,2,3], Wei ZHANG [1,2,], Qingda LI [1,2,3],
[1)]College of Engineering, Heilongjiang Bayi Agricultural University, Daqing / China;
[2)]Heilongjiang Province Conservation Tillage Engineering Technology Research Center, Daqing / China;
[3)]Key Laboratory of Soybean Mechanized Production, Ministry of Agriculture and Rural Affairs, Daqing / China;
Corresponding author: Jun HU; E-mail: +86 13836962331;E-mail:gcxykj@126.com
DOI: https://doi.org/10.35633/inmateh-69-53

***Keywords:** Conical wind field; Droplet velocity distribution; Atomization effect; Deposition test*

ABSTRACT
Conical wind field anti-drift spray is an innovative form of anti-drift operation using auxiliary air flow, which can resist the generation of vortex, and has the characteristics of reducing the droplets loss with wind at the vertical height. In order to explore the characteristics of spray flow field and droplet deposition performance under conical wind field, the structure and working principle were analyzed based on the basic principle of proton dynamics. Spraytec and PDPA system were used to explore the distribution characteristics of spray flow field. Box-Behnken experimental design was used to analyze the droplet deposition performance. The optimum combination of the working parameters with spray height is 0.46 m, the spray pressure was 0.34 MPa, the conical wind speed was 16.16 m/s, and the droplet deposition amount was 3.39μL·cm^{-2}. The droplet deposition amount was optimal.

摘要
锥形风场式防飘喷雾是利用辅助气流进行防飘作业的一种创新形式，可以抵御绕流涡旋的产生,具有减少雾滴在纵向高度上随风飘失的特性。为探究锥形风场作用下的喷雾流场特性及雾滴沉积性能，基于质子动力学基本定律对其结构和工作原理进行了分析。利用 Spraytec 和 PDPA 系统探究了喷雾流场的分布特点。采用 Box-Behnken 实验设计法分析了各影响因素对雾滴沉积率的影响。最优工作参数为喷雾高度 0.46m，喷雾压力为 0.34MPa，锥风风速为 16.16m/s 时，雾滴沉积量为 3.39μL·cm^{-2}。雾滴沉积量最优。

INTRODUCTION
Atomizing pesticides into fine droplets for spraying is a key link in pesticide application technology (*Zhang et al., 2015; Yang et al., 2012; Zhang et al., 2017*). Droplet size is a key indicator to measure the effect of atomization (*Fritz et al., 2009; Ahmed et al., 2014*). The specific performance is that the smaller the particle size of the droplets, the greater the number, and the more uniform distribution on the leaves, but the risk of evaporative drift and wind drift also increases (*Li et al., 2019*). Therefore, selecting droplets with appropriate particle size is one of the important ways to ensure spray quality. There are many methods to improve the spatial distribution of droplet size, such as electrostatic spray, air-assisted spray, variable spray, etc. (*Liang et al., 2020*). Air-assisted spraying technology improves droplet distribution through directional airflow, increases its deposition rate on the target, and reduces drift (*Yuan et al., 2012*). Currently, air-assisted spraying is mostly used in orchard spraying operations, and air curtains are used in field spraying operations (*Qi et al., 2010*).

The variation law of droplet size, motion characteristics and spatial distribution in gas-liquid two-phase flow field is closely related to droplet drift and deposition behavior (*Zhang et al., 2012; Oliveira et al., 2015*). The mechanism research on the interaction between auxiliary airflow and mist droplets has become a research hotspot in the field of plant protection. The Malvern Spraytec laser particle size analyzer is often used to test the droplet size of agricultural nozzles and analyze their atomization characteristics (*Tang et al., 2016*). *Ru et al.,* (*2016*) also used Spraytec to analyze the droplet size distribution gap between GP-81A series aviation nozzles under wind tunnel conditions and flight conditions. *Yan et al.,* (*2014*) used the Phase Doppler Particle Analyzer (PDPA) to determine the influence of the wind speed and distance at the outlet of the air curtain on the particle size and velocity distribution of the droplets. *Guler et al.,* (*2007*) used PIV to compare the velocity field distributions of standard fan nozzle and the air induction nozzle under wind tunnel conditions. *Sinha et al.,* (*2015*) used PDIA to characterize the spray characteristics from the droplet cone angle and droplet size distribution.

The conical wind field anti-drift spray device has been proved to be a kind of air-assisted auxiliary spray method with excellent anti-drift performance (*Liu et al., 2021*). However, the interaction law between the conical wind field generated by the device and the droplet is still unclear. The size, trajectory and deposition effect of droplets in air-assisted spray are affected by air flow, so the deposition characteristics of droplets affected by air flow should be paid special attention (*Gupta et al., 2012*).

In this paper, according to the theory of proton dynamics, the force model of a single droplet in the moving air medium is established, which is used to describe the action law of the conical wind field on the droplet. The Spraytec Laser Particle Size Analyzer and PDIA were used to establish the droplet spatial size spectrum and reveal the relationship between droplet size distribution and velocity. The optimum combination parameters of droplet deposition were obtained by orthogonal test. This study provides a reference for the application of air-assisted spray technology in the field of plant protection.

MATERIALS AND METHODS

Theoretical analysis of conical wind field anti-drift spray

In order to clarify the anti-drift mechanism of the conical wind field, a Cartesian coordinate system is introduced to establish a schematic diagram of the force of a single droplet under the action of the crosswind and the conical wind field (Fig. 1), and the force of a single droplet is analyzed (without considering the internal force of the droplet group).

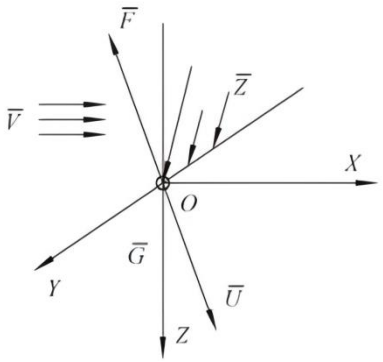


Fig. 1 - The force analysis of droplet under the action of natural wind and conical wind field

Under the combined action of cross wind and conical wind, a moving air medium is formed. The mass and size of a single droplet in it are relatively small, and the interference of the surrounding fluid medium on the droplet can be ignored. Therefore, according to the basic law of proton dynamics, the dynamic equation of the droplet relative to the moving air medium is obtained as

$$m\bar{a} = \overline{F} + \overline{G} \rightarrow m\frac{d\overline{U}}{dt} = \overline{F} + m\bar{g} \tag{1}$$

Where:

a is the droplet acceleration in the flowing air, [m/s^2];
m is the droplet mass, [kg];
U is the relative drift velocity vector, [m/s];
g is the acceleration of gravity, [m/s^2].

According to Euler's method, the resistance F generated by droplet movement in the air medium has a quadratic relationship with the droplet speed (*Pascuzzi et al., 2013; Bulgakov et al., 2018*):

$$F = \frac{mg}{V_{so}^2} \cdot \overline{U}^2 \tag{2}$$

Where: V_{so} is the average rising speed of droplets, [m^2/s^2].

Equations (1) ~ (2) are combined:

$$\frac{\mathrm{d}\overline{U}}{\mathrm{d}t} = -\frac{g}{V_{SO}^2} \cdot \overline{U}^2 \cdot \frac{\overline{U}}{\left|\overline{U}\right|} + g \tag{3}$$

In the Cartesian coordinate system, the simplified differential equations for the motion of a single droplet are obtained:

$$\begin{cases} \frac{d^2x}{dt^2} = -\frac{g}{V_{so}^2} \cdot \left|\overline{U}(t)\right| \cdot U_x(t) \\ \frac{d^2y}{dt^2} = -\frac{g}{V_{so}^2} \cdot \left|\overline{U}(t)\right| \cdot U_y(t) \\ \frac{d^2z}{dt^2} = -\frac{g}{V_{so}^2} \cdot \left|\overline{U}(t)\right| \cdot U_z(t) + g \end{cases} \quad (4)$$

It can be seen from Equation (4) that the speed of droplets in each direction depends on their relative drift vector when moving in the air. By applying conical wind field, the velocity of droplet in target direction is increased and the ability of resisting crosswind is improved. The purpose of spray operation is to prevent and reduce drift through the above measures. The combined wind field formed by the conical wind and the side wind can reduce the longitudinal height of the vortex generation position and reduce droplet drift when the left side wind intrudes into the spray fan to form a surrounding vortex (Fig. 2).



Fig. 2 - Drift state of droplet group before (a) and after (b) conical wind field is applied in crosswind

Structure and flow field distribution of anti-drift spray device

The conical wind field anti-drift spray device connected with HARDI F-110-03 fan nozzle (Fig. 3) was selected for the experiments.

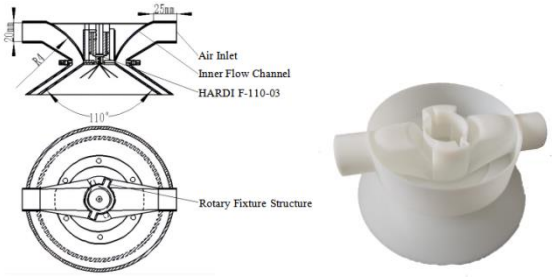


Fig. 3 - Conical wind field anti-drift spray device

The application form of the auxiliary airflow has a significant influence on the droplet motion characteristics (*Hu et al., 2020*). The flow field distribution of the conical wind field anti-drift spray device was simulated (Fig. 4) with the method described in the research of Liu et al., (*2021*).

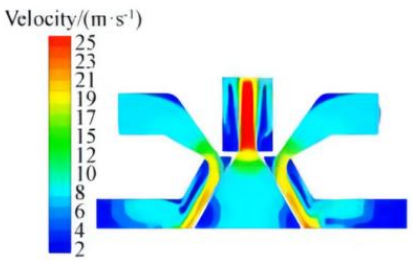


Fig. 4 - Flow field distribution of the conical wind field anti-drift spray device

In order to ensure the stable deposition of droplets on the target, the airflow should meet the final velocity principle (*Hu et al., 2020*). According to the velocity field at the outlet of the device, the conical wind speed is set as five gradients: 0 m/s, 10 m/s, 15 m/s and 20 m/s.

Experimental instruments and conditions of spray flow field

In order to verify the theoretical analysis and explore the influence of conical wind field on droplets, spray experiments were carried out in the Research Center of Plant Protection Machinery and Application Technology (CCAT) of China Agricultural University, Beijing, China. The Laser Particle Size Analyzer Spraytec by Malvern Co., Ltd was used to measure the droplet spatial particle size spectrum (Fig. 5a), and the Droplet Image Analyzer VisiSize P15 (PDIA) by Oxford Lasers Co., Ltd was used to measure the droplet velocity distribution (Fig. 5b).

a b

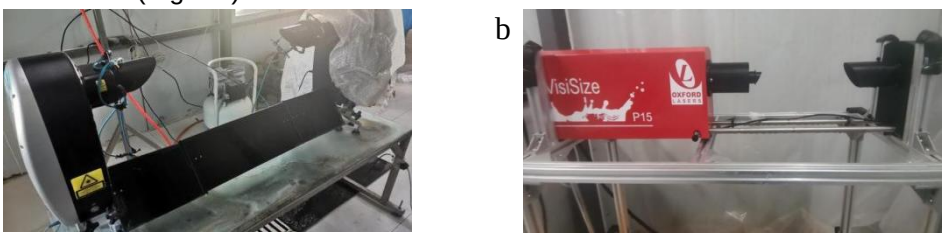


Fig. 5 - Malvern Laser Particle Size Analyzer Spraytec (a), Droplet Image Analyzer VisiSize P15 (b)

The experiment was conducted on November 23, 2020. The temperature was 23°C, and there was no wind during the experiment.

Experimental method design of spray flow field

As the pretest showed that the effective range of the conical wind field acting on droplets effectively was 200 mm beyond the nozzle, the droplets were measured by the method shown in Figure 6.

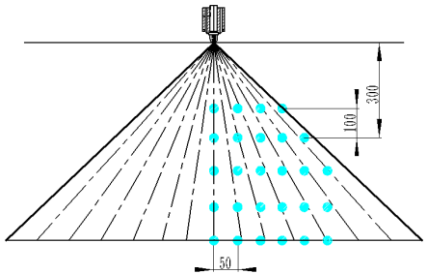


Fig. 6 - Sampling point of spray flow field

For the particle size distribution test, the test nozzle was selected as HARDI F-03-110 fan nozzle, the air supply device was a KOMAX Fan (with duct), the spray liquid was tap water, the spray pressure was 0.3 MPa, and the test index was Dv50. Dv50 also called Volume Median Diameter (VMD), is the droplet diameter when 50% of the spray volume is contained in droplets of lesser diameter. The position where the droplets are easy to drift away is concentrated at the central axis 300-500 mm away from the nozzle (*Song et al., 2011*). For the velocity distribution test, the spray height is selected from 300 mm, 400 mm, 500 mm below the central axis of the nozzle, the spray pressure is 0.3 MPa, 0.4 MPa, and the conical wind speed is 0 m/s, 10 m/s, 15 m/s, 20 m/s. To ensure the accuracy of the test results, each test was repeated 3 times and the average value was taken as the final test result.

Experimental method design of spray deposition test

The conical wind field anti-drift spray device was mounted on the self-propelled plant protection spray truck for orthogonal test, as shown in Fig. 7.



Fig. 7 - Outdoor test of conical wind field anti-drift spray device

The rectangular area formed by soybean plants was selected as the test area, in which the water-sensitive paper was distributed on the top and bottom and overlapped on the soybean plants as far as possible, with a spacing of 300 mm. Model of nozzle was HARDI F-03-110 fan-shaped nozzle; Spray liquid: tap water; Spray pressure: According to the experimental conditions of each group; The amount of droplet deposition (μL·cm^{-2}); Ambient wind speed: 3 m/s (The average wind speed during the test and the wind direction during the test period is generally consistent); Locomotive speed: 2 m/s (Keep constant).

RESULTS

The effect of droplet spatial particle size spectrum

The VMD of the droplets under each conical wind speed obtained according to the test plan are shown in Table 1, and the spatial particle size spectrum of the droplets are shown in Fig. 8.

Table 1

VMD of the droplets under different conical wind speed

Conical wind speed *v*/(m·s^{-1})	*y*/mm	*x*/mm					
		0	50	100	150	200	250
		VMD/μm					
0	200	148.4	157.3	165.4	169.6	-	-
	300	155.5	162.8	172.3	180.1	188.2	-
	400	159.6	171.8	180.4	189.2	197.4	205.4
	500	165.3	179.7	188.3	196.4	203.6	211.7
	600	176.2	189.3	196.5	202.5	213.7	220.6
10	200	146.9	155.6	163.1	166.6	-	-
	300	150.3	158.3	167.4	178.1	186.1	-
	400	156.4	165.4	174.0	182.2	191.0	198.3
	500	160.7	169.2	179.3	186.0	194.6	203.4
	600	169.8	176.7	187.5	193.6	204.5	212.6
15	200	144.0	152.3	161.0	164.4	-	-
	300	148.1	155.5	165.5	175.6	181.0	188.2
	400	153.4	161.1	168.2	178.5	185.7	192.4
	500	156.3	165.2	173.7	181.7	188.0	198.3
	600	165.5	172.4	182.3	188.2	195.8	208.2
20	200	143.1	153.4	162.4	163.2	-	-
	300	146.3	154.3	163.0	175.3	180.2	187.3
	400	152.7	162.5	166.6	176.4	184.6	193.2
	500	154.4	164.1	175.5	180.6	186.4	197.1
	600	163.6	171.2	183.0	187.1	193.6	206.0

It can be seen from Fig. 8 that under the same spray pressure (0.3 MPa), the VMD of droplets are negatively correlated with the conical wind speed. At 500 mm below the nozzle, the mean VMD of droplets decreases by 8.63 μm when 10 m/s conical wind is applied. The VMD of droplets decreased by 5.00 μm on average when the conical wind speed increased from 10 m/s to 15 m/s. But the VMD of droplets decreases only by 1.45 μm, which remains basically unchanged when the conical wind speed increased from 15 m/s to 20 m/s.

Since the nozzle used in this paper is a liquid pressure type, without applying auxiliary wind field, the droplet size distribution and flow velocity are determined by the nozzle aperture and spray pressure, that is, the liquid pressure is the dominant driving force for the atomization. The conical wind field applied in this paper provides additional aerodynamic force for liquid atomization and aggravates the atomization of droplet fragmentation by overcoming the droplet surface tension. An excessively large conical wind field will cause the droplets to collide or even merge, which explains the VMD of droplets located certain areas increase in Table 1.

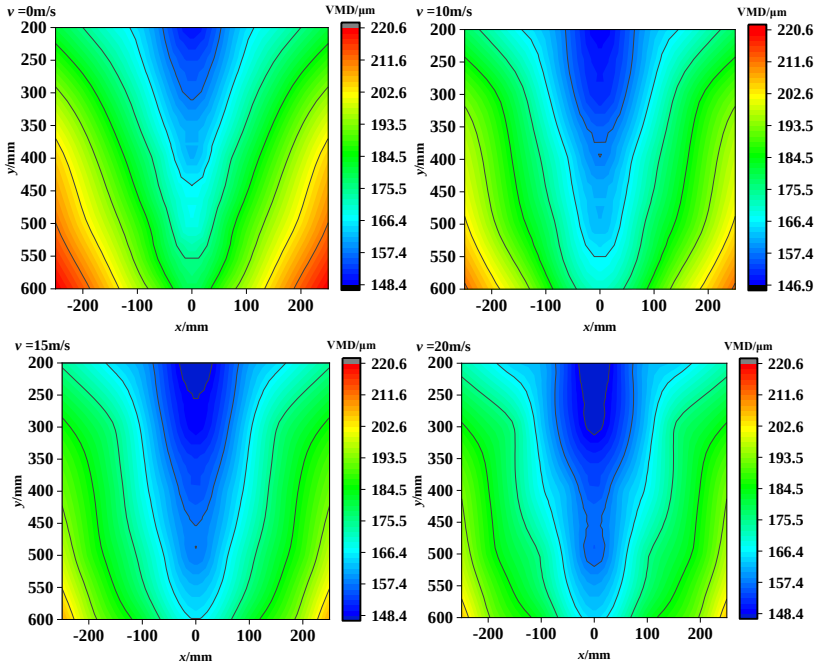


Fig. 8 - The spatial particle size spectrum of the droplets

It can be seen from Table 2 that the overall trend of the change of the average velocity of the droplets decreases with the increase of the spray height, which is caused by the resistance of the droplets during the falling process, and the velocity is constantly attenuated. At the same spray height, the average velocity of droplets increases with the increase of spray pressure, which is due to the large initial kinetic energy of droplets generated under the conditions of high spray pressure.

Table 2

Experiment factor level and coded value

Coded value	The spray height (m)	The spray pressure (MPa)	The conical wind speed ($m \cdot s^{-1}$)
-1	0.450	10	0.2
0	0.475	15	0.3
1	0.500	20	0.4

Under the influence of the conical wind field, the decrease of the average velocity of the droplets show a downward trend with the decrease of the spray pressure. At the distance of about 350 mm from the spray height, the influence of the conical wind on the average velocity of the droplets exceeds the spray pressure.

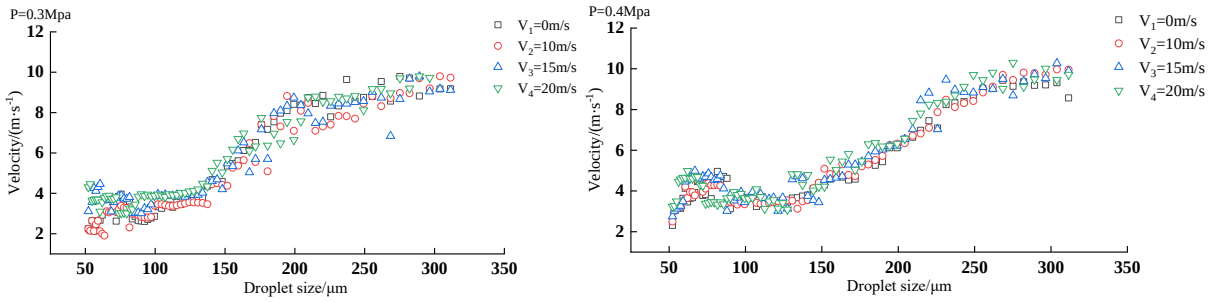


Fig. 9 - Velocity distribution of the droplets under different conical wind speed and spray pressure

The droplet movement speed in the range of 50-150 μm particle size increases obviously with the application of the conical wind field when the spray pressure is 0.3 MPa, which indicates that the droplet speed in this part of the particle size range is related to the conical wind field. The acceleration effect of the conical wind field on this part of the droplets is not obvious when the droplet size is in the range of 150-200 μm. The main body of the conical wind field acting on the movement of the droplet group is 50-150 μm. This is similar to the data law when the spray pressure is 0.4 MPa.

The experiment method and result

This paper uses Box-Behnken as a test method, the amount of droplet deposition as the assessment index. The paper sets out a series of experiments on the spray height (the level value X_1, the coded value x_1), the spray pressure (the level-value X_2, the coded value x_2), the conical wind speed (the level-value X_3, the coded value x_3). The level-value and the coded value of the experiment elements are shown in Table 2. The experimental scheme and the results are shown in Table 3.

Table 3

Experiment factor level and coded value

No.	The spray height, x_1 (m)	The spray pressure, x_2 (MPa)	The conical wind speed, x_3 ($m \cdot s^{-1}$)	The amount of droplet deposition, Y ($\mu L \cdot cm^{-2}$)
1	-1	-1	0	2.71
2	1	-1	0	2.51
3	-1	1	0	3.32
4	1	1	0	2.87
5	-1	0	-1	3.01
6	1	0	-1	2.68
7	-1	0	1	3.39
8	1	0	1	3.01
9	0	-1	-1	2.01
10	0	1	-1	3.03
11	0	-1	1	2.94
12	0	1	1	2.87
13	0	0	0	3.24
14	0	0	0	3.25
15	0	0	0	3.23
16	0	0	0	3.12
17	0	0	0	3.17

The regression model

This research imports the experimental data in Design-Expert 10.0 to make a regression fit, which sets up the regression model of the broken-tea ratio and the assessment index of the sensory evaluation score from different elements, as shown in Eq.(5).

After getting rid of the non-distinctive regression items, the regression model of the broken-tea ratio and the sense assessment index is shown in Eq.(6):

$$Y = 3.20 - 0.17x_1 + 0.24x_2 + 0.19x_3 - 0.063x_1x_2 + 0.013x_1x_3 - 0.27x_2x_3 - 0.020x_1^2 + 0.33x_2^2 - 0.16x_3^2 \quad (5)$$

$$Y = 3.20 - 0.17x_1 + 0.24x_2 + 0.19x_3 - 0.27x_2x_3 + 0.33x_2^2 - 0.16x_3^2 \quad (6)$$

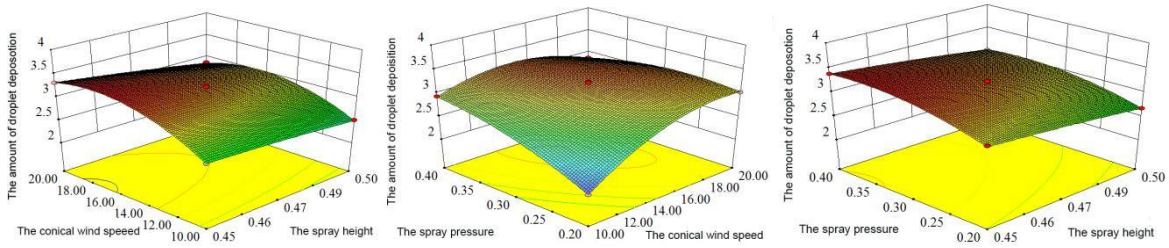
Analysis of the effect of experimental factors

In the regression equation, one element with the factor level o is randomly selected, and the remaining two elements are studied to find out their influence on amount of droplet deposition. The software Design-Expert 10.0 is used to make an analysis to get the response hook face affected by the interaction factors, as shown in Fig. 10.

In Fig. 10 a), this paper finds that if the spray pressure is fixed, the amount of droplet deposition increases first and then decreases with the increase of conical wind speed. With the increase of spray height, the amount of droplet deposition is more suitable in the range of conical wind speed 14 ~ 18 m/s and spray height 0.45 ~ 0.47 m.

In Fig. 10 b), if the spray height is fixed, the amount of droplet deposition increases with the increase of conical wind speed and spray pressure. The amount of droplet deposition is more suitable in the range of conical wind speed 14 ~ 18 m/s and spray pressure 0.27 ~ 0.35 MPa. In this case, the contour lines of the response surface are closed ellipses, indicating that the interaction between conical wind speed and spray pressure is strong and has a maximum value.

In Fig. 10 c), if the conical wind speed is fixed, the droplet deposition increases first and then decreases with the increase of spray pressure. With the increase of spray height, the amount of droplet deposition is more suitable in the range of conical wind speed 14 ~ 18 m/s and spray pressure 0.27 ~ 0.35 MPa. The above analysis is consistent with the significance shown in Eq.(6).



a)Y=f(x1, 0, x3) *b)Y=f(0, x2, x3)* *c)Y=f(x1, x2, 0)*

Fig. 10 - Response surfaces of interactive factors influence on test indexes

The optimization model and the experimental verification

Based on the working performance demand and the actual working condition of the conical wind field anti-drift spray device, this work plans to succeed in the lower conical wind speed, the higher amount of droplet deposition. According to the different elements having different effects, this paper needs to optimize all results. This paper regards amount of droplet deposition as an objective function, makes the optimization design to 3 experimental elements, including the rotating speed of conical wind speed, the spray height and the spray pressure.

The optimization constraint conditions can be conducted as follows:

$$\begin{cases} \max Y \\ s.t. \begin{cases} X_1 \in (0.43, 0.49) \\ X_2 \in (0.25, 0.35) \\ X_3 \in (14.00, 18.00) \end{cases} \end{cases} \quad (7)$$

The influence laws of three experimental factors affecting the amount of droplet deposition is comprehensively considered to get the best parameter combination, using Design-Expert 10.0 software to make an optimization solution. This research gets the optimum working parameter combination, the spray height being 0.46 m, the spray pressure being 0.34 MPa, the conical wind speed being 16.16 m/s, the amount of droplet deposition being 3.39 $\mu L \cdot cm^{-2}$.

In order to use the optimum parameter combination in the actual spray operation, this paper makes the round number of them, the spray height is 0.45 m, the spray pressure is 0.35 MPa, the conical wind speed is 16.00 m/s, 3 repetitive tests are made to get the average value, the amount of droplet deposition is 3.36 $\mu L \cdot cm^{-2}$ which means the experimental results keep an accord with the theoretical results substantially, thus the regression model is good.

CONCLUSIONS

In this paper, the characteristics of spray flow field and droplet deposition of the conical wind field anti-drift spray device are investigated experimentally. The results clearly show that the conical wind field can significantly improve the spatial distribution of droplets, and the optimal combination obtained from the experiment can provide a basis for field spraying operation.

(1) The conical wind field improves the spatial distribution of droplets by intensifying droplet fragmentation and suppressing the entrainment of small droplets. However, when the conical wind speed increases to a certain extent, its effect on the particle size of the droplets to promote the fragmentation will become small or even have no effect.

(2) The conical wind field has a significant effect on the droplet group of 50-150 μm. The average velocity of droplets is positively correlated with spray pressure and conical wind speed, and it decreases continuously with the decrease of height. The research results shows that the conical wind field can supplement the kinetic energy of the small droplets that are easy to drift away, which is helpful for the droplets to settle.

(3) The Box-Behnken was introduced to design the experimental methods, regarding the spray height, the spray pressure, the conical wind speed as the experimental elements, and regarding the amount of droplet deposition as the test indexes, making the series experiments on the operation parameter of the conical wind field anti-drift spray device, finding out that the optimum working parameter combination is the spray height of 0.45 m, the spray pressure of 0.35 MPa, the conical wind speed of 16.00 m/s, and the amount of droplet deposition being 3.39μL·cm^{-2} .

ACKNOWLEDGEMENTS

This research was funded by National Key Research and Development Program Project of China (No.2017YFC1601905-04), Open project of Key Laboratory of Soybean Mechanization Production of Ministry of Agriculture and Rural Affairs (No.SMP202207) and Heilongjiang Province Applied Technology Research and Development Program Project (No.GA21B003). We especially thank for the support of the National Soybean Industry Technology System Post Expert Foundation of China (No.CARS-04-PS30) funded by China Agriculture Research System of MOF and MARA.

REFERENCES

[1] Ahmed, M., Youssef, M. S. (2014) Influence of spinning cup and disk atomizer configurations on droplet size and velocity characteristics. *Chemical Engineering Science,* 107(14), 149–157. https://doi.org/10.1016/j.ces.2013.12.004.

[2] Bulgakov, V., Pascuzzi, S., Nadykto, V. (2018) A mathematical model of the plane-parallel movement of an asymmetric machine and tractor aggregate. *Agriculture,* 8(151), 44–59. https://doi.org/10.3390/agriculture8100151.

[3] Fritz, B. K., Hoffmann, W. C., Lan, Y. (2009) Evaluation of the EPA drift reduction technology (drt) low-speed wind tunnel protocol. *Journal of ASTM International,* 6(4), 183–191. https://doi.org/10.1520/JAI102129.

[4] Guler, H., Zhu, H., Ozkan, H. E., Derksen, R. C., Yu, Y., Kraus, C. R. (2007) Spray characteristics and drift reduction potential with air induction and conventional flat-fan nozzles. *Transactions of the ASABE,* 50(3), 745–754. https://doi:10.13031/2013.23129.

[5] Gupta, P., Sirohi, N., Mishra, I. (2012) Air flow characteristics of an air-assisted sprayer through horizontal crop canopy. *International Journal of Agricultural and Biological Engineering,* 5(1), 1-6. https://doi:10.3965/j.ijabe.20120501.001.

[6] Hu, J., Liu, C. X., Chu, X., Li, Y. F, Sun, S. Y., Zhang, W. (2020) Droplet deposition characteristics of conical wind field anti-drift device. *Transactions of the Chinese Society for Agricultural Machinery,* 51(12), 142-149; 174. https://doi: 10. 6041 / j. issn. 1000-1298. 2020. 12. 015

[7] Li, J. Y., Guo, S., Yao, W. X., Zhan, Y. L., Li, Y. F. (2019) Distribution characteristics of droplet size in rice field and wind tunnel simulation test under airflow operation. *Transactions of the Chinese Society for Agricultural Machinery,* 50(8), 148-156. https://doi: 10. 6041 /j. issn. 1000-1298. 2019. 08. 017

[8] Liang, Z., Fan, G. Q., Wang, G. M., Ding, H., Zhang, X. H. (2020) Distribution model of wind-stressed droplet deposition based on bimodal distribution. *Transactions of the Chinese Society for Agricultural Machinery,* 51(4), 28-37. https://doi: 10. 6041 /j. issn. 1000-1298. 2020. 04. 003

[9] Liu, C. X., Hu, J., Li, Y. F., Zhao, S. X., Zhang, W., Li, Q. D. (2021) Optimization of the inner flow channel of conical wind field anti-drift spray device and anti-drift characteristics. *Transactions of the CSAE,* 37(22), 11-20. https://doi:10.11975/j.issn.1002-6819.2021.22.002

[10] Oliveira, R. B. D., Antuniassi, U. R., Gandolfo, M. A. (2015) Spray adjuvant characteristics affecting agricultural spraying drift. *Engenharia Agricola,* 35(1), 109-116. https://doi.org/10.1590/1809-4430-Eng.Agric.v35n1p109-116/2015

[11] Pascuzzi, S. (2013) The effects of the forward speed and air volume of an air-assisted sprayer on spray deposition in tendone trained vineyards. *Journal of Agricultural Engineering,* 44(18), 125-132. https://doi: 10.4081/jae.2013.e18.

[12] Qi, L. J., Zhao, Y. Q., Wang, J., Ji, R. H., Mang, L. (2010) CFD simulation and experimental verification of droplet dispersion of air-assisted orchard sprayer. *Transactions of the Chinese Society for Agricultural Machinery,* 41(2), 62-67. https://doi:10.3969/j.issn.1000-1298.2010.02.013.

[13] Sinha, A., Prakash, R. S., Mohan, A. M., Ravikrishna, R. V. (2015) Airblast spray in crossflow - structure, trajectory and droplet sizing. *International Journal of Multiphase Flow,* 72(4), 97-111. http://dx.doi.org/10.101 6/jmultiphaseflow.2015.02.008.

[14] Song, J., Liu, Y. J., Zhang, J., He, X. K., Herbst, A. (2011). Drift mechanism of flat fan nozzle. *Transactions of the Chinese Society of Agricultural Machinery,* 42(6), 63-69. https://doi:10.3969/j.issn.1000-1298.

[15] Tang, Q., Chen, L. P., Zhang, R. R., Zhang, B., Yi, T. C., Xu, G. (2016) Atomization characteristics of normal flat fan nozzle and air induction nozzle under high speed airflow conditions. *Transactions of the Chinese Society of Agricultural Engineering,* 32(22), 121-128. http://doi:10.11975/j.issn.1002-6819.2016.22.017

[16] Yang, X. W., Dai, M. L., Song, J. L., Zhao, J. K., He, X. K. (2012) Effect of droplet size, leaf characteristics and angle on pesticide deposition. *Transactions of the Chinese Society of Agricultural Engineering,* 28(3), 70-73. http://doi:10.3969/j.issn.1002-6819.2012.03.013.

[17] Yuan, X., Qi, L. J., Ji, R. H., Zhang, J. H., Huang, S. K. (2012) Analysis on features of air-velocity distribution and droplets deposition pattern for greenhouse air-assisted mist sprayer. *Transactions of the Chinese Society of Agricultural Machinery,* 43(8), 71-77. http://doi: 10. 6041/j.issn. 1000-1298. 2012. 08. 014.

[18] Yan, M. D, Jia., W. D., Mao, H. P., Dong, X., Chen, L. (2014) Experimental investigation of droplet diameter and velocity distributions in air-assist boom sprays. *Transactions of the Chinese Society of Agricultural Machinery,* 45(11), 104-110. http://doi: 10. 6041 /j. issn. 1000-1298. 2014. 11. 016.

[19] Zhang, J. T., Li, S. H., Wen, S., Lan, Y. B., Liao, Y. Y., Zhang, T. M. (2015) Parameter optimization design and experiment of agricultural ultrasonic atomization transducer. *Transactions of the CSAE* 31(12), 8-15. http://doi: 10.11975/j.issn.1002-6819.2015.12.002.

[20] Zhang, H. C., Zheng, J. T., Zhou, H. P., Dorr, G. J. (2017) Droplet deposition distribution and off-target drift during pesticide spraying operation. *Transactions of the Chinese Society for Agricultural Machinery* 48(08), 114-122. http://doi: 10. 6041 /j. issn. 1000-1298. 2017. 08. 012.

[21] Zhang, T., Yang, X. J., Yan, H. R., Wang, J., Dong, X. (2012) Anti-drift technology of super-high clearance boom sprayer with air-assisted system. *Transactions of the Chinese Society for Agricultural Machinery,* 43(12), 77-86. http://doi: 10. 6041 /j. issn. 1000-1298. 2012. 12. 015.

RESEARCH ON THE SPRAY CYLINDER INTERNAL FLOW FIELD AND ITS INFLUENCE ON SPRAYING QUALITY OF FORAGE SEED SPRAY SEEDING MACHINE
/
牧草种子喷播机喷筒内流场及其对喷播质量影响研究

Yan CHEN, Hua GUO *), Shi FU, Rui ZHANG, Ming ZHANG [1]
Department of Information Engineering, Ordos Institute of Technology, Compass, Ordos/ China
Tel: +815849726146; E-mail: guohua716@163.com
Corresponding author: Hua Guo
DOI: https://doi.org/10.35633/inmateh-69-54

Keywords: *pneumatic spraying machine, spraying quality, airflow velocity, spraying performance*

ABSTRACT
The objective of ecological restoration and rehabilitation of grasslands is to recreate the original appearance of damaged or degraded vegetation. From previous research, the pneumatic spraying technology is now more commonly used in the world for vegetation restoration. Pneumatic spraying is relatively inexpensive and causes little damage to the original vegetation, making it one of the most effective techniques for restoring natural grassland vegetation under natural climatic conditions. In this paper, the effect of the spraying machine pipe working airflow on the quality of spraying was studied through simulation analysis and experimental tests. The seeding area of the spraying machine corresponding to different values of the pipe inlet airflow speed was determined. The conclusions show that: 1) the spray pipe inlet airflow velocity has a great influence on the uniformity of spraying. When the airflow velocity is higher than 55 m/s, the spraying is not uniform, while the airflow velocity is lower than 45 m/s, the spraying amplitude is smaller, the operational efficiency is low, which is not conducive to the restoration of degraded grasslands; 2) considering the uniformity of spraying and operational efficiency, the airflow velocity at the inlet of the spray pipe should be between 45 and 55 m/s when the spraying machine is in operation. The seed drop area is changed, by adjusting the airflow velocity of the spray pipe inlet, and the reseeding and leakage area of the seed drop area is reduced, so that the spraying performance of the spraying machine is optimized.

摘 要
草原生态恢复与重建目标是再现被破坏或已退化植被原貌。从前期研究情况看，气力喷播技术目前在世界上应用于植被修复比较普遍。气力喷播技术成本相对较低，对原有植被破坏较小，是在自然气候条件下恢复天然草原植被的有效技术手段之一。本文通过仿真分析和试验测试研究了气力喷播机喷筒工作气流对喷播质量的影响，确定了不同数值喷筒入口气流速度所对应的喷播机落种区域。结论表明：1）喷筒入口气流速度对喷播均匀性有很大影响，当气流速度高于 55 m/s 时，喷播不均匀，当气流速度低于 45 m/s 时，喷播幅度较小，作业效率低，不利于退化草原修复；2）考虑喷播均匀性和作业效率，喷播机工作时喷筒入口气流速度应在 45~55 m/s 之间，且通过调节喷筒入口气流速度改变了种子的落种区域，减小了落种区域重播、漏播面积，实现了对喷播机喷播性能的优化。

INTRODUCTION
The goal of grassland ecological restoration and reconstruction is to reproduce the original vegetation that has been damaged or degraded, and to rebuild a healthy ecosystem (*Chen et al.,2007; Chen et al., 2022; Jiang et al., 2023*). The time and cost of ecological restoration depend on the size of the restoration area, degree of degradation, and restoration techniques employed *(Jiang et al., 2023; Long et al., 2002)*. Currently, the main techniques for grassland vegetation restoration include enclosure, artificial seeding, aerial seeding, and pneumatic seeding. Among them, pneumatic seeding is a widely used and effective technique, with relatively low cost and short restoration period *(Liang et al., 2015; Yue et al., 2022)*. It also causes minimal damage to the existing vegetation, making it one of the most effective means of restoring natural grassland vegetation under natural climatic conditions *(Mu et al., 2012)*.

[1]*Yan Chen, Lecturer Ph.D. Eng.; Hua Guo, Prof M.S. Eng.; Shi Fu, Lecturer M.S. Eng.; Rui Zhang, Lecturer M.S. Eng.; Ming Zhang, Lecturer M.S. Eng.*

Pneumatic seeding operation for degraded grassland vegetation restoration involves spraying coated grass seeds onto the degraded land. The grass seeds and coating adhere to the soil surface, creating conditions for plant growth. With the help of rainwater, the grass seeds can take root and germinate, thereby completing the restoration of degraded grassland vegetation *(Fan et al., 2013)*.

Based on the early spraying experiments, spraying operations are a fast and efficient technique for restoring grassland vegetation under natural climatic conditions (*Wang et al., 2013; Xu et al., 2006; Zhang et al., 2013*). Significant research achievements have been made regarding the use of pneumatic seeders for restoring grassland vegetation. However, during the process of using pneumatic seeders to restore degraded grassland, factors such as the working airflow of the spray pipe have not been considered in relation to the uniformity of spraying.

To improve the spraying quality of the sprayer, this study focused on the 4BQD-40C pneumatic sprayer and investigated the flow field inside the spray pipe, determining its distribution and variation pattern, and analyzed its impact on the seeding area *(Zhang et al., 1997; Cao et al., 2023)*. Based on this, the study analyzed the effects of changing the inlet airflow velocity of the spray pipe on the spraying quality of the sprayer, with the aim of minimizing the area of missed or re-sprayed seeds in the seeding area.

MATERIALS AND METHODS

Principle analysis

4BQD-40C type pneumatic seeder has been improved over many years, and its basic functions are already complete. It is mainly composed of a spray pipe, a seed tube, a seed storage box, a seed dispenser, a fan, and a rotating part, as shown in Fig. 1.

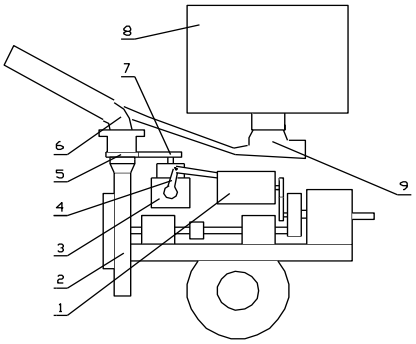


Fig. 1 – Structure diagram of the spraying machine

1 – Worm gear reducer; 2 – Air-blower ;3 – Amplifier; 4 – Rocker 5 – Spray cylinder's gear wheel; 6 – Spray cylinder's Swing mechanism; 7 – Amplifier's output gear; 8 – Material box; 9 – Stuff feeding mechanism

During the spraying process of the sprayer, the coated ice grass seeds are subjected to the action of their own weight and the air flow in the conveying pipe. They enter the seeding device through the metering device and are then transported into the falling seed device. At the outlet of the fan, a throat pipe is installed to generate negative pressure. Due to the negative pressure of the main air duct throat pipe, the ice grass seeds in the falling seed device are sucked in, suspended and accelerated in the main air duct, and then sprayed out with the high-speed air flow of the spray pipe, as shown in Fig. 2. While the sprayer is moving forward under traction, its spray pipe oscillates back and forth within the horizontal plane at an angle of 0° to 180° (*Zhang et al., 1997; Zhao et al., 1997*).

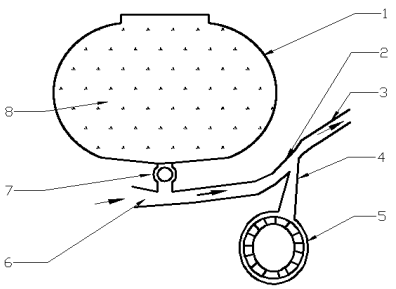


Fig. 2 – Diagram of Sprayer working principle

1 – Material box; 2 – Seed Tube;3 – Spray-duct; 4 – Pipe; 5 – Air-blower; 6 – Air inlet duct; 7 – Seeding Apparatus; 8 – Seed

Spraying quality analysis

The seed is sprayed at high speed through the spray pipe of the sprayer based on the principle of pneumatic conveying. The movement of the seed at the outlet is a combination of the oscillation of the spray pipe and the linear movement of the sprayer. The trajectory of the seed in half a cycle is a trochoid, while the trajectory in the other half of the cycle is another trochoid with the same shape but opposite direction. By magnifying the trajectory of the seed sprayed by the sprayer, it can be seen that the sowing area is enclosed by four curves, as shown in Fig. 3. The sowing area of one cycle of spray pipe oscillation consists of eight curves. When the spray pipe oscillates from counter-clockwise to clockwise, the end curve of the first half cycle is the same as the start curve of the second half cycle, and they are actually the same curve (*Zhang et al., 1997; Zhao et al., 1997*). Therefore, the sowing area is composed of seven different curves. Based on the above analysis, a GUI program is designed in MATLAB software to draw the sowing area of the sprayer, as shown in Fig. 4.

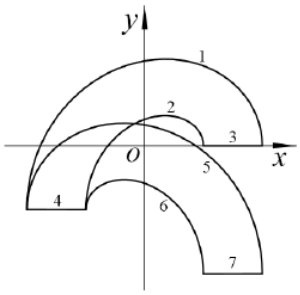


Fig. 3 – Diagram of the falling region

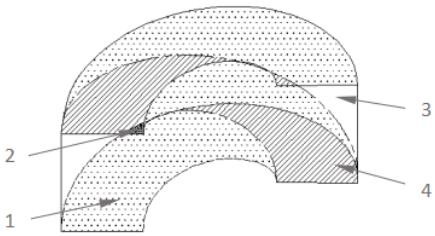


Fig. 4 – Sketch map of missing and broadcast area in seeding area

1 – Normal spraying area; 2 – Secondary spraying area; 3 – Missed spraying area; 4 – One spraying area

According to Fig. 4, the 4BQD-40C pneumatic seed drill shows uneven spraying areas such as reseeding and missed seeding in the seeding area (*Zhang et al., 2013*). The factors affecting this area include the swing frequency of the spray pipe, the air flow velocity of the spray pipe, and the internal flow characteristics of the spray pipe. Among them, the air flow velocity and internal flow characteristics of the spray pipe have a greater impact on spraying quality indicators such as seeding area, spraying bandwidth, seed spraying interval, and spraying uniformity. Therefore, this paper mainly studies the internal flow characteristics of the spray pipe of the seed drill, explores the distribution and variation of the flow field, and reveals the influence of the internal flow field of the spray pipe on the seeding area of the seed drill.

Based on the design principle of the sprayer, the spray pipe area is divided according to Fig. 5. At the same time, ProE software is used to create a 3D model of the spray pipe and seeding tube as shown in Fig.6, and Fluent software is used to conduct numerical simulation research (*Zuo et al., 2020; Xu et al., 2017*).

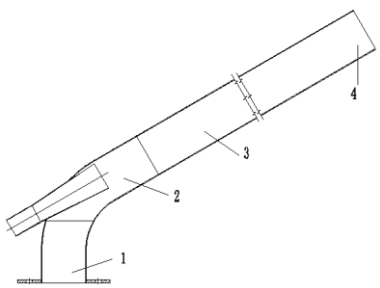


Fig. 5 – Area division of spray cylinder

1 – Spray pipe inlet; 2 – Seed pipe insertion section; 3 – Front section of spraying pipe; 4 – Spraying pipe outlet



Fig. 6 – Simplified three-dimensional model of the seeds convey pipe and spray pipe

Using Pro/E to create a 3D model and import it into Ansys Workbench for model conversion. Then, use Meshing software to perform meshing, as shown in Fig. 7. Finally, use Ansys Fluent 17.0 for flow field simulation analysis (*Chen et al., 2018; Ma et al., 2022; Shen et al., 2022*).

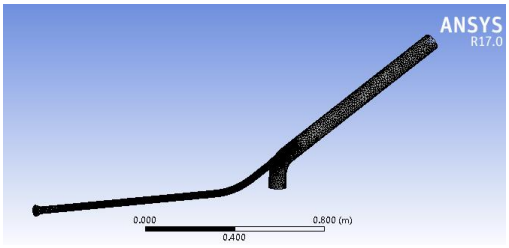


Fig. 7 – Meshing of the seeds convey pipe and spray pipe

In previous research on the 4BQD-40C pneumatic spraying machine, it was found that the maximum airflow velocity at the spray pipe inlet can reach 60 m/s, but when the airflow velocity at the spray pipe inlet is around 47 m/s, the spraying is more uniform and the spraying efficiency is higher (*Zhao et al., 2010*). Based on this, spray pipe inlet airflow velocities of 60 m/s, 55 m/s, 47 m/s, 35 m/s, and 25 m/s were selected for study. When the spray pipe inlet airflow velocity is 60 m/s, the velocity distribution inside the seeding tube and spray pipe is shown in Fig. 8.

As shown in Fig. 8, the velocity distribution of the airflow is relatively uniform in the later stage of the seed tube and the spray pipe. The velocity along the axial direction in the seed tube remains at around 58 m/s, while it remains at around 53 m/s near the tube wall. However, there is a region with higher airflow velocity and an airflow vortex next to the insertion section where the seed tube is connected to the spray pipe, as shown in the enlarged local view in Fig. 9.

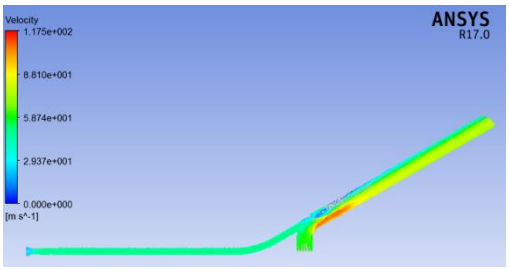


Fig. 8 – Velocity vector diagram in conveying seeds pipe and spray pipe

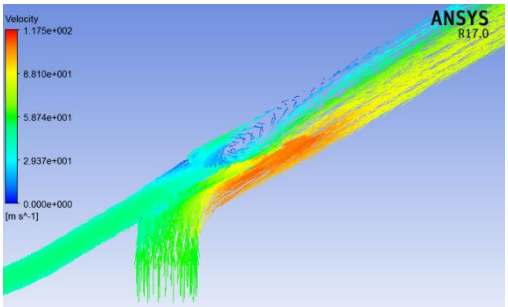


Fig. 9 – Partial enlargement of velocity vector in insertion section of seed conveying pipe

The local airflow in the insertion section of the feeding tube hinders the entry of seeds into the interior of the spray pipe. However, at this point, the seeds already have a certain initial velocity under the action of the airflow, which can overcome the hindrance and enter the spray pipe smoothly. At the same time, according to the velocity distribution vector diagram, it can be seen that after the seeds enter the spray pipe, they are transferred to the area of higher airflow velocity under the action of the airflow vortex and obtain greater energy in this section. By changing the inlet airflow velocity of the spray pipe, the velocity distribution of the airflow in the feeding tube and spray pipe can be obtained. The average values of the velocity of the airflow in the feeding tube and spray pipe are taken on a circular cross-section and the relationship is shown in Table 1.

Table 1

Relationship between inlet airflow velocity of spray cylinder and velocity of inlet of conveying pipe and outlet of spray tube

Inlet airflow velocity of spray cylinder [m/s]	60	55	47	35	25
Inlet airflow velocity of conveying pipe [m/s]	56.5	48.9	39.2	29.6	22.3
Outlet airflow velocity of spray tube [m/s]	78.3	67.9	56.8	42.5	30.6

According to the data fitting in Table 1, the relationship between the inlet airflow velocity of the spray tube and the inlet airflow velocity of the seed delivery tube is as follows:

$$v_s = 0.96v_{pr} - 3.15 \quad (1)$$

where:

v_s represents the airflow velocity in the seed delivery pipe, [m/s]; v_{pr} represents the airflow velocity at the spray pipe inlet, [m/s]. Based on the experiment, it is found that the minimum velocity required for seed suspension is 9.58 m/s. Therefore, according to equation (1), the minimum velocity at the spray pipe inlet should be 13.3 m/s. To ensure smooth seeding, a safety factor of 2.5 is taken, so the minimum spray pipe inlet velocity to be used for the seeder is 35 m/s.

After coating, the equivalent diameter of the ice grass seed was set to 2.5 mm. Numerical analysis was carried out for airflow inlet velocities of 35 m/s, 40 m/s, 47 m/s, 50 m/s, 52 m/s, 55 m/s, and 60 m/s, with a seed dispenser rotating at 18 rpm. The corresponding relationships between the airflow inlet velocity and the seed velocity at the spray pipe outlet are shown in Table 2.

Table 2

Relationship between airflow velocity at sprayer inlet and coated seeds velocity at the outlet of spray cylinder

Inlet airflow velocity of spray cylinder [m/s]	60	55	52	50	47	40	35
Maximum speed of seeds at the outlet of spray pipe [m/s]	16.4~22.5	20.8	19.8	18.5	17.8	14.5	12.5
Minimum seed speed at the outlet of the spray pipe [m/s]	12.8~16.3	14.9	14.3	13.6	12.9	10.3	9.3

From table 2, it can be seen that when the inlet airflow velocity of the spray pipe is 60 m/s, the maximum velocity of seed ejection at the outlet of the spray pipe varies between 16.4 and 22.5 m/s, and the seed ejection velocity is unstable. When the inlet airflow velocity of the spray pipe decreases to 55 m/s, the seed ejection velocity becomes more stable. When the inlet velocity of the spray pipe is between 35 and 55 m/s, the relationship between the maximum seed velocity at the spray pipe outlet and the inlet airflow velocity of the spray pipe is given by the formula:

$$v_{rmax} = 0.42v_{pr}\text{-}2.21 \quad (2)$$

The relationship between the minimum seed velocity at the spray pipe outlet and the airflow velocity at the spray pipe inlet is:

$$v_{rmin} = 0.28v_{pr} - 0.45 \quad (3)$$

According to the above analysis, after seed coating, the maximum seed velocity at the spray pipe outlet is linearly related to the inlet airflow velocity of the spray pipe. Therefore, adjusting the inlet airflow velocity of the spray pipe in the range of 35~55 m/s can change the seed velocity at the spray pipe outlet and adjust the seed sowing area, which lays a foundation for improving the uniformity of the seed sowing machine in the future.

Test conditions

The test site is a relatively flat soil area in the campus of the school, with a temperature range of 17~23°C, and the test was conducted when the wind speed was less than 1.0 m/s. The testing equipment includes one stopwatch, one measuring tape, one electronic scale, one TSI 9565-P multifunctional anemometer, and one hot-wire velocity probe as shown in Fig. 0, with main parameters listed in Table 3.

Table 3

Performance parameters of wind speed probe

Item	Range of measurement [m/s]	Accuracy of measurement [m/s]	Resolution ratio [m/s]	Operating temperature [℃]
Parameter	0~50	±0.015	0.01	-20~50



Fig. 10 – 9565 P multifunction wind meter

Airflow velocity test

This test used an air speed probe to test the airflow velocity at the outlet of the spray pipe and the inlet of the seed delivery tube. Ensure that the seed box, seed delivery tube and spray pipe are clear and free of seed before conducting the test. The frequency converter was adjusted so that the airflow velocity at the inlet of the spray pipe was 40 m/s.

Test spray pipe outlet airflow velocity:

(a) The wind speed probe is placed at the exit position of the spray pipe, perpendicular to the center line of the pipe, with the probe facing the direction of the incoming flow.

(b) Once the data displayed by the wind speed probe has stabilized, the airflow velocity at the outlet of the spray pipe is measured.

(c) The measurement points were selected from the center of the pipe, 10 mm from the center, 20 mm from the center, 30 mm from the center and at the edge of the pipe, and 10 instantaneous values were recorded for each area as the pipe exit airflow velocity.

(d) Calculate the average of each measurement point for the airflow velocity at the spray pipe outlet.

Testing the spray pipe velocity at the inlet of the seed delivery tube:

(a) The wind speed probe is placed at the inlet of the seed tube, perpendicular to the center line of the tube, with the probe facing the direction of incoming flow.

(b) Once the data displayed by the wind speed probe has stabilized, the airflow velocity at the inlet of the seed delivery pipe is measured.

(c) The measurement points were selected at the center of the seed tube, 5 mm from the center, 10 mm from the center and at the edge of the seed tube. 10 instantaneous values were recorded in each area as the airflow velocity at the inlet of the seed tube.

(d) Calculate the average value of each measurement point for the inlet airflow velocity of the seed tube.

Spraying seed range test

A relatively flat soil site was chosen as the test site to give a true picture of the seed drop from the spray pipe. The seed drop in the seed drop area reflects the exit velocity of the seeds from the spray pipe, so the distribution of seeds in the seed drop area was used to verify the velocity of the seeds at the spray pipe exit in the test.

(a) Before starting the test, the test site was gridded as shown in Figure 11. This was done to facilitate the subsequent counting of seeds in the drop zone. The grid size was: 2m x 2m and the grid size of the total seed drop area was: 40m x 40m.

(b) The center line of the total seed drop area is chosen as the location of the spreader, while the edges of the grid are numbered to facilitate subsequent statistics.

(c) For the test, the seed dispenser speed was set to 18 rpm, while the fan was started and the frequency converter operating frequency was changed. The spraying test was carried out at inlet air velocities of 40 m/s, 45 m/s, 47 m/s, 50 m/s and 55 m/s respectively.

(d) After the spraying is completed, four locations in the sprayed seed drop area are selected for measurement at 30º, 60º, 120º and 150º of the canister swing, and the amount of seed dropped at each measurement point is counted separately, and the seed dropped is cleaned up after the count is completed.



Fig. 11 – Grid partition map of experimental area

During the experiment, the seeding rate was fixed at 18 rpm, and the airflow velocity at the spray pipe inlet was adjusted by changing the frequency of the variable frequency drive to 40 m/s, 45 m/s, 47 m/s, 50 m/s, and 55 m/s for seeding tests. After seeding, four locations were selected in the seeding area where the spray pipe swung 30º, 60º, 120º, and 150º, respectively. The seeding amount at each location was counted, and the seeds on the ground were cleaned up after the counting was completed.

During the swing of the spray pipe, the seed distribution range in the seeding area is shown in Fig. 12, R represents the distance from the outer edge of the seeding area to the center of the spray pipe swing, r represents the distance from the inner edge of the seeding area to the center of the spray pipe swing, and the seeding belt is R-r.

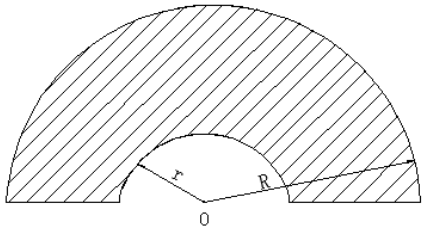


Fig. 12 – Schematic diagram of spraying seed range

RESULTS

Airflow velocity test results

According to Table 4, the airflow velocity near the edge of the spray pipe is the lowest, and gradually increases towards the center of the spray pipe, reaching its maximum value at the center. When the inlet airflow velocity of the spray pipe is 40 m/s, the airflow at the outlet does not change much, except for the low airflow velocity near the edge of the spray pipe. The rest of the velocities are close to, and all greater than, 47 m/s. This is consistent with the simulation results, which indicate that the airflow velocity at the spray pipe outlet is mainly distributed in the range of 47.0-47.8 m/s. Therefore, the numerical simulation results can be considered reliable. However, at the edge of the spray pipe, the simulated airflow velocity is 45.6 m/s, while the experimental measurement is 47.6 m/s, and the difference is relatively large. This may be due to differences in testing methods and measurement errors.

Table 4

The distribution of airflow velocity at the spray pipe outlet when the airflow velocity at inlet is 40 m/s

Location of measuring points	Test value 1 [m/s]	Test value 2 [m/s]	Test value 3 [m/s]	Test value 4 [m/s]	Test value 5 [m/s]	Average value[m/s]
Spraying pipe center	47.83	47.81	47.88	47.91	47.83	47.85
10 mm from the center	47.74	47.77	47.74	47.68	47.69	47.72

20 mm from the center	47.55	47.54	47.61	47.54	47.61	47.57
30 mm from the center	47.33	47.29	47.37	47.30	47.32	47.32
Edge of inner wall of spraying pipe	47.56	47.93	48.02	47.95	47.57	47.81

From Table 5, a similar pattern can be obtained as in Table 4. The airflow velocity at the inlet of the delivery tube gradually decreases from the center to the edge of the tube, with a greater decrease near the wall of the tube. The simulation analysis shows that the airflow velocity at the center of the delivery tube is 34.8 m/s, while the experimental measurement shows 32.5 m/s, indicating a close agreement between the simulation and experimental results. These experimental results demonstrate the correctness of the simulation analysis, and the model and analysis method can be used for further theoretical analysis.

Table 5

The distribution of airflow velocity at the inlet seeds convey pipe when the airflow velocity at inlet is 40 m/s

Location of measuring points	Test value 1 [m/s]	Test value 2 [m/s]	Test value 3 [m/s]	Test value 4 [m/s]	Test value 5 [m/s]	Average value [m/s]
Seed pipe center	32.54	32.47	32.53	32.46	32.51	32.50
5 mm from the center	32.43	32.49	32.51	32.45	32.47	32.47
10 mm from the center	32.31	32.27	32.28	32.32	32.29	32.29
Edge of inner wall of seed delivery pipe	30.98	30.18	30.34	30.91	30.68	30.62

Spraying seed range test results

Put the coated grass seeds into the seeding box, and set the rotary speed of the seeder to 18 rpm. By changing the inlet airflow velocity of the spray pipe, the sowing area of the seeds was tested, and the results are shown in Table 6. When the inlet airflow rate of the spray pipe is high, the outer edge R of the sowing area is also large, indicating that the speed of the seeds at the spray pipe outlet increases with the increase of the inlet airflow rate. When the airflow rate decreases from 55 m/s to 45 m/s, although both the farthest and closest distances of the sowing area decrease, the sowing width remains basically unchanged at 10.7 m and 10.2 m. Therefore, when the inlet airflow rate of the spray pipe is in the range of 45-55 m/s, the sowing area can be adjusted by adjusting the inlet airflow rate of the spray pipe. However, when the airflow rate further decreases, the seed cannot form a stable velocity flow when ejected, causing uneven distribution of the sowing points, ultimately affecting the sowing uniformity, and reducing the sowing range and efficiency.

Table 6

Relationship between coated seeds falling area and airflow velocity of spray tube inlet when seeding speed is 18 rpm

Airflow velocity [m/s]	Inner edge of seed falling area's test value 1 [m/s]	Inner edge of seed falling area's test value 2 [m/s]	Inner edge of seed falling area's test value 3 [m/s]	Inner edge of seed falling area's test value 4 [m/s]	Average value of inner edge of seed falling area [m/s]	Outer edge of seed falling area's test value 1 [m/s]	Outer edge of seed falling area's test value 2 [m/s]	Outer edge of seed falling area's test value 3 [m/s]	Outer edge of seed falling area's test value 4 [m/s]	Average value of outer edge of seed falling area [m/s]
55	11.1	11.3	11.2	10.8	11.1	21.6	21.9	21.8	21.7	21.8
50	9.1	9.3	9.2	8.8	9.1	19.3	19.7	19.5	19.4	19.5
47	8.5	8.6	8.5	8.4	8.5	18.9	18.7	18.8	19.0	18.8
45	7.4	7.8	7.7	7.5	7.6	17.5	18.0	17.9	17.6	17.8
40	6.5	5.7	6.2	6.1	6.1	17.0	15.9	16.5	16.4	16.4

CONCLUSIONS

Theoretical analysis was conducted on the impact of the spray pipe inlet airflow velocity on the spray performance of the sprayer, and spray experiments were carried out on coated Timothy grass seeds at different spray pipe inlet airflow velocities, leading to the following conclusions:

(1) When the sprayer is in a no-seed state, numerical simulation and experimental verification were conducted on the spray pipe inlet airflow velocity, revealing the relationship between the spray pipe inlet airflow velocity and the airflow velocities at the spray pipe outlet and the seed delivery tube inlet, laying a theoretical foundation for subsequent research.

(2) Theoretical analysis was conducted on the effect of the inlet airflow velocity of the spraying spray pipe on the spraying performance of the sprayer. Spray tests were also carried out on coated bermudagrass seeds at different inlet airflow velocities of the sprayer. The following conclusions were drawn: It was found from the analysis of the inlet airflow velocity of the spraying spray pipe that with the increase of the inlet airflow velocity, the outer edge R and inner edge r of the seed dropping range increased. However, when the inlet airflow velocity was between 45-55 m/s, the spraying bandwidth remained basically unchanged. When the inlet airflow velocity was lower than 45 m/s, the seed could not form a stable velocity flow upon spraying. Moreover, when the inlet airflow velocity of the spraying spray pipe was 60 m/s, the seed velocity at the outlet of the spray pipe varied greatly, making it unsuitable for spraying operations.

Based on the above analysis, the relationship between the seed distribution area and the spray pipe inlet airflow velocity during spraying has been obtained. Both theoretical analysis and experimental verification show that uneven spraying occurs when the airflow velocity is higher than 55 m/s, and the spraying range is small with low efficiency when the airflow velocity is lower than 45 m/s, which is not conducive to degraded grassland restoration. Considering the spraying uniformity and operation efficiency, the spray pipe inlet airflow velocity should be set between 45-55 m/s during operation, and the seed distribution area can be adjusted by adjusting the airflow velocity to reduce the area of seed re-sowing and seed leakage, and optimize the spraying performance of the sprayer.

ACKNOWLEDGEMENT

The authors were funded for this project by the University scientific research projects in Inner Mongolia Autonomous Region (NJZY22207).

REFERENCES

[1] Chen, R. Q., Yan, J., (2007). Application of spraying grass planting in geological disaster control project in three Gorges Reservoir area (喷播植草在三峡库区地质灾害治理工程中的应用). *Journal of Express Water Resources&Hydropower Information*, Vol. 18, pp. 21-22+26, Hubei/China.

[2] Chen, Y. D., Wang, C.B., (2022). Analysis of the application of guest soil spraying re-greening technology in road maintenance in loess areas (客土喷播复绿技术在黄土地区公路养护中的应用分析). *Transport Manager World*, Vol. 674(28), pp. 137-139, Beijing/China.

[3] Chen, Y., (2018). *Research on Automatic Variable Spraying Technology and Related Parameter Optimization of Spraying Machine Based on Multisource Information* (基于多源信息的喷播机自动变量喷播技术及相关参数优化研究). PhD thesis. Univ. Inner Mongolia agricultural, Hohhot/China.

[4] Cao, A. N., Wu, C. D., Zhang, B., et al., (2023). Simulation and Analysis of Spray Barrel Motion for Unmanned spray Vehicles Replacing Pesticides (替代农药无人喷雾车的喷筒运动仿真及分析). *Research on Agricultural Mechanization*, Vol. 45(08), pp. 10-17, Heilongjiang/China.

[5] Fan, C. M., (2013). *Optimization and experimental studies of spray cylinder swing frequency for4BQD-40C vehicle-mounted spray seeding machine* (4BQD-40C 型车载式喷播机喷筒摆动频率的优化及试验验证). Master's thesis. Univ. Inner Mongolia agricultural, Hohhot/China.

[6] Jiang, Y. D., Liu, X., Zheng, Y., (2023). Current status of grassland resource degradation in Inner Mongolia and exploration of ecological restoration (内蒙古草地资源退化现状及生态修复探索). *Grassland and Grass Industry*, Vol. 35(01), pp. 57-61, Hohhot/China.

[7] Long, A. H., Xu, Z. M., (2002). On several problems of ecological restoration and reconstruction in northwest (西北地区生态恢复与重建若干问题的思考). *Transactions of the Chinese Ecological Economics Society,* Vol. 03, pp. 42-48, Lanzhou/China.

[8] Liang, W., Li, Y. K., (2015). Finite element analysis of drilling jumbo sliding rail used in coal mine based on ANSYS workbench (基于 ANSYS Workbench 的煤矿用凿岩台车滑轨的有限元分析). *Journal of Coal Mine Machinery*, Vol. 36(05), pp. 93-95, Heilongjiang/China.

[9] Mu, H. C., Zhang, C., (2012). Calculation and analysis of the spray sowing chart of pneumatic spray sowing equipment (气力喷播机喷撒图的计算与分析). *Journal of Forestry Machinery & Woodworking Equipment*, Vol. 40(07), pp. 36-40, Heilongjiang/China.

[10] Ma, W., Fang, H. Y., Xiao, P., (2022). Design and analysis of fertilizer spraying equipment based on ANSYS (基于 ANSYS 的肥设料喷洒设备计与分析). *Machinery Management Development*, Vol. 37(12), pp. 1-2+7, Shanxi/China.

[11] Shen, X. Y., (2022). Analysis of mechanical properties of beams with non-uniform sections based on ANSYS (基于 ANSYS 的非均匀截面梁力学特性分析). *Journal of Baoshan College*, Vol. 41(05), pp. 59-64, Yunnan/China.

[12] Wang, A. T., (2013). *Study on automatic control system for the seeding of 4BQD-40 pneumatic spraying seeding-machine* (4BQD-40 型气力喷播机排种自动控制系统的研究). Master's thesis. Inner Mongolia Agricultural Univ., Hohhot/China.

[13] Xu, H.Y., (2006). *Reasons and prevention models of grassland deterioration in Damao banner Inner Mongolia* (4BQD-40 型气力喷播机排种自动控制系统的研究). Master's thesis. Univ. Chinese Academy of Agricultural Sciences, Beijing/China.

[14] Xu, J.C., Zhang, W.J., (2017). Ultimate load analysis based on ASME Ⅷ-2 large open-hole receiver (基于 ASME Ⅷ-2 大开孔接管的极限载荷分析). *Chemical Equipment and Piping*, Vol. 54(04), pp. 1-6+16, Shanghai/China.

[15] Yue, Y., Tian, H.Q., Liu, F., Zhang, T., Li, D. P., Wang, D., (2022). Analysis of vibration characteristics for rubbing machine based on modal test (基于模态试验的揉碎机振动特性分析). *INMATEH Agricultural Engineering*, Vol. 68(3), pp. 41-50, Romania. https://doi.org/10.35633/inmateh-68-04

[16] Zhang, Y., Fan, C. M., Chen, Z., Wang, J. W., (2013). Optimization and experiment of spray cylinder swing frequency for spray seeding machine (喷播机喷筒摆动频率的优化及试验). *Transactions of the Chinese Society of Agricultural Engineering (Transactions of the CSAE)*, Vol. 29(7), pp. 24-29, Beijing/China.

[17] Zhang, Y., Mu, H. C., Zhao, W. H., Pei, D. S., Wen, C. F., (1997). The design of main functions of 4BQD-40 pneumatic spraying seeding-machine (4BQD-40 型气力喷播机的主要性能设计). *Journal of Inner Mongolia Forestry College*, Vol. 04, pp. 58-66, Hohhot/China.

[18] Zhang, Y., Zhao, W. H., Mu, H. C., Gao, S. F., (1997). Determination of the jet-tube swinging frequency for 4BQD-40 air spray-sower (4BQD-40 型气力喷播机喷筒摆动频率的选择). *Journal of Inner Mongolia Institute of Agriculture & Animal Husbandry*, Vol. 04, pp. 90-93, Hohhot/China.

[19] Zhao, W.H., Zhang, Y., Mu, H. C., Sun, P. S., (1997). Design of the jet-flow sowing machine of 4BQD-40 air spray-sower (4BQD-40 气力喷播机喷射式排种器设计). *Journal of Forestry Machinery & Woodworking Equipment*, Vol. 06, pp. 10-12, Hohhot/China.

[20] Zhang, X. H., Gao, X., Chen, T. Y., Wang, A. T., Wang, H. C., (2013). Study on improvement and experiment for the spray pipe of 4BQD-40 pneumatic spraying seeding-Machine (4BQD-40 型气力喷播机喷筒的改进与试验研究). *Journal of Agricultural Mechanization Research*, Vol. 35(03), pp. 188-191, Hohhot/China.

[21] Zhao, W. C., Zeng, A. J., (2010). *Study on atomization performance of air spraying sprayer for grassland locusts* (草原灭蝗风送式喷雾机喷筒雾化性能研究). Master's thesis. Univ. Inner Mongolia agricultural, Hohhot/China.

[22] Zuo, A. D., (2020). Discussion on the evaluation method and results of ANSYS-based ultimate load analysis (基于 ANSYS 的极限载荷分析评定方法与结果讨论). *Chemical Equipment and Piping*, Vol. 57(03), pp. 1-7, Shanghai/China.

STUDY ON PHENOTYPIC CHARACTERISTICS OF MILLET BASED ON 3D MODEL
/
基于三维模型的谷子表型特征分析研究

Lili SUN [1], Yaoyu LI [2)], Yuzhi WANG [2)], Weijie SHI[2)], Wuping ZHANG [2)], Xiaoying ZHANG [3)], Huamin ZHAO [1)], Fuzhong LI [2,*)]

[1)] College of Agricultural Engineering, Shanxi Agricultural University, Taigu, Shanxi / China
[2)] College of Software, Shanxi Agricultural University, Taigu, Shanxi / China
[3)] Department of Basic, Shanxi Agricultural University, Taigu, Shanxi / China
Tel: +8603546287093; E-mail: lifuzhong@sxau.edu.cn
Corresponding author: Li Fuzhong
DOI: https://doi.org/10.35633/inmateh-69-55

Keywords: *Millet phenotype, Camera calibration, 3D reconstruction, Point cloud filtering, Character extraction*

ABSTRACT

As one of the ancient cultivated crops in China, millet has the characteristics of high nutritional value, drought resistance and barrenness. It also plays an important role in ensuring the supply of food in our country. At present, most of the millet breeding work uses manual extraction of phenotypic information, which is labor-intensive and inefficient. Therefore, the development of an automated, efficient and accurate millet phenotype detection method has practical significance for the extraction of the millet genome. In this study, a combination of sparse reconstruction based on Structure from Motion (SfM) and Patch-based Multi-View Stereo (PMVS) was used to select three different varieties of millet. A total of 81 samples of 9 samples in each period were reconstructed to obtain a 3D model of millet. The combination of conditional filtering and statistical filtering is used to remove the noise points generated during the photographing process, and finally the obtained point cloud data is used to measure the agronomic traits of millet such as plant height and leaf area. The results show that the interval angle of 5° is the best reconstruction angle of millet. The coefficient of determination R^2 of point cloud measurement results and manual measurement data regression analysis is higher than 0.94, indicating that the method used for 3D reconstruction has high applicability to different millet in different periods and high-throughput measurement of millet by the method in this paper is feasible. This study provides a theoretical basis for a millet phenotypic information measurement device.

摘要

谷子作为中国古老的栽培作物之一，具有营养价值高、抗旱耐贫瘠等特点。对我国粮食的供给保障也具有重要作用。目前，谷子育种工作多采用手工提取表型信息，劳动量大，效率低下，所以发展一种自动化、高效且精确的谷子表型检测方法对于谷子基因组的提取具有实际意义。本研究采用了基于运动恢复结构（SfM Structure from Motion）的稀疏重建和基于面片的多视角立体几何（PMVS Patch-based Multi-View Stereo）相结合的方法，对三个不同品种的谷子选取三个不同时期每个时期 9 个样本，共 81 个样本进行三维重建得到谷子的三维模型。利用条件滤波和统计滤波相结合去除在拍照过程中产生的噪声点，最后利用得到的点云数据对谷子进行株高、叶面积等农艺性状的测量。结果表明隔角度为 5° 为谷子的最佳重建角度。点云测量结果与人工测量数据回归分析决定系数R^2均高于 0.94，表明采用的方法进行三维重建对于不同时期不同谷子有较高的适用性并且通过本文的方法对谷子进行高通量测量是切实可行的。本研究为谷子表型信息测量设备提供了理论基础。

INTRODUCTION

China has the largest millet cultivation area and the largest yield in the world. The sown area accounts for more than 90% of the world's sown area. Millet belongs to the Gramineae setaria, with strong drought

[1]*Lili SUN, Ph.D. Eng.; Yaoyu LI, M.S. Stud. Eng.; Yuzhi WANG, M.S. Stud. Eng.; Weijie SHI, M.S. Eng.; Wuping ZHANG, Prof. Ph.D. Eng.; Xiaoying ZHANG, Prof. Ph.D. Eng.; Huamin ZHAO, Ph.D. Eng. ; Fuzhong LI, Prof. Ph.D. Eng..*

resistance and desert resistance, being the ideal crop of dry farming, in Inner Mongolia, Shaanxi, Shanxi and other areas of arid agricultural areas widely planted.

Recently, computer vision has been widely used in crop phenotypic research. The commonly used method is through the image processing technology from crops two-dimensional or three-dimensional images to extract the relevant properties parameters, production forecast and related analysis, etc. 3D models of crops contain spatial information that two-dimensional images do not have, from which more comprehensive and more real phenotypic parameters can be extracted, such as leaf area, plant type, photosynthesis related parameters, etc. (*Gao T. et al., 2021, Xu B. et al., 2017, Rupnik E. et al., 2018, Collier S. et al., 2017*.)

In recent years, more and more people are combining computer vision technology with agriculture to help breeders analyze and screen crop varieties for salt tolerance, drought tolerance and disease resistance. Automatic extraction of sorghum morphological characteristics was realized by 3D point cloud data analysis (*Xiang L, et al., 2019*). *Fang Wei et al. (2016)* proposed a fast 3D reconstruction method for obtaining traits of high-throughput plant types. *Qiu Q. et al. (2019)* used 3D LiDAR point cloud to conduct high-throughput phenotypic analysis on maize plants in the field. *Hu (2018)* calculated crop plant height in the field with UAV high throughput. He used Kinect V2 to obtain color images and depth images of citrus trees, and removed the background by depth threshold segmentation method, and carried out real-time 3D reconstruction of orange tree crowns, which was used for citrus picking barriers. *Syngelaki M. et al., (2018),* designed Photogrammetry system. This system constructed a stereo photogrammetry system consisting of a digital single-lens reflex camera, a lighting platform for placing petri dishes and an Arduino board to control the image acquisition process. The camera was mounted on a bracket. The camera can rotate at 30°, 45° and 60°, so as to obtain multi-view sequence images in different directions. Then Opencv and PCL technologies are used to conduct THREE-DIMENSIONAL reconstruction of biological samples in petri dishes. *He et al. (2017)* built a low-cost multi-view stereo imaging system, which can collect image data of Strawberry Fruit 360. Grass was constructed based on SFM and MVS technology. *Wen et al. (2021)* proposes a 3D phytomer-based geometric modelling method with maize (Zea Mays) as the representative plant. Specifically, conversion methods between skeleton and mesh models of 3D phytomer are specified. *Schipper et al. (2023)* calibrated and validated an existing functional structural plant model (FSPM), which combines plant morphology with a ray tracing model to estimate light absorption at leaflet level."

MATERIALS AND METHODS

Experimental materials

Three representative millet varieties, namely Jingu 21, Dabaigu, and Yuanping Xiaogu, were selected as experimental materials. Under the same temperature, humidity and light conditions, 30 plants were selected from each variety, and 10 plants were selected from jointing stage, heading stage and filling stage respectively for measurement.

Imaging system mainly includes a visible light camera (Cannon EOS 1300D), Hong Xing Yang electric rotating platform, 4 pieces of the LED face plate, a programmable logic controller and computer system objects are shown in Fig. 1. A fixed camera on a tripod, height and back angle of depression all can be adjusted according to actual condition. Rotating platform can be rotation angle according to need and time interval set.



Fig. 1 – Imaging system

In this paper, Zhang Zhengyou calibration method (*Zhou, et al., 2009*) was used to obtain the internal and external parameters and distortion coefficient of the camera to correct the camera. The plants were placed on the rotating platform, and the camera was used to take photos of millet. Different intervals were selected at 1°, 2°, 3°, 5°, 10° and 15°, respectively, and six groups of millet photos with different sequences were obtained. When taking photos, the distance between the camera and the position between the plants should be kept within 25 cm, and all the leaves of the plant should be in the field of view of the camera. Rotate once each time, and take photos when all the leaves of the plant do not shake.

3D reconstruction method

In image-based 3D reconstruction of crops, images are acquired by camera, then sparse reconstruction based on motion recovery structure is carried out, and then the reconstructed sparse point cloud is reconstructed based on faceted multi-view stereo geometry. Finally, point cloud filtering is carried out to obtain clear 3D point cloud image.

The main algorithm principle is as follows:

Sparse reconstruction based on SfM

Feature detection and matching: it is the first step of 3D reconstruction to efficiently and accurately detect and match feature points in the image. The feature points of the image are composed of key points and descriptors. Key points are feature points with image location information, some of which also have direction and scale information. Descriptors are used to describe the information of pixels around key points. Generally speaking, the design principle of descriptors is that similar descriptors should be designed according to similar features in appearance. Therefore, when matching, two feature points can be regarded as the same feature points as long as their descriptors are close in the vector space (*Steve H. et al., 2015*).

The detection and matching steps of feature points are as follows: firstly, extract the pixel of feature in the image. The scale-invariant feature transform (SIFT) algorithm was adopted to construct scale space by differential Gaussian convolution of images at different scales (*Lowe D., 2004*). Non-maximum suppression was used to determine the feature points, remove the low contrast points, and then remove the edge points by Hessian matrix, and then determine the main direction of the feature points. Finally, descriptors of feature points are calculated according to the key points obtained. In order to keep the invariance of scale, when calculating the descriptors of feature points, the image is usually transformed to a unified scale space and scale factors are added. Similar to scale invariance, in order to maintain rotation invariance, the direction information of key points is added to the calculation of feature point descriptors. Finally, the matching is carried out according to the descriptors of feature points.

Basic matrix estimation

There are polar geometric constraints for the same point in different images (*Qi Z. et al., 2018*). Antipolar geometry is the internal projective geometry between two views, independent of landscape structure and dependent only on the internal and external parameters of the camera. Essentially, the antipolar geometry between two views is the geometry of the intersection between the image plane and the plane bundle whose axis is the baseline (the line connecting the centers of the two cameras).

As a mathematical expression of the polar geometry constraint, the basic matrix only depends on the internal and external parameters of the camera, and the specific expression is as follows:

$$F = K^T t \times RK^{-1} \quad (1)$$

where:

K represents the internal parameter of the camera, R and T represent rotation and translation of the camera.

Essential matrix estimation

The intrinsic matrix is obtained by removing the camera's internal parameters from the basic matrix. Its purpose is to constrain the matching obtained before, and the matching obtained becomes geometric consistent matching. The specific expression of the intrinsic matrix is as follows:

$$E = t \times R \quad (2)$$

Three-dimensional point cloud computing

Using the known coordinates of the matching points and the internal and external parameters of the camera, the 3D coordinates of the matching points are restored. Through iterative calculation, new images are constantly added, and the sparse point cloud of millet is finally obtained.

PMVS Patch-based Multi-view Stereo (MVS)

Since sparse point cloud contains less information, dense reconstruction is needed to obtain the dense point cloud of millet. The basic idea of MVS is to find the point of image consistency among different images in an image sequence. MVS can be divided into three categories (*Seitz S., 2006*): dense reconstruction based on voxel, the rest on another, and dense reconstruction based on fusion of dense depth map reconstruction, including the rest based on another dense reconstruction does not require any initial information, such as initial bounding box or initial parallax scope, its applicable scope is very broad, so this paper selected based on the dense reconstruction.

As shown in Fig. 2 in the dense reconstruction based on the plane, the plane P is determined by its center $C(p)$ and the unit normal vector $N(p)$ pointing to the camera shooting it. A reference image $R(p)$ is associated with each facet P, and $R(p)$ selects the image that is nearly parallel to the facet P, which has the smallest distortion. Conversely, the reference plane determines the orientation and scope of the rectangle, perpendicular to $n(p)$, so that the projection of one of its edges in $R(p)$ is parallel to the image pixel row, and its corresponding minimum area in $R(p)$ is $\mu \times \mu$. One is $S(p)$, which means P is visible in the image, but there is an image that is not easy to be recognized or blocked by objects. $T(p)$ represents the image where P is really seen, and $R(p)$ is naturally contained in $S(P)$. Two strong constraints are added to the plane model. First, the constraint of local width consistency is added to require the projection texture of each plane P to be continuous on at least γ images. Second, to add global visual consistency, it is required that the surfaces do not block each other in $S(p)$.

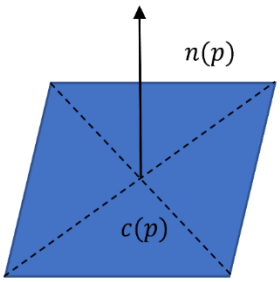


Fig. 2 – Sketch map

Each image I was associated with a regular cell $C(I,J)$, whose size was $\beta_i \times \beta_i$ pixels, trying to correspond to a facet for each cell, as shown in Fig. 3 Cell $C\ (I,j)$ tracks two different sets of reconstructed facet sets $Q_I(i,j)$ and $Q_f(i,j)$, among which two facet sets may be visible in $C(i,j)$: if $I \in T(p)$, another is stored in the $Q_I(i,j)$, if $I \in S(p)/T(p)$, is stored in the $Q_f(i,j)$. At the same time, associate the surface center of $C(i,j)$ and $Q_f(i,j)$ with the center depth of the camera nearest to it, which is equivalent to assigning a depth map to each image I, which will be used in the subsequent visual calculation.

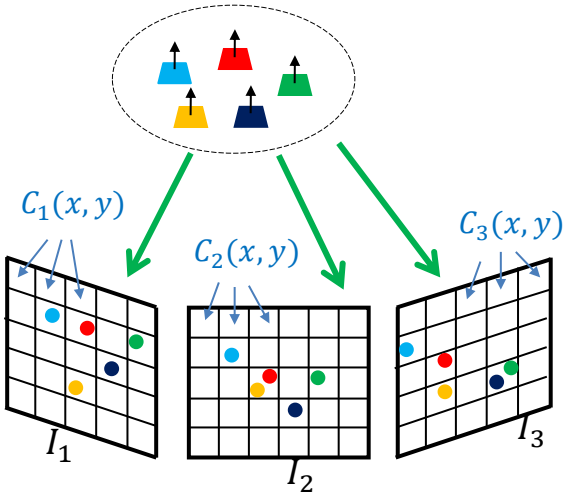


Fig. 3 – Image and cell diagram

Given a surface p, its projection normalized correlation function (NCC) $N\ (p, I, J)$ on two images I and J is used to measure their gray consistency. Given a surface p, its reference image is $R(p)$, and the image set $T(p)$ of truly visible p can be calculated by maximizing its average NCC value to find the position $C(p)$ of the surface and its normal vector $n(p)$.

$$\bar{N}(p) = \frac{1}{|T(p)|-1}\sum_{I\in T(p),I\notin R(p)} N(p,R(p),I) \quad (3)$$

In order to simplify the calculation, $c(p)$ is appointed to simplify the worthiest problem into three dimensions on the ray composed of the optical center of the reference camera and the corresponding image points, that is, to obtain the depth and the yaw Angle and pitch Angle of the normal vector $n(p)$ on the ray, and then obtain the group optimization parameters by using the conjugate gradient method. In the actual calculation, a simple method is used to obtain initial estimates of $c(p)$ and $n(p)$.

The above process is based on the assumption that the surface of the scene or object is a diffuse reflection surface, but when the object or scene reflection surface is specular reflection or there are obstacles, the above method cannot obtain the ideal effect. The influence of the non-diffuse plane can be reduced by ignoring the images with smaller normalized cross-correlation mean value. That is, a threshold α is set in advance, and the image will be adopted only when the luminosity difference between the image and its reference image $R(p)$ is less than the threshold α.

$$N^*(p,R(p),I) = \{I|I \in T(p), N(p,R(p),I) \le \alpha\} \quad (4)$$

$$\bar{N}(p) = \frac{1}{|T(p)|-1}\sum_{I\in T(p),I\notin R(p)} N^*(p,R(p),I) \quad (5)$$

By limiting the brightness difference value, the algorithm effectively avoids the occurrence of non-diffuse reflection or obstacles in the image $R(p)$.

The visibility of each facet is determined by the set of images $S(p)$ and $T(p)$ from which it can be seen (partially or truly visible). In the process of dense reconstruction, two slightly different methods are used to reconstruct $S(p)$ and $T(p)$ respectively. After the matching stage is completed, the surface is reconstructed by matching features, and the visibility of the surface must be determined by the consistency of gray level. Specifically, the image whose NCC value of the connected image set exceeds a certain threshold value is initialized.

$$S(p) = T(p) = \{I|N(p,R(p),I) > \alpha_0\} \quad (6)$$

On the other hand, in the diffusion process, the surfaces are associated with the depth of the left and right images after sufficiently dense reconstruction, and for each surface, $S(p)$ is obtained by specifying a threshold value for its depth. That is: $S(p) = \{I|d_I(p) \le d_I(i,j) + \rho_1\}$. Where $d(p)$ is the ray depth of P on corresponding image I, $d_I(i,j)$ is the depth in cell $C(i,j)$ related to image I and plane p, and ρ_1 is the distance at depth $C(p)$ after the displacement β_1 of corresponding image $R(p)$. Once S(p) is estimated, gray consistency is used to determine where the plane P is actually seen.

Through $T(p) = \{I \in S(p)|N(p,R(p),I) > \alpha_1\}$ is Confirmed, this method requires the reference image $R(p)$ to be the real p, otherwise this method will fail. In order to avoid this situation, relevant methods to deal with this problem will be introduced later in this paper. The reliability and consistency of visual information can also be improved by iterative matching and filtering.

PMVS algorithm needs to establish at least one facet for each image cell $C(i,j)$, and this process mainly has three steps:

✓ Firstly, feature matching. The motion recovery structure algorithm can obtain the sparse point cloud structure and camera parameters of the scene. Therefore, the output of the motion recovery structure algorithm is used as the input in this study to complete the process of initialization of sparse surface slices without feature extraction and matching. According to the sparse point cloud information, the root node of the octree can be initialized, that is, a cube that just completely covers the sparse point cloud.

✓ Secondly, surface diffusion, in which a sparse set of surfaces is obtained from a dense set of surfaces, that is, new surfaces are added around existing surfaces by iterative method until they cover the entire surface of the object or scene. More intuitively, given two faces p and p', if they are stored in adjacent cells $C(i,j)$ and $C'(i,j)$ of the same image I, and their tangent planes are adjacent, the two faces are said to be adjacent and only new adjacent faces are created where diffusion is necessary, i.e., the face set $Q_i(i',j')$ is empty, and there are no elements in $Q_f(i',j')$ and p is n adjacent relation, where the n nearest neighbor relation of p and p' is:

$$|(c(p)-c(p'))\cdot n(p)|+|(c(p)-c(p'))\cdot n(p')|<2\rho_2 \quad (7)$$

The calculation method for ρ_1 is the same as that for ρ_2, which is the corresponding distance where the midpoint of $c(p)$ and $c(p')$is depth after $R(p)$ shift β_1 of the corresponding image.

✓ Thirdly, surface filtering: The purpose of filtering is to remove the surfaces inside and outside the scene or object surface and get an accurate dense point cloud model. Filtering has two steps, further implementing the principle of viewpoint consistency in the front diffused and reconstructed surfaces and removing false matching the first filter is to remove the surfaces outside the real scene or object surface. Suppose there is a sheet p_0, belonging to the set of sheets U containing it. Remove sheet p_0 if sheet p_0 satisfies the following equation. More intuitively, if sheet p_0 is an external value, then the value of $N(p_0)$ and $T(p_0)$ should be small and p_0 is more likely to be removed. The second filter is to remove objects in the scene or real internal surface, using the image depth map, related recalculate the rest for each another $S(p_0)$ and $T(p_0)$, when $|T(p_0)|<\gamma$, remove p_0. Notice that the way you compute $S(p_0)$ and $T(p_0)$ is different from the way you get them in the diffusion process, because after the reconstruction of p_0, more p_0 has been reconstructed.

Finally perform a weak regularization process: p, rest for each another statistical image set $S(p)$ contains its cells and facets in surrounding cells, cell and around for n and p in rest if a group of another neighbor is less than the proportion of the $\varepsilon=0.25$, p was removed as a value outside the threshold of α_1 initial value is 0.7, the diffusion and filtering iterative steps after the completion of the threshold value of α_1 set the value of 1.

$$|T(p_0)|\bar{N}(p_0)<\sum_{p_j\in U}\bar{N}(p_j) \quad (8)$$

The dense point cloud of millet was obtained by using PMVS algorithm for sparse point cloud structure obtained by SfM and internal and external parameters of camera.

Conditional filter and statistical filter remove noise points

There are a large number of noise points in Formula 8. Only by removing noise points, outliers and holes in filtering pretreatment, can the subsequent steps such as registration, feature extraction and surface reconstruction be better carried out. In this paper, conditional filtering and statistical filtering are used to remove noise points.

RESULTS AND DISCUSSION

Influence of interval angle on point cloud precision

The data sets of the images of the three millet varieties in the same growth cycle were named as Dabaigu_ n, Jingu 21_ n and Yuanping Xiaogu_ n according to different rotation interval angles (n=1,2,3,5,10,15) and n is the interval angle between two adjacent pictures of the dataset. By 3D reconstruction of 18 datasets, the effects of different varieties on the reconstruction accuracy at different intervals were tested.

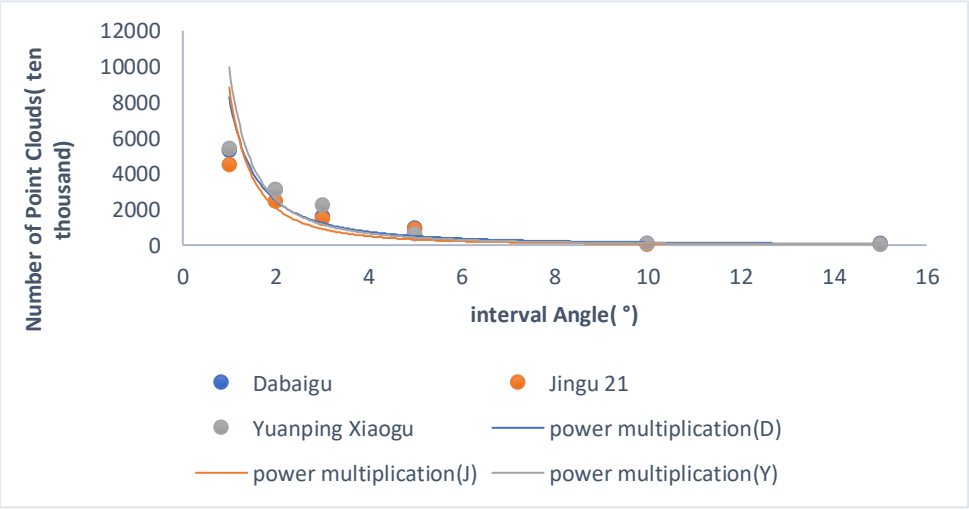


Fig. 4 - Number of point clouds for different varieties of millet at different intervals

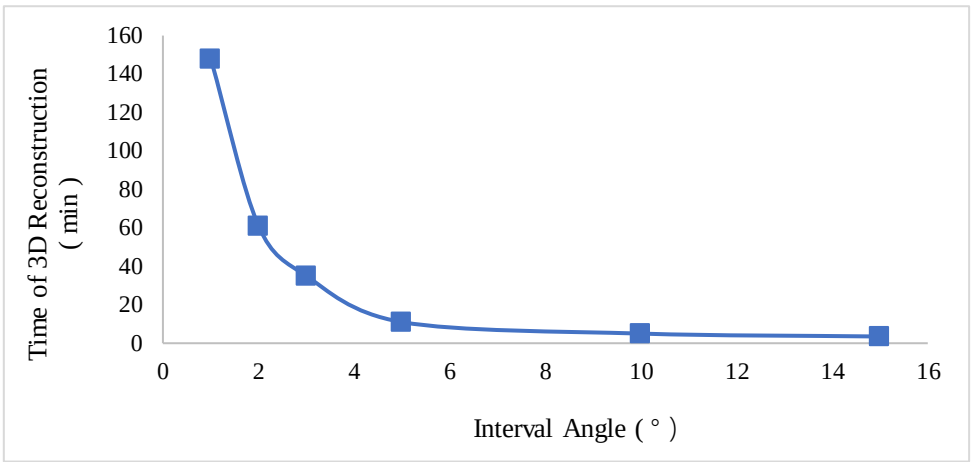


Fig. 5 - Time of 3D reconstruction of millet at different intervals

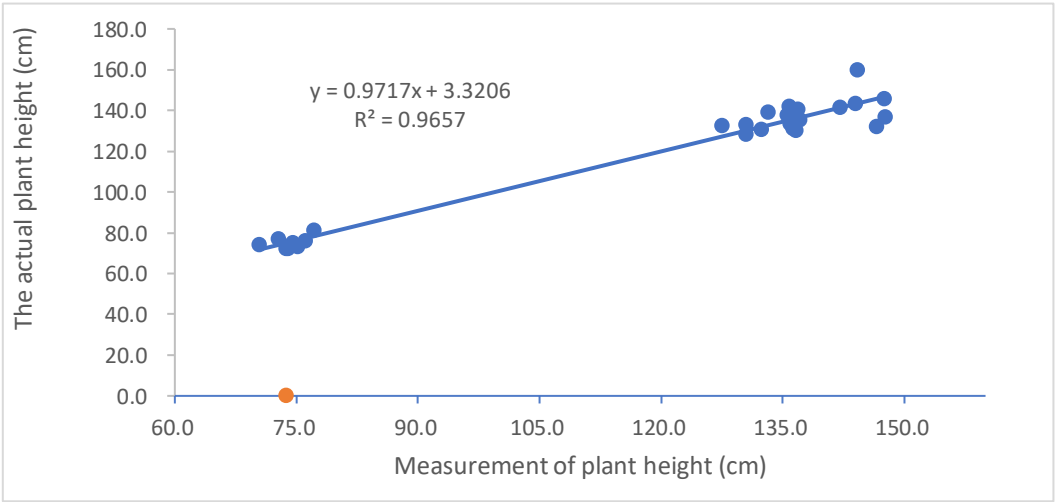
It can be seen from Fig.5 that the smaller the interval angle, the more reconstructed views, the more points of the reconstructed result cloud, and the closer the reconstructed result is to the reality. According to Figures 5 and 6, when the interval angle is less than 5, the number of point clouds keeps increasing, but the running time of the program will increase significantly. Therefore, considering the processing time and point cloud precision comprehensively, interval angle 5 is the best reconstruction interval angle.

Measurement of millet phenotype

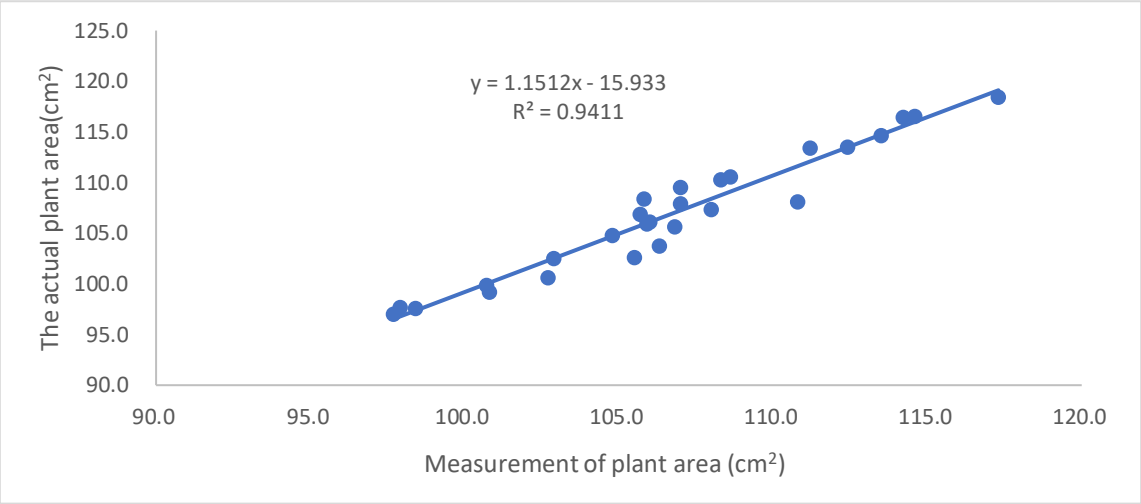
In this paper, 3D reconstruction was carried out for the three varieties at jointing stage, heading stage and filling stage, and 9 plants were selected in each stage and 81 plants in total were photographed for reconstruction. Each plant was photographed at an interval Angle of 5. A total of 72 photos were taken to obtain three-dimensional point cloud reconstruction, and the obtained point cloud data were used to calculate the plant height, leaf area and other agronomic traits of the samples.

Phenotype measurement method

The phenotypic traits measured in this paper were defined as follows: Plant height is from the highest point of the plant to the edge of the planting pot. The leaf area is the sum of leaf areas of all point clouds on each leaf of millet. 3D reconstruction of three varieties of millet was carried out to obtain the corresponding point cloud data, and the point cloud data was used to measure the phenotype of millet. The 3D measured area and manual measured area (real area) as well as the 3D measured plant height and real plant height of the three varieties of millet were regression, as shown in Fig. 5. It can be seen from the figure that the coefficient $R2$ between the measured leaf cumulus cloud area and the artificial real measured area of Dabaigu, Yuanping Xiaogu and Jingu 21 are 0.94, 0.94 and 0.94 respectively; The coefficient $R2$ between the measured cloud height and the measured artificial height were 0.97, 0.97 and 0.96; The correlation between them was tested and the results showed that the correlation was significantly different at the level of 0.05. It is proved that the high throughput measurement of plant height and leaf area by three-dimensional model has high accuracy.

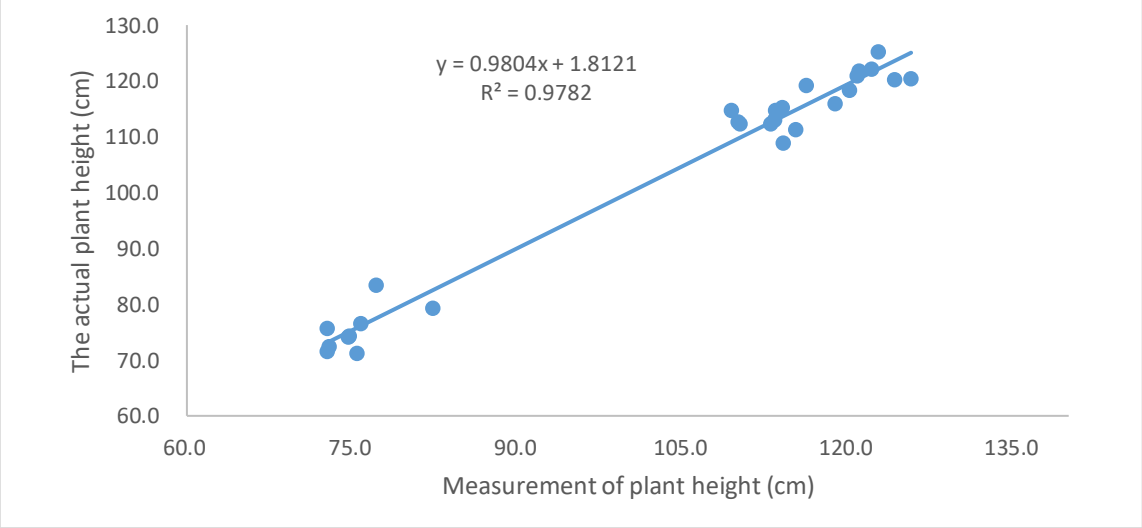


a)



b)

Fig. 6 - Comparison of 3D measurement data of Jingu 21 with real data



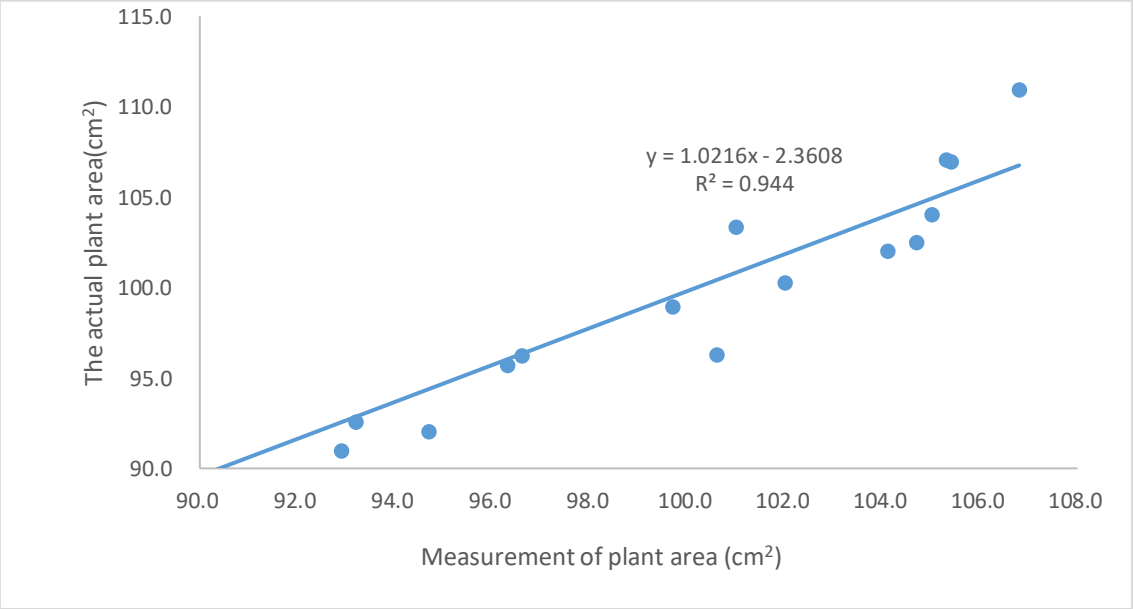


Fig. 7 - Comparison of 3D measurement data of Yuanping Xiaogu with real data

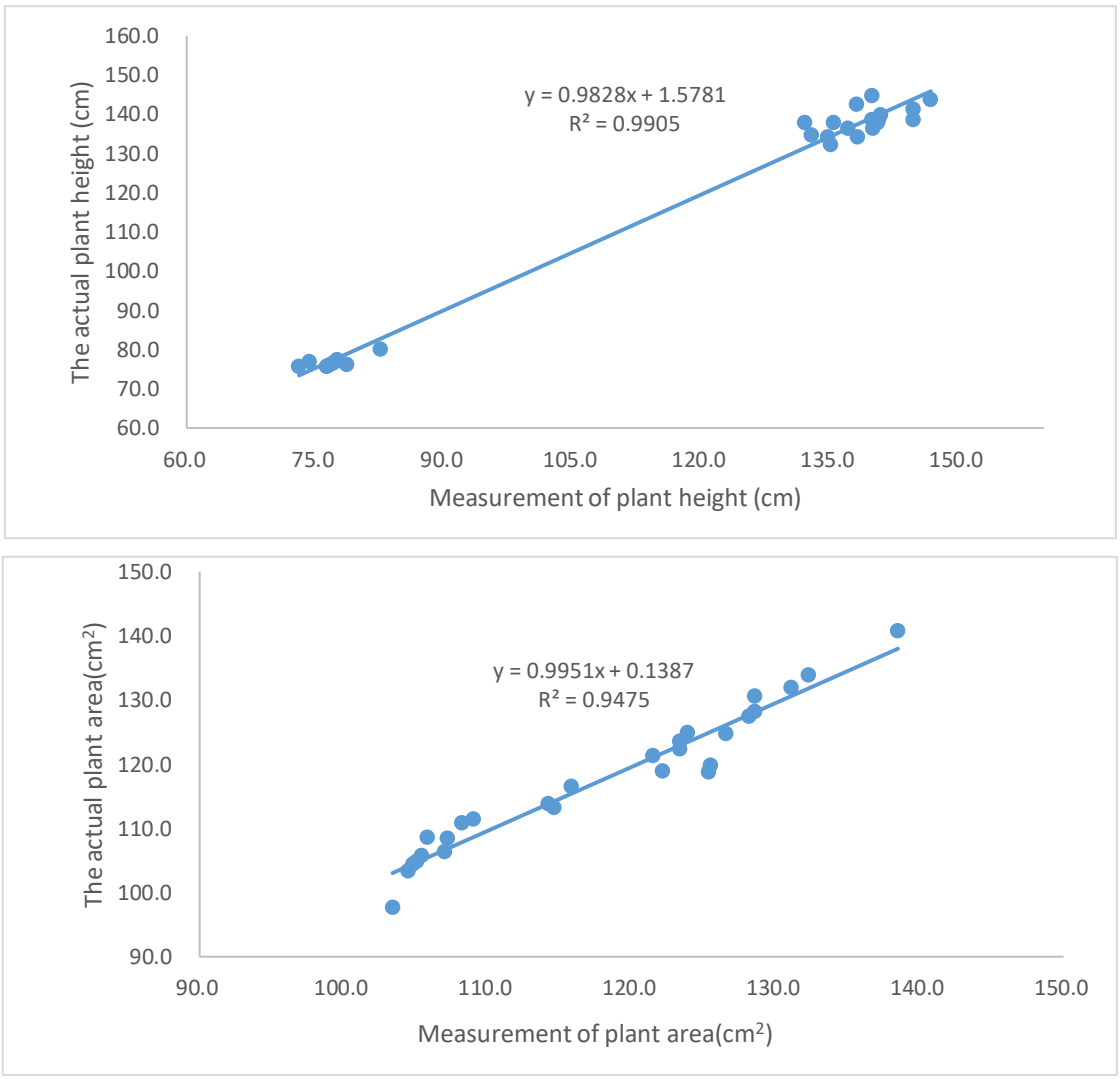


Fig. 8 - Comparison of 3D measurement data of Dabaigu with real data

Table 1

Analysis of phenotypic differences between varieties

Variety	Leaf area (cm2)	Plant height (cm)
Dabaigu	113.87 a	123.30 a
Yuanping Xiaogu	103.69 b	104.58 b
Jingu21	92.33 c	100.20 b

Note: Different lowercase letters in the same column indicate a significant difference of P<0.05.

As can be seen from Table 1, at the significant level of 0.05, the difference in leaf area among the three varieties was caused by the difference among varieties, and the difference in plant height among Dabaigu, Yuanping Xiaogu and Jingu 21 was caused by the difference among varieties.

CONCLUSIONS

This paper studies a method to reconstruct three-dimensional point cloud of millet by image sequence. The method uses SfM and PMVS to carry out 3D reconstruction of millet, and uses conditional filtering and statistical filtering to filter the point cloud of millet. Through the comparison of the reconstruction accuracy and speed of the shooting data set of 3 different millet varieties with different interval angles, it was concluded that when the shooting interval was 5, the reconstruction accuracy of millet met the experimental requirements and the time was faster. Then, the 3D point cloud data of millet was used to analyze the plant height of millet, nondestructive measurement of leaf area, and regression analysis and manual analysis of the measured data.

When the spacing Angle was 5, the determining coefficients of plant height and leaf area of three kinds of millet were higher. In conclusion, the method adopted in this paper has high applicability to millet samples of different varieties and different periods, and provides a reliable basis for the analysis of 3D phenotypic traits of millet. However, the parameters measured in the study are still few, and further research is needed on how to obtain the number of leaves and canopy structure of millet from point cloud data.

ACKNOWLEDGEMENT

The authors were funded for this project by the Major research and development Projects of Shanxi Province, China (2022ZDYF127), the Basic Research Project of Shanxi Province (202103021224123) and Science and Technology Innovation Fund Project of Shanxi Agricultural University(2018YJ43).

REFERENCES

[1] Collier S., Paschke P., Kay R. R., et al. (2017). Image based modeling of bleb site selection. *Scientific Reports*, Vol.7, pp. 6692, UK.

[2] Gao T., Zhu F., Paul P., et al. (2021). Novel 3D Imaging Systems for High-Throughput Phenotyping of Plants. *Remote Sensing*, Vol. 13, pp. 2113, China.

[3] He J. Q., Harrison R. J., Li B. (2017). A novel 3D imaging system for strawberry phenotyping. *Plant Methods*, Vol. 13, pp. 93 UK.

[4] Lowe D. (2004) Distinctive image features from Scale-Invariant Keypoints. *International Journal of Computer Vision*, Vol. 60, pp. 91-110, UK.

[5] Qi Z., Wang Z., Huang J, et al. (2018) Invalid-point removal based on epipolar constraint in the structured-light method. *Optics and Lasers in Engineering*, Vol. 105, pp.173-181, China.

[6] Qiu Q., Sun N., Bai H., et al. (2019). Field-Based High-Throughput Phenotyping for Maize Plant Using 3D LiDAR Point Cloud Generated With a "Phenomobile". *Frontiers in plant science*, Vol. 10, pp. 554, China.

[7] Rupnik E, Pierrot-Deseilligny M, Delorme A. (2018). 3D reconstruction from multi-view VHR-satellite images in MicMac. *Isprs Journal of Photogrammetry and Remote Sensing*, Vol. 139, pp. 201-211, France.

[8] Schipper, R., van der Meer, M., de Visser, P. H. B., et al. (2023). Consequences of intra-canopy and top LED lighting for uniformity of light distribution in a tomato crop. *Frontiers in plant science*, Vol.14, pp. 1012529, Netherlands.

[9] Seitz S. (2006) A comparison and evaluation of multi-view stereo reconstruction algorithms. *Proceedings of the 2006 IEEE Computer Society Conference on Computer Vision and Pattern Recognition (CVPR'06)*, Vol.1, pp. 519-526, US.

[10] Steve H., Arko L., Jon O. (2015) The Impact of the Calibration Method on the Accuracy of Point Clouds Derived Using Unmanned Aerial Vehicle Multi-View Stereopsis. *Remote Sensing*, Vol.7, pp. 11933-11953, Australia.

[11] Syngelaki M, Hardner M, Oberthuer P, et al. (2018) A new method for non-invasive biomass determination based on stereo photogrammetry. *Bioprocess and Biosystems Engineering*, Vol. 41, pp.369-380, China.

[12] Wen, W., Wang, Y., Wu, S., et al. (2021). 3D phytomer-based geometric modelling method for plants-the case of maize. *Frontiers in Plant Science*, Vol. 13, plab055, China.

[13] Xiang L, Bao Y, Tang L, et al. (2019). Automated morphological traits extraction for sorghum plants via 3D point cloud data analysis. *Computers and Electronics in Agriculture*, Vol. 162, pp. 951-961, China.

[14] Xu B., Yang L. F., Lei B., et al. (2017). A Study of the Accuracy Improvement Strategy for Multi-view 3D Reconstruction Instrument Based on Automatic Calibration Technology. *Acta Geoscientica Sinica*, Vol. 38, pp. 243-248, China.

[15] Zhou F. Q., Cai F. H. (2009), Camera Calibration Method Based on Non-metric Distortion Correction. *Journal of Mechanical Engineering*, Vol.45, pp. 228-232, China.

STATISTICAL ANALYSIS OF FATIGUE DAMAGE LIFE OF CORN KERNELS
/
玉米籽粒疲劳损伤寿命统计分析

Bolong WANG [1], Zhiyong LIN [1], Mingjie GAO [1], Guohai ZHANG [1], Duanyang GENG [1], Zhou SHI [2※]
[1] School of Agricultural Engineering and Food Science, Shandong University of Technology, Zibo 255091, China
[2]School of Mechanical Engineering, Shandong University of Technology, Zibo 255049, China
Tel: +86-15553346919; E-mail: shizhou2023@163.com
DOI: https://doi.org/10.35633/inmateh-69-56

Keywords: *fatigue damage; quasi-brittle fracture; fitted equation; normal distribution*

ABSTRACT
It is urgent to study the damage mechanism of corn kernels and find ways of reducing the rate of kernel breakage in mechanical threshing. This paper, by studying the mechanical curves and deformation characteristics of corn kernels with different moisture contents, points out the brittle mechanical characteristics of corn kernel damage fracture with low moisture content, and clarifies the variation law of mechanical properties of kernels with moisture contents. The experimental data of fatigue load - fatigue life curves of corn kernels with different moisture contents were described by the power function equation. At the same time, the fatigue life and damage characteristics of kernel with different moisture content were analyzed, and the accuracy of the fitting equation was verified. Through mathematical statistical analysis, the normal distribution curve of fatigue life was fitted, and the variation law of normal distribution curve with moisture content and fatigue load was determined.

摘 要
研究玉米籽粒损伤机理，降低籽粒破碎率是当前机械脱粒的热门问题。通过研究不同含水率玉米籽粒的力学曲线与变形特点，确定了低含水率玉米籽粒损伤断裂的脆性力学特点，明确了籽粒力学特性随含水率变化规律。采用幂函数方程描述了不同含水率玉米籽粒的疲劳载荷 F_j-疲劳寿命 N_j 曲线试验数据，对不同含水率籽粒的疲劳寿命及损伤特点进行了分析，并验证了拟合方程结果的准确性；通过数理统计分析，拟合了疲劳寿命正态分布曲线，确定了正态分布曲线随含水率、疲劳载荷的变化规律。

INTRODUCTION
Corn is the most productive food crop in the world, which has been planted in more than 170 countries and regions. In 2021, about 206.77 million hectares of corn were planted worldwide *(Geng D. et al., 2019; Wang J. et al., 2019; Zhang C.G., 2016)*. Corn is not only one of the world's three major staple crops, but also an important raw material for medicine, chemical industry and light industry, and an indispensable high-quality roughage for animal husbandry. Therefore, corn production plays an important role in world food security, industrial production and animal husbandry development *(Berry N.K. et al., 2014; CHENG M. et al., 2022)*. The comprehensive crushing rate of corn kernel harvest remains high, and there are serious threshing damage and food loss and waste problems *(Chen Z. et al., 2021; Xiangqian D. et al., 2022; Yang Y. et al., 2021; Yin X. et al., 2021)*. Therefore, to explore the low loss threshing technology of corn grain, reduce the loss of corn grain harvest and improve the efficiency of agricultural production, is the current research hotspot and difficulty in the field of agricultural engineering.

The mechanical property of corn kernel is a key index to study corn threshing damage, which provides a data basis for the design of corn threshing device, and many scholars have conducted a lot of research on this *(Chen Z. et al., 2022; Kruszelnicka W. et al., 2021 Yiren Q. et al., 2022)*. Brass, Srivastava and Kustermam et al. conducted impact and shear tests on corn kernels, respectively, and initially determined the modulus of elasticity of corn kernels, and proved that the moisture content has a significant effect on the performance of corn kernels *(Geng D. et al., 2017; Shi Z. et al., 2018; Zhang X. et al., 2015)*.

[1] *Wang Bolong, As. Ph.D. Eng; Lin Zhiyong, M.S. Stud. Eng; Gao Mingjie, M.S. Stud. Eng; Zhang Guohai, As. Ph.D. Eng; Geng Duanyang, As. Ph.D. Eng;Shi Zhou As. Ph.D. Eng.*

Volkova's, Mohamed et al. conducted a detailed study on the impact resistance of corn kernels, obtained the corresponding loading force-deformation curves, and conducted a preliminary study on the crushing pattern of corn kernels *(Shahbazi F. et al., 2012; Zhang X. et al., 2015; Zhang Y.L. et al., 2007)*.

Gao Lianxing's group at Shenyang Agricultural University conducted experiments on the hydrostatic breaking, impact mechanical properties, and threshing characteristics of corn seed kernels *(Li X. et al., 2007; Liu M. et al., 2013; Zhang Y.L. et al., 2007)*. Li Xinping's group at Henan University of Science and Technology, Zhao Wuyun's group at Gansu Agricultural University have studied the mechanical properties of a corn cob, breaking laws, and threshing performance on seeds *(Li X., 2010; Putri R E.et al., 2015; Wang B. et al., 2018)*.

MATERIAL AND METHODS

Materials and Instruments

The corn kernels used in all experiments in this paper, with the same moisture content, regular shape and no damage in appearance. After strict detection and screening, the corn variety is Zhengdan 958 (semi-horse-toothed type, thousand kernel weight 307 g).

The main experimental instruments are Olympus SZX16 microscope, microcomputer controlled electronic testing machine WDW-100M, Instron 8872 fatigue testing machine, etc.

Research Methodology

The research route used in this paper is shown in Figure 1.

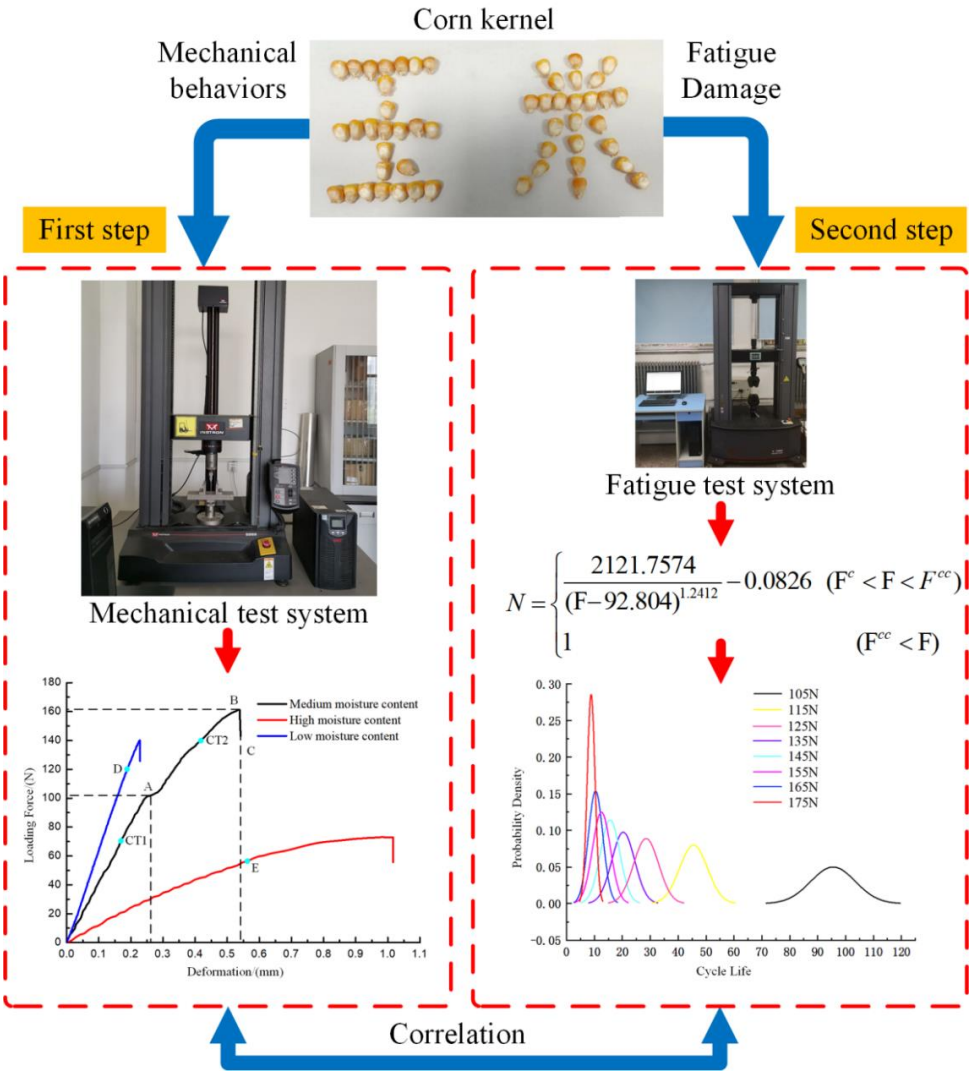


Fig. 1 - Research roadmap of corn kernel

By studying the macro-mechanical properties and fatigue damage of corn kernels with different moisture contents, the variation law of the mechanical properties and deformation characteristics of corn kernels with moisture content are obtained, and the fatigue life-fatigue load of corn kernels is clarified, which provides theoretical guidance for the structural improvement of corn kernel harvesters and harvesting methods.

RESULTS AND DISCUSSION

Mechanical properties of corn kernels

The mechanical curves of corn kernels with different moisture contents were measured by the Mechanical test system. Figure 2 shows the mechanical curves of three kinds of corn kernels with high, medium and low moisture contents, of which the three moisture contents were 30%, 21%, and 14%, respectively. It can be seen from the figure that the mechanical curves of corn kernels with different moisture contents vary greatly, which shows that the moisture content has a great influence on the deformation characteristics of corn kernels.

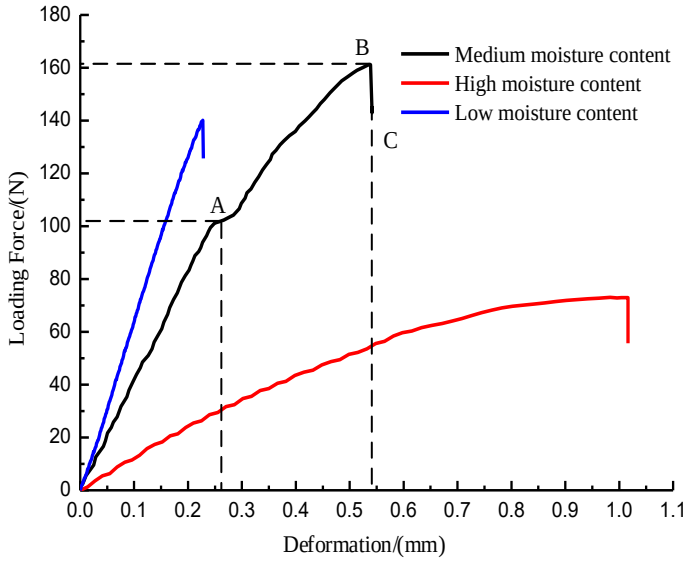


Fig. 2 - Loading force-deformation curve of corn kernels

According to Fig.2, compared with the other two moisture contents, the mechanical curve of corn kernel with 21% moisture content has obvious stages, which can be divided into three stages: 0A, AB and BC.

(1) Linear elasticity stage (0A segment):

When the loading force F on the corn kernel is less than the critical load F^c (not reaching point A), defects such as micro-cracks and voids in the corn kernel cannot break through the bond between starch granules and the protein between the granules after being stressed, and continue to develop to form macroscopic defects. Therefore, in this stage, the internal defects of corn kernels basically do not absorb energy, and damage evolution basically does not occur. During this stage, the macro mechanics of corn kernels is linear elasticity.

(2) Nonlinear strain-hardening stage (AB segment):

When the loading force F on the corn kernel exceeds the critical loading force F^c (above point A), but is lower than the maximum loading force F^{cc} of the corn kernel, the internal defects of the kernel absorb energy, and the micro-cracks break through the bonding of starch particles and proteins. Hence, more and more micro-cracks will grow steadily, and the crack radius will gradually increase. However, the majority of cracks will stop growing as they hit a stronger interface, and one or even a few cracks will continue to grow and expand through the section, and continuous damage will occur inside the corn kernel. Therefore, the loading force -deformation exhibited a nonlinear relationship and the corn kernels produced some plastic deformation.

(3) Loading force drop stage (BC section):

When the external loading force F exceeds the maximum loading force F^{cc}, the internal defects formed in the AB segment will rapidly develop into macroscopic cracks and cause the corn kernel to change from continuous damage to local damage. On the macroscopic level, the bearing capacity of corn kernels decreases rapidly, and one or more macroscopic cracks are formed due to the development and evolution of micro-cracks, and the kernels will be completely broken.

It can be seen from the above that the mechanical and deformation characteristics of corn kernels with medium moisture content conform neither to the mechanical properties of brittle materials, nor to the mechanical properties of ductile materials. They conform to the mechanical properties of quasi-brittle materials. The mechanical curves of corn kernels with high moisture content and low moisture content are shown in Fig.2.

It can be seen that from the beginning of loading to the breaking of the kernels, corn kernels with low moisture content basically manifested a linear change, while those with high moisture content exhibited a nonlinear relationship. High moisture content corn kernel micro-defects are gradually growing and internal damage is gradually developing and evolving into macro-cracks, which eventually lead to kernel breakage.

Fatigue damage of corn kernels

In this part, the fatigue life and damage evolution of corn kernels under continuous external loading force F will be discussed.

Fatigue damage life of corn kernels

To study the damage of corn kernels under continuous external loading forces, it is necessary to first define a dimensionless damage function D, which is a function of the number of cycles n and the damage life $N(F)$. The function satisfies the boundary conditions,

$$\begin{aligned} D(0,N) &= 0 \\ D(N,N) &= 1 \end{aligned} \tag{1}$$

Under one action of external loading force F, the damage is $D(1,N)$, where N is the fatigue life. Theoretically, at the critical load F^c, N should be infinite. But the actual damage performance still needs to be verified by a large number of experiments.

(1) No damage stage:

When the external loading force is lower than F^c, it can be cycled for infinite times, but when the external loading force is higher than F^c, it can be cycled for a limited number of times. In this paper, the validation experiments were conducted in 100 sets using corn kernels with 21% moisture content and 40N external loading force. The results showed that the kernels all produced significant macroscopic damage when the cycles exceeded 500 times. This is because corn kernels are not ideal isotropic homogeneous materials, and there are microscopic defects inside the kernels, which will gradually undergo meso damage after the force is applied. Therefore, even if the degree of damage is small, macroscopic damage can occur when the cycle is large enough.

(2) Fatigue damage stage:

The corn kernels with two different moisture contents (21% and 30%) are used in this part of the experiment and the comparison experiment is conducted between the corn kernels with two moisture contents. 100 groups of fatigue damage experiments on corn kernels were conducted under each fatigue load F_j, and these 100 groups of life were averaged to obtain a set of average life data N_j corresponding to F_j. Table 1 and Table 2 show the data from fatigue damage experiments of corn kernels with 21% and 30% moisture content respectively. The smaller the fatigue life, but the fatigue life of corn kernels with different moisture contents under different loading forces still needs further analysis, and there is no qualitative conclusion on the law of fatigue damage accumulation of corn kernels. Therefore, further research is needed on the data in the tables.

Table 1

Experiment on fatigue damage of corn kernels with 21% moisture content

Fatigue load F_j (N)	Average fatigue life (Time)	Maximum fatigue life (Time)	Minimum fatigue life (Time)
105	95.5	117	80
115	45.3	60	35
125	28.5	42	22
135	20.3	33	15
145	15.6	26	11
155	12.5	22	9
165	10.4	18	6
175	8.8	13	2

Note: *"Time" means the number of times*

Table 2

Experiment on fatigue damage of corn kernels with 30% moisture content

Fatigue load F_j （N）	Average fatigue life（Time）	Maximum fatigue life（Time）	Minimum fatigue life（Time）
20	69.6	83	52
30	20.9	28	14
40	10.4	15	7
50	6.4	10	4
60	4.3	7	2
70	3.2	5	1

Fig.3 and Fig.4 are the fatigue load F_j and fatigue life N_j curves of corn kernels with 21% and 30% moisture contents respectively. Combining the characteristics of the curves shown in the figures and the results of the previous research on corn kernel damage, the curves can be estimated and described by the power function equation:

$$(N + a)(F - F_0)^m = C \tag{2}$$

Where: N is the fatigue life; F is the external loading force; F_0 is the linear elastic/non-linear elastic transition critical load F^c; a, m, F_0, and C are all undetermined constants.

After taking the logarithm of the above equation, the following equation can be obtained:

$$log(N + a) + m\, log(F - F_0) = log\, C \tag{3}$$

In the double logarithmic coordinate system, $log(N+a)$ and $log(F-F_0)$ have a linear relationship, where F_0 is the linear elastic/non-linear elastic transition critical load F^c, and a, m, F_0, and C are all undetermined constants. The power function formula is employed to fit the test data of the fatigue load F_j curve and the fatigue life N_j curve to maximize the correlation coefficient of the linear fitting.

Through calculation, the constants of corn kernels with 21% and 30% moisture contents can be obtained respectively: "a=0.0826, m=1.2412, F_0=92.8404, C=2121.7574" and "a=0.1343, m=1.6540, F_0=10.6047, C=2836.2839". At this time, the $log(N+a)$ and $log(F-F_0)$ linear correlation coefficients R of the corn kernels with two different moisture contents exceeded 0.99. Therefore, the fitting equations of the fatigue load F_j and fatigue life N_j curves of corn kernels with two different moisture contents can be obtained.

Among them, the fitting equation for the corn kernels with 21% moisture content is:

$$N = \begin{cases} \frac{2121.7574}{(F-92.804)^{1.2412}} - 0.0826 & (F^c < F < F^{cc}) \\ 1 & (F^{cc} < F) \end{cases} \tag{4}$$

and the fitting equation for the corn kernels with 30% moisture content is:

$$N = \begin{cases} \frac{2836.2839}{(F-10.6047)^{1.6540}} - 0.1343 & (F^c < F < F^{cc}) \\ 1 & (F^{cc} < F) \end{cases} \tag{5}$$

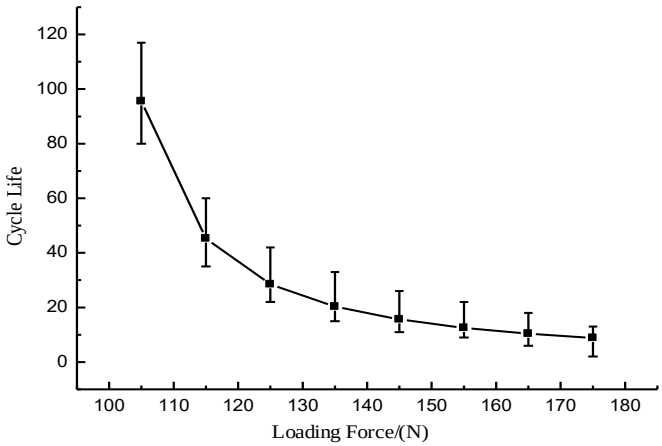


Fig. 3 - Fatigue load-fatigue life curve of corn kernels with 21% moisture content

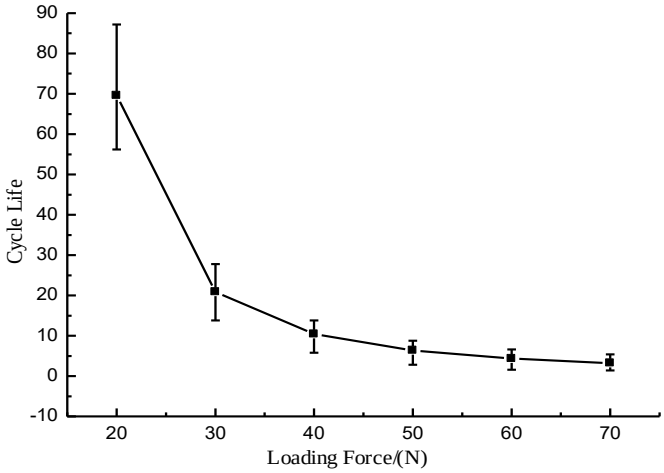


Fig. 4 - Fatigue load-fatigue life curve of corn kernels with 30% moisture content

From the fitting formula, Fig.6 and Fig.7, it can be obtained that in theory, the critical load F^c of linear elastic/non-linear elastic transition caused by damage to corn kernels with 21% moisture content is about 93N and the maximum loading force F^{cc} fluctuates in the ranges from about 170N to 190N; the critical load F^c of linear elastic/non-linear elastic transition caused by corn kernel damage with 30% moisture content is about 11N and the maximum loading force F^{cc} ranges from about 65N to 80N.

Distribution pattern of fatigue damage life

Corn kernels with 21% moisture content were used as experimental samples in this study. The number of cycles was recorded when the kernel was destroyed under a 175N fatigue load, and the number of cycles was statistically analyzed.

The histograms are shown in Fig.5. The arithmetic mean $\overline{x}$ and standard deviation S of the kernel cycle life samples were determined from the following equations.

$$\bar{x} = \frac{1}{n}\sum_{i=1}^{n} x_i \tag{6}$$

$$S = \sqrt{\frac{1}{n-1}\sum_{i=1}^{n}(x_i - \bar{x})^2} \tag{7}$$

Where, x_i is the fatigue life of each kernel, and n is the sample size.

Bringing the groups of data in the histogram into the above formula, the arithmetic mean $\overline{x} = 8.73$ and standard deviation S = 1.64 are obtained, respectively. According to the probability theory, a large number of random variables are independent of each other, and the results are normally distributed. Meanwhile, the individual corn kernels in this part of the study are independent of each other. Therefore, the fatigue life of corn kernel is in accordance with normal distribution, and satisfies $\mu=\overline{x}$, σ=S. The corresponding normal distribution curve is shown in Fig.5, and the expression of the probability density function for the fatigue life can be expressed as:

$$y = \frac{1}{\sigma\sqrt{2\pi}} e^{-\frac{1}{2}(\frac{x-u}{\sigma})^2} \tag{8}$$

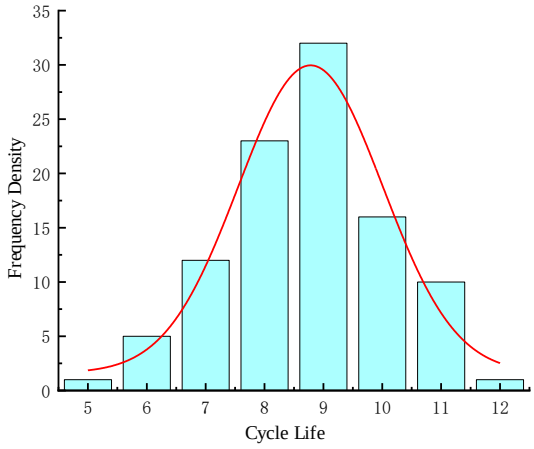


Fig. 5 - Frequency density of corn kernels with 21% moisture content under 175N fatigue load

In order to compare the fatigue life distribution of corn kernels under different fatigue loads, two sets of fatigue experiments were carried out at 21% and 30% moisture content, respectively. The fatigue load and average fatigue life are shown in Table 1 and Table 2, and the fatigue life distribution results of kernels under each fatigue load are shown in Fig.6 and Fig.7. Fig.6 shows the normal distribution of the fatigue life of corn kernels with 21% moisture content under different fatigue loads. It can be seen that, the larger the fatigue load, the smaller the arithmetic mean μ value and standard deviation σ of fatigue life. Fig.7 shows the distribution of fatigue life of corn kernels with 30% moisture content. Similarly, the larger the fatigue load, the smaller the arithmetic mean μ value and standard deviation σ of fatigue life. But compared with 21% moisture content, the arithmetic mean value of fatigue life decreased, and the standard deviation increased. This indicates that the fatigue life distribution of corn kernels is more concentrated, and the upper boundary of fatigue life is closer to the arithmetic mean under the same fatigue life probability density.

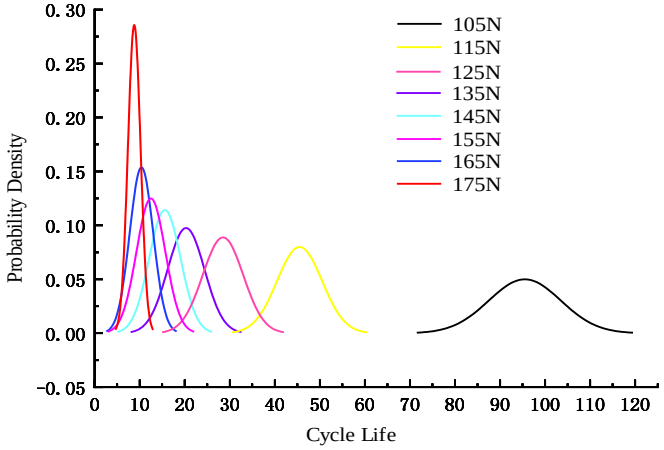


Fig. 6 - Normal distribution curve of fatigue life probability density of corn kernels with 21% moisture content

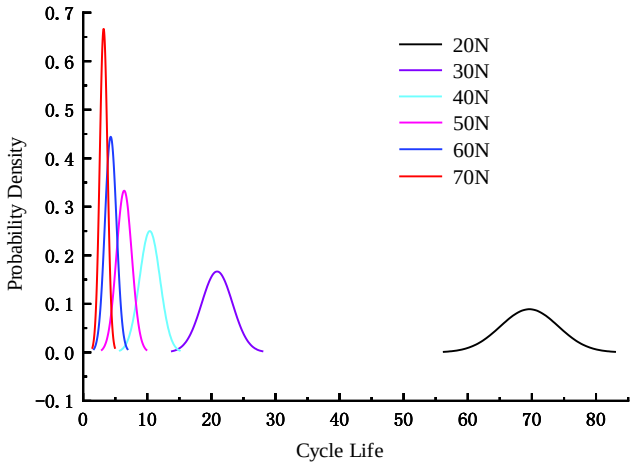


Fig. 7 - Normal distribution curve of fatigue life probability density of corn kernels with 30% moisture content

CONCLUSIONS

(1) By studying the mechanical curves and deformation characteristics of corn kernels, points out the brittle mechanical characteristics of corn kernel damage fracture with low moisture content. With the increase of moisture content, it turns into quasi brittle fracture. And the linear elasticity deformation stage gradually decreased, the maximum loading force that grain can bear increased first and then decreased.

(2) The power function is used to describe the test data of fatigue load F_j and fatigue life N_j curve, and the fitting equation of fatigue load F_j fatigue life N_j curve is obtained, and the accuracy of the fitting equation is verified.

(3) The fatigue life distribution pattern of corn kernels under various loading forces was studied, the normal fatigue life distribution curve was fitted, and the corresponding arithmetic mean and standard deviation were determined. The corresponding arithmetic mean value and standard deviation are determined. The higher the moisture content, the more concentrated the probability density distribution, and the smaller the arithmetic mean and standard deviation.

ACKNOWLEDGEMENT

This work was supported by the National Key Research and Development Program of China (2021YFD2000502,2021YFD200050204), and Shandong Province Modern Agricultural Industrial Technology System Talent Project (SDAIT-02-12).

REFERENCES

[1] Berry N.K, Fielke J.M, Saunders C. (2014), Determination of impact energy to devitalise annual ryegrass (Lolium rigidum) seed from one impact using double and single sided impacts [J]. *Biosystems Engineering*, 118:138–146.

[2] Cheng M., Yanling S U N, Zhuo C, et al. (2022), Effect of low-temperature on the vibration impact comminution performance of wheat bran [J]. *INMATEH-Agricultural Engineering*, 68(3), pp.110-118. https://doi.org/10.35633/inmateh-68-11.

[3] Chen Z., Wassgren C, Ambrose R P K. (2022), Development and validation of a DEM model for predicting impact damage of maize kernels [J]. *Biosystems Engineering*, 224: 16-33.

[4] Chen Z., Wassgren C, Ambrose R P K. (2021), Measured damage resistance of corn and wheat kernels to compression, friction, and repeated impacts [J]. *Powder Technology*, 380: 638-648.

[5] Geng D., Li Y., Meng F. et al. (2019), Design and Experiment on Vertical Polygonal Roller Snapping Ears of Corn Harvester Based on Excitation Theory [J]. *Journal of Agricultural Engineering*, 50(05):124-132

[6] Geng D., Yuhuan L.I., Ke H.E. et al. (2017), Design and Experiment on Gripping Delivery Mechanism for Vertical-rollers Type of Corn Harvester [J]. *Transactions of the Chinese Society for Agricultural Machinery*, 48(011):130-136.

[7] Kruszelnicka W. (2021), Study of selected physical-mechanical properties of corn grains important from the point of view of mechanical processing systems designing [J]. *Materials*, 14(6): 1467.

[8] Li X. (2010), Detecting and Research on Characteristics and Mechanism of Inner Mechanical Cracks of Corn Seed Kernels [J]. *Transactions of the Chinese Society for Agricultural Machinery*, 41(12):143-147.

[9] Liu M., Xinping L.I., Zhang Y.. (2013), Test and Analysis on the Cut Damage of Maize Seed Kernel[J]. *Agricultural Science & Technology and Equipment*.

[10] Putri R.E., Yahya A., Adam N.M. et al. (2015), Related fracture resistance with moisture content in different grain orientation of paddy grain [J]. *J. Biol. Agric. Healthc*, 5: 64-70.

[11] Shahbazi F, Dolwlatshah A, Valizadeh S. (2012), Mechanical damage to wheat and triticale seeds related to moisture content and impact energy [J]. *Agricultural Engineering International: CIGR Journal*, 14(4): 150-155.

[12] Shi Z., Kou S. (2018), Inverse reconstruction of fracture splitting connecting rod and its strength and fatigue life [J]. *Journal of Failure Analysis and Prevention*, 18(3): 619-627.

[13] Wang B., Wang J., Dongdong D.U. (2018), Finite element analysis of dynamic impact damage process of maize kernel based on HyperMesh and LS-DYNA [J]. *Journal of Zhejiang University (Agriculture and Life Sciences)*, (4):465-475.

[14] Wang J., Li Y., Zheng M., et al. (2019), Structural Characteristics and Development Trend of Key Equipment of Corn Harvesting Machinery [J]. *Journal of Agricultural Mechanization Research*, 041(009):1-8.

[15] Xiangqian D., Zheng H., Xuan J.I.A., et al. (2022), Calibration and experiments of the discrete element simulation parameters for rice bud damage [J]. *INMATEH-Agricultural Engineering*, 68(3), pp.659-668. https://doi.org/10.35633/inmateh-68-65

[16] Yang Y., Guo X. X., Liu H. F. et al. (2021), The effect of solar radiation change on the maize yield gap from the perspectives of dry matter accumulation and distribution. *Journal of Integrative Agriculture*, 20(2): 482-493.

[17] Yin X., Hou J., Ming B. et al. (2021), Kernel position effects of grain morphological characteristics by X-ray micro-computed tomography (μCT) [J]. *International Journal of Agricultural and Biological Engineering*, 14(2): 159-166.

[18] Yiren Q., Yaoming L., Lizhang X., et al. (2021), Study on the rape pod shatter resistance suitable for low-loss harvesting of harvester reel [J]. *INMATEH-Agricultural Engineering*, 63(1), pp.281-290. https://doi.org/10.35633/inmateh-63-28

[19] Zhang C. G. (2016), *Structural optimization of the cleaning screen for maize grain harvester* [D]. Harbin: Northeast Agricultural University.

[20] Zhang X.W., Yi K.C., Gao L.X. (2015) Contacting mechanics analysis during impact process between maize seeds and threshing component[J]. *Chinese Agricultural Science Bulletin*, 31(14): 285-290.

[21] Zhang Y.L., Gao L.X., Liu H.L. et al. (2007), Experimental Study on Corn Kernel Shear Crash[J]. *Journal of Agricultural Mechanization Research*, 000(005):136-138.

HEAT TRANSFER CHARACTERISTICS OF AN EVAPORATOR EQUIPPING AN AIR HANDLING UNITS FOR CEREAL SEED STORAGE FACILITY
/
CARACTERISTICILE DE TRANSFER DE CĂLDURA ALE UNUI VAPORIZATOR CARE ECHIPEAZA O CENTRALA DE TRATARE A AERULUI DESTINATA UNUI DEPOZIT DE SEMINȚE DE CEREALE

Iulian UTA[1)]; Valentin APOSTOL*[1)]; Horatiu POP[1)]; Viorel BADESCU[1)]; Constantin PAVEL*[1)]; Claudia IONITA[1)1]
Faculty of Mechanical Engineering and Mechatronics, University Politehnica of Bucharest / Romania
Tel: +040744570329 E-mail: apostol.crvprofesional@gmail.com; cornel.pavel@stud.mec.upb.ro
Corresponding author: Apostol Valentin; Constantin Pavel

DOI: https://doi.org/10.35633/inmateh-69-57

Keywords: *cereal seed, air handling units, air conditioning, mathematical model, heat exchanger*

ABSTRACT
In this paper the evaporator from the air handling units (AHU) is being studied, this being connected to an air conditioning installation with mechanical compression of vapors. In a previous analysis, the heat exchanger (HEX) was checked to see if it complied with the cooling capacity relative to the heat exchange surface by finding the specific criteria equations. A follow-up to the previous article is to calculate based on the thermodynamic cycle, what happens if the refrigerant is replaced with other new refrigerants in the field of air conditioning in order to improve the performance of the air conditioning system (ACS), finding the refrigerant with a low Global warming potential (GWP) and with an appropriate flammability class. The moisture content of seeds is one of the most important storage parameters affecting their quality. In order to obtain the desired effect, the temperature and humidity of the air must be maintained in the warehouse with an air treatment unit. In this study, it is desired to replace the refrigerant and preserve the refrigerating power from the evaporator, by changing the degree of sub-cooling from the condenser. Due to the fact that the temperature in the ambient environment changes substantially during a calendar year and the condenser of the air conditioning installation has the same configuration, thus the decrease in the ambient temperature will result in the appearance of the sub-cooling process and an increase in the performance of the installation.

REZUMAT
In aceasta lucrare se studiază vaporizatorul de la o unitate de tratare a aerului (UTA), ce este racordată la o instalație frigorifică cu comprimare mecanică de vapori. Într-o analiză anterioară, schimbătorul de căldură (HEX) a fost verificat pentru a vedea dacă a respectat capacitatea de răcire în raport cu suprafața de schimb de căldură prin găsirea ecuațiilor criteriale specifice. O continuare a articolului anterior este de a calcula pe baza ciclului termodinamic, ce se întâmplă daca agentul frigorific este înlocuit cu alți agenți frigorifici noi in domeniul aerului condiționat, in scopul îmbunătățirii performantelor sistemului de aer condiționat (ACS), pentru a identifica agentul frigorific cu un potențial de încălzire globală (GWP) scăzut și cu o clasă de inflamabilitate adecvată. Conținutul de umiditate al semințelor este unul dintre cei mai importanți parametri de depozitare care afectează calitatea acestora. Pentru a obține efectul dorit trebuie menținute in depozit o temperatură şi o umiditate a aerului, utilizând o centrala de tratare aer. In acest studiu se dorește înlocuirea agentului frigorific şi păstrarea puterii frigorifice de la vaporizator, prin modificarea gradului de subrăcire de la condensator. Datorită faptului că temperatura din mediul ambiant se modifică substanțial pe parcursul unui an calendaristic şi condensatorul instalaţiei de climatizare aer are aceeași configurație, prin scăderea temperaturii ambiante va rezulta apariția procesului de subrăcire şi o creștere a performanței instalaţiei.

[1] *Iulian Uta, Stud.; Valentin Apostol, Prof. Ph.D. Eng.; Horatiu Pop, Assoc.Prof. Ph.D. Eng.; Viorel Badescu, Prof. Ph.D. Eng.; Constantin Pavel, Stud.; Claudia Ionita, Lecturer Ph.D. Eng.*

INTRODUCTION

Cereals are one of the most important sources of nutrition for most of the world's population. Maintaining the quality of cereal grains is essential between harvest and use. An important preservation method is the control of moisture content. Excess moisture content can encourage the growth of bacteria and fungi and the development of insects and mites in the seeds.

Grain drying involves both heat and mass transfer processes. Mathematical modeling of grain drying can provide a better understanding of the physical and thermal processes during drying *(Ebrahimifakhar et al., 2020).*

Storage conditions of temperature and relative humidity are essential to preserve the quality of the seeds and to ensure storage stability. Seed moisture content, storage temperature, relative humidity, air O_2 and CO_2 concentrations, and storage duration are the most critical parameters for seed postharvest life. The rate of degenerative or seed damage processes increases as the moisture content of the seeds increases. If the moisture content is high enough, the biological activity in the seed will produce enough heat to spoil the seeds if they are not well aerated. Seeds with high moisture are more prone to heat damage than seeds with lower moisture levels. Seeds with moisture content above 18% are subject to excessive damage during storage and processing. Thus, the storage time is reduced, and quality losses occur in seeds with high moisture (>18%). However, seeds with moisture content below 15% are increasingly resistant to impact damage. The respiration rate of seeds with lower moisture content decreases by over 18% *(Kibar et al., 2019).*

The refrigerant is a fluid substance or mixture, usually used in a thermodynamic cycle with a reversible phase transition from a liquid to a gas and back. Refrigerators, air conditioners, heat pumps, water coolers and many other devices use refrigerants as an intermediate fluid to transfer heat between two sources.

A brief history of the past, present, and likely future of natural refrigeration agents is presented in figure 1 *(Abas et al., 2018).*

In a previous article, the evaporator in the AHU was checked in terms of cooling capacity relative to the heat exchange surface by finding in the literature the criterion equation of the indoor convection coefficient that verifies the dimensions of the evaporator in the equipment *(Uta, I. et al., 2022).*

The objective of this study is to analyze, based on the thermodynamic cycle, which parameters or which components change at the air conditioning system, by replacing the refrigerant with other agents in the field of air conditioning, keeping the rest of the data unchanged.

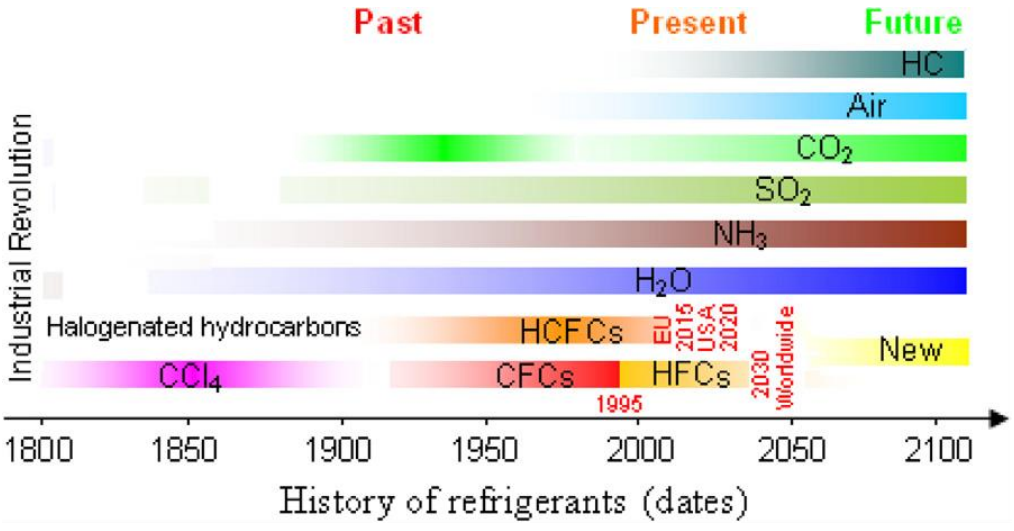


Fig. 1 – Diagram with the history of synthetic and natural refrigerants
(Abas et al., 2018; Uta, I. et al., 2022)

MATERIALS AND METHODS

The technical characteristics of the air conditioning installation

Within the Thermodynamics department of the POLITEHNICA University of Bucharest is an air conditioning installation fully equipped with an air treatment plant and refrigeration unit, Figure 2, where operating parameters can be determined *(Uta I. et al., 2022).*



Fig. 2 - General views of the experimental system

Figure 3 exemplifies the hydraulic diagram of the ACS, which shows the main elements of the installation such as the compressor, the evaporator, the condenser and the rolling valve. Figure 4 shows the thermodynamic cycle of ACS with characteristic state points *(Uta, I. et al., 2022).*

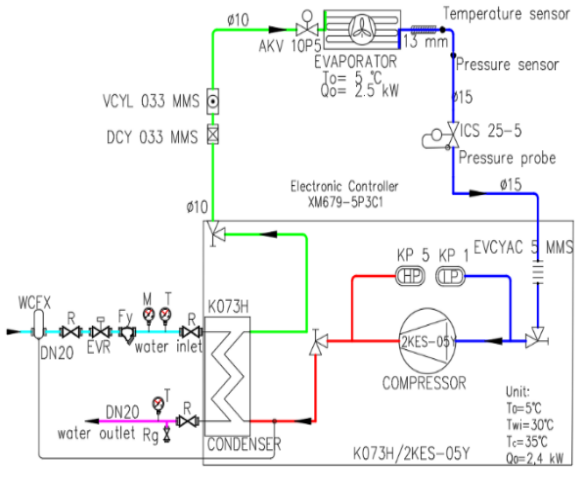


Fig. 3 - Hydraulic diagram of the refrigeration system

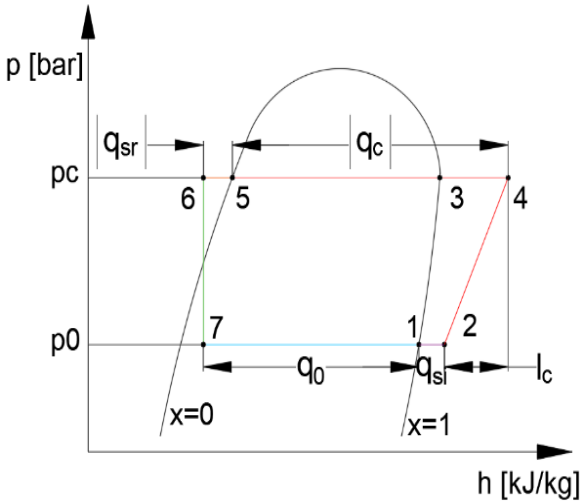


Fig. 4 - Thermodynamic cycle of the VCRS

Heat transfer takes place on the surface of the evaporator by cooling the humid air by the following ways: forced convection on the outside of the HEX, mass exchange by condensing the relative humidity of the air on the surface of pipes and sheets, conduction through the metal wall of pipes and of sheets, convection to boiling.

The evaporator is a surface heat exchanger that achieves the refrigeration effect by forced convection with a fan. The process takes place with phase change, in which the refrigerant takes heat from the cooled environment or from the air in our case, and the cooled air reaches the desired room.

The technical data of the AHU evaporator are known, they have been measured and it consists of: copper pipes, fins or aluminum sheets, with galvanized sheet metal housing, with a single row of pipes *(IDewa B, 2017*; *Uta I. et al., 2022).*

Table 1

Characteristics of the AHU evaporator *(www.komfovent.com)*

Evaporator coil	**Length [mm]: 180**	**Pressure drop [Pa]: 7**	
Coil code	DX-G10-01R-0755-0300-130/-10-1×05C-24F-M1-C40-IS2-RC-1×½/1×22		Int. headers

Air volume [m³/s]	0.28	Capacity [kW]	2.50
Sensible capacity [kW]	1.62	Latent capacity [kW]	0.88
Safety on capacity [%]	56	Air off dry bulb [°C]	25.2
Air on dry bulb [°C]	30.0	Air off wet bulb /RH [°C / %]	19.7 / 61
Air on wet bulb/RH [°C / %]	21.9 / 50	Face velocity [m/s]	1.27
Air pressure drop coil (Wet) [Pa]	7	Fluid flow rate [kg/hr]	58.35
Air pressure drop coil (Dry) [Pa]	5	Subcooling temperature [K]	5.0
Rfrigerant R134A		Superheat temperature [K]	5.0
Condensing temperature [°C]	35.0	Condensation [kg/hr]	1.22
Evaporating temperature [°C]	5.0	Inlet connection	1x½
Refrigerant Pressure Drop [kPa]	0	Outlet connection	1x22
Fin spacing [mm]	2.4	Connection type	Filet
Fin material	Al	Internal volume [dm³]	0.72
Max high pressure [bar]	42	Drain pan type	Flat
Max high temperature [°C]	80		

The evaporator for cooling the air, works with forced convection, the transmission of heat between the hot air and the refrigerant when boiling inside the pipes takes place by forced convection on the outside, mass exchange, conduction through the metal wall and boiling convection. *(Stamatescu, C., 1979)*

The compressor of the air conditioning system is a component that circulates the refrigerant throughout the installation and in which the theoretical compression process takes place, it allows the mechanical increase of the refrigerant pressure in order to suck the vapors from the evaporator and force them to enter the condenser. The compressor is of the semi-hermetic type, with the dimensions shown in figure 5 and with the technical data from table 2, where it was selected with Software Bitzer.

Table 2

Compressor data sheet

Refrigeration compressor Bitzer, type 2KES-05Y-40S

	Speed compressors	**Bore**	**Stroke**	**No of cylinder**	**Dead space volume**	**Max temperature**	**Max pressure**
Unit of measurement	[rot/min]	[mm]	[mm]	[cylinder]	[%]	[°C]	[bar]
Rotation	nr	D	S	i	ε_0	t	p
Value	1550	30	33	2	5	70	32

Type: Semi-hermetic Reciprocating Compressors

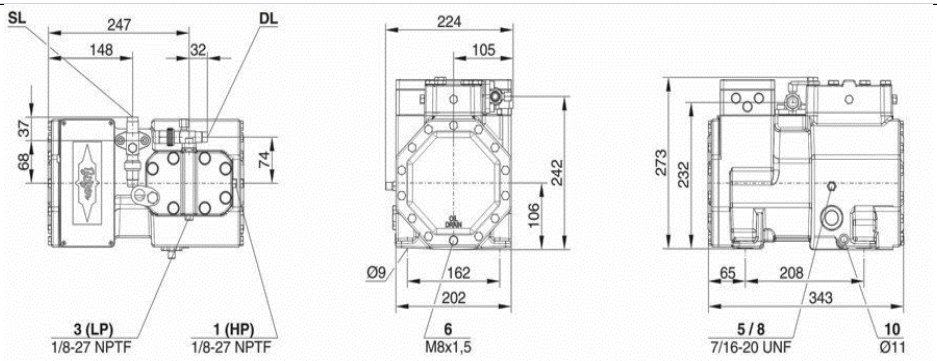


Fig 5 - Compressor dimensions and connections
(www.bitzer.de)

The condenser is a surface heat exchanger that has the role of dissipating the heat accumulated in the refrigerant into the water. The amount of heat is equal to the sum of the heat absorbed in the evaporator and the heat produced by the compression of the agent vapors in the compressor.

The heat transfer medium is water at a temperature lower than that corresponding to the condensing pressure. The condenser process can be compared to the evaporator process except that it is of the opposite "sign", is the conditional change is from vapor to liquid.

The air conditioning system condenser is of multitube type and has the dimensions according to figure 6, and the technical and operational data can be found in table 3.

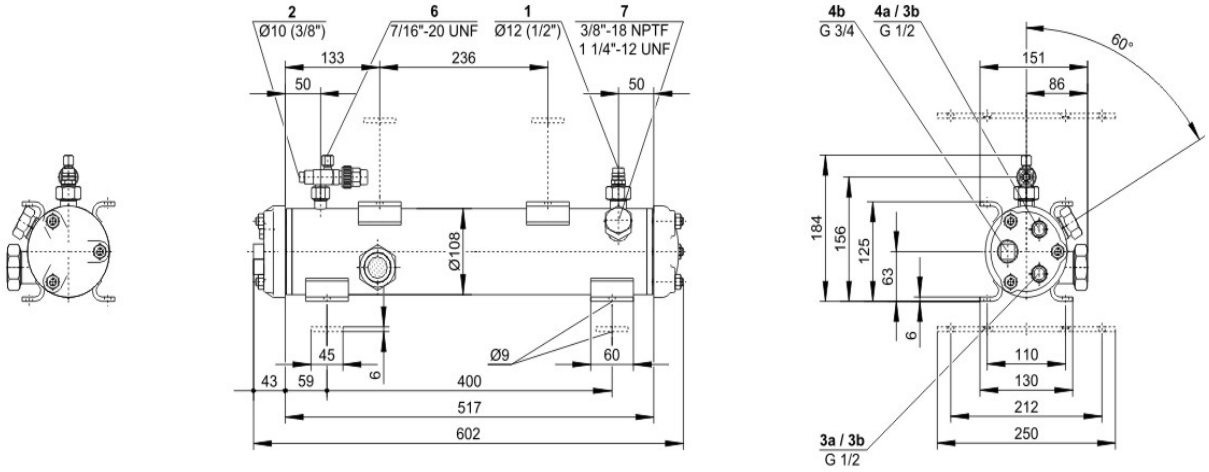


Fig. 6 - Condenser dimensions and connections *(www.bitzer.de)*

Table 3

Condenser data sheet

Condenser Bitzer, type K073H	Water-cooled multitube exchanger		
Weight [kg]	11	Height [mm]	184
With [mm]	602	Jacket tube diameter [mm]	108
Refrigerant inlet [mm]	12 / ½"	Refrigerant outlet [mm / "]	10 / 3/8"
Coolant inlet (2 passes) ["]	2 x1/2"	Coolant outlet (2 passes) ["]	¾"
Coolant inlet (4 passes) ["]	1/2"	Coolant outlet (4 passes) ["]	1/2"
Receiver volume refrigerant [dm^3]	3,4	Max pressure refrigerant [bar]	33
Max. Operating Temperature [°C]	120	Max pressure coolant side [bar]	10

Mathematical analysis of the evaporator from the air conditioning system

This article is a continuation of the mathematical analysis of the evaporator performed in a previous work, where the chosen criterion equation was the one that verifies the dimensional data of the heat exchanger, such as: pipe diameters, pipe length, number of fins, fin thickness, but at the same time we also calculate technical parameters: cooling capacity, indoor convection coefficient, coefficient global heat exchange *(Uta, I. et al., 2022).*

By changing the order of the equations, the previous article *(Uta, I. et al., 2022)*, one can determine the resulting cooling capacity or what other data will be modified by replacing the refrigerant R134a with other refrigerants in the field of air conditioning, while maintaining the rest of the parameters unchanged.

The notations used in the formulas below can be identified in the Nomenclature (Table 4) at the end of the paper work. With these data, the air flow surfaces through the exchanger can be determined and the mass flow of humid air can we calculated:

$$\Delta H = H_1 - H_2 \left[\frac{kJ}{kg}\right] \tag{1}$$

$$\dot{m}_{aum} = \frac{\dot{Q}_o}{\left(1+x_1\right)\cdot\Delta H}\left[\frac{kg}{s}\right] \tag{2}$$

Calculation of the humid air volume flow and the mass vapor flow:

$$\dot{V} = \frac{\dot{m}_{aum}}{\rho_m} \cdot 3600 \left[\frac{m^3}{h}\right] \quad (3)$$

$$\dot{m}_v = \dot{m}_{aum} \cdot \left(x_1 - x_2\right) \left[\frac{kg}{s}\right] \quad (4)$$

Equivalent diameter calculation *(Neacsu E, 1977):*

$$D_{equ} = 2 \cdot H \left[m\right] \quad (5)$$

The length of all sheets and the length of the measured pipe:

$$L_{fin} = n_{fin} \cdot s \left[ml\right] \quad (6)$$

$$L_{pipe} = L - L_{pipe} \left[m\right] \quad (7)$$

Flow rate and air rate of flow through HEX *(Neacsu E, 1977*):

$$A_{exchanger} = \left(L_{pipe} \cdot H_{exchanger}\right) - \left(n_{pipes} \cdot L_{pipe} \cdot d_e\right) \left[m^2\right] \quad (8)$$

$$w_{air} = \frac{\dot{m}_{aum}}{\rho_m \cdot A_{exchanger}} \left[\frac{m}{s}\right] \quad (9)$$

The surface of the pipe without fins reported at 0.8 meters of pipe:

$$A_B = \pi \cdot d_e \cdot \left(L - n_{fin} \cdot \frac{s}{L}\right) \left[m^2\right] \quad (10)$$

The surface of the fins is 0.8 meters of pipe:

$$A_N = \left[\left(R \cdot H - \frac{\pi \cdot {d_e}^2}{4}\right) \cdot 2 + \left(2 \cdot R + 2 \cdot H\right) \cdot s\right] \cdot \frac{n_{fin}}{L} \left[m^2\right] \quad (11)$$

Total area reported 0.8 meters of pipe *(Stamatescu C., 1979):*

$$A_T = A_B + A_N \left[m^2\right] \quad (12)$$

In order to establish the outdoor convection coefficient, the heat transfer characteristics of the air are determined, the Reynolds criterion and the Nusselt criterion have been calculated.

To determine the exterior convection coefficient, the following data are required: the kinematic viscosity of the air at medium temperature $\nu_{air} \left[\frac{m^2}{s}\right]$, average air density at medium temperature $\rho_{air} \left[\frac{m^3}{kg}\right]$, thermal conductivity of air at medium temperature $\lambda_{air} \left[\frac{W}{m \cdot K}\right]$, dynamic viscosity of air at medium temperature $\eta_{air} \left[\frac{N \cdot s}{m^2}\right]$, thermal conductivity of aluminum $\lambda_{Al} \left[\frac{W}{m \cdot K}\right]$, its values are established φ from *(Stamatescu C., 1979).*

$$\eta_{air} = \nu_{air} \cdot \rho_{air} \left[\frac{N \cdot s}{m^2}\right] \quad (13)$$

$$\mathrm{Re} = \frac{w_{air} \cdot D_{equ}}{\nu_{air}} \left[-\right] \quad (14)$$

In order to determine the Nusselt criterion, the values of the constants C and n are needed. They are chosen from *Stamatescu C., (1979)*: $C = 0.096; n = 0.72$

$$Nu = C \cdot \mathrm{Re}^{n} \cdot \left(\frac{d_e}{a}\right)^{-0,54} \cdot \left(\frac{H}{a}\right)^{-0,14} \left[-\right] \quad (15)$$

Determination of the exterior convection coefficient *(Stamatescu,C., 1979):*

$$\alpha_n = \frac{Nu \cdot \lambda_{air}}{a} \left[\frac{W}{m^2 \cdot K}\right] \quad (16)$$

It is considered that the real distribution of temperatures in the rib is replaced by a constant average temperature, where it was shown that by solving the differential equation of conductivity under the conditions of uniqueness from the variation of temperatures in a solid depend on a parameter *(Stamatescu C., 1979):*

$$m = \sqrt{\frac{2 \cdot \alpha_n}{\lambda_{Al} \cdot s}} \left[-\right] \quad (17)$$

Feature and efficiency fin *(Stamatescu C., 1979):*

$$X = \frac{\varphi \cdot d_e}{2} \cdot m \left[-\right] \quad (18)$$

$$\eta_n = \frac{\tanh \cdot (X)}{(X)} \left[-\right] \quad (19)$$

The external convection coefficient was obtained by analytical calculation, referring to the entire ribbed surface of HEX.

Convection coefficient in the dry air area relative to the total area *(Stamatescu C., 1979):*

$$\alpha_c = \frac{\alpha_n}{A_T} \cdot \left(\eta_n \cdot A_N + A_B\right) \left[\frac{W}{m^2 \cdot K}\right] \quad (20)$$

Exterior convection coefficient relative to the total area *(Stamatescu C., 1979):*

$$\sigma = 4 \cdot \alpha_C \left[\frac{W}{m^2 \cdot K}\right] \quad (21)$$

$$\alpha_{ext} = \frac{\sigma \cdot \left(h_m - h_p\right)}{t_m - t_p} \left[\frac{W}{m^2 \cdot K}\right] \quad (22)$$

The refrigerant for ACS is R134a, thus determining its thermophysical properties at the inlet to the evaporator and at the evaporating temperature of 5°C, such as the density of R134a , $\rho_{R134a} \left[\frac{kg}{m^3}\right]$ kinematic viscosity R134a – liquid, $\nu_{R134a,l} \left[\frac{m^2}{s}\right]$ thermal conductivity R134a – liquid , $\lambda_{R134a,l} \left[\frac{W}{m \cdot K}\right]$, specific heat R134a – liquid , $c_{p_{R134a,l}} \left[\frac{J}{kg \cdot K}\right]$, dynamic viscosity R134a – liquid , $\eta_{R134a,l} \left[\frac{N \cdot s}{m^2}\right]$ *(ASHRAE, 2009)*

$$\eta_{R134a,l} = \rho_{R134a,l} \cdot \upsilon_{R134a,l} \left[\frac{N \cdot s}{m^2}\right] \quad (23)$$

The diameter of the inner pipe can be deduced from the existing evaporator measurements and thus determine the flow rate of the agent inside the existing pipe and the inner surface of the pipe on a pipe 0.8 meters long.

$$A_{pipe} = \frac{\pi \cdot d_i^{\,2}}{4} \left[m^2\right] \quad (24)$$

R134a agent flow rate through the pipe *(ASHRAE, 2009):*

$$w_{R134a} = \frac{\dot{m}_o}{A_{teava} \cdot \rho_{R134a,l} \cdot 5} \left[\frac{m}{s}\right] \quad (25)$$

In the following, we apply Shah criterion equations which check the existing HEX to determine the interior convection coefficient, the pipe length, and the overall heat exchange coefficient. *(Shah M, 1982)*

In the calculation of the criteria equations for the indoor convection coefficient, the following data are required: the thermal conductivity of copper *(Neacsu E, 1977)*: $\lambda_{Cu} \left[\frac{W}{m \cdot K}\right]$.

The evaporator pipes are made of copper and have a thickness of: $\delta_{pipe}[m]$ gravitational acceleration *(ASHRAE, 2009)*: $g \left[\frac{m}{s^2}\right]$, latent heat of evaporating for R134a to $t_0 = 5°C]$: $\alpha_{fg} \left[\frac{kJ}{kg}\right]$ *(Elsayed A, 2011)*

Determination of the Reynolds criterion *(Neacsu E, 1977; Mostafa G., 2008)*

$$\mathrm{Re}_{R134a} = \frac{\rho_{R134a,l}.w_{R134a} \cdot di}{\eta_{R134a,l}}\left[-\right] \tag{26}$$

Determination of the Reynolds criterion at the evaporator inlet *(Elsayed A., 2011; Shah M., 1982)*

$$\mathrm{Re}_{R134a,l} = \mathrm{Re}_{R134a} \cdot \left(1 - x_4\right)\left[-\right] \tag{27}$$

Determining the Prandtl criterion *(Collier J., 1996)* and the coefficient of mass velocity of the fluid *(Mostafa G., 2008):*

$$\mathrm{Pr}_{R134a,l} = \frac{c_{pR134a,l} \cdot 10^3 \cdot \eta_{R134a,l}}{\lambda_{R134a}}\left[-\right] \tag{28}$$

$$q'' = \frac{\dot{Q}_o}{A_{pipe} \cdot 5}\left[\frac{W}{m^2}\right] \tag{29}$$

$$G = \frac{\dot{m}_o}{A_{pipe} \cdot 5}\left[\frac{kg}{m^2 \cdot s}\right] \tag{30}$$

The coefficient Bo and the coefficient α_f are calculated *(ASHRAE, 2009; Shah, M, 1982)*

$$Bo_{R134a} = \frac{q''}{G \cdot \alpha_{fg}}\left[-\right] \tag{31}$$

$$\alpha_f = 0{,}023 \cdot \mathrm{Re}_{R134a,l}^{\ 0,8} \cdot \mathrm{Pr}_{R134a}^{\ 0,4} \cdot \frac{\lambda_{R134a,i}}{d_i}\left[\frac{W}{m^2 \cdot K}\right] \tag{32}$$

This determines the convection coefficient inside the pipes *(ASHRAE, 2009; Shah, M, 1982)*

$$Co = \left(\frac{1 - x_4}{x_4}\right)^{0,8} \cdot \left(\frac{\rho_{R134a,\upsilon}}{\rho_{R134a,l}}\right)^{0,5}\left[-\right] \tag{33}$$

$$Frl = \frac{G^2}{\rho_{R134a,l}^{\ 2} \cdot g \cdot d_i}\left[-\right] \tag{34}$$

$$\alpha_{R134a} = F \cdot \left(Bo_{R134a,l}^{0,5}\right) \cdot \exp\left(2{,}47\left(Co\left(0{,}38 \cdot Frl^{-0,3}\right)^n\right)^{-0,15}\right) \cdot \alpha_f\left[\frac{W}{m^2 \cdot K}\right] \tag{35}$$

Global heat exchange coefficient *(Collier, J., 1996)*

$$k = \frac{1}{\left(\frac{1}{\alpha_{ext}}\right) + \left(\frac{A_T}{A_{pipe}}\right) \cdot \left(\frac{1}{\alpha_{R134a}} + \frac{\delta_{pipe}}{\lambda_{Cu}}\right)}\left[\frac{W}{m^2 \cdot K}\right] \tag{36}$$

The average temperature difference is calculated by neglecting the steam overheating heat, so the total length of the HEX pipe can be determined.

Maximum and minimum temperature difference at the evaporator *(Mostafa, G., 2008; Collier, J., 1996):*

$$\Delta t_{\max} = t_1 - t_0\left[^oC\right] \tag{37}$$

$$\Delta t_{\min} = t_2 - t_0\left[^oC\right] \tag{38}$$

Average logarithmic temperature difference at evaporator *(Mostafa, G., 2008; Collier, J., 1996):*

$$\Delta t_{m\log} = \frac{\Delta t_{\max} - \Delta t_{\min}}{\ln\left(\frac{\Delta t_{\max}}{\Delta t_{\min}}\right)}\left[^oC\right] \tag{39}$$

The cooling capacity of the evaporator is determined by the equation below:

$$\dot{Q}_o = \left(L_{total} \cdot k \cdot \Delta t_{m\log} \cdot A_T\right) \cdot 0.8\left[W\right] \tag{40}$$

RESULTS

The calculations have been done using Engineering Equations Solver and the following operational conditions of the VCRS: evaporating temperature: $t_0 = 5℃$; condensing temperature: $t_c = 35℃$; cooling capacity: $\dot{Q}_o = 2.5\ kW$; subcooling degree: $\Delta_{sr} = 5℃$; superheating degree: $\Delta_{si} = 5℃$; refrigerant R134a inside evaporator pipes; moist air outside evaporator pipes and the following parameters: inlet air temperature in the evaporator: $t_{ia} = 30℃$; relative humidity of the air at the inlet: $\varphi_{ia} = 50\%$; air temperature at the outlet: $t_{oa} = 25.2℃$; relative humidity of the air at the outlet: $\varphi_{oa} = 61\%$; air flow by volume: $\dot{V} = 1000\frac{m^3}{h}$;

Below, a graphical comparison will be made between different refrigerants in the field of air conditioning, to see what the differences are if the R134a refrigerant is replaced.

In figure 8, the degree of subcooling at the outlet of the condenser was analyzed in relation to the convection coefficient inside the pipe for different refrigerants in the field of air conditioning. notice how the value of the function decreases in relation to the variable.

This graph can be divided into two areas, agents with the lowest values around the refrigerant R134a, and in the upper part of the graph refrigerants around R410a, with the highest values of the indoor convection coefficient, at the degree of subcooling with the lowest values, as the value of the degree of subcooling increases, the values of α_{int} decrease for the studied refrigerants.

In order to have a high-performance air-conditioning system, the variation of the degree of subcooling in relation to the cooling capacity for the studied refrigerants as substitutes for R134a was analyzed. It is observed in figure, that there are quasi-constant values of the cooling capacity for all refrigerants in relation to the value of the degree of subcooling.

In the lower part of the graph, there are two refrigerants R1234yf and R515A, the latter has as a base agent R1234ze(E) being an azeotropic agent, in the middle part of the graph are the newly studied refrigerants such as R454B, R452B and R466A, having better performances compared to R134a, and in the upper area of the graph are represented refrigerants, R410A, R32 and R407C, with the best performances of the refrigerating power, with an average increase of 40% compared to R134a.

This analysis resulted in a quasi-constant refrigerating power for all agents studied as substitutes for R134a, thus the total refrigerating power increases due to the fact that we have an increase in density due to vaporization pressure and due to the reduction of the compression ratio, a higher mass flow result.

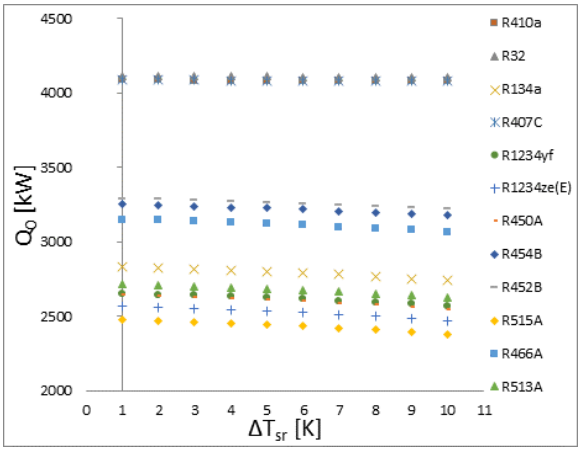


Fig. 7 - Influence of cooling degree on cooling capacity for R134a substituents

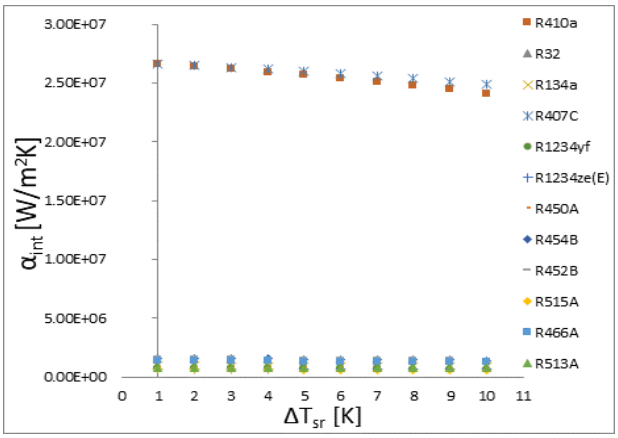


Fig. 8 - Influence of the degree of subcooling on the internal convection coefficient for R134a substituents

The influence of the degree of subcooling at the exit from the condenser was studied, taking into account the heat exchange coefficient for different refrigerants in the field of air conditioning, where a slight decrease in the overall heat exchange coefficient is observed as the value of the degree of subcooling increases for refrigerants in the lower part of the graph, and in the upper part refrigerants have quasi-constant values as the value of the degree of subcooling increases.

The graph in figure 9 can be divided into three groups, respectively in the lower part you can find the refrigerants R515A and R1234yf, with the lowest values, in the middle part you can find the newly studied agents R454B, R452B and R466A, and in the lower part at the top of the graph, there are 3 refrigerants with the best performances at the lowest values of the degree of subcooling, they have an average increase of 40% compared to R134a. The best value of the global heat exchange coefficient is with refrigerants R410A, R32 and R407C.

In figure 10, the influence of the degree of subcooling over the quality at the inlet to the evaporator was examined, where it has a tendency to decrease linearly in relation to the variation of the degree of subcooling; the more liquid enters the evaporator, the higher the efficiency of the heat exchanger.
The graph in figure 10 can be divided into three groups, respectively at the bottom is the cooling agent R32 with the lowest values, most agents occupy the idle of the graph, where the refrigerant R513a is highlighted with an increase of 10% compared to R134a, and in the upper part of the chart there are 2 refrigerants with the highest values, respectively R407C, R1234yf, they have an average increase of 20% compared to R134a.

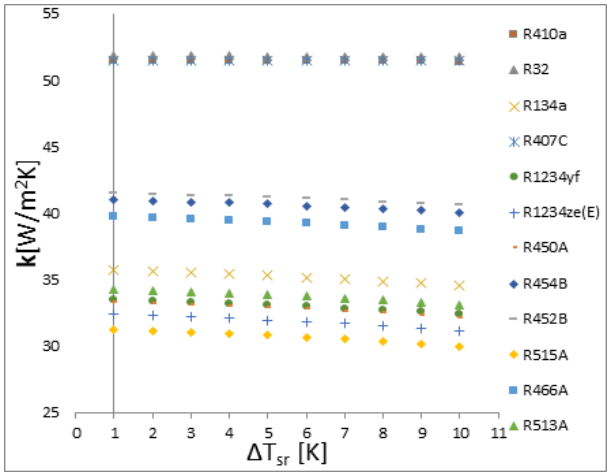


Fig. 9 - Influence of the degree of subcooling on the overall heat exchange coefficient for R134a substituents

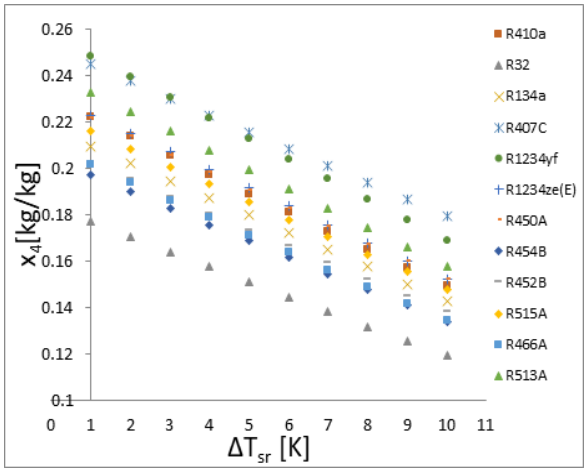


Fig. 10- Influence of the degree of subcooling on the vapor inlet quality for R134a substituents

The influence of the degree of subcooling is represented in figure 11, taking into account the enthalpy of the refrigerant at the entrance to the evaporator, the general orientation for all refrigerants is of linear decrease compared to the increase of the degree of subcooling.

As in the previous graphs and in this graph, it can be divided into 3 areas, in the lower area there are agents around R134a, in the middle part there are new studied agents R454B, R452B and R466A, but also R407C, and in the upper part they remained only agents R32 and R410a with the best performances.

In the graph from figure 12, the degree of subcooling is studied according to the enthalpy of the refrigerant at the condenser exit, so the general direction of refrigerants is increasing in relation to the degree of subcooling. At the bottom of the figures, agent R466A is represented, with the lowest values, and agent R452B is represented with the highest values.

It can be observed that at low values of the degree of subcooling, all agents have similar results, and as the degree of subcooling increases, several antifreeze agents with the highest values R452B and R454B are differentiated.

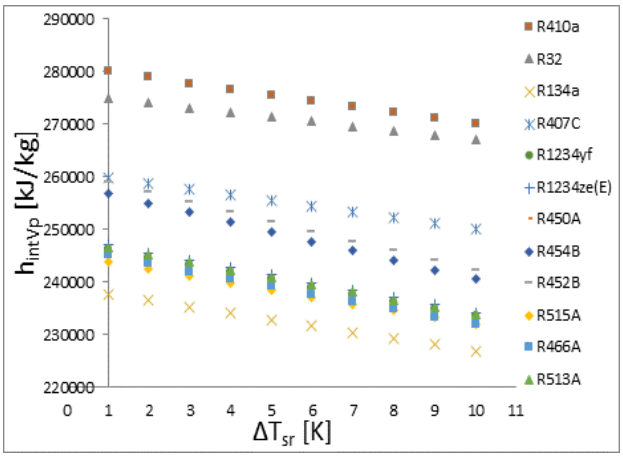


Fig. 11 - Influence of the degree of subcooling on the enthalpy at the input to the evaporator for R134a substituents

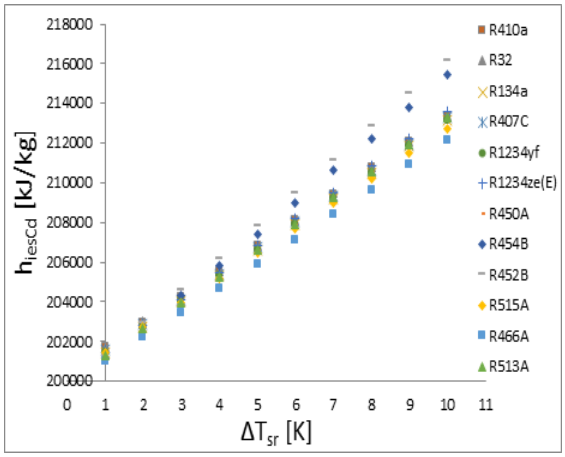


Fig. 12- Influence of the degree of subcooling on the enthalpy at the outlet of the condenser for R134a substituents

CONCLUSIONS

The values of vapor quality at the inlet of the evaporator directly influence the convection coefficient inside the pipes, so we analyzed the variation of the degree of subcooling in relation to the convection coefficient inside the pipes, where we noticed that as the degree of subcooling increases, t the cooling capacity of the heat exchanger decreases, because not enough liquid enters it to realize the heat transfer; the degree of subcooling is influenced by the condensation temperature.

The refrigerant R1234ze(E) is considered a resident agent of R134a, having similar or weaker characteristics in terms of energy and refrigeration performance, with a GWP of 1, but with a flammability class of A2L, this agent can be replaced without making too many changes in the air conditioning system.

A perspective refrigerant with the best performance is the agent R452B, it had the highest values in the graphs among the new refrigerants studied, with a GWP of 676, with a flammability class of A2L, but to replace R134a, the whole installation must be checked, so that it can withstand the higher working pressure, the refrigerant oil must be replaced and the rolling valve must be adjusted to achieve the appropriate liquid injection.

The air conditioning system maintains its cooling capacity when the refrigerant is replaced, and, by adjusting the sub-cooling process, the performance of the air conditioning system increases.

In the next stage, an experimental study will be performed on the air conditioning system with air treatment plant to analyze the installation parameters and model the results, comparing them with the technical data from the equipment manufacturer, and then the refrigerant will be replaced and a comparative study between agents will be performed.

Table 4

NOMENCLATURE

Symbols			
A_{pipe}	Pipe area [m^2]	$Pr_{R134,l}$	Prandlt's liquid criterion [-]
d_i	Inside diameter [m]	Q_0	Cooling capacity [kW]
H_{sc}	Height exchanger [m]	q''	The transferred heat flow [W/m^2]
H_1	Enthalpy at point 1 [kJ/kg]	Re	Reynolds criterion [-]
H_m	Average enthalpy [kJ/kg]	Re_{R134a}	Reynolds criterion for R134a [-]
h_p	Enthalpy at the wall [kJ/kg]	$Re_{R134a,l}$	Reynolds criterion liquid R134a [-]
k	The overall heat exchange coefficient [W/m^2 K]	R	The length of the rectangular fin [m]
L_{pipe}	Measured pipe length [m]	s	The thickness of a fin [m]
m_o	Mass flow [kg/s]	t_m	Medium temperature [°C]
m_{aum}	Mass flow rate of moist air [kg/s]	t_p	Wall temperature [°C]
n_{fin}	The number of fins	V	Volumetric flow of moist air [m^3/h]
n_{pipe}	The number of pipes	w_{air}	Air flow speed [m/s]
Nu	Nusselt criterion [-]	X	Characteristic of the fin [-]
w_{R134a}	Flow rate of R134a [m/s]	x_1	The moisture content of the air [kg/kg]

Greek Symbols

α_n	Convection coefficient for outside [W/m^2K]	$\lambda_{R134a,l}$	Thermal conductivity of R134a [W/mK]
$\lambda_{R134a,l}$	Thermal conductivity of R134a [W/mK]	v_{air}	Kinematic viscosity of air [m^2/s]
v_{air}	Kinematic viscosity of air [m^2/s]	$v_{R134a,l}$	Kinematic viscosity of R134a [m^2/s]
$v_{R134a,l}$	Kinematic viscosity of R134a [m^2/s]	η_n	Yield fin[-]
η_n	Yield fin[-]	η_{air}	Dynamic air viscosity [N s/m^2]
η_{air}	Dynamic air viscosity [N s/m^2]	$\eta_{R134a,l}$	Dynamic viscosity of R134a [N s/m^2]
$\eta_{R134a,l}$	Dynamic viscosity of R134a [N s/m^2]	ρ_{air}	Air density [kg/m^3]
ρ_{air}	Air density [kg/m^3]	$\rho_{R134a,l}$	Density of liquid R134a [kg/m^3]
$\rho_{R134a,l}$	Density of liquid R134a [kg/m^3]	$\rho_{R134a,v}$	Vapor density of R134a [kg/m^3]
$\rho_{R134a,v}$	Vapor density of R134a [kg/m^3]	ρ_m	Medium density [kg/m^3]
ρ_m	Medium density [kg/m^3]	φ_m	Average relative humidity of the air [%]
φ_m	Average relative humidity of the air [%]	$\lambda_{R134a,l}$	Thermal conductivity of R134a [W/mK]

REFERENCES

[1] Abas, N., Kalair, A., R., Khan, N., Haider, A., Saleem, Z., Saleem, M., (2018). Natural and synthetic refrigerants, global warming: A review, *Renewable and Sustainable Energy Reviews*, Vol. 90, pp. 557-569, Pakistan.

[2] *ASHRAE: Fundamentals. SI Edition*, Atlanta (404) 636-8400 (2009)

[3] Collier, J., Thorne, J., (1996). *Convective Boiling and Condensation*, Clarendon Press, Oxford

[4] Ebrahimifakhar, A., Yuill, D., (2020). Inverse estimation of thermophysical properties and initial moisture content of cereal grains during deep-bed grain drying, *Biosystems Engineering,* Vol. 196, United States.

[5] Elsayed, A, (2011). *Heat Transfer in Helically Coiled Small Diameter Tubes for Miniature Cooling Systems*. The School of Mechanical Engineering, University of Birmingham, Edgbaston, Birmingham

[6] Ghiaasiaan, S. Mostafa G., (2008). *Two-Phase Flow*, Boiling and Cambridge University Press, Cambrige

[7] IDewa M.C. Santosa, Baboo L. Gowreesunker, Savvas A. Tassou, Konstantinos M. Tsamos, Yunting Ge, (2017). Investigations into air and refrigerant side heat transfer coefficients of finned-tube CO2 gas coolers, *International Journal of Heat and Mass Transfer*, Vol. 107, pp.168-180

[8] Kibar, H., Kibar, B., (2019). Changes in some nutritional, bioactive and morpho-physiological properties of common bean depending on cold storage and seed moisture contents, *Journal of Stored Products Research,* Vol. 84, Turkey.

[9] Neacsu, E., M., (1977). *Tabele, diagrame si formule termotehnice*., Timisoara, Romania

[10] Satish, G., Kandlikar, M., (1999). *Handbook of Phase Change: Boiling and Condensation*. Printed by Edwards Brothers

[11] Shah, M.M., P. E. (1982). *Chart Correlation for Saturated Boiling Heat Transfer: Equations and Further Study*, 2673

[12] Stamatescu, C., (1979*), Refrigeration Technique Calculation and construction of industrial refrigeration machines and installations (Tehnica Frigului Calculul si constructia masinilor si instalatiilor frigorifice industrial)*. Vol. 2, Editura Tehnica, Bucharest, Romania

[13] Uta, I., Apostol, V., Pop, H., Pavel, C., Alqaisy, SJS., Badescu, V.,Taban, D., Ionita, C.(2022). Mathematical modeling of an evaporator by using different criterial equations, *INMATEH-Agricultural Engineering,* Vol. 67, pp. 562-572, Romania. https://doi.org/10.35633/inmateh-67-55

[14] *** WINTADS_AMALVA_V1.10.0064.1_26042019, S.: www.komfovent.com. (Accessed 2019)

[15] ***Bitzer Software version v6.15.1, r. In: www.bitzer.de.

[16] ***EES: *Engineering Equation Solver | F-Chart Software: Engineering*; www.fchart.com/ees/.

ELECTRIC DRIVE SYSTEM POWERED BY Li-ION BATTERIES FOR AQUATIC BIOMASS HARVESTER

/

SISTEM DE ACȚIONARE ELECTRICĂ PENTRU ECHIPAMENT DE RECOLTAT BIOMASA ACVATICA, ALIMENTAT DIN BATERII Li-ION

Emil TUDOR[1*)], Mihai-Gabriel MATACHE [2)], Ionuț VASILE[1)], Ion-Cătălin SBURLAN[1)], Vasilica ȘTEFAN [*2)]

[1)] INCDIE ICPE-CA / Romania; [2)]INMA Bucharest / Romania;

Tel: +40 755 015 614; E-mail: emil.tudor@icpe-ca.ro; valistefan.inma@yahoo.com

DOI: https://doi.org/10.35633/inmateh-69-58

Keywords: *electric harvester, specific energy consumption, mixed load, efficiency*

ABSTRACT

The development of an electric vehicle harvester for aquatic vegetation is a technical challenge for researchers due to specific requirements: high-torque operation at low travel speeds, high maneuverability, high load capacity, low draught, and affordable price. The collective of authors proposed an electro-hydraulic architecture based on paddles driven by hydraulic motors for propulsion and auxiliary services also driven by motors and hydraulic actuators. The proposed energy source for the aquatic harvester is electric batteries, it was developed a system of 33 kWh Li-Ion batteries connected in parallel, which power an electronic converter and a 14.5 kW rated power electric motor that drives a hydraulic double-circuit pump. The vehicle can be controlled remotely. The paper presents the prototype made and the results obtained during laboratory tests performed for the electric powering system.

ABSTRACT

Dezvoltarea unui echipament electric pentru recoltat biomasa lacustră reprezintă o provocare tehnică pentru cercetători, datorită cerințelor specifice: operare cu cuplu ridicat la viteze mici de deplasare, manevrabilitate ridicată, capacitate mare de încărcare, pescaj redus și preț abordabil. Colectivul de autori a propus o arhitectură electro-hidraulică bazată pe zbaturi antrenate de motoare hidraulice pentru propulsie și de servicii auxiliare acționate tot cu motoare și cu actuatoare hidraulice. Sursa de energie propusă pentru echipamentul de recoltat biomasa acvatica fiind bateriile electrice, a fost dezvoltat un sistem de baterii de 33 kW tip Li-Ion conectate în paralel care alimentează un convertizor și un motor electric de 14,5 kW putere nominală care antrenează o pompă hidraulică cu dublu circuit. Vehiculul poate fi comandat de la distanță. Lucrarea prezintă prototipul realizat și rezultatele obținute în timpul testelor de laborator efectuate pentru sistemul de acționare electrică.

INTRODUCTION

The main objective of this article is to describe the electric drive of an electric-powered aquatic harvester, underlining key features, technical solutions, novelty, and benefits of the proposed architecture.

The aquatic harvesters are used mainly for eliminating the weed developed alongside the lake shores, restricting navigation, and worsening the water for the fish (*Waltham, et al., 2020*).

According to specific literature, weed infestation, such as microalgae, phytoplankton underwater vegetation, and floating vegetation represents an additional oxygen-consuming load on water bodies, that in situations of low daytime photosynthesis, cannot be compensated by the natural oxygenation process, leading to a saturation of zero percent oxygen in the water body.

Several harvesters were developed previously, most of them based on Diesel power, which could be replaced by electric-powered vehicles to improve environmental care (*Marin and Biriș, 2021*). For larger harvesters, the diesel-hydraulic solution is usually used. Even though these kinds of machines fulfill their role as harvesters very well, the polluting factor and costs of diesel fuel cannot be ignored.

For small lake needs, the most suitable solution is, where the electric drive was noticed, the remote operation, and the fact that the harvester can be transported with a regular trailer attached to a normal car. Still, this solution is not able to cut the weed on the lakes, which is the major challenge in maintaining a clean and open lake or river.

Speaking about electrical-operated ships *(Athina, et al., 2022*), one can find that the electric harvester can have built-in sensors for sensing the quality of the water, and, based on the information provided, can perform automated tasks to clean the water until a specified quality is attained.

An electric drive for a boat must contain the same components as an electric drive for cars, mainly electric energy storage, an electronic power converter, one or several electric motors, and mechanical converters such as hydraulic pumps, gearboxes, and actuators *(Sonam, et al., 2016),* (*Un-Noor, et al., 2017*).

Some researchers are implementing a fuel-cell range extender based on hydrogen, similar to the surface EV solutions *(Shigeyuki, et al., 2019).* The authors claim an energy capacity of 65 kWh which can power a 2.6-tone boat for 13 hours at a speed of 8 km/h.

The solution for weed harvester propelling is the one that uses paddles for pulling the boat, instead of a normal propeller, mainly because high torque can be obtained at low speed *(Pratama and Hesty, 2019).*

To drive the paddles at low rotational speed, the most suitable solution is to use hydraulic motors instead of electric motors *(Yun, et al., 2016).*

Boats using electric drives for propulsion are seldom used, especially special boats with particular needs, such as the towing boat *(Moussodji and De Berdarditis, 2015)* which has a power converter that operates the bow thrusters to ensure fine maneuverability in stationary water.

The crop harvesters are using the remote control, especially when they want to optimize the crop field route, and when using multiple synchronized harvesters *(Juostas and Jotautiene, 2022)*.

One of the key features that electric drive is endorsing is the diagnosis of the system, online and offline, and even remote diagnosis which can be performed by a specialist located in the office and connected with the harvester by GSM data *(Gong, et al., 2021).*

The energy storage system recommended to be used by the EV industry is the Li-ION batteries, especially those which are providing compliance with the R100 EU rules of safety and are suitable for use in electric boats, as well *(Zhicheng, et al., 2019).*

The solution to extending the range of the vehicle is the multiplication of the used batteries. The classic solution for small voltage and high energy is the parallel connection of the Li-Ion packs *(Lv, et al., 2019).*

Within the paper, is presented a proposed electro-hydraulic architecture based on paddles driven by hydraulic motors for propulsion and auxiliary services also driven by motors and hydraulic actuators. The work presents the main electrical components of the prototype and their corresponding laboratory tests.

MATERIALS AND METHODS

The selected solution was comprised of an electric motor powered by a power inverter supplied from several Li-Ion energy storage batteries, connected to a hydraulic pump with two circuits, one serving for paddles control via a hydraulic double circuit proportional distributor, and the latter for auxiliary services, as cutting, loading, and orientation. The solution can be seen in Figure 1.

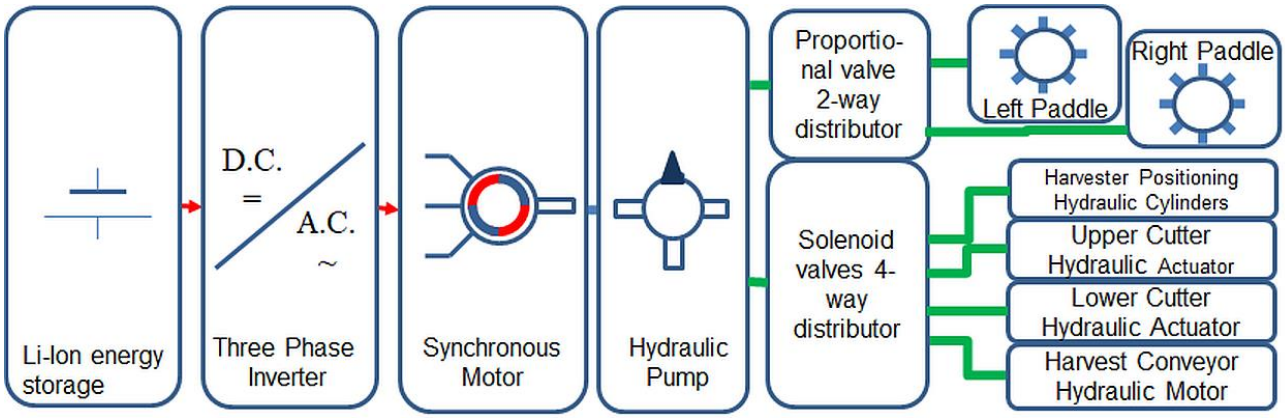


Fig. 1 - The principle of operation of the aquatic harvester

The harvester has to be controlled using a remote control board that provides special controls for the throttle (linear forward and backward, with two independent channels), and on-off switches for auxiliaries. Some low-level diagnose have to be available remotely.

Dimensioning of the equipment is thoroughly described in *(Tudor, et. al., 2022)*. The energy storage battery type Li-Ion consists of three packs previously homologated for hybrid trucks, parallel-connected for larger energy capacity (33kWh) while maintaining a low battery voltage (<60 Vdc). The proposed autonomy of the boat is 90 minutes of operation. The three-phase inverter and the interior permanent magnet synchronous motor IPSM are designed to be used on electric boats operating at less than 60 Vdc nominal voltage. The hydraulic pump has two circuits, one for propelling the boat paddles and one for auxiliary services.

The harvester has three main operating modes:

- Harvesting, with throttle active at low speed and high torque, and with cutting and loading active;
- Transfer, with the full throttle active, based on continuous regulation of the right and of the left paddle in order to control the direction;
- Charging, with throttle and auxiliary inactive.

For modes of Harvesting and Transfer, the electric motor has to be controlled at a steady speed, while the load is controlled by the hydraulic system using the proportional valves and the solenoid valves, as requested. The motor shall be started by an individual command from the remote control panel.

Charging is adapted to use a single-phase 6 kW supply, which is available more often near the lake shores than the three-phase 22 kW ones. The charger must be placed on the dock, thus keeping only the ultra-low voltage on the boat, and avoiding the dangerous voltage (230 Vca).

Furthermore, the load capacity of the harvester must be better than 2 m^3 of biomass, assuming that a payload of 400-500 kg of aquatic vegetation is loaded.

RESULTS

Li-ION Batteries for Energy Storage

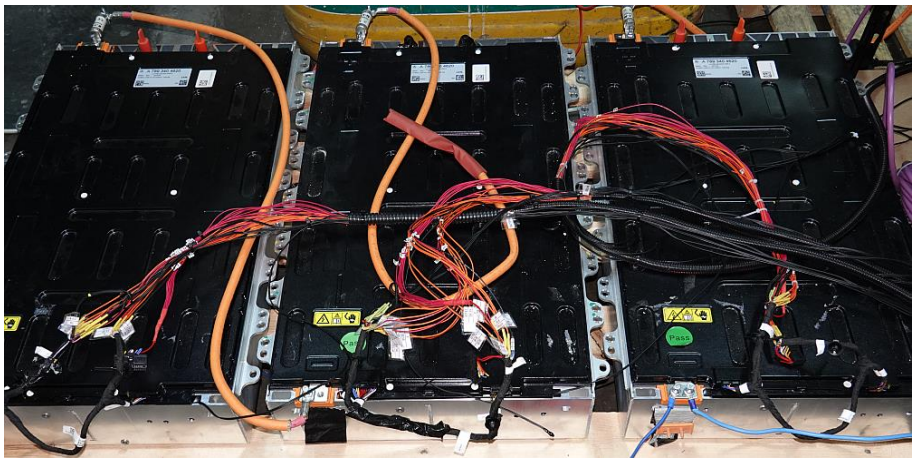
Based on autonomy requirements and the estimator of the needed power for harvesting, some packs developed for mild hybrid trucks were selected from the available REESS batteries, with these characteristics:

Table 1

REESS module characteristics

Open-circuit voltage V_0	58.7 Vdc
Rated capacity C	188 Ah
Rated energy stored E_0	11 kWh
Mass	51.7 kg
Rated cell voltage V_{c0}	3.67 Vcc
Max/min cell voltage	4.2 Vdc / 2.5 Vdc
Dimensions Lxlxh	643x372x116 mm

One pack consists of 2 parallel prismatic modules of 3.72 Vdc and 94 Ah, 16 of those being series connected. The modules are placed on an aluminum case providing liquid cooling. The top of the pack is covered with a black plastic sheet. The power connections are made using two plates.



a.



b.

Fig. 2 - The batteries for energy storage during lab testing and the final assembly during the indoor test

There are several solutions for cell charge balancing, charging and discharging control, overheating overvoltage, and under-voltage. There are named, globally, as BMS systems (Battery Management Systems). In our application, three dependent units are used, each one for its battery, especially for redundancy. The BMS are using some DC contactors, current transducers, and thermistors to connect with the battery. There are located inside a cubicle separated from the batteries but located nearby (Figure 3a.).

Also, for the battery charger was selected a solution with one 6.6kW external charger, connected using a DC line and serial and control communication link. The charger is presented in Figure 3b.



a. b.

Fig. 3 - The BMS cubicle and the DC charger

The experiments with the battery pack were performed in the lab with the devices connected on a test bench supplied by a bidirectional converter able to perform charging and discharging (cycler). The results are presented in Figure 4.

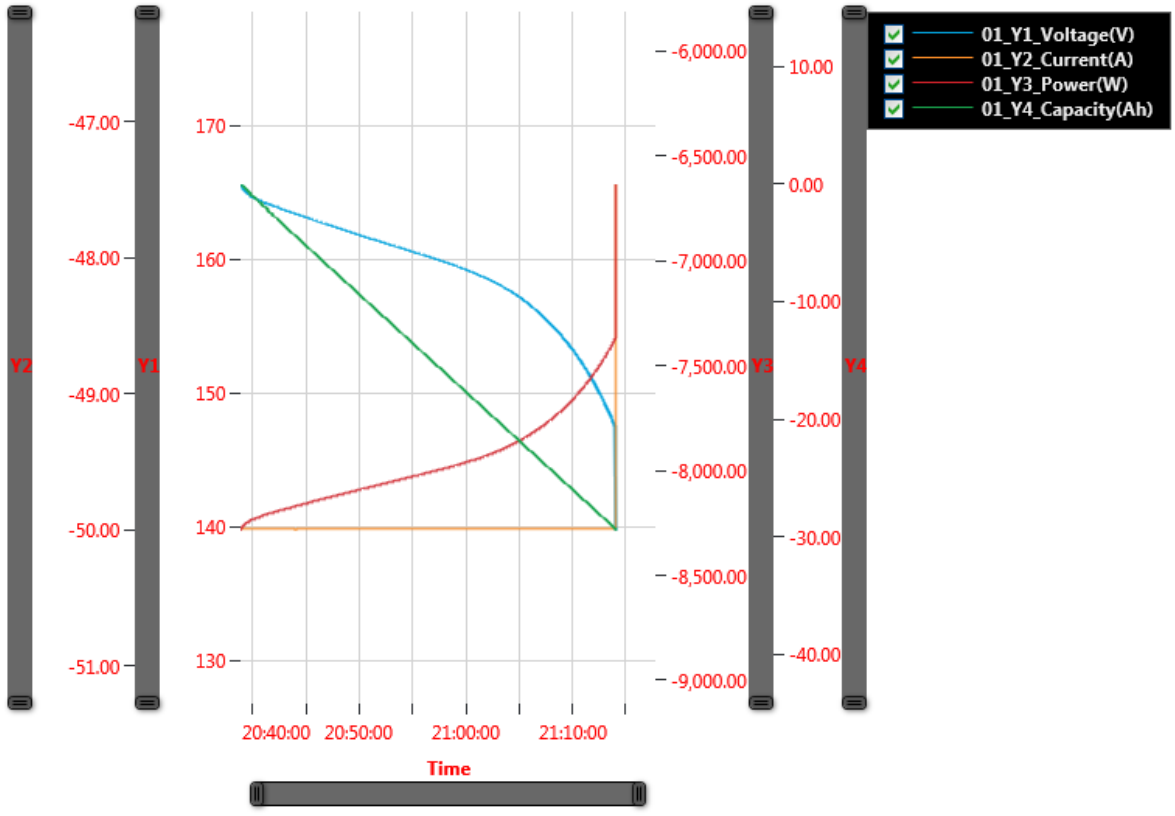


Fig. 4 - Discharge test performed on the bench with batteries connected in series

On the test, the batteries were series connected, thus the voltage starts from 164 Vdc. The initial current provided to the regeneration converter is 50 Adc, but, due to the current limitation from the minimum cell voltage, the current drops down to 48 Adc after 38 minutes.

When the minimum cell voltage protection was triggered, the BMS unit stops the charger. This test simulates the BMS behavior when batteries voltage drops below the lower limit of cell voltage.

Additional tests were performed with the whole equipment mounted on the harvester vehicle, where the batteries were connected in parallel and charged with the charger presented in Figure 3b. The interest was in the CC-CV curve of the charging current (Constant Current - Constant Voltage), as presented in Figure 5.

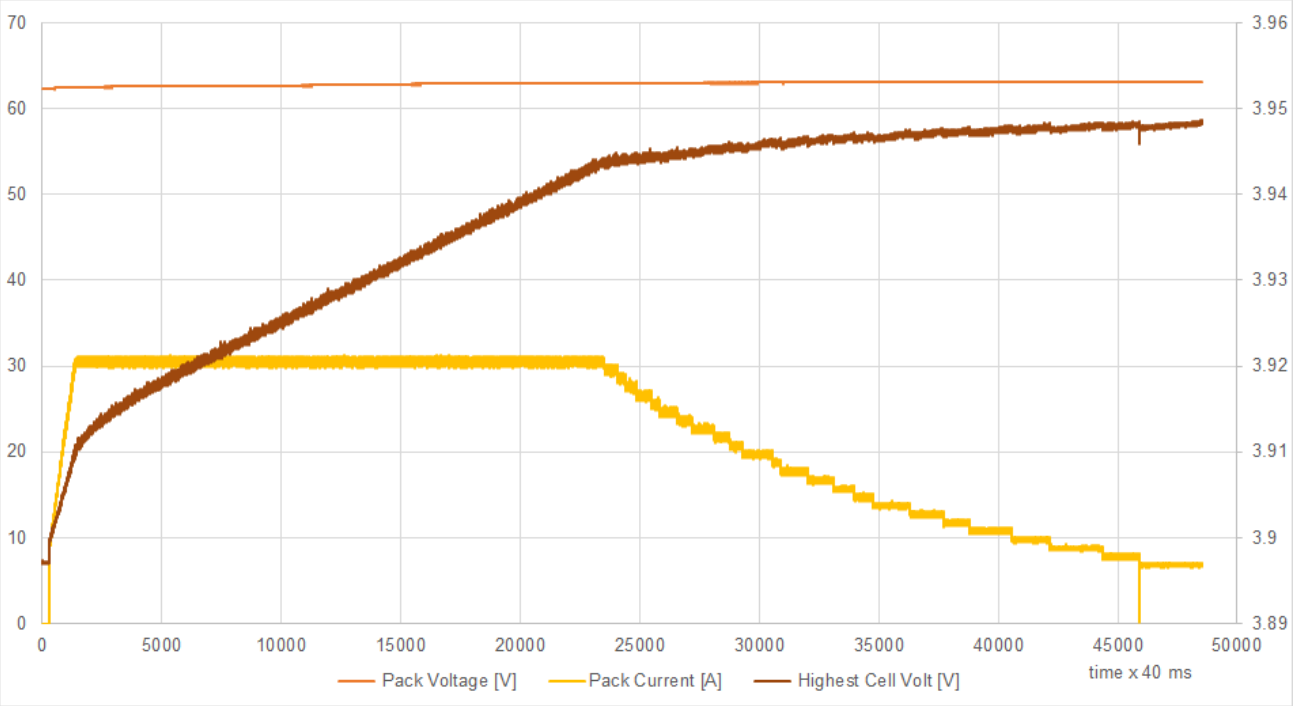


Fig. 5 - CC-CV charging up to max-cell voltage

The charging is performed with Constant Current until the cell voltage is near the maximum value (moment 24000 in Figure 5) when cell voltage balancing is enabled and the requested current limit was reduced. After the cell voltage reached the maximum value for more than 1 s, the constant voltage operation was enabled, and the current limit was reduced to zero, as can be seen in Figure 5 at moment 46000. Because of the cell balancing the charging was re-launched at a lower voltage.

IPMSM motor and three-phase inverter

The electric motor selected for this application was an Internal Permanent Magnet Synchronous Motor developed for electric boats and a dedicated control inverter, both being able to be operated when supplied from a 60 Vdc battery. The motor is a three-phase Y permanent magnet synchronous motor. For overheating, it has a temperature sensor, and for speed control, it has a sin/cos encoder.

The inverter is dedicated to the speed and torque control of 3-phase AC and IPMSM motors. Intended for use as electric traction or hydraulic pump motor controllers for mobile, on-vehicle applications that use a 24-96 Vdc nominal battery supply. The control technique is Field Oriented Control (FOC) algorithms, which can generate the maximum possible torque and efficiency on a wide speed range. The inverter is using the motor's encoder position information in the control loop, as there is extremely important to know the magnet's localization for the optimal control of the motor.

Their main characteristics are:

Table 2

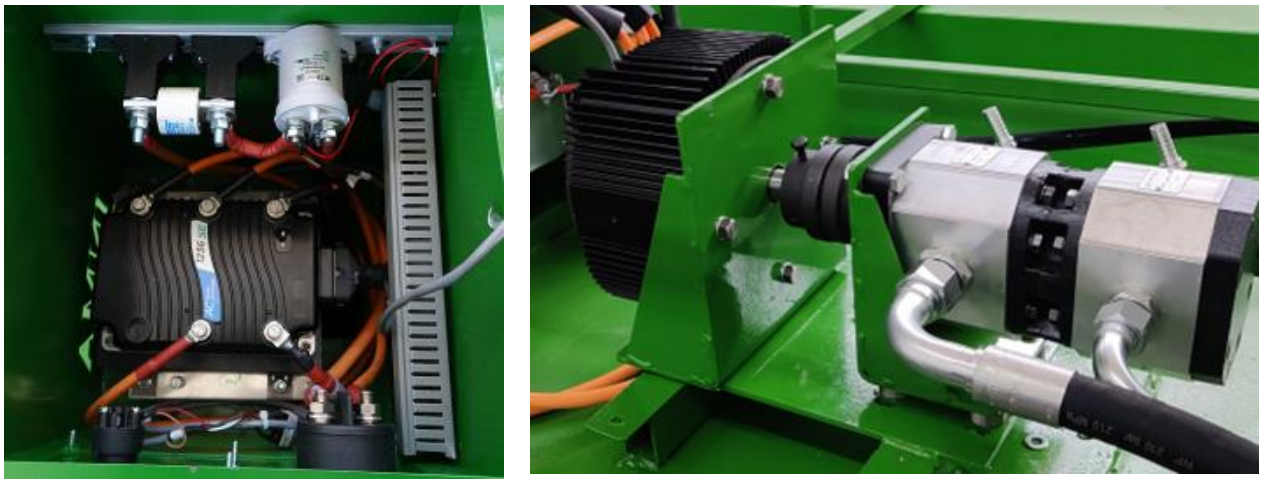
Motor and Inverter characteristics

MOTOR		INVERTER	
Motor's rated power	14.5 kW	Inverter's rated power	24 kW
Maximum power	44 kW	Maximum power	34 kW

MOTOR		INVERTER	
Maximum speed	6000 rpm	Maximum frequency	300 Hz
Rated voltage	48-120 Vdc	Rated voltage	48-96 Vdc
Rated current	250 Aac	Rated current	250 Aac
Maximum current	550 Aac	Maximum current	350 Aac
Mass	20.15 kg	Mass	4.12 kg

To control the electric motor at a specific speed, there must be several external components involved, such as a microprocessor controller, DC contactor, DC power switch, fuse, heatsink, and vents. All those were located in the cubicle near the electric motor, joining the power inverter. The cables between the inverter and the motor are 0.3 m long. The inverter is presented in Figure 3a.

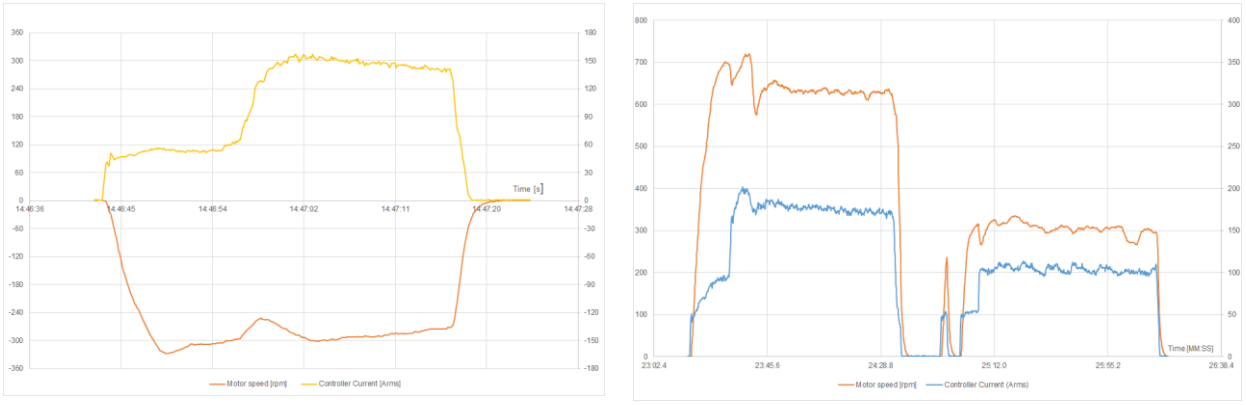
The electric motor is coupled with the hydraulic pump using an axial elastic transmission. The mounting system is revealed in Figure 3b.



a. b.

Fig. 6 - The inverter and the electric motor mounted on the harvester during indoor tests

The electric drive consisting of a motor and inverter is controlled by a dedicated microcontroller which is receiving commands from a remote control and starts the motor with a preregistered speed and current slope when selected. Figure 7 is presenting some stability tests for the electric drive, analyzing the stability of the speed regulator under variable load.



a. b.

Fig. 7 - Motor speed (left axis) and inverter current (right axis) when applying a hydraulic load at 300 rpm and 600 rpm

It could be observed that the electric motor can maintain the speed while the hydraulic load goes on (Figure 7a, moment 14:46:56) and off as imposed by the driver, the speed is quite stable and the current is adjusted adequately. The start is smooth, from 0 to 300 rpm in 6 seconds, and the stop is faster, being performed in 3 seconds.

The whole aquatic harvester boat is a complex machine, which involves several electric and hydraulic powering systems which can fulfill all the requested tasks. Figure 7 is presenting the general 3D project and the picture of the boat in the laboratory where the indoor tests were performed for adjustments of the electronics and the settings of the proportionality of the hydraulic valves.

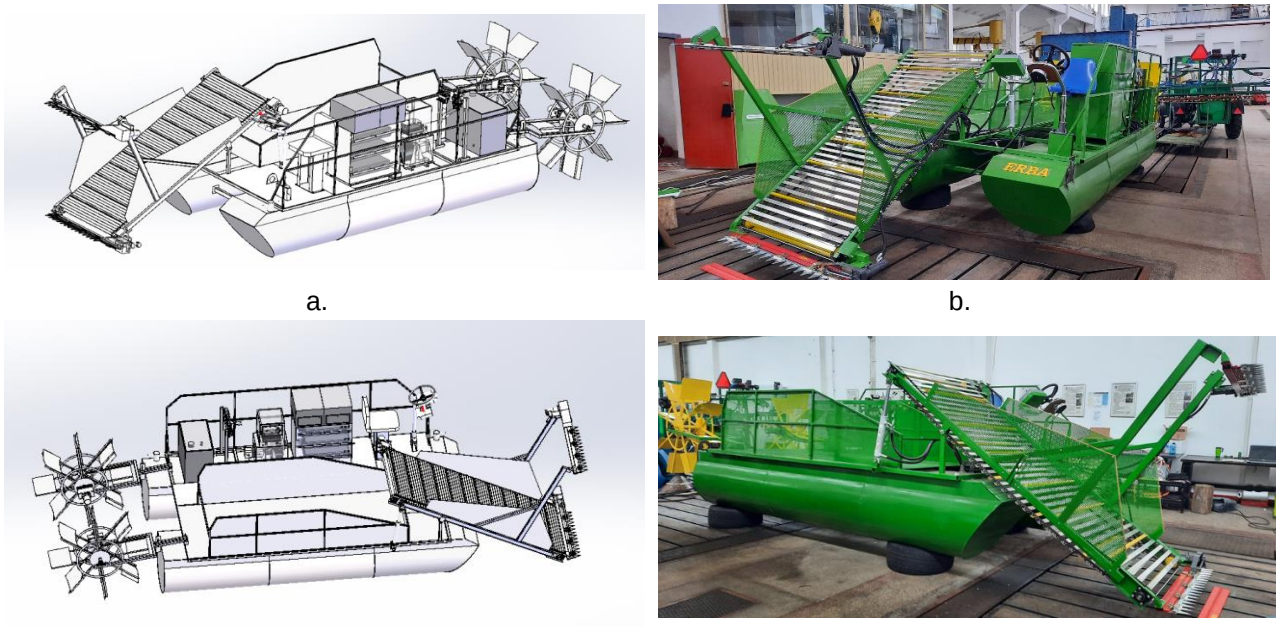


Fig. 8 - The aquatic harvester boat design and prototype during indoor tests

CONCLUSIONS

The prototype of an aquatic harvester boat powered by an electrohydraulic powertrain supplied by traction batteries was completed. All the electric functions were tested using the methodology. The power requested by the hydraulic systems is maintained in the designed range when the electric motor's speed and the hydraulic valves are correlated. There were measured individual loads from 0.7 up to 1.2 kW for auxiliaries and 1-3 kW for each paddle, thus making the rated power of the motor of 14.5 kW suitable for the boat operating in Harvester mode.

For Transfer mode, because the shape of the boat is particular, the currents must be measured while the paddles are pushing the boat, including the influence of the paddle insertion on the water. Further adjustments of the powertrain could be performed, if necessary.

For Charging mode, it is expected to have a 5 h charge from 20 to 90 % of the battery's state-of-charge SOC. Faster charging can be performed if a power outlet is available, in that case, the liquid cooling of the batteries becomes mandatory.

The weight of the vehicle is optimum for the requested payload, autonomy, and specific operational functions. A balancing adjustment was performed indoors and must be verified while on the water.

The boat is prepared for outside tests in water when autonomy, speed, and harvesting efficiency shall be evaluated and optimized.

ACKNOWLEDGEMENT

This work was supported by a grant from the Romanian Research and Innovation Ministry, through Sectorial Plan, contract no. 1PS/2021 and through Programme 1 – Development of the national research and development system, subprogramme 1.2 – Institutional Performance – Projects for financing excellence in RDI, contract no. 25PFE.

REFERENCES

[1] Athina D., Rohit M. P., Praagna G. S. S. K., Malekar E., Shireen K., Ramya B., (2022), Design and Implementation of An Intelligent IoT Based Solar Powered Aqua Harvester to Improve Blue Revolution, *7th International Conference on Communication and Electronics Systems (ICCES)*, pp. 1775-1782, Coimbatore, India.

[2] Gong L., Sharma A., Abdul Bhuiya M., Flaih Awad H., Youssef M. Z., (2021), An Artificial Intelligence Based Fault Monitoring of Power Trains: Design & Implementation, *IEEE Applied Power Electronics Conference and Exposition (APEC)*, pp. 2761-2768, India.

[3] Juostas A, Jotautiene E., (2022), Study of Combine Harvester Remote Monitoring Systems for Fuel Consumption and Environmental Impact Control, *Chemistry Proceedings*, Vol. 10(1):13, MDPI Basel, ISSN: 2673-4583, Switzerland

[4] Lv J., Lin S., Song W., Chen M., Feng Z., Li Y., Ding Y., (2019), Performance of LiFePO4 batteries in parallel based on connection topology, *Applied Energy*, Vol 252, Elsevier, ISSN 0306-2619, Netherlands.

[5] Marin F., Biriș S. Șt., (2021), Research on increasing the performance of combine harvesters by developing and implementing intelligent parameter adjustment systems, *Proceedings of the ISB-INMATEH International Symposium*, pp.450-455, ISSN 2537 – 3773, Bucharest, Romania

[6] Moussodji J., De Bernardinis A., (2015), Electric hybridization of a bow thruster for riverboat application, *2015 IEEE Transportation Electrification Conference and Expo (ITEC),* IEEExplore, pp. 1-6, DOI: 10.1109/ITEC.2015.7165811, Dearborn, MI, USA.

[7] Pratama A.-E., Hesty A., (2019), Design Aquatic Weed and Trash Skimmer Boat with Paddle Wheel in Kalimas River Surabaya (Desain Aquatic Weed and Trash Skimmer Boat dengan), *Jurnal Teknik ITS*, Vol. 2, No. 2, ISSN:2337-3539, Indonesia.

[8] Shigeyuki M., Mori K., Yamada T., Oya T., Koizumi K., Ikeda H., Kojima K., (2019), The Evolution of a Newly Developed FCV-Loaded Electric Boat, *Journal of Asian Electric Vehicles*, Vol. 17(2), pp.1835-1840, ISSN: 1883-6038, Japan.

[9] Tudor E., Matache M.G., Vasile I., Sburlan I.C., Stefan V., (2022), Automation and Remote Control of an Aquatic Harvester Electric Vehicle, *Sustainability,* Vol. 14, No. 10, art. 6360.MDPI-Basel, ISSN:2071-1050, Switzerland.

[10] Un-Noor F., Padmanaban S., Mihet-Popa L., Mollah M. N., Hossain E., (2017) A Comprehensive Study of Key Electric Vehicle (EV) Components, Technologies, Challenges, Impacts, and Future Direction of Development, *Energies* Vol. 10, Art.1217, MDPI-Basel, ISSN:1996-1073, Switzerland.

[11] Waltham N.J., Pyott M., Buelow C., Wearne, L, (2020), Mechanical harvester removes invasive aquatic weeds to restore water quality and fish habitat values on the Burdekin floodplain, *Ecol Manag Restor*, Vol. 21, pp. 187-197, Wiley, USA.

[12] Sonam Y., Park J.H., Lee S.S., Yoo C., (2016), Hydraulic circuit analysis for the electro-hydrostatic actuator system, (2016) *16th International Conference on Control, Automation and Systems (ICCAS)*, IEEE, pp. 178-181, Korea.

[13] Zhicheng S., Zhou B., Meng Q., Dai T., Li S., (2019), Trend Analysis of Electric Vehicle's Power Consumption Based on EV-TEST, (2019), *International Conference on Advances in Construction Machinery and Vehicle Engineering (ICACMVE)*, IEEE, pp. 291-294, China.

CALIBRATION AND EXPERIMENTS OF THE SIMULATION BONDING PARAMETERS FOR PLUG SEEDLING SUBSTRATE BLOCK

/

穴盘苗基质块仿真粘结参数标定与试验

Hongbin BAI[1)], Xuying LI*[1)], Fandi ZENG[1)], Qiang SU[1)], Ji CUI[1)], Junyue WANG[1,2)], Yongzhi ZHANG[1)]

[1)] Inner Mongolia Agricultural University, College of Mechanical and Electrical Engineering, Hohhot/China;

[2)] China Academy of Agricultural Mechanization Science Hohhot Branch Co., Ltd. Hohhot/China

Tel: +86 04714309215; E-mail: bhb81571@163.com

DOI: https://doi.org/10.35633/inmateh-69-59

Keywords: *Simulation; Seedling substrate block; Parameter calibration; Bonding model*

ABSTRACT

To accurately simulate the interactions between the plug seedlings and the planter during the planting process and explore the damage mechanism of the plug seedling substrate block, the bonding parameters of plug seedling substrate block were calibrated by the discrete element method. The physical puncture test showed that the average of maximum force of the cone indenter on substrate block measured by texture analyzer was 4.633 N. A Hertz-Mindlin with the bonding model was established for the substrate block in EDEM software. A virtual calibration experiment was designed with the puncture force of substrate block as the evaluation index. The two-level factorial test and the steepest climbing test were used to screen out the significant parameters and the optimal interval. Then, the Box-Behnken test and the optimization solution were used to obtain the optimal bonding parameter combination of the substrate block particles. Finally, the optimal parameter combination was simulated and verified. The relative error of the maximum puncture force between the simulated value and the measured value was 1.88%, which indicated that the bonding parameters of the substrate block obtained by calibration were accurate and reliable.

摘要

为准确模拟栽植过程中穴盘苗与栽植器间的相互作用，探究穴盘苗基质块的破损机理，采用离散元法校准了穴盘苗基质块的粘结参数。通过物理穿刺试验测得锥形压头对基质块的最大穿刺力平均值为 4.633 N。应用 Hertz-Mindlin with bonding 模型对基质块进行建模，并以最大穿刺力为评价指标，采用二水平析因试验和最陡爬坡试验筛选出显著性参数和最优区间，通过 Box-Behnken 试验和优化求解，得到基质块颗粒的最佳粘结参数组合，针对最优参数组合进行仿真验证，得出仿真值和实测值最大穿刺力相对误差为 1.88%，表明标定所得基质块粘结参数准确可靠。

INTRODUCTION

Transplanting is an agriculture task that involves transferring and planting seedlings grown uniformly in a nursery to a field (*Hwang et al., 2020; Kumar G et al., 2011*). The use of seedling transplanting technology can effectively avoid the impacts of catastrophic weather, create favorable conditions, and increase the survival rates of seedlings (*Kumi F et al., 2016; Zhichao Cui et al., 2022*). The seedlings grow on the substrate block and absorb nutrients from it (*Yongshuang Wen et al., 2021; Luhua Han et al., 2019*). However, during processes of mechanized transplanting, the collision between the plug seedling and the components of machines is unavoidable, which can easily cause mechanical damage to the seedling substrate block, thus seriously affecting the transplanting quality and causing economic losses (*Lvhua Han et al., 2013; Huili Wang et al., 2017*).

The interaction between the plug seedling and components of the transplanting machine is often complicated, and the traditional test and theoretical methods can not accurately analyze the damage mechanism of the seedling substrate block during the collision. In recent years, discrete element method and simulation software EDEM have been widely used in the field of agriculture, providing a new way to study the contact characteristics between agricultural materials and mechanical parts, and promoting the research and development of agricultural equipment and the optimization of related working parameters (*Aikins KA et al., 2023; Obermayr M et al., 2014*).

At present, relevant scholars have conducted a lot of research on agricultural materials based on the discrete element method, and have completed discrete element modeling and simulation research on materials such as potatoes (*Zhongcai Wei et al., 2020*), soil (*Li J. et al., 2022*), seed (*Xuejie Ma et al., 2022; Bhupendra M.G. et al., 2018*), corn straw (*Shuhong Zhao et al., 2021*) and so on. Before the simulation, it is necessary to accurately establish the discrete element model of the material and define the simulation parameters of the model to ensure the reliability of simulation results.

The simulation parameters are usually obtained by direct measurement and parameter calibration. *Ghodki et al.,* (*2019*), calibrated the discrete element simulation parameters of soybean pellets. *Wu et al*., (*2017*), designed the rest-angle simulation test based on the Box-Behnken principle and realized the contact parameter calibration of the discrete element model of cohesive soil. *Zhang et al.,* (*2022*), measured the maximum shear force of water chestnuts by shear test, and used it as a reference to conduct simulation parameter calibration of water chestnut bonding parameters by a screening test, response surface variance analysis, and regression equation optimization method. *Feng et al.,* (*2016*) and *Wu et al.,* (*2021*), respectively measured the simulation parameters of the substrate block of Antrata and strawberry plug seedlings by direct measurement method. *Yuan et al.,* (*2020*) and *Sheng et al.,* (*2021*), used the Hertz-Mindlin with bonding model to calibrate the simulation parameters of the soil model with the actual soil firmness as the target value.

In order to accurately establish the discrete element model of the plug seedling substrate block and ensure the reliability of the subsequent discrete element simulation results for the transplanting process, the physical test and simulation test were combined to calibrate the bonding parameters of the substrate block. The maximum puncture force of the cone indenter on the substrate block was obtained through a physical puncture test. Based on this, the two-level factorial test, steepest climb test and Box-Behnken test were carried out successively to calibrate the discrete element simulation bonding parameters of the substrate block.

MATERIALS AND METHODS

Test material

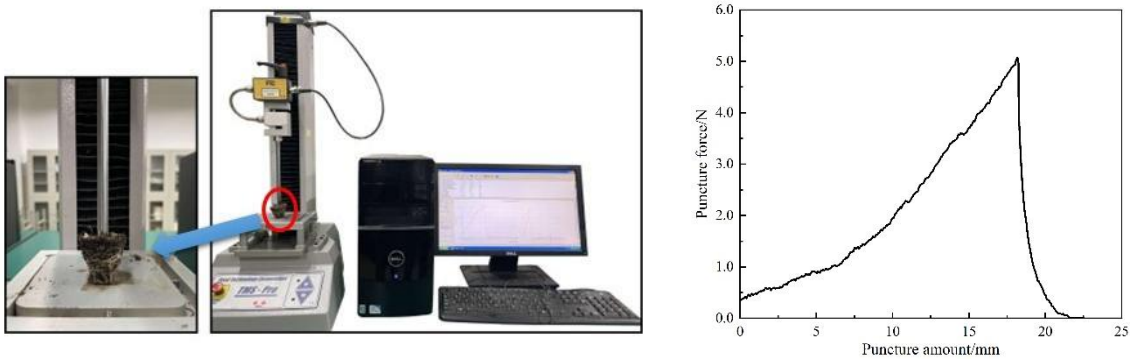
A typical variety of oil sunflower seedlings, Tonghui 562, was selected as the test subject, as shown in Figure 1. The seedlings were cultivated at the Hohhot Modern Agriculture Development Base. The age of seedlings was 30 d. The moisture content of the substrate block was about 60%. The seedling substrate was a mixture of charcoal, perlite, and vermiculite. The volume ratio was as follows: 3:1:1 of charcoal, perlite, and vermiculite, respectively.



Fig. 1 - Oil sunflower plug seedlings at the planting stage

Physical puncture test of the seedling substrate block

The TMS-Pro texture analyzer was used to perform the puncture test on the seedling substrate block to obtain the actual reference value reflecting the bonding parameters, as shown in Figure 2a. During the test, the forward speed of puncture was set to 30 mm/s, the return speed was 45 mm/s, the puncture height ratio was 60%, the trigger force was 0.34 N, and a data point was collected every 0.1 seconds. The experiment was repeated 10 times, and the average value of the maximum puncture force of the cone indenter on the substrate block was 4.633 N, which was used as the physical reference value of the bonding parameters for the virtual calibration test. Figure 2b shows the change curve of puncture force and puncture amount after the puncture test.



a. Puncture test of seedling substrate block b. Puncture force-amount curve

Fig. 2 - Puncture test process and result curve

Substrate block discrete element model construction

The Hertz-Mindlin with bonding model is often used in the case of material breakage and fracture. The model is bonded by multiple particles, and the bonding bonds are formed between the particles. When the model is subjected to external force, the bonding bonds between the particles will change, and the formed particle clusters will produce fracture and crushing effects. Therefore, the Hertz-Mindlin with the bonding model is more suitable for the study of the contact mechanism between materials and mechanical components (*Shijie Feng, 2020*).

The seedling substrate block is an inverted square quadrangle with a relatively regular shape, so a conventional modeling approach was used to create a simulation model of the substrate block and cone indenter, with all dimensions consistent with the physical tests. The discrete element model of the substrate block was established by referring to the reference *Zhang et al.,* (*2022*), and the simulation model of the substrate block composed of particles was obtained. As shown in Figure 3, the radius of the particles is set to 1 mm, the number of particles in the mantle is 3882, and a total of 11151 bonds are generated. Table 1 shows the parameters of mechanical properties (density, Poisson's ratio, modulus of elasticity), and the basic contact parameters (coefficient of collision recovery, coefficient of static friction, and coefficient of dynamic friction) between a substrate block and stainless steel (*Ying Wang et al., 2014; Feng T, 2016; Shijie Feng, 2020*).

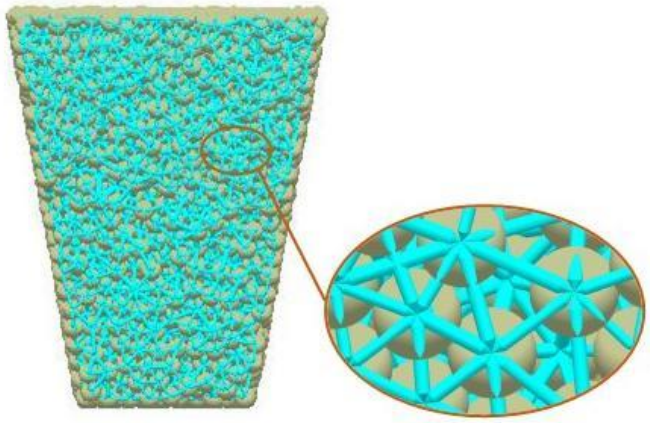


Fig. 3 - Discrete element simulation model of the seedling substrate block

Table 1

Mechanical properties and basic contact parameters

Mechanical properties parameters		Basic contact parameters	
Parameters	**Values**	**Parameters**	**Values**
Substrate block density/[kg/m^3]	395	Block-block collision recovery coefficient	0.20
Substrate block Poisson's ratio	0.43	Block-block static friction coefficient	0.65
Substrate block elasticity modulus/[Pa]	1.25×10^6	Block-block dynamic friction coefficient	0.43
stainless steel density/[kg/m^3]	7850	Steel-block collision recovery coefficient	0.21
stainless steel Poisson's ratio	0.35	Steel-block static friction coefficient	0.44
stainless steel elasticity modulus/[Pa]	7.0×10^{10}	Steel-block dynamic friction coefficient	0.13

TEST METHODS

Two-level factorial test

The two-level factorial test can quickly screen out the significant influence on the test index under the condition of many influencing factors. It greatly reduces the number of tests. According to the Hertz-Mindlin with bonding model, the breakage of the bond between particles is related to the particle contact radius X_1, the normal stiffness per unit area X_2, the tangential stiffness per unit area X_3, the critical normal stress X_4, the critical tangential stress X_5 and the bonding radius X_6. The initial range of bonding parameters was determined by reviewing the relevant literature (*Ying Wang et al., 2014; Feng T, 2016; Shijie Feng, 2020*) and extensive pre-tests, and are summarized in Table 2. Based on the determined range of bond parameters, a total of 16 sets of two-level factorial tests were designed, as shown in Table 3.

Table 2

Simulation test parameters range

Simulation parameters	Low level	High level
Particle contact radius X_1 [mm]	1.2	2.0
Normal stiffness per unit area X_2 [N/m^3]	1.0×10^6	8.0×10^6
Tangential stiffness per unit area X_3 [N/m^3]	1.0×10^6	8.0×10^6
Critical normal stress X_4 [Pa]	2200	3000
Critical tangential stress X_5 [Pa]	2200	3000
Bonding radius X_6 [mm]	1.2	2.0

Steepest climbing test

To quickly determine the range of the optimal values, based on the two-level factorial test, the steepest climbing test was carried out on the screened significant factors. During the experiment, the relative error between the maximum simulated puncture force and the physical reference value was used as the evaluation index. The non-significant bonding parameter takes the intermediate level value in the two-level factorial test, and the significant parameter gradually increases within the value range according to the set step size.

The relative error calculation formula is shown in Eq. (1).

$$e = \frac{|F_P - F_S|}{F_P} \times 100\% \quad (1)$$

Where: e is the relative error, %; F_P is the physical reference value of puncture force, N; F_S is the maximum simulated puncture force, N.

Box-Behnken test

Based on the results of the two-level factorial test and the steepest climbing test, the Box-Behnken test was designed using Design-Expert 13 software to obtain the best combination of bonding parameters for the simulation. Test parameter No. 5 in the steepest climbing test was taken as the intermediate level, and test parameters No. 6 and No. 4 were taken as high and low levels respectively for the Box-Behnken test, and the maximum puncture force of the simulation test was taken as the evaluation index.

Calibration result verification

To check whether the calibrated parameters can be used in subsequent discrete element simulation studies, so that the simulated puncture force value is closest to the physical reference value, it is necessary to optimize and solve the regression equation in the optimization module of the Design-Expert 13 software, and compare with the physical reference value to verify the accuracy and reliability of the parameter calibration.

RESULTS AND DISCUSSION

Two-level factorial test and significance analysis

The two-level factorial test scheme and results are shown in Table 3. Minitab 19 software was used to conduct variance analysis on the test results, and the significant results of each simulation parameter were obtained, as shown in Table 4. As can be seen from Table 4, the normal stiffness per unit area (X_2) and bonding radius (X_6) have an extremely significant effect on the maximum puncture force; the tangential stiffness per unit area (X_3) has a significant effect on the maximum puncture force; the influence of other parameters on the maximum puncture force is not significant.

Table 3

Two-level factorial test scheme and results

No.	X_1	X_2	X_3	X_4	X_5	X_6	Maximum puncture force
	[mm]	[$\times 10^6$N/m^3]	[$\times 10^6$N/m^3]	[Pa]	[Pa]	[mm]	[N]
1	2.0	1.0	8.0	3000	2200	1.2	1.993
2	1.2	1.0	1.0	2200	2200	1.2	0.765
3	1.2	1.0	8.0	2200	3000	2.0	3.050
4	1.2	8.0	1.0	3000	3000	1.2	2.320
5	2.0	1.0	1.0	2200	3000	1.2	0.798
6	2.0	8.0	8.0	3000	3000	2.0	5.980
7	1.2	1.0	8.0	3000	3000	1.2	2.232
8	1.2	8.0	8.0	2200	2200	1.2	2.080
9	1.2	8.0	1.0	2200	3000	2.0	5.010
10	2.0	1.0	1.0	3000	3000	2.0	2.290
11	2.0	1.0	8.0	2200	2200	2.0	2.230
12	1.2	8.0	8.0	3000	2200	2.0	4.990
13	2.0	8.0	1.0	3000	2200	1.2	2.400
14	1.2	1.0	1.0	3000	2200	2.0	1.930
15	2.0	8.0	8.0	2200	3000	1.2	4.230
16	2.0	8.0	1.0	2200	2200	2.0	4.830

Table 4

Variance analysis of two-level factorial test

Parameter	Degree of freedom	Sum of squares	Mean square	F-value	P-value
Model	6	32.904	5.484	11.89	0.001
X_1	1	0.352	0.352	0.76	0.405
X_2	1	17.123	17.123	37.11	<0.0001**
X_3	1	2.594	2.594	5.62	0.042*
X_4	1	0.082	0.082	0.18	0.684
X_5	1	1.376	1.376	2.98	0.118
X_6	1	11.377	11.377	24.66	0.001**
Residual	9	4.152	0.461		

*Note: ** indicates an extremely significant effect (p<0.01),* indicates a significant effect (p<0.05). Same as below*

Analysis of the steepest climbing test

The three significant parameters obtained from the two-level factorial test were subjected to the steepest climbing test. The test design and results are shown in Table 5. With the gradual increase of the value of each significant parameter, the maximum puncture force of the cone indenter on the seedling substrate block gradually increases, and the relative error between the simulated puncture force and the physical reference value decreases first and then increases. Among them, under the parameter combination corresponding to the No.5 test, the relative error is the smallest, and the optimal range can be determined near the No.5 test.

Table 5

Schemes and results of steepest climbing test

No.	X_2	X_3	X_6	Maximum puncture force	Relative Error
	[$\times 10^6$N/m^3]	[$\times 10^6$N/m^3]	[mm]	[N]	[%]
1	0.9	0.9	1.1	0.600	87.04
2	2.5	2.5	1.3	1.766	61.86
3	4.1	4.1	1.5	2.970	35.85
4	5.7	5.7	1.7	4.150	10.37
5	7.3	7.3	1.9	4.980	7.56
6	8.9	8.9	2.1	5.910	27.65

Box-Behnken test results and analysis

Based on the steepest climbing test results, the Box-Behnken response surface test was carried out on the three parameters of normal stiffness per unit area (X_2), tangential stiffness per unit area (X_3), and bonding

radius (X_6). The test parameter levels is shown in Table 6. The Box-Behnken test schemes and results are shown in Table 7, and the Box-Behnken test analysis of variance is shown in table 8.

Table 6

Parameter levels code table

Level	Test parameters		
	X_2 [$\times 10^6$N/m^3]	X_3 [$\times 10^6$N/m^3]	X_6 [mm]
-1	5.7	5.7	1.7
0	7.3	7.3	1.9
1	8.9	8.9	2.1

Table 7

Box-Behnken test schemes and results

No.	X_2 [$\times 10^6$N/m^3]	X_3 [$\times 10^6$N/m^3]	X_6 [mm]	Maximum puncture force [N]
1	-1	1	0	4.22
2	0	1	-1	4.34
3	0	0	0	4.98
4	0	0	0	4.98
5	0	-1	-1	4.52
6	-1	-1	0	4.20
7	0	0	0	4.89
8	-1	0	1	4.57
9	1	1	0	4.35
10	1	0	-1	4.61
11	0	1	1	4.51
12	1	0	1	4.55
13	1	-1	0	4.88
14	0	0	0	4.73
15	0	0	0	4.73
16	-1	0	-1	3.72
17	0	-1	1	4.84

Table 8

Analysis of variance for Box-Behnken test results

Source of variance	Mean square	Degree of freedom	Sum of squares	F-value	P-value
Model	0.186	9	1.670	17.32	0.0005**
X_2	0.353	1	0.353	32.85	0.0007**
X_3	0.130	1	0.130	12.11	0.0103*
X_6	0.205	1	0.205	19.07	0.0033**
$X_2 X_3$	0.076	1	0.076	7.04	0.0328*
$X_2 X_6$	0.207	1	0.207	19.28	0.0032**
$X_3 X_6$	0.006	1	0.006	0.52	0.4927
X_2^2	0.431	1	0.431	40.08	0.0004**
X_3^2	0.071	1	0.071	6.60	0.0371*
X_6^2	0.136	1	0.136	12.67	0.0092**
Residual	0.011	7	0.075		
Lack of Fit	0.004	3	0.012		

Design-Expert 13 software was used to perform multiple regression fitting on the test results in Table 7, and the regression equation with the cone indenter's puncture force on the seedling substrate block as the target value and X_2, X_3, X_6 as the variables was obtained:

$$F = -134.43 + 13.27X_2 + 4.72X_3 + 87.84X_6 - 0.22X_2X_3 - 2.84X_2X_6 - 0.47X_3X_6 - 0.50X_2^2 - 0.21X_3^2 - 17.98X_6^2 \quad (2)$$

The results of the Box-Behnken test ANOVA (analysis of variance) are shown in Table 8. Perform the ANOVA on the test results, where X_2, X_6, X_2X_6, X_2^2, and X_6^2 all have extremely significant effects on the maximum puncture force; X_3, X_2X_3, and X_3^2 has a significant effect on the maximum puncture force; the remaining parameters have no marked effect on the maximum puncture force. The p-value of the quadratic regression models is less than 0.001, where the regression model coefficient of determination R^2=0.957 and Adjusted R^2=0.902 are both close to 1 and with a coefficient of variation C.V.=2.27%. The results showed that the regression model reliably reflects the real situation. According to the above regression equation, the response surfaces of the interaction of each significance parameter to the maximum puncture force were obtained respectively, as shown in Figure 4.

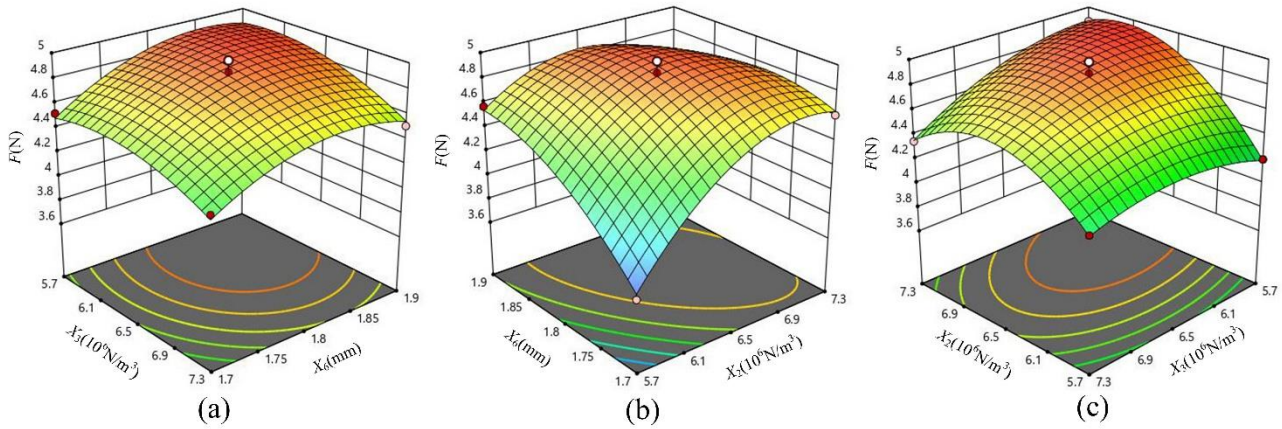


Fig. 4 – Box-Behnken test results response surface

Note: (a) Effect of tangential stiffness per unit area and bonding radius on maximum puncture force; (b) Effect of bonding radius and normal stiffness per unit area on maximum puncture force; (c) Effect of normal stiffness per unit area and tangential stiffness per unit area on maximum puncture force.

Seedling substrate block simulation test validation

Optimization of the regression equation is made to obtain the optimal combination of bonding parameters for substrate seedling block, using the physical reference value 4.633 N as the target value by Design-Expert 13.0 software: the normal stiffness per unit area (X_2) is 7.3×10^6 N/m^3, the tangential stiffness per unit area (X_3) is 6.775×10^6 N/m^3, and the bonding radius (X_6) is 1.813 mm. The other bonding parameters were taken as the intermediate level values in the two-level factorial test.

In order to verify the accuracy and reliability of the simulation calibration, the above parameters are used as the EDEM simulation parameters to simulate the puncture test of the seedling substrate block. The simulation validation test was repeated 3 times. The average of maximum puncture force of substrate block is 4.72 N, with a relative error of 1.88% compared with the physical reference value of 4.633 N. T test was performed on the sample using SPSS software, and P=0.799>0.05 was obtained, indicating that there was no significant difference between the simulated puncture force and the physical reference value. The test comparison is shown in Figure 5. In the simulated puncture test, the interaction between the cone indenter and the seedling substrate block is represented using the substrate block bonding bond.

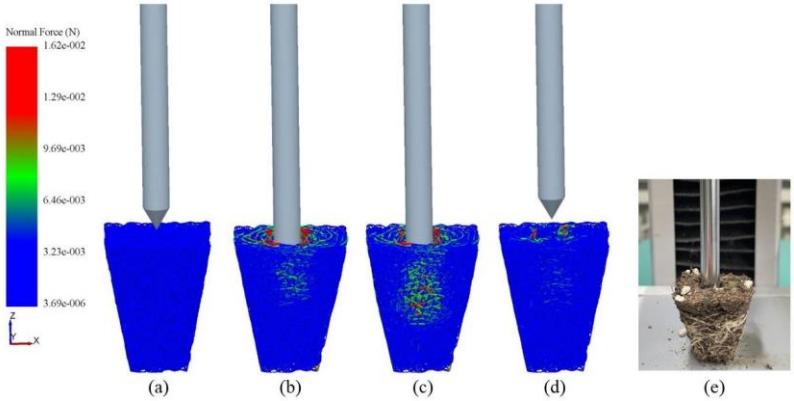


Fig. 5- Experiment comparison on puncturing of seedling substrate block

Note: (a) Cone indenter Puncture preparation stage; (b) Cone indenter puncture stage; (c) Cone indenter punctured to lowest point; (d) Return of the cone indenter to the initial stage of the puncture; (e) Physical puncture test.

CONCLUSIONS

Based on Hertz-Mindlin with bonding model, combined with physical test and virtual calibration test, the discrete element simulation parameters of plug seedling substrate block were calibrated, and the optimal parameter combination of the substrate block bonding model was obtained and verified. The calibration results can improve the precision of simulated transplanting experiment and optimize the parameters of field transplanting operation. The main conclusions are as follows:

(1) Two-level factorial test and steepest climbing test were used to screen out the parameters which had significant influence on the puncture force of the plug seedling substrate block.

(2) A Box-Behnken response surface test was performed to establish a second-order regression model of the puncture force on the significance parameters. The model was optimally solved for the physical reference value (4.633 N), and the best combination of parameters was obtained as follows: the normal stiffness per unit area (X_2) is 7.3×10^6 N/m^3, the tangential stiffness per unit area (X_3) is 6.775×10^6 N/m^3, and the bonding radius (X_6) is 1.813 mm.

(3) The T-test showed that P=0.799>0.05, indicating that there was no significant difference between the maximum puncture force of the physical test and that of the simulated test, and the relative error is 1.88%, which further verifies the authenticity and reliability of the simulation parameters.

ACKNOWLEDGEMENTS

We acknowledge that this work was supported by the National Natural Science Foundation of China (No. 32160423) and the Natural Science Foundation of Inner Mongolia Autonomous Region of China (No. 2021MS05048).

REFERENCES

[1] Hwang S.J., Park J.H, Lee J.Y. et al. (2020). Optimization of main link lengths of transplanting device of semi-automatic vegetable transplanter. *Agronomy*, 10(12), 1938.

[2] Kumar G., Raheman H. (2011). Development of a walk-behind type hand tractor powered vegetable transplanter for paper pot seedlings. *Biosystems Engineering*, 110(2), 189-197.

[3] Kumi F., Mao H., Li Q. et al. (2016). Assessment of Tomato Seedling Substrate-Root Quality Using X-Ray Computed Tomography and Scanning Electron Microscopy. *Applied Engineering in Agriculture*, 32(4), 1-11.

[4] Zhichao Cui, Chunsong Guan, Tao Xu et al. (2022). Development status of technology and equipment of substrate block seedling cultivation and transplanting (基质块育苗移栽技术与装备发展现状). *Journal of Chinese Agricultural Mechanization*, 43(05), 29-34.

[5] Yongshaung Wen, Leian Zhang, Xuemei Huang et al. (2021). Design of and Experiment with Seedling Selection System for Automatic Transplanter for Vegetable Plug Seedlings. *Agronomy*, 11(10), 2031.

[6] Luhua Han, Kumi F, Hanping Mao et al. (2019). Design and tests of a multi-pin flexible seedling pick-up gripper for automatic transplanting. *Applied engineering in agriculture*, 35(6), 949-957.

[7] Lvhua Han, Hanping Mao, Jianping Hu et al. (2019). Experiment on mechanical property of seedling pot for automatic transplanter (穴盘苗自动移栽钵体力学特性试验). *Transactions of the Chinese Society of Agricultural Engineering*, 29(02), 24-29.

[8] Huili Wang, Yong Zhou, Peitong Wang et al. (2017). Mechanical properties of cotton bowl seedling and cotton bowl (棉花钵苗和钵体的力学特性试验). *Journal of Huazhong Agricultural University*, 36(02), 117-122.

[9] Aikins K.A., Ucgul M., Barr J.B. et al. (2023). Review of Discrete Element Method Simulations of Soil Tillage and Furrow Opening. *Agriculture*, 13(3), 541.

[10] Obermayr M., Vrettos C., Eberhard P. et al. (2014). A discrete element model and its experimental validation for the prediction of draft forces in cohesive soil. *Journal of Terramechanics*, 53, 93–104.

[11] Zhongcai Wei, Guosu Liang, Xueqiang Li et al. (2020). Parameter Optimization and Test of Potato Harvester Wavy Sieve Based on EDEM (基于离散元的马铃薯收获机波浪形筛面参数优化与试验). *Transactions of the Chinese Society for Agricultural Machinery*, 51(10), 109-122.

[12] Li J., Xie S., Liu F. et al. (2022). Calibration and testing of discrete element simulation parameters for sandy soils in potato growing areas. *Applied Sciences*, 12(19), 10125.

[13] Xuejie Ma, Zhanfeng Hou, Min Liu. (2022) Calibration of simulation parameters of coated particles and analysis of experimental results. *INMATEH-Agricultural Engineering*, 67(2), 233-242.
[14] Bhupendra M Ghodki, K. Charith Kumar, T.K. Goswami. (2018). Modeling breakage and motion of black pepper seeds in cryogenic mill. *Advanced Powder Technology*, 29(5), 1055-1071.
[15] Shuhong Zhao, Lianlong Gao, Yiwen Yuan et al. (2022). Maize straw motion law in subsoiling operation using discrete element method (基于离散元法的深松作业玉米秸秆运动规律). *Transactions of the Chinese Society of Agricultural Engineering*, 37(20), 53-62.
[16] Ghodki, Bhupendra M. Patel, ManishNamdeo, RohitCarpenter et al. (2019). Calibration of discrete element model parameters: soybeans. *Computational particle mechanics*, 6(1), 3-10.
[17] Wu T., Huang W., Chen X. et al. (2017). Calibration of discrete element model parameters for cohesive soil considering the cohesion between particles (考虑颗粒间黏结力的黏性土壤离散元模型参数标定). *Journal of South China Agricultural University*, 38(03), 93-98.
[18] Zhang G., Chen L., Liu H. et al. (2022). Calibration and experiments of the discrete element simulation parameters for water chestnut (荸荠离散元仿真参数标定与试验). *Transactions of the Chinese Society of Agricultural Engineering*, 38(11), 41-50.
[19] Feng T. (2016). *Optimization design and test research of plug seedlings end-effector in greenhouse* [Master's thesis], Beijing University of Technology.
[20] Wu D. (2021). *Design and experiment of small electric strawberry directional transplanter machine* [Master's thesis], Jiangsu University.
[21] Yuan J., Li J., Zou L. et al. (2020). Optimal Design of Spinach Root-cutting Shovel Based on Discrete Element Method (基于离散元的菠菜收获机根切铲优化设计与试验). *Transactions of the Chinese Society for Agricultural Machinery*, 51(S2), 85-98.
[22] Sheng Y. (2021). *Improved Design and Experimental Research of Straw Forage Harvester Based on Discrete Element Method* [Master's thesis], Inner Mongolia Agricultural University.
[23] Shijie Feng. (2020). *Study on Pick-up System and Pot Body Damage Mechanism of Rape Pot Seedling Based on Movable Tray* [Doctor's thesis], Hunan Agricultural University.
[24] Ying Wang, Jianneng Chen, Jiawei Wu et al. (2014). Mechanics property experiment of broccoli seedling oriented to mechanized planting (用于机械化栽植的西兰花钵苗力学特性试验). *Transactions of the Chinese Society of Agricultural Engineering*, 30(24), 1-10.

OPTIMIZATION OF SCREW CONVEYING OF KNEADED CORN STALKS BASED ON DISCRETE ELEMENT METHOD
/
基于离散元法的揉碎玉米秸秆螺旋输送的优化

ZhiPeng FAN, Zhe MA, HongBo WANG*, ZhiHong YU
College of Mechanical and Electronic Engineering, Inner Mongolia Agricultural University, Hohhot / China
Tel: +86 13739981395; E-mail: wanghb@imau.edu.cn
DOI: https://doi.org/10.35633/inmateh-69-60

Keywords: *screw conveyor, kneading corn stalks, discrete elements, parameter optimization*

ABSTRACT
In order to explore the conveying mechanism of kneaded corn stalk in the screw conveyor and improve the conveying performance of the screw conveyor, the study of the screw conveying process of kneaded corn stalk was carried out, and the simulation model of the screw conveying process was established by using the discrete element method. The results showed that: The pitch, feed amount and screw shaft speed have significant effects on the productivity and power of screw conveying, and there are significant interactions. The optimal parameters of the multi-factor simulation optimization test were 319.428 mm pitch, feed amount of 71.062 kg/min, screw shaft speed of 117.034 r/min, corresponding productivity of 71.517 kg/min and power of 769.84 W. This study reveals the screw conveying mechanism of kneaded corn stalk, verifies the feasibility of using discrete element simulation to analyse the conveying process of kneaded corn stalk, and provides a theoretical basis for improving and optimizing the screw conveying device.

摘要
为了探究揉碎玉米秸秆在螺旋输送机中的输送机理，提高螺旋输送机的输送性能，该研究揉碎玉米秸秆螺旋输送过程中的螺距、喂入量、螺旋轴转速进行单因素、多因素试验和离散元仿真。结果表明：螺距、喂入量、螺旋轴转速对螺旋输送的生产率和功率有显著影响，且存在显著的交互作用；多因素仿真寻优试验的最优参数结果为螺距 319.428 mm、喂入量 71.062 kg/min、螺旋轴转速 117.034 r/min，对应的生产率为 71.517 kg/min，功率为 769.84 W。该研究揭示了揉碎玉米秸秆的螺旋输送机理，验证了运用离散元仿真分析揉碎玉米秸秆输送过程的可行性，同时为改进和优化螺旋输送装置提供理论依据。

INTRODUCTION
Maize is an important food crop and feed crop, with great production potential, high economic benefits, edible, feed and a variety of industrial uses, and has an important strategic position in ensuring food security. According to statistics, China's corn production in 2021 was about 270 million tons, accounting for about 23% of the world's total production, second only to the United States. As an inevitable product in the corn production process, corn stalk has a very high annual yield. Corn stalk itself is relatively tall and has high crude fibre content, and transportation and processing are relatively difficult, which leads to a low comprehensive development utilization rate of this resource *((Wang, 2022)*.

Screw conveyor is one of the important equipment in the process of crop harvesting and agricultural fibre material processing. Screw conveyor can continuously transport materials, and is widely used in the transportation of agricultural materials with the advantages of simple and compact structure, easy installation, convenient operation and maintenance *(Wu, 2022)*. However, the conveying performance of the screw conveyor directly affects the quality and productivity of material harvesting and processing, and also affects the energy consumption of the conveying equipment itself.

Emulation Discrete Element Method (EDEM) is mainly used for simulation and analysis of particle processing and manufacturing equipment production process in industrial production. Modelling by discrete element method and simulating and analysing the entire production process can intuitively display the macroscopic motion state changes and the force and energy transfer between microscopic particles, which is convenient for studying the operation of the equipment and further improving and optimizing.

ZhiPeng Fan, M.S. Stud.; Zhe Ma, M.S. Stud.; HongBo Wang, Professor, Correspondent author; ZhiHong Yu; Professor

In recent years, this method has also been widely used in agricultural fields such as agricultural tools, seeds and soil research, providing a theoretical basis for the improvement and optimization of agricultural machinery *(Hu et al., 2022; Liu et al., 2022; Li et al., 2022; Chen et al., 2023; Wang et al., 2022)*.

At present, *Youwang et al*., *(2020)*, simulated and analysed the conveying process of the horizontal screw feeder through EDEM software, and obtained the influence of the number of feed points on the productivity, filling rate and conveying speed of the feeder. *Tingzhou et al*., *(2019)*, carried out simulation test analysis on the three factors (inclination, pitch, speed) affecting the screw conveying capacity of grain, and obtained the significance relationship and the best parameter combination of the three factors. *Jiangtao et al*., *(2017)*, used EDEM software to analyse the discrete element of the conveying process of the screw conveying device under different pitches and speeds, and obtained the best parameter combination. *Yaoyu*, *(2020)*, analysed the discrete element of the internal conveyor force of the double screw conveyor, and obtained the law that the double screw conveyor was affected by the screw shaft speed, screw blade pitch, conveyor tilt angle and its own wheelbase when transporting grains, and the particle mass flow rate changed with the geometric and physical parameters of the conveyor.

In the previous research, our research group made a theoretical analysis of the screw conveying process of kneaded corn stalks. The influence mechanism of structural parameters and motion parameters on productivity and power consumption was analysed. The significance analysis and optimization analysis of three factors (pitch, screw shaft speed, and feed amount) that significantly affect the specific power consumption were carried out through experiments results, and the optimal combination of parameters were found. The eigen parameters and contact parameters of kneaded corn stalks were calibrated by discrete element calibration method, and an accurate discrete element model of screw conveying of kneaded corn stalks was established *Zhao et al., 2019; Liu et al., 2022; Wulan et al., 2015,2016,2019; Li, 2015)*.

In this study, a combination of experiment and simulation was used to study the screw conveying process of kneaded corn stalks. A discrete element model was established, and single-factor tests of pitch, feed amount and screw shaft speed were carried out with productivity and power as indicators. On this basis, the Box-Behnken response surface method was used to do the experiments, and the mathematical model between each index and the three factors was found. Through the analysis of variance (ANOVA) of its significance and optimization verification, the whole screw conveying process of kneaded corn stalks was optimized, which provided a theoretical basis for the design and improvement of the actual screw conveying device.

MATERIALS AND METHODS

SELECTION OF MATERIALS

The test materials were taken from the surrounding farmland of Wuchuan County, Hohhot, Inner Mongolia Autonomous Region, China, in October 2021, and the variety was Bian 31. The 9R-40 type kneading machine was used for kneading, and the filament body with a length of less than 100 mm and a width of 2~8 mm was obtained, with an average moisture content of 60%. The moisture content of materials was done with reference to the determination method of moisture in food according to the national food safety standard. The calculation formula is as follows.

$$Material\ moisture\ content=[(fresh\ matter\ quality\text{-}dry\ matter\ mass)/fresh\ matter\ quality]\times 100\% \quad (1)$$

TEST BENCH CONSTRUCTION AND MODELING

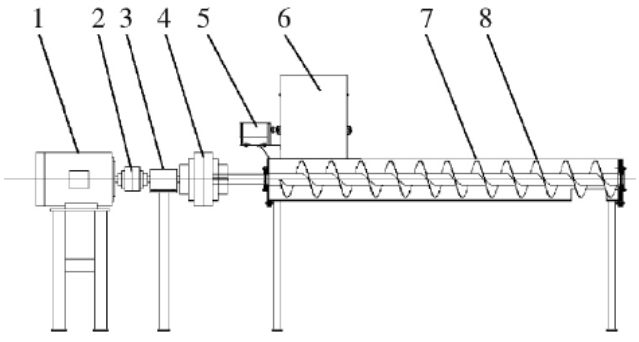
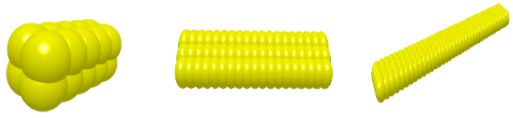


Fig. 1 - Screw conveyor test bench

1 – Electric motor; 2 – Coupling; 3 – Speed torque measuring instrument; 4 – Coupling; 5 – Single-phase DC speed regulating motor; 6 – Feed box; 7 – Shell; 8 – Screw shaft

The screw conveying test bench built in this study is mainly composed of motor, speed torque measuring instrument, feeder, casing and screw shaft (Figure 1). The feed inlet size is 260 mm×400 mm, the outer diameter of the screw blade is 250 mm, the diameter of the centre shaft is 60 mm, the gap between the screw blade and the shell is 5~8 mm, the conveying length is 2500 mm, and the pitch, screw shaft speed and feeder speed are adjustable.

Kneaded corn stalks have complex and diverse shapes. Due to the different materials of each part of the corn stalk itself (core, leaves, husks, nodules, etc.), this paper divides the kneaded corn stalks into straw core, straw husks and straw leaves, and other parts are ignored because they account for less. In order to reduce the complexity of simulation calculation without affecting the accuracy of simulation, the shape and size of straw core, husks and leaves are simplified to a certain extent, and the results are: core: 12 mm×6 mm×6 mm, husks: 20 mm×4 mm×2 mm, leaves: 20 mm×2.5 mm×1 mm. Their discrete element models are shown in Figure 2. The screw conveyor model is established for 1:1 with the test bench screw conveyor housing and screw shaft, as shown in Figure 3.



a. Straw core *b. husks* *c. Leaves*

Fig. 2 - Discrete element model of straw core, husks and leaves

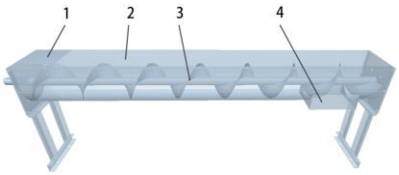


Fig. 3 - Discrete element model of screw conveying device

1 – Pellet factory; 2 – Screw conveyor shell; 3 – Screw shaft; 4 – Discharge outlet

Table 1

Eigen parameters of the parts of kneaded corn stalks and 45-steel

Parameters	Values	Parameters	Values
Density of straw core	62 kg/m^3	Density of husks	798 kg/m^3
Shear modulus of straw core	1.52×10^8 Pa	Shear modulus of husks	8.88×10^8 Pa
Poisson's ratio of straw core	0.032	Poisson's ratio of husks	0.317
Density of leaves	152 kg/m^3	Density of 45	7.85×10^3 kg/m^3
Shear modulus of leaves	5.842×10^8 Pa	Shear modulus of 45	8×10^7 Pa
Poisson's ratio of leaves	0.284	Poisson's ratio of 45	0.31

Table 2

Contact parameters between the parts of the kneaded corn stalks and 45-steel

Contact Parameters	Values	Contact Parameters	Values
Static friction coefficient of straw core-straw core	2.705	Collision restitution coefficient of husks-husks	0.380
Rolling friction coefficient of straw core-straw core	0.350	Static friction coefficient of husks-leaves	0.380
Collision restitution coefficient of straw core-straw core	0.390	Rolling friction coefficient of husks-leaves	0.377
Static friction coefficient of straw core-husks	0.900	Collision restitution coefficient of husks-leaves	0.385
Rolling friction coefficient of straw core-husks	0.345	Static friction coefficient of husks-45-steel	0.325
Collision restitution coefficient of straw core-husks	0.400	Rolling friction coefficient of husks-45-steel	0.270
Static friction coefficient of straw core-leaves	0.930	Collision restitution coefficient of husks-45 steel	0.425
Rolling friction coefficient of straw core-leaves	0.325	Static friction coefficient of leaves-leaves	0.411
Collision restitution coefficient of straw core-leaves	0.395	Rolling friction coefficient of leaves-leaves	0.335
Static friction coefficient of straw core-45-steel	1.030	Collision restitution coefficient of leaves-leaves	0.335
Rolling friction coefficient of straw core-45-steel	0.365	Static friction coefficient of leaves-45-steel	0.380
Collision restitution coefficient of straw core-45-steel	0.415	Rolling friction coefficient of leaves-45-steel	0.215
Static friction coefficient of husks-husks	0.665	Collision restitution coefficient of leaves-45-steel	0.395
Rolling friction coefficient of husks-husks	0.295		

When setting the Eigen parameters and contact parameters of the kneaded corn stalks model, directly use the data obtained from the previous test and calibration. In the pre-processing section of EDEM software, the volumes V-N (0.05,1) of the straw core, husks and leaves are set in Bulk Material, and other parameters are set according to Table 1 and Table 2.

The parameters set to 45-steel in Equipment Material are shown in Table 1. In Geometries, three pellet plants are set up at the screw conveyor inlet to produce straw core, husks, and leaves respectively, and the total production ratio is 3:4:16; the particle contact model in Physics is set up as Hertz-Mindlin (no slip) and Standard Rolling Friction. In the simulation section of EDEM software, set the time step to 2.214×10^{-7} s and total time to 5 s. The interval between storing data is 0.01 s. The grid size is $3xR_{min}$, where R_{min} means the minimum particle radius.

SCREW CONVEYING TEST OF KNEADED CORN STALKS

Since it is necessary to study the screw conveying performance of kneaded corn stalks, the efficiency and power consumption of kneaded corn stalks screw conveying are selected as the indicators.

Through the review of paper *(Wulan et al., 2016)* and the analysis of the screw conveying process of kneaded corn stalks, these factors are selected for this test: pitch, speed and feed amount. It can be seen that when the pitch of the screw blade of the screw conveyor is 160~300 mm, the feed amount is 10~70 kg/min, and the screw shaft speed is 50~148 r/min. The screw conveyor can meet the stable conveying requirements of kneaded corn stalks. And the factor levels are shown in Table 3.

Table 3

Test factors' levels

Level	1	2	3	4	5	6
Pitch [mm]	160	220	250	300	335	355
Feed amount [kg/min]	10	25	40	55	70	85
Screw shaft speed [r/min]	50	73	94	117	132	148

During single factor test of pitch, the feed amount is 40 kg/min, the speed is 94 r/min. The screw conveying test of kneaded corn stalks is carried out with the pitch as the variable. The results are shown in Figure 4. It can be seen from the figure that the productivity shows an upward trend with the increase of the pitch; and when the pitch reaches 335 mm, the inflection point occurs, and the productivity begins to decline; the power continues to rise with the increase of the pitch.

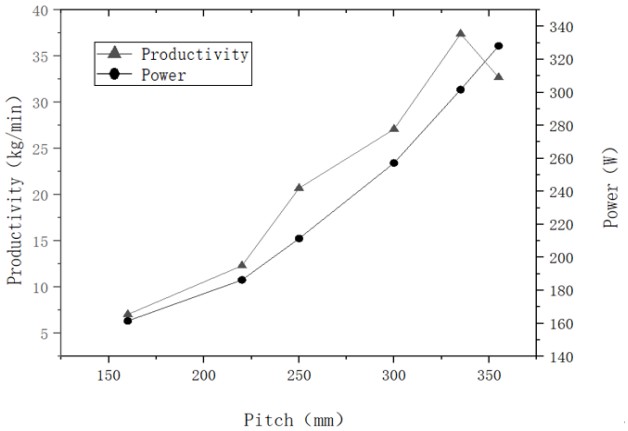
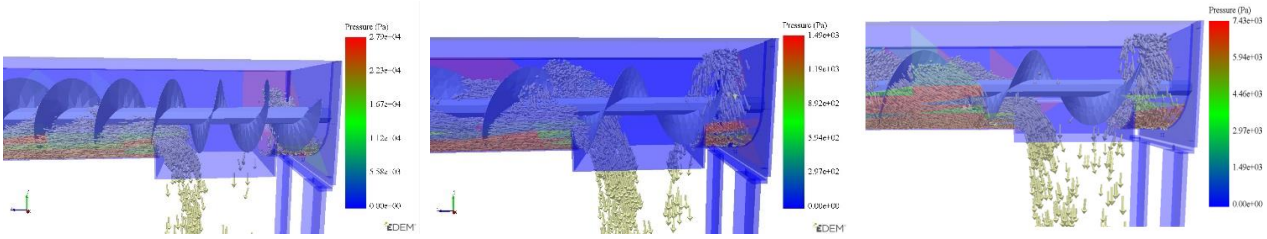


Fig. 4 - Relationship between pitch, productivity and power

Figure 5 are simulations of single factor screw conveying process of different pitches. In order to observe its motion law more intuitively, the particles of the three types of kneaded corn stalks in the figure are replaced by arrows in their own movement direction, and the blue, green and red areas in the figures represent the area of pressure on the shell of the body (the same below). It can be seen from the figures that with the increase of the pitch (Fig. 5a to 5b), the screw rising angle increases at the same time, and the movement space of the particles is also increasing, so the fluidity is enhanced and the productivity is improved; while the red area is significantly increased, representing that the friction area and friction between the particles and the body are increasing, so the power is also increasing; as the pitch continues to increase (Fig. 5b to 5c), the

screw rising angle increases at the same time, and the circular motion of the particles increases significantly, so the productivity tends to decrease, and the friction area and friction between the particles and the body are also increasing, so the power continues to increase.



a. Pitch as 160 mm *b. Pitch as 335 mm* *c. Pitch as 355 mm*

Fig. 5 - Screw conveying simulation of different pitches

During single factor test of feed volume, the pitch is 355 mm, the speed is 94 r/min, and the screw conveying test of kneaded corn stalks is carried out with the feed amount as the variable. The results are shown in Figure 6, and it can be seen from the figure that the productivity shows an upward trend with the increase of the feed volume; the power tends to increase with the increase of feed.

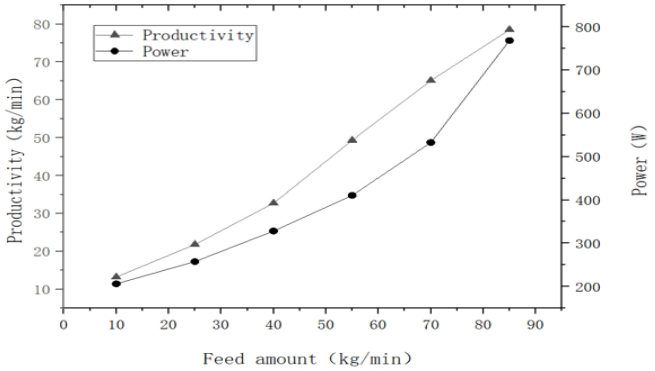
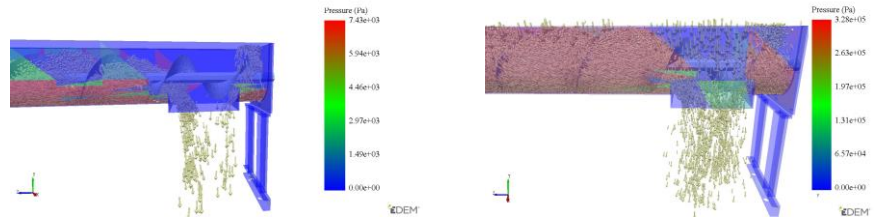


Fig. 6 - Relationship between pitch, productivity and power



a. Feed amount as 40 kg/min *b. Feed amount as 85 kg/min*

Fig. 7 - Screw conveying simulation of different feed volumes

As can be seen in Figure 7, with the increase of feed volume (Fig. 7a to 7b), the productivity is increasing, and the red area is significantly increased, which means that the friction area and friction between particles and the body, particles and blades are increasing, so the power is also increasing.

During single factor test of screw shaft speed, the pitch is 355 mm, the feed amount is 40 kg/min, and the screw conveying test of kneaded corn stalks is carried out with the screw shaft speed as the variable. The results are shown in Figure 8, it can be seen from the figure that the productivity increases with the increase of the screw shaft speed, and when the screw shaft speed reaches 117 r/min, the inflection point occurs, and the productivity begins to decline; the power always shows an upward trend with the increase of the speed of the screw shaft.

It can be seen from Figure 9 that with the increase of the speed of the screw shaft (Fig. 9a to 9b), the fluidity of particles is enhanced, the productivity is constantly increasing, and the red area is also increasing, which means that the friction area and friction between the particles and the body are increasing, so the power is also increasing; as the speed of the screw shaft continues to increase (Fig. 9b to 9c), due to the action of centrifugal force, the circular motion of particles increases significantly, and the axial movement decreases, so the productivity tends to decrease, and the friction area and friction between particles and the body are still increasing, so the power continues to increase.

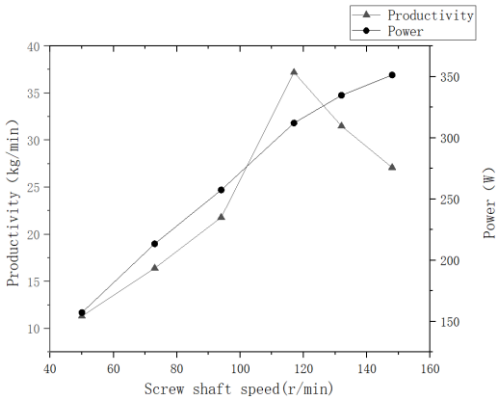
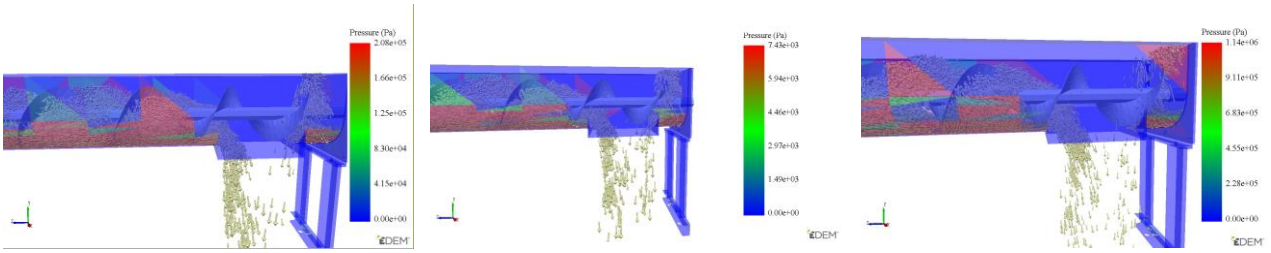


Fig. 8 - Relationship between screw shaft speed, productivity and power



a. Screw shaft speed as 50 r/min *b. Screw shaft speed as 94 r/min* *c. Screw shaft speed as 148 r/min*

Fig. 9 - Screw conveying simulation of different screw shaft speeds

BOX-BEHNKEN TEST AND ANALYSIS

In order to obtain the influence of multiple factors on productivity and power evaluation indicators, the last three levels of each factor are taken at a high level (+1) and a low level (-1), and the factors and their levels are shown in Table 4, and the Box-Behnken experiments are designed by using Design Expert software. Other non-significant parameters are averaged from physical tests. The Box-Behnken experimental design and results of significant contact parameters are shown in Table 5.

Table 4

Box-Behnken test parameter level table

Level	Pitch – A [mm]	Feed amount – B [kg/min]	Screw shaft speed - C [r/min]
-1	300	55	117
0	335	70	132
+1	355	85	148

Box-Behnken experiment design and results **Table 5**

Experimental group	A	B	C	Productivity [kg/min]	Power [W]
1	-1	-1	0	41.3	457.3
2	1	-1	0	43.4	482.7
3	-1	1	0	65.5	712.4
4	1	1	0	67.2	747.5
5	-1	0	-1	69.3	694.2
6	1	0	-1	71.4	735.4
7	-1	0	+1	65.5	835.7
8	1	0	+1	63.8	874.1
9	0	-1	-1	47.5	513.2
10	0	1	-1	82.8	895.8
11	0	-1	+1	38.7	574.3
12	0	1	+1	73.2	958.4
13	0	0	0	55.4	654.3
14	0	0	0	63.5	738.5
15	0	0	0	65.6	764.5
16	0	0	0	63.1	749.8
17	0	0	0	58.2	671.1

The multiple regression analysis of the experimental results in Table 5 is carried out by Design-Expert software, and the quadratic polynomial regression model of screw conveying productivity (Y_1) and power (Y_2) of kneaded corn stalks are established.

$$Y_1 = 222.6561 + 0.28854A + 5.36956B - 6.33944C - 0.001455AB + 0.000117AC - 0.00086BC - 0.000238A^2 - 0.027244B^2 + 0.022976C^2 \quad (2)$$

$$Y_2 = 386.26531 + 29.12865A + 59.94399B - 109.18962C + 0.005879AB - 0.001642AC + 0.001613BC - 0.043795A^2 - 0.366867B^2 + 0.425931C^2 \quad (3)$$

ANOVA of the Box-Behnken experiment results of productivity as indicator **Table 6**

Source of variation	Sum of Squares	df	nagMean Square	F-value	P-value	
Model	2106.09	9	234.01	11.45	0.0020	significant
A	13.01	1	13.01	0.6363	0.4513	
B	1676.20	1	1676.20	82.01	< 0.0001	
C	142.80	1	142.80	6.99	0.0333	
AB	1.44	1	1.44	0.0705	0.7983	
AC	0.0100	1	0.0100	0.0005	0.9830	
BC	0.1600	1	0.1600	0.0078	0.9320	
A^2	0.1364	1	0.1364	0.0067	0.9372	
B^2	158.22	1	158.22	7.74	0.0272	
C^2	128.30	1	128.30	6.28	0.0407	
Residual	143.07	7	20.44			
Lack of Fit	72.18	3	24.06	1.36	0.3754	not significant
Pure Error	70.89	4	17.72			
Cor Total	2249.16	16				
R^2	0.9364	C.V.%	7.44	Adeq Precision	11.8102	

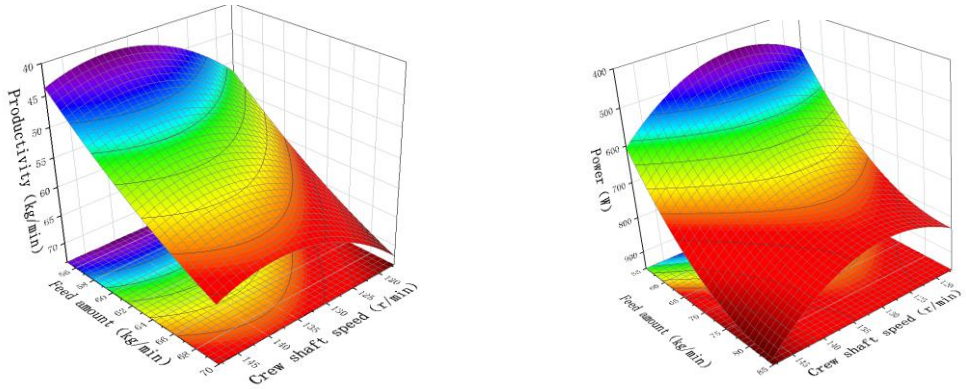
ANOVA of the Box-Behnken experiment results of power as indicator **Table 7**

Source of variation	Sum of Squares	df	nagMean Square	F-value	P-value	
Model	3.034E+05	9	33706.54	11.48	0.0020	significant
A	2453.50	1	2453.50	0.8360	0.3910	
B	2.069E+05	1	2.069E+05	70.50	< 0.0001	
C	20391.90	1	20391.90	6.95	0.0336	
AB	23.52	1	23.52	0.0080	0.9312	
AC	1.96	1	1.96	0.0007	0.9801	
BC	0.5625	1	0.5625	0.0002	0.9893	
A^2	4618.67	1	4618.67	1.57	0.2499	
B^2	28689.17	1	28689.17	9.78	0.0167	
C^2	44090.23	1	44090.23	15.02	0.0061	
Residual	20544.10	7	2934.87			
Lack of Fit	10720.91	3	3573.64	1.46	0.3526	not significant
Pure Error	9823.19	4	2455.80			
Cor Total	3.239E+05	16				
R^2	0.9366	C.V.%	7.64	Adeq Precision	12.5885	

Table 6 and Table 7 are regression ANOVA results for models Y_1 and Y_2, respectively. From Table 6, it can be seen that the P-value of regression model is 0.002 which is less than 0.05, indicating that the model is significant; The coefficient of determination R^2 is 0.9364, indicating that the model Y_1 can accurately reflect the influence of factors on productivity. The misfit value is 0.3754, which is more than 0.05, indicating that the factors not considered in the test have little impact on the test results. The coefficient of variation is 7.44%, which is less than 10%, indicating that the obtained model fits well with the actual experiment. The signal-to-noise ratio is 11.8102, indicating that the model has good precision and strong response signal. Table 7 shows that the model Y_2 is also successfully established.

In summary, both models can be used as predictive models for the screw conveying of kneaded corn stalks. From the ANOVA results of the models, it can be seen that the feed amount (B) and the screw shaft speed (C) have a significant impact on productivity and power.

In order to obtain the relationship between the influencing significant factors and the response value more intuitively, the stereoscopic atlas of the response surface of the model is got by using Design-Expert software, as shown in Figure 8.



a. The influence surface of feed volume and screw shaft speed on productivity

b. The influence surface of feed amount and screw shaft speed on power

Fig. 10 - The response surface atlas of interaction effects

As can be seen from Figure 8, the impact of feed volume increasing on productivity continues to grow. The effect of increased screw shaft on productivity shows a trend of increasing first and then decreasing. The influence of screw shaft speed increasing on productivity and power continues to increase.

RESULTS

After comprehensive analysis and optimization by Design-Expert software, the best process parameters of screw conveying are finally obtained as pitch of 319.428 mm, feeding amount of 71.062 kg/min, and screw shaft speed of 117.034 r/min. The corresponding production rate is 71.517 kg/min and the power is 769.84 W. Through EDEM software simulation and t-test explanation, the optimization results are reliable.

CONCLUSIONS

In this study, the kneaded corn stalks and screw conveying device are modelled by discrete element method, the screw conveying process of kneaded corn stalks was simulated, and the law affecting productivity and power consumption is revealed by changing the pitch, feed amount and screw shaft speed. And then the discrete-element simulation software is used to analyse the significance of three factors and obtain the optimal solution, namely the pitch of 319.428 mm, the feed amount of 71.062 kg/min, and the screw shaft speed of 117.034 r/min. The simulation verification by EDEM software shows that there is no significant difference, indicating the reliability of the optimization results.

This study also verifies the scientific rationality of the simulation of the screw conveying process of kneaded corn stalks by discrete element method, reveals the screw conveying mechanism of kneaded corn stalks, and the research results can provide a scientific and reasonable basis for the improvement and optimization of screw conveying device. On this basis, the discrete element method can be used to further reveal the wear and tear mechanism of the screw conveying device, which provides a theoretical basis for the design optimization of related conveying machinery and equipment.

REFERENCES

[1] Chen C., Ma X. D., Liu F. Y., Du Y. L., Zang F. (2023). Discrete element simulation study on grain separation in dustpan under eccentric pendulum (偏心摆振下圆簸箕中谷物分离的离散元模拟研究), *Journal of Agricultural Mechanization Research*, vol. 45, issue 05, pp. 13-19.

[2] Hu W. H., Yang F. Z., Zhao G. D., Lin Y. L., Huang K. (2022). Analysis and optimization of working parameters of vertical rotary tillage knife based on discrete element method (基于离散元法的立式旋耕刀工作参数分析与优化), *Journal of Chinese Agricultural Mechanization*, vol. 43, issue 10, pp. 25-32, 41.

[3] Li X. Y., Wang C. G. (2015). Experimental study on the performance of corn stover on LS screw conveyor (玉米秸秆在 LS 型螺旋输送机上的性能试验研究), *Agricultural Mechanization Research*, vol. 37, issue 02, pp. 161-165.

[4] Li X. Y., Liao M., Yang J., Zheng R. K. (2022). Discrete element parameter calibration and seeding verification of Qiang live grains and perlite (羌活籽粒和珍珠岩的离散元参数标定及排种验证), *Chinese Journal of Agricultural Mechanization*, vol. 43, issue 08, pp. 40-46.

[5] Liu Y. Y., Yu S. J., Xu B., Wang X. L., Song F. C. (2022). Research and experiment of in-situ ploughing in facility agriculture based on discrete element (基于离散元的设施农业就地翻土犁的研究与试验), *Journal of Jilin University*, vol. 1, issue 11.

[6] Ning T. Z., Li Y., Gu Y. N. (2019). Research on conveying capacity of inclined screw conveyor based on EDEM (基于 EDEM 的倾斜螺旋输送机输送能力研究), *Journal of Mudanjiang Normal University*, issue 04, pp. 38-41.

[7] Qi J. T., Meng J. W., Kan Z., Li C. S., Li Y. P. (2017). Analysis and test of feed performance of double helix cow feed device based on EDEM (基于 EDEM 的双螺旋奶牛饲喂装置给料性能分析与试验), *Transactions of the Chinese Society of Agricultural Engineering*, vol. 33, issue 24, pp. 65-71.

[8] Wang P. F., Li J. P., Liu H. J., Zhang J. L. (2022). Application and practice of EDEM software in agricultural machinery teaching (基于 EDEM 软件在农业机械教学中的应用与实践), *Agriculture and Technology*, vol. 42, issue 06, pp. 54-57.

[9] Wang Z. G. (2021). Exploration on comprehensive utilization pathways of maize straw (玉米秸秆综合利用途径探究), *China Animal Health*, vol. 23, issue 05, pp. 102+104.

[10] Wu Y. L., Hou S. L., Zhao L. X., Tian T. S., Meng H. B. (2013). Development status and prospect of straw conveying technology and equipment (秸秆输送技术与设备发展现状及展望), *Research on Agricultural Mechanization*, vol. 35, issue 09, pp. 11-15+29.

[11] Wulan T. Y., Wang C. G., Qi X. H., Yan J. G., Wang J. L. (2015). Analysis and optimization of working parameters of vertical rotary tillage knife based on discrete element method (揉碎玉米秸秆螺旋输送性能试验分析), *Journal of Chinese Agricultural Mechanization*, vol. 31, issue 21, pp. 51-59.

[12] Wulan T. Y., Wang C. G., Zhao F. C., Wang X. R. (2019). Parameter test optimization of screw conveying device for kneading corn stalk (揉碎玉米秸秆螺旋输送装置参数试验优化), *Journal of China Agricultural University*, vol. 24, issue 02, pp. 115-122.

[13] Wulan T. Y., Wang C. G., Xie S. S., Zhao Y. Y. (2015). Research on power consumption of corn stover transported by screw conveying device (螺旋输送装置输送玉米秸秆功耗研究), *Research on Agricultural Mechanization*, vol. 30, issue 10, pp. 45-49.

[14] Wulan T. Y., Wang C. G., Qi X. H., Wang X. R., Wang H. C. (2016). Theoretical model analysis and experiment of spiral transport of crushed corn stalk (揉碎玉米秸秆螺旋输送理论模型分析与试验), *Transactions of the Chinese Society of Agricultural Engineering*, vol. 32, issue 33, pp. 18-26.

[15] Wulan T. Y. (2016). Research on screw conveying mechanism of kneaded corn stalk (揉碎玉米秸秆螺旋输送机理研究), *Inner Mongolia Agricultural University*.

[16] Xin Y. Y. (2020). Material conveying characteristics and wear mechanism of double screw conveyor based on discrete element method (基于离散元法双螺旋输送机物料输送特性及磨损机理), *Liaoning Petrochemical University*.

[17] Zhao F. C., Wang C. G., Wulan T. Y. (2019). Research on parameter optimization of spiral conveying device (螺旋式输送装置参数优化研究), *China Agricultural Science and Technology Review*, vol. 21, issue 06, pp. 70-78.

[18] Zhang Y. W., Wang W., Liu H. Y., Zhang W. G., Lu J. C. (2020). Simulation analysis of multi-point feed horizontal screw feeder based on EDEM (基于 EDEM 的多点进料水平螺旋给料机仿真分析), *Port Loading and Unloading*, issue 06, pp. 10-13+51.

THREE-DIMENSIONAL RECONSTRUCTION AND CHARACTER EXTRACTION OF CORN PLANTS BASED ON KINECT SENSOR
/
基于Kinect传感器的玉米植株三维重构与性状提取

Yuanyuan SUN[1)], Xuchang WANG*[2)], Kaixing ZHANG[3)]
[1)] College of Modern Equipment Academy, Changzhou Vocational Institute of Industry Technology, Changzhou / China;
[2)] Yantai CIMC Raffies Offshore Ltd, Yantai / China;
[3)] College of Mechanical and Electronic Engineering, ShanDong Agricultural University, Tai'an / China
E-mail: s18853853891@163.com
Corresponding author: Xuchang Wang
DOI: https://doi.org/10.35633/inmateh-69-61

Keywords: *Kinect sensor, 3D reconstruction, point cloud segmentation, ellipse fitting, growth parameters*

ABSTRACT
Aiming at the problems of low precision, strong subjectivity, and continuous measurement in the current measurement methods of corn phenotypic traits, a method of measuring corn phenotypic traits with high precision, low cost, easy carrying and continuous measurement was proposed. Firstly, the three-dimensional scanning device Kinect 2.0 is used to collect corn information and process and reconstruct the collected point cloud. Then, the stem and leaf point clouds were segmented by straight-through filtering, ellipse fitting and region growth segmentation. Finally, the phenotypic parameters of corn were obtained by triangulation and plane fitting for the segmented corn leaves, and the accuracy was analyzed. The results showed that the accuracy of corn plant height was 97.622 %, the average relative error of stem long axis was 9.46 %, the average relative error of stem short axis was 11.17 %, and the accuracy of leaf area was 95.577 %. Studies have shown that this method provides a new method for continuous measurement of phenotypic traits in corn.

摘要
针对目前玉米表型性状测量方法存在精度低，主观性强，不能连续性测量等问题，提出一种精确度高、耗费少、便携且可连续性测量的玉米表型性状测量方法。首先，采用三维扫描设备Kinect 2.0 采集玉米信息并对采集后的点云进行处理和三维重建。然后，利用直通滤波、椭圆拟合、区域增长分割方法分割出玉米茎秆叶片等数据。最后，对分割后的玉米叶片等利用三角面片化以及平面拟合等方法获取玉米植株表型参数并对其进行精度分析。结果表明：算法测量株高精确度为97.622%，茎秆长轴的平均测量相对误差为9.46%，茎秆短轴平均测量相对误差为11.17%，叶片面积精确度为95.577%。研究表明，本文方法为玉米的表型性状测量提供一种连续性测量新方法。

INTRODUCTION
Corn is an important food crop and an important source of feed. Accurate acquisition of phenotypic traits such as plant height, stem diameter, leaf perimeter and area in the process of corn growth is of great significance for understanding crop growth, yield estimation, disease resistance detection and breeding (*Zila Jia et al, 2019*). Traditional crop phenotypic traits are mainly measured manually. This method is inefficient, has no uniform measurement standard, and cannot continuously measure crops (*Yingbo Song, 2015; Jay S., 2015*). With the development of industry, researchers began to apply image processing and machine vision for crop phenotype detection. Hui quantified and evaluated the canopy structure of plant populations in two and three dimensions using multi-view stereo (MVS) techniques, and monitored plant growth and development from seedling to fruiting stage. (*Hui et al, 2018*). *He et al.* built a set of multi-view stereo imaging system, collected 360°image data of strawberry fruit, carried out three-dimensional reconstruction, and extracted character parameters (*He et al, 2017*). Aksoy constructed an imaging system using a robotic arm and cameras to monitor different tobacco plants, measuring their growth parameters and leaf growth rates (*Aksoy E.E. et al, 2015*).

Yuanyuan Sun, Lecture M.S. Eng.; Xuchang Wang), Engineer M.S. Eng.; Kaixing Zhang, Prof. Ph.D. Eng.*

Based on the structured light scanner, Li obtained the three-dimensional point cloud of cotton, reconstructed the three-dimensional model, and measured the phenotypic traits (*Yaochen Li, 2019*). Qian Wu realized the recognition and segmentation of overlapping fruits by using color features and three-dimensional geometric features through Kinect v2, which provided an important reference for the research on robotic fruit picking (*Qian Wu, 2022*). WU used Kinect v2 sensor to obtain multi-view images of rice, and carried out three-dimensional reconstruction of rice plants by contour projection and inverse projection methods (*WU D, 2020*). Jie Ding proposed a modeling method for rotationally symmetric objects based on Kinect. For rotationally symmetric objects with weak structures, the model can be obtained by rotating fitting boundary (*Jie Ding, 2019*).

At present, the instruments and technologies for crop 3D reconstruction based on point cloud include Lidar, multi-eye stereo camera, TOF (Time of flight) camera, etc. Kinectv2 sensor is widely used in information agriculture because it has the function of real-time synchronous acquisition of depth information and color information, and has the advantages of good precision, low cost and good compatibility. Measurements based on two-dimensional images are often inaccurate due to occlusion between plants and are not suitable for measuring morphological parameters such as leaf area. Due to the special shape of corn, general trait measurement method is not applicable to it. Therefore, this paper proposes a three-dimensional reconstruction method based on Kinect 2.0 and a phenotypic parameter extraction method based on ellipse fitting for corn. Through experimental verification, the method proposed in this study can extract crop phenotypic parameters non-destructively and accurately, which is of great significance for understanding crop growth status, crop detection, yield estimation, disease resistance detection and breeding.

MATERIALS AND METHODS

Experimental Materials and Data Acquisition

The hardware measurement system for corn collection is mainly composed of six parts: control host, Kinect 2.0, tripod, disc and controller. The turntable system is shown in Fig. 1. Capturing the corn plant point cloud scene with Kinect is shown in Fig. 2.

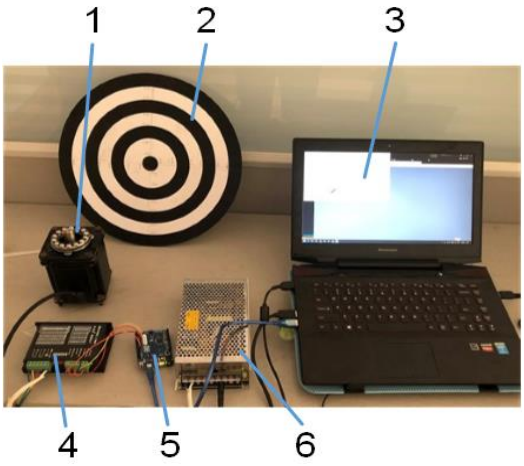


Fig. 1 - Schematic diagram of measurement composition

1-Stepper motor; 2-Disc; 3-Control host; 4-Driver; 5-Arduino control board; 6-Switching power supply



Fig. 2 - Acquisition of corn point cloud data

1-Collection objects; 2-Disc; 3-Kinect 2.0; 4-Control host; 5-Tripod

Based on the Windows 10 operating system, this study used the turntable method to scan the corn information. Within the effective range of Kinect v2 (0.5m ~ 5.0m) (*Jin Zhou, 2013*), the closer the distance is, the higher the accuracy will be. Therefore, under the premise of meeting the use conditions, it should be as close to the corn as possible. The rotation angle was 36°, and the rotation was 9 times to obtain all the information of the corn plant. Based on Kinect 2.0, the color information and depth information of corn plant are obtained and converted into color image and depth image. The depth coordinate space (512 × 424) and color coordinate space (1920 × 1080) of Kinect are registered by using the principle of coordinate system conversion and converted into 3D color point cloud. Fig. 3 is the obtained color depth map.

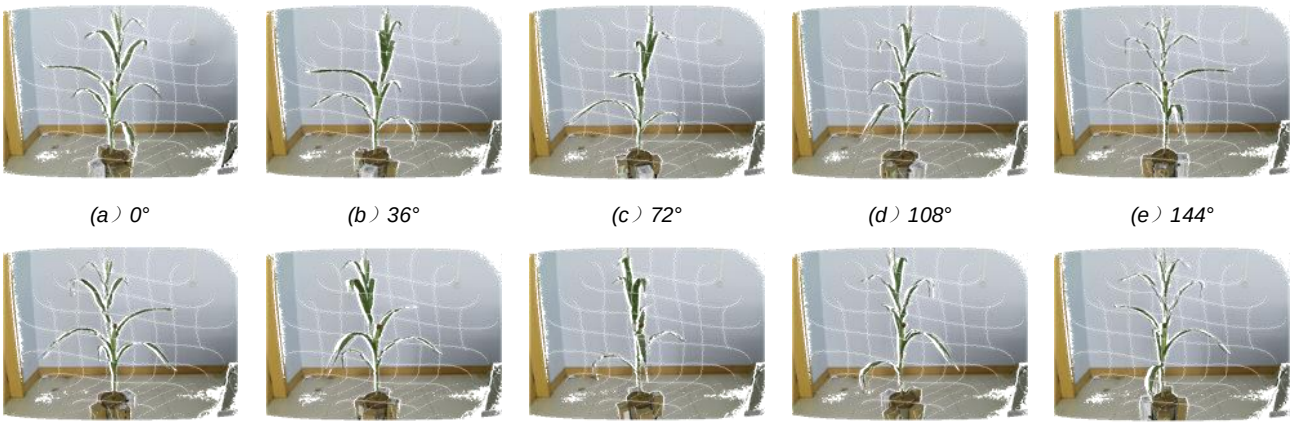


Fig. 3 - Color depth map obtained from ten directions

Three-dimensional reconstruction of corn

(1) Point cloud data noise reduction

Due to the uneven surface of corn leaves and the presence of small villi, the reflection of light will be affected to produce noise points. Noise points will affect the accuracy of 3D reconstruction (*Gang Liu et al, 2022; Song Bi et al, 2021*). The obtained corn background point cloud is removed by direct filtering (*Archibald R. et al, 2019*). For the noise points around the point cloud model, this study uses a statistical filtering method to remove them. The idea of statistical filtering is to traverse all point clouds in the point cloud model, and judge whether the point needs to be deleted by the average distance from all points to their neighborhood points. The ten directional point clouds after statistical filtering are shown in Fig. 4. From Fig. 4, it can be seen that the noise points around the target point cloud after statistical filtering are deleted, which improves the accuracy of the point cloud model.

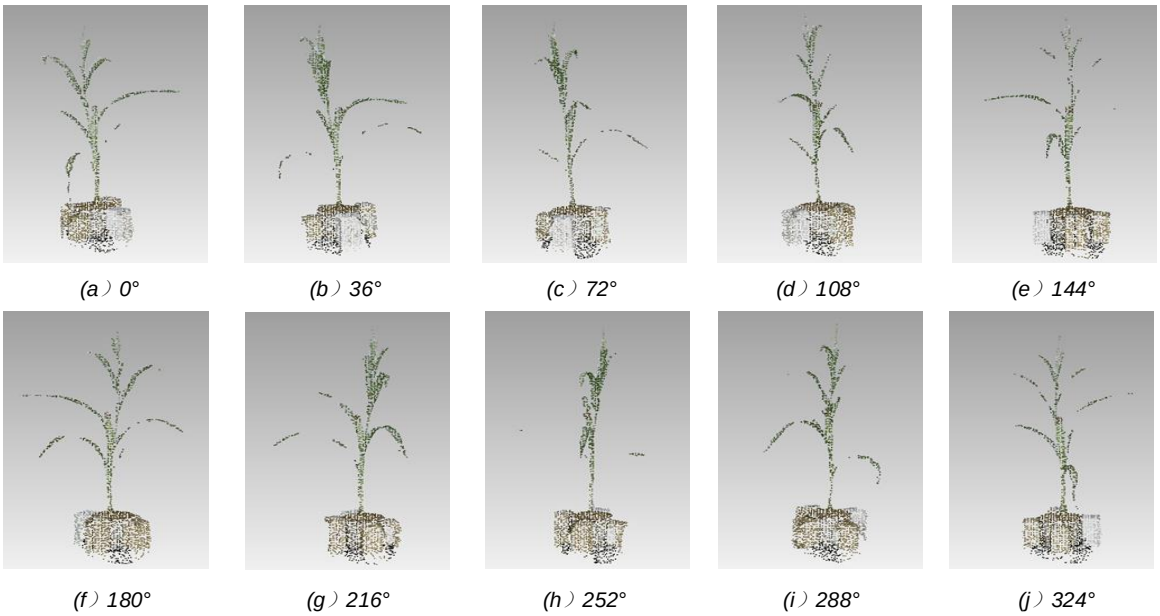


Fig. 4 - Ten direction point clouds after statistical filtering

(2) Point cloud matching and simplification

The local point cloud registration is carried out by manual registration for coarse registration and Iterative Closest Point (ICP) algorithm for fine registration. Before manual coarse registration of point clouds, two adjacent point cloud sets are selected, and four distant feature points are selected from the two point cloud sets for coarse registration.

At this time, the two point cloud sets roughly coincide. In order to reduce the error and improve the registration accuracy, the ICP algorithm is used to perform fine registration. The ICP algorithm finds the corresponding points of two matching point clouds by iteration or search. The Euclidean distance is used as the objective function to iterate continuously, and the rotation matrix and translation matrix of the point cloud are obtained to minimize the error function of the registration point cloud, the point cloud matching of corn is shown in Fig. 5.

The point cloud data after matching is redundant, and too much point cloud data will affect the processing speed and the accuracy of phenotype parameter extraction. Commonly used point cloud simplification methods include curvature-based simplification, random sampling simplification, and bounding box method. The point cloud data after matching is streamlined based on the above method, and the results are shown in Fig. 6. Fig. 6(a) shows the results of curvature-based simplification, with a simplification rate of 30%. The simplified point cloud and the leaf boundary information are seriously lost, and the distribution of leaf point cloud is uneven, which affects the accuracy of the subsequent triangular mesh generation of corn leaves. Fig. 6(b) shows the results of random sampling simplification. The simplification rate is 30%, and there is loss of corn leaf boundary point cloud. Fig. 6(c) shows the simplification of corn plant based on bounding box method, and the simplification spacing is 0.0078. After simplification, the point cloud feature of corn retains the feature information of leaf vein and leaf edge, and the point cloud distribution is relatively uniform, which is convenient for leaf triangular surface to calculate leaf area.



Fig. 5 - Effect diagram of point clouds registration

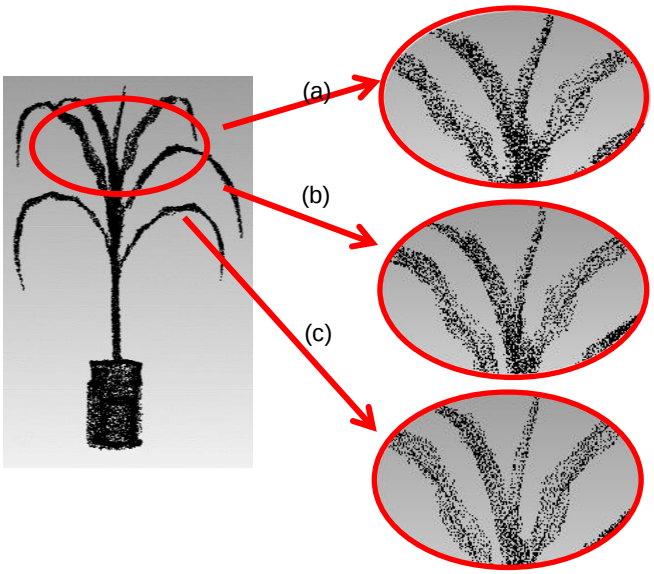


Fig. 6 - Effect diagram of Point cloud simplification

(a)Curvature-based simplification (b) Random sampling simplification (c) Bounding box method

In summary, the simplification of corn plants based on bounding box method can retain more phenotypic characteristics when the number of point clouds is similar, and the point cloud distribution is uniform, which is convenient for subsequent leaf triangular patching. Therefore, this study selected bounding box method for corn plant point cloud simplification.

Segmentation of corn point clouds

During data acquisition, the Kinect 2.0 uses its own inherent coordinate system to generate three-dimensional point clouds. The principal component direction of the model is inconsistent with the direction of the three-dimensional coordinate axis. Therefore, before the point cloud processing, the point cloud centroid is rotated to the coordinate origin position, so that the corn stalk is along the z-axis direction. Based on the z-axis information, the target point cloud is divided into corn plants and flower pot, and the segmentation effect is shown in Fig. 7 (a).

(1) Ellipse fitting of corn stalk

In this paper, six-point clouds are selected for ellipse fitting based on the least square method, and all point clouds are traversed to calculate the distance between the point cloud data and the fitting ellipse. When the distance is less than the set threshold, the point is considered to be a standard point. When the distance between all point clouds and the fitting ellipse is calculated, the number of standard points is counted. Repeat the above process until the remaining point cloud is less than six.

Compare the number of point clouds satisfied after each fit. The fitting when the number of point clouds is the largest is the optimal ellipse fitting, and the optimal ellipse fitting parameters are obtained. According to the fitting ellipse, the point cloud of the corn plant point cloud inside the ellipse is extracted, and the segmentation effect is shown in Fig. 7(b).



(a)Removal of flowerpot point cloud *(b) Stem extraction of point cloud*

Fig. 7 - Segmentation of Corn point cloud

(2) Region growing segmentation algorithm

Before the leaf segmentation, the topological relationship of the point cloud is established to search the point cloud, and the point with the smallest curvature is selected as the initial point. Several neighborhood points of the initial point are calculated, and whether these neighborhood points can meet the established growth rules is judged. If the growth rules are met, the search point is classified into the region and used as a new sub-seed point. If only the angle between the seed point and the normal vector of the neighborhood point is within the set threshold range, the neighborhood point is only classified into the same region. Traverse all point clouds and repeat the previous step to continuously add new seed points until no new seed points appear. Repeat the above operation process until all point clouds are divided. The principle of region growing segmentation algorithm is shown in Fig. 8. The segmentation results are represented by different colors, and different colors represent different classes. The segmentation effect is shown in Fig. 9.

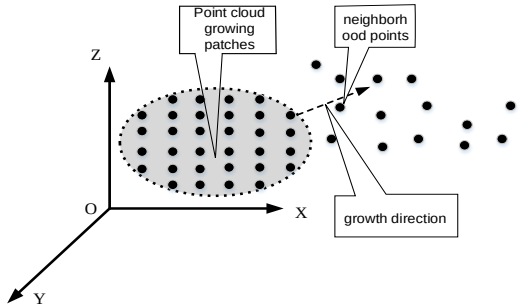


Fig. 8 - Schematic diagram of region growing segmentation algorithm

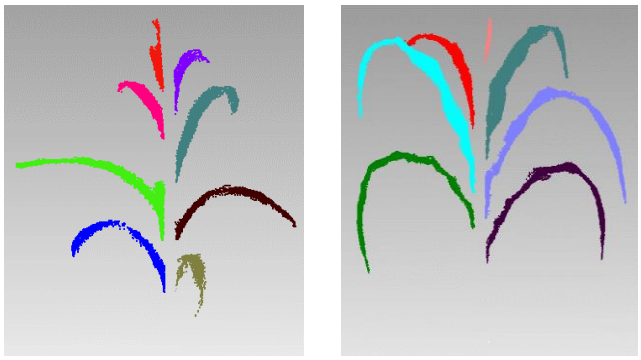


Fig. 9 - Corn point clouds after leaf segmentation

Extraction and accuracy analysis of corn phenotypic parameters

(1) Height measurement of corn

The direction of corn stover after coordinate transformation is along the Z-axis. For the corn point cloud after removing the pot, traverse all the points to get the height of the corn plant, namely the Z-coordinate distance between the highest point and the lowest point of the corn plant. The schematic diagram of corn height extraction is shown in Fig. 10.

(2) Measurement of corn stalk

The stalk diameter of corn can be represented by a fitted elliptic feature, as shown in Fig. 11. The stalk diameter of corn can be calculated according to the long axis and the short axis.

The long and short axes of the fitting ellipse are as follows:

$$\begin{cases} X = \dfrac{BE - 2CD}{4AC - B} \\ Y = \dfrac{BD - 2AE}{4AC - B} \end{cases} \quad (1)$$

$$\begin{cases} L = \dfrac{2(AX + CY + BXY - 1)}{A + C + \sqrt{(A - C) + B}} \\ S = \dfrac{2(AX + CY + BXY - 1)}{A + C - \sqrt{(A - C) + B}} \end{cases} \quad (2)$$

Where:

X_c and Y_c are the X and Y coordinates of the ellipse center;

L and S are the long half axis and short half axis of ellipse respectively;

A, B, C are parameters of fitting elliptic equation.

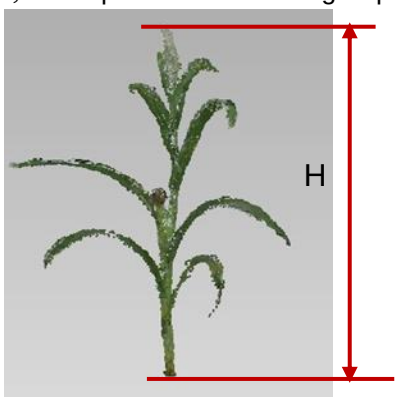


Fig. 10 - Height measurement of corn

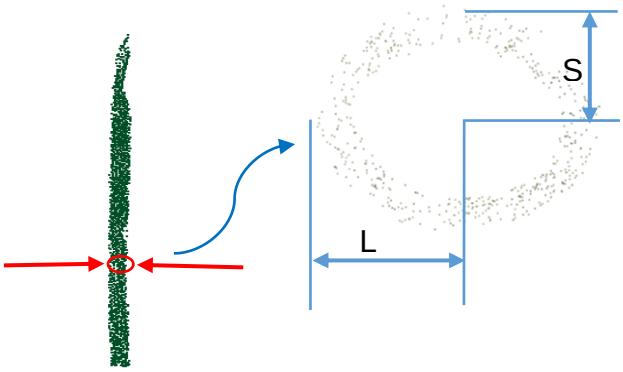
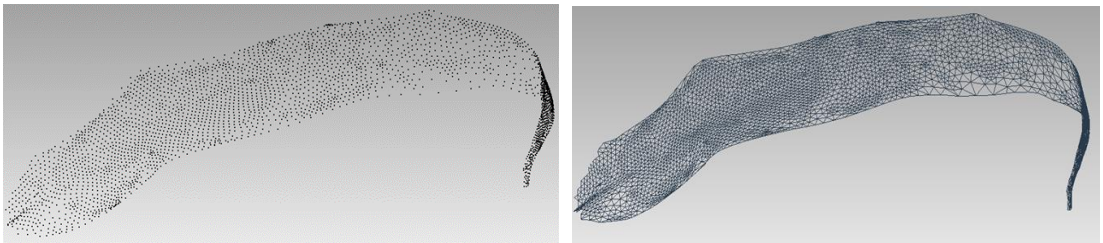


Fig. 11 - Schematic diagram of corn stalk diameter extraction

(3) Measurement of leaf circumference and area of corn

Since the obtained three-dimensional point cloud is scattered points, it cannot display the surface information of the crop directly obtained. Therefore, it is necessary to triangulate the point cloud greedy projection. The threshold of triangular patching is set as follows: the maximum plane angle is 45°, and the maximum angle and minimum angle of each triangle are 10° and 150° respectively. The point cloud of corn leaves is triangularized as shown in Fig. 12(a), and the effect is shown in Fig. 12(b).



(a) Leaf point cloud *(b) Triangulation of leaf point clouds*

Fig. 12 - Greedy Projection Triangulation

The three-dimensional point clouds of the blade are transformed into triangular patches with topological relations by greedy projection triangulation algorithm (*Hui Chen et al., 2021*). The corn leaf model is composed of several small triangles. Each triangle contains the original three-dimensional point cloud information. The side length of the three sides of the triangle is calculated by the vertex coordinates of the triangle, and then the triangle area can be calculated by Helen formula. The area of each triangle is calculated by traversing all triangles in the corn leaf model, and then the area of all triangles is summed to get the corn leaf area.

Helen's formula and the area sum formula are as follows:

$$S_i = \sqrt{p_i(p_i - a_i)(p_i - b_i)(p_i - c_i)} \quad (3)$$

$$S = \sum_{i=1}^{n} S_i \quad (4)$$

Where:

S is corn leaf area;

S_i is the area of the i^{th} small triangle;

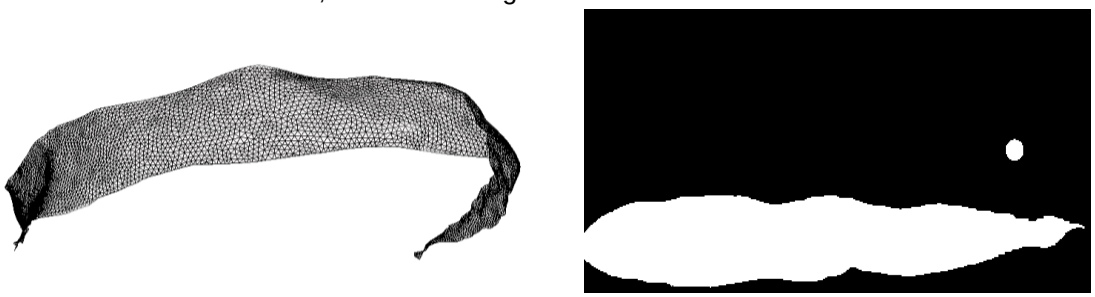
p_i is half of the area of the i^{th} triangle;

a_i, b_i, c_i are the length of three sides of the triangle;

n is the total number of patches;

i is the number of face index.

The artificial measurement of corn leaves is to cut the corn leaves with scissors, spread the leaves and place them on the whiteboard. At the same time, a black circle with a diameter of 1 cm is placed on the whiteboard, and a camera is used to shoot in the vertical direction of the whiteboard to obtain images containing corn leaves and circles. Based on the image processing module in Matlab, the circumference and area of corn leaves are calculated, as shown in Fig. 13.



(a) Triangulation of three-dimensional leaves *(b) Binarization of leaf point cloud*

Fig. 13 - Treatment of leaves

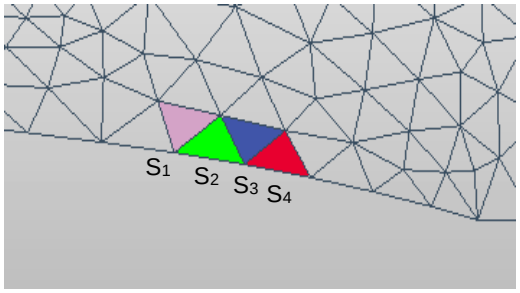


Fig. 14 - Example diagram of boundary triangle

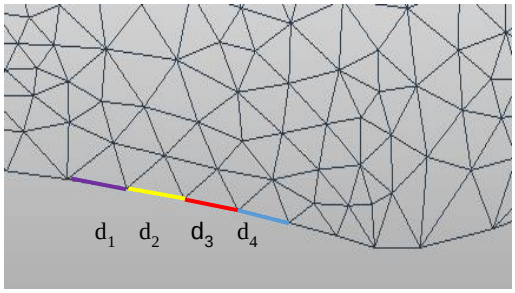


Fig. 15 - Diagram of side length

Retrieve all triangles to find the corn leaf boundary triangle that has two sides with other triangles triangle, they do not share with other triangles side length is added, the result is the blade circumference. The boundary triangles are red and yellow triangles in the corn boundary triangles as in Fig. 14, and the boundary triangles are not co-edges with other triangles such as *d1, d2, d3, d4* in Fig. 15.

RESULTS

The effective detection range of Kinect v2 is 0.5~4.5 m, the vertical direction Angle is 60 degrees, and the detection range is within 3.5 to achieve a good effect. At this time, the maximum object collected is 4 meters, which fully meets the information collection requirements of corn in each growth period. The accuracy of the measurement of the phenotypic parameters of the point cloud 3D model is evaluated by comparing the phenotypic parameters measured by manual measurement and the parameters measured by the algorithm measurement. The accuracy is evaluated based on the determination coefficient (R^2), root mean square error (RMSE) and mean absolute percentage error (MAPE).

These formulas are as follows:

$$R^2 = \frac{\sum_{i=1}^{n}(X_i - \bar{X})(Y_i - \bar{Y})}{\sqrt{\sum_{i=1}^{n}(X_i - \bar{X})^2}\sqrt{\sum_{i=1}^{n}(Y_i - \bar{Y})^2}} \quad (5)$$

Where:

n is the leaf number of corn plant;

X_i is a manual measurement of phenotypic parameters;

$\bar{X}$ is the average value of phenotypic parameters measured manually;

Y_i is the phenotypic parameter of 3D model;

$\bar{Y}$ is the average of phenotypic parameters of three-dimensional model.

$$MAPE = \frac{1}{n}\sum_{i=0}^{n}\frac{|x_{ai} - x_{mi}|}{x_{mi}} \times 100\% \quad (6)$$

$$RMSE = \sqrt{\frac{1}{n}\sum_{i=0}^{n}(x_{ai} - x_{mi})^2} \quad (7)$$

Where:

MAPE is the average absolute percentage error; *RMSE* is the root mean square error;

n is the number of corn plant samples;

x_{ai} is algorithm measurement data;

x_{mi} is manual measurement data.

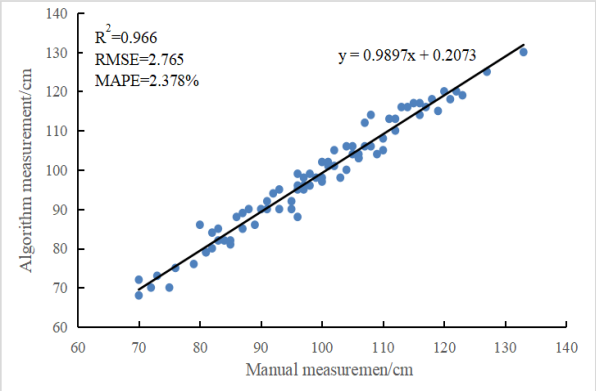


Fig. 16 - Scatter plot of comparison between manual measurement and algorithm measurement of corn plant height

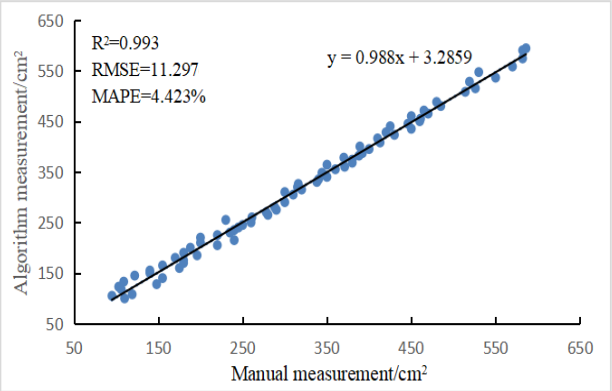


Fig. 17 - Scatter diagram of comparison between manual measurement and algorithm measurement of corn leaf area

Table 1

Comparison between manual measurement and algorithm measurement of corn stalk diameter

Number	Long axis				Short axis			
	Manual measure-ment / mm	Algorithmic measurement / mm	Measure-ment error / mm	Relative error / %	Manual measure-ment / mm	Algorithmic measure-ment / mm	Measure-ment error / mm	Relative error / %
1	24.96	23.03	1.93	7.73	21.56	22.02	0.46	2.13
2	33.84	34.44	0.60	1.78	26.59	22.17	4.42	16.62
3	33.26	32.51	0.75	2.25	26.11	27.63	1.52	5.82
4	35.73	38.36	2.63	7.36	30.49	29.05	1.44	4.72
5	41.45	44.17	2.72	6.56	31.16	27.23	3.86	12.39
6	32.03	35.65	3.62	11.30	25.01	22.04	2.97	11.88
7	33.71	30.76	2.95	8.75	28.67	22.44	6.23	21.73
8	28.16	29.53	1.37	4.87	25.61	21.38	4.23	16.52

Table 1
(continuation)

Number	Long axis				Short axis			
	Manual measure-ment / mm	Algorithmic measurement / mm	Measure-ment error / mm	Relative error / %	Manual measure-ment / mm	Algorithmic measure-ment / mm	Measure-ment error / mm	Relative error / %
9	32.01	25.67	6.34	19.81	25.98	20.36	5.62	21.63
10	33.48	41.59	8.11	24.22	23.26	25.55	2.29	9.85
11	28.66	26.22	2.44	8.51	21.63	16.71	4.92	22.75
12	32.82	43.66	10.84	33.03	27.49	26.26	1.23	4.47
13	34.97	37.53	2.56	7.32	25.57	22.37	3.20	12.51
14	38.62	38.33	0.29	0.75	27.41	29.18	1.77	6.46
15	30.25	31.50	1.25	4.13	26.21	24.39	1.82	6.94
16	31.43	33.20	1.77	5.63	23.64	27.51	3.87	16.37
17	29.91	30.17	0.26	0.87	24.34	23.17	1.17	4.81
18	25.41	30.84	5.43	21.37	22.64	21.78	0.86	3.80
19	29.82	28.87	0.95	3.19	24.46	20.85	3.61	14.76
20	35.19	31.74	3.45	9.80	23.38	25.06	1.68	7.19
Average value	32.29	33.39	3.01	9.46	25.56	23.86	2.86	11.17

The algorithm and manual measurement of corn plant height are shown in Fig. 16. The determination coefficient is 0.966, the average absolute percentage error is 2.378%, the root mean square error is 2.765 cm, and the accuracy of the algorithm for measuring plant height is 97.622%. The results show that the plant height measurement method has high accuracy, and the algorithm measurement value has good consistency with the manual measurement value. The accuracy of corn leaf area is shown in Fig. 17. The determination coefficient of corn leaf area is 0.993, the average absolute percentage error is 4.423%, the root mean square error is 11.927cm^2, and the accuracy of the algorithm for measuring plant height is 95.577%. The analysis results show that the algorithm measurement results are in good agreement with the two-dimensional experimental measurement results, which indicates that the algorithm measurement method of corn leaves can accurately measure the perimeter and area of corn leaves. The comparison between manual measurement and algorithm measurement of corn stem diameter is shown in Table 1. The average measurement error of the long axis of corn stem diameter is 3.01 mm, and the average measurement relative error is 9.46%. The average measurement error of the short axis of corn stem diameter is 2.86 mm, and the average measurement relative error is 11.17%. The results show that the stem extraction and measurement methods proposed in this study have high accuracy and can meet the needs of use.

CONCLUSIONS

Based on the existing machine vision research, this paper proposes a new method of three-dimensional model reconstruction and feature segmentation for corn. Based on Kinect 2.0 combined with turntable method, corn plants are scanned to obtain corn point cloud. In the three-dimensional reconstruction of corn plants with complete information after manual rough registration and ICP fine registration, the reconstruction method improves the operation speed and measurement accuracy. The ellipse fitting and region growing segmentation algorithm for corn shape features are used to segment the characteristics of flower pot, stem and leaf. This method has high efficiency, high precision, no damage and continuous measurement. The corn plant model and the segmented corn leaves are measured. The measurement accuracy of the corn plant height algorithm is 97.622%. The average relative errors of corn stem length and short axis were 10.27% and 12.71% respectively. The measurement accuracy of corn leaf area algorithm is 95.577%. Experimental results showed that this method could extract crop phenotype parameters nondestructively and accurately. In the future, Kinect sensor is considered to be placed on a three-wheeled cart to directly collect corn information in the field. This study is of great significance for understanding crop growth status, crop detection, yield estimation and disease resistance detection.

REFERENCES

[1] Aksoy E. E., Abramov A., Worgotter F., et al. (2015). Modeling leaf growth of rosette plants using infrared stereo image sequences [J]. *Computers and Electronics in Agriculture*, 110:78-90.

[2] Archibald R., Bao F., et al. (2019). A direct filter method for parameter estimation. *Journal of Computational Physics*, 398: 108871.

[3] Ding J., Chen J., Zhou A. et al. (2019). 3D Modeling of the Rotationally Symmetric Objects Using Kinect [C]//*2019 IEEE 4th International Conference on Image, Vision and Computing (ICIVC). IEEE*, 685-689.

[4] Dongyu Ren et al. (2022). A 3D reconstruction method of fruit tree branches based on Kinect v2 sensor (基于 Kinect v2 传感器的果树枝干三维重建方法) [J]. *Transactions of the Chinese Society for Agricultural Machinery*, 53(S2):197-203.

[5] Gang Liu, Yohan Yin et al. (2022). Cherry canopy denoising and registration method based on three-dimensional point cloud (基于三维点云的群体樱桃树冠层去噪和配准方法). *Transactions of the Chinese Society of Agricultural Machinery*. 1-11.

[6] He JQ, Ha Rison R.J. et al. (2017). A novel 3D image system for strawberry phenotyping [J]. *Plant Methods*, 13(1):1-8.

[7] Hui F., Zhu J., Hu P. et al. (2018). Image-based dynamic quantification and high-accuracy 3D evaluation of canopy structure of plant populations. *Annals of Botany*, 121(5): 1079-1088.

[8] Hui Chen, Tingting Wang et al. (2021). Three-dimensional Measurement Method of Leaf Area of Irregular Plants Based on Motion Restoring Structure (基于运动恢复结构的无规则植物叶片面积三维测量方法). *Transactions of the Chinese Society of Agricultural Machinery*. 52(04): 230-238.

[9] Jay S., Rabatel G., Hadoux X., et al. (2015). Infield crop row phenotyping from 3D modelling performed using structure from motion. *Computers and Electronics in Agriculture*, 110: 70-77.

[10] Jin Zhou et al. (2013). Fast reconstruction of 3D human body using Kinect (使用 Kinect 快速重建三维人体) [J]. *Journal of Computer Aided Design and Graphics,* 25(6): 873-879.

[11] Qian Wu. (2022). *Segmentation and registration of citrus point cloud based on Kinect v2 camera (基于 Kinect v2 相机的柑橘点云分割与配准研究)* [D].*Guangxi Normal University*. DOI:10.27036/d.cnki.ggxsu. 2022.001585.

[12] Song Bi, Yuhao Wang, (2021). LiDAR point cloud denoising method based on adaptive radius filter (基于自适应半径滤波的农业导航激光点云去噪方法研究) [J]. *Transactions of the Chinese Society for Agricultural Machinery*, 52(11): 234-243.

[13] Wu D., Ye J.L., Wang K. et al. (2020) Research on 3D reconstruction method of potted rice based on contour projection [J]. *Agric. Sci. Technol*., 22:87-95.

[14] Xiong X., Yu L., Yang W., et al. (2017). A high-throughput stereo-imaging system for quantifying rape leaf traits during the seedling stage. *Plant Methods*, 13(1): 1-17.

[15] Xu Wu, Luling Wen, Dongdong Liang et al. (2019), Comparative Study of Surface Reconstruction Algorithms Based on Point Cloud Data (基于点云数据的曲面重建算法比较研究), *Journal of Anhui Normal University (Natural Science Edition)*, 042(001): 46-50.

[16] Yingbo Song, Wei Guo, Hongquan Zhang, et al. (2015). Practical application of image processing techniques for measuring leaf area of corn (图像处理技术在玉米叶面积测量中的实际应用). *Journal of Agriculture*, 5(8): 111-114.

[17] Yaochen Li. (2019). *Measurement of Morphological Characteristics of Cotton Seedlings Based on Structured Light Imaging (基于结构光成像的棉花幼苗形态特征测量)*. Huazhong Agricultural University.

[18] Zila Jia, Yungang Bai, Biao Cao, (2019), Effects of different water treatments on plant growth and yield of silage corn under mulched drip irrigation in northern Xinjiang (北疆寒旱区不同水分处理对膜下滴灌青贮玉米植株生长与产量的影响). *Chinese Agricultural Science Bulletin*, 35(16): 6-14.

STUDY ON THE UNIFORMITY OF SPRAYING SEEDS WITH 4BQD-40C SPRAYING SEEDER MACHINE
/
4BQD-40C 型喷播机喷播落种均匀性研究

Yan CHEN, Hua GUO *), Shi FU, Rui ZHANG, Ming ZHANG [1]
Department of Information Engineering, Ordos Institute of Technology, Compass, Ordos/ China
Tel: +815849726146; E-mail: guohua716@163.com
Corresponding author: Hua Guo
DOI: https://doi.org/10.35633/inmateh-69-62

Keywords: *spraying quality, seed distribution trajectory, swinging frequency, forward speed*

ABSTRACT
The working parameters of the pneumatic sprayer, such as the sprayer's attitude, working airflow, and spraying amount, have an impact on the evenness of seed distribution during the process of vegetation restoration on degraded grasslands. This article focuses on the 4BQD-40C pneumatic sprayer and analyzes the impact of the sprayer's forward speed, the airflow velocity at the sprayer's inlet, and the frequency of the sprayer's swinging nozzle on the spraying quality. The conclusion shows that: 1) the equation of the seed distribution trajectory of the sprayer was obtained, laying the foundation for subsequent research; 2) the swinging frequency of the nozzle is the key factor affecting the spraying quality of the sprayer, and the optimal swinging frequency of the nozzle corresponding to different forward speeds of the sprayer was obtained based on the established trajectory equation; 3) when the sprayer performs spraying operations with the optimized forward speed and swinging frequency, the trajectory of the sprayer's seed distribution was analyzed. It was found that when the nozzle swings at each optimal frequency, the trajectory of the seed distribution is the same, and the sum of the re-sprayed and missed areas in the seed distribution area is equal.

摘要
气力喷播机对退化草地进行植被修复的过程中，喷播机的工作参数，如喷播机姿态、工作气流和喷播量对喷播均匀性均有影响。本文以4BQD-40C 型气力喷播机为研究对象，分析喷播机前进速度、喷筒入口气流速度及喷筒摆动频率对喷播质量的影响。结论表明：1）得到了喷播机的落种轨迹方程，为后续研究奠定基础；2）得出喷筒摆动频率是影响喷播机喷播质量的关键因素，依据建立的轨迹方程对喷播机不同前进速度对应的喷筒摆动频率进行了优化，得到喷播机不同前进速度对应的喷筒最优摆动频率；3）当喷播机以优化后的前进速度与摆动频率进行喷播作业时，对喷播机的落种轨迹进行了分析，发现喷筒在各个最优摆动频率摆动时，种子的落种轨迹相同，且此时在落种区域内，重播、漏播面积之和相等。

INTRODUCTION
From the results of the preliminary spraying experiments, spraying operations are an efficient and fast technique for restoring grassland vegetation under natural climatic conditions. Significant research achievements have been made in the related studies on vegetation restoration on degraded grasslands using pneumatic sprayers *(Jin et al., 2023; Wang et al., 2015; Zhang et al., 2013; Xuan et al., 2016; Grella et al., 2020; Tai et al., 2022; Wang et al., 2023)*. However, in the process of using pneumatic sprayers for vegetation restoration on degraded grasslands, the impact of the sprayer's working parameters, such as the sprayer's attitude, working airflow, spraying amount, and their relationship with the existing vegetation coverage have not been fully considered. Although the reciprocating swinging spraying method of the 4BQD-40C sprayer nozzle can increase the operational range and spraying area, it also has a certain impact on the spraying quality. The spraying quality of the sprayer can be measured by the evenness of seed distribution in the seed distribution area, mainly manifested by the size of the re-sprayed and missed areas in the seed distribution area.

[1] *Yan Chen, Lecturer Ph.D. Eng.; Hua Guo, Prof M.S. Eng.; Shi Fu, Lecturer M.S. Eng.; Rui Zhang, Lecturer M.S. Eng.; Ming Zhang, Lecturer M.S. Eng.*

The term "Replay seeding area" refers to the area where seeds have been sown more than once during the spraying operation, while "Missed seeding area" refers to the area where no seeds have been sown during the spraying operation (*Kang et al., 2019; Wu et al., 2022*). The main factors that affect the uniformity of seed sowing by the sprayer seeding machine are the forward speed of the machine, the air flow velocity at the nozzle inlet, and the oscillation frequency of the nozzle. Changing the air flow velocity and oscillation frequency of the nozzle based on the machine's different posture information is the most convenient and effective method to improve the quality of seed sowing by the sprayer seeding machine. This paper mainly studies the relationship between the forward speed of the 4BQD-40C sprayer seeding machine, the air flow velocity at the nozzle inlet, the oscillation frequency of the nozzle, and the areas of seed sowing with overlapping or missing seeds.

MATERIALS AND METHODS

Establish trajectory equation

The 4BQD-40C pneumatic sprayer seeding machine swings its spray nozzle back and forth around its center from 0 to 180 degrees during the seeding process to increase its coverage area, resulting in a complex seed drop trajectory. To study the seeding area of the machine, it is necessary to establish the seed drop trajectory equation first, and then analyze the seed drop area based on this equation *(Wang et al., 2012; Liu et al., 2020; Xing et al., 2020; Cujbescu et al., 2022)*.

The forward travel speed of the sprayer seeding machine is v. The sprayer nozzle swings back and forth around its own center in the horizontal plane, with a swing angle ranging from 0 to 180 degrees. One swing cycle is completed when the nozzle swings back and forth once, and the swing frequency is denoted as n_b. Taking the opposite direction of the forward direction of the sprayer as the positive direction of the y-axis, and the limit position of the nozzle swinging counterclockwise as the positive direction of the x-axis, a coordinate system is established with the swinging center of the nozzle as the origin. The motion state of the seeds at the nozzle outlet is analyzed (*Akhalaya et al., 2021;* Cao *et al., 2023; Liao et al., 2022; Tabeei et al., 2021*).

The initial position of the nozzle is at the counter clockwise limit position, which coincides with the positive direction of the x-axis. The nozzle swings around its own center for one period T, and there are two different trajectories for the seeds, as shown in Fig. 1. In the first half period of swinging, the seed's trajectory is represented by curve AB, while in the second half period, the seed's trajectory is represented by curve BC. If the swinging angular velocity of the nozzle is ω, the spraying time is t, and the velocity of the seed at the nozzle outlet is v_r, then the angle between the nozzle and the positive x-axis during the swinging process is ω_t (*Zhang et al., 2012*).

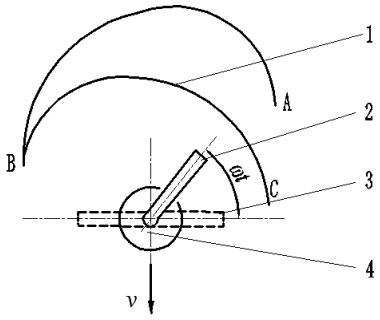


Fig. 1 - Sketch map of dropping seeds trajectory

1 – Trajectories for the seeds; 2 – Spray barrel; 3 – Limit position of spray barrel; 4 – Turntable

The initial position of the spray barrel is aligned with the positive direction of the x-axis, and the spray barrel swings in a counterclockwise direction, forming an acute angle λ with the x-axis. When the swing time is $t \in [\pi/2\omega, \pi/\omega]$, it can be obtained $\lambda = \omega t$, the seed velocity at the outlet of the spray barrel can be analyzed as shown in Fig. 2a. At this time, the partial velocity equation of the seed along the coordinate axis direction is:

$$\begin{cases} v_x = -v_r \cdot sin\omega t \\ v_y = v_r \cdot cos\omega t - v \end{cases} \quad (1)$$

When the swing time $t\in[\pi/2\omega, \pi/\omega]$, it can be obtained $\lambda=\pi-\omega t$, the seed velocity at the outlet of the spray barrel can be analyzed as shown in Fig. 2b. At this time, the partial velocity equation of the seed along the coordinate axis direction is:

$$\begin{cases} v_x = -v_r \cdot sin(\pi - \omega t) \\ v_y = -v_r \cdot cos(\pi - \omega t) - v \end{cases} \quad (2)$$

When the swing time $t\in[\pi/\omega, 3\pi/2\omega]$, it can be obtained $\lambda=\omega t-\pi$, the seed velocity at the outlet of the spray barrel can be analyzed as shown in Fig. 2c. At this time, the partial velocity equation of the seed along the coordinate axis direction is:

$$\begin{cases} v_x = v_r \cdot sin(\omega t - \pi) \\ v_y = v_r \cdot cos(\omega t - \pi) - v \end{cases} \quad (3)$$

When the swing time $t\in[3\pi/2\omega, 2\pi/\omega]$, it can be obtained $2\pi-\omega t$, the seed velocity at the outlet of the spray barrel can be analyzed as shown in Fig. 2d. At this time, the partial velocity equation of the seed along the coordinate axis direction is:

$$\begin{cases} v_x = v_r \cdot sin(2\pi - \omega t) \\ v_y = -v_r \cdot cos(2\pi - \omega t) - v \end{cases} \quad (4)$$

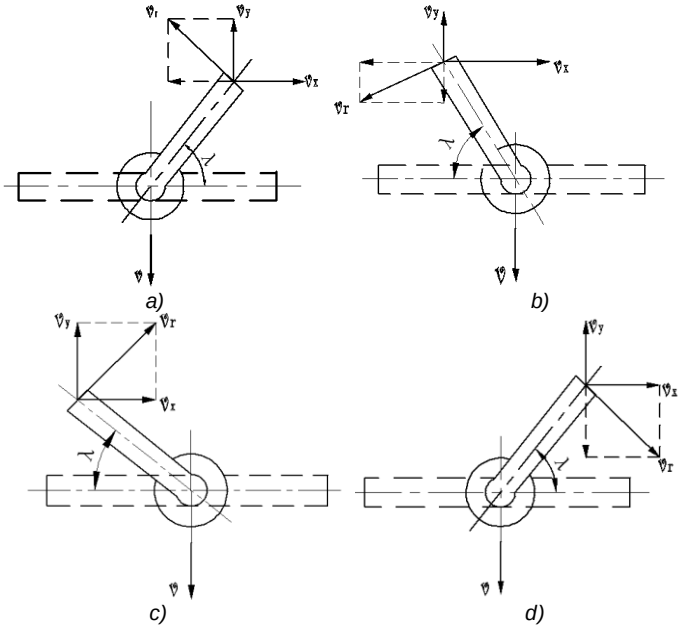


Fig. 2 - Diagram of the velocity analysis of the seed at the outlet of spray pipe

After sorting out Equations (1), (2), (3), and (4), the following equations can be obtained for the velocity of the seed at the outlet of the spray barrel. When $t\in[0, \pi/\omega]$, the trajectory of the nozzle barrel is shown in Section AB in Fig. 1, and the velocity equation of Equation (5) is obtained. When $t\in[\pi/\omega, 2\pi/\omega]$, the trajectory of the nozzle barrel is shown in Section BC in Fig. 1, and the velocity equation of Equation (6) is obtained:

$$\begin{cases} v_x = -v_r \cdot sin\omega t \\ v_y = v_r \cdot cos\omega t - v \end{cases} \quad (5)$$

$$\begin{cases} v_x = -v_r \cdot sin\omega t \\ v_y = -v_r \cdot cos\omega t - v \end{cases} \quad (6)$$

By integrating Equations (5) and (6), the following expression is obtained, where c_1 and c_2 are constants.

$$\begin{cases} x = v_r/\omega \cdot cos\omega t + c_1 \\ y = v_r/\omega \cdot sin\omega t - v \cdot t + c_2 \end{cases} \quad (7)$$

$$\begin{cases} x = v_r/\omega \cdot cos\omega t + c_1 \\ y = -v_r/\omega \cdot sin\omega t - v \cdot t + c_2 \end{cases} \quad (8)$$

Set the spray barrel length of the sprayer to l, while $x=l$, $v_r=\omega l$. At this point, $c_1=c_2=0$, so the trajectory equations for AB and BC segments are shown in Equation (9) and (10).

$$\begin{cases} x = l \cdot cos\omega t \\ y = l \cdot sin\omega t - v \cdot t \end{cases} \quad (9)$$

$$\begin{cases} x = l \cdot cos\omega t \\ y = -l \cdot sin\omega t - v \cdot t \end{cases} \quad (10)$$

Therefore, the trajectory equation of the seed with the spray barrel of the sprayer swinging back and forth for one cycle can be expressed as:

$$\begin{cases} x = l \cdot cos\omega t \\ y = |l \cdot sin\omega t| - v \cdot t \end{cases} \quad (11)$$

Analysis of seed falling area

Upon enlarging the trajectory of the seeds sprayed by the sprayer, it can be seen that the seed distribution area is enclosed by four curves, forming a belt-shaped pattern as shown in Fig. 3. The seed distribution area for one swing cycle of the nozzle barrel consists of eight curves. When the nozzle barrel transitions from counterclockwise swing to clockwise swing, the end curve of the first half cycle coincides with the start curve of the second half cycle, and they are the same curve. Therefore, the actual seed distribution area is composed of seven different curves. Based on Equation (11), the equation of each curve can be obtained as shown in Equations (12)-(18) (*Fan et al., 2013*).

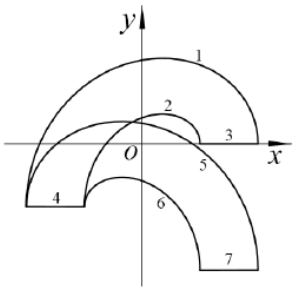


Fig. 3 - Diagram of the falling region

$$\begin{cases} x_1 = R \cdot cos\omega t \\ y_1 = R \cdot sin\omega t - v \cdot t \end{cases} \quad t \in (0, \frac{T}{2}) \quad (12)$$

$$\begin{cases} x_2 = r \cdot cos\omega t \\ y_2 = r \cdot sin\omega t - v \cdot t \end{cases} \quad t \in (0, \frac{T}{2}) \quad (13)$$

$$y_3 = -v \cdot t \quad t = 0, x \in [r, R] \quad (14)$$

$$y_4 = -v \cdot t \quad t = \frac{T}{2}, x \in [-r, -R] \quad (15)$$

$$\begin{cases} x_5 = R \cdot cos(\pi - \omega t) \\ y_5 = R \cdot sin(\pi - \omega t) - v \cdot t \end{cases} \quad t \in (\frac{T}{2}, T) \quad (16)$$

$$\begin{cases} x_6 = r \cdot cos(\pi - \omega t) \\ y_6 = r \cdot sin(\pi - \omega t) - v \cdot t \end{cases} \quad t \in (\frac{T}{2}, T) \quad (17)$$

$$y_7 = y_3 - v \cdot t \quad t = T, x \in [r, R] \quad (18)$$

In the equation, T is the swing period of the spray barrel, R is the distance from the outer edge of the seed landing area to the center of the spray barrel swing, and r is the distance from the inner edge of the seed landing area to the center of the spray barrel swing.

According to the above analysis, a GUI interface program is designed in Matlab software to draw the seed distribution area of the sprayer, as shown in Fig. 4.

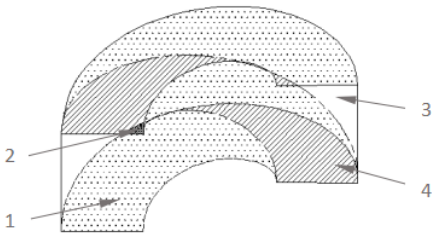


Fig. 4 - Sketch map of missing and broadcast area in seeding area

1 – Normal spraying area; 2 – Secondary spraying area; 3 – Missed spraying area; 4 – One spraying area

Based on the above analysis, a GUI program for designing the spray seeding area was developed in Matlab software, as shown in Fig. 4. To analyze the re-seeding and missed seeding areas in the seeding area, the curve intersection method was used to determine the re-seeding and missed seeding areas in the seeding area. From Fig. 4, it can be seen that in one swing cycle of the nozzle, there are normal seeding areas, re-seeding areas, and missed seeding areas, and these areas appear twice symmetrically in one swing cycle. Since the shapes of the re-seeding and missed seeding areas are irregular, the calculus method of finding the area of a rectangle was used to calculate the re-seeding and missed seeding areas in the spray seeding area.

For ease of calculation, the coordinates of the leftmost and rightmost projections of the seeding area onto the x-axis are [-R, R]. Then, the seeding area is divided into n equal parts, with an integration step size of h is:

$$h = \frac{R-(-R)}{n} \tag{19}$$

The area of replanting and missed seeding in the seed falling area is:

$$S = h\sum_{i=1}^{m}|f_i(x) - f_{i+1}(x)| \tag{20}$$

In the equation, $f_i(x)$ represents the outer boundary curve equation of the seed falling area in the second half of the swing cycle, $f_{i+1}(x)$ represents the inner boundary curve equation of the seed falling area in the first half of the swing cycle, and x represents the horizontal coordinate value of the spray range (*Fan et al., 2013*).

Analysis of seed drop uniformity

As shown in Fig. 4, uneven seeding areas such as replanting and missed seeding appear in the seed falling area, mainly caused by the combined motion of the swinging of the spray barrel and the forward movement of the sprayer. Therefore, the relationship between the frequency of the spray barrel swing and the forward speed of the sprayer has a significant impact on the area of replanting and missed seeding in the seed falling area.

Based on the established trajectory equation and seed falling area of the sprayer, and with the forward speed of the sprayer fixed, the replanting and missed seeding areas were calculated for different swing frequencies of the spray barrel, and the minimum total area of replanting and missed seeding was found. This corresponded to the optimal swing frequency of the spray barrel for the given forward speed, thus achieving optimization of the swing frequency. Before optimization, the relationships between the forward speed of the sprayer, swing frequency of the spray barrel, and the total area of replanting and missed seeding were established separately. Then, a unified relationship was established using optimization methods.

The optimization variables are the nozzle oscillation frequency n_b and the forward speed of the sprayer v, with the minimum total area of replanting and missed seeding in the seed falling area as the optimization objective. During the optimization process, the area of the replanting region is denoted as S_C, and the area of the missed seeding region is denoted as S_L, both in units of square meters. The optimization function is given by equation (21) (*Chen et al., 2018*).

$$S(v, n_b) = S_c + S_L \tag{21}$$

Based on the actual situation, the following constraints are set for the objective function:

- The proportion of replanting area to the total seed falling area should be less than or equal to 20%.
- The proportion of missed seeding area to the total seed falling area should be less than or equal to 20%.
- According to the literature, the maximum speed of a tractor in the field is 20 km/h, which is equivalent to a maximum speed of 5.6 m/s. Therefore, only forward speeds of 0~6 m/s are considered in optimizing the nozzle oscillation frequency.
- The oscillation frequency of the nozzle should be less than or equal to 20 min^{-1}, which is determined by the motor speed and transmission ratio.

For the convenience of optimizing the swing frequency of the nozzle, various parameters are set on the Matlab GUI program interface. At the same time, the calculated optimal swing frequency of the nozzle and the minimum replanting and missed seeding area are displayed on the GUI interface (Fig. 5).

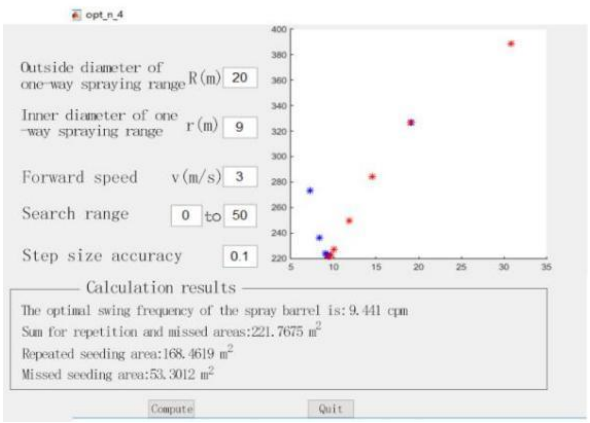


Fig. 5 - Optimization of GUI program interface for swinging frequency of spray cylinder

The optimization of the spraying tube swing frequency was conducted for different forward speeds of the sprayer seeding machine. The relationship between the optimal swing frequency of the spraying tube and different forward speeds of the sprayer seeding machine is shown in Table 1.

Table 1

Optimal swing frequency of spray cylinder corresponding to different forward speeds

Forward speed [m/s]	0.5	1	1.5	2	2.5	3	3.5	4	4.5	5	5.5	6
Swing frequency [rpm]	1.6	3.1	4.7	6.3	7.8	9.4	11.1	12.6	14.2	15.7	17.3	18.9

According to Table 1, the optimal frequency of the nozzle swing is proportional to the forward speed of the sprayer. Furthermore, it was found through analysis of the seed falling trajectory that the optimal frequency corresponding to the optimized seed falling trajectory results in the same area of replanting and missed seeding. Therefore, verification of the spraying swing under a commonly used working speed is sufficient.

Seed falling uniformity test

The experimental site was selected in a relatively flat soil field at Inner Mongolia Agricultural University. The experiment was conducted under the condition of wind speed less than 1 m/s and temperature of 15-20℃. The experimental equipment used in this experiment was 4BQD-40C pneumatic seeder (as shown in Fig. 6), several packages of coated rye grass seeds, a TSI 9565-P multifunctional anemometer, a hot wire anemometer probe, a tape measure, a stopwatch, and several bags of white powder.



Fig. 6 - 4BQD-40C type pneumatic sprayer seeding machine

Check the components of the sprayer to ensure that they are in good condition during operation. Choose a relatively flat soil site for the experiment to ensure that the seeds sprayed land smoothly on the ground and there is minimal splashing, which can reflect the actual working conditions of the sprayer. Count the amount of seeds in the seeding area, record the area of the replay and leakage in the seeding area, and compare the data obtained from the experiment with the simulated data to obtain the optimal swing frequency of the nozzle corresponding to different forward speeds of the sprayer.

Before the experiment, the working area was divided into a grid using a tape measure and white powder. The grid size was: 2m x 2m and the grid size of the total seed drop area was: 40m x 40m. The centerline of the total seeding area was selected as the position of the sprayer, and the grid edges were numbered for later statistical analysis. In this experiment, the sprayer was tested at forward speeds of 0.3 m/s and 0.5 m/s with different optimal nozzle swing frequencies (as shown in Table 2).

Table 2

The sprayer seeding machine speed is 0.3 m/s and 0.5 m/s, corresponding frequency of the spray cylinder swing

Forward speeds [m/s]	Swing frequencies 1 [rpm]	Swing frequencies 2 [rpm]	Swing frequencies 3 [rpm]	Swing frequencies 4 [rpm]	Swing frequencies 5 [rpm]
0.3	0.75	0.84	0.94	1.02	1.11
0.5	1.25	1.40	1.57	1.70	1.85

Before starting the experiment, the following steps were taken:

- Set the inlet air velocity of the nozzle to 50 m/s using the frequency converter.
- Adjust the seeding rate to 0.63 rpm.
- Set the frequency of the frequency converter according to the corresponding values in Table 3 obtained from Equation (22).
- Adjust the initial position of the nozzle to its counterclockwise limit position.
- Adjust the forward speed of the sprayer to 0.3 m/s.
- Set the distance from the starting position of the sprayer to the edge of the grid behind the sprayer to be 20 m, as the maximum seeding distance is 20 m when the inlet air velocity of the nozzle is 50 m/s.
- Set the centerline of the grid as the predefined path of the sprayer (Fig. 7) and determine the end position of the sprayer according to Equation (23).

$$f = 50 \cdot \frac{n_b}{n_0 \cdot i} \quad (22)$$

$$s = v \cdot T = v \cdot \frac{60}{n_b} \quad (23)$$

The formula is as follows: n_b is the oscillation frequency of the spray nozzle of the sprayer; n_0 is the rated speed of the motor that drives the nozzle oscillation, n_0= 2840 rpm; i is the transmission ratio, and the motor and nozzle are connected by a gear transmission, i = 1/60; T is the oscillation period of the nozzle.

Table 3

Frequency of frequency converter corresponding to different spray cylinder swings

Swing frequencies [rpm]	0.75	0.84	0.94	1.02	1.11	1.25	1.40	1.57	1.70	1.85
Converter frequency [Hz]	0.80	0.89	1.00	1.08	1.18	1.33	1.48	1.66	1.80	1.96

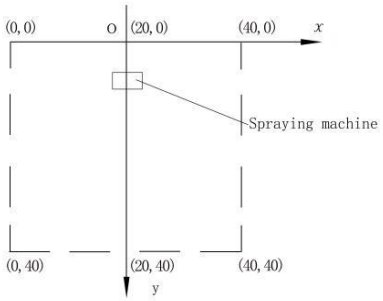


Fig. 7 - Predefined path schematic of a sprayed machine

During the experiment, the sprayer seeding machine traveled at a constant speed along a pre-defined path according to the set forward speed. At the start position for spraying, the aerial sprayer seeding machine was activated, and the seeding motor was started along with the swinging of the nozzle. The sprayer seeding machine stopped working after one cycle of nozzle swinging, and the experimental data was then collected. The ground seeds were cleaned up after the data collection was completed, preparing for subsequent experiments. Five experiments were conducted with varying frequencies of nozzle swinging while the sprayer seeding machine was traveling at a speed of 0.3 m/s. The experimental process at a forward speed of 0.5 m/s was identical to that at a forward speed of 0.3 m/s, except for the change in nozzle swinging frequency.

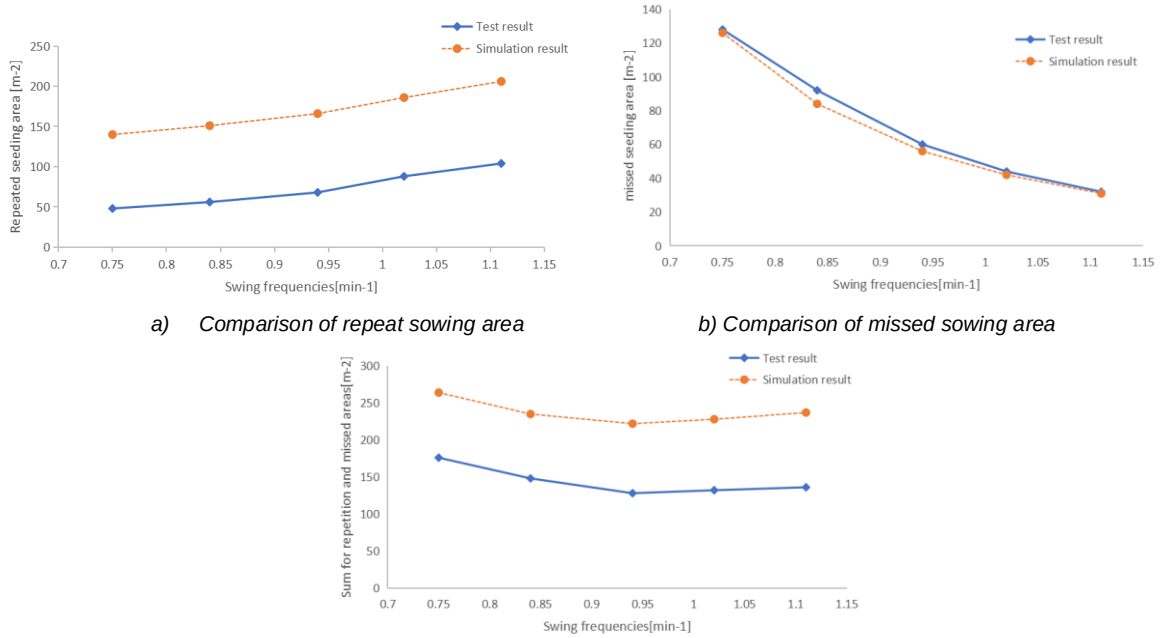
RESULTS

The experimental analysis record table was identical to the ground grid used during the experiment. During the experiment, the seeding amount in each grid was recorded when the sprayer seeding machine was traveling at a speed of 0.3 m/s. The experimental data and simulation results were analyzed and the analysis results are shown in Table 4. During the experiment, the re-seeding and leakage areas of the spraying region were calculated. The leakage area was defined as the grid area with a seeding amount of 0, while the re-seeding area was defined as the grid area with a seeding amount greater than the average seeding amount of the spraying region. The experimental results were compared with the simulation analysis results, as shown in Fig. 8.

Table 4

Results of reseeded and missed areas at different oscillation frequencies when the sprayer forward speed is 0.3m/s.

Swing frequencies [rpm]	Repeated seeding area of the test [m^2]	Missed seeding area of the test [m^2]	Sum for repetition and missed areas of the test [m^2]	Repeated seeding area of the simulation [m^2]	Missed seeding area of the simulation [m^2]	Sum for repetition and missed areas of the simulation [m^2]
0.75	48	128	176	140	126	264
0.84	56	92	148	151	84	235
0.94	68	60	128	166	56	222
1.02	88	44	132	186	42	228
1.11	104	32	136	206	31	237



a) Comparison of repeat sowing area

b) Comparison of missed sowing area

c) Comparison of the sum of repeated and missed sowing areas

Fig. 8 - Comparison of rebroadcast and missed area results when the speed is 0.3 m/s

From Fig. 8, it can be observed that as the frequency of nozzle swinging increases, the re-seeding area of the spraying region increases while the leakage area decreases. When the frequency of nozzle swinging is 0.94 rpm, the sum of the re-seeding and leakage areas is minimized. At this frequency, the seed distribution in the spraying region is relatively even. This result is consistent with the simulation analysis, which found that the optimal frequency of nozzle swinging for a sprayer seeding machine traveling at a speed of 0.3 m/s is 0.94 rpm, thus validating the correctness of the simulation analysis. However, Fig. 8 also shows that there is a certain difference between the re-seeding and leakage areas obtained from the experimental data and the simulation analysis results, which is mainly due to statistical errors. Nevertheless, the overall trend of the results is similar.

Simultaneously, the recorded data for the sprayer seeding machine traveling at a speed of 0.5 m/s shows the seed distribution in each grid of the experimental area obtained by changing the frequency of nozzle swinging. The experimental results are analyzed and compared with the simulation results in Table 5. When the sprayer seeding machine travels at a speed of 0.5 m/s, both the simulation and experimental results show that the re-seeding area in the spraying region increases with the increase of nozzle swinging frequency while the leakage area decreases. At the optimal frequency of nozzle swinging, the sum of the re-seeding and leakage areas is minimized. This result is consistent with the analysis results obtained when the sprayer seeding machine travels at a speed of 0.3 m/s.

Table 5

Results of reseeded and missed areas at different oscillation frequencies when the sprayer forward speed is 0.5m/s

Swing frequencies [rpm]	Repeated seeding area of the test [m^2]	Missed seeding area of the test [m^2]	Sum for repetition and missed areas of the test [m^2]	Repeated seeding area of the simulation [m^2]	Missed seeding area of the simulation [m^2]	Sum for repetition and missed areas of the simulation [m^2]
1.25	40	140	180	141	119	260
1.40	44	100	144	151	83	234
1.57	60	64	124	168	54	222
1.70	80	52	132	181	45	226
1.85	100	36	136	200	36	236

Reseeded and missed area after spray canister operation at an optimum oscillation frequency of 0.94 rpm with a sprayer advance speed of 0.3 m/s. This was compared with the reseeded and missed area after the spray barrel was operated at an optimum oscillation frequency of 1.57 rpm at a forward speed of 0.5 m/s of the sprayer. The results are shown in Table 6. Table 6 shows that when the forward speed of the spreader is changed and the spray nozzle is operated at the corresponding optimum oscillation frequency, the sum of the reseeded missed areas obtained statistically in the seed drop area is essentially equal and the seed drop trajectories are similar, which is consistent with the conclusions obtained from the simulation.

Table 6

Comparison of replanting and missing area in the falling area when the forward speed is 0.3 m/s and 0.5 m/s

Forward speeds [m/s]	Repeated seeding area of the test [m^2]	Missed seeding area of the test [m^2]	Sum for repetition and missed areas of the test [m^2]
0.3	68	60	128
0.5	60	64	124

CONCLUSIONS

Spraying quality is an important indicator for evaluating the spraying performance of a sprayer seeding machine. Through simulation analysis, numerical simulation, and experimental analysis, the factors affecting the spraying quality of the sprayer seeding machine were analyzed, and the following conclusions were drawn:

(1) Analyzing the seed trajectory of the spray seeder, an equation for the seed trajectory was obtained, laying the foundation for subsequent research.

(2) By analyzing the influence of the swing frequency of the nozzle on the spray quality of the spray seeder, the optimal swing frequency of the nozzle corresponding to different forward speeds of the spray seeder was obtained through optimization based on the established trajectory equation.

(3) When the spray seeder performs seeding operations at the optimized forward speed and swing frequency of the nozzle, an analysis of the seed trajectory was conducted. It was found that when the nozzle swings at various optimal frequencies, the seed trajectory remains the same, and the sum of the areas of over-seeding and under-seeding is equal within the seeding area.

ACKNOWLEDGEMENT

The support of the University scientific research projects in Inner Mongolia Autonomous Region (NJZY22207) for this research is greatly appreciated.

REFERENCES

[1] Akhalaya, B. Kh; Shogenov, Yu Kh; Starovoitov, S., (2021). Effect of Design Changes in Pneumatic Seeding Devices on Quality Indicators of Seeding. *Russian Agricultural Sciences*, Vol. 47(1), pp. 93-98.

[2] Chen, Y., (2018). *Research on Automatic Variable Spraying Technology and Related Parameter Optimization of Spraying Machine Based on Multisource Information*. PhD thesis. Univ. Inner Mongolia agricultural, Hohhot/China.

[3] Cao, A. N., Wu, C. D., Zhang B., et al., (2023). Simulation and Analysis of Spray Barrel Motion for Unmanned spray Vehicles Replacing Pesticides (替代农药无人喷雾车的喷筒运动仿真及分析). *Research on Agricultural Mechanization*, Vol. 45 (08), pp. 10-17, Heilongjiang/China.

[4] Cujbescu, D., Gageanu, L., Persu, C., Gheorghe, G., (2022). Numerical simulation of seed distribution of a pneumatic seed meter. *INMATEH-Agricultural Engineering*, Vol. 66(1), pp. 41-48, Bucharest/ Romania. https://doi.org/10.35633/inmateh-66-04

[5] Fan, C. M., (2013). *Optimization and experimental verification of nozzle swing frequency of 4BQD-40C vehicle-mounted spraying machine* (4BQD-40C 型车载式喷播机喷筒摆动频率的优化及试验验证). Master's thesis. Inner Mongolia Agricultural Univ., Hohhot/China.

[6] Grella, M., Miranda-Fuentes, A., Marucco, P., & Balsari, P., (2020). Field assessment of a newly-designed pneumatic spout to contain spray drift in vineyards: evaluation of canopy distribution and off-target losses. *Pest Management Science*. Vol. 76(12), pp. 4173-4191, Lanzhou/China.

[7] Jin, X. G., Wen, F., Bai, Y. Y. T., Xu, Q. Q., Wang, J., Huang, Q. J., Hu, R. M., Li, M., Zhang, G. H., Lv, J. B., (2023). Effects of Different Seeding Rates of Millet on Main Agronomic Characters and Yield in Tongliao Area, Inner Mongolia (内蒙古通辽地区糜子不同播种量对主要农艺性状和产量的影响). *Journal of Agriculture and Technology*, Vol. 43 (05), pp. 10-12, Jilin/China.

[8] Kang, T. T., Li, Z., Gao, Y. C., (2019). Evaluation of the Comprehensive Benefits of Ecological Restoration of Mountainous Oasis Desert Systems in Arid Areas of Northwest China (西北干旱区山地-绿洲-荒漠系统生态恢复综合效益评估). *Journal of Ecology*, Vol. 39 (20), pp. 7418-7431, Beijing/China.

[9] Liu, W., (2020). *Research on Monitoring and Controlling Technology of Wheat Planter Seeding Volume Based on Information of Seeding Flow* (基于排种流量信息的小麦播种机播种量监测调控技术研究). PhD thesis. Univ. Jiangsu University, Zhenjiang/China.

[10] Liao, C. Q., Chen, J., Geng, F. Z., Tang, X. M., (2022). Airflow basin structure numerical optimisation analysis and suction nozzle characteristics experimental study of vacuum-vibration tray precision seeder. *Journal of Agricultural Engineering*, Vol. 53(4), Italy.

[11] Tai, Z. K., (2022). *Design and experiment of seed metering device for coated caragana seed spray seeder* (包衣柠条种子喷播机排种器设计与试验) [D]. Univ. Inner Mongolia agricultural, Hohhot/China.

[12] Tabeei, A., Keikhosravani, A., Samimi, A., Mohebbi-Mohebbi-Kalhori, D., Zakeri, M., (2021). Experimental evaluation of parameters affecting the coating performance of urea seeds in a prototype bottom external mixing spray two-fluid nozzle fluidized bed granulator. *Chemical Engineering Research & Design*, Vol. 172, pp. 242-253, England.

[13] Wang, D., Gao, Y., Xu, A., Wang, Z., Yu, H., Ren, W., (2015). Effects of Different Improvement Measures on Degraded Sheep grass Pasture (不同改良措施对退化羊草草地的影响). *Journal of Grassland and Livestock*. Vol. 223(6), pp. 22-24, Sichuan/China.

[14] Wang, A. T., (2012). *Study on the Automatic Control System of Seed Discharge for 4BQD-40 Pneumatic Planter* (4BQD-40 型气力喷播机排种自动控制系统的研究). Master's thesis. Inner Mongolia Agricultural Univ., Hohhot/China.

[15] Wu, M. H., Qian, Y., (2022). The Effectiveness and Challenges of China's Ecological Civilization Construction: An Analysis Based on Provincial Data (中国生态文明建设成效与面临的挑战——基于省域数据的分析). *Journal of Administrative Forum*, Vol. 29 (05), pp. 147-153, Heilongjiang/China.

[16] Wang, B. S., Liao, Q. X., Wang, L., Shu, C. X., Cao, M., Du, W. B., (2023). Design and Test of Air-Assisted Seed-Guiding Device of Precision Hill-Seeding Centralized Seed-Metering Device for Sesame. *Agriculture-Basel*, Vol. 13(2).

[17] Xuan, C., Chen Z., Liu H., Song T., Xue J., Liang, T., (2016). Wind erosion resistance of different restoration modes in Siziwang Banner grassland restoration experimental area (四子王旗草地修复试验区不同修复模式的抗风蚀试验). *Transactions of the Chinese Society of Agricultural Machinery*, Vol. 47(8), pp. 164-170, Beijing/China.

[18] Xing, H., Wang, Z., Luo, X., He, S., Zang, Y., (2020). Mechanism modeling and experimental analysis of seed throwing with rice pneumatic seed metering device with adjustable seeding rate. *Computers and Electronics in Agriculture*, Vol. 178(2), pp. 105697, England.

[19] Zhang, Y., Fan, C. M., Chen, Z., Wang, J. W., (2013). Optimization and experimental verification of swing frequency of nozzle boom in spraying machine (喷播机喷筒摆动频率的优化及试验). *Transactions of the Chinese Society of Agricultural Engineering*, Vol. 29(7), pp. 24-29, Beijing/China.

[20] Zhang, X.H., (2012). *Experimental research and improved design of 4BQD-40 pneumatic seeder* (4BQD-40 型气力喷播机改进设计与试验研究). Master's thesis. Inner Mongolia Agricultural Univ., Hohhot/China.

DESIGN AND EXPERIMENTAL STUDY OF A SMART TREE WHITEWASH DEVICE BASED ON HUMAN–COMPUTER INTERACTION
/
基于人机交互智能树干涂白装置的设计与实验研究

Haichao WANG [1)], Zheying ZONG [*2)], Yi QIN [2)], Yingjie DU2), Zhen WANG[2)], Chunhui ZHANG [*2)]
[1)] Inner Mongolia Agricultural University, College of Energy and Transportation Engineering, Inner Mongolia/ China
[2)] Inner Mongolia Agricultural University, College of Mechanical and Electrical Engineering, Inner Mongolia / China
Tel: +86 10 0471-4309215, +86 10 0471-5315864; E-mail: zongzheying@163.com, zhchunhui1979@126.com
Corresponding authors: Zong Zheying, Zhang Chunhui
DOI: https://doi.org/10.35633/inmateh-69-63

Keywords: *Trunk whitening device, diameter at breast height (DBH) measurement, human–machine interaction, tree maintenance*

ABSTRACT
Tree whitewash has the functions of parasite prevention and cold protection and is therefore commonly used in the maintenance and management of trees. At present, tree whitewash mainly relies on manual operation, which has the problems of low efficiency, poor quality, and uneven distribution of the whitewash agent. To address this issue, this study developed a smart tree whitewash device based on human–computer interaction. The device was controlled mainly by a programmable logic controller (PLC). Once the trunk information collected by sensors was received by the PLC, it would control the up and down motions of the ball screw to manipulate the mechanical arm for whitewash. In addition, a Mitsubishi GT12 touch screen was adopted to facilitate system operation. Subsequently, a whitewash experiment was performed on poplar trunks with lengths of 10–35 cm using three different whitewash devices, i.e., a backpack sprayer, a semi-automatic tree sprayer, and the proposed smart tree whitewash device; the efficiency and the amount of whitewash agents used were compared. The results suggested that as the tree diameter at breast height increased, the amount of required whitewash agent elevated accordingly. In this case, the time required by the backpack sprayer and the semiautomatic tree sprayer to complete the job both increased, whereas that required by the smart tree whitewash device remained almost identical. In terms of work efficiency, the time required by the smart whitewash device to whitewash a tree was 109.89 s, which was approximately 1/2 of the time required by the backpack sprayer or 2/3 of that required by the semiautomatic tree spraying device. Meanwhile, the amount of whitewash agent required by the smart whitewash device to whitewash a tree was 140.23 g, which was approximately 0.46 of the amount required by the backpack sprayer or 0.74 of that required by the semiautomatic tree spraying device. Therefore, it was concluded that the proposed smart tree whitewash device could not only improve the work efficiency of tree whitewash but also greatly reduce the amount of whitewash agent required, thereby decreasing the cost and minimising environmental pollution. This study provides theoretical guidance and technical support for future research on smart tree whitewash devices.

摘要
树木刷粉具有预防寄生虫和御寒的功能，因此常用于树木的养护和管理。目前，树木刷白主要依靠人工操作，存在效率低、质量差、刷白剂分布不均匀等问题。针对这一问题，本研究开发了一种基于人机交互的智能树干涂刷装置。该装置主要由可编程控制器(PLC)控制。PLC接收到传感器采集到的主干信息后，通过控制滚珠丝杠的上下运动来操纵机械臂进行粉刷。并采用三菱GT12触摸屏，方便系统操作。随后，在10-35 cm的杨树树干上进行了刷白试验，试验采用3种不同的刷白装置，即背包式刷白机、半自动刷白机和本发明的智能刷白装置；比较了该方法的漂白效率和用量。结果表明，随着树径胸高的增加，所需的漂白剂用量也相应增加。在这种情况下，背包喷雾器和半自动树木喷雾器完成这项工作所需的时间都增加了，而智能树木粉刷设备所需的时间几乎相同。在工作效率方面，智能刷树装置刷树时间为109.89 s，约为背包式喷雾器刷树时间的1/2或半自动喷雾器刷树时间的2/3。同时，智能刷白装置刷白树木所需的刷白剂用量为140.23 g，约为背包式喷雾器所需用量的0.46，或半自动刷白装置所需用量的0.74。因此，本文提出的智能树木涂刷装置不仅可以提高树木涂刷工作效率，而且可以大大减少所需的刷白剂用量，从而降低成本，减少环境污染。本研究为未来智能树干刷白设备的研究提供了理论指导和技术支持。

INTRODUCTION

Trees can easily freeze and crack in the early spring. This is especially the case for large trees with darker colours, thicker trunks, and weaker bark *(Liu, 2017)*. Trunk whitening can effectively mitigate such issues. The whitening agent can form an alkaline layer on the surface of the tree trunk to prevent the invasion of pathogens, kill the parasites and bacteria on the bark, accelerate the healing of tree wounds, and prevent animals from chewing on the bark *(Zhang, 2018)*.

The whitening equipment is mainly divided into three categories. The first type, a knapsack sprayer, is the most widely used *(He et al., 2016; Guo et al., 2019)*. This equipment mainly relies on manual spraying and it is difficult to control the range of the spray, which can cause low-quality spraying. Furthermore, when whitening trees with a small diameter at breast height (DBH), a large part of the whitening agent is lost into the air. The second category is a semi-automatic tree-spraying device. Although this type of device has special designs for the container, it requires manual operation and is susceptible to interference from the external environment. The third category includes more advanced whitening machines; however, most of them are in the theoretical-research stage and the production cost is relatively high *(Chen, 2018)*.

In response to the above problems, this paper proposes an intelligent tree-trunk whitening device, based on human–machine interaction, which uses ultrasonic sensors to measure the diameter of the tree trunk and transmits it to the programmable logic controller (PLC). The PLC controls a three-dimensional screw that drives the manipulator to spray the trunk and uses a Mitsubishi GT12 touch screen to achieve human–machine interaction. Such a design is user-friendly, versatile, and environmentally friendly. The performance of the proposed smart tree whitewash device was compared to that of a backpack sprayer and a semiautomatic tree spraying device. The results of this study can provide theoretical guidance and technical support for future research on smart tree whitewash devices.

MATERIALS AND METHODS

DESIGN PLAN

This design uses the Mitsubishi PLCFX2N-48MR programmable logic controller (hereinafter referred to as the PLC), an HC-SR04 ultrasonic ranging sensor, a human–machine interface, and other equipment to realize the electrical control of the whitening device. With a programmable controller as the core and an ultrasonic ranging sensor and human–machine interface as auxiliary tools, the design constitutes a manual/automatic electrical control system that integrates the collection and processing of live-wood DBH measurements and intelligently whitens the tree according to the different DBH *(Sun et al., 2018)*.

The PLC sends a pulse trigger signal to the ultrasonic distance-measuring sensor through the analogue/digital (A/D) conversion module of the PLC, and a high-level output is obtained at the receiving port. When the high-level output is received, a timer is started. When this port reaches a low level, we can read the timer value and calculate the measured time to obtain the DBH of the tree. The measurement result is fed back to the PLC, and the moving speed of the manipulator and the spraying amount of the discharge port are matched, according to the DBH of different trees *(Masood et al., 2020)*. The device is divided into two control modes: manual and automatic.

The whitening-agent tank has a built-in level gauge. When the whitening agent is insufficient or overfilled, the human–machine interface will remind the user to replenish or stop the paint supply, respectively. The system structure diagram is shown in Figure 1.

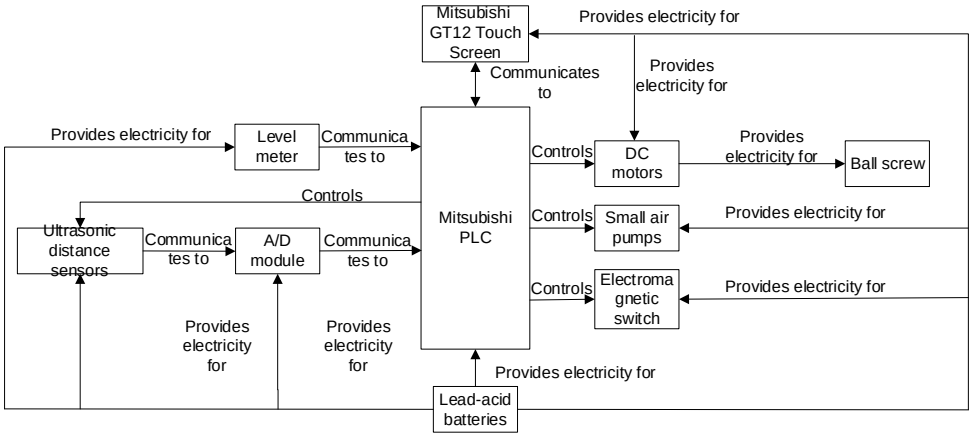


Fig. 1 - System Structure

HARDWARE DESIGN

Hardware

The mechanical part of this design is composed of a manipulator, a ball screw, a direct-current (DC) motor, an ultrasonic ranging sensor, a small air pump, a nozzle, an electromagnetic switch, a tank, a rubber tube, and a float-level gauge inside the whitening-agent charging barrel. It adopts two semi-circular clip structures, which are opened and closed by an electromagnetic switch. The manipulator is connected to the ball screw, and the DC motor controls the movement of the ball screw to spray up and down.

In this design, three ultrasonic distance-measuring sensors are installed, and placed at equal distances above the circular clamp. Three special nozzles are installed in the inner groove of the clip. The diameter of the liquid outlet is slightly larger than that of an ordinary water nozzle. Because lime water is more likely to block the output than water, the wide-mouth nozzle can be used for a better discharge. The sprayed liquid from each nozzle can cover a 120° range.

The whitening agent is pressurized from the tank by a small air pump, fully mixed, and then injected into the manipulator through a hose. The float-level gauge in the tank can sense the height of the solution in the tank and sends it to the human–machine interface. The interface can provide operators with information, such as whether to replenish the solution, whether the container has been filled, and the status of the battery. The mechanical-structure diagram is shown in Figure 2.

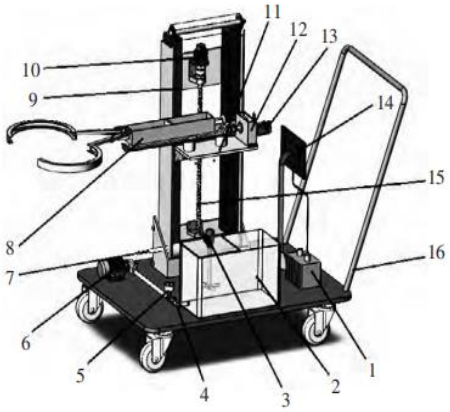


Fig. 2 - Mechanical Structure

1. Storage battery. 2. Tank. 3. Float-level meter. 4. Regulator. 5. Water meter. 6. Small air pump. 7. Hose. 8. Manipulator. 9. Lifting platform. 10. DC motor. 11. Cage. 12. Gearbox. 13. DC motor. 14. Human–machine interface. 15. Ball screw. 16. Cart.

Selecting Device Types

PLC

Compared to the PLCs of other companies, the PLC produced by Mitsubishi has the advantages of intuitive and easy-to-understand programming, detailed instructions, dedicated positioning instructions, and easy-to-control servo and stepping motors *(Li et al., 2015)*. Hence, this design uses the Mitsubishi PLC as the control. However, the PLC models produced by Mitsubishi Corporation are numerous, and each has its own characteristics. The FX2N-48MR model PLC was selected as the main controller *(Jiang et al., 2020)*, and its parameters are shown in Table 1.

Table 1

PLC FX2N-48MR Parameters

Name	Value
I/O Count	48
Output	Relay
Power	24 V DC
Rated Voltage	100–240 V AC
Rate Frequency	50 / 60 Hz

A/D module

The A/D module can convert the external analogue signal into a digital signal. This design mainly uses the Mitsubishi PLC, so the A/D module uses the FX0N-3A module *(Tang et al., 2021)*. This module has two analogue-signal input channels and one analogue-signal output channel. The input/output signals can be either voltage or current. The main performance parameters are shown in Table 2.

Table 2

FX0N-3A Main Characteristics

A/D Conversion	Input Voltage	Input Current
Analogue input range	0–10 V DC	4–30 mA DC
Effective digital output	8-digit binary	
Conversion time	100 ms	
D/A conversion	Output Voltage	Output Current
Analogue output range	0–10 V DC	4–30 mA DC
Effective digital input	8-digit binary	

Ultrasonic distance-measuring sensor

Compared with several types of ultrasonic ranging sensors on the market, the sensor performance of the HC-SR04 is better *(Gunawan et al., 2019)*, the control is simple, and the price is low. Specific performance parameters are shown in Table 3.

Table 3

HC-SR04 Performance Parameter Table

Characteristic	Value
Operating Voltage	5 V
Ultra-small quiescent working current	< 5 mA
Accuracy	0.3 cm
Blind spot	< 2 cm

Human–machine interface

The human–machine interface of the Mitsubishi GT12 series has a flexible and scalable configuration. It can be connected with the Mitsubishi-series PLC for data communication and control, and the operation is simple. Its specific performance parameters are shown in Table 4.

Table 4

Human–Machine Interface GT12(640×480) Parameters

Characteristic	Value
Screen Size	12.1 inch
Resolution	640×480
Input Voltage	DC 24 V (+25%, -20%)
Power	< 11 W
Current	< 29 A (10 ms)(max)
Temperature	-20 °C–60 °C

Float–level gauge

The float-level gauge has a simple structure, is convenient to debug, and can be widely used in high-pressure and viscous media. It fits in perfectly with the working environment of our device. Its specific performance parameters are shown in Table 5.

Table 5

Float-Ball Level-Gauge Performance Parameters

Characteristic	Value
Range	0–3500 mm
Supply voltage	12–36 V DC
Precision	±2.5% F.S.
Nominal pressure	≤ 2.5 MPa
Temperature	-20–120 °C

I/O distribution and PLC peripheral wiring diagram

I/O distribution

The I/O distribution of the selected device includes 14 inputs and six outputs. The final I/O allocation table is shown in Table 6.

Table 6

I/O Distribution

Input			
Number	**Module**	**Location**	**Function**
1	SB1	X000	Power off
2	SB2	X001	Power on
3	SB3	X002	Raise mechanical arm
4	SB4	X003	Lower small mechanical arm
5	SB5	X004	Lower medium mechanical arm
6	SB6	X005	Lower large mechanical arm
7	SB7	X006	Initiate spraying
8	SB8	X007	Stop spraying
9	SQ1	X010	Upper limit switch
10	SQ4	X011	Lower limit switch
11	s	X012	Virtual Switch (Small Trees)
12	m	X013	Virtual Switch (Medium Trees)
13	l	X014	Virtual Switch (Large Trees)
14	FR	X015	Overload protection
Output			
Number	Module	Location	Function
1	KM1	Y0000	Raise mechanical arm
2	KM2	Y0011	Lower mechanical arm
3	KM3	Y002	Run pump
4	L1	Y003	Mechanical rising indicator
5	L2	Y004	Mechanical lowering indicator
6	L3	Y005	Pump-running indicator

PLC peripheral wiring diagram

According to the I/O allocation table combined with the selected hardware, the peripheral wiring diagram of the PLC is shown in Figure 3.

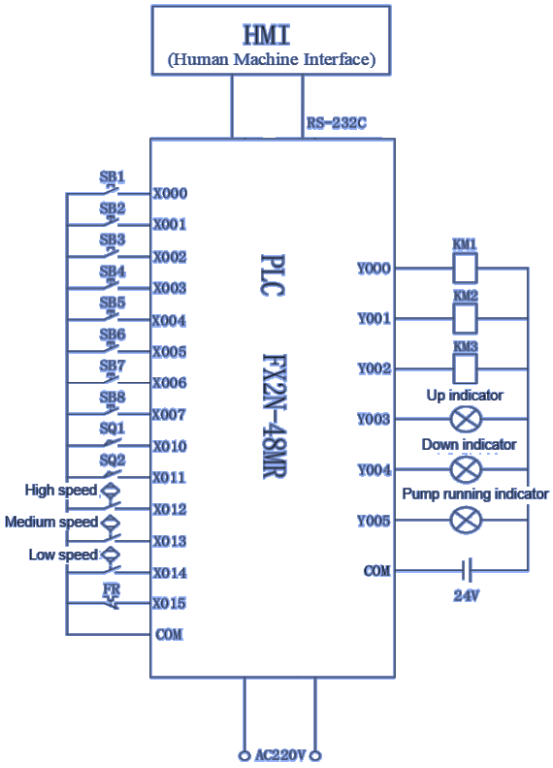


Fig. 3 - Peripheral wiring diagram

SOFTWARE DESIGN

Working principle

The data measured by the HC-SR04 ultrasonic distance-measuring sensor are transmitted to the PLC through the A/D module, and the PLC executes the program to control the DC motor to drive the three-dimensional screw movement. It thereby controls the raising and lowering movements of the manipulator and the opening and closing of the spray valve.

In view of the differences of tree diameters at breast height, to achieve better adaptability and a higher use efficiency of the whitening agent, the automatic mode control has three different spraying modes for small, medium, and large trees *(Teimouri et al., 2020)*. (See Table 7 for the parameters.) The operating can use manual mode to select different speeds, start or stop spraying, and other operations, according to their needs.

Table 7

Three Spraying Modes and their Parameters

Mode	DBH/cm	Manipulator Movement Speed/(cm/s)	Output Pressure/MPa
Small Trees	DBH < 15	8	0.15
Medium Trees	15 ≤ DBH < 30	6	0.20
Large Trees	30 ≤ DBH	4	0.25

Work process

The workflow of this design is divided into three parts, as shown in Figure 4.

Preparation stage: The PLC controls the manipulator to encircle the tree trunk, measure its DBH, and select the appropriate spraying operation mode.

Spraying stage: The PLC controls the DC motor and valve switch to whiten and spray the trunk.

Ending stage: After the spraying operation is completed, the PLC recycling manipulator completes the whitening operation of the entire tree trunk.

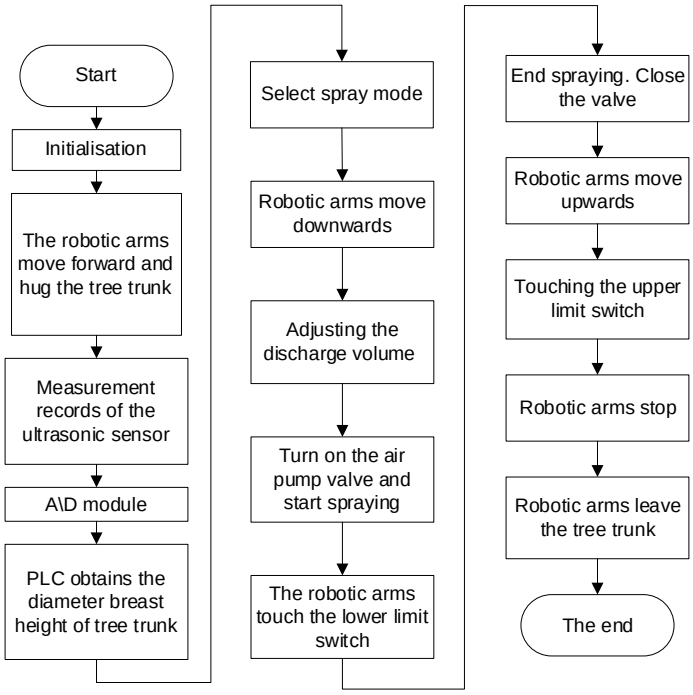


Fig. 4 - Work Process

Simulation software

Human–machine interface

To facilitate the staff's work, manual and automatic operation modes are set on the human–machine interface for trees with different DBH. The automatic mode is divided into three modes. After measuring the distance with the ultrasonic distance-measuring sensor installed on the ring clamp of the manipulator, the PLC calculates and selects the corresponding mode for spraying, so that trees of different DBH can be evenly covered with the whitening agent. The manual mode allows the operator to select operations, such as start spraying, stop feeding, and select speed, according to their needs. The human–machine interaction interface is shown in Figure 5.

Manual control mode

The operator starts by pressing the main start switch. When s/he presses the manipulator start button, the manipulator starts to move up, and the indicator light turns on. The upwards movement stops after it touches the travel switch. If the user presses the start button of the feed, the spray indicator light turns on. By pressing the down button, the staff can choose the corresponding speed, according to the tree's conditions. For example, if the manual control mode is selected, the DBH < 15, the downward-movement indicator light turns on, and the DBH is displayed as 11 cm, and the speed is displayed as 8 cm/s, and the Liquid is displayed as 46L. The manipulator simultaneously moves down to complete the spraying work. When the manipulator reaches the bottom end and touches the travel switch, the movement and spraying stop. The human–machine interface is shown in Figure 6.

Automatic Control Mode

The ultrasonic distance-measuring sensor measures the breast diameter of the tree and feeds the data back to the PLC. After the PLC has finished the calculation, a mode is automatically selected for whitening. The manipulator starts to work at the top end. The material is discharged, while the manipulator moves down the tree. When it reaches the bottom end and touches the travel switch, the spraying and moving stop. The user should raise the manipulator to the highest position again to prepare for the next whitening. For example, if the automatic control mode is selected, the 30 > DBH > 15, the downward-movement indicator light turns on, and the DBH is displayed as 27 cm, and the speed is displayed as 6 cm/s, and the Liquid is displayed as 45L. The manipulator simultaneously moves down to complete the spraying work. When the manipulator reaches the bottom end and touches the travel switch, the movement and spraying stop. The human–machine interface is shown in Figure 7.

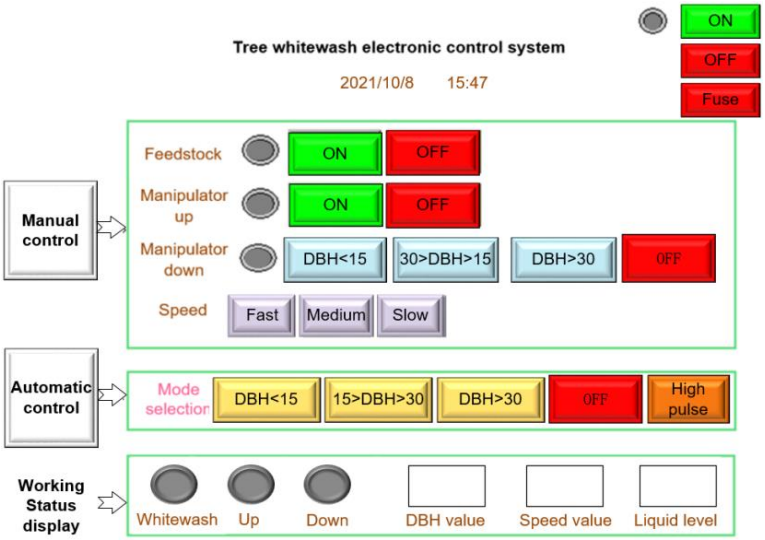


Fig. 5 - Human–machine interface

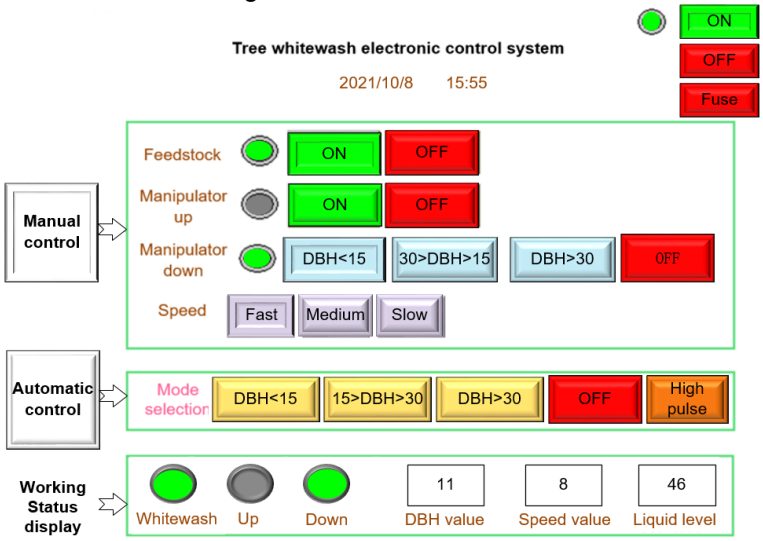


Fig. 6 - Manual control. Human–machine interaction interface simulation diagram

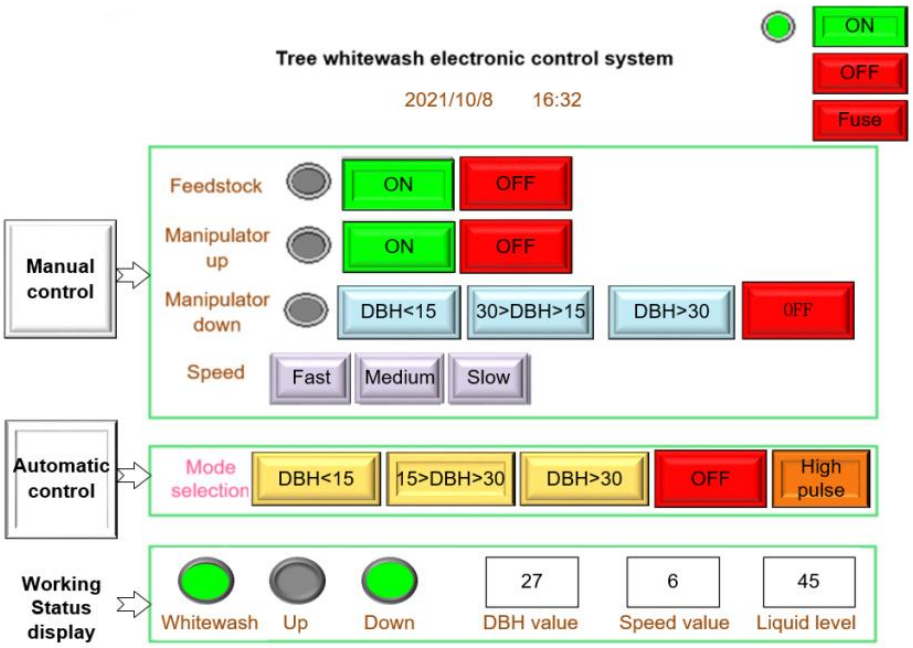


Fig. 7 - Automatic control. Human–machine interaction interface simulation diagram

RESULTS AND ANALYSIS

On October 8, 2021, 36 poplar trees with a diameter of 10–35 cm at breast height were selected on the Hohhot campus of the Inner Mongolia Agricultural University. The selected samples were divided into three groups, each consisting of trees with similar diameters at breast height. Subsequently, the trunks of these poplar trees were whitewashed with a backpack sprayer, a semiautomatic spraying device, and the proposed smart tree whitewash device to a height of 1.4 m from the ground. The Senle® tree whitewash agent was used after being diluted with water at a ratio of 1: 3. Finally, the operation time and the amount of the whitewash agent required by the different devices to complete the job were recorded, as shown in Table 8 and Figure 8.

Table 8

Comparison results of different tree whitewash devices

Tree diameter at breast height	Backpack sprayer		Semi-automatic tree spraying device		Smart tree whitewash device	
	Operation time	Amount of whitening agent	Operation time	Amount of whitening agent	Operation time	Amount of whitening agent
[cm]	[s]	[g]	[s]	[g]	[s]	[g]
10	165.23	203.57	140.85	92.01	94.14	89.11
11	166.25	212.11	145.86	105.14	94.35	89.98
14	173.35	230.98	151.98	119.08	100.58	101.25
18	177.01	236.65	156.11	126.01	98.35	112.25
21	178.20	255.85	157.58	135.32	105.36	121.01
23	188.56	461.57	159.40	143.52	111.10	123.23
24	189.44	380.52	161.12	157.67	96.35	123.89
27	190.38	386.11	166.18	173.35	99.63	134.21
29	200.25	392.22	167.87	183.25	101.25	138.24
31	204.38	303.24	172.14	188.50	109.89	140.23
33	207.91	412.4	178.38	193.87	108.32	148.32
35	214.35	418.47	181.26	206.35	99.98	156.21
Average	187.94	324.47	161.56	152.01	101.61	123.16

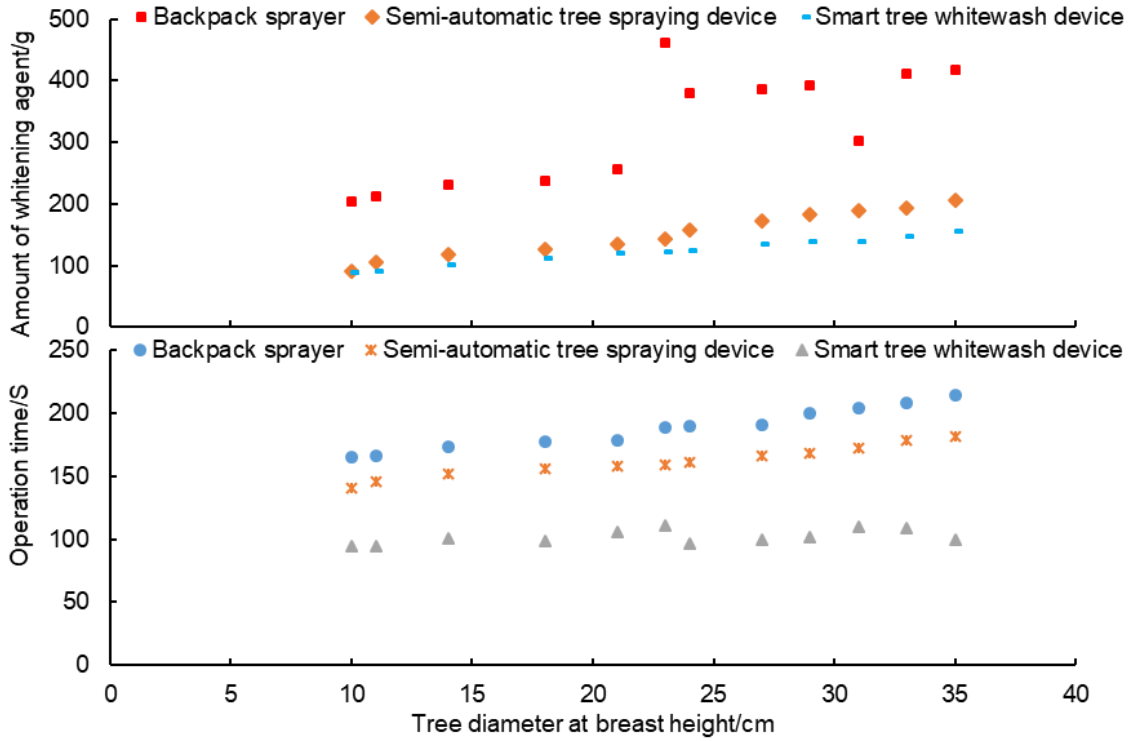


Fig. 8 - Analysis of test results of different white coating machines

Table 8 and Figure 8 shows that as the tree diameter at breast height increased, the amount of whitewash agent required increased accordingly. Additionally, the time required by the backpack sprayer and the semiautomatic tree sprayer to complete the job both increased, whereas that required by the smart tree whitewash device remained almost identical. In terms of work efficiency, the time required by the smart whitewash device to whitewash a tree was 109.89 s, which was approximately 1/2 of the time required by the backpack sprayer or 2/3 of that required by the semiautomatic tree spraying device. Meanwhile, the amount of whitewash agent required by the smart whitewash device to whitewash a tree was 140.23 g, which was approximately 0.46 of the amount required by the backpack sprayer or 0.74 of that required by the semiautomatic tree spraying device. Therefore, it was concluded that the proposed smart tree whitewash device could not only improve the work efficiency of tree whitewash but also considerably reduce the amount of required whitewash agent, thereby decreasing the cost and minimising environmental pollution.

CONCLUSIONS

Hardware and software parts comprise the two major elements of the intelligent trunk-whitening device, based on human–machine interaction, and the working principle was analysed. This design used the PLC as the control core and an ultrasonic distance sensor to measure the diameter of the trees at breast height. The device then matched the corresponding whitening speed and output, which effectively solved the problems of uneven whitening and the waste of whitening agent. Based on the PLC and combined with a human–machine interface, the operation was simpler, the spraying was more uniform, and the quality and efficiency of trunk whitening were effectively improved.

A comparison of the proposed device with two other commercially available tree whitewash devices indicated that the time required by the smart whitewash device to whitewash a tree was 109.89 s, which was approximately 1/2 of the time required by a backpack sprayer or 2/3 of that required by a semiautomatic tree spraying device. Moreover, the amount of whitewash agent required by the smart whitewash device to whitewash a tree was 140.23 g, which was approximately 0.46 of the amount required by the backpack sprayer or 0.74 of that required by the semiautomatic tree spraying device.

The smart tree whitewash device developed in this study has the advantages of a uniform spraying effect, short operation time, and an even distribution of the whitewash agent, thereby effectively improving both the quality and the efficiency of tree whitewash.

ACKNOWLEDGEMENTS

We acknowledge that this work was financially supported by the Science and Technology Project of Inner Mongolia (No. 2020GG0078), the National Natural Science Foundation of China Regional Science Foundation (No. 52069018), the Major Science and Technology Projects of Inner Mongolia Autonomous Region (No. 2020ZD0009), the Natural Science Foundation of Inner Mongolia Autonomous Region (No.2021BS03019), and Inner Mongolia Autonomous Region Scientific research projects of colleges and universities (NJZY19288).

REFERENCES

[1] Chen H., (2018), Design of reverse alarm system based on ultrasonic ranging, *Internal Combustion Engine & Parts*, vol.3, Issue 20, pp. 5-7, China;

[2] Guo H.K., (2019), Design of elevator control system considering acceleration and deceleration based on PLC and its human-machine interface, *Electric Engineering*, vol.1, Issue 24, pp. 12-14, China;

[3] Gunawan A A N., Sumadiyasa M, (2019), Water level detection system based on ultrasonic sensors HC-SR04 and ESP8266-12 modules with telegram and buzzer communication media. *Instrumentation Mesure Métrologie*, vol. 18, Issue 3, pp. 305-309, Canadian;

[4] He C., Hong X.F., Liu K.Z., (2016), An improved technique for nondestructive measurement of the stem volume of standing wood, *Journal of the South African Forestry Association*, vol.78, Issue 1, pp. 53-60, China;

[5] Jiang X.H., Hu C., Zhang G.X., Wang H., He H., Ge J., (2020), A study on self-adaptive system of intelligent trunk brushing device based on SolidWorks. *Manufacturing Automation*, vol. 42, Issue 8, pp. 103-105, China;

[6] Liu B., (2017), Research and promotion strategy of new technology of tree whitening, *Modern Horticulture*, vol.1, Issue 2, pp. 60, China;

[7] Li H.C., Yuan W., Liu X.F., Wang H., Ding D.C., Lin Z.H., (2015), Design and analysis of a tree-trunk whitewashing device. *Mechanical Engineer*, vol. 3, Issue 2, pp. 188-190, China;

[8] Masood B., Song G., Baig S., Rasheed M.B., Hou J., (2020), Measurements and characterization of low and medium voltage residential, commercial and industrial NB-PLC networks for AMI. *IET Generation, Transmission and Distribution*, vol.14, Issue 3, pp. 12-14, China;

[9] Sun L.H., Fang L.M., Tang L.H., Liu J.J., (2018), Developing portable system for measuring diameter at breast height, *Journal of Beijing Forestry University*, vol.40, Issue 9, pp. 82-89, China;

[10] Tang L.S., Hou J., Cui Y F., (2021), Research and development of tree trunk whitening device based on man-machine cooperation. *Forest Engineering*, vol. 37, Issue 1, pp. 38-44, China;

[11] Teimouri M., Podlaski R, (2020), Modelling Tree's diameter using mixture of skewed Student's t distributions [J]. *Canadian Journal of Forest Research*, vol. 50, Issue 10, pp. 1-108, Canadian;

[12] Zhang L., (2020), Selection of the optimum cold-proof treatment with white paint on plum by using subordinate function method, *Molecular Plant Breeding*, vol.18, Issue 6, pp. 2070-2076, China.

ON-STREAM SOIL DENSITY MEASURING
/
ВИЗНАЧЕННЯ ПОТОКОВОЇ ЩІЛЬНОСТІ ҐРУНТУ

Volodymyr KRAVCHUK [1)], Mikhailo IVANIUTA [*1)], Viacheslav BRATISHKO [2)], Yuri HUMENIUK [2)], Vitaly KURKA [2)]

[1)]The Institute of Bioenergy Crops and Sugar Beet National Academy of Agrarian Sciences of Ukraine / Ukraine

[2)] National University of Life and Environmental Sciences of Ukraine / Ukraine

Tel: +380995044767; E-mail: ur6hdc@ukr.net

DOI: https://doi.org/10.35633/inmateh-69-64

Keywords: *tillage; soil compaction; soil density; water content of soil; devices for measuring soil density.*

ABSTRACT

The article is focused on the determination of the nonlinear relationships between soil compaction, density, and water content. It was found that these properties can be described by the second-order models and used for improving devices for the on-stream soil density measuring. The models for determining the density of loamy soil (at a water content of 20%) in the range from 0.9 to 1.6 g/cm^3 with an extremum of 1.35 g/cm^3 were improved. A device for the on-stream soil density measuring is proposed. The device operates within the soil compaction range from 0.3 to 1.2 MPa and water content from 10 to 30% at the angle of inclination of the kinematic link γ from 15 to 40 degrees. The obtained results can be used in the adaptation of the proposed device for use in precision agriculture.

РЕЗЮМЕ

В статті наведено результати теоретичних та експериментальних досліджень з визначення нелінійних зв'язків твердості, щільності та вологості ґрунту. Встановлено, що зазначені характеристики можна описати моделями другого порядку та використовувати з метою удосконалення пристроїв потокового визначення щільності ґрунту. Обґрунтовано моделі визначення щільності в діапазоні 0.9-1.6 г/см3 з екстремумом у значеннях 1.35 г/см3 при вологості 20% суглинистого ґрунту. Запропонований пристрій забезпечує отримання зазначених показників щільності ґрунту в межах його твердості 0,3-1,2 МПа, вологості 10-30% при зміні кута нахилу кінематичної ланки γ від 15 до 40 градусів. Результати досліджень можуть бути адаптовані для застосування в сучасних технологіях точного (керованого) землеробства.

INTRODUCTION

The phase composition of the soil is largely affected by soil tillage (*Voytyuk et al., 2015, Hudz et al, 2010, Kravchuk, 2018*) as it is formed under the action of working elements of machines. Tillage improves plant conditions, increases soil fertility, and protects the ground from water and wind erosion. Tillage helps reach the optimal soil structure in the root soil layer by changing the mechanical characteristics of the soil. The optimal phase composition of soil for most crops is a three-phase disperse system, which consists of a solid (mineral and organic parts), a liquid (water), and a gaseous (air) part (Fig. 1). From the standpoint of solid mechanics, the soil can be defined as a porous body in which the solid particles are crushed and mixed with other components (water and air). Compaction and bulk density are the main physical properties of the soil.

Compaction derives from the potential energy of inter-structural adhesive bonds of the soil. In a broader sense, compaction is an indicator of the deformation of the soil boundary state as a result of the interaction between applied external mechanical forces and resistance reactions of internal stresses (*Shvets et al., 2014*). In the process of tillage, soil undergoes a complex stress state leading to elastic, plastic deformation, and fracture, resulting in changes in the size and volume of soil particles. These changes relate to the indicator of bulk density (*Hudz et al., 2010, Shvets et al., 2014*).

Analysis of the literature allowed us to conclude that there is a nonlinear correlation between soil density and compaction (*Kushnarev et al., 2010*). The relationship between compaction and bulk density received much attention in the works of Kushnarev et al. *(2010)* and Ajit K. Srivastava et al. *(2006*). It was also found that soil compaction is largely influenced by the water content and chemical composition of the soil.

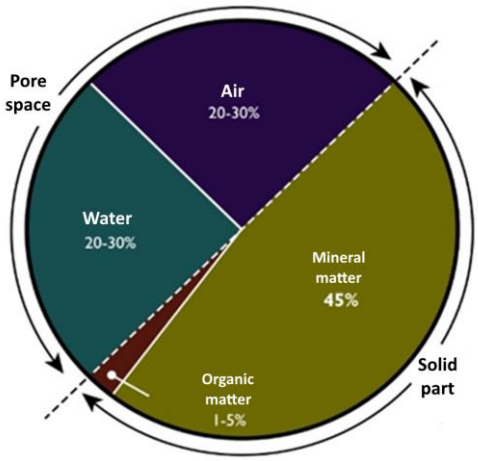


Fig. 1 - Soil phase composition optimal for plants
(Hudz et al., 2010)

There are two known methods of soil compaction measuring − stationary and on-stream (*Kushnarev et al., 2010*). The first method deploys devices operating by the method of contact selective determination using a compaction meter. In the stationary devices, the measuring plunger moves perpendicular to the soil surface. The on-stream method is based on the selective interaction of the measuring body of the device. In this method, the mechanical resistance of the soil is a function of the resistance response and time R(t), and bulk density is determined with the use of dependencies that include the water content of the soil.

In the context of advanced agrotechnologies, e.g., precision agriculture, searching the limits of relations between soil compaction, density, and water content is necessary for the development of the protocols for the on-stream soil density testing and adaptation of agricultural machines to the specific agrotechnical requirements. *The purpose of the research* was to study the diapason of nonlinear correlations between soil compaction, bulk density, and water content, which can be used in the improvement of the devices for on-stream soil density measuring.

MATERIALS AND METHODS

Soil density was assessed in accordance with DSTU ISO 11272 (weighting of the dry mass). The water content of soil was determined in accordance with GOST 28268 (oven drying). Compaction was measured with the use of the soil compaction meter SC-900 (USA) by the method of stationary measurements.

Analysis of the response surface (RSM) between independent variables of bulk density X_1 and water content of soil X_2 and the response function with the compaction values Y was performed according to the Box-Wilson method *(Box et al., 1951, Kravchuk et al., 2016*). The method is based on the correlation relationships between the values of soil density and compaction and the use of empirical coefficients (Table 1). The relationship between soil density and compaction can be described by the second-order polynomial equation (*Kushnarev A., et al., 2010*) (Fig. 2):

$$\rho = a + bp + cp^2; \quad (1)$$

Where:

ρ - soil bulk density, [g/cm^3];
p – soil compaction, [N/cm^2];
a, b, c are empirical coefficients.

Table 1

Empirical coefficients for different methods of soil tillage
(*Kushnarev et al., 2010***)**

Method of tillage	*a*	*b*	*c*
Ploughing	698	0.039	0.00038
Deep tollage	657	0.038	0.00062
Subsurface tillage	0.720	0.048	0.0080

Ajit K. Srivastava et al. (2006) found that soil density is largely affected by water content and chemical composition of the soil, as the consistency and structural bonds change due to adhesion, which leads to a change in soil compaction.

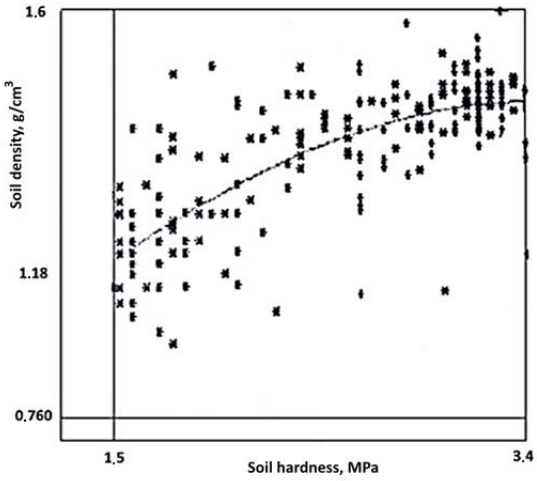


Fig. 2 - Correlation relationships between soil compaction and density in the 0-300 mm layer (*Kushnarev et al., 2010*)

We studied the correlations between soil density and compaction using a device for on-stream soil compaction measuring (Kravchuk et al., 2021). The device consists of a frame *1*, a kinematic link *2*, an angle sensor of the kinematic link *3*, an arrow *4*, a damper *5*, a roller *6*, a plunger *7*, a holder *8*, a cone *9*, a position sensor of the measuring roller *10*, and a position sensor of the measuring body *11* (Fig. 3).

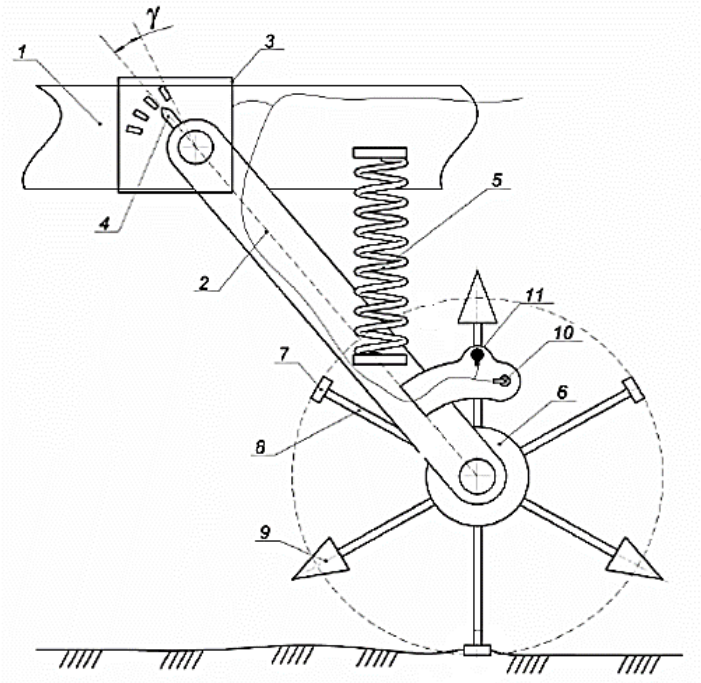


Fig. 3 – Device for soil compaction measuring (*Kravchuk et al., 2021*)

The device was tested in a soil channel (8.5 m x 1.2 m x 0.6 m) filled with typical loamy soil of various humidity and density in accordance with the experimental design. Starting from the initial position of the device (indicated by the position sensor of the measuring roller), the kinematic link under the action of a spring (stiffness 18 N/mm) alternatively presses the plunger and the cone to the soil surface. Due to the action of the damper, the plungers and cones alternately immerse into the soil to a certain depth. In the process of immersing the plunger, which depends on the soil compaction and the spring stiffness, the kinematic link is set to a certain angle γ, which is registered by the angle sensor sequentially for each of the measuring bodies.

Soil compaction is calculated based on the values of the angle of inclination of the kinematic link at the moment when the sensor of the measuring body position is in the vertical position.

The relations between the soil properties were studied with the use of the developed device in the full factorial experiment. Three measurements of compaction were taken for each value of soil density and water content. To verify the adequacy of the correlation models, Fisher's approach was exploited, which is based on the exploitation of either a null or alternative hypothesis to the results of experimental studies. Verification of the hypothesis was carried out based on the assessment of the level of significance *p* in Fisher's test. As a null hypothesis, it is assumed that soil density and water content have no correlations with compaction.

A full two-factor experiment 2^k (k = 2) was carried out according to *Oliveira et al., (2019) and Borovikov (2013*). The analysis of variance involved the compilation of a scale of values and factors (Fig. 4) and a matrix with obtained results (Table 3). The studied characteristic was the position angle γ of the kinematic link determined by the sensor, which varied depending on the soil compaction.

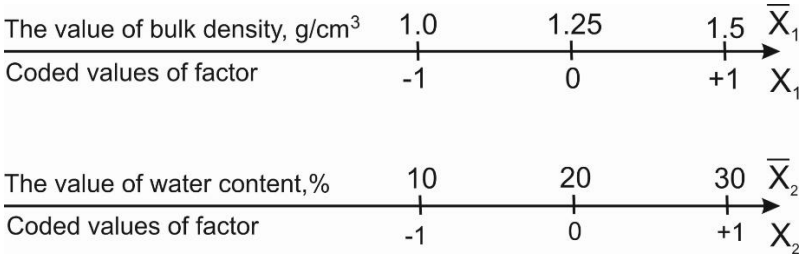


Fig. 4 – Scale of levels and values of the experimental factors

The null hypothesis was adopted regarding the correlations between the factors of soil density and water content with the compaction function, which are related to each other as random variables. To reject the null hypothesis, an additional test was performed (line 10 in Table 2) with the analysis of variance. Statistical data processing was carried out by the variance analysis methods as described by *Borovikov (2013*) using the software Statistica, with replications of *ANOVA* based on the table of empirical data.

Table 2

Experiment planning matrix 2^2 and data

Experiment number	X_1	X_2	$\overline{X_1}$, (g/cm³)	$\overline{X_2}$, (%)	Y	*P*, (MPa)	γ, (°)
1	-1	-1	1.0	10	y_1	0.30	35
2	0	-1	1.25	10	y_2	0.35	34
3	+1	-1	1.5	10	y_3	0.38	34
4	-1	0	1.0	20	y_4	0.90	23
5	0	0	1.25	20	y_5	0.95	22
6	+1	0	1.5	20	y_6	1.20	17
7	-1	+1	1.0	30	y_7	0.40	33
8	0	+1	1.25	30	y_8	0.50	31
9	+1	+1	1.5	30	y_9	0.55	30
10	+1	+1	1.5	30	y_{10}	0.58	29

RESULTS

The results of the analysis of variance are given in Tables 3 and 4. The number of bulk density gradations a = 3; the number of water content gradations b = 3; the number of the experiment replication r = 1; the total number of observations n = 10; the total number of degrees of freedom v = 9; the type of approximation – the least-squares method (LSM). The coefficient of determination R^2=0.74. *SS* is the total sum of the squares of deviations; *cc is* the degree of freedom; *MS* is the variance; *F* is the Fisher criterion; *L is* the difference between the values of the responses at the largest and smallest values of the factors; *Q* is the quadratic nonlinear effect.

Table 3

Results of the variance analysis

FACTOR	SS	ss	MS	F	p
Bulk density, g/cm^3 (1L)	0.25	1	0.25	3.04	0.16
Bulk density, g/cm^3 (Q)	0.26	1	0.26	3.25	0.15
Water content, % (*2*L)	0.34	1	0.34	4.18	0.11
Water content, % (Q)	0.02	1	0.02	0.22	0.66
1L to 2L (interaction)	0.00	1	0.00	0.01	0.92
Error	0.32	4	0.08		
Total SS	1.24	9			

From Table 3, it can be concluded that in the first approximation, the obtained *p* values of the significance level of the Fisher test of all cases of compaction exceed 0.05; therefore, the null hypothesis cannot be rejected. However, to clarify the correlations, the null hypothesis must be replaced with an alternative one. From a statistical point of view, this indicates the presence of a nonlinear correlation between bulk density, water content, and compaction due to the adhesive bonds between structural aggregates of soil.

The results of the additional testing nonlinearity of the correlations between compaction, density, and water content of soil are shown in Table 4.

Table 4

Results of the additional testing nonlinearity of the correlation

Factor	SS	ss	MS	F	p
Bulk density, g/cm^3 (1L)	0.25	1	0.25	197.13	0.045
Bulk density, g/cm^3 (Q)	0.26	1	0.26	210.30	0.044
Water content, % (2L)	0.34	1	0.34	271.08	0.039
Water content, % (Q)	0.02	1	0.02	14:30	0.165
1L to 2L (interaction)	0.00	1	0.00	0.79	537
Loss of coherence	0.32	3	0.11	86.05	0.079
Error	0.00	1	0.00		
Total SS	1.24	9			

The results of the additional test showed that *p*-values >0.05 were obtained only for the quadratic nonlinear effect of water content, which confirmed the adequacy of the second-order model. Non-linear relationships between water content and soil compaction are described by the response surface (Figs. 5, 6), contour plots of the region of maximum compaction values (Figs. 7, 8), and equations 2, 3.

From Figs. 5.6 it follows that a 10% decrease in water content leads to a 0.35 MPa decrease in soil compaction. This can be explained by the increasing fragility of loamy soil due to a decrease in the adhesion of the structural bonds, which was confirmed by previous research (*Terfaya et al., 2018; Cheng et al., 2021*).

We obtained the maximum value for the internal adhesive bonds of the loamy soil structure. The total soil compaction was 1.1 MPa at a bulk density of 1.35 g/cm^3 and water content of 20%. With an increase in water content to 30%, a 0.55 MPa decrease in compaction was observed, which can be explained by a decrease in adhesive bonds due to the substitution of inter-structural bonds with capillary ones. The substitution leads to a decrease in the force of internal friction when shear stresses are applied, as confirmed by *Cheng et al. (2021) and Nawaz et al. (2013*).

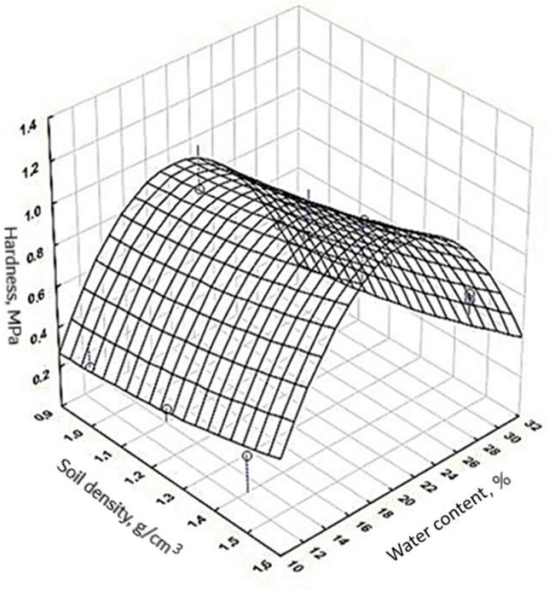


Fig. 5 – Diagram of the response surface of correlations between soil compaction, bulk density, and water content

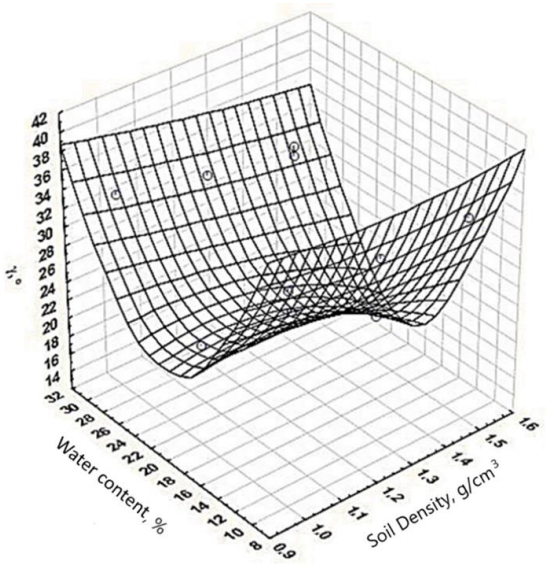


Fig. 6 – Diagram of the response surface of correlations between the angle γ, soil density, and water content

The response surface equation for compaction is the following:

$$Z = -1.33 - 0.58x - 0.24y + 0.32x^2 + 0.006xy + 0.006y^2 + 0 \quad (2)$$

The response surface equation for the kinematic link position sensor is the following:

$$Z = 67.37 + 10.91x - 4.76y - 5.42\,x^2 - 0.2xy + 0.12y^2 + 0 \quad (3)$$

Contour graphs (Fig. 7−8) made it possible to set the range of values of the maximum soil compaction in more detail. The maximum compaction (1 MPa) was observed in the bulk density diapason from 1.5 to 1.6 g/cm^3 and water content diapason from 1 to 23% at the determined values of the angle of the kinematic link from 18 to 22 degrees.

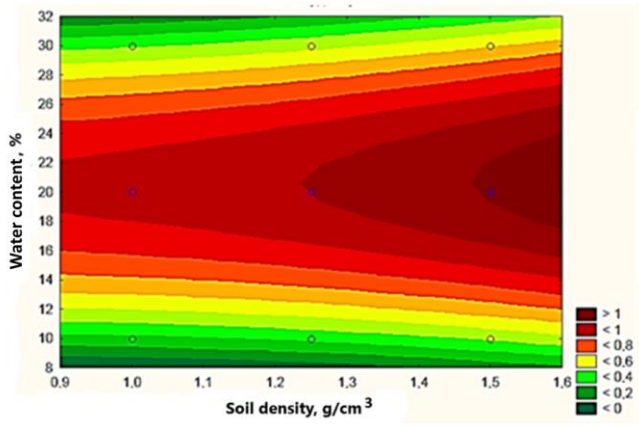


Fig. 7 – Contour graph of soil compaction *P*, bulk density MPa, and water content relations

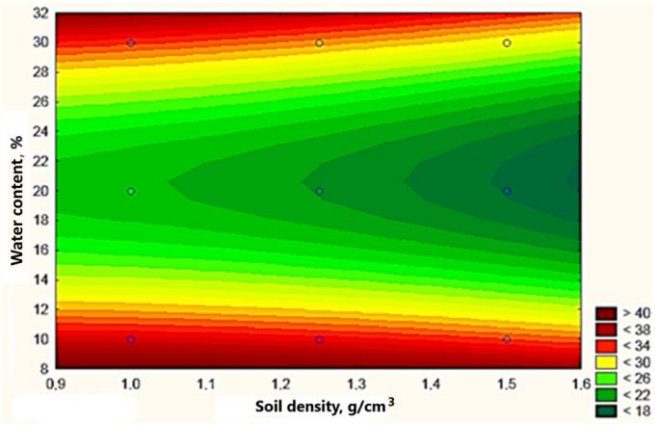


Fig. 8 – Contour graph of angle γ, bulk density, and water content relations

To sum up, the study revealed, that soil, as a porous natural body, has a bearing capacity to support plant life. In the process of tillage, soil's physical and mechanical properties change depending on the water content, which is consistent with the results of *Khishvand et al. (2017)* and *Panigrahi Goyal (2021*).

In modern farming systems, major agrophysical properties of soil should be taken into account to reach efficient use of agricultural machines for soil tillage.

CONCLUSIONS

The method of the on-stream soil density measuring during the tillage operations will be promising under the condition that nonlinear models of correlations between soil compaction and water content are taken into account. The second-order models may be used for the on-stream measuring of soil bulk density in the range from 0.9 to 1.6 g/cm^3 with a maximum value of 1.35 g/cm^3 and water content of 20%. The proposed device is promising for use in precision agriculture. It provides measuring soil density values within the soil compaction range between 0.3 and 1.2 MPa at a water content of 10−30% and a change in the angle of inclination of the kinematic link γ from 15 to 40 degrees.

REFERENCES

[1] Ajit K. Srivastava, Carroll E. Goering, Roger P. Rohrbach, Dennis R. Buckmaster (2006). *Engineering Principles of Agricultural Machines*, 2nd edition, / American Society of Agricultural and Biological Engineers ASABE, Niles Road, St. Joseph, MI 49085-9659 USA. ISBN 1-892769-50-6. 559 p.

[2] Borovikov V.P. (2013). *A popular introduction to modern data analysis in the system STATISTICA*. Moscow: Hot line-telecom. ISBN 978-5-9912-0326-5. 288 p.

[3] Box, G.E.P. and Wilson, K.B. (1951). On the Experimental Attainment of Optimum Conditions. *Journal of the Royal Statistical Society* Series B, 13, 1-45. https://doi.org/10.1111/j.2517-6161.1951.tb00067.x

[4] Cheng, J.; Zheng, K.; Xia, J.; Liu, G.; Jiang, L.; Li, D. (2021), Analysis of Adhesion between Wet Clay Soil and Rotary Tillage Part in Paddy Field Based on Discrete Element Method. *Processes*, Vol.9, p.845. https://doi.org/10.3390/pr9050845.

[5] DSTU ISO 11272 (2001). Soil quality. *Determination of bulk density per dry mass*. National standard of Ukraine. Derzhspozhivstandart. Kyiv.

[6] GOST 28268 (1989). *Methods for determining moisture, maximum hygroscopic moisture, and moisture of stable wilting of plants*. Standartinform. Moscow.

[7] GOST 12536 (1979). Soils. Methods of laboratory granulometric (grain size) and microaggregate distribution. Standartinform. Moscow.

[8] Hudz' V. P., Primak I.D., Budyonny Yu, V., Tanchik S. P. (2010). *Farming*: textbook /Kyiv, Center of educational literature. ISBN 978-611-01-0064-9. 464 p.

[9] Khishvand M., Nazem M., Sloan SW. Carter JP. (2017). Application of the third medium method for frictionless contact problems in geomechanics*, Computers and* Geotechnics, Vol.85:117–125,

[10] Kravchuk V.I., Ivaniuta M.V. Shustik L.P. (2021). *Device for operative determination of physical and mechanical properties of soil. Ukraine*, Pat No 147335

[11] Kravchuk V.I., (2018). *Research and experimental investigation of agricultural machinery and technologies: development and diversification* / Doslidnitske, UkrNDIPVT im. Pogorilogo, ISBN 978-617-657-042-4. 240 p.

[12] Kravchuk V.I., Khaylis G.A., Kushnarev A.S., (2016). *Research agricultural machinery: textbook / Doslidnitske*, UkrNDIPVT im. Pogorilogo, ISBN 978-617-657-026-4. 328 p.

[13] Kushnarev A., Kravchuk V., Kushnarev S., Dyuzhaev V. (2010). Monitoring of soil density in the arable horizon in the system of precision (managed) farming. *Machinery and technology of agro-industrial complex*, V №9 (12). Doslidnyts'ke. ISSN 2306-1391. pp. 12:16

[14] Nawaz M.F., Bourrié G. & Trolard F. (2013). Soil compaction impact and modelling. A review. *Agron. Sustain*. V. 33, pp. 291–309. https://doi.org/10.1007/s13593-011-0071-8.

[15] Oliveira L.G., de Paiva, A.P., Balestrassi, P.P., Ferreira, J.R., da Costa, S.C. and da Silva Campos, P.H., (2019). Response surface methodology for advanced manufacturing technology optimization: theoretical fundamentals, practical guidelines, and survey literature review", *International Journal of Advanced Manufacturing Technology*, Vol. 104 Nos. 5-8, pp. 1785-1837.

[16] Panigrahi B., Goyal M. R. (2021). *Modeling Methods and Practices in Soil and Water Engineering. Oakville*, ON L6L 0A2. Apple Academic Press. 375p.

[17] Shvets V.B., Boyko I.P., Vynnykov Y.L. Zotsenko M.L., Petrakov O.O., Solodjankin O.V., Shapoval V.G., Shashenko O.M., Bida S.V. (2014). *Soil mechanics. Bases and foundations (abridgement)*: Textbook / Dnipropetrovsk: «Porogi», 2014. – 231 p.

[18] Terfaya N., Berga A., Raous M., Abou-Bekr N. (2018). Contact Model Coupling Friction and Adhesion: Application to Pile/Soil Interface. *International Review of Civil Engineering, Praise, Worthy Prize*, V.9 (1), pp.20. https://hal.archives-ouvertes.fr/hal-03038978.

[19] Voytyuk D.G., Aniskevych L.V., Ishchenko V.V. (2015). *Agricultural machinery*: textbook / Kyiv, Agroeducation, ISBN 978-617-7283-06-4. 679 p.

EFFECT OF CONTROLLED-RELEASE FERTILIZER ON MAIZE YIELD AND NUTRIENT UPTAKE UNDER A FERTILIZER ONE-TIME POINT-APPLIED SYSTEM

/

一次性机械化穴施缓释复合肥对玉米产量和养分吸收的影响

Xin DU[1, 2], Cailing LIU*), Changqing LIU[1, 2], Meng JIANG[1)], Hao YUAN[1)]
[1)] College of Engineering, China Agricultural University, Beijing 100083/ China;
[2)] School of Mechanical Engineering, Jiangsu Ocean University, Lianyungang 222005/ China
Tel: 0086-010-62737502; E-mail: cailingliu@163.com
Corresponding author: Cailing Liu
DOI: https://doi.org/10.35633/inmateh-69-65

***Keywords:** Maize; Nutrient uptake; Fertilizer; Fertilizer point-applied*

ABSTRACT

Currently, maize production in China suffers from many problems, such as excessive fertilizer application, inefficient fertilizer use, and insufficient agricultural labour. The effect of one-time mechanical point-applied fertilization of controlled-release compound fertilizer in the root-zone on yield and nutrient uptake was investigated to explore efficient fertilization patterns for fertilizer decrease and yield increase in maize. The selected fertilizer was a controlled-release granular fertilizer (24-6-10 for N-P_2O_5-K_2O) with six treatments in the application program: 1) no fertilizer (CK); 2) application of a one-time banding fertilizer (BDP) 5 cm off the seeds between rows and 10 cm deep; 3) application of a one-time point-applied fertilization (RZF) 5 cm off seed in the row and 10 cm deep; 4) application of a one-time point-applied fertilization (90% RZF) 10% fertilizer reduction 5 cm off seed in the row and 10 cm deep; 5) application of a one-time point-applied fertilization (80% RZF) 20% fertilizer reduction 5 cm off seed in the row and 10 cm deep; 6) application of a one-time point-applied fertilization (70% RZF) 30% fertilizer reduction 5 cm off seed in the row and 10 cm deep. The results showed that RZF increased yield by 5.84% over BDP, and the difference was significant, indicating that mechanized point-applied fertilization of fertilizer can replace manual point-applied fertilization application operations and achieve increased crop yield. The agronomic utilization rate of fertilizer of 12.35% and the bias productivity of 5.31% were higher in RZF than in BDP, and the differences were significant, indicating that one-time mechanical point-applied fertilization in the root zone significantly improved fertilizer utilization and reduced fertilizer loss.

摘要

针对夏玉米现有施肥模式下施肥量大、肥效低导致面源污染大、单产低的问题，通过研究根区一次性机械化穴施缓释复合肥对夏玉米产量和养分吸收的影响，探索减肥增产的玉米高效施肥模式。选用肥料为缓释颗粒肥（N-P_2O_5-K_2O 为 24-6-10），施肥方案共设 6 个处理，分别为：1）不施肥(CK)；2）行间偏离种子 5 cm、深 10 cm 一次性条施(BDP)；3）行间偏离种子 5 cm、深 10 cm 一次性穴施(RZF)；4）减肥 10%行间偏离种子 5 cm、深 10 cm 一次性穴施(90%RZF)；5）减肥 20%行间偏离种子 5 cm、深 10 cm 一次性穴施(80%RZF)；6）减肥 30%行间偏离种子 5 cm、深 10 cm 一次性穴施(70%RZF)。结果显示，根区一次性机械化穴施缓释复合肥（RZF）比一次性条施（BDP）增产 5.84%，且差异显著，说明机械化穴施肥料可以代替人工穴施肥作业，实现作物增产。RZF 的肥料农学利用率 12.35%、偏生产力 5.31%均比 BDP 高，且差异显著，说明根区一次性机械化穴施肥料显著提高了肥料利用率，减少了肥效损失和面源污染。RZF 与 BDP 相比，植株高度无显著差异，但植株茎粗、叶面积、伤流量和根系干物质量差异显著，说明根区施肥可促进根系生长，增大根长和根表面积，从而导致吸收水肥的能力更强，进一步表现为伤流量显著增大，从而提高地上部生长发育，增大叶面积，提高光合作用强度和碳水化合物的积累，实现籽粒增产。

INTRODUCTION

Maize (Zea mays L.) is one of the most widely grown crops in the world and ranks first for planting area and total production in China (*Hu et al.*, 2016). Maize is important for China's food production and food security (*MaCao*, 2021). Arable land in China is scarce, and the per capita area of arable land is approximately 0.1 ha and less than 40% of the world average (*Shan et al.*, 2021).

Xin Du, Ph.D. Stud.; Cailing Liu, Prof. Ph.D.; Changqing Liu, Ph.D. Stud.; Meng Jiang, Ph.D. Stud.; Hao Yuan, Ph.D. Stud.*

Therefore, increasing maize productivity has become an important aspect to ensure food security (*Usman et al.*, 2021). However, to obtain high yields within short periods, growers often use large amounts of fertilizers, which cause fertilizer losses, waste resources and challenges to sustainable development of agricultural production (*Luan et al.*, 2020; *Ren et al.*, 2020; *Xu et al.*, 2019). Experts and scholars at home and abroad have done a lot of research to improve crop yields and fertilizer utilization (*Shi et al.*, 2020), but mostly focused on fertilizer varieties (*Anstoetz et al.*, 2015), dosage (*Wei et al.*, 2019) and fertilizer application locations (*Jiang et al.*, 2018), etc. Different fertilizer application methods directly affect the effectiveness of fertilizer and crop yield, and are the basis for achieving high crop yields and improving fertilizer efficiency.

The conventional fertilizer application mode applies fertilizer in a one-time banding fertilizer at a distance of 5~10 cm from the seed row and 10 cm deep at the time of maize sowing, and some conventional fast-acting fertilizers are in the soil far away from the roots with low root efficiency, so that the roots cannot absorb the nutrients released by the fertilizer particles in time, and the excess fertilizer nutrients leave the cultivated soil due to runoff, leaching or gaseous loss, thus causing groundwater or atmospheric pollution (*Ye et al.*, 2010; *Zhu*, 2013; *Chen et al.*, 1995). Recent studies have found that ammonia volatilization and runoff losses are significantly reduced when urea is point-applied to the root zone, greatly improving nitrogen fertilizer utilization (*Cao et al.*, 1984; *SavantDe Datta*, 1980). Wang (2013) believes that fertilizer application in the root zone ensures the best match between fertilizer and the active range of the root system, which in turn affects the migration and transformation of nutrients in the soil, the morphology and distribution characteristics of the root system, and thus acts on the uptake and transfer of nutrients to the above-ground parts of the crop to achieve a yield increase.

Zhou *et al.* (2020) found that a one-time root zone point-applied application under the monopoly furrow full film cover planting method was beneficial to nitrogen concentration of in the soil tillage layer, improving the efficiency of nitrogen utilization by summer maize and promoting dry matter accumulation and improving summer maize yield. Liu *et al.* (2017) found that by applying N fertilizer in the root zone of rice with a single point-applied, the apparent utilization rate of N fertilizer increased by 22.6%-30.6% and the loss of N decreased from 73.0% to 29.7% compared to the previous application, indicating that the application of N fertilizer in the root zone significantly increased the storage time of fertilizer nutrients in the soil and improved the efficiency of the utilization of N fertilizer in rice.

Chen *et al.* (2014) proposed a technique of simultaneous lateral deep fertilization of rice, and the results showed that the yield increase ranged from 5.86% to 13.41% compared with manual spreading of fertilizer. Jiang *et al.* (2018a; 2019; 2018b) studied the one-time root zone point-applied application of urea to maize than the one-time banding application of urea and farmers' customary split application of nitrogen increased yield by 9.8% and 8.8%, respectively, and the apparent utilization rate of nitrogen fertilizer increased by 12.4% and 8.3%, respectively, and found that the one-time root zone point-applied application of urea can achieve the effect of slow and controlled release fertilizer and improve the utilization rate of nitrogen fertilizer.

Zhang *et al.* (2020) used an indoor simulation experiment to study the nutrient transport pattern of nitrogen, phosphorus and potassium under the point-applied application of urea, ammonium polyphosphate and potassium chloride compound fertilizers, and found that the nitrification of ammonium nitrogen under fertilizer point-applied application conditions was inhibited by the high concentration of nutrients between fertilizers, thus delaying the conversion of ammonium nitrogen to nitrate nitrogen, which was an important reason for the continuous and efficient supply of nitrogen fertilizer in the root zone primary application technique. Guo *et al.* (2020) showed that full inter-plant point-applied application increased plant yield by 3.70%, biomass above-ground by 3.56%, and the accumulation of N and P nutrients by 11.24% and 19.44% compared to the open-row strip application.

From the above studies, it can be seen that most of the research reports on point-applied application of fertilizers in the root zone are on manual application of a single fast-acting fertilizer, focusing on basic research on the mechanism of fertilizer transport, dynamic diffusion and migration patterns of nutrients, and spatial and temporal distribution characteristics of root morphology. Little research has been reported on the interactions between the soil, machine and plant on maize yield and the efficiency of nutrient system. Based on the point-applied fertilization planter for maize developed by the project team (*Du et al.*, 2022), this paper investigated the effects of one-time mechanical application of slow-release compound fertilizer on the yield and nutrient utilization efficiency of maize during the whole fertility period through two years of field trials, aiming to provide technical and theoretical support for fertilizer reduction and maize yield increase.

MATERIALS AND METHODS

Overview of the test field

The test site is located in XiaoDuzhuang Village, Shenze Town, Shenze County, Shijiazhuang City, Hebei Province, China, at 115°13'48.1" E longitude and 38°12'5.4" N latitude, with the average annual temperature of 12.4 ºC, frost-free period of 188 days, average annual sunshine duration of 2714.1 hours, average annual rainfall of 489.8 mm, and temperate continental monsoon climate, with precipitation accounting for 54% of the annual precipitation during the test period (June-September). The previous crop was winter wheat, with a stubble height of 15-20 cm and a straw quantity of 0.66 kg/m^2. The soil of the test site was in the transition zone of tidal soil and brown soil, with a soil capacity of 1.37 g/cm^3 and a water content of 23.6%.

Experimental design

This study used the "Zhengdan 958" maize flat dentate hybrid produced by Henan Dacheng Seed Industry Co., Ltd. as the research object, with 60 cm spacing between rows and 25 cm spacing between plants, and single grain precision sowing. The selected fertilizer was a controlled-release granular fertilizer（24-6-10 for N-P_2O_5-K_2O）with six treatments in the application program: 1) no fertilizer (CK); 2) a one-time banding fertilizer application (BDP) 5 cm off the seeds between rows and 10 cm deep (735 kg/ha); 3) one-time point-applied fertilization (RZF) 5 cm off seed in the row and 10 cm deep (735 kg/ha); 4) one-time point-applied fertilization (90% RZF) 10% fertilizer reduction 5 cm off seed in the row and 10 cm deep (661.5 kg/ha); 5) one-time point-applied fertilization (80% RZF) 20% fertilizer reduction 5 cm off seed in the row and 10 cm deep (588 kg/ha); 6) one-time point-applied fertilization (70% RZF) 30% fertilizer reduction 5 cm off seed in the row and 10 cm deep (514.5 kg/ha).

The plot size was 2.4 m × 25 m (4 row zones, 100 plants per row, 400 plants in total), with 3 replications and randomized group arrangement. Field management measures such as pest and weed control and irrigation were consistent among different treatments. The field trial period was from June to September of 2020 and 2021, respectively.

Measurement items and methods

Collection and determination of plant samples

Five plants for each repetition were randomly selected to measure plant height and stalk diameter (diameter of maize stalk base) at the elongation, flared, spanning and grouting stages, respectively; five plants were randomly selected to measure plant leaf area at the cob position (single leaf area = leaf length × leaf width × 0.75) at the flared, spanning and grouting stages, respectively.

Collection and determination of soil samples

Root system determination: Five plants for each repetition were randomly selected at the spanning stage of maize, and the soil was dug out with a 30 cm radius and 30 cm depth, the soil was rinsed off with water, and the roots were dried at 80°C for 12 h and weighed for dry weight.

Determination of root injury flow: 5 plants for each repetition were randomly selected at the flared, spanning and grouting stage, respectively. At 18:00, cut the stalk horizontally with a sharp blade from a height of 10 cm above the ground and keep the incision flat, quickly put on the pre-prepared wound fluid collection bag, and fasten it with a cable tie. The collection belt is an intact transparent sealed bag with dry absorbent cotton inside. Weigh before use (W_1) and make a label, collect for 12 hours (the wound fluid should not exceed the saturated absorption capacity of absorbent cotton), remove the collection bag, and weigh again (W_2) to obtain the root wound flow $W = W_2 - W_1$.

Production and seed counting

After maturity, maize ears were harvested from the whole plot of each treatment, and the number of harvested ears was calculated and the average number of grains per ear was determined. The 1000-grain weight is based on the average 1000-grain weight of the tested varieties in the past three years. The final grain yield is 85% of the product of the number of ears per hectare, the number of grains per ear and the 1000-grain weight.

Calculation of relevant indicators and statistical methods

Agronomy efficiency (AE, kg/kg) = [yield in fertilized area (kg/ha)- yield in the control area (kg/ha)]/ nutrient application (kg/ha)

Partial factor productivity (PFP, kg/kg) = yield (kg/ha) / nutrient application (kg/ha)

SPSS 19.0 software was used for variance analysis, and Duncan's new multiple range method was used to judge the significant difference between treatments ($P<0.05$), and Origin2018 software was used to draw.

RESULTS

Effect of different fertilizer application methods on maize plant height and stalk diameter

It can be seen from Figure 1 that, compared with CK, the one-time mechanized fertilization in the root zone increased the plant height by 26.77%-36.67%. At the elongation stage, the maize plant height of BDP was slightly higher than that of RZF, and the plant height decreased gradually with the decrease of fertilization amount. The plant height of RZF maize was slightly higher than that of BDP by 2.50%-4.03% at the flared, spanning and grouting stages, and the plant height of RZF gradually decreased by 6.66%-15.52% with the decrease of fertilization rate. There was no significant difference in maize plant height between BDP and RZF during the whole growth period, but RZF had higher plant height.

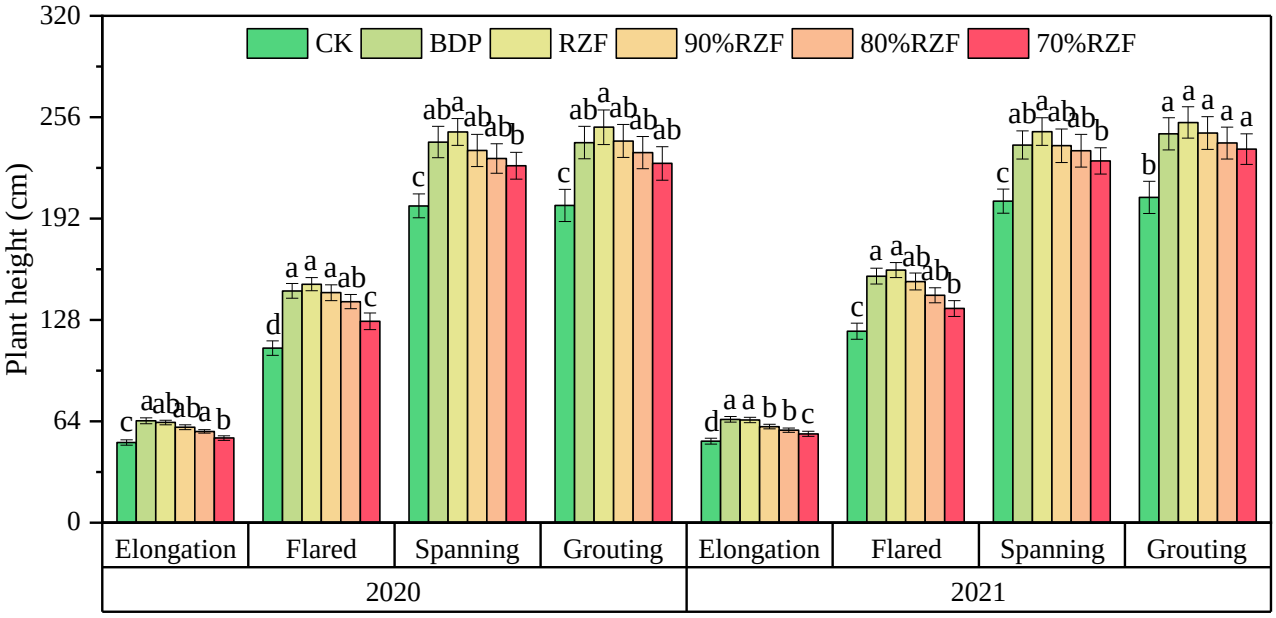


Fig. 1 – Effect of fertilizer application method on maize plant height

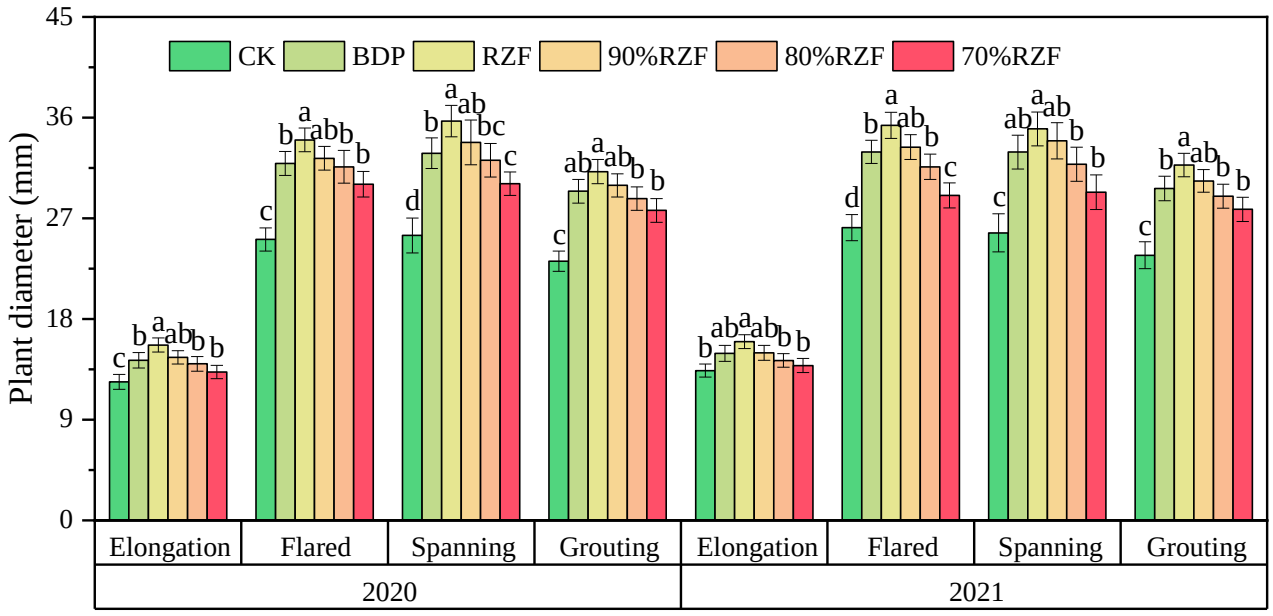


Fig. 2 – Effect of fertilizer application method on maize stalk diameter

As shown in Figure 2, compared with CK, one-time mechanized fertilization in the root zone increased stem diameter by 19.32%-40.17%. The stem diameter of RZF was 5.98%-9.54% larger than that of BDP at the elongation stage, flared stage, spanning stage and grouting stage, and the stem diameter of RZF plants decreased gradually by 11.14%-17.74% with the decrease of fertilization rate. The maize stalk diameter of RZF was significantly larger than that of BDP during the whole growth period.

Effect of different fertilizer application methods on maize leaf area

As can be seen from Figure 3, compared with CK, the one-time mechanized fertilization in the root zone increased the leaf area by 25.58%-32.56%, and the difference was significant. The maize leaf area of RZF was slightly higher than that of BDP by 6.63%-9.96% in the whole growth period, and the difference was significant. The leaf area of RZF plants decreased gradually by 12.10%-16.36% with the decrease of fertilization amount, and the difference was significant. There was no significant difference in maize leaf area between 90% RZF and BDP. RZF had the largest maize leaf area, indicating greater photosynthetic capacity and greater potential for yield increase.

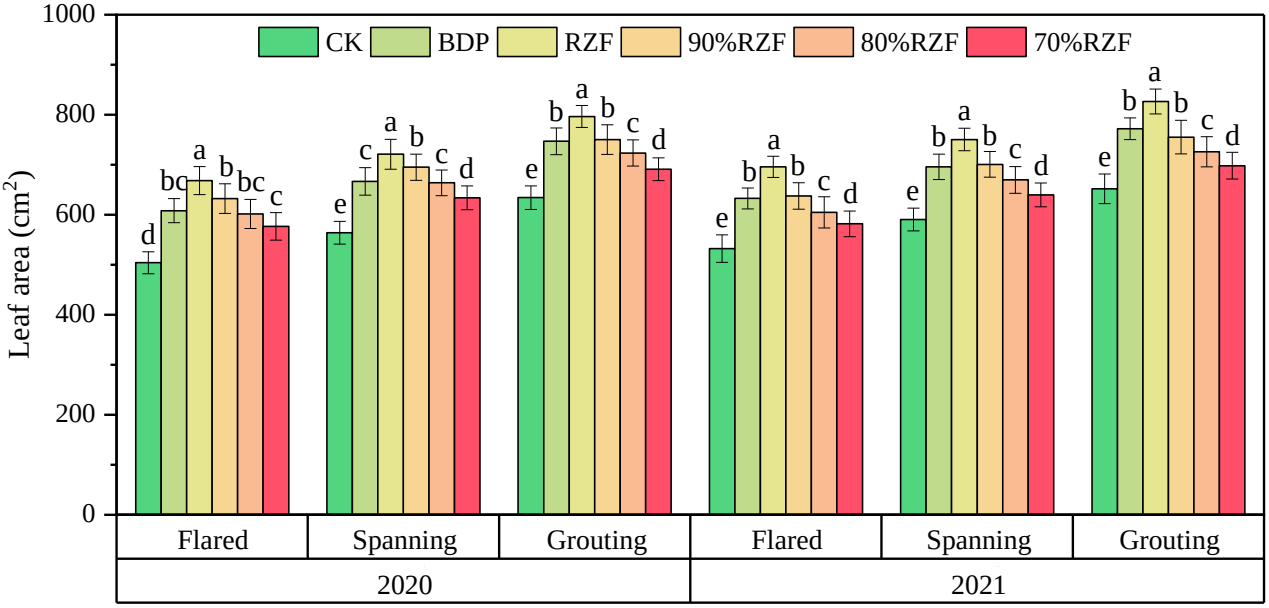


Fig. 3 – Effect of fertilizer application method on maize leaf area

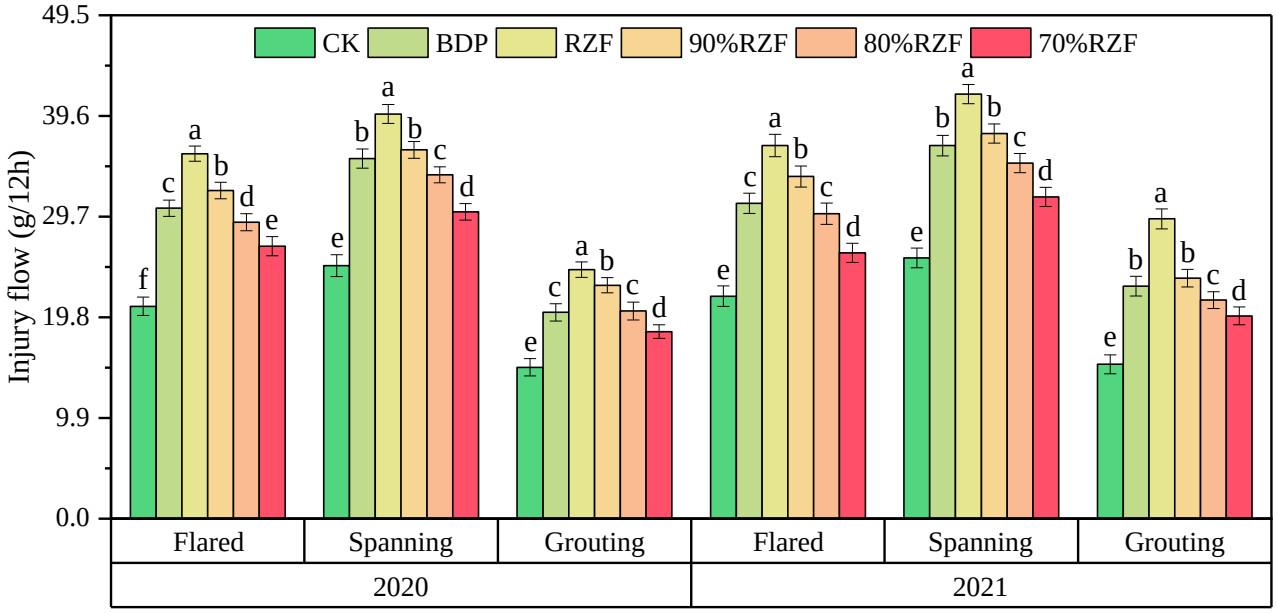


Fig. 4 – Effect of fertilizer application method on maize injury flow

Effect of different fertilizer application methods on maize injury flow

As can be seen from Figure 4, compared with CK, one-time mechanized fertilization in the root zone increased the injury flow by 59.93%-94.21%, and the difference was significant. In the whole growth period, the maize injury flow of RZF was slightly higher than that of BDP by 12.37%-28.92%, and the difference was significant. With the decrease of fertilization rate, the plant injury flow of RZF gradually decreased by 24.18%-32.37%, and the difference was significant. There was no significant difference in maize injury flow between 90% RZF and BDP. RZF had the largest maize injury flow, which indicated that the root system had a stronger ability to absorb water and fertilizer and had a greater potential for increasing yield.

Effect of different fertilizer application methods on maize dry matter mass of root system

As can be seen from Figure 5, compared with CK, one-time mechanized fertilization in the root zone increased root dry matter by 141.94%-144.62%, and the difference was significant. The maize root dry matter of RZF was slightly higher than that of BDP by 10.65%-10.88%, and the difference was significant. The root dry matter of RZF plants decreased gradually by 21.16%-26.73% with the decrease of fertilization amount, and the difference was significant. There was no significant difference in maize root dry matter between 90% RZF and BDP. RZF had the largest root dry matter, indicating that the more developed the root system, the greater the root length and root surface area, the stronger the ability to absorb water and fertilizer, and the greater the potential for increasing yield.

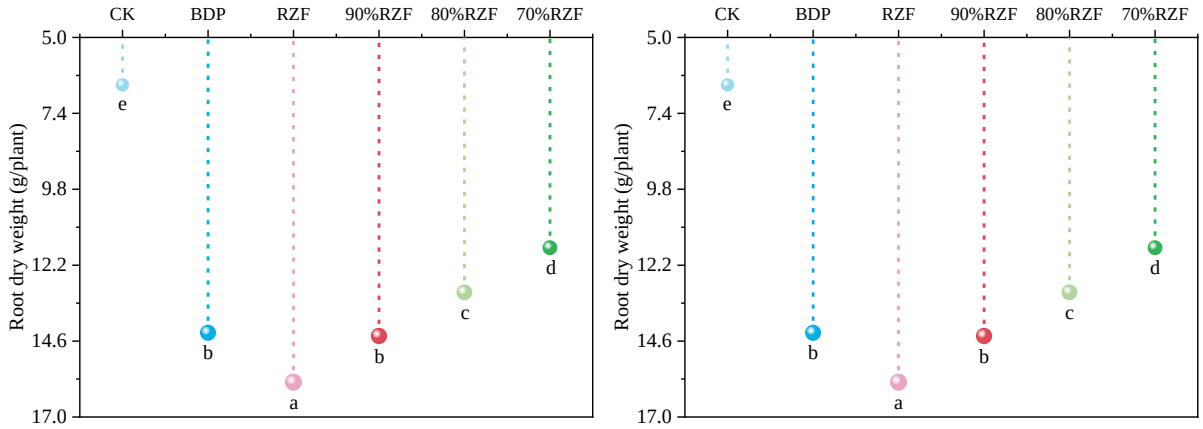


Fig. 5 – Effect of fertilizer application method on maize dry matter mass of root system

Effect of different fertilizer application methods on maize yield and fertilizer utilization

It can be seen from Table 1 that the average 2-year yield of maize under the six treatments was 5700.76 kg/ha~10067.92 kg/ha. The grain yield of BDP and RZF treatments was the highest, and the yield of RZF was 5.83% higher than that of BDP, and the difference was significant. The maize yield of RZF decreased gradually by 15.15% with the decrease of fertilization amount, and the yield difference between treatments was significant when the fertilizer decrease was 10%. The yield difference between BDP and 90% RZF was not significant, indicating that the effect of RZF and BDP on yield was not obvious when losing 10%.

Table 1

Effect of fertilizer application method on maize yield and fertilizer utilization

Treatment	2020			2021		
	Grain yield (kg/ha)	RE (kg/kg)	PFP (kg/kg)	Grain yield (kg/ha)	RE (kg/kg)	PFP (kg/kg)
CK	5424.54 e	-	-	5976.98 e	-	-
BDP	9480.52 b	13.796 b	32.247 e	9545.51 b	14.017 c	32.468 e
RZF	10013.85 a	15.610 a	34.061 d	10121.97 a	15.978 a	34.428 d
90%RZF	9411.58 b	15.068 a	35.569 c	9535.13 b	15.535 ab	36.036 c
80%RZF	8927.27 c	14.893 a	37.956 b	9025.46 c	15.310 ab	38.374 b
70%RZF	8496.95 d	14.929 a	41.287 a	8517.69 d	15.030 b	41.388 a

It can be seen from Table 1 that the 2-year agronomy efficiency of maize under the six treatments was 13.796 kg/kg~15.978 kg/kg. BDP had the lowest agronomy efficiency of 13.796 kg/kg, compared with RZF, 90% RZF, 80% RZF and 70% RZF, the agronomy efficiency increased by 13.57%, 10.33%, 8.59% and 7.72%, respectively, and the differences were significant. There was no significant difference in agronomy efficiency between RZF, 90% RZF, 80% RZF and 70% RZF. Compared with BDP, RZF can effectively improve the agronomy efficiency rate of fertilizers, indicating that root zone fertilization can improve fertilizer efficiency and reduce nutrient loss. It can be seen from Table 1 that the average partial factor productivity of maize in 2 years under the six treatments was 32.357 kg/kg~41.338 kg/kg. The partial factor productivity of BDP was the lowest at 32.357 kg/kg, compared with RZF, 90% RZF, 80% RZF and 70% RZF, the partial factor productivity increased by 5.83%, 10.65%, 17.95% and 27.75%, respectively, and the difference was significant. There were significant differences in partial factor productivity among RZF, 90% RZF, 80% RZF and 70% RZF. Compared with BDP, RZF can effectively improve the partial factor productivity of fertilizer, indicating that root zone fertilization can improve grain yield under the premise of the same fertilization amount.

DISCUSSIONS

Compared with the conventional one-time banding fertilizer application, the one-time mechanized point-applied application of slow-release compound fertilizer in the root zone increased the yield by 5.63% and 6.04% in 2020 and 2021, respectively, indicating that the fertilization method of RZF can increase crop yield. At the same time, there is no significant difference in the yield between 90% RZF and BDP in 2020 and 2021, indicating that RZF cannot reduce the yield compared with BDP when the fertilizer dosage is reduced by 10%, which improves the fertilizer efficiency and utilization rate. Jiang (*Jiang et al.*, 2018) found that RZF increased maize yield by 9.8% compared with BDP, which was higher than the results of this study by 5.63% and 6.04%. Because this paper uses the self-developed maize no-till point-applied fertilization planter, the fertilization position, the spatial distribution of fertilizer particles in the soil, and the accumulation form may change to a certain extent during machine fertilization, resulting in a low degree of yield increase. However, it is also proved from a side view that applying fertilizer to the active growth area of the maize root system and matching the fertilizer nutrients with the nutrient absorption of maize can improve the nutrient utilization rate, increase and stabilize the yield.

Compared with BDP, RZF can increase fertilizer agronomic utilization rate by 12.35% and partial factor productivity by 5.31% while increasing yield. Other scholars also have similar research results. Jiang (*Jiang et al.*, 2018) found that RZF can improve fertilizer agronomic efficiency by 20.96-35.86% and partial factor productivity by 6.44%-8.39% compared with BDP. Zhang (*Zhang et al.*, 2020b) believed that the nitrification of ammonium nitrogen under the condition of point-applied fertilization in the root zone was inhibited by the high concentration of nutrients in the fertilizer field, which delayed the conversion of ammonium nitrogen to nitrate nitrogen and ensured the continuous and efficient supply of nitrogen fertilizer. Zhou (*Zhou et al.*, 2020b) believed that fertilizer point-applied can effectively reduce the contact area between fertilizer particles and soil, resulting in low nutrient release efficiency, prolonging nutrient supply time, and improving nutrient absorption efficiency.

CONCLUSIONS

The one-time mechanized RZF of slow-release compound fertilizer in the root zone increased the yield by 5.84% compared with the one-time BDP, and the difference was significant. The fertilizer agronomic efficiency of RZF was 12.35% and the partial productivity of 5.31% was higher than that of BDP, and the difference was significant. Compared with BDP, RZF has no significant difference in plant height, but there are significant differences in plant stem diameter, leaf area, wound flow and root dry matter mass, indicating that root zone fertilization can promote root growth. It shows that fertilization in the root zone can promote root growth, increase root length and root surface area, resulting in a stronger ability to absorb water and fertilizer, which is further manifested as a significant increase in injury flow, thereby improving the growth and development of shoots, increasing leaf area, and improving photosynthesis intensity, and ultimately achieve fertilizer decrease and increase production.

ACKNOWLEDGEMENT

This work was financially supported by National Key Research and Development Plan of China (2017YFD0700703).

REFERENCES

[1] Anstoetz, M., Rose, T. J., Clark, M. W., et al. (2015). Novel applications for oxalate-phosphate-amine metal-organic-frameworks (OPA-MOFs): can an Iron-based OPA-MOF be used as slow-release fertilizer? *Plos One*, *10*(12).

[2] Cao, Z., De Datta, S. K., Fillery, I. R. P. (1984). Nitrogen-15 balance and residual effects of urea-N in wetland rice fields as affected by deep placement techniques. *Soil Science Society of America Journal*, *48*(1), 203-208.

[3] Chen, X., Luo, X., Wang, Z., et al. (2014). Experiment of synchronous side deep fertilizing technique with rice hill-drop drilling. *Transactions of the Chinese Society of Agricultural Engineering*, (16), 1-7.

[4] Chen, Z., Yuan, F., Yao, Z., et al. (1995). The movement and leaching loss of NO_3-N in profile of Chao soil in Beijing. (北京潮土NO_3-N在土体中的移动特点及其淋失动态) *Journal of Plant Nutrition and Fertilizers,* (02), 73-81.

[5] Du, X., Liu, C., Jiang, M., Yuan, H. (2022). Design and development of fertilizer point-applied device in root-zone. *Applied Engineering in Agriculture*, *38*(3), 559-571.

[6] Guo, Y., Yin, H., Chang, F., et al. (2020). Inter-plant hole application of fertilizer: effect on yield and nutrient absorption of summer maize. (株间穴施对夏玉米产量和养分吸收的影响) *Journal of Agriculture*, *10*(03), 43-48.
[7] Hu, S., Luebberstedt, T., Zhao, G., et al. (2016). QTL mapping of low-temperature germination ability in the maize IBM Syn4 RIL population. *Plos One*, *11*(3).
[8] Jiang, C., Lu, D., Zu, C., Zhou, J., Wang, H. (2018a). Root-zone fertilization improves crop yields and minimizes nitrogen loss in summer maize in China. *Scientific Reports*, *8*(1).
[9] Jiang, C., Lu, D., Zu, C., et al. (2018b). One-time root-zone N fertilization increases maize yiel d, NUE and reduces soil N losses in lime concretion black soil. *Scientific Reports*, *8*. http://doi.o rg/10.1038/s41598-018-28642-0.
[10] Jiang, C., Ren, X., Wang, H., et al. (2019). Optimal Nitrogen Application Rates of One-Time Root Zone Fertilization and the Effect of Reducing Nitrogen Application on Summer Maize. *Sustainability*, *11*(10), 2979.
[11] Jiang, C., Wang, H., Lu, D., et al. (2018). Single fertilization of urea in root zone improving crop yield, nutrient uptake and use efficiency in summer maize. (一次性根区穴施尿素提高夏玉米产量和养分吸收利用效率) *Transactions of the Chinese Society of Agricultural Engineering*, *34*(12), 146-153.
[12] Liu, X., Chen, X., Wang, H., et al. (2017). Effects and principle of root-zone one-time N fertilization on enhancing rice (*Oryza sativa* L.) N use efficiency. *Soils*, *49*(05), 868-875.
[13] Luan, H., Gao, W., Huang, S., et al. (2020). Substitution of manure for chemical fertilizer affects soil microbial community diversity, structure and function in greenhouse vegetable production systems. *Plos One*, *15*(2).
[14] Ma, J., Cao, Y. (2021). Genetic dissection of grain yield of maize and yield-related traits through association mapping and genomic prediction. *Frontiers in Plant Science*, *12*.
[15] Ren, H., Cheng, Y., Li, R., et al. (2020). Integrating density and fertilizer management to optimize the accumulation, remobilization, and distribution of biomass and nutrients in summer maize. *Scientific Reports*, *10*(1).
[16] Savant, N. K., De Datta, S. K. (1980). Movement and distribution of ammonium-N following deep placement of urea in a wetland rice soil. *Soil Science Society of America Journal*, *44*(3), 559-565.
[17] Shan, Y., Lv, M., Zuo, W., et al. (2021). Sewage sludge application enhances soil properties and rice growth in a salt-affected mudflat soil. *Scientific Reports*, *11*(1).
[18] Shi, Y., Zhu, Y., Wang, X., et al. (2020). Progress and development on biological information of crop phenotype research applied to real-time variable-rate fertilization. *Plant Methods*, *16*(1).
[19] Usman, B., Nawaz, G., Zhao, N., et al. (2021). Programmed editing of rice (Oryza sativa L.) OsSPL16 gene using CRISPR/Cas9 improves grain yield by modulating the expression of pyruvate enzymes and cell cycle proteins. *International Journal of Molecular Sciences*, *22*(1).
[20] Wang, H., Zhou, J. (2013). Root-zone fertilization——a key and necessary approach to improve fertilizer use efficiency and reduce non-point source pollution from the cropland. *Soils*, *45*(05), 785-790.
[21] Wei, S., Wang, X., Li, G., et al. (2019). Plant density and nitrogen supply affect the grain-filling parameters of maize kernels located in different ear positions. *Frontiers in Plant Science*, *10*. http://doi.org/10.3389/fpls.2019.00180.
[22] Xu, X., He, P., Pampolino, M. F., et al. (2019). Spatial variation of yield response and fertilizer requirements on regional scale for irrigated rice in China. *Scientific Reports*, *9*.
[23] Ye, Z., Chu, G., Ye, J., et al. (2010). A comparison of mobility and availability of granular and fluid phosphate fertilizers in calcareous soils under laboratory conditions. *Journal of Plant Nutrition and Fertilizers*, *16*(06), 1433-1438.
[24] Zhang, L., Song, H., Chen, X., et al. (2020). Primary study on nutrient migration under hole fertilization in soils. (穴施条件下肥料养分在土壤中迁移规律的初步研究) *Soils*, *52*(06), 1145-1151.
[25] Zhou, C., Li, Y., Chen, P., et al. (2020). Effects of Single Application of Fertilizer on Yield and Nitrogen Utilization of Mulching Summer Maize. *Transactions of the Chinese Society for Agricultural Machinery*, *51*(10), 329-337.
[26] Zhu, Z., Jin, J. (2013). Fertilizer use and food security in China. *Journal of Plant Nutrition and Fertilizers*, *19*(02), 259-273.

DESIGN AND TEST OF POTATO CONVEYING AND GRADING DEVICE WITH VARIABLE SPACE
/
变间距式马铃薯输送分级装置设计与试验

Xin HE[1)], Longfei LI [1)], Xing LIU [1)], Yumeng XIAO [1)], Taowei JIAO[1)], Wei LI*[1)]
[1)] Northwest A&F University College of Mechanical and Electronic Engineering, Shaanxi Yangling 712100, China
Tel: +86-139-0925-8177; E-mail: liweizibo@nwsuaf.edu.cn
DOI: https://doi.org/10.35633/inmateh-69-66

Keywords: *potato, conveying and grading device, variable space, grading accuracy, potato damage rate*

ABSTRACT

This paper proposed a technical idea of joint operation of conveying and grading and developed a potato conveying and grading device with variable space to realize efficient grading in the field because of the difficulties of field grading in the process of potato harvesting in the hilly mountains of northwest China. Based on field measurement of potato size distribution, the clearance between rotating plates of potato conveying and grading device was determined. The key structural parameters of the rotating plate were obtained by referring to the structure and relevant parameters of the conveying and grading device. Moreover, the conveyor chain elevation angle of the conveying and grading device was determined through the dynamics analysis of potatoes on the conveying and grading device. The inclined plane test determined the inclination angle of the potato guide plate. To reduce the damage to potatoes in the process of conveying and grading, damage analysis was carried out. Finally, Field tests were conducted with conveyor chain elevation angle, unit forward speed, and the conveyor chain line speed as test factors, and the grading accuracy and the damage rate of the potato conveying and grading device as test indexes. The test results showed that when the conveyor chain elevation angle, unit forward speed, and conveyor chain line speed were 21.0°, 0.8 m/s, and 1.3 m/s, respectively, the grading accuracy was 91.4% and the rate of potato damage was 0.88%. The operational performance of the prototype was stable, and all the test evaluation indicators could meet the agronomic requirements of the potato harvester.

摘要

针对西北丘陵山区马铃薯收获过程中田间分级困难的问题，提出了输送分级联合作业的技术思路，并研制了一种变间距式马铃薯输送分级装置，以实现田间高效分级。在实地测量马铃薯尺寸分布基础上，确定马铃薯输送分级装置的转动板间隙。参考输送分级装置结构和相关参数，得到转动板关键结构参数。通过对输送分级装置上的马铃薯进行动力学分析，确定输送分级装置输送链的提升角度。通过斜面试验确定了导薯板的倾角。为了减少马铃薯在输送分级过程中的损伤，进行了损伤分析。最后，以输送链提升角度、机组前进速度和输送链线速度为试验因素，以马铃薯输送分级装置的分级准确率和损伤率为试验指标进行田间试验。试验结果表明，当输送链提升角度、机组前进速度和输送链线速度分别为21.0°、0.8m/s和1.3m/s时，分级准确率为91.4%，损伤率为0.88%。样机运行性能稳定，各项试验评价指标均满足马铃薯收获机的农艺要求。

INTRODUCTION

Potato is the world's third most important food crop, with high nutritional value and a wide planting range *(Koga et al., 2013; Zheng et al., 2021)*. China's potato industry has grown rapidly in recent years, with its planted area and production ranking first in the world *(Kang et al., 2014; Yang et al., 2016; Zhou et al., 2015; Luo et al., 2021)*. At this stage, China's potato harvesting mainly uses a two-stage harvesting method, where the dug potatoes are laid on the ground, followed by manual picking, sorting, and conveying*(Kumar and Tripathi, 2017; Wei et al., 2019)*. In this mode, the potato conveying and grading process goes through multiple processes, which can easily cause mechanical damage and spoilage of potatoes. At the same time, the subjectivity and inconsistency of people in the grading process can easily lead to production waste *(Razmjooy et al., 2012; Wei et al., 2018; Yang et al., 2018)*. Therefore, the design of a mechanical potato conveying and grading device is of great significance in improving the quality and efficiency of grading operations.

Lv et al. (2019) developed a roller potato conveying and grading device, and *Wang Xiangyou et al*. developed a paddle roller push-type potato cleaning and sorting machine *(Wang et al., 2017)*. However, it widely suffered from the disadvantages of large size, poor field adaptability, and difficulty adapting to complex plots of land such as hilly and mountainous areas. With the development of spectral detection, spectral imaging, and other technologies, UV cameras, hyperspectral cameras, NMR and X-rays, and other potato sorting techniques came into being*(Zhou et al., 2015; Aleixos et al., 2002; Al-Mallahi et al., 2008; Blasco et al., 2009; Dacal-Nieto et al., 2009; Kong et al., 2012; Rady and Guyer, 2015)*. However, they have not been widely used due to the expense and difficulty of applying directly to field operations. Therefore, a potato conveying and grading device with a low damage rate and high grading accuracy is urgently needed to improve the economic efficiency of potato cultivation.

For this reason, this study proposed the technical idea of "rod group translational conveying, potato soil separation at the front end, rotating plate variable position grading." Designed a variable space potato conveying and grading device. By designing and experimentally verifying the key components of the conveying and grading device and studying the movement mechanism of potatoes on the grading device, efficient and low-loss grading of potatoes in the field can be achieved.

MATERIALS AND METHODS

Whole machine structure and working principle

Whole machine structure

Fig. 1 shows the whole machine structure of the variable space potato conveying and grading device. The whole machine mainly consists of a lifting device, gear shifter, diesel engine, frame, rear walking wheel, transmission device, conveying and grading device, depth limiting wheel, front walking wheel, pick-up shovel, potato toggle device, etc. A diesel engine powers the whole machine. The lifting device can change the height of the conveying and grading device relative to the ground to adapt to different terrain conditions. The pick-up shovel can pick up potatoes on the ground. The potato toggle device can move potatoes into the conveying grading device. The conveying and grading device can realize the conveying and grading of potatoes. The whole machine can complete the operation of potato collection, picking up, potato soil separation, and grading.

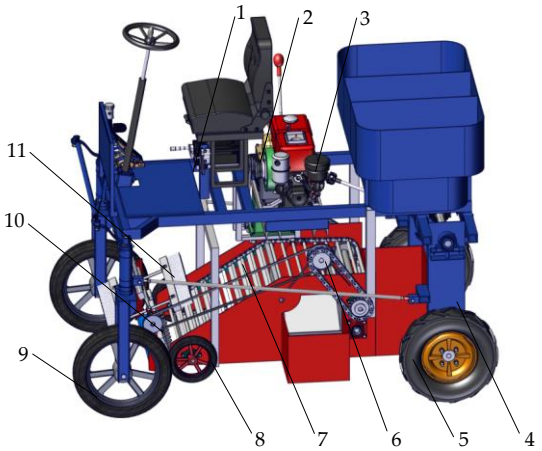


Fig. 1 - Structure diagram of the whole machine

1 – Lifting device; 2– gear shifter; 3 – diesel engine; 4 – frame; 5 – rear walking wheel; 6 – transmission device; 7 – conveying and grading device; 8 – depth limiting wheel; 9 – front walking wheel; 10 – pick-up shovel; 11 – potato toggle device

Working principle and technical parameters

The working principle of the variable space conveying and grading device is shown in Figure 2. In the field operation, while the conveying and grading device moved forward, the conveying chain drived the potatoes backward. The potatoes on the surface of the field and the soil they carry entered the conveying and grading de-vice under the joint action of the pick-up shovel and the potato toggle device and, in the process, completed the preliminary separation of potatoes and soil. Under the action of the conveying and grading device, potatoes were transported backward while the potato soil was further separated, and at its back end, the rotation of the rotating plate made the rotating plate clearance change to complete the potato grading. The device can effectively solve the damage caused by multiple mechanical operations on potatoes in the harvesting process, shorten the time of potato harvesting operations, and thus improve operational efficiency. Its main technical parameters are shown in Table 1.

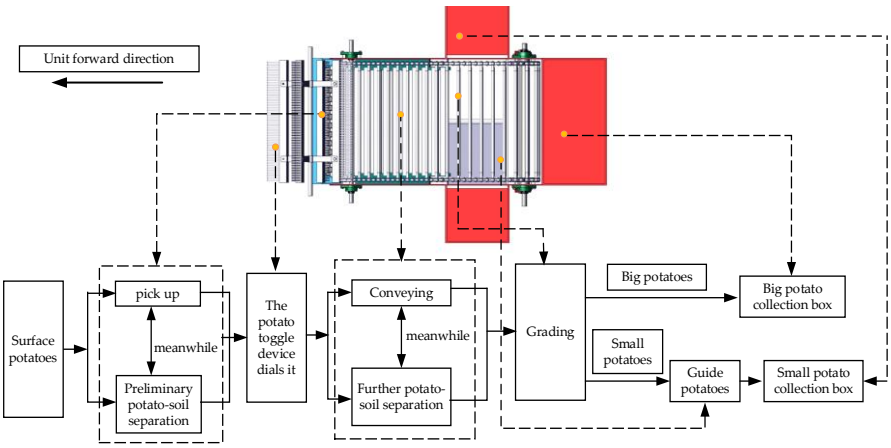


Fig. 2 - Working principle diagram of variable pitch potato conveying and grading device

Table 1

Main technical parameters of variable space potato conveying and grading device

Projects	Title 2
Diesel engine power/kW	23
Whole machine size (length× width× height)/mm× mm× mm	2000× 1300× 1600
Conveying and grading device size(length× width× height)/mm× mm× mm	1500× 800× 600
Number of harvests and rows	Single ridge and double row
Operation width/mm	1100
Travel speed/(m/s)	0.7-1.3
Net working time productivity/(hm^2/h)	0.18-0.32

Design and analysis of conveying and grading device

The structure of conveying and grading device is shown in Fig. 3, which consists of the side plate, conveying chain, rotating plate, fixed guide rail, connecting rod, large potato collection box, small potato collection box, potato guide plate, etc. It adopted the technical idea of "rod group translational conveying, potato soil separation at the front end, rotating plate variable position grading ". Specifically, the connecting rod on the conveying chain was installed with the rotating plate, and the rotating plate can be rotated around the connecting rod. Combined with the fixed guide rail installed at the bottom of the front end of the conveyor chain, the rotating plate at the front end of the conveyor grading device can be supported by the fixed guide rail and be in a flat extension state, and the stage was taken as the lifting stage I. As there was no fixed guide rail at the rear end of the conveying and grading device, the rotating plate lost its supporting role and rotated in a vertical state under the action of its gravity, and the stage was taken as the lifting stage II. So the smaller potatoes fell first and entered the small potato collection boxes on both sides along the guide plate. In comparison, the larger potatoes were transported back to the large potato collection boxes at the rear, thus achieving grading.

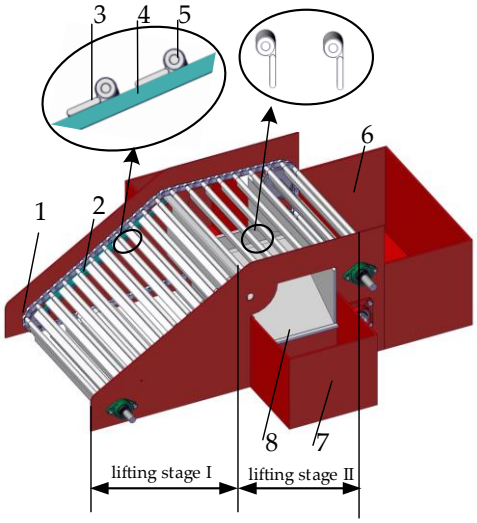


Fig. 3 - The structure of conveying and grading device

1 – side panel; 2– conveyor chain; 3 – rotating plate; 4 – fixed guide rail; 5 – connecting rod; 6 – large potato collection box;7 – small potato collection box; 8 – potato guide plate

Design of rotating plate

Determination of the rotating plate clearance

In the lifting stage I, potatoes were transported backward along the conveyor chain, and the mixed soil fell through the rotating plate clearance. In lifting stage II, when the potato thickness was less than the rotating plate clearance, the potato dropped from the rotating plate clearance, so the rotating plate gap was determined based on the potato size distribution.

Referring to the official Chinese standards for potato grades and specifications (NY/T 1066-2006, 2006) and the actual situation in Guyuan City, Ningxia, China, the potatoes were divided into two grades using 200g mass as the limit. Less than 200g of potatoes for small potatoes can be used as a seed or commercial potatoes, and greater than or equal to 200g for large potatoes can be sold directly as edible potatoes.

After the field measurement of the test object " Qingshu 9 " in Xiji County, Guyuan City, Ningxia, the potatoes were divided into spherical and ellipsoidal to clearly and accurately describe the distribution of potatoes*(Geng et al., 2019)*. According to its morphological characteristics, sphericity S_P was introduced to classify potatoes. When $S_P > 0.85$, potatoes were spherical, and when $S_P \leqslant 0.85$, potatoes were ellipsoida *(Liu et al., 2018)*. The results of potato sample measurements are shown in Table 2.

The sphericity S_P is defined as:

$$S_p = \left(\frac{\frac{\pi}{6} l_s \omega_s t_s}{\frac{\pi}{6} l_s^3}\right)^{\frac{1}{3}} = \left(\frac{\omega_s t_s}{l_s^2}\right)^{\frac{1}{3}} = \frac{(l_s \omega_s t_s)^{\frac{1}{3}}}{l_s} \quad (1)$$

where:

l_s is the length of the potato, [mm];
ω_s is the width of the potato, [mm];
t_s is the thickness of the potato, [mm].

Table 2

Results of potato sample measurements

Type	Thickness range (mm)	Average mass (g)	Average thickness (mm)	Thickness size distribution (mm)	Proportion (%)
Small spherical potato	20~30	16.4	26.9	25.1~28.6	0.5
	30~40	40.5	36.1	31.9~39.8	4.9
	40~50	68.3	44.5	40.0~49.1	1.9
	50~60	116.95	54.55	52.1~59.6	2.2
Small ellipsoidal potato	20~30	30.5	26.9	23.0~29.9	3.3
	30~40	70.0	36.2	30.2~40.0	11.5
	40~50	126.9	44.5	40.1~50.0	32.1
	50~60	160.1	53.2	50.1~59.9	7.6
Big ellipsoidal potato	40~50	221.2	47.9	42.3~49.8	2.3
	50~60	263.7	55.0	50.2~59.9	28.6
	60~70	360.0	62.8	60.6~67.1	5.1

The small potatoes of " Qingshu 9 " had two shapes: spherical and ellipsoidal, of which small spherical potatoes accounted for 9.5%, and the thickness was mainly concentrated in 31.9~39.8mm, with an average thickness of 36.1mm in this range. Small ellipsoidal potatoes accounted for 54.5%, with the thickness mainly concentrated in the range of 40.1~50.0mm, and the average range thickness is 44.5mm. Large ellipsoidal potatoes accounted for 36%, with thickness mainly concentrated in the range of 50.2~59.9mm, and the average range thickness is 55.0mm. To ensure that the potatoes cannot fall from the rotating plate clearance in lifting stage I, the rotating plate clearance was 31mm in lifting stage I. To ensure that as many small potatoes as possible fell into the small potato collection box through the clearance of the rotating plate and large potatoes entered the large potato collection box at the back side in the lifting stage II, to achieve two-stage grading in the lifting stage II successfully. According to Table 2, the value range of the clearance of the rotating plate in the lifting stage II was 44.5~55.0mm, and the clearance of the rotating plate in the lifting stage II was 52.0mm.

Determination of structural parameters of the rotating plate

From Fig. 4(a), it can be seen that the rotating plate is in flat extension under the action of the fixed guide rail in the lifting stage i. The clearance C_l of the rotating plate in this stage is:

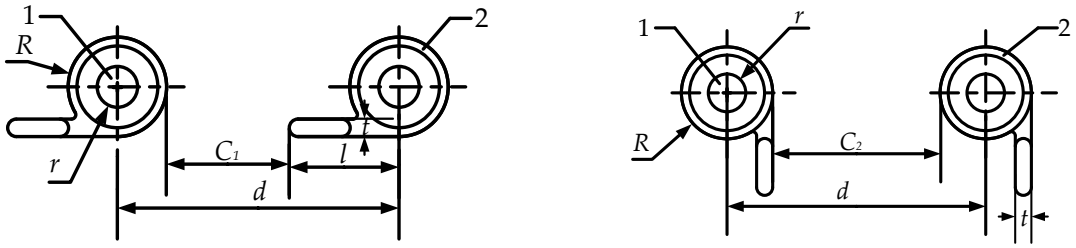
$$C_1 = d - R - l \quad (2)$$

where:

d is the center distance of the connecting rod, [mm];
R is the outer diameter of the rotating plate, [mm];
l is the extended length of the rotating plate, [mm].

From Fig. 4(b), it can be seen that there is no fixed guide rail in the lifting stage II and the rotating plate is in the vertical stage. The clearance of the rotating plate C_2 in this stage is:

$$C_2 = d - 2R \tag{3}$$



(a) rotating plate at lifting stage I (b) rotating plate at lifting stage II

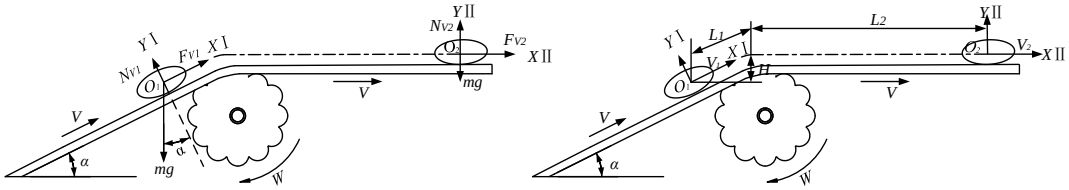
Fig. 4 - Structural Diagram of Rotating Plate

1 – connecting Rods; 2– rotating plate

The outer diameter R, the extended length l, the rotating plate's thickness t, and the connecting rod's center distance d need to satisfy equations (2) and (3). Referring to the structure and relevant parameters of the potato harvester conveying and grading device, the outer diameter of the rotating plate R was 15mm, the inner diameter *r* was 8mm, the extended length l was 36mm, and the thickness *t* was 3mm.

Determination of elevation angle of conveyor chain

The elevation angle of the conveyor chain was an important factor that affected the movement time and state of potatoes and greatly influenced the grading efficiency and accuracy. To determine the conveyor chain elevation angle, the dynamics analysis of potatoes was carried out. The potatoes were subjected to the supporting force of the conveyor chain N_{V1}, N_{V2}, the friction force of the conveyor chain F_{V1}, F_{V2}, and the potatoes' gravity mg. O_1 and O_2 were the cores of potatoes in the lifting stage I and lifting stage II, respectively. In lifting stage I, the conveying direction along the conveyor chain was the XI axis, and the vertical conveyor chain direction was the YI axis. In lifting stage II, the conveying direction along the conveyor chain was the XII axis. The vertical conveyor chain direction was the YII axis. The coordinate system shown in Figure 5 is established.



(a) Potato stress analysis (b) Potato movement analysis

Fig. 5 - The dynamics analysis of potatoes

From Fig. 5(a), it can be seen that the potatoes were subjected to frictional force F_{V1} in the lifting stage I is:

$$F_{V1} = \mu mgsoc\alpha \tag{4}$$

where:

m is the mass of potatoes, [kg];

μ is the coefficient of friction of potatoes in the lifting stage I;

α is the angle between the conveyor chain and the horizontal plane in the lifting stage I, [°].

Assuming that the potato enters conveying and grading device through the pick-up shovel at a speed of V_0, the speed V_1 of the potato at the O_1 position is:

$$V_1 = V_0 + (\mu cos\alpha - sin\alpha)gt_1 \tag{5}$$

where:

t_1 is the time from the potato entering the lifting stage I to moving to point O_1, [s].

It can be seen from Fig. 5 (b) that the friction force F_{V2} of potatoes in the lifting stage II is:

$$F_{V2} = \mu mg \tag{6}$$

Potatoes moved from O_1 to O_2 on the conveyor chain, ignoring the bouncing of potatoes in this process. According to the theorem of conservation of energy, we can get the following:

$$\frac{1}{2}mV_2^2 = \frac{1}{2}mV_1^2 + F_{V1}L_1 + F_{V2}L_2 - mgH \quad (7)$$

where:

V_2 is the speed of the potato at O_2, [m/s];

L_1 is the distance of the potato from O_1 to the end of the lifting stage I, [m];

L_2 is the length of potato movement from the endpoint of the lifting stage I to O_2, [m];

H is the height of the potato from O_1 to O_2, [m].

In Fig. 5(b), the length L_1 is related to the height H as:

$$H = L_1 sin\alpha \quad (8)$$

Combining the above equations yields:

$$V_2 = \sqrt{[V_0 + (\mu cos\alpha - sin\alpha)gt_1]^2 + 2\mu g(cos\alpha L_1 + L_2) - 2gsin\alpha L_1} \quad (9)$$

To sum up, potatoes moved backward, relying on the friction between them and the conveyor chain. It can be seen from Formula (9) that the speed of the potato in the lifting stage II, namely the grading stage, was related to the inclination angle α of the conveyor chain in lifting stage I. Considering the extension relationship between the conveying and grading device and the pick-up shovel and the relevant agronomic requirements of potato harvesting machinery, the value range of the conveyor chain elevation angle in this paper was 13°-23°.

Design of potato guide plate

The role of the potato guide plate was to ensure that potatoes falling from the clearance between the rotating plates of the conveying and grading device could enter the small potato collection boxes on the left and right sides through the potato guide plate. To ensure that potatoes did not accumulate on the potato guide, the sliding friction angle of the potato-steel plate needed to be measured. This measurement test was carried out with a homemade inclinometer composed of a bench, a pulley, a gearbox, an inclined surface, and a steel wire. Since the friction received by the material was related to its material, shape, and quality of the object *(Cui et al., 2013)*, to ensure the reliability of the test data, potatoes with the maximum, intermediate, and minimum S_p and mass values were selected as test objects in the actual potato measurement data in Section 2.1. The test results are shown in Table 3.

Table 3

Potato-plate sliding friction angle test results

No	Length (mm)	Width (mm)	Thickness (mm)	Mass (g)	S_p	Shape	Potato-plate sliding friction angle (°)
1	24.67	32.43	32.93	41.4	1.21	spheroidal	26.2
2	72.92	50.49	39.86	81.7	0.72	ellipsoidal	26.8
3	128.11	56.49	45.73	168.1	0.54	ellipsoidal	27.5
4	155.39	80.1	61.8	482.1	0.59	ellipsoidal	27.3
5	84.69	61.3	49.14	126.4	0.75	ellipsoidal	26.6
6	28.38	28.19	25.13	12.3	0.96	spheroidal	26.2
			average value				26.8

Through many measurements, the sliding friction angle between the potato and steel plate was 26°~28°, the average value was 26.8°, and the maximum value was 27.5°. When the tilt angle of the guide plate was too large, the momentum of the potatoes sliding down was too large, which would increase the collision phenomenon of the potatoes and the potato collection box, thus causing damage to the potatoes. So the tilt angle of the guide plate was 28°.

Analysis of potato damage

To reduce the mechanical damage of potatoes in mechanized harvesting, the damage analysis of potatoes was carried out *(Bao et al., 2021; Bentini et al., 2006; Opara and Pathare, 2014)*. The potato was regarded as a particle, ignoring the influence of air resistance and potato rolling in the potato's process of potato movement. The potato from the end of the lifting stage I moved to lifting stage II for an oblique throwing motion. This transition phase trajectory is shown in Figure 6.

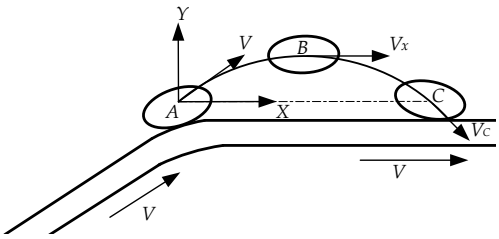


Fig. 6 - Trajectory of potato movement in the transition phase

Taken the center of mass of the potato at the end of lifting stage I as the origin A of the coordinate system, the horizontal to the right was the positive direction of the X axis, and the vertical to the up was the positive direction of the Y axis, established a rectangular coordinate system.

The collision speed V_C between the potato and the rotating plate when the potato is obliquely thrown down to position *C* is:

$$V_C = V \tag{10}$$

where: V is the conveyor chain line speed, [m/s].

When the potato collided with the rotating plate, the collision speed between the potato and the rotating plate was the main factor that caused damage to the potato *(Lv et al., 2020)*. From equation (10), the conveyor chain speed *V* can be reduced to lower the collision speed V_C. Since the linear speed, *V* of the conveyor chain, was less than the forward speed of the unit (the value range is 0.7-1.4 m/s), it was not conducive to the smooth transmission of potatoes on the conveying and grading device *(Lv et al., 2015)*. So the conveyor chain linear speed V should not be too small, and the value range of the linear speed V was 0.7~2.1 m/s.

RESULTS

Field experiment

Experimental conditions

The field experiment was conducted in November 2021 in Yangling District, Xianyang City, Shaanxi Province (34°28′N, 108°07′E). The potatoes were spread out in the field with a length of 10 m and a width of 1 m to simulate the state of the field after excavation work, and the field test is shown in Figure 7.



Fig. 7 - Field experiment

Test parameters and evaluation indexes

According to the results of the transport mechanics analysis of potatoes in the process of conveying and grading, the elevation angle of the conveyor chain, the forward speed of the unit, and the line speed of the conveyor chain were determined as the three primary parameters of the test study. According to the provisions of NY/T 1130-2006 Potato Harvesting Machinery, the essential evaluation indexes in the potato conveying and grading process: grading accuracy Y_1 and potato damage rate Y_2 were taken as the test indexes.

$$Y_1 = \frac{n_1}{N} \times 100\% \tag{11}$$

$$Y_2 = \frac{n_2}{N} \times 100\% \tag{12}$$

where:

N is the total mass of potatoes entering the conveying and grading unit, [kg];

n_1 is the total mass of potatoes correctly graded, [kg];

n_2 is the total mass of potatoes damaged after conveying and grading, [kg].

Experimental protocol and analysis of results

Experimental protocol and results

A quadratic orthogonal rotating combination test method was used to verify the grading performance of the conveying classifier and the potato damage. The forward speed of the unit was 0.7~1.3 m/s, the elevation angle of the conveyor chain was 13°~23°, and the speed of the conveyor chain was 0.7~2.1 m/s were used as the test factors, and the grading accuracy and potato damage rate were used as the test indexes. The test results analyzed the significance of the three test factors, and the parameters were optimized according to the actual needs to obtain the optimal combination of each factor. The coded levels of the test factors are shown in Table 4, and the test scheme and results are shown in Table 5.

Table 4

Code values and levels of factors

Code value x_j	test factors		
	conveyor chain elevation angle x_1 (°)	unit forward speed x_2 (m/s)	conveyor chain speed x_3 (m/s)
-1.682	13	0.7	0.7
-1	15	0.8	1.0
0	18	1	1.4
1	21	1.2	1.8
1.682	23	1.3	2.1

Table 5

Experimental protocol and results

No	test factors			Y_1 (%)	Y_2 (%)
	x_1 (°)	x_2 (m/s)	x_3 (m/s)		
1	15	0.8	1	85.6	2.3
2	21	0.8	1	90.4	0.9
3	15	1.2	1	84.3	3.4
4	21	1.2	1	87.1	1.9
5	15	0.8	1.8	87.3	3.9
6	21	0.8	1.8	91.3	2.6
7	15	1.2	1.8	86.5	4.3
8	21	1.2	1.8	94.2	3.7
9	13	1.0	1.4	83.4	4.3
10	23	1.0	1.4	92.2	2.0
11	18	0.7	1.4	91.1	1.9
12	18	1.3	1.4	88.0	3.5
13	18	1.0	0.7	85.9	1.4
14	18	1.0	2.1	89.5	4.0
15	18	1.0	1.4	91.4	2.3
16	18	1.0	1.4	91.8	2.2
17	18	1.0	1.4	92.7	2.4
18	18	1.0	1.4	89.9	2.3
19	18	1.0	1.4	91.0	2.1
20	18	1.0	1.4	90.2	2.5
21	18	1.0	1.4	91.3	2.5
22	18	1.0	1.4	90.6	2.2
23	18	1.0	1.4	92.1	2.2

Experimental results and analysis

Design-Expert 13.0 software was used to fit multiple regression to the test results in Table 5 to obtain the regression equation of grading accuracy Y_1 and potato damage rate Y_2. And test the significant influence of each test factor on the working performance of the coveying and grading device.

(1) grading accuracy Y_1

By analyzing and fitting the test results, Table 6 provides the ANOVA of grading accuracy. According to the ANOVA results, the model F=19.52, indicating that the model was significant; P<0.0001, showing that the model term was significant. For the test index grading accuracy, the main order of influence of each test factor and the interaction between factors was x_1, x_3, x_3^2; x_1^2, x_2x_3, x_2^2, x_2, x_1x_3, x_1x_2; where x_1, x_3, x_3^2; x_1^2 had a highly significant influence(P<0.01); x_2x_3, x_2^2 had a significant influence (0.01<P<0.05); x_2 had a slightly significant influence(0.05<P<0.1); x_1x_3, x_1x_2 had no significant influence(P>0.1). After removing the insignificant factors x_1x_3 and x_1x_2, the regression equation of each test factor and the interaction between factors on the grading accuracy Y_1 was obtained as follows:

$$Y_1 = 17.97960 + 5.53791x_1 + 10.40392x_2 + 14.02373x_3 + 10.46875x_2x_3 - 0.130711x_1^2 - 13.94211x_2^2 - 7.57349x_3^2 \quad (13)$$

Table 6

ANOVA of grading accuracy

Source	Sum of squares	Degree of freedom	Mean square	F	P
Model	170.84/168.38	9/7	18.98/24.05	19.52/23.88	<0.0001***/<0.0001***
x_1	85.14/85.14	1/1	85.14/85.14	87.54/84.54	<0.0001***/<0.0001***
x_2	4.36/4.36	1/1	4.36/4.36	4.48/4.33	0.0542*/0.0551*
x_3	23.60/23.60	1/1	23.60/23.60	24.27/23.44	0.0003***/0.0002***
x_1x_2	0.3612	1	0.3612	0.3714	0.5527
x_1x_3	2.10	1	2.10	2.16	0.1654
x_2x_3	5.61/5.61	1/1	5.61/5.61	5.77/5.57	0.0320**/0.0322**
x_1^2	21.99/21.99	1/1	21.99/21.83	22.61/21.83	0.0004***/0.0003***
x_2^2	4.94/4.94	1/1	4.94/4.94	5.08/4.91	0.0421**/0.0426**
x_3^2	23.33/23.33	1/1	23.33/23.33	23.99/23.17	0.0003***/0.0002***
residual	12.64/15.11	13/15	0.9726/1.01		
Lack of fit	6.09/8.55	5/7	1.22/1.22	1.49/1.49	0.2941/0.2929
Error	6.56/6.56	8/8	0.8194/0.8194		
Total	183.49/183.49	22/22	18.98/24.05	19.52/23.88	<0.0001***/<0.0001***

Note: / Posterior values represent ANOVA results for Y_2 after excluding non-significant test indicators;
**** extremely significant (P<0.01), ** significant (0.01<P<0.05), * slightly significant (0.05<P<0.1).*

(2) potato damage rate Y_2

By analyzing and fitting the test results, Table 7 provides the ANOVA of the potato damage rate. According to the ANOVA results, the model F=21.57, indicating that the model was significant; P<0.0001, showing that the model term was significant. For the test index potato damage rate, the main order of influence of each test factor and the interaction between factors was x_2, x_3, x_3^2; x_1^2, x_1, x_1x_3, x_2^2, x_2x_3, x_1x_2; where x_2, x_3, x_3^2; x_1^2 had a highly significant influence(P<0.01); x_1, x_1x_3 had a significant influence (0.01<P<0.05); x_2^2 had a slightly significant influence; x_2x_3, x_1x_2 had no significant influence. After removing the insignificant factors x_2x_3 and x_1x_2, the regression equation of each test factor and the interaction between factors on the potato damage rate Y_2 was obtained as follows:

$$Y_2 = 19.73157\text{-}1.55255x_1 - 4.68117x_2 - 2.42073x_3 + 0.104167x_1x_3 + 0.033198x_1^2 + 3.49218x_2^2 + 0.873045x_3^2 \quad (14)$$

Table 7

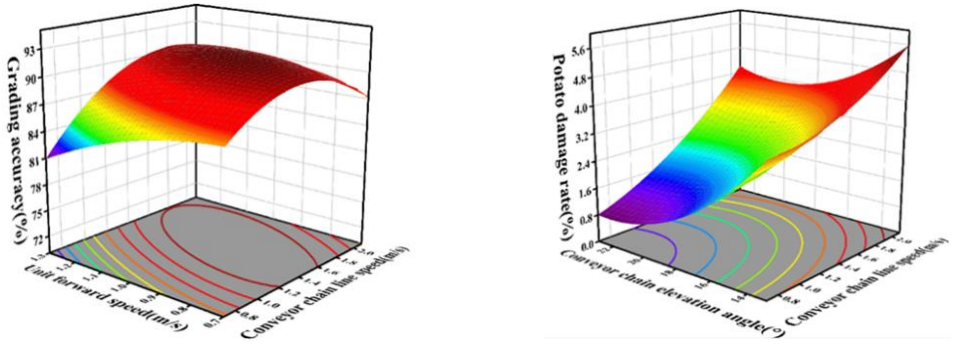
ANOVA of potato damage

Source	Sum of squares	Degree of freedom	Mean square	F	P
Model	18.51/18.42	9/7	2.06/2.63	99.97/110.43	< 0.0001***/< 0.0001***
x_1	5.50/5.50	1/1	5.50/5.50	267.45/230.89	< 0.0001***/< 0.0001***
x_2	2.90/2.90	1/1	2.90/2.90	140.87/121.61	< 0.0001***/< 0.0001***
x_3	7.88/7.88	1/1	7.88/7.88	382.97/330.62	< 0.0001***/< 0.0001***
x_1x_2	0.0450	1	0.0450	2.19	0.1630
x_1x_3	0.1250/0.1250	1/1	0.1250/0.1250	6.08/5.25	0.0284**/0.0369**
x_2x_3	0.0450	1	0.0450	2.19	0.1630
x_1^2	1.42/1.42	1/1	1.42/1.42	68.96/59.53	< 0.0001***/< 0.0001***
x_2^2	0.3100/0.3100	1/1	0.3100/0.3100	15.07/13.01	0.001964***/0.0026***
x_3^2	0.3100/0.3100	1/1	0.3100/0.3100	15.07/13.01	0.0019***/0.0026***
residual	0.2674/0.3574	13/15	0.0206/0.0238		
Lack of fit	0.1074/0.1974	5/7	0.0215/0.0282	1.64/1.41	0.4408/0.3187
Error	0.1600/0.1600	8/8	0.0200/0.0200		
Total	18.78/18.78	22/22			

Note: / Posterior values represent ANOVA results for Y_1 after excluding non-significant test indicators;
**** extremely significant (P<0.01), ** significant (0.01<P<0.05), * slightly significant (0.05<P<0.1).*

Response surface analysis

Design-Expert 13.0 software was used to analyze the experimental results. The response surface with significant interaction of the conveyor chain elevation angle x_1, unit forward speed x_2, and conveyor chain line speed x_3 on the test index grading accuracy Y_1 and potato damage rate Y_2 was obtained, as shown in Figure 8.



(a) x_1=18° (b) x_2=1m/s

Fig. 8 - Response surfaces of grading accuracy and the potato damage rate

When the conveyor chain elevation angle x_1=18°, the response surface between the unit forward speed and the conveyor chain line speed is shown in Figure 8(a). When the conveyor chain line speed was certain, the grading accuracy Y_1 increased gradually as the forward speed of the unit decreased. The reason was that as the unit forward speed increased, the number of potatoes entering the conveying and grading device per unit of time exceeded the maximum grading capacity of the conveying and grading unit, so the grading accuracy decreased. When the forward speed of the unit was fixed, the grading accuracy Y_1 tended to increase and decrease as the conveyor chain speed increased. The reason was that the conveyor chain line speed affected the residence time of potatoes on the conveying and grading device. When the conveyor chain line speed was too low, the potatoes stayed too long, which would cause the potatoes to be blocked. When the conveyor chain line speed was large, the potato residence time was too short, and some potatoes were transported to the large potato collection box without grading.

When the forward speed of the unit x_1=1m/s, the response surface between the conveyor chain line speed and the conveyor chain elevation angle is shown in Figure 8(b). When the conveyor chain elevation angle was certain, the potato damage rate Y_2 showed a gradual increase as the speed of the conveyor chain increased. The reason was that when the conveyor chain line speed was larger, the potato from lifting stage, I was thrown to lifting stage II. The greater the fall speed, the more likely to cause damage to potatoes. When the conveyor chain line speed was certain, the potato damage rate gradually increased as the conveyor chain elevation angle decreased. The reason was that when the conveyor chain elevation angle was small, potatoes were prone to accumulation, increasing the friction between the potatoes and the conveyor chain, while the potatoes stayed on the conveyor chain for a longer time, thus increasing the potato damage. Among them, the effect of conveyor chain line speed on potato damage rate was greater than that of conveyor chain elevation angle.

Parameter optimization

To obtain the best combination of test factors with higher grading accuracy and lower injury rate of potatoes, Design-Expert 13.0 was used for parameter optimization, and the optimization constraints were selected as follows:

$$\begin{cases} \max Y_1(x_1, x_2, x_3) \\ \min Y_2(x_1, x_2, x_3) \\ s.t. \begin{cases} 13° < x_1 < 23° \\ 0.7m/s < x_2 < 1.3m/s \\ 0.7m/s < x_3 < 2.1m/s \end{cases} \end{cases} \quad (14)$$

The optimization result was that the best grading effect was achieved when the conveyor chain elevation angle, unit forward speed, and conveyor chain line speed were 21.0°, 0.8 m/s, 1.3 m/s, the grading accuracy was 91.9%, and the damage rate was 1.4%.

Experimental validation

During the test, each test index of the potato conveying and grading device was adjusted to the optimal parameters. The potatoes' grading accuracy and the potato damage rate were measured several times under the same test conditions as above to obtain the results shown in Table 8.

Table 8

Grading accuracy and damage rate of potatoes at optimal parameters

No.	test factors			Y_1 (%)	Y_2 (%)
	x_1 (°)	x_2 (m/s)	x_3 (m/s)		
1	21.0	0.8	1.3	90.35	1.1
2	21.0	0.8	1.3	90.88	1.34
3	21.0	0.8	1.3	91.28	0.89
4	21.0	0.8	1.3	91.22	0.68
5	21.0	0.8	1.3	92.4	0.83
6	21.0	0.8	1.3	92.1	0.45
average value	21.0	0.8	1.3	91.4	0.88

As can be seen from Table 8, the conveyor chain elevation angle, unit forward speed, and conveyor chain line speed were 21.0°, 0.8 m/s, and 1.3 m/s, respectively. Through six tests, the average grading accuracy and potato damage rate were 91.4% and 0.88%, respectively, which met the agronomic requirements of potato harvesting machinery (grading accuracy ≥ 85%, damage rate ≤ 3%).

CONCLUSIONS

(1) A variable space potato conveying and grading device was designed in this study by measuring the potato size distribution in the field and referring to the structure and relevant parameters of the conveying and grading device. The clearance and structure parameters of the rotating plate were determined, and the conveyor chain elevation angle was determined by dynamics analyzing the potatoes on the conveying and grading unit. The inclined plane test determined the inclination angle of the potato guide plate. The main factors affecting the mechanical damage of potatoes were determined by analyzing the damage of potatoes from the end of lifting stage I to lifting stage II.

(2) Through the field test of the prototype, the regression model of test indexes and test factors was established, and the parameters were optimized. The test results showed that when the conveyor chain elevation angle, unit forward speed, and conveyor chain line speed were 21.0°, 0.8 m/s, and 1.3 m/s, respectively, the grading accuracy was 91.4% and the rate of potato damage was 0.88%. Hence, the grading effect was the best. The operational performance of the prototype was stable, and all the test evaluation indicators could meet the agronomic requirements of the potato harvester. It can effectively solve the problem of damage to potatoes caused by multiple mechanical operations in the harvesting process, shorten the time for handling potatoes after harvesting operations and improve operational efficiency.

ACKNOWLEDGEMENT

This research was funded by the Key Research and Development Program Major (Key) Projects of Ningxia Hui Autonomous Region (2019BFF02003) and the Key Industry Chain Innovation Project of Shaanxi Province (2018ZDCXL-NY-03-06).

REFERENCES

[1] Al-Mallahi, A., Kataoka T., & Okamoto H. (2008). Discrimination between potato tubers and clods by d etecting the significant wavebands, *Biosystems Engineering*, 100(3), 329-337. https://doi.org/10.1016/j.biosystemseng.2008.04.013.

[2] Aleixos, N., Blasco J., Navarron F., & Molto E. (2002). Multispectral inspection of citrus in real-time usi ng machine vision and digital signal processors, *Computers and Electronics in Agriculture*, 33(2), 121-137. https://doi.org/10.1016/s0168-1699(02)00002-9.

[3] Bao, G., Wang G., Wang B., Hu L., Xu X., Shen H., & Ji L. (2021). Study on the drop impact characteri stics and impact damage mechanism of sweet potato tubers during harvest, *Plos One*, 16(8), e025585 6. https://doi.org/10.1371/journal.pone.0255856.

[4] Bentini, M., Caprara C., & Martelli R. (2006). Harvesting damage to potato tubers by analysis of impact s recorded with an instrumented sphere, *Biosystems Engineering*, 94(1), 75-85. https://doi.org/10.1016/j.biosystemseng.2006.02.007.

[5] Blasco, J., Aleixos N., Cubero S., Gomez-Sanchis J., & Molto E. (2009). Automatic sorting of satsuma, (Citrus unshiu) segments using computer vision and morphological features, *Computers and Electroni cs in Agriculture*, 66(1), 1-8. https://doi.org/10.1016/j.compag.2008.11.006.

[6] Cui, T., Liu J., Yang L., Zhang D., Zhang R., & Lan W. (2013). Experiment and simulation of rolling frict ion characteristics of corn seeds based on high speed camera, *Transactions of the Chinese Society of Agricultural Engineering*, 29(15), 8. https://doi.org/10.3969/j.issn.1002-6819.2013.15.005.

[7] Dacal-Nieto, A., Vázquez-Fernández E., Formella A., Martin F., Torres-Guijarro S., & González-Jorge H. (2009). A genetic algorithm approach for feature selection in potatoes classification by computer visi on. In *2009 35th Annual Conference of IEEE Industrial Electronics*, 1955-1960. https://doi.org/10.1109/IECON.2009.5414871.
[8] Geng, J., Wang S., Gao Z., Liu Z., & Rao X. (2019). Influence of initial orientations on potato conveyor trajectories by machine vision, *Computers and Electronics in Agriculture*, 163(38), 104838. https://doi.org/10.1016/j.compag.2019.05.047.
[9] Kang, W. Q., Fan M. S., Ma Z., Shi X. H., & Zheng H. L. (2014). Luxury Absorption of Potassium by Po tato Plants, *American Journal of Potato Research*, 91(5), 573-78. https://doi.org/10.1007/s12230-014-9386-8.
[10] Koga, N., Kajiyama T., Senda K., Iketani S., Tamiya S., & Tsuda S. (2013). Energy efficiency of potato production practices for bioethanol feedstock in northern Japan, *European Journal of Agronomy*, 44, 1-8. https://doi.org/10.1016/j.eja.2012.07.001.
[11] Kong, Y., Gao X., Li H., Zhang M., Yang Z., Mao H., & Yang Q. (2012). Potato grading method of mas s and shapes based on machine vision, *Transactions of the Chinese Society of Agricultural Engineerin g*, 28(17), 143-48. https://doi.org/10.3969/j.issn.1002-6819.2012.17.021.
[12] Kumar, D., & Tripathi A. (2017). Performance evaluation of tractor drawn potato digger cum -elevator, 7(2), 433-48.
[13] Liu, W. Z., He J., Li H. W., Li X., Zheng K., & Wei Z. C. (2018). Calibration of Simulation Parameters fo r Potato Minituber Based on EDEM, *Transactions of the Chinese Society for Agricultural Machinery*, 49 (5), 125-35,42. https://doi.org/10.6041/j.issn.1000-1298.2018.05.014.
[14] Luo, Q., Gao M., Zhang S., & Lun R. (2021). Comparative analysis on potato industry between china a nd other countries, *Chinese Journal of Agricultural Resources and Regional Planning*, 42(7), 1-8. https://doi.org/10.7621/cjarrp.1005-9121.20210701.
[15] Lv, J., Tian Z., Yang Y., Shang Q., & Wu J. E. (2015). Design and experimental analysis of 4U2A type double-row potato digger, *Transactions of the Chinese Society of Agricultural Engineering*(6), 17-24. https://doi.org/10.3969/j.issn.1002-6819.2015.06.003.
[16] Lv, J., Yang X., LV Y., Li Z., Li J., & Du C. (2020). Analysis and Experiment of Potato Damage in Proce ss of Lifting and Separating Potato Excavator, *Transactions of the Chinese Society for Agricultural Mac hinery*, 51(1), 103-13. https://doi.org/10.6041/j.issn.1000-1298.2020.01.011.
[17] Lv, J., Yu J., Feng X., Li Z., Li J., & Liu Z. (2019). Design and Experiment of Roller Potato Grading Machine, *Transactions of the Chinese Society for Agricultural Machinery*, 50(2), 323-32. https://doi.org/10.6041/j.issn.1000-1298.2019.02.037.
[18] Opara, U. L., & Pathare P. B. (2014). Bruise damage measurement and analysis of fresh horticultural p roduce-A review, *Postharvest Biology and Technology*, 91, 9-24. https://doi.org/10.1016/j.postharvbio.2013.12.009.
[19] Rady, A.M., & Guyer D.E. (2015). Rapid and/or nondestructive quality evaluation methods for potatoes *Computers and Electronics in Agriculture*, 117, 31-48. https://doi.org/10.1016/j.compag.2015.07.002.
[20] Razmjooy, N., Mousavi B. S., & Soleymani F. (2012). A real-time mathematical computer method for p otato inspection using machine vision, *Computers & Mathematics with Applications*, 63(1), 268-79. https://doi.org/10.1016/j.camwa.2011.11.019.
[21] Wang, X., Sun J., Xu Y., Li X., & Cheng P. (2017). Design and Experiment of Potato Cleaning and Sort ing Machine, *Transactions of the Chinese Society for Agricultural Machinery*, 48(10), 316-22,279. https://doi.org/10.6041/j.issn.1000-1298.2017.10.040.
[22] Wei, Z., Li H., Sun C., Su G., Liu W., & Li X. (2019). Experiments and analysis of a conveying device f or soil separation and clod-crushing for a potato harvester, *Applied engineering in agriculture*, 35(6), 987-96. https://doi.org/10.13031/aea.13283.
[23] Wei, Z. C., Li H. W., Sun C. Z., Li X., Liu W. Z., Su G., & Wang F. (2018). Improvement of potato harve ster with two segment of vibration and wave separation, *Transactions of the Chinese Society of Agricul tural Engineering*, 34(12), 42-52. https://doi.org/10.11975/j.issn.1002-6819.2018.12.006.
[24] Yang, H., Shang S., Ni Z., Liu Z., & Guo D. (2018). Design and experiment of vertical circular separatin g and conveying device for potato combine harvester, *Nongye Gongcheng Xuebao/Transactions of the Chinese Society of Agricultural Engineering*, 34(3), 10-18. https://doi.org/10.11975/j.issn.1002-6819.2018.03.002.
[25] Yang, R., Yang H., Shang S., Xu P., Cui G., & Liu L. (2016). Design and Test of Poking Roller Shoving Type Potato Harvester, *Transactions of the Chinese Society for Agricultural Machinery*, 47(7), 119-26. https://doi.org/10.6041/j.issn.1000-1298.2016.07.017.
[26] Zheng, Z. Q., Zhao H. B., Liu Z. D., He J., & Liu W. Z. (2021). Research Progress and Development of Mechanized Potato Planters: A Review, *Agriculture-Basel*, 11(6), 521. https://doi.org/10.3390/agriculture11060521.
[27] Zhou, K., Jensen A. L., Bochtis D. D., & Sorensen C. G. (2015). Simulation model for the sequential in -field machinery operations in a potato production system, *Computers and Electronics in Agriculture*, 116, 173-86. https://doi.org/10.1016/j.compag.2015.06.018.

ANALYSIS AND IMPROVEMENT OF SINGLE-PHASE FLOW FIELD INSIDE THE CRUSHING CHAMBER OF MACHINE FOR LENTINUS EDODES STIPE CRUSHING
/
香菇柄成松机成松室内单相流场分析与改进

Yang LI [1,2], Yanjun LI [3], Pei LI [4] [1]

[1] Chinese Academy of Agricultural Mechanization Sciences Group Company Limited, Beijing 100083, China
[2] National Key Laboratory of Agricultural Equipment Technology, Beijing 100083, China
[3] Weifang University, Weifang, Shandong 261061, China
[4] Shandong University of Technology, Zibo, Shandong 255000, China
Tel: +86-18811778308; E-mail: tanfeiyuxie@163.com
DOI: https://doi.org/10.35633/inmateh-69-67A

Keywords: *FLUENT; simulation; machine for lentinus edodes stipe crushing; flow field.*

ABSTRACT

In order to analyze the flow field inside the crushing chamber of machine for lentinus edodes stipe crushing and improve performance of the machine based on the results of the flow field analysis, this paper applied the computational fluid dynamics software FLUENT to numerically simulate the flow field inside the crushing chamber of the machine for lentinus edodes stipe crushing. Thus, the flow field characteristics and flow state inside the crushing chamber were intuitively displayed, and the visualization of the flow field in the crushing chamber was realized. Then, the wind speed value obtained by simulation was compared with the value measured by experiment, and the average relative error between them was less than 10%. Finally, according to the simulation results of flow field, the flow field generated by one air inlet and two air inlets was analyzed, and then the blade structure, outlet area parameters, and rotation speed parameters were compared, simulated and optimized. Results analysis: the pressure distribution and velocity distribution of the flow field inside the crushing chamber were obtained, and the optimal structure and parameters were two inlets, the rotation speed of 2000 r/min and the outlet area of 160×80 mm^2, the crushing chamber with the new blade parameters and structure had greater turbulent kinetic energy and velocity gradient, which was more favorable to the discharge, and provided a basis for further optimization and improvement of the crushing machine.

摘 要

为了对香菇柄成松室进行内部流场分析以及根据流场分析结果对成松室进行改进，本文应用计算流体力学软件 FLUENT 对香菇柄成松机成松室的内部流场进行数值模拟，从而直观显示了成松机腔体内的流场特性和流动状态，实现了成松室流场的可视化。然后对仿真所得的风速值和试验测得的值进行对比，得出二者平均相对误差小于 10%，最后根据流场模拟结果，对一个进风口和两个进风口内流场进行分析，然后对刀片结构，出料口面积参数，转速参数进行对比模拟分析优化。结果分析:得到了成松室内流场的压力分布和内部流场速度分布，并依据仿真结果得到两个进风口，转速为 2000r/min，出料口面积为 160×80 ㎜^{2}，新型刀片的参数与结构下的成松室具有更大的湍动能和速度梯度，更有利于出料，并为成松机的进一步优化改进提供基础。

INTRODUCTION

Lentinus edodes stipe is hard to chew, but it has high nutritional value, so the group has developed the machine for lentinus edodes stipe crushing, whose key component, the striking device, is cleverly designed and consists of 72 blades, 18 discs and 17 sleeves through the spiral mounting structure, which can well realize the striking and conveying of materials. The working principle of the machine for lentinus edodes stipe crushing is that the lentinus edodes stipe is broken up and formed into a crushed shape conforming to the quality evaluation standard through the collision and rubbing effect between the high-speed rotating blades and the materials by using the striking principle, and is discharged from the outlet through the centrifugal fan (*Liu Liangdong, 2016*). So, the machine for lentinus edodes stipe crushing can realize the industrialization and large-scale production, and the effect of lentinus edodes stipe crushing is also good, which has greater economic and social benefits, so the in-depth research on the machine for lentinus edodes stipe crushing also becomes important.

[1] *Yang LI*, Ph.D. Stud. Eng.; Yanjun LI, Ph.D. Stud. Eng.; Pei LI, Ph.D. Stud. Eng.*

As the material inside the crushing chamber is highly susceptible to the influence of the internal airflow, the magnitude of the internal airflow also affects the material discharge and the lentinus edodes stipe crushing effect of the crushing chamber.

In addition to this, the crushing efficiency is largely constrained by the internal circulation layer (*Wang Xiaofeng, 2008*), resulting in low crushing efficiency and high energy consumption of the crushing machine. However, the complex flow field inside the crushing chamber cannot be viewed with the naked eye, so numerical simulation is an effective method to study the complex flow field inside the equipment in depth (*Darelius A. et al, 2008; Barailler F. et al, 2006*). Canadian scholar Dennis Ramo simulated the airflow field distribution inside a traction forage harvester on FLUENT 6.1 (*Lammers, 2005*). Gong Jun from Lanzhou University of Technology performed FLUENT numerical simulation of the flow field inside the pulverizing chamber of a turbulent ultrafine pulverizer with different leaf types, and the simulation results clearly demonstrated the flow field structure inside the pulverizing chamber (*Gong Jun, et al, 2006*). *Peiyu Shen et al* used FLUENT software to simulate the flow field inside the high-speed cutting and crushing chamber of agricultural materials and derived the pressure and velocity distribution of the internal flow field as well as the optimal impeller blade shape and blade deflection angle and impeller speed (*Shen Peiyu et al, 2010)*. Due to the complex internal flow field of the machine for lentinus edodes stipe crushing, it is difficult to obtain it by experimental means or other methods. In this paper, the internal flow field distribution is numerically simulated by using Fluent, a fluid dynamics software, and the distribution state of the internal flow field is obtained by analyzing the flow field in it, and some structural parameters and operation parameters are improved to provide the basis for further optimization of the machine for lentinus edodes stipe crushing.

MATERIALS AND METHODS

The overall design of prototype

- **Prototype introduction**

The machine for lentinus edodes stipe crushing developed by the group was used as the research object, in which the structure of the machine is shown in Figure 1. The crushing machine adopts the principle of forming lentinus edodes stipe floss by striking, after the lentinus edodes stipe is treated by the pre-treatment process, the lentinus edodes stipe is added into the cylinder inside the housing through the feed hopper, and the lentinus edodes stipe is moved to the outlet under the negative pressure generated by the fan and the striking and pushing action of the rotor device, during the moving process, the high-speed rotating blades collide and knead with the lentinus edodes stipe repeatedly, so as to break the lentinus edodes stipe into a fine stipe shape and realize the soft formation of the lentinus edodes stipe. The lentinus edodes stipe is crushed and the crushed lentinus edodes stipe is discharged through the discharge port for post-processing to obtain the required lentinus edodes stipe floss. The generated dust is discharged from the machine through the centrifugal dust collector.

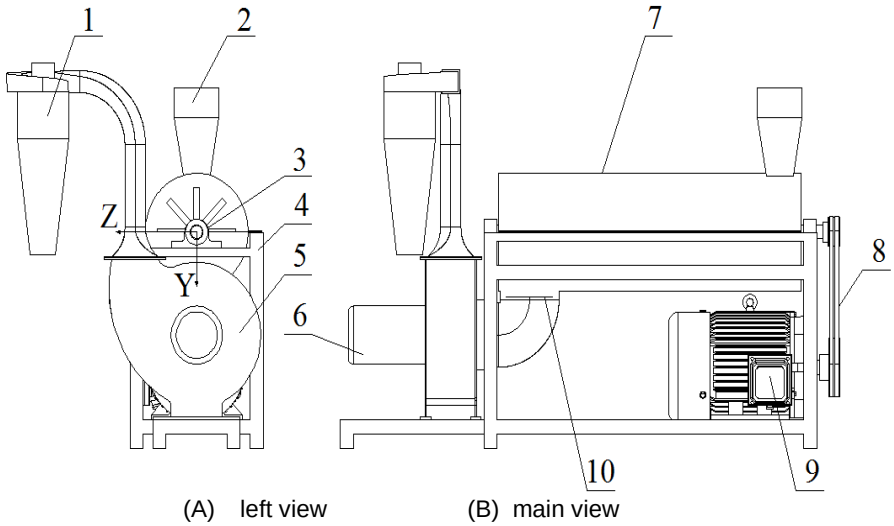


Fig. 1 - Structure of the machine for lentinus edodes stipe crushing
1. Centrifugal dust collector; 2. Feed hopper; 3. Rotor; 4. Frame; 5. Fan; 6. fan motor; 7. Shell; 8. Belt drive; 9. Main motor; 10. Discharge port

Table 1

Parameters of the crushing chamber of the machine for lentinus edodes stipe crushing

Mating power (kW)	3
Rotation Speed (r/min)	2200
Number of blades	72
The distance between the end of the blade and the cylinder (mm)	7
Discharge port area (mm^2)	160×80
Sleeve length (mm)	50
Blade thickness (mm)	5
Tool Type	Straight Blade

Theoretical calculation method

- **Mathematical model**

The comparison between the Reynolds number and the boundary Reynolds number is used to determine whether the flow inside the crushing chamber is turbulent or laminar. The measured velocity at the outlet is 21.14 m/s, and the Reynolds number is calculated from Equation (1) (*Huang Yihui, 2011*).

$$\mathrm{Re} = \frac{vd}{V} \tag{1}$$

where: v - velocity; d - inlet hydrodynamic diameter; V - aerodynamic viscosity.

$$d = \frac{2ab}{a+b} \tag{2}$$

where: a, b are the length and width of the rectangle of the exit section.

From the formula (2), it can be derived from the exit of the hydraulic diameter of 106.67mm, and the standard aerodynamic viscosity is 15×10^{-6} m^2/s, so the airflow Reynolds number at the exit is 1.5×10^5, the Reynolds number is greater than 2300, that is, it belongs to turbulent flow.

Secondly, we define the coordinates of the crushing chamber to clarify the X, Y and Z directions of the machine, so as to facilitate the analysis and verification of the velocity-pressure clouds and the velocity of the points on the opposite side.

X - the direction in which the spindle is located.

Y-direction perpendicular to the inlet and outlet, i.e. radial direction.

Z-direction perpendicular to X-axis, Y-axis.

The study is solved numerically using the standard k-e model with the control equations including the mass conservation equation, the momentum conservation equation, the turbulent kinetic energy k equation and the dissipation rate equation, which are expressed as the following general equations (*Wang Juan et al, 2010; Zhai Zhiping et al, 2008*):

$$\frac{\partial(\rho\phi)}{\partial t} + \frac{\partial(\rho u\phi)}{\partial x} + \frac{\partial(\rho v\phi)}{\partial y} + \frac{\partial(\rho w\phi)}{\partial z} = \frac{\partial}{\partial x}\left(\Gamma\frac{\partial\phi}{\partial x}\right) + \frac{\partial}{\partial y}\left(\Gamma\frac{\partial\phi}{\partial y}\right) + \frac{\partial}{\partial z}\left(\Gamma\frac{\partial\phi}{\partial z}\right) + S \tag{3}$$

where:

$\emptyset$ - generalized variable; Γ - diffusion coefficient; S - source term;

u-x velocity in x direction; v-y velocity in Y direction; w-z velocity in Z direction; ρ - density; t - time.

- **Calculation area and mesh generation**

The complexity of the flow channel model is simplified by considering the crushing chamber as a completely closed area and omitting all the small gaps and chamfers (*Cao Liying et al, 2010*). The shaft and blade set as a whole, omitting the connections between each structure, the small gaps between the blades and the cutterhead, between the blades and the shaft and between the sleeve and the shaft do not affect the magnitude of the negative pressure in the flow field, so the shaft and blades set can be built directly as a single body.

Boolean subtraction operations were performed on the whole model to cut out the flow paths to form the rotational and stationary domains (*Zhu Lianhua et al, 2015)*. The fluid medium in the simulation is air with a density of 1.225 kg/m^3, and the air flow space of the crushing chamber is selected as the calculation region, i.e., the air flow enters from the inlet and exits from the outlet of the crushing chamber.

The model created with the 3D software PROE, as shown in Figure 2, is imported into the pre-processing software ICEM CFD of FLUENT for meshing. The whole calculation area is divided into five parts, namely two inlet runners, outlet runners, rotor set runners, and circular housing runners. Due to the spatial complexity of the computational region, the mesh division uses a more adaptable non-structural tetrahedral mesh (*Cao Yuan et al, 2015)*. After the grid division is completed, the quality of the grid is also checked, and the quality of the grid is still checked mainly by the numerical cells of Equisize Skew and Minimum Value, which is the minimum volume of the cell and requires that it must be greater than 1, otherwise it cannot be used (*Qianpu Wang et al, 2001; Robert Johansson et al, 2014; Bo Yuan Lim et al, 2016*). According to the size of the area using different sizes of the grid, the whole crushing chamber is divided into a total of 1965284 cells, the model after the grid division is shown in Figure 3.

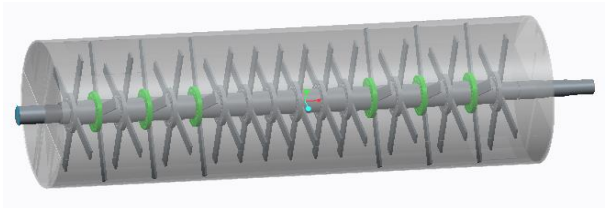


Fig. 2 - Three dimensional geometric solid model of the crushing chamber

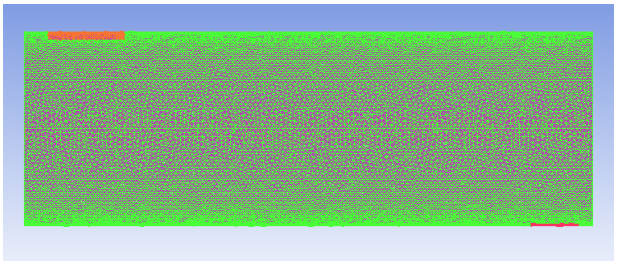


Fig. 3 - Meshing of computational region

- **Multiple coordinate reference systems and boundary conditions**

The FLUENT software provides three models describing the rotational motion of fluids: the multi-reference system model, the slip mesh model, and the dynamic mesh model to deal with the case of relative motion between multiple objects, which are widely used for solving problems of turbine engines, impeller machinery, and mixing apparatus (*Song Yongqi, 2007*).The MRF model is a calculation method based on the steady-state flow field (*Li Weidong et al, 2017*) and is the simplest of the rotation models, which divides the computational domain into a rotating part and a stationary part, and uses the rotating and stationary coordinate systems to perform the calculation separately, without the need for internal and external iterations, thus saving computational time. The MRF model reduces the flow field inside the crushing chamber to a transient flow field of the blades at a given location (*Shang Tan et al, 2014*) .While the sliding grid model and the dynamic grid model are suitable for calculating the unsteady flow field, the calculation time is long (*Pei Yaowu, 2014*), for the simulation and analysis of the relatively simple rotating model, this rotating flow field can be simulated approximately with the MRF model, and the same results can be obtained to match the actual situation. In this paper, multiple reference coordinate systems are used for the calculation, which requires the establishment of interface surfaces between the moving and stationary regions for energy transfer. The rotor group area is established on the kinematic reference system, and the rest of the wall area such as the shell area is established on the fixed coordinate system.

The inlet and outlet of the crushing chamber are the pressure inlet and pressure outlet respectively. The default setting is used for the pressure inlet, and the pressure measured at the pressure outlet is 940Pa.

- **Numerical calculation method**

The calculations are performed using the standard k-e model with no-slip wall boundary conditions, i.e., the relative velocity is zero (*Zong Quanli et al, 2013*). The flow simulation in the near-wall region was performed using standard wall functions and the pressure-velocity coupling was solved using the standard SIMPLE algorithm (*R. Aghaei tog et al, 2008; Guo Yuhang, 2015*).

The convergence was dynamically monitored by checking the residuals during the solution process, with a convergence accuracy of 0.001. The setting of the relaxation factor should also be reasonable, too high for the analysis to converge and too low to maintain accuracy.

RESULTS AND ANALYSIS

Simulation test

The numerical calculation converges at 765 steps and the calculation is completed. For the analysis, the point (0.648, 0.03, -0.03) is used as the coordinates of the center point of the crushing cylinder, and the central section of the Z-axis including the inlet and outlet is selected to analyze the flow field with the flow of air in the inlet and outlet. In addition, to analyze the pressure and velocity distribution in the vicinity of the blade, a cross-section including the blade was selected for analysis, so one of the cross sections with X=0.674 was chosen, which shows the distribution of the flow field into the cylinder after the Boolean operation on the blade and has obvious characteristics of easy analysis. From Fig.4, it can be seen that the entire crushing cylinder is in a negative pressure state, and the absolute value of wind pressure increases from the inlet to the outlet in order. This can ensure that the material in the process of conveying is relatively smooth, but also can make the lentinus edodes stipe floss has met the requirements of the smooth discharge rather than being repeatedly struck into powder.

In addition, it can be seen from Figs.5 and 6 that the airflow velocity at the tip of the blade is maximum, and then gradually decreases until it reaches 0 in the area where it will reach the shell area. This is because the rotation of the blade drives the fluid to rotate together, thus generating centrifugal force, and when the gas flows in the cylinder, the linear velocity of the fluid increases as the radius increases, and the energy gained by the fluid increases.

Fig.7 shows that the negative pressure at the center of the rotor has a pattern, the closer to the center, the greater the negative pressure value. And in the near the cylinder wall due to the high-speed rotation of the blade generated by the centrifugal force, resulting in the near-wall area of the pressure value is relatively small. And from the figure can also be derived from the blade near the tip, the blade back wind side of the negative pressure is larger, while in the blade tip windward side of the negative pressure is smaller, so that the entire blade pressure difference. The back of the knife tip is a suction surface, and the negative pressure inside the entire cylinder is superimposed, resulting in a greater negative pressure on the back. Fig. 8 shows the velocity vector diagram of the whole crushing cylinder, from which the trajectory of the fluid can be seen. With the high-speed rotating motion of the blade, the fluid is in a spiral motion in the crushing cylinder, instead of just rotating, which just reflects the conveying role of this crushing machine and is also in line with the actual situation.

Fig.9 shows the velocity distribution in axial and radial positions at a speed of 2200 r/min obtained by numerical simulation. The graph shows that the velocity of the fluid is smaller at the position close to the spindle, but as the distance from the spindle increases, the velocity of the fluid also starts to increase, except that it starts to increase slowly at about 68 mm from the barrel wall, and then increases more rapidly, while at the tip of the tool, the linear velocity reaches its maximum. In the gap between the end of the blade and the cylinder wall, the velocity of the fluid decreases dramatically because the blade has difficulty in applying the required kinetic energy to the fluid, resulting in a distinct "cliff structure" (*Zhang Hongwei, 2013*). As shown in Figure 9(b), the fluid velocity is small and varies gently in the area between the blades, while it is larger in the area above the blades.

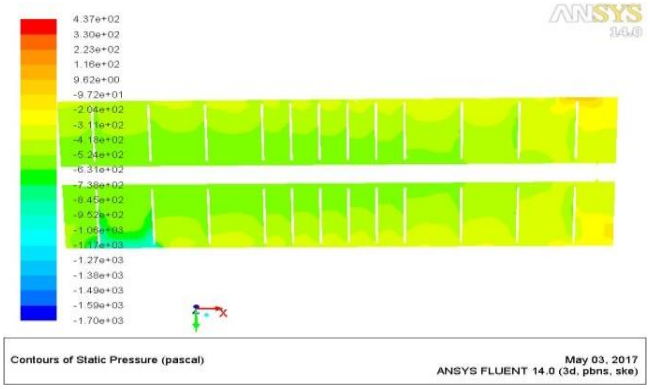


Fig. 4 - Pressure contour plot at plane position Z=-0.03m

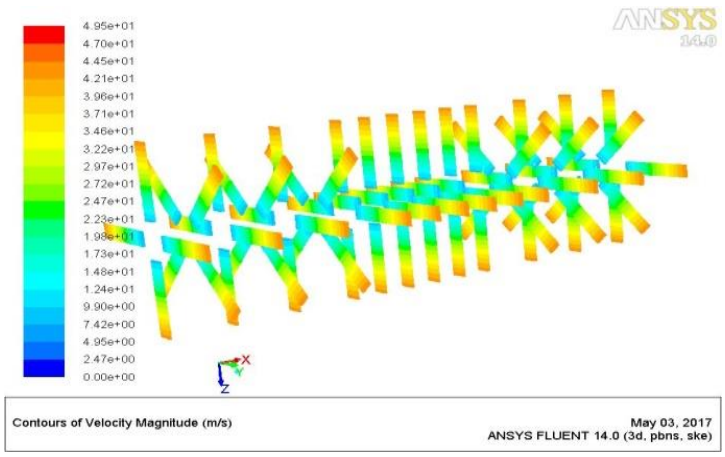


Fig. 5 - Velocity contour for the blade group

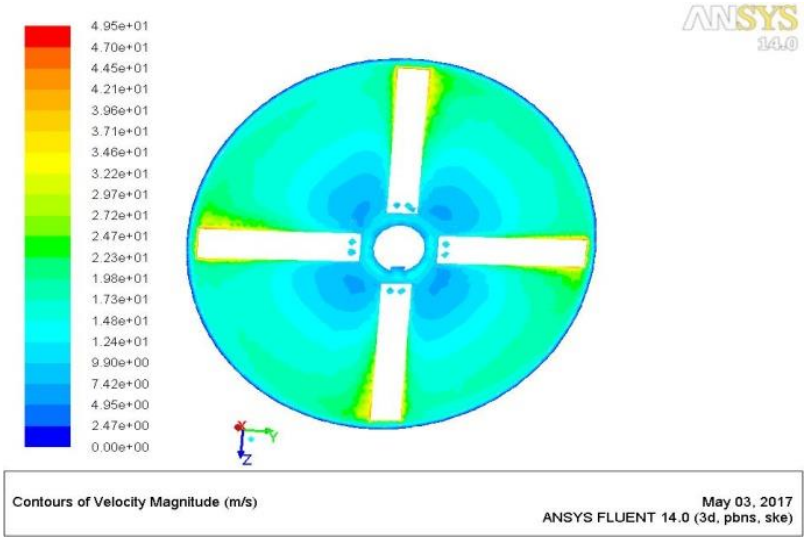


Fig. 6 - Velocity contour plot at plane position X=0.674m

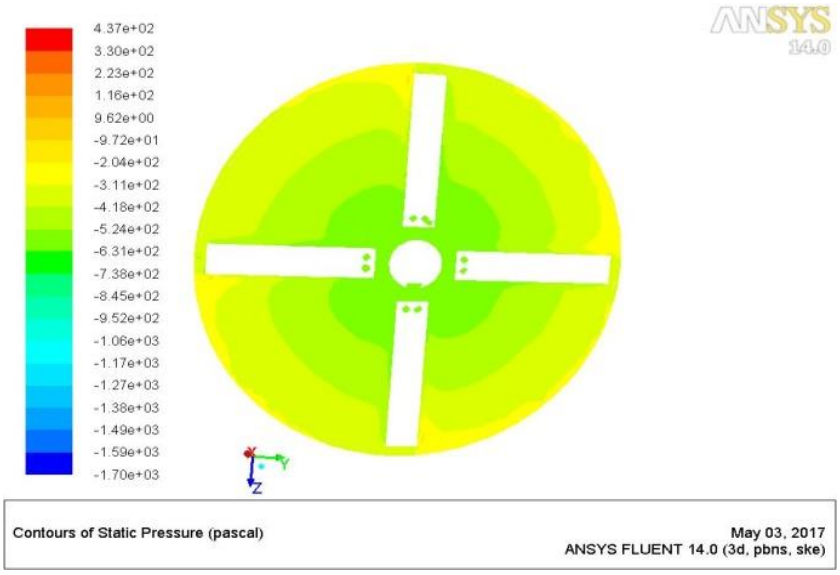


Fig. 7 - Pressure contour plot at plane position X=0.674m

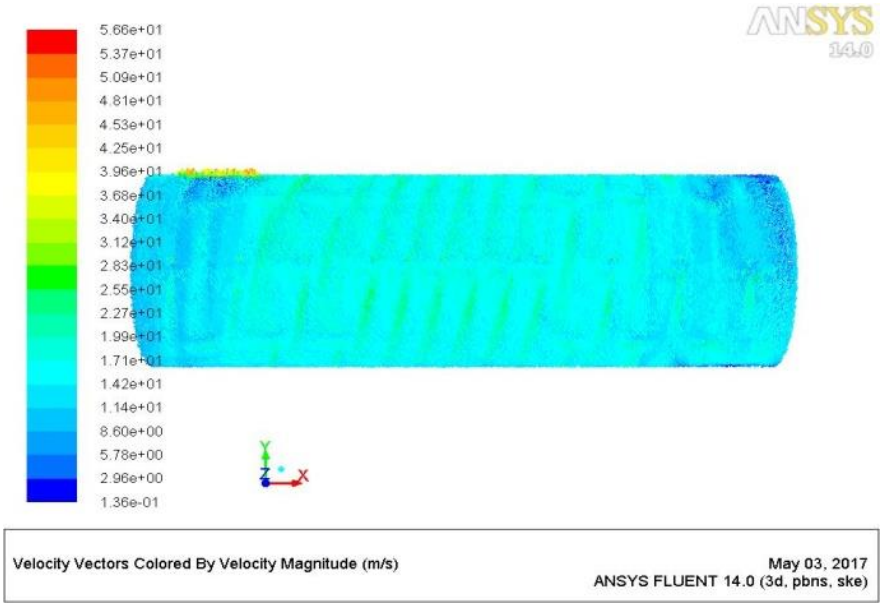
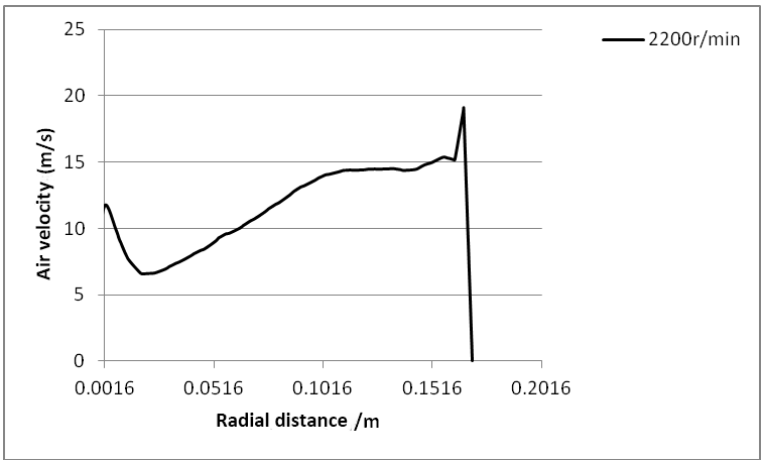
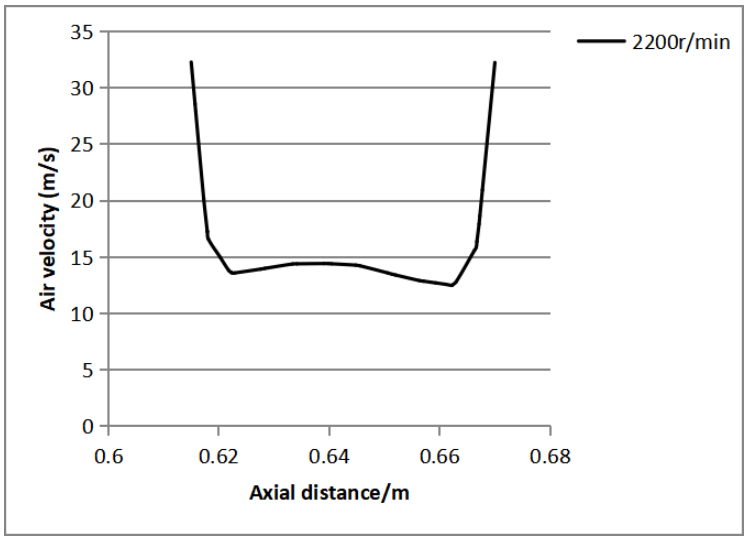


Fig. 8 - Velocity vector for the crushing cylinder



(a) Variation of the velocity inside the crushing chamber from the rotating shaft to the cylinder wall



(b) Variation of fluid velocity along the axial direction between adjacent blades

Fig. 9 - Velocity distribution at a 2200r/min shaft speeds for the crushing chamber

Verification of the correctness of the numerical simulation method

- **Experimental validation**

(1) Test instrument and measurement point arrangement

In order to test the reliability of the simulation, the airflow speed at the measurement point was measured under no-load conditions at 1800r/min, 2000r/min and 2200r/min, respectively, using a KXYL-600B digital pressure-velocity-airflow meter under the simultaneous rotation of the fan motor and the spindle motor.

The measurement points are measured as follows: the Pitot cylinder is fixed on the upper part of the cylinder wall, and the position of the Pitot cylinder inside the cylinder is changed by adjusting the clamps in the up and down direction to measure the fluid velocity at different spatial points. The position is mainly measured by vernier calipers, and the value is taken every 5 mm along the Y direction between the two blades in the middle of the cylinder, as shown in Fig.10.

The coordinates of the measured points should correspond to the coordinates of the numerical simulation to compare the error between the test value and the simulation value. The coordinates of each measurement point are:1:(0.648,-0.11,-0.03)2: (0.648,-0.115,-0.03)3: (0.648,-0.12,-0.03)4: (0.648,-0.125,-0.03)5: (0.648,-0.13,-0.03)6:(0.648,-0.135,-0.03)7:(0.648,-0.14,-0.03)8:(0.648,-0.145,-0.03)9:(0.648,-0.15,-0.03)10:(0.648,-0.155,-0.03)11:(0.648,-0.16,-0.03)12:(0.648,-0.165,-0.03).

Each measurement point was repeated at least three times and the average of the three test results was recorded. The experimental equipment for measuring the airflow velocity in the crushing chamber is shown in Fig.11.

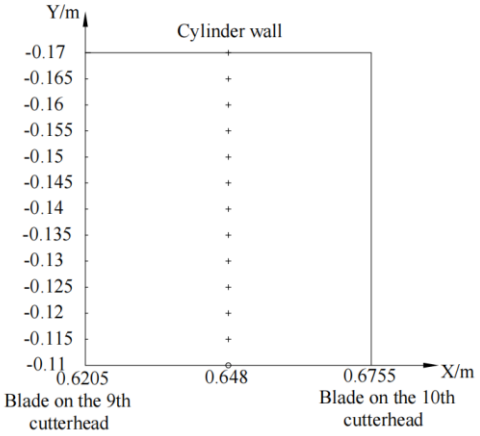


Fig. 10 - The layout of measurement positions for fluent velocities



Fig. 11 - Experimental equipment for measuring fluid velocities of flow field in the crushing chamber

(2) Comparative analysis of test results and simulation results

The test results measured along the radial direction of the crushing chamber were compared with the simulated results, as shown in Fig. 12. From the figure, it can be seen that the trend of the velocity distribution obtained from the simulation is the same as the test value, except that the simulated velocity value is larger, which is because the simulation is carried out under ideal conditions, ignoring factors such as air leakage and friction between the airflow and the blade and wall surface. The exit velocity is measured for

different outlet areas and speeds to further verify the simulation results. To further verify the simulation results, this paper makes further verification for different outlet areas and different speeds, measures the speed at the center of the outlet, and compares the area-weighted average outlet speed obtained from the simulation with the actual measured outlet speed at the center, as shown in Table 2, the average relative error between the simulated speed value and the actual measured speed value is about 10%, which proves that the simulation results are feasible.

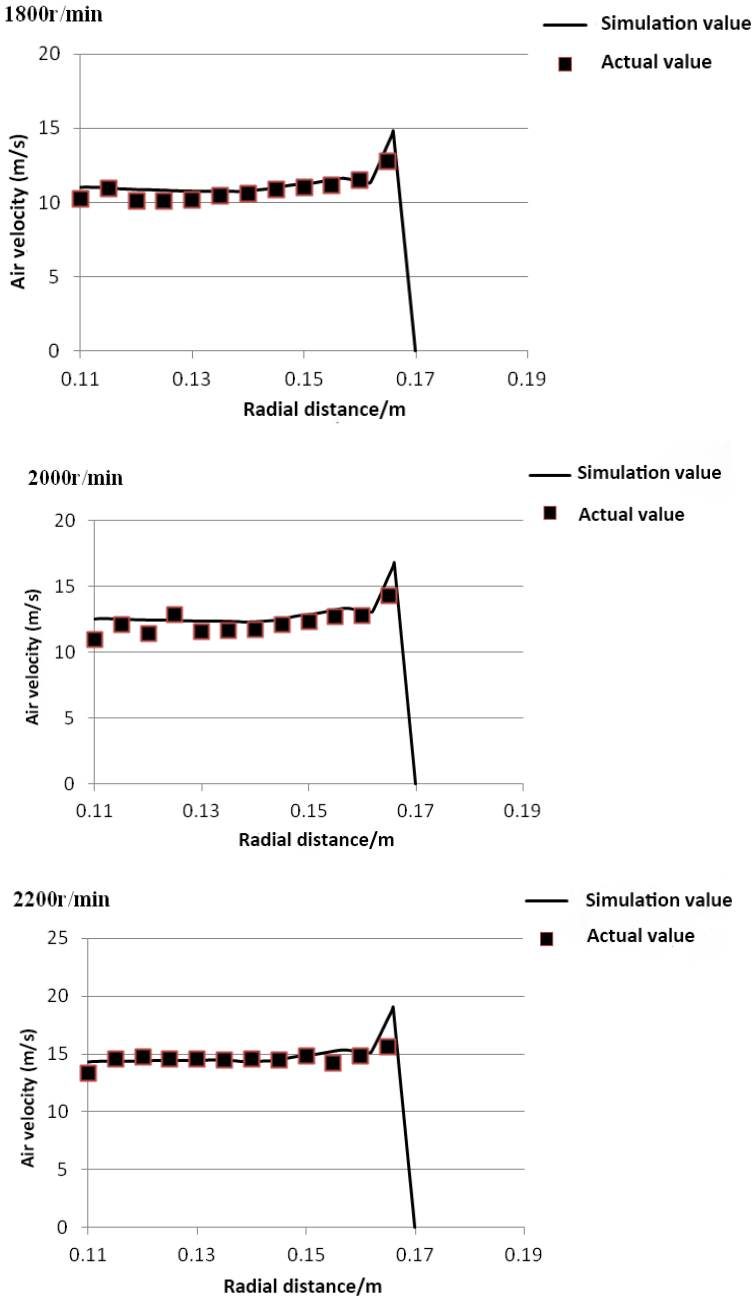


Fig.12. Comparison between measured and simulated results of air velocity measured by Y to each measuring point

Table 2

Comparison of simulation and measured velocity at different speeds and outlets

Rotational Speed(rpm)	Discharge port area(mm²)	Simulation speed value(m/s)	Measured speed value(m/s)	Error
1800	160×50	24.29	22.15	8.8%
	160×80	20.77	18.01	13.3%
	160×160	16.49	15.8	4.2%
2000	160×50	25.92	23.3	10.1%
	160×80	21.91	19.98	8.8%
	160×160	17.5	16.6	5.1%

Table 2

Comparison of simulation and measured velocity at different speeds and outlets

2200	160×50	27.53	25.5	7.4%
	160×80	23.31	21.14	9.3%
	160×160	18.81	17.49	7%

Analysis of the improvement of the crushing chamber

- **Improvement to the structure of the cylinder**

It can also be seen from Fig. 4 above that there is a gradient change in pressure at the inlet, when the wind comes in from the inlet, it moves from the inlet to the outlet, and a small part of the wind is discharged from the upper and lower gap between the first row of blades and the wall of the cylinder to continue forward conveying, most of the wind is hindered by the barrier formed by the high speed rotating blades and forms a vortex at the inlet, so that the lentinus edodes stipe cannot continue to be conveyed to the left end with the airflow, making it strike repeatedly at the inlet and concentrate on the right end of the cylinder. To break this phenomenon, an 80mm air inlet is specially opened on the lower cover cylinder at the right end of the lentinus edodes stipe, causing the negative pressure value at the left end to be larger than that at the right end, thus breaking the wind balance at the inlet, so that the lentinus edodes stipe can be transported from the lower right end to the left end due to the pressure gradient, and the lentinus edodes stipe is processed into stipe floss by repeated action with the striking device during the transport process, and finally enters the fan from the outlet under the action of negative pressure.

Fig.13 is the pressure cloud diagram without the lower end air inlet section, from the diagram it can be seen that because the lower end of the cylinder did not open the air inlet, resulting in the lower end does not have pressure gradient distribution, lentinus edodes stipe when being fed from the inlet, due to the existence of no pressure difference, and cannot be discharged from the upper and lower gap of the first row of blades, but has been circling at the entrance, still forming a vortex, unable to discharge, so the machine, in addition to the inlet, also needs to open an air inlet in the lower cover cylinder auxiliary, to break the wind balance and fast discharge.

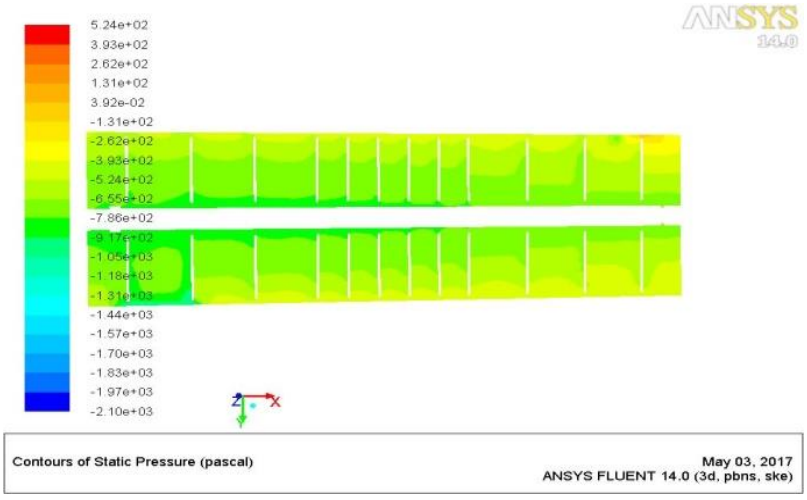


Fig. 13 - Pressure contour plot at plane position Z=-0.03m for no air inlet

- **Improvement of blade structure**

From Fig. 5 and Fig. 6, we can conclude that the airflow speed at the center of the rotor is very small, and the airflow speed in the area swept by the blade is larger. Only one-third of the blades play the role of real striking, and the rest of the blades only play the role of increasing the line speed of the blade tip to improve the quality of the stipe floss, so the structure of the blades can be improved, especially the position of the blades from the tip of one-third. Given the above analysis of the internal flow field of the lentinus edodes stipe into the crushing chamber, the blade structure is now improved by thickening the part of the original straight blade one-third from the tip, increasing 5mm to 8mm, and the improved blade structure is shown in Fig.14.

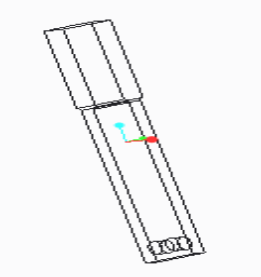


Fig. 14 - Schematic diagram of the improved blade

The turbulent kinetic energy and the transverse velocity gradient and longitudinal velocity gradient were obtained by numerical simulation of the flow fields of these two blades separately without changing other parameters. From Table 3, it can be seen that after the improvement, the turbulent kinetic energy is not only significantly increased, but also the speed gradient is significantly increased, which is more conducive to material conveying and preventing excessive crushing. In addition, the service life of the blades has become longer.

Table 3

Volume average values of turbulent energy for the different blade structure

Blade Structure	Turbulent kinetic energy(m^2/s^2)	Lateral speed gradient(s^{-1})	Longitudinal speed gradient(s^{-1})
Straight Blade	1.665	-90.53	3.2
New blades	2.191	-119.34	2.98

- **Simulation analysis and comparison of flow field for different speed**

Rotational speed is one of the important parameters of machine for lentinus edodes stipe crushing. The higher the speed, the stronger the collision and rubbing between the material and the material, and the greater the centrifugal force on the material, the higher the efficiency, but the higher the energy consumption and the greater the vibration of the machine. Therefore, the smoothness of the discharge as well as the quality of stipe floss formation should be used as a measure to select the appropriate speed under different process conditions.

Keeping the other structural parameters of the model unchanged, the rotational speed of the flow field simulation was changed, and the numerical simulations were performed for the flow fields at 1800 r/min, 2000 r/min, and 2200 r/min, and the volume weighted average value of each energy consumption at different rotational speeds, the velocity gradient values and the maximum negative pressure and maximum velocity values were obtained, as shown in Table 4 and Table 5. Kolmogorov argued that in turbulent flows with large Reynolds number, the energy spectrum of locally isotropic turbulence can be derived by the method of gauge analysis (*Kolmogorovan,1962*).

The only possible form of the dimensionless energy spectrum is Kolmogorov's -5/3 power law (referred to as the -5/3 energy spectrum):

$$E(k) = \alpha \varepsilon^{2/3} k^{-5/3} \quad (4)$$

where:

$E(k)$ is the turbulent energy spectrum, dimensionless; α (also written as Ck) is the Kolmogorov constant; k is the turbulent kinetic energy, m^2/s^2; ε is the turbulent dissipation rate, m^2/s^3.

In terms of velocity gradient, as the speed increases, the value of velocity gradient increases and the shear force between fluids increases. Therefore, based on the energy spectrum and velocity gradient data, the speed of 2000 r/min is selected as a suitable speed value.

Table 4

Volume average values of turbulent energy at different shaft speeds

Rotational Speed (rpm)	V_{max} (m/s)	$-P_{max}$ (Pa)	Turbulent kinetic energy (m^2/s^2)	Turbulent dissipation rate (m^2/s^3)	-5/3 Energy spectrum
1800	42.6	-1329	1.066	343.57	44.10
2000	46	-1506	1.159	415.18	43.52
2200	49.5	-1699	1.274	498.15	41.97

Table 5

Volume average values of velocity gradient at different shaft speeds

Rotational Speed (rpm)	Transverse fluid velocity gradient (s^{-1})	Longitudinal fluid velocity gradient (s^{-1})
1800	-69.63	2.66
2000	-81.34	2.75
2200	-95.4	2.88

- **Simulation analysis and comparison of flow field for different outlet areas**

The size of the outlet area mainly affects the air volume of the suction fan, and the size of this air volume has a great influence on the discharge of lentinus edodes stipe floss and the quality of the stipe floss. If the outlet area is too large, the air volume becomes large, and the material stays in the crushing chamber for a smaller time, which affects the quality of the stipe floss; if the outlet area is too small, the air volume is not enough, which affects the discharge of the material, so that the material that reaches the quality requirement cannot be discharged in time. So, the area of the outlet should have a suitable value.

The simulation model is changed, the outlet area is changed, and the simulation analysis and comparison are carried out for different outlet areas respectively, and the volume-weighted average value of energy consumption parameters and velocity gradient distribution of the three outlet areas are obtained, as shown in Table 6. As shown in Table 6, with the increase of the outlet area, the turbulent kinetic energy of the flow field inside the crushing chamber increases, and the turbulent energy spectrum decreases, i.e., the effective energy utilization decreases, the turbulent dissipation rate increases, the maximum negative pressure increases, and the maximum linear velocity decreases.

However, as far as the outlet flow rate is concerned, the outlet flow rate was 0.191 kg/s, 0.245 kg/s, and 0.31 kg/s with the increase of the outlet area, respectively, in increasing. And in terms of Table 7 velocity gradient, the transverse velocity gradient decreases as the outlet port area increases, which is not conducive to the transport of lentinus edodes stipe floss, so on comprehensive consideration, the outlet port area of 160×80 mm^2 is selected as a suitable outlet port area parameter.

Table 6

Volume average values of turbulent energy for the different discharge area

Area (mm^2)	V_{max} (m/s)	$-P_{max}$ (Pa)	Turbulent kinetic energy (m^2/s^2)	Turbulent dissipation rate (m^2/s^3)	-5/3 Energy spectrum
160×50	52.4	-1414	1.018	395.02	52.26
160×80	49.5	-1699	1.274	498.15	41.97
160×160	47	-2296	1.665	663.52	32.52

Table 7

Volume average values of velocity gradient for the different discharge area

Area (mm^2)	Transverse fluid velocity gradient (s^{-1})	Longitudinal fluid velocity gradient (s^{-1})
160×50	-99.98	2.78
160×80	-95.4	2.88
160×160	-90.53	3.2

CONCLUSIONS

(1) Using FLUENT14.0 software to simulate and analyze the flow field inside the crushing chamber of machine for lentinus edodes stipe crushing, the flow field distribution state and basic characteristics of the internal flow field of the crushing chamber, the main working part of the machine for lentinus edodes stipe crushing, were obtained through the simulation analysis of the flow field inside the crushing chamber, and the visualization of the flow field of the complex crushing chamber was realized.

From various cloud diagrams, it can be seen that the flow field velocity increases with the increase of radius until it reaches the cylinder wall velocity quickly will be 0, and the pressure on the backwind side of the blade is greater than that on the windward side. And a detailed theoretical analysis of the opening of the air inlet at the lower end of the cylinder was carried out, and it was concluded that the opening of the air inlet at the lower end could effectively improve the pressure state inside the crushing chamber, break the wind balance at the inlet, and promote the conveying of materials.

(2) By comparing the experimental values obtained from the actual measurement of the velocity at the discharge port and the velocity between the blades at different rotational speeds and different discharge port areas with the simulated values obtained from the simulation of the flow field in the crushing chamber using FLUENT software, it is concluded that the error between the simulated data values and the actual measured values is within 10%, which indicates that the simulation analysis is feasible.

(3) By analyzing the flow field, the problems of the flow field are derived, and then the pelletizing cylinder is improved. In other words, according to the simulation results obtained from the simulation of the crushing chamber with different speed, blade structure, outlet area and structure, and combined with the evaluation indexes such as turbulent kinetic energy, turbulent energy spectrum, velocity gradient, outlet flow rate and maximum velocity and maximum negative pressure, it is concluded that under the conditions of 2000r/min speed, 160×80 mm^2 outlet area and new blade, the flow field in the crushing chamber The turbulence energy of the new blade is greater and the velocity gradient is higher, which is more conducive to the conveying of materials, and provides a theoretical basis for further optimization of the crushing machine.

ACKNOWLEDGEMENT

This research was developed within the framework of the project “China Machinery Industry Group Co., Ltd. Major science and technology”.

REFERENCES

[1] Aghaei Tog R., Tousi A.M., Tourani A., (2008), Comparison of turbulence methods in CFD analysis of compressible flows in radial turbomachines, *Aircraft Engineering and Aerospace Technology*, *80*(6), 657-665.

[2] Bo Yuan Lim, Rosnah Shamsudin, B.T. Hang Tuah Baharudin, (2016), Performance evaluation and CFD multiphase modeling for Multistage Jatropha Fruit Shelling Machine, I*ndustrial Crops and Products, 85,* 125-138.

[3] Cao Liying, Wu Pei, Ma Yanhua, (2010), Analysis on single-phase flow field of hammer mill based on FLUENT, *Cereal & Feed Industry*, (12), 45-47.

[4] Cao Yuan, Wang Jianxin, Cao Liying, (2015), Optimization anysis of a new feed mill structure based on fluent, *Feed Industry*, *36*(3), 5-8.

[5] Darelius Anders, Rasmuson Anders, Van Wachem Berent, (2008), CFD simulation of the high shear mixing process using kinetic theory of granular flow and frictional stress models, *Chemical Engineering Science*,*63*(8):2188-2197.

[6] Dennis Lammers, (2005). *Determination of the air and crop flow behavior in the blowing unit and spout of a pull -type forage harvester*, Saskatchewan: University of Saskatchewan.

[7] Fabien Barailler, Mourad Heniche, Philippe A, (2006), CFD analysis of a rotor-stator mixer with viscous fluids, *Chemical Engineering Science*, *61*(9):2888-2894.

[8] Gong Jun, Song Yongqi, Guo Runlan, (2006), Numerical simulation of flow on a new model of comminuting mill, *Modern Manufacturing Engineering*, (11), 97-99.

[9] Guo Yuhang, (2015), *Numerical Simulation of Gas Solid Two Phase Flow Vertical Screw Conveyor*, Taiyuan: Taiyuan University of Science & Technology.

[10] Huang Yihui, (2011), *Study on O-SEPA Classifier’s Structure and Its Fluid Field Characteristics*, Wuxi: Jiangnan University.

[11] Kolmogorovan, (1962), A refinement of previous hypotheses concerning the local structure of turbulence in incompressible viscous fluid for very large Reynolds number, *Journal of fluid mechanics*, *13*(1), 82-85.

[12] Li Weidong, Yao Qi, (2017), Optimization analysis for impeller inlet of artificial heart pump with hydraulic suspension based on CFD, *Beijing Biomedical Engineering*,*36*(1):21-28.

[13] Liu Liangdong, (2016), *Design and Experimental Test of a Machine for Processing lentinus edodes stipe into floss*, Wuhan: Hua Zhong Agricultural University.
[14] Min Jin, Chunguang Wang, Pengpeng Wang, (2020), CFD Numerical simulation of temperature and airflow distribution in pigsty based on grid independence verification, *INMATEH Agricultural Engineering, 61*(2), 241-250.
[15] Qianpu Wang, Morten Chr., Melaaen, Sunil R., De Silva, (2001), Investigation and simulation of a cross-flow air classifier, *Powder technology*, *120*(3), 273-280.
[16] Pei Yaowu, (2014), *Simulation and Analyzation on Flow Field in Crashing Cavity of New-type Feed Hammer Mill*, Baotou:Inner Mongolia University of Science&Technology.
[17] Robert Johansson, Magnus Evertsson, (2014), CFD simulation of a centrifugal air classifier used in the aggregate industry, *Minerals Engineering*, *63*, 149-156.
[18] Shang Tan, Guo Guisheng, (2014), *Analysis of Fluid-structure Interaction and Simulation of Internal Flow Field for Cornstalk Rubbing Silk Machine,* Yangling: Northwest A&F University.
[19] Shen Peiyu, Zhao Hao, Zhang Yuzhong, (2010), Numerical simulation of fluid field for high-speed cutting grinding, *Transactions of the Chinese Society for Agricultural Machinery*,*41*(09):60-65.
[20] Song Yongqi, (2007), *Numerical Simulation on Superfine Comminuting Mill with Turbulence*, Lanzhou: Lanzhou University of Technology.
[21] Wang Xiaofeng, (2008), *Study on the Flow Patterns of Comminuting Process in a Superfin*, Wuxi: Jiangnan University.
[22] Wang Juan, Wang Chunguang, Wang Fang, (2010), Numerical simulation on three-dimensional turbulence air flow of 9R-40 rubbing and breaking machine based on Fluent software, *Transactions of the CSAE*, *26*(2), 165-169.
[23] Zhai Zhiping, Wang Chunguang, (2008), Numerical simulation and optimization for air flow in an impeller blower, *Transactions of the Chinese Society for Agricultural Machinery*, (06),84-87.
[24] Zhang Hongwei, (2013), *Numerical Simulation and Experimental Measurement of Single-phase Turbulent Flow in Stirred Media Mill*, Guangzhou: South China University of Technology.
[25] Zhu Lianhua, Song Qiang, Ze Xiangbo, (2013), Numerical simulation of the flow field of household soybean milk machine with the S shape blade, *Special Topics on Structure and Design Appliances,* (9), 60-62.
[26] Zong Quanli, Zheng Tiegang, Liu Huanfang, (2013), Numerical simulation and analysis on whole flow field for drip self-cleaning screen filter, *Transactions of the Chinese Society of Agricultural Engineering, 29*(16), 57-65.

WRITING INSTRUCTIONS

Article Types

Three types of manuscripts may be submitted:

1. **Regular articles:** These should describe new and carefully confirmed findings, and experimental procedures should be given in sufficient detail for others to verify the work. The length of a full paper should be the minimum required to describe and interpret the work clearly (max.10 pages, even number);
2. **Reviews:** Submissions of reviews and perspectives covering topics of current interest are welcome and encouraged (max.12 pages, even number).

Manuscripts should be written in English (American or British usage is accepted, but not a mixture of these) and submitted **electronically** at the following e-mail addresses: ***inmatehjournal@gmail.com***
Please be sure to include your full affiliation and e-mail address (see Sample manuscript)
The authors are responsible for the accuracy of the whole paper and references.
There are allowed 2 papers by each first author.
The text layout should be in single-column format. To avoid unnecessary errors it is strongly advised to use the "spell-check" and "grammar check" functions of your word processor.

Review Process

All manuscripts are reviewed by 2 members of the Scientifically Review Office. Decisions will be made as rapidly as possible and the journal strives to return reviewers' comments to authors in approx.3 weeks.
The editorial board will re-review manuscripts that are accepted pending revision.

NOTE:

Submission of a manuscript implies: that the work described has not been published before (excepting as an abstract or as part of a published lecture or thesis) that it is not under consideration for publication elsewhere.

1. REGULAR ARTICLES

- Manuscripts should be concise, in ***1.15 line spacing***, and should have 2 cm all over margins. The font should be ***Arial 10 pt.*** Ensure that each new paragraph is clearly indicated, using **TAB at 1 cm**.
- Title will be ***Arial 12 pt***. and explicit figures will be ***Arial 9 pt***.
- Text will be written in English.
- Chapters' titles are written by ***Arial 10 pt, Bold, Uppercase*** (e.g. **INTRODUCTION, MATERIALS AND METHODS**), between chapters is left a space for 10 pt. At the beginning of each paragraph, TAB of 1 cm.
- The paper body will be written in ***Arial 10 pt., Justify alignment***.

TITLE ***Arial 12 pt., Uppercase, Bold, Center*** *(in English language)* and ***Bold Italic*** *(in native language)*.
Should be a brief phrase describing the contents of the paper. Avoid long titles; a running title of no more than 100 characters is encouraged (without spaces).

AUTHORS ***ARIAL 9, Bold, Centre alignment***
Under the paper's title, after a space (enter) 9 pt., write ***authors' names*** and ***affiliations (Arial 8 pt.-Regular)***
When the paper has more than one author, their name will be followed by a mark (Arabic numeral) as superscript if their affiliation is different. Less than 6 authors.
Corresponding author's name (next row), ***(Arial 8 pt.)***. Should be added also: phone, fax and e-mail information, for the paper corresponding author (***font: 8 pt., Italic***).

KEYWORDS ***(In English)*** about 4 to 7 words that will provide indexing references should be listed (title: ***Arial 10pt, bold italic,*** text ***Arial 10 pt., italic***).

A list of non-standard *Abbreviations* should be added. In general, non-standard abbreviations should be used only when the full term is very long and used often. Each abbreviation should be spelled out and introduced in parentheses the first time it is used in the text. Standard abbreviations (such as ATP and DNA) need not to be defined.
ABSTRACT ***(in English and Native language, Arial 10 pt.)***, the title *bold*; the text of abstract: *italic*) should be informative and completely self-explanatory, briefly present the topic, state the scope of the experiments, indicate significant data, and point out major findings and conclusions. The Abstract should be max.250 words. Complete sentences, active verbs, and the third person should be used, and the abstract should be written in the past tense. Standard nomenclature should be used and abbreviations should be avoided. No literature should be cited.
INTRODUCTION (***Arial 10 pt.)*** should provide a clear statement of the problem, the relevant literature on the subject, and the proposed approach or solution. It should be understandable to colleagues from a broad range of scientific subjects. We should refer to the current stage of researches performed in the field of the paper to be published, by quoting up-to-date specialty studies, preferably published after 2006, excepting certain referential specialty

books/studies, especially papers issued in magazines/journals/conferences/ISI quoted symposia or in other international data bases, which are well known and available.

MATERIALS AND METHODS (***Arial 10 pt.***) should be complete enough to allow experiments to be reproduced. However, only truly new procedures should be described in detail; previously published procedures should be cited, and important modifications of published procedures should be mentioned briefly. Methods in general use need not be described in detail.

RESULTS (***Arial 10 pt.***) should be clarity presented. The results should be written in the past tense when describing findings in the authors' experiments. Results should be explained, but largely, without referring to the literature. Discussion, speculation and detailed interpretation of data should not be included in the Results, but should be put into the Conclusions section.

CONCLUSIONS (***Arial 10 pt.***) The main conclusions drawn from results should be presented in a short Conclusions section. Do not include citations in this section.

Formulae, symbols and abbreviations: Formulae will be typeset in Italics (preferable with the Equation Editor of Microsoft Office 2003) and should be written or marked as such in the manuscript, unless they require a different styling. They should be referred to in the text as Equation (4) or e.g. (4). The formulae should be numbered on the right side, between brackets ***(Arial 10 pt.)***:

$$P = F \cdot v \quad (1)$$

Terms of the equation and the unit measure should be explained, e.g.

P is the power, [W];
F – force, [N];
v – speed, [m/s]

SI units must be used throughout.

Tables should be self-explanatory without reference to the text. The details of the methods used in the experiments should preferably be described in the legend instead of in the text. The same data should not be presented both in table and graph form or repeated in the text.
Table's title will be typed ***Arial 9 pt, Bold, Centered***
In the table, each row will be written Arial 9 pt, single-spaced throughout, including headings and footnotes.
The table should be numbered on the right side, ***Arial 10 pt.***

Figures ***(Arial 9 pt., Bold, Center)***should be typed in numerical order (Arabic numerals). Graphics should be high resolution (e.g.JPEG).Figure number is followed by what represent the figure or graph e.g.:

Fig.1 – Test stand

Legend: ***Arial 8 pt, Italic, Center,*** e.g.:
1 - plansifter compartments; 2- break rolls; 3 – semolina machines; 4 – reduction rolls; 5 – flour

ACKNOWLEDGMENTS (***Arial 10 pt.***) of people, grants, funds etc should be brief (*if necessarily*).

REFERENCES (***Arial 10 pt.***)
(In alphabetical order, in English and in the original publication language).
Minimum 10 references, last 10 years, minimum 3 references from the last 2 years

It can be used "*References*" tool from the *Word Editor*. **APA Style (American Psychological Association)**
https://apastyle.apa.org/style-grammar-guidelines/references/examples

All references must be provided in English
Authors are fully responsible for the accuracy of the references.

References should be **alphabetically**, with complete details, as follows:

Examples:
Books: https://apastyle.apa.org/style-grammar-guidelines/references/examples/book-references

Jackson, L. M. (2019). *The psychology of prejudice: From attitudes to social action* (2nd ed.). American Psychological Association. https://doi.org/10.1037/0000168-000
Kesharwani, P. (2020). *Nanotechnology based approaches for tuberculosis treatment*. Academic Press.
Sapolsky, R. M. (2017). *Behave: The biology of humans at our best and worst*. Penguin Books.

Torino, G. C., Rivera, D. P., Capodilupo, C. M., Nadal, K. L., & Sue, D. W. (2019). *Microaggression theory: Influence and implications*. John Wiley & Sons. https://doi.org/10.1002/9781119466642

In text:

- ***Parenthetical citations***: (Jackson, 2019; Sapolsky, 2017)
- ***Narrative citations***: Jackson (2019) and Sapolsky (2017)

Journal Article:

https://apastyle.apa.org/style-grammar-guidelines/references/examples/journal-article-references

Grady, J. S., Her, M., Moreno, G., Perez, C., & Yelinek, J. (2019). Emotions in storybooks: A comparison of storybooks that represent ethnic and racial groups in the United States. *Psychology of Popular Media Culture*, *8*(3), 207–217. https://doi.org/10.1037/ppm0000185

In text:

- ***Parenthetical citation***: (Grady et al., 2019)
- ***Narrative citation***: Grady et al. (2019)

Conference or Symposium:

https://apastyle.apa.org/style-grammar-guidelines/references/examples/conference-proceeding-references

Duckworth, A. L., Quirk, A., Gallop, R., Hoyle, R. H., Kelly, D. R., & Matthews, M. D. (2019). Cognitive and noncognitive predictors of success. *Proceedings of the National Academy of Sciences*, *USA*, *116*(47), 23499–23504. https://doi.org/10.1073/pnas.1910510116

In text:

- ***Parenthetical citation***: (Duckworth et al., 2019)
- ***Narrative citation***: Duckworth et al. (2019)

Dissertation / Thesis:

https://apastyle.apa.org/style-grammar-guidelines/references/examples/published-dissertation-references

Zambrano-Vazquez, L. (2016). *The interaction of state and trait worry on response monitoring in those with worry and obsessive-compulsive symptoms* [Doctoral dissertation, University of Arizona]. UA Campus Repository. https://repository.arizona.edu/handle/10150/620615

In text:

- ***Parenthetical citations***: (Kabir, 2016; Miranda, 2019; Zambrano-Vazquez, 2016)
- ***Narrative citations***: Kabir (2016), Miranda (2019), and Zambrano-Vazquez (2016)

https://apastyle.apa.org/style-grammar-guidelines/references/examples/unpublished-dissertation-references

Harris, L. (2014). *Instructional leadership perceptions and practices of elementary school leaders* [Unpublished doctoral dissertation]. University of Virginia.

In text:

- ***Parenthetical citation***: (Harris, 2014)
- ***Narrative citation***: Harris (2014)

Patents: Names and initials of authors, year (between brackets), patent title (Italic), patent number,country:

Grant, P. (1989). *Device for Elementary Analyses*. Patent. No.123456. USA.

Legal regulations and laws, organizations:

https://apastyle.apa.org/style-grammar-guidelines/references/examples/iso-standard-references

International Organization for Standardization. (2018). *Occupational health and safety management systems—Requirements with guidance for use* (ISO Standard No. 45001:2018). https://www.iso.org/standard/63787.html

Occupational Safety and Health Administration. (1970). *Occupational safety and health standards: Occupational health and environmental control: Occupational noise exposure* (OSHA Standard No. 1910.95). United States Department of Labor. https://www.osha.gov/laws-regs/regulations/standardnumber/1910/1910.95

In text:

- ***Parenthetical citations***: (International Organization for Standardization, 2018; Occupational Safety and Health Administration, 1970)
- ***Narrative citations***: International Organization for Standardization (2018) and Occupational Safety and Health Administration (1970)

Web references: The full URL should be given in text as a citation, if no other data are known. If the authors, year, and title of the documents are known and the reference is taken from a website, the URL address has to be mentioned after these data.

Citation in text

Please ensure that every reference cited in the text is also present in the reference list (and vice versa).

Do not cite references in the Abstract and Conclusions !.

Unpublished results, personal communications as well as URL addresses are not recommended in the references list.

Making personal quotations (one, at most) should not be allowed, unless the paper proposed to be published is a sequel of the cited paper. Articles in preparation or articles submitted for publication, unpublished, personal communications etc. should not be included in the references list.

Citations style

Text: All citations in the text may be made directly (or parenthetically) as bellow.

- ***single author:*** the author's name (without initials, unless there is ambiguity) and the year of publication:
  "as previously demonstrated *(Brown, 2010)*".
- ***two authors:*** both authors' names and the year of publication: *(Adam and Brown, 2008; Smith and Hansel, 2006; Stern and Lars, 2009)*
- ***three or more authors:*** first author's name followed by "et al." and the year of publication: "As has recently been shown *(Werner et al., 2005; Kramer et al., 2000)* have recently shown ...."

Citations of groups of references should be listed first alphabetically, then chronologically.

Units, Abbreviations, Acronyms

- Units should be metric, generally SI, and expressed in standard abbreviated form.
- Acronyms may be acceptable, but must be defined at first usage.

2. REVIEWS

Summaries, reviews and perspectives covering topics of current interest in the field, are encouraged and accepted for publication. Reviews do not have the requirements for regular articles. However, should include: (*) an introductory chapter, (**) a careful and critical presentation of the relevant aspects of the topic approached and (***) emphasis of the aspects that aren't known and require further research to progress. Reviews should be concise (max. 12 pages).

Edited by: INMA Bucharest
6, Ion Ionescu de la Brad Blvd., sect. 1, Bucharest, ROMANIA
Tel: +4021.269.32.60; Fax: +4021.269.32.73
https:// inmateh.eu
e-mail: ***inmatehjournal@gmail.com***